CODEN: JASMAN 4966

THE JOURNAL of the Acoustical Society of America

Vol. 103, No. 3 March 1998

SOUNDINGS SECTION

(Continued)

CONTENTS—*Continued from preceding page*

(Continued)

CONTENTS—*Continued from preceding page*

(Continued)

CONTENTS—*Continued from preceding page*

NOTES CONCERNING ARTICLE ABSTRACTS

1. The number following the abstract copyright notice is a Publisher Item Identifier (PII) code that provides a unique and concise identification of each individual published document. This PII number should be included in all document delivery requests for copies of the article.
2. PACS numbers are for subject classification and indexing. See June and December issues for detailed listing of acoustical classes and subclasses.
3. The initials in brackets following the PACS numbers are the initials of the JASA Associate Editor who accepted the paper for publication.

SOUNDINGS

This front section of the *Journal* includes acoustical news, views, reviews, and general tutorial or selected research artcles chosen for wide acoustical interest and written for broad acoustical readership.

ACOUSTICAL NEWS—USA

Elaine Moran
Acoustical Society of America, 500 Sunnyside Boulevard, Woodbury, New York 11797

Editor's Note: *Deadline dates for news items and notices are 2 months prior to publication.*

New Fellows of the Acoustical Society of America

Walter L. Clearwaters—For contributions to submarine sonar development.

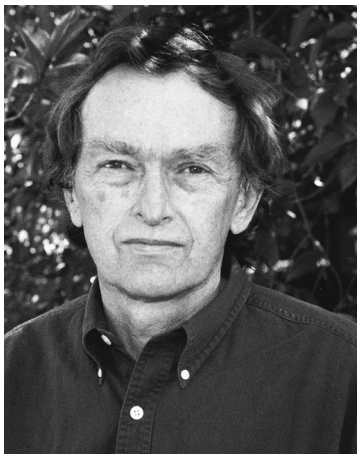

Andrew S. Harris—For contributions to airport noise analysis.

Marjorie R. Leek—For contributions to complex sound perception by the hearing impaired.

Malvin C. Teich to receive IEEE Leeds Award

Malvin C. Teich, professor of electrical & computer engineering, biomedical engineering, and physics at Boston University, has been named the 1997 recipient of the IEEE Morris E. Leeds Award by the Institute of Electrical and Electronics Engineers, Inc. This award recognizes Teich for outstanding contributions to electrical measurement using infrared and nonlinear heterodyne detection. He received the award at the 1997 Lasers and Electro-Optics Society Annual Meeting on 10 Nov. 1997 in San Francisco.

Teich joined the faculty of Boston University in 1995. He is director of the Quantum Optics Laboratory and a member of the Center for Photonics Research. He is also professor emeritus of engineering science and applied physics at Columbia University.

Teich earned a bachelor's degree in physics from MIT, a master's in electrical engineering from Stanford University, and a doctorate from Cornell University. He is the author and co-author of more than 200 technical publications and holds one patent. He is a Fellow of the Acoustical Society of America, the IEEE, the Optical Society of America, the American Physical Society, and the American Association for the Advancement of Science.

Teich's previous awards include the IEEE Browder J. Thompson Memorial Prize, a Guggenheim Fellowship, and the Memorial Gold Medal of Palacký University in the Czech Republic.

INCE announces noise meetings and seminars

The Institute of Noise Control Engineering (INCE) has announced that an 8-page *Invitation to Participate* at NOISE-CON 98 is available. NOISE-CON 98, the 1998 National Conference on Noise Control Engineering, will be held at the Ypsilanti Marriott at Eagle Crest Conference Resort in Ypsilanti, Michigan on 5–8 April 1998. NOISE-CON 98 is being organized in cooperation with the Society of Automotive Engineers; it will open with a reception on Sunday evening, 5 April. The theme of NOISE-CON 98 is *Transporting Noise Control to the 21st Century; Planning for a Quiet Future.* Many papers will be devoted to transportation noise control, but papers in all areas of noise control engineering will be presented.

The *Invitation to Participate* also contains information on the 1998 Sound Quality Symposium, SQS 98, which will be held at the same hotel on 9 April. A joint registration fee for both NOISE-CON 98 and SQS 98 is available.

Two seminars will be held in conjunction with NOISE-CON 98 at the same hotel; both seminars will be held on 3–4 April. Andrew S. Harris, Carl E. Hanson, and Christopher W. Menge of Harris Miller Miller and Hanson will present a seminar titled **Recent Developments in Transportation Noise**. J. Stuart Bolton of Purdue University will present a seminar titled **Noise Control Materials: Properties and Effective Use**.

Printed copies of the two seminar flyers and the *Invitation to Participate* are available from the Institute of Noise Control Engineering, P.O. Box 3206, Arlington Branch, Poughkeepsie, NY 12603. Telephone: (914) 462-4006; Fax: (914) 463-0201; E-mail: INCEUSA@aol.com. Those with access to the Internet will find all of the information by connecting to: http://users.aol.com/noiseconf/invite98.html

Regional Chapter report

Madras, India Chapter: On the joyous occasion of the formation of the Madras Chapter (MIRC) by ASA, Officers of MIRC honored D. Srini-

 0001-4966/98/103(3)/1231/2/$10.00

FIG. 1. Chapter officers present D. Srinivasan with honorary membership in the Madras, India Regional Chapter of ASA (l–r): B. Chakraborty (President), C. P. Vendhan (Treasurer), D. Srinivasan, S. Suresh (Vice President), Hari S. Paul (Secretary).

vasan, first chair of organizational meeting, as an honorary member of the chapter (see Fig. 1). Twenty-four papers including 3 invited papers were presented in the third technical sessions at Goa. Four best student paper awards were given in technical sessions. Six awards were presented to the secondary level students at the Fair out of the 15 projects received by the chapter. More than 40 participants attended the meeting.

Credit goes to B. Chakraborty and C. S. Murty for the successful third technical sessions at Goa, Western part of India. The chapter would like to widen its base to include all of India.

HARI S. PAUL
Secretary

USA Meetings Calendar

Listed below is a summary of meetings related to acoustics to be held in the U.S. in the near future. The month/year notation refers to the issue in which a complete meeting announcement appeared.

1998

5–8 April	NOISE-CON 98, Ypsilanti, MI [Noise Control Foundation, P. O. Box 2469, Arlington Branch, Poughkeepsie, NY 12603, Tel.: 914-462-4006; Fax: 914-463-0201; E-mail: noisecon98@aol.com; WWW: users.aol.com/noisecon98/nc98_cfp.html].
4–7 June	7th Symposium on Cochlear Implants in Children, Iowa City, IA [Center for Conferences and Institutes, The University of Iowa, 249 Iowa Memorial Union, Iowa City, IA 52242-1317, Tel.: 800-551-9029; Fax: 319-335-3533].
20–26 June	135th meeting of the Acoustical Society of America/16th International Congress on Acoustics, Seattle, WA [ASA, 500 Sunnyside Blvd., Woodbury, NY 11797, Tel.: 516-576-2360; Fax: 516-576-2377; E-mail: asa@aip.org, WWW: http://asa.aip.org].
26 Jun–1 July	International Symposium on Musical Acoustics, ISMA 98, Leavenworth, WA [Maurits Hudig, Catgut Acoustical Society, 112 Essex Ave., Montclair, NJ 07042, Fax: 201-744-9197; E-mail: catgutas@msn.com, WWW: www.boystown.org/isma98].
7–12 July	Vienna and the Clarinet, Ohio State Univ., Columbus, OH [Keith Koons, Music Dept., Univ. of Central Florida, P.O. Box 161354, Orlando, FL 32816-1354, Tel.: 407-823-5116; E-mail: kkoons@pegasus.cc.ucf.edu].
9–14 Aug.	International Acoustic Emission Conference, Hawaii [Karyn S. Downs, Lockheed Martin Astronautics, PO Box 179, M.S. DC3005, Denver, CO 80201, Tel.: 303-977-1769; Fax: 303-971-7698; E-mail: karyn.s.downs@lmco.com].
13–17 Sept.	American Academy of Otolaryngology—Head and Neck Surgery, San Francisco, CA [American Academy of Otolaryngology—Head and Neck Surgery, One Prince St., Alexandria, VA 22314, Tel.: 703-836-4444; Fax: 703-683-5100].
12–16 Oct.	136th meeting of the Acoustical Society of America, Norfolk, VA [ASA, 500 Sunnyside Blvd., Woodbury, NY 11797, Tel.: 516-576-2360; Fax: 516-576-2377; E-mail: asa@aip.org, WWW: http://asa.aip.org].

1999

15–19 March	Joint meeting: 137th meeting of the Acoustical Society of America/Forum Acusticum [Acoustical Society of America, 500 Sunnyside Blvd., Woodbury, NY 11797, Tel.: 516-576-2360; Fax: 516-576-2377; E-mail: asa@aip.org; WWW: asa.aip.org].
27–30 June	ASME Mechanics and Materials Conference, Blacksburg, VA [Mrs. Norma Guynn, Dept. of Engineering Science and Mechanics, Virginia Tech, Blacksburg, VA 24061-0219, Fax: 540-231-4574; E-mail: nguynn@vt.edu; WWW: http://www.esm.vt.edu/mmconf/]. Deadline for receipt of abstracts: 15 January 1999.

OBITUARIES

This section of the Journal publishes obituaries concerning the death of Fellows of the Society and other acousticians eminent in the world of acoustics. When notified, the Editor-in-Chief solicits a summary of the person's life and contributions from an ASA member thoroughly familiar with the details, if possible. If a promised obituary is never received, a brief obituary notice may be published later.

William Ranger Farrell • 1926–1997

William Ranger Farrell, a Fellow of the Society, and one of its highly creative members in architectural acoustics, died on 16 February in Mystic, Connecticut. For many years he had struggled valiantly against the debilitating effects of a stroke (partial paralysis and aphasia) that had ended his consulting career at its peak in 1976.

He spent his early years at the Perkins Institute for the Blind in Watertown, Massachusetts, where his father was the Director. After graduating in 1943 from Cambridge's Brown and Nichols School he joined the US Navy Officer Training Program at Brown University. After World War II he entered MIT's School of Architecture, receiving his professional degree in 1951. His career in acoustics began in 1953, when he joined the pioneering acoustical consulting firm of Bolt Beranek and Newman (BBN), after being captivated by the lectures of Professor Robert Newman at the MIT School of Architecture. He often worked with world-famous architects as clients, including Eero Saarinen, Minoru Yamasaki, Philip Johnson, and I. M. Pei. He convinced two of his MIT classmates (Bill Cavanaugh in 1954 and Parker Hirtle later) to join him at BBN. Ranger developed many consulting projects with New York City architects and BBN opened a branch office there. He headed the New York office until 1965, then left to teach at the Parsons School of Design and to form the firm of Ranger Farrell Associates in Tarrytown, New York, where his enthusiasm for acoustical consulting flourished. He continued consulting on internationally prestigious projects, and to produce ideas for acoustical products and devices for creating better acoustical environments. One example was the invention of a flow-resistive sound-absorbing fabric, which now is widely used to reduce noise and reverberation in air-supported structures, especially sports facilities.

Throughout his consulting career Ranger presented and co-authored many technical papers in architectural acoustics. He also taught acoustics courses at architectural schools at Rhode Island School of Design, Yale University, and Cooper Union. Ranger was able to persuade clients to fund acoustical research in areas where adequate criteria and practical solutions to problems were sorely needed. For example, he convinced a major acoustical materials manufacturer that their products needed to solve the common problem of inter-office acoustical privacy. The result was their sponsorship of pioneering speech privacy research at BBN, which produced more accurate speech privacy criteria and unique design tools for solving speech privacy problems in buildings. The work was reported in a paper entitled ''Speech Privacy in Buildings'' [J. Acoust. Soc. Am. **34**, 475–492 (1962)], which Ranger co-authored with colleagues Cavanaugh, Hirtle, and Watters. This landmark paper was subsequently published in the ''Benchmark Papers in Acoustics.''

Ranger had married Helena Fenn in 1946, and she was his constant companion, business partner, and speech therapist after his stroke until her death in 1983. During Helena's illness Ranger faithfully took her to cancer therapy at the Massachusetts General Hospital. Later he found fulfillment as a research volunteer for a long-term MIT/MGH stroke research program at MGH's neuropsychology laboratory. Dr. Hildebrandt and her research staff marveled at his perseverance and contributions to the research program despite his severe speech communication handicap.

Ranger is survived by two daughters, Debra Dolinski of Como, Italy, and Suzi Peck of Sharon, Massachusetts, and four grandchildren. A family memorial service was held in the summer of 1997 in Mystic, Connecticut. Ranger will be missed by his friends and professional colleagues.

WILLIAM J. CAVANAUGH
PARKER W. HIRTLE

Harold Frederick Schuknecht • 1917–1996

Harold Frederick Schuknecht, M.D., a Fellow of the Society, Professor Emeritus of the Department of Otology and Laryngology at Harvard Medical School, and Chief Emeritus of the Department of Otolaryngology at the Massachusetts Eye and Ear Infirmary, died on 19 October 1996. He was a world renowned clinical otologist, otopathologist, teacher, and scholar.

Dr. Schuknecht was born 10 February 1917 in South Dakota. After undergraduate training at the University of South Dakota he graduated from the Rush Medical College in Chicago in 1940. He served a one-year internship at Mercy Hospital in Des Moines where he met his wife, Anne Bodle. Then he served as a flight surgeon with the 15th Air Force in the Mediterranean Theater in World War II. He was awarded the Soldier's Medal for heroism. He then completed his residency training at the University of Chicago Clinics in 1949.

As a faculty member at the University of Chicago School of Medicine his clinical activities were largely confined to head and neck surgery and endoscopy. In 1951 he shared first prize for an exhibit on the surgical management of carcinoma of the paranasal sinuses. His paper on maxillectomy is still a classic. In 1953 he became Associate Surgeon at the Henry Ford Hospital in Detroit where he pursued basic scientific investigations into the pathophysiology of deafness. In 1961 he became Chair of the Department of Otology and Laryngology at Harvard and Chief of Otolaryngology at the Massachusetts Eye and Ear Infirmary. He was among the first surgeons in the United States to perform the modern stapedectomy procedure. The equipment he designed for mastoid tympanoplasty is still in wide clinical use.

Dr. Schuknecht was an accomplished investigator in anatomy, physiology, and pathology of the ear. His research included determination of auditory thresholds in experimental animals and the use of behaviorally conditioned animals in a series of classical experiments, including the study of traumatic hearing loss, and the behavioral effects of partial section of the auditory nerve. The principal focus of his research work at Harvard was the importance of the underlying anatomy of the ear to understanding the pathology of the ear. It can be said that Dr. Schuknecht reestablished the histologic and scientific basis for modern medical and surgical otologic intervention, based on his lifelong study and documentation of human temporal bones. His contributions to this area are many, but of particular interest were studies of otosclerosis, Meniere's disease and other vestibular disorders, and presbycusis. The second edition of his magnum opus, *Pathology of the Ear*, was completed in 1993 and will remain a classic in otopathology, and at the same time provides fundamental information for every otologic surgeon. His scholarly career includes the publication of over 300 original articles, editorials, and reviews, and seven books devoted to anatomy, pathology, and surgery of the ear.

In addition to his clinical expertise, Schuknecht was a willing and gifted teacher. His temporal bone collection established at the Massachusetts Eye and Ear Infirmary now contains over 1500 sets of well-documented specimens. This collection and his willing expert mentorship attracted residents and postgraduate students from many nations. Students honored him in 1973 by the establishment of the International Otopathology Society, also known as the Schuknecht Society. The Society has more than 120 members from 30 countries who meet in scientific sessions every three years.

Dr. Schuknecht is survived by his wife, Anne; his daughter Judy Burness of Santa Rosa, California; his son Jim of Seattle, Washington; and two grandsons, Alexander and Nathan Schuknecht.

Medicine in general and the specialty of otology in particular has lost a giant, and many of us have lost a marvelous colleague and good friend. Through his meticulous writings and scientific collections and the training of hundreds of fellows, residents, and students, his clinical and scientific contributions will continue to influence scientific inquiry and the practice of otology.

(from information provided by)
JOSEPH B. NADEL, JR., M.D.
Harvard Medical School

 0001-4966/98/103(3)/1241/1/$10.00

REVIEWS OF ACOUSTICAL PATENTS

Daniel W. Martin
7349 Clough Pike, Cincinnati, Ohio 45244

The purpose of these acoustical patent reviews is to provide enough information for a Journal reader to decide whether to seek more information from the patent itself. Any opinions expressed here are those of reviewers as individuals and are not legal opinions. Printed copies of United States Patents may be ordered at $3.00 each from the Commissioner of Patents and Trademarks, Washington, DC 20231.

Reviewers for this issue:

GEORGE L. AUGSPURGER, *Perception Incorporated, Box 39536, Los Angeles, California 90039*
HARVEY H. HUBBARD, *325 Charleston Way, Newport News, Virginia 23606*
SAMUEL F. LYBARGER, *101 Oakwood Road, McMurray, Pennsylvania 15317*
D. LLOYD RICE, *11222 Flatiron Drive, Lafayette, Colorado 80026*
CARL J. ROSENBERG, *Acentech Incorporated, 33 Moulton Street, Cambridge, Massachusetts 02138*
ERIC E. UNGAR, *Acentech Incorporated, 33 Moulton Street, Cambridge, Massachusetts 02138*
ROBERT C. WAAG, *University of Rochester Medical Center, 601 Elmwood Avenue, Rochester, New York 14642*

5,672,830

43.35.Yb MEASURING ANISOTROPIC MECHANICAL PROPERTIES OF THIN FILMS

John A. Rogers *et al.*, assignors to Massachusetts Institute of Technology
30 September 1997 (Class 73/597); originally filed 4 October 1994

''Anisotropic mechanical properties of thin films are measured by exciting time-dependent waveguide acoustic modes in the thin film sample with a pair of excitation pulses from an excitation laser. The waveguide acoustic modes are then optically detected by diffracting a probe laser beam off the excited modes. The probe beam is detected to generate an electronic signal. The anisotropic moduli and related properties in the film are determined by analyzing the electronic signal using a mathematical inversion procedure.''—DWM

5,676,015

43.35.Zc CAVITATION CONTROLLED ACOUSTIC PROBE FOR FABRIC SPOT CLEANING AND MOISTURE MONITORING

Shuh-Haw Sheen *et al.*, assignors to The University of Chicago
14 October 1997 (Class 73/73); filed 6 September 1994

''A method and apparatus are provided for monitoring a fabric. An acoustic probe generates acoustic waves relative to the fabric. An acoustic sensor, such as an accelerometer is coupled to the acoustic probe for generating a signal representative of cavitation activity in the fabric. The generated cavitation activity representative signal is processed to indicate moisture content of the fabric... . A feedback control signal is generated responsive to the generated cavitation activity representative signal. The feedback control signal can be used to control the energy level of the generated acoustic waves and to control the application of a cleaning solution to the fabric.''—DWM

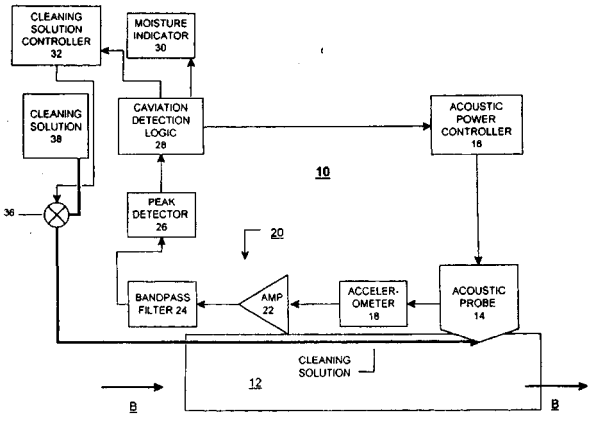

5,675,655

43.38.Hz SOUND INPUT APPARATUS

Shinichi Hatae, assignor to Canon Kabushiki Kaisha
7 October 1997 (Class 381/26); filed in Japan 28 April 1994

The patent shows a sound input apparatus employing a microphone system having a mid microphone facing forward and two side microphones

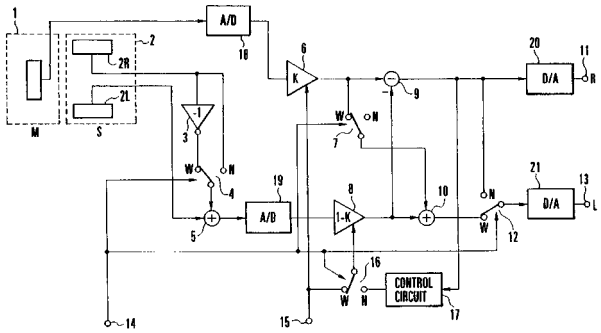

facing sideways. The objective of the system is to obtain a relatively narrow forward pickup pattern to reduce the effects of ambient noise.—SFL

5,659,157

43.38.Ja 7TH ORDER ACOUSTIC SPEAKER

Daniel W. Shulte, Santa Rosa, CA
19 August 1997 (Class 181/156); filed 21 March 1995

A loudspeaker is mounted in opening **10**. All of the other tubes and vents connect chambers with other chambers or with the outside world. If everything is juggled just so, the frequency response has the shape of a triple-tuned bandpass filter. The patent document includes comparative mea-

 0001-4966/98/103(3)/1243/10/$10.00

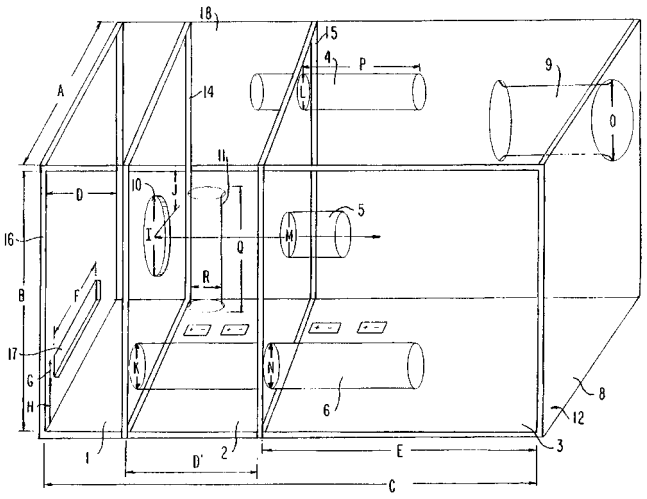

surements showing that, over the same low-frequency range, the output of the Shulte design is about 6 dB greater than that of a popular commercial bandpass loudspeaker. (The patent says 9 dB, but not the way I interpret the curves.) Since the internal volume of the larger box is about 4.25 times that of the smaller, the difference in efficiency is to be expected.—GLA

5,664,024

43.38.Ja LOUDSPEAKER

Akihiro Furuta *et al.*, assignors to Matsushita Electric Industrial Company
2 September 1997 (Class 381/199); filed in Japan 25 April 1994

The patent describes a sophisticated loudspeaker design having a radiating surface that is an edge-driven vault-shaped diaphragm. Numerous variations and practical details are analyzed in relation to measured performance.—GLA

5,606,289

43.38.Lc AUDIO FREQUENCY POWER AMPLIFIERS WITH ACTIVELY DAMPED FILTER

Robert C. Williamson, assignor to Carver Corporation
25 February 1997 (Class 330/297); filed 7 June 1995

This is an elaboration of earlier patent 5,543,753 for which this patent is a continuation. Its main application is in audio-frequency amplifiers containing tracking power supplies. An active damping control circuit moves poles contributed by the power supply output inductor to locations away from the right half of the *s* plane, where they can be compensated without instability.—GLA

5,644,635

43.38.Si METHOD AND DEVICE FOR ECHO CANCELLATION

Werner Armbruster, assignor to U.S. Philips Corporation
1 July 1997 (Class 379/390); filed in Germany 22 December 1994

Adaptive filters are commonly used to cancel echoes in duplex loudspeaking telephones. Signal levels must be closely matched for the filter to operate at its best. This short patent describes a method of automatic gain control that operates independently of the loudspeaker amplifier, the microphone amplifier, and the location of the loudspeaker relative to the microphone.—GLA

5,657,384

43.38.Si FULL DUPLEX SPEAKERPHONE

Daniel W. Staudacher and Harbhajan S. Virdee, assignors to Tandy Corporation
12 August 1997 (Class 379/388); filed 10 March 1995

The first part of the patent document is an excellent two-page summary of duplex speakerphone operation and adaptive filter theory. This speakerphone ''...minimizes the amount of digital signal processing required to maintain full duplex operation by holding the signal dynamic range within predetermined limits.''—GLA

5,677,964

43.38.Si EARPHONE

Ming-Han Sun, Tapei, Taiwan
14 October 1997 (Class 381/187); filed 16 September 1996

The patent shows a small earphone that feeds into a cavity provided with two outlets adapted to receive ends of a length of thin flexible tubing. The tubing surrounds the earphone and is fitted over the auricle. Sound expands and contracts the tubing wall to produce an audible signal.—SFL

5,680,465

43.38.Si HEADBAND AUDIO SYSTEM WITH ACOUSTICALLY TRANSPARENT MATERIAL

James H. Boyden, assignor to Interval Research Corporation
21 October 1997 (Class 381/25); filed 5 April 1995

The patent shows an acoustical system mounted on a band around the head. Transducers to radiate sound are positioned on opposite sides of the head, close to the ears. Signals to the headband device are delivered from loudspeakers that may be mounted on the shoulders or chest of the wearer. In one version the transducers share a common enclosure and are driven 180 degrees out of phase, so that low frequencies are enhanced.—SFL

5,649,019

43.38.Tj DIGITAL APPARATUS FOR REDUCING ACOUSTIC FEEDBACK

Samuel L. Thomasson, Gilbert, AZ
15 July 1997 (Class 381/83); filed 1 May 1995

This is a continuation of patent 5,412,734. In a public address system or hearing aid the signal from a microphone is not only amplified but also is mixed with an ultrasonic pulse-width-modulated version of itself before being sent to the loudspeaker or earphone. Any acoustic feedback includes the PWM signal which, in theory at least, can be used for electronic echo cancellation. The previous patent relied on analog circuitry. The digital version described here is said to be easier to adjust and modify.—GLA

5,598,478

43.38.Vk SOUND IMAGE LOCALIZATION CONTROL APPARATUS

Yoshiaki Tanaka *et al.*, assignors to Victor Company of Japan
28 January 1997 (Class 381/17); filed in Japan 18 December 1992

The audio processing requirements for video games can be reduced to manageable size by restricting virtual sound images to a 180-degree lateral arc. The apparatus expands the field to 360 degrees, using a pair of convolvers in small, relatively inexpensive circuitry.—GLA

5,602,922

43.38.Vk METHOD AND APPARATUS FOR PROCESSING AN AUDIO SIGNAL BY SURROUND MODES

Young-Man Lee, assignor to Samsung Electronics Company
11 February 1997 (Class 381/18); filed in Republic of Korea 19 August 1993

A key for the appropriate surround-sound processing model (''large hall,'' ''nightclub,'' etc.) can be inaudibly encoded in the audio signal, and then used by the surround-sound processor, so that the listener does not have to make decisions, decisions.—GLA

5,604,809

43.38.Vk SOUND FIELD CONTROL SYSTEM

Hiroshi Tsubonuma and Hirofumi Yanagawa, assignors to Pioneer Electronic Corporation
18 February 1997 (Class 381/17); filed in Japan 31 October 1994

The subjective lateral spread of artificial reverberation is enhanced by filtering and cross-feeding signals between left and right channels.—GLA

5,633,981

43.38.Vk METHOD AND APPARATUS FOR ADJUSTING DYNAMIC RANGE AND GAIN IN AN ENCODER/DECODER FOR MULTIDIMENSIONAL SOUND FIELDS

Mark F. Davis, assignor to Dolby Laboratories Licensing Corporation
27 May 1997 (Class 395/2.39); filed 7 June 1995

The patent is a division of patent number 5,583,962. The patent discloses a digital method for encoding multi-channel audio, that is, ''...audibly superior to known 4-2-4 matrix systems with enhanced decoding,'' yet which conserves substantial bandwidth relative to prior art discrete and matrix systems. The patent document is well written, comprehensive, and will be of interest to readers involved with digital audio.—GLA

5,682,712

43.40.Ph STEEL-RUBBER SEISMIC ISOLATION BEARING

Zoltan A. Kemeny, assignor to MM Systems of Arizona
4 November 1997 (Class 52/167.7); filed 27 October 1995

This patent discloses ''a seismic isolation bearing for bridges, buildings and machines with steel reinforced rubber body and external or internal tapered steel pin uniform yielders. The pins are fixed to load plates and intersect in mid-plate...'' as shown. ''Vertical bearing stiffness is greatly controlled by the size of a central hole, passing vertically through the bearing.'' The tapered pins slide freely in the mid-plate holes for vertical motion, and the pins bend when the bearing deflects in shear motion. When the lateral component of the earthquake vibrations ceases, the stiffness of the bent pins restores the bearing and its supported structure to the original position where the pins are centered in the holes of the mid-plate.—DWM

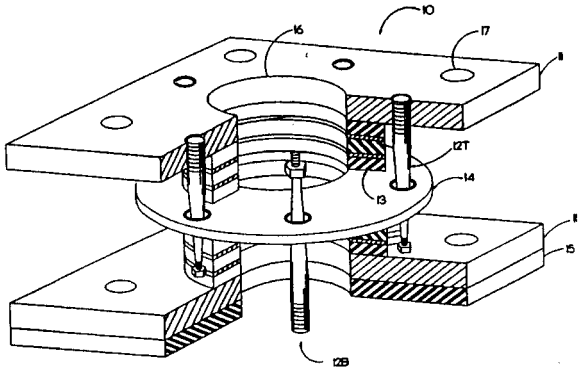

5,638,720

43.40.Tm VEHICLE TRANSMISSION SHIFTING SYSTEM VIBRATION DAMPING ARRANGEMENT

Armin Weinhart *et al.*, assignors to Bayerische Motoren Werke Aktiengesellschaft
17 June 1997 (Class 74/473 R); filed in Germany 5 May 1994

This patent describes an arrangement for reducing the vibrations that are transmitted from a vehicle transmission to the gear shift lever. The shift rod that connects the lever to the transmission is made of two parallel rods that are interconnected by two pin-and-sleeve assemblies. Vibration attenuation is provided by clearance between each pin and its sleeve, and by an elastic layer that occupies some of the clearance space.—EEU

5,654,402

43.40.Tm TURBINE BLADE VIBRATION DAMPENING

Charles C. Cornelius *et al.*, assignors to Solar Turbines, Incorporated
8 July 1997 (Class 416/190); filed 10 April 1996

Each of the blades in a turbine wheel assembly in this patent has one or more slots with a flat rectangular cross section near its outer tip. The slots are configured to accept metal straps, so that these straps form circumferential belts. When the wheel spins, centrifugal forces push the straps outward, enhancing the friction between the outer surfaces of the straps and the inner surfaces of the slots. This friction, of a magnitude that can be selected in the design processes by suitable choices of strap materials and cross-sectional dimensions, contributes to the damping of turbine blade vibrations involving relative motions of the blades.—EEU

5,663,943

43.40.Tm VIBRATION DAMPING SUSPENSION MECHANISM FOR RECORDED DATA REPRODUCING APPARATUS

Tatsuya Yanagisawa *et al.*, assignors to Pioneer Electronic Corporation
2 September 1997 (Class 369/75.1); filed in Japan 6 February 1992

This vibration damping support mechanism for a recorded data reproducing apparatus (e.g., a CD player) allows the player to be installed in either a horizontal or vertical position. The mechanism does so without shifting the tensioning direction of damper springs, thus protecting the playback device from external vibration and shock.—CJR

5,650,853

43.40.Vn VIBRATION RESISTANT INTERFEROMETER

Toshio Honda and Katsuyuki Okada, assignors to Fuji Photo Optical Company
22 July 1997 (Class 356/359); filed in Japan 12 October 1994

This interferometer is intended for the accurate measurement of the surface shape of optical elements and the like in the presence of external vibrations and/or air turbulence. It incorporates an active system which maintains the optical path difference between a reference light component and an object light component at a predetermined value. An interference fringe image is analyzed by a computer to calculate the shape of the sample

surface or its vibration or tilt, and to generate signals to actuate PZT elements that support a reference plate.—EEU

5,660,251

43.40.Vn VIBRATION DAMPING DEVICE FOR DISC BRAKE

Yukio Nishizawa and Hironobu Saka, assignors to Sumitomo Electric Industries
26 August 1997 (Class 188/73.35); filed in Japan 26 May 1995

This patent describes an active vibration damping device for stopping squeaks of a disc brake that are caused by the oscillations of the rotor. The system works by first detecting the vibration of the disc rotor; then that signal is used to oscillate the disc rotor (out of phase) so as to cancel out the vibrations of the disc rotor. Thus, squeaks can be suppressed more effectively than with a conventional vibration damping mechanism.—CJR

5,647,377

43.50.Gf NOISE SUPPRESSOR APPARATUS

Joe Shinabarger, Carson City, Michigan
15 July 1997 (Class 128/864); filed 19 March 1996

This patent relates to the control of coughing and sneezing noises as they may impact the stalking of prey by a hunter. Passive acoustical treatments are arranged inside an appropriately vented portable chamber into which the hunter may cough or sneeze.—HHH

5,649,419

43.50.Gf ROTATING ACOUSTICALLY LINED INLET SPLITTER FOR A TURBOFAN ENGINE

Larry A. Schaut, assignor to the Boeing Company
22 July 1997 (Class 60/226.1); filed 27 January 1995

The patent relates to the control of fan noise radiating forward from turbofan engines. An acoustically treated ring is attached by struts to the spinner of the engine, and is thus located ahead of the fan blades and near

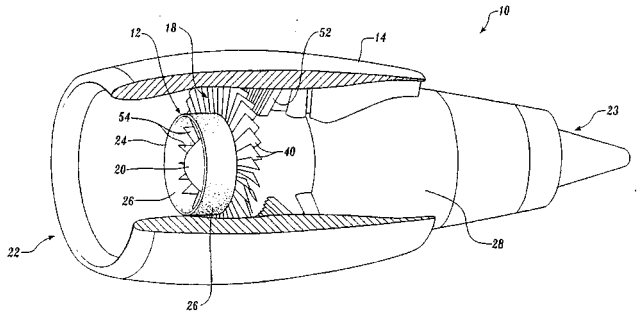

the axis of rotation. The acoustical linings on the ring are positioned near the source of the noise in the primary flow region and are effective in absorbing forward-radiating fan noise.—HHH

5,650,599

43.50.Gf NOISE CANCELLATION METHOD AND APPARATUS

Peter E. Madden *et al.*, assignors to Northrop Grumman Corporation
22 July 1997 (Class 181/218); filed 8 May 1995

The patent relates to noise reduction for exhaust flows such as those from jet engines during ground testing. The exhaust flow is contained within a diverging conduit containing both active and passive treatments for noise control. Passive treatments are focused on the high-frequency portions of the spectrum, whereas active noise control is aimed at frequencies below about 80 Hz. Eight loudspeaker systems may be interconnected in a multi-input, multi-output, control scheme or incorporated in a single-input, single-output scheme.—HHH

5,651,249

43.50.Gf EXHAUST MUFFLER STRUCTURE FOR INTERNAL COMBUSTION ENGINE

Yoshiaki Nagao *et al.*, assignors to Kioritz Corporation
29 July 1997 (Class 60/302); filed in Japan 22 April 1994

This patent relates to the muffling of the exhaust noise of small internal combustion engines such as air-cooled two-cycle gasoline engines used for mowers and chain saws. The muffler housing is designed such that it comes apart in halves to expedite the servicing of the catalyzer element which consists of cloth layers supported by stainless steel nets.—HHH

5,661,272

43.50.Gf ENGINE NOISE REDUCTION APPARATUS

Francesco E. Ianetti, Raleigh, North Carolina
26 August 1997 (Class 181/256); filed 27 January 1995

This patent relates to the reduction of exhaust noise of an internal combustion engine while minimizing the back pressure on the engine. Per-

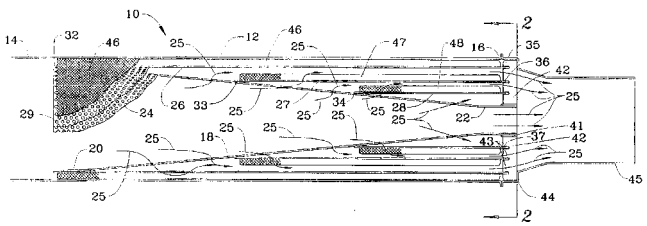

forated metal rings are spaced concentrically around a perforated conical flow guide. Passive absorptive acoustical material (metallic or ceramic) is inserted between the rings in such a manner as to allow the exhaust gases to flow freely through the intervening spaces.—HHH

5,655,361

43.50.Gf SOUND ABSORBING APPARATUS FOR A SUPERSONIC JET PROPELLING ENGINE

Kimihiro Kishi, assignor to Mitsubishi Jukogyo Kabushiki Kaisha
12 August 1997 (Class 60/266); filed in Japan 14 September 1994

This patent relates to reducing exhaust noise of a turbofan engine. Exhaust nozzle liners consisting of vented honeycomb structures are proposed for sound absorption. Provision is made for inducing low-temperature

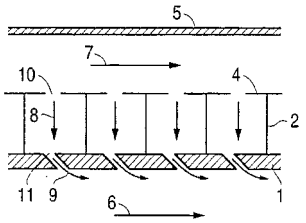

fan discharge air through the honeycomb liners for the purpose of structural cooling.—HHH

5,677,958

43.50.Ki ACTIVE SOUND DAMPER

Frank Juergen Lehringer, assignor to Leistritz AG & Co Abgastechnik
14 October 1997 (Class 381/71); filed in Germany 7 July 1993

Tube **11** might be an auto exhaust pipe. The noise produced at exit **13** is surrounded by a correctional sound field generated by loudspeaker **2**. The

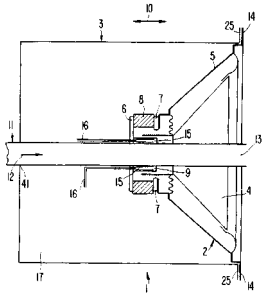

coaxial configuration results in a small, efficient active noise canceller.—GLA

5,665,943

43.55.Ev NESTABLE SOUND ABSORBING FOAM WITH REDUCED AREA OF ATTACHMENT

Peter D'Antonio, assignor to RPG Diffuser Systems, Incorporated
9 September 1997 (Class 181/295); filed 15 June 1995

Various configurations of sound-absorbing plastic foam (cut in one or two dimensions to mimic sine waves, saw tooth cross sections, triangular, etc.) allow the material to be nested, increase its exposed surface area, decrease the overall amount of material that needs to be used for a given

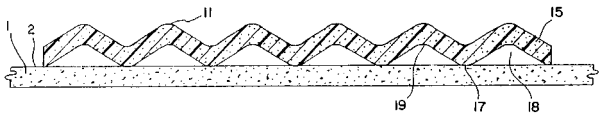

performance, minimize the rear surface area, which is in direct attachment to a flat wall; provide rear air cavities (thus adding additional low frequency absorption), and in so doing, it is said to increase the absorptive properties by 15% to 50%.—CJR

5,661,273

43.55.Ti SOUNDPROOF WALL

Bill Bergiadis, Valencia, CA
26 August 1997 (Class 181/290); filed 7 June 1995

This wall combines a wood wool facing (like shredded wood fiber form board) with insulation and furring channels and studs to become a sound insulating barrier, with a sound absorptive surface.—CJR

5,675,935

43.55.Ti DOOR SEALING MECHANISM

Chen-Yi Lin, Taipei, Taiwan
14 October 1997 (Class 49/306); filed 5 July 1995

The patent is for a movable drop sill said to be able to seal the top and/or bottom of a door to prevent sound leakage. A flexible tip is attached to a movable holder which, when extended, seals to the bottom sill or top lintel around a doorway. The seal withdraws when the door is open.—CJR

5,678,364

43.55.Ti SOUNDPROOF WALL

Hiroshi Shima and Toshiyuki Watanabe, assignors to Bridgestone Corporation
21 October 1997 (Class 52/169.3); filed in Japan 20 July 1994

The patented configuration of a sound wall (for a highway noise barrier) has a ''Y'' shape with secondary branches off the primary branches of

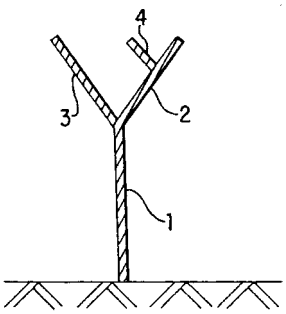

the ''Y'' to provide additional attenuation of diffracted sound, without having to increase the height of the wall.—CJR

5,673,328

43.66.Ts BONE CONDUCTING HEARING AID

Rudolf Wandl and Kurt Schermann, assignors to Viennatone GmbH
30 September 1997 (Class 381/181); filed in Austria 7 October 1992

The patent shows a bone vibrator of a type that might be used in a bone conduction eyeglass hearing aid. The magnetic system includes a permanent magnet, a coil, an armature, a spring holding the armature, and a conductor button that presses against the mastoid bone. A rubber bearing typically holds a rather stiff support spring for the conductor button in the

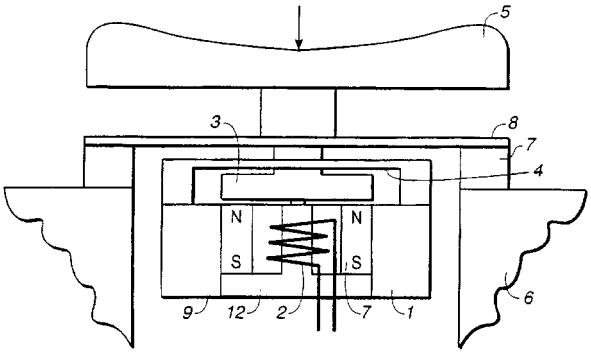

usual design. The patent calls for a considerably lower stiffness, not exceeding 0.4 N/cm, for the support spring **8** to increase the difference between the useful signal and the spurious signal delivered to the mastoid. This permits the size of the bone receiver to be substantially reduced without loss of efficiency.—SFL

5,680,466

43.66.Ts OMNIDIRECTIONAL HEARING AID

Joseph Zelikovitz, Grove, OK
21 October 1997 (Class 381/68.1); filed 6 October 1994

The patent is directed toward detecting sounds in the auditory field associated with the less sensitive ear and transmitting these detected sounds to the more sensitive normal or partially impaired ear. The output of a microphone at the poorer ear is supplied to a radio transmitter adjacent to that ear, and is picked up by a radio receiver at the better ear.—SFL

5,680,467

43.66.Ts HEARING AID COMPENSATING FOR ACOUSTIC FEEDBACK

Roy Skovgaard Hansen, assignor to GN Danavox A/S
21 October 1997 (Class 381/68.2); filed in Denmark 31 March 1992

A hearing aid with digital electronic compensation for acoustic feedback is shown. The circuit includes a noise generator for the insertion of noise and an adjustable digital filter for the adaptation of the feedback sig-

nal. The adaptation takes place using a correlation circuit that includes a digital circuit to carry out a statistical evaluation of the filter coefficients in the correlation circuit, and changes the feedback function accordingly.—SFL

5,679,001

43.70.Ep CHILDREN'S SPEECH TRAINING AID

Martin J. Russell *et al.*, assignors to the United Kingdom of Great Britain and Northern Ireland
21 October 1997 (Class 434/185); filed in the United Kingdom 4 November 1992

''A children's speech training aid compares a child's speech with models of speech, stored as sub-word acoustic models, and a general speech model to give an indication of whether or not the child has spoken correctly... . The stored acoustic models are formed by first recording a plurality of words by a plurality of children from a given list of single words. These recordings are then processed off-line to give a basic acoustic model

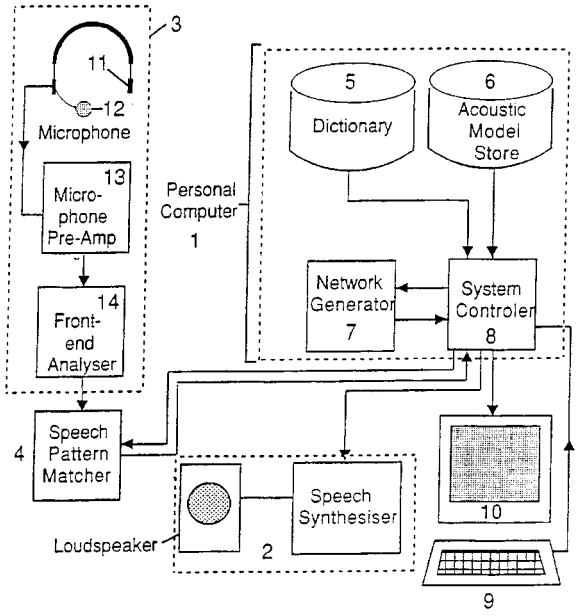

of an acceptable or correct sound for each phoneme in the context of the pre- and proceeding phonemes. The acoustic models are Hidden Markov models. The limits of acceptable pronunciation applied to different words and children may be adjusted by variable penalty values applied in association with the general speech acoustic model.''—DWM

5,664,052

43.72.Ar METHOD AND DEVICE FOR DISCRIMINATING VOICED AND UNVOICED SOUNDS

Masayuki Nishiguchi and Jun Matsumoto, assignors to Sony Corporation
2 September 1997 (Class 704/214); filed in Japan 15 April 1992

This voiced/unvoiced/silence detector is based on the calculation of signal statistics within each subblock of the speech signal. Blocks of 256 samples (32 ms) are divided into subblocks of 8 samples (1 ms) length. For

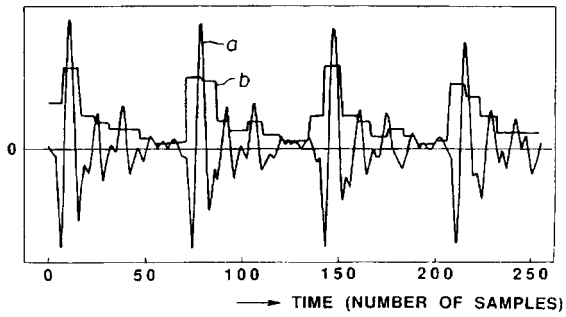

each subblock, the arithmetic mean, geometric mean, rms, standard deviation, and peak value are computed. Measures such as the ratio of arithmetic mean to geometric mean are compared to thresholds to determine a voicing measure for each subblock.—DLR

5,666,464

43.72.Ar SPEECH PITCH CODING SYSTEM

Masahiro Serizawa, assignor to NEC Corporation
9 September 1997 (Class 104/207); filed in Japan 26 August 1993

This speech coding system performs individual pitch analyses over multiple subframes of each input frame. A sequence of subframe pitch values is determined so as to minimize the average prediction gain over the frame. Candidates from the neighborhood of the ideal pitch-period sequence are selected based on the inner product of the input signal and each code vector. The period having minimum waveform distortion is then selected for the frame.—DLR

5,664,053

43.72.Gy PREDICTIVE SPLIT-MATRIX QUANTIZATION OF SPECTRAL PARAMETERS FOR EFFICIENT CODING OF SPEECH

Claude Laflamme *et al.*, assignors to Universite De Sherbrooke
2 September 1997 (Class 704/219); filed 3 April 1995

This linear prediction coding system improves the accuracy of fit of LP parameters within each speech frame by dividing the frame into two (or more) subframes. A split-matrix computation performs separate analyses on

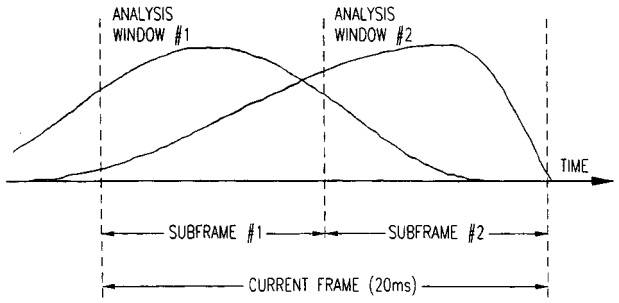

each subframe. A vector quantization by frame captures the subframe pattern with roughly the same bit rate as would be required for full-frame LP analysis.—DLR

5,664,054

43.72.Gy SPIKE CODE-EXCITED LINEAR PREDICTION

Huan-Yu Su, assignor to Rockwell International Corporation
2 September 1997 (Class 704/219); filed 29 September 1995

According to this patent, a code excited (CELP) vocoder typically uses a differential code to represent the amplitude of successive pitch periods. When a previous pitch period waveform is known, the new one can be

predicted knowing only the amplitude step and the period. However, the scheme fails for the first period of each voiced segment. This system reinitializes the prior period buffer to a pulse pattern after each unvoiced interval, providing a better match for the first period of the voiced segment.—DLR

5,664,055

43.72.Gy CS-ACELP SPEECH COMPRESSION SYSTEM WITH ADAPTIVE PITCH PREDICTION FILTER GAIN BASED ON A MEASURE OF PERIODICITY

Peter Kroon, assignor to Lucent Technologies, Incorporated
2 September 1997 (Class 704/223); filed 7 June 1995

This linear predictive coder divides the pitch prediction loop into an adaptive codebook portion and a fixed codebook portion. A pitch predictor filter allows an adjustable gain value ranging from 0.2 to 0.8, depending on a measure of the periodicity. The final gain is then based on the filter adjustable gain plus a gain value from the adaptive codebook result of the previous frame.—DLR

5,664,057

43.72.Gy FIXED BIT RATE SPEECH ENCODER/ DECODER

Antony Henry Crossman and Brant Martin Helf, assignors to PictureTel Corporation
2 September 1997 (Class 704/229); filed 7 July 1993

This speech coder performs a spectral analysis by dividing a FFT output into bands. The band energies are then coded using a nonlinear quantization of the differences of band energy variances from the mean energy.

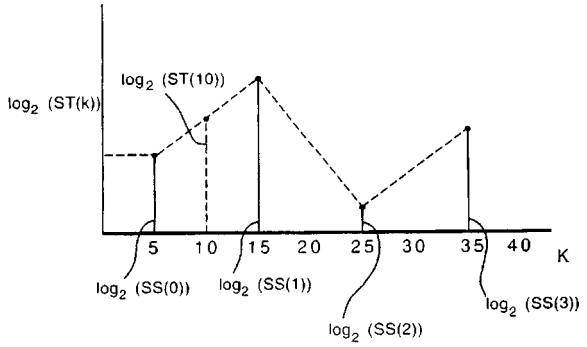

Bands with greater energy use larger step sizes. The step size calculation is iterated until the desired coding efficiency is reached.—DLR

5,666,465

43.72.Gy SPEECH PARAMETER ENCODER

Kazunori Ozawa, assignor to NEC Corporation
9 September 1997 (Class 704/222); filed in Japan 10 December 1993

This vector-quantizing speech coder uses a type of perceptual masking computation to generate the spectral weighting coefficients used in the codebook search. A typical critical band power spectrum is processed to determine weighting coefficients corresponding to auditory masking threshold values. The weighting coefficients are then used to generate speech signals for comparison with codebook entries.—DLR

5,664,050

43.72.Ja PROCESS FOR EVALUATING SPEECH QUALITY IN SPEECH SYNTHESIS

Bertil Lyberg, assignor to Telia AB
2 September 1997 (Class 704/251); filed in Sweden 2 June 1993

The idea behind this patent is to use a speech recognizer to listen to and evaluate a speech synthesizer. The recognizer would be trained with a set of speakers' voices having the characteristics desired in the synthetic voice. In operation, the recognizer would report how the synthetic voice compared with the recognition training data. The obvious shortcoming is that synthesizers generally tend to do fairly well in those aspects of speech which are more or less understood. They are inadequate in just those aspects which recognizers tend to ignore, such as inflection and variations in duration and allophonic structure.—DLR

5,664,051

43.72.Ja METHOD AND APPARATUS FOR PHASE SYNTHESIS FOR SPEECH PROCESSING

John C. Hardwick and Jae S. Lim, assignors to Digital Voice Systems, Incorporated
2 September 1997 (Class 704/206); filed 24 September 1990

This speech analysis method, intended mainly for use in speech synthesizers, is based on the extraction of magnitude and phase of the harmonics during voiced speech. However, the phase information is not encoded for transmission. Instead, a phase value for each harmonic is computed at the receiver. The computed phase value is modulated by a random jitter factor, which is said to eliminate largely the buzzy effect often heard in synthetic speech.—DLR

5,640,450

43.72.Kb SPEECH CIRCUIT CONTROLLING SIDETONE SIGNAL BY BACKGROUND NOISE LEVEL

Osamu Watanabe, assignor to Kokusai Electric Company
17 June 1997 (Class 379/392); filed in Japan 8 July 1994

This is a telephone microphone circuit that monitors the on-going background noise level and adjusts the sidetone and received signal levels accordingly. A second microphone on the backside of the handset picks up

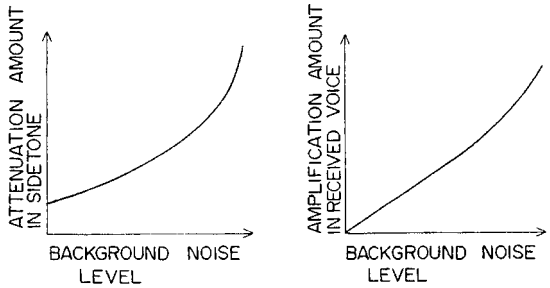

the background noise level with much less speech signal. The transmitted signal is kept at a desired level despite near-end noise level changes.—DLR

5,651,096

43.72.Ne MERGING OF LANGUAGE MODELS FROM TWO OR MORE APPLICATION PROGRAMS FOR A SPEECH RECOGNITION SYSTEM

Matthew G. Pallakoff *et al.*, assignors to Apple Computer, Incorporated
22 July 1997 (Class 395/2.84); filed 14 March 1995

This is an operating system software component for use with a speech recognizer in a computer system where multiple applications may be under concurrent control by speech input. The patented component integrates information on the desired voice interaction from each application into a unified grammar, allowing voice inputs to be recognized and directed to an application without depending on a specific application already being activated.—DLR

5,664,058

43.72.Ne METHOD OF TRAINING A SPEAKER-DEPENDENT SPEECH RECOGNIZER WITH AUTOMATED SUPERVISION OF TRAINING SUFFICIENCY

George Vysotsky, assignor to NYNEX Science & Technology
2 September 1997 (Class 704/243); filed 12 May 1993

The patent describes a strategy to be followed during template updating with new token data in an isolated-phrase speech recognizer. Although the patent title suggests that the strategy itself provides the supervision, it is actually a (manually) supervised procedure in that the strategy is to be followed only during ''training'' (i.e., the system always knows what item has been spoken). The strategy involves computing distances between the new token, other tokens of the same phrase, and competing tokens of other phrases.—DLR

5,644,059

43.72.Ne SELF-LEARNING SPEAKER ADAPTATION BASED ON SPECTRAL VARIATION SOURCE DECOMPOSITION

Yunxin Zhao, assignor to Panasonic Technologies, Incorporated
2 September 1997 (Class 701/254); originally filed 29 April 1993

This speaker adaptation method for a speech recognizer employs a technique of separating any speaker-specific biases from the multi-speaker probability distributions. The system is initially trained by a number of speakers following known procedures. A specific test speaker (say, speaker Q) then identifies himself to the system. The system then recognizes Q's input using the independent distributions, but accumulates new data representing Q's deviations from the general set. Future inputs by speaker Q are then adjusted before recognition proceeds.—DLR

5,666,466

43.72.Pf METHOD AND APPARATUS FOR SPEAKER RECOGNITION USING SELECTED SPECTRAL INFORMATION

Qiguang Lin *et al.*, assignors to Rutgers, The State University of New Jersey
9 September 1997 (Class 704/246); filed 27 December 1994

This patent covers a modified method of computing cepstral vectors from a speech signal for use in a speaker recognizer system. Following a typical FFT amplitude spectrum analysis, the spectral vector is truncated, retaining a band from the speech midrange, perhaps 1 or 2 kHz, up to the

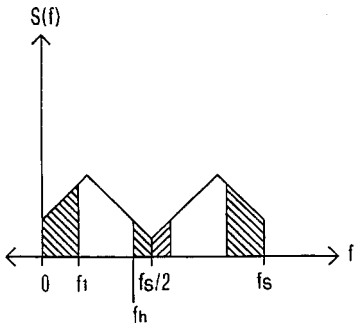

highest frequency allowed by the chosen sample rate. This band is said to retain the information most critical to the speaker's identity. Cepstral vectors are computed from the limited spectral band in a typical manner.—DLR

5,686,679

43.75.Kk PERCUSSION INSTRUMENT WITH TONE BARS FOR EXACTLY GENERATING TONES ON A SCALE

Minoru Nakano and Hiroaki Ohmuro, assignors to Yamaha Corporation
11 November 1997 (Class 84/402); filed in Japan 20 January 1995

In the vibraphone of this patent the bottom of each metal bar **11** has recesses **11r**, **11s**, and **11t** shaped to tune the frequencies of the first three

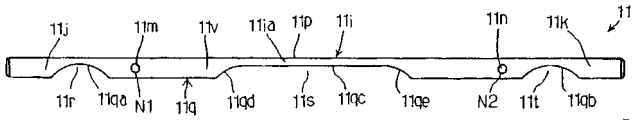

modes of transverse vibration to a frequency ratio of 1:4:8, in order to bring the mode frequencies into octave relationships.—DWM

5,684,262

43.75.Rs PITCH-MODIFIED MICROPHONE AND AUDIO REPRODUCING APPARATUS

Junichi Nakamura and Masakazu Nakamura, assignors to Sony Corporation
4 November 1997 (Class 811/654); filed in Japan 28 July 1994

The apparatus disclosed in this patent is intended to extend the art of karaoke singing. The tape or disk playback device **1** which provides a musical accompaniment signal heard by the singer singing into microphone **11** is supplied to two channels. The normal channel includes amplifier **2**, converter **3**, equalizer **4**, mixer **5**, and digital-to-analog converter **6**. A central processing unit **21** receives playback signal through decoder **22** and converted singing signal through sound level detector **17**. A tone converter **16**, under the control of CPU **21**, produces one or more additional voice signals in synchronism with the original singing voice signal, and mixes the original

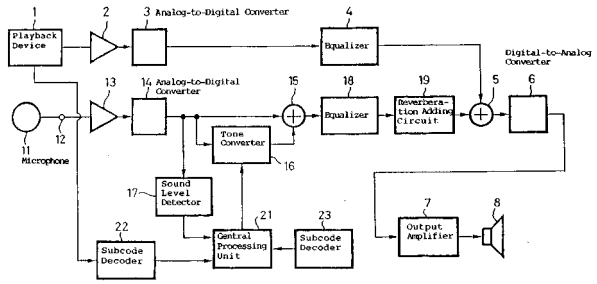

with the additional voice signals in mixer **15**. Reverberation is added to the mixed voices, then mixed with the playback accompaniment signal for amplification and electroacoustic radiation. The purpose is to provide a duet or chorus of voices for which the relative frequency intervals are determined by chords in the music from the tape or record being played.—DWM

5,686,682

43.75.Tv ELECTRONIC MUSICAL INSTRUMENT CAPABLE OF ASSIGNING WAVEFORM SAMPLES TO DIVIDED PARTIAL TONE RANGES

Osamu Ohshima and Tokiharu Ando, assignors to Yamaha Corporation
11 November 1997 (Class 84/603); filed in Japan 9 September 1994

In this digital electronic musical instrument a variety of waveform samples is stored. The musical scale is divided into a number of partial tone ranges. An equal number of different waveforms is selected, and each waveform is assigned to a different partial tone range so that tones played in each range are sounded with different waveforms.—DWM

5,684,260

43.75.Wx APPARATUS AND METHOD FOR GENERATION AND SYNTHESIS OF AUDIO

James E. Van Buskirk, assignor to Texas Instruments, Incorporated
4 November 1997 (Class 84/604); filed 9 September 1994

This sound synthesizer comprises a digital signal processor programmed for selecting waveform spectral values to generate a composite waveform; for generating noise spectral values; and for combining the noise spectral values and composite waveform to provide digital signals that are then converted to analog signals. The text and figures of this patent occupy only 20 pages, a typical size for a computer music patent, but an appendix illustrating the computer program expands the length of the patent document to over 500 pages.—DWM

5,686,683

43.75.Wx INVERSE TRANSFORM NARROW BAND/ BROAD BAND SOUND SYNTHESIS

Adrian Freed, assignor to the University of California
11 November 1997 (Class 84/625); filed 23 October 1995

''An additive sound synthesis process for generating complex, realistic sounds is realized in a computationally efficient manner. In accordance with one aspect of the invention, polyphony is efficiently achieved by dosing the energy of a given partial between separate transform sums corresponding to different channels. In accordance with another aspect of the invention, noise is injected by randomly perturbing the phase of the sound, either on a per-partial basis or on a transform-sum basis. In the latter instance, the phase is perturbed in different regions of the spectrum to a degree determined by the amount of energy present in the respective regions of the spectrum. In accordance with yet another aspect of the invention, a transform sum representing a sound is processed in the transform domain to achieve with great economy effects achievable only at much greater expense outside the transform domain.''—DWM

5,684,460

43.80.Qf MOTION AND SOUND MONITOR AND STIMULATOR

Michael V. Scanlon, assignor to the United States of America
4 November 1997 (Class 340/573); filed 9 May 1996

This patent discloses a system for monitoring the normal breathing sounds, heartbeats, and movements of an infant lying on a fluid-filled pad such as a ''baby water bed.'' The sound and vibration signals picked up by sensors in the pad are transmitted to a monitoring system. When these normal signals cease, as in sudden infant death syndrome (SIDS), the system sends stimulation signals (e.g., light, sound, and shaker vibration) to the infant. Recent medical studies have shown that resuscitation may be possible by immediate stimulation. The stimulator may also be used in a gentle fashion to soothe and quiet an infant after awakening. The sensors' output can be transmitted to a remote location for monitoring by a parent or other person.—DWM

5,630,416

43.80.Vj ULTRASONIC DIAGNOSTIC PROBE

Shiro Uchikura and Narutaka Nakao, assignors to Fujitsu, Ltd.
20 May 1997 (Class 128/660.08); filed in Japan 19 September 1994

This probe, intended for use in the esophagus, includes a mechanism to swing the transducer around an axis parallel to the face of the transducer, and a mechanism that rotates the transducer around an axis perpendicular to the face of the transducer. The rotating mechanism contains a pedestal support that permits the swinging motion. The swinging is accomplished using a wire that is connected to the pedestal.—RCW

5,630,417

43.80.Vj METHOD AND APPARATUS FOR AUTOMATED CONTROL OF AN ULTRASOUND TRANSDUCER

Alan W. Peterson and Robert M. Perlman, assignors to Acuson Corporation
20 May 1997 (Class 128/660.08); filed 8 September 1995

In this patent a transducer is rotated by a motor via a mechanical coupling. The motor is controlled using a microprocessor, a state machine, and an encoder. Two methods of control are described. In the first method, the state machine is initialized by providing a speed and target position and the speed is automatically determined from the initialization. In the second method, two speeds, the target position, and a position near the target are provided and the transducer rotates toward the target initially using the first speed and then using the second speed after the transducer passes the position near the target.—RCW

5,634,464

43.80.Vj METHOD AND APPARATUS FOR ULTRASOUND IMAGING AND ATHERECTOMY

Yue-Teh Jang and Axel F. Brisken, assignors to Cardiovascular Imaging Systems
3 June 1997 (Class 128/660.03); filed 6 June 1995

An ultrasonic transducer in a catheter is fixed to a cutter. The transducer is moved longitudinally within a blood vessel while in a fixed radial position. Ultrasonic reflections are received and processed to display an image of an axial plane through the vessel. Different axial planes are imaged by rotating the transducer to a different angular orientation and repeating the longitudinal motion.—RCW

5,632,277

43.80.Vj ULTRASOUND IMAGING SYSTEM EMPLOYING PHASE INVERSION SUBTRACTION TO ENHANCE THE IMAGE

Christopher S. Chapman and John C. Lazanby, assignors to Siemens Medical Systems, Incorporated
27 May 1997 (Class 128/660.07); filed 28 June 1996

This system utilizes two transmissions of amplitude-modulated signals in which the carrier phase of the second pulse differs from that of the first pulse and the echoes arising from these pulses are combined.—RCW

43.80.Vj CONTINUOUS DISPLAY OF CARDIAC BLOOD FLOW IMAGING

Daniel C. Schmiesing *et al.*, assignors to Advanced Technology Laboratories

3 June 1997 (Class 128/661.08); filed 9 June 1995

Blood flow information is determined and displayed using a Doppler noise threshold that is determined by the operating characteristics of the imaging system. Spectral Doppler data is compared to this threshold to identify a valid peak velocity. Peak velocity values are interpolated and displayed in place of artifactual values caused by valve motion. Intervals over which cardiovascular performance is computed are selected using the R-wave of an ECG trace and the selected intervals are highlighted for the user.—RCW

43.80.Vj ULTRASONIC TRANSESOPHAGEAL PROBE WITH DETACHABLE TRANSDUCER TIP

George P. Gruner, assignor to Advanced Technology Laboratories

3 June 1997 (Class 128/662.06); filed 15 December 1995

This probe includes an articulation section that is formed by interconnected links. Articulation is controlled from the handle of the probe and the position of articulation may be locked, but the lock can be overcome by force of the esophagus against the tip of the probe when it is withdrawn in a locked and bent position. An indication of locking is displayed on the handle of the probe and on the screen of the ultrasonic imaging system.—RCW

The solution for the propagation of sound in a toroidal waveguide with driven walls (the acoustitron)[a)]

Christopher C. Lawrenson,[b)] L. Dwynn Lafleur,[c)] and F. Douglas Shields
Jamie Whitten National Center for Physical Acoustics, Coliseum Drive, University, Mississippi 38677

(Received 31 July 1995; revised 3 September 1997; accepted 10 October 1997)

This paper describes the theory of sound propagation in a toroidal waveguide with driven walls. This configuration has the advantage of simulating a tube of infinite length. The general solution for the velocity potential is derived in terms of an arbitrary function which represents the angular dependence of the disturbance of the driving wall. Two different cases are considered. The first is a toroid with the wall driven at a single angular position. The second case is a toroid with walls driven such that a traveling wave is generated in the wall with a controllable wave number and frequency. A traveling wave is produced inside the toroid when the circumference of the toroid is a whole number of wavelengths for the wave in the wall. The amplitude of the traveling wave is a function of the intrinsic speed of sound in the medium inside the toroid. A device we call an *acoustitron* was constructed to verify the results of the latter case. Experimental results agree well with those predicted by theory. © *1998 Acoustical Society of America.* [S0001-4966(98)02102-X]

PACS numbers: 43.10.Ln, 43.20.Mv, 43.20.Ks [JEG]

INTRODUCTION

The vast majority of studies of sound propagation in acoustic waveguides deal with the case of passive walls.[1–5] In other words, the walls are considered either rigid or elastic but are not active sources of acoustic energy. Previous works dealing with sound propagation in curved tubes have considered only the case of rigid walls[6–11] and porous walls.[12,13] In this paper, the case of a toroid with rigid walls will first be considered, then the case of one with driven walls. It will be seen that the solution for the rigid wall case will give some insight to the driven wall solution.

In 1960, H. E. von Gierke described a device to David Blackstock that consisted of a tube in a ring configuration (he called it an ''acoustitron'' because of the close resemblance to a cyclotron), with a single source attached to the ring via a port. The device used was to produce a progressive wave traveling in one direction around the ring. At resonance, when the circumference was equal to $n\lambda$, the excitation added by the source would be in phase with the traveling wave, and therefore be able to build up very high pressure levels. According to Blackstock, von Gierke was able to produce very high sound pressure levels with a relatively small source.[14] In attempting to reproduce the experiment, Blackstock discovered that he could not keep the source from exciting a backward traveling as well as forward traveling wave so that the resulting wave was not the progressive-wave type sought.[15]

Work began at the National Center for Physical Acoustics to study the propagation of sound in infinitely long straight tubes with driven walls, which followed from Lord Rayleigh's work.[2] Experimentally, such a system could be represented by a toroidal waveguide which has an infinite effective path length. This led to the idea of building a tube consisting of multiple sources mounted equally spaced around a toroidal waveguide. Again, because of the close resemblance to a cyclotron, the authors have called this device an ''acoustitron.'' Part of the theoretical and experimental work in the present paper discusses the production of a traveling wave in such a waveguide.

Experiments undertaken to verify the theoretical results will also be described. In particular, the construction and analysis of the acoustitron will be detailed. The manner in which walls are driven to produce traveling waves is described, and the experimental results verifying the existence of the waves are given.

I. THEORY

The geometry considered theoretically throughout this paper is that of a toroidal duct with a rectangular cross section. Let the toroid have an inside radius of a and an outside radius b as shown in Fig. 1. The height of the toroid is $z=h$ with the base assumed to be in the x-y plane. Solutions will be sought in the form of waves traveling in the azimuthal direction. The wave equation in terms of the velocity potential, $\Phi(r,t)$, is given by

$$\nabla^2\Phi=\frac{1}{c^2}\frac{\partial\Phi}{\partial t}, \tag{1}$$

where the velocity potential is related to the particle velocity and pressure by $\mathbf{u}=\nabla\Phi$ and $p=-\rho_0(\partial\Phi/\partial t)$, respectively. The general solution can be written as

$$\Phi=\sum_m\,[A_rJ_m(k_rr)+B_rY_m(k_rr)]\times[A_z\,\cos(k_zz)+B_z\,\sin(k_zz)]e^{i(m\theta-\omega t)}, \tag{2}$$

where

[a)]''Selected research articles'' are ones chosen occasionally by the Editor-in-Chief that are judged (a) to have a subject of wide acoustical interest, and (b) to be written for understanding by broad acoustical readership.

[b)]Present address: MacroSonix Corp., 1570 East Parham Road, Richmond, VA 23228.

[c)]Permanent address: Department of Physics, University of Southwestern Louisiana, Lafayette, LA 70504.

 0001-4966/98/103(3)/1253/8/$10.00

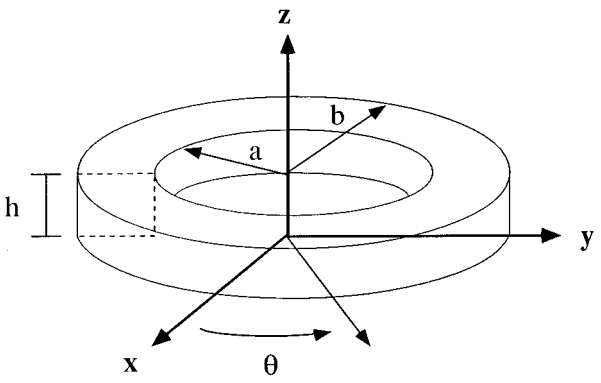

FIG. 1. The toroidal waveguide.

$$k_r^2=\frac{\omega^2}{c^2}-k_z^2, \tag{3}$$

and m must be an integer because of the requirement that $\Phi(r,\theta,z,t)=\Phi(r,\theta+2\pi,z,t)$. Note that the real part of Eq. (2) must be evaluated to get to the real quantity $\Phi(r,t)$. Because the propagation of sound is defined to be along θ, it is convenient to think of m as analogous to a wave number. Following the convention of Krasnushkin,[16] m will be referred to as the *angular wave number*.

A. Rigid wall condition

In a toroid with rigid walls, the normal component of the fluid particle velocity is zero at the walls, i.e.,

$$\left.\frac{\partial\Phi_m}{\partial z}\right|_{z=0}=\left.\frac{\partial\Phi_m}{\partial z}\right|_{z=h}=0, \tag{4}$$

$$\left.\frac{\partial\Phi_m}{\partial r}\right|_{r=a}=\left.\frac{\partial\Phi_m}{\partial r}\right|_{r=b}=0, \tag{5}$$

for a given value of angular wave number m. Using Eq. (2) with these boundary conditions yields

$$B_z=0, \quad k_z=\frac{n\pi}{h} \quad (n=0,\pm1,\pm2,\ \ldots), \tag{6}$$

and

$$J_m'(\beta)Y_m'(\beta b/a)-J_m'(\beta b/a)Y_m'(\beta)=0, \tag{7}$$

where $\beta\equiv k_r a$. If β_{mp} is the pth root of Eq. (7) for a given m, Eq. (3) yields

$$\omega_{mnp}=c\sqrt{\left(\frac{\beta_{mp}}{a}\right)^2+\left(\frac{n\pi}{h}\right)^2}, \tag{8}$$

where ω_{mnp} are the characteristic (or normal mode) frequencies.

The solution for the velocity potential can then be written as

$$\Phi=\sum_{m=-\infty}^{\infty}\sum_{n=0}^{\infty}\sum_{p=-\infty}^{\infty}A_{mnp}\left[J_m\left(\frac{\beta_{mp}r}{a}\right)-Y_m\left(\frac{\beta_{mp}r}{a}\right)\frac{J_m'(\beta_{mp})}{Y_m'(\beta_{mp})}\right]\cos\left(\frac{n\pi z}{h}\right)e^{i(m\theta-\omega_{mnp}t)}. \tag{9}$$

A similar result was derived by Rostafinski[8] and Grigor'yan.[10]

Now consider Eq. (7) for the case of a toroid whose width is much less than its radius, i.e., $b/a=1+\epsilon$, where $0<\epsilon\ll1$ so that

$$J_m'(\beta)Y_m'(\beta+\epsilon\beta)-J_m'(\beta+\epsilon\beta)Y_m'(\beta)=0. \tag{10}$$

Expanding the Bessel functions for $\beta\epsilon\ll1$ in a Taylor series expansion yields

$$0=J_m'(\beta)Y_m''(\beta)-J_m''(\beta)Y_m'(\beta)+\frac{\epsilon\beta}{2}[J_m'(\beta)Y_m'''(\beta)-J_m'''(\beta)Y_m'(\beta)]+\mathcal{O}(\beta^2\epsilon^2). \tag{11}$$

Using identities for the difference of the products of Bessel and Neumann function derivatives[17] yields,

$$\beta\approx m\sqrt{\frac{2-3\epsilon}{2-\epsilon}}, \tag{12}$$

or from Eq. (8),

$$\omega_{mn}\approx c\sqrt{\left(\frac{m}{a}\right)^2\left(\frac{2-3\epsilon}{2-\epsilon}\right)+\left(\frac{n\pi}{h}\right)^2}. \tag{13}$$

Consider the case of $n=0$, i.e., no variation of wave properties in the z direction. Expanding the square root to first order in ϵ yields

$$\omega_m\approx\frac{mc}{a}\left(1-\frac{1}{2}\epsilon\right). \tag{14}$$

These characteristic frequencies correspond to those of integral wavelengths along the ''center'' circumference of the toroid. This can be demonstrated by considering a straight duct of length $l=\pi(a+b)$, the ''center'' circumference of the toroid. The frequencies of waves with an integral number of wavelengths over l are $\omega=2\pi mc/l$. Using $b=a(1+\epsilon)$, the frequencies of waves that fit in this straight duct are

$$\omega=\frac{mc}{a}\left(1+\frac{1}{2}\epsilon\right)^{-1}\approx\frac{mc}{a}\left(1-\frac{1}{2}\epsilon\right), \tag{15}$$

which is identical to Eq. (14). Note that the similarity of the toroid to a straight duct requires that $\beta\epsilon=k_r a\epsilon\ll1$, so that this approximation is only valid for wavelengths that are large compared to the width of the tube. Therefore, in this limit, the shape of the bend has no effect on sound propagation. This result is the same as derived by Rostafinski,[8] and even earlier by Lord Rayleigh.[18]

B. Driven wall condition

Let the outer and inner radial walls of the toroid now be driven with an angular dependent velocity function $f(\theta)$ between $-\pi < \theta \leqslant \pi$, while the top and bottom walls are kept rigid, i.e.,

$$\left.\frac{\partial \Phi_m}{\partial z}\right|_{z=0} = \left.\frac{\partial \Phi_m}{\partial z}\right|_{z=h} = 0, \tag{16}$$

$$\left.\frac{\partial \Phi_m}{\partial r}\right|_{r=a} = V_0 f(\theta) e^{-i\omega t}, \tag{17}$$

$$\left.\frac{\partial \Phi_m}{\partial r}\right|_{r=b} = -V_0 f(\theta) e^{-i\omega t}, \tag{18}$$

where V_0 is the velocity amplitude of the wall. Note that the inner and outer walls move in opposite directions, as indicated by the minus sign in Eq. (18).

Equation (16) again yields the result for k_z given by Eq. (6). Because there is no z dependence in the boundary conditions, there will be no variation of wave properties in the z direction, i.e., $n=0$.

As stated earlier, a general solution in terms of θ without any restrictions on the frequency and angular wave number of the wall is desired. For this reason, it is convenient to write the θ dependence of the driven boundary condition as the sum over all possible angular wave numbers in the wall by Fourier decomposing $f(\theta)$. Therefore,

$$f(\theta) = \sum_{l=-\infty}^{\infty} A_l e^{il\theta}, \tag{19}$$

where

$$A_l = \frac{1}{2\pi} \int_{-\pi}^{\pi} f(\theta') e^{-il\theta'} d\theta'. \tag{20}$$

An expression describing the driving wall in terms of θ is all that is then required to solve for the velocity potential.

C. Application of boundary conditions

1. Single driving element

Consider the case of a toroid with all rigid walls except for a single set of driving elements located on both inside and outside walls at θ_d, i.e., Blackstock's configuration, so that

$$f(\theta) = \delta(\theta - \theta_d). \tag{21}$$

For convenience, the x-y axes will be oriented so that $\theta_d = 0$. When substituted into Eq. (20), the result is

$$A_l = \frac{1}{2\pi}. \tag{22}$$

Using this with Eq. (19), Eqs. (17) and (18) become

$$\left.\frac{\partial \Phi_m}{\partial r}\right|_{r=a} = \sum_{l=-\infty}^{\infty} \frac{V_0}{2\pi} e^{i(l\theta - \omega t)}, \tag{23}$$

$$\left.\frac{\partial \Phi_m}{\partial r}\right|_{r=b} = \sum_{l=-\infty}^{\infty} -\frac{V_0}{2\pi} e^{i(l\theta - \omega t)}. \tag{24}$$

Note that the amplitude of each angular wave number component will be the same so that each positive wave number has a corresponding negative wave number of the same amplitude. The result will therefore be a standing wave inside the toroid.

Using the general solution for the velocity potential, Eq. (2), in the above (excluding the z dependence) yields,

$$\sum_{l=-\infty}^{\infty} \frac{V_0}{2\pi} e^{il\theta} = \sum_{m=-\infty}^{\infty} k_r [A_m J'_m(k_r a) + B_m Y'_m(k_r a)] e^{im\theta}, \tag{25}$$

$$\sum_{l=-\infty}^{\infty} -\frac{V_0}{2\pi} e^{il\theta} = \sum_{m=-\infty}^{\infty} k_r [A_m J'_m(k_r b) + B_m Y'_m(k_r b)] e^{im\theta}, \tag{26}$$

where $k_r = \omega/c$.

Multiplying both sides of Eqs. (25) and (26) by $\exp(-ij\theta)$, where j is an integer, and integrating over $d\theta$ from $-\pi$ to π yields,

$$\frac{V_0}{2\pi} = A_m k_r J'_m(k_r a) + B_m k_r Y'_m(k_r a), \tag{27}$$

$$-\frac{V_0}{2\pi} = A_m k_r J'_m(k_r b) + B_m k_r Y'_m(k_r b). \tag{28}$$

Solving for A_m and B_m and substituting into Eq. (2), the general solution for the velocity potential becomes

$$\Phi = \frac{V_0}{2\pi k_r} \sum_{m=-\infty}^{\infty} \frac{1}{\Delta_m} \{[Y'_m(k_r a) + Y'_m(k_r b)] J_m(k_r r) - [J'_m(k_r a) + J'_m(k_r b)] Y_m(k_r r).\} e^{i(m\theta - \omega t)}, \tag{29}$$

where

$$\Delta_m \equiv J'_m(k_r a) Y'_m(k_r b) - J'_m(k_r b) Y'_m(k_r a). \tag{30}$$

Comparison to Eq. (7) reveals that the frequencies satisfying $\Delta_m = 0$ are the characteristic frequencies of the rigid wall toroid, ω_{mp}, given by Eq. (8) with $n=0$.

The corresponding normalized pressure is

$$\frac{p}{\rho_0 c V_0} = i \sum_{m=0}^{\infty} \frac{1}{\Delta_m} \{[Y'_m(k_r a) + Y'_m(k_r b)] J_m(k_r r) - [J'_m(k_r a) + J'_m(k_r b)] Y_m(k_r r)\} \times \cos(m\theta) e^{-i\omega t}, \tag{31}$$

where $Y_{-m}(x) = (-1)^m Y_m(x)$ and $J_{-m}(x) = (-1)^m J_m(x)$ has been used. Note that the real part of this quantity must be evaluated to get to the real quantity $p(r,t)$. This pressure corresponds to a standing wave inside the toroid with a frequency dependent amplitude. As pointed out above, the behavior of Δ_m is such that when the driving frequency corresponds to a characteristic frequency of the rigid wall toroid, this term is zero. This will result in an infinite pressure with the driving element located at a pressure antinode. Even in the nonideal case, therefore, the pressure amplitude is expected to be greater at the characteristic frequencies than at

other frequencies. As shown earlier, when $a \ll \lambda$, these characteristic frequencies are those that fit a whole number of wavelengths along the circumference of the toroid.

As mentioned earlier, Blackstock was unable to produce a traveling wave with a single driver, which is consistant with theory.

2. Entire driven wall

Now consider the case of a toroidal waveguide with a sinusoidal wave propagating between $-\pi < \theta \leqslant \pi$ with an angular phase velocity Ω along both inside and outside walls. In other words, the walls are driven with a controllable wave number and frequency. No restrictions will be placed on the choice of Ω so that in general, a discontinuity in the driven wall will exist at $\theta = \pi$. As will be seen, this driver configuration is capable of producing traveling waves under certain conditions. The chosen θ dependence will be

$$f(\theta) = e^{i\omega\theta/\Omega}. \tag{32}$$

(Note that $\Omega = \Omega_m$ is not required, i.e., the value of ω/Ω is not necessarily an integer.) When substituted into Eq. (20), the result is

$$A_l = \frac{\sin(\omega/\Omega - l)\pi}{(\omega/\Omega - l)\pi}. \tag{33}$$

For this driving condition, the amplitude of each angular mode will vary as a function of frequency and angular phase velocity.

Equations (17) and (18) then become

$$\left.\frac{\partial \Phi_m}{\partial r}\right|_{r=a} = \sum_{l=-\infty}^{\infty} V_0 \frac{\sin(\omega/\Omega - l)\pi}{(\omega/\Omega - l)\pi} e^{il\theta} e^{-i\omega t}, \tag{34}$$

$$\left.\frac{\partial \Phi_m}{\partial r}\right|_{r=b} = \sum_{l=-\infty}^{\infty} -V_0 \frac{\sin(\omega/\Omega - l)\pi}{(\omega/\Omega - l)\pi} e^{il\theta} e^{-i\omega t}. \tag{35}$$

Using the general solution for the velocity potential given by Eq. (2) and excluding the z dependence yields

$$\sum_{l=-\infty}^{\infty} V_0 \frac{\sin(\omega/\Omega - l)\pi}{(\omega/\Omega - l)\pi} e^{il\theta} = \sum_{m=-\infty}^{\infty} k_r [A_m J'_m(k_r a) + B_m Y'_m(k_r a)] e^{im\theta}, \tag{36}$$

$$\sum_{l=-\infty}^{\infty} -V_0 \frac{\sin(\omega/\Omega - l)\pi}{(\omega/\Omega - l)\pi} e^{il\theta} = \sum_{m=-\infty}^{\infty} k_r [A_m J'_m(k_r b) + B_m Y'_m(k_r b)] e^{im\theta}, \tag{37}$$

where $k_r = \omega/c$.

Following the same path used in the previous section, the general solution for the velocity potential becomes

$$\Phi = \frac{V_0}{k_r} \sum_{m=-\infty}^{\infty} \frac{1}{\Delta_m} \{[Y'_m(k_r a) + Y'_m(k_r b)] J_m(k_r r) - [J'_m(k_r a) + J'_m(k_r b)] Y_m(k_r r)\} \times \frac{\sin(\omega/\Omega - m)\pi}{(\omega/\Omega - m)\pi} e^{i(m\theta - \omega t)}, \tag{38}$$

where Δ_m is again defined by Eq. (30).

The corresponding pressure is

$$p = \frac{i\omega\rho_0 V_0}{k_r} \sum_{m=-\infty}^{\infty} \frac{1}{\Delta_m} \{[Y'_m(k_r a) + Y'_m(k_r b)] J_m(k_r r) - [J'_m(k_r a) + J'_m(k_r b)] Y_m(k_r r)\} \times \frac{\sin(\omega/\Omega - m)\pi}{(\omega/\Omega - m)\pi} e^{i(m\theta - \omega t)}, \tag{39}$$

where it is understood that the real part of this quantity must be evaluated to get to the real quantity $p(r,t)$.

Again, note that the driving frequencies which produce infinite response are the resonant frequencies of the rigid wall toroid for the case of $n = 0$. Since Δ_m is independent of the angular phase velocity, this resonance occurs at the characteristic frequencies regardless of the value of Ω, even if an integral number of wavelengths does not fit in the toroid. This means that although the walls are moving (that is, they are not rigid) the amplitude of the sound in the fluid will depend mostly on the intrinsic speed of sound, which appears in the function Δ_m. Such a result in a tube with passive walls can only occur when the walls are rigid, which for the case of dense fluids (i.e., liquids), is often very difficult to obtain.

Consider the case of $k_r a \neq \beta_{mp}$ such that the velocity potential remains finite. If the ratio of the angular frequency to the angular phase velocity is such that $\omega/\Omega = q$, where q is an integer, then

$$\Phi \propto \sum_{m=-\infty}^{\infty} \frac{\sin(q-m)\pi}{(q-m)\pi} = \delta_{qm}. \tag{40}$$

This means only the angular wave number corresponding to $m = q$ will contribute to the velocity potential; Φ will represent a traveling wave. Such a wave will have an amplitude that is independent of angular position, and a phase difference between any two positions corresponds to the propagation time for the driven wave in the fluid.

If $\omega/\Omega \approx m$, the dominant term in the sum in Eq. (38) is the one corresponding to that value of m, with small contributions from other angular wave numbers. In this case, the sound in the duct is no longer a pure traveling wave, but it is also not a pure standing wave. However, if the choice of ω/Ω is such that the contribution of sound due to $m < 0$ is the same as that for $m > 0$, then the result will be that of a standing wave inside the toroid.

D. Cross-sectional geometries

The choice of theoretically describing the torus with a rectangular cross section was made because the wave equation in toroidal coordinates is not separable. On the other

hand, it is experimentally more convenient to build a toroid with a circular cross section. The following addresses the plausibility of comparing the theoretical case of a rectangular cross section to experimental results obtained from a circular cross section.

It has been shown in Sec. II A that for wavelengths long compared to the width of the toroid, the shape of the bend can be ignored. Therefore, the toroid can be thought of as an infinitely long tube with a driven wall that is periodic along the center axis. In a thermally conducting tube filled with a viscous fluid, the propagation characteristics of sound in pores[19–21] can be expressed in terms of the characteristic pore radius, given as twice the transverse pore area divided by the pore perimeter. For a circular cross section it is the radius r and for a rectangular cross section of height a and width b, the characteristic pore radius is $ab/(a+b)$. If $a=b=2r$, then both geometries will have the same value. In the wide tube limit, the boundary layer is only a small fraction of the cross-sectional area, so the difference in geometry would only affect the attenuation. In the next section it will be shown that this difference is unimportant.

Therefore, the propagation characteristics of sound in both cases will be the same. A similar result was also observed experimentally by Cummings[13] in curved tubes with rectangular and circular cross sections.

E. Attenuation

In order to compare theory to experiment, it is necessary to include losses in the ideal solution. One way that this is done is by considering the wave number in the fluid to be complex. Once the value of this wave number is determined, Eq. (39) can be used to solve for the pressure in the toroid.

The complex wave number can be written as

$$\overline{k}=k-i\alpha, \tag{41}$$

where α is the *absorption coefficient* and $k=\omega/c$. The sources of attenuation are the various mechanisms that take energy out of the system. In the case of the relatively soft walled plastic tubing used in the acoustitron (see Sec. III) the loss due to the yielding tube wall is much greater than the viscous and thermal losses within the gas inside the tube. This yielding wall loss is given by[22]

$$\alpha=\mathrm{Re}\left(\frac{\rho_0 c}{Z}\right)\frac{1}{a}, \tag{42}$$

where a is the inside radius of the tube, a' is the radius to the center of the wall, and

$$Z=\frac{\rho_0 c}{a\alpha_{CW}^R}+i\left(\frac{\mathrm{Re}(Y)T}{aa'\omega}-\omega\rho_\omega T\right). \tag{43}$$

If α is plotted versus frequency, its maximum value $\alpha_R=\rho_0 c/Z_r$ occurs at ω_0. Then in terms of ω_0 and α_R, the absorption is given by[23]

$$\alpha=\alpha_R\left[1+\left(\frac{\rho_w}{\rho_0}\right)^2\left(\frac{\omega\alpha_R}{c}\right)^2\left(\frac{a}{a'}\frac{\omega_0^2}{\omega^2}-1\right)^2\right]^{-1}, \tag{44}$$

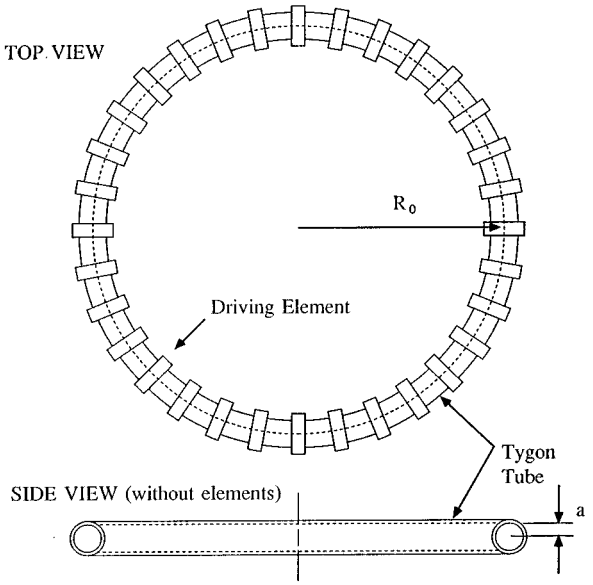

FIG. 2. The acoustitron.

where ρ_w is the density of the wall. The resonant frequency in terms of Young's modules is given by, $\omega_0=\sqrt{\mathrm{Re}(Y)/aa'\rho_w}$.

II. EXPERIMENT

To verify the theoretical results for sound propagation in a toroidal waveguide with driven walls, a device was built that is called an *acoustitron*. It consisted of a length of Tygon® tubing (''TYGON'' is a registered trademark of Norton Company) with the ends connected to form a torus. Mounted around the outside were 32 evenly spaced piezoceramic rings (poled in the radial direction) as shown in Fig. 2. The radius, R_0, was 19.40 cm and the inside tube radius, a, was 1.27 cm. Each element was glued to the torus to maximize the coupling between the driver and the tube wall.

Sound pressure measurements were made using a Brüel & Kjær $\frac{1}{8}$ in. microphone (type 4138) inserted through an airtight opening in the wall of the tube. The protective grille was carefully removed and the microphone diaphragm was positioned flush with the tube wall so it was perpendicular to the z axis in the z plane bisecting the torus. A Hewlett-Packard 35665A signal analyzer was configured to record the sound pressure level (SPL) measured with the microphone.

A digital delay circuit was constructed to drive the 32 acoustitron elements with a specific time delay between elements. The circuit produces 32 analog output signals from a single input signal from either an external analog source, or an internal programmed waveform. For the case of external input, the analog signal was received through an 8-bit analog-to-digital converter and loaded into the high speed memory of a Texas Instruments TMS320C30 Digital Signal Processor (DSP) located inside an IBM-PC compatible computer. Software consisted of a PC-side program that allowed the parameters to be set in the DSP, and a DSP-side program which controlled the operation of the DSP.

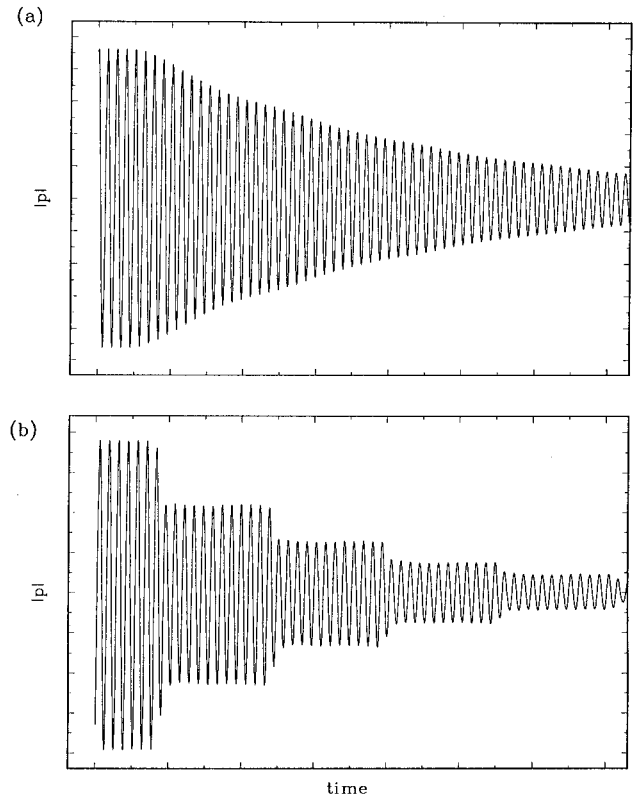

FIG. 3. Examples of decay measured for the case of (a) a traveling wave in the acoustitron and (b) a standing wave produced by a single driving element.

III. RESULTS

A. Entire driven wall

Measurements of the pressure amplitude as a function of frequency and Ω/Ω_0 were made, where $\Omega = c/R_0$, and Ω_0 was the angular phase velocity corresponding to the intrinsic speed of sound in the medium, which for this experiment was $\Omega_0 = 1773$ rad/s. This ratio is analogous to an angular Mach number. As pointed out in theory, the peaks in the response of the acoustitron correspond to the characteristic frequencies of a rigid wall toroid with identical dimensions. From the frequency positions of the peaks and the known circumference of the acoustitron, the intrinsic speed of sound in the fluid can be determined using Eqs. (7) and (8).

The value of α was measured as a function of frequency by measuring the decay of waves inside the toroid. Figure 3(a) shows the decay of a traveling wave and Fig. 3(b) the decay of a standing wave produced by driving a single element half the circumference away from the observing microphone. For the standing wave case, the driving frequency was 12 times the fundamental frequency and the microphone was located approximately opposite the driving element. Therefore the number of cycles in the first step is about 6, and the remainder of the steps is exactly 12. The driving frequency used in both cases was about 3900 Hz. Figure 4 shows the plot of α versus frequency. Shown also is the plot of Eq. (44) with values of α_R and ω_0 adjusted to fit the curve.

For the case of traveling waves, the absorption coefficient for the driving frequency was determined by fitting an exponential curve to the pressure peaks in the region of decay. For the standing wave case, the absorption coefficient was determined using $\ln(A_2/A_1)/C$ where A_1 and A_2 were the amplitudes of adjacent steps with $A_2 > A_1$, and C was the circumference corresponding to R_0.

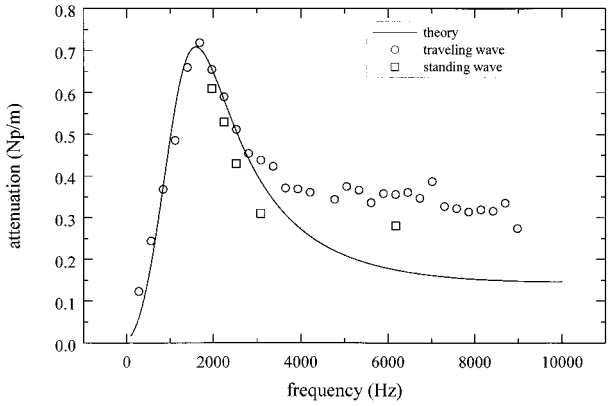

FIG. 4. Measured values of absorption coefficient in the acoustitron along with theory. The frequencies plotted as circles correspond to traveling waves inside the acoustitron. Standing wave values are plotted as squares.

An approximate value for V_0 was obtained by measuring the displacement of the tube wall at three different positions between two driving elements with a laser Doppler vibrometer. At low frequencies the amplitude was nearly independent of frequency. The value of V_0 used in Eq. (39) was 1.0×10^{-9} m/V.

The SPLs calculated by Eq. (39) are plotted as functions of frequency for three different values of Ω/Ω_0 (0.85, 1.0, and 1.2) and shown in Figs. 5–7 . The complex k_r is obtained as explained above from Eq. (41). Shown also are the experimental curves. For $\Omega \geqslant \Omega_0$, the predicted SPLs match the measured SPLs quite well for all frequencies. For $\Omega < \Omega_0$, theoretical and experimental data match well for low frequencies, but deviations are apparent at higher frequencies, the lower the Ω the more the deviation. The reason for this is as follows. Recall that the boundary condition used in the theoretical case was that of a continuously driven wall where the wave number in the fluid was equal to the wave

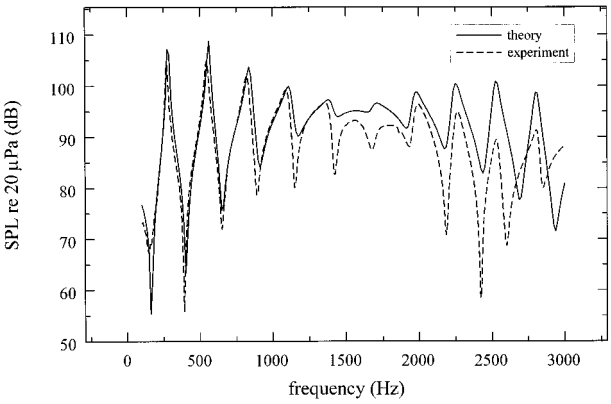

FIG. 5. Comparison of predicted to measured values of the sound pressure level inside the acoustitron for $\Omega/\Omega_0 = 0.85$.

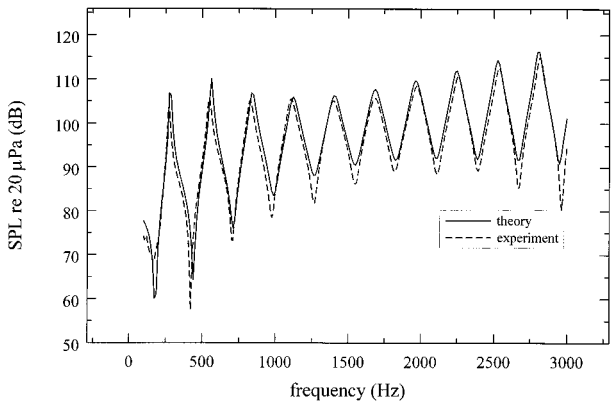

FIG. 6. Comparison of predicted to measured values of the sound pressure level inside the acoustitron for $\Omega/\Omega_0=1.00$.

number in the wall. In the experimental tube, however, driving elements are spaced a finite distance apart. As Ω decreases, the speed of the wave in the wall decreases, and for a fixed frequency, the wavelength decreases. This means that there are fewer elements per wavelength so that the wall appears more like a series of point drivers separated by passive walls instead of a continuously driven wall derived in theory.

B. Traveling waves

The theoretical solution for the sound pressure in a toroid with driven walls shows that if the ratio of the angular phase velocity Ω and the angular frequency ω of the driven wall is an integer, the resulting sound wave will be a traveling wave. This is equivalent to saying that there are an integral number of wavelengths along the circumference of the toroid. For traveling waves, the amplitude of the sound wave is independent of position and the phase shift measured between two locations in the tube corresponds to the propagation time between them.

There are two straightforward methods for experimentally finding combinations of ω and Ω that produce traveling waves in the acoustitron. One method is to record the complex pressure at two different positions in the acoustitron at a

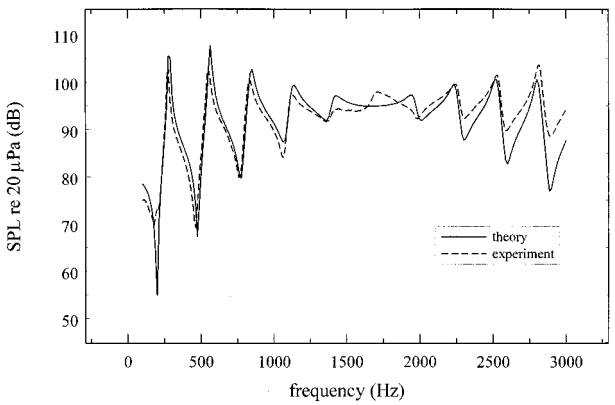

FIG. 7. Comparison of predicted to measured values of the sound pressure level inside the acoustitron for $\Omega/\Omega_0=1.20$.

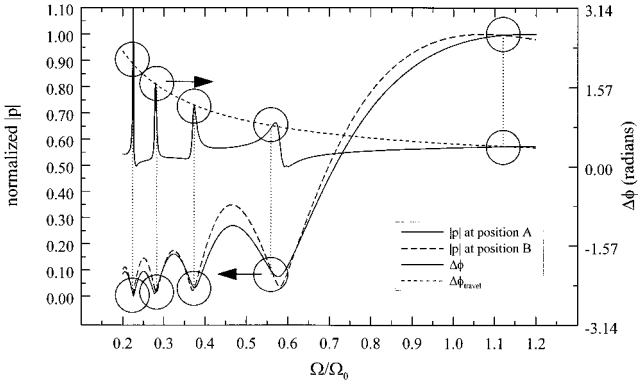

FIG. 8. Theoretical comparison of the complex pressure at two arbitrary positions (labeled A and B) inside the acoustitron.

given frequency as a function of angular phase velocity. The presence of traveling waves can then be observed by looking for values of Ω/Ω_0 that produce identical amplitudes and a phase difference equal to the propagation time for the speed of the wave in the wall. A theoretical example of this method is shown in Fig. 8 which consists of the theoretical complex pressure at two different positions along θ inside the acoustitron for an arbitrary frequency. These plots were generated using Eq. (39).

A second method for detecting traveling waves is to record the frequency dependence of the sound pressure at different positions in the acoustitron for a given angular phase velocity. The traveling waves can then be determined by looking for values of frequency that produce identical amplitudes at all positions. As seen in Fig. 8, it is possible to match pressure amplitudes at two different positions, yet not have a traveling wave. The graph shows the magnitude $|p|$ and the phase difference $\Delta\phi_{\text{travel}}$ of the pressure at both positions as functions of angular phase velocity. The line labeled as $\Delta\phi_{\text{travel}}$ is the phase difference corresponding to the propagation time determined by Ω. The values of Ω/Ω_0 that produce traveling waves are indicated by circles. By taking measurements at unevenly spaced angular positions, the need to check for the proper phase is eliminated. Both of these methods are suitable for making the desired measurements.

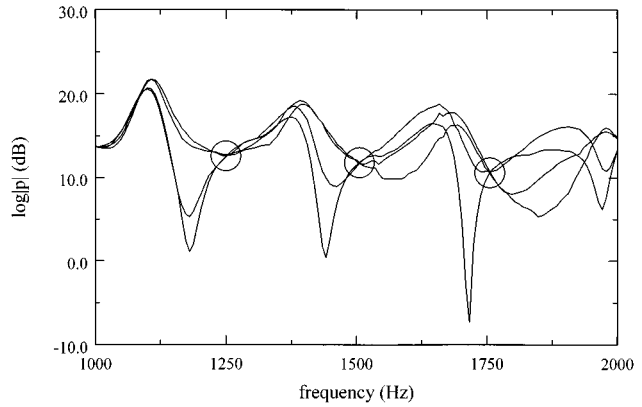

FIG. 9. Experimental values of the magnitude of the pressure at four different positions inside the acoustitron. The frequencies that yield traveling waves are indicated by circles, where $\Omega/\Omega_0=0.9$.

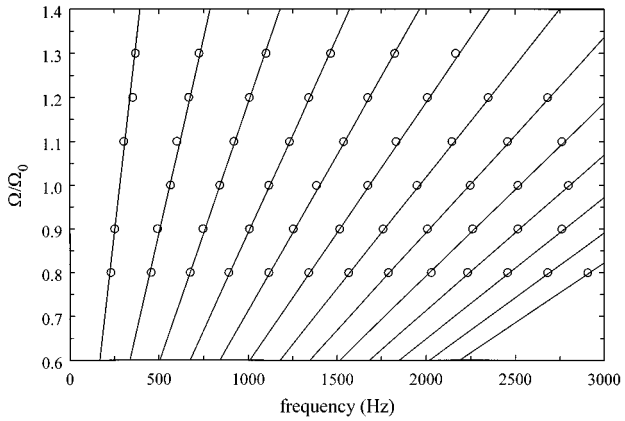

FIG. 10. Comparison of theoretical (solid lines) and experimental (empty circles) results for combinations of frequency and angular phase velocity that yield traveling waves in the acoustitron.

In this study, it was easier to sweep frequencies than to sweep angular phase velocities.

In order to make measurements at different positions inside the acoustitron, the element receiving output from the first output channel was varied, effectively ''moving'' the microphone around the tube. An example of sound pressures measured in the acoustitron at various microphone positions is shown in Fig. 9. Frequencies at which the sound pressure is the same at all four positions, i.e., a traveling wave, can be clearly seen in this data set. This data set is typical of all others used to produce Fig. 10.

Figure 10 shows experimentally determined combinations of Ω and ω that produced traveling waves in the acoustitron. (Error bars are approximately the size of the symbols used in the plot.) Theoretically predicted values, which are determined from $\Omega = \omega n$, where n is an integer, are indicated by the solid lines. It is clear from this data that traveling waves are occuring at combinations of frequencies and angular phase velocities as predicted by theory.

IV. CONCLUSION

The theory for sound propagation in a toroidal waveguide with driven walls has been presented. The general result was expressed in terms of walls driven with an arbitrary angular dependence. For the simple case of a single driving element, the resulting sound in the toroid corresponds to standing waves at specific determined frequencies. For the case of a wall driven with a controllable wave number and frequency, the sound wave produced in the toroid ranges from a traveling wave (when Ω/ω is an integer), to a standing wave (when the sum of the Fourier amplitudes for $m < 0$ are equal to those for $m > 0$). When these conditions are not met, the sound wave inside the toroid is a combination of both traveling and standing waves.

An acoustitron was built to experimentally verify the latter case, and the results are well represented by theory. The existence of traveling waves when $\Omega/\omega = n$ was specifically demonstrated.

ACKNOWLEDGMENTS

The authors wish to thank Frank Lacy for his work with the electronics and his programming of the DSP, and David Blackstock for his interest and invaluable assistance. Useful discussions with Robin Cleveland, Mark Hamilton, and Steve Garrett are gratefully appreciated. This work was supported by the Office of Naval Research.

[1] G. Kirchhoff, ''Ueber den Einflufs der Warmeleitung in einem Gase auf die Schallbewegung,'' Ann. Phys. Chem. **134**, 177–193 (1868).
[2] J. W. Strutt (Lord Rayleigh), *The Theory of Sound* (Dover, New York, 1945), 2nd ed., Vol. 2, Section 348–350.
[3] H. Tijdeman, ''On the propagation of sound waves in cylindrical tubes,'' J. Sound Vib. **39**, 1–33 (1975).
[4] T. C. Lin and G. W. Morgan, ''Wave propagation through fluid contained in a cylindrical, elastic shell,'' J. Acoust. Soc. Am. **28**, 1165–1176 (1956).
[5] V. A. Del Grosso, ''Errors in ultrasonic propagation parameter measurements. Part 4—Effect of finite thickness solid tubes enclosing the liquid cylinder of interest,'' Naval Research Laboratory Technical Report No. 6852, Naval Research Laboratory, Washington, DC, 1958.
[6] W. C. Osborne, ''Higher mode propagation of sound in short curved bends of rectangular cross-section,'' J. Sound Vib. **45**, 39–52 (1976).
[7] M. El-Raheb, ''Acoustic propagation in rigid three-dimensional waveguides,'' J. Acoust. Soc. Am. **67**, 1924–1930 (1980).
[8] W. Rostafinski, ''On the propagation of long waves in curved ducts,'' J. Acoust. Soc. Am. **52**, 1411–1420 (1972).
[9] W. Rostafinski, ''Analysis of propagation of waves of acoustic frequencies in curved ducts,'' J. Acoust. Soc. Am. **56**, 11–15 (1974).
[10] F. E. Grigor'yan, ''Theory of sound wave propagation in curvilinear waveguides,'' Sov. Phys. Acoust. **14**, 315–321 (1969).
[11] M. El-Raheb and P. Wagner, ''Acoustic propagation in a rigid torus,'' J. Acoust. Soc. Am. **71**, 1335–1346 (1982).
[12] S. H. Ko and L. T. Ho, ''Sound attenuation in acoustically lined curved ducts in the absence of fluid flow,'' J. Sound Vib. **53**, 189–201 (1977).
[13] A. Dummings, ''Sound transmission in curved duct bends,'' J. Sound Vib. **35**, 451–477 (1974).
[14] D. T. Blackstock (private communication).
[15] D. T. Blackstock, ''High intensity sound research, 1961–1978,'' Applied Research Laboratories Technical Report No. ARL-TR-79-36, Applied Research Laboratories, The University of Texas at Austin, 21 June 1979, pp. 8–9.
[16] P. E. Krasnushkin, ''Waves in curved tubes,'' Uch. Zap. Mosk. Gos. Univ., No. 75, Bk. 2, Pt. 2, 9–27 (1945).
[17] G. N. Watson, *A Treatise on the Theory of Bessel Functions* (Cambridge U.P., Cambridge, 1962).
[18] J. W. Strutt (Lord Rayleigh), *The Theory of Sound* (Dover, New York, 1945), 2nd ed., Vol. 2, Section 263.
[19] W. P. Arnott, H. E. Bass, and R. Raspet, ''General formulation of thermoacoustics for stacks having arbitrarily shaped pore cross sections,'' J. Acoust. Soc. Am. **90**, 3228–3237 (1991).
[20] M. R. Stinson and Y. Champoux, ''Propagation of sound and the assignment of shape factors in model porous materials having simple pore geometries,'' J. Acoust. Soc. Am. **91**, 685–695 (1992).
[21] M. R. Stinson, ''The propagation of plane sound waves in narrow and wide circular tubes, and generalization to uniform tubes of arbitrary cross-sectional shape,'' J. Acoust. Soc. Am. **89**, 550–558 (1991).
[22] P. M. Morse, *Vibration and Sound* (American Institute of Physics, Woodbury, New York, 1981), 2nd ed., p. 307.
[23] C. C. Lawrenson, Ph.D. thesis, The University of Mississippi, 1994.

Cancellation model of pitch perception[a)]

Alain de Cheveigné
Laboratoire de Linguistique Formelle, CNRS/Université Paris 7, 2 place Jussieu, case 7003, 75251, Paris, France and ATR Human Information Processing Research Laboratories, 2-2 Hikaridai, Seikacho, Soraku-gun, Kyoto 619-02, Japan

(Received 7 May 1997; accepted for publication 13 October 1997)

A model of pitch perception is presented involving an array of delay lines and inhibitory gating neurons. In response to a periodic sound, a *minimum* appears in the pattern of outputs of the inhibitory neurons at a lag equal to the period of the sound. The position of this minimum is the cue to pitch. The model is similar to the autocorrelation model of pitch, multiplication being replaced by an operation similar to subtraction, and maxima by minima. The two models account for a wide class of pitch phenomena in very much the same way. The principal goal of this paper is to demonstrate this fact. Several features of the cancellation model may be to its advantage: it is closely related to the operation of harmonic cancellation that can account for segregation of concurrent harmonic stimuli, it can be generalized to explain the perception of multiple pitches, and it shows a greater degree of sensitivity to phase than autocorrelation, which may allow it to explain certain phenomena that autocorrelation cannot account for. [S0001-4966(98)00902-3]

PACS numbers: 43.10.Ln, 43.66.Ba, 43.66.Hg, 43.64.Bt [JWH]

INTRODUCTION

The autocorrelation model of pitch perception dates back to Licklider's ''duplex'' model of pitch perception (Licklider, 1951, 1956, 1959, 1962). Licklider imagined a network of delay lines and coincidence counters arranged along two axes: frequency (inherited from peripheral filtering) and delay (over the range of periods that can evoke pitch). The network calculated an array of autocorrelation functions (ACF), one for each channel of the peripheral filter. In response to a periodic tone, activity within the network was greatest along a ''ridge'' spanning the frequency dimension at a lag equal to the period. [An example of a similar pattern produced by the model of Meddis and Hewitt (1991a, b) is displayed in Fig. 3(a).]

Despite its appeal, Licklider's model fell on a blind spot of auditory theory. For many years, favor went mainly to the ''pattern matching'' models of pitch perception of Wightman (1973), Terhardt (1974), and Goldstein (1973), in spite of the fact that they are tributary to a high-resolution spectral analysis (also present in Licklider's model, but of secondary importance). They also require explicit pattern matching mechanisms: Fourier transformation in the case of Wightman (1973), and learning in the case of Terhardt (1974), whereas pattern matching comes ''for free'' in Licklider's model. In his model, the fundamental period is calculated simply by looking across channels for a peak common to several channels, and this operation succeeds whether individual components are resolved within channels or not. Pattern matching models are not specific about how pattern matching is implemented physiologically, whereas Licklider's model is both specific and reasonably plausible.

Licklider's model lacked a precise rule to derive a quantitative pitch estimate. This was repaired by Meddis and Hewitt (1991a, b; Meddis and O'Mard, 1997), who chose perhaps one of the simplest possible rules: the autocorrelation pattern is summed across the frequency dimension to obtain a summary autocorrelation function (SACF) and the pitch is derived from the first major peak in this function (the ''period peak'') [Fig. 4(a)]. Meddis and Hewitt also undertook the task of simulating the behavior of their model in response to a set of stimuli that evoke pitch phenomena important for pitch theory (missing fundamental, pitch shifts of inharmonic complexes, etc.). This helped dispel several common misconceptions, such as that the ACF might be excessively sensitive to phase if calculated in the time domain, or on the contrary excessively *insensitive* to phase. The hair cell transduction model of Meddis (1988) included in the simulation of their pitch model was instrumental in demonstrating second-order effects such as phase sensitivity that may arise in a physiologically realistic implementation of the autocorrelation model. The ''pitch dominance region,'' of crucial importance for the thesis of pattern matching, emerged in their model as a consequence of the relative weights of low- versus high-frequency channels, and the breakdown of neural firing synchrony at high frequencies. This was corroborated by Cariani and Delgutte (1996a, b), who recorded from the auditory nerve of the cat in response to a range of stimuli important for auditory theory, and showed that in most cases the pitch could be readily derived from the shape of autocorrelation histograms (ACH).

The ACH (or all-order interspike interval histogram) used by Cariani and Delgutte is a relatively recent way of processing recordings from auditory neurons (Ruggero, 1973; Boerger, 1974; Evans, 1983; Shofner, 1991). More common has been the first-order interspike interval histogram (ISIH) (Rose *et al.*, 1967). The abundance of physiological data reported in this format led to several models similar to those of Licklider or Meddis and Hewitt (1991a, b), but using arrays of ISIHs rather than autocorrelation functions (Moore, 1977; van Noorden, 1982).

[a)]''Selected research articles'' are ones chosen occasionally by the Editor-in-Chief that are judged (a) to have a subject of wide acoustical interest, and (b) to be written for understanding by broad acoustical readership.

Licklider's model has inspired computational models of pitch (Lyon, 1984; Lazzaro and Mead, 1989; Slaney, 1990) and auditory scene analysis (Lyon, 1983; Weintraub, 1985; Cooke, 1991; Brown, 1992; Meddis and Hewitt, 1992; Lea, 1992) involving two-dimensional autocorrelation arrays. The array is usually summed across the frequency dimension to obtain a summary function similar to the SACF of Meddis and Hewitt. This summary ACF is close in shape to the ACF of the *raw waveform*, and the latter can be used as a simpler model of similar predictive power (Yost, 1996; Yost *et al.*, 1996). The pulse-ribbon and strobed auditory integration (SAI) models of Patterson (Patterson, 1987; Patterson *et al.*, 1992) are related to autocorrelation. The SAI is in effect the cross correlation between the neural response within each channel with a strobe signal consisting of a single pulse per stimulus period, and the pattern it produces is visually quite similar to autocorrelation.

In its modern form(s), the autocorrelation model of pitch appears to becoming accepted to the same degree as ''pattern-matching'' models. Nevertheless it is not altogether without problems. For one thing, there is as yet little evidence of a two-dimensional autocorrelation map organized according to frequency and lag, despite some evidence for amplitude modulation maps in the inferior colliculus of the cat (Langner and Schreiner, 1988; Langner, 1992). Licklider (1959) noted, however, that an orderly layout should not necessarily be expected. More generally, there is not strong evidence of delay lines of sufficient duration (up to 10–20 ms). This weakness is not entirely specific to autocorrelation. Other models require elements not very different from delay lines (the SAI's signal buffer, for example), or else are rather vague about the physiological operations that they would involve (a ''Fourier transformer,'' for example). It would be unfair to fault autocorrelation for making its requirements explicit. In favor of autocorrelation is evidence for the closely related cross-correlation model of binaural interaction (Jeffress, 1948) found in the MSO and IC of the cat (Yin and Chan, 1990; Yin *et al.*, 1987) and equivalent centers in the owl (Konishi *et al.*, 1988).

Autocorrelation is also difficult to reconcile with some aspects of pitch perception. It works equally well for stimuli consisting of unresolved harmonics as for resolved harmonics, yet there is evidence that the resolved harmonics dominate the pitch percept (Houtsma, 1995). Pitches from resolved and unresolved channels should be readily comparable, yet Carlyon and Shackleton (1994) found that such is not the case. Kaernbach and Demany (1996) found that the pitch of high-pass filtered pulse trains depended on the statistics of first-order intervals between pulses, rather than all-order intervals as one would expect based on autocorrelation.

Another example that the AC model does not readily account for is the difference in percept evoked by certain time-reversed stimuli. Patterson (1994a, b) presented subjects with stimuli consisting of sine-wave carriers shaped with repeated ''damped'' (exponential decay) or ''ramped'' envelopes (same shape, but time reversed). Examples are shown in Fig. 9. The carrier frequency is 800 Hz, the repetition rate 40 Hz, and the half-time (time to it takes for the wave to decrease by half) is a 4 ms. These stimuli will be used later on in this paper for illustration purposes. Both evoked a pitch corresponding to the sine wave carrier, but the pitch was much stronger for ramped than for damped sine waves. The two stimuli have identical spectra and autocorrelation functions, and the AC model does not readily explain why they evoke different sensations.

Despite these problems, the AC model remains a good first-order model, attractive in terms of simplicity, explanatory power, and physiological plausibility. The purpose of this paper is to point out that a similar model can be obtained by replacing the multiplication by subtraction (or excitatory by inhibitory neural interaction). This new model will be referred to loosely as the ''cancellation model of pitch perception.'' The equivalence between autocorrelation and cancellation is illustrated for three variants of the AC model (waveform based, discharge probability based, spike based). On the strength of this equivalence we may assume that major pitch phenomena explainable by autocorrelation models (Meddis and Hewitt, 1991a, b; Cariani and Delgutte, 1996a, b; Yost *et al.*, 1996) are equally well explained by their cancellation counterparts.

Although cancellation and autocorrelation pitch models are equivalent to a first approximation, several features of cancellation make it attractive. For one, cancellation is a flexible and powerful ''building block'' in that it leaves a residue that may be analyzed in turn, in a succession of estimate–cancel–estimate operations. For another, the way cancellation may be implemented physiologically makes it relatively sensitive to time reversal, and this might account for the time-order-dependent phenomena reported by Patterson (1994a, b).

I. SUBTRACTION VERSUS MULTIPLICATION AT THE WAVEFORM LEVEL

The autocorrelation function of a waveform $s(t)$ may be understood as the result of applying a kind of nonlinear ''filter'' to the waveform

$$P_\tau(t) = s(t)s(t-\tau) \tag{1}$$

and then integrating over time

$$\mathrm{ACF}(\tau) = \int_{-\infty}^{\infty} P_\tau(\theta)\, d\theta. \tag{2}$$

In practice the summation is usually performed over a sliding window to obtain a running autocorrelation function indexed by time:

$$\mathrm{ACF}_t(\tau) = \int_{-\infty}^{t} w(\theta - t) P_\tau(\theta)\, d\theta, \tag{3}$$

where $w(\theta - t)$ is a window function that emphasizes values near t. The integration can be seen as a kind of low-pass filter that smooths the quantity $P_\tau(t)$ so that the ACF pattern does not fluctuate too much over time.

As an example, let us consider a waveform made up of ten equal amplitude harmonics of 200 Hz in sine phase (Fig. 1). The ACF of this waveform is shown in Fig. 2(a). The ACF shows peaks at the origin and at 5 ms, period of the

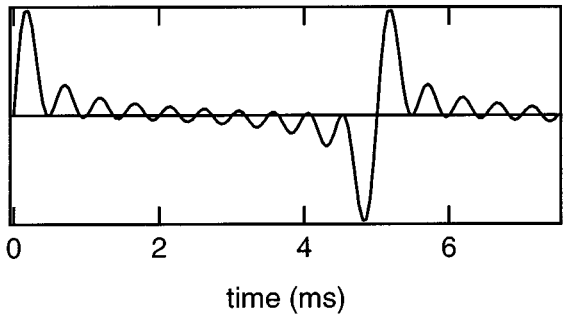

FIG. 1. Waveform consisting of the first ten harmonics of 200 Hz added with equal amplitudes in sine phase.

waveform, as well as at multiples of 5 ms (not visible in the figure). The position of the first ''period peak'' is the cue to the pitch according to models of pitch perception based on the autocorrelation function of the waveform (Yost, 1996). In this example, summation was performed over a square window covering two periods of the waveform (10 ms). In general, in this paper, integration windows are chosen so as to minimize fluctuation of the pattern (ACF or other) over time, rather than according to psychophysical or physiological estimates. If the windows were chosen too short (for example, shorter than the fundamental period), the shape of the pattern would differ according to where in time it was sampled, with the risk of inconsistent or misleading conclusions. A model using short windows is incomplete unless it specifies how such a ''pulsating'' pattern is processed to obtain a relatively stable percept such as pitch.

The product of $s(t)$ and $s(t-\tau)$ may be replaced by their squared difference $D_\tau(t)=[s(t)-s(t-\tau)]^2$ to obtain an average ''squared difference function'' (SDF):

$$\mathrm{SDF}_t(\tau)=\int_{-\infty}^{t} w(\theta-t)D_\tau(\theta)\,d\theta. \tag{4}$$

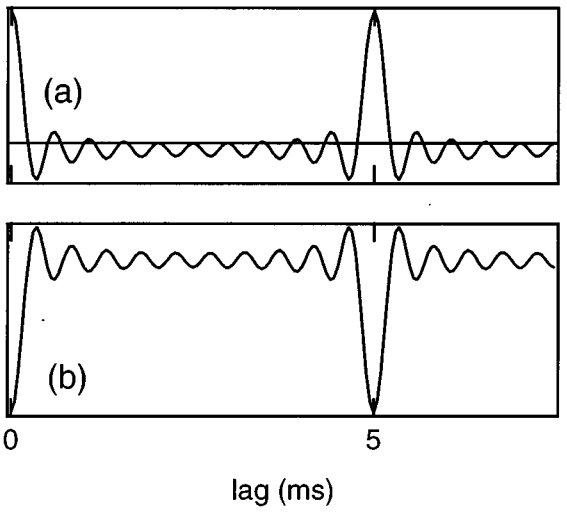

FIG. 2. (a) Running autocorrelation function (ACF) of the waveform of Fig. 1, calculated over a 10-ms window. (b) Average squared difference function (SDF) of the same waveform.

Figure 2(b) shows an example of this function calculated using the same window as for the ACF. The SDF looks like a mirror image of the ACF. Whereas the ACF showed a peak at the origin and at the period (and its multiples), the SDF shows dips in those positions. In fact, $D_\tau(t)$ and $P_\tau(t)$ are related:

$$D_\tau(t)=s^2(t)+s^2(t-\tau)-2s(t)s(t-\tau) \tag{5}$$

$$=P_0(t)+P_0(t-\tau)-2P_\tau(t) \tag{6}$$

implying a similar relation between SDF and ACF. If the integration window is large enough, fluctuations of $\mathrm{ACF}_t(0)$ with t are small and we have

$$\mathrm{SDF}_t(\tau)=2[\mathrm{ACF}_t(0)-\mathrm{ACF}_t(\tau)]. \tag{7}$$

Comparing Fig. 2(a) and (b), it is clear that the SDF could replace the ACF as the basis of a pitch perception model, if the ''pitch peak'' cue were replaced by a ''pitch valley'' cue. A pattern similar to the SDF might arise within a coincidence network like that of Licklider, but involving *inhibitory* rather than excitatory interaction between time-domain patterns of neural activity. This idea is explored in more detail in the next two sections.

It should be noted that the SDF is closely related to the average magnitude difference function (AMDF) that has been used to estimate the fundamental frequency (F_0) of speech (Ross *et al.*, 1974). The difference between the two, apart from the discrete sample notation, is that the AMDF sums absolute values whereas the SDF sums their squares:

$$\mathrm{AMDF}_i(\tau)=\sum_{j=i}^{i+N} |s(j)-s(j-\tau)|. \tag{8}$$

II. SUBTRACTION VERSUS MULTIPLICATION OF DISCHARGE PROBABILITY

Instead of the waveform, we consider discharge probability within each channel of a model of peripheral filtering and hair-cell transduction (Meddis and Hewitt, 1988). Following the model of Meddis and Hewitt (1991a, b), the ACF of each probability function was calculated to obtain a pattern of activity over two dimensions: characteristic frequency (inherited from peripheral frequency analysis) and the lag dimension of the autocorrelation function. Figure 3(a) shows the pattern evoked by the previous pulse train. A ''ridge'' is visible at 5 ms, period of the waveform, as well as at the origin. If the ACFs are summed across channels, the resulting summary autocorrelation function (SACF) shows a peak at 5 ms [Fig. 4(a)]. The position of this ''period peak'' is the cue to pitch in Meddis and Hewitt's (1991a, b) pitch perception model. In this example the ACF used a 10-ms square integration window rather than the 2.5-ms exponential window used by Meddis and Hewitt.

The ACF pattern might represent the activity across a neural network of delay lines and coincidence neurons in which direct and delayed spike trains interact in *excitatory* fashion. It is possible to imagine a similar network in which the spike trains would interact in *inhibitory* fashion. For example, a coincidence detector might fire with a probability

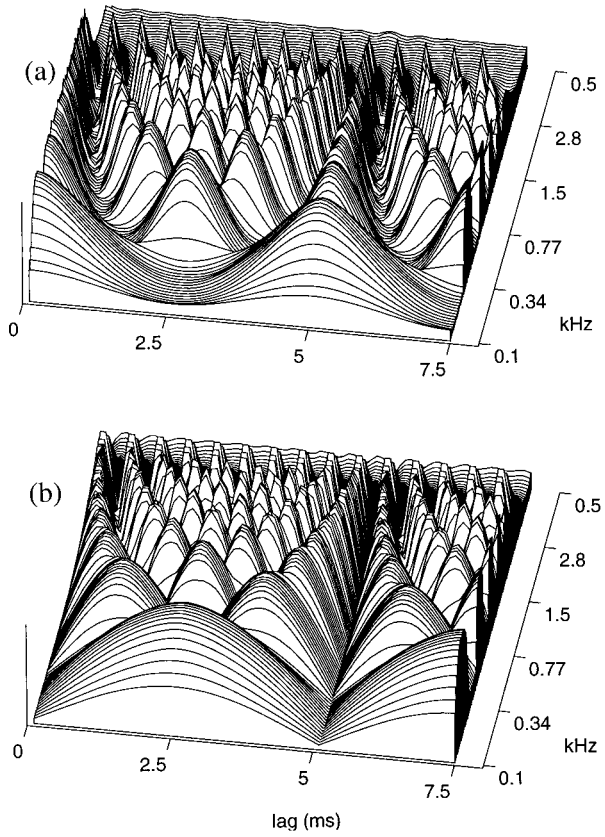

FIG. 3. (a) Array of autocorrelation functions calculated from discharge probabilities produced by a model of peripheral filtering and transduction in response to the waveform of Fig. 1. There are 100 channels, spaced uniformly between 100 and 5000 Hz on an ERB scale. (b) Array of average half-wave rectified difference functions (RDF) in response to the same waveform.

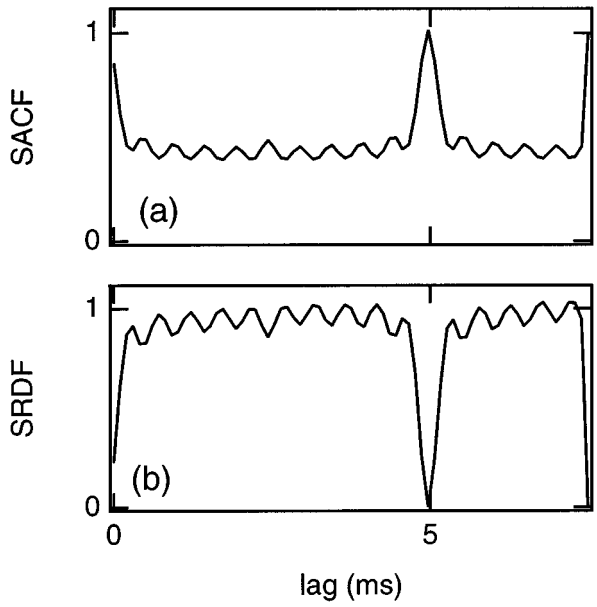

FIG. 4. (a) Summary autocorrelation function (SACF) in response to the waveform of Fig. 1. (b) Summary average half-wave rectified difference functions (SRDF) in response to the same waveform.

proportional to the difference between spike densities along direct and delayed pathways, as assumed in the ''neural cancellation filter'' of de Cheveigné (1997a):

$$R_\tau(t) = \max(0, s(t) - s(t-\tau)), \tag{9}$$

where $s(t)$ and $R_\tau(t)$ are instantaneous firing probability densities at the input and output of the cancellation filter, respectively. The half-wave rectifying max ( ) operation reflects the fact that probabilities cannot be negative [the firing probabilities $s(t)$ themselves are approximate versions of the half-wave rectified basilar membrane motion, so half-wave rectification occurs twice within the model]. The activity within an array of such filters, indexed by delay, may be represented by a function similar to the SDF, but in which the squared difference is replaced by a *half-wave rectified* difference. We denote this average ''rectified difference function'' as RDF:

$$\mathrm{RDF}_t(\tau) = \int_{-\infty}^{t} w(t-\theta) R_\tau(\theta)\, d\theta. \tag{10}$$

Figure 3(b) shows the pattern evoked by the previous pulse train. A ''valley'' is visible at 5 ms, period of the waveform, as well as at the origin. If the RDFs are summed across channels, the resulting summary half-wave rectified difference function (SRDF) shows a dip at 5 ms [Fig. 4(b)]. The position of this ''period dip'' could be taken as the cue to pitch, resulting in a pitch perception model very similar to that of Meddis and Hewitt (1991a, b). It is interesting to note that, for a perfectly periodic stimulus such as this one, the background-to-dip ratio is infinite for the SRDF, whereas the peak-to-background ratio is finite (about 2 in this case) for the SACF.

Equation (9) represents a hypothetical gating neuron that fires with a probability proportional to the *difference* of firing probabilities at its excitatory and inhibitory synapses. More general interaction may be easier to model explicitly with spike trains, either recorded physiologically or generated by a stochastic spike generation model. That is the subject of the next section.

III. INHIBITORY VERSUS EXCITATORY COINCIDENCE COUNTING

A. Spike generation model

Instead of the raw waveform, or discharge probabilities, we consider spike trains produced by a model of spike generation, driven by probability functions produced by the previous model of peripheral filtering and haircell transduction. Spike times were generated stochastically according to an inhomogeneous Poisson process with a refractory period (Schroeder and Hall, 1974; Johnson, 1980; Johnson and Swami, 1983; Carney, 1993). The model produces lists of ''spike'' times similar to those recorded in physiological experiments. Histograms (peristimulus, period, interval, autocorrelation) derived from model spike data are similar to those reported in the literature, suggesting that the model reproduces the essential aspects of spike train statistics.

Figure 5(a) shows an example of an autocorrelation histogram (ACH) derived from the 500-Hz channel of the model in response to 100 repetitions of a 100-ms portion of

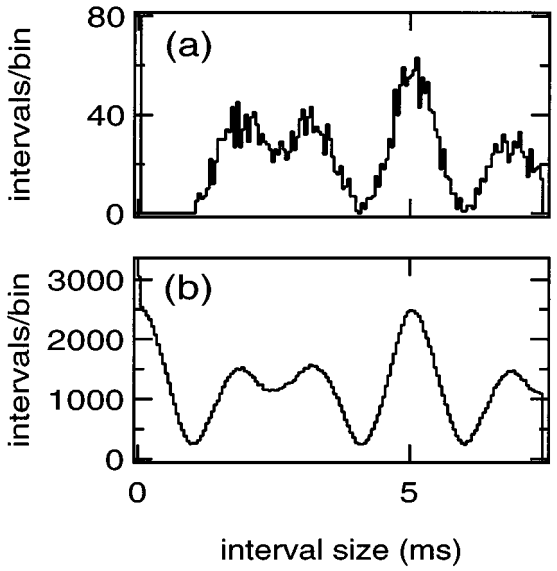

FIG. 5. (a) Autocorrelation histogram (ACH) of a single-fiber spike train produced by the spike generation model in response to the waveform of Fig. 1. The ''fiber's'' characteristic frequency was 500 Hz, and the histogram was calculated from 100 repetitions of the 100-ms stimulus. The first 20 ms of each spike train were discarded to remove the onset transient response. Bin width is 100 μs. (b) The ACH calculated from the same data, sorted to simulate the activity of 100 fibers of similar characteristics. Note the reduced ''noise,'' and the lack of the gap due to refractory effects.

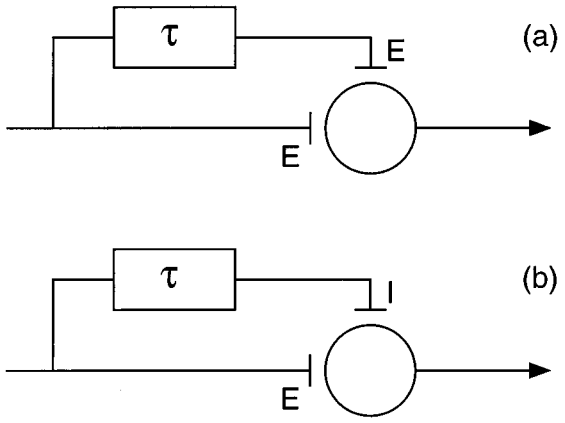

FIG. 6. (a) Excitatory gating neuron. The neuron fires if spikes arrive simultaneously along the direct and delayed pathways. (b) Inhibitory gating neuron. The neuron fires if a spike arrives along the direct path, unless a spike arrives simultaneously along the delayed path.

the waveform displayed in Fig. 1 (the initial 20 ms of each spike train were discarded to eliminate the transient response at onset). The ''gap'' below 1 ms is due to the refractory period, and the peak at 5 ms reflects the period of the waveform. This histogram reflects the statistics of intervals between spikes within a *single* fiber. It is reasonable to assume that the auditory system might take into account interspike intervals within a *group* of similar fibers, as this makes more efficient use of the available information. In practice, the interval statistics of a group of N similar fibers can be simulated by taking the list of spike times for N presentations of the stimulus to the same fiber (time being measured relative to stimulus onset), and sorting it. Figure 5(b) shows a histogram obtained after sorting spike data in this fashion. The ''spikes'' are the same as displayed in Fig. 5(a), but the ACH is less noisy and lacks a gap at short intervals. The sorted-spike ACH is equivalent to the autocorrelation of the peristimulus histogram (PST) (Palmer, 1992)

The sample at zero in Fig. 5(b) counts coincidences of spikes ''with themselves,'' and is equal to the number of spikes in the spike train. This sample is often not represented in histograms of neural data, but its presence is congruent with the definition of autocorrelation. In Fig. 5(a) the value of that bin (3048) is outside the range of the graph. The value of the zero lag bin does not depend on bin width, whereas that of all other bins does. The prominence of this bin relative to the rest of the histogram thus depends on bin width.

B. Excitatory coincidence network

Licklider's (1951) model involved an array of coincidence or gating neurons similar to the one schematized in Fig. 6(a). The neuron fires if and only if spikes arrive simultaneously via direct and indirect pathways (with a certain tolerance). More precisely, each spike arriving along the delayed pathway opens a ''window'' during which a spike arriving along the direct pathway may be transmitted. In our simulation the window was square and its duration was 0.05 ms (exponential windows were also tested with roughly similar results). Sorted spike trains produced by the spike generator were fed to an array of gating neurons covering a range of delays from 0 to 7.5 ms with 0.02-ms resolution. The number of spikes transmitted as a function of delay is displayed in Fig. 7(a). This plot is similar in aspect to the autocorrelation histogram [Fig. 5(b)]. The size of the coincidence window determines the relative height of the sample at zero lag.

If a similar simulation is performed in other channels

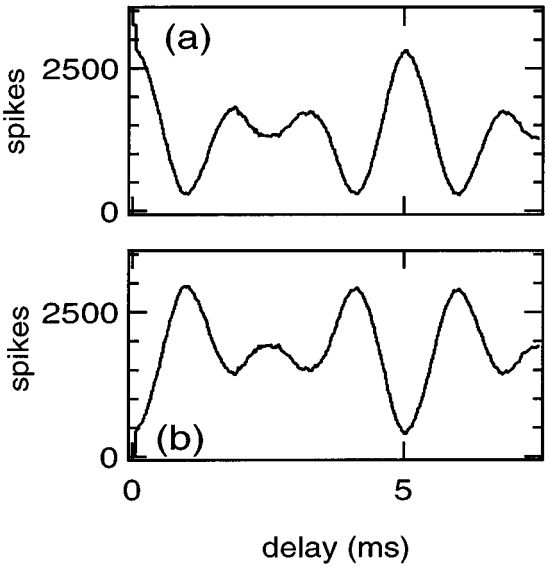

FIG. 7. (a) Pattern of activity at the output of an array of excitatory gating neurons [Fig. 6(a)] in response to the waveform of Fig. 1. The channel's characteristic frequency is 500 Hz. The coincidence window is square with a width of 0.05 ms. Delays are sampled with a resolution of 0.02 ms. (b) Pattern of activity at the output of an array of inhibitory gating neurons [Fig. 6(a)] in response to the same waveform. Parameters are the same as for (a).

(not shown), a peak appears at the same position (5 ms), as predicted by Licklider and verified by Cariani and Delgutte (1996a, b) with recordings from the auditory nerve.

C. Inhibitory coincidence network

The excitatory gating neuron of Fig. 6(a) may be replaced by the inhibitory gating neuron of Fig. 6(b). Each spike arriving along the delayed pathway opens a ''window'' during which a spike arriving along the direct pathway will *not* be transmitted. An array of such inhibitory gating neurons was simulated with the same data and similar parameters as for the excitatory network. The result is plotted in Fig. 7(b). The pattern is the mirror image of that plotted in Fig. 7(a). The dip at 5 ms can serve as a cue to the pitch of the stimulus, playing the same role as the peak in Fig. 7(a). The size of the coincidence window determines the depth of this dip.

In summary, in each version of the AC model, multiplication can be replaced by subtraction (or excitatory gating by inhibitory gating) to produce an equivalent cancellation model. To a first approximation the behavior is the same, and these cancellation-based models can account for the same class of pitch effects as their autocorrelation-based counterparts. In addition to the examples reported here, the models were simulated with a variety of stimuli (missing fundamental, inharmonic complexes, synthetic vowels, rippled noise, etc.). Peaks and dips generally occurred at the same positions for autocorrelation and cancellation, although in some cases there were differences in the strength of the pitch cue (Sec. IV B).

IV. WHY SUBTRACT?

So far we have emphasized the similarity between models based on multiplication and subtraction. Why then consider the latter, given that autocorrelation models are successful and well established? To the extent that the two are equivalent, a cancellation-based model may be regarded as an alternative implementation of its autocorrelation-based counterpart. Even if it performs no better than autocorrelation, cancellation offers a fresh perspective. Physiologists might find use for a model in which *minima* of activity are given the importance usually attributed to maxima. In addition, cancellation is a flexible ''building block'' for auditory modelling, and its implementation implies properties that might explain second-order effects that AC models have difficulty accounting for.

A. Cancellation as a building block of auditory processing

There is evidence, from experiments on concurrent vowel identification, that concurrent harmonic sounds are segregated by a mechanism of *cancellation* of harmonic interference. Although other models of harmonic cancellation have been proposed (Meddis and Hewitt, 1992), one effective way to perform the operation is with a ''neural'' filter similar to that illustrated in Fig. 6 or defined by Eq. (9) (de Cheveigné, 1993, 1997a). Harmonic cancellation requires an estimate of the period of the interference. While this can be obtained from a variety of period-estimation models, for example ACF based, it is expedient to derive it from the cancellation filter itself, by searching for a minimum of Eq. (10) as a function of its parameter τ (de Cheveigné, 1997a). Given that the period-estimation principle is successful in that context, it makes sense to apply it also to pitch perception.

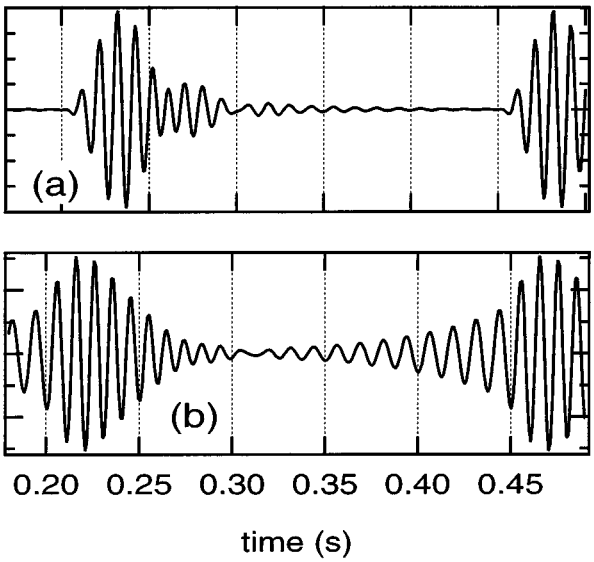

FIG. 8. (a) Damped sine wave stimulus filtered by a gammatone filter of center frequency 1040 Hz. (b) Same for the ramped sine wave.

Harmonic cancellation may also be used to build a model of the perception of *multiple pitches* evoked by concurrent periodic sounds. The situation is common in music when several instruments play together, and trained listeners can accurately estimate the pitches of concurrent periodic sounds, even if there are no differences in onset or spectral envelope (Nordmark, 1978). Multiple periods may be estimated recursively in a succession of estimate–cancel–estimate steps, or in parallel according to a joint cancellation algorithm. The principle was applied with success to F_0 estimation of pairs of natural spoken voices by de Cheveigné (1993), who found that it was superior to several other two-period estimation algorithms. It can be generalized to an arbitrary number of concurrent periodic signals (de Cheveigné and Kawahara, 1997). Examples of the effectiveness of harmonic cancellation for reinforcing the representation of a nondominant period may be found in de Cheveigné (1993, 1997a). If cancellation-based estimation can successfully handle multiple pitches, it makes sense to invoke it in the limit case of a single pitch. A link between harmonic sound segregation and pitch (though not necessarily via this model) was an ingredient of a model that explained the pitch shifts of mistuned partials observed by Hartmann and Doty (1996) (de Cheveigné, 1997b).

Harmonic cancellation allows interfering components to be ''peeled away'' from a target, but it can also serve another purpose. Responses of single peripheral channels to stimuli with transient waveforms show ringing effects due to basilar membrane filtering. This is illustrated in Fig. 8 for a 1040-Hz channel responding to the damped and ramped stimuli that we mentioned before (Fig. 9). This corresponds to a channel

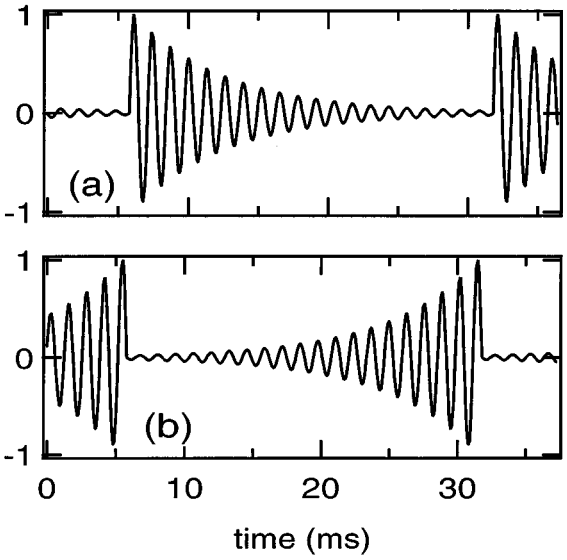

FIG. 9. (a) ''Damped'' sine wave stimulus as used by Patterson (1994a, b). Carrier frequency is 800 Hz, modulation frequency is 40 Hz, and half-life is 4 ms. (b) Similar ''ramped'' sine wave stimulus.

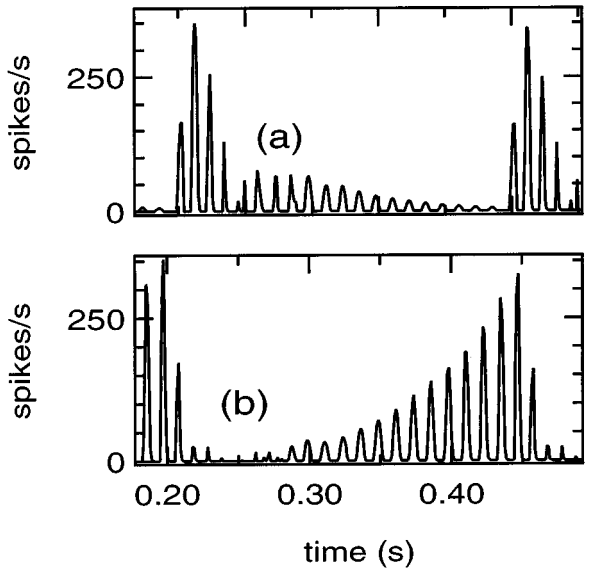

FIG. 10. (a) Damped sine wave stimulus filtered by a gamma tone filter of center frequency 1040 Hz, followed by a hair cell model, followed by a cancellation filter tuned to 0.962 ms (period of the gammatone filter center frequency). (b) Same for the ramped sine wave.

tuned slightly higher than the 800-Hz carrier (cf. Figs 6 and 7 of Patterson, 1994a). The response to the ramped stimulus [Fig. 8(b)] can be decomposed into two intervals: an interval of ringing excited by the sharp offset of the previous ramp, with a periodicity of about 1040 Hz, and an interval of gradual onset of the current ramp, with a periodicity of 800 Hz. The response to the damped stimulus is more complex: ringing and stimulus interact throughout the modulation period. The auditory system faces a difficult problem in analyzing such patterns in the time domain, as they reflect both the stimulus and less interesting resonance characteristics.

Certain models incorporate schemes to remove the effects of ringing. Weintraub (1985) subtracted from the 2-D autocorrelation pattern the same pattern obtained in response to white noise. The response to noise reflects only basilar membrane filtering, and subtracting it was expected to remove some effects of filter ringing. The Patterson–Holdsworth software suite (Patterson *et al.*, 1992) includes a temporal adaptation stage designed to reduce the effects of ringing (Holdsworth, 1990). Additionally in that model, as in multichannel autocorrelation models (Meddis and Hewitt, 1991a, b), ringing effects within individual channels are averaged out by summation over channels.

Ringing effects can also be removed by harmonic cancellation. Figure 10(a) represents the basilar membrane filter response of Fig. 8(a) filtered by a cancellation filter tuned to 0.962 ms (inverse of the gammatone filter's center frequency). Figure 10(b) shows the same processing in the case of the ramped stimulus. Suppression of ringing effects is evident in both cases. The fine structure of the response reflects the stimulus carrier (800 Hz) and its envelope resembles that of the stimulus. There is no evidence of the filter's ringing periodicity. It is perhaps premature to include a ''ringing suppressor'' in every model of auditory processing, but this example illustrates well the power and flexibility of cancellation as a building block for neural ''signal processing'' models.

It is interesting to note the following modification that may be of use in the case of an amplitude-varying stimulus or impulse response:

$$R'_\tau(t) = \max(0, s(t) - \alpha s(t-\tau)). \tag{11}$$

A value of $\alpha < 1$ is sufficient to suppress a decreasing signal, whereas a value greater than 1 is required to suppress a ramped signal. The extra parameter compromises parsimony, but the auditory system (supposing it employs this form of time-domain cancellation) might find such fine tuning useful.

Cancellation has been proposed as a mechanism to explain binaural release from masking (Durlach's Equalization-Cancellation model, 1963).

B. Temporal asymmetry

The product $P_\tau(t) = s(t)s(t-\tau)$ summed in the ACF is symmetric in $s(t)$ and $s(t-\tau)$ [Eq. (3)]. The ACF is therefore not affected by a reversal of the time axis. The same is true of the SDF that sums the squared difference [Eq. (4)]. Therefore, neither can account for the greater pitch strength of ramped versus damped stimuli observed by Patterson (1994a, b). The hair cell transduction stage used by Meddis and Hewitt (1991a, b) introduces a certain degree of sensitivity to temporal asymmetry, but Irino and Patterson (1996) showed that it is insufficient to account for the asymmetry in pitch strength. Based on the relative insensitivity of the ACF to time reversal, Patterson (1994b) argued in favor of the strobed temporal integration (STI) process incorporated in his auditory image model (AIM) (Patterson *et al.*, 1995). However, Irino and Patterson (1996) showed that a sensitivity to temporal asymmetry may be the consequence of a variety of other ''delta-gamma'' processes that arise at various stages of auditory processing. The delta-gamma operator em-

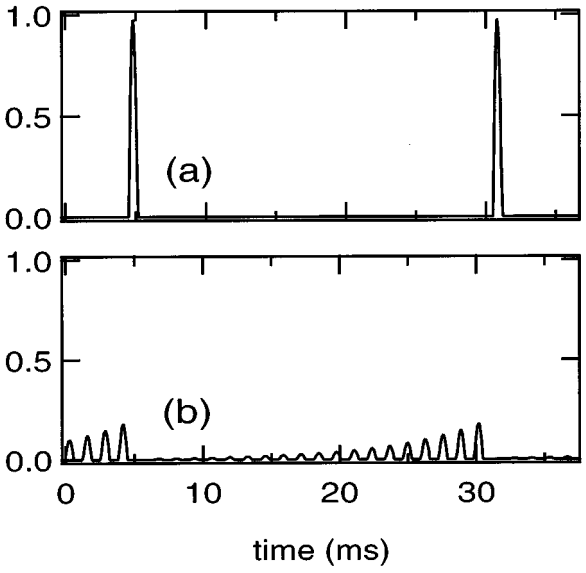

FIG. 11. (a) Cancellation filter output for an input consisting of a half-wave-rectified damped sine wave. Lag is 1.25 ms (period of the 800-Hz carrier). (b) Same for the ramped sine wave. The vertical scale of both graphs was normalized by dividing by the peak output observed in the damped case.

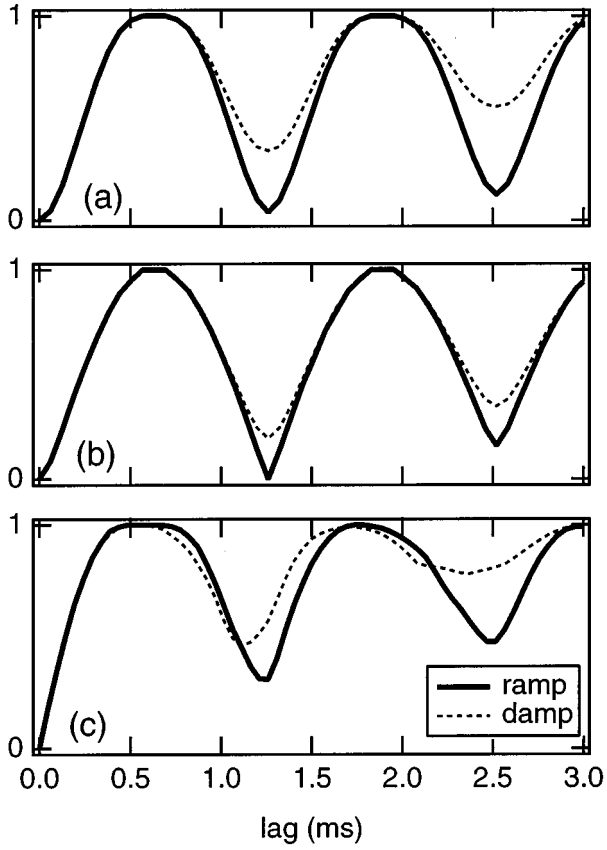

FIG. 12. (a) Modified RDF for a ramped (full line) or damped (dotted line) sine wave. The RDF was modified by raising $R_\tau(t)$ to the square before integration. It was calculated from the half-wave rectified waveform (no filtering or haircell transduction). (b) Same, but the RDF was modified by replacing $R_\tau(t)$ by $R'_\tau(t)$ [Eq. (11)] with $\alpha=1.3$. (c) The RDF calculated from a single channel of the basilar membrane model tuned to 1040 Hz with ringing suppression, in response to the ramped (full line) and damped (dotted line) stimuli. The channel was processed by half-wave rectification followed by a cancellation filter tuned to 1040 Hz (ringing suppression), followed by the unmodified RDF.

phasizes the portion of signals for which the derivative of the envelope is positive rather than negative. It turns out that the half-wave rectified difference $R_\tau(t)$ involved in the RDF model has such a property.

The effect of a time reversal is illustrated in the case of the ramped and damped stimuli in Fig. 11, for a delay of 1.25 ms, period of the 800-Hz carrier. For this illustration, the quantity $R_\tau(t)$ was calculated directly from the half-wave rectified stimulus waveform, to avoid compounding effects of basilar membrane filtering and haircell transduction. For the damp, the first peak of each resonance is reflected in $R_\tau(t)$, but each successive peak falls in the ''shadow'' of its predecessor and is suppressed. The result is a single pulse per modulation period. For the ramped signal (b), $R_\tau(t)$ is a ramped series of pulses at the period of the carrier. When peripheral filtering is included the picture is less clear, but it remains true that $R_\tau(t)$ is asymmetric and sensitive to time reversal. The consequences of this asymmetry depend upon other details of the model. It turns out the RDF itself, as defined in Eq. (10) is *not* sensitive to a time reversal, despite the strong asymmetry of the quantity $R_\tau(t)$ that it integrates.

There are at least three ways by which the asymmetry can be reintroduced. One is to replace $R_\tau(t)$ by its square before summation. This is illustrated in Fig. 12(a). The dips in the RDF are deeper for the ramped stimulus (full line) than for the damped stimulus (dotted line). If pitch strength is a function of the depth of the pitch cue, the pitch should be stronger for ramped than for damped stimuli, as observed by Patterson (1994a, b). Note that if a compressive nonlinearity were applied before integration instead of a expansive nonlinearity (square), the opposite asymmetry would have resulted.

A second way to reintroduce an asymmetry is to replace $R_\tau(t)$ by $R'_\tau(t)$, as defined in Eq. (11), with a value of α greater than 1. This is illustrated in Fig. 12(b). The dips in the RDF are considerably deeper for ramped than for damped stimuli. Again, the opposite asymmetry would have resulted if $\alpha<1$. A third way to introduce temporal asymmetry is to assume ringing suppression as described in Sec. IV A. As evident in Fig. 10, the ramped waveform is more successfully salvaged than the damped waveform. This results again in deeper dips in the RDF for ramped than for damped stimuli [Fig. 12(c)].

In order to determine whether such asymmetries might be sufficient to account for the experimental results of Irino and Patterson (1996), ramped stimuli of half-lives 4, 8, 16, and 32 ms were matched by damped stimuli with half-lives chosen to produce the same depth of the period cue, according to the procedure of Irino and Patterson. An asymmetry factor was calculated using their equation. The first scheme [Fig. 12(a)] yielded a value of 2.16, close to the value of 2.3 observed experimentally for sinusoidal carriers. For the second scheme [Fig. 12(b)], it was impossible to find a damped stimulus long enough to match the extremely deep period dip obtained for ramps. There is no upper limit to the asymmetry

factors that can be ''predicted'' with this scheme. Finally, the third scheme [Fig. 12(c)], based on a single 1040-Hz channel, yielded an asymmetry factor of 0.95, and other channels yielded similar values. The values of these three schemes bracket those observed experimentally.

In conclusion, the ''neural cancellation filter'' is inherently sensitive to a time reversal, and this can readily result in a difference in the strength of pitch cues. The ACF is by definition insensitive to phase, although hair-cell adaptation and transduction introduce a certain degree of phase sensitivity in practice. A short integration window also causes phase dependencies, but a model based on a short window is not properly defined unless it specifies how the fluctuating pattern (ACF or other) should be sampled in time. Differences in sensitivity to phase are a minor exception to our main conclusion that ACF and cancellation models are equivalent and can be used interchangeably.

V. SUMMARY

Multiplication or excitatory neural interaction as used in the family of autocorrelation models of pitch perception can be replaced by subtraction or inhibitory neural interaction to form a corresponding family of cancellation models. The behavior of the models is the same to a first approximation, and cancellation models can account for much the same set of pitch phenomena as autocorrelation models. To a second approximation, the cancellation models differ in some ways from their autocorrelation counterparts. Whereas autocorrelation is largely phase insensitive, cancellation-based models show a sensitivity to phase that may allow them to account for phenomena such as the different sensations evoked by stimuli reversed in time. Cancellation is more flexible as a ''building block'' for auditory processing than multiplicative or excitatory interaction, as it leaves a ''residue'' that can be analyzed in turn. Cancellation models can thus be built to account for the perception of multiple pitches evoked by concurrent harmonic sounds such as simultaneous musical notes. Harmonic cancellation seems to be a major mechanism underlying F_0-guided segregation, and it makes sense to assume that the other main ''client'' of periodicity, namely pitch, is derived from a cancellation-based mechanism. Indeed, given that the need for sound segregation is probably older and more important for survival than musical pitch perception, one could speculate that pitch might be a ''spin-off'' of mechanisms that evolved for the purpose of sound segregation.

The cancellation model has the same requirement of delay lines as does the AC model (and also neural cancellation models of F_0-guided segregation), and the lack of physiological evidence for these delay lines is a major problem. It is conceivable that the delay lines exist but that technical difficulties prevent recording from them directly. It is also possible that patterns involving *minima* of activity were overlooked by researchers expecting maxima. If so, the different perspective taken by the present model might be of use in future investigations.

What sets the AC model apart from the pattern matching models of Wightman (1973), Terhardt (1974), and Goldstein (1973) is not so much its principle of time-domain periodicity estimation as the fact that it does not require a separate stage of pattern matching. For ''unresolved'' channels the pitch cue is obtained directly from the ACF and from ''resolved'' channels it is obtained by simple comparison or summation of ACFs across channels. Pattern matching is often thought of as being based on place cues, but this is not essential. Goldstein and Srulovicz (1977) suggested that the spectral pitches required for pattern matching could be determined from auditory nerve fiber interspike interval statistics, measured by ISI histograms. The ISI histogram can be replaced advantageously in this role by the AC histogram, and autocorrelation in turn might be replaced by cancellation, to form a pattern-matching model in which spectral pitch cues are cancellation based. The advantage of cancellation over the AC or ISI histograms in this context is that partials that are too close to be resolved by peripheral filtering might be resolved within channels by the multiple period estimation version of the cancellation model. That is important if one is to account for the perception of the pitches of concurrent sounds, whose partials may be very close in frequency. The disadvantage of this proposition, relative to the AC model or the models discussed in Secs. I–III, is of course that it leaves out entirely the issue of how pattern matching is performed. On the other hand, as periods of most harmonics are shorter than the fundamental period, the problem of delay lines is somewhat eased.

Carlyon (1996, 1997) found that two concurrent sounds restricted to a spectral region where their components were not resolvable (3900–5400 Hz) did not evoke two pitches. This contradicts, at least in those conditions, our proposal that several periods may be determined within the same channel. Carlyon has investigated other situations in which perceptual acuity differs between stimuli made of ''unresolved'' components (high frequency and/or closely spaced) and those made of ''resolved'' components (low frequency and/or widely spaced). Performance on pitch tasks is usually best for the latter, and comparison between the two may be poor (Carlyon and Shackleton, 1994). All this argues against a single mechanism that treats all spectral regions alike, such as the AC model or the models of Secs. I–III, and rather in favor of a pattern-matching mechanism for the resolved region (for how else can we explain the importance of resolution?). By ''resolved,'' it is usually understood that peripheral filters are sufficiently sharp to resolve partials of each sound *by itself.* It is not clear how this property might extend to partials of sounds that are mixed, in particular with small F_0 differences (ΔF_0). In one concurrent vowel experiment, a ΔF_0 of 0.4% improved identification of a vowel that was 15 dB weaker than its competitor. In another, a ΔF_0 of 3% improved identification of a vowel that was 25 dB weaker than its competitor (de Cheveigné, 1997c). In such difficult conditions, it is hard to imagine a partial of the weaker vowel being isolated within any channel, and this casts doubt on whether ''resolvable'' partials are actually resolved when F_0-guided segregation occurs. Within the context of the neural cancellation model that Sec. III is based upon, the advantage of the region of ''resolved partials'' might be explained by the fact that neural cancellation is imperfect, and better performed after a first step of linear analysis has improved

the signal-to-noise ratio (see also Meddis and O'Mard, 1997 for another explanation). It is clear that this issue requires more investigation.

ACKNOWLEDGMENTS

Simulation of gammatone filtering and hair cell transduction was based on Malcolm Slaney's ''Auditory Toolbox'' Matlab code (Slaney, 1993). Minoru Tsuzaki, Peter Cariani, John Culling, Bob Carlyon, Bill Yost, and Ray Meddis made useful comments on earlier versions of the manuscript.

Boerger, G. (**1974**). ''Coding of repetition pitch in the cochlear nucleus of the cat,'' in *Facts and Models in Hearing*, edited by E. Zwicker and E. Terhardt (Springer-Verlag, Berlin), pp. 206–215.

Brown, G. J. (**1992**). ''Computational auditory scene analysis: a representational approach,'' Sheffield, Department of Computer Science, unpublished doctoral dissertation.

Cariani, P. A., and Delgutte, B. (**1996a**). ''Neural correlates of the pitch of complex tones. I. Pitch and pitch salience,'' J. Neurophysiol. **76**, 1698–1716.

Cariani, P. A., and Delgutte, B. (**1996b**). ''Neural correlates of the pitch of complex tones. II. Pitch shift, pitch ambiguity, phase-invariance, pitch circularity, rate-pitch and the dominance region for pitch,'' J. Neurophysiol. **76**, 1717–1734.

Carlyon, R. P. (**1996**). ''Encoding the fundamental frequency of a complex tone in the presence of a spectrally overlapping masker,'' J. Acoust. Soc. Am. **99**, 517–524.

Carlyon, R. (**1997**). ''The effects of two temporal cues on pitch judgments,'' J. Acoust. Soc. Am. **102**, 1097–1105.

Carlyon, R. P., and Shackleton, T. M. (**1994**). ''Comparing the fundamental frequencies of resolved and unresolved harmonics: Evidence for two pitch mechanisms?,'' J. Acoust. Soc. Am. **95**, 3541–3554.

Carney, L. H. (**1993**). ''A model for the responses of low-frequency auditory-nerve fibers in cat,'' J. Acoust. Soc. Am. **93**, 401–417.

Cooke, M. P. (**1991**). ''Modelling auditory processing and organisation,'' Sheffield, Department of Computer Science, unpublished doctoral dissertation.

de Cheveigné, A. (**1993**). ''Separation of concurrent harmonic sounds: Fundamental frequency estimation and a time-domain cancellation model of auditory processing,'' J. Acoust. Soc. Am. **93**, 3271–3290.

de Cheveigné, A. (**1997a**). ''Concurrent vowel segregation III: A neural model of harmonic interference cancellation,'' J. Acoust. Soc. Am. **101**, 2857–2865.

de Cheveigné, A. (**1997b**). ''Harmonic fusion and pitch shifts of inharmonic partials,'' J. Acoust. Soc. Am. **102**, 1083–1087.

de Cheveigné, A. (**1997c**). ''Ten experiments in concurrent vowel segregation,'' ATR Human Information Processing Research Labs, Tech. Rep. TR-H-217.

de Cheveigné, A., and Kawahara, H. (**1997**). ''Modeling the perception of multiple pitches,'' Proc. IJCAI Workshop on Computational Auditory Scene Analysis, Nagoya (August 1997) (a preliminary draft is available at: http://www.hip.atr.co.jp/~alain/ijcai97.ps).

Durlach, N. I (**1963**). ''Equalization and cancellation theory of binaural masking-level differences,'' J. Acoust. Soc. Am. **35**, 1206–1218.

Evans, E. F. (**1983**). ''Pitch and cochlear nerve fibre temporal discharge patterns,'' in *Hearing—Physiological Bases and Psychophysics*, edited by R. Klinke and R. Hartmann (Springer-Verlag, Berlin), pp. 140–146.

Goldstein, J. L. (**1973**). ''An optimum processor theory for the central formation of the pitch of complex tones,'' J. Acoust. Soc. Am. **54**, 1496–1516.

Goldstein, J. L., and Srulovicz, P. (**1977**). ''Auditory-nerve spike intervals as an adequate basis for aural frequency measurement,'' in *Psychophysics and Physiology of Hearing*, edited by E. F. Evans and J. P. Wilson (Academic, London), pp. 337–347.

Hartmann, W. M., and Doty, S. L. (**1996**). ''On the pitches of the components of a complex tone,'' J. Acoust. Soc. Am. **99**, 567–578.

Holdsworth, J. (**1990**). ''Two dimensional adaptive thresholding,'' APU AAM-HAP Report, Vol. 1, Annex 4, MRC APU, Cambridge.

Houtsma, A. J. M. (**1995**). ''Pitch perception,'' in *Hearing*, edited by B. C. J. Moore (Academic, London), pp. 267–295.

Irino, T., and Patterson, R. (**1996**). ''Temporal asymmetry in the auditory system,'' J. Acoust. Soc. Am. **99**, 2316–2331.

Jeffress, L. A. (**1948**). ''A place theory of sound localization,'' J. Comp. Physiol. Psychol. **41**, 35–39.

Johnson, D. H. (**1980**). ''The relationship between spike rate and synchrony in responses of auditory-nerve fibers to single tones,'' J. Acoust. Soc. Am. **68**, 1115–1122.

Johnson, D. H., and Swami, A. (**1983**). ''The transmission of signals by auditory-nerve fiber discharge patterns,'' J. Acoust. Soc. Am. **74**, 493–501.

Kaernbach, C., and Demany, L. (**1996**). ''Psychophysical evidence against the autocorrelation theory of pitch perception'' (submitted).

Konishi, M., Takahashi, T. T., Wagner, H., Sullivan, W. E., and Carr, C. E. (**1988**). ''Neurophysiological and anatomical substrates of sound localization in the owl,'' in *Auditory Function–Neurobiological Bases of Hearing*, edited by G. M. Edelman, W. E. Gall, and W. M. Cowan (Wiley, New York), pp. 721–745.

Langner, G. (**1992**). ''Periodicity coding in the auditory system,'' Hearing Res. **60**, 115–142.

Langner, G., and Schreiner, C. E. (**1988**). ''Periodicity coding in the inferior colliculus of the cat. I. Neuronal mechanisms,'' J. Neurophysiol. **60**, 1799–1822.

Lazzaro, J., and Mead, C. (**1989**). ''Silicon modeling of pitch perception,'' Proc. Natl. Acad. Sci. USA **86**, 9597–9601.

Lea, A. (**1992**). ''Auditory models of vowel perception,'' Nottingham University, unpublished doctoral dissertation.

Licklider, J. C. R. (**1951**). ''A duplex theory of pitch perception,'' Experientia **7**, 128–134.

Licklider, J. C. R. (**1956**). ''Auditory frequency analysis,'' *Information Theory*, edited by C. Cherry (Butterworth, London), pp. 253–268.

Licklider, J. C. R. (**1959**). ''Three auditory theories,'' in *Psychology, a Study of Science*, edited by S. Koch (McGraw-Hill, New York), Vol. I, pp. 41–144.

Licklider, J. C. R. (**1962**). ''Periodicity pitch and related auditory process models,'' Int. Audiol. **1**, 11–36.

Lyon, R. (**1984**). ''Computational models of neural auditory processing,'' IEEE ICASSP, 36.1(1–4).

Meddis, R. (**1988**). ''Simulation of auditory-neural transduction: further studies,'' J. Acoust. Soc. Am. **83**, 1056–1063.

Meddis, R., and Hewitt, M. J. (**1991a**). ''Virtual pitch and phase sensitivity of a computer model of the auditory periphery. I: Phase identification,'' J. Acoust. Soc. Am. **89**, 2866–2882.

Meddis, R., and Hewitt, M. J. (**1991b**). ''Virtual pitch and phase sensitivity of a computer model of the auditory periphery. II: Phase sensitivity,'' J. Acoust. Soc. Am. **89**, 2883–2894.

Meddis, R., and Hewitt, M. J. (**1992**). ''Modeling the identification of concurrent vowels with different fundamental frequencies,'' J. Acoust. Soc. Am. **91**, 233–245.

Meddis, R., and O'Mard, L. (**1997**). ''A unitary model of pitch perception,'' J. Acoust. Soc. Am. **102**, 1811–1820.

Moore, B. C. J. (**1977**). *An Introduction to the Psychology of Hearing* (Academic, London) (reprinted in 1996).

Nordmark, J. O. (**1978**). ''Frequency and periodicity analysis,'' in *Handbook of Perception, Vol. IV—Hearing*, edited by E. C. Carterette and P. P. Friedman (Academic, New York), pp. 243–282.

Palmer, A. R. (**1992**). ''Segregation of the responses to paired vowels in the auditory nerve of the guinea-pig using autocorrelation,'' in *Audition Speech and Language*, edited by M. E. H. Schouten (Mouton-DeGruyter, Berlin), pp. 115–124.

Patterson, R. D. (**1987**). ''A pulse ribbon model of peripheral auditory processing,'' in *Auditory Processing of Complex Sounds*, edited by W. A. Yost and C. S. Watson (Erlbaum, Hillsdale, NJ), pp. 167–179.

Patterson, R. D. (**1994a**). ''The sound of a sinusoid: time-domain models,'' J. Acoust. Soc. Am. **94**, 1419–1428.

Patterson, R. D. (**1994b**). ''The sound of a sinusoid: spectral models,'' J. Acoust. Soc. Am. **96**, 1409–1418.

Patterson, R. D., Allerhand, M., and Guiguère, C. (**1995**). ''Time-domain modeling of peripheral auditory processing: a modular architecture and a software platform,'' J. Acoust. Soc. Am. **98**, 1890–1894.

Patterson, R. D., Robinson, K., Holdsworth, J., McKeown, D., and Zhang, C. (**1992**). ''Complex sounds and auditory images,'' in *Auditory Physiology and Perception*, edited by Y. Cazals, K. Horner, and L. Demany (Pergamon, Oxford), pp. 429–446.

Rose, J. E., Brugge, J. F., Anderson, D. J., and Hind, J. E. (**1967**). ''Phase-

locked response to low-frequency tones in single auditory nerve fibers of the squirrel monkey,'' J. Neurophysiol. **30**, 769–793.
Ross, M. J., Shaffer, H. L., Cohen, A., Freudberg, R., and Manley, H. J. (**1974**). ''Average magnitude difference function pitch extractor,'' IEEE Trans. Acoust., Speech, Signal Process. **ASSP-22**, 353–362.
Ruggero, M. A. (**1973**). ''Response to noise of auditory nerve fibers in the squirrel monkey,'' J. Neurophysiol. **36**, 569–587.
Schroeder, M. R., and Hall, J. L. (**1974**). ''Model for the mechanical to neural transduction in the auditory receptor,'' J. Acoust. Soc. Am. **55**, 1055–1060.
Shofner, W. P. (**1991**). ''Temporal representation of rippled noise in the anteroventral cochlear nucleus of the chinchilla,'' J. Acoust. Soc. Am. **90**, 2450–2466.
Slaney, M. (**1990**). ''A perceptual pitch detector,'' ICASSP-90, pp. 357–360.
Slaney, M. (**1993**). ''An efficient implementation of the Patterson-Holdsworth auditory filter bank,'' Apple Computer technical report #35.
Terhardt, E. (**1974**). ''Pitch, consonance and harmony,'' J. Acoust. Soc. Am. **55**, 1061–1069.
van Noorden, L. (**1982**). ''Two channel pitch perception,'' in *Music, Mind, and Brain*, edited by M. Clynes (Plenum, London), pp. 251–269.
Weintraub, M. (**1985**). ''A theory and computational model of auditory monaural sound separation,'' University of Stanford, unpublished doctoral dissertation.
Wightman, F. L. (**1973**). ''The pattern-transformation model of pitch,'' J. Acoust. Soc. Am. **54**, 407–416.
Yin, T. C. T., and Chan, J. C. K. (**1990**). ''Interaural time sensitivity in media superior olive of cat,'' J. Neurophysiol. **64**, 465–488.
Yin, T. C. T., Chan, J. C. K., and Carney, L. H. (**1987**). ''Effects of interaural time delays of noise stimuli on low-frequency cells in the cat's inferior colliculus. III. Evidence for cross-correlation,'' J. Neurophysiol. **58**, 562–583.
Yost, W. A. (**1996**). ''Pitch strength of iterated rippled noise,'' J. Acoust. Soc. Am. **100**, 3329–3335.
Yost, W. A., Patterson, R., and Scheft, S. (**1996**). ''A time domain description for the pitch strength of iterated rippled noise,'' J. Acoust. Soc. Am. **99**, 1066–1078.

A multiresolution analysis of scattering by a pair of local regions of complex heterogeneity

Ben Zion Steinberg
Department of Interdisciplinary Studies, Faculty of Engineering, Tel-Aviv University, Tel-Aviv, 69978 Israel

John J. McCoy
School of Engineering, The Catholic University of America, Washington, DC 20064

(Received 18 November 1996; accepted for publication 30 September 1997)

The scattering by a pair of spatially disjoint local regions of complex (multiscale) stiffness heterogeneity in an unbounded thin linearly elastic plate is investigated. Issues of the mutual interaction of the spatially disjoint scatterers and its manifestation within a homogenized, or effective, formulation governing large scale response fields are the focus. It is shown analytically and numerically that while one must incorporate scatterer/scatterer coupling for estimating the large scale response field, one can neglect this coupling in estimating the effective measures for describing the scatterers. © *1998 Acoustical Society of America.* [S0001-4966(98)00502-5]

PACS numbers: 43.20.Bi, 43.20.Fn [ANN]

INTRODUCTION

An investigation of the scattering of time-harmonic, elastic waves by a spatially limited region of highly structured heterogeneity in an otherwise homogeneous plate bounding a fluid half space, was reported in a recent series of papers.[1–5] The heterogeneity refers to a variation of a plate property, i.e., the bending stiffness or the surface mass density. Primary attention was applied to a specific regime of parameters which characterize the scattering problems, and the research issues relevant to these parameters. To set the issues of the present work in a proper context, we briefly describe the characteristics of the scattering problems and the research issues addressed.

The length, λ, of the flexural waves which would obtain in a homogeneous background plate response is one parameter. This is used to distinguish between a macroscale and a microscale, as applying to a variation that is observed in distances of the order of λ and much smaller than λ (say $\lambda/20$ and smaller), respectively. A *complex scatterer* is described as a local region of heterogeneity which requires description on both the macro and micro scales. Thus, the size of the region of heterogeneity is of a macroscale length. Then, the variation in the heterogeneity can have two components, a macroscale component observed in distances of the order of λ and a microscale component observed in distances much smaller than λ. The plate response in the presence of the articulated complex heterogeneity can similarly be resolved into macroscale and microscale components. The microscale, or ''detail,'' component is a variation which averages to zero over distances of the order of λ. It is only the macroscale component of the plate response, also termed the spatially smoothed plate response, that results in acoustic field which radiates to significant distances from the plate. Variation in the plate response that is described on length scales smaller than λ results in an acoustic field, in the fluid half space, which lies in the evanescent part of the spectrum. The specific research issues addressed in Refs. 1–5 relate to the effects of the microscale heterogeneity on the macroscale response. A self-consistent formulation expressed only in the macroscale component of the plate response was developed. The ''footprint'' of the small scale interior heterogeneity structure, i.e., the microscale heterogeneity, appears in the obtained formulation as an ''across-scale coupling operator,'' or ''effective material operator'' (EMO). It is this operator, then, that describes the complex scatterer as determining the far-radiated acoustic field.

The norm of this across-scale coupling operator was shown to vanish in the case of a heterogeneity in the mass density of the plate.[1] The physical implication of this is: a mass density variation, which averages to zero over regions of the size of a fraction of a wavelength, has no effect on the component of the plate response, which results in a radiation of sound to far distances. The norm of the across-scale coupling operator was shown to be finite in the case of a heterogeneity in the local bending stiffness of the plate.[2,3] The physical implication of this is: a bending stiffness variation which averages to zero over regions of the size of a fraction of a wavelength does affect the component of the plate response which radiates as sound to far distances in a fluid bounded by the plate. Now, let $h(x)$ denote a heterogeneity of a complex scatterer character; $h(x)=m(x)$ or $h(x)=q(x)$ for a mass or stiffness heterogeneity, respectively. An effective measure of $h(x)$ is defined as the *smooth* heterogeneity $h^{(\mathrm{eff})}(x)$ that gives rise to a plate response identical to the smooth component of the plate response associated with $h(x)$. Thus, the complex scatterer $h(x)$ and its effective measure $h^{(\mathrm{eff})}(x)$ ''look the same'' when observed in the far field, but $h^{(\mathrm{eff})}(x)$ is ''simpler'' than $h(x)$. With the results articulated above, $m^{(\mathrm{eff})}(x)$ is merely the smooth component of $m(x)$, while $q^{(\mathrm{eff})}(x)$ cannot be obtained by a mere smoothing of $q(x)$. The existence of the effective measure $q^{(\mathrm{eff})}(x)$ and its derivation in the context of multiresolution analysis are first treated in Refs. 3 and 4.

The study reported in this paper is of the effects of a second complex scatterer located some fixed distance from

the first. It is shown analytically and numerically that the across-scale coupling operator which applies for the pair of scatterers is equal to the algebraic sum of those which apply for the isolated scatterers. The demonstration will be limited to the case of a bending stiffness variation; the demonstration for a mass variation follows in a similar manner, but is much less interesting in comparing zero with the sum of zeros.

Before presenting the details of the study, the issue to be studied might be further clarified. There is no question that the ''smoothed'' plate *response field* for the pair of scatterers cannot be estimated by summing the similarly smoothed plate *response fields* obtained for each of the scatterers in isolation. The coupling effects of multiple scattering are well appreciated. The issue is whether the effects of this coupling can be correctly estimated by a formulation expressed in the smoothed response field, in which the rule for obtaining the *across-scale-coupling* operator of the two scatterers need not incorporate any scatterer/scatterer coupling.

A major advantage of the two-step approach of first estimating the across-scale-coupling operator and then solving for the smoothed plate response field is the demonstrated conclusion that one can neglect all scatterer/scatterer coupling in the first step. This coupling is only significant in the second step, in a formulation that does not require calculations involving heterogeneity on scales of the order of the interior structure of the scatterers.

The outline of the paper is as follows: In Sec. I, the mathematical framework for resolving heterogeneity and response fields according to length scales and the derivation of the formulation governing the smoothed component of the response field in a general scattering formulation are reviewed. The application of these to scattering in a thin, linearly elastic plate which contains a stiffness heterogeneity of the complex character articulated above is demonstrated in Sec. II. Then, in Sec. III, the heterogeneity as a pair of scatterers, separated by an arbitrary but fixed distance and each containing an interior structure, is introduced. The size of the individual scatterers are restricted to be of the size of a wavelength, defined for a narrow-band excitation and the homogeneous background plate; the interior structures describe a variation on a scale that is a factor of 20 to 50 times smaller. Subject to these restrictions, it is shown that in the asymptotic regime in which 20 to 50 is a large number, the across-scale-coupling operator depends only on the local properties of the plate, i.e., the properties in a neighborhood of a size equal to a fraction of a wavelength. In Sec. IV, numerical results for the effective measures obtained for the pair of scatterers and obtained by adding the results for the two scatterers in isolation are shown and compared. Also presented are calculations of the smoothed component of the plate response field obtained for the pair of scatterers and obtained by adding the results of response fields for the two scatterers in isolation. Clearly demonstrated is while one must incorporate scatterer/scatterer coupling for estimating the smoothed response field, one can neglect this coupling in estimating the effective measures. Finally, in Sec. IV, summary remarks are offered.

I. A WAVELET BASED PHASE-SPACE

The theory of multiresolution decomposition (MRD) and orthogonal wavelets[6,7] provides a natural framework for the study of inter-scale coupling processes. There is a rapidly growing literature on the application of wavelet transformations to operators, e.g., the studies reported in Refs. 8–12. The main concern the studies reported is computational, to reduce the number of operations required for the inversion of certain classes of operators by applying wavelet transformations and thereby reducing a densely populated matrix to one that is sparsely populated. The approach followed will not reduce the number of operations for the complex scatterer problem of interest here, however, since its effectiveness requires a smoothness in the system heterogeneity. In a study more closely related to the complex scatterer problem,[13] the MRD theory was used to achieve a numerical homogenization, i.e., to formulate an equation with slowly varying coefficients whose solution has the same large scale behavior as that of the original equation. While this study has some relationship to previous studies of the present authors,[1,2] the motivations were clearly different. Thus, the work in Ref. 13 is devoted mainly to a sophisticated ''decimation'' process in which efficient numerical algorithm for estimating the large scale response component is developed. Left unaddressed are all of the questions articulated in the Introduction of the present paper. Addressing these questions requires a different viewpoint and, subsequently, a different analysis. Below the MRD theory is briefly summarized in a manner tailored to the class of problems of interest.

A. Representation of functions

Some terminology is required. A wavelet-based phase-space representation of a function is expressed as a linear sum; i.e., a synthesis, of *shifted* and *dilated* window functions, termed ''wavelets.''[6] The term ''mother wavelet'' is used to identify a particular window function, the shifts and dilations of which result in an appropriate ''wavelet system.'' Then, the term ''discrete'' applies if the linear sum for representing a function requires only finite increments of shift and dilation. Finally, the term ''orthogonal'' applies if the wavelets are mutually orthogonal. Discrete, orthogonal wavelet systems represent a particular class of systems; a mathematical description of the system can be given in terms of the properties of the mother wavelet used for generating it.

One can truncate the wavelet sum at some arbitrarily chosen dilation, and thereby suppress variability on scales larger than the one that corresponds to the cutoff dilation. This truncation can be identified with a ''high-pass'' filtering. The truncated representation can once again be made complete by adding its ''complement'' to it. Moreover, this complement can be given representation as a linear sum of shifted window functions. The window function to be shifted is a properly dilated function that has a precise relationship to the mother wavelet. This function is termed a ''scaling function.'' Like the mother wavelet, the scaling function is defined independently of an absolute length. For an orthogonal system, the set of shifted, properly dilated replicas of the scaling function are mutually orthogonal among themselves and are orthogonal to the wavelets.

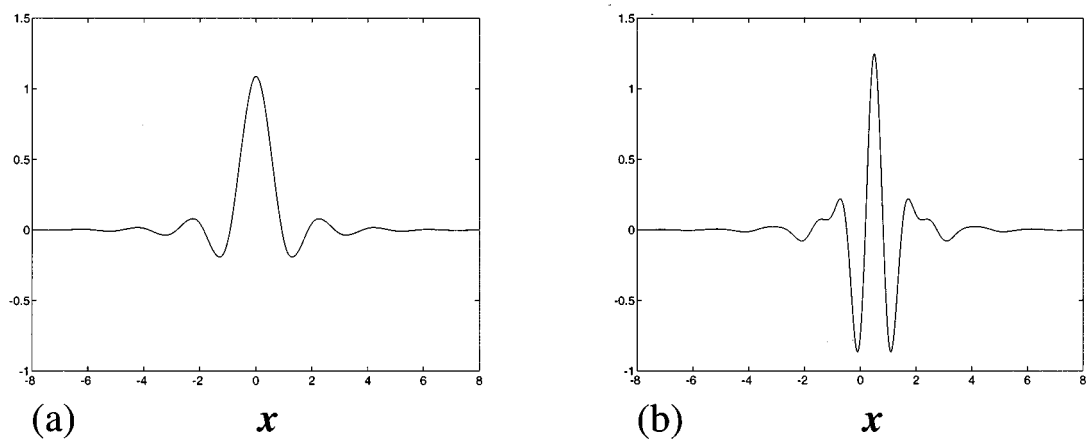

FIG. 1. The cubic spline Battle–Lemarie multiresolution system. (a) The scaling function $\phi(x)$. (b) The wavelet $\psi(x)$.

The complete representation of an arbitrary function in terms of its ''smooth'' component, represented by a sum of shifted, properly dilated replicas of the scaling function, and its ''detail'' component, represented by a truncated sum of wavelets, is expressed by

$$f(x)=f^s(x)+f^d(x), \tag{1a}$$

where

$$f^s(x)=\sum_n F^s_{jn}\phi_{jn}(x), \quad F^s_{jn}=\langle f,\phi_{jn}\rangle, \tag{1b}$$

and

$$f^d(x)=\sum_{m=j}\sum_n F^d_{mn}\psi_{mn}(x), \quad F^d_{mn}=\langle f,\psi_{mn}\rangle. \tag{1c}$$

The $\phi_{jn}=2^{j/2}\phi(2^jx-n)$ are the shifted (n), properly dilated (j) replicas of the scaling function and the $\psi_{mn}=2^{m/2}\psi(2^mx-n)$ are the wavelets. $\langle\cdot,\cdot\rangle$ denotes a scalar product. Notice that the wavelet sum is truncated at the dilation level, $m=j$. The described representation applies for discrete, orthogonal wavelet systems.

One particular scaling function and its associated mother wavelet, the cubic-spline Battle–Lemarie system,[6,7] provide the framework for our studies. These are illustrated in Fig. 1.

The partial sum represented by $f^s(x)$ describes that *component* of the variation of $f(x)$ that applies for length scales equal to the chosen reference length scale 2^{-j} or larger. The partial sum of $f^d(x)$, given by a specified value for m, describes that *component* of the variation of $f(x)$ that applies for the specified length scale 2^{-m}. This interpretation suggests the terminology of a ''multiscale decomposition'' in referring to the representation.

B. Representation of operators

The set of functions defined by the wavelets, truncated at an arbitrarily chosen dilation level (j), and the properly dilated replicas of the scaling function provide for a matrix representation of an operator. Let $\mathscr{A}$ denote an arbitrary operator. Its matrix representation can be partitioned into four submatrices $(\mathbf{A}^{(s,s)},\mathbf{A}^{(s,d)},\mathbf{A}^{(d,s)},\mathbf{A}^{(d,d)})$, with elements defined as follows:

$$\begin{aligned}
A^{(s,s)}_{jn,jn'}&=\langle\mathscr{A}\phi_{jn},\phi_{jn'}\rangle,\\
A^{(s,d)}_{jn,m'n'}&=\langle\mathscr{A}\phi_{jn},\psi_{m'n'}\rangle,\\
A^{(d,s)}_{mn,jn'}&=\langle\mathscr{A}\psi_{mn},\phi_{jn'}\rangle,\\
A^{(d,d)}_{mn,m'n'}&=\langle\mathscr{A}\psi_{mn},\psi_{m'n'}\rangle.
\end{aligned} \tag{2}$$

There is a dual interpretation to the four submatrices as describing a partitioning of the operator $\mathscr{A}$ defined on a function space which, for the theory of a multiresolution decomposition, is required to be an $L_2(R)$ space. This dual interpretation accepts the four submatrices as representing the action of the $\mathscr{A}$ operator on the two subspaces of $L_2(R)$, the subspace of smooth functions and of detail functions, as this term is determined by the chosen reference scale. Thus, for the submatrices $\mathbf{A}^{(s,s)}$ and $\mathbf{A}^{(d,s)}$, the operator acts on the subspace of smooth functions; for the submatrices, $\mathbf{A}^{(s,d)}$ and $\mathbf{A}^{(d,d)}$, the action is applied to the subspace of detail functions. For the submatrices $\mathbf{A}^{(s,s)}$ and $\mathbf{A}^{(d,d)}$, the result on the action is ''projected'' onto the same function subspace on which the action was applied. For the submatrices $\mathbf{A}^{(d,s)}$ and $\mathbf{A}^{(s,d)}$, the result of the action is projected on the complement of the function subspace to that on which the action was applied. The suggested terminology is that $\mathbf{A}^{(s,s)}$ and $\mathbf{A}^{(d,d)}$ represent intrascale operators, while $\mathbf{A}^{(d,s)}$ and $\mathbf{A}^{(s,d)}$ represent interscale operators.

C. Representations of scattering problems

The scattering problem can be expressed as an integral equation with the algebraic structure,

$$w=w_0+\mathscr{G}\mathscr{H}w, \tag{3}$$

where w is a measure of the wave field in the structure, i.e., the plate; w_0 is the same measure for a structure with the region of heterogeneity absent; $\mathscr{H}$ is an operator that describes the interaction of the wave field with a scatterer, and $\mathscr{G}$ is an operator that describes the distribution of the effects of this interaction throughout the structure; it is a propagator. Depending on the specifics of the scatterer, the $\mathscr{H}$ operator can be algebraic, differential, or perhaps require an integral, i.e., nonlocal, representation. The $\mathscr{G}$ operator is nonlocal.

Applying the Galerkin method to an integral equation represented by Eq. (3) results in a system of algebraic equations on the coefficients for describing $w(x)$ in a wavelet-based phase-space.[1–4] This system of algebraic equations can be interpreted, then, as providing a phase-space representation of a scattering problem. To ''solve'' the scattering problem, one first inverts the constructed system of algebraic equations to obtain the coefficients of $w(x)$, followed by the synthesis of Eqs. (1a)–(1c).

The system of algebraic equations governing the coefficients of $w(x)$ can be written as follows:

$$(I-\Phi)\vec{s}-C\vec{d}=\vec{s}_0, \quad -\overline{C}\vec{s}+(I-\Psi)\vec{d}=0. \tag{4}$$

The coefficients of $w(x)$ which apply to the properly dilated replicas of the scaling function are collected in $\vec{s}$ and those which apply to the wavelet functions are collected in $\vec{d}$. Thus, $\vec{s}$ represents $w^s(x)$ and $\vec{d}$ represents $w^d(x)$.

The matrix operators $\mathbf{\Phi}$, $\mathbf{\Psi}$, $\mathbf{C}$, $\overline{\mathbf{C}}$ are the four submatrices that represent the combined operator $\mathscr{G}\mathscr{H}$ via a decomposition similar to (2) with $\mathscr{A}=\mathscr{G}\mathscr{H}$: $\mathbf{\Phi}=\mathbf{A}^{ss}$, $\mathbf{\Psi}=\mathbf{A}^{dd}$, $\overline{\mathbf{C}}=\mathbf{A}^{sd}$, $\mathbf{C}=\mathbf{A}^{ds}$. The matrix elements are given by

$$\begin{aligned}
&\Phi_{n',n}=\langle \mathscr{G}\mathscr{H}\phi_{jn},\phi_{jn'}\rangle,\\
&\Psi_{m'n',mn}=\langle \mathscr{G}\mathscr{H}\psi_{mn},\psi_{m'n'}\rangle,\\
&C_{n',mn}=\langle \mathscr{G}\mathscr{H}\psi_{mn},\phi_{jn'}\rangle,\\
&\overline{C}_{m'n',n}=\langle \mathscr{G}\mathscr{H}\phi_{jn},\psi_{m'n'}\rangle.
\end{aligned} \tag{5}$$

A formulation tuned to govern the smoothed response measure $\vec{s}$ can be derived from (4) via a two-step procedure. In the first step one uses the lower half of (4) to formally solve for $\vec{d}$ in terms of $\vec{s}$,

$$\vec{d}=(\mathbf{I}-\mathbf{\Psi})^{-1}\overline{\mathbf{C}}\vec{s}. \tag{6}$$

This last result states that the relation between $\vec{d}$ and $\vec{s}$ (or the relation between the small scale and large scale responses) is independent of the problem forcing, and it proves to be useful in subsequent derivations. An exact, self-consistent formulation governing $\vec{s}$ is obtained now by substituting Eq. (6) back in the upper half of Eq. (4),

$$(\mathbf{I}-\mathbf{\Phi}-\mathbf{C}(\mathbf{I}-\mathbf{\Psi})^{-1}\overline{\mathbf{C}})\vec{s}=\vec{s}_0. \tag{7}$$

D. The footprint of small scale structure in large scale response

The interpretation of a scaling function as a low pass filter with a cutoff spatial frequency determined by the scale 2^{-j} conveys the interpretation of the matrix operator $\mathbf{\Phi}$ as a representation of $\mathscr{G}\mathscr{H}$ smoothed on a reference scale 2^{-j}. Thus, the small scale structure information in $\mathbf{\Phi}$ has been eliminated. The effect of the small scale structure on the large scale response is expressed via the presence of the operator $\mathbf{C}(\mathbf{I}-\mathbf{\Psi})^{-1}\overline{\mathbf{C}}$, termed the *across scales coupling operator* or the *effective material operator* (EMO). A general measure of the potential degree of this effect is the EMO norm; if $\|\mathrm{EMO}\|\ll\|\mathbf{\Phi}\|$, then the small scale structure has practically no effect on the large scale response. If these norms are comparable, then a small scale heterogeneity can have a significant effect on the large scale response. An estimate of the EMO norm requires one to specify the structure of the operators $\mathscr{G}$ and $\mathscr{H}$.

Of special interest is the case in which $\mathscr{H}$ is an algebraic multiplication operator and $\mathscr{G}$ is an integral operator. Then, for every $f(x)$ one has

$$\mathscr{H}f(x)=h(x)f(x), \tag{8}$$

$$\mathscr{G}f(x)=\int \Gamma(x,y)f(y)dy, \tag{9}$$

provided the integral exists. Here $h(x)$ and $\Gamma(x,y)$ are known functions, the former represents a heterogeneity field and the latter represents a response measure associated with an appropriately defined background problem (usually one defined by a constant coefficients differential equation). It has been shown[1–4] that when $\mathscr{H}$ and $\mathscr{G}$ take the form of Eqs. (8) and (9), the EMO norm is essentially determined by the irregularity order of $\Gamma(x,y)$ at the origin $x=y$. For highly irregular kernels the EMO norm can be $O(1)$, whereas for smooth kernels $\|\mathrm{EMO}\|\ll 1$. The former represents the cases for which the small scale heterogeneity can have a significant effect on the large scale response, and the latter represents cases in which it has practically no effect. Another result that holds in the latter case follows directly from Eq. (6),

$$\|\vec{d}\|\ll\|\vec{s}\|\Leftrightarrow\|w^d\|\ll\|w^s\|. \tag{10}$$

This result will prove to be extremely important.

II. SCATTERING ON A THIN LINEARLY ELASTIC PLATE

The differential equation governing the motion of a thin linearly elastic plate with a one-dimensional stiffness heterogeneity, $Q(x)$, subject to a time harmonic line forcing, $F(x)$, is given by

$$\frac{d^2}{dx^2}\left[Q(x)\frac{d^2}{dx^2}w(x)\right]-\omega^2 m w(x)=F(x), \tag{11}$$

where $w(x)$ is the flexural (transverse displacement) response of the plate, m is the surface mass density of the plate, and ω is the radian frequency. The time harmonic dependence $e^{-i\omega t}$ has been suppressed. We shall define the local normalized (nondimensional) fluctuating component of $Q(x)$ via the relation

$$Q(x)=Q_0[1+q(x)], \tag{12}$$

in which the constant Q_0 is interpreted as the stiffness associated with the homogeneous ''background'' plate. The constants Q_0, m and ω define the background wave number,

$$K_{f_0}=\left(\frac{\omega^2 m}{Q_0}\right)^{1/4}. \tag{13}$$

It is the wave number of the free waves that propagate in the homogeneous background plate. For convenience, we shall normalize the physical coordinate x with respect to the background wave number via

$$x \mapsto \frac{K_{f_0} x}{2\pi} = \frac{x}{\lambda_{f_0}}. \tag{14}$$

Here λ_{f_0} is the wavelength associated with K_{f_0}. Expressed in the new dimensionless variable, x, the equation of motion takes the form

$$\frac{d^2}{dx^2}\left[(1+q(x))\frac{d^2}{dx^2}w(x)\right] - (2\pi)^4 w(x) = f(x), \tag{15}$$

where $f(x) = (\lambda_{f_0}^4/Q_0)F(x)$ is the normalized forcing. A formulation governing the background plate is readily obtained from Eq. (15) by setting $q(x)=0$. Similarly, the corresponding Green's function $G(x)$ satisfies

$$\frac{d^4}{dx^4}G(x-x') - (2\pi)^4 G(x-x') = -\delta(x-x'), \tag{16}$$

where $\delta(x)$ is the Dirac delta function. The last equation can be solved analytically. The result is

$$G(x) = -\frac{1}{32\pi^3}(ie^{i2\pi|x|} - e^{-2\pi|x|}). \tag{17}$$

With the help of Eqs. (16)–(17), Eq. (15) can be transformed to an integral equation formulation. To achieve this, the term containing the heterogeneity, $(d^2/dx^2)[q(x)(d^2/dx^2)w(x)]$, is moved to the right hand side, and the solution, $w(x)$, written as a convolution of the background problem Green's function $G(x)$, with the extended source term, $f(x) - [q(x)w''(x)]''$. The result is

$$w(x) = w_0(x) + \int G(x-y)[q(y)w''(y)]''dy, \tag{18}$$

where $w_0(x)$ is the background system response to the forcing $f(x)$,

$$w_0(x) = -\int G(x-y)f(y)dy. \tag{19}$$

Equation (18) is integro-differential. It can be transformed to a Fredholm integral equation of the second kind governing $w''(x)$—the inverse of the local radii of curvature of the plate. Thus, taking a second derivative of Eq. (18) with respect to x obtains

$$u(x) = u_0(x) + \int G''(x-y)[q(y)u(y)]''dy, \tag{20}$$

where $u(x) = w''(x)$ and $u_0(x) = w_0''(x)$. Next the rhs is integrated by parts twice, and Eq. (16) used to express the fourth derivative of $G(x)$ in terms of $G(x)$. The result is

$$u(x) = u_0(x) + \int \Gamma(x,y)q(y)u(y)dy, \tag{21a}$$

where $\Gamma(x,y)$ is a kernel function given by

$$\Gamma(x,y) = (2\pi)^4 G(x-y) - \delta(x-y). \tag{21b}$$

This is a second kind Fredholm integral equation scattering formulation, identical to that in Eq. (3) with the special forms in Eqs. (8) and (9). It is seen in Eq. (21b) that the kernel associated with the integral equation formulation is highly irregular. In light of the discussion in Sec. I D and Refs. 2–4, the conclusion follows that a small-scale stiffness heterogeneity [small-scale variation of $q(x)$] can have a significant effect on the large-scale response $u^s(x)$. This is demonstrated numerically in Sec. IV.

An alternative formulation, similar in form to that of $u(x)$ in Eq. (21a), but with a smoother kernel can be derived. Performing the integration over $\delta(x-y)$ and moving the result to the left hand side obtains

$$u(x)[1+q(x)] = u_0(x) + (2\pi)^4 \int G(x-y)q(y)u(y)dy. \tag{22}$$

This suggests a rewriting the scattering formulation in terms of the normalized local bending moment, $T(x)$:

$$T(x) = u(x)[1+q(x)], \tag{23}$$

which yields $(u_0(x) = T_0(x))$

$$T(x) = T_0(x) + (2\pi)^4 \int G(x-y)r(y)T(y)dy, \tag{24a}$$

with

$$r(y) = \frac{q(y)}{1+q(y)} = 1 - \frac{1}{1+q(y)}. \tag{24b}$$

This scattering formulation, written now on the bending moment $T(x)$, has the same standard form of Eq. (13) with Eqs. (8) and (9)—a property shared also by the scattering formulation (21a). However, unlike the formulation in (21a), the integral operator kernel function $(2\pi)^4 G(x-y)$ as well as its first two derivatives are continuous at the origin $(x=y)$. Thus, the corresponding EMO norm is very small compare to $\|\mathbf{\Phi}\|$ (see, for example, Refs. 2–4). Thus, small scale variation of $r(x)$ has practically no effect on large scale response. As a consequence, the scattering formulation governing the large scale component of $T(x)$ is identical to Eq. (24a), but with $r(x)$ replaced by its large scale component $r^s(x)$,

$$T^s(x) = T_0(x) + (2\pi)^4 \int G(x-y)r^s(y)T^s(y)dy, \tag{25a}$$

where, with Eq. (24b),

$$r^s(y) = 1 - \left(\frac{1}{1+q(y)}\right)^s. \tag{25b}$$

Furthermore, the local constitutive relation (23), in conjunction with (10) can be approximated by $(\|T^s\| \gg \|T^d\|)$

$$u^s(x) \simeq T^s(x)\left(\frac{1}{1+q(x)}\right)^s. \tag{26}$$

From Eqs. (25a)–(26) it is seen that the only heterogeneity measure relevant for the computation of $u^s(x)$ is $(1/[1+q(x)])^s$. In other words,

$$\frac{1}{1+q^{(\mathrm{eff})}(x)}=\left(\frac{1}{1+q(x)}\right)^{s}$$

$$\Rightarrow q^{(\mathrm{eff})}(x)=\left[\left(\frac{1}{1+q(x)}\right)^{s}\right]^{-1}-1, \tag{27}$$

where $q^{(\mathrm{eff})}(x)$ is the effective measure of the heterogeneity variation $q(x)$. The computational role of $q^{(\mathrm{eff})}$ is clarified by the following steps. Use Eq. (27) to express the relation in Eq. (26) in terms of $q^{(\mathrm{eff})}(x)$,

$$T^{s}(x)\simeq u^{s}(x)[1+q^{(\mathrm{eff})}(x)]. \tag{28}$$

Similarly, express $r^{s}(x)$ in Eq. (25b) in terms of $q^{(\mathrm{eff})}(x)$,

$$r^{s}(x)=\frac{q^{(\mathrm{eff})}}{1+q^{(\mathrm{eff})}(x)}. \tag{29}$$

Use the last two expressions to rewrite the integral equation formulation (25a) in terms of $u^{s}(x)$ and $q^{(\mathrm{eff})}(x)$,

$$u^{s}(x)[1+q^{(\mathrm{eff})}(x)]=u_{0}(x)+(2\pi)^{4}\int G(x-y)\times q^{(\mathrm{eff})}(y)u^{s}(y)dy, \tag{30}$$

an alternative form of which is

$$u^{s}(x)=u_{0}(x)+\int \Gamma(x,y)q^{(\mathrm{eff})}(y)u^{s}(y)dy, \tag{31}$$

where $\Gamma(x,y)$ is the same kernel as that of the complete formulation written for $u(x)$ in Eqs. (21a) and (21b). Thus, the formulation written directly for the large scale response measure $u^{s}(x)$ is identical to that written for $u(x)$, with the heterogeneity $q(x)$ replaced by its effective measure $q^{(\mathrm{eff})}(x)$. Certainly, one can use now Eq. (31) as a starting point, and reverse the steps that lead from the differential equation (11) to the integral equation formulation. The resultant differential equation formulation is then

$$\frac{d^{2}}{dx^{2}}\left[Q^{(\mathrm{eff})}(x)\frac{d^{2}}{dx^{2}}w^{s}(x)\right]-\omega^{2}mw^{s}(x)=F(x), \tag{32}$$

where $w^{s}(x)$ is the large scale response component, and $Q^{(\mathrm{eff})}(x)=1+q^{(\mathrm{eff})}(x)$.

III. THE TWO SCATTERERS EXPERIMENT

The only nonlocal operation involved with the computation of $q^{(\mathrm{eff})}(x)$ is the smoothing. The rest are algebraic. The smoothing operator, however, becomes local when observed on length scales that are large compared to the smoothing length scale 2^{-j} (reference scale). One usually chooses the reference scale to faithfully describe variations on the length scale of the background wavelength λ. Thus, the reference scale 2^{-j} shall be, say, $\lambda/4$ or $\lambda/8$. It follows that the effective property measure is local with respect to the wavelength.

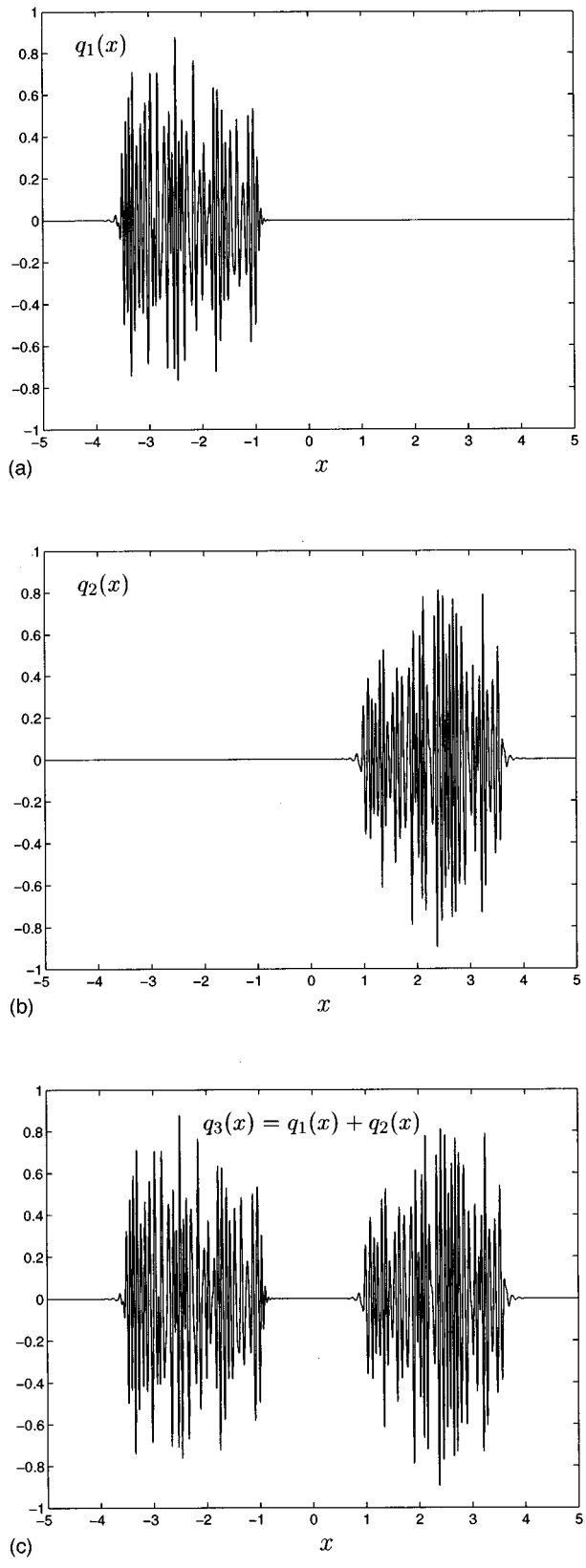

FIG. 2. Examples of stiffness heterogeneity that constitute complex scatterers. (a) Complex scatterer $q_1(x)$. (b) Complex scatterer $q_2(x)$. (c) Complex scatterer $q_3(x)=q_1(x)+q_2(x)$.

Let $q_1(x)$ and $q_2(x)$ be two highly structured stiffness heterogeneity functions, and let $q_3(x)$ be the stiffness heterogeneity that corresponds to the sum of the two heterogeneity measures,

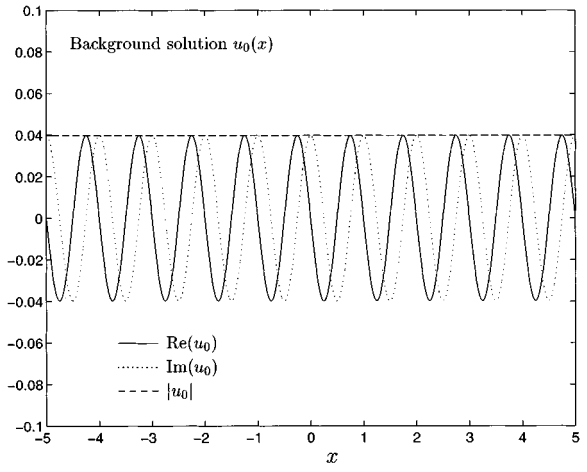

FIG. 3. The backgroud system response $u_0(x)=G(x-x')$.

$$q_3(x)=q_1(x)+q_2(x). \tag{33}$$

Let I_1 and I_2 be the intervals in space in which $q_2(x)\neq 0$ and $q_1(x)\neq 0$, respectively. Assume the intervals do not overlap. If the distance between I_1 and I_2 is measured on the large scale, the local property of the effective measure yields

$$q_3^{(\mathrm{eff})}(x)=q_1^{(\mathrm{eff})}(x)+q_2^{(\mathrm{eff})}(x). \tag{34}$$

That is: *effective measures can be superimposed, if their corresponding scatterers are isolated when observed on the large scale.*

IV. NUMERICAL EXAMPLE AND CONCLUSIONS

The nondimensional (normalized) formulation (15) with the normalized space coordinate system denoted by (14) is to be used throughout this section. Thus, the length scale associated with the background system response equals one unit [see (17)]. The reference, or smoothing, length scale, 2^{-j}, is chosen to correspond to $\lambda/8$, thus $j=3$. Two complex scatterers were synthesized with a random number generator. The corresponding stiffness distributions $q_1(x)$ and $q_2(x)$ are shown in Fig. 2(a) and (b). Their supports are spatially disjoint. A third complex heterogeneity $q_3(x)$ given by the sum of $q_1(x)$ and $q_2(x)$ [see Eq. (33)] is shown in Fig. 2(c). In all three complex scatterers, the length scale for observing the inner structure is in the order of $\lambda/20$ ($\lambda=1$). The outer dimensions of $q_1(x)$ and of $q_2(x)$ as well as the spatial separation between them are in the order of a few λ. With the chosen reference scale, the smooth component of the heterogeneity vanish,

$$q_i^s(x)=0 \quad \text{for } i=1,2,3. \tag{35}$$

Thus, the scatterers under consideration possess only microscale heterogeneity.

Assume the system is subject to a point forcing $f(x)=\delta(x-x')$ located at $x'=-10$. The background system response to this forcing is given by $u_0(x)=G(x-x')$, where $G(x)$ is given in Eq. (17). This background response is shown in Fig. 3. Denote by $u_i^s(x)$, $u_i^d(x)$, and $u_i(x)$ the macroscale, microscale, and complete responses associated with the heterogeneity $q_i(x)$, subject to the forcing $f(x)$.

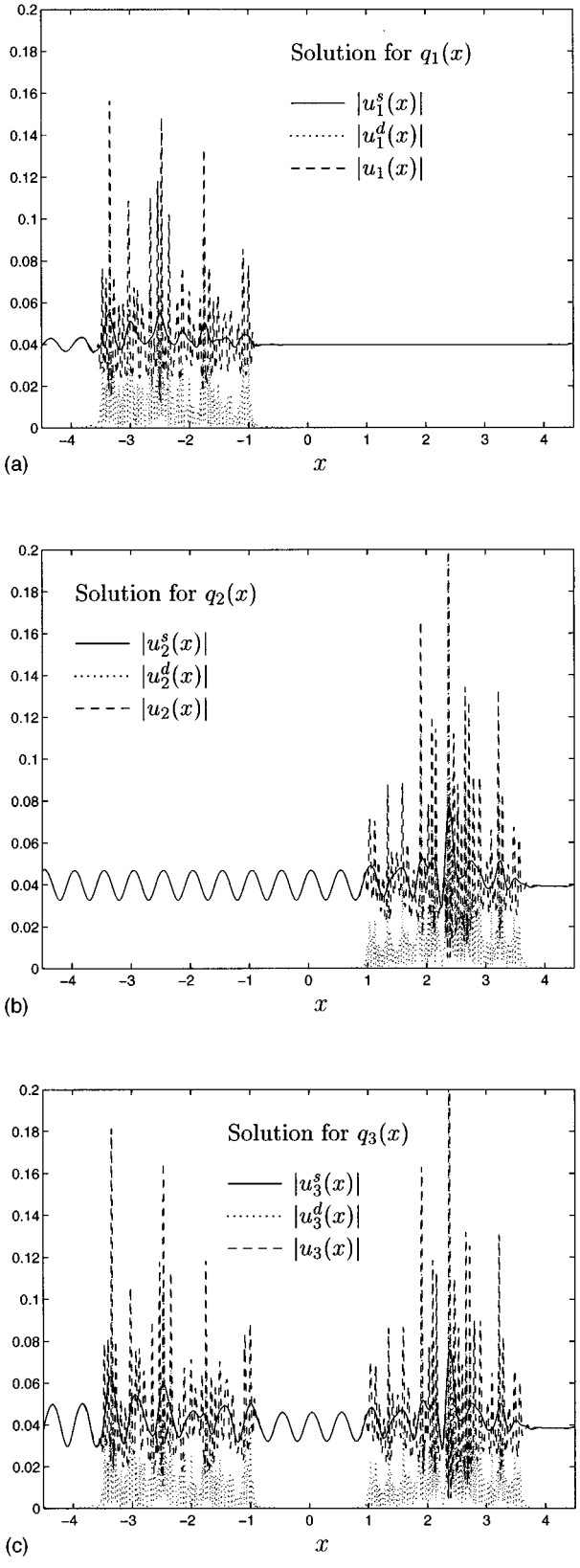

FIG. 4. Magnitudes of $u^s(x)$, $u^d(x)$, and $u(x)$ associated with (a) $q_1(x)$, (b) $q_2(x)$, and (c) $q_3(x)$.

Consider the following demonstration of a footprint of the microscale heterogeneity in the macroscale response. Figure 4(a)–(c) applies to the plate responses associated with $q_1(x)$, $q_2(x)$, and $q_3(x)$, respectively. Shown are the mag-

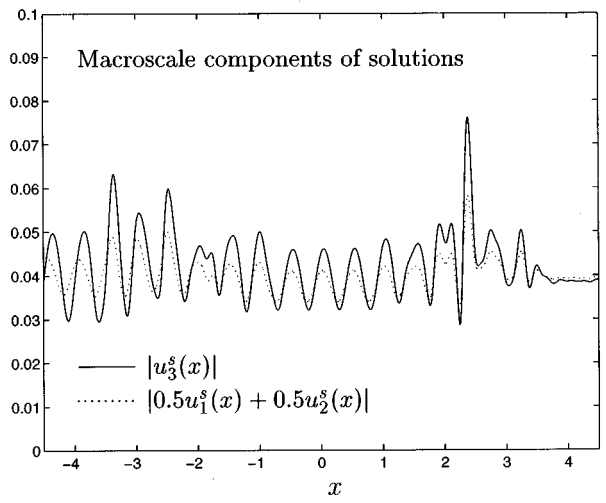

FIG. 5. Magnitudes of the macroscale response $u_3^s(x)$ and the synthetic field $\overline{u}(x)=\frac{1}{2}u_1^s(x)+\frac{1}{2}u_2^s(x)$.

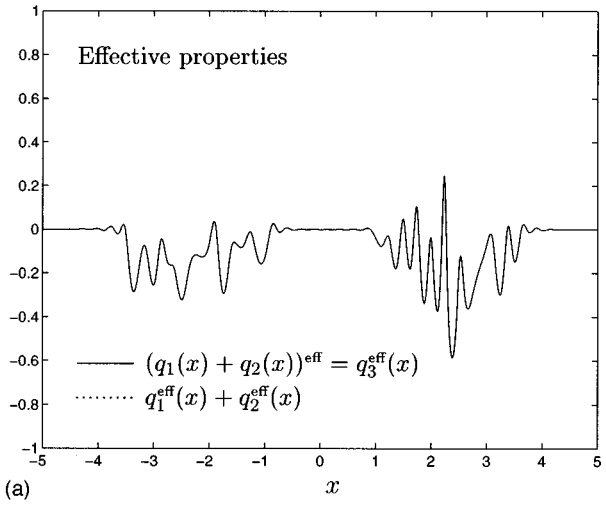

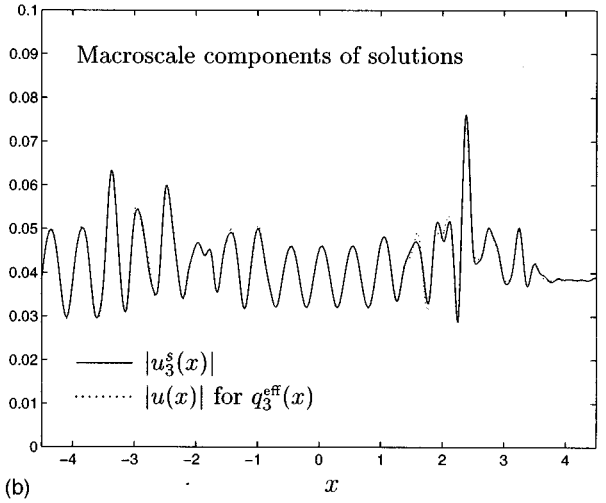

FIG. 6. Effective measures. (a) $q_3^{(\text{eff})}(x)$—the effective measure of $q_3(x)$—compared to $q_1^{(\text{eff})}(x)+q_2^{(\text{eff})}(x)$. (b) The field associated with the stiffness distribution $q_3^{(\text{eff})}(x)$ compared to the macroscale component of the field associated with $q_3(x)$.

nitudes of the complete response $u_i(x)$ and the magnitudes of its macroscale and microscale components $u_i^s(x)$ and $u_i^d(x)$. Clearly, $u_i^s(x)$ in all cases differ considerably from the background system response shown in Fig. 3. Thus, as anticipated by the presented analysis, small scale stiffness heterogeneity can have a significant effect on large scale response.

Figure 5 allows a comparison of $u_3^s(x)$ with the synthetic field $\overline{u}(x)=\frac{1}{2}u_1^s(x)+\frac{1}{2}u_2^s(x)$. The multiplication factor 1/2 has been inserted in the latter to make the total source intensities of $u_3^s(x)$ and of $\overline{u}(x)$ equal. It is seen that the magnitudes differ considerably. Thus, *one must incorporate scatterer/scatterer coupling for estimating the macroscale response component.*

Finally, Fig. 6 contains a demonstration that the effective measures for a pair of spatially disjoint scatterers is correctly given by the algebraic sum of the effective measures for the isolated scatterers. Thus, the lines representing the effective measure of $q_3(x)$ and the sum of the effective measures of $q_1(x)$ and $q_2(x)$, in Fig. 6(a), are indistinguishable to within the graphic resolution of the figure. Figure 6(b) contains a demonstration of the fidelity of the effective measure in determining the macroscale response, $u_3^s(x)$, by reproducing the *complete* response associated with $q_3^{(\text{eff})}(x)$. The curves are in good agreement. These last results are consistent with the assertion in Sec. III that *one can neglect scatterer/scatterer interaction in estimating the effective measures.*

ACKNOWLEDGMENTS

This research was supported in part by The Israel Science Foundation administered by The Israel Academy of Science and Humanities.

[1] B. Z. Steinberg and J. J. McCoy, ''Towards local effective parameter theories using multiresolution decomposition,'' J. Acoust. Soc. Am. **96**, 1130–1143 (1994).
[2] B. Z. Steinberg and J. J. McCoy, ''Effective measures for nonstationary microscale stiffness variation using multiresolution decomposition,'' J. Acoust. Soc. Am. **98**, 3516–3526 (1995).
[3] B. Z. Steinberg and J. J. McCoy, ''A class of one dimensional stiffness microstructures resulting in identical macroscale response,'' Wave Motion **23**, 237–258 (1996).
[4] B. Z. Steinberg and J. J. McCoy, ''A study of the effective properties of mass and stiffness microstructure—A multiresolution approach,'' Q. Appl. Math. (to appear).
[5] B. Z. Steinberg and J. J. McCoy, ''A multiresolution study of effective properties of complex electromagnetic systems,'' IEEE Trans. Antennas Propag. (to appear).
[6] I. Daubechies, *Ten Lectures on Wavelets*, CBMS–NSF Series in Applied Mathematics (SIAM, Philadelphia, 1992).
[7] S. G. Mallat, ''A theory for multiresolution signal decomposition: the wavelet representation,'' IEEE Trans. Pattern. Anal. Mach. Intell. **11**, 674–693 (1989).
[8] G. Beylkin, R. Coifman, and V. Rokhlin, ''Fast wavelet transforms and numerical algorithms I,'' Commun. Pure Appl. Math. **44**, 141–183 (1991).
[9] B. Alpert, G. Beylkin, R. Coifman, and V. Rokhlin, ''Wavelet bases for the fast solution of the second-kind integral equations,'' SIAM J. Sci. Stat. Comput. **14**, 159–184 (1993).
[10] S. Jaffard and Ph. Laurencot, ''Orthonormal wavelets, analysis of operators, and applications to numerical analysis,'' in *Wavelets: A Tutorial in Theory and Applications*, edited by C. K. Chui (Academic, New York, 1992).

[11] B. Z. Steinberg and Y. Leviatan, ''On the use of wavelet expansions in the method of moments,'' IEEE Trans. Antennas Propag. **AP-41**, 610–619 (1993).
[12] B. Z. Steinberg and Y. Leviatan, ''A multiresolution study of two-dimensional scattering by metallic cylinders,'' IEEE Trans. Antennas Propag. **44**, 572–579 (1996).
[13] M. E. Brewster and G. Beylkin, ''A multiresolution strategy for numerical homogenization,'' Appl. Comput. Harmonic Anal. **2**, 327–349 (1995).

Inhomogeneous absorption and geometric acoustics

F. D. Tappert
Division of Applied Marine Physics, University of Miami, RSMAS, Miami, Florida 33149

(Received 16 June 1997; accepted for publication 23 November 1997)

The conventional formulation of geometric acoustics in the presence of inhomogeneous (spatially varying) absorption is examined. This formulation is found to fail under conditions of multipath propagation, because interference between ray paths is not taken into account when the absorptive losses are calculated. The example of high-frequency attenuation due to a surface bubble layer is studied, and Weston's correction term is discussed. © *1998 Acoustical Society of America.* [S0001-4966(98)03003-3]

PACS numbers: 43.20.Dk, 43.20.Hq, 43.30.Cq [JEG]

INTRODUCTION

The geometric acoustics approximation is an efficient technique for modeling propagation in waveguides that are range dependent, especially at high frequencies and for broadband signals (see, e.g., Weinberg and Keenan[1]). Due to accumulated phase errors, however, the geometric approximation is not uniformly valid in range, and it breaks down at sufficiently large ranges. Precise estimates of this breakdown range, such as that given by Tappert and Tang[2] in a situation characterized by ray chaos, are difficult to confirm.

In this paper, another cause for concern about the uniform validity of geometric acoustics is investigated. Suppose that the non-negative volume absorption coefficient α depends on position $\mathbf{r}$ in a significant way: $\alpha=\alpha(\mathbf{r})$. This is called inhomogeneous absorption. In ocean acoustics, for example, α depends on the temperature $T(\mathbf{r})$ and it is typical that $T(\mathbf{r})$ varies rapidly with depth in the thermocline and varies rapidly with range at ocean fronts. Another example drawn from ocean acoustics is resonant absorption due to a near-surface bubble layer, in which case α varies with depth on a scale of a few meters or less. If a ray trajectory is denoted by $\mathbf{r}(s)$, where s is the distance along the ray, then the cumulative absorption along this ray is

$$\beta=\int \alpha(\mathbf{r}(s))ds, \tag{1}$$

and the ray amplitude is attenuated by the amount

$$\Gamma=\exp(-\beta). \tag{2}$$

This is the conventional description of absorption within the framework of the geometric approximation.

The above-described conventional treatment of inhomogeneous absorption has been called[3] ''non-deviative absorption,'' because the ordering of absorption in the asymptotic expansion leading to geometric acoustics is such that the rays do not deviate from their trajectories in the absence of absorption. An alternative approach, called[3] ''deviative absorption,'' requires the introduction of complex-valued ray trajectories $\mathbf{r}(s)$. Then $\alpha(\mathbf{r}(s))$ must be analytically continued into the complex plane, which is not in general possible because in most applications $\alpha(\mathbf{r})$ is given in tabular form. Furthermore, it is not known (even conceptually) how to compute complex-valued eigenrays in realistic waveguides. For these reasons, all practical ray-trace models known to the author use the above conventional method for treating inhomogeneous absorption.

There are at least three difficulties with treating inhomogeneous absorption by the conventional method of geometric acoustics. These are enumerated below.

(1) Since $\alpha(\mathbf{r})$ also depends on the acoustic frequency f, often as a fairly rapidly varying function of f, predictions of broadband signal propagation may require computations of β, specified in Eq. (1) above, for many different frequencies. This reduces the efficiency advantage of ray-tracing models compared to full-wave models, but in principle it is not a fundamental difficulty.

(2) At finite frequencies, the ray trajectories are actually tubes having a transverse width that can be estimated asymptotically in terms of the range-dependent Fresnel radius. Then the integrand in the β integral, specified in Eq. (1) above, should contain a weighting function to allow for the thickness of the ray tube. This would greatly complicate ray tracing. Even more, the Fresnel radius is inversely proportional to the square root of frequency, and as in point (1) above predictions of broadband signal propagation would require these complicated computations to be done at many frequencies. These appear to be serious difficulties for ray tracing with inhomogeneous absorption, and have not been implemented to the author's knowledge.

(3) For waveguide propagation, the occurrence of multipaths is typical. According to the above formulas, absorption is calculated along each ray without regard for other rays. However, destructive interference between multipaths can cause attenuation to be greatly reduced because no absorption can occur in regions where the field amplitude is zero. Since the above formulas for ray attenuation do not take into account multipath interference, there appears to be a fundamental flaw in the conventional formulation of geometric acoustics in the case of inhomogeneous absorption. The third of these difficulties is the main subject of this paper.

In the reduced wave equation, the absorption coefficient appears in a product of the form $\alpha(\mathbf{r})p(\mathbf{r})$, where $p(\mathbf{r})$ is the acoustic field. Thus if $p(\mathbf{r})$ is small in some region due to multipath interference, then little attenuation occurs in this

region even though $\alpha(\mathbf{r})$ is large. An estimate of the multipath effect can be made as follows. Consider two locally plane waves separated by the angle θ. Multipath interference gives nulls of the acoustic field in the transverse direction separated by $\Delta z \sim 1/k_0 \sin\theta$, where $k_0 = 2\pi f/c_0$ is the reference wave number and f is the acoustic frequency. If the length scale of the inhomogeneous absorption in the transverse direction is l, then validity of the geometric approximation requires that $l \gg \Delta z$, or

$$k_0 l \sin\theta \geqslant 1. \tag{3}$$

For fixed angle θ, this condition is always satisfied for a sufficiently high frequency. For fixed frequency, however, this condition is not satisfied for a sufficiently small θ, and then geometric acoustics with inhomogeneous absorption breaks down. In other words, the geometric approximation is not uniformly valid in the multipath angle θ. A particular example of this nonuniform validity has previously been recognized by Weston.[4]

In the remainder of this paper, these ideas are analyzed quantitatively. The analysis is based on the first-order parabolic approximation[5] because this approximation is often adequate for waveguide propagation where the grazing angles are small, and because this approximation allows explicit and physically intuitive calculations to be made. In Sec. I, this small-angle parabolic approximation with inhomogeneous absorption is introduced for propagation in the two-dimensional vertical plane. The equations of conventional geometric acoustics within the parabolic approximation are developed in Sec. II, with special attention given to the effects of inhomogeneous absorption on the ray amplitudes. Section III discusses multipath propagation using a coherent summation over eigenray amplitudes and phases, and it is shown that geometric acoustics contains a fundamental flaw in the presence of inhomogeneous absorption. This flaw is dramatically illustrated in Sec. IV, where the attenuation of sound waves due to a near-surface bubble layer is considered and Weston's correction term[4] is obtained. The main results are summarized and discussed in Sec. V.

I. PARABOLIC APPROXIMATION

Throughout this paper, the depth z increases downward from the surface boundary at $z=0$, and the range r increases outward from the source at $r=0$. The acoustic pressure p is related to the parabolic envelope function ψ by

$$p(z,r) = (R_0/r)^{1/2}\psi(z,r)\exp(ik_0 r), \tag{4}$$

where $R_0 = 1$ m is the reference range, and $k_0 = 2\pi f/c_0$ is the reference wave number. Here f is the acoustic frequency and c_0 is the reference sound speed. The parabolic wave equation is

$$ik_0^{-1}\frac{\partial\psi}{\partial r} = -\frac{1}{2k_0^2}\frac{\partial^2\psi}{\partial z^2} + U(z,r)\psi, \tag{5}$$

where the complex-valued potential function is

$$U(z,r) = u(z,r) - i\alpha(z,r)/k_0. \tag{6}$$

The real part of the potential is

$$u(z,r) = [1 - n^2(z,r)]/2, \tag{7}$$

and the acoustic index of refraction is specified as a function of the sound speed $c(z,r)$ as

$$n(z,r) = c_0/c(z,r). \tag{8}$$

The imaginary part of the potential contains the volume absorption coefficient per unit distance, $\alpha(z,r) \geqslant 0$. The frequency dependence of the absorption coefficient is suppressed in the notation, although of course it is important in practice. Validity of the first-order parabolic approximation requires that

$$|u(z,r)| \ll 1, \tag{9}$$

and that

$$\alpha(z,r)/k_0 \ll 1. \tag{10}$$

The second inequality is interpreted as the condition that the absorption per wavelength must be small.

The initial condition for an omnidirectional source at depth z_0 is

$$\psi(z,0) = (2\pi i R_0/k_0)^{1/2}\delta(z - z_0). \tag{11}$$

The conventional transmission loss from the source to the field point at (z,r), in units of dB *re*: 1 m, is

$$\begin{aligned}\mathrm{TL} &= -10\log_{10}[|p(z,r)|^2] \\ &= -10\log_{10}[(R_0/r)|\psi(z,r)|^2].\end{aligned} \tag{12}$$

At very small ranges, the potential term U in Eq. (5) can be ignored. This yields $|\psi(z,r)|^2 \approx R_0/r$, and then TL $\approx 20\log_{10}(r/R_0)$, which is the conventional expression for spherical spreading in ocean acoustics. This explains the source normalization in Eq. (11). The boundary condition at the surface is

$$\psi(0,r) = 0, \tag{13}$$

which is called the pressure-release condition. The boundary condition at great depths is due to attenuation within the bottom, and is

$$\lim_{z\to\infty}\psi(z,r) = 0. \tag{14}$$

With the above initial condition and boundary conditions, Eq. (5) is a well-posed problem.

II. PARABOLIC RAY TRACING WITH ABSORPTION

The geometric approximation to the solution of Eq. (5) is found by putting the ansatz

$$\psi(z,r) = a(z,r)\exp[ik_0 s(z,r)] \tag{15}$$

into Eq. (5), and then expanding the amplitude a in an asymptotic series,

$$a = a^{(0)} + k_0^{-1}a^{(1)} + \cdots. \tag{16}$$

This is essentially a high-frequency approximation, $k_0^{-1} \to 0$.

To leading order, the parabolic eikonal equation is obtained:

$$\frac{\partial s}{\partial r}+\frac{1}{2}\left(\frac{\partial s}{\partial z}\right)^2+u(z,r)=0. \tag{17}$$

It is important to note that only u, the real part of U, appears in the eikonal equation. This is because the imaginary part, α/k_0, is formally one order higher in the asymptotic expansion. The parabolic ray equations follow from Eq. (17) by defining the grazing angle of propagation as

$$\theta=\frac{\partial s}{\partial z}, \tag{18}$$

and the total derivative along a ray as

$$\frac{d}{dr}=\frac{\partial}{\partial r}+\theta\,\frac{\partial}{\partial z}. \tag{19}$$

Then by taking the partial derivative of Eq. (17) with respect to z, one obtains the parabolic ray equations[5]

$$\frac{dz}{dr}=\theta, \quad \frac{d\theta}{dr}=-\frac{\partial u}{\partial z}. \tag{20}$$

The initial conditions are $z(0)=z_0$, and $\theta(0)=\theta_0$. Each ray in the fan of rays from the source is labeled by the value of the parameter θ_0, which is interpreted as the launch angle. Thus the solutions of the ray equations are denoted as $z(r,\theta_0)$ and $\theta(r,\theta_0)$. The eikonal function along the ray labeled by θ_0 is found to be

$$s(r,\theta_0)=\int_0^r[\tfrac{1}{2}\theta^2(r',\theta_0)-u(z(r',\theta_0),r')]dr'. \tag{21}$$

Next the ray variational equations are obtained for the two quantities $\xi(r,\theta_0)=\partial z/\partial\theta_0$ and $\eta(r,\theta_0)=\partial\theta/\partial\theta_0$. By differentiating Eq. (20) with respect to θ_0, one obtains the linear equations

$$\frac{d\xi}{dr}=\eta, \quad \frac{d\eta}{dr}=v(r,\theta_0)\xi, \tag{22}$$

where

$$v(r,\theta_0)=-\frac{\partial^2}{\partial z^2}\,u(z(r,\theta_0),r). \tag{23}$$

The initial conditions are $\xi(0)=0$ and $\eta(0)=1$. Caustic contact points along the ray labeled by θ_0 occur at the ranges where $\xi(r,\theta_0)=0$. Five functions have been defined along a ray labeled by θ_0; these are z, θ, s, ξ, and η. The sixth such quantity, $\zeta(r,\theta_0)=\partial s/\partial\theta_0$, is not independent since it can be shown that $\zeta=\theta\xi$.

To next order in the expansion parameter k_0^{-1}, the ''transport equation'' for the ray amplitude $a^{(0)}$ is obtained. Dropping the superscript (0) for notational convenience, this linear equation is

$$\frac{\partial a}{\partial r}+\frac{\partial s}{\partial z}\,\frac{\partial a}{\partial z}+\frac{1}{2}\,\frac{\partial^2 s}{\partial z^2}\,a=-\alpha(z,r)a. \tag{24}$$

Note that the absorption coefficient α first enters the asymptotic expansion in this order. Using Eqs. (18) and (19), this equation for the ray amplitude becomes

$$\frac{da}{dr}+\frac{1}{2}\,\frac{\partial\theta}{\partial z}\,a=-\alpha(z,r)a. \tag{25}$$

It is readily found that

$$\frac{\partial\theta}{\partial z}=\frac{\partial\theta}{\partial z_0}\Big/\frac{\partial z}{\partial z_0}=\frac{\eta}{\xi}. \tag{26}$$

From the variational equations, Eq. (22), it follows that

$$\frac{\eta}{\xi}=\xi^{-1}\,\frac{d\xi}{dr}=\frac{d}{dr}\ln\,\xi. \tag{27}$$

and thus the amplitude equation becomes

$$\frac{da}{dr}+\frac{a}{2}\,\frac{d}{dr}\ln\,\xi=-\alpha(z,r)a. \tag{28}$$

This equation is readily solved to yield

$$a(r,\theta_0)=\tilde{a}(r,\theta_0)\Gamma(r,\theta_0). \tag{29}$$

Here $\tilde{a}(r,\theta_0)$ is the geometric spreading factor given by

$$\tilde{a}(r,\theta_0)=[R_0/\xi(r,\theta_0)]^{1/2}, \tag{30}$$

and the ray attenuation factor is given by

$$\Gamma(r,\theta_0)=\exp[-\beta(r,\theta_0)], \tag{31}$$

where

$$\beta(r,\theta_0)=\int_0^r\alpha(z(r',\theta_0),r')dr'. \tag{32}$$

The normalization in Eq. (30) follows from the discussion below Eq. (12) and the fact that $\xi\approx r$ for sufficiently small r. The correct branch of the square-root function in Eq. (30) is determined by the Keller–Maslov index that is familiar from the general theory of geometric acoustics. The new result here is Eq. (32) which has been shown to follow rigorously from the conventional formulation of geometric acoustics within the parabolic approximation.

III. MULTIPATH PROPAGATION

In general, for waveguide propagation there are many ray paths that connect the point source at $(z_0,0)$ to a point receiver at (Z,R). This is called multipath propagation. Since several uniformly valid methods for treating caustics are known, and in this paper the main topic is inhomogeneous absorption that is an entirely distinct phenomenon, it is henceforth assumed that the receiver location is not at a caustic of the wave field.

The condition that rays from the source pass through the receiver, called the eigenray condition, is

$$z(R,\theta_0)=Z. \tag{33}$$

Roots of this equation are denoted by θ_{0j}, $j=1,2,...,J$. Thus there are J paths, and one of them is labeled by the index j. The jth ray trajectory is $z_j(r)=z(r,\theta_{0j})$, $\theta_j(r)=\theta(r,\theta_{0j})$. Then the eikonal function at the receiver is

$$s_j=\int_0^R[\tfrac{1}{2}\theta_j^2(r')-u(z_j(r'),r')]dr'. \tag{34}$$

The geometric spreading factor at the receiver for the jth ray is

$$\tilde{a}_j = [R_0/\xi(R,\theta_{0j})]^{1/2}, \tag{35}$$

and the attenuation is

$$\Gamma_j = \exp(-\beta_j), \tag{36}$$

where

$$\beta_j = \int_0^R \alpha(z_j(r'),r')dr'. \tag{37}$$

The total field at the receiver is then obtained by coherent addition of all multipaths:

$$\psi(Z,R) = \sum_{j=1}^{J} \tilde{a}_j \Gamma_j \exp(ik_0 s_j). \tag{38}$$

It is worth noting that this expression may be rewritten as

$$\psi(Z,R) = \sum_{j=1}^{J} \tilde{a}_j \exp(ik_0 \hat{s}_j), \tag{39}$$

where the complex-valued eikonal function $\hat{s}_j$ is given by

$$\hat{s}_j = \int_0^R [\tfrac{1}{2}\theta_j^2(r') - U(z_j(r'),r')]dr'. \tag{40}$$

Here, $U(z,r)$ is the complex-valued potential function specified in Eq. (6) that contains absorption in the imaginary part. The ray trajectories in this integral are real valued, however, so this conventional treatment of inhomogeneous absorption is not the ''deviative'' absorption developed in Ref. 3, where the ray trajectories are complex valued.

Multipath interference is certainly included in this formulation of geometric acoustics. It should be noted, however, that the attenuation along each ray does not take into account the effects of multipath interference as is clearly indicated in Eq. (37). Therefore when the absorption coefficient is strongly inhomogeneous, which is the main subject of this study, the above expression is not correct. The reason, again, is that the effect of absorption is greatly reduced in regions where multipath interference causes the total field strength to be small. In the limit of a null in the total field, it is physically obvious that no attenuation due to absorption can occur at these points. It is surprising that this flaw in geometric acoustics has not previously been pointed out, except indirectly by Weston[4] for the case discussed in the next section.

IV. SURFACE BUBBLE LOSS AND DECOUPLING

The attenuation of high-frequency sound waves in the ocean due to resonant interaction with bubble clouds has been studied for at least 50 years.[6,7] It is known that the extinction coefficient α, which represents losses to both absorption and scattering, is proportional to the concentration of bubbles. For the wind-generated clouds of bubbles near the sea surface, the mean bubble concentration is commonly assumed to decrease exponentially from its peak at the surface.[4,8–11] With this assumption, the absorption coefficient has the form

$$\alpha(z) = \alpha_0 \exp(-z/l). \tag{41}$$

The two parameters α_0 and l are empirical functions of the acoustic frequency and the surface wind speed. Since these empirical functions are not germane to this article, they are omitted except to mention that the e-folding scale depth of the bubble layer is about 1 m or somewhat less.

For the high frequencies considered in this paper, $f > 10$ kHz, the influence of the bubble layer on the real part of the index of refraction is small,[9] and is henceforth neglected. Further, it is assumed that a ray that specularly reflects from the flat surface at $z=0$ is approximately a straight line within and slightly below the bubble layer. The grazing angle of this ray is $\theta = \text{const}$, and thus $dz/dr = \pm\theta$ in the parabolic approximation. Evaluation of β according to Eq. (32) for a single reflection from the surface of a ray that has a grazing angle θ near the surface yields

$$\beta_R = 2\int_0^\infty \alpha(z)dz/\theta. \tag{42}$$

Here the subscript R denotes the result of conventional ray theory. For the exponential profile in Eq. (41), this integral yields

$$\beta_R = 2\alpha_0 l/\theta. \tag{43}$$

In high-frequency acoustics, it has become customary to define a quantity called the ''surface bubble loss,'' in dB units, as[11]

$$\text{SBL} = -20\log_{10}\Gamma = -20\log_{10}\exp(-\beta) = 8.686\beta. \tag{44}$$

The conventional ray theory result is therefore

$$\text{SBL}_R = 8.686(2\alpha_0 l)/\theta. \tag{45}$$

Either implicitly[9,10,12] or explicitly[1,11] this formula has been widely used in numerical ray-tracing predictions of high-frequency propagation loss for small grazing angles at the surface.

The divergence of SBL_R in Eq. (45) as $\theta \to 0$ is physically absurd, because it violates the basic principle that any boundary loss function must tend toward zero as the grazing angle tends toward zero. According to ray theory, a ray having a smaller grazing angle as it approaches the surface has a longer path length within the lossy surface bubble layer, and therefore suffers greater loss. However, the resulting loss formula cannot be correct for small grazing angles because the loss becomes arbitrarily large. Since the above ray-theoretic calculation leading to Eq. (45) follows rigorously from the conventional equations of geometric acoustics, as derived above in Sec. II, it follows that the conventional formulation of geometric acoustics is seriously flawed in the presence of inhomogeneous absorption. The cause of this flaw is the neglect of multipath interference when calculating attenuation, as was indicated above and is further discussed next.

Near the surface, an up-going ray that is approaching the surface interferes with a down-going ray that has been reflected from the surface. This is called the Lloyd's mirror effect, surface image interference, or surface decoupling. The coherent ray-tracing result above in Eq. (38) correctly describes this effect when there is no absorption. For a plane

wave that has grazing angle θ, the acoustic intensity near the pressure-release surface at $z=0$ is easily found to be

$$I=\text{const}\times\sin^2(k_0\theta z). \tag{46}$$

For a receiver location that is well below the surface bubble layer, this surface-reflected ray is counted as a single ray and the interference between the up-going and down-going components is ignored when calculating the surface bubble loss. This yields the expression in Eq. (45), which is not correct for small grazing angles because this surface image interference effect is then significant.

Weston[4] recently introduced an ingenious correction term that remedies the most serious flaw in the above ray-tracing calculation. Since the quantity β is physically the integral of the product of α and I along a ray, Weston suggests that Eq. (42) should be replaced by

$$\beta_W\approx 4\int_0^\infty \sin^2(k_0\theta z)\alpha(z)dz/\theta. \tag{47}$$

This is reasonable approximation for small SBL, but is not exact because Eq. (46) assumes no absorption and zero sea state. For an exponential loss profile, it is found that

$$\beta_W=\beta_R W, \tag{48}$$

where Weston's correction factor is[4]

$$W=4k_0^2l^2\theta^2(1+4k_0^2l^2\theta^2)^{-1}. \tag{49}$$

Thus the surface bubble loss according to Weston's theory is

$$\text{SBL}_W=\text{SBL}_R W. \tag{50}$$

In the formal limit of infinite frequency, it is clear that

$$\lim_{k_0\to\infty} W=1, \tag{51}$$

and thus geometric acoustics (ray theory) is correct at infinite frequency, as is well known. However, ray theory is not uniformly valid in the grazing angle, since $W\approx 1$ requires that

$$\theta\gg(2k_0l)^{-1}. \tag{52}$$

This is the condition for validity of ray theory for this problem. Thus for any finite frequency, no matter how large, it is always possible to find a grazing angle so small that ray theory is not valid for calculating the surface bubble loss.

According to Weston's theory, the surface bubble loss as a function of grazing angle is

$$\text{SBL}_W=(8.686)(8k_0^2\alpha_0l^3)\theta(1+4k_0^2l^2\theta^2)^{-1}. \tag{53}$$

The maximum value of this function occurs at $\theta=\theta_p=(2k_0l)^{-1}$, and is found to be

$$(\text{SBL}_W)_{\max}=(8.686)(2k_0\alpha_0l^2). \tag{54}$$

If $\theta\ll\theta_p$, then SBL_W decreases linearly to zero as $\theta\to 0$, which is consistent with the basic physical principle enunciated above. Also ray theory overestimates the surface bubble loss by an arbitrarily large amount in this limit. If $\theta\gg\theta_p$, then $\text{SBL}_W\approx\text{SBL}_R$, and the surface bubble loss decreases with increasing grazing angle as θ^{-1}, in accordance with ray theory. This behavior of Weston's theory is physically reasonable.

As a numerical example, consider $f=20$ kHz and $l=0.5$ m. Then $\theta_p\approx 0.012$ rad$\approx 0.68°$. At this grazing angle, ray theory overestimates the surface bubble loss by a factor of 2. Thus if Weston's theory predicts $\text{SBL}_W=10$ dB, then ray theory predicts $\text{SBL}_R=20$ dB, which would be an error of 10 dB. For smaller grazing angles, ray theory errs by even larger amounts in this example.

Although Weston has provided a reasonably good correction to geometric acoustics for the surface bubble loss problem, at least if the loss is not too large, it is not known how to make such a correction for the many other examples of inhomogeneous absorption that are encountered in waveguide propagation problems. Even for the surface bubble loss problem, it would be extremely difficult to extend Weston's theory to the case of a downward refracting sound-speed profile near the surface. For these reasons, the use of ray-based numerical models may not be a reliable prediction method for acoustic waveguide propagation problems, even in the high-frequency regime.

V. SUMMARY AND DISCUSSION

The effects of inhomogeneous absorption in the context of the geometric acoustics approximation have been critically examined. The parabolic ray equations have been rigorously derived with the conventional scaling of terms such that the ray trajectories are not influenced by absorption. It is shown that the effects of absorption are accumulated along each ray in a manner that is physically intuitive. However, since these ray-tracing formulas do not take into account the effects of multipath interference, they can be seriously in error for waveguide propagation in the presence of inhomogeneous absorption. It has been shown in general that the geometric approximation is not uniformly valid in the grazing angle θ, i.e., for any finite acoustic frequency, there exists a small value of θ such that the geometric approximation predicts incorrect results.

For the case of attenuation by near-surface bubble clouds in the ocean, it has been shown that the forward loss predicted by conventional ray-tracing models is seriously in error for grazing angles at the surface less than about 1°, for high acoustic frequencies. In this special case, it is possible to derive an improvement to the ray-tracing result that includes the effects of multipath interference near the surface. The resulting loss formula, due to Weston, restores the correct physical behavior at small grazing angles. Since Weston's theory is a kind of perturbation theory that is valid only if the surface bubble loss is not too large, its domain of applicability is limited.

For large surface bubble loss, there appears to be no available theory to correct the result of conventional ray theory at small grazing angles. Therefore, the author and a graduate research assistant have performed a series of numerical experiments with the PE acoustic model, and have measured the surface bubble loss for different wind speeds (up to 30 kn) and for high frequencies (10–40 kHz) as a function of grazing angle. The results will be reported in a separate paper.[13]

ACKNOWLEDGMENTS

This research was partially supported by the Office of Naval Research, Code 321OA, and by the Naval Undersea Warfare Center, Code 842.

[1] H. Weinberg and R. E. Keenan, ''Gaussian ray bundles for modeling high-frequency propagation loss under shallow-water conditions,'' J. Acoust. Soc. Am. **100**, 1421–1431 (1996).
[2] F. D. Tappert and X. Tang, ''Ray chaos and eigenrays,'' J. Acoust. Soc. Am. **99**, 185–195 (1996).
[3] R. M. Jones, ''Ray theory for lossy media,'' Radio Sci. **5**, 793–801 (1970).
[4] D. E. Weston, ''On the losses due to storm bubbles in oceanic sound transmission,'' J. Acoust. Soc. Am. **86**, 1546–1553 (1989).
[5] F. D. Tappert, ''The parabolic approximation method,'' in *Wave Propagation and Underwater Acoustics*, Lecture Notes in Physics, Vol. 70, edited by J. B. Keller and J. S. Papadakis (Springer-Verlag, New York, 1977), Chap. V, pp. 224–287.
[6] ''Acoustic properties of wakes,'' Part IV of *Physics of Sound in the Sea*, edited by R. Wildt, Vol. 8, Summary Technical Report of Div. 6, National Defense Research Committee, Department of the Navy, Washington, DC, 1946.
[7] C. S. Clay and H. Medwin, *Acoustical Oceanography: Principles and Applications* (Wiley, New York, 1977), Chap. 6, pp. 178–215.
[8] B. D. Johnson and R. C. Cooke, ''Bubble population and spectra in coastal waters: a photographic approach,'' J. Geophys. Res. **84**, 3761–3766 (1979).
[9] J. C. Novarini and D. R. Bruno, ''Effects of the sub-surface bubble layer on sound propagation,'' J. Acoust. Soc. Am. **72**, 510–514 (1982).
[10] M. V. Hall, ''A comprehensive model of wind-generated bubbles in the ocean and predictions of the effects on sound propagation at frequencies up to 40 kHz,'' J. Acoust. Soc. Am. **86**, 1103–1117 (1989).
[11] P. H. Dahl, ''Revisions and notes on a model for bubble attenuation in near-surface propagation,'' Applied Physics Laboratory, University of Washington, Technical Report 9411, November, 1994.
[12] M. Schulkin, ''Surface-coupled losses in surface sound channel propagation. II,'' J. Acoust. Soc. Am. **45**, 1054–1055 (1969).
[13] F. D. Tappert and Jun He, ''Numerical study of surface bubble loss'' (unpublished).

Application of the integral equation method to acoustic wave diffraction from elastic bodies in a fluid layer

Valentin E. Belov, Sergey M. Gorsky, Alexey A. Zalezsky, and Alexey Y. Zinovyev
Institute of Applied Physics, RAS; 46, Ulyanov St., 603600, Nizhny Novgorod, Russia

(Received 13 July 1994; revised 5 September 1997; accepted 4 November 1997)

A method is proposed for solving the wave diffraction problem by employing a system of N space-localized inhomogeneities in a longitudinally homogeneous waveguide. The method combines integral equations and eigenfunction methods. As an illustration of this method, acoustic diffraction is calculated from a system of N, different, parallel cylinders arbitrarily placed in a liquid layer. The problem is reduced to a system of $2N$ integral-functional equations relative to fields excited in elastic bodies and sources of scattered waves on the surface of the cylinders. Standard methods may be used for solving the systems of equations. Numerical solutions are found for various versions of the system of elastic cylinders ($N=1,2$) in a liquid layer with perfectly ''soft'' and ''hard'' walls. The method allows: (1) the calculation of the scattering matrix for reflected and transmitted waves with any given accuracy; (2) the construction of the amplitude-frequency and the phase-frequency characteristics for the matrix elements; and (3) the calculation of the distribution of field sources on the surface of each cylinder and the scattered wave field both in the near and far zones. © *1998 Acoustical Society of America.* [S0001-4966(98)04802-4]

PACS numbers: 43.20.Gp, 43.20.Jr [JEG]

INTRODUCTION

This paper addresses diffraction and resonance scattering of acoustic waves from space-localized inhomogeneities in a fluid waveguide. In many instances, the efficiency of the solutions depends on the methods used in the investigations. Effective numerical simulations have been used based on the methods of eigenfunctions,[1] T-matrices,[2,3] integral equations, auxiliary sources, collocation, and others.[4–6] However, when applied to the problem of diffraction from inhomogeneities in a waveguide, these methods are too unwieldy or have restricted areas of application, outside of which the numerical solutions are either unstable or poorly converging.

In this paper a method is presented that combines integral equations and eigenfunctions for solution of such problems This method represents the space-localized inhomogeneities as a system of elastic bodies of rotation. The problem is reduced to solving a set of simple, singular integral-function equations involving the Fredholm integral of the second kind relative to scattered waves on the surface of the bodies. The efficiency of the method is illustrated by solving for the acoustic wave diffraction from one or more elastic cylinders in a two-dimensional homogeneous layer composed of a perfect compressible liquid.

I. STATEMENT OF THE PROBLEM AND METHOD OF SOLUTION

Consider a planar waveguide filled with a perfect compressible liquid of density, ρ, sound speed, c; and containing N localized inhomogeneities composed of round, elastic, parallel cylinders, each of radius R_ν, density ρ_ν, and having Lame coefficients λ_ν, μ_ν, where $\nu=1,2,...,N$.

A cross section of the waveguide system is shown in Fig. 1. The waveguide is bounded above and below by parallel planes located at $x=0$ and $x=d$. The axes of the embedded cylinders (space-localized inhomogeneities) are parallel to the z axis of the waveguide and cross the $z=0$ plane at points (x_ν, y_ν). The analysis presented here is restricted to the two-dimensional steady-state problem with temporal dependence $\exp(-i\omega t)$.

Within the waveguide the acoustic field is described by

$$P(x,y)=P_e(x,y)+\sum_{\nu=1}^{\infty} P_{s\nu}(x,y), \tag{1}$$

where $P_e(x,y)$ is the pressure field emitted by external sources, and $P_{s\nu}(x,y)$ is the pressure field scattered by the νth cylinder.

Elastic oscillations in each cylindrical body will be described by the scalar potential, $F^{(\nu)}(r_\nu,\varphi_\nu)$, and the z-component of the vector potential of displacements in an elastic body, $\Phi^{(\nu)}(r_\nu,\varphi_\nu)$. The polar coordinate system, (r_ν,φ_ν), which is connected with the rectangular coordinate system, (x,y), by the relationships,

$$x=X_\nu+r_\nu \sin\varphi_\nu, \quad y=Y_\nu+r_\nu\cos\varphi_\nu, \tag{2}$$

where $\nu=1,2,...,N$, corresponds to each cylinder. In the following all variables and parameters that have the dimension of length are considered normalized by d/π.

The problem is reduced to finding fields $P(x,y)$, $P_{s\nu}(x,y)$, $F^{(\nu)}(r_\nu,\varphi_\nu)$, and $\Phi^{(\nu)}(r_\nu,\varphi_\nu)$, which satisfy:

(1) Helmholtz wave equations

$$(\nabla^2+k^2)P(x,y)=0 \tag{3a}$$

in the region $r_\nu\geqslant R_\nu$, $0\leqslant x\leqslant\pi$, $-\infty<y<\infty$;

$$\begin{aligned}&(\nabla^2+k_{l\nu}^2)F^{(\nu)}(r_\nu,\varphi_\nu)=0,\\ &(\nabla^2+k_{t\nu}^2)\Phi^{(\nu)}(r_\nu,\varphi_\nu)=0,\end{aligned} \tag{3b}$$

in the region $0\leqslant r_\nu\leqslant R_\nu$, $0\leqslant\varphi_\nu\leqslant 2\pi$, $\nu=1,2,...,N$, where ∇^2 is the Laplace operator, $k=2d/\lambda$, $k_{t\nu}=kc/c_{t\nu}$, $k_{t\nu}$

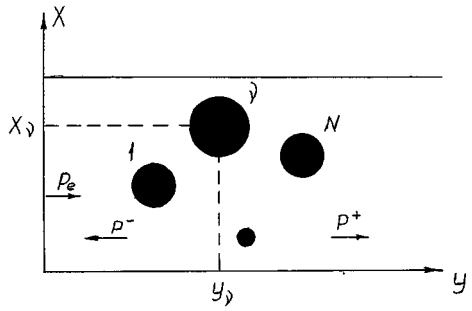

FIG. 1. Schematic cross section of the waveguide showing cylinders and coordinates.

$=kc/c_{t\nu}$ are the wave numbers, λ is the wavelength in a liquid medium of density ρ, $c_{t\nu}=[(\lambda_\nu+2\mu_\nu)/\rho_\nu]^{1/2}$, $c_{t\nu}=[\mu_\nu/\rho_\nu]^{1/2}$.

(2) Boundary conditions on the waveguide walls

$$\left[\alpha_0+\beta_0\frac{\partial}{\partial x}\right]_{x=0}P=0,\qquad \left[\alpha_1+\beta_1\frac{\partial}{\partial x}\right]_{x=x}P=0, \tag{4}$$

where α_0, α_1, β_0, β_1, are constant numbers which are, in general, complex.

(3) Radiation conditions in the y direction.

(4) Coupling conditions joining the total field $P(x,y)$ with the elastic oscillations of N cylinders, each at $r_\nu=R_\nu(\nu=1,2,...,N)$.

They correspond to:

(i) the absence of a tangent component of the stress tensor (a perfect liquid does not transfer tangent stresses)

$$\sigma_{r\varphi}^{(\nu)}|_{r_\nu=R_\nu}=\mu_\nu\left[\frac{\pi}{d}\right]^2\left[2\frac{\partial}{\partial r_\nu}\left(\frac{1}{r_\nu}\frac{\partial F^{(\nu)}}{\partial\varphi_\nu}\right)-k_{t\nu}^2\Phi^{(\nu)}-2\frac{\partial^2\Phi^{(\nu)}}{\partial r_\nu^2}\right]_{r_\nu=R_\nu}=0. \tag{5a}$$

(ii) the continuity of the normal component of the stress tensor

$$\sigma_{rr}^{(\nu)}|_{r_\nu=R_\nu}=2\mu_\nu\left[\frac{\pi}{d}\right]^2\left[\frac{\partial}{\partial r_\nu}\left(\frac{1}{r_\nu}\frac{\partial F^{(\nu)}}{\partial\varphi_\nu}\right)-\frac{\lambda_\nu}{2\mu_0}k_{t\nu}^2F^{(\nu)}+\frac{\partial^2F^{(\nu)}}{\partial r_\nu^2}\right]_{r_\nu=R_\nu}=-P|_{r_\nu=R_\nu}. \tag{5b}$$

(iii) the continuity of the normal component of the displacement vector

$$U_r^{(\nu)}|_{r_\nu=R_\nu}=\left[\frac{\pi}{d}\right]^2\left[\frac{\partial F^{(\nu)}}{\partial r_\nu}+\frac{1}{r_\nu}\frac{\partial\Phi^{(\nu)}}{\partial\varphi_\nu}\right]_{r_\nu=R_\nu}=\frac{1}{\rho(kc)^2}\frac{\partial P}{\partial r_\nu}\bigg|_{r_\nu=R_\nu}. \tag{5c}$$

A solution of the boundary problem will be found in the approximation of a given field $P_e(x,y)$ which may be imagined as a series of a complete eigenfunctions, $P_n(x,y)$, of the boundary value problem (3a)–(4). They have the form

$$P_n(x,y)=\exp(\pm ig_ny)\cdot\sin(\eta_nx-\theta_n), \tag{6}$$

where $g_n=(k_n^2-\eta_n^2)^{1/2}$ are longitudinal wave numbers and η_n are transverse wave numbers. The spectrum of eigenvalues η_n is determined by the dispersion equation

$$\tan(\eta_n\pi)=\frac{-\xi_0+\xi_1}{\xi_0\xi_1+\eta_n^2}\,\eta_n,\qquad \theta_n=\tan^{-1}\left(\frac{\eta_n}{\xi_0}\right),\quad \xi_0=\frac{\alpha_0}{\beta_0},\quad \xi_1=\frac{\alpha_1}{\beta_1}. \tag{7}$$

Eigenfunctions of the corresponding conjugate problem are given by

$$\overline{P_n}(x,y)=\frac{2}{\gamma_n}P_n(x,y),\qquad \gamma_n=\pi+\frac{\xi_1-\xi_0}{(\xi_0-\eta_n^2)(\xi_1-\eta_n^2)}. \tag{8}$$

Using Eq. (6), the field from the sources can be written as

$$P_e(x,y)=\sum_{n=1}^{\infty}A_n\exp(ig_ny)\cdot\sin(\eta_nx-\theta_n), \tag{9}$$

where A_n are given amplitudes. With respect to the (r_ν,ϕ_ν) coordinate system connected with the νth cylinder, the field can be represented as

$$P_e(x,y)=\sum_{m=-\infty}^{\infty}a_{m\nu}J_{m\nu}(kr_\nu)\cdot\exp(im\varphi_\nu), \tag{10}$$

where

$$a_{m\nu}=i^m\sum_{n=1}^{\infty}A_n\exp(ig_nY_\nu)\cdot\sin(g_nx_\nu+m\Psi_\nu-\theta_n),\qquad \Psi_n=\cos^{-1}\left(\frac{\eta_n}{k}\right)-\frac{\pi}{2}. \tag{11}$$

The field $P_{s\nu}(x,y)$ of waves scattered by the νth cylinder will be found as a potential of a simple layer:

$$P_{s\nu}(x,y)=\int_{L_\nu}G_\nu(x,y;x_{\nu0},y_{\nu0})\mu_\nu^0(x_{\nu0},y_{\nu0})dl_{0\nu}, \tag{12}$$

where $\mu_\nu^0(x_{\nu0},y_{\nu0})$ is an unknown function describing the source fields distribution on the surface of the νth cylinder, (x,y) are the coordinates of an observation point, $(x_{\nu0},y_{\nu0})$ are the coordinates of current integration point over the line L_ν, and L_ν is a circle of radius R_ν, centered at the point $x=X_\nu$, $y=Y_\nu$, $dl_{0\nu}=dx_{0\nu}\,dy_{0\nu}$.

The Green's function $G_\nu(x,y;x_{\nu0},y_{\nu0})$ is the solution of

$$(\nabla^2+k^2)G=\delta(x-x_{\nu0})\,\delta(y-y_{\nu0}),\qquad \nu=1,2,...,N, \tag{13}$$

which fits the radiation conditions at $y\to\pm\infty$ and the boundary conditions given by Eq. (4). They have the following form:

$$G_\nu(x,y;x_{\nu 0},y_{\nu 0})=\sum_{n=1}^{\infty} G_{\nu n}(x,y;x_{\nu 0},y_{\nu 0}),$$

$$G_{\nu n}=\frac{i}{\gamma_n g_n}\sin(\eta_n x-\theta_n)\sin(\eta_n x_{\nu n}-\theta_n)\times\begin{cases}\exp(ig_n(y-y_{\nu 0})), & y\geqslant y_{\nu 0},\\ \exp(ig_n(y_{\nu 0}-y)), & y\leqslant y_{\nu 0}.\end{cases} \tag{14}$$

Since $dl_{0\nu}=R_\nu d\varphi_{0\nu}$, denoting $\mu_0(\varphi_0)=R_\nu\mu_\nu^0(\varphi_{\nu 0})$, it is possible to turn to a single integral in Eq. (13):

$$P_{s\nu}(x,y)=\int_0^{2\pi} G_\nu(x,y;R_\nu,\varphi_{\nu 0})\cdot\mu_\nu(\varphi_{\nu 0})d\varphi_{0\nu}. \tag{15}$$

The use of Green's function in Eq. (12) in the form (14) allows the problem to be reduced to finding a distribution of the sound field sources μ_ν^0 on N cylinders each, that will fit the continuity conditions (5).

Distribution of the potentials $F^{(\nu)}(r_\nu,\varphi_\nu)$ and $\Phi^{(\nu)}\times(r_\nu,\varphi_\nu)$ in the elastic cylinders will be found as a series of the respective eigenfunctions of a cylinder,

$$F^{(\nu)}(r_\nu,\varphi_\nu)=\sum_{m=-\infty}^{\infty} B_{\nu m}J_m(k_{t\nu}r_\nu)\exp(im\varphi_\nu),$$

$$\Phi^{(\nu)}(r_\nu,\varphi_\nu)=\sum_{m=-\infty}^{\infty} C_{\nu m}J_m(k_{t\nu}r_\nu)\exp(im\varphi_\nu). \tag{16}$$

Substituting expressions (10), (15), and (16) into (5) gives the correlation,

$$C_{\nu m}=i\,\frac{\Phi_{1m}(k_{t\nu}r_\nu)}{\Phi_{2m}(k_{t\nu}r_\nu)}B_{\nu m},\quad -\infty<m<\infty, \tag{17}$$

$$\sum_{m=-\infty}^{\infty}[z_{1m}^\nu B_{\nu m}-kJ_m'(kR_\nu)a_{m\nu}]\exp(im\varphi_\nu)=\left[\frac{\partial}{\partial r_\nu}\left(\sum_{l=1}^{N}P_{sl}\right)\right]_{r_\nu=R_\nu},$$

$$\sum_{m=-\infty}^{\infty}[z_{2m}^\nu B_{\nu m}+J_m(kR_\nu)a_{m\nu}]\exp(im\varphi_\nu)=-\left[\left(\sum_{l=1}^{N}P_{sl}\right)\right]_{r_\nu=R_\nu}, \tag{18}$$

where $\nu=1,2,...,N$, and

$$z_{1m}^\nu=\frac{\rho(kc)^2(\pi/d)^2}{R_\nu\Phi_{2m}(k_{t\nu}R_\nu)}[k_{t\nu}R_\nu J_m(k_{t\nu}R_\nu)\Phi_{2m}(k_{t\nu}R_\nu)]-mJ_m'(k_{t\nu}R_\nu)\Phi_{1m}(k_{t\nu}R_\nu),$$

$$z_{1m}^\nu=\frac{\mu_\nu(\pi/d)^2}{R_\nu\Phi_{2m}(k_{t\nu}R_\nu)}[\Phi_{3m}(k_{t\nu}R_\nu)\Phi_{2m}(k_{t\nu}R_\nu)-\Phi_{1m}(k_{t\nu}R_\nu)\Phi_{1m}(k_{t\nu}R_\nu)],$$

$$\Phi_{1m}(x)=2m[xJ_m'(x)-J_m(x)],$$

$$\Phi_{2m}(x)=-2\left[xJ_m'(x)+\left(\frac{x^2}{2}-m^2\right)J_m(x)\right],$$

$$\Phi_{3m}(x)=2x^2\left[J_m''(x)-\frac{\lambda_\nu}{2\mu_\nu}J_m(x)\right].$$

The right-hand parts of Eqs. (18) contain the sums of N integrals over lines L_ν ($\nu=1,2,...,N$). At $l\neq\nu$ they are obvious Riemann's integrals. At $l=\nu$ they are singular and make no sense in the obvious (Riemann's) interpretation. They obtain a definite sense by introducing the Cauchy principal value of the integral. If at $l\neq\nu$, the fields P_{sl} and radial derivatives $(\partial P_{sl}/\partial r_\nu)$ are continuous functions along the line L_ν, at $l=\nu$ the derivatives $(\partial P_{sl}/\partial r_\nu)$ have a break of the first kind, which equals $\mu_\nu(\varphi_\nu)$ in magnitude. Thus the integrals of P_{sl} in Eq. (15), and $(\partial P_{sl}/\partial r_\nu)$ in the right-hand parts of Eqs. (18) should be understood in the sense of the principal value with a transfer of the differentiation operators immediately on the function being interacted. In terms of these remarks the correlations (18) can be represented as a system of $2N$ singular Fredholm integral equations of the second kind relative to the functions $\mu_\nu(\varphi_\nu)$ and the coefficients $B_{\nu m}$:

$$\sum_{m=-\infty}^{\infty}[z_{1m}^\nu B_{\nu m}-kJ_m'(kR_\nu)a_{m\nu}]\exp(im\varphi_\nu)=\mu_\nu(\varphi_\nu)+\sum_{l=1}^{N}\int_0^{2\pi}L_{\nu l}(\varphi_\nu,\varphi_{l0})\cdot\mu_1(\varphi_{l0})d\varphi_{l0},$$

$$\sum_{m=-\infty}^{\infty}[z_{2m}^\nu B_{\nu m}+J_m(kR_\nu)a_{m\nu}]\exp(im\varphi_\nu)=-\sum_{l=1}^{N}\int_0^{2\pi}K_{\nu i}(\varphi_\nu,\varphi_{l0})\cdot\mu_1(\varphi_{l0})d\varphi_{l0}, \tag{19}$$

where $\nu=1,2,...,N$, and,

$$K_{\nu l}=[G_l(x_\nu,y_\nu;x_{l0},y_{l0})]_{r_\nu=R_\nu},\quad x_\nu=X_\nu+R_\nu\sin\varphi_\nu,$$

$$L_{\nu l}=\left[\frac{\partial G_l}{\partial r_\nu}(x_\nu,y_\nu;x_{l0},y_{l0})\right]_{r_\nu=R_\nu},\quad y_\nu=Y_\nu+R_\nu\cos\varphi_\nu, \tag{20a}$$

$$K_{l\nu}=\sum_{n=1}^{\infty}K_{l\nu}^n(\varphi_\nu,\varphi_{l0}),\quad x_{l0}=X_l+R_l\sin\varphi_{l0},$$

$$L_{l\nu}=\sum_{n=1}^{\infty}L_{l\nu}^n(\varphi_\nu,\varphi_{l0}),\quad y_{l0}=Y_l+R_l\cos\varphi_{l0},$$

$$K_{\nu l}^{n}=\frac{i}{\gamma_n g_n}\sin(\eta_n x_\nu-\theta_n)\sin(\eta_n x_{l0}-\theta_n)\times\exp[\pm ig_n(y_\nu-y_{l0})],$$

$$L_{\nu l}^{n}=\frac{1}{\gamma_n}\sin(\eta_n x_{l0}-\theta_n)\left[\frac{\eta_n}{ig_n}\sin(\varphi_\nu)\cos(\eta_n x_\nu-\theta_n)\pm\cos(\varphi_\nu)\sin(\eta_n x_\nu-\theta_n)\right]\exp[\pm ig_n(y_\nu-y_{l0})]. \tag{20b}$$

Here the top sign corresponds to the region $y_\nu \geqslant y_{l0}$, and the lower sign corresponds to the region $y_\nu \leqslant y_{l0}$.

In performing calculations, convergence of the series (20b) is improved by separating asymptotics $(k\to 0)$ and representing them as

$$K_{\nu l}=\overline{K}_{\nu l}+\sum_{n=1}^{\infty}(K_{l\nu}^{n}-\overline{K}_{\nu l}^{n}),$$

$$L_{\nu l}=\overline{L}_{\nu l}+\sum_{n=1}^{\infty}(L_{l\nu}^{n}-\overline{L}_{\nu l}^{n}),$$

where

$$\overline{K}_{\nu l}^{n}=K_{\nu l}^{n}+O(n^{-2}),\quad \overline{L}_{\nu l}^{n}=L_{\nu l}^{n}+O(n^{-2}),$$
$$\overline{K}_{\nu l}=\sum_{n=1}^{\infty}\overline{K}_{l\nu}^{n},\quad \overline{L}_{\nu l}=\sum_{n=1}^{\infty}\overline{L}_{l\nu}^{n}. \tag{21}$$

The functions $\overline{K}_{\nu\nu}(\varphi_\nu,\varphi_{\nu 0})$ and $\overline{L}_{\nu\nu}(\varphi_\nu,\varphi_{\nu 0})$ have singularities of the kind $K_{\nu\nu}\approx\ln(\varphi_\nu-\varphi_{\nu 0})$ and $L_{\nu\nu}\approx(\varphi_\nu-\varphi_{\nu 0})^{-1}$. In performing numerical calculations their values are connected at the points $\varphi_\nu=\varphi_{\nu 0}$ to give the following average values:

$$K_{\nu\nu}(\varphi_\nu,\varphi_{\nu 0})=\tfrac{1}{2}\lim_{\Delta\to 0}[K_{\nu\nu}(\varphi_\nu,\varphi_\nu+\Delta)+K_{\nu\nu}(\varphi_\nu,\varphi_\nu-\Delta)],$$

$$L_{\nu\nu}(\varphi_\nu,\varphi_{\nu 0})=\tfrac{1}{2}\lim_{\Delta\to 0}[L_{\nu\nu}(\varphi_\nu,\varphi_\nu+\Delta)+L_{\nu\nu}(\varphi_\nu,\varphi_\nu-\Delta)].$$

The main values of the integrals from Eq. (19) are separated. The rest of series (21) is quickly converging and has no singularities.

The Galerkin–Ritz method with basis function $\exp(im\varphi_\nu)$ is used to solve the system of equations. Each of those is used for the pair of equations with their own subscript ''ν.'' Because the functions $\mu_\nu(\varphi_\nu)$ are determined on the interval $0\leqslant\varphi_\nu\leqslant 2\pi$ and the integrals $\int_0^{2\pi}|\mu_\nu(\varphi_\nu)|d\varphi_\nu$ exist because of the finiteness of the field $P_{s\nu}$, they can be represented as Fourier series

$$\mu_\nu(\varphi_\nu)=\sum_{p=-\infty}^{\infty}b_{p\nu}\exp(ip\varphi_\nu);$$
$$b_{p\nu}=\frac{1}{2\pi}\int_0^{2\pi}\mu_\nu(\varphi_\nu)\exp(ip\varphi_\nu)d\varphi_\nu \tag{22}$$

and put into Eq. (19). Then each pair of equations in (19) should be multiplied by the functions $\exp(im\varphi_\nu)/2\pi$ with a corresponding subscript ''ν'' and integrated over φ_ν from 0 to 2π. As a result an inhomogeneous infinite system of linear algebraic equations relative to the coefficients $b_{p\nu}$ and $B_{p\nu}$ $(\nu=1,2,...,N)$ is obtained. After simple transformations it can be expressed as:

$$b_{m\nu}+\sum_{l=1}^{N}\left[\sum_{p=-\infty}^{\infty}b_{pl}M_{pm}^{l\nu}\right]=P_{pm}^{\nu}a_{m\nu}, \tag{23}$$

$$B_{\nu m}=-\frac{1}{z_{2m}^{\nu}}\left[J_m(kR_\nu)a_{m\nu}+\sum_{l=1}^{N}\left[\sum_{p=-\infty}^{\infty}b_{pl}N_{pnt}^{l\nu}\right]\right], \tag{24}$$

where $\nu=1,2,...,N$, $-\infty<m<\infty$, and

$$M_{pm}^{l\nu}=\frac{1}{2\pi}\int_0^{2\pi}\left\{\int_0^{2\pi}[L_{\mu l}(\varphi_\nu,\varphi_{l0})-z_{\nu m}K_{\nu l}(\varphi_\nu,\varphi_{l0})]\times\exp[i(p\varphi_{l0}-m\varphi_\nu)]d\varphi_{\nu 0}\right\}d\varphi_\nu,$$

$$N_{pm}^{l\nu}=\int_0^{2\pi}\left\{\int_0^{2\pi}K_{\nu l}(\varphi_\nu,\varphi_{l0})\times\exp[i(p\varphi_{l0}-m\varphi_\nu)]d\varphi_{\nu 0}\right\}d\varphi_\nu, \tag{25}$$

$$P_{pm}^{\nu}=-[kJ_m'(kR_\nu)+z_{\nu p}J_p(kR_\nu)]\delta_{pm},$$

where $z_{\nu m}=z_{lm}^{\nu}/z_{2m}^{\nu}$.

Solutions of the system of equations in (23) permit one to calculate completely the distribution of the fields $P(x,y)$ and $P_s(x,y)$ in a waveguide and the potentials $F^{(\nu)}(r_\nu,\varphi_\nu)$ and $\Phi^{(\nu)}(r_\nu,\varphi_\nu)$ in elastic bodies. The scattered wave field distribution $P_s(x,y)$ should be calculated, especially in the near zone, by the following formula:

$$P_s(x,y)=\sum_{\nu=1}^{N}\sum_{p=-\infty}^{\infty}\int_0^{2\pi}B_{p\nu}G_\nu(x,y;x_{\nu 0},y_{\nu 0})\times\exp(ip\varphi_{\nu 0})d\varphi_{\nu 0}, \tag{26}$$

where asymptotic $(k\to 0)$ parts should be also separated in the expression of Green's function G_ν.

The potential distributions $F^{(\nu)}(r_\nu,\varphi_\nu)$ and $\Phi^{(\nu)}\times(r_\nu,\varphi_\nu)$ as well as the distribution of the field sources $\mu_\nu(\varphi_\nu)$ on the surface of the elastic bodies can be easily calculated by Eqs. (16), (22), (24), and (25).

If a system of N elastic bodies is placed in some infinite volume of the waveguide, it can be considered as a waveguide node loaded on two semi-infinite regular waveguides limited by reference planes $y=y_0\leqslant\min(Y_\nu-R_\nu)$ and $y=y_1\leqslant\max(Y_\nu+R_\nu)$. In each of these waveguides the fields $P_s(x,y)$ of scattered waves can be conveniently represented as a set of natural modes of a homogeneous waveguide. For $y<y_0$,

$$P_s^-(x,y)=\sum_{n=1}^{N} A_n^- \sin(\eta_n x-\theta_n)\exp(-ig_n y),$$
$$A_n^-=i\sum_{\nu=1}^{N} \frac{\exp(ig_n Y_\nu)}{g_n\gamma_n} \sum_{m=-\infty}^{\infty} i^m b_{m\nu} J_m(kR_\nu) \times\sin(\eta_n X_\nu - m\Psi_n-\theta_n), \tag{27}$$

and for $y>y_1$,

$$P_s^+(x,y)=\sum_{n=1}^{N} A_n^+ \sin(\eta_n x-\theta_n)\exp(-ig_n y),$$
$$A_n^+=i\sum_{\nu=1}^{N} \frac{\exp(ig_n Y_\nu)}{g_n\gamma_n} \sum_{m=-\infty}^{\infty} i^m b_{m\nu} J_m(kR_\nu) \times\sin(\eta_n X_\nu + m(\Psi_n+\pi)-\theta_n). \tag{28}$$

By means of Eqs. (27) and (28) it is possible to calculate the amplitude- and phase-frequency characteristics (AFC and PFC) of waveguide modes in the waveguide system being considered. When calculating $P_s(x,y)$ in the region of the waveguide mode it is necessary to take into account the sources of the field placed both on the left and on the right of the plane $y=\text{const}$, on which the observation point is disposed. On the left of it they are placed on the entire surface of the cylinders, for which $Y_\nu+R_\nu<y$ and on the part of the surface of the cylinders crossing the plane $y=\text{const}$, for which $Y_\nu<y$; on the right of this plane—on the entire surface of the cylinders with $Y_\nu-R_\nu>y$ and on the corresponding part of the cylinders, which cross the plane $y=\text{const}$. As a result, in this region the field of scattered waves, $P_s(x,y)$, can be represented as a set of waveguide modes propagating both in the positive and in the negative directions of the y axis. In this case, their amplitudes prove to be essentially dependent on coordinate y.

II. ANALYSIS OF THE DIFFRACTION FIELD STRUCTURE

Using the method described above, it is possible to calculate, with a given accuracy all parameters and functions, which are necessary for a detailed analysis of both the entire field distribution $P(x,y)$ and the diffracted wave structure $P_s(x,y)$. By means of the coefficients $b_{m\nu}$ obtained by solving the system (23), it is possible to find the amplitudes $B_{m\nu}$ and $C_{m\nu}$ [Eqs. (17) and (24)], to calculate the scattered field distribution $P_s(x,y)$ [Eqs. (26)–(28)], the potentials $F^{(\nu)}\times(r_\nu,\varphi_\nu)$ and $\Phi^{(\nu)}(r_\nu,\varphi_\nu)$ in each of the elastic cylinders [Eq. (10)], amplitudes of the normal modes, A_n^- and A_n^+, in reflected and transmitted waves [Eqs. (27), (28)], etc. This makes it possible not only to analyze in detail the structure of the wave diffracted at the elastic cylinders, but also to investigate its dependence on material and geometric parameters of the elastic bodies and the waveguide in any frequency range. The phenomena, due to the resonance excitation of elastic oscillations of the cylinders and the features of the field distribution both in the near and far zones are of most interest in this respect.

The field outside the node can be described by an incident field and the response of the waveguide node to it. This response is determined by a set of diffracted waves, leaving the node or damping as a distance from the node increases. Because the system is linear, for full description of the entire field it is sufficient to calculate a scattering matrix $\hat{S}$ which determines the bond between the amplitudes in the incident and scattered waves:

$$\mathbf{A}=\hat{S}^-\cdot\mathbf{A}^-, \quad \mathbf{A}=\hat{S}^+\cdot\mathbf{A}^+, \tag{29}$$

where $\mathbf{A}=(A_n)$, $\mathbf{A}^-=(A_n^-)$, $\mathbf{A}^+=(A_n^+)$ are the vectors, the component of which are the complex mode amplitudes in the incident, reflected, and transmitted wave, respectively. $\hat{S}^-=\|S_{nm}^-\|$ is a matrix of scattering to the first regular waveguide. $\hat{S}^+=\|S_{nm}^+\|$ is a transmission matrix from the first waveguide to the second one. The elements of these matrices are the ratio of the corresponding amplitudes of waveguide modes in the incident, reflected, and transmitted waves:

$$S_{nm}^-=\frac{A_m^-}{A_n}, \quad S_{nm}^+=\frac{A_m^+}{A_n}, \tag{30}$$

where S_{nm}^- and S_{nm}^+ are called reflection and transmission factors of modes of order n.

Using Eqs. (27) and (28) it is easy to calculate the elements of these matrices and therefore perform full analysis of the structure of the fields $P(x,y)$ and $P_s(x,y)$ outside the waveguide node. The field distribution and the features of its structure in the area of the waveguide node can be investigated by calculating the fields using Eq. (26).

The waveguide node area can be considered as a resonator with diffraction losses by radiation. In fact, it is a waveguide analog of an open resonator. Determination of the eigenfrequencies and oscillations of such a resonator is most important in the spectral boundary-value problem. Solving this problem is of great significance when the resonance scattering of waves in a waveguide is investigated. Based on the physical precondition that a spectrum of open waveguide structures is discrete it is possible to reduce the boundary-value problem to a uniform system of linear algebraic equations:

$$b_{m\nu}+\sum_{l=1}^{N}\left[\sum_{p=-\infty}^{\infty} b_{pl}M_{pm}^{l\nu}\right]=0, \tag{31}$$

where $\nu=1,2,...,N$, $-\infty<m<\infty$, and the matrix elements $M_{pm}^{l\nu}$ are calculated by Eq. (25).

The spectrum of natural wave numbers k_s (or critical frequencies) is determined from the condition, under which the system (31) possesses a nontrivial solution:

$$\det\|l_{pm}+M_{pm}^{l\nu}(k_s)\|=0, \quad l_{nm}=\begin{cases}0, & n\neq m,\\ 1, & n=m.\end{cases} \tag{32}$$

Two points $k=k_s$ on the real axis, where the real and imaginary parts of the determinant are equal to zero simultaneously, determine the critical frequencies of the waveguide.

At points $k=k_s$ the matrix of the system (23) proves to be degenerate. Thus in these calculations Eq. (23) is solved in the full range of the change of k except $k=k_s$.

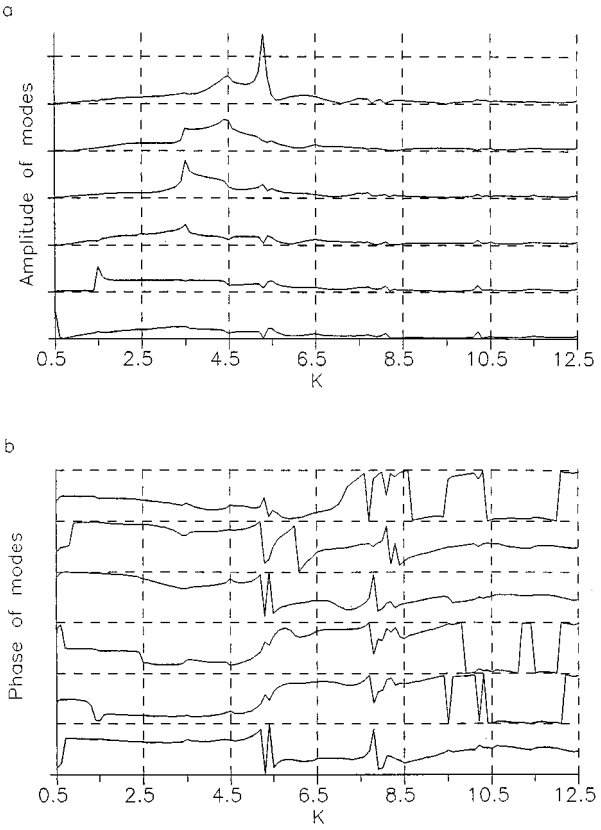

FIG. 2. AFC and PFC for the reflected wave for the first version.

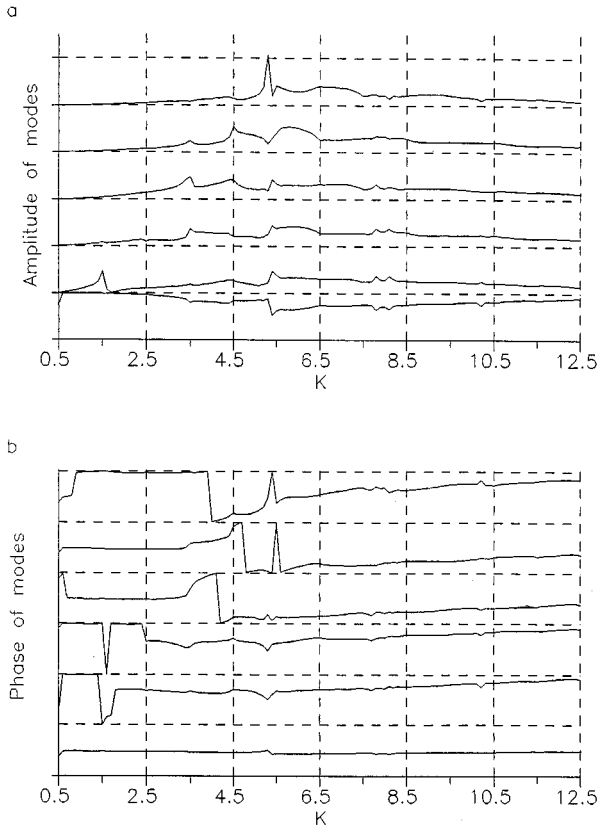

FIG. 3. AFC and PFC for the transmitted wave for the first version.

III. NUMERICAL RESULTS

To analyze the main appropriateness of the waveguide mode diffraction at elastic bodies in a layer of liquid, and to show the possibilities of the method proposed, the solution of the problem is found for one of the versions of the waveguide system corresponding to the following values of the parameters: $\alpha_0=\beta_1=0$, $\alpha_1=\beta_0=0$, e.g., for a waveguide with perfectly ''soft'' and ''hard'' walls. In this case, the expressions for $P_e(x,y)$ (9) and the items $G_{\nu n}$ in Green's function (14) take the following form:

$$P_e(x,y)=\sum_{n=0}^{\infty} A_n \cos\left[\left(n+\frac{1}{2}\right)x\right]\exp(ig_n y),$$

$$G_{\nu n}=\frac{1}{ng_n}\cos\left[\left(n+\frac{1}{2}\right)x\right]\cos\left[\left(n+\frac{1}{2}\right)x_{0\nu}\right]$$

$$\times\begin{cases}\exp[ig_n(y-y_{\nu 0})], & y\geqslant y_{\nu 0},\\ \exp[ig_n(y_{\nu 0}-y)], & y\leqslant y_{\nu 0},\end{cases} \tag{33}$$

$$g_n=[k^2-(n+0.5)^2]^{1/2}.$$

In the calculations, the waveguide mode with $n=0$ and $A_0=1$ was taken as $P_e(x,y)$; the parameters of the liquid were $\rho=10^3$ kg/m^3, $c=1493$ m/s. In the present paper the results of calculations are provided for the following versions of mutual location and number of elastic cylinders in the waveguide:

1. $N=1 \quad X_1=\dfrac{\pi}{2}, \quad Y_1=10^3, \quad R_1=\dfrac{\pi}{20},$

2. $N=2 \quad X_1=X_2=\dfrac{\pi}{2}, \quad Y_1=10^3,$

$$Y_2=Y_1+0.5, \quad R_1=R_2=\frac{\pi}{20}.$$

The material parameters are: $\rho_\nu=7.7\times10^3$ kg/m^3, $\lambda_\nu=2.22\times10^8$ Pa, and $\mu_\nu=16\times10^8$ Pa.

A. Amplitude- and phase-frequency characteristics of a scattered wave

The reduction method is usually used to solve Eq. (23). Its convergence and efficiency are determined by the structure of the matrix $\|1+M_{pm}^{l\nu}\|$ and by behavior of the matrix elements when the subscripts $|p|$, $|m|$ increase for every block with given l and ν.

As a result of the numerical experiment it is found that the real and imaginary parts of the matrix elements $M_{pm}^{l\nu}$ for any given values of l and ν, as a distance from the center in any direction grows, decrease by 3–4 orders at least. Distribution of the matrix elements in the central part of each block, naturally, possesses different properties at different frequencies and for different versions of a waveguide system. However, in general, their behavior is the same when $|p|$ and $|m|$ increase: in the block with $l=\nu$ diagonal matrix elements $\|1+M_{pm}^{l\nu}\|$ approach 1 by module, nondiagonals ones are considerably different from 0 at $|p|$, $|m|<5$ only. Such a structure of the matrix ensures fast convergence of the reduction method when solving system (23). Numerical

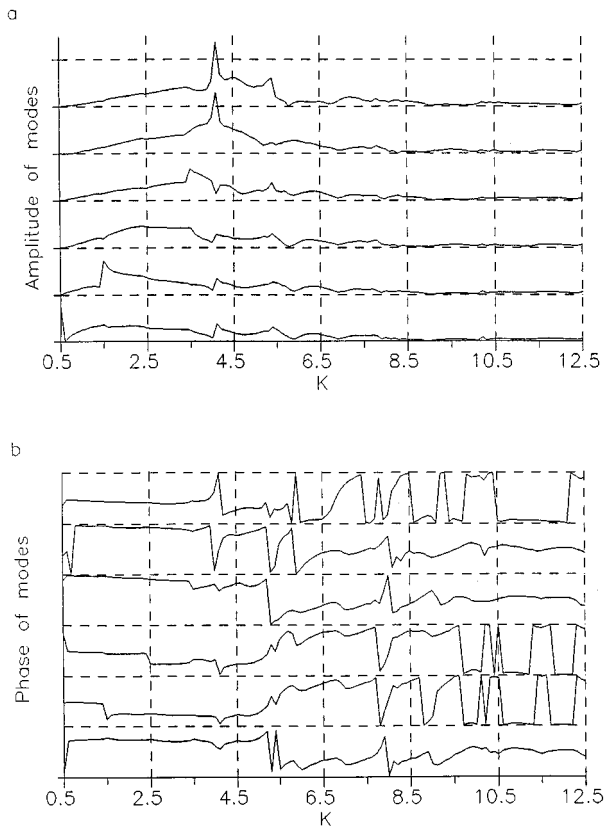

FIG. 4. AFC and PFC for the reflected wave for the second version.

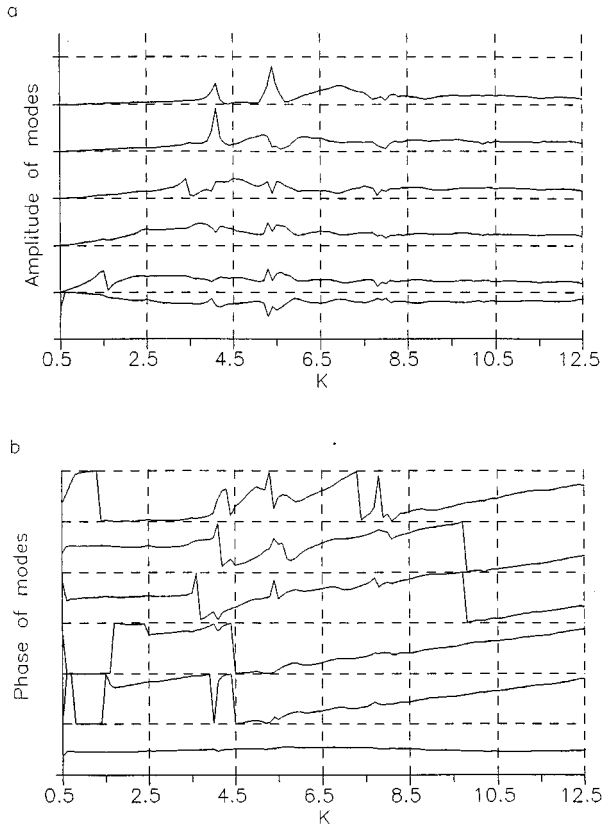

FIG. 5. AFC and PFC for the transmitted wave for the second version.

estimates show that it is sufficient to use the truncated matrices of dimension 15×15 to calculate the coefficients $b_{m\nu}$ with an accuracy of 10^{-4}.

Figures 2–5 show AFC and PFC of the waveguide modes in the reflected $A_p^- = S_{0p}^-$ (Figs. 2, 4) and transmitted $A_p^+ = S_{0p}^+$ (Figs. 3, 5) waves for each version of the system of elastic bodies in the waveguide ($N=1,2$). AFC and PFC of the modes are depicted in strips corresponding to their order p; width of AFC strip is equal to 1, that of PFC strip -2π, the lower strip corresponds to $p=0$. Analysis of AFC and PFC curves shows the following:

(1) In the vicinity of the critical frequency of each waveguide mode, a sharp increase of its amplitude and great advance of its phase are observed; there are no appreciable changes of the amplitudes and phases of other modes in this case. This is explained by a sharp increase of the density of the mode energy because of the multiple reflection at waveguide walls. These phenomena were first observed in optics when light waves are scattered by diffraction gratings, and they are called the Wood's anomalies.

(2) Sharp changes of the amplitudes and phases of the waveguide modes occur in the vicinity of natural or resonance frequencies $k_s \neq n+0.5$ of the waveguide system. In the first case such changes were observed in one mode characteristics, but here they take place in the AFC and PFC of all waveguide modes. In this last case resonance oscillations of elastic cylinders with a high quality factor are excited in the vicinity of the resonance frequencies. For their existence, ''participation'' of all waveguide modes of the system is necessary. The values of the eigenfrequencies k_s and of the quality factor value, which determines the nature of the changes of the mode amplitudes and phases, considerably depend on geometric and material parameters of the waveguide and the elastic bodies.

(3) In both versions, in transmitted and reflected waves, the amplitudes both of propagating and nonpropagating modes are considerably different from 0, especially in the region of resonance scattering. It means that nonpropagating modes play an important role where the field is formed in the area of the waveguide node and it is necessary to take them into account for determination of the propagating mode amplitudes outside the waveguide node e.g., in the far zone.

(4) In general, the eigenfrequency spectrum also depends on the number and mutual location of the elastic cylinders. It is easy to determine the values of the natural and resonance frequencies k_s for each version by the AFC and PFC curves shown in Figs. 2–5. It is necessary to note that in the cases considered here the spectra (k_{sn}) contain eigenfrequencies which are practically the same for both (for example, $k_s \approx 5.3$).

B. $P(x,y)$ in the near and far zones; $\mu_\nu(R_\nu,\phi_\nu)$ on the surface

A brief analysis of the full field, $P(x,y)$, in the near and far zones, and of the field sources, $\mu_\nu(R_\nu,\varphi_\nu)$, on the surface of elastic cylinders, will be given. To analyze the field structure in the immediate proximity of the cylinders, the distribution of the field sources $\mu_\nu(R_\nu,\varphi_\nu)$ on each cylinder

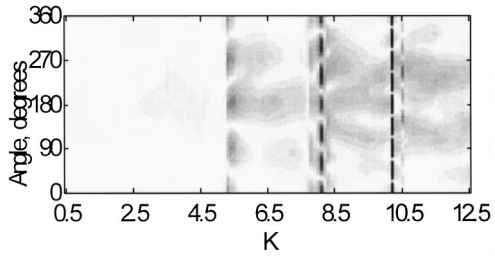

FIG. 6. Distribution of $|\mu_\nu(R_\nu,\varphi_\nu)|$ for the first version. Dark areas correspond to high density and light areas correspond to low density of source distributions.

surface, depending on the length of the incident wave, has been calculated. The distribution of the module $|\mu_\nu(R_\nu,\varphi_\nu)|$ on each cylinder and its dependence on the wave number k are shown in Figs. 6 and 7 for versions 1, 2 of the system of elastic cylinders. It shows that the nature of the distribution of $\mu_\nu(R_\nu,\varphi_\nu)$ considerably depends on the frequency and mutual location of the cylinders in the waveguide. For each elastic body it is possible to separate frequencies in the vicinity of which functions μ_ν increase sharply by amplitude, and their structure corresponds to high quality factor oscillations of an elastic cylinder at one of its eigenfrequencies. For version 1 (Fig. 6) it is possible to separate wave numbers $k \sim 6$, in the vicinity of which a natural azimuthal mode of order $m=2$ has the highest quality factor. In the vicinity of $k \sim 8.5$, this is a model of order $m=3$. In the vicinity of $k \sim 10.5$, $m=4$. For version 2 [Fig. 7(a) and (b)] on the two cylinders, respectively, those orders are the following: $k \sim 4.8$, $m=1$, and $k \sim 10.5$, $m=4$. Outside these areas the value of $|\mu_\nu(R_\nu,\varphi_\nu)|$ is substantially less, and the intensity of oscillations of the elastic bodies is correspondingly small.

The distribution of the full field, $P(x,y)$, calculated by

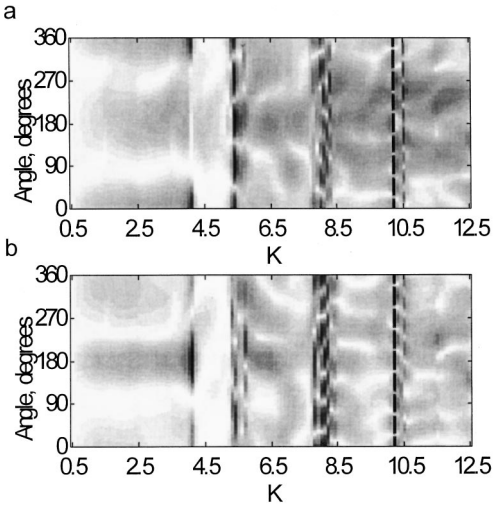

FIG. 7. Distribution of $|\mu_\nu(R_\nu,\varphi_\nu)|$ for the second version. (a) is on the first cylinder and (b) is on the second cylinder. Dark areas correspond to high density and light areas correspond to low density of source distributions.

Eqs. (26)–(28) at a frequency $k=5.3$ for both versions of the system of elastic cylinders in the waveguide is shown in Fig. 8. The scattering cylinders are marked by dark circles to

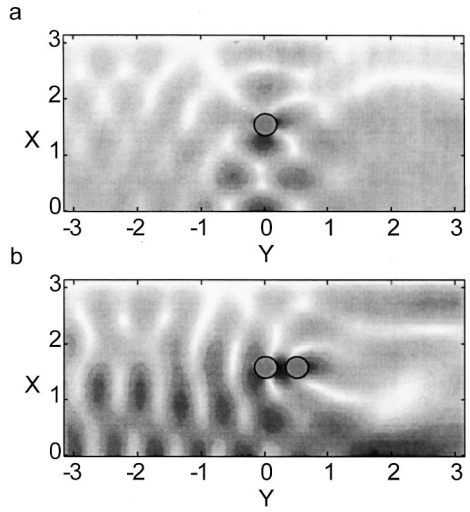

FIG. 8. Distribution of $|P(x,y)|$. (a) is for one cylinder and (b) is for two cylinders. In each case only the external field has been calculated where dark areas correspond to high sound pressure levels and light areas correspond to low sound pressure levels.

respective scale. These figures show the field structure, especially in the near zone, e.g., in the area of the waveguide node, to be rather complicated. Its features depend appreciably on the parameters of the waveguide and scattering bodies, their number and mutual location. It appears in the differences of the field structure both in the near and far zones between different versions of inhomogeneities in the waveguide system.

IV. SUMMARY

A method has been presented for solving wave diffraction problems by employing a system of N space-localized inhomogeneities in a longitudinally homogeneous waveguide. The method combined integral equations and eigenfunction methods to reduce the problem to a system of $2N$ integral-functional equations relative to fields excited in elastic bodies and sources of scattered waves on the surface of cylinders. The method allows: (1) the calculation of the scattering matrix for reflected and transmitted waves with any given accuracy; (2) the construction of the amplitude-frequency and the phase-frequency characteristics for the matrix elements; and, (3) the calculation of the distribution of field sources on the surface of each cylinder and the scattered wave field both in the near and far zones.

[1] P. C. Waterman, ''New formulation of acoustic scattering,'' J. Acoust. Soc. Am. **45**, 1417–1430 (1969).
[2] M. F. Werby and G. T. Tango, ''Applications of the extended boundary condition equations to scattering from fluid-loaded bounded object,'' Eng. Anal. **5**, 12–20 (1988).
[3] M. F. Werby and S. A. Chin-Bing, ''Some numerical techniques and their use in the extension of T-matrix and null-field approaches to scattering,'' Comput. Math. Appl. **11**, 717–731 (1985).
[4] B. Z. Katsenelenbaum, ''Diffraction at a large hole in a wide waveguide,'' USSR Acad. Sci. Rep. **144**, 322–325 (1992).
[5] P. Gerstoft and H. Schmidt, ''A boundary element approach to ocean seismoacoustic facet reverberation,'' J. Acoust. Soc. Am. **89**, 1629–1642 (1991).
[6] A. Boag, Y. Leviatan, and A. Boag, ''Analysis of acoustic scattering from fluid cylinders using a multifilament source model,'' J. Acoust. Soc. Am. **83**, 1–8 (1988).

Fluid column resonances of water-filled cylindrical shells of elliptical cross section

Paul A. Chinnery and Victor F. Humphrey
School of Physics, University of Bath, Bath BA2 7AY, United Kingdom

(Received 10 April 1997; accepted for publication 20 November 1997)

The acoustic resonances of a submerged fluid-filled cylindrical shell are analyzed as the shell cross section is deformed from circular to elliptical geometry. A schlieren visualization system is used to image standing wave fields within insonified water-filled shells of different eccentricities, and to locate the resonance frequencies of the fluid column. The acoustic behavior of elliptical cavities with infinite and finite surface impedances are modeled and the theory used to predict the resonance frequencies of the fluid column and calculate the pressure distribution in the acoustic field. As the symmetry of the circular shell is broken by deforming it to the more general ellipse the resonance spectrum changes; mode splittings and level crossings are observed as the eccentricity increases. The experimental observations of resonance patterns and frequency variation are in good agreement with the theoretical predictions. © *1998 Acoustical Society of America.* [S0001-4966(98)01603-8]

PACS numbers: 43.20.Ks, 43.35.Sx [ANN]

INTRODUCTION AND BACKGROUND

Although considerable work has been done on the scattering and resonance behavior of cylindrical objects, most of it has concentrated on the special case of cylinders having circular cross section. Much of the early work involving circular cylinders concerned itself with the scattered field; the resonance behavior itself received comparatively limited attention, until the Resonance Scattering Theory was introduced by Flax *et al.*[1] in 1978. The scattering and resonance behavior of such simple objects has recently been reviewed by Veksler[2] and has been summarized in review articles by Flax *et al.*[3] and Gaunaurd.[4] Comparatively little attention has been given to the more general case of the elliptical cylindrical geometries. The importance of target resonances is now well established, and experimental techniques have been developed to isolate and identify resonances by analyzing the scattered field; see, for example, Tsui *et al.*[5] and Maze and Ripoche.[6] The Resonance Scattering Theory predicts that energy builds up inside the structure at frequencies corresponding to resonances of the target. This is obviously particularly true of hollow objects having a fluid cavity which can resonate, and it is therefore expected that measurements of the pressure inside the fluid column will give a good indication of where the resonances lie. However, achieving this in a noninvasive manner is not easy; any hydrophone placed in the wave field would perturb it. In recent papers[7–9] the authors have investigated the use of schlieren for studying two-dimensional standing wave fields and used the technique to examine the fluid column resonances of water-filled cylindrical shells in a noninvasive manner. The technique is here applied to cylindrical cavities of elliptical cross section and used to validate a model of the fluid column resonances.

Early work involving scattering by infinite (two-dimensional) elliptical cylinders is described in Bowman *et al.*[10] and references therein. Elliptical cylinders were considered by Burke[11] who applied the Mathieu function solution to penetrable and impenetrable elliptical cylinders and gave low-frequency approximations. The Mathieu function approach was also used by Harumi[12] who studied scattering by a ribbon. Goel and Jain[13] have considered the penetrable elliptical cylinder using a Green's function approach.

Simon and Radlinski[14] investigated elastic wave scattering by an elliptical cylindrical shell by combining the *T*-matrix[15] method with thin shell theory. Radlinski and Simon[16] modified the previous formalism and applied it to scattering from elliptical cylindrical shells in a fluid. Plastic, steel, and iron shells were considered, and a significant dependence upon incident angle and eccentricity of the shell was shown. Baskar *et al.*[17] also applied the coupled thin-shell *T*-matrix method to the scattering of acoustic waves from a thin elliptical cylindrical shell in a fluid. Another method for thin shells is that of Borovikov and Veksler[18] who used the geometrical theory of diffraction to study scattering by elliptical shells. Thicker elliptical shells were studied by Pillai *et al.*,[19] again using *T*-matrix methods. Rigid and elastic cylinders of elliptical cross section were previously studied by Pillai, *et al.*[20] and scattering by rigid cylindrical objects of various cross section by Varadan *et al.*[21]

Burke and Twersky[22] studied a grating of elliptical cylinders and Brigham *et al.*[23] studied the scattering by planar arrays of elliptical shells. Other theoretical approaches to noncircular cylindrical geometries have recently appeared. The elliptical geometry has been investigated by Stepanishen and Ramakrishna[24] using internal source distribution and singular value decomposition methods. A new method involving conformal mappings, referred to as the Fourier matching method, is described by DiPerna and Stanton[25] and deals with scattering by cylindrical objects of noncircular geometries, including the elliptical cylinder.

The resonance modes of cavities of complex geometry can also be investigated using perturbation techniques. A recent book by Trusler[26] gives a good overview of the acoustics of closed systems, focusing on perturbations in the shapes of cavities, and the impedance of the boundary. Perturbation methods were used by Aldoshina and Olyushin[27] to

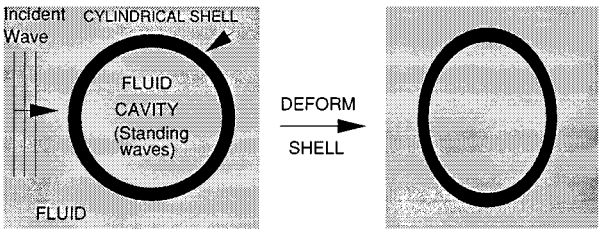

FIG. 1. Fluid columns of circular and elliptical geometry within the cavities of cylindrical shells.

calculate the resonance frequencies of enclosures having complex geometry and impedance boundaries.

Much of the literature is concerned with the acoustics of evacuated (or air filled) shells where the principal mechanisms contributing to the scattering behavior are the propagation of surface waves around the cylinder perimeter, and vibrations of the elastic shell. For fluid-filled shells the fluid column resonances are also important. Maze *et al.*[28] experimentally identified several kinds of resonance associated with the circular cylindrical shell. The majority of the resonances were modes of the fluid column. The resonances of the fluid column within cylindrical structures have not received as much attention as the external (scattering) problem. The use of a schlieren technique for visualizing the interaction of acoustic waves with cylindrical objects was described by Knapp and Humphrey[29] and Humphrey *et al.*[30] This technique enabled several classes of resonance of the fluid-filled circular cylindrical shell to be identified by examining the *interior* fluid.[31] Prior to this work the schlieren technique had rarely been used to study the acoustic resonances of fluid-filled cylindrical shells, although the visualization of elastic resonances of transparent solid cylinders had been achieved; see, for example, Dardy *et al.*[32] and Sittig and Coquin.[33] No experimental results concerning visualization of the fluid column resonances of elliptical cylindrical shells (or cavities) are known to the authors, although the focusing of a shock wave in an elliptical cavity was observed using a schlieren technique by Gustafsson.[34]

In this paper the perturbation of the acoustic fluid column resonances of insonified water-filled shells are investigated experimentally using a schlieren visualization system, and results compared with theoretical predictions for the modes of vibration of elliptical cavities. The scattering problem is illustrated schematically in Fig. 1. When insonified by a plane wave the fluid column within such a shell resonates at frequencies determined by the geometry of the cavity and the impedance that the shell presents to the interior acoustic fluid. The aim of the present work is to investigate the sensitivity of this resonance behavior to changes in the shape of the shell as an initially circular sample is deformed. Measurements are made with 1.6-mm-thick brass cylindrical shells of inner radius (b) 14.25 mm over a kb range 11–15, for eccentricities up to 0.6.

The fluid column resonances manifest themselves in both the scattered acoustic field, and in the field within the fluid column. By calculating the partial wave amplitudes in the normal mode series expansion[2] for a circular cylindrical shell, different families of resonances can easily be identified. Although for shells of circular geometry the scattering problem can be solved exactly, for elliptical shells of constant thickness this is not possible because inner and outer boundaries are not represented in the same elliptical coordinate system. Therefore in this paper we consider only the interior problem, neglecting the incident wave. This approach is justified as it is the fluid column resonances that are of interest, and, as will be shown, these lie close to the eigenmodes of the cavity.

The theory for the modes of vibration of a circular cavity with rigid (infinite impedance) boundary is briefly summarized and extended to a cavity with finite surface impedance, representing the impedance of the shell. The acoustic wave equation is then solved in elliptical coordinates, again considering infinite and finite surface impedances.

In Secs. I and II we discuss the theoretical determination of the resonance frequencies and identification of the different modes of circular and elliptical cavities. The experimental technique used to locate and identify resonances is described in Sec. III. Results are presented in Sec. IV where comparison is made between theory and experiment.

I. CIRCULAR CYLINDRICAL SHELLS

Relevant features of the theory of plane wave scattering by circular cylindrical shells are briefly stated and simple models for calculating the resonance frequencies and wave fields of the fluid cavity are presented for comparison.

A. Normal mode series

The normal mode series solution has been widely used for studying the acoustic behavior of targets of separable geometry; for a recent review see Ref. 2. The essence of the method is to expand all acoustic and elastic wave fields as harmonic series. In the circular geometry these series involve products of Bessel functions and circular functions.

For a plane wave normally incident on a cylindrical shell the pressure field in the external fluid (P_{ex}) is the sum of the incident pressure (P_{in}) and the scattered pressure (P_{sc}), $P_{\mathrm{ex}}=P_{\mathrm{in}}+P_{\mathrm{sc}}$, where

$$P_{\mathrm{in}}(r,\phi)=e^{i(k\cdot r)}=P_0\sum_n \varepsilon_n i^n J_n(kr)\cos n\phi,$$
$$P_{sc}(r,\phi)=P_0\sum_n \varepsilon_n i^n B_n(ka)H_n^1(kr)\cos n\phi. \tag{1}$$

where ε_n equals 1 if $n=0$ and 2 if $n>0$, the coefficients B_n are determined from the boundary conditions, and J_n and H_n^1 are respectively Bessel and Hankel functions of order n. Similarly, the field inside the cavity is given by

$$P_{\mathrm{fl}}(r,\phi)=P_0\sum_n \varepsilon_n i^n A_n(ka)J_n(kr)\cos n\phi, \tag{2}$$

where A_n are coefficients determined from the boundary conditions.

The boundary conditions at the inner ($r=b$) and outer ($r=a$) interfaces of the shell require the continuity of normal stress ($\mathscr{T}$) and displacement (U), and the vanishing of all tangential stresses:

$$U_r(a)=U_{\mathrm{ex}}(a),\quad U_r(b)=U_{\mathrm{fl}}(b),$$
$$\mathscr{T}_{rr}(a)=P_{\mathrm{ex}}(a),\quad \mathscr{T}_{rr}(b)=P_{\mathrm{fl}}(b), \tag{3}$$
$$\mathscr{T}_{r\phi}(a)=0,\quad \mathscr{T}_{r\phi}(b)=0.$$

Here, subscripts ex and fl refer to the external and internal fluids, respectively, and variables on the left-hand side of each equation refer to the elastic shell. The displacements within the shell are found by expressing the displacement vector in terms of scalar and vector potentials, each potential satisfying the Helmholtz equation and being expanded in normal mode series. Stress-displacement relations allow the components of the stress tensor (τ) to be calculated, and the boundary conditions solved to find the unknown coefficients in the normal mode series [Eqs. (1) and (2)].

The backscattered field is expressed as a dimensionless normalized form function:

$$f(r,\phi)=\sqrt{\frac{2r}{a}}\,\frac{P_{\mathrm{sc}}(r,\phi)}{P_{\mathrm{in}}}. \tag{4}$$

Resonances of the fluid-filled shell manifest themselves as sharp changes in this form function. Also, if the acoustic field inside the cavity is calculated [Eq. (2)] at or close to these frequencies, resonance modes are observed.

B. Cavity resonances within rigid boundary

The above theoretical formalism constitutes an *exact* solution for the scattering of a plane wave from a circular cylindrical shell insonified normal to its axis. All of the resonance modes of this coupled elasto-acoustic scatterer are allowed for in the theory and can potentially be identified in the form function or interior pressure field.

However, for the fluid column resonances, a simpler technique is expected to yield the frequencies and pressure distributions of the resonance modes. If the impedance mismatch between the inner fluid (density ρ_f) and the (fluid loaded) elastic shell is large, the inner interface ($r=b$) can be approximated to a rigid boundary so that the normal components of particle velocity (V) vanish:

$$V_r(b)=\dot{U}_r(b)=\frac{i}{\omega\rho_f}\left.\frac{\partial P_{\mathrm{fl}}}{\partial r}\right|_{r=b}=0. \tag{5}$$

Substituting the normal mode expansion for P_{fl} (2) into (5) yields

$$J_n'(kb)=0, \tag{6}$$

having roots ($k_{n,m}$) corresponding to the free vibrational modes (n,m) of the fluid column with rigid boundary.

The locations of resonance modes associated with the vibration of the elastic shell or Stoneley wave propagation cannot be found in this manner. For these, the full normal mode series solution must be employed (Sec. I A).

C. Cavity resonances within impedance boundary

In reality the cavity does not have a rigid boundary. We consider the fluid-loaded elastic shell to present a mechanical input impedance (Z_{inp}) to the acoustic fluid within the cavity. At the inner interface (b) the boundary conditions require that the radiation impedance on the surface is equal to the input impedance of the shell. The radiation impedance in the fluid is P_{fl}/V_r where V_r is given by Eq. (5), and the boundary condition ($P_{\mathrm{fl}}/V_r=Z_{\mathrm{inp}}$) reduces to

$$Z_{\mathrm{inp}}\left.\frac{\partial P_{\mathrm{fl}}}{\partial r}\right|_b+i\omega\rho_f P_{\mathrm{fl}}(b)=0. \tag{7}$$

Using the normal mode series expansion for P_{fl} [Eq. (2)] we obtain

$$J_n'(kb)+i\,\frac{\rho_f c_f}{Z_{\mathrm{inp}}}\,J_n(kb)=0 \tag{8}$$

having a series of roots $k_{n,m}$ which are the free modes of vibration (no incident field) of the fluid column, subject to finite impedance boundary conditions.

The exact mechanical impedance of the circular shell (Z_{inp}) can of course be derived from the formalism of the previous section, but we here consider two approximations that will be employed later, and which result in greatly simplified expressions.

First we approximate the fluid-loaded elastic shell to a fluid-loaded fluid shell (of circular cross section) and the input impedance to the normal impedance of such a shell. In doing this we are neglecting shear waves in the shell because we are principally concerned with near normal wave components. The resulting expression for the impedance is

$$Z_{\mathrm{circ}}=-iZ_L\,\frac{iZ_L[Y_n(k_la)J_n(k_lb)-J_n(k_la)Y_n(k_lb)]+Z_w[J_n(k_lb)Y_n'(k_la)-Y_n(k_lb)J_n'(k_la)]}{iZ_L[Y_n(k_la)J_n'(k_lb)-J_n(k_la)Y_n'(k_lb)]+Z_w[J_n'(k_lb)Y_n'(k_la)-Y_n'(k_lb)J_n'(k_la)]}, \tag{9}$$

where Y_n are Bessel functions of the second kind, $Z_L=\rho c_l$ is the impedance of the layer material (density ρ and compressional wave velocity c_l), k_l is the wave number in the layer, and Z_w is the impedance of the external loading fluid (density ρ_f, velocity c_f), given by

$$Z_w=\left.\frac{P_{\mathrm{sc}}}{V_r}\right|_{r=a}=-i\rho_f c_f\,\frac{H_n^1(ka)}{H_n^{1\prime}(ka)}. \tag{10}$$

Here, the impedance of the external fluid (Z_w) is derived from the expression for the scattered field [P_{sc}, see Eq. (1)]. This expression reduces to

$$Z_{\mathrm{circ}}=\rho c_l\,\frac{4/\pi^2k_l^2ab-i(\chi r_n s_n+p_n q_n/\chi)}{\chi^2+q_n^2/\chi}, \tag{11}$$

where $\chi=Z_w/\rho c_l$, and r_n, s_n, p_n, and q_n are products of Bessel functions and their derivatives, as shown in Eq. (9)

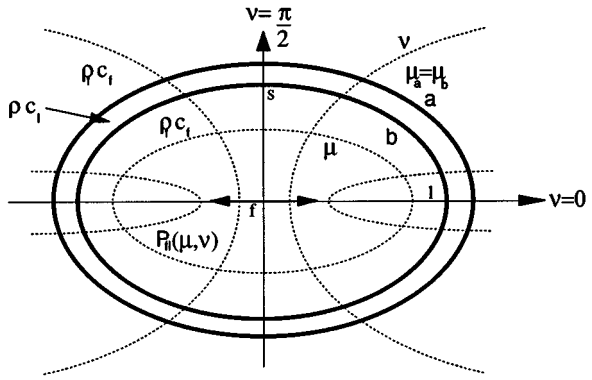

FIG. 2. Elliptical coordinate system and geometry of the elliptical shell.

and defined in Abramowitz (Ref. 35, p. 361).

As might be expected, in the limit whereby $ka \sim kb$ are sufficiently large that asymptotic expansions for J_n, Y_n, and H_n are valid, expression (11) reduces to the normal input impedance of a planar layer (Z_{flat}) with a fluid half-space backing, characterized only by the density of the layer, its compressional wave velocity, and its thickness. The derivation is well known (see, for example, Ref. 36) and will not be repeated here. The resulting expression for Z_{flat} is

$$Z_{\text{flat}} = Z_L \frac{Z_w + iZ_L \tan(k_l d)}{Z_L + iZ_w \tan(k_l d)}, \tag{12}$$

where $Z_w = \rho_f c_f$ is the contribution from the loading fluid half-space, and $d = a - b$ is the layer thickness.

The use of either of these impedances [Eq. (11) or (12)] in expression (8) yields an equation whose solutions are expected to better approximate the resonance frequencies of the fluid column than the roots of $J_n'(kb) = 0$ [Eq. (6)] do.

II. CAVITY RESONANCES OF ELLIPTICAL CYLINDRICAL SHELLS

A. Rigid boundary

As will be demonstrated the fluid column resonances of a circular shell lie close to the free modes of vibration of the fluid column within a rigid or finite impedance boundary, the theory for which is presented above. An analogous approach is used to solve for the deformed/elliptical cavities. The free modes of vibration (i.e., with no incident wave) of a fluid column with elliptical boundary are calculated as solutions of the wave equation in elliptical coordinates. The geometry and parameters of the problem are given in Fig. 2.

1. Elliptical coordinates

The coordinates μ, ν represent families of confocal ellipses and hyperbolae, respectively. An ellipse having ''pseudo-radial'' coordinate μ has an eccentricity $e = \text{sech}(\mu)$ and the distance between foci is $f = 2le$, where, for all ellipses having the same circumference, the semi-major axis (l) and semi-minor axis (s) are related by $(s + l)/2 = b$, where b is the radius of the limiting circle ($e = 0$) from which the ellipse is deformed. If the inner and outer boundaries of the shell (denoted b and a, respectively) are parallel, then $\mu_a = \mu_b = \tanh^{-1}(s/l)$ and the boundaries have the same eccentricity, but different interfocal distances f_a, f_b. In the circular limit, $\cosh(\mu) \to \infty$, $f_a \cosh(\mu)/2 \to a$ and $f_b \cosh(\mu)/2 \to b$ as the foci coalesce ($f = 0$); a and b are then the outer and inner radii of the circular shell.

2. Wave equation and its solutions

Writing the Helmholtz equation for a pressure field P in elliptical coordinates, we obtain

$$\frac{\partial^2 P}{\partial \mu^2} + \frac{\partial^2 P}{\partial \nu^2} + \frac{f^2}{4} k^2 (\cosh^2 \mu - \cos^2 \nu) P = 0. \tag{13}$$

The separation of variables $P(\nu, \mu) = \Theta(\nu) j(\mu)$ yields the two equations

$$\frac{\partial^2 \Theta(\nu)}{\partial \nu^2} + \left(\iota - \frac{f^2 k^2}{8} \cos 2\nu \right) \Theta(\nu) = 0 \tag{14}$$

and

$$\frac{\partial^2 j(\mu)}{\partial \mu^2} - \left(\iota - \frac{f^2 k^2}{8} \cosh 2\mu \right) j(\mu) = 0, \tag{15}$$

where ι is the separation constant. Equation (14) is Mathieu's equation and has solutions of period π and 2π, each of which can have even (e) or odd (o) symmetry about $\nu = 0$. These solutions are the ''Mathieu functions'' which are infinite series of circular functions:

$$\begin{aligned}
\Theta &= ce_{2n}(\nu, q) = \sum_{r=0}^{\infty} A_{2r}^{2n} \cos(2r\nu) \quad (\text{e}, \pi), \\
\Theta &= ce_{2n+1}(\nu, q) = \sum_{r=0}^{\infty} A_{2r+1}^{2n+1} \cos((2r+1)\nu) \quad (\text{e}, 2\pi), \\
\Theta &= so_{2n}(\nu, q) = \sum_{r=0}^{\infty} B_{2r}^{2n} \sin(2r\nu) \quad (\text{o}, \pi), \\
\Theta &= so_{2n+1}(\nu, q) = \sum_{r=0}^{\infty} B_{2r+1}^{2n+1} \sin((2r+1)\nu) \quad (\text{o}, 2\pi),
\end{aligned} \tag{16}$$

where ce are *even* Mathieu functions, so are *odd* Mathieu functions, the coefficients A and B are found from recursion relations,[35] and q is a dimensionless parameter given by

$$2q = \frac{f^2 k^2}{8}. \tag{17}$$

For the same value of ι, Eq. (15), known as the ''modified Mathieu equation,'' has corresponding solutions

$$
\begin{aligned}
j &= je_{2n}(\mu,q) = \sum_{r=0}^{\infty} A_{2r}^{2n} \cosh(2r\mu), \quad (\mathrm{e},\pi) \\
j &= je_{2n+1}(\mu,q) \\
&= \sum_{r=0}^{\infty} A_{2r+1}^{2n+1} \cosh((2r+1)\mu), \quad (\mathrm{e},2\pi) \\
j &= jo_{2n}(\mu,q) = \sum_{r=0}^{\infty} B_{2r}^{2n} \sinh(2r\mu), \quad (\mathrm{o},\pi) \\
j &= jo_{2n+1}(\mu,q) \\
&= \sum_{r=0}^{\infty} B_{2r+1}^{2n+1} \sinh((2r+1)\mu), \quad (\mathrm{o},2\pi)
\end{aligned}
\tag{18}
$$

where je and jo are ''radial Mathieu functions,'' and even and odd symmetry, respectively.

The solution of the Helmholtz equation for the pressure P consists of the functions

$$
P_n(\nu,\mu) = \begin{Bmatrix} ce_n(q,\nu) je_n(q,\mu) \\ so_n(q,\nu) jo_n(q,\mu) \end{Bmatrix}, \tag{19}
$$

each product being associated with a particular value of ι, which is in turn dependent upon n and q (and hence k). Boundary conditions applied at $\mu=\mu_b$ limit the values of q to a discrete set of real eigenvalues. Note that in the limit $q\to 0$,

$$
\begin{aligned}
ce_n(q,\nu) &\to \cos n\phi, \\
so_n(q,\nu) &\to \sin n\phi, \\
je_n(q,\mu) &\to jo_n(q,\mu) \to J_n(kr),
\end{aligned}
\tag{20}
$$

the functions become the familiar circular functions.

3. Boundary conditions

At a rigid boundary the component of particle velocity normal to the inner surface of the shell must vanish. In a manner analogous to that of Sec. I B the resonance modes $(q_{n,m})$ of the elliptical cavity with rigid boundary are calculated as solutions of

$$
je_n'(q_b,\mu_b) = 0, \quad jo_n'(q_b,\mu_b) = 0, \tag{21}
$$

from which the wave numbers can be calculated from $q_b = f_b^2 k^2/16$. The fact that $je \to jo$ as $q\to 0$ implies that $q_{n,m}^{(e)} \to q_{n,m}^{(o)}$ and hence

$$
k_{n,m}^{(e)} \to k_{n,m}^{(o)} \quad \text{as} \quad f\to 0, \tag{22}
$$

which is simply the statement that the odd and even resonance frequencies are equal in the circular limit. For the $n=0$ case, only even solutions exist.

In summary, there exists a series of normal modes characterized by their symmetry, and by the integers n and m. We denote these normal modes (n,m,e) (even solutions) and (n,m,o) (odd solutions), and we can write the pressure distributions of these modes

$$
\begin{aligned}
P_{n,m}^{(e)}(\nu,\mu) &= ce_n(q_{n,m}^{(e)},\nu) je_n(q_{n,m}^{(e)},\mu) \quad (\text{even}), \\
P_{n,m}^{(o)}(\nu,\mu) &= so_n(q_{n,m}^{(o)},\nu) jo_n(q_{n,m}^{(o)},\mu) \quad (\text{odd}).
\end{aligned}
\tag{23}
$$

B. Impedance boundary

The solution of the internal problem involving a finite impedance boundary was discussed in Sec. I C for the circular geometry. This technique is now applied to the elliptical geometry. As with the rigid boundary formalism, solutions of even and odd symmetry, and period π and 2π, exist; but for brevity we shall suppress reference to them, and their arguments, referring only to a solution denoted $P(x)$, where x is a or b and the arguments may be deduced from the context of the equation.

At the inner boundary (b) the normal component of velocity in the fluid column (V_r) is related to the pressure (P_{fl}) by

$$
V_r(b) = \frac{i}{\omega\rho_f} \frac{dP_{\mathrm{fl}}(b)}{dn} = \frac{i}{\omega\rho_f} \frac{1}{h_\mu} \frac{dP_{\mathrm{fl}}(b)}{d\mu}, \tag{24}
$$

where ω is the angular frequency, $dn = h_\mu d\mu$ is normal to the ellipse, and the metric $h_\mu = f_b\sqrt{(\cosh(2\mu_b)-\cos(2\nu))/8}$ is a function of the angular coordinate (ν). The boundary conditions at b can be written

$$
\frac{P_{\mathrm{fl}}(b)}{V_r(b)} = Z_{\mathrm{inp}}, \tag{25}
$$

where Z_{inp} is the mechanical surface impedance of the shell and P_{fl}/V_r is the radiation impedance on the inner surface. Combining (24) and (25), we obtain

$$
\frac{dP_{\mathrm{fl}}(b)}{d\mu} + i \frac{\omega\rho_f h_\mu}{Z_{\mathrm{inp}}} P_{\mathrm{fl}}(b) = 0. \tag{26}
$$

The actual impedance of the shell (Z_{inp}) is properly given by

$$
Z_{\mathrm{inp}} = \frac{P_{\mathrm{lay}}(b)}{V_{\mathrm{lay}}(b)} = \frac{P_{\mathrm{lay}}(b)}{\dfrac{i}{\omega\rho} \dfrac{1}{h_\mu} \dfrac{dP_{\mathrm{lay}}}{d\mu}\Big|_b}, \tag{27}
$$

where P_{lay}, the pressure in the layer, depends upon boundary conditions at the outer boundary a. Substituting this expression into (26) yields

$$
P_{\mathrm{fl}}'(b) + i \frac{\omega\rho_f}{X_{\mathrm{inp}}} P_{\mathrm{fl}}(b) = 0, \quad \text{where} \quad X_{\mathrm{inp}} = \frac{P_{\mathrm{lay}}(b)}{\dfrac{i}{\omega\rho} \dfrac{dP_{\mathrm{lay}}}{d\mu}\Big|_b}, \tag{28}
$$

this equation having no angular dependence. Knowledge of Z_{inp} (or X_{inp}) would constitute a complete solution of the scattering problem. Unfortunately Z_{inp} is unknown, and cannot be computed. In the present study we do not calculate X_{inp} exactly, but seek an approximation, as follows.

In the circular limit $(f\to 0)$, $d\mu \to dn/b$ and so

$$
X_{\mathrm{inp}} \to \frac{Z_{\mathrm{circ}}}{b}, \tag{29}
$$

where Z_{circ} is the input impedance of a circular shell of inner radius b. The use of Z_{circ} for eccentricities greater than zero amounts to the approximation that the input impedance is that of a circular shell irrespective of eccentricity. The impedance of the circular shell can be approximated to that of an acoustic shell characterized by only one velocity [as in

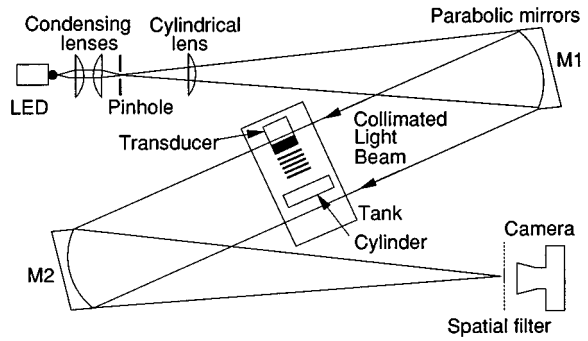

FIG. 3. The schlieren visualization system.

Eq. (11)]. As in Sec. I we can further approximate the surface impedance to the input impedance of a planar layer (Z_{flat}) having the same thickness [Eq. (12)]. Both expressions (11) and (12) have been found to give very similar values for the surface input impedance, and produced insignificant differences in the final results. Therefore in the present study the simpler expression for the planar layer is used throughout. With these approximations, Eq. (28) becomes

$$P'_{\text{fl}}(b) + i\,\frac{\rho_f c_f kb}{Z_{\text{flat}}}\,P_{\text{fl}}(b) = 0. \tag{30}$$

The roots of (30) are $q^{e/o}_{n,m}$ and the corresponding wave numbers are $k^{e/o}_{n,m}$ [found from Eq. (17)]. As before each (n,m) labels a pair of resonances (even and odd) that are degenerate in the circular limit. The results of the rigid boundary approximation emerge from the above formalism (30) as the special case $Z_{\text{inp}} \to \infty$; i.e., $P'_{\text{fl}}(b) = 0$.

III. EXPERIMENTAL SYSTEM

The measurements were made using a schlieren technique described in greater detail in several previous papers.[7,29–31] The schlieren system is shown in Fig. 3. A high-power light-emitting diode is used as the optical source, a pair of condensing lenses focus the light onto a pinhole, and a parabolic mirror is used to collimate the resulting light beam which is passed though a tank of water containing the acoustic field. In the tank a transducer (resonant at 450 kHz, driven in continuous mode) is positioned with its axis perpendicular to that of the light beam and insonifies the cylindrical shell (suspended using nylon thread) normal to its axis. The light emerging from the tank it focused by another parabolic mirror and forms a diffraction pattern whose side orders contain the light that has been diffracted out of the main beam by the pressure variations in the acoustic field. The central order is blocked and the remaining light combined using the lens of a camera (still or video) to form an image of the acoustic field. For low acoustic pressures the resulting optical image approximates the square of the acoustic pressure field.[7] In the present application the resonances of the shell are located by varying the frequency applied to the transducer and observing the optical image using a video camera. At the resonance frequencies standing wave fields can be clearly seen in the fluid column.

TABLE I. Fluid column resonances of a brass cylindrical shell of radii a and b ($b/a = 0.90$) showing comparison of kb values determined experimentally using the schlieren system and determined using different theoretical models. The full elasticity theory is used for the plane wave calculations (Sec. I).

		Plane wave theory		Free vibrations	
	Experiment schlieren	Pressure distribution	Form function	Rigid boundary	Impedance boundary
Mode	kb	kb	kb	kb	kb
(3,3)	11.46	11.45	11.45	11.35	11.44
(1,4)	11.80	11.79	11.80	11.71	11.79
(4,3)	12.79	12.78	12.78	12.68	12.77
(7,2)	13.03	13.01	13.01	12.93	13.04
(2,4)	13.26	13.25	13.25	13.17	13.24
(0,5)	13.41	13.40	13.40	13.32	13.39
(5,3)	14.10	14.09	14.09	13.99	14.06
(8,2)	14.21	14.19	14.19	14.12	14.21
(3,4)	14.67	14.66	14.66	14.59	14.65

IV. RESULTS

The experimental system has been used to locate and image resonances of circular and elliptical shells and results are compared with the predictions made using the model described in Secs. I and II.

A. Fluid column resonances of a brass cylindrical shell of circular cross section

In order to assess the system performance the resonance behavior of a circular brass cylindrical shell was investigated. This shell had radii of (b) 14.25 mm and (a) 15.85 mm, giving a radii ratio (b/a) of 0.90. All samples used in the measurements had a length of 100 mm. Using the experimental system, the fluid column resonances of the brass shell were located; results are presented for the frequency band stretching from the (3,3) mode to the (3,4) mode and are given in Table I.

The experimental results are given in the second column, and theoretical predictions, made by examining the computed pressure distribution in the fluid column and in the far-field form function, are given in the third and fourth columns. The fifth and sixth columns give results for the free vibrations of the fluid column with both infinite and finite impedance boundary conditions. The velocities within brass were taken to be 4372 m s^{-1} (compressional) and 2180 m s^{-1} (shear), the density of brass was 8485 kg m^{-3}, and the velocity and density of the fluid (water) were 1473 m s^{-1} and 998 kg m^{-3}, respectively.

The results obtained using the finite impedance boundary model are seen to be in good agreement with the experimental results, and a significant improvement upon the rigid boundary approximation. From this we conclude that the impedance boundary formulation is perfectly adequate for calculating the resonance frequencies of the cavity.

The computed backscattered form function is shown in Fig. 4(a). A great many narrow resonances can be seen, many of them being due to the fluid column. The narrow frequency band ($kb = 11 \to 15$) is shown in Fig. 4(b) and the frequencies of the fluid column resonances located with the schlieren technique are marked as vertical lines in the figure.

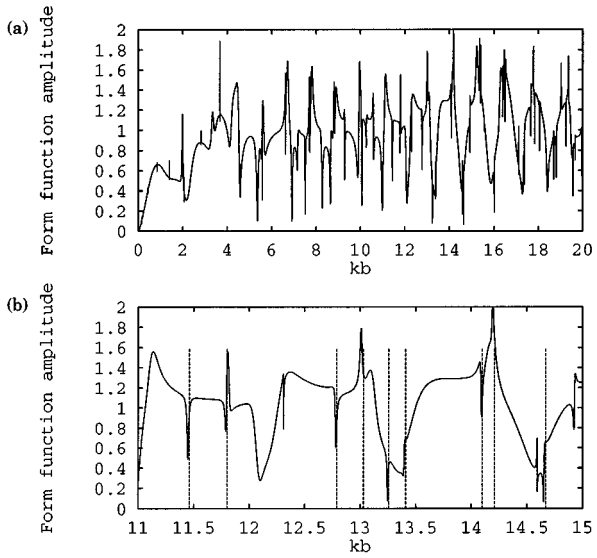

FIG. 4. (a) Backscattered far-field form function of the cylindrical shell. (b) Resonances located using the schlieren technique; comparison of experimentally determined frequencies (vertical lines) with the predicted plane wave form function (solid line) over a narrow band of frequencies.

These are seen to agree well with the sharp features in the form function.

A schlieren image of the (3,3) fluid column resonance mode of this shell has been presented previously[7] and other examples of resonance modes of circular shells are given in Knapp *et al.*[37] and Chinnery and Humphrey.[8]

B. Elliptical shell—experimental results

Of the nine fluid column modes located in the circular sample (Table I), six were chosen for further investigation as the shell was deformed. The six modes, in ascending order of frequency were (3,3), (1,4), (4,3), (2,4), (0,5), and (3,4). All of these resonances were found between 190 and 250 kHz with the present experimental arrangement.

The resonances within five brass cylindrical shells of differing eccentricity were located and photographed using the schlieren system and compared with theoretical predictions made using the model presented in Sec. II. Taking the internal semi-minor axis of each sample to be s, and defining a deformation parameter $\gamma = 1 - s/b$, the five samples had deformations of $\gamma = 0\%$, 3.4%, 6%, 8%, and 10.4%. All the samples were 100 mm long and made by distorting samples of the same cylindrical shell as that described previously.

The angle that the acoustic beam made with the major axis of the ellipse was varied, depending on the symmetry of the resonance sought: all even solution resonances were found by insonifying along the major axis; the odd solution resonances required insonification at other angles in order to properly excite the modes. In all cases the cylinder was insonified normal to its own axis.

The experimentally determined resonance frequencies are given in Table II and shown in Fig. 5 for comparison with those of the circular sample. The distribution of resonances of the deformed cavities is initially rather confusing; many more modes are detected than for the circular sample, and the resonance patterns of many of these modes do not resemble those of the circular shell, and cannot be easily classified. The ordering and classification of the data given in Table II is only possible after undertaking the theoretical investigations described in the next section.

TABLE II. Normalized frequencies (kb) of fluid column resonance modes of deformed cavities (of different eccentricities) located with schlieren.

γ	0%	3.4%	6.0%	8.0%	10.4%
Eccentricity	0	0.36	0.46	0.52	0.59
Mode	kb	kb	kb	kb	kb
(3,3,o)	11.46	11.46	11.48	11.52	11.59
(3,3,e)	⋯	11.37	11.28	11.21	11.17
(1,4,o)	11.80	12.12	12.32	12.55	12.86
(1,4,e)	⋯	11.76	11.84	11.94	12.11
(4,3,o)	12.79	12.77	12.75	12.75	12.79
(4,3,e)	⋯	12.74	12.63	12.52	12.45
(2,4,o)	13.26	13.36	13.48	13.63	13.83
(2,4,e)	⋯	13.12	13.12	13.18	13.29
(0,5,e)	13.41	13.74	13.97	14.25	14.57
(3,4,o)	14.67	14.69	14.75	14.84	14.99
(3,4,e)	⋯	14.52	14.44	14.42	14.50

C. Elliptical shell—theoretical results

The model described in Sec. II can be used to predict the behavior of the fluid column modes as the eccentricity of an initially circular cavity is increased.

Concentrating on the six modes that were the subject of the experimental investigation, the model was used to calculate the frequencies [Eq. (30)] of the modes at different eccentricities and to calculate the acoustic field in the cavity [Eq. (23)]. The variation of resonance frequency with deformation is shown in Fig. 6 where it is seen that each resonance of the circular shell splits into two as the symmetry is broken, except for an $n=0$ resonance at $kb \approx 13.4$, which is isolated. The agreement between theory and experiment is good enough to allow the experimental data to be interpreted; each of the experimentally observed resonances can be associated with a particular branch of the plot, and thus ultimately with a resonance of the circular (undeformed) cavity.

All of the even solutions [except (0,5)] have an initial decrease in the kb value as the shell is initially deformed. As it is deformed still further, however, the kb values begin to increase again and eventually become greater than the initial values for a circular shell. Comparison of the (3,3,e) and

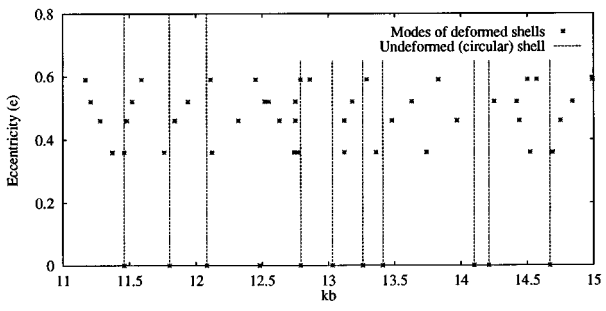

FIG. 5. Experimental locations of resonances in deformed shells (points) compared with locations for undeformed shells (vertical lines).

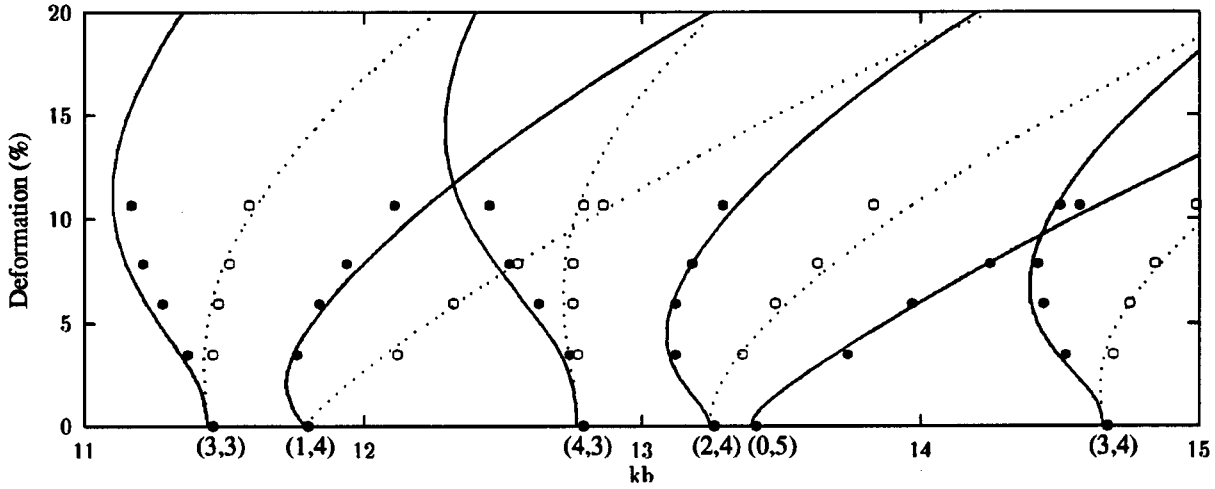

FIG. 6. Variation of frequency (kb) with deformation (γ) for selected fluid column resonance modes (n,m,e/o). Theory (lines) and experimental observation [points; even (●) and odd (○) modes].

(3,4,e) modes show that the number of wavelengths across the diameter (m) does not play such a large part in the variations as does the order (n). The odd solutions behave differently. The $n=3$ and $n=4$ resonances show a slight decrease before k begins increasing, while the lower-order modes begin increasing immediately.

Degeneracies—or level crossings—can be seen to exist at certain eccentricities where the curves cross. As the deformation increases to high values, all the resonance frequencies increase, as might be expected considering that the volume decreases as the eccentricity increases (since the circumference is constant).

The remaining differences between the experimental results and the theoretical predictions are thought to be mainly due to a certain amount of ''flattening'' that occurred along the portions of the ellipse in contact with the jaws of the press with which they were produced. This flattening is only noticeable for the highly eccentric samples.

In Figs. 7 and 8 theoretical predictions of the schlieren images are presented alongside experimentally obtained results for the field inside the fluid column. The theoretical plots show the optical distribution calculated using a value of the Raman–Nath parameter of 3.4, which has been shown[7] to give a reasonably accurate representation of both the pressure distribution and the experimental images. It should be noted that the even/odd symmetry of the modes refers to symmetries in the pressure field itself and not in the optical images. The (3,4) fluid column mode is shown for three of the deformed samples of differing eccentricity. Modes lying on the odd branch (Fig. 7) resemble the (3,4) mode of the circular cavity (not shown), but the even modes (Fig. 8) are very different in appearance from anything previously seen in the circular cavity. Only small deformations are necessary to alter the appearance of many resonances significantly. The agreement between theory and experiment is very good, validating the theoretical approach of the previous section, and the approximation of the deformed shells to elliptical cylinders.

Although experimental results could not be obtained for higher eccentricities, the theoretical calculations have been extended to predict the behavior of the wave numbers, and the acoustic field, at these much higher eccentricities.

Figure 9 shows a sequence of images for the (1,4) resonance modes, of both even and odd symmetry, as the ellipse is deformed to high eccentricities. In the circular limit the modes are degenerate and the wave fields identical (except for a 90-deg rotation). The variation of frequency with ec-

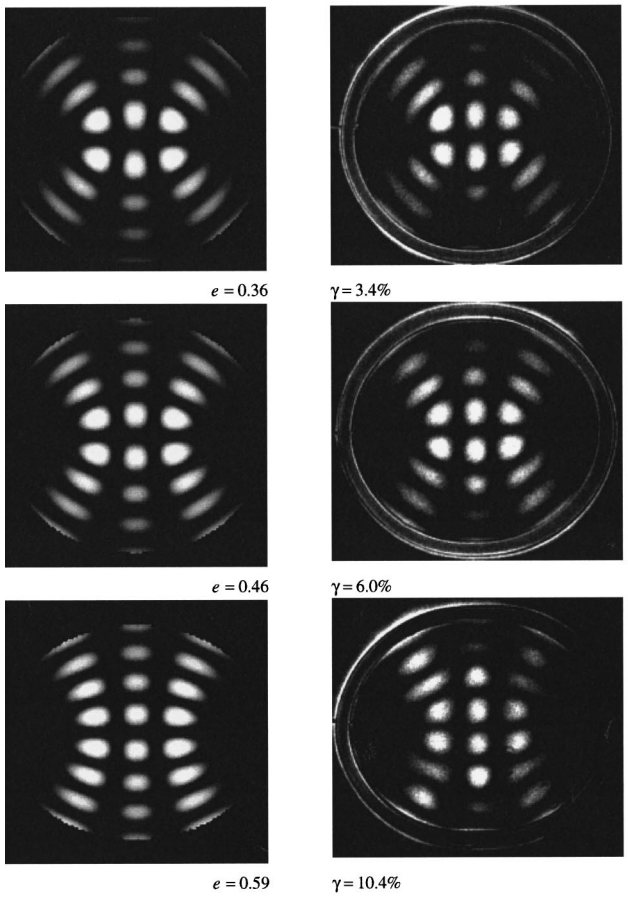

FIG. 7. (3,4,**o**) fluid column resonances of elliptical shells of different eccentricity e (% deformation γ). Theoretical model (left) and schlieren images (right).

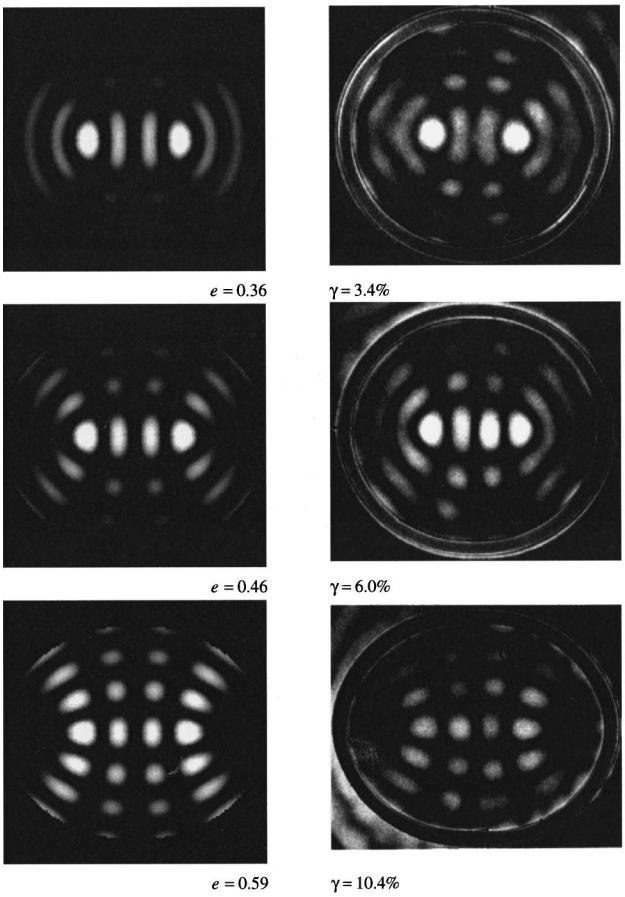

FIG. 8. (3,4,**e**) fluid column resonances of elliptical shells of different eccentricity e (% deformation γ). Theoretical model (left) and schlieren images (right).

centricity was given in Fig. 6. As the eccentricity increases the two modes become quite different.

V. CONCLUSION

This paper has presented an experimental and theoretical study of how the fluid column resonances of circular cylindrical shells behave as they are deformed. The aim has been to investigate the sensitivity of the resonance modes to perturbations in the shape of the structure. Six fluid column resonances were located in five deformed shells of differing eccentricity. The resonances were located using schlieren and photographs of the resonance patterns obtained with the system.

Theoretical models for the standing waves within circular and elliptical cavities have been described, and used to predict the resonance frequencies and acoustic wave fields of the fluid column modes of the cavities. Good agreement with experiment has been obtained when the finite impedance of the shell is included in the model.

The deformed (elliptical) shells are seen to possess many more modes of vibration than the undeformed (circular) shells. Mode splittings occur as the circular symmetry of the shell is broken, and level crossings are observed in the spectra as eccentricity varies.

It has also been shown that predictions of resonance frequency made by examining the form function amplitudes,

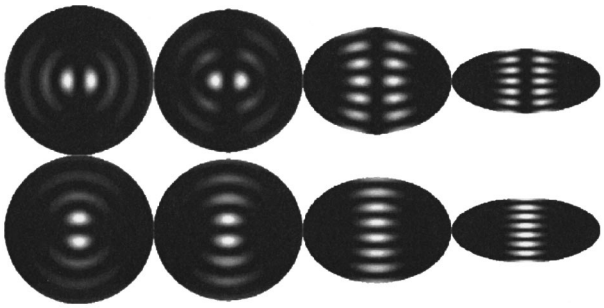

FIG. 9. Predicted pressure distribution of the (1,4) fluid column modes in elliptical cavities of different eccentricity. Even (top) and odd (bottom) solutions.

and interior pressure distributions, were in good agreement with each other, and with experimental measurements made using schlieren. The zeros of $J_n'(kb)=0$ were found to be, in general, slightly lower, revealing the extent to which the shell's finite impedance influences the resonance frequencies of the fluid column.

Other types of resonance of the cylindrical shells (such as shell resonances and Stoneley wave resonances) have not been discussed, although they have all been observed within the elliptical shells using the schlieren system.

The advantages of using the schlieren technique to study the resonance behavior of two-dimensional fluid-filled structures has been demonstrated. The application of this technique to another noncircular geometry has previously been presented by the authors.[9]

ACKNOWLEDGMENT

This work was supported by the Procurement Executive of the Ministry of Defence, UK.

[1] L. Flax, L. R. Dragonette, and H. Überall, ''Theory of elastic resonance excitation by sound scattering,'' J. Acoust. Soc. Am. **63**, 723–731 (1978).
[2] N. D. Veksler, *Resonance Acoustic Spectroscopy* (Springer-Verlag, Berlin, 1993).
[3] L. Flax, G. C. Gaunaurd, and H. Überall, ''Theory of resonance scattering,'' in *Physical Acoustics Vol. XV*, edited by W. P. Mason and R. N. Thurston (Academic, New York, 1981).
[4] G. C. Gaunaurd, ''Elastic and acoustic resonance wave scattering,'' Appl. Mech. Rev. **42**, 143–192 (1989).
[5] C. Y. Tsui, G. N. Reid, and G. C. Gaunaurd, ''Resonant scattering by elastic cylinders and their experimental verification,'' J. Acoust. Soc. Am. **80**, 382–390 (1986).
[6] G. Maze and J. Ripoche, ''Methode d'isolement et d'identification des résonances (MIIR) de cylindres et de tubes soumis à une onde acoustique plane dans l'eau,'' Revue Physique Appl. **18**, 319–326 (1983).
[7] P. A. Chinnery and V. F. Humphrey, ''The schlieren image of two-dimensional ultrasonic fields and cavity resonances,'' J. Acoust. Soc. Am. **101**, 250–256 (1997).
[8] P. A. Chinnery and V. F. Humphrey, ''On the overlapping acoustic resonances of a fluid-filled cavity: schlieren visualisation of an insonified circular-cylindrical shell,'' J. Acoust. Soc. Am. **102**, 1383–1387 (1997).
[9] P. A. Chinnery and V. F. Humphrey, ''Experimental visualization of acoustic resonances within a stadium shaped cavity,'' Phys. Rev. E **53**, 272–276 (1996).
[10] J. J. Bowman, T. B. A. Senior, and P. L. E. Uslenghi (eds.), *Electromagnetic and Acoustic Scattering by Simple Shapes* (Hemisphere, New York, 1987).
[11] J. E. Burke, ''Low-frequency approximations for scattering by penetrable elliptic cylinders,'' J. Acoust. Soc. Am. **36**, 2059–2070 (1964).
[12] K. Harumi, ''Scattering of plane waves by a rigid ribbon in a solid,'' J. Appl. Phys. **32**, 1488–1497 (1961).

[13] G. C. Goel and D. L. Jain, ''Scattering of plane waves by a penetrable elliptic cylinder.'' J. Acoust. Soc. Am. **69**, 371–379 (1981).
[14] M. M. Simon and R. P. Radlinski, ''Elastic wave scattering from elliptical shells,'' J. Acoust. Soc. Am. **71**, 273–281 (1982).
[15] V. K. Varadan and V. V. Varadan (eds.), *Acoustic, Electromagnetic and Elastic Wave Scattering—Focus on the T-matrix Approach* (Pergamon, New York, 1980).
[16] R. P. Radlinski and M. M. Simon, ''Acoustic and elastic wave scattering from elliptic-cylindrical shells,'' J. Acoust. Soc. Am. **93**, 2443–2453 (1993).
[17] S. Baskar, V. V. Varadan, and V. K. Varadan, ''Thin shell theories and acoustic wave scattering by infinitely long cylindrical shells of arbitrary cross section,'' J. Acoust. Soc. Am. **75**, 1673–1679 (1984).
[18] V. A. Borovikov and N. D. Veksler, ''Scattering of sound waves by smooth convex elastic cylindrical shells,'' Wave Motion **7**, 143–152 (1985).
[19] T. A. K. Pillai, V. K. Varadan, V. V. Varadan, and R. P. Radlinski, ''Acoustic wave scattering by elastic cylindrical shells in water,'' J. Acoust. Soc. Am. **74**, 619–624 (1983).
[20] T. A. K. Pillai, V. V. Varadan, and V. K. Varadan, ''Sound scattering by rigid and elastic infinite elliptical cylinders in water,'' J. Acoust. Soc. Am. **72**, 1032–1037 (1982).
[21] V. K. Varadan, V. V. Varadan, and S. J. Tsao, ''Scattering of acoustic waves by rigid cylindrical objects with sharp corners,'' J. Acoust. Soc. Am. **72**, 1957–1964 (1982).
[22] J. E. Burke and V. Twersky, ''On scattering of waves by the infinite grating of elliptic cylinders,'' IEEE Trans. Antennas Propag. **AP-14**, 465–480 (1966).
[23] G. A. Brigham, J. J. Libuha, and R. P. Radlinski, ''Analysis of scattering from large planar gratings of compliant cylindrical shells,'' J. Acoust. Soc. Am. **61**, 48–59 (1977).
[24] P. R. Stepanishen and S. Ramakrishna, ''Acoustic radiation impedances and impulse responses for elliptical cylinders using internal source density and singular value decomposition methods,'' J. Sound. Vib. **176**, 49–68 (1994).
[25] D. T. DiPerna and T. K. Stanton, ''Sound scattering by cylinders of noncircular cross section: A conformal mapping approach,'' J. Acoust. Soc. Am. **96**, 3064–3079 (1994).
[26] J. P. M. Trusler, *Physical Acoustics and Metrology of Fluids* (Hilger, Bristol, 1991).
[27] I. A. Aldoshina and M. V. Olyushin, ''Resonance frequencies and structures of sound fields in the enclosures of acoustical systems,'' Sov. Phys. Acoust. **38**, 529–534 (1992).
[28] G. Maze, J. L. Izbicki, and J. Ripoche, ''Acoustic scattering from cylindrical shells: guided waves and resonances of the liquid column,'' Ultrasonics **24**, 354–362 (1986).
[29] S. M. Knapp and V. F. Humphrey, ''Schlieren visualization of low frequency ultrasonic fields,'' in *Ultrasonics International 89 Conference Proceedings* (Butterworths, London, 1989), pp. 1089–1094.
[30] V. F. Humphrey, S. M. Knapp, and C. Beckett, ''Laboratory studies of acoustic scattering,'' Proc. I.O.A. **12** (1), 91–98 (1990).
[31] V. F. Humphrey, S. M. Knapp, and C. Beckett, ''Visualization of the resonances of a fluid-filled cylindrical shell using a low frequency Schlieren system,'' in *Physical Acoustic*, edited by O. Leroy and M. A. Breazeale (Plenum, New York, 1991), pp. 371–376.
[32] H. D. Dardy, L. Flax, C. F. Gaumond, J. V. Subrahhmanyam, S. Ashrafi, P. K. Raju, and H. Überall, ''Acoustically induced stresses in elastic cylinders and their visualization,'' J. Acoust. Soc. Am. **82**, 1378–1385 (1987).
[33] E. K. Sittig and G. A. Coquin, ''Visualization of plane-strain vibration modes of a long cylinder capable of producing sound radiation,'' J. Acoust. Soc. Am. **48**, 1150–1159 (1970).
[34] G. Gustafsson, ''Experiments on shock-wave focusing in an elliptical cavity,'' J. Appl. Phys. **61**, 5193–5195 (1987).
[35] M. Abramowitz and I. A. Stegun (eds.), *Handbook of Mathematical Functions* (Dover, New York, 1972).
[36] L. M. Brekhovskikh, *Waves in Layered Media* (Academic, London, 1960).
[37] S. M. Knapp, C. Beckett, and V. F. Humphrey, ''Schlieren observation of the resonances of a fluid filled shell,'' in preparation for J. Acoust. Soc. Am. (1998).

Performance bounds for acoustic direction-of-arrival arrays operating in atmospheric turbulence

D. Keith Wilson
U.S. Army Research Laboratory, ATTN: AMSRL-IS-EE, 2800 Powder Mill Road, Adelphi, Maryland 20783

(Received 14 September 1996; accepted for publication 18 November 1997)

A method is described for assessing the precision of wavefront direction-of-arrival (DOA) estimates made by acoustic arrays. Arrays operating in turbulent atmospheric boundary layers are considered. The method involves calculating the Cramer–Rao lower bound, which describes the best obtainable DOA precision (performance) for a given array and environment. For simplicity, it is assumed that the source is monochromatic, and multipath effects are not considered. The predicted performance bounds are found to degrade with increasing propagation distance, increasing frequency, and increasing turbulence strength. Performance predictions using several different three-dimensional turbulence models are compared: isotropic and anisotropic Gaussian models, the von Kármán model, and the Kolmogorov model, with the last in both intermittent and nonintermittent forms. When array performance is limited by turbulence (as opposed to background noise), the turbulence model strongly affects the calculated performance bounds. The results also suggest that degradation in DOA estimates results primarily from shear-generated, small-scale fluctuations in the wind velocity. Large, boundary-layer-scale eddies may still play a significant indirect role by driving intermittent episodes of high wind shear. [S0001-4966(98)01403-9]

PACS numbers: 43.28.Fp, 43.28.Vd [LCS]

INTRODUCTION

Acoustic sensor arrays have long been used to detect, locate, and identify underwater objects. In the atmosphere, however, acoustic arrays have so far been used only rarely; a variety of radar and optical systems are much more widely employed. Still, acoustic systems do offer some potential benefits that can be exploited: they are relatively inexpensive, do not require a line-of-sight propagation path, are unaffected by smoke and other obscurants, and can be used effectively to supplement existing electromagnetic technologies.

One important characteristic of acoustic systems deployed in the atmosphere is that their performance depends strongly on atmospheric conditions. Performance is normally enhanced by still, nighttime conditions, and degraded by atmospheric turbulence occurring during windy conditions or on a sunny day. This is because array beamforming relies on good mutual coherence between the signals received by the individual sensors; turbulence causes a loss of such coherence.

This paper discusses general models for the effect of turbulence on direction-of-arrival (DOA) estimates made by acoustic sensor arrays deployed in the atmosphere. Array performance in the presence of turbulence is quantified by calculating theoretical lower bounds on the precision of the DOA estimates. A general framework for calculating such lower bounds was developed recently by Song and Ritcey[1] and applied to propagation through random fluctuations in the ocean; in this paper I adapt their analysis to the atmospheric case and examine the features of atmospheric turbulence that most strongly affect acoustic array performance. This task is complicated by the varied and complex structure of atmospheric turbulence. Although no completely satisfactory model exists for atmospheric turbulence, comparisons between several atmospheric turbulence models, each of which has its own relative merits and shortcomings, can lead to some important conclusions. The models I consider are an isotropic Gaussian model, an anisotropic Gaussian model developed by Wilson and Thomson,[2] a von Kármán model, and a Kolmogorov model in both nonintermittent and intermittent forms. (Among the models considered in this paper only the Kolmogorov one can be extended to incorporate intermittency.)

The general DOA estimation problem is formulated in two dimensions in this paper. Although the formulation applies to planar arrays having an arbitrary orientation, one must be careful when applying it to a vertical plane. In this case atmospheric refractive effects can complicate matters, so that the DOA may be quite different from the actual source elevation angle. Then accurate assessment of the source elevation will depend on good calculations of refraction, as well as the DOA estimate. On the other hand, when the formulation is applied in a horizontal plane, refractive effects will be less important, and the DOA should correspond reasonably well to the azimuthal bearing of a source. Hence, when I apply the formulation later in this paper, I consider only horizontal array configurations.

For simplicity, the analysis in this paper also assumes that there is a single, monochromatic, plane-wave source. Multipath effects are not considered. The basic analysis, using a matrix representation for sensor cross correlations, is given in Sec. I. Incorporation of turbulence models is discussed in Sec. II. Example calculations of array performance for realistic atmospheric conditions are presented in Sec. III.

I. SENSOR CROSS-CORRELATION ANALYSIS

A. General formulation

Consider an array having N sensors. The signal at each sensor is assumed to have two contributions: one that has propagated through the atmosphere from a source of interest and arrives with a wavefront normal direction ψ, and a second consisting of random noise. The time-varying complex envelopes (phasors) of the two contributions are indicated by $\mathbf{s}(\psi,t)$ and $\mathbf{n}(t)$, respectively. Boldface type is used here to indicate matrices, in this case column vectors having N elements, one element corresponding to each sensor. The source contribution varies in time because of the effect of random turbulent fluctuations on the propagation. The noise contributions, which also vary in time, may be from wind noise or other competing acoustic sources. The total received signal is

$$\mathbf{p}(\psi,t)=\mathbf{s}(\psi,t)+\mathbf{n}(t). \tag{1}$$

The cross correlations between the sensor signals can be written compactly in matrix form as

$$\mathbf{R}_{pp}(\psi)=\langle \mathbf{p}(\psi,t)\mathbf{p}^{*}(\psi,t)\rangle, \tag{2}$$

where the angle brackets indicate the ensemble average, and the asterisk indicates complex conjugation and transposition. Assuming the source signal and noise are uncorrelated, the total cross-correlation matrix is the sum of the source and noise cross-correlation matrices:

$$\mathbf{R}_{pp}(\psi)=\mathbf{R}_{ss}(\psi)+\mathbf{R}_{nn}(\psi). \tag{3}$$

Furthermore, assuming that the noise signals at the sensors are mutually uncorrelated and equal in variance, we have

$$\mathbf{R}_{pp}(\psi)=\mathbf{R}_{ss}(\psi)+\sigma_n^2\mathbf{I}, \tag{4}$$

where σ_n^2 is the noise variance. (The assumption of uncorrelated noise signals may be a poor one in some circumstances, and will need to be scrutinized in future work.) It is convenient to normalize the signals and noise so that $\mathbf{s}(\psi,t)$ has unit variance. Then σ_n^2 becomes a noise-to-signal variance ratio. It is related to the signal-to-noise ratio in decibels (SNR) by $\sigma_n^2=10^{-\mathrm{SNR}/10}$.

Realistic modeling of the source-signal cross-correlation matrix is rather difficult. While $\mathbf{R}_{ss}(\psi)$ depends most importantly on the relative sensor positions, it also depends on several other factors that affect the propagation, such as turbulence, refraction, and absorption of sound by air. For the time being, let us assume perfect plane-wave propagation through a nonturbulent atmosphere. The former assumption is reasonable if the dimensions of the array are small compared to its distance from the source. Then the phase factor representing the delay between wavefront incidence at two array elements m and n is

$$S_{mn}(\psi)=\exp[-ik\rho_{mn}\cos(\psi-\alpha_{mn})], \tag{5}$$

where $k=2\pi/\lambda$ is the wave number, λ is the wavelength, $\rho_{mn}=[(x_m-x_n)^2+(y_m-y_n)^2]^{1/2}$ is the interelement spacing, $\alpha_{mn}=\arctan[(y_m-y_n)/(x_m-x_n)]$ is the angle between the elements, and $\mathbf{x}_m=(x_m,y_m)$ is the location of the mth element. The matrix formed from the phase delays, $\mathbf{S}(\psi)$, is called the *array steering matrix*. In the nonturbulent case, $\mathbf{R}_{ss}(\psi)=\mathbf{S}(\psi)$.

The effect of turbulence can be incorporated using the *transverse mutual coherence function*, or *MCF*. The MCF is defined here by

$$\Gamma(\boldsymbol{\rho}_{mn})=\frac{\langle p_m(t)p_n^{*}(t)\rangle}{\langle p_m(t)p_m^{*}(t)\rangle}, \tag{6}$$

where $p_m(t)$ and $p_n(t)$ are the complex envelopes at two sensors whose separation $\boldsymbol{\rho}_{mn}=\mathbf{x}_m-\mathbf{x}_n$ is parallel to the wavefronts (transverse to the propagation direction). (Because only plane-wave propagation is considered here, the average mean intensity at the two receivers matches, i.e., $\langle p_m p_m^{*}\rangle=\langle p_n p_n^{*}\rangle$.)

I assume now that the coherence between a pair of sensors can be estimated adequately by multiplying the phase factor that would occur in the absence of turbulence by the MCF for wavefront incidence parallel to the sensor pair. The reason why I make this assumption is that there are apparently no results available for the MCF under conditions of oblique wavefront incidence. Hence the turbulence effect is included by setting

$$\mathbf{R}_{ss}(\psi)=\mathbf{S}(\psi)\odot\mathbf{T}, \tag{7}$$

where the symbol $\odot$ indicates the Hadamard matrix product (simple element-by-element multiplication), and

$$T_{mn}=\Gamma(\boldsymbol{\rho}_{mn}). \tag{8}$$

B. Performance bounds

We can quantify the performance of the sensor array by calculating the mean square error, $\langle(\psi-\hat{\psi})^2\rangle$, where $\hat{\psi}$ is the estimated DOA. According to the Cramer–Rao theorem, the minimum mean square error is the inverse of the Fisher information matrix, $\mathbf{J}(\psi)$:[3]

$$\langle(\psi-\hat{\psi})^2\rangle\geqslant\mathbf{J}^{-1}(\psi). \tag{9}$$

The right-hand side of Eq. (9) is called the *Cramer–Rao lower bound* (CRLB). In our case, since we have only one parameter to be determined, ψ, the information matrix is actually a scalar. (For multiple source detection problems, the information matrix would have multiple elements.) Song and Ritcey[1] show, for signals having a joint-Gaussian probability distribution, that

$$\mathbf{J}(\psi)=M\,\mathrm{tr}\left(\mathbf{R}_{pp}^{-1}\frac{\partial\mathbf{R}_{pp}}{\partial\psi}\mathbf{R}_{pp}^{-1}\frac{\partial\mathbf{R}_{pp}}{\partial\psi}\right). \tag{10}$$

In the above, tr ( ) is the trace of the matrix, and M is the number of statistically independent samples used to estimate the correlation matrix of $\mathbf{p}(\psi,t)$.

It must be kept in mind that the Cramer–Rao theorem gives the *minimum* possible error. Since turbulence effects on the propagation are random, the *actual* error is also random. Furthermore, the actual error depends on the DOA estimation method. Among the more common methods are delay/sum beamforming and maximum-likelihood estimation. For the sensor array performance evaluations in Sec. III of this paper, only calculations of the CRLB will be pro-

vided, as opposed to calculations of actual array performance corresponding to specific estimation methods. The calculated errors are therefore intrinsically optimistic. However, it is worth pointing out that Song and Ritcey,[1] in their calculations of random ocean effects on DOA estimates, were able to achieve performance very near the CRLB using the maximum-likelihood method.

For the calculations appearing in Sec. III of this paper, when I refer to the CRLB I will actually mean the square root of $\mathbf{J}^{-1}(\psi)$. My reason for doing so is that the actual CRLB has units $(\text{deg})^2$, and it is more natural to think of the error bounds in plain degrees. The distinction between the actual CRLB and its square root should be clear from the context, because of the difference in units.

As a simple example, let us consider a two-element array. In this case

$$\mathbf{S}(\psi)=\begin{bmatrix} 1 & e^{-ikd\,\cos(\psi-\pi/2)} \\ e^{-ikd\,\cos(\psi+\pi/2)} & 1 \end{bmatrix},$$

$$\mathbf{T}=\begin{bmatrix} 1 & \Gamma(d) \\ \Gamma(d) & 1 \end{bmatrix},$$

and

$$\mathbf{R}_{nn}=\begin{bmatrix} \sigma_n^2 & 0 \\ 0 & \sigma_n^2 \end{bmatrix}.$$

Calculating the derivative of $\mathbf{R}_{pp}=\mathbf{S}\odot\mathbf{T}+\mathbf{R}_{nn}$ with respect to ψ, and its inverse, we find the following result for the CRLB:

$$\mathbf{J}^{-1}(\psi)=\frac{1-\Gamma^2(d)+\sigma_n^2(2+\sigma_n^2)}{2M(kd)^2\Gamma^2(d)\cos^2\psi}. \tag{11}$$

Clearly, the two-element array performs best when the source is broadside ($\psi=0$). In fact, when the source is in a line with the receivers ($\psi=\pi/2$), the CRLB becomes singular. Note also that it is desirable to make kd as large as possible, in order to create a large phase difference between the elements.

At this point, we have now succeeded in relating the lower performance bound for the array to the MCF for the turbulence. The next step is to determine the MCF.

C. The MCF and 2-D structure function

For homogeneous, isotropic, and nonintermittent turbulence, when the parabolic and Markov approximations to the wave equation are valid, the MCF is given by[4–8]

$$\Gamma(\boldsymbol{\rho})=\exp\left\{-\frac{\pi k^2 X}{2}\,[b(\mathbf{0})-b(\boldsymbol{\rho})]\right\}, \tag{12}$$

where $b(\boldsymbol{\rho})$ is the *two-dimensional (2-D) correlation function*[9] of the fluctuation in the squared index of refraction, N, and X is the source/array separation distance. By definition, $N=n^2-1$, where $n=c_0/c$ is the index of refraction, c is the actual sound speed, and c_0 is its ambient value. The speed of sound in the atmosphere depends on both temperature and humidity, being given by[10]

$$c\simeq 20\sqrt{T}(1+0.26h_s), \tag{13}$$

where T is the absolute temperature and h_s is the specific humidity (mass of water vapor divided by the total mass of the moist air). Fluctuations in the sound speed, $c'=c-c_0$, are normally small compared to the ambient value, and the influence of humidity fluctuations is also generally small. With these assumptions

$$N\simeq-\frac{2c'}{c_0}\simeq-\frac{T'}{T_0}, \tag{14}$$

where $c_0=20\sqrt{T_0}$ and $T'=T-T_0$. Hence correlation functions for N are approximately equal to correlation functions for normalized temperature fluctuations.

The 2-D correlation function is defined as the integral, over the direction of propagation, of the usual, 3-D correlation function $R(\mathbf{r})=\langle N(\mathbf{r})N(\mathbf{0})\rangle$.[4] Taking the x (r_1) axis to be the propagation direction, the 2-D correlation is specifically

$$b(\boldsymbol{\rho})=\frac{1}{2\pi}\int_{-\infty}^{\infty}R(r_1,r_2,r_3)\,dr_1, \tag{15}$$

where $\boldsymbol{\rho}=(r_2,r_3)$. When the turbulence is homogeneous and isotropic we may write the 2-D correlation function in an alternative form involving the spectral density function $\Phi(\boldsymbol{\kappa})$. This alternative form is derived using the fact that the 3-D correlation and spectral density functions constitute a Fourier transform pair:

$$R(\mathbf{r})=\int_{-\infty}^{\infty}\Phi(\boldsymbol{\kappa})\exp(i\boldsymbol{\kappa}\cdot\mathbf{r})\,d^3\kappa, \tag{16}$$

$$\Phi(\boldsymbol{\kappa})=\frac{1}{8\pi^3}\int_{-\infty}^{\infty}R(\mathbf{r})\exp(-i\boldsymbol{\kappa}\cdot\mathbf{r})\,d^3r. \tag{17}$$

Now, by Fourier transforming Eq. (16) with respect to r_1, and setting $\kappa_1=0$, we find the following expression equivalent to Eq. (15):

$$b(\boldsymbol{\rho})=\int_{-\infty}^{\infty}\int_{-\infty}^{\infty}\Phi(0,\kappa_2,\kappa_3)\times\exp[i(\kappa_2 r_2+\kappa_3 r_3)]\,d\kappa_2 d\kappa_3. \tag{18}$$

The effect of wind velocity fluctuations on a propagating sound wave is similar to the effect of sound speed fluctuations. By making a parabolic approximation to the acoustic wave equation, Ostashev[11] has shown that, in the presence of turbulent velocity fluctuations, N can be replaced by the following effective value:

$$N_{\text{mov}}=N-2v_1/c_0, \tag{19}$$

in which v_1 is the fluctuation of the velocity component parallel to the direction of propagation. Hence it is natural to consider statistics of a normalized velocity field $u_i=2v_i/c_0$, for example the correlation function

$$R_{ij}(\mathbf{r})=\langle u_i(\mathbf{r})u_j(\mathbf{0})\rangle. \tag{20}$$

When dealing with correlations of a vector field such as u_i, it is necessary to keep track of the orientation of the velocity components relative to the direction of the displacement $\mathbf{r}$. When Eq. (15) is applied to a vector field, we must therefore take care that the correlation function is for the velocity com-

ponents parallel to the propagation path (the direction of integration):

$$b_{\|}(\boldsymbol{\rho}) = \frac{1}{2\pi} \int_{-\infty}^{\infty} R_{11}(r_1, r_2 r_3) dr_1. \tag{21}$$

Note that for an isotropic field Eq. (21) is equivalent to defining $b_{\|}(\boldsymbol{\rho})$ by integrating R_{22} along the r_2 axis, or R_{33} along the r_3 axis. [We could also define a transverse 2-D correlation by making the integration perpendicular to the velocity components (e.g., by integrating R_{11} along the r_2 axis), although this function would apparently have little value in acoustics.]

It is also convenient to define a *two-dimensional structure function* as

$$d(\boldsymbol{\rho}) = 2[b(\mathbf{0}) - b(\boldsymbol{\rho})], \tag{22}$$

and similarly for $b_{\|}(\boldsymbol{\rho})$. The 2-D structure function is the 2-D counterpart of the usual structure function,

$$D(\mathbf{r}) = \langle [N(\mathbf{r}) - N(0)]^2 \rangle = 2[R(\mathbf{0}) - R(\mathbf{r})]. \tag{23}$$

With this definition for the 2-D structure function, Eq. (12) becomes

$$\Gamma(\boldsymbol{\rho}) = \exp\left\{ -\frac{\pi k^2 X}{4} d(\boldsymbol{\rho}) \right\}. \tag{24}$$

D. Incorporating intermittency

When turbulence intermittency[12,13] is included in the model, statistics such as the turbulent dissipation rates and structure functions become *local* properties of the flow; that is, they vary in space and time. We therefore define a local MCF $\tilde{\Gamma}(\boldsymbol{\rho}, \tilde{\epsilon}, \tilde{\chi})$ such that

$$\tilde{\Gamma}(\boldsymbol{\rho}_{mn}, \tilde{\epsilon}, \tilde{\chi}) = \frac{\langle p_m(t) p_n^*(t) | \tilde{\epsilon}, \tilde{\chi} \rangle}{\langle p_m(t) p_m^*(t) | \tilde{\epsilon}, \tilde{\chi} \rangle}, \tag{25}$$

where the vertical bar indicates conditional sampling, and $\tilde{\epsilon}$ and $\tilde{\chi}$ are the local (path-averaged) dissipation rates for turbulent kinetic energy and temperature variance, respectively, defined as[14]

$$\tilde{\epsilon} = \frac{1}{X} \int_0^X \epsilon(\xi) d\xi, \tag{26}$$

$$\tilde{\chi} = \frac{1}{X} \int_0^X \chi(\xi) d\xi. \tag{27}$$

In terms of the dissipation rates, the local structure-function parameters are[15]

$$\tilde{C}_N^2 \simeq \frac{2}{T_0^2} \tilde{\epsilon}^{-1/3} \tilde{\chi}, \tag{28}$$

$$\tilde{C}_u^2 \simeq \frac{8}{c_0^2} \tilde{\epsilon}^{2/3} \tag{29}$$

[see also Eqs. (70) and (77)]. In order for Eq. (25) to be a useful definition, it must be assumed that the period of the acoustic wave is much smaller than the time scales associated with variability in path-averaged turbulence properties. Otherwise it would be impossible to define a time-varying complex envelope $p_m(t)$ that responds to $\tilde{\epsilon}$ and $\tilde{\chi}$. Fortunately, $\tilde{\epsilon}$ and $\tilde{\chi}$ normally vary over intervals of several seconds at the fastest.[16]

One interpretation of Eq. (25) is that if we were to somehow measure the average dissipation rates $\tilde{\epsilon}$ and $\tilde{\chi}$ along the propagation path, and then average numerous samples of p_m and p_n^* for fixed values of $\tilde{\epsilon}$ and $\tilde{\chi}$, we would obtain a statistical estimate for $\tilde{\Gamma}(\boldsymbol{\rho}, \tilde{\epsilon}, \tilde{\chi})$. In practice we might also be able to obtain estimates for $\tilde{\Gamma}$ using a very large array of microphones. If the coherence radius (the value of ρ at which $\tilde{\Gamma}$ decays by a factor $1/e$) is small compared to the array dimensions and the turbulent length scale associated with the intermittency, then we could estimate $\tilde{\Gamma}$ by averaging over a large number of microphone pairs.

For spatially varying structure-function parameters, Tatarskii and Zavorotnyi[17] indicate that the MCF, Eq. (6), should be generalized to the following:

$$\tilde{\Gamma}(\boldsymbol{\rho}, \tilde{\epsilon}, \tilde{\chi}) = \exp\left\{ -\frac{\pi k^2}{4} \int_0^X d(\xi, \boldsymbol{\rho}) d\xi \right\}, \tag{30}$$

in which $d(\xi, \boldsymbol{\rho})$ is the 2-D structure function at a particular time and longitudinal position ξ along the propagation path. It will be shown in Sec. II D that for nonintermittent, inertial subrange turbulence, the 2-D structure function is proportional to the structure-function parameter C_N^2 (or C_u^2) times $\rho^{5/3}$. In the intermittent formulation, C_N^2 is replaced by $\tilde{C}_N^2$, its average value along the propagation path. Using Kolmogorov's inertial-subrange scaling [i.e., Eq. (73) in Sec. II D], we therefore have

$$\tilde{\Gamma}(\rho, \tilde{C}_N^2) = \exp\{0.464 \pi k^2 X \rho^{5/3} \tilde{C}_N^2 / 4\}. \tag{31}$$

For turbulent velocity fluctuations, $\tilde{C}_N^2$ is replaced by $\tilde{C}_u^2$, and the constant 0.464 is replaced by 0.850, in accordance with Eq. (79).

What is needed to complete the formulation of intermittent propagation is a probabilistic model describing the variations in $\tilde{C}_N^2$ and $\tilde{C}_u^2$. Kolmogorov[12] and Obukhov[13] proposed that the local dissipation rates have a log-normal probability density function (pdf) (i.e., $\ln \tilde{\epsilon}$ and $\ln \tilde{\chi}$ are normal). More generally, $\tilde{\epsilon}$ and $\tilde{\chi}$ can be modeled as jointly log-normal.[18] Other researchers have since verified that the log-normal model works reasonably well, except for predicting the ''tails'' of the pdf (i.e., the occurrence of very large or very small values of $\ln \tilde{\epsilon}$ or $\ln \tilde{\chi}$). I use the log-normal model in this paper.

If $\tilde{\epsilon}$ and $\tilde{\chi}$ are jointly log-normal, it follows that $\tilde{C}_N^2$ and $\tilde{C}_u^2$ are jointly log-normal.[19] Therefore the pdf of $\eta = \tilde{C}_N^2$ (or $\eta = \tilde{C}_u^2$) is

$$P(\eta) = \frac{1}{\sqrt{2\pi}\, \eta \sigma_{\ln \eta}} \exp\left[-\frac{(\ln \eta - m_{\ln \eta})^2}{2\sigma_{\ln \eta}^2} \right], \tag{32}$$

where $m_{\ln \eta} = \langle \ln \eta \rangle$ is called the log-mean, and $\sigma_{\ln \eta}^2 = \langle (\ln \eta - m_{\ln \eta})^2 \rangle$ the log-variance. A general property of the log-normal distribution is that

$$m_{\ln \eta} = \ln \langle \eta \rangle - \sigma_{\ln \eta}^2 / 2, \tag{33}$$

allowing us to rewrite $P(\eta)$ as

$$P(\eta)=\frac{1}{\sqrt{2\pi}\,\eta\sigma_{\ln\eta}}\exp\left[-\frac{(\ln(\eta/\langle\eta\rangle)+\sigma^2_{\ln\eta}/2)^2}{2\sigma^2_{\ln\eta}}\right]. \tag{34}$$

This form is more convenient than (32), since in practice we normally have some method for determining $C_N^2=\langle\widetilde{C}_N^2\rangle$, but do not know $\langle\ln\widetilde{C}_N^2\rangle$ directly.

The log-variance of quantities such as the volume-averaged structure-function parameters, in a high Reynolds number flow, obeys the formula[12,20]

$$\sigma^2_{\ln\eta}=\mu\,\ln\left(\frac{\mathscr{L}}{\Delta}\right), \tag{35}$$

where μ is a constant, $\mathscr{L}$ is the integral length scale, and Δ is a linear scale characteristic of the averaging volume. As the averaging volume becomes small in comparison to the large-scale flow features, the log-variance increases. Most recent studies, usually involving either laboratory measurements or numerical flow simulations, suggest the constant μ is in the range 0.15–0.25.[21–23] One notably different result comes from Kukharets's[24] atmospheric measurements, from which he found $\mu=0.800\pm0.343$. J. G. Brasseur[25] has suggested that the discrepancies in measurements of μ result from non-universality of Eq. (35) when it is applied to different flows. It could also be that Kukharet's measurements included substantial *global* intermittency of the type discussed by Mahrt,[26] as opposed to the *small-scale* (turbulent) intermittency considered in this paper. For the calculations in this paper I have set $\mu=0.25$.

Having settled on the log-normal model for $\widetilde{C}_N^2$ and $\widetilde{C}_u^2$, we can now formulate statistics for the local MCF. In particular (considering only $\widetilde{C}_N^2$ for simplicity), we can determine an unconditionally averaged MCF from $P(\widetilde{C}_N^2)$ using the relationship

$$\langle\widetilde{\Gamma}(\rho,\widetilde{C}_N^2)\rangle=\int_0^\infty\widetilde{\Gamma}(\rho,\widetilde{C}_N^2)P(\widetilde{C}_N^2)d\widetilde{C}_N^2. \tag{36}$$

Besides the average MCF, it is important to establish the extreme values between which $\widetilde{\Gamma}(\rho,\widetilde{C}_N^2)$ varies. One method for doing so is to calculate confidence bounds on $\widetilde{\Gamma}(\rho,\widetilde{C}_N^2)$. A normally distributed random variable falls between $m-1.65\sigma$ and $m+1.65\sigma$ 90% of the time. Hence we can calculate 90% confidence bounds on $\widetilde{\Gamma}(\rho,\widetilde{C}_N^2)$ by evaluating Eq. (31) at

$$\begin{aligned}\widetilde{C}_N^2&=\exp(m_{\ln N}\pm1.65\sigma_{\ln N})\\&=C_N^2\,\exp(-0.5\sigma^2_{\ln N}\pm1.65\sigma_{\ln N}),\end{aligned} \tag{37}$$

and similarly for $\widetilde{\Gamma}(\rho,\widetilde{C}_u^2)$.

II. TURBULENCE MODELS FOR THE 2-D STRUCTURE FUNCTION

Most previous spectral models appearing in the atmospheric sciences literature are one-dimensional (e.g., the work summarized by Panofsky and Dutton[27]), but we need full 3-D spectral (or 3-D correlation) models in order to compute the 2-D structure function, which is in turn needed to compute the MCF [Eq. (24)]. Unfortunately, there are currently no (and probably never will be) 3-D turbulence models that are known to work satisfactorily for a wide variety of atmospheric conditions. This is because atmospheric turbulence structure is determined by complex interactions between shear instability, temperature stratification, surface roughness, and the Coriolis force, among other factors. Hence we are forced to consider idealized spectral models. Some specific 3-D spectral models for atmospheric turbulence are discussed in this section.

The first such idealization I consider is the isotropic, homogeneous Gaussian model. The main advantage of the Gaussian model is its analytical convenience. Unfortunately most of the energy in the Gaussian model is concentrated at a single spatial scale; the model cannot represent the broad distribution of energy across spatial scales that is a well-known characteristic of high Reynolds number turbulence. The next model discussed, the Wilson and Thomson[2] model, is also built from Gaussian functions but incorporates certain anisotropic and inhomogeneous properties characteristic of energy subrange (large-scale) eddies in the atmosphere. The third model treated is the isotropic, homogeneous von Kármán model. It has the advantage of describing energy in the smaller scale (*inertial subrange*) eddies much more realistically than the Gaussian models, yet still behaves in a physically reasonable manner in the energy subrange. As such, the von Kármán model is the only one considered in this paper that can be applied to the full turbulence spectrum without obtaining totally unrealistic results. [The dissipation subrange is not considered in this paper, since the dissipative eddies are small (1–10 mm) compared to the acoustic wavelengths of interest.] Finally I consider the Kolmogorov model, which is intended only for the inertial subrange. The Kolmogorov model is developed in this paper by calculating small-scale approximations to the von Kármán model.

For the isotropic Gaussian, von Kármán, and Kolmogorov models, results are given for both scalar and vector fields. Previous authors[11,28,29] have discussed the important distinction between turbulence models for vector and scalar fields, even though it has often been neglected in atmospheric acoustics studies. The Wilson and Thomson model incorporates both scalar and vector fluctuations in a nonrigorous manner.

A. Isotropic Gaussian model

1. Scalar

The scalar version of the isotropic, homogeneous Gaussian model is defined by the normalized correlation function

$$h(r)=\exp\left(-\frac{r^2}{L^2}\right), \tag{38}$$

where $h(r)=R(\mathbf{r})/\sigma^2$, σ^2 is the variance, and L is a length scale parameter. In accordance with Eq. (14), the variance to be used in the model is

$$\sigma^2=\langle N^2\rangle=\frac{\langle T'^2\rangle}{T_0^2}. \tag{39}$$

Besides the correlation, an important fundamental function characterizing a turbulence model is its *specific energy spectrum*, $E_N(\kappa)$. (*Specific* here means per unit mass.) For a

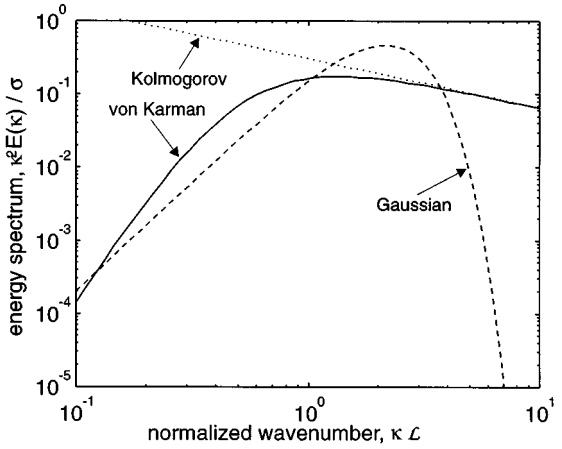

FIG. 1. Comparison of the energy spectral functions for the scalar forms of the Gaussian, von Kármán, and Kolmogorov models.

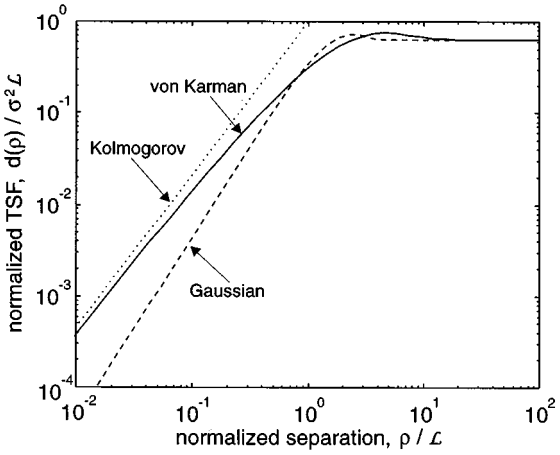

FIG. 2. Comparison of the two-dimensional structure functions corresponding to the Gaussian, von Kármán, and Kolmogorov turbulence models.

scalar, the energy spectrum is $2\pi\kappa^2$ times the 3-D spectrum $\Phi(\boldsymbol{\kappa})$, so the integral of $E_N(\kappa)$ from 0 to ∞ equals one-half the total variance of the field. By Fourier transforming the correlation function, it can be shown that

$$E_N(\kappa)=\frac{\sigma^2\kappa^2L^3}{4\sqrt{\pi}}\exp\left(-\frac{\kappa^2L^2}{4}\right). \tag{40}$$

Since the length scale L is particular to the Gaussian model, comparisons between the Gaussian model and other models are facilitated by relating L to a length scale that can be defined for any well-behaved model. A good choice for the common length scale is the integral length scale, defined as

$$\mathscr{L}=\int_0^\infty h(r)dr. \tag{41}$$

By performing the integration one finds that

$$\mathscr{L}=(\sqrt{\pi}/2)L=0.886L. \tag{42}$$

When the Gaussian energy spectrum is multiplied by κ/σ^2, it becomes a function solely of $\kappa\mathscr{L}$. The energy spectrum thus normalized is plotted in Fig. 1.

From Eq. (15) the 2-D correlation function is

$$b(\rho)=\frac{\sigma^2L}{2\sqrt{\pi}}\exp\left(-\frac{\rho^2}{L^2}\right). \tag{43}$$

Hence, the 2-D structure function is

$$d(\rho)=2[b(0)-b(\rho)]=\frac{\sigma^2L}{\sqrt{\pi}}\left[1-\exp\left(-\frac{\rho^2}{L^2}\right)\right]. \tag{44}$$

This equation is plotted in Fig. 2.

2. Vector

The case of a vector field is somewhat more complicated than the scalar one: two independent normalized correlation functions can be defined, one where the displacement is parallel to the velocity, e.g.,

$$f(r)=R_{11}(r,0,0)/\sigma^2, \tag{45}$$

and the other where it is perpendicular, e.g.,

$$g(r)=R_{11}(0,r,0)/\sigma^2. \tag{46}$$

For a purely rotational flow, such as turbulence, the two correlation functions are related by[30]

$$g(r)=f(r)+\frac{r}{2}\frac{df}{dr}. \tag{47}$$

The full correlation tensor is[30]

$$R_{ij}(r_1,r_2,r_3)=\sigma^2\left[\frac{r_ir_j}{r^2}f(r)+\left(\delta_{ij}-\frac{r_if_j}{r^2}\right)g(r)\right]. \tag{48}$$

Following Ostashev,[11] I define the vector Gaussian model by setting

$$f(r)=\exp\left(-\frac{r^2}{L^2}\right). \tag{49}$$

The variance in the vector model, in accordance with Eq. (19), is

$$\sigma^2=\langle(N-N_{\mathrm{mov}})^2\rangle=\langle u_i^2\rangle=\frac{4\langle v_i^2\rangle}{c_0^2}. \tag{50}$$

Because $f(r)$ is the same as $h(r)$ in the scalar model, it is still true that $\mathscr{L}=(\sqrt{\pi}/2)L$.

The energy spectrum can be found by calculating the Fourier transform, $\hat{f}(\kappa)$, of Eq. (49), and then using the relationship[30]

$$E_u(\kappa)=\sigma^2\kappa^3\frac{d}{d\kappa}\left[\frac{1}{\kappa}\frac{d\hat{f}(\kappa)}{d\kappa}\right]. \tag{51}$$

The resulting energy spectrum is

$$E_u(\kappa)=\frac{\sigma^2\kappa^4L^5}{8\sqrt{\pi}}\exp\left(-\frac{\kappa^2L^2}{4}\right). \tag{52}$$

For a nondivergent, mass-conserving flow, the 3-D spectra are related to the energy spectrum according to[30]

$$\Phi_{ij}(\kappa)=\frac{E_u(\kappa)}{4\pi r^4}(\delta_{ij}\kappa^2-\kappa_i\kappa_j), \tag{53}$$

The 2-D correlation function for the vector Gaussian model can be found from the equation

$$b_{\|}(\rho)=\frac{1}{2}\int_0^\infty \frac{E_u(\kappa_\perp)}{\kappa_\perp} J_0(\kappa_\perp \rho) d\kappa_\perp, \tag{54}$$

which results from substituting Eq. (53) (with $i=j=1$) into (18), and then rewriting the integration in cylindrical coordinates, with $\kappa_\perp$ being the radial wave number in the (κ_2,κ_3) plane. For the Gaussian model, the result of performing the integration is

$$b_{\|}(\rho)=\frac{\sigma^2 L}{2\sqrt{\pi}}\left(1-\frac{\rho^2}{L^2}\right)\exp\left(-\frac{\rho^2}{L^2}\right). \tag{55}$$

Hence, the 2-D structure function for the vector model is

$$\begin{aligned} d_{\|}(\rho)&=2[b_{\|}(0)-b_{\|}(\rho)] \\ &=\frac{\sigma^2 L}{\sqrt{\pi}}\left[1-\left(1-\frac{\rho^2}{L^2}\right)\exp\left(-\frac{\rho^2}{L^2}\right)\right]. \end{aligned} \tag{56}$$

B. Wilson and Thomson model

Wilson and Thomson[2] developed an anisotropic, inhomogeneous, Gaussian model for atmospheric turbulence. The model includes structure from large-scale, buoyantly generated eddies, as well as smaller scale, shear-generated eddies. One inherent limitation of the Wilson and Thomson model is its unrealistic inertial subrange, which results from its Gaussian nature. A second limitation is that the velocity field is essentially treated as an anisotropic scalar field. Despite these limitations the model appears reasonable for the energy subrange, and can be useful for examining the relative contributions of buoyantly and shear-generated turbulence to the scattering.

The Wilson and Thomson model has four independent physical parameters: the surface wind stress τ, the surface temperature flux Q, the boundary-layer inversion height z_i, and the height from the ground z. From these physical parameters, the relevant turbulence scaling parameters can be determined: the *friction velocity* $u_*=\sqrt{\tau/\rho_0}$, the *surface-layer temperature scale* $T_*=-Q/u_*$, and the *free-convection velocity scale* $w_f=(Qgz_i/T_s)^{1/3}$. (The air density is ρ_0, g is gravitational acceleration, and T_s is the surface temperature.)

The Wilson/Thomson model consists of a correlation function having six terms, four attributable to small-scale, shear-generated turbulence, and the other two to large-scale, buoyantly generated turbulence. The correlation function is written in the following form:

$$R(\mathbf{r})=\sum_{i=1}^{6} A_i \exp(-\tilde{\mathbf{r}}\tilde{\mathbf{T}}\mathbf{L}_i^{-2}\mathbf{T}\mathbf{r}), \tag{57}$$

where $\mathbf{r}$ is a coordinate system whose r_1 axis is aligned with the direction of propagation,[31] $\mathbf{T}$ is a rotation matrix that maps the meteorological coordinates to the propagation coordinates, the A_i are variances, and $\mathbf{L}_i$ is a length scale matrix. The parametrizations of the A_i's are $A_1=4T_*^2/T_0^2$ (small-scale temperature variance), $A_2=22(u_*^2/c_0^2)\cos^2\phi$ (small-scale velocity variance, longitudinal), $A_3=18(u_*^2/c_0^2)\sin^2\phi$ (small-scale velocity variance, lateral), $A_4=10(u_*T_*/c_0T_0)\cos\phi$ (temperature-longitudinal velocity covariance), $A_5=0.8(w_f^2/c_0^2)\cos^2\phi$ (large-scale velocity variance, longitudinal), and $A_6=0.8(w_f^2/c_0^2)\sin^2\phi$ (large-scale velocity variance, lateral), where ϕ is the azimuthal angle of propagation, relative to the wind direction. [Note that the A_i's given in Wilson and Thomson's[2] Table II must be multiplied by 4 to bring them in line with the conventions used in this paper (Sec. I C).] The length scale matrix is diagonal, with the nonzero elements being $L_{i,x}=f_{i,x}L_{i,z}$, $L_{i,y}=f_{i,y}L_{i,z}$, and $L_{i,z}$. In terms $i=1$ to 4, $L_{i,z}=z$, and in terms $i=5$ to 6, $L_{i,z}=0.4z_i$. (No summation over repeated indices is implied.) For near ground propagation, $f_{i,x}\simeq 6.3$ and $f_{i,y}\simeq 1.0$ in terms 1 to 4, and $f_{i,x}$, $f_{i,y}\simeq 0.7$ in terms 5 to 6.

For anisotropic turbulence, the 2-D correlation must be determined from Eq. (15). [Note that $b(r_2,r_3)$ here corresponds to $\hat{\rho}(y,z)/2\pi$ in the notation of Ref. 2.] Assuming horizontal propagation, the result of the integration is the 2-D correlation function

$$b(r_2,r_3)=\sum_{i=1}^{6}\frac{A_i}{2}\sqrt{\frac{1}{\pi a_i}}\exp\left(\frac{b_i^2-4a_ic_i}{4a_i}\right)\operatorname{erfc}\left(\frac{b_i}{2\sqrt{a_i}}\right), \tag{58}$$

where

$$a_i=\frac{1}{L_{i,z}^2}(f_{i,x}^2\cos^2\phi+f_{i,y}^2\sin^2\phi),$$

$$b_i=\frac{2}{L_{i,z}^2}(-f_{i,x}^2+f_{i,y}^2)\cos\phi\sin\phi\, r_2,$$

$$c_i=\frac{1}{L_{i,z}^2}[(f_{i,x}^2\sin^2\phi+f_{i,y}^2\cos^2\phi)r_2^2+r_3^2].$$

C. von Kármán model

1. Scalar

The version of the von Kármán model developed here is based on the following form for the energy spectrum of a scalar:

$$E_N(\kappa)=\frac{4\Gamma(\alpha+5/2)}{3\sqrt{\pi}\Gamma(\alpha)}\frac{\sigma^2\kappa^4 l^5}{(1+\kappa^2 l^2)^{\alpha+5/2}}. \tag{59}$$

[A factor such as $\exp(-\kappa^2/\kappa_m^2)$ is sometimes included in the von Kármán spectrum in order to attenuate the spectrum in the dissipation subrange, but since the small eddies of the dissipation subrange are unimportant in low-frequency acoustics, I choose to omit the factor here.] The parameter l is a characteristic length scale, Γ is the gamma function, and α controls the power-law dependence in the inertial subrange ($\kappa l\gg 1$). By integrating Eq. (59) from $\kappa=0$ to $\kappa=\infty$, it can be verified that the total energy in the scalar spectrum is $\sigma^2/2$. Generally we set $\alpha=1/3$ to obtain Kolmogorov's $\kappa^{-5/3}$ power law[32] for the inertial subrange. The von Kármán model is compared to the Gaussian model in Fig. 1. The main difference between the von Kármán and Gaussian models is that the Gaussian model decays much more rapidly at large wave numbers.

As discussed earlier (Sec. II A1), the scalar 3-D spectrum is simply $\Phi(\kappa)=E_N(\kappa)/2\pi\kappa^2$. The correlation function follows by calculating the inverse Fourier transform with respect to all three wave number axes, and then setting $r_2=r_3=0$. The result is

$$h(r)=\frac{2}{\Gamma(1/3)}\left(\frac{r}{2l}\right)^{1/3}\left[K_{1/3}\left(\frac{r}{l}\right)-\left(\frac{r}{3l}\right)K_{2/3}\left(\frac{r}{l}\right)\right], \quad (60)$$

where K_ν is the modified Bessel function of the second kind. Integrals (3.773.6) and (6.726.4) from Gradshteyn and Ryzhik[33] were used to derive this result. The variance parameter in the scalar von Kármán model is the same as in the scalar Gaussian model, Eq. (39). The length scales in the two models can be related via the integral length scale. For the von Kármán model, the integral length scale is found by integrating Eq. (60), with the result

$$\mathscr{L}=\frac{2\sqrt{\pi}\Gamma(5/6)}{3\Gamma(1/3)}\,l=0.498l. \quad (61)$$

We can find the 2-D correlation for the scalar von Kármán model from the energy spectrum using the equation

$$b(\rho)=\int_0^\infty \frac{E_N(\kappa_\perp)}{\kappa_\perp}\,J_0(\kappa_\perp\rho)\,d\kappa_\perp, \quad (62)$$

which follows by rewriting Eq. (18) in cylindrical coordinates. Making the substitution $J_0(x)=(2/x)J_1(x)-J_2(x)$ produces two integrals, each of which is given by the formula (6.565.4) in Ref. 33. The 2-D correlation function resulting from the integrations is

$$b(\rho)=\frac{4\sigma^2 l}{3\sqrt{\pi}\Gamma(1/3)}\left(\frac{\rho}{2l}\right)^{5/6}\left[K_{5/6}\left(\frac{\rho}{l}\right)-\frac{\rho}{2l}\,K_{1/6}\left(\frac{\rho}{l}\right)\right]. \quad (63)$$

The 2-D structure function for the scalar von Kármán model is plotted and compared to the Gaussian function in Fig. 2.

2. Vector

The vector von Kármán energy spectrum $E_u(\kappa)$ is simply three times the scalar spectrum,[34] so that the total energy is $3\sigma^2/2$. The 3-D spectra follow from the energy spectrum using Eq. (53). By Fourier transforming $\Phi_{11}(\boldsymbol{\kappa})$ with respect to all three axes, and then setting $r_2=r_3=0$, one finds

$$f(r)=\frac{2}{\Gamma(1/3)}\left(\frac{r}{2l}\right)^{1/3}K_{1/3}\left(\frac{r}{l}\right). \quad (64)$$

The variance parameter in the vector von Kármán model is the same as the variance in the vector Gaussian model, Eq. (50). The integral length scale, in the direction of the velocity components, is

$$\mathscr{L}=\frac{\sqrt{\pi}\Gamma(5/6)}{\Gamma(1/3)}\,l=0.747l. \quad (65)$$

Since $E_u(\kappa)=3E_N(\kappa)$, and the right-hand side of Eq. (54) is $\frac{1}{2}$ the right-hand side of Eq. (62), the vector 2-D correlation function $b_\parallel(\rho)$ is simply $\frac{3}{2}$ times the scalar result, Eq. (63). The same relationship holds for 2-D structure functions.

D. Kolmogorov model

The Kolmogorov model is based on scaling arguments that apply only in the inertial subrange: for $\rho\ll\mathscr{L}$ in the spatial domain, or $\kappa\mathscr{L}\gg1$ in the wave number domain. Kolmogorov[32] argued that the inertial subrange has universal scaling properties that are independent of the large-scale structure of a particular flow; specifically, inertial subrange statistics depend only on the length scale $1/\kappa$ and the dissipation rate of turbulent kinetic energy ϵ. Actually, the von Kármán model discussed in the previous section has an inertial subrange that satisfies Kolmogorov's hypothesis. Therefore we can essentially derive the Kolmogorov model simply by calculating the appropriate limits of the von Kármán model. However, in the spirit of Kolmogorov's hypothesis, the limiting von Kármán equations still should be reformulated without explicit appearance of σ^2 and l, since those parameters depend primarily on energy subrange structure. In the following development, structure-function parameters are used in lieu of σ^2 and l.

1. Scalar

The structure function for a scalar, such as the fluctuation in the squared index of refraction, is

$$D(r)=\langle[N(\mathbf{r})-N(\mathbf{0})]^2\rangle=2\sigma^2[1-h(r)], \quad (66)$$

with the structure-function parameter defined as

$$C_N^2=\lim_{r\to0}\,D(r)/r^{2/3}. \quad (67)$$

We can find the required limits from Eq. (60), by expanding the modified Bessel functions as Maclaurin series,

$$K_\alpha(\xi)\simeq\frac{\Gamma(\alpha)}{2}\left(\frac{\xi}{2}\right)^{-\alpha}-\frac{\Gamma(1-\alpha)}{2\alpha}\left(\frac{\xi}{2}\right)^{\alpha}. \quad (68)$$

We find that the structure-function parameter for the scalar is

$$C_N^2=\frac{22\sigma^2\Gamma(2/3)}{3\Gamma(1/3)}\left(\frac{1}{2l}\right)^{2/3}\simeq2.34\sigma^2 l^{-2/3}. \quad (69)$$

Note, from Eq. (39), that

$$C_N^2\simeq C_T^2/T_0^2, \quad (70)$$

where C_T^2 is the structure-function parameter for the temperature field. Taking the large κl limit of Eq. (59), and substituting the results for the structure-function parameter, we find

$$E_N(\kappa)=\frac{2^{5/3}}{11\sqrt{\pi}}\,\frac{\Gamma(17/6)}{\Gamma(2/3)}\,C_N^2\kappa^{-5/3}\simeq0.207C_N^2\kappa^{-5/3}. \quad (71)$$

The scalar Kolmogorov energy spectrum is plotted in Fig. 1.

For inertial-subrange separations, the scalar 2-D correlation is

$$b(\rho)=\frac{2\sigma^2 l\Gamma(5/6)}{3\sqrt{\pi}\Gamma(1/3)}\left[1-\frac{11}{5}\,\frac{\Gamma(1/6)}{\Gamma(5/6)}\left(\frac{\rho}{2l}\right)^{5/3}\right]. \quad (72)$$

The 2-D structure function, in terms of the structure-function parameter, is therefore

$$d(\rho)=\frac{\Gamma(1/6)}{5\sqrt{\pi}\Gamma(2/3)}\,C_N^2\rho^{5/3}\simeq 0.464C_N^2\rho^{5/3}. \tag{73}$$

Equation (73) is plotted in Fig. 2.

2. Vector

For vectors, the structure-function parameter is normally defined with a parallel displacement, e.g.,

$$D_{\parallel}(r)=\langle[u_1(r,0,0)-u_1(0,0,0)]^2\rangle=2\sigma^2[1-f(r)], \tag{74}$$

$$C_u^2=\lim_{r\to 0} D_{\parallel}(r)/r^{2/3}. \tag{75}$$

From Eq. (64) one finds

$$C_u^2=\frac{6\sigma^2\Gamma(2/3)}{\Gamma(1/3)}\left(\frac{1}{2l}\right)^{2/3}\simeq 1.91\sigma^2 l^{-2/3}. \tag{76}$$

Note also, from Eq. (50), that

$$C_u^2=\frac{4}{c_0^2}\,C_v^2, \tag{77}$$

where C_v^2 is the structure-function parameter for the velocity field. In terms of the structure-function parameter, the energy spectrum is

$$E_u(\kappa)=\frac{2^{5/3}}{3\sqrt{\pi}}\,\frac{\Gamma(17/6)}{\Gamma(2/3)}\,C_u^2\kappa^{-5/3}\simeq 0.760C_u^2\kappa^{-5/3}, \tag{78}$$

and the 2-D structure function is

$$d_{\parallel}(\rho)=\frac{11}{30}\,\frac{\Gamma(1/6)}{\sqrt{\pi}\Gamma(2/3)}\,C_u^2\rho^{5/3}\simeq 0.850C_u^2\rho^{5/3}. \tag{79}$$

By comparing Eq. (79) to Eq. (73), we see that the vector case is analogous to the scalar case when, in place of C_N^2, we use $C_{\rm eff}^2=(11/6)C_u^2=(22/3)C_v^2/c_0^2$. This result agrees with Ostashev's[11] Eq. (69).

III. RESULTS

A. Long baseline–sensor decorrelation tradeoff

Were it not for cost, limitations of practical beamforming procedures, and turbulence effects, it would be desirable to make DOA arrays as large as possible. This is evident, for example, from the equation for the CRLB of a two-element array, Eq. (11). The CRLB in this case is inversely proportional to the square of the sensor spacing. Increasing the array dimensions is desirable because it increases the phase differences between the sensors, making the measurement less sensitive to noise. On the other hand, large arrays are undesirable when turbulence is significant. Generally one wants the dimensions of the array small in relation to the size of the most energetic turbulent eddies, so that there is good mutual coherence across the array.

The tradeoff between array baseline and turbulent degradation is illustrated by the CRLB calculations shown in Fig. 3. The calculations are for broadside incidence ($\psi=0$) on a five-element uniform linear array, at a normalized distance $kX=1000$ from the source. The spacing $kd(=2\pi d/\lambda)$

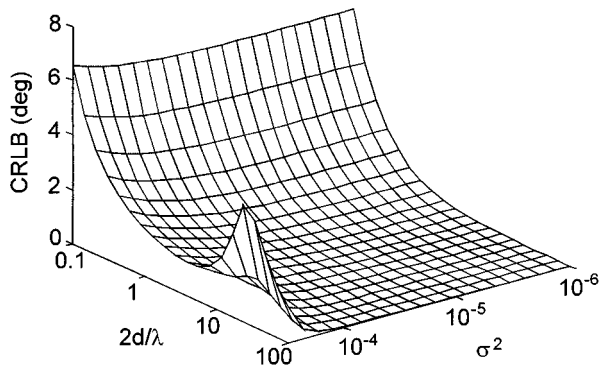

FIG. 3. Effect of changing the array spacing on DOA estimation errors: moderate noise, von Kármán turbulence model case. The array is a five-element uniform line array, and the calculations are for $\sigma_n^2=0.1$, $M=5$, and $k\mathscr{L}=10\pi$.

and strength of the turbulence σ^2 are varied in the figures. The normalized integral length scale is $k\mathscr{L}=10\pi$, and the noise-to-signal variance is $\sigma_n^2=0.1$ (SNR=10). A scalar von Kármán turbulence spectrum was used in this example [Eq. (63)].

For weak turbulence ($\sigma^2\lesssim 10^{-5}$), we can improve array performance essentially without bound by increasing the sensor spacing. Performance is poor for small sensor spacings because phase difference information becomes lost in the measurement noise. For strong turbulence ($\sigma^2\gtrsim 10^{-4}$) array performance is degraded, particularly if the size of the array is comparable to the integral length scale of the turbulence. When this occurs an ''error resonance'' in the CRLB is evident. If array dimensions are either much smaller or much larger than the turbulence length scale, however, array performance suffers little.

Figure 4 is similar to Fig. 3, except that the noise variance has been decreased to $\sigma_n^2=0.01$. Because there is less noise than in the previous example, smaller arrays provide better performance. Although the error resonance is still clearly evident on the figure, now some turbulent degradation of array performance is observed even for the smaller arrays.

Calculations for a scalar Gaussian spectrum, with

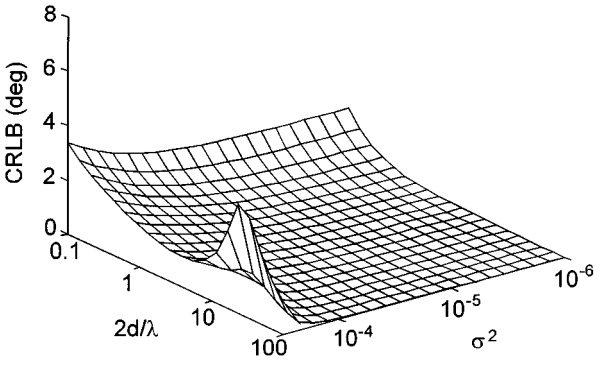

FIG. 4. Effect of changing the array spacing on DOA estimation errors: low noise, von Kármán turbulence model case. Same as Fig. 3, except that the noise variance has been reduced to $\sigma_n^2=0.01$.

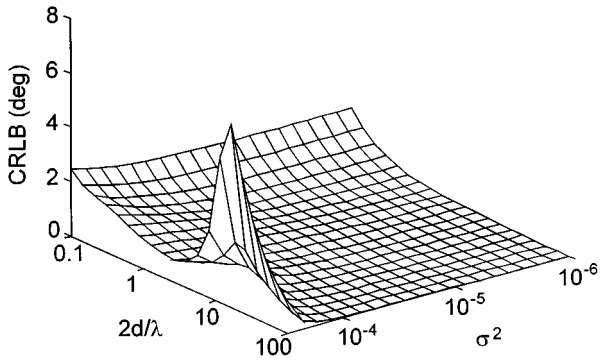

FIG. 5. Effect of changing the array spacing on DOA estimation errors: low noise, Gaussian turbulence model case. Except for the change in the turbulence model, this is the same as Fig. 4.

$\sigma_n^2=0.01$, are shown in Fig. 5. The error resonance in strong turbulence is sharper in the von Kármán spectrum, while the error for small arrays ($2d/\lambda<1$) is somewhat less. This results from the deficiency of the Gaussian model discussed earlier: it does not realistically capture the energy in the inertial-subrange turbulence.

B. Relative contributions of velocity and temperature fluctuations

As discussed in Sec. II B, the Wilson/Thomson model contains separate terms representing the contributions from temperature fluctuations, small- (z-) scale velocity fluctuations, large- (z_i-) scale velocity fluctuations, and temperature/velocity covariance. This allows us to study the relative significance of the different contributions to the overall 2-D structure function, and hence to DOA estimates from a sensor array.

Figure 6(a) shows the 2-D structure function predicted by the Wilson/Thomson model for upwind propagation ($\phi=\pi$). The model parameters were $u_*=0.5$ m/s, $T_*=-0.3$ K, $z=2$ m, and $z_i=1000$ m. These values are representative of the lower atmosphere, on a sunny, somewhat windy afternoon, what atmospheric scientists call a *convective* (buoyantly unstable) boundary layer. Such conditions are favorable to the production of a high variance in temperature. Nonetheless, as clearly shown by the figure, small-scale velocity fluctuations (terms 2 and 3 in the Wilson/Thomson model) dominate the 2-D structure function for transverse separations $r_2\lesssim 10$ m. The large-scale velocity fluctuations become most important only when $r_2\gtrsim 100$ m. The temperature/velocity covariance term plays a minor role when $r_2\lesssim 10$ m, while the contribution from the temperature term is always very small.

Figure 6(b) is similar to (a), except that T_* has been changed to -0.01 K. These values are characteristic of a windy, overcast day (known as a *neutral* boundary layer). As before, small-scale velocity fluctuations dominate the 2-D structure function. Both the temperature and temperature/velocity covariance terms are completely negligible. The contribution from large-scale velocity fluctuations is somewhat diminished.

In conclusion, we see that for sensor separations typical of applications ($r_2\lesssim 10$ m), the contribution from small-scale velocity fluctuations is normally most important, even when the meteorological conditions produce a high temperature variance. Hence in subsequent calculations I focus on the effects of small-scale velocity fluctuations.

Although no plots are shown here, it is worth pointing out that large-scale velocity fluctuations normally dominate the 2-D correlation function (as opposed to the 2-D structure function) in the Wilson/Thomson model. This does not imply, however, that the large-scale turbulence plays a dominant role in determining the signal coherence: the large-scale turbulence causes highly coherent fluctuations in amplitude and phase across the entire array. Therefore plots of the contributions of the various terms to the 2-D correlation (or 3-D correlation or spectrum) can be misleading; plots of the 2-D structure function provide the relevant information.

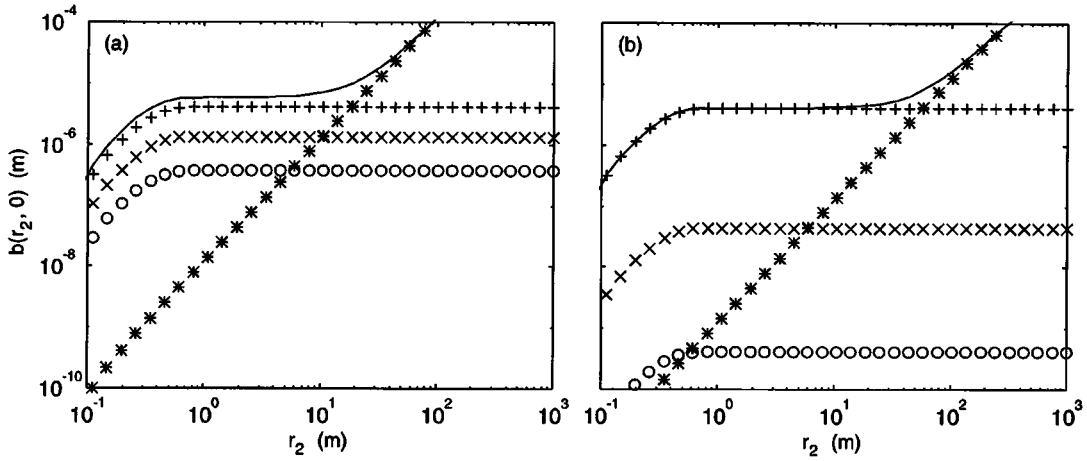

FIG. 6. Two-dimensional structure function as computed from the Wilson and Thomson model. (a) Convective boundary layer case: $u_*=0.5$ m/s, $T_*=-0.3$ K, $z=2$ m, and $z_i=1000$ m. (b) Same as (a), except $T_*=-0.01$ K. The total 2-D structure function is the solid line. Circles are the contribution from temperature fluctuations; ×'s are from temperature/velocity covariance; +'s are from small-scale velocity fluctuations; and *'s are from large-scale velocity fluctuations.

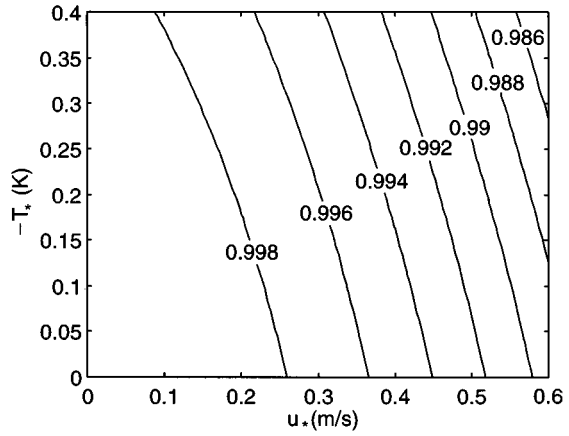

FIG. 7. The MCF calculations as a function of turbulence conditions. The propagation distance was 500 m, the frequency 200 Hz, and the sensor spacing one-half wavelength.

C. Dependence of array performance on meteorological conditions

Figure 7 shows example calculations of the MCF as a function of u_* and T_*, using the Wilson/Thomson model. The calculations are for r_2 equal to one-half wavelength, $f=200$ Hz, $z=2$ m, $z_i=1000$ m, and propagation distance $X=500$ m. The MCF is observed to depend more strongly on u_* than on T_*, since u_* characterizes the strength of the small-scale velocity fluctuations. When winds are light (small u_*), however, the MCF does decrease somewhat with increasing T_*. The resulting CRLB is shown in Fig. 8 for a horizontal, five-element, uniform line array, at broadside incidence, with spacing $\lambda/2$. The noise variance was $\sigma_n^2=0.01$, and the number of samples was $M=5$.

D. Model intercomparisons

In this subsection comparisons of CRLB calculations from the various turbulence models (Sec. II) are presented. The array configuration is again a five-element line array

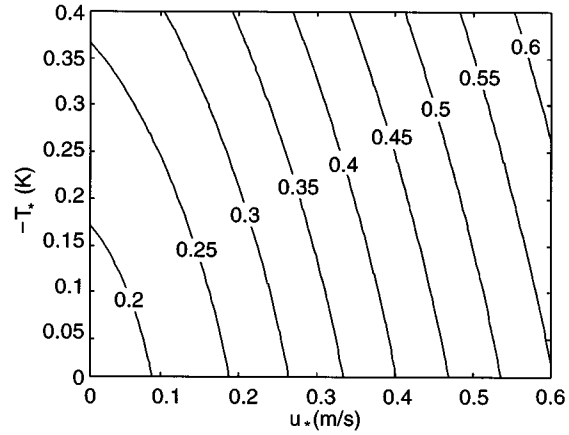

FIG. 8. The CRLB (in degrees) as a function of turbulence conditions, for a five-element uniform line array at broadside incidence. The propagation distance was 500 m, the frequency 200 Hz, and the sensor spacing one-half wavelength.

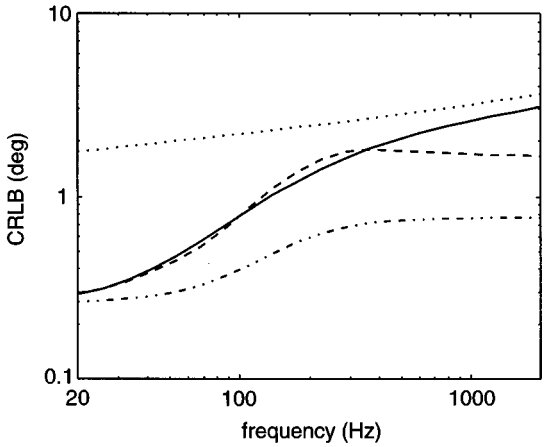

FIG. 9. Comparison of the CRLB's for a five-element uniform line array, at broadside incidence, using various turbulence models ($\sigma_n^2=0.01$, $M=5$, $X=500$ m, and $d=\lambda/2$). Solid line: von Kármán model. Dashed line: Isotropic Gaussian model. Dotted line: Kolmogorov model. Dash-dotted line: Wilson/Thomson model.

with spacing $\lambda/2$, and also $\sigma_n^2=0.01$, $M=5$. Meteorological conditions were representative of a windy, neutral atmosphere: $u_*=0.5$ m/s, $T_*=-0.01$ K, and $z_i=1000$ m. The resulting calculations are shown in Fig. 9.

Let us first consider the Gaussian model calculations. In the Wilson/Thomson model, since the contribution from small-scale velocity fluctuations is most important, the model can be approximated by its $i=2$ term for upwind propagation:

$$b(r_2,r_3)\simeq\frac{6.3zA_2}{2\sqrt{\pi}}\exp\left(-\frac{r_2^2+r_3^2}{z^2}\right). \tag{80}$$

Although the full Wilson/Thomson model was used in the calculations, the approximation above reproduces the behavior of the full model quite well in this case. The isotropic, vector Gaussian model used in the calculations in Fig. 9 was Eq. (55), with $\sigma^2=A_2$ and $L=z$:

$$b_{\|}(\rho)=\frac{zA_2}{2\sqrt{\pi}}\left(1-\frac{\rho^2}{z^2}\right)\exp\left(-\frac{\rho^2}{z^2}\right). \tag{81}$$

Note that because z is used for the length scale, the Gaussian model actually has been made inhomogeneous.

The figure shows that the CRLB predictions for the two types of Gaussian models are similar. The CRLB for the isotropic model is somewhat larger, though, by a nearly constant factor. This can be explained by a comparison of Eqs. (80) and (81). The coefficient preceding the exponential in the Wilson/Thomson model is larger by 6.3, the ''stretching factor'' for eddy elongation by the wind. As a result of this stretching the Wilson/Thomson model predicts that there will be less loss of coherence. It would be very interesting to look for this effect of turbulent anisotropy in experimental data.

It is also evident that the CRLB for the isotropic Gaussian and Wilson/Thomson models does not change quickly with frequency when the frequency is very low or very high. A transition occurs between the two ''plateaus,'' in the frequency range 40 Hz$\lesssim f\lesssim$400 Hz. The low-frequency plateau

is the frequency region where array performance is limited by noise. In the high-frequency plateau, turbulence has caused the coherence between the array elements to fall nearly to zero, so that further increases in frequency have little effect on array performance.

The same variance and integral length scales were used in the vector von Kármán and Kolmogorov models as in the isotropic Gaussian model. Given the Gaussian length scale, the von Kármán length scale l follows by equating integral length scales in Eqs. (42) and (65). The structure-function parameter in the Kolmogorov model was determined from Eq. (76).

The isotropic Gaussian and von Kármán models are nearly the same for low and moderate frequencies, $f \lesssim 400$ Hz. Only when the array dimensions become smaller than the turbulence length scale ($\sim z$) do the two models start to diverge. The two models do not agree well for small arrays because the von Kármán model has a realistic inertial subrange; the Gaussian model contains essentially no energy at these eddy scales.

The Kolmogorov model converges to the von Kármán model at high frequency (small sensor spacings). The CRLB predictions from the Kolmogorov model are much too high at frequencies less than several hundred Hertz, since that model is reasonable only in the inertial subrange. But even as the frequency is increased above several hundred Hertz, the Kolmogorov model converges to the von Kármán model very slowly. The reason for this slow convergence can be understood mathematically if we retain higher-order terms in the expansion, Eq. (68). We then see that the next term in the expansion for $d(\rho)$ (after the $\rho^{5/3}$ term) is proportional to $\rho^{7/3}$. Hence the ratio of the second to the third term in the expansion decreases only as $\rho^{-2/3}$, and the Kolmogorov model works only marginally well. However, there is also a deeper, physical reason why the Kolmogorov model does not work particularly well for describing the 2-D correlation and structure functions. We see from the integral definition of the 2-D correlation, Eq. (15), that the 2-D correlation is strongly affected by the large, energetic eddies in the direction of propagation. When the Kolmogorov model is used, the effect of these large eddies is neglected. Hence the Kolmogorov model for the 2-D structure function is a small-scale approximation to a quantity that inherently depends on large-scale structure. This observation ties in with the one made above during the comparison of the Wilson/Thomson and isotropic, Gaussian models: that anisotropy, a large-scale aspect of turbulence structure, can have a significant effect on the 2-D correlation.

Although they are not shown here, similar model comparisons were performed for a convective atmosphere ($u_* = 0.5$ m/s, $T_* = -0.3$ K, and $z_i = 1000$ m). The results were nearly identical to Fig. 9. There was a slight decrease in the CRLB as computed from the Wilson and Thomson model, due to the increased presence of large, buoyantly driven eddies.

E. Calculations with intermittency

For intermittent wave scattering calculations, the ''strength'' of turbulence in the inertial subrange is allowed to fluctuate in space and time. We can model this variability by defining structure-function parameters local to the propagation path, $\tilde{C}_N^2$ and $\tilde{C}_u^2$, as discussed in Sec. I D. Only Kolmogorov-type inertial subrange models (Sec. II D) can be adapted to intermittent calculations.

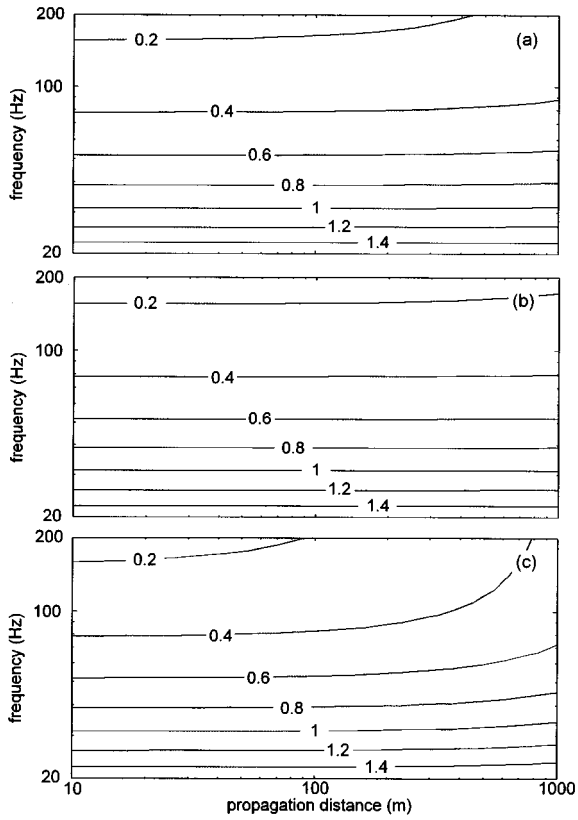

FIG. 10. The CRLB calculations for a five-element uniform line array in weak turbulence ($u_* = 0.1$ m/s). (a) Nonintermittent calculation. (b) Intermittent calculation, lower confidence bound at 5%. (c) Intermittent calculation, upper confidence bound at 95%.

In the following calculations, I consider only the effect of shear-generated (small-scale) velocity fluctuations, since temperature fluctuations are normally less important. As a result, the mean dissipation rate of turbulent kinetic energy is[35]

$$\varepsilon = \frac{u_*^3}{k_v z}, \tag{82}$$

where $k_v \simeq 0.4$ is von Kármán's constant. The mean structure function parameter for velocity fluctuations [from Eq. (29), which applies approximately to the means of ε and C_u^2, as well] is hence

$$C_u^2 \simeq 15 \frac{u_*^2}{c_0^2 z^{2/3}}. \tag{83}$$

First let us consider CRLB for fairly weak turbulence, $u_* = 0.1$ m/s, as shown in Fig. 10. For these calculations, the separation between array elements was 1 m, and $z = 2$ m, $\sigma_n^2 = 0.01$, $M = 5$. The integral length scale used in Eq. (35) was $0.3 z_i$.[36] This length scale is characteristic of the large, boundary-layer size eddies that exist in convective boundary layers. Since the earlier calculations suggested that it was

mostly the small-scale, shear-generated eddies that affected the MCF, we might be tempted at first to use a smaller integral length scale. However, it is the large, convective eddies that produce locally high wind shear, and hence cause locally intense small-scale turbulence. Therefore the intermittency occurs on the scale of the largest eddies.

Part (a) of Fig. 10 is the result when intermittency effects are neglected. For most of the propagation distances and frequencies shown on the plot, the CRLB is nearly independent of the distance, since array performance is affected primarily by sensor noise. At the very highest frequencies and longest propagation distances, however, there is some degradation of array performance; in this region array performance is affected by turbulence.

Parts (b) and (c) of Fig. 10 show the results when intermittency is incorporated into the calculation. The former is the 5% lower confidence bound, whereas the latter is the 95% upper bound [see Eq. (37)]. That is, as a result of intermittency the CRLB fluctuates such that it is bounded by the values shown in the figures 90% of the time. These fluctuations can be substantial, at least for propagation distances longer than several hundred meters and frequencies that are not extremely low. For example, at 80 Hz and 1000 m, array performance is noise limited when the turbulence is ''quiet'' (the lower confidence bound). During an episode of active turbulence (the upper confidence bound), however, the CRLB increases by about 50%.

Calculations for fairly strong turbulence are shown in Fig. 11. Dramatic fluctuations in the array performance are now evident at all but the shortest propagation distances and lowest frequencies. For example, at 80 Hz and 100 m, the CRLB fluctuates between about 0.4 and 0.8 deg. At 80 Hz and 1000 m, the CRLB fluctuates between 0.6 and 2 deg.

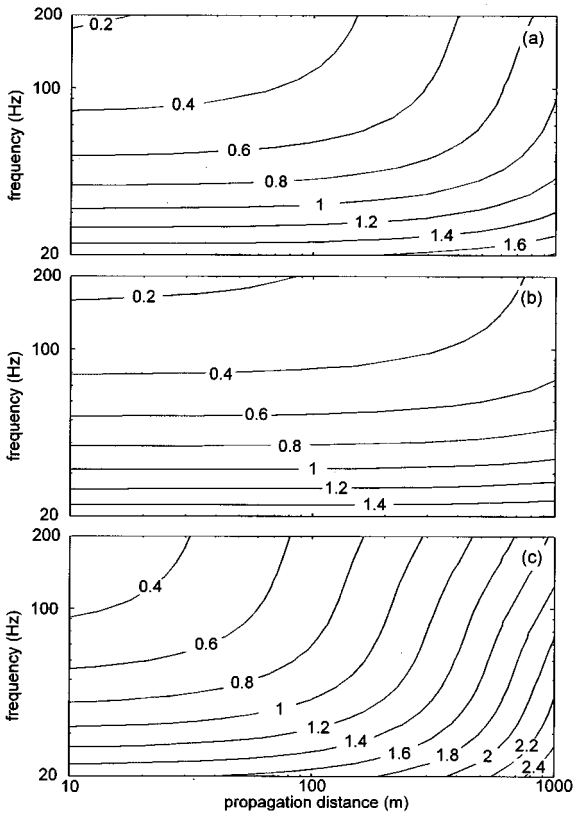

FIG. 11. The CRLB calculations for a five-element uniform line array in strong turbulence ($u_* = 0.5$ m/s). (a) Nonintermittent calculation. (b) Intermittent calculation, lower confidence bound at 5%. (c) Intermittent calculation, upper confidence bound at 95%.

IV. CONCLUSIONS

This paper has provided a theoretical analysis, using various atmospheric turbulence models, of the performance bounds of acoustic arrays used for direction-of-arrival (DOA) estimation. The calculations show that the accuracy of DOA estimates, near to the source and/or at low frequency, is controlled by the ambient noise. As the separation between the source and receiving array, and the source frequency, are increased, array performance degrades as a result of turbulence. The distance and frequency at which the turbulence effect becomes important depends on the ambient noise levels and the strength of the turbulence.

For an unstable, daytime boundary layer, the calculations strongly suggest that small-scale velocity fluctuations, generated by near-ground turbulent shear instabilities, play a much more significant role in degrading the coherence of a propagating acoustic wavefront than either temperature fluctuations or large-scale velocity fluctuations. (Temperature fluctuations would probably play a more significant role in a stable, nocturnal boundary layer, since stable conditions favor the development of sharp temperature gradients.)

The turbulence models considered in this paper were each found to have inherent strengths and limitations. The isotropic Gaussian model is easy to manipulate analytically, but is unrealistic for high Reynolds number turbulence. The isotropic von Kármán model is much more realistic than the Gaussian model, but like the Gaussian model its application to atmospheric turbulence is problematic, because the parameters cannot be chosen to agree well with the known features of atmospheric turbulence. The Kolmogorov model has well-defined parameters and can work reasonably well when inertial subrange turbulence is most important in the scattering. Unfortunately, acoustic wavelengths are often large enough that inertial subrange modeling is unsatisfactory, particularly for the 2-D structure function, since it depends somewhat on large-scale turbulence structure. The Wilson and Thomson (anisotropic Gaussian) model might be reasonable in some applications where energy subrange turbulence is most important.

Some very significant effects of turbulent anisotropy and intermittency on arrays were evident in the model calculations, and it would be worthwhile to look for these in future field studies. The 2-D structure function, used to calculate array coherence, is dependent on large-scale turbulence structure even for small separations between array elements. Hence, it is affected by energy subrange properties of turbulence such as anisotropy. It appears that the 2-D structure function may be increased (and hence coherence improved) in the directions upwind and downwind from a source.

It also appears that intermittency can cause dramatic fluctuations in signal coherence on windy days. There will be some periods, lasting several seconds to a minute, when accurate DOA estimations can be obtained. Then a strong gust

of wind can momentarily cause the accuracy of the DOA estimations (the Cramer–Rao lower bound) to degrade by several hundred percent. Algorithms for tracking acoustic sources should be made robust to such temporary degradations when possible.

[1] B.-G. Song and J. A. Ritcey, ''Angle of arrival estimation of plane waves propagating in random media,'' J. Acoust. Soc. Am. **99**, 1370–1379 (1996).

[2] D. K. Wilson and D. W. Thomson, ''Acoustic propagation through anisotropic, surface-layer turbulence,'' J. Acoust. Soc. Am. **96**, 1080–1095 (1994).

[3] L. L. Scharf, *Statistical Signal Processing: Detection, Estimation, and Time Series Analysis* (Addison–Wesley, Reading, MA, 1991).

[4] R. Dashen, ''Path integrals for waves in random media,'' J. Math. Phys. **20**, 894–920 (1979).

[5] V. I. Tatarskii, *The Effects of the Turbulent Atmosphere on Wave Propagation* (Keter, Jerusalem, 1971).

[6] S. M. Rytov, Y. A. Kravtzov, and V. I. Tatarskii, *Principles of Statistical Radio Physics, Part 4: Wave Propagation through Random Media* (Springer, Berlin, 1989).

[7] V. E. Ostashev, G. Goedecke, F. Gerdes, R. Wandelt, and J. Noble, ''Line-of-sight sound propagation in the turbulent atmosphere with Gaussian correlation functions of temperature and wind velocity fluctuations,'' in *Proceedings of the Seventh International Symposium on Long Range Sound Propagation* (Ecole Centrale de Lyon, Lyon, France, 1996), pp. 349–357.

[8] Instead of Eq. (12), the formula for the MCF is often given as (Ref. 6) $\Gamma(\rho)=\exp\{-\pi^2k^2X\int_0^\infty[1-J_0(\kappa_\perp\rho)]\Phi(0,\kappa_2,\kappa_3)\kappa_\perp\, d\kappa_\perp\}$, where J_0 is the Bessel function of the first kind, and $\kappa_\perp^2=\kappa_2^2+\kappa_3^2$. Using the identity $J_0(z)=(1/2\pi)\int_0^{2\pi}\exp(iz\cos\theta)d\theta$, and the definition for the 2-D correlation function, Eq. (18), one can show Rytov *et al.*'s formula to be equivalent to Eq. (12).

[9] Previous authors have called the two-dimensional correlation function the *transverse* correlation function. This terminology can lead to confusion when discussing correlations of vector fields, since in that context a transverse correlation is one whose displacement is perpendicular to the velocity components. I prefer *two-dimensional*, because the definition involves setting one of the wave numbers in $\Phi(\kappa_1,\kappa_2,\kappa_3)$ to zero and then taking the inverse Fourier transform in the remaining two directions. Thus it is the Fourier counterpart of the two-dimensional spectrum, which is defined by setting one of the displacements in the correlation function $R(r_1,r_2,r_3)$ to zero, and then taking the forward Fourier transform in the remaining two directions. Note that the 2-D correlation function in this paper equals $\hat{\rho}/2\pi$ in Ref. 4.

[10] G. S. K. Wong and T. F. W. Embleton, ''Variation of specific heats and of specific heat ratio in air with humidity,'' J. Acoust. Soc. Am. **76**, 555–559 (1984). Equation (13) was derived using $c=(\gamma RT_0/M)^{1/2}$, with $M=(29+18h)/(1+h)$ [from Wong and Embleton's Eq. (2)], and $\gamma=1.4-0.086h$ [Wong and Embleton's Eq. (7), evaluated at 20 °C], where h is the molar concentration of water vapor. For small h, one finds $c\simeq 20.03\sqrt{T_0}(1+0.16h)$. Equation (13) then follows using $h_s\simeq 0.622h$. [See, for example, ANSI S1.26-1995, ''American National Standard Method for the Calculation of the Absorption of Sound by the Atmosphere'' (Acoustical Society of America, New York, 1995).]

[11] V. E. Ostashev, ''Sound propagation and scattering in media with random inhomogeneities of sound speed, density and medium velocity,'' Waves Random Media **4**, 403–428 (1994).

[12] A. N. Kolmogorov, ''A refinement of previous hypotheses concerning the local structure of turbulence in a viscous incompressible fluid at high Reynolds number,'' J. Fluid Mech. **13**, 82–85 (1962).

[13] A. M. Obukhov, ''Some specific features of atmospheric turbulence,'' J. Fluid Mech. **273**, 77–81 (1962).

[14] It is worth pointing out that Eq. (28) involves a line average of the structure-function parameter, whereas Kolmogorov's (Ref. 12) theory of intermittent turbulence explicitly deals only with volume averages. This issue did not arise in a previous paper I coauthored (Ref. 16), since the scattering treatment in that paper involved volume averages of structure functions. Fortunately there is good reason to think that Kolmogorov's log-normal model also applies to line averages. The derivation presented by Gurvich and Yaglom (Ref. 20) in favor of the log-normal law applies to line averages just as well as volume averages. In fact, experimental verification of the log-normal model has generally relied on line averages.

[15] R. A. Antonia, E. J. Hopfinger, Y. Gagne, and F. Anselmet, ''Temperature structure functions in turbulent shear flows,'' Phys. Rev. A **30**, 2704–2707 (1984).

[16] D. K. Wilson, J. C. Wyngaard, and D. I. Havelock, ''The effect of turbulent intermittency on scattering into an acoustic shadow zone,'' J. Acoust. Soc. Am. **99**, 3393–3340 (1996).

[17] V. I. Tatarskii and V. U. Zavorotnyi, ''Wave propagation in random media with fluctuating turbulent parameters,'' J. Opt. Soc. Am. A **2**, 2069–2076 (1985).

[18] C. W. Van Atta, ''Influence of fluctuations in local dissipation rates on turbulent scalar characteristics in the inertial subrange,'' Phys. Fluids **14**, 1803–1804 (1971).

[19] D. K. Wilson, ''Scattering of acoustic waves by intermittent temperature and velocity fluctuations,'' J. Acoust. Soc. Am. **101**, 2980–2982 (1997).

[20] A. S. Gurvich and A. M. Yaglom, ''Breakdown of eddies and probability distributions for small-scale turbulence,'' Phys. Fluids , S59–S65 (1967).

[21] F. Anselmet, Y. Gagne, E. Hopfinger, and R. A. Antonia, ''High-order velocity structure functions in turbulent shear flows,'' J. Fluid Mech. **140**, 63–89 (1984).

[22] K. R. Sreenivasan and P. Kailasnath, ''An update on the intermittency exponent in turbulence,'' Phys. Fluids A **5**, 512–514 (1993).

[23] L.-P. Wang, S. Chen, J. G. Brasseur, and J. C. Wyngaard, ''Examination of hypotheses in the Kolmogorov refined turbulence theory through high-resolution simulations. Part 1. Velocity field,'' J. Fluid Mech. **309**, 113–156 (1996).

[24] V. P. Kukharets, ''Investigation of variability of the structure characteristic of temperature in the atmospheric boundary layer,'' Izv. Atmos. Ocean. Phys. **24**, 578–582 (1988) (English translation).

[25] J. G. Brasseur, 1996, personal communication.

[26] L. Mahrt, ''Intermittency of atmospheric turbulence,'' J. Atmos. Sci. **46**, 79–95 (1989).

[27] H. A. Panofsky and J. A. Dutton, *Atmospheric Turbulence: Models and Methods for Engineering Applications* (Wiley, New York, 1984).

[28] D. Juvé, P. Blanc-Benon, and P. Chevret, ''Sound propagation through a turbulent atmosphere: influence of the turbulence model,'' in *Proceedings of the Sixth International Symposium on Long Range Sound Propagation*, edited by D. I. Havelock and M. R. Stinson (NRC Canada, Ottawa, Canada, 1994), pp. 270–282.

[29] V. E. Ostashev, G. Goedecke, B. Brähler, V. Mellert, and H. Auvermann, ''Coherence functions of plane and spherical sound waves in the turbulent atmosphere with von Karman spectra of temperature and wind velocity fluctuations,'' in *Proceedings of the Seventh International Symposium on Long Range Sound Propagation* (Ecole Centrale de Lyon, Lyon, France, 1996), pp. 349–357.

[30] G. K. Batchelor, *The Theory of Homogeneous Turbulence* (Cambridge U.P., Cambridge, 1953).

[31] In Ref. 2, primes were used to indicate the propagation coordinates. The unprimed coordinate system was the meteorological coordinates. I have used the opposite convention in this paper, in order to be consistent with the presentation of the isotropic models.

[32] A. N. Kolmogorov, ''The local structure of turbulence in incompressible viscous fluid for very large Reynolds numbers,'' C. R. Acad. Sci. URSS **30**, 301–305 (1941).

[33] I. S. Gradshteyn and I. M. Ryzhik, *Table of Integrals, Series, and Products* (Academic, San Diego, 1994).

[34] Only a functional equivalence is implied here. The variance and length scale parameters in $E_N(\kappa)$ and $E_u(\kappa)$ can have different values and units.

[35] R. B. Stull, *An Introduction to Boundary Layer Meteorology* (Kluwer, Dordrecht, 1988).

[36] D. H. Lenschow and B. B. Stankov, ''Length scales in the convective boundary layer,'' J. Atmos. Sci. **43**, 1198–1209 (1986).

The unidentified object problem in a shallow ocean

R. P. Gilbert
Department of Mathematical Sciences, University of Delaware, Newark, Delaware 19716

T. Scotti and A. Wirgin
Laboratoire de Mecanique et d'Acoustique, UPR 7051 du CNRS, 31 Chemin Joseph Aiguier, 13402 Marseille Cedex 20, France

Y. S. Xu
Department of Mathematics, University of Tennessee, Chattanooga, Tennessee 37403

(Received 17 February 1997; accepted for publication 15 December 1997)

This work addresses the inverse problem of the identification of a passive three-dimensional impenetrable object in a shallow-water environment. The latter is assumed to have flat perfectly reflecting (sound-soft top and sound-hard bottom) boundaries and therefore acts as a guide for acoustic waves. These waves are employed to interrogate the object and the scattered acoustic wavefield is measured on the surface of a (virtual) vertically oriented cylinder (of finite or infinite radius, corresponding to near- or far-field measurements) fully enclosing the object. The direct scattering problem is resolved in approximate manner by employing, in a local manner, the known separated-variable solution for a scattering by a vertically oriented cylinder in a perfect waveguide. The inverse problem is resolved in the same manner (i.e., with the same approximate field ansatz) by least-squares matching of theoretical fields (for trial objects) to the measured field. Examples are given of successful shape reconstructions for two types of immersed objects. This manner of solving approximately both the forward and inverse problems is generalized to the case of a body of shallow water with an elastic seabed. [S0001-4966(98)05303-X]

PACS numbers: 43.30.Gv [DLB]

INTRODUCTION

Remote localization and identification of *sources* in shallow water is an inverse problem of strategic interest. It has been largely addressed over the past 20 years,[1–4] and can now be solved by a variety of available tools involving matched field processing, mode filtering, beamforming of modal amplitudes, boundary, or domain integral field representations (for pulsating sources of nonzero support and/or sources in the presence of unknown objects), etc.[4–8]

The inverse (domain) problem of the localization and identification of a *passive object* in the same body of water also has important practical applications (identification of seamounts, mineral deposits, submarines, submerged wreckages, and navigational obstacles, etc.), and has received fairly considerable attention.[9–25] Only recently have attempts been made to deviate from the usual (generally nonautomatized) signature-recognition strategy[25] to that of the achievement of full-fledged (automatized) parameter estimation (the parameters being those associated with the location and shape of the object, assuming the sources and underwater environment to be known).[9–11,17,18,21,24,26–29]

Both of the previously cited problems, closely related to their counterparts in direct and inverse electromagnetic wave propagation problems in waveguides,[30,31] are fundamentally ill-posed, but the reconstruction of sources (of known support) is a linear problem whereas the identification of a passive object is a nonlinear problem associated with complicated forward scattering phenomena. The latter have been examined by a great variety of tools involving ray models, coupled modes, normal mode expansions, T-matrix methods, Herglotz potentials, single scattering approximations, slender body approximations, complete family of (generally nonorthogonal) functions representations (including the Rayleigh partial wave and equivalent source expansions), boundary integral representations appealing to various forms of Green's functions (for a guide with rigid, elastic, poroelastic bottom), etc.[5,21,26,32–53] The complexity of propagation is greatly increased by the elastic or poroelastic nature of the seabed and it is only recently that these factors have been taken rigorously into account for the purpose of solving inverse problems, namely by the construction of the guide Green's functions.[13,37,38,40,54] (Other important, but more mathematical issues, concerning the uniqueness of solutions to the direct scattering problem in the guide and the solvability of the inverse problem of an obstacle in a shallow water guide, have also been treated.[14,15,16,21,22,54]

Herein we reconsider the inverse domain problem of the identification of an object in shallow water. The spirit of our contribution is similar to that of Refs. 17 and 21, which both treat a 3-D object in a water-filled guide with perfectly reflecting boundaries, and[29] which treats a 2-D (cylindrical) object in an equally perfect guide. However, these studies are rather computer intensive in that no attempt is made therein to obtain approximations to the solution of the associated direct problem during the inversion. A reconstruction process that takes hours (if not days) of computation is not particularly appropriate for identifying a moving 3-D object (e.g., submarine). To be able to carry out such a task, we employ an *approximation* of the solution of the direct problem which is a generalization of the ICBA (intersecting canonical body approximation) used successfully in previous

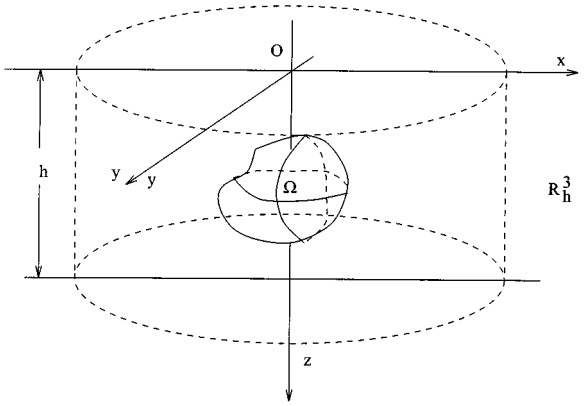

FIG. 1. An unknown object in the water column R_h^3.

studies of direct and inverse problems involving 2-and 3-D bodies in *free space*.[55–59] Whereas in our previous studies on 3-D bodies we employed canonical solutions of the problem of scattering by a *sphere in free space*, we found it more appropriate herein to employ canonical solutions for a *circular cylinder in a waveguide* in conjunction with a scheme that turns out to be similar to the DCA (deformed cylinder approximation) of Stanton.[60] Another interesting feature of the proposed method is that it lends itself to a rather straightforward generalization for treating the case of an elastic (penetrable) seabed.

I. IMPENETRABLE BODY IN A SHALLOW OCEAN

The problem is to determine the shape of a submerged acoustically soft object in a finite depth ocean. To illustrate our method we limit the discussion to a uniform ocean with a totally reflecting bottom. The more realistic cases can be considered by using our method for constructing Green's functions for nonhomogeneous oceans with elastic and poroelastic seabeds.[32,33,38,45] In addition, it is not difficult to generalize the analysis to the cases of acoustically hard or penetrable objects.

We assume the ocean has depth h, and denote the region occupied by the ocean as $R_h^3 = R^2 \times [o,h]$. An object embedded in the ocean is denoted by Ω (see Fig. 1). The differential equation describing the acoustic pressure u is

$$(\Delta + k^2)u = 0 \quad \text{in} \quad R_h^3 \backslash \overline{\Omega}, \tag{1}$$

it being understood that the $\exp(-i\omega t)$ temporal dependence is implicit, with ω the angular frequency and t the time variable. The total field u may be decomposed into an incident wave u^i and a scattered wave u^s as $u = u^i + u^s$. The boundary conditions on the seabed, sea surface and object (occupying the domain Ω) are

$$\left.\frac{\partial u}{\partial z}\right|_{z=h} = 0, \quad u|_{z=0} = 0, \quad u|_{\partial\Omega} = 0. \tag{2}$$

In addition, the scattered field satisfies an appropriate radiation condition for $r \to \infty$, with r the radial coordinate in the cylindrical coordinate system r, θ, z. We make the following basic assumptions:

(1) The measured field is known in both phase and amplitude at a set of points lying on a cylinder of radius r_b enclosing the object.
(2) The scattering surface is acoustically soft (Dirichlet boundary condition).
(3) The space $R_h^3 \backslash \overline{\Omega}$ is occupied by a homogeneous fluid in which the speed of sound is $c = \omega/k$.
(4) The incident waves are normal mode waves, i.e., they may be expanded as

$$u^i(r,\theta,z) = \sum_{n=1}^{N} \phi_n(z_0)\phi_n(z) e^{ika_n \boldsymbol{\alpha}\cdot\mathbf{r}}, \tag{3}$$

where

$$N = \left[\frac{1}{2} + \frac{kh}{\pi}\right], \quad \text{and}$$

$[\cdot]$ denotes the integer part of the term,

$$\phi_n(z) = \sqrt{\frac{2}{h}} \sin\left(\frac{(2n-1)\pi z}{2h}\right), \quad n = 1,2,\ldots .$$

$$a_n = \sqrt{1 - \frac{(n-\frac{1}{2})^2 \pi^2}{k^2 h^2}},$$

z_0 is a fixed number, $0 < z_0 < h$,

$k =$ wave number,

$$\boldsymbol{\alpha} = (\alpha_1, \alpha_2), \quad |\boldsymbol{\alpha}| = 1, \quad \boldsymbol{\alpha} = (\cos\theta_0 \ \sin\theta_0),$$

$$\mathbf{r} = (x_1, x_2), \quad |\mathbf{r}| = r, \quad \mathbf{r} = r(\cos\theta, \sin\theta).$$

[Note that the definition of N signifies that we are restricting ourselves to propagative (i.e., nonevanescent) incident modes.]

(5) The scattering obstacle is described by the set

$$\Omega = \{(r,\theta,z) | 0 \leqslant r < \rho(\theta,z), \ 0 \leqslant \theta < 2\pi, \ 0 < z < h\}.$$

II. FIELD REPRESENTATION

Regardless of the shape of the scatterer, outside any cylinder D_d enclosing the body Ω the total wave field can be represented in $R_h^3 \backslash D_d$, by

$$u(r,\theta,z) = u^i(r,\theta,z) + \sum_{n=1}^{\infty}\sum_{m=0}^{\infty} \phi_n(z) H_m^{(1)}(ka_n r) \times [A_{nm}\cos(m\theta) + B_{nm}\sin(m\theta)]. \tag{4}$$

In view of Ref. 61 (p. 1371) the identity

$$e^{ikr\cos\phi} = \sum_{m=0}^{\infty} \epsilon_m i^m \cos(m\phi) J_m(kr), \tag{5}$$

we may write

$$e^{ika_n \boldsymbol{\alpha}\cdot\mathbf{r}} = e^{ika_n r\cos(\theta-\theta_0)} = \sum_{m=0}^{\infty} \epsilon_m i^m \cos(m(\theta-\theta_0)) J_m(ka_n r).$$

Hence, this allows us the following representation for the ''plane'' incident wave

$$u^i(r,\theta,z)=\sum_{n=1}^{N}\sum_{m=0}^{\infty}\phi_n(z_0)\phi_n(z)\epsilon_m i^m \times\cos(m(\theta-\theta_0))J_m(ka_n r), \tag{6}$$

where J_m, $H_m^{(1)}$ are the mth order Bessel and Hankel functions of the first kind, respectively,

$$\epsilon_m=1 \quad \text{for } m=0, \quad \epsilon_m=2 \quad \text{for } m>0.$$

III. DETERMINATION OF THE RADIUS OF AN UNKNOWN CIRCULAR CYLINDRICAL OBJECT

A. Forward problem

Suppose we consider a circular cylindrical object coaxial with the z-axis, namely,

$$D_a=\{(r,\theta,z)|r=a,\ 0\leqslant\theta<2\pi,\ 0\leqslant z\leqslant h\}.$$

Then if we have an acoustically soft-boundary cylinder D_a, the Dirichlet condition $u(a,\theta,z)=0$ for $0\leqslant\theta<2\pi$, $0\leqslant z\leqslant h$ holds. Using Eqs. (5) and (6), and the orthogonality of the functions $\{\phi_n(z)\cos m\theta,\ \phi_n(z)\sin m\theta\}$, one finds

$$A_{nm}=\begin{cases}-\epsilon_m i^m\phi_n(z_0)\cos(m\theta_0)\dfrac{J_m(ka_n a)}{H_m^{(1)}(ka_n a)} & \text{for } 1\leqslant n\leqslant N\\ 0, \quad \text{for } n>N,\end{cases}$$

$$B_{nm}=\begin{cases}-\epsilon_m i^m\phi_n(z_0)\sin(m\theta_0)\dfrac{J_m(ka_n a)}{H_m^{(1)}(ka_n a)} & \text{for } 1\leqslant n\leqslant N\\ 0, \quad \text{for } n>N.\end{cases}$$

Thus the total pressure field may be represented as

$$u(r,\theta,z)=u^i(r,a,z)+\sum_{n=1}^{N}\sum_{m=0}^{\infty}c_{nm}(a)\cos[m(\theta-\theta_0)]\phi_n(z)H_m^{(1)}(ka_n r), \tag{7}$$

where

$$c_{nm}(a)=-\epsilon_m i^m\phi_n(z_0)\frac{J_m(ka_n a)}{H_m^{(1)}(ka_n a)}. \tag{8}$$

B. Inverse problem

Assume the acoustic field is measured at the points (r_b,θ^q,z^p) where the indices range over $q\in\{1,2,...,Q\}$ and $p\in\{1,2,...,P\}$. The field at these points is given by $u^*(r_b,\theta^q,z^p)$ where $r_b>a$ is a constant.

The inverse problem is to determine $\eta^{qp}=\eta(\theta^q,z^p)$ for $q\in\{1,...,Q\}$ and $p\in\{1,...,P\}$ such that (match of the data to its mathematical representation)

$$u^*(r_b,\theta^q,z^p)-\left[u^i(r_b,\theta^q,z^p)+\sum_{n=1}^{N}\sum_{m=0}^{M}c_{nm}(\eta^{qp})\times\cos\ m(\theta^q-\theta_0)\phi_n(z^p)H_m^{(1)}(ka_n r_b)\right]\simeq 0. \tag{9}$$

Note that $\eta(\theta^q,z^p)$ is not identically equal to the radius a because we have truncated the m-series for numerical purposes. For each (p,q), (9) yields at least one solution for the ''radius'' of the unknown cylinder.

IV. DETERMINATION OF THE SHAPE OF A THREE-DIMENSIONAL BODY

The above idea can be extended to three-dimensional bodies which may be represented by a shape function $\rho(\theta,z)$ as

$$D=\{(r,\theta,z)|r=\rho(\theta,z),\ 0\leqslant\theta<2\pi,\ 0\leqslant z\leqslant h\},$$

where $\rho(\theta,z)\geqslant 0$. As before we first need to represent the solution to the direct problem.

Remark. Ω is an open set whose topological boundary is a subset of D. D may contain a number of line segments which are not boundary points. Using the method in Scotti and Wirgin[56,57] we extend this to the truncated cylindrical geometry. The analogy between the present problem and that of the circular cylinder suggests the following approximation of the field:

$$u(r,\theta^q,z^p)\simeq u^i(r,\theta^q,z^p)+\sum_{n=1}^{N}\sum_{m=0}^{M}c_{nm}(\rho(\theta^q,z^p)), \quad \cos m(\theta^q-\theta_0)\phi_n(z^p)H_m^{(1)}(ka_n r). \tag{10}$$

The first term in this expression represents the measured field whereas the second term is the total field representation on a cylinder of radius r. (Actually Scotti and Wirgin[57,58] use a sphere rather than a cylinder and they are working in R^3 rather than in a waveguide.) Due to Eq. (9), the coefficients $c_{nm}(\rho(\theta^q,z^p))$ are given by

$$c_{nm}(\rho(\theta^q,z^p))=-\epsilon_m i^m\phi_n(z_0)\frac{J_m(ka_n\rho(\theta^q,z^p))}{H_m^{(1)}(ka_n\rho(\theta^q,z^p))}. \tag{11}$$

Since $J_n(\xi)$ is bounded as $\xi\to 0$, and $H_m^{(1)}(\xi)\to\infty$ as $\xi\to 0$ we have

$$c_{nm}(\rho)\to 0 \ \text{ as } \rho\to 0 \ \text{ for all } n,m. \tag{12}$$

Remark. Equation (10) implies that

(1) If $u(r,\theta^q,z^p)\approx u^i(r,\theta^q,z^p)$, then it follows that $c_{nm}=0$ and $\rho(\theta^q,z^p)=0$.
(2) This method is reasonable only if from $\rho(\theta^q,z^p)=0$ it follows that $u(r,\theta^q,z^p)\approx u^i(r,\theta^q,z^p)$. An example of such a region where this happens is a cylinder-like region where $\rho(\theta^q,z^p)\geqslant a>0$ for some a.

We formulate the inverse problem as determining the discretized shape function $\rho^{qp}=\rho(\theta^q,z^p)$ on the index set $q\in\{1,...,Q\}$ and $p\in\{1,...,P\}$ such that

$$u^*(r_b,\theta^q,z^p)-\left[u^i(r_b,\theta^q,z^p)+\sum_{n=1}^{N}\sum_{m=0}^{M}c_{nm}(\rho^{qp})\cdot\cos\ m(\theta^q-\theta_0)\cdot\phi_n(z^p)H_m^{(1)}(ka_n r_b)\right]\simeq 0. \tag{13}$$

Here $u^*(r_b,\theta^q,z^q)$ are given data and the sum represents the total field expression for a cylinder with radius ρ^{qp}.

V. CASE OF THE ELASTIC SEABED

For the shallow ocean with an elastic seabed, in addition to the Helmholtz equation holding in the ocean

$$(\Delta + k^2)u = 0 \quad \text{in} \quad R_k^3 \backslash \overline{\Omega},$$

we have to add the acoustic equations for the elastic seabed. These are

$$\begin{aligned} &\partial_r \sigma_{rr} + \partial_z \sigma_{rz} + \frac{1}{r}(\sigma_{rr} - \sigma_{\theta\theta}) + \rho\omega u_r = 0 \\ &\partial_r \sigma_{rz} + \partial_z \sigma_{zz} + \frac{1}{r}\sigma_{rz} + \rho\omega^2 u_z = 0. \end{aligned} \tag{14}$$

Replacing the stresses σ_{rr}, σ_{zz}, and shear σ_{rz} by Hooke's law for an isotropic material.

$$\begin{aligned} \sigma_{rr} &= \lambda e + 2\mu \partial_r u_r \\ \sigma_{\theta\theta} &= \lambda e + \frac{2\mu}{r} u_r \\ \sigma_{rz} &= \mu(\partial_z u_r + \partial_r u_z), \end{aligned} \tag{15}$$

we obtain the Navier displacement equations.

Actually these equations hold for the entire ocean-seabed system if we set $\mu = 0$ in the ocean. The constitutive equation for the ocean becomes, once we recognize $\sigma_{rr} = \sigma_{\theta\theta} = \sigma_{zz} := p$,

$$p = \lambda e,$$

The boundary, transition conditions are given by

$$\begin{aligned} &p(r,0) = 0, \\ &u_z(r,h^-) = u_z(r,h^+), \\ &\sigma_{zz}(r,h^+) = p(r,h^-), \\ &\sigma_{rz}(h^+) = 0, \\ &u_z(r,b^-) = \sigma_{rz}(r,b^-) = 0. \end{aligned} \tag{16}$$

The last two conditions represent the seabed lying over a rigid, smooth, formation. The method we outline below carries over for different conditions at $z = b^-$, such as the condition for complete reflection at a very rigid surface

$$u_z(r,b^-) = \partial_z \sigma_{zz}(r,b^-) = 0.$$

If we seek seabed solutions in the separated form

$$u_r = \alpha(z) H_1(cr), \quad u_z = \beta(z) H_0(cr), \tag{17}$$

then we obtain a system of ordinary differential equations,

$$\begin{aligned} &(\mu\alpha')' + [\rho\omega^2 - (\lambda + 2\mu)c^2]\alpha - c\mu'\beta - c(\lambda + \mu)\beta' = 0, \\ &((\lambda + 2\mu)\beta')' + [\rho\omega^2 - \mu c^2]\beta + c\lambda'\alpha + c(\lambda + \mu)\alpha' = 0. \end{aligned} \tag{18}$$

In his Ph.D. thesis, Lin[45] provides an inner-product for the ocean-seabed system. (In Refs. 38 and 54 an inner product which depended on the eigenvalue was obtained. Lin managed to remove the eigenvalue from this expression, which makes the inner product useful in the present context.) In terms of the vector functions $\Phi := \langle \phi, \alpha, \beta \rangle$, $F := \langle f, a, b \rangle$

$$(\Phi, F) := \int_0^h \phi \overline{f} + \omega^2 \rho_0 \int_h^b \mu\beta \overline{b} + \omega\rho_0 \int_h^b (\mu\alpha' \overline{a'} - \rho_s \omega^2 \alpha \overline{a}). \tag{19}$$

The functions ϕ, f are defined in the ocean $[o,h]$; whereas, α, a, β, b are defined in the seabed $[h,b]$. In order to find ϕ one must also find α, β. How to do this is outlined in Refs. 38, 45, and 54. The model eigenfunctions we designate as

$$\Phi_n := \langle \phi_n, \alpha_n, \beta_n \rangle.$$

If $n \neq m (\Phi_n, \Phi_m) = 0$; except for a countable number of frequencies ω we have shown $(\Phi_m, \Phi_m) = \|\Phi_m\| \neq 0$. In terms of this inner product we can express the Green's function due to a source at z_0 $(0 < z_0 < h)$ for the ocean-seabed system as

$$G(\tau, z, z_0) = \frac{i}{4} \sum_{j=0}^{\infty} \frac{1}{(\Phi_n, \Phi_n)} \phi_n(z) \phi_n(z_0) H_0^{(1)}(\sqrt{c_n} r).$$

We can now proceed to develop the procedure for the unknown target problem for the case of the elastic seabed.

If we choose our incoming wave as before

$$\begin{aligned} u^i(r, \theta, z; \boldsymbol{\alpha}) &= \sum_{n=0}^{N} \frac{\phi_n(z)\phi_n(z_0)}{(\Phi_n, \Phi_n)} e^{ika_n \boldsymbol{\alpha} \cdot \mathbf{r}} \\ &= \sum_{n=1}^{N} \sum_{m=0}^{\infty} \frac{\phi_n(z)\phi_n(z_0)}{(\Phi_n, \Phi_n)} \epsilon_m i^m \\ &\quad \times \cos(m[\theta - \theta_0]) J_m(ka_n r). \end{aligned} \tag{20}$$

Then we may still write the solution in the water column as

$$\begin{aligned} u(r, \theta, z) = u^i(r, \theta, z) + \sum_{n=1}^{\infty} \sum_{m=0}^{\infty} \phi_n(z) H_m^{(1)}(ka_n r) \\ \times [A_{nm} \cos(m\theta) + B_{nm} \sin(m\theta)]. \end{aligned}$$

Then we clearly obtain the same formula for the coefficients A_{nm}, B_{nm} or for that matter

$$c_{nm}(a) = -\frac{\epsilon_m i^m \phi_n(z_0)}{(\Phi_n, \Phi_n)} \frac{J_m(ka_n\theta)}{H_m^{(1)}(ka_n a)},$$

except that here the ϕ_n are the first term of the triplet $\Phi_n := \langle \phi_n, \alpha_n, \beta_n \rangle$. The method works formally for the elastic seabed. We believe an inner product may be found for the poroelastic case too, but we have not been successful in obtaining it.

In the next section we consider some numerical experiments for the case of a totally reflective seabed. We shall present numerical experiments for the case of inhomogeneous oceans over elastic seabeds in another paper.

VI. SOME NUMERICAL EXPERIMENTS

In this section we present the results of some numerical experiments for two types of objects in a guide with totally reflecting seabed and the following parameters: the ocean depth $h = 10$, the wave number $k = 5$, (corresponding to the number of propagating modes $N = 16$). The scattered field is detected at a cylindrical area with radius $r_b = 2$.

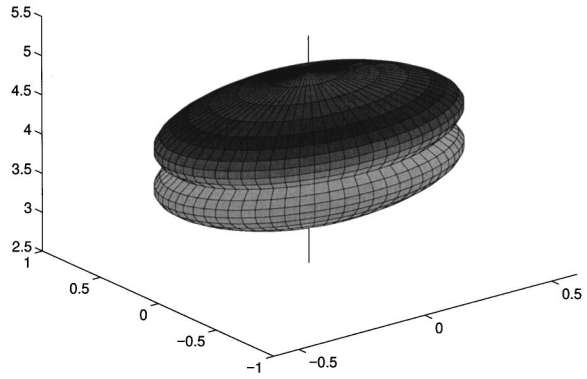

FIG. 2. Example 1: Original.

For each object the computation proceeded in two steps. The first step concerned numerical simulations of ''measured'' data on the measurement cylinder of radius r_b. This was done, for each incident wave and the required set of indices p,q, via Eqs. (10) and (11) wherein the truncation was taken to be $M=30$ to insure a high accuracy of the measured field. The second step consisted in solving Eq. (13) (wherein the truncation was taken to be $M=10$ to reduce computational cost, and to avoid the *inverse crime*) in a least-squares sense for each $\eta(\theta^q,z^p)$ by employing ''measured'' data for five incident waves with $(\theta_0,z_0)=[(25+j)\pi/20,(5+3j)/10]$, $j=1,2,3,4,5$. This was done with the MATLAB minimization function leastsq using, for each (p,q) the initial guess $\eta(\theta^q,z^p)=1$. All other computations were done using the Matlab language and routines.

In Figs. 2–8 we present graphs of two numerical experiments.

A. Example 1: (Figs. 2–5)

The original object is

$$\mathcal{D}:=\{(r,\theta,z)\,|\,r=\rho(\theta,z),\ 0\leqslant\theta<2\pi,\ 0<z<10\},$$

where

$$\rho(\theta,z):=\begin{cases}0 & \text{if } 0<z<3\\ |(z-3)(z-4.5)| & \text{if } 3\leqslant z\leqslant 4\\ |(z-3.5)(z-5)| & \text{if } 4\leqslant z\leqslant 5\\ 0 & \text{if } 5<z<10.\end{cases}$$

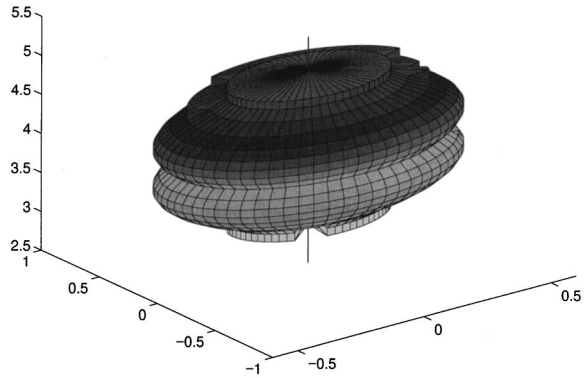

FIG. 3. Example 1: Reconstruction.

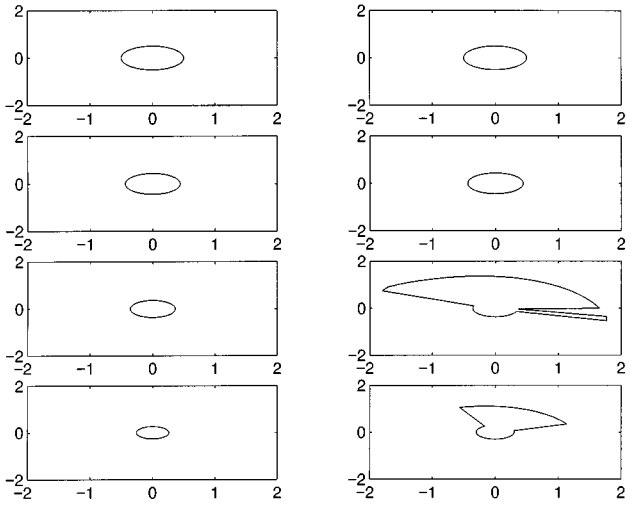

FIG. 4. Example 1: These are z sections of the object at $z=4.5$, 4.6, 4.7, and 4.8. On the left are the original z-sections and on the right the reconstructed ones.

In the example we chose $P=100$, $Q=64$. The numerical results are given in Figs. 2–5. Figure 2 is the original object, and the reconstruction is given in Fig. 3. Figures 4 and 5 show z slices of the original body (left column) and its reconstructed image (right column). In Fig. 4, the values of z are (from top to bottom) 4.5, 4.6, 4.7, and 4.8. Figure 5 is a modification of Fig. 4 by a post-treatment, i.e., we cut off wings and spikes based on the assumption that the object has no such sharp prominences.

B. Example 2: (Figs. 6–8)

The original object is

$$\rho(\theta,z):=\left(0.2+\sin\frac{3\pi z}{h}\right)^2(1-0.5\cos(3\theta)),$$

$$0<z<10,\ 0\leqslant\theta<2\pi.$$

Here we chose $P=40$, $Q=32$.

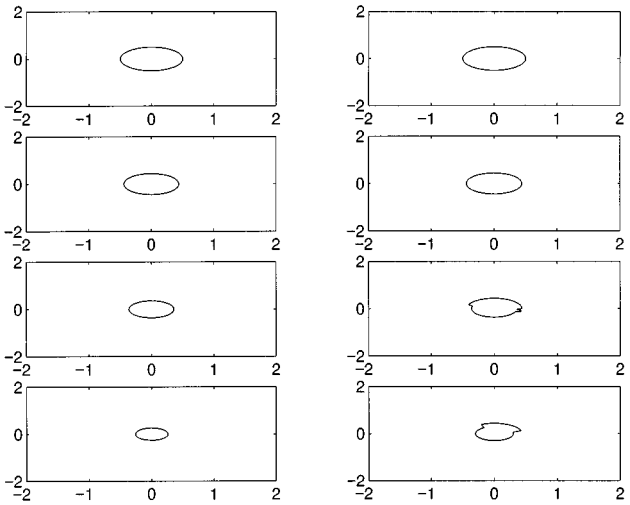

FIG. 5. Example 1: These are z sections of the object at $z=4.5$, 4.6, 4.7, and 4.8. On the left are the original z-sections and on the right the post-processed, reconstructed ones.

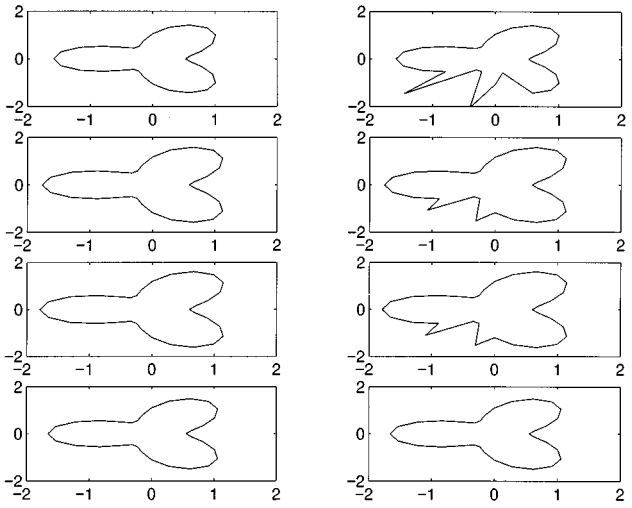

FIG. 6. Example 2: These are z sections of the object at $z=4.25$, 4.5, 4.75, 5.0. On the left are the original z-sections and on the right the reconstructed ones.

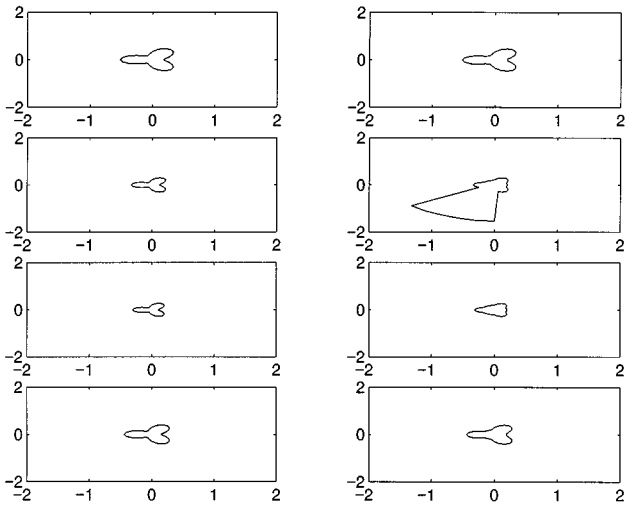

FIG. 8. Example 2: These are z sections of the object. On the left are the original z-sections at $z=6.25$, 6.5, 6.75, 7.0, and on the right the reconstructed ones.

The numerical results are given in Figs. 6–8, where the pictures on the left are the z-slices of the original body, and those on the right are the z slices of the reconstructed image. In Fig. 6, the values of z are (from top to bottom) 4.25, 4.5, 4.75, 5.0. In Fig. 8, the values of z are (from top to bottom) 6.25, 6.5, 6.75, 7.0.

VII. DISCUSSION OF RESULTS AND CONCLUSIONS

It is obvious, from the choice of parameters, that we have not addressed herein the specific problem of the localization of the object. As a matter of fact, we assumed that the z axis cut through the object (and that the latter was starlike in each z slice) so that the only locational information to be recovered concerned the position (depth) of the object along the z axis. Actually, the presented analysis enables one to recover position parameters in the x-y plane as well under the aforementioned hypotheses.[55,56] If, on the other hand, the z axis does not cut through the object (and/or the latter is not starlike in each z slice), then the presented analysis is not sufficient to reconstruct and locate the object. However, it is not difficult to adapt the analysis to treat these situations; the main changes are that the computational burden is increased (while remaining reasonable).

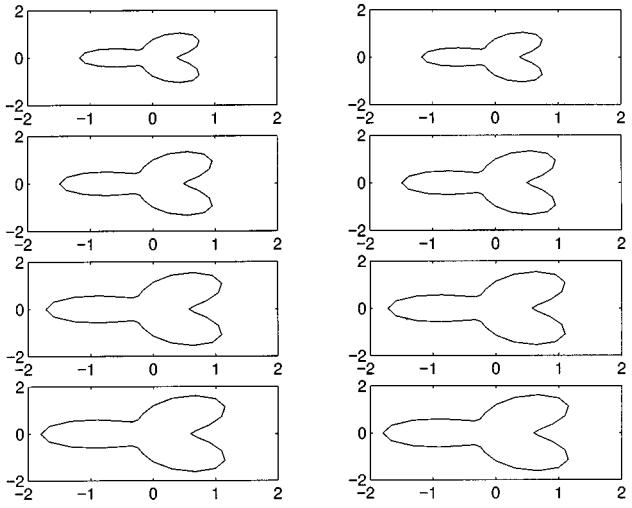

FIG. 7. Example 2: These are z sections of the object at $z=4.25$, 4.5, 4.75, 5.0. On the left are the original z-sections and on the right the post-processed, reconstructed ones.

As concerns the issue of computations, it should be stressed that the presented results *for 3-D bodies* were obtained in a matter of tens of seconds on a personal computer with a Pentium processor. This should be compared with the hours of calculation and large computational power usually required for solving direct as well as inverse scattering problems for *3-D (and even 2-D) bodies* when no approximation is made of the scattered field.

Employing the generalized ICBA technique appears to be justified by the fact that the obtained reconstructions are rather good for a variety of object shapes. The more-or-less prominent reconstruction errors, visible at the poles of the objects in Fig. 4 and in some of the z sections of Figs. 4–8, are probably due to the fact that the least-squares scheme is returning local minima for certain values of p,q. These (false) solutions can be eliminated by suitable regularization strategies or by post-treatment of the reconstructed images.[56]

In conclusion, this paper reports our attempt to develop an effective method for shape determination in a waveguide. The major achievement of this paper is the effectiveness of the method and its reasonable accuracy. There are other issues in inverse problems for underwater acoustics, including from a mathematical aspect the uniqueness and sensitivity, and from a practical aspect a more realistic model of the ocean and other assumptions. However, it is out of the scope of this paper to address these issues. We have cited a reasonable number of references, including our papers in the area. Interested readers can find further discussion in those papers.

This paper considers only an impenetrable object with a soft boundary. It would be interesting to find whether this method can be modified to handle other kinds of objects. Currently we are trying to modify it for the hard boundary case.

We wish to point out that our method depends on the

normal mode representation. The method may fail if such a representation is not valid. On the other hand, if there exists a normal mode representation, then our method will be able to apply even if the ocean has a rough bottom or is inhomogeneous. The accuracy of the normal mode representation is the most crucial point of our method. More studies concerning this aspect will be conducted in the future.

Last but not least, the material presented in Sec. V, provides the means of treating, in the same manner, the more realistic case of a guide with elastic seabed. Our results for reconstructions of objects in such guides will be presented elsewhere.

[1] H. P. Bucker, ''Use of calculated sound fields and matched-field detection to locate sound sources in shallow water,'' J. Acoust. Soc. Am. **59**, 368–373 (1976).

[2] M. J. Hinich, ''Maximum likelihood estimation of the position of a radiating source in a waveguide,'' J. Acoust. Soc. Am. **66**, 480–483 (1979).

[3] J. M. Ozard, ''Matched field processing in shallow water for range, depth and bearing determination: Results of experiment and simulation,'' J. Acoust. Soc. Am. **86**, 744–753 (1989).

[4] C. Rozier and D. Lesselier, ''Inversion of a cylindrical vibrating body in shallow water from aspect-limited data using filtered SVD and the L-curve,'' Acust. Acta Acust. **82**, 717–728 (1996).

[5] F. B. Jensen, W. A. Kuperman, M. B. Porter, and H. Schmidt, *Computational Ocean Acoustics* (AIP, New York, 1994).

[6] Y. Xu and Y. Yan, ''Boundary integral equation method for source localization with a continuous wave sonar,'' J. Acoust. Soc. Am. **92**, 995–1002 (1992).

[7] Y. Xu and Y. Yan, ''A boundary integral equation method for acoustic source localization in a waveguide with inclusions,'' J. Comput. Acoust. **2**, 133–145 (1994).

[8] T. C. Yang, ''A method of range and depth estimation by modal decomposition,'' J. Acoust. Soc. Am. **82**, 1736–1745 (1987).

[9] T. S. Angell, R. E. Kleinman, C. Rozier, and D. Lesselier, ''Uniqueness and complete families for an acoustic waveguide problem,'' Wave Motion (submitted).

[10] P. Carrion, ''Reflection tomography in underwater acoustics,'' J. Acoust. Soc. Am. **97**, 1318–1321 (1995).

[11] P. Carrion and G. Boehm, ''Tomographic imaging of opaque and low-contrast objects in range-independent waveguides,'' J. Acoust. Soc. Am. **91**, 1440–1446 (1992).

[12] R. P. Gilbert and Z. Lin, ''Near field acoustic approximations in a shallow ocean,'' preprint (1996).

[13] R. P. Gilbert, Z. Lin, and J. L. Buchanan, ''Direct and inverse problems in ocean acoustics,'' Nonlinear Anal. **30**, 1535–1546 (1997).

[14] R. P. Gilbert and Y. Xu, ''Starting fields and far fields in ocean acoustics,'' Wave Motion **11**, 507–524 (1989).

[15] R. P. Gilbert and Y. Xu, ''Dense sets and the projection theorem for acoustic harmonic waves in a homogeneous finite-depth ocean,'' Math. Meth. Appl. Sci. **12**, 69–76 (1990).

[16] R. P. Gilbert and Y. Xu, ''The propagation problem and far-field patterns in a stratified finite-depth ocean,'' Math. Meth. Appl. Sci. **12**, 199–208 (1990).

[17] R. P. Gilbert and Y. Xu, ''Generalized Herglotz functions and inverse scattering problems in finite depth oceans, in Inverse Problems,'' *SIAM Proceedings Applied Mathematies 63*, edited by J. Corones *et al.* (SIAM, Philadelphia, 1992).

[18] R. P. Gilbert and Y. Xu, ''The seamount problem,'' in SIAM special issue on the occasion of Prof. I. Stakgold's 70th birthday, *Nonlinear Problems in Applied Mathematics*, edited by T. Angell *et al.* (SIAM, Philadelphia, 1996), pp. 140–149.

[19] D. Lesselier and B. Duchene, ''Wavefield inversion of objects in stratified environments. From backpropagation schemes to full solutions,'' in *Review of Radio Science 1993–1995*, edited by R. Stone (Oxford U.P., Oxford, 1996), pp. 235–268.

[20] N. C. Makris, F. Ingenito, and W. A. Kuperman, ''Detection of a submerged object insonified by surface noise in an ocean waveguide,'' J. Acoust. Soc. Am. **96**, 1703–1724 (1994).

[21] Y. Xu, ''Direct and inverse scattering of acoustic waves in shallow oceans,'' Doctoral thesis, University of Delaware, 1990.

[22] Y. Xu, ''An injective far-field pattern operator and inverse scattering problem in a finite depth ocean,'' Proc. Edinb. Math. Soc. **34**, 295–311 (1991).

[23] Y. Xu, T. C. Poling, and T. Brundage, ''Direct and inverse scattering of harmonic acoustic waves in an inhomogeneous shallow ocean,'' in *Computational Acoustics*, edited by D. Lee *et al.*, IMACS 91, Vol. 2 (North-Holland, Amsterdam, 1993), pp. 21–43.

[24] T. C. Yang, ''Scattering from boundary protuberances and reverberation imaging,'' J. Acoust. Soc. Am. **93**, 231–242 (1993).

[25] T. C. Yang and T. W. Yates, ''Scattering from an object in a stratified medium. II. Extraction of scattering signature,'' J. Acoust. Soc. Am. **96**, 1020–1031 (1994).

[26] R. P. Gilbert, Y. Xu, and P. Thejll, ''An approximation scheme for the three-dimensional scattered wave and its propagating far-field pattern in a finite depth ocean,'' Z. Angew. Math. Mech. **72**, 459–480 (1992).

[27] C. Rozier, D. Lesselier, and T. Angell, ''Optimal shape reconstruction of a perfect target in shallow water,'' in Proceedings of the 3rd European Conference on Underwater Acoustics, Heraklion (1996).

[28] D. Rozier, D. Lesselier, T. Angell, and R. Kleinman, ''Reconstruction of an impenetrable obstacle immersed in a shallow water acoustic waveguide,'' in Proc. Conf. Problemes Inverses Propagation et Diffraction D'Ondes, Aix-les-Bains (1996).

[29] C. Rozier, D. Lesselier, T. Angell, and R. Kleinman, ''Shape retrieval of an obstacle immersed in shallow water from single-frequency farfields using a complete family method,'' Inverse Probl. (submitted).

[30] S. Russenschuck, ''Synthesis, inverse problems and optimization in computational electromagnetics,'' Int. J. Numer. Model.—Electron. Networks Devices Fields **9**, 45–57 (1996).

[31] J. Schwinger and D. S. Saxon, *Discontinuities in Waveguides* (Gordon and Breach, New York, 1968).

[32] J. L. Buchanan and R. P. Gilbert, ''Transmission loss in the far field over a seabed with rigid substrate assuming the Biot sediment model,'' J. Comput. Acoust. **4**, 29–54 (1996).

[33] J. L. Buchanan and R. P. Gilbert, ''Transmission loss in the far field over a one-layer seabed assuming the Biot sediment model,'' Z. Angew. Math. Mech. **77**, 121–135 (1997).

[34] J. L. Buchanan, R. P. Gilbert, and Y. Xu, ''Green's function for acoustic pressure over a poroelastic seabed,'' preprint (1996).

[35] T. W. Dawson, ''Acoustic scattering in a three-dimensional oceanic waveguide using boundary integral methods,'' J. Acoust. Soc. Am. **90**, 2609–2622 (1991).

[36] T. W. Dawson and J. A. Fawcett, ''A boundary integral equation method for acoustic scattering in a waveguide with nonplanar surfaces,'' J. Acoust. Soc. Am. **87**, 1110–1125 (1990).

[37] R. P. Gilbert, K. Khashanah, and Y. Xu, ''An unidentified inclusion problem for a shallow ocean, I: Construction of the Green's function,'' Comput. Acoust. **2**, 1–19 (1993).

[38] R. P. Gilbert and Z. Lin, ''Acoustic field in a shallow stratified ocean with a poroelastic seabed,'' Z. Angew. Math. Mech. **77**, 677–688 (1997).

[39] R. P. Gilbert and Y. Xu, ''Scattering of acoustic waves by an ellipse in a shallow ocean,'' in *Advances in Computer Methods for Partial Differential Equations VII*, edited by R. Vichnevetsky *et al.* (IMACS, 1992), pp. 287–293.

[40] R. P. Gilbert and Y. Xu, ''The coefficient problem for a shallow ocean with an unknown inhomogeneity and an elastic seabed,'' preprint (1996).

[41] G. A. Grinblat, A. A. Kleshchev, and K. V. Smirnov, ''Acoustic fields of spheroidal scatterers and radiators in a plane waveguide,'' Acoust. Phys. **39**, 36–38 (1993).

[42] R. H. Hackman and G. S. Sammelmann, ''Acoustic scattering in an inhomogeneous waveguide: Theory,'' J. Acoust. Soc. Am. **80**, 1447–1458 (1986).

[43] R. H. Hackman and G. S. Sammelmann, ''Multiple-scattering analysis for a target in an oceanic waveguide,'' J. Acoust. Soc. Am. **84**, 1813–1825 (1988).

[44] F. Ingenito, ''Scattering from an object in a stratified medium,'' J. Acoust. Soc. Am. **82**, 2051–2059 (1987).

[45] Z. Lin, ''Some direct and inverse problems for inhomogeneous media,'' Doctoral thesis, University of Delaware, 1997.

[46] I.-T. Lu, ''Analysis of acoustic wave scattering by scatterers in layered media using the hybrid ray-mode (boundary integral equation) method,'' J. Acoust. Soc. Am. **86**, 1136–1142 (1989).

[47] G. S. Sammelmann and R. H. Hackman, ''Acoustic scattering in a homogeneous waveguide,'' J. Acoust. Soc. Am. **82**, 324–336 (1987).

[48] A. Sarkassian, ''Method of superposition applied to scattering from a target in shallow water,'' J. Acoust. Soc. Am. **95**, 2340–2345 (1994).
[49] A. Sarkassian, ''Multiple scattering effects when scattering from a target in a bounded medium,'' J. Acoust. Soc. Am. **96**, 3137–3144 (1994).
[50] M. I. Taroudakis, ''A coupled-mode formulation for the solution of the Helmholtz equation in water in the presence of a conical sea-mount,'' J. Comput. Acoust. **4**, 101–121 (1996).
[51] M. Tran-Van-Nhieu, ''Scattering from slender bodies in a homogeneous waveguide,'' J. Acoust. Soc. Am. **88**, 2880–2888 (1990).
[52] T. W. Wu, ''On computational aspects of the boundary element method for acoustic radiation and scattering in a perfect waveguide,'' J. Acoust. Soc. Am. **96**, 3733–3743 (1994).
[53] Y. Xu and Y. Yan, ''An approximate boundary integral method for acoustic scattering in shallow oceans,'' J. Comput. Acoust. **1**, 61–75 (1993).
[54] R. P. Gilbert and Z. Lin, ''Acoustic waves in shallow inhomogeneous ocean with a layer of sediment,'' Acustica **82**, 729–737 (1996).
[55] T. Scotti and A. Wirgin, ''Location and shape reconstruction of a soft body by means of canonical solutions and measured scattered sound fields,'' C. R. Acad. Sci. Paris II b **330**, 641–646 (1995).
[56] T. Scotti and A. Wirgin, ''Shape reconstruction using diffracted waves and canonical solutions,'' Inverse Probl. **11**, 1097–1111 (1995).
[57] T. Scotti and A. Wirgin, ''Location and shape reconstruction of an impenetrable 3D body by matching measurements of scattered sound to a canonical body field representation,'' Proceedings of the 2nd International Conference Inverse Problems Engineering Theory and Practice, Le Croisic (1996).
[58] T. Scotti and A. Wirgin, ''Shape construction of a penetrable homogeneous 3D scattering body via the ICBA,'' Proc. Conf. Problemes Inverses Propagation et Diffraction D'Ondes, Aix-les-Bains (1996).
[59] A. Wirgin and T. Scotti, ''Wide-band approximation of the sound field scattered by an impenetrable body of arbitrary shape,'' J. Sound Vib. **194**, 537–572 (1996).
[60] T. K. Stanton, ''Sound scattering by cylinders of finite length. III. Deformed cylinders,'' J. Acoust. Soc. Am. **86**, 691–705 (1989).
[61] P. M. Morse and H. Feshbach, *Methods of Theoretical Physics* (McGraw-Hill, New York, 1953).

Nonlinear acoustic scattering from a gassy poroelastic seabed

Frank A. Boyle and Nicholas P. Chotiros
Applied Research Laboratories, The University of Texas at Austin, P.O. Box 8029, Austin, Texas 78713-8029

(Received 13 December 1996; accepted for publication 24 November 1997)

A model for difference frequency backscatter from trapped bubbles in sandy sediments was developed. A nonlinear volume scattering coefficient was computed via a technique similar to that of Ostrovsky and Sutin [''Nonlinear sound scattering from subsurface bubble layers,'' in *Natural Physical Sources of Underwater Sound,* edited by B. R. Kerman (Kluwer, Dordrecht, 1993), pp. 363–373], which treats the case of bubbles surrounded by water. Biot's poroelastic theory is incorporated to model the acoustics of the sediment. Biot fast and slow waves are included by modeling the pore fluid as a superposition of two acoustic fluids with effective densities that differ from the pore fluid's actual density and account for its confinement within sediment pores. The principle of acoustic reciprocity is employed to develop an expression for the backscattering strength. Model behavior is consistent with expectations, based on the known behavior of bubbles in simpler fluid media. © *1998 Acoustical Society of America.* [S0001-4966(98)02803-3]

PACS numbers: 43.30.Ma, 43.25.Dc [JHM]

INTRODUCTION

The subject of acoustic scattering from the ocean floor has generated considerable interest over the past several decades. Because there is no general agreement on what the dominant scattering mechanisms are, many models exist that are based on different scattering mechanisms. Some[1,2] assume that scattering occurs at the fluid/sediment interface, while others[3–7] consider scattering from within the sediment volume below the interface. Possible volume scattering mechanisms include variations in the refractive index of the sediment caused by local variations of the sound speed or density, the sediment grains, occlusions between grains, and trapped gas bubbles. It is reasonable that, when gas is present in sufficient quantity, gas bubble scattering should dominate; bubbles in resonance are very strong scatterers of sound, with scattering cross sections typically 1000 times their geometric cross sections.[8] The model of Boyle and Chotiros[7] suggests that very small amounts of gas (fluid gas fractions of 10^{-5} or less) are sufficient to dominate other scattering mechanisms. At present, no practical method of measuring, *in situ*, such small amounts of gas exists.

Significant ambiguity can exist between the acoustic returns from gas concentrations and other types of scatterers; a hard rock interface can resemble a pocket of trapped gas. This introduces uncertainty into acoustic methods of sediment classification. Finding an effective way of distinguishing gas bubble acoustic returns from other types is therefore critical.

One way in which gas bubbles differ from other kinds of scatterers is in their nonlinear scattering character. Water has a nonlinearity parameter B/A of about 5 to 6 compared with a value of 8–12 for water-saturated sand.[9] The value for a bubbly liquid is much higher.[10]

One way of identifying bubble returns is to ensonify the sediment with a parametric signal and measure the scattered sound at combination frequencies. This procedure has been successfully employed to detect bubbles in the water column.[11]

The problem of identifying gas bubbles trapped within sediment pores is considerably more complicated than that involving bubbles in the water column. Recent experiments[12,13] suggest that sandy sediments are best modeled acoustically via Biot's[14,15] poroelastic theory. This type of treatment differs from others in that it models a saturated sediment as a two-phase medium, consisting of a semirigid matrix of sediment grains, through which the pore fluid is allowed to flow. An outstanding feature of Biot's theory is that two compressional waves are predicted, in addition to the shear wave. In the so-called Biot fast wave, the pore fluid and grain structure move approximately in phase. This wave is analogous to the compressional wave that would exist in an equivalent elastic medium. The other type of compressional wave, called the Biot slow wave, consists of the solid and fluid parts of the medium moving out of phase. Experiment suggests that both types of waves can be significant. For trapped bubble scattering purposes, shear waves can be neglected since they couple only weakly into the pore fluid that contains the bubbles.

As a bubble expands, it carries with it the surrounding pore fluid. Partial confinement within sediment pores will cause the fluid to behave as if it had an effective density different from its actual density. Since the mechanics of fluid confinement are different for Biot fast and slow waves, the pore fluid will have two different effective densities, depending on whether fast or slow waves are propagating. As a result, the pore fluid's acoustic impedance and the bubble's resonance frequency and damping constant are specific for each of the Biot waves. Furthermore, whereas for a fluid model these quantities can generally be treated as constants, in the Biot case they are functions of frequency.

In this paper, an expression for the difference frequency scattering coefficient from a bubbly sediment is developed. It separately models scattering from Biot fast and slow waves

by modeling the medium as a superposition of two acoustic fluids. One fluid supports the fast wave while the other supports the slow wave. This is attained by assigning an appropriate effective density and acoustic impedance to each fluid. The densities and impedances are obtained from the Biot model of Stern *et al.*[16]

In Sec. I, an expression for the difference frequency scattering coefficient of a single bubble in an acoustic fluid is derived. The fluid's effective density, and therefore its acoustic impedance and the bubble's resonance frequency and damping constant, are allowed to vary with frequency. In Sec. II, the scattering coefficient from a distribution of bubble sizes is computed. Section III contains a calculation of the effective backscattering strength of the interface above a bubbly Biot medium. Conclusions are discussed in Sec. IV.

I. CALCULATION OF THE DIFFERENCE FREQUENCY SCATTERING COEFFICIENT FROM A SINGLE BUBBLE

Ostrovsky and Sutin[17] derived an expression for the difference frequency scattering coefficient of a bubble in an unbounded fluid. The following treatment follows theirs but is modified to allow the fluid's density and related parameters to vary with the applied acoustic frequency. These modifications are necessary for the modeling of bubbles in a Biot medium in Sec. III.

Zabolotskaya and Soluyan[18] derived the following equation of motion for a bubble surface:

$$\ddot{V}+\omega_0^2 V-\alpha V^2-\mu(2\ddot{V}V+\dot{V}^2)+\omega\delta\dot{V}=-\epsilon P, \tag{1}$$

where V is a perturbation in the bubble's volume, P is the acoustic pressure incident upon the bubble, ω is the frequency of volume oscillations, and δ is the bubble's damping constant, an expression for which is given by Devin.[8,19] The resonance frequency ω_0 and the coefficients α, μ, and ϵ are given by

$$\omega_0^2=\frac{3\gamma b\beta P_{\mathrm{eq}}}{\rho R_{\mathrm{eq}}^2}, \tag{2}$$

$$\mu=\frac{1}{8\pi R_{\mathrm{eq}}^3}, \tag{3}$$

$$\epsilon=\frac{4\pi R_{\mathrm{eq}}}{\rho}, \tag{4}$$

$$\alpha=3\beta(\gamma+1)\omega_0^2, \tag{5}$$

where γ is the ratio of specific heats of the gas inside the bubble, P_{eq} is the ambient static pressure, and R_{eq} is the bubble equilibrium radius, which is assumed small in comparison with the acoustic wavelength. The factors b and β account for surface tension and thermal conductivity, detailed expressions for which are given by Medwin.[8]

The quantities ω_0, α, δ, and ϵ will vary with the applied frequency since they depend on the fluid density ρ, which, in the context of the Biot theory, effectively varies with frequency. One implication is that the bubble does not possess a single unique resonance frequency but rather a ''transresonance,'' in which the resonance frequency varies with the applied frequency. In the following text, the subscripts ''1,'' ''2,'' or ''Ω'' specify the appropriate acoustic frequency for a frequency-dependent variable. For example, the resonance frequency ω_0 of a bubble that is driven at frequency ω_1 is denoted ''ω_{01}.''

A solution for V in Eq. (1) is needed, given a biharmonic acoustic pressure incident upon the bubble:

$$P=P_1\cos(\omega_1 t+\varphi_1)+P_2\cos(\omega_2 t+\varphi_2), \tag{6}$$

where P_1 and P_2 are amplitudes and φ_1 and φ_2 are corresponding phases of two superimposed incident pressure signals with frequencies ω_1 and ω_2. As an ansatz, let V be of the form

$$V=V_1\cos(\omega_1 t+\xi_1)+V_2\cos(\omega_2 t+\xi_2)+V_\Omega\cos(\Omega t+\xi_\Omega)+\Psi, \tag{7}$$

where $\Omega=\omega_1-\omega_2$ is the difference frequency. V_i and ξ_i are amplitudes and phases of superimposed components of V. ''Ψ'' comprises all other terms, including those involving the sum frequency and higher harmonics of the driving frequencies ω_1 and ω_2. To solve for V_1 and V_2, it is only necessary to consider the linear part of (1):

$$\ddot{V}=\omega_0^2 V+\omega\delta\dot{V}=-\epsilon P, \tag{8}$$

where ω_0, δ, and ϵ are functions of the frequency ω of V. The linear part of V is given by

$$V_{\mathrm{lin}}=V_1\cos(\omega_1 t+\xi_1)+V_2\cos(\omega_2 t+\xi_2). \tag{9}$$

Upon substituting Eqs. (9) and (6) into Eq. (8),

$$\begin{bmatrix}(\omega_{01}^2-\omega_1^2)V_1\cos(\omega_1 t+\xi_1)+\delta_1\omega_1^2 V_1\sin(\omega_1 t+\xi_1)\\ +(\omega_{02}^2-\omega_2^2)V_2\cos(\omega_2 t+\xi_2)+\delta_2\omega_2^2 V_2\sin(\omega_2 t+\xi_2)\end{bmatrix} =\begin{bmatrix}-\epsilon_1 P_1\cos(\omega_1 t+\varphi_1)\\ -\epsilon_2 P_2\cos(\omega_2 t+\varphi_2)\end{bmatrix}. \tag{10}$$

If Eq. (10) is valid for all possible values of time t, the ω_1 and ω_2 components must satisfy it separately. Hence

$$(\omega_{01}^2-\omega_1^2)V_1\cos(\omega_1 t+\xi_1)+\delta_1\omega_1^2 V_1\sin(\omega_1 t+\xi_1)=-\epsilon_1 P_1\cos(\omega_1 t+\varphi_1), \tag{11}$$

$$(\omega_{02}^2-\omega_2^2)V_2\cos(\omega_2 t+\xi_2)+\delta_2\omega_2^2 V_2\sin(\omega_2 t+\xi_2)=-\epsilon_2 P_2\cos(\omega_2 t+\varphi_2). \tag{12}$$

By equating magnitudes on either side of Eqs. (11) and (12), the amplitudes V_1 and V_2 are obtained:

$$V_1=\frac{\epsilon_1 P_1}{\sqrt{(\omega_{01}^2-\omega_1^2)^2+\delta_1^2\omega_1^4}}, \tag{13}$$

$$V_2=\frac{\epsilon_2 P_2}{\sqrt{(\omega_{02}^2-\omega_2^2)^2+\delta_2^2\omega_2^4}}. \tag{14}$$

To find the difference frequency component V_Ω of the bubble volume perturbation V, it is necessary to consider the complete nonlinear equation, Eq. (1). The Ω components of Eq. (1)'s linear terms are given by substitution of Eq. (7):

$$(\omega_0^2 V)_\Omega=\omega_0^2 V_\Omega\cos(\Omega t+\xi_3), \tag{15}$$

$$(\omega\delta\dot{V})_\Omega = \omega\delta\Omega V_\Omega \sin(\Omega t+\xi_3), \tag{16}$$

$$(\ddot{V})_\Omega = -\Omega^2 V_\Omega \cos(\Omega t+\xi_3). \tag{17}$$

The first nonlinear term in Eq. (1) is $(-\alpha V^2)$. To find the Ω component of V^2, apply expression (7):

$$V^2 = V_1^2 \cos^2(\omega_1 t+\xi_1) + 2V_1V_2 \cos(\omega_1 t+\xi_1)\cos(\omega_2 t + \xi_2) + V_2^2 \cos^2(\omega_2 t+\xi_2) + \text{higher-order terms}. \tag{18}$$

By invoking the trigonometric identity,

$$\cos(a)\cos(b) = \tfrac{1}{2}(\cos(a+b)+\cos(a-b)), \tag{19}$$

the difference frequency component of V^2 can be computed:

$$(V^2)_\Omega = V_1V_2 \cos[\Omega t+(\xi_1-\xi_2)]. \tag{20}$$

In similar fashion, the difference frequency components of the other nonlinear terms in Eq. (1) can be computed:

$$(\ddot{V}V)_\Omega = \frac{(-\omega_1^2-\omega_2^2)}{2} V_1V_2 \cos[\Omega t+(\xi_1-\xi_2)], \tag{21}$$

$$(\dot{V}^2)_\Omega = \omega_1\omega_2 V_1V_2 \cos[\Omega t+(\xi_1-\xi_2)]. \tag{22}$$

The total Ω component of Eq. (1) is the sum of contributions from each of its terms. Therefore by substituting Eqs. (15)–(17) and (20)–(22) into Eq. (1) and noting that the incident pressure P has no difference frequency component,

$$\begin{aligned}\{&-\Omega^2 V_\Omega \cos(\Omega t+\xi_3) + \omega_{0\Omega}^2 V_\Omega \cos(\Omega t+\xi_3)\\ &-\alpha_\Omega V_1V_2 \cos[\Omega t+(\xi_1-\xi_2)]\\ &-\mu(-\omega_1^2-\omega_2^2)V_1V_2 \cos[\Omega t+(\xi_1-\xi_2)]\\ &-\mu\omega_1\omega_2 V_1V_2 \cos[\Omega t+(\xi_1-\xi_2)]\\ &+\delta_\Omega\Omega^2 V_\Omega \sin(\Omega t+\xi_3)\} = 0,\end{aligned} \tag{23}$$

where $\omega_{0\Omega}$, α_Ω, and δ_Ω are the values of ω_0, α, and δ, at the difference frequency Ω. Rearranging,

$$\begin{aligned}&(\omega_{0\Omega}^2-\Omega^2)V_\Omega \cos(\Omega t+\xi_3) + \delta_\Omega\Omega^2 V_\Omega \sin(\Omega t+\xi_3)\\ &\quad = (\alpha_\Omega - \mu(\omega_1^2+\omega_2^2-\omega_1\omega_2))V_1V_2 \cos[\Omega t+(\xi_1-\xi_2)].\end{aligned} \tag{24}$$

Expression (24) is an equality of harmonic signals. For two harmonic signals to be equal, their magnitudes and phases must be equal. By equating the magnitudes on either side of (24),

$$\begin{aligned}&\left|\sqrt{(\omega_{0\Omega}^2-\Omega^2)^2+\delta_\Omega^2\Omega^4}V_\Omega\right|\\ &\quad = \left|(\alpha_\Omega-\mu(\omega_1^2+\omega_2^2-\omega_1\omega_2))V_1V_2\right|.\end{aligned} \tag{25}$$

Hence the amplitude of the difference frequency oscillations of the bubble volume V is

$$V_\Omega = \left|\frac{(\alpha_\Omega-\mu(\omega_1^2+\omega_2^2-\omega_1\omega_2))V_1V_2}{\sqrt{(\omega_{0\Omega}^2-\Omega^2)^2+\delta_\Omega^2\Omega^4}}\right|. \tag{26}$$

Upon inserting expressions (13) and (14) for V_1 and V_2,

$$V_\Omega = \left|\frac{(\alpha_\Omega-\mu(\omega_1^2+\omega_2^2-\omega_1\omega_2))\epsilon_1\epsilon_2 P_1P_2}{\sqrt{(\omega_{0\Omega}^2-\Omega^2)^2+\delta_\Omega^2\Omega^4}\sqrt{(\omega_{01}^2-\omega_1^2)^2+\delta_1^2\omega_1^4}\sqrt{(\omega_{02}^2-\omega_2^2)^2+\delta_2^2\omega_2^4}}\right|. \tag{27}$$

This expression reduces to that of Zabolotskaya and Soluyan[18] for the special case of a simple fluid medium, in which case ω_0, α, and δ are independent of frequency.

As the bubble volume oscillates at frequency Ω, a pressure $P_\Omega(r)$ is generated in the surrounding fluid at distance r from the bubble center. Landau and Lifshits' expression,[20,21] relating a bubble's far-field acoustic pressure amplitude P_Ω to its volume perturbation amplitude V_Ω, is given by

$$P_\Omega(r) = \frac{\Omega^2\rho_\Omega V_\Omega}{4\pi r}. \tag{28}$$

Upon substituting Eq. (27) for V_Ω in Eq. (28),

$$P_\Omega(r) = \frac{\Omega^2\rho_\Omega}{4\pi r}\left|\frac{(\alpha_\Omega-\mu(\omega_1^2+\omega_2^2-\omega_1\omega_2))\epsilon_1\epsilon_2 P_1P_2}{\sqrt{(\omega_{0\Omega}^2-\Omega^2)^2+\delta_\Omega^2\Omega^4}\sqrt{(\omega_{01}^2-\omega_1^2)^2+\delta_1^2\omega_1^4}\sqrt{(\omega_{02}^2-\omega_2^2)^2+\delta_2^2\omega_2^4}}\right|. \tag{29}$$

The bubble's difference frequency scattering coefficient is defined as the scattered power at frequency Ω, divided by the total incident intensity:

$$\sigma = 4\pi r^2\left(\frac{\langle p_\Omega v_\Omega\rangle}{\langle p_1v_1\rangle+\langle p_2v_2\rangle}\right), \tag{30}$$

where p_i and v_i are complex pressures and velocities. In terms of the scattered and incident pressure amplitudes P_i, this can be written as

$$\sigma = 4\pi r^2\left(\frac{[(P_\Omega(r))^2/|Z_\Omega|]\cos\phi_\Omega}{(P_1^2/|Z_1|)\cos\phi_1+(P_2^2/|Z_2|)\cos\phi_2}\right), \tag{31}$$

where $Z_i = d\mathbf{p}/d\mathbf{v}_i$ is the acoustic impedance of the medium, and ϕ_i is the phase angle between the fluid velocity and acoustic pressure at frequency i. Substitution of Eq. (29) for $P_\Omega(r)$ in Eq. (31) yields

$$\sigma=\left|\frac{\Omega^4\rho_\Omega^2(\alpha_\Omega-\mu(\omega_1^2+\omega_2^2-\omega_1\omega_2))^2\epsilon_1^2\epsilon_2^2P_1^2P_2^2}{4\pi[(\omega_{0\Omega}^2-\Omega^2)^2+\delta_\Omega^2\Omega^4][(\omega_{01}^2-\omega_1^2)^2+\delta_1^2\omega_1^4][(\omega_{02}^2-\omega_2^2)^2+\delta_2^2\omega_2^4][P_1^2(\zeta_\Omega/\zeta_1)+P_2^2(\zeta_\Omega/\zeta_2)]}\right|, \tag{32}$$

where

$$\zeta_i=\frac{|Z_i|}{\cos\,\phi_i}. \tag{33}$$

Upon substituting Eqs. (2)–(5), the following expression for the bubble scattering coefficient is obtained:

$$\sigma=\left|\frac{\pi\Omega^4\rho_\Omega^2(3(\gamma+1)\omega_{0\Omega}^2-\omega_1^2-\omega_2^2+\omega_1\omega_2)^2P_1^2P_2^2}{R_{\rm eq}^2\rho_1^2\rho_2^2[(\omega_{0\Omega}^2-\Omega^2)^2+\delta_\Omega^2\Omega^4][(\omega_{01}^2-\omega_1^2)^2+\delta_1^2\omega_1^4][(\omega_{02}^2-\omega_2^2)^2+\delta_2^2\omega_2^4][P_1^2(\zeta_\Omega/\zeta_1)+P_2^2(\zeta_\Omega/\zeta_2)]}\right|. \tag{34}$$

II. DIFFERENCE FREQUENCY SCATTERING COEFFICIENT FROM A DISTRIBUTION OF BUBBLES IN AN ACOUSTIC FLUID

Equation (34) is an expression for the scattering coefficient of a single bubble. To write a simple expression for the scattering coefficient from a volume containing a size distribution of bubbles, an assumption is made that resonance scattering dominates and that a single scattering assumption is valid.[7] The volume scattering coefficient can then be written in the following form:

$$\beta=\int_0^\infty \sigma n(R_{\rm eq})dR_{\rm eq}, \tag{35}$$

where $R_{\rm eq}$ is the equilibrium bubble radius and $n(R_{\rm eq})$ is the bubble size density function, defined as

$$n(R_{\rm eq})=\frac{dN(R_{\rm eq})}{dR_{\rm eq}}, \tag{36}$$

where $N(R_{\rm eq})$ is the number of bubbles per unit volume with radii less than $R_{\rm eq}$.

A combination of Eqs. (34) and (35) results in an integral that is very difficult to solve analytically. In this section, an approximate expression is obtained, based on a technique originally employed by Wildt.[22] It is based on the following three assumptions:

(1) Most of the scattering is from bubbles with radii near the resonance radius.
(2) The bubble size density function is approximately constant in each range of bubble sizes that contribute.
(3) The damping constant δ is approximately constant in each range of bubble sizes that contribute.

Medwin's[8] expression for the resonance angular frequency ω_0 in terms of the equilibrium bubble radius is

$$\omega_0=\frac{\sqrt{3\gamma b\beta P_{\rm eq}/\rho}}{R_{\rm eq}}, \tag{37}$$

where γ is the ratio of specific heats, $P_{\rm eq}$ is the ambient pressure, ρ is the ambient density, and b and β are quantities that account for surface tension and thermal conductivity.

By inversion, the resonance radius R_r is given in terms of applied frequency ω:

$$R_0=\frac{\sqrt{3\gamma b\beta P_{\rm eq}/\rho}}{\omega}. \tag{38}$$

By combination of (37) and (38),

$$\frac{\omega_0}{\omega}=\frac{R_0}{R_{\rm eq}}. \tag{39}$$

By combining Eqs. (39) and (34),

$$\sigma_\Omega=\frac{\pi\rho_\Omega^2[3(\gamma+1)\omega_0^2-\omega_1^2-\omega_2^2-\omega_1\omega_2]^2P_1^2P_2^2}{\rho_1^2\rho_2^2R_{\rm eq}^2\omega_1^4\omega_2^4[(R_{01}^2/R_{\rm eq}^2-1)^2+\delta_1^2][(R_{02}^2/R_{\rm eq}^2-1)^2+\delta_2^2][(R_{0\Omega}^2/R_{\rm eq}^2-1)^2+\delta_\Omega^2][P_1^2(\zeta_\Omega/\zeta_1)+P_2^2(\zeta_\Omega/\zeta_2)]}, \tag{40}$$

where R_{01}, R_{02}, and $R_{0\Omega}$ are resonance radii when the bubble is driven at frequencies ω_1, ω_2, and ω_Ω, respectively.

By inspection, it is clear that Eq. (40) will have maxima when $R=R_{01}$, $R=R_{02}$, and $R=R_{0\Omega}$. The height of these maxima will be determined by the values of the damping constants δ_1, δ_2, and δ_Ω. Assumption (1) is a statement that the maxima are high enough that most of the contribution to the integral in Eq. (35) comes from bubbles with radii very close to R_{01}, R_{02}, or $R_{0\Omega}$:

$$\begin{aligned}\beta&=\beta_1+\beta_2+\beta_\Omega\\&=\int_{R_{01}-\epsilon}^{R_{01}+\epsilon}\sigma n(R_{\rm eq})dR_{\rm eq}\\&\quad+\int_{R_{02}-\epsilon}^{R_{02}+\epsilon}\sigma n(R_{\rm eq})dR_{\rm eq}+\int_{R_{0\Omega}-\epsilon}^{R_{0\Omega}+\epsilon}\sigma n(R_{\rm eq})dR_{\rm eq}.\end{aligned} \tag{41}$$

Consider β_Ω, which is the contribution from bubbles with radius close to $R_{0\Omega}$:

$$\beta_\Omega = \int_{R_{0\Omega}-\epsilon}^{R_{0\Omega}+\epsilon} \sigma n(R_{\rm eq}) dR_{\rm eq} = \frac{\rho_\Omega^2 P_1^2 P_2^2}{\rho_1^2 \rho_2^2 \omega_1^4 \omega_2^4 [P_1^2(\zeta_\Omega/\zeta_1) + P_2^2(\zeta_\Omega/\zeta_2)]} \times \int_{R_{0\Omega}-\epsilon}^{R_{0\Omega}+\epsilon} \frac{[3(\gamma+1)\omega_0^2 - \omega_1^2 - \omega_2^2 - \omega_1\omega_2]^2 n(R_{\rm eq}) dR_{\rm eq}}{R_{\rm eq}^2 [(R_{01}^2/R_{\rm eq}^2 - 1)^2 + \delta_1^2][(R_{02}^2/R_{\rm eq}^2 - 1)^2 + \delta_2^2][(R_{0\Omega}^2/R_{\rm eq}^2 - 1)^2 + \delta_\Omega^2]}. \quad (42)$$

According to assumption (2), the bubble size density function $n(R_{\rm eq}) = n(R_{0\Omega})$ is constant within the narrow range of bubble radii about $R_{0\Omega}$. Assumption (1) states that, within the integral, the bubble equilibrium radius is approximately equal to the resonance radius $R_{0\Omega}$. Therefore, according to Eq. (39), the resonance frequency can be approximately by $\omega_0 = \Omega$. The second and third factors in the denominator of Eq. (42) do not change significantly across the bubble radius ranges and can be approximated as constants with $R_{\rm eq} = R_{0\Omega}$. Hence

$$\beta_\Omega = \frac{\pi \rho_\Omega^2 [3(\gamma+1)\Omega^2 - \omega_1^2 - \omega_2^2 - \omega_1\omega_2]^2 P_1^2 P_2^2 n(R_{0\Omega})}{\rho_1^2 \rho_2^2 \omega_1^4 \omega_2^4 [P_1^2(\zeta_\Omega/\zeta_1) + P_2^2(\zeta_\Omega/\zeta_2)][(R_{01}^2/R_{0\Omega}^2 - 1)^2 + \delta_1^2][(R_{02}^2/R_{0\Omega}^2 - 1)^2 + \delta_2^2]} \int_{R_{0\Omega}-\epsilon}^{R_{0\Omega}+\epsilon} \frac{dR_{\rm eq}}{R_{\rm eq}^2 [(R_{0\Omega}^2/R_{\rm eq}^2 - 1)^2 + \delta_\Omega^2]}. \quad (43)$$

To solve this integral, the following variable transformation is made:

$$q = \frac{R_{0\Omega}}{R_{\rm eq}} - 1, \quad dq = -\frac{R_{0\Omega}}{R_{\rm eq}^2} dR_{\rm eq}. \quad (44)$$

The integral in Eq. (43) is then given by

$$I = \int_{R_{0\Omega}-\epsilon}^{R_{0\Omega}+\epsilon} \frac{dR_{\rm eq}}{R_{\rm eq}^2 [(R_{0\Omega}^2/R_{\rm eq}^2 - 1)^2 + \delta_\Omega^2]} = \int_{q1}^{q2} \frac{-dq}{R_{0\Omega}[((q)(q+2))^2 + \delta_\Omega^2]}, \quad (45)$$

where

$$q_1 = \frac{R_{0\Omega}}{(R_{0\Omega}-\epsilon)} - 1, \quad q_2 = \frac{R_{0\Omega}}{(R_{0\Omega}+\epsilon)} - 1. \quad (46)$$

Since, according to assumption (1), the contribution to the integral is from a narrow range of bubble radii near $R_{\rm eq} = R_{0\Omega}$, the variable q is always small. Hence the following approximation can be made:

$$(q(q+2))^2 \cong 4q^2. \quad (47)$$

When this approximation is applied, the integral reduces to

$$I = \frac{1}{R_{0\Omega}} \int_{-\infty}^{\infty} \frac{dq}{[4q^2 + \delta_\Omega^2]}, \quad (48)$$

where the limits of integration have been expanded out to infinity. This is reasonable since the contribution to the integral is small outside the original limits of q_1 and q_2. The resulting definite integral is tabulated:[23]

$$I = \frac{1}{R_{0\Omega}} \frac{\pi}{2\delta_\Omega}. \quad (49)$$

Combine (43), (45), and (49) to get an expression for β_Ω:

$$\beta_\Omega = \frac{\pi \rho_\Omega^2 [3(\gamma+1)\Omega^2 - \omega_1^2 - \omega_2^2 - \omega_1\omega_2]^2 P_1^2 P_2^2 n(R_{0\Omega})}{\rho_1^2 \rho_2^2 \omega_1^4 \omega_2^4 [P_1^2(\zeta_\Omega/\zeta_1) + P_2^2(\zeta_\Omega/\zeta_2)][(R_{01}^2/R_{0\Omega}^2 - 1)^2 + \delta_1^2][(R_{02}^2/R_{0\Omega}^2 - 1)^2 + \delta_2^2]} \frac{1}{R_{0\Omega}} \frac{\pi}{2\delta_\Omega}. \quad (50)$$

β_1 and β_2 can be obtained by repeating the procedure of Eqs. (42)–(50) over bubble size ranges about R_{01} and R_{02}. The results are

$$\beta_1 = \frac{\pi \rho_\Omega^2 [3(\gamma+1)\omega_1^2 - \omega_1^2 - \omega_2^2 - \omega_1\omega_2]^2 P_1^2 P_2^2 n(R_{01})}{\rho_1^2 \rho_2^2 \omega_1^4 \omega_2^4 [P_1^2(\zeta_\Omega/\zeta_1) + P_2^2(\zeta_\Omega/\zeta_2)][(R_{0\Omega}^2/R_{01}^2 - 1)^2 + \delta_\Omega^2][(R_{02}^2/R_{01}^2 - 1)^2 + \delta_2^2]} \frac{1}{R_{01}} \frac{\pi}{2\delta_1}, \quad (51)$$

$$\beta_2 = \frac{\pi \rho_\Omega^2 [3(\gamma+1)\omega_2^2 - \omega_1^2 - \omega_2^2 - \omega_1\omega_2]^2 P_1^2 P_2^2 n(R_{02})}{\rho_1^2 \rho_2^2 \omega_1^4 \omega_2^4 [P_1^2(\zeta_\Omega/\zeta_1) + P_2^2(\zeta_\Omega/\zeta_2)][(R_{0\Omega}^2/R_{02}^2 - 1)^2 + \delta_\Omega^2][(R_{01}^2/R_{02}^2 - 1)^2 + \delta_1^2]} \frac{1}{R_{02}} \frac{\pi}{2\delta_2}. \quad (52)$$

III. DIFFERENCE FREQUENCY SCATTERING STRENGTH OF A GASSY SEAFLOOR

In Ref. 7, an expression was developed for the linear backscattering strength of a sediment interface due to trapped bubbles within the volume below the interface. In this section, the same treatment will be followed in developing an expression for difference frequency backscatter of a parametric signal.

In Sec. III A, an expression is derived for the scattered pressure from an element of sediment volume, based on the Biot theory and the principle of acoustic reciprocity. In Sec.

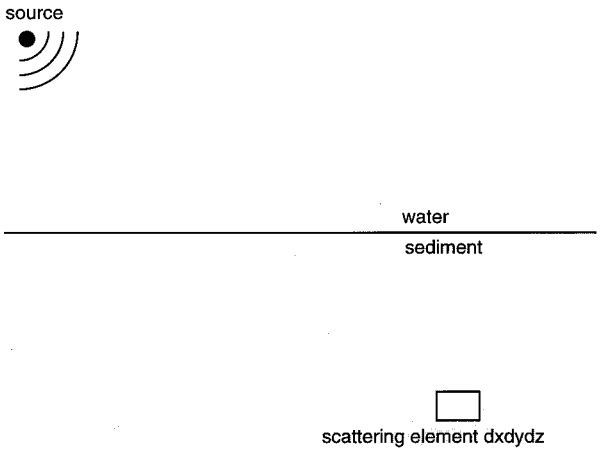

FIG. 1. Backscatter from an element of sediment volume.

III B, an expression is obtained for the effective scattering coefficient per unit area of sediment interface.

A. Scattered pressure from an element of sediment volume by reciprocity

Acoustic reciprocity is invoked in this section to describe the acoustic pressure scattered back to a projector in the water column from an ensonified element of sediment volume. In order to invoke reciprocity, the assumption is made that all sound propagates linearly through the medium. The nonlinearity treated here describes how sound is generated by the scatterer, rather than how it propagates after being scattered. This linear acoustic propagation assumption is consistent with the single scattering assumption made in Eq. (35) above; if neighboring scatterers with a common resonance frequency are widely spaced, their nonlinear contribution to propagation will be small.

Consider an acoustic source in the water column and an element of sediment volume that scatters sound, as in Fig. 1. The source and scatterer are both assumed to be much smaller than the acoustic wavelength. One can surround them each with virtual spheres that are large in comparison with the wavelength, as in Fig. 2. The spheres surrounding the source and scatterer will be called the ''source sphere'' and the ''scatterer sphere,'' respectively.

The source sphere starts with a surface velocity v_0, which generates a pressure P at the scatterer. The scatterer sphere responds with a surface velocity v, which in turn induces a scattered pressure P_v back at the source. The pressures and surface velocities are related by the principle of acoustic reciprocity, which states that, in a linear medium, the source and scatterer can be swapped with no change in the relationship between transmit and receive signals. This swapping of positions can be interpreted to represent the backscatter case. In terms of pressures and velocities, reciprocity states that

$$\frac{P}{v_0}=\frac{P_v}{v}. \tag{53}$$

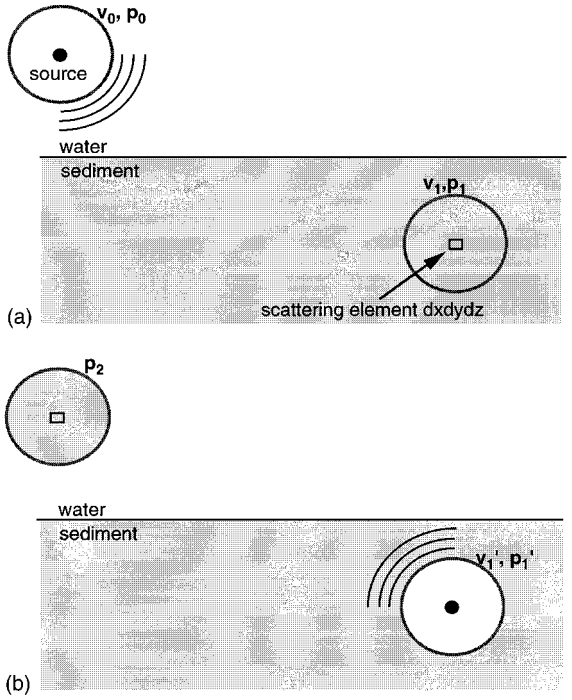

FIG. 2. Calculation of backscatter by acoustic reciprocity, (a) Acoustic propagation of incident sound; the virtual sphere surrounding the source as surface velocity $\mathbf{v}_0$ and pressure $\mathbf{p}_0\cdot\mathbf{v}_1$ and $\mathbf{p}_1$ are the pore fluid velocity and pressure induced at the scatterer. (b) Acoustic propagation of backscattered sound; the virtual sphere surrounding the scatterer has surface velocity $\mathbf{v}_1'$ and pressure $\mathbf{p}_1'\cdot\mathbf{p}_2$ is the backscattered pressure induced at the source.

The surface velocities can be related to the local acoustic pressures and impedances:

$$v_0=\frac{P_0}{Z_0}, \tag{54}$$

$$v=\frac{\eta P}{Z}, \tag{55}$$

where Z_0 and Z are the acoustic impedances in the fluid above and in the sediment. η is a transfer function from incident pressure P to scattered pressure ηP at the surface of the scatterer sphere. It includes the combined effects of scattering at the element $dx\ dy\ dz$ and propagation from the scatterer to the surface of the surrounding virtual sphere. As illustrated in Fig. 2, this propagation takes place as if it were in the water column. If the water column's attenuation is neglected, the average square magnitude of η is

$$\langle|\eta|^2\rangle=\frac{\sigma_{bv}\ dx\ dy\ dz}{4\pi r_s^2}, \tag{56}$$

where r_s is the radius of the virtual spheres and σ_{bv} is the scattering cross section, defined as the ratio of scattered power to incident intensity. By combining Eqs. (53)–(56), an expression is obtained for the square magnitude of the pressure returned to the projector:

$$\langle |P_v|^2 \rangle = \int \left| \frac{P}{P_0/Z_0} \right|^2 \frac{\sigma_{bv}}{4\pi r_s^2} \left| \frac{P}{Z} \right|^2 dx\, dy\, dz. \tag{57}$$

Since the sediment under consideration is a Biot medium supporting fast and slow waves, the acoustic intensity returned to the projector has two components:

$$\langle |P_v|^2 \rangle = \int \left| \frac{P_f + P_s}{P_0/Z_0} \right|^2 \left(\frac{\sigma_{bvf}}{4\pi r_s^2} \left| \frac{P_f}{Z_f} \right|^2 + \frac{\sigma_{bvs}}{4\pi r_s^2} \left| \frac{P_s}{Z_s} \right|^2 \right) \times dx\, dy\, dz, \tag{58}$$

where σ_{bvf} and σ_{bvs} are the scattering cross sections, per unit sediment volume, associated with the fast and slow waves. The quantities Z_f, Z_s, P_f, and P_s are, respectively, the fast and slow wave acoustic impedances and the acoustic pressures carried by the fast and slow wave. The quantity inside the parentheses is the square magnitude of the scatter's surface velocity. The factor $|(P_f+P_s)/(P_0/Z_0)|^2$ converts this to the backscattered pressure magnitude squared.

Equation (58) involves linear scattering, where all propagation and scattering occurs at a single defined frequency. For parametric scattering, the incident sound upon the scatterer is at two primary frequencies. Some of the sound scatters at combinations of these two primary frequencies, including their difference frequency. In this case, the magnitude squared of the difference frequency backscattered pressure is

$$\langle |P_{v\Omega}|^2 \rangle = \int \chi \left[\frac{\beta_f}{4\pi r_s^2} \left(\left| \frac{P_{1f}}{Z_{1f}} \right|^2 + \left| \frac{P_{2f}}{Z_{2f}} \right|^2 \right) + \frac{\beta_s}{4\pi r_s^2} \left(\left| \frac{P_{1s}}{Z_{1s}} \right|^2 + \left| \frac{P_{2s}}{Z_{2s}} \right|^2 \right) \right] dx\, dy\, dz, \tag{59}$$

where β_f and β_s are difference frequency scattering coefficients, β in Eq. (41). The subscripts f and s specify, respectively, whether a Biot fast or slow wave is being scattered. P_{1f} and P_{2f} are fast wave acoustic pressures incident upon the scattering element $dx\, dy\, dz$ at the primary frequencies ω_1 and ω_2. P_{1s} and P_{2s} are slow wave acoustic pressures incident upon the element. Z_{1f}, Z_{2f}, Z_{1s}, and Z_{2s} are the corresponding partial acoustic impedances.

The quantity inside the brackets is the difference frequency component of the scattering sphere's surface velocity. The factor χ converts this to the backscattered pressure returned to the projector. According to the principle of acoustic reciprocity, this is given by

$$\chi = \left| \frac{P_{\Omega f} + P_{\Omega s}}{P_{\Omega 0}/Z_{\Omega 0}} \right|^2, \tag{60}$$

where $P_{\Omega f}$ and $P_{\Omega s}$ are the fast and slow acoustic pressures that would be induced at the difference frequency Ω upon the scattering element if the fluid surrounding the source were driven at frequency Ω with velocity $P_{\Omega 0}/Z_{\Omega 0}$.

B. Difference frequency backscattering strength of sediment interface

In the following, a difference frequency backscattering strength for the sediment interface is defined. The definition is similar to that for linear scattering from bubbles.[7] As illustrated in Fig. 3, the effective surface backscattered pressure P_s per unit area $dx\, dy$ of sediment interface is a sum of contributions from all volume scattering elements below the interface:

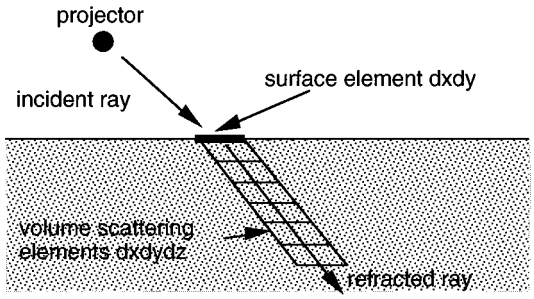

FIG. 3. Effective interface backscatter due to volume scattering.

$$\langle |P_s|^2 \rangle = \int_0^\infty \left| \frac{P_{\Omega f} + P_{\Omega s}}{P_{\Omega 0}/Z_{\Omega 0}} \right|^2 \left[\frac{\beta_f}{4\pi r_s^2} \left(\left| \frac{P_{1f}}{Z_{1f}} \right|^2 + \left| \frac{P_{2f}}{Z_{2f}} \right|^2 \right) + \frac{\beta_s}{4\pi r_s^2} \left(\left| \frac{P_{1s}}{Z_{1s}} \right|^2 + \left| \frac{P_{2s}}{Z_{2s}} \right|^2 \right) \right] dz. \tag{61}$$

It is convenient to define P_{su} as the difference frequency scattered pressure at unit distance from the interface element $dx\, dy$:

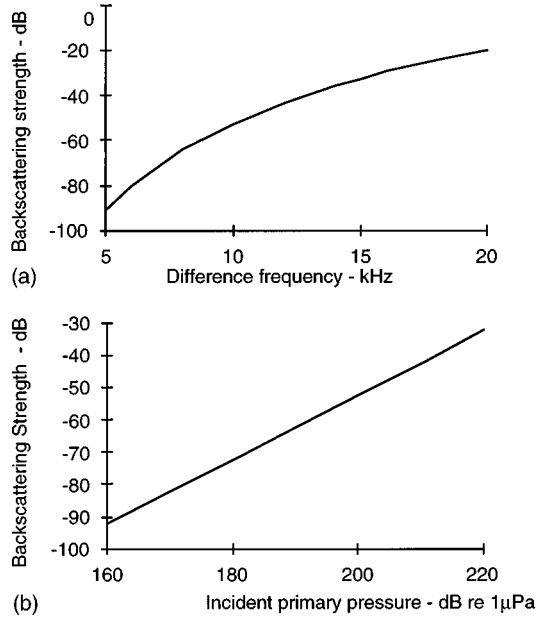

FIG. 4. Predicted parametric backscattering strengths over a gassy sand with geoacoustic properties given in Table I. (a) Backscattering strength versus difference frequency for a source level of 200 dB *re*:1 μPa and center frequency of 42 kHz, at normal incidence. (b) Backscattering strength versus source level (at primary frequencies) for a difference frequency of 10 kHz and center frequency of 42 kHz, at normal incidence.

$$|P_{su}| = |P_s| \frac{r}{r_{1m}} e^{r\alpha}, \tag{62}$$

where r is the distance between the source in the water column and the scattering element $dx\ dy$, and α is the absorption in the water column. The difference frequency backscattering strength of the interface is defined as

$$\mathrm{BS}_\Omega = 10 \log \frac{\langle |P_{su}|^2 \rangle}{|P_{\mathrm{inc1}} + P_{\mathrm{inc2}}|^2}, \tag{63}$$

where P_{inc1} and P_{inc2} are the primary wave pressures, at frequencies ω_1 and ω_2, that are incident upon the interface. Upon substituting (61) and (62) into (63),

$$\mathrm{BS}_\Omega = 10 \log \frac{\left(\frac{r}{r_{1m}}\right)^2 e^{2r\alpha} \int_0^\infty \left| \frac{(P_{\Omega f} + P_{\Omega s})}{(P_{\Omega 0}/Z_{\Omega 0})} \right|^2 \left[\frac{\beta_f}{4\pi r_s^2} \left(\left|\frac{P_{1f}}{Z_{1f}}\right|^2 + \left|\frac{P_{2f}}{Z_{2f}}\right|^2 \right) + \left(\frac{\beta_s}{4\pi r_s^2}\right) \left(\left|\frac{P_{1s}}{Z_{1s}}\right|^2 + \left|\frac{P_{2s}}{Z_{2s}}\right|^2 \right) \right] dz}{|P_{\mathrm{inc1}} + P_{\mathrm{inc2}}|^2}. \tag{64}$$

Figure 4(a) is a plot of the difference frequency backscattering strength modeled by Eq. (64) for a typical coarse sandy sediment. The sediment parameters are listed in Table I. The backscattering strength in this figure increases with frequency. This is consistent with expectations, which are based on the input bubble size density function, shown in Fig. 5. This bubble size density function was derived from the measured grain size distribution as described in Ref. 7. Over the frequency range of Fig. 4(a), the bubble size density function increases as the bubble radius decreases. Since the model is based on resonance scattering from bubbles, an increase in the scattering strength with frequency is expected.

The sediment parameters are listed in Table I. The backscattering strength in this figure increases with frequency because of the bubble size density function, which decreases with bubble size. Since the model is based on resonance scattering from bubbles, this means that the backscattering strength should increase with frequency, which is consistent with the model's behavior.

In Fig. 4(b), the dependence of the backscattering strength on the incident primary pressure is plotted. The two primary pressures are assumed in this figure to have the same amplitude. The backscattering strength increases linearly with the primary signal pressure.

IV. CONCLUSIONS

A model for parametric backscatter from trapped bubbles in sandy sediments has been developed. It is based on the nonlinear behavior of a gas bubble in an acoustic fluid, with modifications that allow the treatment of bubbles in a poroelastic medium. These modifications consist of assigning the pore fluid effective densities and acoustic impedances that characterize the Biot fast and slow waves.

The model's predictions are consistent with expectations. The backscattering strength increases linearly with source strength, which is identical to the case for parametric scattering from bubbles in an acoustic fluid. The increase in parametric backscattering strength with frequency is consistent with the frequency range described in Fig. 4 and the input bubble size distribution shown in Fig. 5.

Similar parametric scattering models have been developed for bubbles in water,[11] and they compare reasonably well with experimental measurements. The work reported in this paper allows an application of the technique described in Ref. 11 to gas bubbles that might be trapped within sedi-

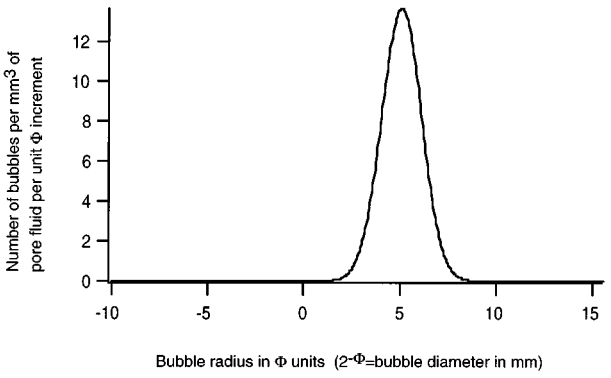

FIG. 5. Input bubble size density function N computed from grain size distribution according to Ref. 7.

TABLE I. Geoacoustic input parameters for parametric scattering strengths of Fig. 4.

Parameter	Units	
Fluid density	(kg/m^3)	1000
Fluid bulk modulus	(Pa)	2.25×10^9
Porosity		0.4
Grain density	(kg/m^3)	2650
Mean grain diameter	(ϕ)[a]	1.0
Standard deviation	(ϕ)[a]	1.0
Pore size parameter	(m)	1.796×10^{-4}
Viscosity	(kg/m s)	1.0×10^{-3}
Permeability	(m^2)	6.45×10^{-10}
Virtual mass parameter		1.75
Grain bulk modulus	(Pa)	7.0×10^9
Frame shear modulus	(Pa)	2.61×10^7
Shear log decrement		0.15
Frame bulk modulus	(Pa)	5.3×10^9
Bulk log decrement		0.15
Gas bulk modulus	(Pa)	2.48×10^5
Gas density	(kg/m^3)	1.22
Gas heat conductivity	(cal/m s °C)	5.6×10^{-3}
Gas specific heat (const press)	(cal/kg)	240
Gas specific heat ratio, C_p/C_v		1.4
Bubble surface tension	(N/m^2)	0.075
Bubble/pore volume ratio		0.625
Gas content		1.0×10^{-5}

[a] $\phi = -\log_2$ (grain diameter in millimeters).

ment. At present, however, the authors are not aware of any experimental measurements of parametric scattering strengths from sediments where the gas bubble size distributions are known. When they become available, such data are needed to test and further develop this model.

ACKNOWLEDGMENTS

This work was supported by the Office of Naval Research, under management by the Applied Physics Laboratory, The University of Washington, under subcontract 449382.

[1] R. E. Patterson, ''Backscatter of sound from a rough boundary,'' J. Acoust. Soc. Am. **35**, 2010–2013 (1963).
[2] C. S. Clay and H. Medwin, *Acoustical Oceanography: Principles and Applications* (Wiley, New York, 1977).
[3] J. H. Stockhausen, ''Scattering from the volume of an inhomogeneous half-space,'' Naval Research Establishment (Dartmouth, N. S.) Report No. 63/9, 1963.
[4] D. R. Jackson, D. P. Winebrenner, and A. Ishimaru, ''Application of the composite roughness model to high-frequency bottom backscattering,'' J. Acoust. Soc. Am. **79**, 1410–1422 (1986).
[5] P. C. Hines, ''Theoretical model of acoustic backscatter from a smooth seabed,'' J. Acoust. Soc. Am. **88**, 324–334 (1990).
[6] N. G. Pace, ''Low frequency acoustic backscatter from the seabed,'' Proceedings, Inst. Acoust. **16**, 181–188 (1994).
[7] F. A. Boyle and N. P. Chotiros, ''A model for high frequency backscatter from gas bubbles in sandy sediments,'' J. Acoust. Soc. Am. **98**, 531–541 (1995).
[8] H. Medwin, ''Counting Bubbles Acoustically, a Review,'' Ultrasonics **15**, 7–13 (1977).
[9] J. M. Hovem, ''The nonlinearity parameter of saturated marine sediments,'' J. Acoust. Soc. Am. **66**, 1463–1467 (1979).
[10] V. G. Welsby and M. H. Safar, ''Acoustic non-linearity due to microbubbles in water,'' Acustica **22**, 177–182 (1969/70).
[11] T. G. Leighton, R. J. Lingard, A. J. Walton, and J. E. Field, ''Acoustic bubble sizing by combination of subharmonic emissions with imaging frequency,'' Ultrasonics **29**, 319–323 (1991).
[12] N. P. Chotiros and M. L. Ramaker, ''High frequency acoustic penetration of sandy ocean sediments,'' presented at 121st Meeting of the Acoustical Society of America, J. Acoust. Soc. Am. **89**, 1908(A) (1991).
[13] F. A. Boyle and N. P. Chotiros, ''Experimental detection of a slow acoustic wave in sediment at shallow grazing angles,'' J. Acoust. Soc. Am. **91**, 2615–2619 (1992).
[14] M. A. Biot, ''Theory of propagation of elastic waves in a fluid saturated porous solid I. Low frequency range,'' J. Acoust. Soc. Am. **28**, 168–178 (1956).
[15] M. A. Biot, ''Theory of propagation of elastic waves in a fluid saturated porous solid. II. Higher frequency range,'' J. Acoust. Soc. Am. **28**, 179–191 (1956).
[16] M. Stern, A. Bedford, and H. R. Millwater, ''Wave reflection from a sediment layer with depth-dependent properties,'' J. Acoust. Soc. Am. **77**, 1781–1788 (1985).
[17] L. A. Ostrovsky and A. M. Sutin, ''Nonlinear sound scattering from subsurface bubble layers,'' in *Natural Physical Sources of Underwater Sound*, edited by B. R. Kerman (Kluwer, Dordrecht, 1993), pp. 363–370.
[18] E. A. Zabolotskaya and S. I. Soluyan, ''Emission of harmonic and combination-frequency waves by air bubbles,'' Sov. Phys. Acoust. **18**, 396–398 (1973), Eqs. 7 and 18.
[19] C. Devin, ''Survey of thermal, radiation, and viscous damping of pulsating air bubbles in water,'' J. Acoust. Soc. Am. **31**, 1654–1667 (1959).
[20] E. A. Zabolotskaya and S. I. Sutin, ''Emission of harmonic and combination-frequency waves by air bubbles,'' Sov. Phys. Acoust. **18**, 396–398 (1973).
[21] L. D. Landau and E. M. Lifshits, *Mechanics of Continuous Media* (GITTL, Moscow, 1953) (in Russian).
[22] R. Wildt, ''Acoustic Theory of Bubbles,'' *Physics of Sound in the Sea* (N.D.R.C. Summary Technical Report Div. 6, Washington, DC, 1946, Chap. 28, Vol. 8).
[23] *Schaum's Outline Series: Mathematical Handbook of Formulas and Tables*, edited by M. R. Speigel (McGraw-Hill, New York, 1968).

Plane-wave reflection from a solid layer with nonuniform density, sound speed, and shear speed

Alvin J. Robins
BAeSEMA Ltd., Apex Tower, 7 High Street, New Malden, Surrey KT3 4LH, England

(Received 26 April 1996; revised 20 January 1997; accepted 24 November 1997)

This paper considers the problem of calculating the reflection coefficient of a plane wave incident on an inhomogeneous elastic solid layer of finite thickness, overlying a semi-infinite, homogeneous solid substrate. The physical properties of the inhomogeneous layer, namely the density, compressional (sound) speed, shear speed, and attenuation, are all assumed to vary with depth. It is shown that, provided terms involving the gradient of the shear speed and of the shear modulus are ignored, and volume coupling between compressional and shear waves is neglected, analytical solutions of the resulting equations can be obtained. The assumptions made are justified at most frequencies of practical interest in underwater acoustics. In the case of a solid whose density and shear speed are constant, the results obtained are exact solutions of the full equations of motion, and may usefully be compared with numerical solutions in which the variation in sound speed through the layer is represented by a number of homogeneous sublayers. It is concluded that, with realistic sediment and substrate properties, a surprisingly large number of sublayers can be needed to give accurate results. [S0001-4966(98)02503-X]

PACS numbers: 43.30.Ma, 43.20.Fn, 43.20.Gp [JHM]

INTRODUCTION

The problem of calculating the reflection coefficient of a plane wave incident on a marine sediment has been the subject of a large number of studies, most of which treat the sediment as a homogeneous fluid or solid. The assumption of homogeneity is sometimes justified for thin sediments,[1–3] and simplifies the analysis considerably. This is particularly useful for ray path models (e.g., Refs. 2, 4 and 5), which can be more illuminating than full wave equation solutions in illustrating the dominant physical processes. Nevertheless, it is often necessary to be able to model layers with continuously varying properties, representing the majority of observed thick sediments.[6,7] This is usually done using numerical methods, either by dividing a nonuniform layer into a number of homogeneous sublayers[8,9] or by numerical integration of the wave equation to define the ''propagator matrix,''[10,11] thus avoiding the need to discretize the sediment layer. Mitchell and Lemmon[12] use a ray theory approach, tackling the problem of a thick, nonuniform fluid sediment by dividing it into layers in which the sound speed and attenuation vary linearly with depth.

Numerical techniques are able to deal with arbitrary variations of sediment parameters. It is, however, clearly desirable to be able to generate analytical solutions for an inhomogeneous layer, if only to verify the results from numerical models. A number of well-known solutions are available for inhomogeneous fluids,[13] but the literature on nonuniform solids is relatively sparse. Gupta[14] has obtained an analytical solution for a solid of constant density in which the compression and shear wave velocities, c and v, both vary linearly with depth. However, Gupta's solution is valid only for the ratio $c/v=\sqrt{3}$, so it is limited in application. More recently, Hall[15] has used the Born approximation to produce a semi-analytical model of a sea bed of constant density, in which the shear modulus is zero at the sea floor and exhibits a power law dependence on depth. Hall's analysis is aimed at low frequencies, where the gradient of the shear modulus has an impact on reflectivity via P-S coupling.

The purpose of the present paper is to provide an analytical model of compression and shear waves in an inhomogeneous solid whose density, sound speed, shear wave speed, and attenuation all vary continuously with depth. An earlier paper[16] provided solutions for a solid of nonuniform density, whose compression and shear wave speeds are both constant. That study included the continuous conversion of compression to shear waves arising from the effect of a density gradient, but its restriction to an isovelocity medium meant that the solutions are of limited practical significance. It was also assumed that the shear modulus is small compared with the bulk modulus.

We now show that the approximation of a small shear modulus can be abandoned, but we retain the assumption that its gradient can be neglected. Continuous volume coupling between compression and shear waves, resulting from density gradient effects, is also neglected. Both assumptions are justified at most frequencies of practical interest in underwater acoustics.[11,16–18] Under these conditions it is possible to obtain analytical solutions of the resulting equations for a solid layer whose properties all vary continuously with depth. In the special case of constant density and shear speed, the solutions satisfy the complete equation of motion, so no approximation is involved. The solutions are incorporated into a three-layer model of ocean, sediment, and substrate (the substrate being treated as a semi-infinite, homogeneous solid), and are used to determine the reflection coefficient of an incident plane wave in the upper (fluid) layer.

I. EQUATIONS OF MOTION IN AN ELASTIC MEDIUM

This section presents the mathematical model describing the propagation of plane shear and compression waves in an inhomogeneous solid. The equation of motion in an inhomogeneous, isotropic elastic medium is written as[19]

$$\rho \frac{\partial^2 \mathbf{u}}{\partial t^2} = \nabla[(\lambda+2\mu)\nabla\cdot\mathbf{u}] - \nabla\times(\mu\nabla\times\mathbf{u}) - 2(\nabla\mu)\nabla\cdot\mathbf{u} + 2(\nabla\mu\cdot\nabla)\mathbf{u} + 2\nabla\mu\times(\nabla\times\mathbf{u}), \quad (1)$$

where $\mathbf{u}$ is the particle displacement vector, ρ is the density, and λ, and μ are the Lamé parameters. The compression and shear wave speeds c and v are related to λ and μ by[20]

$$\rho c^2 = \lambda + 2\mu, \quad \rho v^2 = \mu. \quad (2)$$

Equations for the compression and shear waves are derived, making the assumption that terms involving the gradient of the shear wave speed and shear modulus may be neglected. There is no restriction on the variation of sound speed. Reference 16 made the additional assumption that the shear modulus is small compared with the bulk modulus, which is equivalent to the assertion that $v^2 \ll c^2$. However, we show below that this latter assumption can be abandoned. This means that the resulting equations are exact for a medium whose shear modulus and shear speed (and therefore also the density) are constant. There is of course a degree of approximation involved in applying the simplified equations to a solid whose density or shear speed vary with depth. We can gain an idea of the validity of the approximation by considering the magnitude of the neglected shear terms in relation to those retained. Each of the terms involving μ and its gradients, on the right-hand side of Eq. (1), is either a product of μ and a second derivative of $\mathbf{u}$ or a product of $\nabla\mu$ and a first derivative of $\mathbf{u}$. The magnitudes of the first and second spatial derivatives of $\mathbf{u}$ are given approximately by $k|\mathbf{u}|$, $k^2|\mathbf{u}|$, respectively, where k is the dilatational wave number.

We may also write

$$|\nabla\mu| \simeq \frac{\Delta\mu}{h},$$

where h is the thickness of the inhomogeneous layer and $\Delta\mu$ is the change in μ across the layer. Thus the ratio of the magnitude of the shear gradient terms to that of the terms proportional to μ is given approximately by

$$\left(\frac{\Delta\mu}{h}\,k\right) \Big/ (\mu k^2) = \frac{\Delta\mu}{(kh)\mu}.$$

We can expect the approximation of neglecting shear gradients to be valid if this ratio is small. In a consolidated sediment the change in μ across the layer will be less than the mean value $\bar{\mu}$. For an unconsolidated sediment, where μ may be very small at the surface, the value of $\Delta\mu$ could be greater than the mean value. However, even in this case $\Delta\mu/\bar{\mu}$ would not exceed 2 (assuming a linear variation of μ through the sediment). Hence the above condition will be satisfied provided the dimensionless wave number (kh) is significantly greater than 1. Thus the neglect of shear gradient terms is essentially a high-frequency approximation, as noted by Vidmar and Foreman,[11] although in practice it is applicable even at fairly low frequencies. Vidmar and Foreman suggest that, for typical deep-sea marine sediments, gradient terms may be neglected for frequencies above about 10 Hz.

Returning to the equation of motion, neglect of the $\nabla\mu$ terms in Eq. (1) gives

$$\frac{\partial^2 \mathbf{u}}{\partial t^2} = \frac{1}{\rho}\nabla[(\lambda+2\mu)\nabla\cdot\mathbf{u}] - \frac{\mu}{\rho}\nabla\times(\nabla\times\mathbf{u}). \quad (3)$$

It is usual to describe compression waves by means of an equation for the pressure p, defined by

$$p = -\kappa\nabla\cdot\mathbf{u}, \quad (4)$$

where $\kappa = \lambda + 2/3\mu$ is the bulk modulus. This procedure was followed in Ref. 16.

However, we note here that the first term on the rhs of Eq. (3) contains the expression $(\lambda+2\mu)\nabla\cdot\mathbf{u} = \rho c^2\nabla\cdot\mathbf{u}$, which is similar to the above expression for p (and identical to $-p$ in the fluid case). This leads us to try working in terms of a ''modified compressional potential'' p^*, defined by

$$p^* = -\rho c^2\nabla\cdot\mathbf{u} = p(1-4v^2/3c^2)^{-1}. \quad (5)$$

It turns out that the choice of the variable p^* in preference to p enables us to write equations which are valid for a solid with large shear modulus. Taking the divergence of Eq. (3), and neglecting $\nabla(\mu/\rho)$, gives

$$\frac{\partial^2 D}{\partial t^2} = \nabla\cdot\left[\frac{1}{\rho}\nabla[(\lambda+2\mu)D]\right] = -\nabla\cdot\left(\frac{1}{\rho}\nabla p^*\right), \quad (6)$$

where

$$D = \nabla\cdot\mathbf{u} = -p^*/(\rho c^2). \quad (7)$$

Hence the equation for p^* becomes

$$\frac{1}{c^2}\frac{\partial^2 p^*}{\partial t^2} = \nabla^2\mathbf{p}^* - \frac{1}{\rho}\nabla\rho\cdot\nabla p^*. \quad (8)$$

This is identical to the usual wave equation for pressure in an inhomogeneous fluid.[21] In a fluid medium, p^* is simply equal to the pressure p.

We now seek an equation governing the shear wave, and begin by writing the displacement $\mathbf{u}$ in the general form

$$\mathbf{u} = \nabla\phi + \nabla\times\boldsymbol{\psi} \quad (9)$$

where ϕ is a scalar potential related to p^* by

$$\nabla^2\phi = \nabla\cdot\mathbf{u} = -p^*/(\rho c^2) \quad (10)$$

and $\boldsymbol{\psi}$ is a vector potential describing the rotational component of the motion. Hall[15] notes that this simple Helmholtz representation of the displacement field cannot be used in an inhomogeneous medium if shear speed gradient effects are to be modeled. In those circumstances the more general formulation described by Richards[17] is required. However, Eq. (9) is adequate to describe the displacement if the gradients of both the shear speed v and the shear modulus (ρv^2) are neglected. Exact equations result in the case of a fluid of variable density or a solid of constant density and shear speed.

We now look for plane wave solutions in which the motion is confined to the (x,z) plane, so we may write

$$\boldsymbol{\psi}=(0,\psi,0), \tag{11}$$

where the scalar ψ is a function of x and z only. Hence

$$\boldsymbol{\nabla}\times\mathbf{u}=\boldsymbol{\nabla}\times(\boldsymbol{\nabla}\times\boldsymbol{\psi})=-\nabla^2\boldsymbol{\psi}. \tag{12}$$

Thus Eq. (3) can be written in the form

$$\frac{\partial^2\mathbf{u}}{\partial t^2}=-\frac{1}{\rho}\,\boldsymbol{\nabla}p^*+\frac{\mu}{\rho}\,\nabla^2(\boldsymbol{\nabla}\times\boldsymbol{\psi}). \tag{13}$$

The equation for $\boldsymbol{\psi}$ is obtained by taking the curl of Eq. (13). Neglecting the gradient of the shear speed, this results in

$$\nabla^2\left\{\frac{1}{v^2}\,\frac{\partial^2\boldsymbol{\psi}}{\partial t^2}-\nabla^2\boldsymbol{\psi}\right\}=-\frac{1}{(\rho v)^2}\,\boldsymbol{\nabla}\rho\times\boldsymbol{\nabla}p^*. \tag{14}$$

This equation is the same as given in Ref. 16, except for the replacement of p by p^*. Thus, if gradients of v and μ are small, the problem of calculating plane wave propagation in an inhomogeneous solid reduces to the solution of Eqs. (8), (10), and (14) for p^*, ϕ, and $\boldsymbol{\psi}$, from which the displacement field can be deduced using Eq. (9).

The term on the rhs of Eq. (14) represents continuous P to S wave conversion due to a density gradient, and has been discussed in Ref. 16. In that paper, analytical solutions were presented for an isovelocity layer of varying density, including the continuous coupling effect. Those solutions are of limited application to real sediments, in which refraction plays a dominant role. The problem of obtaining analytical solutions to Eq. (14) for a *refracting* medium is a complex one, and has not been addressed here. However, at most frequencies of interest we can neglect the coupling between P and S waves due to density gradient effects.[16] The source term on the rhs of Eq. (14) is then set to zero, and the equation for $\boldsymbol{\psi}$ can be written as the simple wave equation

$$\frac{1}{v^2}\,\frac{\partial^2\boldsymbol{\psi}}{\partial t^2}=\nabla^2\boldsymbol{\psi}. \tag{15}$$

[Omission of the ∇^2 factor outside the bracket in Eq. (14) is equivalent to ignoring solutions of Laplace's equation which would appear as source terms on the rhs of Eq. (15), but which can be excluded here since we have neglected volume coupling.]

We now show that, with this approximation, there is no need to solve explicitly for the scalar displacement potential ϕ. Substituting for $\boldsymbol{\nabla}^2\boldsymbol{\psi}$ in Eq. (13) gives

$$\frac{\partial^2\mathbf{u}}{\partial t^2}=-\frac{1}{\rho}\,\boldsymbol{\nabla}p^*+\frac{\partial^2}{\partial t^2}\,(\boldsymbol{\nabla}\times\boldsymbol{\psi}). \tag{16}$$

Comparison with Eq. (9) shows that

$$\frac{\partial^2}{\partial t^2}\,(\boldsymbol{\nabla}\phi)=-\frac{1}{\rho}\,\boldsymbol{\nabla}p^*, \tag{17}$$

which reduces to

$$\boldsymbol{\nabla}\phi=\frac{1}{\rho\omega^2}\,\boldsymbol{\nabla}p^* \tag{18}$$

when we make the usual assumption of an $\exp(-i\omega t)$ time dependence. Hence the irrotational component of the displacement can be found directly in terms of p^* using Eq. (18) without the need to solve Eq. (10) for ϕ. Note that, if we take the curl of Eq. (18), we deduce that $\boldsymbol{\nabla}\rho\times\boldsymbol{\nabla}p^*=0$, which is precisely the approximation made in arriving at Eq. (15). Numerical results presented later in this paper indicate that the neglect of volume coupling is justified at frequencies of practical importance, for density profiles typical of marine sediments.

Returning to the equation for p^*, Eq. (8) is now further transformed to a form suitable for coping with variable density. Following Refs. 16 and 22, we define new variables w and q by

$$w=\rho^{-1/2},\quad q=\rho^{-1/2}p^*. \tag{19}$$

Substituting w and q for ρ and p^* in Eq. (8) results in

$$\frac{1}{c^2}\,\frac{\partial^2 q}{\partial t^2}=\nabla^2 q+\frac{q}{w}\,\nabla^2 w. \tag{20}$$

For plane waves in a horizontally stratified layer we write

$$q=\exp[i(k_x x-\omega t)]q_1, \tag{21}$$

$$\boldsymbol{\psi}=\exp[i(k_x x-\omega t)]\boldsymbol{\psi}_1, \tag{22}$$

where q_1 and $\boldsymbol{\psi}_1$ are functions of depth only. The equations for q_1 and $\boldsymbol{\psi}_1$ then become

$$\frac{d^2q_1}{dz^2}+\left[k_p^2-k_x^2-\frac{1}{w}\,\frac{d^2w}{dz^2}\right]q_1=0, \tag{23}$$

$$\frac{d^2\psi_1}{dz^2}+[k_s^2-k_x^2]\psi_1=0, \tag{24}$$

where

$$k_p=\omega/c,\quad k_s=\omega/v. \tag{25}$$

II. SPEED AND DENSITY PROFILES

A variety of speed and density profiles can be defined leading to analytical solutions of Eqs. (23) and (24),[13,23] but many of these solutions are difficult to evaluate numerically. Here we have chosen profiles that result in relatively simple solutions. These are adequate to demonstrate the effects of variable density and shear speed in a refracting sediment.

The density profile is defined by the equation

$$\rho=\frac{Ae^{\alpha z}}{(e^{\alpha z}+a)^2}=\frac{A}{4a}\,\mathrm{sech}^2\left[\frac{1}{2}\,(\alpha z-\log a)\right]. \tag{26}$$

This ''sech-squared'' profile corresponds to

$$w(z)=\rho^{-1/2}=A^{-1/2}[e^{(1/2)\alpha z}+ae^{-(1/2)\alpha z}], \tag{27}$$

which gives

$$\frac{1}{w}\,\frac{d^2w}{dz^2}=\mathrm{const}=\frac{1}{4}\,\alpha^2. \tag{28}$$

Equation (28) enables a variety of profile shapes to be modeled by appropriate choice of A, a, and α. It is discussed in detail in Ref. 22, which examines the effect of density profile shape on reflection from a refracting fluid layer. The choice

TABLE I. Sediment and substrate properties. All densities are normalized with respect to $\rho_0 = 1050\ \mathrm{kg/m^3}$, and all speeds with respect to $c_0 = 1544$ m/s. All losses are in dB per wavelength.

	Top of sediment	Bottom of sediment	Substrate
Density	1.457	2.181	2.419
Sound speed	0.979	1.509	2.267
Shear speed	0.259	0.518	1.1335
Pressure loss	0.12	0.24	0.1
Shear loss	1.0	1.5	0.2

of $a=0$ results in the well-known exponential density profile.[24]

The sound and shear speeds are represented by either a constant value or a ''linear k^2'' profile, in which the square of the refractive index varies linearly with depth. This type of profile is described by an equation of the form

$$\text{speed} = (B+\beta z)^{-1/2}, \tag{29}$$

where B and β are constants. Unlike the density profile, there is no scope for altering the shapes of the speed profiles, which are determined uniquely by prescribing the speeds at the top and bottom of the sediment. With a constant speed the solution of Eq. (23) or (24) is a combination of exponentials, while a linear k^2 profile gives a solution in terms of Airy functions.[13] Losses are modeled in the usual way, by allowing the sound and shear speeds to take complex values.[13]

III. MODEL OF SEDIMENT AND SUBSTRATE

The three-layer model used to calculate reflection coefficients treats the upper layer as a semi-infinite, lossless fluid and the lower layer as a semi-infinite, lossy elastic solid. The inhomogeneous solid layer representing the sediment has the density and velocity profiles described in the previous section. The properties chosen for this study are representative of a thick terrigenous sediment overlying sedimentary rock.[6] The reference density ρ_0 and sound speed c_0 (that is, the values in the upper layer) are set to $1050\ \mathrm{kg/m^3}$ and 1544 m/s, respectively. All other properties are expressed as dimensionless quantities, normalized with respect to these values. Table I shows the parameters chosen for a typical sediment and substrate. The parameter ''a'' in Eq. (27) is set to 0.519. This gives a density profile having $d\rho/dz=0$ at the bottom of the sediment. The resultant shape is close to that of measured profiles,[23] and is plotted in Fig. 1. Velocity profiles defined by a linear k^2 speed law (Fig. 2) are less successful in modeling measured sound and shear speed profiles, since they give shapes which are concave upwards, while measured profiles are generally concave downwards. However, the intention of this paper is to model the effects of depth-varying properties in a solid layer, and in particular to compare analytical with numerical solutions. It is not essential for this purpose to simulate a real environment in any detail. Alternative speed profiles are known[13,23] which are better representations of measured profiles, and for which exact solutions of the Helmholtz equation can be found. However, the solutions are difficult to evaluate numerically and so have not been pursued here. Work is currently in progress on obtaining approximate solutions for more realistic profiles. It is intended to make this work the subject of a later publication.[25]

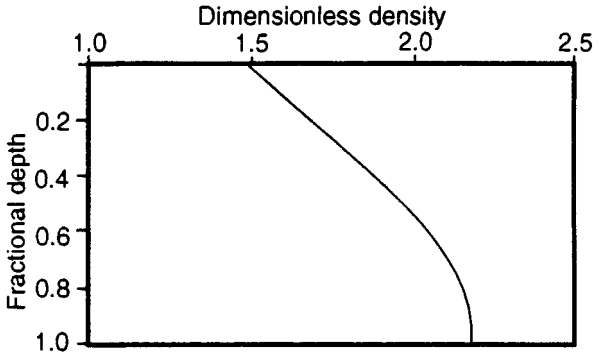

FIG. 1. Density profile given by Eq. (27) with $a=0.519$ and using density values from Table I.

The reflection coefficient for a plane wave incident from the upper layer is calculated, at each frequency and grazing angle of interest, by applying the usual boundary conditions,[26] namely, continuity of normal displacement and normal stress components at both interfaces, continuity of tangential displacement and tangential stress at the lower (solid/solid) interface, and zero tangential stress at the upper (fluid/solid) interface. We present the last of these conditions in detail by way of example. The tangential stress component τ_{xz} in the inhomogeneous layer is given by[20]

$$\frac{1}{\mu}\,\tau_{xz} = \frac{\partial u_x}{\partial z} + \frac{\partial u_z}{\partial x}.$$

Substituting for the velocity components using Eqs. (9), (18), and (19) results in

$$\frac{1}{\mu}\,\tau_{xz} = \frac{2ik_x}{\omega^2}\, w\,\frac{\partial q}{\partial z} - \frac{\partial^2 \psi}{\partial z^2} - k_x^2 \psi. \tag{30}$$

Setting $\tau_{xz}=0$ at the upper interface gives a linear equation in four unknowns, these being the multipliers of the exponential or Airy functions of which q and ψ are composed. Similar equations result from the other six boundary conditions, giving seven equations for seven unknowns, one of which is the required amplitude reflection coefficient R.

It is possible, in principle, to solve the equations analytically, thereby arriving at an explicit expression for R. This procedure was followed for the case of a fluid sediment and substrate,[22] where a system of four equations is to be solved. However, even in that relatively simple case the expressions are quite complicated. Except in the limits of very low or very high frequency they do not provide any additional insight into the physics of the problem. In the present case, where seven equations are to be solved, the expressions would be much more complex. Therefore the final step of calculating R is performed by solving the 7×7 matrix equation numerically. Nevertheless we refer to the solutions as ''analytical'' because all the coefficients of the equations are

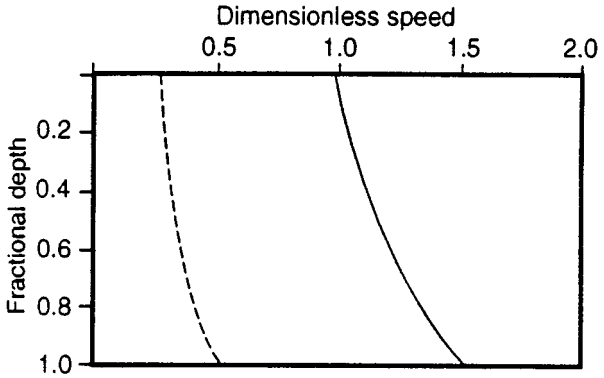

FIG. 2. Linear k^2 speed profiles using values from Table I: ——— compressional speed; ——— shear speed.

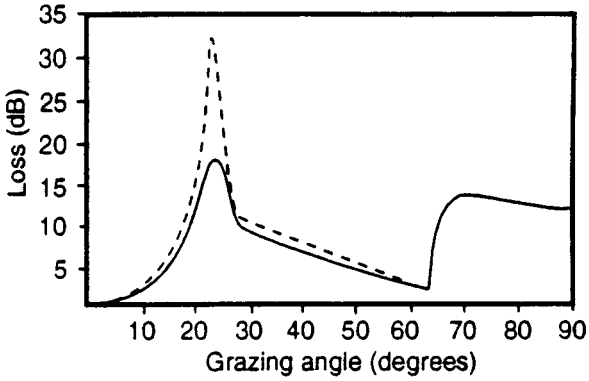

FIG. 3. Comparison of analytical reflection loss with SAFARI for an isovelocity sediment with varying density at $k_0h=2$: ——— analytical; ——— SAFARI.

analytical expressions, and because the results do not depend on numerical integration or on discrete layering of the sediment.

Solutions are presented in the following section, which also includes comparisons with the SAFARI fast field program.[27] The numerical technique employed by SAFARI deals with an inhomogeneous layer by dividing it into a number of sublayers, in each of which the density, shear speed, shear attenuation, and compressional attenuation are constant. The compressional wave speed is also required to be constant for solid sediments, but a ''linear k^2'' variation is permitted in each sublayer in the fluid case. Thus, although SAFARI is capable of providing exact solutions, its accuracy can be affected by the number of sublayers used to model a nonuniform sediment. This limitation is illustrated below.

IV. NUMERICAL RESULTS AND DISCUSSION

The following results show that the approximations made, in order to arrive at analytical solutions, are valid at frequencies of practical importance. The results also illustrate the limitations of modeling an inhomogeneous sediment using homogeneous sublayers. All results are shown as graphs of reflection loss versus grazing angle for a constant value of the dimensionless frequency $k_0h=\omega h/c_0$, where h is the sediment thickness. Reflection loss is defined in the usual way, namely as $-20\log_{10}|R|$.

A. Isovelocity sediment

First we examine the simple case of an isovelocity sediment of variable density. The density properties are as given in Table I, while the sound and shear speeds are assumed to have the ''top of sediment'' values of Table I throughout the whole layer. The variation in shear modulus is thus due entirely to the density variation. It has been shown that the neglected terms are of decreasing significance as frequency increases, and this is confirmed by the numerical results. Figure 3 compares the analytical solution with SAFARI, at the dimensionless frequency $k_0h=2$. One hundred sublayers were used to represent the density variation in the sediment. At this low frequency the neglected terms in the equations of motion are significant. This leads to errors in the analytical results in the grazing angle range 20° to 30°, where the peak in reflection loss is considerably under predicted. Agreement improves at higher grazing angles and is excellent for angles above 64° (the critical angle for generation of compression waves in the substrate). The sharp change in the slope of the loss curve at 28° is attributed to the onset of propagating shear waves in the substrate, leading to higher losses than would otherwise occur in the range 28° to 64°. At the higher frequency $k_0h=8$ (Fig. 4) the neglected terms are of much less importance, and the analytical solution agrees very well with SAFARI for the whole range of grazing angle. The differences are too small to be plotted. Figure 4 shows a reflection loss peak of about 8 dB at low grazing angle. This is due to destructive interference between the compression waves reflected from the water/sediment and sediment/substrate interfaces. This mechanism for high loss at low grazing angle has been discussed by Hastrup.[28]

B. Refracting sediment with constant density and shear speed

As noted above, the SAFARI results of Figs. 3 and 4 were produced using 100 uniform sublayers of equal thickness to represent the inhomogeneous sediment. This number is more than adequate to describe a layer of variable density[22] since the sublayer thickness is much less than a wavelength. Indeed, it is common to use about 10–25 sub-

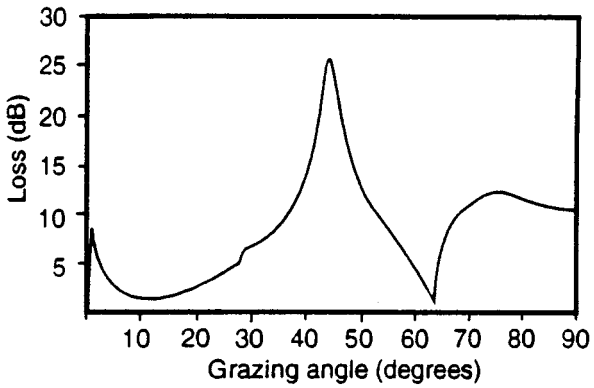

FIG. 4. Reflection loss for an isovelocity sediment with varying density, at $k_0h=8$, as predicted by both SAFARI and analytical solution.

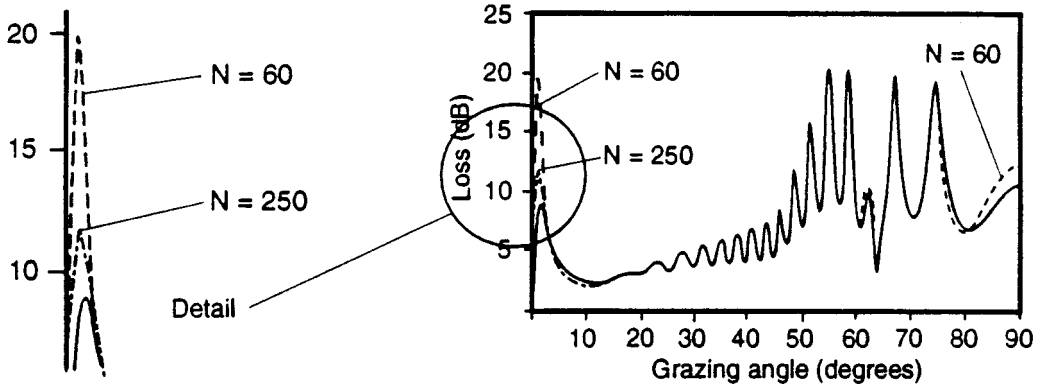

FIG. 5. Comparison of exact analytical solution with SAFARI for a refracting solid sediment of constant density and shear speed at $k_0h=60$: ——— exact solution; ——— SAFARI.

layers to model a nonuniform layer,[15,29] even when all its properties vary with depth. Under some circumstances this can lead to large errors, as shown by the following example of a refracting solid layer with constant density and shear speed. Remembering that the analytical results are exact solutions of Eq. (1) if shear speed and shear modulus are constant, this case is ideal for comparison with SAFARI to examine the sensitivity of the solution to the number of sublayers. The sound speed and compression wave attenuation at the top and bottom of the sediment are as given in Table I, while the density, shear speed, and shear attenuation take the ''top of sediment'' values throughout. We consider the dimensionless frequency $k_0h=60$ which, for the chosen value of c_0, would correspond to a frequency of 147 Hz with a sediment thickness of 100 m, or 14.7 Hz for a thickness of 1 km. An estimate of the number of sublayers needed for accuracy can be made by following the guideline given by Schmidt,[27] who states that a sublayer thickness of one-quarter wavelength should be enough in most cases. Based on the minimum compressional wavelength in the layer, this indicates that 40 sublayers should suffice at $k_0h=60$. An alternative estimate is obtained by considering ray paths near the top of the sediment. A simple Snell's law calculation for the chosen speed profile shows that rays in the upper layer, incident at small grazing angles, will reach a maximum depth of 7.4% of the sediment thickness before returning to the upper layer. Therefore one would expect to have to subdivide the sediment into at least 14 sublayers (assuming they are of equal thickness) if rays at small grazing angles are to experience any change in sound speed within this depth. With a more stringent criterion of (say) 4 sublayers between the surface and the ray turning depth, at least 54 sublayers are required.

We have used the compressional speed rather than the shear speed to estimate the number of sublayers, because the lower value of shear speed gives rise to much steeper angles of shear waves within the sediment, thus ensuring that penetration of shear waves into the sediment is much greater than that of compressional waves for small grazing angles. The discretization needed is therefore expected to be determined by the compressional profile in this case. This is confirmed by numerical results for solid and fluid sediments, presented below.

A number of SAFARI runs were carried out, with the sediment divided into various numbers N of sublayers of equal thickness. (Non-uniform layering of the sediment could have been used, but for present purposes this extra complication was not considered worthwhile.) Figure 5 compares the exact solution with SAFARI, for $N=60$ and $N=250$. We see from the exact result that there is a reflection loss peak of 9 dB at about 2° grazing angle, similar to the peak in Fig. 4. Again this is due to destructive interference, but in this case the interference is between the refracted wave penetrating the sediment, and the component reflected directly from the water/sediment interface. This can occur only for sediments whose surficial sound speed is less than that in the water, allowing penetration of the sediment by rays at low grazing angle. The mechanism has been discussed by Ainslie and Harrison.[30] The SAFARI result with 60 sublayers gives a reflection loss peak of 20 dB, which is grossly in error. At higher grazing angles the loss curve is generally well predicted, although there is still a 2 dB error even at normal incidence. The errors are due to the inability of a limited number of simple plane waves, generated at the sublayer interfaces, to match correctly the phase and amplitude of the exact solution over the whole angle range. The matching is particularly poor at low angles where only a small proportion of the 60 sublayers are penetrated by the incident wave. Increasing N by a factor of about 4, to a total of 250, gives much better agreement, as shown in Fig. 5. However, there is still a 2.5 dB error in the low grazing angle peak, despite the fact that there are now 19 sublayers between the upper interface and the ray turning depth. The error at normal incidence is reduced from 2 to 0.5 dB (not shown in the diagram). An increase in N by a further factor of 4, to a total of 1000 sublayers, eliminates the discrepancies except at the low angle peak, where there is a residual error of 0.5 dB (not plotted in Fig. 5).

It is remarkable that such a fine layering of the sediment should be needed to get an accurate result. One would normally expect reliable solutions using a discretization one or two orders of magnitude coarser than the 1000 sublayers

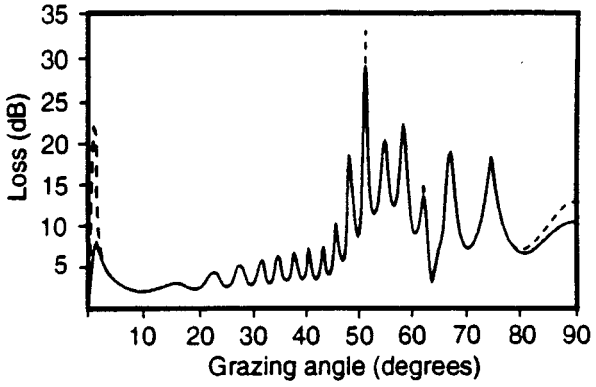

FIG. 6. Comparison of exact analytical solution with SAFARI for a refracting fluid sediment of constant density at $k_0h=60$: ——— exact solution; ——— SAFARI.

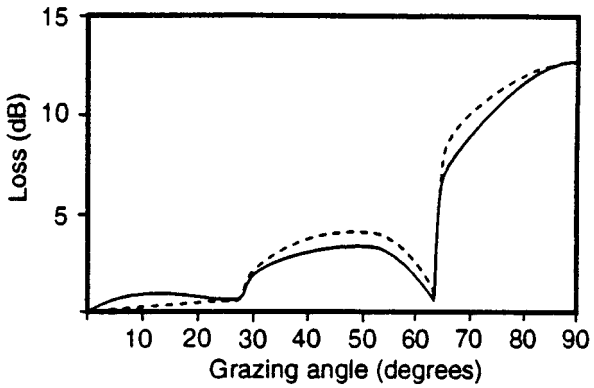

FIG. 7. Comparison of analytical solution with SAFARI for a sediment of variable density, sound speed, and shear speed at $k_0h=2$: ——— analytical; ——— SAFARI.

required here, as reported by Gupta,[29] for example. The problem is attributed entirely to the need to discretize the sound speed profile into constant speed sections when modeling a solid sediment, which is a feature of the SAFARI model used in this study.[27] By contrast, if the sediment can be modeled as a fluid, then the sound speed can be represented as a continuous function, using a linear k^2 profile in each sublayer. Under these conditions an accurate solution can be obtained with a very modest number of sublayers. Lekner[31] has noted the gains in accuracy and efficiency that can be made with inhomogeneous sublayers. Figure 6 plots the analytical solution, at $k_0h=60$, for a fluid sediment whose sound speed and density properties are the same as in Fig. 5. The solution given by SAFARI for this case, with only ten sublayers and using a linear k^2 speed profile in each sublayer, replicates the analytical solution very closely. The differences are too small to be shown in Fig. 6. However, if we discretize the sound-speed profile into constant speed segments (as would be needed with a solid sediment), then even with 60 sublayers we get a poor result. It is seen from Fig. 6 that the SAFARI solution with a discretized profile again fails to predict the low angle peak. The result is very similar to that for the solid sediment.

The reflection loss peak of Figs. 5 and 6 is dependent on the destructive interference mechanism mentioned above. At frequencies for which this mechanism does not operate, one would expect to get a good solution from SAFARI with a much reduced number of sublayers. However, it should be noted that the sediment and substrate parameters chosen for Fig. 5 were not specially selected as a ''pathological case,'' but used representative values for a real ocean bottom (albeit with the sediment density and shear speed held constant in order to get an exact solution).

With general variations in sediment properties, for which no analytical solutions are available, a numerical method is, of course, a necessity. When using the SAFARI model it will not be possible to predict beforehand whether any predetermined value of N is large enough to give an accurate result. One can, of course, make estimates of the number of sublayers required in any given circumstances using the methods discussed above, but the results of Figs. 5 and 6 show clearly that it is important to experiment with different numbers of layers to ensure convergence to the correct solution, as recommended by Schmidt.[27] It is not considered feasible to give a general criterion for selecting N which can be guaranteed to work in all cases.

C. General case

Next we turn to a case in which all the sediment properties vary with depth, as in Table I. The dimensionless shear modulus ρv^2 varies considerably in this case, from 0.098 at the top of the sediment to 0.585 at the bottom, so this example is a severe test of the validity of the approximations made earlier. Figures 7 and 8 compare the analytical solutions with SAFARI at dimensionless frequencies of 2 and 20, respectively. The SAFARI solutions used 400 sublayers, which was confirmed as adequate for convergence. Figure 7 ($k_0h=2$) shows that the analytical solution reproduces the shape of the loss curve correctly, but at this low frequency the neglected gradient terms are large enough to give inaccuracies in the solution. Agreement is much improved at $k_0h=20$, which is more representative of frequencies of practical interest. Figure 8 shows that the two solutions are indistinguishable over most of the grazing angle range. The error does not exceed 0.3 dB at any angle.

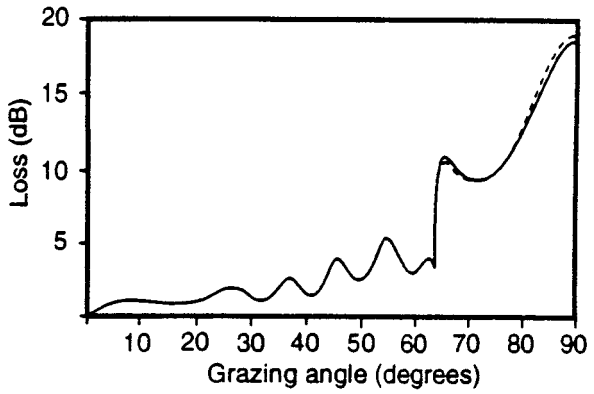

FIG. 8. Comparison of analytical solution with SAFARI for a sediment of variable density, sound speed, and shear speed at $k_0h=20$: ——— analytical; ——— SAFARI.

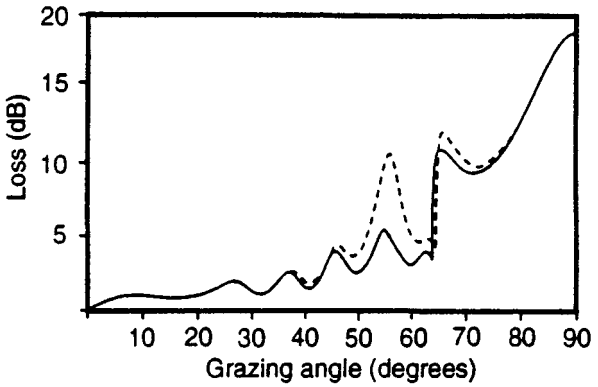

FIG. 9. Reflection loss for constant and variable sediment shear speeds at $k_0h=20$: ——— variable shear speed; ——— constant shear speed.

Finally, Fig. 9 illustrates the error incurred by neglecting the shear speed variation in the sediment. The solid line in this graph corresponds to a shear speed varying as shown in Table I (i.e., doubling between top and bottom of the sediment), while the broken line gives the result for a shear speed held constant at the ''top of sediment'' value throughout. There is a range of grazing angles (approximately 46° to 74°) where differences are apparent between the two loss curves. The critical angle for generation of compression waves in the substrate is 64°. Reflection loss is dominated by this mechanism for higher angles, and we see only a fairly small effect of the shear speed profile. Likewise, at low angles the reflection loss is controlled by the properties of the upper part of the sediment. The shear profile will have an impact on reflection loss via the conversion of compression to shear waves at the sediment/substrate interface, which will occur if the grazing angle is large enough for compression waves to reach the lower interface. This corresponds to grazing angles greater than $\cos^{-1}(1/1.509)=48.5°$, which is close to the value for which the shear profile begins significantly to affect the results in Fig. 9. Note that the differences between the two curves in Fig. 9 are unconnected with any error arising from the neglect of the shear gradient terms in Eq. (1). At this frequency ($k_0h=20$) the neglected terms have only a small effect, as illustrated by the SAFARI comparison of Fig. 8. Therefore, while shear profile effects can be ignored for angles close to zero or near normal incidence, the shear speed variation must be represented to get correct results over the whole angle range even when the shear gradient terms in the equations of motion are negligible. This is especially important in cases where an interface wave is generated at the sediment/substrate boundary, since in those circumstances the value of shear speed at the interface is critical.

V. CONCLUSIONS

It has been shown that, by making a suitable choice of variables, analytical solutions can be obtained of the equations for shear and compression wave propagation in an inhomogeneous solid. The solutions are valid for a medium with nonuniform density, sound speed, and shear speed provided we can ignore terms involving the gradient of shear speed or shear modulus, and can also ignore volume coupling between shear and compression waves due to density gradients. These approximations are justified at most frequencies of practical interest in underwater acoustics. For a medium whose shear speed and shear modulus are constant the solutions are exact, with no restriction on the magnitude of the shear speed. Such solutions are valuable for making comparisons with results obtained via numerical methods. The case of a refracting solid with constant density and shear speed has been used to show that a very large number of sublayers can sometimes be needed to model an inhomogeneous solid sediment accurately using the SAFARI model.

[1] S. J. Hughes, D. D. Ellis, D. M. F. Chapman, and P. R. Staal, ''Low-frequency acoustic propagation loss in shallow water over hard-rock seabeds covered by a thin layer of elastic-solid sediment,'' J. Acoust. Soc. Am. **88**, 283–297 (1990).
[2] N. R. Chapman and D. M. F. Chapman, ''A coherent ray model of plane-wave reflection from a thin sediment layer,'' J. Acoust. Soc. Am. **94**, 2731–2738 (1993).
[3] J. M. Hovem and A. Kristensen, ''Reflection loss at a bottom with a fluid sediment over a hard solid half-space,'' J. Acoust. Soc. Am. **92**, 335–340 (1992).
[4] P. J. Vidmar, ''Ray path analysis of sediment shear wave effects on bottom reflection loss,'' J. Acoust. Soc. Am. **68**, 639–648 (1980).
[5] M. A. Ainslie, ''Plane-wave reflection and transmission coefficients for a three-layered elastic medium,'' J. Acoust. Soc. Am. **97**, 954–961 (1995).
[6] E. L. Hamilton, ''Geoacoustic modelling of the sea floor,'' J. Acoust. Soc. Am. **68**, 1313–1340 (1980).
[7] E. L. Hamilton, ''Acoustic properties of sediments,'' in *Acoustics and Ocean Bottom, Proceedings of 2nd F.A.S.E. Conference*, Madrid, Spain, June 1987 (C.S.I.C., Madrid, 1987).
[8] H. P. Bucker, J. A. Whitney, G. S. Yee, and R. R. Gardner, ''Reflection of low-frequency sonar signals from a smooth ocean bottom,'' J. Acoust. Soc. Am. **37**, 1037–1051 (1965).
[9] G. J. Fryer, ''Reflectivity of the ocean bottom at low frequency,'' J. Acoust. Soc. Am. **63**, 35–42 (1978).
[10] S. R. Rutherford and K. E. Hawker, ''Effects of density gradients on bottom reflection loss for a class of marine sediments,'' J. Acoust. Soc. Am. **63**, 750–757 (1978).
[11] P. J. Vidmar and T. L. Foreman, ''A plane-wave reflection loss model including sediment rigidity,'' J. Acoust. Soc. Am. **66**, 1830–1835 (1979).
[12] S. K. Mitchell and J. J. Lemmon, ''A ray theory model of acoustic interaction with the ocean bottom,'' J. Acoust. Soc. Am. **66**, 855–861 (1979).
[13] L. M. Brekhovskikh, *Waves in Layered Media* (Academic, New York, 1980), pp. 188–192.
[14] R. N. Gupta, ''Reflection of elastic waves from a linear transition layer,'' Bull. Seismol. Soc. Am. **66**, 701–717 (1966).
[15] M. V. Hall, ''Acoustic reflectivity of a sandy seabed: A semianalytic model of the effect of coupling due to the shear modulus profile,'' J. Acoust. Soc. Am. **98**, 1075–1089 (1995).
[16] A. J. Robins, ''Generation of shear and compression waves in an inhomogeneous elastic medium,'' J. Acoust. Soc. Am. **96**, 1669–1676 (1994).
[17] P. G. Richards, ''Weakly coupled potentials for high-frequency elastic waves in continuously stratified media,'' Bull. Seismol. Soc. Am. **64**, 1575–1588 (1974).
[18] G. J. Fryer, ''Compressional-shear wave coupling induced by velocity gradients in marine sediments,'' J. Acoust. Soc. Am. **69**, 647–660 (1981).
[19] J. F. Hook, ''Separation of the vector wave equation of elasticity for certain types of inhomogeneous, isotropic media,'' J. Acoust. Soc. Am. **33**, 302–313 (1961).
[20] H. Kolsky, *Stress Waves in Solids* (Dover, New York, 1963), pp. 9, 13.
[21] E. Skudrzyk, *The Foundations of Acoustics* (Springer-Verlag, New York, 1971), p. 282.
[22] A. J. Robins, ''Reflection of a plane wave from a fluid layer with continuously varying density and sound speed,'' J. Acoust. Soc. Am. **89**, 1686–1696 (1991).

[23] A. J. Robins, ''Exact solutions of the Helmholtz equation for plane wave propagation in a medium with variable density and sound speed,'' J. Acoust. Soc. Am. **93**, 1347–1352 (1993).
[24] I. Tolstoy, ''Effects of density stratification on sound waves,'' J. Geophys. Res. **70**, 6009–6015 (1965).
[25] A. J. Robins, ''Bottom reflection loss from an inhomogeneous solid layer using wave functions calculated by means of the Langer approximation,'' in preparation.
[26] J. Miklowitz, *The Theory of Elastic Waves and Waveguides* (North-Holland, Amsterdam, 1978), pp. 156–169.
[27] H. Schmidt, ''Seismo-acoustic fast field algorithm for range independent environments—users guide,'' SACLANT Report SR-113 (1988).
[28] O. F. Hastrup, ''Some bottom-reflection loss anomalies near grazing and their effect on propagation in shallow water,'' in *Bottom-interacting Ocean Acoustics*, edited by W. A. Kuperman and F. B. Jensen (Plenum, New York, 1980), pp. 135–152.
[29] R. N. Gupta, ''Reflection of plane acoustic waves from transition layers with arbitrary variation of velocity and density,'' Bull. Seismol. Soc. Am. **56**, 633–642 (1966).
[30] M. A. Ainslie and C. H. Harrison, ''Reflection of sound from deep water inhomogeneous fluid sediments,'' in *Proc. Annual Meeting of the Canadian Acoustical Association*, edited by A. Cohen (Canadian Acoust. Assoc., Toronto, 1989).
[31] J. Lekner, ''Matrix methods in reflection and transmission of compressional waves by stratified media,'' J. Acoust. Soc. Am. **87**, 2319–2324 (1990).

Depth-pressure relationships in the oceans and seas

Claude C. Leroy
Private consultant, Cabinet d'Etudes en Acoustique Sous-Marine, 41 rue du Docteur Clément, 83330 Le Plan du Castellet, France

François Parthiot
Chief of Department of Underwater systems at GENAVIR, IFREMER, B.P. 330, 83507 La Seyne-sur-Mer Cedex, France

(Received 28 March 1997; accepted for publication 21 November 1997)

Two sets of equations, covering all world oceans and seas, are presented to calculate pressure from depth for the computation of sound speed, and depth from pressure for use in ocean engineering. They are based on the algorithm of UNESCO 1983 [N. P. Fofonoff and R. C. Millard, Jr., Unesco Tech. Papers in Mar. Sci. No. 44 (1983)], and on calculations from temperature and salinity profiles. The pressure to depth conversion is presented first. The equations can be used in those cases where the desired accuracy is reduced to ± 0.8 m. The equations to convert depth to pressure provide an overall accuracy between ± 8000 Pa and ± 1000 Pa. This leads to errors in sound speed consistently smaller than ± 0.02 m/s. The discussion, and comparisons with results and other formulas, suggest that the new equations are a substantial improvement on the previous simplified ones, which should now be abandoned. © *1998 Acoustical Society of America.* [S0001-4966(98)02103-1]

PACS numbers: 43.30.Pc, 43.30.Es [DLB]

INTRODUCTION

The need to obtain pressure at sea from depth and location is found in many applications of underwater acoustics. The main topic is sound propagation, which depends on the variation of the speed of sound with depth and range. As the local speed of sound in the ocean varies with temperature T, salinity S, and pressure P, and because the precise laboratory measurements leading to the equations for the speed of sound were made in conditions where pressure was the measured parameter, the basic equations use pressure and not depth. Depth, however, must be used in the various calculations of sound propagation such as based on ray theory, etc. The temperature and salinity profiles in the sea are often obtained from *in situ* measurements that can be made as a function of depth or pressure, completed at great depth by values from data banks. Most of these, like that of Levitus[1] for instance, and atlases, give T and S as a function of depth, not pressure. In all, for a specific sound propagation calculation, the user is mostly faced with the problem of converting depth into pressure for the calculation of sound speed. For this reason several simple formulas have been proposed.[2–5] Their accuracy was limited to a final precision of ± 0.5 to ± 1 m/s on sound speed, which was regarded as satisfactory up to ten years ago. This is no longer the case, especially in acoustic tomography, and an improvement by a factor of 10 is desirable. The reverse problem, that of pressure to depth conversion, has received considerable attention from oceanographers. The desired accuracy is indeed very high for such problems as the calculation of the motions of water masses, internal waves, etc. The procedure developed by Fofonoff and Millard[6] (UNESCO 83), here usually abbreviated as F-M or U83, is well adapted to the problem of calculating depth Z from pressure P, and a modest PC can easily handle the calculations once the specific program has been loaded. One must, however, enter $T(P)$ and $S(P)$ profiles by a number of layers with constant values, the sampling depending on the profiles and on the final desired accuracy.

A need arose three years ago at IFREMER to develop a simple method for calculating in real time the depth of a ROV or a deep towed fish down to 6000 m to an accuracy within only ± 1 m, from a pressure gauge installed on the vehicle. It was decided to perform the complete oceanographic calculation with a number of selected T and S profiles covering the oceans and seas worldwide, and to determine from the results whether a limited number of simple equations applicable to very large areas could give depth within this accuracy from pressure and latitude only. This study, carried out by the authors, concluded that a single equation could account for 80% of worldwide conditions with an accuracy better than ± 0.8 m. A set of ten alternative corrective terms could be developed for the other areas, especially the closed basins, with an accuracy of better than ± 0.2 m in most cases. The success of this procedure encouraged Leroy to attempt to develop equations for the reverse problem, the Z to P transformation, for which he had proposed an equation in 1968.[2] It was found that a single equation could cover most of the world with an accuracy better than ± 8000 Pa, leading for sound speed to errors smaller than ± 0.02 m/s. A set of ten different corrective terms, for the same areas as considered in the P to Z transformation, was developed, providing an accuracy of the order of ± 2000 Pa. All of these figures are stated on the assumption that the U83 algorithm to convert P into Z is correct. Both results are presented here, starting briefly with the simplified P to Z transformation.

I. CONVERSION OF PRESSURE INTO DEPTH

According to Fofonoff and Millard,[6] the depth Z in the ocean is obtained from pressure and latitude by the equation:

 0001-4966/98/103(3)/1346/7/$10.00

$$Z = Z_s(P,\phi) + \frac{\Delta D}{9.8}, \tag{1}$$

which is obtained by solving the hydrostatic equation

$$\int_0^Z gz\phi \, dZ = \int_0^P V_{TSP} \, dP. \tag{2}$$

Here, $Z_s(P,\phi)$ is a universal expression giving depth in what is called by oceanographers the ''standard ocean'' (an ideal medium in temperature and salinity with $T=0\,^\circ$C and $S=35‰$). The term D, called the geopotential anomaly, accounts for the difference in temperature and salinity structure from the standard ocean.

The complete formulation of F-M for $Z_s(P,\phi)$ reads, when P is expressed in megaPascal (MPa) instead of decibar:

$$Z_s = \frac{9.726\,59\times10^2 P - 2.512\times10^{-1}P^2 + 2.279\times10^{-4}P^3 - 1.82\times10^{-7}P^4}{g(\phi) + 1.092\times10^{-4}P}, \tag{3}$$

where $g(\phi)$ is given by the international formula for gravity

$$g(\phi) = 9.780\,318(1 + 5.2788\times10^{-3}\,\sin^2\,\phi - 2.36\times10^{-5}\,\sin^4\,\phi). \tag{4}$$

Although any personal computer can easily handle such calculations, it can be of interest to note that the following simplified formulation gives departures smaller than ±0.03 m in all situations:

$$Z_s(P,\phi) = \frac{9.7266\times10^2 P - 2.512\times10^{-1}P^2 + 2.28\times10^{-4}P^3 - 1.8\times10^{-7}P^4}{9.7803(1 + 5.3\times10^{-3}\,\sin^2\,\phi) + 1.1\times10^{-4}P}. \tag{5}$$

This formula was used in the deep vehicle localization problem, where the final accuracy desired was only ±1 m.

We shall call corrective term proper to an area i the quantity $\delta f_i = \Delta D/9.8$, and rewrite Eq. (1) as

$$Z = f(P,\phi) + \delta fi(Z) \tag{6}$$

with $f(P,\phi) \equiv Z_s(P,\phi)$, given by Eqs. (3) plus (4) or Eq. (5).

The geopotential anomaly is given through $\Delta D = \int_0^P \delta(T,S,P)dP$. The order T, S, P has been chosen in place of the more usual S, T, P, in order to be consistent with the common use in underwater acoustics and in data banks for temperature and salinity. In practice, the integral for ΔD is replaced by a summation over a number of layers where the quantity δ, called the specific volume anomaly, is considered to be constant. $\delta(TS,P)$ is given by: $\delta(T,S,P) = V(T,S,P) - V(0,35,P)$ where V is specific volume.

The method of calculating $\delta(T,S,P)$ is fully explained in Ref. 6, Part 3 and will not be repeated here. We mention only that the algorithm contains polynomial developments that use 45 coefficients and constants, each with 4–9 significant figures. This method has been programmed and applied with a number of T and S profiles covering the world oceans. Various questions had to be examined regarding the justification for using smoothed profiles such as those given by data banks like that of Levitus[1] or oceanographic atlases, the effect of sampling, that of seasonal variations, etc. The first problem to solve was the transformation of the profiles given in depth into profiles in pressure. This was done by using the simplified equation of the form $P = P(Z,\phi)$ proposed in 1978 by Lovett.[3] The use of this equation was preferred to that of Leroy[2] after a preliminary investigation. It was then found, for the purpose of achieving an accuracy ''better than ±1 m,'' that the sampling used in Levitus[1] (with Z transformed into P) was totally satisfactory: the difference between the values of Z obtained when using this sampling, and those obtained from various enriched profiles, derived from the original one by inserting points through interpolations on fourth degree Newton polynomials, was smaller than ±0.05 m. As for the seasonal variations and the smoothing (comparison with the use of detailed measured profiles), these never led to errors greater than ±0.1 m at depth in the worst cases.

The results of the study in the open oceans are expressed by the equation

$$\delta f_0(P) = P/(P+1) + 5.7\times10^{-2}P. \tag{7}$$

This equation was found to represent all open oceans situations within better than ±0.8 m with two exceptions: (i) the North Eastern Atlantic area between 30° and 35 °N, for which a separate equation $\delta f_1(P)$ is given in Table I, and (ii) circumpolar waters around the Antarctic. In that case, another equation $\delta f_2(P)$, also given in Table I, was found to give an accuracy better than ±0.01 m at various places for latitudes higher than 50 °S. However, the intermediate waters between the Antarctic ones and the common South Atlantic, Indian, and Pacific Oceans cannot be described with one single equation, and this is a unique particular case.

All closed basins were subsequently examined sytematically, and a total set of 9 further simple equations for $\delta f_i(P)$ was found capable of covering all of them, with an accuracy better than ±0.2 m in most cases. All of these equations are presented in Table I. More comments about those basins will be given in the next chapter when considering the depth to pressure conversion.

II. CONVERSION OF DEPTH INTO PRESSURE

Since it was found in the study of the pressure to depth conversion by simple formulas that solutions of the form of Eq. (6) could give accuracies from ±0.8 to ±0.1 m, it was

TABLE I. Corrective terms $\delta f_i(P)$ to be added to Eqs. (3)–(4) or Eq. (5) for obtaining depth Z(in m) from pressure P (in MPa) in the various areas of the world.

No.	Area of applicability	Latitude	Expression for $\delta f_i(P)$	Accuracy (±m)
0	Common oceans between 60° N and 40° S	as appropriate	$P/(P+1)+5.7\times10^{-2}P$	0.8
1	North Eastern Atlantic	id (30–35°)	$P/(P+2)+3\times10^{-2}P$	0.3
2	Circumpolar Antarctic waters	as appropriate	$4\times10^{-2}P-2\times10^{-4}P^2$	0.1
3	Mediterranean Sea	id	$-7\times10^{-2}P+2\times10^{-3}P^2$	0.2
4	Red Sea	id	None	0.2
5	Arctic ocean	id	None	0.1
6	Sea of Japan	id	(a) $6\times10^{-2}P$	0.1
			(b) $\delta f_0(P)$	0.8
7	Sulu Sea	8°	$0.9P/(P+1)+0.17P+7\times10^{-4}P^2$	0.2
8	Halmahera basin	0°	$0.8P/(P+0.5)+0.125P$	0.1
9	Celebes basin	4°	$1.2P/(P+1)+6.7\times10^{-2}P$	0.4
	Weber deep	6°	$+2.2\times10^{-4}P^2$	
10	Black Sea	43°	$1.1P$	0.1
11	Baltic Sea	60°	$1.8P$	0.1

though that corresponding accuracies, viz., always better than ±8000 Pa, could be obtained by reversing the P to Z algorithm.

A global reversal of Eq. (6) was judged inappropriate because it would have led to a formulation with corrective terms to be applied prior to use the equation reversing that for depth in the standard ocean. Instead, solutions of the form $P_i(Z,\phi)=h(Z,\phi)-\delta h_i(Z)$ [$h(Z,\phi)$ reversing $f(P,\phi)$ and δh_i being positive] were sought. It was obvious from the previous study that these corrective terms would follow the same geographical distribution as the δf_i of Table I.

The inversion of the equation giving Z from P and ϕ in the standard ocean [Eq. (2) plus (3) from F-M] was carried out by calculating a fourth degree Newton polynomial joining 5 (P,Z) doublets for latitude 45°, with Z between 0 and 8000 m. This provided an equation for $h(Z,45)$, whose coefficients were simplified by trial and error until an acceptable form was found to fit the whole range 0–11 000 m. To account for latitude, intuition suggested a form $h(Z,\phi)=h(Z,45)\times(g(\phi)-aZ)/(g(45)-aZ)$. It was considered that the use of the complete equation for gravity was not necessary and that a simpler one like in Eq. (5) could be sufficient. Finally, the following equation was adopted.

$$h(Z,\phi)=h(Z,45)\times k(Z,\phi), \tag{8}$$

with, Z being in meters and P in megaPascal,

$$h(Z,45)=1.008\,18\times10^{-2}Z+2.465\times10^{-8}Z^2-1.25\times10^{-13}Z^3+2.8\times10^{-19}Z^4, \tag{9}$$

$$k(Z,\phi)=(g(\phi)-2\times10^{-5}Z)/(9.806\,12-2\times10^{-5}Z), \tag{10}$$

$$g(\phi)=0.7803(1+5.3\times10^{-3}\sin^2\phi). \tag{11}$$

The accuracy of Eqs. (8)–(11) was checked to be within ±500 Pa over the entire range of possibilities for depth and latitude by systematic computer calculations. Depth was calculated from pressure using the complete formulation given by Eqs. (3) plus (4), and pressure calculated back from the obtained depth through Eqs. (8)–(11).

The calculation of the various corrective terms was performed by an iterative process in order to ensure maximum accuracy.

In the open oceans between latitudes 60° N and 40° S one single corrective term can be adopted, which reads

$$\delta h_0(Z)=0.8Z/(Z+100)+6.2\times10^{-6}Z. \tag{12}$$

The other corrective terms are given in Table II.

Figure 1 gives the results for the open oceans. The investigation was extended to the greatest depths and not limited to 8000 m as in the ROV problem. Figure 2 gives the results for the closed basins. Figure 2(a) is drawn with the same horizontal scale as Fig. 1, with the three curves corresponding to the common open oceans for comparison. The correction for the Sea of Japan remains within the ±8000 Pa of Eq. (12), but the separate more precise equation given in Table II can be used if desired. The Arctic Ocean and the Red Sea do not require corrective terms, the former because its characteristics are close to those of the standard ocean, and the latter because it is not deep enough for the geopotential anomaly to be significant. For the Mediterranean, the corrective term has a different sign from the others, and a second degree equation is needed for accuracy. Figure 2(b), drawn with a different scale, presents the results for Indonesian closed basins. These are very numerous and information about them may be found for example in Ref. 7. It was found, as in the reverse problem, that except for the basins specifically mentioned in Fig. 2(b) and Table II, the corrective terms can be approximated by Eq. (12). The Sulu Sea needs a quite different correction, as already pointed out by Lovett[3] who claimed that it as the third most irregular case in the world, after the Baltic and the Black Sea. These two last exceptional cases, with low-saline water, are illustrated in Fig. 2(c), with again a different scale.

TABLE II. Corrective terms $\delta h_i(Z)$ to be subtracted from the values given by Eqs. (8)–(11) for obtaining pressure P (in MPa) from depth Z (in m) in the various areas of the world.

No.	Area of applicability	Latitude	Expression for $\delta h_i(Z)$	Accuracy ($\pm 10^3$ Pa)
0	Common oceans between 60° N and 40° S	as appropriate	$1.0\times10^{-2}Z/(Z+100)+6.2\times10^{-6}Z$	8
1	North Eastern Atlantic	id (30–35°)	$8\times10^{-3}Z/(Z+200)+4.0\times10^{-6}Z$	3
2	Circumpolar Antarctic waters	as appropriate	$8\times10^{-3}Z/(Z+1000)+1.6\times10^{-6}Z$	1
3	Mediterranean Sea	id	$-8.5\times10^{-6}Z+1.4\times10^{-9}Z^2$	2
4	Red Sea	id	None	2
5	Arctic Ocean	id	None	1
6	Sea of Japan	id	(a) $7.8\times10^{-6}Z$	1
			(b) $\delta h_0(Z)$	8
7	Sulu Sea	8°	$1.0\times10^{-2}Z/(Z+100)+1.6\times10^{-5}Z+1.0\times10^{-9}Z^2$	<1
8	Halmahera basin	0°	$8\times10^{-3}Z/(Z+50)+1.3\times10^{-5}Z$	<1
9	Celebes basin	4°	$1.2\times10^{-2}Z/(Z+100)+7.0\times10^{-6}Z+2.5\times10^{-10}Z^2$	2
	Weber deep	6°		
10	Black Sea	43°	$1.13\times10^{-4}Z$	1
11	Baltic Sea	60°	$1.8\times10^{-4}Z$	1

III. DISCUSSION

A. Pressure to depth conversion

A simple formulation giving depth as a function of pressure and latitude was given in the instruction manual of Bisset-Berman.[8] It reads

$$Z=\frac{9.7512P}{1+5.3\times10^{-3}\sin^2\phi}-2.07\times10^{-4}P^2$$

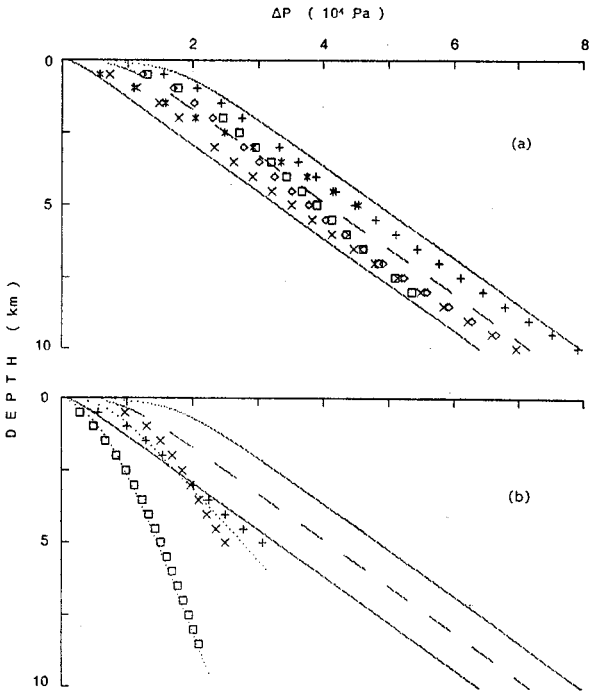

FIG. 1. Pressure corrections $\Delta P=\delta h_i(Z)$ to be subtracted from $h(Z,\phi)$ as given by Eqs. (8)–(11) to account for the geopotential anomalies. (a) Main oceans: + Pacific (Marianna trench); × Pacific (Kouril trench); * North Atlantic (Puerto Rico trench); ◇ South Atlantic; □ Indian Ocean. (b) Special cases: + and × North-East Atlantic; □ Antarctic circumpolar water.

with Z in m and P in kg/cm^2 above atmospheric. The results obtained from this equation are higher by $+0.1-+4$ m than those given by Eqs. (8)–(11) without the corrective term, i.e., for the standard ocean. If the Bisset-Berman equation is considered to be applicable to the real common oceans, then it gives results that are lower than Eqs. (8)–(11) completed by the corrective term given in Eq. (12), the difference lying between -1 to -4.5 m.

As more simplified equations to calculate pressure P from depth Z have been proposed, useful comparisons can be made by examining the reverse problem.

B. Depth to pressure conversion

The conversion of depth to pressure has been the subject of several publications. The first simple equation seems to have been proposed by Leroy[2] in 1968, for the purpose of calculating sound speed. The basic equation was applicable to the main oceans and reads for pressure above atmospheric:

$$P=0.102\,506(1+5.28\times10^{-3}\sin^2\phi)Z+2.524\times10^{-7}Z^2 \quad (13)$$

with P in kg/cm^2. Simple modified versions without the gravity term were proposed for the Black Sea and the Baltic Sea (the Sulu Sea had been forgotten). The development of these equations was carried out by solving

$$P=\int_0^Z \rho_{TSZ}\, g_{Z\phi}\, dZ \quad (14)$$

with linear approximations of ρ_{TSZ} and $g_{\phi Z}$. The first one was adjusted from graphs by Bialek[9] and a modified expression of gravity versus depth was used for the second. The resulting second degree expression in Z was integrated in closed form, with a third degree term that could be neglected.

Ten years later, in an attempt to revise the Del Grosso's[10] NRL II equation for the speed of sound in sea water, Lovett proposed for calculating pressure what he

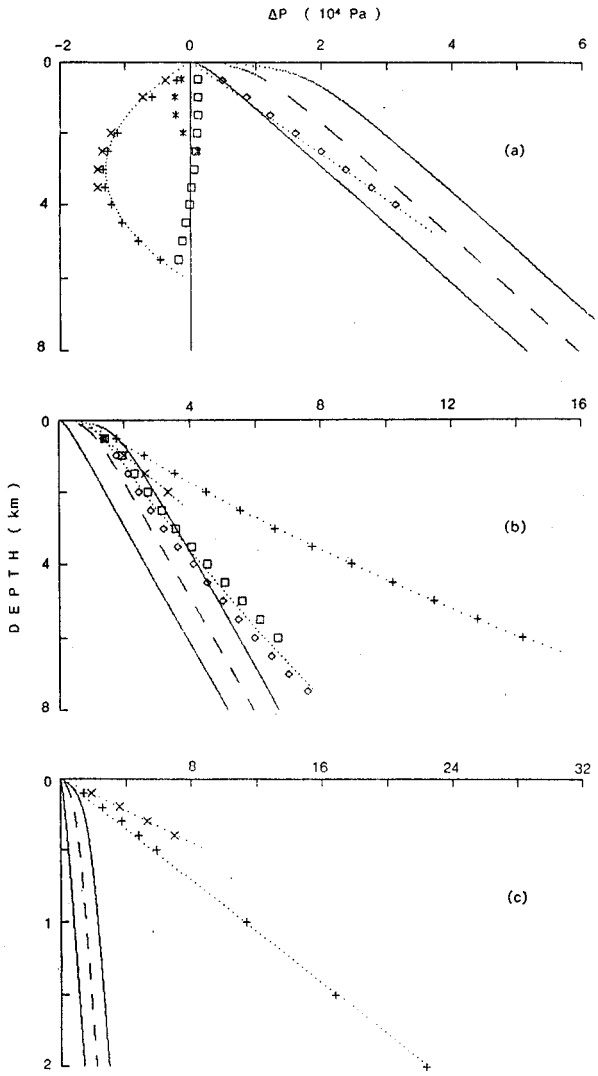

FIG. 2. Pressure corrections $\Delta P = \delta h_i(Z)$ to be subtracted from $h(Z,\phi)$ to account for the geopotential anomalies in the closed basins. (a) Miscellaneous: + Mediterranean Sea; × Red Sea; ◇ Sea of Japan; □ Arctic Ocean. (b) Indonesian basins: + Sulu Sea; × Halmahera basin; ◇ Weber deep; □ Celebes basin. (c) Low saline basins: + Black Sea; × Baltic Sea.

called a ''modified version of Leroy's simplified equation'' (Ref. 3, p. 1716). This reads, with P in dbar:

$$P = 1.005\,240\,5(1 + 5.28\times10^{-3}\sin^2\phi)Z + 2.36 \times 10^{-6}Z^2. \quad (15)$$

The conversion of Leroy's equation to use dbar instead of kg/cm^2 gives, in fact, exactly the same figures for the first degree term, and only the coefficient of the second degree term is different (2.475×10^{-6} instead of 2.36×10^{-6}).

In a paper published in 1981 Mackenzie[11] pointed out that most authors of publications about sound propagation did not mention the method they had employed to obtain pressure from depth in the unavoidable calculation of sound speed. He himself did not propose equations but employed a development that had long been used by oceanographers[12–14] based upon the resolution of Eq. (14) by summation over homogeneous layers. This method is summarized in Appendix A of Ref. 11, which gives all the necessary coefficients, but requires the introduction of T and S profiles.

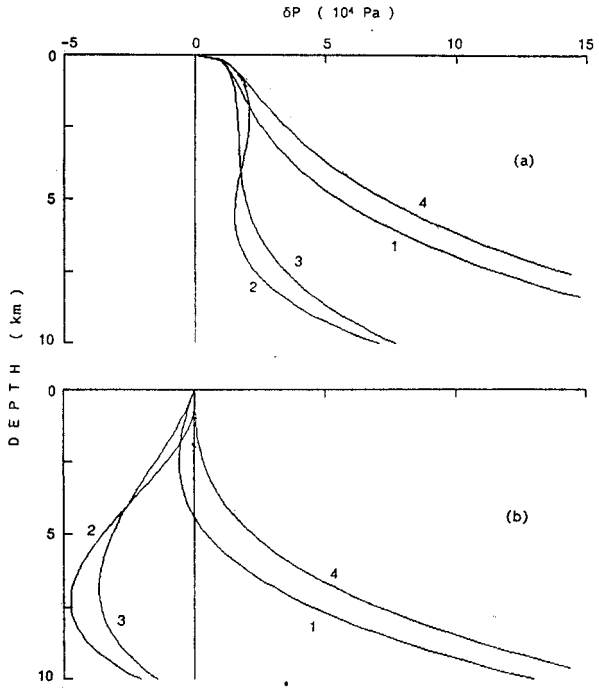

FIG. 3. Differences δP between pressure given by various equations and the present one [Eqs. (8)–(11)]. (a) With the corrective term for common oceans. (b) Without the corrective term. 1—Leroy 1968 (Ref. 2); 2—Bisset-Berman inverted (Ref. 8); 3—Lovett (Ref. 3); 4—Siess (Ref. 4).

A simplified equation to calculate pressure from depth and latitude was presented in 1982 by Siess[4] in an unpublished communication. With P in dbar it reads:

$$P = 1.0082Z(1 - 2.64\times10^{-3}\cos 2\phi + 2.45\times10^{-6}Z).$$

This equation in fact concerns the standard ocean, but Siess had compared it with that of Leroy for the common oceans. Purely by accident these two equations do not much differ once Leroy's is reformulated to use decibars and $\cos 2\phi$ instead of $\sin^2\phi$. This is why Leroy, in a review of sound speed in ''Neptunian'' waters written in 1988,[5] adopted without further investigation a compromise between his 1968 equation and that of Siess. It reads, with P in dbar:

$$P = 1.008Z(1 - 2.64\times10^{-3}\cos 2\phi + 2.45\times10^{-6}Z)$$

which, for comparison with Eq. (15), can be reformulated as

$$P = 1.005\,34(1 + 5.294\times10^{-3}\sin^2\phi)Z + 2.46 \times 10^{-6}Z^2.$$

C. Comparison of the results

The difference δP between the pressure calculated by the present Eqs. (8)–(11) taken as the reference, and those obtained from the equations of Leroy (1968), Lovett, Bisset-Berman (inverted), and Siess are illustrated in Fig. 3 for a latitude of 45°. Figure 3(a) corresponds to the common oceans situation, with the corrective term of Eq. (12). Figure 3(b) gives the differences obtained when Eqs. (8)–(11) are

applied without the corrective term, i.e., for the standard ocean. One can observe that there exists a definite discrepancy between the new equation and the simplified previous ones, in particular those of Leroy and Siess. This deserved more investigation.

We found that Siess had carried out his mathematical development in small quantities up to the third degree in Z, but had deliberately neglected the last term in his numerical application because it gave an accuracy of 0.2% which was considered sufficient for the computation of sound speed. By calculating and adding this last term, and by using one more significant figure in the coefficients of the previous ones, the equation of Siess can be reformulated, with P in dbar, as

$$P = 1.008\,18Z(1 - 2.64\times10^{-3}\cos 2\phi + 2.453\times10^{-6}Z - 1.3\times10^{-11}Z^2). \quad (16)$$

The results given by this modified equation are in much better agreement with those of our present equations [Eqs. (8)–(11)] for the standard ocean: the maximum differences between the calculated pressures are reduced from 1.4×10^5 Pa to $\pm2\times10^3$ Pa only at depth for all latitudes. As for Leroy's 1968 equation (developed in greater detail in a SACLANTCEN Report,[15] we discovered that its second degree term was extremely sensitive to the two simple linear aproximations used for density and gravity. The fit to the Bialek's data made in Ref. 2, Fig. 1, p. 652 reads, with density in g/cm^8: $\rho(Z) = 1.002\,74 + 2.4\times10^{-6}Z$. If we adopt instead the law $\rho(Z) = 1.0028 + 2.3\times10^{-6}Z$, not much difference can be seen of the figure! If, in addition, we use for the gradient of gravity with depth the classical value 2.2×10^{-6} (instead of 2.4×10^{-6}) the second degree term of Leroy, for P in dbar, becomes $2.367\times10^{-6}Z$, which differs from the original formulation ($2.475\times10^{-6}Z$ as seen above), and is much closer to that adopted by Lovett in Eq. (15). In all, we can conclude that the disagreements between the present equations and the original equations of Leroy and Siess are now fully explained.

To improve the motivation for publishing the present discussion we have compared our results with the various data presented by Mackenzie in his 1981 publication.[11] In Table AI, page 810, values of pressure versus depth in the Marianna trench are given down to 10 916 m. Equations (8)–(11) used with the common ocean corrective term gives, after transformation for units, the same values within ±0.05 kg/cm^2. Table I, page 809 in the same reference, presents a set of data from 15 locations covering the world, used by Mackenzie to establish the average variation of pressure with depth for building his proposed equation for sound speed. In this case the data are values of depth as a function of pressure. They have been compared with the results obtained from Eqs. (5)–(7) presented in Chapter I for the reverse problem and found in good agreement (better than ±0.9 m), but with one exception: (Point C) south of Alaska, where an unexpected departure of 1.6 m is observed. As the T and S profiles used by Mackenzie were not given, and as his calculation was based on less recent algorithms the observe differences may be understandable.

A final comment needs to be made about the exactness of the data used in this development to assess the accuracy claimed. The first concerns the equation of state of sea water, which needs to be exact, and the second concerns the oceanographic data. On that subject, a question that could be raised is the transformation of pressure into depth when the original measurements used for establishing the data banks had used pressure. Was the P to Z conversion, including the latitude effect, properly made? It would be worth investigating this point, but we think, considering the intermediate steps of our computation, that the errors introduced would most probably be of second order. To summarize, the set of corrective terms $\delta h_i(Z)$ or $\delta f_i(P)$ should not suffer from substantial errors, and little improvement could be expected from further work. The main terms for the standard ocean could easily be modified if a new equation of state were proved to be significantly more accurate.

IV. CONCLUSION

Based on the algorithm of Fofonoff and Millard (UNESCO 83), a simplified formulation for use in ocean engineering has been developed for converting pressure into depth in oceans and seas. Its general expression is:

$$Z = f(P,\phi) + \delta f_i(P),$$

where $f(P,\phi)$ stands for the standard ocean and $\delta f_i(P)$ is a simple corrective term applicable to a particular area. One main term can cover 80% of the world conditions, found in open oceans, with an accuracy better than ±0.8 m. Ten alternative terms are provided for special cases, including all closed basins, with accuracies better than ±0.2 m in most applications. This method enables to calculate depth within always better than ±1 m from pressure and latitude only, without having to perform XBT measurements or use data banks. The proper corrective term $\delta f_i(P)$ is selected according to the surveyed area.

Equations to obtain pressure from depth, for use in calculating sound speed, have been developed from the inversion of the $Z(P,\phi)$ equation for the standard ocean and calculations proper to the various areas studied in the previous section have been made. The general formulation is

$$P = h(Z,\phi) - \delta h_i(Z),$$

where $h(Z,\phi)$ is given by the set of equations [Eqs. (8)–(11)] and the $\delta h_i(Z)$ are given by Table II. The equations provide worldwide coverage with overall accuracies between ±500 Pa and ±8000 Pa. This corresponds to errors lower than ±0.02 m/s when calculating sound speed, which is appropriate with an accurate equation like that of Del Grosso.[10] It is believed, under the assumption that the Fofonoff and Millard algorithm for calculating pressure is exact, that the previous simplified equations giving pressure versus depth, like Leroy's in particular and even Lovett's, should now be abandoned.

ACKNOWLEDGMENTS

The presentation of the pressure to depth conversion by simple equations was sponsored by IFREMER through its

subsidiary GENAVIR. The work on the calculation of pressure from depth was supported by the LSM Department of the CTSN (DCN, French Navy, Toulon).

[1] S. Levitus, *Climatological Atlas of the World Ocean*, NOAA prof. Paper No. 13 (U.S. Government Printing Office, Washington, DC, 1982).
[2] C. C. Leroy, ''Formulae for the calculation of underwater pressure in acoustics,'' J. Acoust. Soc. Am. **44**, 651–653 (1968).
[3] J. R. Lovett, ''Merged seawater sound-speed equations,'' J. Acoust. Soc. Am. **63**, 1713–1718 (1978).
[4] IPA Siess, ''Relation entre pression et immersion dans l'océan,'' (relationship between pressure and depth in the ocean), Annex to letter 293 EPSHOM/E/OC (1982) (in French).
[5] C. C. Leroy, ''La vitesse du son dans les eaux neptuniennes—Synthèse et mise à jour'' (Speed of sound in Neptunian waters—Review and updating), Consultant Report for CERDSM No. ACS 88/02/03 (1988) (in French).
[6] N. P. Fofonoff and R. C. Millard, Jr., ''Algorithms for computation of fundamental properties of seawater,'' Unesco Tech. Papers in Mar. Sci., No. 44 (1983).
[7] H. U. Sverdrup, M. W. Johnson, and R. H. Fleming, ''The water masses and currents in the oceans,'' in *The Oceans—Their Physics, Chemistry, and General Biology* (Prentice-Hall, Englewood Cliffs, NJ, 1942, reissued 1970), Chap. XV, pp. 735–738.
[8] ''Instruction manual for salinity/temperature/depth/sound velocity measuring systems models 9040'' (Bisset Berman, San Diego, CA, 1971).
[9] E. L. Bialek, ''Handbook of oceanographic tables,'' U.S. Naval Ocean Office, SP-68 (1966).
[10] V. A. Del Grosso, ''New equation for the speed of sound in natural waters (with comparisons to other equations),'' J. Acoust. Soc. Am. **56**, 1084–1091 (1974).
[11] K. V. Mackenzie, ''Nine-term equation for sound speed in the oceans,'' J. Acoust. Soc. Am. **70**, 807–812 (1981).
[12] N. P. Fofonoff and C. Froese, ''Program for oceanographic computations and data processing on the electronic computer ALWAC III-E,'' Fish. Res. Board of Canada, Rep. 25 (1958).
[13] N. P. Fofonoff and S. Sabata (same title as above), Fish. Res. Board of Canada, Rep. 27 (1958).
[14] H. E. Sweers, ''A comparison of methods used to calculate sigma-T, specific volume anomaly and dynamic height,'' J. Marine Tech. Soc. **5**, 7–26 (1971).
[15] C. C. Leroy, ''A universal formula for the calculation of underwater pressure in acoustic studies,'' SACLANT ASW Research Centre Technical Report No. 108 (1968).

Three-dimensional wave propagation through single crystal solid–liquid interfaces

Yichi Lu[a] and Haydn N. G. Wadley
Intelligent Processing of Materials Laboratory, School of Engineering and Applied Science, University of Virginia, Charlottesville, Virginia 22903

(Received 18 April 1997; accepted for publication 22 October 1997)

Large differences in the ultrasonic velocity of the solid and liquid phases of semiconductors have stimulated an interest in the use of laser ultrasonic methods for locating and characterizing solid–liquid interfaces during single crystal growth. A previously developed two-dimensional ray tracing analysis has been generalized and used to investigate three-dimensional ultrasonic propagation across solid–liquid interfaces in cylindrical bodies where the receiver is located at an arbitrary position relative to the source. Numerical simulations of ultrasonic ray paths, wavefronts, and time of flight have indicated that ultrasonic sensing in the diametral plane is a preferred sensing configuration since the transmitted, reflected, and refracted rays all propagate in this plane, significantly simplifying analysis of the results. While other sensing configurations can also provide information about solid–liquid interfaces, they require a more complicated analysis because the planes in which reflected and refracted rays propagate are not known *a priori*, and fewer ray paths are accessible for interface interrogation because of large refractions. © *1998 Acoustical Society of America.* [S0001-4966(98)00203-3]

PACS numbers: 43.35.Bf [HEB]

INTRODUCTION

The Bridgman growth of single crystal semiconductor materials with low thermal conductivity often results in poor crystal quality and a low yield of useful wafers for microelectronic, optoelectronic, or infrared detector applications.[1–6] The crystal quality is thought to be largely controlled by the velocity and curvature of the solid–liquid interface during the growth process. The best crystal quality usually results from a planar or slightly convex interface shape that propagates at a uniform slow rate along the axis of the boule. Thus sensing and control of the solid–liquid interface during crystal growth appears to be a key step toward improving crystal quality. In most systems of interest, large decreases in ultrasonic velocity accompany melting. The large difference in the ultrasonic velocity between the solid and the liquid phases of most semiconductor materials, together with the recent emergence of noninvasive laser ultrasonics, have stimulated an interest in using ultrasonics to monitoring solid–liquid interfaces during single crystal growth.[7–9]

In previous work,[10] the severe ray bending associated with the large velocity change at liquid–solid interfaces has been shown to require a detailed ray tracing analysis to use ultrasonic time of flight (TOF) projection data for characterizing a solid–liquid interface. Using a two-dimensional analysis, a detailed study of ray paths, wavefronts, and TOF of ultrasound signals propagating on either the transverse or diametral planes of liquid single crystal solid bodies was reported. Numerical simulations indicated that the magnitude and direction of the group velocity, the solid–liquid velocity ratio, and the curvature of the interface together controlled the ray bending behavior, and thus determined ultrasonic paths across the interface. These theoretical studies indicated that when the ray paths through an interface could be computed, the interface location and curvature could be reconstructed from sparse ultrasonic TOF data collected on the diametral plane. Laser ultrasonic experiments conducted on benchtop models have recently confirmed that the interface location and curvature can indeed be reconstructed from the measured TOF data using a simple nonlinear least squares algorithm, an axisymmetric interface model, and the ray tracing algorithm, developed in Ref. 10.[11]

The sensor configurations explored to date have been constrained by our limited understanding of wave propagation at anisotropic solid–liquid interfaces. The availability of only 2-D wave propagation algorithms required the placement of sources and receivers on the transverse or diametral plane where both the transmitted and refracted rays must propagate. Here, we generalize the 2-D wave propagation analysis to 3-D, and allow the receiver to be located at arbitrary positions relative to the source. Similar to our previous work[10] we study only the (fastest) quasilongitudinal wave mode. The diffracted rays have been studied in our previous work. We employ a matrix/vector approach for the 3-D ray tracing analysis that has previously been developed for isotropic materials.[12] The key step in analyzing the 3-D wave propagation in anisotropic materials is shown to be the determination of the usually unknown plane in which both the reflected and transmitted rays propagate. With this plane determined, the procedure for constructing elastic stiffness tensors and the Christoffel equations that govern wave propation velocity in the local coordinate systems of the interface then become the same as the 2-D case.[10] Numerical simulations of ray paths, wavefronts, and TOF are presented for both convex and concave interface shapes with the ultrasonic source/receiver located either above or below the interface. It

[a]Now at Southwest Research Institute, NDE Science and Technology Division, 6220 Culebra Road, San Antonio, TX 78228-0510.

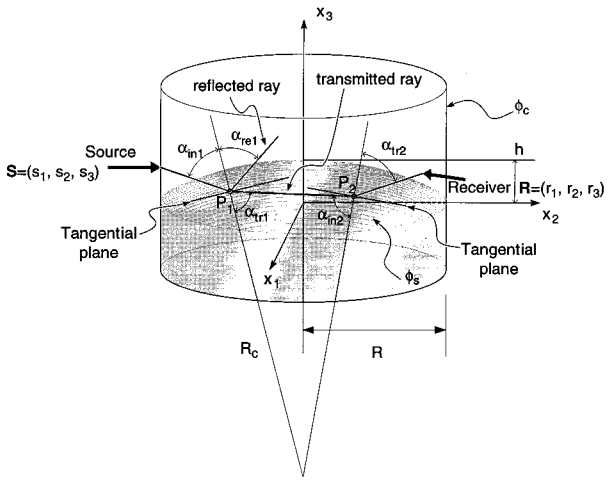

FIG. 1. An illustration of 3-D ray tracing in a single crystal solid–liquid body.

will be shown that rays traveling in nondiametral planes can be used for interface sensing. However, because the plane in which the reflected and transmitted rays propagate is not known beforehand (and needs to be determined at each intersection point of the ray path with the interface), analysis of TOF data is considerably more complex. When diametral plane access is available, it appears to be the preferred approach for sensing axisymmetric interfaces.

I. RAY PATH ANALYSIS

Consider a circular crystal cylinder of radius R (Fig. 1). The axis of the cylinder is chosen to coincide with the x_3 axis of our coordinate system. Following Shah[12] the outer boundary surface of the cylinder, ϕ_c, can be expressed as:

$$\phi_c = \mathbf{x}^T \mathbf{A}_c \mathbf{x} - c_c = 0, \tag{1}$$

where $\mathbf{x}=(x_1, x_2, x_3)$, and

$$\mathbf{A}_c = \begin{bmatrix} 1 & 0 & 0 \\ 0 & 1 & 0 \\ 0 & 0 & 0 \end{bmatrix}, \quad c_c = R^2. \tag{2}$$

We assume that the solid–liquid interface is a spherical cap with a radius, R_c, centered on the x_3 axis. The intersection of the solid–liquid interface and the cylinder lies in the x_1-x_2 plane. Thus the interface is symmetric with respect to both the x_1-x_3 and the x_2-x_3 planes. The interface, ϕ_s, can be expressed as:

$$\phi_s = \mathbf{x}^T \mathbf{A}_s \mathbf{x} + \mathbf{B}_s^T \mathbf{x} + c_s = 0, \tag{3}$$

where

$$\mathbf{A}_s = \begin{bmatrix} 1 & 0 & 0 \\ 0 & 1 & 0 \\ 0 & 0 & 1 \end{bmatrix}. \tag{4}$$

For convex interfaces,

$$\mathbf{B}_s = \begin{bmatrix} 0 \\ 0 \\ 2(R_c - h) \end{bmatrix}, \quad c_s = h^2 - 2R_c h, \quad h > 0. \tag{5}$$

For concave interfaces,

$$\mathbf{B}_s = \begin{bmatrix} 0 \\ 0 \\ -2(R_c + h) \end{bmatrix}, \quad c_s = h^2 + 2R_c h, \quad h < 0. \tag{6}$$

In Eqs. (5) and (6), h defines the interface convexity (Fig. 1). The interface is flat when $h=0 (c_s=0)$. In terms of the cylinder radius, R, and the convex interface convexity, h, the interface radius of curvature R_c, can be expressed as:

$$R_c = \frac{R^2 + h^2}{2h}. \tag{7}$$

We let $\mathbf{S}$ be a prescribed source point, and $\mathbf{l}$ be the initial ray direction vector pointing from the source point, $\mathbf{S}$. $\mathbf{P}_1$ and $\mathbf{P}_2$ are then the first and the second intersection points of a general ray path propagating through the interface to a receiver point R; $\mathbf{t}_1$ and $\mathbf{r}_1$ are then the transmitted and reflected ray direction vectors at $\mathbf{P}_1$, while $\mathbf{t}_2$ is the transmitted ray direction vector at $\mathbf{P}_2$. Thus

$$\mathbf{P}_1 = \mathbf{S} + L_1 \mathbf{l}, \tag{8}$$

where L_1 is the distance from $\mathbf{S}$ to $\mathbf{P}_1$.

Since $\mathbf{P}_1$ is on the interface, it satisfies Eq. (3):

$$\mathbf{P}_1^T \mathbf{A}_s \mathbf{P}_1 + \mathbf{B}_s^T \mathbf{P}_1 + c_s = 0. \tag{9}$$

Substituting Eq. (8) into Eq. (9) yields

$$L_1^2 (\mathbf{l}^T \mathbf{A}_s \mathbf{l}) + L_1 (2\mathbf{S}^T \mathbf{A}_s \mathbf{l} + \mathbf{B}_s^T \mathbf{l}) + (\mathbf{S}^T \mathbf{A}_s \mathbf{S} + \mathbf{B}_s^T \mathbf{S} + c_s) = 0. \tag{10}$$

Equation (10) yields two roots for L_1. When both roots are complex, the ray path does not intersect the interface; when both roots are real and positive the smaller one is the correct solution for L_1; when one root is positive and the other is negative, the positive one is the solution for L_1 (the negative root is for the ray traveling in the opposite direction with respect to $\mathbf{l}$); when both roots are real and negative, then the ray travels away from the interface (it does not intersect the interface).

The normal, $\mathbf{N}_1=(n_1, n_2, n_3)$, at $\mathbf{P}_1$ to the interface can be obtained from the gradient of the interface:

$$\mathbf{N}_1 = \frac{\nabla \phi_s}{\sqrt{(\nabla \phi_s)^T (\nabla \phi_s)}}, \tag{11}$$

where

$$\nabla \phi_s = 2\mathbf{A}_s \mathbf{P}_1 + \mathbf{B}_s \tag{12}$$

is the gradient of the interface at $\mathbf{P}_1$. The normal of the interface, $\mathbf{N}_1$, is chosen such that it always points into the liquid $(n_3 > 0)$.

The incident angle α_{in1} at $\mathbf{P}_1$ to the interface can now be expressed as:

$$\cos \alpha_{in1} = -\mathbf{l} \cdot \mathbf{N}_1. \tag{13}$$

To determine the plane in which reflected and transmitted rays propagate, we notice that when a ray is incident upon an interface, both the reflected and transmitted rays

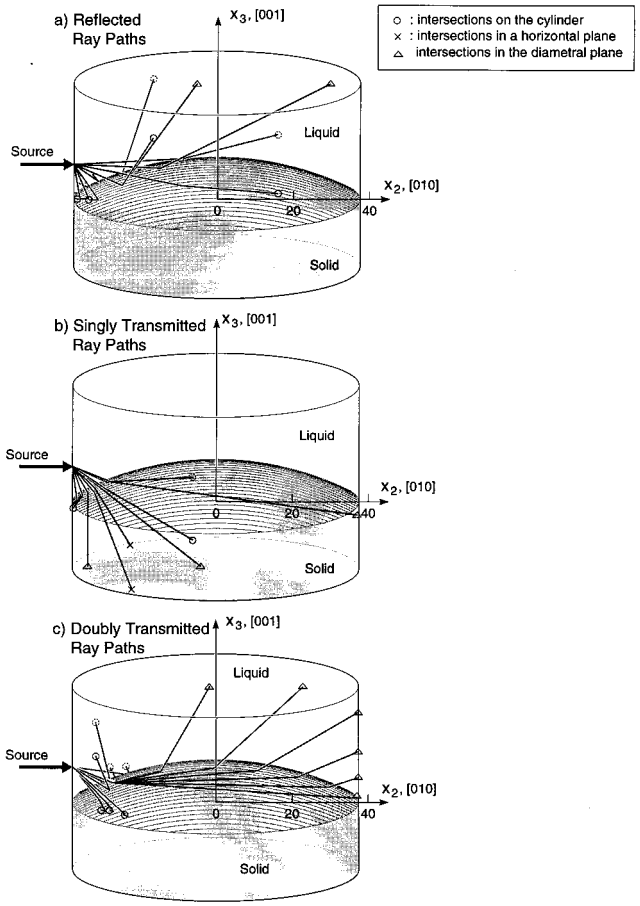

FIG. 2. Ray paths for a convex interface, $h=15$ mm, $s_3=15$ mm. (a) Reflected ray paths; (b) singly transmitted ray paths; (c) doubly transmitted ray paths.

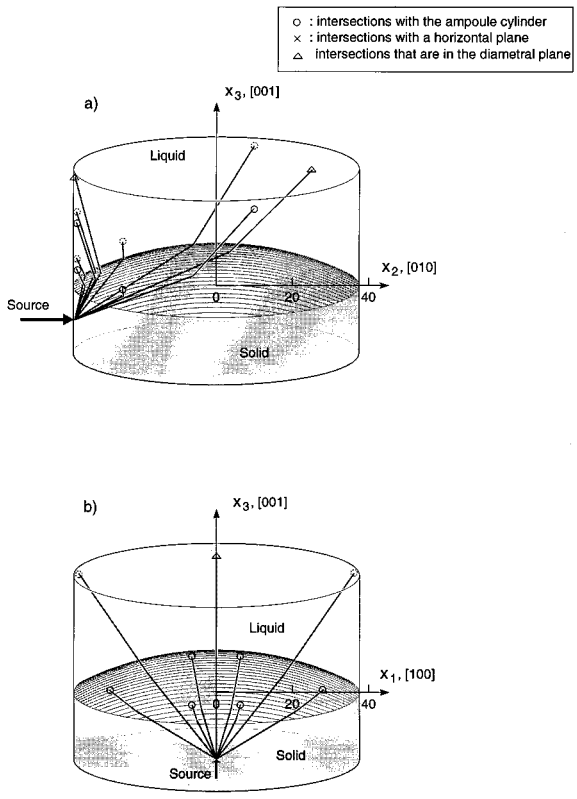

FIG. 3. Transmitted ray paths for a convex interface, $h=15$ mm, $s_3=-15$ mm. (a) The viewing direction is parallel to the x_1 axis; (b) the viewing direction is parallel to the x_2 axis.

propagate in the plane defined by the incident vector, **l**, and the normal to the interface, $\mathbf{N}_1$, at the intersection point $\mathbf{P}_1$.[13–19] If **r** is an arbitrary vector in the plane, this plane is given as:

$$(\mathbf{r}-\mathbf{P}_1)\cdot(\mathbf{l}\times\mathbf{N}_1)=0, \tag{14}$$

where $(\mathbf{l}\times\mathbf{N}_1)$ is the normal to the plane at $\mathbf{P}_1$.

To determine the reflected and transmitted ray paths emitting from $\mathbf{P}_1$ and propagating in the plane defined by Eq. (14), we first need to determine an expression for the stiffness tensor in the plane. We introduce a local coordinate system (x_1',x_2',x_3') in which the x_2' axis is in the $\mathbf{N}_1$ direction, the x_3' axis is in the $(\mathbf{l}\times\mathbf{N}_1)$ direction, and the x_1' axis is in the direction defined by $[\mathbf{N}_1\times(\mathbf{l}\times\mathbf{N}_1)]$ which is tangential to the interface. Using the directional cosines between (x_1,x_2,x_3) and (x_1',x_2',x_3') the expression of the stiffness tensor in the local (x_1',x_2',x_3') coordinate system can now be obtained following the procedure described by Auld.[10,15] Knowing the plane in which the incident, reflected, and transmitted rays propagate and the expression of the elastic stiffness tensor in the local (x_1',x_2',x_3') coordinate system, the problem of determining the reflected and transmitted ray paths becomes 2-D, and can thus be solved using the procedures described in a previous publication.[10]

When the source point is in the liquid, the direction vectors of the transmitted rays in the solid, $\mathbf{t}_1$, and reflected rays in the liquid, $\mathbf{r}_1$, can be shown to be

$$\mathbf{t}_1=\frac{\nu_g}{\nu_l}\,\mathbf{l}+\left[\frac{\nu_g}{\nu_l}\cos(\alpha_{in1})-\cos(\alpha_{tr1})\right]\mathbf{N}, \tag{15}$$

$$\mathbf{r}_1=\mathbf{l}+2\cos(\alpha_{in1})\mathbf{N}_1, \tag{16}$$

where v_g is the magnitude of the group velocity in the solid, α_{tr1} is the refraction angle in the solid, Fig. 1. When the source point is in the solid, all rays intersecting the interface are transmitted into the liquid due to the smaller liquid velocity and the smaller refraction angle. The refraction direction vector in the liquid in this case is:

$$\mathbf{t}_1=\frac{\nu_l}{\nu_g}\,\mathbf{l}-\left[\frac{\nu_l}{\nu_g}\cos(\alpha_{in1})-\cos(\alpha_{tr1})\right]\mathbf{N}_1. \tag{17}$$

For a convex interface and a source point above the interface, a transmitted ray path may intersect the interface again at $\mathbf{P}_2$; the point $\mathbf{P}_2$ is obtained in exactly the same way as $\mathbf{P}_1$. This type of ray is called a doubly transmitted ray. When the source point is below a concave interface, there is only one intersection point on the solid–liquid interface due to the interface curvature and the smaller refraction angle in the liquid resulting from the smaller liquid velocity. The ray with a single intersection point on the interface is called singly transmitted ray. Using $\mathbf{t}_1$ and $\mathbf{r}_1$, the second intersection point $\mathbf{P}_2$ and the reflected ray point **R** leaving $\mathbf{P}_1$ can be written as

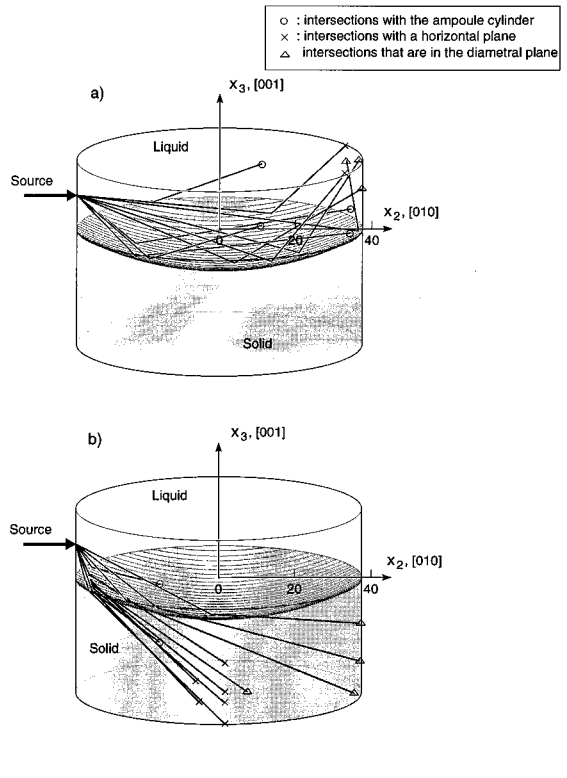

FIG. 4. Ray paths for a concave interface, $h=-15$ mm, $s_3=15$ mm. (a) Reflected ray paths; the viewing direction is parallel to the x_1 axis; (b) reflected ray paths; the viewing direction is parallel to the x_2 axis; (c) transmitted ray paths; the viewing direction is parallel to the x_1 axis; (d) transmitted ray paths; the viewing direction is parallel to the x_2 axis.

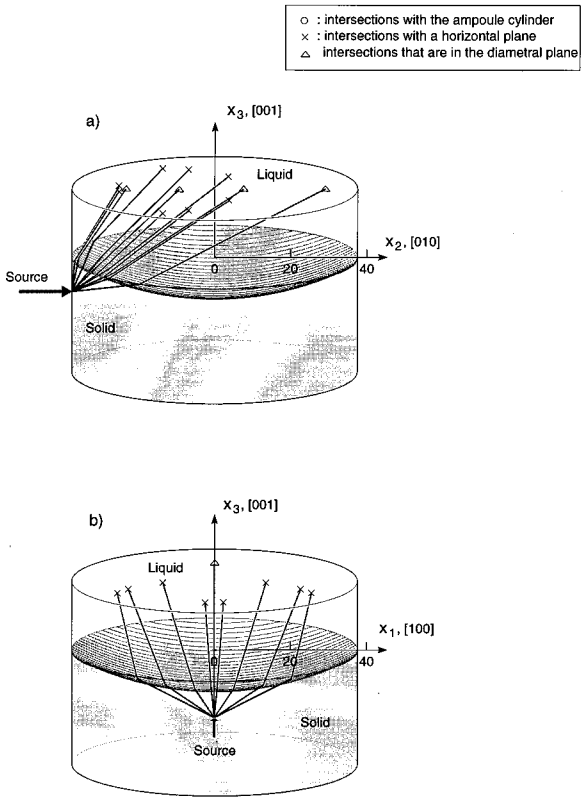

FIG. 5. Transmitted ray paths for a concave interface, $h=-15$ mm, $s_3=-15$ mm. (a) The viewing direction is parallel to the x_1 axis; (b) the viewing direction is parallel to the x_2 axis.

$$\mathbf{P}_2=\mathbf{P}_1+L_2\mathbf{t}_1, \quad \mathbf{R}=\mathbf{P}_1+L_R\mathbf{r}_1, \tag{18}$$

where L_2 is the distance from $\mathbf{P}_1$ to $\mathbf{P}_2$, L_R is the length of the reflected ray leaving $\mathbf{P}_1$.

When there is a second intersection point $\mathbf{P}_2$, the direction vector $\mathbf{t}_2$ for the transmitted ray at $\mathbf{P}_2$ is

$$\mathbf{t}_2=\frac{\nu_l}{\nu_g}\,\mathbf{t}_1-\left[\frac{\nu_l}{\nu_g}\cos(\alpha_{in2})-\cos(\alpha_{tr2})\right]\mathbf{N}_2, \tag{19}$$

where α_{in2} and α_{tr2} are the angles of the incident and transmitted rays, $\mathbf{N}_2$ is the normal to the interface at $\mathbf{P}_2$, Fig. 1. All rays eventually intersect the cylinder at $\mathbf{P}_3$. The distance between $\mathbf{P}_2$ and $\mathbf{P}_3$ when there is a second intersection point on the solid–liquid interface, or between $\mathbf{P}_1$ and $\mathbf{P}_3$ when there is no second intersection point, can be solved by substituting either $\mathbf{P}_2$ or $\mathbf{P}_1$ into Eq. (9) where $\mathbf{A}_s$ and c_s are replaced by $\mathbf{A}_c$ and c_c in Eq. (2), and $\mathbf{B}_s$ is set to be zero. The reflected ray path is then given by $\mathbf{S}$, $\mathbf{P}_1$, and $\mathbf{R}$, and the singly transmitted ray path by $\mathbf{S}$, $\mathbf{P}_1$, $\mathbf{P}_3$, while the doubly transmitted ray path is given by $\mathbf{S}$, $\mathbf{P}_1$, $\mathbf{P}_2$, and $\mathbf{P}_3$.

II. NUMERICAL IMPLEMENTATION

To numerically simulate wave propagation we use the material constants of germanium (Ge) because its elastic constants as functions of temperature are available for both the solid and the liquid. The analysis can easily be extended to any anisotropic material (cubic or noncubic) with known elastic properties. We use the values of elastic stiffness constants, c_{ij}, of Ge at 900 °C (Ref. 20) to represent the solid.

$$c_{11}=108.45 \text{ GPa}, \quad c_{12}=108.45 \text{ GPa}, \quad c_{44}=108.45 \text{ GPa}. \tag{20}$$

At this temperature the solid density $\rho=5.26$ g/cm^3.[21] The sound velocity in the liquid (at a temperature just above the Ge melting temperature of 937 °C) is taken to be 2.71 mm/μs.[22] In all cases $R=37.5$ mm.

To analyze a representative convex interface shape, we take $h=15$ mm. For a source point above the interface at $(0,-R,15 \text{ mm})$, Fig. 2(a), (b), and (c) shows reflected, singly transmitted, and doubly transmitted ray paths. When the initial ray directions, $\mathbf{l}$, are in the diametral plane, all ray paths remain in the plane. When the initial ray directions are not in the diametral plane the reflected and transmitted rays travel away from the diametral plane. This arises because when the source point is in the liquid, the convex liquid–solid interface acts as a divergent lens to ray paths (see Fig. 6 of Ref. 10 for rays traveling in the 2-D transverse plane of a liquid cylinder containing a solid core). Notice that most forward propagating doubly transmitted ray paths are in the diametral plane with a narrow incident angle region; the doubly transmitted rays that do not propagate in the diametral plane propagate backward due to severe ray bending.

The singly transmitted ray paths for the same convex interface but with a source located below the interface at $(0,-R,-15)$ are shown in Fig. 3(a) and (b). For this configuration, all rays that intersect the interface are refracted into the liquid due to the smaller liquid velocity. No doubly

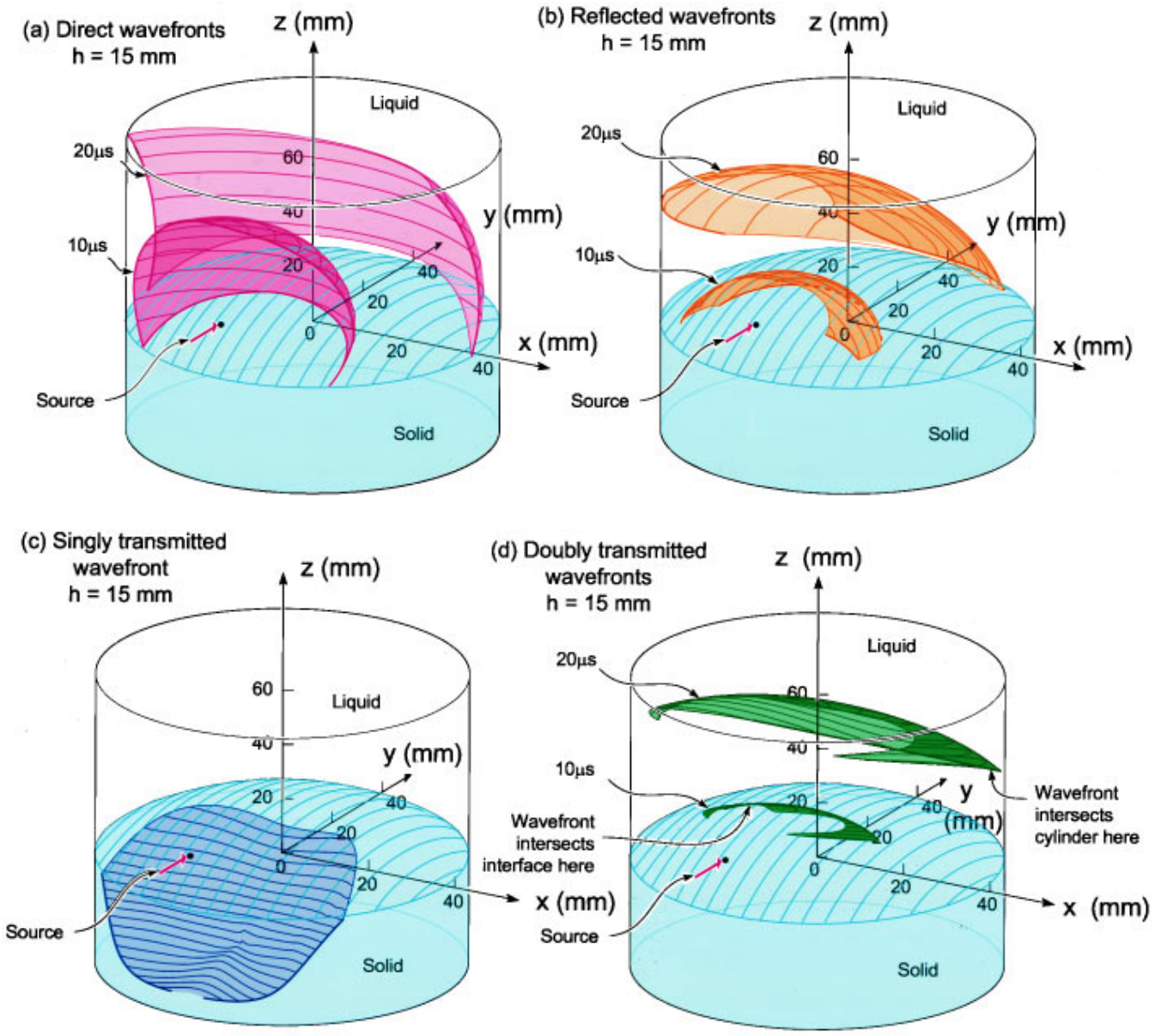

FIG. 6. Wavefronts for a convex interface, $h=15$ mm, $s_3=15$ mm. (a) Direct wavefronts; (b) reflected wavefronts; (c) singly transmitted wavefront; (d) doubly transmitted wavefronts. Thick lines are intersections of wavefronts with either the solid–liquid interface or the ampoule's cylindrical surface.

transmitted ray paths exist for this configuration. Rays are seen to again travel in the diametral plane when the initial ray direction vector is also in the diametral plane. When the initial ray directions are not in the diametral plane, the ray paths are bent by the interface toward the diametral plane, similar to rays traveling in the transverse plane of a solid cylinder containing a liquid core (see Fig. 5 of Ref. 10).

Figure 4(a) and (b) shows reflected and singly transmitted ray paths, for a concave interface with $h=-15$ mm and a source point above the interface at $(0,-R,15\ \text{mm})$. The reflected ray paths travel toward the diametral plane due to the interface curvature, while the transmitted ray paths are bent away from the diametral plane due to the larger refraction angle in the solid. When the source point is below the interface at $(0,-R,-15\ \text{mm})$ [Fig. 5(a) and (b)] the transmitted ray paths are bent toward the diametral plane due to the smaller refraction angle in the liquid. There are no doubly transmitted rays since all rays that intersect the interface are refracted into the liquid due to the smaller refraction angle in the liquid.

With the ray paths fully analyzed, we can draw several important conclusions concerning optimal laser ultrasonic sensing configurations. When the initial ray directions are in the diametral plane and the interface curvature is symmetric with respect to the plane, rays always travel in the diametral plane. Thus the plane in which reflected and transmitted rays travel is known *a priori* and it is straightforward to then determine the ray path between prescribed source and receiver points. When the initial ray directions are not in the diametral plane, the planes in which reflected and transmitted rays travel are not known beforehand and must be determined in order to obtain the reflected and transmitted ray paths. The orientation of the plane *depends on the interface curvature and the incident ray direction vector and is not*

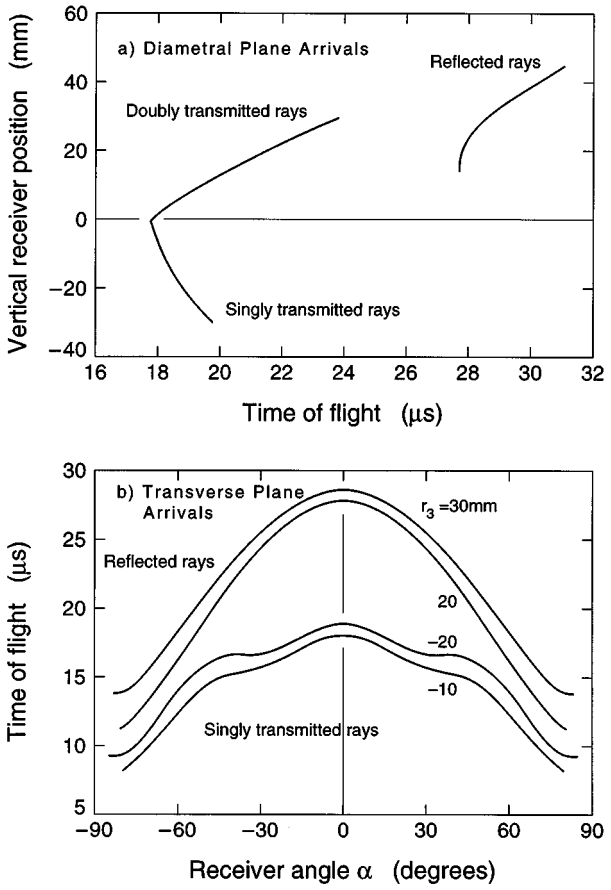

FIG. 7. Time of flight projection data for a convex interface, $h=15$ mm, $s_3=15$ mm. (a) Diametral reflected, singly transmitted, and doubly transmitted ray paths as functions of the vertical receiver coordinate, r_3; (b) circumferential reflected and singly transmitted ray paths as functions of the receiver angle α.

known a priori. The bending of rays occurs near the solid–liquid interface and, for interface reconstruction purposes, this is easier to account for in the diametral plane than in other planes. Thus for ultrasonic characterization of a solid–liquid interface, positioning the ultrasonic source and receiver in the diametral plane should always be the preferrable sensor approach. There are no fundamental difficulties to using ray paths in nondiametral planes for interface sensing; it is just a more complex and time consuming task. In fact, the very large refractions in nondiametral plane configurations imply a high sensitivity to the exact interface geometry, and so this off-diametral approach might be pursued if additional curvature reconstruction accuracy were needed.

III. WAVEFRONT SURFACES

Ultrasonic signals can be detected only at points where the wavefronts intersect the crystal surface. Wavefronts are obtained by connecting points along ray paths with the same traveling time. Here we only show wavefronts for a convex interface shape, $h=15$ mm, where the source point is above the interface at $(0,-R,15)$. Figure 6(a) shows the wavefronts for the direct rays in the liquid. The wavefronts are spherical, centered at the source point since the liquid velocity is isotropic. Notice that the bottom edge of the wavefront after 20μs of propagation does not touch the interface due to the screening effect of the interface. Figure 6(b) shows wavefronts for the reflected rays that are reflected by the solid–liquid interface into the liquid region. Notice that the reflected wavefront at 10 μs intersects the ampoule cylinder at only two small separate sections. The wavefront for singly transmitted rays after 10 μs propagation is shown in Fig. 6(c). It has a ridge shaped area below the source, which is due to the smaller group velocity on the (100) crystal plane of this cubic material. Due to the high velocity in the solid, the singly transmitted wavefront at 20 μs has propagated out of the region shown in Fig. 6(c). The doubly transmitted wavefronts are shown in Fig. 6(d). These wavefronts have larger y values than the corresponding wavefronts for the reflected rays because the doubly transmitted rays have traveled a significant distance in the solid which has a higher velocity than the liquid. The relatively thick middle portion and the thin wings of the wavefronts in Fig. 6(d) indicate that the region where it is possible to detect the doubly transmitted rays is greater near the diametral plane.

IV. TIME OF FLIGHT PROJECTIONS

To use ultrasonic TOF data for interface characterization, we are interested in ray paths that intersect the solid–liquid interface and thus carry information about the interface. To illustrate, we study the four following situations.

A. A convex interface, $h=15$ mm, and source point above interface at $(0,-R,15)$

Figure 7(a) and (b) shows the diametral and transverse plane TOF projection results, respectively. In Fig. 7(b) the receiver angle, α, corresponds to the angle of deviation from the diametral plane projected onto the transverse plan (see Fig. 4 of Ref. 10 for additional details). The reflected, singly transmitted, and doubly transmitted signals can all be detected in the diametral plane [Fig. 7(a)]. The TOF data for the reflected ray paths increase with the vertical receiver position due to the longer propagation distance and the smaller liquid velocity. TOF values of both the singly and doubly transmitted ray paths increase with the vertical distance between the source and the receiver. The minimum TOF value for the transmitted ray paths is reached when the receiver point meets the interface at $r_3=0$.

Most doubly transmitted rays travel in the diametral plane [Fig. 2(c)] therefore a circumferential scan of the receiver around the crystal cylinder is unlikely to detect doubly transmitted signals except near the diametral plane. In the transverse planes reflected and singly transmitted TOF data increase with reducing $|\alpha|$ because of the longer propagation distance. TOF values for the reflected ray paths increase as the receiver point is raised. Those for the singly transmitted ray paths decrease as the receiver point is moved closer to the interface.

B. A convex interface, $h=15$ mm, and source point below interface at $(0,-R,-15)$

Diametral and transverse plane TOF projection data are shown in Fig. 8(a) and (b). These are no doubly transmitted

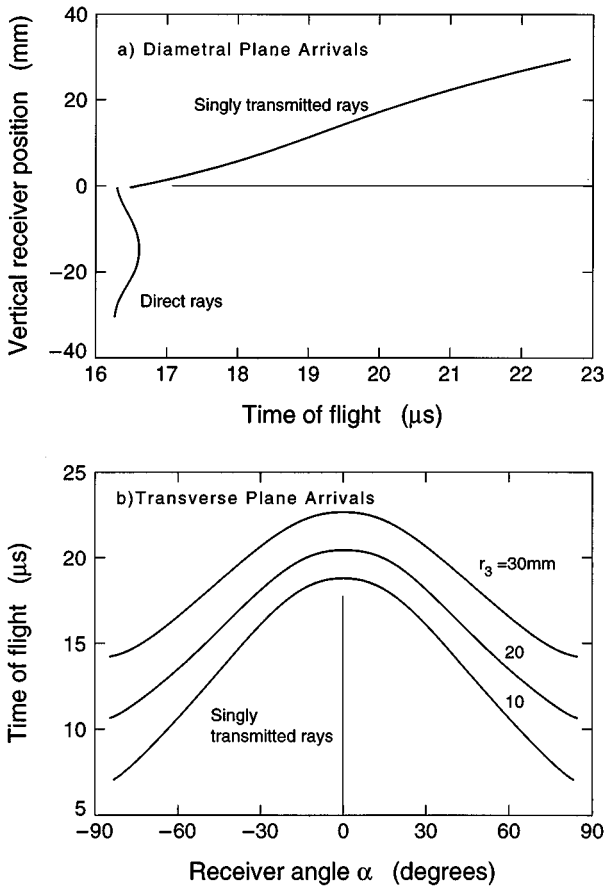

FIG. 8. Time of flight projection data for a convex interface, $h=15$ mm, $s_3=-15$ mm. (a) Direct and singly transmitted ray paths as functions of the vertical receiver coordinate, r_3; (b) singly transmitted ray paths as functions of the receiver angle α.

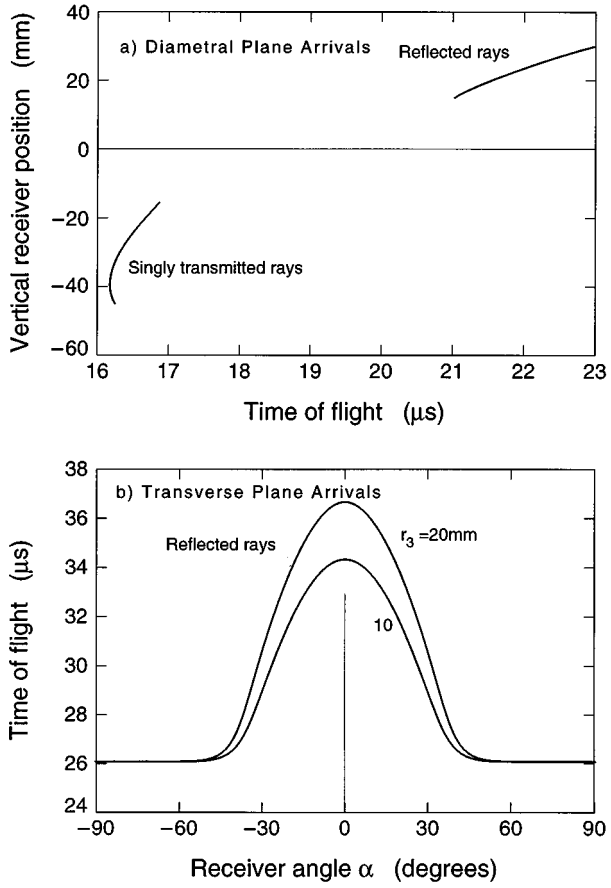

FIG. 9. Time of flight projection data for a concave interface, $h=-15$ mm, $s_3=15$ mm. (a) Diametral reflected and singly transmitted ray paths as functions of the vertical receiver coordinate, r_3; (b) reflected ray paths as functions of the receiver angle α.

ray paths as discussed above. In the diametral plane when the receiver is below the interface, only the TOF for the direct ray paths can be detected, and its behavior is fully described by the group velocity on this {100} plane.[10] The TOF values for the transmitted ray paths increase with the vertical receiver position due to the longer propagation distances and a smaller liquid velocity. By comparing the diametral TOF data between Fig. 7(a) and Fig. 8(a) we see that the location of the convex interface with respect to the source point can be readily determined by translating the receiver point in the diametral plane. The transmitted transverse plane TOF data are similar to those of Fig. 7(b) when the source is above the interface but the TOF values are smaller.

C. A concave interface, $h=-15$ mm, and source point above the interface at $(0,-R,15)$

Diametral and transverse plane TOF projection data are shown in Fig. 9(a) and (b). The diametral reflected rays can be detected only when $r_3>s_3$ due to the interface curvature [Fig. 4(a)] while the transmitted rays can be detected only when $r_3<-15$ mm due to the large refraction angle in the solid [Fig. 4(b)]. However, except for the rays in the diametral plane, the transmitted rays intersect the outer sample surface well below the interface (due to the interfaces curvature), and so only the circumferential TOF data for reflected rays are shown in Fig. 9(b). They have a steep hump near $\alpha=0$. It is clear by comparing Fig. 7 with Fig. 9 that the interface is convexity, or concave can be easily determined either from the diametral or circumferential TOF data.

D. A concave interface, $h=-15$ mm, and source point below interface at $(0,-R,-15)$

Diametral and transverse plane TOF projection data are shown in Fig. 10(a) and (b). The diametral plane TOF for the direct ray paths can be detected only when $r_3>s_3$, due again to the screening effect of the interface. The diametral TOF of transmitted ray paths can be detected only when $r_3>36$ mm because of the smaller refracted angle in the liquid [Fig. 5(a)]. By comparing the diametral TOF data in Figs. 8(a) and 10(a), we see again that the interface convexity can be determined from the diametral TOF data alone due to the different functional behavior of the projection data sets at $a=0$.

In Fig. 10(b) the maximum in the TOF data for the direct ray paths is caused by the anisotrophy of the solid velocity and the change in ray propagation distance as rays are swept from the $-x_1$ to the x_2 direction (Fig. 1). The small differences in the $r_3=-20$ and -30 mm data are also a consequence of the solid velocity anisotrophy. By comparing Fig. 10(b) with Fig. 8(b), it can again be seen that the interface convexity can be determined from transverse plane projections when the source point is below the interface.

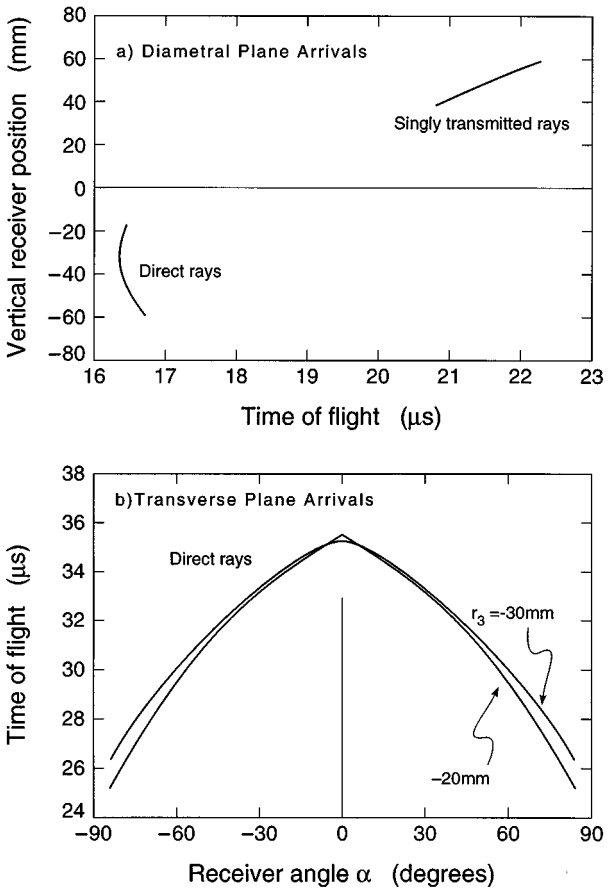

FIG. 10. Time of flight projection data for a concave interface, $h=-15$ mm, $s_3=-15$ mm. (a) Direct and singly transmitted ray paths as functions of the vertical receiver coordinate, r_3; (b) direct ray paths as functions of the receiver angle α.

An inspection of TOF data in Figs. 7, 8, 9, and 10 also indicates that a greater diversity of ray paths (i.e., reflected, singly/doubly transmitted) can be detected near the interface in the diametral plane than in other nondiametral planes, indicating again that ultrasonic sensing in the diametral plane is likely to be the preferred sensing configuration.

V. CONCLUSIONS

A method has been developed for the calculation of three-dimensional ray paths, wavefront shapes, and TOF values during ultrasonic propagation through cylindrical single crystal solid–liquid bodies. It has been demonstrated that both the interface location and convexity strongly influence ultrasonic TOF projection data. Positioning sensors near the diametral plane is the preferred sensing configuration for solid–liquid interface sensing because: (1) the plane in which reflected and transmitted rays propagate is known beforehand; and (2) more ray paths (reflected, transmitted, etc.) are available in this plane for interface reconstruction purposes. There is no fundamental difficulty in using ray paths in other nondiametral planes; it is just more complicated and fewer ray paths are available for interface reconstruction. The TOF projection data and different interface curvatures are distinctively different for different interface curvatures, providing a promising real time direct method for solid–liquid interface characterization during the vertical Bridgman single crystal growth.

ACKNOWLEDGMENTS

This work has been performed as a part of the research of the Infrared Materials Producibility Program conducted by a consortium that includes Johnson Matthey Electronics, Texas Instruments, II-VI Inc., Loral. the University of Minnesota, and the University of Virginia. We are grateful for the many helpful discussions with our colleagues in these organizations. The consortium work has been supported by ARPA/CMC under Contract No. MD A972-91-C-0046 monitored by Raymond Balcerak.

[1] M. C. Flemings, *Solidification Processing* (McGraw-Hill, New York, 1974).
[2] T. Fu and W. R. Wilcox, ''Influence of insulation on stability of interface shape and position in the vertical Bridgman–Stockbarger technique,'' J. Cryst. Growth **48**, 416–424 (1980).
[3] M. Pfeiffer and M. Mühlberg, ''Interface shape observation and calculation in crystal growth of CdTe by the vertical Bridgman method,'' J. Cryst. Growth **118**, 269–276 (1992).
[4] P. Rudolph and M. Mühlberg, ''Basic problems of vertical Bridgman growth of CdTe,'' Mater. Sci. Eng. B **16**, 8–16 (1993).
[5] S. Brandon and J. J. Derby, ''Internal radiative transport in the vertical Bridgman growth of semitransparent crystals,'' J. Cryst. Growth **110**, 481–500 (1991).
[6] S. Kuppurao, J. J. Derby, and S. Brandon, ''Modeling the vertical Bridgman growth of cadmium zinc telluride. I. Quasi-steady analysis of heat transfer and convection,'' J. Cryst. Growth **155**, 93–102 (1995).
[7] R. L. Parker and J. R. Manning, ''Application of pulse-echo ultrasonics to locate the solid/liquid interface during solidification and melting,'' J. Cryst. Growth **79**, 341–353 (1986).
[8] C. K. Jen, Ph. de Heering, P. Sutcliffe, and J. F. Bussiere, ''Ultrasonic monitoring of the molten zone of single crystal germanium,'' Mater. Eval. **49**, 701–707 (1991).
[9] F. A. Mauer, S. J. Norton, Y. Grinberg, D. Pitchure, and H. N. G. Wadley, ''An ultrasonic method for reconstructing the two dimensional liquid–solid interface in solidifying bodies,'' Metall. Trans. B **22**, 467–473 (1991).
[10] Yichi Lu and Haydn N. G. Wadley, ''Two-dimensional wave propagation in cylindrical single-crystal solid–liquid bodies,'' J. Acoust. Soc. Am. **98**, 2663–2680 (1995).
[11] D. T. Queheillalt, Y. Lu, and H. N. G. Wadley, ''Ultrasonic sensing of the location and shape of a solid/liquid interface,'' J. Acoust. Soc. Am. **101**, 843–853 (1997).
[12] Pravin M. Shah, ''Ray tracing in three dimensions,'' Geophysics **38**, 600–604 (1973).
[13] F. I. Fedorov, *Theory of Elastic Waves in Crystals* (Plenum, New York, 1968).
[14] M. J. P. Musgrave, *Crystal Acoustics* (Holden-Day, San Francisco, 1970).
[15] B. A. Auld, *Acoustic Fields and Waves in Solids* (Krieger, Malabar, FL, 1990).
[16] E. G. Henneke, ''Reflection-refraction of a stress wave at a plane boundary between anisotropic media,'' J. Acoust. Soc. Am. **51**, 210–217 (1971).
[17] E. G. Henneke and G. L. Jones, ''Critical angle for reflection at a liquid–solid interface in single crystals,'' J. Acoust. Soc. Am. **59**, 204–205 (1976).
[18] A. Atalar, ''Reflection of ultrasonic waves at a liquid–solid interface,'' J. Acoust. Soc. Am. **73**, 435–440 (1983).
[19] S. I. Rokhlin, T. K. Bolland, and L. Adler, ''Reflection and refraction of elastic waves on a plane interface between two generally anisotropic media,'' J. Acoust. Soc. Am. **79**, 906–918 (1986).
[20] Yu. A. Burenkov and S. P. Nikanorov, ''Elastic properties of germanium,'' Sov. Phys. Solid State **12**, 1940–1942 (1971).
[21] V. M. Glasov, S. N. Chizhevskaya, and N. N. Glagoleva, *Liquid Semiconductors* (Plenum, New York, 1969).
[22] V. M. Glazov, A. A. Aivazov, and V. I. Timoshenko, ''Temperature dependence of the velocity of sound in molten germanium,'' Sov. Phys. Solid State **18**, 684–685 (1976).

Ultrasonic propagation in metal powder-viscous liquid suspensions

Frederick T. Schulitz, Yichi Lu,[a] and Haydn N. G. Wadley[b]
Intelligent Processing of Materials Laboratory, School of Engineering and Applied Science, University of Virginia, Charlottesville, Virginia 22903

(Received 1 March 1997; accepted for publication 11 November 1997)

The need to measure the volume fraction of metal powder during the slurry casting synthesis of metal matrix composites has stimulated a new interest in ultrasonic propagation in metal powder-viscous liquid suspensions. Using model slurries, a systematic series of ultrasonic tests have been conducted to experimentally identify the frequency dependent relationships between ultrasonic velocity/attenuation and the particle volume fraction, the suspending liquid's viscosity and the particle's shape. For slurries with the compositions and viscosities typical of those used in slurry casting, the velocity decreases and the attenuation increases with particle fraction. The data have been compared to predictions of the Harker–Temple hydrodynamic model for these systems. The velocity measurements were well predicted by the model with a difference between measured and predicted velocities of about 0.25%. The ultrasonic attenuation was underpredicted by this model in part by its use of a rule of mixtures and by its failure to incorporate the intrinsic absorption/scattering within the powder phase.
[S0001-4966(98)01003-0]

PACS numbers: 43.35.Bf [HEB]

INTRODUCTION

Metal matrix composites (MMCs) consisting of light, high melting temperature metals (such as titanium) reinforced with stiff, strong SiC or Al_2O_3 fibers are expanding the limits of engineering design.[1] They allow the synthesis of aerospace components with property profiles (i.e., combinations of specific modulus, strength, toughness, and creep rupture strength, etc.) that are unchievable with monolithic metal alloys or ceramics.[2] However, the insertion of these materials into many applications has been hindered by the limitations of current processing technologies which must avoid the aggressive chemical reactions between constituents that can lead to fiber-matrix interface damage, fiber dissolution, and a degradation of matrix and fiber properties.[3–7] The recent emergence of a continuous slurry (tape) casting technique[8–10] now promises a low cost, solid state synthesis route for MMC manufacture that completely eliminates liquid metal-ceramic fiber contact.

The attributes of the finished composite components fabricated using a slurry casting technique depend strongly on the characteristics of the initial slurry system. Thus particle volume fraction, particle size distribution, slurry viscosity, and slurry homogeneity can all affect macro-, meso-, and microscopic characteristics of composite components. For instance, a high particle loading in the slurry beneficially reduces macro-shape change during subsequent hot isostatic pressing, but at the expense of an increased slurry viscosity which decreases slurry infiltration of the fiber mat and results in the touching of fibers in completed components. Because local variations in particle fraction can also be harmful during the processing of MMC components, the best composites are obtained when particle volume fractions and slurry viscosities are constantly maintained near optimized values. This requires that the slurry system remains homogeneously mixed throughout the casting process. The ability to maintain a homogeneous, controlled particle loading is limited by many factors, including particle settling due to gravity clustering, and/or incomplete mixing, selective pick-up of particles during infiltration and solvent evaporation. It is believed that these problems could be controlled by on-line sensing of the slurries' composition.

Both ultrasonic velocity and attenuation measurements might enable *in situ* determination of the particle volume fraction, particle size distribution, slurry viscosity, and slurry homogeneity during slurry casting. When the ultrasonic wavelength is much longer than the particle size, a slurry can be approximated as an ultrasonically homogeneous medium. In this case, the ultrasonic velocity, $\nu = 1/\sqrt{\beta\rho}$ where β is its effective compressibility (the inverse of the bulk modulus), and ρ is its density.[11,12] Since the density of metal particles ($\sim 5\ \mathrm{kg\ m^{-3}}$) is greater than that of the liquid ($\sim 1.5\ \mathrm{kg\ m^{-3}}$), the overall density of such a slurry increases with the particle volume fraction. However, the effective compressibility of the suspension decreases with the particle volume fraction since the compressibility of solid particles (2×10^{-3}–$40\times10^{-3}\ \mathrm{m^2/GN}$) is much smaller than that of the liquid (0.2–$1.0\ \mathrm{m^2/GN}$). When the particle volume fraction is relatively low (say less than 40%), the increase in the overall density with particle fraction is more than offset by the decrease in overall compressibility, and the ultrasonic velocity decreases monotonically with the particle fraction. Since most slurries for tape casting have particle loadings of 25%–30% or less (otherwise they are too viscous to rapidly cast), the existence of a monotonic velocity-particle fraction

[a]Now at Southwest Research Institute, NDE Science and Technology Division, 6220 Culebra Road, San Antonio, TX 78228-0510.
[b]Author to whom correspondence should be addressed.

relation near these particle loadings could provide an ideal basis for ultrasonic particle volume fraction determination.

The ultrasonic attenuation coefficient also depends on the particle volume fraction. This dependence is thought to result from ultrasonic scattering by the particles, by acoustic energy dissipation in the viscous liquid near the particle surface and from heat conduction between the liquid and the solid particles.[13] The attenuation contributions of these processes are all likely to increase with particle loading and the liquid's viscosity. Thus the ultrasonic attenuation might also provide a way of sensing either particle volume fraction or the suspending liquid's viscosity (i.e., its composition). Thus both ultrasonic velocity and attenuation measurements might be of use for the on-line sensing of tape casting processes.[14]

Ultrasonic propagation models that involve a detailed analysis of particle loading effects are important both for interpreting ultrasonic measurements and for ensuring that all significant physical contributions have been properly considered in the design of a sensor. The development of predictive models for ultrasonic propagation in suspensions involves two steps: first the interaction between the surrounding viscous liquid and a *single* solid particle is solved and then the *collective* effects of a volume of particles on ultrasonic propagation are determined. Good predictive models for the ultrasonic velocity in suspensions have been developed for wavelength regions that are much larger than the particle size.[15] McClements and Povey[16] have recently completed a comprehensive review of the other models. It should be noted that ultrasonic attenuation has been more difficult to accurately predict, and, sometimes, as much as an order of magnitude difference is observed between the predicted and measured attenuation coefficients.

There are two approaches available for the formal development of a model based either on a wave scattering[17–21] or a hydrodynamic approach.[22,23] To determine the interaction between the viscous liquid and a single solid particle, the wave scattering approach decomposes the total wave field into incident and scattered wave fields. Both the incident and the scattered fields are expressed as infinite eigenfunction series and the expansion coefficients are obtained by matching the displacement, velocity, tractions, temperature, and heat flux at the liquid–solid particle interface. After obtaining the scattered field, the collective effects of a volume of particles on ultrasonic propagation are obtained by a summation over the total number of particles. Since particle–particle interactions are ignored, the approach is an independent scattering one, and can only strictly be applied to dilute suspensions. In the hydrodynamic approach, the Stokes formula[24] is used to describe the interaction between a single solid particle and a surrounding Newtonian viscous liquid. For this model, the collective effects of a high particle fraction on ultrasonic propagation have been approximated using a rule of mixtures and so this approach may better represent the behavior of the concentrated slurries encountered in composite processing.

Here we experimentally investigate the use of ultrasound for the noninvasive sensing of a slurry's particle volume fraction and effective viscosity, and examine the predictive accuracy of the hydrodynamic modelling approach.[22] Using a model laboratory slurry system consisting of Ti-alloy particles (of known shape and size distribution) suspended in liquid mixtures of glycerol and water whose viscosity could be varied over the range of typical tape casting slurries, we have evaluated the feasibility of using a piezoelectric ultrasonic sensor methodology for measuring ultrasonic velocity and attenuation for a variety of suspensions. Both velocity and attenuation measurements are found to be sensitive to the particle volume fraction, and either can be used to sense local particle fraction variations in slurries. While the Harker and Temple hydrodynamic model (the H-T model)[22] appears to incorporate the phenomena that govern the ultrasonic velocity dependence on particle volume fraction up to particle fractions of 0.35, the model can only predict ultrasonic attenuation for the particle volume fractions below 20% due to the use of a rule of mixtures in the model and the failure to incorporate the intrinsic scattering and absorption of the powder itself.

TABLE I. Liquid properties at 25 °C (Refs. 23, 25, 26).

Fluids (volume % of constituents)	Bulk modulus (GPa)	Density (kg/m^3)	Velocity (m/s)	Viscosity (Pa s)
100% glycerol	4.59	1260	1909	1.5
95% glycerol+5% water	4.37	1250	1870	0.58
90% glycerol+10% water	4.14	1239	1828	0.25
85% glycerol+15% water	3.97	1228	1798	0.13
80% glycerol+20% water	3.79	1217	1765	0.076
75% glycerol+25% water	3.64	1205	1738	0.046
100% water	2.24	1000	1497	0.001
Suspending liquids for tape casting	1.7	1100	1545	0.15

I. SLURRY SYSTEM

A typical MMC tape casting slurry consists of a mixture of viscous liquids with an effective shear viscosity of about 0.15 Pa s containing 10–200μm diameter solid metal particles with a volume fraction of about 20%. The suspending liquids used here consisted of mixtures of (highly viscous) glycerol and water. The glycerol and water mixtures were chosen because of their similar viscosities to the binder/solvent combinations used in tape casting slurry. Since the glycerol/water volume fractions (and thus the viscosity) of such mixtures can be easily manipulated, this system allowed the effects of liquid viscosity upon the ultrasonic velocity and attenuation to be systematically studied. The viscosity, density, and sound velocity of the components and their mixtures studied are listed in Table I.[25,26]

Two types of metal powder particles were used in the study. The first were Ti-3 wt. % Al powders with a nearly spherical shape; Fig. 1(a). Their theoretical density, $\rho_0 = 4.459\ g/cm^3$, while their bulk modulus, $B = 141$ GPa. A cross sectional analysis of the particles revealed that a few contained closed pores. Overall the particle porosity was determined to be 2.2%, and so an effective density, $\rho = 0.978\ \rho_0 = 4.361\ g/cm^3$, was used in subsequent calculations. The second system consisted of nonspherical Ti-6 wt. % Al-4 wt. % V; Fig. 1(b). Their theoretical density, ρ_0

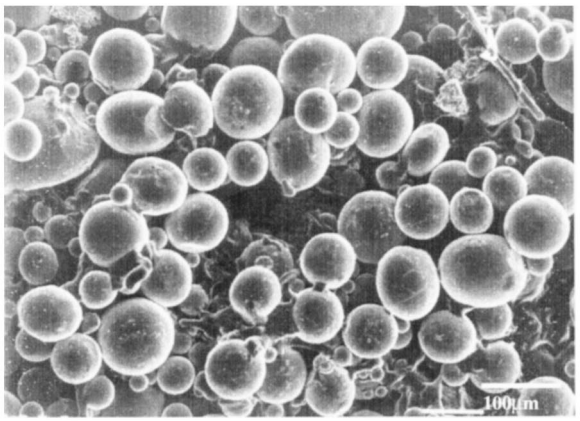

(a) Ti-3Al powder particles

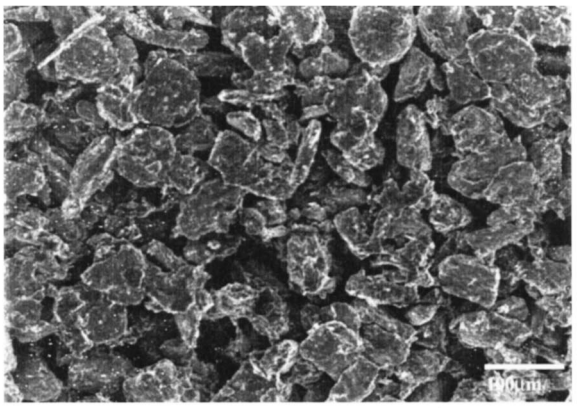

(b) Ti-6Al-4V powder particles

FIG. 1. Micrographs showing (a) spherical Ti-3 Al powder particles, and (b) nonspherical Ti-6 Al-4 V powder particles.

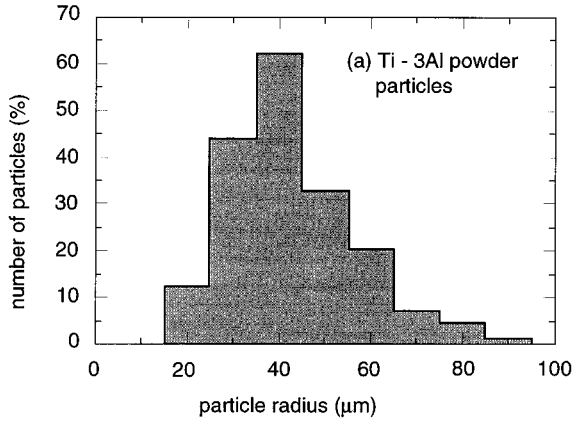

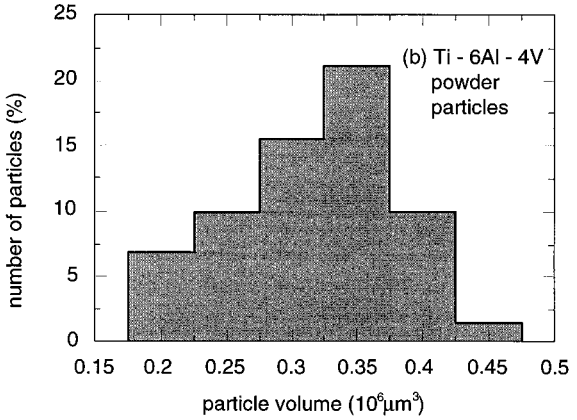

FIG. 2. (a) Ti-3 Al powder particle radius distribution; (b) Ti-6 Al-4 V powder particle volume distribution.

$=4.457$ g/cm^3 and their bulk modulus, $B=141$ GPa. A cross sectional analysis of these particles indicated negligible porosity. Both particles sets had a fairly broad size/volume distribution; Fig. 2. The spherical Ti-3 Al particle system was chosen for ease in modeling, while the nonspherical Ti-6 Al-4 V powders were selected to assess the effects of particle shape which is not always spherical in practice.

II. MEASUREMENT SYSTEM

A. Ultrasonic test cell

The ultrasonic test cell consisted of two collinear transducers in a pitch-catch arrangement; Fig. 3. To increase the signal strength in these sometimes very lossy slurries, a focused piezoelectric transducer was used to generate ultrasonic pulses and an unfocused transducer with a matching central frequency was used to receive ultrasonic signals. Four pairs of 1-in. diameter (Panametrics) transducers with center frequencies of 0.46 MHz, 0.87 MHz, 2.10 MHz, and 4.80 MHz were used for the ultrasonic testing. The transmitting transducer was mounted on a three point adjustable plate allowing for precise collinear alignment of the two transducers; the receiving transducer was fixed to a piston controlled by a micrometer allowing the distance between the transmitter and the receiver to be continuously varied. The measured distance between the two transducers had a precision of about $\pm 10\ \mu$m. Parallelism between the two transducers was considered achieved by maximizing the amplitude of the detected signal. The ultrasonic test system used in conjunction with the test cell consisted of a MATEC MBS 8000 velocity and attenuation measurement system, a Marconi 2022C signal generator, a LeCroy 9400 digital oscilloscope (8 bits vertical resolution, 1-ns sampling resolution) and a 15-MHz low-pass filter to eliminate high-frequency noise. A theoretical model due to Lu *et al.*[27] for focused transducers was used to calculate the acoustic field intensity for each combination of transducers and mixtures of glycerol and water; the acoustic intensity was then used to correct attenuation measurements for beam spreading or convergence.

B. Data collection

The test cell micrometer position was set to zero at a reference propagation distance, L_0. Velocity and attenuation measurements were then made as the distance between transducers was increased in steps of about 3.0 ± 0.1 cm. A slurry sample was then placed in the test cell and the reading of the micrometer was recorded. This, together with the reference distance, L_0, gave the distance between the transmitter and the receiver. The raw data were collected in the form of receiver transducer waveforms on a digital oscilloscope. The entire data acquisition process was automated using a data acquisition program LABVIEW at a rate of about one wave-

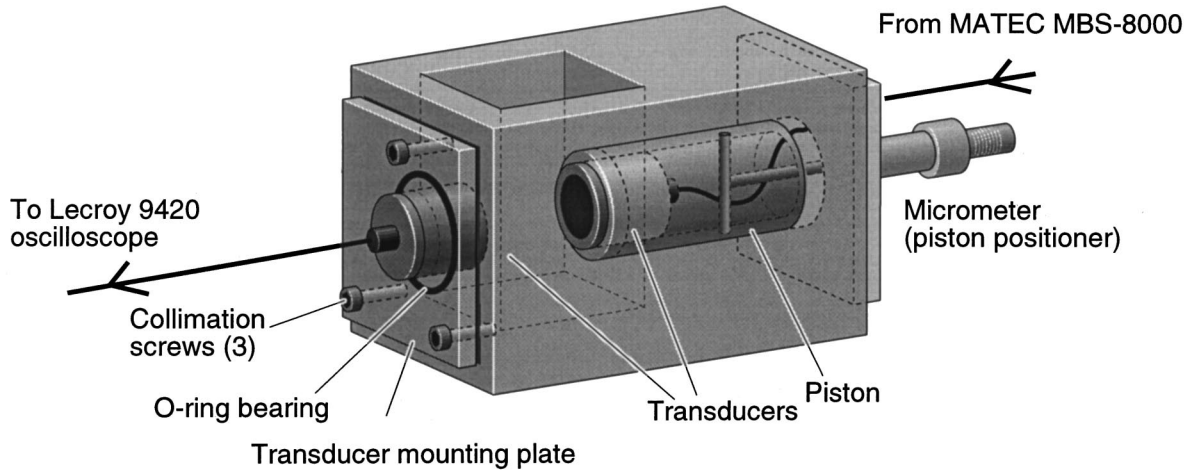

FIG. 3. The ultrasonic test cell used for the experimental study.

form every 2 s to allowed experiments to be conducted rapidly and to avoid potential settling of the slurry during the measurement. All measurements were taken at the ambient temperature.

C. Velocity/attenuation determination

The ultrasonic velocity was determined by measuring the travel time of the first peak in each waveform. If L was the distance between two transducers and t the time lapse between the trigger time and the first peak in the waveform, then the ultrasonic velocity $v=L/t$. We obtained a linear relationship between the measured time interval, t, and the propagation distance, L, with an estimated error of ± 2.5 m/s, or about 0.14% for a typical velocity of 1800 m/s.

A differential scheme was used to determine the attenuation. The maximum amplitudes, A_1, A_2, A_3, of three waveforms corresponding to three different propagation distances, L_1, L_2, L_3, (for the same frequency and slurry composition) were measured. The attenuation was obtained as: $\alpha(\mathrm{dB})=20\log[(A_3-A_1)/(A_2-A_1)]/(L_3-L_2)$. The numerical attenuation values for each set of data were then averaged.

III. SUSPENDING LIQUID BEHAVIOR

Acoustic properties of both glycerol and water have been extensively investigated by many researchers.[13,28–31] These two liquids (and therefore their mixtures) are so called associate liquids.[13,28–31] Their volume viscosity, η_v, is of the same order as their shear viscosity, η_s, and thus the effects of the volume viscosity on ultrasonic attenuation should not be ignored.[13,28–31] The acoustic velocity, v_{liq}, and attenuation, α_{liq}, of the liquid mixtures without particle loading can be expressed as[13]

$$\nu_{\mathrm{liq}}=\sqrt{\frac{\frac{2B}{\rho'}\left[1+\left(\frac{\omega}{\omega_\nu}\right)^2\right]}{1+\sqrt{1+\left(\frac{\omega}{\omega_1}\right)^2}}},$$
$$\alpha_{\mathrm{liq}}=\frac{\omega}{2B}\frac{\nu\rho'}{\left(\frac{\omega}{\omega_\nu}+\frac{\omega_\nu}{\omega}\right)}, \tag{1}$$

where $\omega=2\pi f$ is the angular frequency, f is the sound frequency, ν is the velocity, ρ' is the effective liquid density, and

$$\omega_\nu=\frac{B}{\eta_\nu+\frac{4}{3}\eta_s} \tag{2}$$

is the characteristic frequency of the mixtures.

The measured ultrasonic velocity and attenuation of glycerol/water mixtures are shown in Fig. 4 and Fig. 5. Equation (1) was used to predict both the velocity and the attenuation. The shear viscosity of the mixture was taken from Ref. 26, and the volume viscosity was determined to be $\eta_v=0.8\eta_s$ by fitting experimental data with Eq. (1). There is an excellent match between the measured velocity and the predicted velocity; Fig. 4(b). Since the velocity for the mixture of either 90% glycerol and 10% water or 80% glycerol and 20% water is almost constant at all test frequencies ($v=1828$ m/s for 90% glycerol and 10% water, and $=1763$ m/s for 80% glycerol and 20% water), we conclude that both the ultrasonic frequency and the viscosity have a vanishing effect on the velocity, and the increase in the velocity is a result of an increase in the bulk modulus due to the increasing glycerol volume fraction (see Table I).

The attenuation was found to rapidly increase with the glycerol volume fraction and the test frequency; Fig. 5. We found that Eq. (1) fits measured attenuation data well by taking $\eta_v=0.8\eta_s$. It severely underestimated the measured data if $\eta_v=0.0$, confirming that the volume viscosity plays a

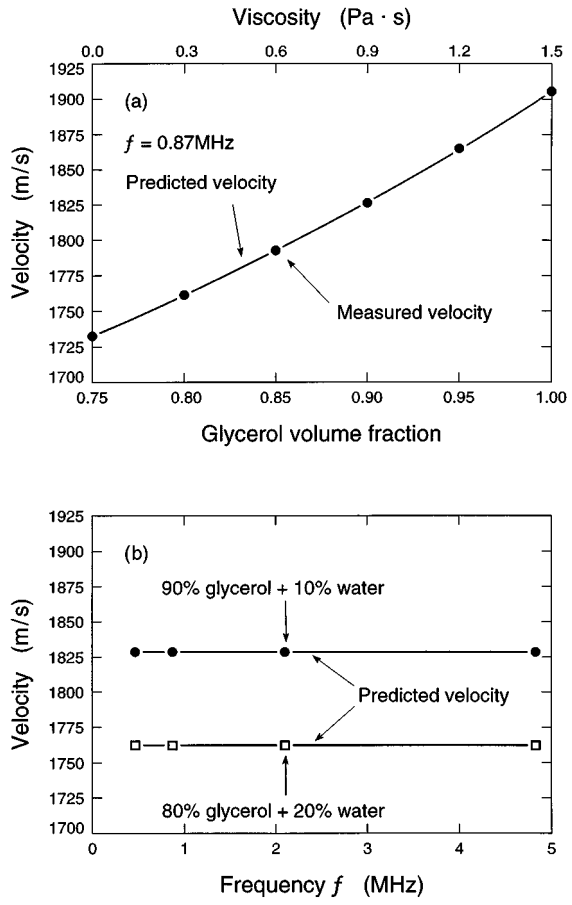

FIG. 4. The measured ultrasonic velocity of the suspending liquid as a function of (a) glycerol and water volume fractions, (b) test frequency.

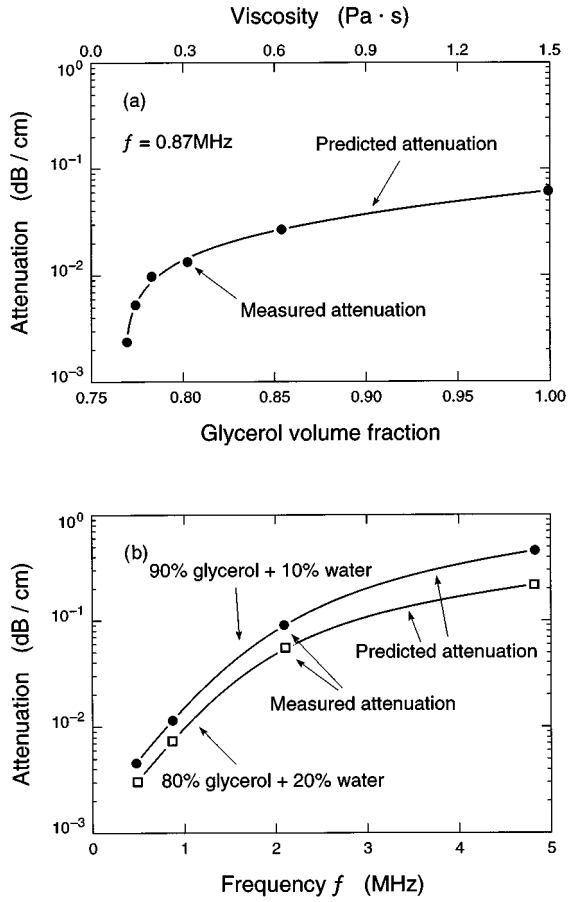

FIG. 5. The measured ultrasonic attenuation of the suspending liquid as a function of (a) glycerol and water volume fractions, (b) test frequency.

very significant role in ultrasonic propagation in viscous liquids, and its effects should not be neglected in attenuation predictions for slurries.

IV. POWDER SLURRY BEHAVIOR

A. Results

Figures 6 and 7 show typical examples of the measured ultrasonic velocity of both spherical Ti-3 Al and nonspherical Ti-6 Al-4 V particles suspended in two glycerol and water mixtures (90% glycerol+10% water and 80% glycerol +20% water) as a function of particle volume fraction for test frequencies 0.46 and 2.1 MHz. For particle volume fractions up to 0.35, the velocity decreased monotonically with the particle volume fraction. The slope was steepest near the volume fraction of 0.25—fortuitously close to the value used in many slurry casting processes. The velocity for Ti-3 Al powder suspensions was always greater than that for Ti-6 Al-4 V particle suspensions, principally because of the (often hollow) Ti-3 Al powders' smaller effective density. The velocity of the slurries were also strongly affected by the suspending liquid's composition. For example, Fig. 8 displays the measured velocity-glycerol volume fraction relationship for a slurry containing a 20% volume fraction of Ti-3 Al powders at a test frequency of 0.87 MHz. The velocity is a strong, monotonic functions of the suspending liquid's composition.

The ultrasonic attenuation as a function of particle volume fraction is shown in Figs. 9 and 10 at test frequencies of 0.46 and 2.1 MHz. The attenuation was a strongly increasing function of both particle fraction and test frequency. The size of the particles appears to affect the attenuation, with the larger Ti-6 Al-4 V powder particles (the average particle radius was 47.5 μm, deduced from the particle volume measurements) exhibiting a higher attenuation than the Ti-3 Al powder particles (the average particle size was 37.5 μm).

The ultrasonic attenuation exhibits a strong monotonic increase as particle volume fraction and/or ultrasonic frequency increase; Figs. 9 and 10. The attenuation also monotonically increases with the liquid's viscosity; Fig. 8. Figure 8 shows attenuation as a function of volume percentage of glycerol for a 20% volume fraction of Ti-3 Al particles at 0.87-MHz frequency. Clearly, the attenuation is a strong monotonic function of the suspending liquid's composition. In particular, it is clear that as the suspending liquid's viscosity increases (glycerol content rises), the attenuation of the slurry rises exponentially. A comparison of Figs. 5 and 8 reveals that the presence of powder synergistically increases the attenuation contribution of the liquid, and clearly reveals the very strong effect of viscosity upon ultrasonic attenuation by suspended particles.

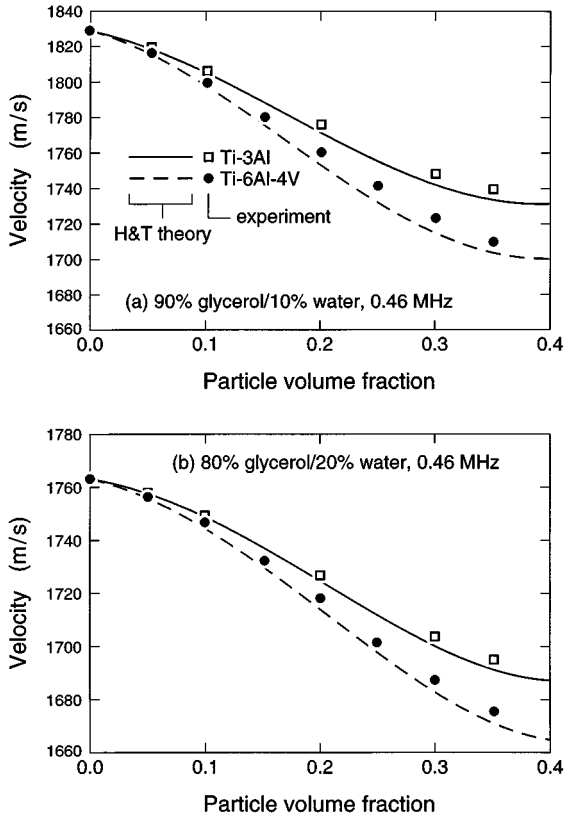

FIG. 6. The measured and H-T model predicted velocities as functions of particle volume fraction at 0.46 MHz (a) 90% glycerol and 10% water; (b) 80% glycerol and 20% water.

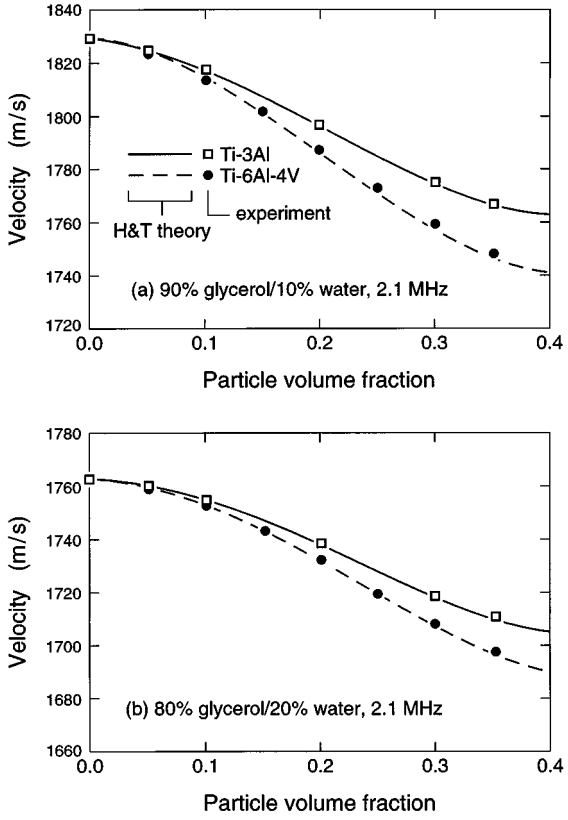

FIG. 7. The measured and H-T model predicted velocities as functions of particle volume fraction at 2.1 MHz. (a) 90% glycerol and 10% water; (b) 80% glycerol and 20% water.

B. Discussion

1. Sensor opportunities

Within the 0.0–0.35 particle volume fraction range, the measured velocity is a monotonic function of powder particle fraction (Figs. 6 and 7) and is consistent with the dominance of increase in slurry density over the compensating decrease in slurry compressibility. The ultrasonic velocity also monitonically increases with the suspending liquid's or the powder particle's velocity (e.g., see Figs. 8 and 6). Changes in the particle volume fraction, particle size, ultrasonic frequency, and liquid viscosity all affect the ultrasonic attenuation.

The experimental velocity/attenuation trends with particle volume fraction shown above can be empirically fitted by simple monotonic relationships. Thus once provided with premeasured calibration data relating either the ultrasonic velocity or attenuation to the particle volume fraction, a subsequent ultrasonic measurement during slurry casting could be converted to particle fraction, providing the basis for a real time ultrasonic particle volume measurement. Because of the relatively small error in measured velocity (± 2.5 m/s) and the fairly strong dependence of velocity upon particle volume fraction, the particle volume fraction could be obtained to within 5% from the velocity measurement near the 0.2 volume fraction region of practical interest.

The attenuation relationship (e.g., Figs. 9 and 10) could also be used for sensing volume fraction. However, attenuation measurements have relatively larger uncertainties (the largest measurement error was about ± 1 dB/cm), and a weaker dependence upon particle fraction around the 0.2 volume fraction region of interest. The attenuation is also a strong function of the suspending liquid's viscosity. This, together with the difficulty of avoiding signal losses from other causes, may pose additional practical problems for a particle volume fraction sensor based solely on amplitude measurements. It is of interest to note that since the velocity measurements give a good indication of particle volume fraction, the ability to make reliable attenuation measurements would provide a potential method to determine the viscosity of the suspending liquid. This then provides a prac-

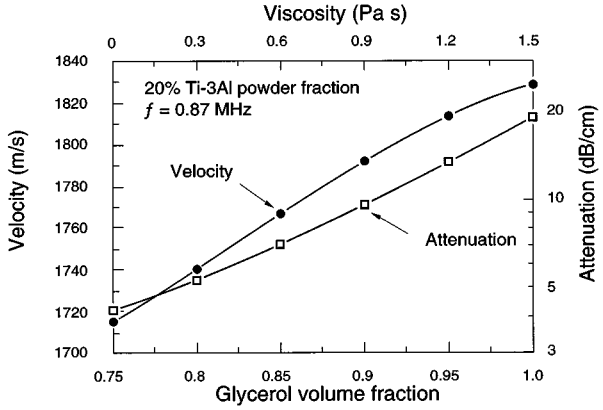

FIG. 8. The measured velocities and attenuation for a 20% Ti-3 Al particle volume fraction at 0.87 MHz as a function of glycerol volume fraction.

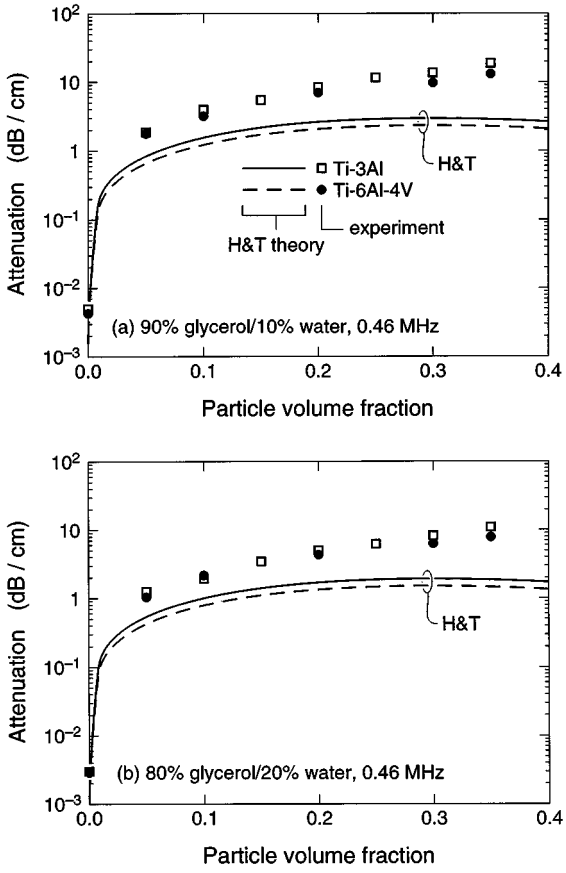

FIG. 9. The measured and H-T model predicted attenuation as a function of particle volume fraction at 0.46 MHz. (a) 90% glycerol and 10% water; (b) 80% glycerol and 20% water.

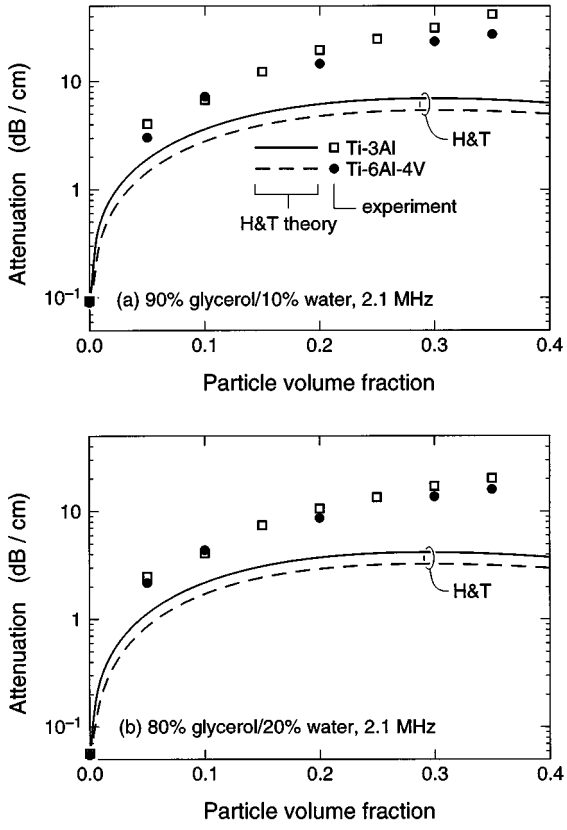

FIG. 10. The measured and H-T model predicted attenuation as a function of particle volume fraction at 2.1 MHz. (a) 90% glycerol and 10% water; (b) 80% glycerol and 20% water.

tical way to monitor changes in the liquid's composition through relationships between viscosity and composition (e.g., Fig. 8).

2. Wave propagation predictions

In Harker and Temple's (H-T) hydrodynamic model[22,23] the complex effective wave number, k, is used to determine the velocity and attenuation. The effective wave number is given by

$$k^2=\omega^2[(1-\varphi)\beta_l+\varphi\beta_s] \times \frac{\rho_l[\rho_s(1-\varphi+\varphi S)+\rho_l S(1-\varphi)]}{\rho_s(1-\varphi)^2+\rho_l[S+\varphi(1-\varphi)]}, \tag{3}$$

where

$$S=\frac{1}{2}\left(\frac{1+2\varphi}{1-\varphi}\right)+\frac{9}{4}\sqrt{\frac{2\eta_s}{a^2\rho_l\omega}} +i\left(\frac{9}{4}\left[\sqrt{\frac{2\eta_s}{a^2\rho_l\omega}}+\frac{2\eta_s}{a^2\rho_l\omega}\right]\right). \tag{4}$$

The velocity and the attenuation coefficient are obtained from Eqs. (3) and (4) using:

$$v=\frac{\omega}{\mathrm{Re}(k)}, \quad \alpha(\mathrm{dB})=20(\log_{10} e)\,\mathrm{Im}(k). \tag{5}$$

The measured ultrasonic velocity and attenuation data have been compared to predictions of the H-T model using the thermophysical data for the liquids found in Table II. Since the H-T model strictly applies only to spherical particles, the volume, V, of the Ti-6 Al-4 V particles was used to deduce an equivalent particle radius $a=\sqrt[3]{3V/4\pi}$. The predicted velocity values are shown and compared with measurements in Figs. 6 and 7. Overall the comparison between the predicted and measured velocity values is very good. It is clear from both Figs. 6 and 7 that the velocity is a function both of particle and glycerol volume fractions; neither the test frequency nor the viscosity significantly affect the velocity. At lower frequencies, the H-T model slightly overestimates the rate of the velocity decrease with the powder particle volume fraction. As the frequency increases the agreement between the experimentally determined ultrasonic

TABLE II. Thermophysical data used in H-T model (Ref. 33).

Property (Symbol)	Glycerol ($C_3H_8O_3$)	Water
Thermal conductivity (K)	0.292 W/m	0.6071 W/m
Viscosity (η)	923 mPa s	0.893 mPa s
Density (ρ)	1.2613 g/cm^3	1.0 g/cm^3
Specific heat at the constant pressure (Cp)[a]	218.9 J mol^{-1} K^{-1}	75.3 J mol^{-1} K^{-1}
Thermal expansion coefficient (α)	0.52×10^3/°C	0.206×10^3/°C

[a]Basic Laboratory and Industrial Chemicals, *A CRC Quick Reference Handbook*, edited by D. R. Lide (CRC, Boca Raton, 1993).

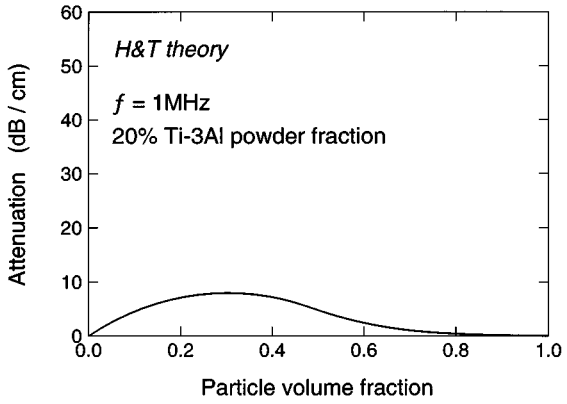

FIG. 11. Predicted attenuation as a function of particle volume fraction for Ti-3 Al particles, $f=1$ MHz; water volume fraction in the liquid: 20%.

velocities and the model becomes excellent. Generally, the relative error between the measured and predicted velocities is around 0.25%.

The predicted attenuation values are compared with the data in Figs. 9 and 10. It can be seen that the H-T model compares fairly well for low (say less than 0.2) volume fractions of powder. In general, it underestimates the attenuation of the mixtures. This may be linked to the H-T model's use of a simple viscosity relation that does not recognize volume viscosity. This term in the constitutive response of associative liquids clearly has a significant effect on attenuation (Fig. 5). However, we also note that while the measured attenuation always increases monotonically with the particle volume fraction, the predicted values peak at about a 30% particle volume fraction. Figure 11 shows the attenuation as a function of particle volume fraction predicted by the H-T model for a volume fraction from zero to unity. Clearly, the model can no longer be valid when the particle volume fraction exceeds the theoretical limit for spherical particle packing (0.67 for a random packing). The drop in predicted attenuation above a volume fraction of 0.3 is a consequence of the zero assumed attenuation of the solid phase and the use of a rule of mixtures in the derivation of the H-T model. The validity of the rule of mixtures relation restricts the validity of the H-T model to particle volume fractions of no more than 20%.[32] The use of the rule of mixtures, combined with the assumption of no solid phase attenuation even reduces the predicted attenuation in the 0.1–0.2 particle volume fraction region, and appears to be a significant contributor to the discrepancy between modeled and measured attenuation.

In spite of the attenuation modeling discrepancy, it is clear that provided the viscosity of the suspending liquid is known, there exists a promising basis for ultrasonic determination of particle volume fraction from either a velocity or an attenuation measurement. The precision of the measurement might be increased by using both attenuation and velocity data at a specific frequency and/or ultrasonic measurements over a range of frequencies. It is interesting to note that Figs. 6 and 7 show that the liquid viscosity has a vanishingly weak effect upon velocity, whereas Figs. 9 and 10 show attenuation measurements are much more viscosity dependent. Thus a combination of the two measurements might enable the determination of both viscosity and the particle volume fraction of a slurry.

V. CONCLUSION

Ultrasonic sensor concepts have been assessed for their potential for monitoring metal particle volume fractions during a slurry casting step in the manufacture of fiber reinforced MMCs via tape casting. Model laboratory slurry systems consisting of two Ti-alloy powders of known size and shape distributions suspended in mixtures of glycerol and water with controllable viscosity were used to investigate the relationship between particle shape, slurry composition, liquid viscosity, and the velocity/attenuation of ultrasound. The slurries had viscosities that spanned those of a typical tape casting slurry. The experiments reveal a monotonic decrease in velocity with increasing particle volume fraction and water content. The attenuation monotonically increased with particle volume fraction, viscosity, and test frequency.

An ultrasonic velocity measurement appears to offer the best precision for determining the particle volume fraction. The use of attenuation data has the potential for additional recovery of the slurry's viscosity. Because of the relatively small error in velocity measurement (± 2.5 m/s) and the fairly strong dependence of velocity upon particle volume fraction, the particle volume fraction could be obtained to within 5% from the velocity measurement. Attenuation measurements have larger uncertainties (the largest measurement error was about ± 1 dB/cm) and this may pose potential problems for a sensor technology solely based upon amplitude measurements.

The Harker and Temple hydrodynamic model was used to analyze both the velocity and attenuation results. The velocity measurements were well predicted by the H-T model, the relative error between the measured and predicted velocities is around 0.25%, suggesting that the model could be used to convert velocity data to particle volume fraction. Ultrasonic attenuation trends with particle fraction, liquid viscosity, and test frequency were reproduced well by the model. However, the absolute attenuations were underestimated by the model. This arises in part from the use of a rule of mixtures (which limits its useful range to a particle volume fraction of less than about 20%) and its failure to incorporate scattering/absorption in the metal phase.

ACKNOWLEDGMENT

This work has been jointly supported by the High Performance Composites Consortium through an ARPA contract (R. B. Crowe, Program Manager) and Virginia Center for Innovative Technology.

[1] J. Doychak, JOM. **44**, 46 (1992).
[2] D. F. Adams, *Mechanics of Composite Materials*, edited by G. P. Sendeckyi (Academic, New York, 1974), Chap. 5.
[3] N. A. James, D. J. Lovett, and C. M. Warick, Composites: Design, Manufacture and Application, ICCM VIII, edited by S. W. Tsai and G. S. Springer, SAMPE **2**, I1 (1992).
[4] M. S. Misra and S. G. Fishman, Composites: Design, Manufacture and Application, ICCM VIII, edited by S. W. Tsai and G. S. Springer, SAMPE **2**, 18A1 (1992).
[5] T. Onzawa, A. Suzumura, and J. H. Kim, Composites: Design, Manufac-

ture and Application, ICCM VIII, edited by S. W. Tsai and G. S. Springer, SAMPE **2**, J1 (1992).
[6] W. J. Whatley and F. E. Wawner, J. Mater. Sci. Lett. **4**, 173 (1985).
[7] S. Ochiai and Y. Murakami, J. Mater. Sci. Lett. **14**, 831 (1979).
[8] D. G. Backman, JOM **42**, 17 (1990).
[9] J. F. Edd and J. T. Niemann, ''Scale-up of a tape casting process for continuous fiber-reinforced metal and intermetallic matrix composites,'' in *Titanium Aluminide Composites*, edited by P. R. Smith, S. J. Balsone, and T. Nicholas, WL-TR-91-4020, 158-173 (1991).
[10] J. T. Niemann and J. F. Edd, ''Fabrication of titanium aluminide composites by tape casting,'' in *Titanium Aluminide Composites*, edited by P. R. Smith, S. J. Balsone, and T. Nicholas, WL-TR-91-4020, 300-314 (1991).
[11] A. B. Wood, *A Textbook of Sound* (G. Bell, London, 1941).
[12] R. J. Urick, J. Appl. Phys. **20**, 283 (1948).
[13] A. B. Bhatia, *Ultrasonic Absorption: An Introduction to the Theory of Sound Absorption and Dispersion in Gases, Liquids and Solids* (Dover, New York, 1967).
[14] H. N. G. Wadley, ''Intelligent processing of high performance materials,'' in Proceedings of the 41st Sagamore Conference, edited by W. N. Roy, S. M. Walsh, Plymouth, MA, 57–94 (1995).
[15] A. Ishimaru, *Wave Propagation and Scattering in Random Media* (Academic, New York, 1977).
[16] D. J. McClements and M. J. W. Povey, ''Ultrasonic velocity as a probe of emulsions and suspensions,'' Adv. Colloid Interface Sci. **27**, 285–316 (1987).
[17] P. M. Morse and K. U. Ingard, *Theoretical Acoustics* (McGraw-Hill, New York, 1968).
[18] C. J. T. Sewell, Philos. Trans. R. Soc. London, Ser. A **210**, 239 (1910).
[19] P. S. Epstein, Applied Mechanics—Th von Karman Anniversary Volume, pp. 162–188, California Institute of Technology, California (1941).
[20] P. S. Epstein and R. R. Carhart, J. Acoust. Soc. Am. **25**, 553 (1953).
[21] J. R. Allegra and S. A. Hawley, J. Acoust. Soc. Am. **51**, 1545 (1971).
[22] A. H. Harker and J. A. G. Temple, ''Velocity and attenuation of ultrasound in suspensions of particles in fluids,'' J. Phys. D **21**, 1576–1588 (1988).
[23] A. H. Harker and J. A. G. Temple, Ultrasonics **29**, 427 (1991).
[24] G. G. Stokes, Trans. Camb. Philos. Soc. **9**, 8 (1851).
[25] *Basic Laboratory and Industrial Chemicals, A CRC Quick Reference Handbook*, edited by D. R. Lide (CRC, Boca Raton, 1993).
[26] *CRC Handbook of Chemistry and Physics*, 77th ed. (CRC, Boca Raton, 1996), pp. 15–16.
[27] J. Lu, H. Zou, and J. F. Greenleaf, ''Biomedical ultrasound beam forming,'' Ultrasound Med. Biol. **20**, 403 (1994).
[28] T. A. Litovitz, ''Liquid relaxation phenomena and the glass state,'' in *Non-Crystalline Solids*, edited by V. D. Fréchette (Wiley, New York, 1958).
[29] K. F. Herzfeld and T. A. Litovitz, *Absorption and Dispersion of Ultrasonic Waves* (Academic, New York, 1959).
[30] R. B. Lindsay, *Mechanical Radiation* (McGraw-Hill, New York, 1960).
[31] T. A. Litovitz and C. M. Davis, ''Structural and shear relaxation in liquids,'' in *Physical Acoustics*, Vol. IIA, edited by W. P. Mason (Academic, New York, 1965).
[32] R. M. Christensen, *Mechanics of Composite Materials* (Wiley, New York, 1979).
[33] M. F. Ashby and D. R. Jones, *Engineering Materials*, II (Pergamon, New York, 1982), p. 10.

Acoustoelastic measurements on aluminium alloy by means of a contact and a non-contact (LFB acoustic microscopy) technique

T. Berruti and M. M. Gola
Dipartimento di Meccanica, Politecnico di Torino, Cso. Duca degli Abruzzi 24, 10129 Torino, Italy

G. A. D. Briggs
Department of Materials, University of Oxford, Parks Road, Oxford OX1 3PH, United Kingdom

(Received 10 July 1996; accepted for publication 18 October 1997)

Two independent experimental techniques for measuring the acoustoelastic effect on a sample of AA 6082 T6 aluminium alloy are tested and compared. A non-contact technique using acoustic microscopy and a contact technique using two point wedges as receivers are employed. The two techniques use different approaches in the velocity measurements. The wave frequency is also different—225 MHz for the microsocpy technique and 5 MHz for the contact device. Two different systems to load the sample are also employed. The results confirm the validity of the measurements and of the techniques employed. © *1998 Acoustical Society of America.*
[S0001-4966(98)00403-2]

PACS numbers: 43.35.Cg, 43.35.Pt [HEB]

INTRODUCTION

The acoustoelastic effect, which is the small dependence of the ultrasonic wave velocity on the stress state of the material through which it travels, has been studied from the middle of this century and many theoretical and experimental approaches have been developed. Different experiments[1–5] using Rayleigh surface waves have given evidence that the wave velocity depends linearly on the stress; this effect is described by constants, characteristic of a material, called ''acoustoelastic constants,'' relating the change in wave velocity with the stress. These constants depend on the material parameters (elastic constants) in the ''natural'' unstressed state which may be unknown or not known with sufficient accuracy.[6,7] For this reason it is often preferable to apply known stress steps to a sample and measure the velocity variation in order to deduce directly the material ''acoustoelastic constants'' rather than expressing the dependence of the velocity on stress through a relation involving the material elastic constants.

The acoustoelastic effect is relatively small; in some materials the effect is strong enough to be measured while in others it is almost impossible to detect. Very precise measurements are required, and it is essential to be sure that the acoustoelastic effect is being measured rather than any other secondary effect due to the measuring system. The goals of this work have been to employ two completely different measurement techniques on the same sample loaded in different ways and to compare the values of the acoustoelastic constant obtained. Previous experiments had already demonstrated that the variation of velocity with stress in a silicon wafer could be measured by quantitative acoustic microscopy.[7] In the present experiments, a bar of 6082 T6 aluminium alloy was tested and the value of the acoustoelastic constant along its axis was determined with two independent techniques: a non-contact technique using acoustic microscopy, and a contact technique using two point wedges as receivers. Good agreement was found between the measurements, confirming their validity and also the validity of the techniques employed.

I. LINE-FOCUS BEAM ACOUSTIC MICROSCOPY

The acoustic microscope can be used to determine ultrasonic velocity of waves travelling on the surface of a specimen.[8] It consists of a ZnO transducer mounted on a sapphire lens. The lens has a cylindrical surface, with the axis of the cylinder parallel to the sample surface, to give a line-focus beam in order to excite Rayleigh waves along a single direction in the sample.[9] The sample stage allows tilting around two axes for alignment with the lens axis, and the sample can be scanned under the control of a computer which also records the lens signal. For quantitative measurements the sample is scanned toward the lens, as shown in Fig. 1. The distance by which the sample is moved closer to the lens relative to the focus is the defocus z. The total signal V received by the transducer is the sum of two rays: the ray which is normally reflected from the specimen surface and the ray associated with a surface wave. As the amount of defocus changes, the path lengths of the normally incident ray and of the ray coming from the specimen surface change at different rates so that the total signal at the transducer fluctuates as the two rays go in and out of phase with each other.[9] The response of the transducer to this total signal is measured by a lock-in amplifier, and the values obtained are acquired by the computer and plotted versus the amount of defocus, giving a so-called $V(z)$ curve. In Fig. 2 is shown an example of $V(z)$ curve for a 6082 T6 aluminium alloy sample. By comparing the rates of change of the two path lengths with defocus the period of the oscillations in $V(z)$ can be expressed as:[9–11]

$$\Delta z = \frac{\lambda_0}{2(1-\cos\ \theta_R)}, \tag{1}$$

 0001-4966/98/103(3)/1370/7/$10.00

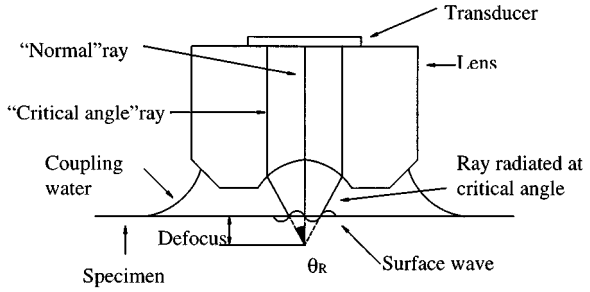

FIG. 1. Schematic diagram of an acoustic lens.

where λ_0 is the wavelength of longitudinal waves in water and θ_R the critical angle for surface wave excitation. By using Snell's law $\sin \theta_R = v_0/v_R$ with v_0 the velocity of longitudinal waves in water, relationship (1) may be inverted to give the Rayleigh wave velocity V_R in the measurement area in terms of Δz, the frequency f, and the velocity v_0:

$$v_R = v_0 \left[1 - \left(1 - \frac{v_0}{2 f \Delta z} \right)^2 \right]^{-1/2}. \quad (2)$$

The data analysis routine to obtain the period Δz from the $V(z)$ curve[8] includes the following main steps:

- filtering the curve to remove unwanted high frequency oscillations;
- subtraction of a reference $V(z)$ curve, previously obtained using a material with no excitation of waves in the specimen, to remove the geometric effect of the acoustic lens;
- different filtering to remove unwanted low frequency components;
- Fourier transformations to get a final value of Δz.

II. POINT CONTACT MEASUREMENTS

A surface wave is excited in the sample; the measurement consists in detecting the surface wave at two points with a fixed separation, and calculating its velocity from the time of flight between the two points.[12] The equipment for these measurements is a commercial Rayleigh wave generator (Krautkramer MSWS), and a pair of commercial longitudinal transducers (Panametrics A5038-SM(I)) which act as receivers and are coupled to the surface being measured

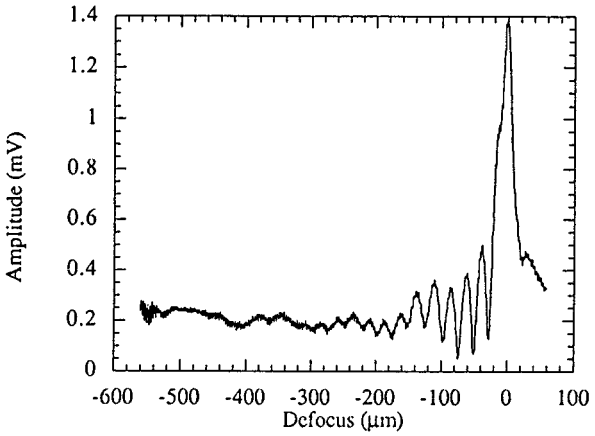

FIG. 2. $V(z)$ curve for 6082 T6 aluminium alloy sample.

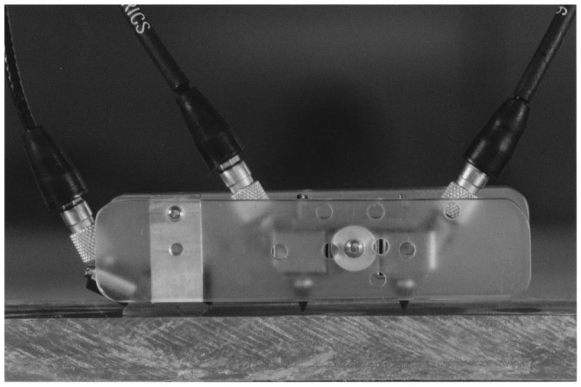

FIG. 3. The point contact measurement assembly.

through steel elements (Fig. 3 and Fig. 4). These three probes employed piezoelectric crystals of 0.25 in. diameter to transmit and receive longitudinal waves at 5 MHz. The transmitter is aligned with the receivers by means of plastic guides which permit small rotations to maintain their alignment in case of imperfectly plane surface.

The transmitter generates longitudinal waves which are converted by the plastic wedge into surface waves. These waves reach the steel elements in contact with the surface and their shear components generate in each steel element longitudinal waves detected by the piezoelectric probe fixed on it. The delay time between the two received signals is the time of flight between the two steel elements. Whatever mathematical method is employed to determine this time of flight (see later discussion), it will give the most accurate results when the signals detected by the receivers have similar amplitude and waveform. The shape of the steel elements is relevant to the detection of the waves. Different shapes of

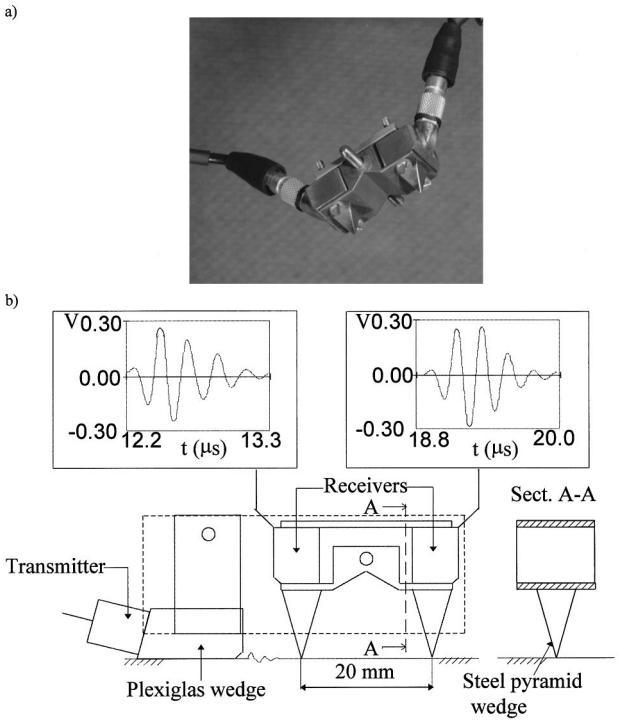

FIG. 4. (a) Picture of the receivers steel pyramid. (b) Point contact measurement device and received signals.

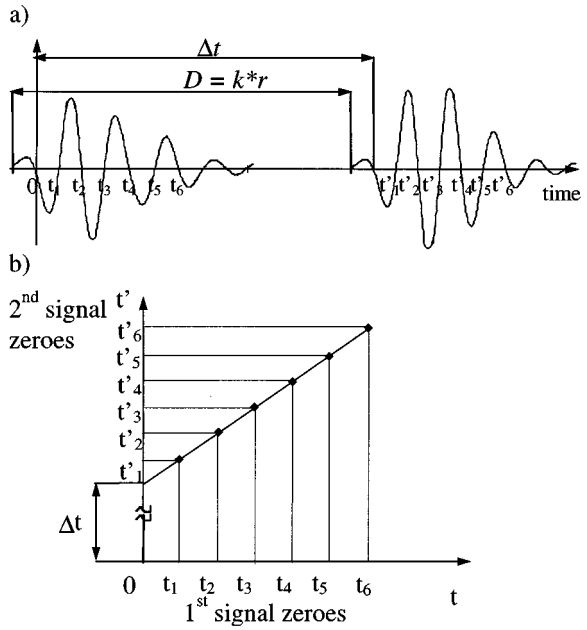

FIG. 5. (a) Two signals with a shift of Dt. (b) 45° regression line fitting the first six zeros of the two signals.

receiver steel elements were examined and tested. Initially elements with linear contact were explored, because it was believed that this would produce higher signals. Both wedges and half cylinders were tried, but it was found that although these arrangements gave a high signal, they also gave high variability because the two elements would never touch the surface in the same way. The point contact version which proved to be the best compromise is shown in Fig. 3 and Fig. 4. The pyramid elements are made of hardened steel (0.88% C, 1.8% Mn, 0.2% V) (heated at 800 °C, cooled in oil, tempered at 300 °C). A 40° vertex was chosen to prevent internal reflections on the wedge surfaces. The result is a received signal with an initial pulse well isolated from the following wavetrain.

A. Electronic apparatus

The measurement transducers are connected to a broadband ultrasonic pulser-receiver (PANAMETRICS 5052GTA-2) which excites the transmitter and receives and amplifies the switched signals from the two receiving probes (Fig. 5). The pulser is set to excite the transmitter with a repetition rate of 200 kHz, maximum input energy 94 μJ and a damping of 500 Ω, which determines the minimum pulse length. The received pulses are amplified by 40 dB and then displayed on a digital oscilloscope (Fluke PM3382) where the vertical resolution is set at 50 mV per division (10 divisions). Each trace displayed on the oscilloscope screen is the average of 32 consecutive signals. The digital oscilloscope is connected to a personal computer where the two switched waveforms are stored sequentially.

B. Time of flight calculation

The signals received by the digital oscilloscope are transferred to the computer for analysis. After acquisition of the first trace (detected by the first receiver), a constant delay

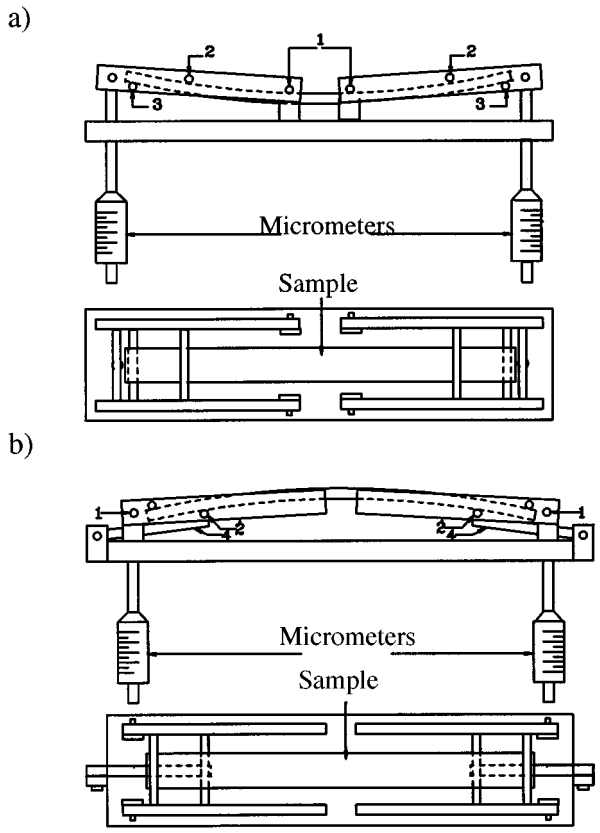

FIG. 6. Four-point bending system. (a) Compressive stress in the upper surface of the sample. (b) Tensile stress in the upper surface of the sample.

$D=6620$ ns is set on the oscilloscope to visualize and acquire the second trace (second receiver). The scale is set at 100 ns per division with 10 divisions on the screen. The computer acquires 50 points per division i.e. the points are spaced $r=2$ ns apart.

Only the zero crossings of the signals from the two receivers are taken into account $[t_1,t_2,\ldots,t_1',t_2',\ldots$ in Fig. 5(a)]. These points are plotted against one another [Fig. 5(b)], and the points obtained are fitted with a 45° straight line. The intersection of this line with the y axis is the delay between the two signals, i.e. the time of flight of the surface wave between the two receivers. In general the first six zeros of the signals are involved in this calculation since they are the more aligned on a 45° straight line. The method requires that the signals detected by the two receivers should be similar. As an alternative method of analysis, the cross correlation of the signals can be calculated, enabling their shift to be found from the maximum of the cross correlation function. The two methods are equivalent (no appreciable difference in the acoustoelastic constant values),[12] the advantage of the first one is that it is more rapid than the second.

III. SAMPLE LOADING SYSTEM

The jig used to load the sample at different loading steps is a four-point bending system where two micrometers can be used to increase or decrease the strain in the sample. As is shown in Fig. 6(a) and (b) the sample can be loaded in order to have compressive or tensile stress on its upper surface. In

the first case the sample support rotates about the four central pivots (1). The sample held between the two pairs of pins (2) and (3) is deformed thanks to their relative movement during the rotation about the pivots (1). Pins (2) and (3) are covered with rubber to avoid longitudinal sample sliding during the loading phase. In the case of tensile stress on the upper surface [Fig. 6(b)] the forces for the sample deformation are applied to the inner pins (2) by means of the micrometers through the levers (4); this solution has been chosen to simplify mounting problems on the microscope stage.

In both cases the stress induced on the upper surface of the sample has been calculated as a function of the micrometer displacement, and checked by means of a strain gauge applied parallel to the sample axis on the tensile surface of the measurement area. During the measurement another strain gauge is applied to a sample of the same material to compensate for temperature fluctuations.

IV. SAMPLE PREPARATION

The alloy tested in the experiments was AA 6082 T6 (Si 0.7–1.3%, Fe 0.5%, Cu 0.1%, Mn 0.1–0.4%, Mg 0.6–1.2%, Cr 0.25%, Zn 0.2%, Ti 0.1%). The sample was a 150 mm long bar with a rectangular section 15×2.5 mm^2. It is cut from a rolled aluminium alloy sheet. A good planarity of the sample is required to avoid errors due to the lens-surface misalignments. A good polished finish is also required since the surface wave velocity, measured with the acoustic microscope, is influenced by surface roughness. The sample was ground and polished to mirror quality (roughness 0.04 μm) by means of grinding papers of decreasing grain size and followed by diamond paste from 6 to 1 μm.

The surface has been imaged using another acoustic microscope: OXSAM, operating at 350 MHz. The defocus could be adjusted to optimise the sensitivity to features affecting the propagation of Rayleigh waves, which at this frequency sample a depth of about 10 μm. Figure 7 presents a picture of the measured area with the lens focused on the surface together with a picture in which the lens defocused by $z=8$ μm.

V. ACOUSTIC MICROSCOPE MEASUREMENTS

The loading device was positioned on the acoustic microscope stage so that the lens was in the central part of the sample with its cylindrical cavity axis perpendicular to the sample axis. The loading jig was held on the stage by means of a partial vacuum inside the stage. The microscope stage was levelled in order to make the vertical axis of the lens be perpendicular to the specimen surface. The measurements have been performed in the rolling direction.

At zero load a scan was made to measure the velocity of the Rayleigh waves in different points of the sample (Fig. 8). There is a variation of a few meters per second from point to point. The measurement aperture of the line focus beam is about 0.5 mm; an average occurs during a single measurement so that the orientation of the grains, whose dimensions are of the same order as the wavelength (10 μm), as shown in Fig. 7, does not influence the velocity values. A reason of the velocity variation along the axis (Fig. 8) could be that the alignments of the sample stage have been done with the lens positioned in the centre of the sample; moreover the sample is hand-polished and probably not uniformly flat along its axis. Therefore detection of the stress effect requires that the lens is held in the same relative position with the sample during the loading cycles. The measurement proceeds from the largest stress (either tensile or compressive) down to zero. The largest sample deflection allows better adjustment of the longitudinal position of the sample so that the lens focuses where the sample is locally horizontal.

To detect the longitudinal position of zero slope the lens

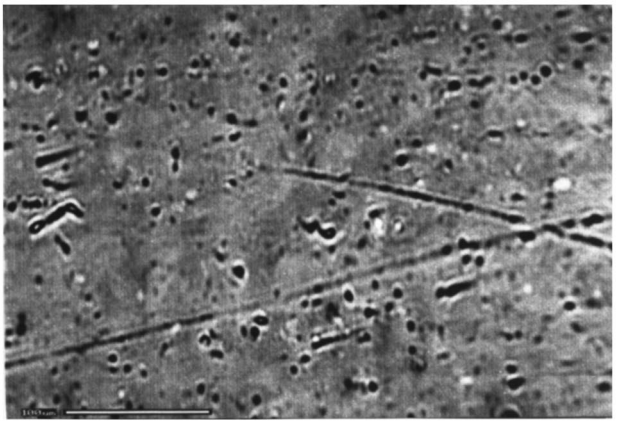

FIG. 7. Surface acoustic images by means of the acoustic microscope OXAM with (a) the lens focused on the surface and (b) defocus $z=8$ μm.

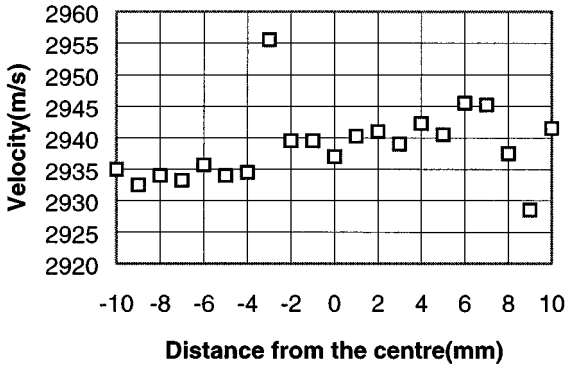

FIG. 8. Rayleigh wave velocity as a function of position along the sample axis.

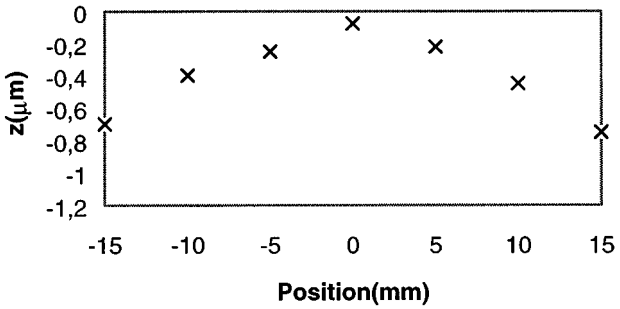

FIG. 9. Sample deformation topography in the case of tension on the sample top surface.

was scanned in order to find the focal position in different points along the sample longitudinal axis. The sample vertical displacement as a function of the horizontal lens position is plotted in Fig. 9 for a case with the top surface of the sample in tension. The region where the sample surface is horizontal was moved under the lens for the subsequent measurement. During the unloading steps the sample deformation decreased while maintaining its curvature coaxial with the cylindrical cavity lens: The deformed sample topography is verified each loading step by a scan like Fig. 9. Keeping the lens coaxial with the sample curvature ensures that the z-scan is normal to the sample surface.

For each sample deformation step, ten $V(z)$ curves were acquired from which ten values of velocity were calculated. The acoustic velocity in the water depends on the temperature, which was measured using a thermocouple. The temperature in the room was kept constant by an air conditioning system and the microscope is in a protective enclosure. For each deformation the mean of the ten velocity values was plotted versus the surface stress values measured by the strain gauges. The resulting graph is shown in Fig. 10, with the line of best fit. The error bars are the standard deviations of the measurements. The acoustoelastic constant K is defined as:

$$v - v_0 = K \cdot (\sigma - \sigma_0), \tag{3}$$

where v_0 Rayleigh wave velocity with an initial stress σ_0.

The slope of the best fit line in the graph of Fig. 10 is then a measure of acoustoelastic constant of the material. The value of this constant is given in Table I, together with its error calculated with 95% confidence.

TABLE I. Acoustoelastic constants and v_0 values obtained in different tests. The errors are calculated with 95% confidence.

6082 T6 aluminium alloy Polished surface	Acoustic microscope	Contact points device	
	Four-point bending	Four-point bending	Pure tensile stress
K ($m\,s^{-1}\,MPa^{-1}$)	0.066	0.065	0.062
v_0 ($m\,s^{-1}$)	2938.6	2976.6	2976.1
err in K ($m\,s^{-1}\,MPa^{-1}$)	0.010	0.006	0.016
err in v_0 ($m\,s^{-1}$)	0.7	0.4	1.2

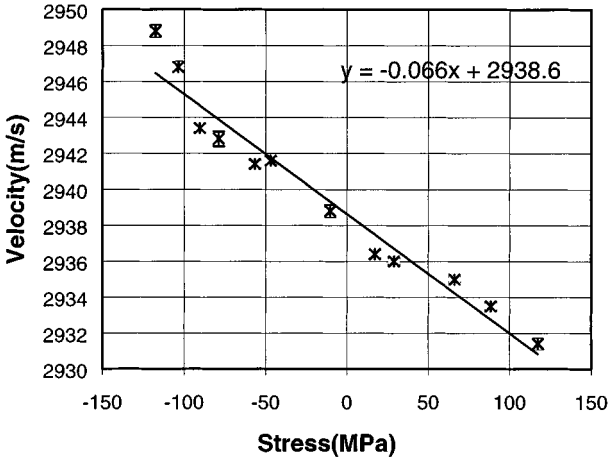

FIG. 10. 6082 T6 aluminium alloy sample, LFB acoustic microscopy measurements.

The acoustoelastic constant value is in good agreement (inside 10%) with that found on a sample, loaded in pure traction, of the same aluminium alloy group (AlMgSi) by J. D. Achenbach *et al.*[13]

VI. MEASUREMENTS WITH THE CONTACT DEVICE

A. Bending test

The measurements with the point contact device were taken on the same sample after the microscope measurements to avoid the scratches due to the contact device tips disturbing the high frequency acoustic microscope measurements. The contact point device is held in contact with the sample loaded in the four-point bending system by two small weights (80 g), one between the two receivers, and the other on the transmitter. A thin layer of coupling oil was spread under the transmitter wedge. As in the case of the acoustic microscope the sample is unloaded in steps starting from maximum concave deformation to zero and from the maximum convex deformation to zero. For each step the surface stress was measured by strain gauges and the wave velocity was measured ten times, each time after lifting and replacing the contact device. The frequency was 5 MHz, giving a Rayleigh wavelength of 0.6 mm. The value of the stress influencing the velocity has been calculated as the mean value of the stress over a depth equal to the characteristic depth z_c shown in Fig. 11. The depth z_c has been calculated[8] as the position of the centre of the area subtended by the exponential function expressing the decay of the wave from the surface. Different values of the depths z_c are summarised in

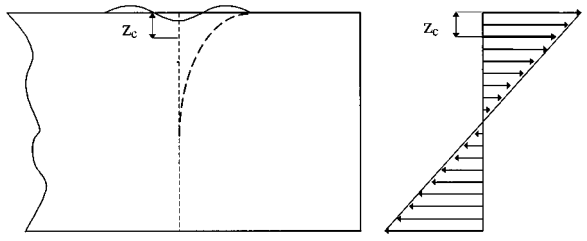

FIG. 11. Variation of the stress field through the sample thickness.

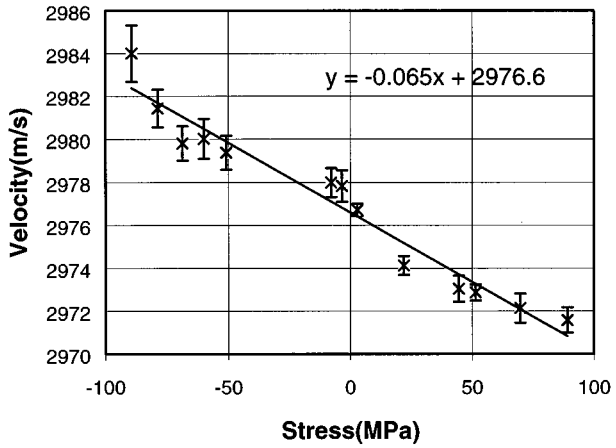

FIG. 12. Contact point device measurements of Rayleigh velocity versus mean stress encountered by the Rayleigh wave on a 6082 T6 aluminium alloy sample loaded in four-point bending.

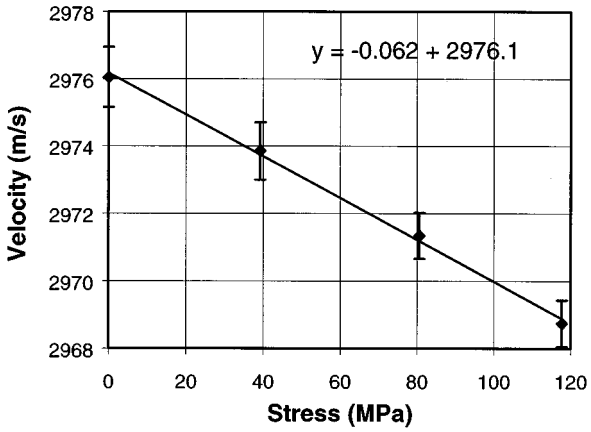

FIG. 13. 6082 T6 aluminium alloy sample, contact point device measurements. Loading system: pure tensile stress.

Ref. 8 (Table 6.2) for different values of Poisson ratio of the material. In the case of aluminium alloy the Poisson ratio is 0.3 and the characteristic depth z_c 0.6 wavelength.

In Fig. 12 the mean of ten velocity measurements for each loading step is plotted against the value of stress estimated in this way; the error bars are the standard deviations of the measurements at each value of stress.

Each velocity value was calculated from the time of flight of a Rayleigh wave and the distance of the two contact points. For each loading step the distance between the tips is corrected of a term due to the sample curvature (obtained from geometrical considerations). In the case of maximum sample deformation (surface stress near the yield point 120 MPa) the increasing of the wave path between the two tips due to the sample curvature is about 0.06%.

In Fig. 12 the slope of best fit line is, as in Fig. 10, an approximation of the acoustoelastic constant of the material. The value of this constant and its error calculated with 95% confidence are shown in Table I.

B. Tensile test

The same sample was subsequently tested applying pure tensile stress by means of an hydraulic tensile machine. In this case no correction of the distance for the sample curvature was necessary. As in the previous case for each loading step the velocity was measured ten times, each time after removing and replacing the contact device. The mean of each set of ten measurements with its standard deviation is plotted in Fig. 13 versus the stress on the surface (no stress gradient is present). The value of the acoustoelastic constant (slope of the best fit line) and its error calculated with 95% confidence are shown in Table I.

The acoustoelastic constant value is in good agreement (inside the measurement errors) with that found on a sample, loaded in pure traction, of the same aluminium alloy group (AlMgSi) by B. G. Martin.[14] Comparisons with results from other authors[2–5] are not significant because they tested different alloys.

VII. INFLUENCE OF THE TEXTURE

The sample has a strong texture since it was cut from a rolled aluminium sheet. If the texture changes with the depth, Rayleigh waves propagating with two different penetration depths (10 μm in tha case of LFB and 0.6 mm for point contact device), could be influenced by two different textures.

The effect of two different texture on the measurement obtained after application of loads on the sample could be:

- translation of the curve applied stresses velocity without changing its slope,
- change of the acoustoelastic constant due to texture orientation variation along the thickness.

The first effect does not influence the values of the acoustoelastic constants obtained by means of the two techniques.

The second effect, if present, could be hidden in the difference between the acoustoelastic constants obtained by means of the two techniques. Measurements of texture orientations along the sample thickness have not carried on in this context so that this effect has not been proved. Comparison with values of acoustoelastic constants obtained by other authors[13,14] seems to indicate that any variation associated with texture, if present, is less than 10%.

VIII. CONCLUSIONS

After the preparation of the sample the experiments have been developed in three different phases:

1—measurements with the LFB non-contact technique, sample loaded in a four-point bending device;

2A—measurements with the ''contact device,'' sample loaded in a four points bending device;

2B—measurements with the ''contact device,'' sample loaded in a pure tensile machine.

In step 1 the graph of Fig. 10 has been obtained. There is some scatter in the results, but there is also a systematic variation in the Rayleigh velocity with stress. A similar variation was found when the sample was subsequently

tested with a completely different and independent technique on the same four-point bending device (step 2A), as shown in Fig. 12.

The comparison with the measurements obtained in step 1 with those obtained in step 2A shows good agreement in the acoustoelastic constant values to within 5%. The two techniques differ by the velocity measurements: The velocity inferred from the microscopy technique measurments is a phase velocity (see the Appendix) while that obtained from the contact device is a group velocity; the frequency also is different 225 MHz and 5 MHz.

The velocity values measured in the two techniques differ by about 40 m s^{-1}. The contact technique is set more for comparative velocity measurements rather than absolute; in fact each velocity value depends on the accuracy with which the separation between the receiver tips distance is known. Thus, for example, assuming a tip separation $d=19.88$ mm rather than $d=20$ mm decreases the velocity values by about 40 m s^{-1} without altering the value of the velocity variation with the stress (acoustoelastic constant), which is the parameter we are really interested in.

To check the influence of the sample curvature due to the bending, in step 2B the contact device was employed on the sample loaded in pure tensile stress. Satisfactory agreement of the acoustoelastic constant value with the previous value (from the bending system) confirms that the sample curvature and the particular loading system adopted have little influence on the measurements.

These experiments confirm the possibility of stress measurements in bent specimen by the LFB acoustic microscopy. Testing a non-homogeneous material at 225 MHz increases the measurement difficulties since the acoustic lens must be kept in the same point (specimen curvature coaxial with the lens cavity) during the loading and unloading phases. The cross comparison with a contact measurement technique tested on the specimen loaded in bent and pure tensile confirms the validity of the measurements.

ACKNOWLEDGMENTS

The authors wish to thank the British Council and the Ministero dell'Università e della Ricerca Scientifica for providing grants for travel and accommodation.

APPENDIX

From LFB acoustic microscope measurements, phase velocity can be computed. The velocity of the surface wave is obtained from oscillations in the transducer signal $V(z)$ which can be understood in terms of interference between two reflected components. The analysis of these oscillations assumes waves of a single frequency (135–144, Ref. 8). In this case it is not even meaningful to speak of group velocity, since at a single frequency there can be no dispersion (indeed the concept is then meaningless). For practical reasons a pulse must be used in the experiment (though the pulse length in the LFB microscope contains many more oscillations than in an imaging microscope), and therefore more than one frequency is present. But no attempt is made to determine the group velocity of the pulse, and in more advanced microscopes special electronic circuits are used to ensure that the measurement is made on a single frequency component of the spectrum within the pulses (64–73, Ref. 8). The propagation direction arises as a further question in anisotropic materials, since even when there is no dispersion with frequency, the Pointing vector (which gives the direction of the group velocity) is not in general parallel to the wave vector (which gives the direction of the group velocity). In the LFB microscope it is again the phase velocity that can be deduced, since the nature of the cylindrical lens means that while beam steering by the anisotropy may affect the strength of the oscillations in the lens signal $V(z)$, it cannot affect their period. Thus the azimuthal propagation angle phi of the surface waves measured in an LFB microscope refers to the direction of the wave vector (which is perpendicular to the axis of the cylindrical lens), and not the direction of group velocity (240–251, Ref. 8). In this context the ray model of the $V(z)$ effect may seem a little confusing at first, since rays are associated with energy flow, but more careful analysis shows that any deviation of the ray in the surface from the wave vector cancels out, and it is indeed the phase velocity (in the direction of the wave vector) that can be deduced.

[1] G. R. Gerhart, ''Rayleigh wave velocity for a stress induced slightly anisotropic solid,'' J. Acoust. Soc. Am. **60**, 1085–1088 (1976).
[2] K. Jassby and D. Saltoun, ''Use of ultrasonic Rayleigh waves for the measurement of applied biaxial surface stresses in alluminium 2024-t351 alloy,'' Mater. Eval. **40**, 198–205 (1982).
[3] K. Jassby and D. Kishoni, ''Experimental technique for measurement of stress-acoustic coefficients of rayleigh waves,'' Exp. Mech. **23**(1), 74–80 (1983).
[4] P. P. Delsanto, R. B. Mignogna, and A. V. Clark, ''Ultrasonic texture and stress measurements in anisotropic polycristalline aggregates,'' J. Acoust. Soc. Am. **87**, 215–224 (1990).
[5] S. Kobayashi, ''Stress measurement by use of Rayleigh waves,'' in *Residual Stresses III*, edited by H. Fujiwara, T. Abe, and K. Tanaka (Elsevier Applied Science, London, 1992), Vol. 2, pp. 1109–1114.
[6] A. F. Jankowsky and T. Tsakalakos, ''The effect of strain on the elastic constants of noble metals,'' J. Phys. F: Met. Phys. **15**, 1279–1284 (1985).
[7] A. Briggs, *Advances in Acoustic Microscopy* (Plenum, New York, 1995), pp. 209–244.
[8] A. Briggs, *Acoustic Microscopy* (Oxford University Press, New York, 1992), pp. 78–164.
[9] J. Kushibiki and N. Chubachi, ''Material characterization by line-focus beam acoustic microscope,'' IEEE Trans. Sonics Ultrason. **32**, 189–212 (1985).
[10] W. Parmon and H. L. Bertoni, ''Ray interpretation of the material signature in the acoustic microscope,'' Electron. Lett. **15**, 684–686 (1979).
[11] A. Atalar, ''A physical model for acoustic signatures,'' J. Appl. Phys. **50**, 8237–8239 (1979).
[12] T. Berruti and M. M. Gola, ''Acoustoelastic determination of stresses in steel using Rayleigh ultrasonic waves,'' in *Non-destructive Characterization of Materials VII*, edited by A. L. Bartos, R. W. Green, Jr., and C. O. Ruud (Transtec Publications Ltd., Zurich, 1996), Vol. 1, pp. 171–178.
[13] Y. Lee, J. O. Kim, and J. Achenbach, ''Measurement of stresses by line focus acoustic microscopy,'' Ultrasonics **32**, 359–365 (1994).
[14] B. G. Martin, ''The measurement of surface and near-surface stress in aluminium alloys using ultrasonic Rayleigh waves,'' Mater. Eval. **32**, 229–234 (1974).

The acoustic emissions from single-bubble sonoluminescence

Thomas J. Matula, Ibrahim M. Hallaj, Robin O. Cleveland, and Lawrence A. Crum
Applied Physics Laboratory, University of Washington, 1013 NE 40th Street, Seattle, Washington 98105

William C. Moss
Lawrence Livermore National Laboratory, P.O. Box 808, Livermore, California 94550

Ronald A. Roy
Department of Aerospace and Mechanical Engineering, Boston University, 110 Cummington Street, Boston, Massachusetts 02215

(Received 3 February 1997; accepted for publication 24 November 1997)

Detailed measurements of the acoustic emissions from single-bubble sonoluminescence have been made utilizing both a small 200-μm aperture PVDF needle hydrophone, and a focused 10-MHz transducer. Signals obtained with the needle hydrophone show a fast (5.2 ns), probably bandlimited rise time and relatively large pulse amplitude ($\approx$1.7 bar). Below the sonoluminescence threshold, the emissions are observable, but considerably smaller in amplitude ($\approx$0.4 bar). Several signals are observed with the 10-MHz transducer and correspond to acoustic emissions from the bubble during the main collapse, as well as from the rebounds. Experiments reveal that the acoustic emissions occur at or near the minimum bubble radius. Calculations of the peak pressures and pulse widths are compared with experimental data.
[S0001-4966(98)03203-2]

PACS numbers: 43.35.Ei [HEB]

INTRODUCTION

The discovery of single-bubble sonoluminescence[1] or SBSL, in which a single cavitation bubble is acoustically driven to transduct sound energy into light energy in a stable and repeatable fashion, has generated a great amount of interest in the scientific community resulting in remarkable experimental discoveries.[1–9] Though the transduction mechanism is still greatly debated, the dynamical motion of the bubble [radius versus time, or $R(t)$ curve] can be described via the equations of nonlinear bubble dynamics.[10] These equations predict the overall motion quite well, as confirmed using light scattering techniques.[11]

Most studies of sonoluminescence bubbles have centered on the light emission. In this paper we focus on the acoustic emissions from SBSL, where we attempt to make detailed measurements of the emission characteristics. The motivation for this study arises, in part, from previous measurements of the acoustic emissions using homemade hydrophones, in which the output signal appears to show evidence of shock-induced ringing of the hydrophone.[12] (Evidence for acoustic emissions can also be observed by placing a pill transducer to the outside of a levitation cell; the shape of the driving sinusoid becomes distorted when the levitated bubble is near the sonoluminescence threshold.)

Previous studies of the acoustic emissions from cavitation bubbles have typically involved cavitation fields, whereby many bubbles are cavitating in a transient fashion. Hence typical experiments rely on spectral characteristics of the ''noise'' signal, since individual signals are hard to distinguish and correlate with a particular bubble.[13] With SBSL, we can directly observe the correlated emission from a single cavitating bubble and, using light-scattering techniques, monitor the dynamical motion simultaneously.[14] In this paper, we attempt to quantify some of those observations. In particular, we have attempted to measure the acoustic pulse amplitude and pulse width. Furthermore, we have attempted to relate the location (in time) of the acoustic pulse with the radial oscillations of the cavitating bubble. Our techniques do not employ signal averaging, and hence, retain certain characteristics of the pulse that might otherwise average out due to jitter in signal triggering.[15]

Finally, we compare our measurements with calculations for the radiated pressure from a cavitation bubble. In one case we assume that the bubble wall generates the observed pressure pulse; in another case we assume the observed pulse is due to a shock wave originating from inside the bubble. We find that the pulse amplitude calculated using the internal shock-wave method is consistent with experimental measurements, however, the pulse width does not agree with measurements. Calculations of the acoustic emissions based on the bubble wall motion, on the other hand, overestimate the pulse amplitude, but are consistent with the pulse width.

I. EXPERIMENT

Our experiment was performed in a quartz cylindrical levitation cell (7.5-cm tall by 4.5-cm diameter) closed at the bottom with a glass plate, and open on top to the atmosphere. The levitation cell is filled with degassed (with air, to approximately 15% of saturation), filtered, room-temperature water to a height of 6.0 cm. The driving frequency of 33.8 kHz corresponds to the fundamental resonance (a single-pressure antinode located at the center) of this cell. The pressure field along the axis of the cell was measured with a (low-frequency) calibrated Dapco needle hydrophone.[16] The acoustic emission can be observed using either a needle hydrophone or a focused transducer, as described below. The

 0001-4966/98/103(3)/1377/6/$10.00

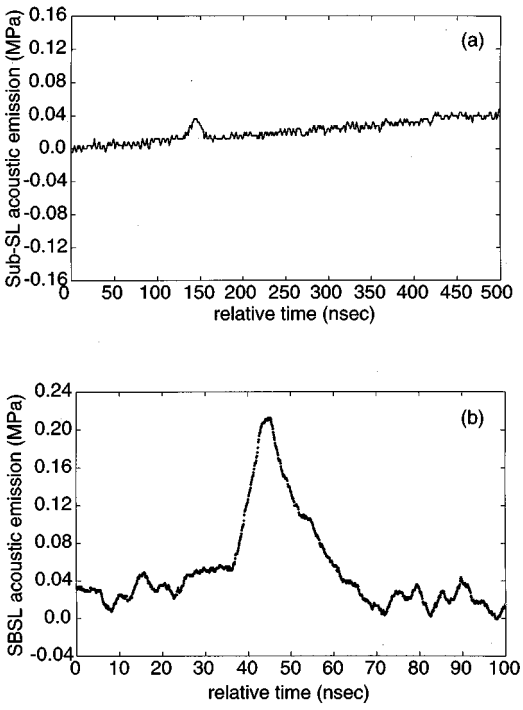

FIG. 1. Typical signal observed for a bubble (a) below, and (b) above the luminescence threshold, measured with a calibrated 0.25-mm aperture needle hydrophone. The measured rise time of the signal in (a) is approximately 10 ns. The general increasing trend in the signal over these time scales is due to the changing drive pressure amplitude. The measured rise time (5.2 ns) and amplitude (1.7 bar) in (b) may be limited by the 100-MHz bandwidth preamp, as well as the finite curvature of the wavefront, as discussed in the text.

levitation cell is mounted on a three-dimensional translation stage so that fine control of the positioning can be obtained.

A. Needle hydrophone measurement

In this experiment a (high-frequency) calibrated 5-cm-long needle hydrophone (Precision Acoustics,[17] model 340) is used to measure acoustic emissions from a cavitating bubble, both below, and above the sonoluminescence threshold. The hydrophone employs a polyvinylidene fluoride (PVDF) sensor with an aperture of 200 μm. The PVDF thickness is 9 μm (with a sound speed in PVDF of about 2250 m/s, the $\lambda/2$ resonance occurs at 125 MHz). A 20-dB preamp (Precision Acoustics model HP1, manufacturers rated bandwidth of 100 MHz) is attached directly to the hydrophone. The output is then delivered to another preamp (EG&G) model 115, 100-MHz bandwidth, 20-dB gain) before being delivered to a fast digitizing oscilloscope (LeCroy 9362, 1.5-GHz analog bandwidth, 10-GS/s digitizing rate). The location of the hydrophone, approximately 1 mm above the bubble, is the closest we could come without disturbing the bubble significantly (at this separation distance, we could not employ signal averaging due to the slight jitter of the bubble).

Figure 1 illustrates signals observed from a cavitating bubble using this system. Below the sonoluminescence threshold [shown in Fig. 1(a)] the signal is weak ($\approx$0.4 bar), and shows a rise time of approximately 10 ns. The pulse width is approximately 20 ns (the drive pressure amplitude, $P_a \approx 0.9$ bar, for this case). We note that this signal is not necessarily typical of all signals observed below the threshold. Repeatable measurements are difficult to obtain due to the instability of the bubble. This signal represents one of the larger amplitude signals that we were able to obtain. Smaller amplitude signals can be more rounded than shown here, probably due to a slight misalignment between the bubble and hydrophone. This issue is discussed later. (We note that it would be difficult to make a series of progressive measurements of the acoustic emission amplitude as the bubble is driven from below the light-emission threshold to above the threshold, due to the jitter, or dancing motion of the bubble as the threshold is approached.)

Above the SBSL threshold [Fig. 1(b)], the signal amplitude is much larger (approximately 1.7 bar) and sharpens, with a 5.2-ns rise time (10%–90% transition). The measured rise time approaches the bandwidth of our system,[18] so that the actual pulse may have a slightly faster rise time and higher amplitude (the drive pressure amplitude for this case was $\approx$1.5 bar). Note that at a distance of 1 mm, the curvature of the wavefront differs from planar by approximately 0.3%. This slight difference may add as much as 3 ns to the detected rise time of the pulse, assuming the hydrophone edges are as equally sensitive as the center portion of the hydrophone. Thus our measurements are limited by the finite curvature of the wavefront, and by the bandwidth of our detector.

The pulse width of the signal above the threshold is about 25 ns. In addition, one can see small perturbations on the back side of the pulse, near 54 and 63 ns. We believe these perturbations are due to reflections of the signal within the 9-μm-thick PVDF (the travel time between the front and back portion of the PVDF is $\approx$4 ns). Taking these perturbations into account, the pulse width of the SBSL emission is similar to the pulse width observed for a bubble below the sonoluminescence threshold. (Also note that needle hydrophones can resonate via reflections within the needle itself. In our case, these reflections occur at a much lower frequency, and are delayed in time relative to the appearance of the main signal.)

B. Focused transducer measurement

A 10-MHz focused transducer (focal length=25 mm, aperture size=6.35 mm) was also employed for observing the acoustic emission from cavitating bubbles.[19] For this experiment the transducer was positioned in the levitation cell, with care taken not to trap air beneath the concave transducer element. The face of the transducer sat 5 mm below the water line and was positioned for maximum response from the bubble emission. The output of the transducer was either input directly into a digitizing oscilloscope (LeCroy 9450, 400 MHz), or into a 40-dB preamp before being delivered to the oscilloscope (the distinction is made clear below).

In this experiment we also measured simultaneously the radius versus time curve for the bubble using a light scattering technique. We used an argon/ion laser (at 200 mW), with an emission at 514 nm for these measurements. The intensity

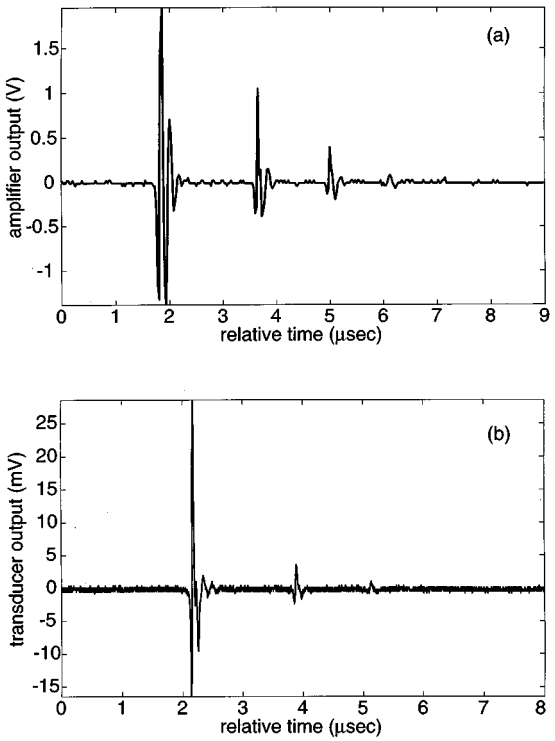

FIG. 2. Pressure pulses from an SBSL bubble measured with the focused transducer. The output from the transducer (a) with and (b) without a secondary 40-dB preamp. In (a) the first pulse amplitude causes distortion in the preamp, such that no amplitude comparisons can be made of that particular signal with the other pulses.

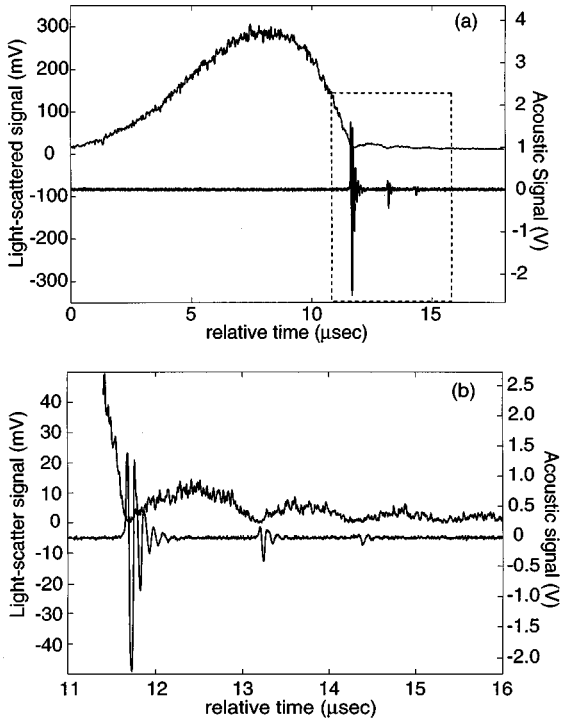

FIG. 3. (a) A single-shot $R(t)$ curve as measured using our light-scattering system, with the corresponding acoustic signature. (b) A detailed view of the boxed area in (a). The acoustic data is shown here shifted in time equal to the time necessary for sound to travel from the bubble to the transducer, about 16.77 μs.

scattered from the bubble was observed with a photomultiplier tube (RCA 9495 KB). The method is described in more detail elsewhere.[1,11]

Figure 2 illustrates the large acoustic signals observed from SBSL being driven near its maximum light output ($P_a \approx 1.5$ bar) with (a) and without (b) the added 40-dB preamp. The initial signal from each pulse corresponds to a positive pressure incident on the transducer, as verified with the needle hydrophone. The remainder of each separate signal is probably due to transducer ringing (the ringing occurs at 10 MHz).

The initial spikes in Fig. 2(a) and (b) correspond to the acoustic emission from SBSL at or near the minimum of the bubble radius, where the light emission is also observed. This was verified by recording the time delay between the light emission [using a photomultiplier tube (PMT)] and the acoustic emission, taking into account the travel time of the acoustic pulse from the bubble to the transducer. We used a pulse–echo technique to measure the travel time,[20] which was found to be $16.77 \pm 0.025\ \mu$s. The estimated error comes from resolving the true arrival time of the pulse. There is also a small systematic error in the pulse–echo measurements, since we ''pinged'' off the bubble during its growth phase, and not near the bubble minimum. Assuming the echo originated when the bubble was 20 μm, we estimate the added propagation time from a bubble of 1 μm to be 13 ns.

Because of the high signal-to-noise ratio (due in part to the geometrical gain from focusing), we are also able to observe several of the smaller pulses associated with the rebounds. This can be verified by simultaneous measurements of the $R(t)$ curve using our light scattering system. Figure 3 shows a single-shot $R(t)$ curve together with the single-shot acoustic emission pulses. In Fig. 3(a) the general features for both the light scattered data and acoustic emission data are shown, and in Fig. 3(b) an expanded view of the boxed region is shown, clearly showing the correspondence of the $R(t)$ curve and acoustic emission pulses (for this figure the acoustic emission data was shifted by a time corresponding to the acoustic travel time to the transducer).

The addition of a 40-dB preamp allowed us to compare the relative amplitudes of the rebound, or afterbounce emissions (see Fig. 2); however, with the preamp in place, the initial signal amplitude becomes distorted due to its relatively large amplitude. Thus for comparisons, we examine the relative amplitude of the large main signal with the first afterbounce emission without the preamp, and then compare the relative afterbounce emissions using the preamp.

II. DISCUSSION

The acoustic emission measured with the needle PVDF hydrophone clearly shows that the SBSL-generated acoustic pulse has a fast rise time and relatively large amplitude, suggesting the presence of a shock emitted from the bubble. If we assume the pulse is only affected by spherical spreading, then a measured pressure amplitude of 1.7 bar (at ≈ 1 mm) implies that near the bubble minimum ($\approx 1\ \mu$m), the pressure would be 1700 bar [acoustic Mach number of 1.13 (Ref.

21)]. This prediction is a lower bound, since absorption and instrumental effects have been neglected. In the Appendix we show that we can estimate the effects of attenuation (other than spherical spreading) if we assume that the measured pulse nearly corresponds to the actual pulse. This allows us to estimate the pulse spreading and amplitude reduction that would occur because of absorption and finite-amplitude effects. The results show that, for $r \geqslant 5\ \mu$m, neither linear absorption nor finite-amplitude effects affect the pressure pulse to any significant degree, so that *if* the measured pulse is nearly representative of the actual pulse, spherical spreading is the dominant attenuation mechanism, and pulse spreading is minimal (we emphasize our measurement is close to the bandwidth limitations of our system, so that it is possible that the actual pulse has a shorter rise time and a larger amplitude, and the resulting analysis from the Appendix is thus an approximation).

Comparisons of the measured pressure amplitude with calculations can be insightful. For instance, one-dimensional (1-D) hydrodynamic simulations of a collapsing bubble have shown that a shock wave can be generated within a bubble during its collapse.[22–24] This shock wave converges, reflects, then diverges from the center of the bubble. Meanwhile, the radius of the bubble continues to decrease until the diverging shock wave reaches it, after which the radius begins to increase. The shock wave continues to propagate into the liquid, where its strength diminishes rapidly due to spherical divergence. The calculated shock pressure amplitude is approximately 2 bar at a distance of 1 mm from the center of a nitrogen bubble, with $R_0 = 4.5\ \mu$m and $R_{\max} = 44\ \mu$m.

This calculated pressure amplitude agrees with our measured pressure amplitude (at 1 mm from the bubble). It is important to note, however, that the calculated amplitudes are sensitive to the initial conditions, including the gas content in the bubble; for a nitrogen bubble with $R_0 = 4.5\ \mu$m and $R_{\max} = 36\ \mu$m, the shock pressure amplitude is approximately 1.2 bar at a distance of 1 mm from the bubble (compared to 2 bar for $R_{\max} = 44\ \mu$m).

Although consistent with the measured peak amplitude, the hydrodynamic simulations predict that the pulse width be approximately 40 ps at 1 mm from the bubble center. The measured pulse width is near 20 ns.

In the above analysis, the radiated pressure results from acoustic waves interior to the bubble, propagating out into the fluid. However, one would expect acoustic emissions even with a spatially uniform gas pressure in the bubble. In this case, the acoustic emission would be due to the large decelerations that arrests the bubble wall's inward collapse. We can examine this deceleration mechanism for acoustic radiation from a radially pulsating bubble, subject to simplifying assumptions. For the sake of conciseness, we leave the details to the interested reader.[25–27] The calculation depends on the radius-time dynamics of the bubble, which we obtain via the Keller equation.[28] Note that pressures calculated with this method should overestimate the actual pressure, since not all loss mechanisms are included in the Keller equation, nor is the Keller equation strictly valid near where the radiated pressure originates.

Nevertheless, using this deceleration-mechanism method for calculating the radiated pressure, we find that the maximum pressure amplitude at the location of the hydrophone (for an equilibrium radius of $R_0 = 4.5\ \mu$m and a driving pressure of $P_a = 1.5$ bar) is about 15 bar. As in the previous hydrodynamic simulations, this method also shows a similar variability in the radiated pressure with initial conditions (e.g., a driving pressure of $P_a = 1.3$ bar yields a maximum pressure amplitude of about 5 bar at 1 mm). Interestingly, the pulse width calculated using this method is 20 ns. Thus although the peak pressures are overestimated (as one would expect), the pulse width is consistent with the measured values.

Further insight can be obtained from data obtained with the focused transducer. Although the focused transducer is not calibrated, and ringing is evident, we expect the peak signal is proportional to the pressure amplitude. The observed reduction in amplitude after each rebound is not predicted by either model discussed here. Both models consistently overpredict the (relative) rebound amplitudes, indicating that further dissipation terms are needed to better predict the rebound dynamics.

From these calculations we cannot positively discern whether the emission is from the bubble wall, as it arrests its inward collapse, or whether the emission is due to a shock wave propagating from the bubble interior. Perhaps the emission is due to both phenomena. For instance, Fig. 1(b) appears to show a small precursor at $t \approx 30$ ns (although difficult to distinguish among the other wiggles, the precursor always shows up as an almost flat signal lasting ≈ 10 ns, lacking the normal noise oscillations). This precursor may be due to the initial acceleration from the bubble as it begins to arrest its collapse. However, this precursor may also simply be due to a small misalignment of the needle hydrophone, as is typically observed in similar measurements. A small misalignment causes the pulse to reach the casing of the hydrophone first. This signal propagates faster than the pulse in the water, and reaches the sensor element first, giving the precursor. Careful alignment is thus necessary; also, with misalignment the rise time of the pulse widens, as it takes a longer time for the wavefront to traverse the aperture of the sensor element [as may be the case shown in Fig. 1(a)]. Parenthetically, one might also expect acoustic radiation from translational motion of the bubble as a result of the Bjerknes and buoyancy forces; however, this radiation should be much smaller than the radiation from other means.[12]

Another feature observed with the focused transducer is that the period between successive acoustic emissions decreases. This corresponds to a decrease in the rebound period. The observed decreasing period is due to the varying drive pressure amplitude over the acoustic cycle. During the rebounds, the drive pressure is increasing, causing the bubble to ''ring'' at a higher rate. This decrease in the period between subsequent rebounds can also be observed in our light scatter data, Fig. 3(b).

III. CONCLUSION

Our observations of the correlated acoustic emissions from a single cavitating bubble show that the acoustic emis-

sions originate at or near the local bubble minima. This was accomplished using a focused transducer and pulse–echo technique to determine the travel time of the acoustic emission, and comparing this travel time to the time of light emission for an SBSL bubble. In addition, we have also observed acoustic emissions from the rebounds, as verified by simultaneous light scattering from the bubble. Finally, using a needle hydrophone and fast digitizer, we found that the fast rise time and relatively large amplitude of the observed acoustic signal for an SBSL bubble suggests that a diverging shock wave is propagated through the liquid.

Hydrodynamic simulations correctly predict the pressure amplitude, but not the pulse width. Bubble dynamics equations overpredict the pressure amplitude, but correctly predict the pulse width. Inclusion of other loss mechanisms not currently contained in the theories may further clarify the situation.

Previous measurements at distances of several mm from the bubble have shown that the amplitude does obey spherical spreading.[12] It would be interesting to determine whether the emission is also spherically symmetric. Asymmetric collapse hypotheses could possibly be tested by examining the acoustic emission amplitude at various locations around the bubble. One would expect that an asymmetric bubble collapse would generate an asymmetric (possibly toroidal) acoustic pulse. We are presently examining the possibility that such a measurement can be made accurately.

Finally, the acoustic emission data from the focused transducer also clearly illustrates a simple and inexpensive technique for monitoring the stability of single-bubble sonoluminescence. Minimizing the pulse-to-pulse jitter from the acoustic signal is a means to fine-tuning the sonoluminescence apparatus without the cost and the dark lab environment necessary with light detectors.

ACKNOWLEDGMENTS

We wish to thank Vera Khoklova for helpful conversations, and Todd Brooks for his assistance in the laboratory. This research is supported by NSF, ONR, and the UW Royalty Research Fund. W.C.M.'s work was performed under the auspices of the U.S. Department of Energy at Lawrence Livermore National Laboratory under Contract No. W-7405-Eng-48.

APPENDIX: ESTIMATION OF PULSE BROADENING AND AMPLITUDE REDUCTION BY ABSORPTION AND NONLINEARITIES

The goal of this Appendix is to estimate the effects of absorption and nonlinearities on the acoustic pulse during the propagation from near the bubble, out to 1 mm, where the hydrophone was located. Absorption and nonlinearities result in a broadening of the pulse width and a reduction in the pulse amplitude.

The pulse measured in Fig. 1(b) is typical of those observed in underwater explosions and spark discharges. We modeled the propagation of the pulse as a spherically spreading, progressive, finite-amplitude wave. The assumption of a spherically spreading, progressive wave is valid for a radius greater than approximately 5 μm (that is, large ka). We are not able to model the propagation characteristics at smaller radii; full hydrodynamic methods must be used. (It is interesting to note that using the full hydrodynamic simulations, the acoustic pulse in water comes from within the bubble, as a diverging shock wave. Artificial viscosity is used to match the hydrodynamics with the Rankine–Huginot relation.)

Finite-amplitude acoustics is a valid model in water for acoustic amplitudes up to about 1 kbar (Mach number of 1.08). The equation used to describe pulse propagation, accounting for spreading, nonlinearities, and absorption, is a generalized form of the Burgers equation,[29] given by

$$\frac{\partial P}{\partial r}+\frac{P}{r}-\frac{\beta P}{c_0^3\rho_0}\frac{\partial P}{\partial t'}=\delta\frac{\partial^2 P}{\partial t'^2}, \tag{A1}$$

where P is the pressure, r is the radial distance, c_0 is the ambient speed of sound in the liquid, ρ_0 is the ambient density of the liquid, β is the coefficient of nonlinearity, δ is the linear absorption coefficient, and $t'=t-r/c_0$ is a retarded time. Spherical spreading of the pulse is described by the second term on the left-hand side of Eq. (A1). Nonlinearities are described by the third term, while linear absorption is described by the first term on the right-hand side of Eq. (A1).

Our goal of determining the absorptive and nonlinear losses that result in the observed pressure pulse is hampered by the interaction of the nonlinear and absorption terms in Eq. (A1), which precludes us from using the pulse measured at 1 mm to determine the acoustic pulse close to the bubble. However, if the absorption term is neglected in Eq. (A1), the lossless Burgers equation is obtained. The lossless equation may be solved using the Earnshaw solution, in conjunction with weak shock theory to account for the presence of shocks.[30] The pulse can then be backpropagated to the desired location; the price paid is that shock rise times (at the earlier position of the pulse) cannot be predicted.

For a triangular-shaped pulse there is an analytical solution describing the evolution of the pulse.[31] The pulse measured in Fig. 1(b) was approximated as a triangle wave with amplitude 2 bar and duration 20 ns. Backpropagation to $r=5\,\mu$m (the limit for validity using this approach) using weak shock theory, produced a prediction of a triangle wave of amplitude 412 bar and duration 19.4 ns (small-signal acoustics would predict 500 bar and 20 ns). The effect of finite-amplitude effects appeared to be quite small. A full numerical solution of the generalized Burgers equation[32] was then used to forward propagate the triangle wave from $r=5\,\mu$m to $r=1$ mm. At $r=1$ mm the code predicted a triangular-shaped pulse with a rise time of 2 ns. The predicted rise time is a little shorter than actually observed and indicates that the bandwidth of the hydrophone and finite curvature of the wavefront may have limited the rise-time measurement; there may also have been a slight misalignment between the hydrophone and bubble, resulting in a broadening of the pulse.

This approach is limited to estimating the effects of absorption and nonlinearities for a radius $r\geqslant 5\,\mu$m. It benefits from the fact that we can use the measured pulse character-

istics to estimate the losses, which appear to be small over the range considered. In any case, the measured pulse amplitude and rise time represents a lower and upper bound, respectively, to the actual pulse.

[1] D. F. Gaitan, L. A. Crum, C. C. Church, and R. A. Roy, ''Sonoluminescence and bubble dynamics for a single, stable, cavitation bubble,'' J. Acoust. Soc. Am. **91**, 3166–3183 (1992).

[2] B. P. Barber, R. Hiller, K. Arisaka, H. Fetterman, and S. Putterman, ''Resolving the picosecond characteristics of synchronous sonoluminescence,'' J. Acoust. Soc. Am. **91**, 3061–3063 (1992).

[3] R. Hiller, S. Putterman, and B. P. Barber, ''Spectrum of synchronous picosecond sonoluminescence,'' Phys. Rev. Lett. **69**, 1182–1184 (1992).

[4] R. G. Holt, D. F. Gaitan, A. A. Atchley, and J. Holzfuss, ''Chaotic sonoluminescence,'' Phys. Rev. Lett. **72**, 1376–1379 (1994).

[5] R. Hiller, K. Weninger, S. J. Putterman, and B. P. Barber, ''Effect of noble gas doping in single bubble sonoluminescence,'' Science **445**, 248–250 (1994).

[6] T. J. Matula, R. A. Roy, P. D. Mourad, W. B. McNamara, and K. S. Suslick, ''Comparison of multibubble and single-bubble sonoluminescence spectra,'' Phys. Rev. Lett. **76**, 2602–2605 (1995).

[7] R. G. Holt and D. F. Gaitan, ''Observation of stability boundaries in the parameter space of single bubble sonoluminescence,'' Phys. Rev. Lett. **77**, 3791–3794 (1996).

[8] J. B. Young, T. Schmiedel, and W. Kang, ''Sonoluminescence in high magnetic fields,'' Phys. Rev. Lett. **77**, 4816–4819 (1996).

[9] K. Weninger, S. J. Putterman, and B. P. Barber, ''Resolving the moment of collapse of a sonoluminescing bubble,'' J. Acoust. Soc. Am. **100**, 2716(A) (1996).

[10] For a review, cf. T. G. Leighton, *The Acoustic Bubble* (Academic, New York, 1994), pp. 302–308.

[11] B. P. Barber and S. J. Putterman, ''Light scattering measurements of the repetitive supersonic implosion of a sonoluminescing bubble,'' Phys. Rev. Lett. **69**, 3839–3842 (1992).

[12] S. M. Cordry, ''Bjerknes forces and temperature effects in single-bubble sonoluminescence,'' Ph.D. thesis, University of Mississippi, 1995.

[13] Measurements of the transient collapse of individual cavitation bubbles have been made previously. See, e.g., S. L. Ceccio and C. E. Brennen, ''Observations of the dynamics and acoustics of traveling bubble cavitation,'' J. Fluid Mech. **233**, 633–610 (1991); S. Fujikawa and T. Akamatsu, ''Effects of the non-equilibrium condensation of vapour on the pressure wave produced by the collapse of a bubble in a liquid,'' J. Fluid Mech. **97**, 481–512 (1980).

[14] I. M. Hallaj, T. J. Matula, R. A. Roy, and L. A. Crum, ''Measurements of the acoustic emission from glowing bubbles,'' J. Acoust. Soc. Am. **100**, 2717(A) (1996).

[15] Recent measurements of the acoustic emission using a fiber-optic hydrophone [Gompf (private communication)] show similar characteristics to our data, but because of the decreased sensitivity, the fiber-optic hydrophone must employ signal averaging.

[16] The custom needle hydrophone obtained by Dapco (Dapco Industries, Inc., 241 Ethan Allen Highway, Ridgefield, CT 06883) was calibrated against a B&K 8103 calibrated hydrophone via a substitution calibration in a 4-l ''tank'' filled with degased water. A PZT glued to the bottom of the tank was used to set up a standing wave within the tank, at the appropriate frequency. The Dapco sensitivity was found to be -266 ± 1.5 dBV/μPa.

[17] Precision Acoustics, 1 Colliton Walk, Dorchester DT1 1TZ, England.

[18] Assuming a single-pole, or lag network, the bandwidth of a system is related to the rise time of a signal by $\mathrm{BW}\times\tau_r\approx0.35$. Thus the fastest rise-time signal we can observe is $\tau_r\approx0.35/\mathrm{BW}\approx3.5$ ns. See, e.g., Malvino, *Electronic Principles* (McGraw-Hill, New York, 1984), pp. 426–428.

[19] Panametrics, Inc. (800) 225-8330. We also observed the acoustic emission from SBSL using 5 and 30 MHz focused transducers.

[20] The pulse–echo technique consists of a Panametrics 502U pulser–receiver connected to the transducer. A pulse is sent out at a particular phase of the sound field (triggered with an SRSDG345 delay generator) so that the pulse is incident on the bubble during the growth phase, which gives a larger echo signal. In this configuration the time difference between the pulse and echo was measured to be 33.53 ± 0.05 μs, and corresponds to twice the travel time from the bubble to the transducer. Note that the travel time from a 1-μm bubble would add approximately 13 ns.

[21] The Mach number is given by $M=V/c$; $V=c+0.5\beta p_{\mathrm{sh}}/\rho c$, where $c\approx1500$ m/s is the ambient sound speed, $\beta\approx3.5$ is the coefficient of nonlinearity, $p_{\mathrm{sh}}\approx1700$ bar is the shock overpressure, and $\rho\approx1000$ kg/m^3 is the density of water. Thus we obtain $M\approx1.13$. See, e.g., A. D. Pierce, *Acoustics: An Introduction to its Physical Principles and Applications* (Acoustical Society of America, New York, 1989), 2nd ed., pp. 589–590.

[22] C. C. Wu and P. H. Roberts, ''A model of sonoluminescence,'' Proc. R. Soc. London, Ser. A **445**, 323–349 (1994).

[23] W. C. Moss, D. B. Clarke, J. W. White, and D. A. Young, ''Hydrodynamic simulations of bubble collapse and picosecond sonoluminescence,'' Phys. Fluids **6**, 2979–2985 (1996).

[24] W. C. Moss, D. B. Clarke, J. W. White, and D. A. Young, ''Sonoluminescence and the prospects for table-top microthermonuclear fusion,'' Phys. Lett. A **211**, 69–74 (1996).

[25] V. A. Akulichev, ''Pulsations of Cavitation Voids,'' in *High-Intensity Ultrasonic Fields*, edited by L. D. Rozenberg (Plenum, New York, 1971), pp. 203–259.

[26] E. Cramer, ''The dynamics and acoustic emission of bubbles driven by a sound field,'' in *Cavitation and Inhomogeneities*, edited by W. Lauterborn (Springer-Verlag, Berlin, 1979), pp. 54–63.

[27] C. C. Church, ''A theoretical study of cavitation generated by an extracorporeal shock wave lithotripsy,'' J. Acoust. Soc. Am. **86**, 215–227 (1989).

[28] See V. Kamath, A. Prosperetti, and F. N. Egolfopoulos, ''A theoretical model of sonoluminescence,'' J. Acoust. Soc. Am. **94**, 248–260 (1993). A spatially uniform pressure inside the bubble is assumed, and a van der Waals equation of state is used ($R_0/a=8.54$, where a is the excluded radius). The driving frequency $f=33.5$ kHz, the speed of sound in water $c=1480$ m/s, the viscosity of water is $\mu=1$ cP, and the surface tension coefficient is $\sigma=72$ dyn/cm.

[29] D. T. Blackstock, ''Connection between the Fay and Fubini solutions for plane sound waves of finite amplitude,'' J. Acoust. Soc. Am. **39**, 1019–1026 (1966).

[30] K. A. Naugol'nykh, S. I. Soluyan, and R. V. Khokhlov, ''Spherical waves of finite-amplitude in a viscous thermally conducting medium,'' Sov. Phys. Acoust. **9**, 42 (1963).

[31] D. T. Blackstock, ''Nonlinear Acoustics (Theoretical),'' in *American Institute of Physics Handbook* (McGraw-Hill, New York, 1972), 3rd ed., Chap. 3n.

[32] R. O. Cleveland, M. F. Hamilton, and D. T. Blackstock, ''Time-domain modeling of finite-amplitude sound in relaxing fluids,'' J. Acoust. Soc. Am. **99**, 3312–3318 (1996).

Rayleigh wave dispersion due to a distribution of semi-elliptical surface-breaking cracks

Claudio Pecorari[a)]
Materials Department, Oxford University, Oxford OX1 3PH, England

(Received 5 August 1997; accepted for publication 17 September 1997)

A model describing changes of Rayleigh wave velocity caused by distributions of two-dimensional, surface-breaking cracks is presented. The results are obtained by extending an approach recently presented by the same author [C. Pecorari, J. Acoust. Soc. Am. **100**, 1542–1550 (1996)] for the analogous problem concerning distributions of one-dimensional cracks. The method developed in the previous article to evaluate the effective elastic constants of a cracked surface is presented here again and its assumptions are discussed in greater detail. A comparison between theoretical predictions and experimental results is also presented. © *1998 Acoustical Society of America.* [S0001-4966(98)05002-4]

PACS numbers: 43.35.Pt, 43.35.Cg, 43.35.Zc [HEB]

INTRODUCTION

Polishing the surface of ceramic components inevitably introduces microdamage in the region proximal to the surface of the sample. Surface damage appears in the form of surface roughness, residual stresses, and distributions of microcracks. Of the three, the latter is the one which most strongly affects the level of performance and lifetime of ceramic components.

Pattern and shape of microcracks generated by surface polishing depend on the shape of the particles used in the process. Particles of round shape generate cracks which are similar to those produced in a Hertzian indentation test. Such cracks appear at the surface of the sample as semicircles in the wake of the particle motion; they are roughly parallel to each other, and they extend in depth in a diverging conical shape. Particles with sharp edges, on the other hand, generate cracks similar to those produced during a Vickers indentation test. They are of three kinds: lateral, median, and radial cracks. Lateral cracks run parallel to the surface, and are responsible for material removal. Median and radial cracks extend normally to the surface into the bulk, with the cracks along the polishing direction usually being deeper than those normal to it. The depth of these cracks is of the order of a few microns.[1]

The complete characterization of complex, random structures, such as those of crack distributions generated during surface polishing, requires the knowledge of a large number of parameters. The need for a variety of techniques enabling the study of different properties of such systems is, therefore, apparent. Surface acoustic waves (SAW), and in particular Rayleigh waves, have been widely used in NDE to characterize both mechanical and structural properties of solids in their near-surface regions. Of relevance to the present subject, for example, Chu *et al.*,[2] and Hefetz and Rokhlin[3] investigated thermal shock damage in ceramics by means of ultrasonic waves. They used measurements of leaky Rayleigh wave velocity to obtain the effective shear modulus of the cracked material under the assumption that the cracks were distributed uniformly in the whole bulk of the sample. The case in which the distribution of cracks exists only in the near-surface region was not dealt with, and, to the best of this author's knowledge, an exhaustive theoretical model describing the interaction of a Rayleigh wave with a distribution of surface cracks has not yet been developed. In a recent article,[4] this author proposed a heuristic model to predict Rayleigh wave velocity changes due to a distribution of one-dimensional, noninteracting, surface-breaking cracks. According to this approach, a real medium having a cracked surface is modeled by an effective medium consisting of an anisotropic layer on an isotropic substrate. The elastic properties of the substrate are those of the uncracked host medium, whereas those of the effective layer are modified by the crack distribution. Since both the actual system and the effective medium are inhomogeneous, the mean field supported by them cannot have the same dependence on the space variables as a Rayleigh wave. Thus the phase velocity of a Rayleigh wave propagating on a cracked surface is calculated as that of the lowest surface mode supported by the effective layered system described above. Velocity reductions of up to 3% were predicted for distribution of cracks having a depth of 0.03λ, where λ is the wavelength of the unperturbed Rayleigh wave.

In this work, the effective medium approach outlined above is extended to the case of a two-dimensional distribution of semielliptical cracks. Kachanov's method[5] is presented here again in some detail to allow the addition of critical comments to the discussion reported in the previous article. A comparison between theoretical predictions and the experimental results presented by Tardy *et al.*[6] concludes the paper.

I. A HEURISTIC MODEL FOR A CRACKED SURFACE

This approach is developed in the low-frequency limit, and neglects crack interaction.[4] Kachanov's approach[5] is used to evaluate the effect of the crack distribution on the elastic properties of the near-surface region. Like any other effective medium approach, Kachanov's method requires the identification of a representative volume element (RVE). In this work, as in the preceding article,[4] the crack distribution is essentially two dimensional, and, therefore, a representa-

[a)]The author's new address is now Institute for Advanced Materials, SCI Unit, P.O. Box 2, 1755 ZG, Petten, The Netherlands.

 0001-4966/98/103(3)/1383/5/$10.00

tive surface element (RSE) should be used. However, since the cracks extend outside the RSE and their elastic response is nonlocal, the evaluation of the average properties of the near-surface region requires the use of a volume element which contains the whole extent of the cracks included in a RSE.

If a statistically homogeneous, three-dimensional distribution of defects is introduced in a homogeneous medium, the latter can be represented by an effective medium which is still homogeneous. On the other hand, a two-dimensional distribution which is contained in a three-dimensional host medium inevitably changes the average structural properties of the system. In this case, a medium representing the average properties of the real system must reflect the average inhomogeneous structure of the latter. Also, as a consequence of the structural change just mentioned, the coherent field associated with a Rayleigh wave propagating over a cracked surface may be expected to have a different spatial dependence, though it must satisfy the same boundary conditions enforced on a Rayleigh wave.

The strain field, $\boldsymbol{\epsilon}(\mathbf{x})$, in the near-surface region of a system with a uniform distribution of two-dimensional cracks, which are all parallel to the y-z plane and have the same depth, h, can be written as follows:

$$\boldsymbol{\epsilon}(\mathbf{x})=\mathbf{S}^0:\boldsymbol{\sigma}(\mathbf{x})+\frac{1}{2}\sum_{r=1}^{N}[\mathbf{b}(\mathbf{x}_r)\hat{n}_r+\hat{n}_r\mathbf{b}(\mathbf{x}_r)]\times\delta(x-x_r)u(\Omega_r). \tag{1}$$

In Eq. (1), $\mathbf{S}^0$ is the compliance tensor of the uncracked material, $\boldsymbol{\sigma}(\mathbf{x})$ is the total stress field, $\mathbf{b}(\mathbf{x}_r)$ is the crack opening displacement (COD) of the rth crack, $\hat{n}_r$ is the unit vector normal to the crack faces, and $u(\Omega_r)$ is the characteristic function of the rth crack, i.e., $u(\Omega_r)=1$ if $\mathbf{x}\in\Omega_r$, and $u(\Omega_r)=0$ if $\mathbf{x}\notin\Omega_r$. The symbol Ω_r represents the area of the rth crack. Since the cracks are parallel to each other, a frame of reference can be chosen so that $\hat{n}_r=\hat{x}=(1,0,0)$. The delta function dependence of $\boldsymbol{\epsilon}(\mathbf{x})$ on the variable x is to be ascribed to the displacement discontinuity localized on the crack face. Although not explicitly included in the notation, both strain and stress fields depend on the location of the N cracks. Assuming that the cracks are distributed uniformly over a RSE, A, that is, the distribution is characterized by a constant probability density function, $w(\mathbf{x}_1'',\mathbf{x}_2'',\ldots,\mathbf{x}_N'')=1/A^N$, the average strain field is found to be

$$\langle\boldsymbol{\epsilon}(\mathbf{x})\rangle_w=\mathbf{S}^0:\langle\boldsymbol{\sigma}(\mathbf{x})\rangle_w+\frac{1}{2A^N}\int_{\Pi A}\int\int\sum_{r=1}^{N}[\mathbf{b}(\mathbf{x}_r)\hat{n}_r+\hat{n}_r\mathbf{b}(\mathbf{x}_r)]\delta(x-x_r)u(\Omega_r)d\mathbf{x}_1''\,d\mathbf{x}_2''\cdots d\mathbf{x}_N'', \tag{2}$$

where the symbol $\langle\cdot\rangle_w$ represents the ensemble average, and $\mathbf{x}_1'',\mathbf{x}_2'',\ldots,\mathbf{x}_N''$ are the projections of the corresponding position vectors on the x-y plane.

A local relationship between the coherent strain and stress fields cannot be found at this stage because the COD is a nonlocal quantity with respect to the stress applied to the crack faces. This fact prevents the definition of a local effective medium, as it is done for three-dimensional crack distributions.[5] However, physical intuition suggests that the cracked surface may still be modeled as a local, homogeneous layer with reduced elastic constants which can be derived from the average elastic response of the crack distribution. On this assumption rests the heuristic character of this model. The average elastic response of the cracked surface can be evaluated by using the local relationship between the COD and the applied stress field averaged over the whole surface of the crack. Also note that the average coherent stress field so obtained is not required to satisfy the same boundary conditions as the coherent field. The averaging of both sides of Eq. (2) over the crack depth, h, yields

$$\langle\boldsymbol{\epsilon}(x)\rangle=\mathbf{S}^0:\langle\boldsymbol{\sigma}(x)\rangle+\frac{1}{2Ah}\int_{Ah}\int\sum_{r=1}^{N}[\mathbf{b}(\mathbf{x}_r)\hat{n}_r+\hat{n}_r\mathbf{b}(\mathbf{x}_r)]\delta(x-x_r)u(\Omega_r)d\mathbf{x}_r''\,dz. \tag{3}$$

If the incident wave propagates in the x direction, then the average field is expected to be independent on y. With this in mind, after the integration over the volume $V=Axh$ is carried out, Eq. (3) can be written as

$$\langle\boldsymbol{\epsilon}(x)\rangle=\mathbf{S}^0:\langle\boldsymbol{\sigma}(x)\rangle+\frac{N\Omega}{2Ah}[\langle\mathbf{b}(x)\rangle\hat{n}+\hat{n}\langle\mathbf{b}(x)\rangle],\quad\text{for } 0<z<h, \tag{4}$$

$$\langle\boldsymbol{\epsilon}(\mathbf{x})\rangle=\mathbf{S}^0:\langle\boldsymbol{\sigma}(\mathbf{x})\rangle,\quad\text{for } z>h, \tag{4'}$$

where the assumption that the cracks are identical has been made explicit. By introducing into Eq. (4) the crack density $\nu=N/A$, and the crack compliance tensor, B_{ij}, defined by

$$\langle\mathbf{b}(x)\rangle_i=hB_{ij}\langle\boldsymbol{\sigma}(x)\rangle_{jk}n_k,\quad i,j,k=1,2,3, \tag{5}$$

the ijth component of $\langle\boldsymbol{\epsilon}(x)\rangle$ for $0<z<h$ becomes

$$\langle\boldsymbol{\epsilon}(x)\rangle_{ij}=S^0_{ijrs}\langle\boldsymbol{\sigma}(x)\rangle_{rs}+\frac{\nu\Omega}{2}[B_{ir}n_sn_j+B_{jr}n_sn_i]\times\langle\boldsymbol{\sigma}(x)\rangle_{rs}. \tag{6}$$

If B_{ij} is given in terms of the crack normal and shear compliances, B_1, B_2, and B_3,[1] Eq. (6) can also be written as follows:

$$\langle\boldsymbol{\epsilon}(x)\rangle_{ij}=\Big\{S^0_{ijrs}+\frac{\nu\Omega}{2}[2(B_1-B_2)n_in_jn_rn_s+B_2(n_jn_s\delta_{ir}+n_in_s\delta_{jr})+(B_3-B_2)\times(n_jn_s\delta_{i3}\delta_{r3}+n_in_s\delta_{j3}\delta_{r3})]\Big\}\langle\boldsymbol{\sigma}(x)\rangle_{rs}, \tag{7}$$

or

$$\langle\boldsymbol{\epsilon}(x)\rangle_{ij}=(S^0_{ijrs}+\Delta S_{ijrs})\langle\boldsymbol{\sigma}(x)\rangle_{rs},\quad\text{for } 0<z<h. \tag{7'}$$

Equations (7′) and (4) show that the average elastic properties of the actual system can be represented by a homogeneous surface layer of depth h lying on a homogeneous substrate (Fig. 1). Consistency would require the use of the coherent field in the evaluation of the COD, and, conse-

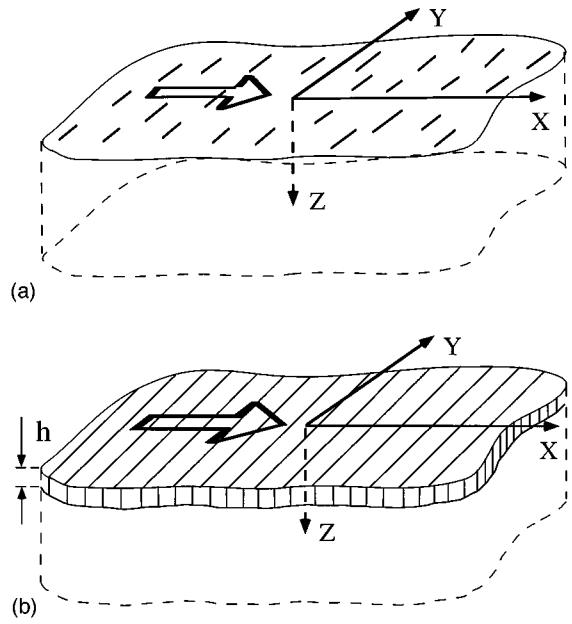

FIG. 1. Surface with a distribution of two-dimensional cracks (a), and the effective medium consisting of a substrate of the host material supporting an homogeneous, anisotropic layer (b). The reference frame used in this work is also illustrated.

quently, of B_1, B_2, and B_3 [Eq. (5)]. However, since the crack distribution is supposed to cause just a small perturbation to the Rayleigh wave, the true coherent field may be substituted by the stress field carried by a Rayleigh wave for this purpose.

When a crack is subjected to an inhomogeneous stress field, the quantities B_1, B_2, and B_3 may show a slight dependence on h/λ even within the range of values considered here for this parameter, and, therefore, they cannot be considered to describe intrinsic properties of the crack. Nonetheless, for a given set of crack compliance constants, B_1, B_2, and B_3, that is, for a given applied stress field, $S^0_{ijrs}+\Delta S_{ijrs}$ can be used to define the elastic properties of an *ad hoc* effective layer. A convenient mathematical way to obtain explicit expressions for the components ΔS_{ijrs} in terms of B_1, B_2, and B_3, is to assume the layer to be subjected to a constant test stress field, $\langle \boldsymbol{\sigma}(x)\rangle_{rs}=(\sigma/2)(\delta_{rm}\delta_{sn}+\delta_{sm}\delta_{rn})$. Then,

$$\Delta S_{ijrs}=\frac{\nu\Omega}{2}\,[\,\gamma_{ijrs}+(\alpha_{js}\delta_{ir}+\alpha_{jr}\delta_{is}+\alpha_{is}\delta_{jr}+\alpha_{ir}\delta_{js}) +(\beta_{is}\delta_{j3}\delta_{r3}+\beta_{ir}\delta_{j3}\delta_{s3}+\beta_{js}\delta_{i3}\delta_{r3} +\beta_{jr}\delta_{i3}\delta_{s3})\,], \tag{8}$$

where

$$\alpha_{ij}=B_2 n_i n_j\,, \tag{9a}$$

$$\beta_{ij}=(B_3-B_2)n_i n_j\,, \tag{9b}$$

$$\gamma_{ijrs}=4(B_1-B_2)n_i n_j n_r n_s\,. \tag{9c}$$

If a distribution of identical cracks which are parallel to the wave front of the propagating Rayleigh wave, that is, $\hat{n}=\hat{x}$, is considered, then the only nonzero elements of the extra compliance tensor ΔS_{IJ} are $\Delta S_{11}=2\nu\Omega B_1$, $\Delta S_{55}=\nu\Omega B_3/2$, $\Delta S_{66}=\nu\Omega B_2/2$. Here, Voigt's notation has been used. For the purpose of determining the change of phase velocity of a Rayleigh wave propagating along the x direction on a surface with cracks parallel to the y-z plane, only the extra compliances ΔS_{11} and ΔS_{55} need to be calculated.

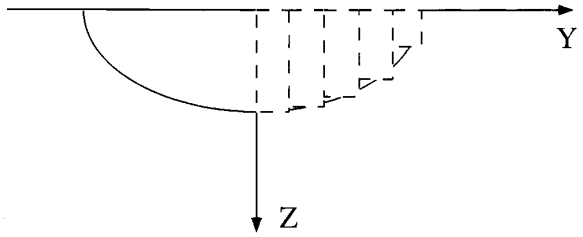

FIG. 2. Partitioning of the crack faces.

II. NUMERICAL RESULTS

A fundamental step in modeling the layer's elastic properties is the evaluation of the crack opening displacement, $\mathbf{b}(\mathbf{x})$. In this work the cracks are assumed to be semielliptical with an aspect ratio of 3 to 1. The surface of each crack of the distribution is $\Omega=3\pi h^2/2$. A correct numerical procedure to evaluate the COD of a two-dimensional surface-breaking crack requires the use of the components of the appropriate Green's tensor as kernels of the integral equations for the components of COD.[7] Unfortunately, the implementation of such a scheme is very computing intensive. In this work, an approximated scheme proposed by Zhang and Achenbach[8] is adopted to estimate the COD of an individual crack.

Let the crack surface be divided in narrow strips which extend from the surface into the bulk of the material, and terminate at the crack front. As shown in Fig. 2, the depth of each strip changes with its position relative to the center line of the crack. The COD of the two-dimensional crack within each strip is then approximated by that of a one-dimensional crack having the same depth as the strip. The COD of a one-dimensional crack is evaluated first by solving the appropriate integral equation for the dislocation densities, and then by integrating the latter along the crack depth. For further details about the numerical aspect of the problem concerning the evaluation of the COD of a one-dimensional crack, the reader is referred to Achenbach *et al.*[9] and Achenbach and Brind.[10]

The method just described is expected to overestimate the COD of a two-dimensional crack. Unfortunately, no exact results for the COD of a two-dimensional, surface-breaking crack insonified by a Rayleigh wave have been found in the literature. The lack of benchmark results makes it difficult to estimate the error associated with the approximation used here.

Once the COD is available, the components of the crack compliance tensor, B_{ij}, can be calculated from Eq. (6), and with those the components of the extra compliance tensor of the fictitious layer can be readily estimated. The numerical results which follow are obtained for an alumina (Al_2O_3) half-space with the following values of the bulk phase velocities and the mass density: $V_L=10\,822\ \mathrm{m\,s^{-1}}$, V_T

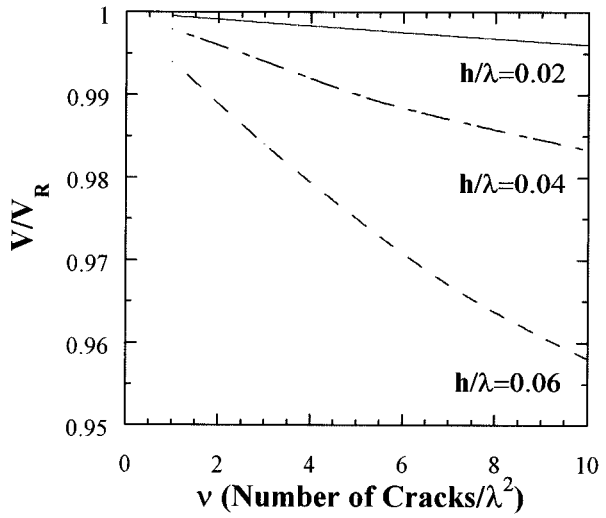

FIG. 3. Normalized Rayleigh phase velocity versus crack density for three values of the normalized crack depth.

$=6163\ \mathrm{m\ s^{-1}}$, and $\rho=3970\ \mathrm{kg\ m^{-3}}$. The phase velocity of the coherent field is evaluated according to the procedure outlined in Ref. 4.

Figure 3 presents the normalized phase velocity of a Rayleigh wave plotted versus the crack density for three values of the crack depth, h/λ. The plots illustrate that the effect of cracking on the wave velocity is almost negligible for values of the normalized crack depth, h/λ, below 0.02, even for a crack density as large as 10 cracks/λ^2. However, Fig. 3 also shows that cracks of depth quite smaller than the Rayleigh wavelength may cause a decrease of the wave velocity which is measurable, for instance, with a line-focus acoustic microscope.

Figure 4 illustrates the dependence of the normalized velocity on the normalized crack depth for three values of the crack density. For crack densities lower than 1 crack/λ^2, the variations of the wave velocity are smaller than 1% for crack depths in the range $h/\lambda \leqslant 0.06$. For crack densities higher than 1 crack/λ^2, variations of the crack depths cause

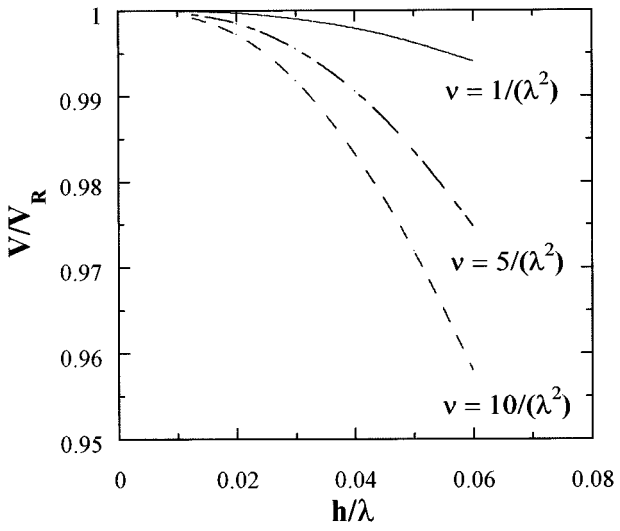

FIG. 4. Normalized Rayleigh phase velocity versus normalized crack depth for three values of the crack density.

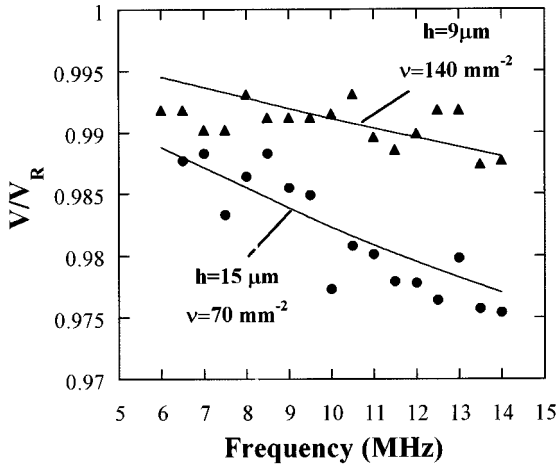

FIG. 5. Theoretical (lines) and experimental (dots) results: a comparison.

velocity changes of rapidly increasing magnitude.

The different behavior shown by the normalized velocity when plotted versus the normalized crack density (Fig. 3) or versus the normalized crack depth (Fig. 4) can be understood as follows. When the crack density is changed and the normalized crack depth is maintained constant, the dispersion is entirely due to the change of the mechanical properties of the layer. On the other hand, when the crack depth changes while the crack density is maintained constant, the variation of the phase velocity is affected not only by the change of the elastic constants according to Eq. (8), but also by the change of the layer thickness. In other words, there is an additional effect due to the change of geometry of the system.

Recently, Tardy *et al.*[6] have reported experimental dispersion curves of Rayleigh waves propagating on ground ceramic surfaces. Such data have been acquired by means of line-focus quantitative acoustic microscopy performed in pulse mode. Of the three curves presented by Tardy *et al.*, the one which did not show significant dispersion in the frequency range between 6 and 14 MHz was used here to obtained the value of the unperturbed Rayleigh wave velocity. This value was used to normalize the other experimental data, which are reported in Fig. 5. The depth of the cracks in the surfaces was also measured directly by the authors, and values of 20 and 12 μm were reported for the maximum damage depth in the two surfaces. It is known[11] that cracks in ground surfaces tend to be aligned along the grinding direction, and, therefore, to be mostly parallel and in close proximity to each other. This type of crack distributions can be suitably approximated by the idealized distributions considered in this work. Simulations were run by using effective crack depths of 15 and 9 μm in order to account for cracks of depth smaller than the maximum. Furthermore, semielliptical cracks with an excessively large aspect ratio of 3 to 1 were considered in the model in order to account for the close proximity of the cracks in the real distributions. As Fig. 5 illustrates, a sufficiently good agreement between experimental results and theoretical predictions have been obtained for values of the crack density equal to 70 and 140 cracks per

mm^2. Scherer *et al.*[12] have estimated densities of crack-like defects of the order of 10^3 mm^{-2} in rather more damaged surfaces by means of high-frequency acoustic microscopy. Thus the values of 70 and 140 cracks per mm^2 are to be considered at least plausible.

III. CONCLUDING REMARKS

In this article, a heuristic model to predict variations of phase velocity of a Rayleigh wave propagating on a surface with a uniform distribution of semielliptical cracks which are parallel to each other and normal to the direction of propagation of the SAW has been presented. The heuristic nature of the model requires the validity of its predictions to be sought by means of a comparison with either experimental results or theoretical predictions based on alternative approaches. The comparison presented here between experimental results available in the literature and theoretical predictions have shown that, the heuristic nature of this model notwithstanding, the model contains the correct physical elements and adequately describes the experimental results obtained on surfaces which can be dealt with by this model.

Although, at this stage, the numerical implementation of the model is affected by a ''systematic'' error due to the approximation chosen for the evaluation of the COD, this should not be seen as an intrinsic limitation of the model. Such an error could be removed by a correct evaluation of the COD which may be obtained at the cost of greater computational effort. The model itself, however, could also be improved by allowing, for instance, the cracks to have different depths, and different orientations with respect to each other and to the direction of propagation of the Rayleigh wave (see Pecorari[4]).

ACKNOWLEDGMENTS

This work is part of a project funded by the EPSRC (Grant No. GR/L/27633). The author wishes to thank Dr. D. A. Mendelsohn for numerous discussions about the problem of scattering of a Rayleigh wave from a one-dimensional, surface-breaking crack, and Dr. S. G. Roberts for providing the author with the basic knowledge about surface damage in brittle material, and with the distinct impression that there is still a lot more for this author to learn about it. The encouragement of Dr. G. A. D. Briggs is also appreciated.

[1] C. C. Anya and S. G. Roberts, ''Indentation fracture toughness and surface flaw analysis of sintered alumina/SiC nanocomposites,'' J. Eur. Ceram. Soc. **16**, 1107–1114 (1996).
[2] Y. C. Chu, M. Hefetz, and S. I. Rokhlin, ''Evaluation of microcrack thermal shock damage in ceramics: Modeling and experiments,'' AD **27**, Fracture and Damage, ASME, 95–102 (1992).
[3] M. Hefetz and S. I. Rokhlin, ''Thermal shock damage assessment in ceramics using ultrasonic waves,'' J. Am. Chem. Soc. **75**, 1839–1845 (1992).
[4] C. Pecorari, ''Modeling variations of Rayleigh wave velocity due to distributions of one-dimensional surface-breaking cracks,'' J. Acoust. Soc. Am. **100**, 1542–1550 (1996).
[5] M. Kachanov, ''Effective elastic properties of cracked solids: Critical review of some basic concepts,'' Appl. Mech. Rev. **45**, 304–335 (1992).
[6] F. Tardy, M. H. Noroy, L. Paradis, and J. C. Baboux, ''Material characterization by a Rayleigh wave velocity measurement,'' Ultrasonic Testing (http://ultrasonic.de/backup/bupl_e.htm), November 1996.
[7] D. E. Budreck and J. D. Achenbach, ''Three-dimensional elastic wave scattering by surface-breaking cracks,'' J. Acoust. Soc. Am. **86**, 395–406 (1989).
[8] C. Zhang and J. D. Achenbach, ''Dispersion and attenuation of surface waves due to distributed surface-breaking cracks,'' J. Acoust. Soc. Am. **88**, 1986–1992 (1990).
[9] J. D. Achenbach, L. M. Keer, and D. A. Mendelsohn, ''Elastodynamic analysis of an edge crack,'' J. Appl. Mech. **47**, 551–556 (1980).
[10] J. D. Achenbach and R. J. Brind, ''Scattering of surface waves by a sub-surface crack,'' J. Sound Vib. **76**, 43–56 (1981).
[11] D. B. Marshall, A. G. Evans, B. T. Khuri-Yakub, J. W. Tien, and G. S. Kino, ''The nature of machining damage in brittle materials,'' Proc. R. Soc. London, Ser. A **385**, 461–475 (1983).
[12] V. Scherer, S. U. Fassbender, G. Weised, and W. Arnold, ''Microscopic characterization of machined high-performance ceramics using acoustical, optical and mechanical NDT techniques,'' Proceedings of the 99th Annual Meeting of the American Ceramic Society, 1997 (to be published).

Thermoacoustic streaming in a resonant channel: The time-averaged temperature distribution

Ashok Gopinath and Nicole L. Tait[a)]
Department of Mechanical Engineering, Naval Postgraduate School, Code ME/Gk, Monterey, California 93943

Steven L. Garrett
Graduate Program in Acoustics, P. O. Box 30, The Pennsylvania State University, State College, Pennsylvania 16804

(Received 7 April 1997; accepted for publication 20 November 1997)

The problem of thermoacoustic streaming in a plane parallel resonant channel, representative of the stack in a thermoacoustic engine, has been developed in a general dimensionless form. The utility of such a formulation and its wide ranging applicability to different solid–fluid combinations is demonstrated by which a consistent account of all the energy-exchange mechanisms can be made. Certain (wide-gap, thick-wall) simplifications are initially made to arrive at more manageable forms of the time-averaged temperature distributions of interest in both the fluid gap, and the channel walls. These simplifications clarify the origin of the thermoacoustic effect and provide a description of the responsible physical mechanisms based on which the validity of the ''bucket-brigade'' model is examined. The unexpected role of a little-known second-order thermal expansion coefficient is pointed out. It is shown that the conjugate wall–fluid coupling is crucial in yielding the large time-averaged axial temperature gradients that can be induced in the channel. In particular, the heat transfer rates at the ends of the channel are found to play an important role in determining the magnitude of these time-averaged gradients. The more general and practically useful case of arbitrary channel gap widths is also treated and it is found that for ideal gas working fluids there is an optimum channel gap width for which the axial thermal stratification in the channel is maximized. A comparison of the predictions from this study with available experimental data shows very good agreement. [S0001-4966(98)02203-6]

PACS numbers: 43.35.Ud, 43.35.Ty, 43.25.Nm, 43.20.Ks [HEB]

LIST OF SYMBOLS

$\langle \ldots \rangle$	time average of enclosed quantity
B	$(\beta_m T_m)^2\ (c_m^2/c_p T_m)$ [$=(\gamma-1)$ for an ideal gas]
Bi_1	Biot number at $x=x_1$, h_1/kK_s
Bi_2	Biot number at $x=x_2$, h_2/kK_s
c.c. [. . .]	complex conjugate of enclosed quantity
c	speed of sound in the fluid, ω/k [m/s]
c_p	isobaric specific heat [J/kg K]
Ec	Eckert number, $U_0^2/2c_p\Delta T_{\mathrm{ref}}$
f	frequency [Hz]
g, g_0, g_2	functions defined in Eqs. (32), (33)
G	functions defined in Eq. (A3)
h_1	heat transfer coefficient at $x=x_1$ [W/m^2 K]
h_2	heat transfer coefficient at $x=x_2$ [W/m^2 K]
k	wave number, $2\pi/\lambda$ [m^{-1}]
K_f	fluid thermal conductivity [W/m K]
K_s	solid thermal conductivity [W/m K]
K_{fs}	dimensionless parameter, $(K_f/K_s)\ (l/\delta_\nu)$
l	channel wall half-thickness [m]
m	eigenvalues in Eqs. (19), (20)
M	Mach number, U_0/c_m
p^*	fluid pressure [Pa]
p_m	quiescent fluid pressure [Pa]
p	dimensionless fluid pressure, $(p^*-p_m)/\varrho_m c_m U_0$
P_0	acoustic pressure amplitude, $\varrho_m c_m U_0$ [Pa]
$q^{*\prime\prime}$	heat flux [W/m^2]
q_w''	dimensionless wall heat flux [Eq. (33)]
$\Re\{ \ldots \}$	real part of enclosed quantity
t^*	time [s]
t	dimensionless time, ωt^*
t_s	dimensionless time, $\kappa_s t^*/l^2$
T_f^*	fluid temperature [K]
T_s^*	solid temperature [K]
T_i^*	*steady* fluid–wall interface temperature [K]
T_m	quiescent fluid temperature [K]
ΔT_{ref}	reference temperature difference [K]
u^*	x component of velocity [m/s]
u	dimensionless x component of velocity, u^*/U_0
U_0	acoustic velocity amplitude [m/s]
v^*	y component of velocity [m/s]
v	dimensionless y component of velocity, $v^*/[U_0(y_0 k)]$
x^*	axial coordinate [m]
x	dimensionless axial coordinate, kx^*
x_1, x_2	x coordinates of channel ends
$\overline{x}$	x coordinates of channel midpoint, $(x_1+x_2)/2$
Δx	dimensionless channel length, (x_2-x_1)
δx	dimensionless channel length, $\delta x=2\Delta x/\pi$

[a)]Formerly in the U. S. Naval Reserve.

$y^*, \hat{y}^*$ normal coordinate in fluid [m]
y dimensionless normal coordinate in fluid, y^*/y_0
y_s^* normal coordinate in wall [m]
y_s dimensionless normal coordinate in wall, y_s^*/l
y_0 channel gap half-width [m]

Greek letters
β fluid thermal expansion coefficient [1/K]
γ ratio of isobaric to isochoric specific heats
δ_ν viscous penetration depth, $\sqrt{2\nu/\omega}$ [m]
δ_κ fluid thermal penetration depth, $\sqrt{2\kappa_f/\omega}$ [m]
δ_s solid thermal penetration depth, $\sqrt{2\kappa_s/\omega}$ [m]
ϵ_s complex constant defined in Eq. (13)
η dimensionless normal coordinate in fluid, $\hat{y}^*/\delta_\nu$
η_0 dimensionless gap half-width, y_0/δ_ν
$\eta_0\sqrt{\sigma}$ dimensionless gap half-width, y_0/δ_κ
κ_f fluid thermal diffusivity [m^2/s]
κ_s solid thermal diffusivity [m^2/s]
λ wavelength [m]
ν kinematic viscosity [m^2/s]
ξ ''second-order'' thermal expansion coefficient [Eq. (23)]
ϱ^* fluid density [kg/m^3]
ϱ_m quiescent fluid density [kg/m^3]
ϱ dimensionless fluid density, $(\varrho^*-\varrho_m)/M\varrho_m$
σ Prandtl number
ϕ dimensionless fluid temperature, $(T_f^*-T_m)/\Delta T_{\text{ref}}$
Φ dimensionless solid temperature, $(T_s^*-T_m)/\Delta T_{\text{ref}}$
φ dimensionless *steady* fluid-wall interface temperature, $(T_i^*-T_m)/\Delta T_{\text{ref}}$
ω angular frequency [rad/s]
Ω_n eigenvalues in Appendix B

Superscripts
* represents dimensional quantities

Subscripts
f fluid
s solid
m quiescent conditions
0,1,2,... order in solution expansion [Eq. (8)]

BACKGROUND AND INTRODUCTION

Thermoacoustics can be simplistically defined as the physics of the interaction of thermal and acoustic fields, especially in the form in which one gives rise to a significant component of the other. A more careful description may be found in the general review article by Rott[1] from which it becomes clear that the field of thermoacoustics can be broadly classified into essentially two main branches on the basis of cause and effect, namely: (a) time-averaged heat/temperature-gradient *driven* fluid oscillations, and (b) time-averaged heat/temperature gradients *induced by* fluid oscillations.

The former topic includes, among other issues, the vast body of work on Rijke (and related) tubes and has received considerably far more attention than the latter (see the recent comprehensive review by Raun *et al.*[2]). It is however only the latter topic with which this paper is concerned, and has been most aptly named *thermoacoustic streaming* by Rott,[1] by analogy with *acoustic streaming*, to describe the significant second-order time-averaged heat transfer effects produced by the interaction of strong acoustic fields with rigid boundaries. In the context of commonly used terminology in the thermoacoustic engine literature, this paper deals primarily with the thermoacoustic streaming effects associated with the ''refrigerator'' mode (vice the ''prime-mover'' mode) of operation of a thermoacoustic engine. Notable early contributions to this area of thermoacoustic streaming were made by Rott[3] and Merkli and Thomann[4] (see also references in the paper by Rott[1] to a series of studies with his co-workers), and more recently by Jeong and Smith,[5] and on a related subject by Bauwens.[6] This topic has gained particular prominence in the past decade or so, due to its applicability to the fundamental processes of interest in the *stack* region of a thermoacoustic engine. Wheatley *et al.*[7–9] and Hofler[10] have provided some preliminary discussions of the theory of such engines and obtained experimental data using a **T**hermo**A**coustic **C**ouple (TAC) model of the stack, confirming the basic nature of the heat-generating mechanism underlying thermoacoustic streaming. An account of related developments with relevance to thermoacoustic engines, along with a more detailed review of both the principles of operation and the references in the literature, may be found in a fine tutorial article by Swift.[11] (The notation here is largely based on this tutorial article.)

Atchley *et al.*[12] have also conducted further detailed experiments using TACs to obtain a better quantitative comparison with the theory, especially at practically relevant high acoustic drive ratios. Numerical methods have also been used by Cao *et al.*[13] to study the energy transport rates in such TACs. Reports of more detailed experimental performance studies may be found in the papers by Swift[14] and Olson and Swift[15] on the overall effect of loading on such thermoacoustic engines. Various engine geometries have been explored, such as the radial wave engine discussed by Arnott *et al.*[16] In addition, various stack geometries and their thermoacoustic effects have also been investigated, such as the pinstack (with some superior features) treated by Swift and Keolian.[17] A general porous medium formulation has been provided by Arnott *et al.*[18] for arbitrarily shaped stack cross sections. This paper however deals only with a simple representative configuration, i.e., a plane-parallel channel stack geometry in a straight resonant duct, so as to concentrate attention on some fundamental thermoacoustic effects in the stack which form the primary focus of this study. The traveling wave mode of operation and the associated Stirling engine effects of a thermoacoustic engine which have been studied theoretically and experimentally by Raspet *et al.* and Kordomenos *et al.*[19–21] for the case of an *inviscid ideal gas* are not treated here; this paper deals strictly with the resonant

standing wave mode of operation, although for the more general case of a real viscous heat-conducting fluid (gas or liquid).

The promise of the applicability of thermoacoustic engines as a practical and environmentally benign means of generating a useful refrigerating effect has been discussed by Hofler,[22] Garrett *et al.*[23,24] and Swift,[25] and successful overall optimization studies have been initiated by Minner *et al.*[26] and Wetzel and Herman.[27] In this regard, research attention has more recently turned to obtaining a detailed understanding of the various ''subsystems'' in a thermoacoustic engine which have been identified as potential bottlenecks to future development, especially for operation at more practically relevant high acoustic drive ratios for which nonlinear effects are significant. This aspect has received much attention for the ''prime-mover'' mode of operation, from the viewpoint of stability or threshold of start-up, and subsequent build-up of the acoustic field as evidenced by the experimental studies of Atchley *et al.*[28–31] and Arnott *et al.*,[32] and the more recent theoretical explanations offered by Watanabe *et al.*[33] and Yuan *et al.*[34] However the thermoacoustic streaming behavior in the ''refrigerator'' mode of operation relevant to this paper has received less attention, although there is considerable interest in (for instance) the fluid and heat transport behavior inside (and in the vicinity of) the stack, with application to impedance behavior, energy flux densities and heat transfer rates to the adjoining heat exchangers. The recent experimental work of Wetzel and Herman[35] using holographic interferometry, and the numerical work of Worlikar and Knio[36] point to the complicated fluid mechanics in these regions and are features deserving of greater scrutiny in the future.

This study re-examines some of the above noted basic aspects of thermoacoustic streaming theory responsible for explaining the manner in which such significant time-averaged thermal effects may be created by the interaction of strong acoustic fields with rigid boundaries. The model problem chosen comprises the plane-parallel geometry of a channel in a resonant duct supporting a plane standing sound wave (as shown in Fig. 1). The focus in this paper is on the time-averaged temperature distribution induced in the walls and fluid gap of such a channel due to the presence of the acoustic field. The motivation for this fundamental study comes from a review of the literature which shows that in the majority of the earlier studies of such thermoacoustic effects in a channel, the general approach has been to *assume a priori* the presence of a significant mean axial temperature gradient in the channel, and to *only then* determine the overall energy transport rates by a suitable integration across the channel cross section. Such an approach however does not readily afford a basic understanding/explanation of the actual *origin* of this mean temperature gradient that is induced by the interaction of the walls with the acoustic field. In fact, any steady thermal stratification which may be induced should clearly be a manifestation of the thermoacoustic streaming effect, and is accordingly shown here to arise from a systematic solution of the governing Navier–Stokes equations. And of those earlier authors who *have not* assumed an *a priori* presence of a steady temperature gradient, such as

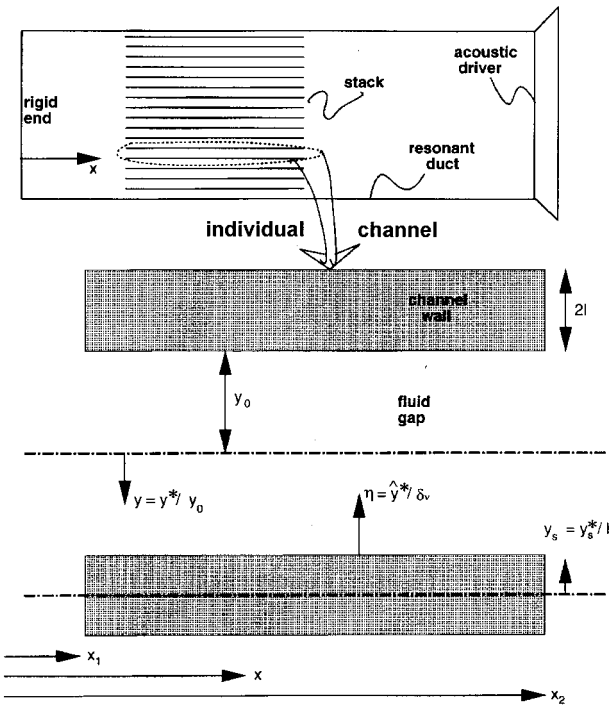

FIG. 1. Definition sketch of the problem statement showing the stack of plane-parallel channels in the resonant duct, and a magnified view of one such channel.

Merkli and Thomann[4] or Jeong and Smith,[5] the focus has been on the thermoacoustic effects *only* in the fluid, and the conjugate wall–fluid thermal coupling has not been included, thus prohibiting prediction of the large mean axial temperature gradients that can be induced in the channel. Furthermore, the work thus far has been largely based on *dimensional* analyses which has unfortunately led to some omissions, and not allowed a clear account of the nature of *all* the energy exchange mechanisms responsible for this time-averaged thermal effect, a feature that is explained in more detail later in this paper.

It is shown here that a systematic framework based on a *dimensionless* formulation of the governing equations, which also accounts for conjugate effects due to the fluid–wall coupling, yields a self-consistent description of the scales involved and provides a clear indication of the source of the large time-averaged axial thermal stratification that can be induced in a resonant channel, for both *gaseous and nongaseous* working fluids. The predictions from this theory are found to be in very good agreement with available experimental data in the literature. As noted earlier, fundamental studies of this nature, but based on a different approach, have been recently conducted by Watanabe *et al.*[33] and Yuan *et al.*[34] to offer a theoretical explanation, however, of the ''prime-mover'' mode of operation of a thermoacoustic engine. A similar strategy (involving similitude arguments) has also been used by Olson and Swift,[37] although for a very different purpose, i.e., to identify the controlling global dimensionless parameters which describe the overall workings of a thermoacoustic engine with the intent of proper dimensionless presentation of experimental data, and to understand scalability issues of these engines. Such a dimensionless ap-

proach has also been used by Qi[38] to study the effects of compressibility on acoustic streaming due to a plane wave at a rigid boundary.

The layout of the remainder of the paper is as follows: the governing equations and the solution procedure are outlined in Sec. I, and the leading order first harmonic quantities are obtained in Sec. II with some important boundary conditions laid out at the end of Sec. II. The time-averaged temperature distribution is considered in Sec. III; the role of a second-order thermal expansion coefficient is discussed in Sec. III A and a physical explanation of the source of the thermoacoustic effect is provided in Sec. III B, along with a description of the resulting behavior due to the wall–fluid coupling, which is provided in Sec. III C and Sec. III D. Some comparisons with available experimental data have been carried out in Sec. IV and finally conclusions are drawn in Sec. V. Appendix A includes a treatment of the more general version of the problem considered in the main body of the paper. Appendix B provides details of the heat conduction problem analyzed in Sec. III C and Sec. III D.

I. FORMULATION AND GOVERNING EQUATIONS

The Navier–Stokes equations are used to describe the effects of a plane standing acoustic field whose direction of oscillation is aligned with the axis of the plane-parallel geometry of a channel as shown in Fig. 1. The single channel, also shown magnified in Fig. 1, represents a ''unit cell'' in a multitude of channels, all of which are enclosed in an outer larger resonant duct supporting the standing acoustic field. This collection of channels is the typical configuration representative of the *stack* of a thermoacoustic engine. The focus here is on the time-averaged temperature distribution induced in the fluid gap and walls of one such channel, due to its interactions with the resonant acoustic field.

In the initial quiescent state (in the absence of the acoustic field), at a mean pressure, p_m, and density, ϱ_m, the fluid and channel walls are taken to be isothermal at the quiescent temperature, T_m. In the presence of the acoustic field, the corresponding disturbance variables are defined and nondimensionalized in the following manner:

$$\begin{aligned} &t=\omega t^*,\quad x=kx^*,\quad y=y^*/y_0,\\ &u=u^*/U_0,\quad v=v^*/U_0y_0k,\\ &\varrho=(\varrho^*-\varrho_m)/[\varrho_m(U_0/c_m)],\\ &p=(p^*-p_m)/\varrho_m c_m U_0,\quad \phi=(T_f^*-T_m)/\Delta T_{\rm ref}, \end{aligned} \tag{1}$$

where it may be noted that the scaling in the definition of ϱ includes a U_0/c_m factor in anticipation of the expected solution form. In the narrow acoustic waveguide approximation ($y_0^2k^2\ll 1$) being treated, the pressure $p\equiv p(x,t)$, and the boundary layer nature of the governing equations in dimensionless form are

$$\frac{\partial\varrho}{\partial t}+\mathrm{M}\left(u\frac{\partial\varrho}{\partial x}+v\frac{\partial\varrho}{\partial y}\right)+(1+\mathrm{M}\varrho)\left(\frac{\partial u}{\partial x}+\frac{\partial v}{\partial y}\right)=0, \tag{2}$$

$$(1+\mathrm{M}\varrho)\left[\frac{\partial u}{\partial t}+\mathrm{M}\left(u\frac{\partial u}{\partial x}+v\frac{\partial u}{\partial y}\right)\right]=-\frac{\partial p}{\partial x}+\frac{1}{2\eta_0^2}\frac{\partial^2 u}{\partial y^2}, \tag{3}$$

$$\begin{aligned} &(1+\mathrm{M}\varrho)\left[\frac{\partial\phi}{\partial t}+\mathrm{M}\left(u\frac{\partial\phi}{\partial x}+v\frac{\partial\phi}{\partial y}\right)\right]\\ &\quad=\frac{1}{2\sigma\eta_0^2}\frac{\partial^2\phi}{\partial y^2}+\frac{\mathrm{Ec}}{\eta_0^2}\left(\frac{\partial u}{\partial y}\right)^2\\ &\qquad+2(\beta T_f^*)\mathrm{Ec}\left[\frac{1}{\mathrm{M}}\frac{\partial p}{\partial t}+\frac{1}{2\eta_0^2}\left(u\frac{\partial^2 u}{\partial y^2}\right)\right.\\ &\qquad\left.-(1+\mathrm{M}\varrho)u\left(\frac{\partial u}{\partial t}+\mathrm{M}u\frac{\partial u}{\partial x}+\mathrm{M}v\frac{\partial u}{\partial y}\right)\right], \end{aligned} \tag{4}$$

wherein use has been made of Eq. (3) to arrive at Eq. (4). These equations are to be accompanied by a suitable equation of state for the fluid.

The important dimensionless parameters in these equations are the Mach number, M, the gap width parameter, $\eta_0\equiv y_0/\delta_\nu$ (or its counterpart y_0/δ_κ related through the Prandtl number), and the Eckert number, Ec as defined below:

$$\mathrm{M}=\frac{U_0}{c_m},\quad \eta_0^2=\left(\frac{y_0}{\delta_\nu}\right)^2=\frac{y_0^2\omega}{2\nu},\quad \mathrm{Ec}=\frac{U_0^2}{2c_p\Delta T_{\rm ref}}. \tag{5}$$

In the definition of the Eckert number, Ec, above, since the channel walls and the fluid are allowed to naturally develop their temperature field from an initially uniform quiescent value of T_m, and since there is no mean temperature gradient that is externally imposed or artificially assumed, there is thus no obvious choice for the reference temperature difference, $\Delta T_{\rm ref}$. As a result $\Delta T_{\rm ref}$ will later be simply chosen to be its intrinsic value such that we have the case of $\mathrm{Ec}\equiv 1$. However it may be noted that the above formulation with $\Delta T_{\rm ref}$ in the definition of Ec is retained, since it allows a more general dimensionless treatment (dealt with elsewhere) of the reverse scenario of this problem, i.e., the so-called ''prime-mover'' mode of operation of the thermoacoustic engine, in which case cause and effect are reversed, and a mean axial temperature gradient is in fact externally imposed in the channel walls (immersed in an otherwise quiescent fluid), to spontaneously induce an acoustic field.

As for boundary conditions, the velocity field in the fluid is made to satisfy no-slip conditions along the channel walls ($y=1$), and symmetry conditions about the center plane of the fluid gap ($y=0$). The thermal field in the fluid is suitably coupled with that of the wall via continuity requirements on the temperature, and the heat flux, at the wall-fluid interface ($y=1$). The boundary conditions for the fluid at the ends of the channel ($x=x_1,x_2,\ 0\leqslant y\leqslant 1$) are discussed in greater detail later at the end of Sec. II.

In the solid material of the wall itself, heat is assumed to be transferred by simple isotropic conduction for which the unsteady temperature distribution is governed by

$$\frac{\partial^2\Phi}{\partial y_s^2}+l^2k^2\frac{\partial^2\Phi}{\partial x^2}=2\frac{l^2}{\delta_s^2}\frac{\partial\Phi}{\partial t}\equiv\frac{\partial\Phi}{\partial t_s} \tag{6}$$

subject to the appropriate temperature and heat-flux continuity boundary conditions at the wall-fluid interface ($y_s=1$),

and symmetry about the wall center plane ($y_s=0$). The channel wall ends too ($x=x_1,x_2$, $0\leqslant y_s\leqslant 1$); the relevant boundary conditions are provided at a suitable stage later in Sec. III C. For the bulk of the paper the channel is taken to be half-wavelength long and sufficiently wide to facilitate a quick development of the fundamental ideas behind the mechanism being studied, and to allow ready comparisons with some key results available in the literature. However the development that follows is general enough to handle shorter channels (with narrower gaps) as well, as is demonstrated in Appendix A and, also by successful application of the results to experimental data for shorter channels as described in Sec. IV.

To begin with, as a trivial check, it is verified that the homogenous solution set

$$(\varrho,u,v,p,\phi,\Phi)=(\mathbf{0}) \tag{7}$$

corresponding to the basic undisturbed state, identically satisfies the above governing equations for the fluid and the solid portions. Furthermore, if so desired, the incompressible limit may be conveniently analyzed by ignoring the density fluctuations, i.e., by simply setting $\varrho=0$, although some important physics would be lost with this simplistic approximation. More importantly, it is only now that one can seek a self-consistent series expansion solution in powers of the parameter, $\mathrm{M}\ll 1$, which clearly emerges as the proper perturbation parameter in the above system of equations as explained by Crighton[39] and also used by Qi.[38] Such a procedure allows a careful accounting of all the energy-exchange mechanisms, and interestingly reveals the role of a little-known second-order thermal expansion coefficient as discussed later in Sec. III A. In general, the solution to the above equations may now be developed with the remaining dimensionless parameters treated as arbitrary $O(1)$ numbers, although for the bulk of this study emphasis will be on cases for which the gap width η_0 is sufficiently large so as to arrive at the principal results quickly, and to also allow comparisons with available results in the literature. However cases of smaller gap widths [$\eta_0=O(1)$], which are practically more relevant in thermoacoustic engines are also dealt with in Appendix A, and help establish a procedure for predicting optimum gap widths in stack design.

The solution procedure adopted is briefly outlined below. For a typical dependent variable, u for example, the solution is now sought in a series of the form

$$u=u_1+\mathrm{M}u_2+\mathrm{M}^2u_3+\cdots, \tag{8a}$$

except for the series for ϕ and Φ which are

$$(\phi,\Phi)=\frac{1}{\mathrm{M}}(\phi_0,\Phi_0)+(\phi_1,\Phi_1)+\mathrm{M}(\phi_2,\Phi_2)+\mathrm{M}^2(\phi_3,\Phi_3)+\cdots \tag{8b}$$

and have, in addition, ϕ_0 and Φ_0 terms, respectively, representing $O(1/\mathrm{M})$ contributions. It is worthwhile to note that though it may appear that the $O(1/\mathrm{M})$ terms in the above series for ϕ and Φ are singular, they are indeed removable singularities, which are required to be present in that particular form due to the coefficient of the $\partial p/\partial t$ term in Eq. (4). In general the symbols for the dependent variables in the above series represent complex quantities, although their physically meaningful real parts are of course understood, i.e., a symbol such as $\zeta(x,y,t)$ would represent the real part, $\Re\{\overline{\zeta}(x,y)e^{\mathrm{int}}\}$, where $\overline{\zeta}(x,y)$ is the ''complex amplitude,'' and integer $n\geqslant 0$ is the nth harmonic. The symbol ζ stands for any of the dependent variables ϱ, u, v, p, ϕ, or Φ. It may be noted that for the time-independent contributions which are ultimately the quantities of interest in this study, $n=0$, in which case $\overline{\zeta}(x,y)$ is necessarily real. For ease of manipulation, the solutions are later also expressed in terms of a dimensionless normal coordinate measured from the wall as

$$\eta=\hat{y}^*/\delta_\nu=\eta_0(1-y) \tag{9}$$

and defined in the schematic in Fig. 1.

II. THE LEADING ORDER SOLUTION

The leading order solution of the governing equations provides a description of the variation of the first harmonic quantities of the imposed standing wave. Solution of the $O(1)$ balance of the equation of motion [Eq. (3)] yields the velocity distribution

$$\overline{u_1}=i\frac{d\overline{p_1}}{dx}\left[1-\frac{\cosh(1+i)y\,\eta_0}{\cosh(1+i)\,\eta_0}\right], \tag{10}$$

where $u_1\equiv\overline{u_1}(x,y)e^{it}$ and $p_1\equiv\overline{p_1}(x)e^{it}$ with the variation $\overline{p_1}(x)$ governed by a suitable wave equation which is determined later at the end of Sec. II.

For the leading $O(1/\mathrm{M})$ temperature contributions in the fluid and wall portions, $\phi_0\equiv\overline{\phi_0}(x,y)e^{it}$ and $\Phi_0\equiv\overline{\Phi_0}(x,y)e^{it}$, respectively, in Eq. (8), and the solutions of the governing Eqs. (4) and (6) give

$$\overline{\phi_0}=2\,\mathrm{Ec}(\beta_m T_m)\overline{p_1}(x)\left[1-\frac{1}{1+\varepsilon_s}\frac{\cosh(1+i)y\,\eta_0\sqrt{\sigma}}{\cosh(1+i)\,\eta_0\sqrt{\sigma}}\right], \tag{11}$$

while in the wall region for $\delta_s^2k^2\ll 1$,

$$\overline{\Phi_0}=2\,\mathrm{Ec}(\beta_m T_m)\overline{p_1}(x)\frac{\varepsilon_s}{1+\varepsilon_s}\left[\frac{\cosh(1+i)y_s l/\delta_s}{\cosh(1+i)l/\delta_s}\right], \tag{12}$$

from which it is clear that both $\overline{\phi_0}$ and $\overline{\Phi_0}$ have an axial distribution which is determined by the as yet unknown form of $\overline{p_1}(x)$. In the above expressions ε_s is a complex constant defined as

$$\epsilon_s=\sqrt{\frac{(K\varrho c_p)_f}{(K\varrho c_p)_s}}\frac{\tanh[(1+i)y_0/\delta_\kappa]}{\tanh[(1+i)l/\delta_s]}. \tag{13}$$

Admittedly the above results are not all completely new (see the Appendix in Ref. 11), although the above forms are revealing and clearly present the *scale* of the temperature fluctuations in both the fluid and solid, from which it is a straightforward matter to deduce the dimensional quantities of interest. For instance, for channels with sufficiently thick walls ($l/\delta_s\geqslant 2$), and wide gaps ($y_0/\delta_\kappa\geqslant 2$), ϵ_s is essentially

a real constant, and for typical solid–*gas* combinations being considered for which $(K\varrho c_p)_s \gg (K\varrho c_p)_f$, it follows that $\epsilon_s \to 0$. Under these conditions it may be deduced from Eqs. (11) and (12) that the dimensional magnitude of the first harmonic temperature fluctuations in the fluid and the solid are entirely consistent with the expected values, i.e., of $O(\mathrm{M}(\gamma-1)T_m)$ and $O(\epsilon_s \mathrm{M}(\gamma-1)T_m)$ in the fluid and solid, respectively. It may be noted that in the above results the fluid thermal expansion coefficient has been expressed as the sum of a leading order contribution about the mean quiescent state (represented by the subscript ''m''), and a higher $O(\mathrm{M})$ contribution as

$$\beta T_f^* = \beta_m T_m + O(\mathrm{M}), \quad \text{where} \quad \beta_m = -\frac{1}{\varrho_m}\left(\frac{\partial \varrho^*}{\partial T_f^*}\right)_m . \tag{14}$$

Some important higher order effects associated with the ignored terms of $O(\mathrm{M})$ in the above equation are discussed at a later stage in Eqs. (22) and (23) of Sec. III A.

The first harmonic density fluctuations in the fluid are expressed in terms of the corresponding pressure and temperature fluctuations via a suitable equation of state, $\varrho \equiv \varrho(p,\phi)$. After appropriate manipulation of this equation of state, the first harmonic $O(1)$ density variation $\varrho_1 \equiv \overline{\varrho_1}(x,y)e^{it}$ may be expressed in dimensionless form as

$$\varrho_1 = \gamma p_1 - \frac{\beta_m T_m}{2\mathrm{Ec}} \frac{c_m^2}{c_p T_m}\phi_0, \tag{15}$$

so that

$$\overline{\varrho_1} = \overline{p_1}\left\{ \gamma - \mathrm{B}\left[1 - \frac{1}{1+\epsilon_s} \frac{\cosh(1+i)y\,\eta_0\sqrt{\sigma}}{\cosh(1+i)\,\eta_0\sqrt{\sigma}} \right] \right\}, \tag{16}$$

where the newly introduced fluid property parameter $B \equiv (\beta_m T_m)^2 (c_m^2/c_p T_m)$ simplifies to $(\gamma-1)$ only for the special case of an ideal gas working fluid. Substitution of the above solution forms into an $O(1)$ balance of the continuity equation [Eq. (2)] yields

$$i\overline{\varrho_1} + \frac{\partial \overline{u_1}}{\partial x} + \frac{\partial \overline{v_1}}{\partial y} = 0, \tag{17}$$

wherein $v_1 \equiv \overline{v_1}(x,y)e^{it}$. Using results for $\overline{u_1}$ and $\overline{\varrho_1}$ from Eqs. (10) and (16), respectively, and integrating the above expression once with respect to y, subject to the no-slip condition on the channel wall ($\overline{v_1}=0$ at $y=1$), gives

$$\begin{aligned}\overline{v_1} = {} & i\gamma \overline{p_1}(1-y) + i\frac{d^2\overline{p_1}}{dx^2}\left[(1-y) - \frac{1}{(1+i)\,\eta_0} \right. \\ & \left. \times \left(\tanh(1+i)\,\eta_0 - \frac{\sinh(1+i)y\,\eta_0}{\cosh(1+i)\,\eta_0} \right) \right] \\ & - i\mathrm{B}\overline{p_1}\left[(1-y) - \frac{1}{(1+\epsilon_s)(1+i)\,\eta_0\sqrt{\sigma}} \right. \\ & \left. \times \left(\tanh(1+i)\,\eta_0\sqrt{\sigma} - \frac{\sinh(1+i)y\,\eta_0\sqrt{\sigma}}{\cosh(1+i)\,\eta_0\sqrt{\sigma}} \right) \right]. \end{aligned} \tag{18}$$

Application of the ''no-crossover'' condition $\overline{v_1}=0$ at the fluid gap center plane $y=0$ in the above result, provides the governing ordinary differential equation for the complex pressure amplitude, $\overline{p_1}$, as

$$\frac{d^2\overline{p_1}}{dx^2} + m^2 \overline{p_1} = 0$$

with

$$m^2 = \frac{\gamma - \mathrm{B}[1 - \tanh(1+i)\,\eta_0\sqrt{\sigma}/(1+\epsilon_s)(1+i)\,\eta_0\sqrt{\sigma}]}{[1 - \tanh(1+i)\,\eta_0/(1+i)\,\eta_0]} \tag{19}$$

subject to appropriate boundary conditions at the ends of the channel ($x = x_1, x_2$) which should match with the characteristics of the standing acoustic waveform at these locations in the outer resonant duct. For a solid–*gas* coupling in the presence of sufficiently thickwall and wide-gap channels (such that $l/\delta_s \geqslant 2$ and $y_0/\delta_\kappa \geqslant 2$ so that $\epsilon_s \to 0$), the complex eigenvalues in Eq. (19) take on a far simpler form given by

$$m \approx \pm\left[1 + \frac{(1-i)(\gamma + \sqrt{\sigma} - 1)}{4\,\eta_0\sqrt{\sigma}} + O(\eta_0{}^{-2}) \right], \tag{20}$$

from which it becomes clear that the channel gap has to be sufficiently wide ($\eta_0\sqrt{\sigma} = y_0/\delta_\kappa \gg 1$) for $m \approx \pm 1$ so that the usually assumed simple purely sinusoidal standing wave behavior is applicable even *inside* the channel.

To obtain the pressure distribution inside the stack, $\overline{p_1}(x)$, from Eq. (19), the boundary conditions at the channel ends ($x = x_1, x_2$, $0 \leqslant y \leqslant 1$) have to be specified with care in a manner that is also consistent with measurements of the waveform characteristics that can typically be made in the rest of the resonant duct (see p. 1179 of Ref. 11). For the setup shown in the schematic of Fig. 1, typically the peak acoustic pressure amplitude (P_0) is measured by a microphone or other pressure transducer positioned on the face of the rigid reference end ($x=0$) of the resonator duct. Then for a known resonant excitation frequency in the duct, the acoustic pressure and velocity conditions can now be determined *just outside* the starting end of the stack ($x = x_1^-$) by integrating the above wave equation from the rigid end, $x=0$, up to the starting end, $x = x_1^-$, with $2y_0$ representing the spacing of the resonator duct walls. Standard acoustic techniques allow these quantities to be approximated as $|\overline{p_1}| \approx \cos x_1$ and $|\overline{u_1}| \approx \sin x_1$ at $x = x_1^-$. Subsequently, the desired acoustic pressure and velocity *just inside* the starting end of the stack ($x = x_1^+$) can be determined by virtue of continuity of pressure and ''volumetric velocity'' (volume flow rate obtained by integrating $\overline{u_1}$ across the gap cross-sectional area) across the $x = x_1$ boundary. These conditions thereby specify $\overline{p_1}$ and $d\overline{p_1}/dx$ at $x = x_1^+$ which now serve as the starting conditions for the integration of Eq. (19) for the solution of the acoustic pressure distribution *inside* the stack from one end, $x = x_1^+$, to the other, $x = x_2^-$. The pressure distribution over the remainder of the duct for $x \geqslant x_2^+$ should be such that it matches with the pressure field at the other (typically driver) end of the duct for the tuned resonant frequency of operation.

With a large number of channels in the resonant duct, each of uniform wall thickness ($2l$) and gap width ($2y_0$), continuity across the $x=x_1$ boundary (in going from $x=x_1^-$ to $x=x_1^+$) requires that the pressure itself be uniform, whereas volumetric velocity arguments dictate that the velocity (which depends on the pressure *gradient*) be amplified according to

$$|\overline{p_1}(x_1^+)|=|\overline{p_1}(x_1^-)|,$$
$$\left|\frac{d\overline{p_1}}{dx}(x_1^+)\right|=\left|\frac{d\overline{p_1}}{dx}(x_1^-)\right|\left(1+\frac{l}{y_0}\right), \tag{21}$$

where the ratio l/y_0 is a measure of the ''blockage effect'' in the duct due to the presence of the stack. It must be noted in the above expression that the *dimensional magnitude* of the pressure just outside the stack, at $x=x_1^-$, which is typically determined from an experimental measurement at the rigid far end ($x=0$), is itself a function of this blockage effect in such a way that as $l/y_0\to\infty$, the *dimensional amplitude* $P_0\to 0$ since in this limit the stack simply completely blocks off any acoustic transmission from the driver end to the rigid end of the duct. It is also clear that the ''blockage effect'' in the resonant duct introduced by the presence of the finite thickness of the stack walls could have an influence on the above boundary conditions of importance at the starting end ($x=x_1$) of the stack. Recent work by Worlikar and Knio[36] and Wetzel and Herman[35] has shown that vortex shedding/reattachment flow mechanisms are present in these end regions, whose incorporation into the current model is clearly beyond the scope of this study. Nonetheless, it is seen later that the boundary conditions in Eq. (21) above give a fairly accurate description of the principal mechanisms involved.

For purposes of simplifying the analysis and establishing a universal baseline reference case that does not complicate the issue by involving a dependence on the blockage factor l/y_0, and hence also allows ready comparisons with existing results in the literature (such as those of Merkli and Thomann[4]), this paper deals largely with a certain class of ideal channels. These are channels which are half-wavelength long ($x_2-x_1=\pi$) and start at the rigid end ($x_1=0$) of the duct, so that $|\overline{p_1}|=1$ and $|d\overline{p_1}/dx|=0$ become the convenient starting conditions at $x_1=0^+$ for the solution of Eq. (19). By choosing $x_1=0$ (i.e., stack end flush with rigid end), the need for specifying the l/y_0 parameter has thus been avoided, since it is not explicitly required in the analysis. However it should be noted that the *dimensional* values of the various variables which would be extracted from the *dimensionless* results of this work would still obviously depend on the magnitude of P_0, which in turn does depend on the blockage factor l/y_0. It is therefore noted that the various dimensionless arguments and comparisons to be made hereafter for different parameter values will all be with tacit reference to a given peak acoustic pressure amplitude, P_0, that can in reality be achieved at the rigid end termination of the duct. To arrive at the underlying physics quickly, with minimal digressions, the bulk of this paper deals with such half-wavelength long channels with gaps wide enough ($y_0/\delta_\kappa\gg 1$) such that $|\overline{p_1}(x)|$ is simply $\cos x$, even *inside* the channels of the stack. The more general and interesting case of narrower gap widths (which is also of greater practical interest) is considered in Appendix A, and, as shown later, indicates the presence of considerably modified and distorted pressure waveforms in the stack. Such a general procedure also establishes a proper criterion for the wide gap assumption made in the bulk of the paper, and furthermore predicts optimum gap widths that maximize the axial thermal stratification in the channel which is important from the viewpoint of stack design.

Despite the emphasis on these ideal channels, primarily to help capture and illustrate the underlying physics, it is stressed that the solution methodology developed here is equally well suited to handle even the general case of arbitrary channel lengths and gap widths, as has been demonstrated later in Appendix A, and also in Sec. IV by application of these results to make comparisons with some experimental data for shorter channels available in the literature.

III. THE TIME-AVERAGED TEMPERATURE DISTRIBUTION

Having determined the leading order first harmonic quantities, attention is now turned to determine the primary quantity of interest in this study, i.e., the time-averaged temperature distribution induced by the acoustic field. A search for higher order effects in the energy equation reveals that the leading order first harmonic terms interact in a nonlinear manner to generate an $O(1)$ temperature field, comprising a time-independent component, in addition to the second harmonic contribution. Since all the time-harmonic quantities have a zero temporal mean, it is the experimentally observable, time-independent component of the $O(1)$ temperature distribution which will form the focus of this study.

A. The fluid gap

For the fluid in the channel gap, in this search for $O(1)$ effects arising in Eq. (4), it becomes necessary (as is made clear below) to obtain the higher order terms for βT_f^* which were ignored earlier in Eq. (14) while dealing with leading order effects. A Taylor's series expansion of β based on its thermodynamic definition results in the following dimensionless form (details of the expansion omitted)

$$\beta T_f^*=\beta_m T_m\left[1-\mathrm{M}\left(\varrho_1+\frac{1}{2\,\mathrm{Ec}}\frac{c_m^2}{c_p T_m}\xi_m\phi_0\right)+O(\mathrm{M}^2)\right], \tag{22}$$

where in the $O(\mathrm{M})$ correction above, ξ_m represents a ''second-order'' thermal expansion coefficient defined as

$$\xi_m=\frac{T_m}{\varrho_m\beta_m}\left(\frac{\partial^2\varrho^*}{\partial T_f^{*2}}\right)_m-1 \tag{23}$$

so that for an ideal gas, $\xi_m\equiv 1$. The strength of the present dimensionless approach is well exemplified here since *a dimensional analysis would not be able to anticipate, or re-*

veal, the significance of this fluid property, ξ_m. This thermodynamic modulus, ξ_m, can be expressed in terms of more familiar properties using Maxwell's generalized thermodynamic relations as

$$\left(\frac{\partial c_p}{\partial p}\right)_T = -T\left(\frac{\partial^2(1/\varrho)}{\partial T^2}\right) = \frac{1}{\varrho T}[\beta T(\xi+1) - 2(\beta T)^2],$$

the significance of which has been alluded to by Allen *et al.* (Eq. 4 in Ref. 40) and used by Swift[41] in their exploration of liquids as possible working substances in Stirling or Malone type heat engines.

Based on the above arguments, the solution for the $O(1)$ temperature distribution ϕ_1 is now sought in the form

$$\phi_1(x,y,t) = \phi_{10}(x,y) + \overline{\phi}_{12}(x,y)e^{2it} \tag{24}$$

as a sum of a time-independent term, $\phi_{10}(x,y)$, and a second harmonic, $\phi_{12}(x,y,t) \equiv \overline{\phi}_{12}(x,y)e^{2it}$. The governing differential equation for the key component of interest, i.e., $\phi_{10}(x,y)$, is obtained by grouping together the time-independent contributions arising from the various nonlinear interactions of the first harmonic terms in Eq. (4) to yield

$$\begin{aligned}\frac{1}{2\sigma\eta_0^2}\frac{\partial^2\phi_{10}}{\partial y^2} = &\left\langle \varrho_1\frac{\partial\phi_0}{\partial t}\right\rangle + \left\langle u_1\frac{\partial\phi_0}{\partial x}\right\rangle + \left\langle v_1\frac{\partial\phi_0}{\partial y}\right\rangle \\ &- \frac{\mathrm{Ec}}{\eta_0^2}\left[\left\langle\left(\frac{\partial u_1}{\partial y}\right)^2\right\rangle + \beta_m T_m\left\langle u_1\frac{\partial^2 u_1}{\partial y^2}\right\rangle\right] \\ &+ 2\,\mathrm{Ec}(\beta_m T_m)\left[\left\langle \varrho_1\frac{\partial p_1}{\partial t}\right\rangle\right. \\ &\left. + \frac{1}{2\,\mathrm{Ec}}\frac{c_m^2}{c_p T_m}\xi_m\left\langle\phi_0\frac{\partial p_1}{\partial t}\right\rangle\right],\end{aligned} \tag{25}$$

where the angle brackets, $\langle \ldots \rangle$, denote a time average of the enclosed quantities. It may be noted that use has been made of the result in Eq. (22) to arrive at the last term in $[\ldots]$ on the rhs of Eq. (25) which includes the effect of the second-order thermodynamic modulus, ξ_m.

The above result can now, in principle, be integrated with respect to y, subject to symmetry conditions about the center plane, $y=0$, and proper coupling at the solid–fluid interface, $y=1$, to obtain the desired steady temperature distribution, $\phi_{10}(x,y)$. However the forms of the first harmonic terms from Sec. II required in Eq. (25) make this integration procedure a formidable task requiring a great deal of manipulative labor, and result in unwieldly expressions which do not afford an easy understanding of the underlying physics. Thus this task is relegated to Appendix A, while here a few assumptions are made to restrict the generality of the formulation leading to Eq. (25) to thereby arrive at a more manageable and insightful form of the governing equations. In particular, as noted at the end of Sec. II, the condition on the arbitrariness of the gap width is restricted to now allow only ''wide gaps'' (i.e., cases of $y_0/\delta_\kappa \geqslant 4$ as established in Appendix A), which in view of the applications in mind, is not very restrictive after all (the more general case of narrower/arbitrary gap widths is treated in Appendix A). This assumption allows the first harmonic terms from Sec. II to be expressed in an approximate form in terms of the coordinate, η, with little loss in accuracy [the coordinate *eta* was defined in Eq. (9)]. Consequently the primary results from Sec. II now become

$$\overline{u}_1 \approx i\frac{d\overline{p}_1}{dx}[1 - e^{-\eta(1+i)}], \tag{26}$$

$$\overline{\phi}_0 \approx 2\,\mathrm{Ec}\;\beta_m T_m \overline{p}_1\left[1 - \frac{1}{1+\epsilon_s}e^{-\eta\sqrt{\sigma}(1+i)}\right], \tag{27}$$

$$\overline{\varrho}_1 \approx \overline{p}_1\left\{\gamma - \mathrm{B}\left[1 - \frac{1}{1+\epsilon_s}e^{-\eta\sqrt{\sigma}(1+i)}\right]\right\}, \tag{28}$$

$$\begin{aligned}\overline{v}_1\eta_0 \equiv &\frac{|\overline{v}_1^*|}{U_0\delta_\nu k} \\ &\approx i\gamma\overline{p}_1\eta + i\frac{d^2\overline{p}_1}{dx^2}\left[\eta - \frac{1}{(1+i)}(1 - e^{-\eta(1+i)})\right] \\ &\quad - i\mathrm{B}\overline{p}_1\left[\eta - \frac{1}{(1+\epsilon_s)(1+i)\sqrt{\sigma}}(1 - e^{-\eta\sqrt{\sigma}(1+i)})\right]\end{aligned} \tag{29}$$

with $|\overline{p}_1(x)|$ approximated by its simple wide-gap purely sinusoidal form, $\cos x$ (as noted at the end of Sec. II). These ''wide-gap'' simplifications permit the integration of Eq. (25) to be carried out in a relatively more straightforward manner (compared to the arbitrary gap case), without losing any essential information on the physics behind the thermoacoustic streaming mechanism. The above forms in Eqs. (26)–(29) may be physically interpreted either as the one-wall form of the results in Sec. II (note no dependence on the gap width parameter, η_0), or more meaningfully as inner solutions in a near wall region (in contrast to outer solutions in the core of the channel gap), and thereby effectively decouple the channel walls in this approximation.

The details of the subsequent integration procedure of Eq. (25) have been omitted, except to note that the time average of the product of two typical first harmonic terms, $\zeta \equiv \overline{\zeta}(x,y)e^{it}$, and $\chi \equiv \overline{\chi}(x,y)e^{it}$, in Eq. (25) may be found from the simple rule

$$\langle \overline{\zeta}(x,y)e^{it}\cdot\overline{\chi}(x,y)e^{it}\rangle = \tfrac{1}{2}\Re\{\overline{\zeta}(x,y)\cdot \mathrm{c.c.}[\overline{\chi}(x,y)]\}, \tag{30}$$

where c.c. $[\ldots]$ denotes the complex conjugate of the enclosed quantity.

Results are given below for the usually found combination of properties and parameters for which the constant $\epsilon_s \to 0$. One integration of Eq. (25) yields for the steady transverse temperature gradient in the fluid,

$$\frac{\partial \phi_{10}}{\partial \eta} = \gamma\ \mathrm{Ec}\ \beta_m T_m |\overline{p_1}|^2 \sqrt{2\sigma} e^{-\eta\sqrt{\sigma}} \sin(\eta\sqrt{\sigma} + \pi/4) + \mathrm{Ec}\ \beta_m T_m |\overline{p_1'}|^2 \sqrt{2\sigma} \Bigg[\sqrt{\sigma} e^{-\eta} \sin(\eta + \pi/4) - e^{-\eta\sqrt{\sigma}} \sin(\eta\sqrt{\sigma} + \pi/4)$$
$$- \frac{\sqrt{\sigma}}{1+\sigma} e^{-\eta(1+\sqrt{\sigma})} (\cos(\eta\sqrt{\sigma} - \eta + \pi/4) - \sqrt{\sigma}\cos(\eta\sqrt{\sigma} - \eta - \pi/4)) \Bigg] - \mathrm{Ec}\ \beta_m T_m \sqrt{2\sigma} |\overline{p_1}|^2 e^{-\eta\sqrt{\sigma}}$$
$$\times \Bigg[(\gamma - \mathrm{B}) \sqrt{\sigma} \sin(\eta\sqrt{\sigma} - \pi/4) + \mathrm{B} \left(\sin(\eta\sqrt{\sigma} - \pi/4) + \frac{1}{\sqrt{2}} e^{-\eta\sqrt{\sigma}} \right) + e^{-\eta} (\gamma - \mathrm{B}) \frac{\sigma}{1+\sigma} (\cos(\eta\sqrt{\sigma} - \eta - \pi/4)$$
$$+ \sqrt{\sigma}\cos(\eta\sqrt{\sigma} - \eta + \pi/4)) \Bigg] + \mathrm{Ec} |\overline{p_1'}|^2 \sigma e^{-\eta} [e^{-\eta} - \beta_m T_m \sqrt{2} \sin(\eta + \pi/4)]$$
$$- \mathrm{Ec}\ \mathrm{B} |\overline{p_1}|^2 (\xi_m - \beta_m T_m) \sqrt{2\sigma} e^{-\eta\sqrt{\sigma}} \sin(\eta\sqrt{\sigma} + \pi/4). \tag{31}$$

It may be noted that the result in Eq. (31) is in a fairly general form and has wide ranging applicability to different solid–fluid combinations for which $\epsilon_s \to 0$. For the wide-gap case being treated ($y_0/\delta_\kappa \geqslant 4$ determined in Appendix A), the temperature gradient it predicts at the center plane ($\eta = \eta_0$) is exponentially small, and thus may be assumed to satisfy the center plane symmetry condition. Of greater interest is the temperature gradient predicted at the wall-fluid interface, $\eta = 0$, which in turn determines the *steady* heat exchange rate between the wall and the fluid. With the simple wide-gap purely sinusoidal pressure distribution $|\overline{p_1}(x)| = \cos x$, and with ΔT_{ref} chosen such that $\mathrm{Ec} \equiv 1$ [for reasons noted following Eq. (5)], the driving mean fluid temperature gradient at the wall can be obtained from Eq. (31) as,

$$\left.\frac{\partial \phi_{10}}{\partial \eta}\right|_{\eta=0} = \beta_m T_m \frac{\sqrt{\sigma}}{1+\sigma} [(\sigma\sqrt{\sigma} - 1)\sin^2 x + \{\gamma(1+\sigma)$$
$$+ (\gamma - \mathrm{B})\sqrt{\sigma}(1 - \sqrt{\sigma})\}\cos^2 x]$$
$$+ \sigma(1 - \beta_m T_m)\sin^2 x$$
$$+ \mathrm{B}\sqrt{\sigma}(\beta_m T_m - \xi_m)\cos^2 x. \tag{32}$$

In addition, if the working fluid is a gas which may be treated as ideal, then $\beta_m T_m \equiv 1$, $\xi_m \equiv 1$ and $\mathrm{B} \equiv (\beta_m T_m)^2 (c_m^2/c_p T_m) = (\gamma - 1)$, and the above form in Eq. (32) is further simplified to

$$\left.\frac{\partial \phi_{10}}{\partial \eta}\right|_{\eta=0} = \frac{\sqrt{\sigma}}{1+\sigma} [(\sigma\sqrt{\sigma} - 1)\sin^2 x + (\gamma(1+\sigma)$$
$$+ \sqrt{\sigma}(1 - \sqrt{\sigma}))\cos^2 x]$$
$$= g_0(\sigma, \gamma) + g_2(\sigma, \gamma)\cos 2x,$$

where

$$g_0(\sigma, \gamma) = \frac{\sqrt{\sigma}}{2}(\gamma + \sqrt{\sigma} - 1),$$
$$g_2(\sigma, \gamma) = \frac{\sqrt{\sigma}}{2} \left[\gamma + \frac{(1-\sigma)(1+\sqrt{\sigma})}{(1+\sigma)} \right]. \tag{33a}$$

In this specially chosen limiting form, the result in Eq. (33a) for an ideal gas allows comparisons to be made with the available results in the literature, in particular with those of Merkli and Thomann.[4] Although the resonant channel geometry they considered was different (namely a cylindrical tube), their results can be used here for comparison purposes since for the wide gap approximation purposefully being made here, the boundary layer effects resulting in Eq. (33a) are essentially the same for both cases. The correctness of the form in Eq. (33a) may be verified by specifically making a comparison with Fig. 2 of their paper which shows the axial variation of the *numerically* determined (dimensionless) wall heat flux. The corresponding heat flux scale for nondimensionalization in this study would be $\varrho_m \nu c_m^2 / y_0$ which may be used with Eq. (33a) to obtain the dimensionless heat flux as

$$q_w'' = \frac{q_w^{*''}}{\varrho_m \nu c_m^2 / y_0} = \frac{K_f \Delta T_{\mathrm{ref}} / \delta_\nu}{\varrho_m \nu c_m^2 / y_0} \left.\frac{\partial \phi_{10}}{\partial \eta}\right|_{\eta=0}$$
$$= \tfrac{1}{2} \mathrm{M}^2 \eta_0 g(x; \sigma, \gamma),$$

where

$$g(x; \sigma, \gamma) \equiv \frac{1}{\sigma} \left.\frac{\partial \phi_{10}}{\partial \eta}\right|_{\eta=0}$$
$$= \frac{1}{\sigma} [g_0(\sigma, \gamma) + g_2(\sigma, \gamma)\cos 2x]. \tag{33b}$$

The axial variation of this dimensionless wall heat flux q_w'', and its dependence on σ and γ is represented by the above carefully extracted function $g(x; \sigma, \gamma)$, which is shown in Fig. 2 here for various values of σ, and found to confirm the numerical predictions of Merkli and Thomann (Fig. 2 in Ref. 4), and also the results of Jeong and Smith (Eq. 47 and Fig. 6 in Ref. 5). However, owing to the complicated representation of the final results from their analyses (Eq. 22 in Ref. 4 and Eq. 29 in Ref. 5), little information can be gleaned with regard to the actual physical origin of the energy exchange mechanisms responsible for this time-averaged heat flux effect, a matter which is discussed in greater detail for the case of both gaseous and nongaseous

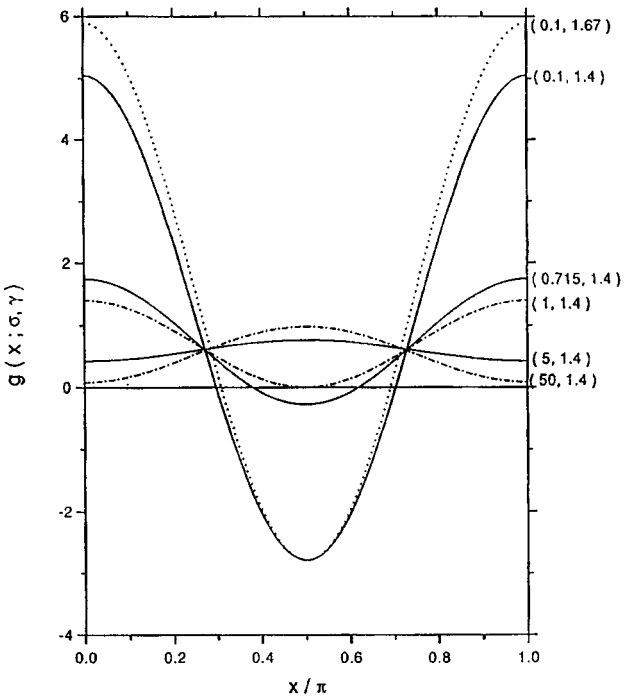

FIG. 2. Axial variation of the dimensionless wall heat flux in the wide-gap limit as described by the function $g(x;\sigma,\gamma)$ in Eq. (33) for various sets of values of (σ,γ) shown on the figure (cf. Fig. 2 of Ref. 4).

working fluids in the following section. In particular it may be noted that, the importance of the previously ignored role of γ is clearly demonstrated in Fig. 2, as characterized by the two curves with $\gamma=1.4$ and $\gamma=1.67$ for the case of $\sigma=0.1$. The reader is reminded that the more general and interesting cases of narrower/arbitrary gap widths are also discussed in Appendix A, and the corresponding heat flux results have been presented in Fig. A3.

B. A physical explanation—The bucket-brigade model

Before proceeding further, at this stage it is worthwhile to exploit the results obtained thus far with this dimensionless formulation, to trace the physical origin of this steady thermoacoustic heating/cooling effect manifest at the wall-fluid boundary, *without* making the ideal gas simplifications which yielded Eq. (33), but instead by analyzing the more general result in Eq. (32) valid for any fluid. Such an exercise would be fruitful since a review of the literature shows that a clear account is not available of the physical mechanisms responsible for this thermal effect, which is in turn ultimately responsible for establishing the mean axial temperature gradient along the channel. Although the arguments that follow are based on results from the wide-gap approximation obtained thus far, the essential physics are preserved even for the arbitrary gap case treated in Appendix A.

To trace the source of this thermoacoustic effect from its governing equations, Eqs. (25) and (32) are carefully compared to determine the term-by-term cause-effect correspondence between the two equations, and to also determine the significance of those terms that subsequently vanish in Eq. (33) due to the ideal gas assumption. Such a comparison shows that the first $\sin^2 x$ term in Eq. (32) is due to the second term on the rhs of Eq. (25), whereas it is the first and third terms on the rhs of Eq. (25) which are responsible for the first $\cos^2 x$ contribution in Eq. (32). The coefficients of these first $\sin^2 x$ and $\cos^2 x$ terms in Eq. (32) then clearly indicate that, for a gas (for instance) which has $\sigma<1$, these terms give rise to a cooling and heating effect, respectively. Since these terms all arise from only the first three terms on the rhs of Eq. (25), it becomes clear now that this thermoacoustic mechanism owes its origin primarily to the time-averaged effects of energy convection (rather than energy dissipation), thus providing a firm footing for the oft-quoted bucket-brigade model (see Refs. 9, 11, and 25). [The ideal gas result in Eq. (A2) from the integral procedure of Appendix A is identical to Eq. (33) but offers an alternative perspective of the same.]

Continuing this comparison procedure it is found that, the pair of terms in the first [. . .] in Eq. (25) with coefficient Ec/η_0^2, represents a combination of viscous dissipation and compressibility work effects which together results in a contribution $\sim\sin^2 x(1-\beta_m T_m)$ to the wall heat flux in Eq. (32). Thus for an ideal gas for which $\beta_m T_m\equiv 1$, contrary to common expectation, viscous dissipation effects *do not* have a net thermal effect *at the wall-fluid interface*, and are instead completely balanced by compressibility work effects and hence *neither* effect is present in Eq. (33). Lastly, the pair of terms in the second [. . .] in Eq. (25) with coefficient $2\,\mathrm{Ec}\,\beta_m T_m$, represents time-averaged expansion work effects arising from temporal changes in the pressure, and makes a contribution $\sim\cos^2 x(\beta_m T_m-\xi_m)$ to the wall heat flux in Eq. (32). Again for the case of an ideal gas for which both $\beta_m T_m\equiv 1$ and $\xi_m\equiv 1$, this term also vanishes as is evident from Eq. (33), indicating that expansion work effects are also unimportant for an ideal gas.

So it may be concluded that for the common case of an ideal gas working fluid in a thermoacoustic engine, it is only the first term representing time-averaged energy convective effects in [. . .] on the rhs of Eq. (32) which makes a nonzero contribution to the thermoacoustic streaming effect, thus resulting in the forms in Eq. (33) in support of the simple ''bucket-brigade'' model. This is especially noteworthy since this model is based on the mechanics of gas parcel oscillation from standard *inviscid* linear acoustic theory and would not be expected to provide an explanation of viscous effects at the wall. Fortuitously, though, the model does work for the particular case of an ideal gas, only due to the energy balances noted in the above paragraph. The issue is however far more involved for the general case of a nongaseous working fluid, such as water (Swift and Fusco,[42] Gabrielson[43]) or liquid-sodium (Migliori and Swift[44]) which have been studied as possible thermoacoustic working fluids, wherein the latter two terms of Eq. (32) are also fully capable of giving rise to significant nonzero contributions to the thermoacoustic heating/cooling effect. Due to the dissipative origin of these additional contributions the simple ''bucket-brigade'' model would be incapable of providing a complete description of the complete mechanics of the process. In view of the above arguments, it can also be inferred that the curves for $\sigma\geqslant 1$ in Fig. 2 (provided here only for comparison with Fig. 2 of Merkli and Thomann[4]) are in fact incomplete

and have little, or no, physical meaning for lack of correspondence with any real fluids since they are based on the ideal gas result in Eq. (33) and hence do not account for any of the additional dissipative effects as noted above. Besides making a note of this important point, this matter is not pursued further (the rest of this paper is devoted only to ideal gas working fluids), simply for lack of more detailed information (in the open literature) on the variation of the fluid properties (thermal expansion coefficients) β and ξ for different candidate liquid working substances which could be used in thermoacoustic engines.

C. The wall-fluid coupling

Having verified the correctness of the above approach (by applying the present general theory to the specific case of an ideal gas in a wide-gap channel to allow corroboration with existing results in the literature), the result for the temperature gradient in Eq. (31) is integrated once more to obtain the *steady* temperature distribution in the fluid,

$$\begin{aligned}\phi_{10} = {} & \gamma\ \mathrm{Ec}\ \beta_m T_m |\overline{p_1}|^2 [1 - e^{-\eta\sqrt{\sigma}} \cos\ \eta\sqrt{\sigma}] + \mathrm{Ec}\ \beta_m T_m |\overline{p_1'}|^2 [\sigma(1 - e^{-\eta}\ \cos\ \eta) - (1 - e^{-\eta\sqrt{\sigma}}\ \cos\ \eta\sqrt{\sigma})] \\ & - \mathrm{Ec}\ \beta_m T_m |\overline{p_1'}|^2 \frac{\sigma}{(1+\sigma)^2} [(1-\sigma)(1 - e^{-\eta(1+\sqrt{\sigma})} \cos(\eta\sqrt{\sigma} - \eta)) + 2\sqrt{\sigma} e^{-\eta(1+\sqrt{\sigma})} \sin(\eta\sqrt{\sigma} - \eta)] \\ & + \mathrm{Ec}\ \beta_m T_m |\overline{p_1}|^2 (\gamma - \mathrm{B}) \left[\sqrt{\sigma} e^{-\eta\sqrt{\sigma}}\ \sin\ \eta\sqrt{\sigma} - \frac{\mathrm{B}}{2(\gamma - \mathrm{B})} (1 - e^{-2\eta\sqrt{\sigma}} - 2e^{-\eta\sqrt{\sigma}}\ \sin\ \eta\sqrt{\sigma}) \right] - \mathrm{Ec}\ \beta_m T_m |\overline{p_1}|^2 \\ & \times (\gamma - \mathrm{B}) \frac{\sigma\sqrt{\sigma}}{(1+\sigma)^2} [2\sqrt{\sigma}(1 - e^{-\eta(1+\sqrt{\sigma})}\ \cos(\eta\sqrt{\sigma} - \eta)) - (1-\sigma) e^{-\eta(1+\sqrt{\sigma})}\ \sin(\eta\sqrt{\sigma} - \eta)] + \frac{1}{2} \mathrm{Ec} |\overline{p_1'}|^2 \\ & \times \sigma [(1 - e^{-2\eta}) - 2\beta_m T_m (1 - e^{-\eta}\ \cos\ \eta)] - \mathrm{Ec}\ \mathrm{B} |\overline{p_1}|^2 (\xi_m - \beta_m T_m) [1 - e^{-\eta\sqrt{\sigma}}\ \cos\ \eta\sqrt{\sigma}] + \varphi(x). \end{aligned} \tag{34}$$

When evaluated at the wall–fluid boundary, $\eta = 0$, the above expression simplifies to only the last term of the rhs, $\varphi(x)$, which represents the as yet undetermined interface temperature at the wall–fluid boundary. This crucial coupling between the wall and the fluid, $\varphi(x)$, represents the large time-averaged axial thermal stratification which can be induced in the channel and has to be determined from a conjugate solution of the temperature distribution in the wall as treated below.

In correspondence with the form of the $O(1)$ temperature distribution in the fluid in Eq. (24), the $O(1)$ temperature distribution in the channel wall is also sought as

$$\Phi_1(x,y,t) = \Phi_{10}(x,y) + \overline{\Phi}_{12}(x,y) e^{2it} \tag{35}$$

with interest being primarily in the time-independent component, $\Phi_{10}(x,y)$. The governing differential equation for this steady-state temperature distribution in the channel wall comes from Eq. (6) as

$$\frac{\partial^2 \Phi_{10}}{\partial y_s^2} + l^2 k^2 \frac{\partial^2 \Phi_{10}}{\partial x^2} = 0 \tag{36}$$

subject to the symmetry condition along its center plane (since each wall of the channel in Fig. 1 is exposed to identical conditions on either side)

$$\frac{\partial \Phi_{10}}{\partial y_s} = 0 \ \text{ at } \ y_s = 0 \tag{37}$$

and the heat flux matching condition at the fluid–wall interface from Eq. (33)

$$\begin{aligned} \left. \frac{\partial \Phi_{10}}{\partial y_s} \right|_{y_s = 1} &= K_{\mathrm{fs}} \left. \frac{\partial \phi_{10}}{\partial \eta} \right|_{\eta = 0} \\ &= K_{\mathrm{fs}} [g_0(\sigma,\gamma) + g_2(\sigma,\gamma) \cos 2x]. \end{aligned} \tag{38}$$

At its ends, $x = x_1, x_2$, $0 \leqslant y_s \leqslant 1$, the channel wall is exposed to a complicated fluid motion pattern as shown in the numerical work of Worlikar and Knio[36] and the experimental observations of Wetzel and Herman,[35] in addition to the time-averaged streaming motion that is present in these regions. Hence, for lack of a more precise measure of the effect of this fluid motion, these end convective conditions are chosen to be characterized by heat transfer coefficients h_1, h_2 respectively, which yield the following boundary conditions at these end faces,

$$\frac{\partial \Phi_{10}}{\partial x} = (-1)^{2,1}\ \mathrm{Bi}_{1,2}\ \Phi_{10}$$

$$\text{at } \ x = x_{1,2} \ \text{ where } \ \mathrm{Bi}_{1,2} = h_{1,2}/kK_s \tag{39}$$

in standard form in terms of Biot numbers. The solution of the conduction problem in the channel wall in Eqs. (36)–(39) is carried out using the standard separation of variables method, the results of which have been summarized in Appendix B. A close inspection of the different parameters in the results in Eqs. (B1)–(B3) shows that the wall–fluid coupling is crucial in determining the time-averaged thermoacoustic streaming effect. Evaluation of the time-averaged temperature at the wall-fluid interface $\Phi_{10}(x, y_s = 1)$ provides the sought after axial temperature variation $\varphi(x)$ in a

manner consistent with Eq. (34). Also embedded in these results is the influence of the acoustics on the fluid motion and heat transfer which is characterized by the heat transfer coefficients h_1 and h_2 at the end faces $x=x_1,x_2$ of the channel walls which are crucial, yet unknown, quantities in this problem. However, due to the complicated representation in Appendix B involving an infinite series solution, it is difficult to readily discern the contribution of the different solid/fluid properties and parameters. To facilitate a better appreciation of the wall-fluid interaction a simple and highly *idealized* case is considered in Sec. III D below.

D. The wall–fluid interface

To appreciate the wall–fluid coupling better, an idealized situation is considered, in which all faces of the channel, except the wall–fluid interface are assumed to be perfectly insulated. In other words, it is assumed for simplicity that there is no heat transfer on the wall end faces at $x=x_1,x_2$ ($\mathrm{Bi}_1=\mathrm{Bi}_2=0$), in addition to the center plane being effectively insulated owing to symmetry as noted in Eq. (37). This case requires a quasi-steady conduction analysis, also outlined in Appendix B, with allowance made for temperature variation of the wall with time (on a diffusive time scale) due to the presence of a time-averaged heat flux with a nonvanishing mean at the wall-fluid boundary [the g_0 part of Eq. (38)], which has no outlet at any of the other boundaries. It is emphasized that this is strictly not a realistic boundary condition and is chosen only to illustrate the wall–fluid coupling in a more lucid manner as shown below. Under these conditions the resulting infinite series solution in Appendix B takes on a particularly simple two-term form (after sufficient time during which the initial transients have decayed), for the special case of a channel which is half-wavelength long ($\Delta x=\pi$). The corresponding axial temperature distribution at the wall–fluid interface corresponding to the last term on the rhs of Eq. (34) can be obtained from Eqs. (B4) and (B5) as $\varphi(x)\equiv\Phi_{10}(x,y_s=1)$, and yields

$$\varphi(x)=K_{\mathrm{fs}}g_0(\sigma,\gamma)(t_s+\tfrac{1}{3})+K_{\mathrm{fs}}g_2(\sigma,\gamma)\frac{\coth 2lk}{2lk}\cos 2x. \tag{40}$$

Despite the gross idealization made in assuming insulated channel ends to arrive at the result above in Eq. (40), its appeal is in its particularly simple form for a half-wavelength long channel which thereby allows further useful deductions to be made as discussed below. Although the first term in the above result indicates a ''slow'' temperature growth with time (on a diffusive time scale), it is spurious in the sense that it is present only because of the insulated ends idealization; for the more realistic cases of non-zero Bi_1, Bi_2 it is clear from the more correct representation in Eqs. (B1)–(B3) that there is of course no such time dependence and the temperature eventually reaches a steady-state distribution. It is also for this reason that it is incorrect to deduce, based on this term, that there is an indefinite growth of temperature with time, since in reality, there is (however small) always a finite heat exchange with the working fluid present at the end faces, due to which the temperature distribution reaches an eventual steady state. Despite these limitations, this idealized problem is of value since it provides much insight through the second term in Eq. (40) above, which is of great interest since it contains the $\coth 2lk/2lk$ temperature magnification introduced due to the wall-fluid coupling and hence provides an explanation for the large axial thermal stratification that can be induced in the channel. This is essentially the same coupling present in the general result in Eqs. (B1)–(B3), although not as patently apparent. It may be recalled that due to this coupling, the axial temperature variation $\varphi(x)$ present at the wall-fluid boundary is by definition transmitted across to the temperature distribution on *both* the fluid and solid sides of this boundary. With this in mind the time-averaged temperature in the fluid described by Eq. (34) may now be viewed as a combination of a large magnitude axial stratification dictated by $\varphi(x)$, on which is superimposed a relatively smaller magnitude transverse variation prescribed by the other terms in Eq. (34). [Note that in Eq. (40) the second term contains a contribution only from the zero time-averaged component $g_2(\sigma,\gamma)$ of the boundary condition in Eq. (38), with the nonzero time-averaged component $g_0(\sigma,\gamma)$ appearing only in the first term. This is merely an artifact of the insulated boundaries idealization—for realistic cases recourse must be made to the more general form in Eqs. (B1)–(B3) in which case both g_0 and g_2 would make a contribution to the time-averaged behavior.]

The idealizations notwithstanding, the above analysis also shows that the *steady* temperature distribution, $\varphi(x)$ in Eq. (40), despite being nominally an $O(1)$ quantity in the series solution form of Eq. (8b), can be considerably amplified due to the wall–fluid coupling. This is further clarified below by considering the *dimensional* magnitude of this temperature term which clearly shows the roles of the different fluid/solid properties and parameters, and their capability to induce a large temperature magnification in the wall and the fluid,

$$\frac{T_i^*-T_m}{T_m}=\frac{K_f}{K_s}\frac{\coth 2lk}{2\delta_\nu k}\frac{c_m^2}{2c_pT_m}\left(\frac{P_0}{\gamma p_m}\right)^2 g_2(\sigma,\gamma)\cos 2x. \tag{41}$$

Despite being the result for a very idealized situation, the above simplified form provides a direct look at the reason behind this magnified temperature gradient, and helps in a better appreciation of the more realistic and general form [in Eqs. (B1)–(B3)] when nonzero heat transfer rates are present at the channel ends.

For completeness, it would also be useful to recall at this stage the major assumptions made in arriving at the simple forms in Eqs. (40) and (41) as listed below:

(1) Boundary layer approximation of the Navier–Stokes equations based on the narrow acoustic waveguide approximation in the channel, $y_0^2k^2\ll 1$.
(2) Small solid thermal penetration depth, $\delta_s k\ll 1$, to allow the approximation which yields the form in Eq. (12).
(3) Sufficiently thick channel walls ($l/\delta_s\geqslant 2$) to approximate the constant ϵ_s in Eq. (13) as real, and to also allow a quasi-steady conduction analysis (in Appendix B) for the case of insulated boundaries.

(4) Sufficiently wide channel gaps ($y_0/\delta_\kappa \geqslant 4$) to approximate the constant ϵ_s in Eq. (13) as real, and to also allow the use of the purely sinusoidal approximation for $\overline{p_1}(x)$ in the simplified forms in Eqs. (26)–(29) for the time averaging in Eq. (25) to ultimately arrive at the result for the $O(1)$ steady temperature distribution ϕ_{10} in Eq. (34).
(5) Combination of fluid–solid properties for which $(K\varrho c_p)_s \gg (K\varrho c_p)_f$ so that $\epsilon_s \to 0$.
(6) Host fluid is a gas ($\sigma < 1$) which may be treated as ideal, so that $\beta_m T_m \equiv 1$, $\xi_m \equiv 1$, and $\mathrm{B} \equiv (\beta_m T_m)^2 (c_m^2/c_p T_m) = (\gamma - 1)$.
(7) Channel half-wavelength long ($x_1 = 0, x_2 = \pi$) with insulated ends at x_1, x_2.

IV. COMPARISONS WITH EXPERIMENTAL DATA

Most of the available experimental data in the literature for this problem has been obtained using a short stack of narrow gap channels (called a **T**hermo**A**coustic **C**ouple or TAC) with walls made from sandwiched fiber glass or metal in the form of sheets/plates or screens. These walls have been carefully inlaid with instrumentation (thermopiles or thermocouples) designed to measure the induced temperature distribution in the channel (see, for instance, Fig. 4 in Ref. 7 or Figs. 2 and 3 in Ref. 12). Data from such experiments have been typically gathered in the form of temperature measurements at various axial locations along the channel wall, and/or, in the form of a net temperature difference induced across the ends of the channel (ΔT_s). Results from the present theory will be compared with available experimental data, although such a comparison must be qualified with certain inherent limitations in the procedure as noted below:

(i) the unknown heat transfer coefficients at the ends of the channel walls;
(ii) edge effects due to a finite lateral extent of the TAC not accounted for in the theory;
(iii) the sandwich nature of the channel walls of the stacks, which introduces uncertainties related to the resistance due to improper bonding of dissimilar materials; and
(iv) difficult to simulate artificially controlled heating/cooling conditions present at the ends of the TAC in some of the experiments.

The above limitations notwithstanding, in the interests of validating the current theory by corroboration with experiment, an attempt has been made to compare the theoretical predictions of this study with earlier experimental data wherever relevant. All comparisons have been made only with data obtained from solid-walled channels (such as plates, and *not* screens or meshes), for which this theory has been developed.

In the absence of any information on the crucial heat transfer behavior at the ends of these channels, the ends faces have initially been simply assumed to be insulated ($\mathrm{Bi}_1 = \mathrm{Bi}_2 = 0$) in these comparisons. Under such conditions, the *dimensional* magnitude of the fluid-wall interface temperature used in these comparisons can be obtained from the time-independent part of Eqs. (B4) and (B5) as,

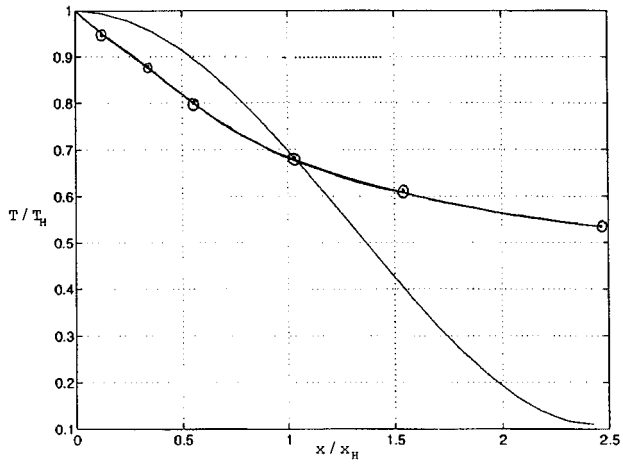

FIG. 3. Mean temperature distribution with axial location. The open circles connected by a curve represent measured temperature data for a fiberglass TAC reproduced from Fig. 10 of Wheatley *et al.* (Ref. 7). The smooth curve is the theoretical prediction from the current study under the same conditions as discussed in Sec. IV A.

$$(T_i^*|_x - T_i^*|_{x_1}) = -\frac{\delta x^2}{8\pi}\left[\frac{2g_2(\sigma,\gamma)}{\gamma\sqrt{\sigma}}\right]\frac{p_m\sqrt{2\kappa_f}}{K_s}\frac{c_m}{\sqrt{\omega}}\left(\frac{P_0}{p_m}\right)^2 \times \sum_{n=1,3,5,\ldots}^{\infty}\frac{(\sin 2x_1 + \sin 2x_2)}{n(n^2-\delta x^2)} \times \coth(2lkn/\delta x)[1-\cos 2n(x-x_1)] \quad (42)$$

and in the above form permits ready comparison with existing forms in the literature. For cases where some information on the heat transfer coefficients at the channel ends can be indirectly deduced, the more general form in Eqs. (B1)–(B3) has been used.

In either case, numerical values of the above infinite series solutions were obtained from a simple computer program. Each program was input with the variables and material properties relevant to the particular experiment being examined, and the infinite series solution in Eqs. (B1)–(B3) or Eqs. (B4)–(B5) and (42) were evaluated. The results of such a comparison process have been presented below for one such representative experimental study.

A. Comparisons with Ref. 7

Wheatley *et al.*[7] measured the temperature distribution in the channels of various TAC configurations which are most suitable for comparisons with this study. Data from these experiments were principally plotted in Figs. 9–13 of their paper, the salient features of a couple of which are discussed and compared below.

In particular, data from a representative figure (Fig. 10 of their paper) has been reproduced in Fig. 3 here, and compared with theoretical predictions from this study. The experimental data are for a fiberglass TAC in a resonant duct with He gas at a mean pressure, $p_m = 2.76$ bar, and frequency, $f = 161$ Hz, with pressure ratios P_0/p_m in the range of 1.6%–3.7%. It is encouraging to note from Fig. 3 that despite the inherent uncertainties in obtaining the experimental parameters, the current theory successfully predicts tem-

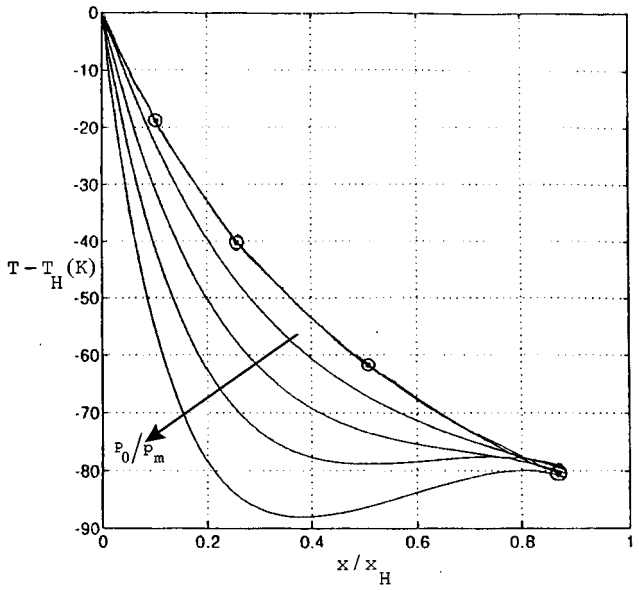

FIG. 4. Mean temperature distribution with axial location. The open circles connected by a curve represent measured temperature data for a fiberglass TAC reproduced from Fig. 11 of Wheatley *et al.* (Ref. 7). The four smooth curves are theoretical predictions from the current study for pressure ratio (P_0/p_m) values of 2.19%, 3.12%, 4.38%, and 6.19% as discussed in Sec. IV A.

perature differences of the O(100°C) as recorded in their paper. Unfortunately a more precise comparison is neither possible nor meaningful because of the lack of more accurate knowledge on the behavior of the flow at the ends of the stack. In particular it is clear from Fig. 3 here that the temperature distribution predicted by this study has a zero slope at the channel ends and is consistent with the insulated ends assumption being made for lack of more detailed information. In contrast, the experimental curve has a finite slope at the ends indicating a cooling effect which is in turn responsible for the general upward shift of the curve. This unknown flow and heat transfer behavior at the channel ends prevents a more accurate extrapolation of our theoretically predicted data with the experimental values, although the general trend is indeed encouraging.

In Fig. 4, a comparison has been made with Fig. 11 of Wheatley *et al.*[7] Here the experimental data are also for a fiber glass TAC in a resonant duct with He gas, but at a mean pressure, $p_m = 1.90$ bar, and frequency, $f = 394$ Hz, for four pressure ratio (P_0/p_m) values of 2.19%, 3.12%, 4.38%, and 6.19%. A more meaningful comparison is possible in this case since the experimental data has been presented in the form of a temperature *difference* rather than an absolute temperature *ratio*. A magnified view of Fig. 11 of their paper has been used to calculate as accurately possible the temperature gradients at the ends of the channel, which was in turn used to determine the Biot numbers. These Biot number values were then used in Eqs. (B1)–(B3) to predict the temperature distribution for the different pressure ratios that were used in the experiment, the results of which have been plotted in Fig. 4 here. Once again the agreement between the experimental data and the predictions from this study is very encouraging, especially at lower pressure ratios. Increasing deviation at higher pressure ratios is probably due to other higher order effects that are not accounted for by the present theory. In addition it is noteworthy that these comparisons can provide us with an estimate (although crude) of the heat transfer coefficients at the ends of the channel, which were found to vary linearly with the acoustic pressure ratio (and hence as the square root of the acoustic streaming velocity and also of the corresponding Reynolds number) for a given set of conditions.

For the ''short-stack'' approximation ($\delta x \ll 1$, stack length short relative to one-quarter wavelength) commonly made in some of the experiments, Eq. (42) may be used to obtain the net temperature difference, ΔT_s, across the ends of the stack as

$$\Delta T_s \equiv (T_i^*|_{x_2} - T_i^*|_{x_1}) \equiv \frac{\delta x^2}{2\pi}\left[\frac{2g_2(\sigma,\gamma)}{\gamma\sqrt{\sigma}}\right]\frac{p_m\sqrt{2\kappa_f}}{K_s}\frac{c_m}{\sqrt{\omega}}\left(\frac{P_0}{p_m}\right)^2 \times \sin 2\overline{x}\sum_{n=0}^{\infty}\frac{\coth(2(2n+1)lk/\delta x)}{(2n+1)^3}[1+O(\delta x^2)]. \tag{43}$$

The series summation in Eq. (43) is rapidly convergent and may be conveniently approximated by its first term with a maximum incurred error of a few percent. Again a comparison of this result with experimental data is encouraging and exhibits the $\sin 2\overline{x}$ dependence measured by Wheatley *et al.* (see Fig. 5 in Ref. 7) and Atchley *et al.* (see Figs. 7 and 8 in Ref. 12). However at this order of approximation, the theory is unable to predict the distortions observed by Atchley *et al.* (see Figs. 9 and 11 in Ref. 12) at high acoustic (drive) pressure ratios.

It may be concluded that despite the inherent limitations in making comparisons with experimental data obtained ''after the fact'' (i.e., under previously prescribed and controlled experimental conditions not precisely applicable to the present study), the extent of verification that has been obtained is encouraging enough to suggest other avenues of research with regard to the transport mechanics at the channel ends.

V. CLOSURE

The fundamental problem of thermoacoustic streaming in a resonant channel (representative of a channel in the stack of a thermoacoustic engine) has been considered to determine the origin of the mean or time-averaged temperature stratification that is induced in the walls and the fluid gap of such a channel. In the course of this study the role of a little known second order thermal expansion coefficient was developed at the beginning of Sec. III A, and used to arrive at the heat flux result for the wide-gap case in Eqs. (32) and (33), which is one of the principal results of this paper. A careful term-by-term comparison was made in Sec. III B to enunciate a sound physical explanation for the origin of this thermoacoustic effect, and to check the validity of the oft-

quoted bucket-brigade model. Based on the more general treatment of the arbitrary gap case in Appendix A, a corrected integral result has been provided in Eq. (A1), and from the standpoint of engine design, optimum channel gap widths have been predicted that can maximize the thermal stratification in the channel. It is found that this behavior is intimately coupled with the requirement for continuity of temperature and heat flux at the wall-fluid interface, and this coupling is crucial in determining the nature of the large axial temperature stratification that can be induced in the channel. This feature was demonstrated by solution of the coupled wall-fluid problem in Appendix B and subsequent successful comparisons in Sec. IV with representative experimental data available in the literature.

A knowledge of the fluid flow and heat transfer behavior at the *ends* of the channel walls is essential to be able to accurately predict the magnitude of the mean temperature gradient that can be established. It is believed that the above time-averaged heat transfer aspects, both inside and at the ends of the channel, are strongly influenced by the behavior of the time-averaged streaming fluid motion which is generated on the walls of the channel. It is hoped that the development in this study would establish a proper framework for the formulation of this problem and allow such higher order effects to be treated in a systematic manner.

ACKNOWLEDGMENTS

Thanks to Dr. G. W. Swift for his comments, and for drawing our attention to Ref. 40. We are grateful to the referees for their comments. We would also like to acknowledge many discussions with Dr. J. Olson which helped better express some of the ideas in this paper. A. G. is grateful for support received from the Naval Postgraduate School and the NASA Micogravity Program. S. L. G. is grateful for support from the Office of Naval Research. This work is based in part on the M. S. thesis of N. L. T.

APPENDIX A

For the case of arbitrary gap widths, it was noted earlier in Sec. III A that the general form in Eq. (25) must be integrated to obtain the time-averaged results. An integral procedure for carrying this out has been implemented in the Appendix of the paper by Merkli and Thomann,[4] which results in a compact form (Eq. 20 of their paper) for the time-averaged heat flux at the wall-fluid interface. However a close inspection of this result and its dependence on only the leading order terms u_1 and ϕ_0 (*but not* v_1) suggests that the time-averaged heat flux is independent of γ, and furthermore for wide gaps (when $|\overline{p_1}| \approx \cos x$) predicts a purely $\cos 2x$-type sinusoidal variation, both these features being clearly inconsistent with the true form in Fig. 2 shown here. The correct form of the result from their integral method obtained here by using Eq. (17) in Eq. (25) yields for the case of an ideal gas working fluid,

$$\left.\frac{1}{2\sigma\eta_0}\frac{\partial\phi_{10}}{\partial y}\right|_{y=1} = \eta_0\int_0^1\left\langle\frac{\partial}{\partial x}(u_1\phi_0)\right\rangle dy + \langle(\eta_0 v_1)\phi_0\rangle\Big|_{y=0}^{y=1}, \tag{A1}$$

where the presence of the previously ignored second term on the rhs may be noted. Application of the wide-gap limiting forms in Eqs. (26), (27), and (29) shows that *both terms* on the rhs of Eq. (A1) make a nonzero contribution to give

$$g(x;\sigma,\gamma) \equiv \left.\frac{1}{\sigma}\frac{\partial\phi_{10}}{\partial\eta}\right|_{\eta=0} = \frac{(1-\sigma\sqrt{\sigma})}{\sqrt{\sigma}(1+\sigma)}\cos 2x + \frac{(\gamma+\sqrt{\sigma}-1)}{\sqrt{\sigma}}\cos^2 x, \tag{A2}$$

which is an alternative form of the ideal gas result in Eq. (33).

For the more general case of arbitrary gap widths, the more complicated time-averaging integration procedure in Eq. (25) to obtain the dimensionless wall heat flux was carried out with the help of the symbolic computational program MAPLE. As noted at the end of Sec. II, for purposes of

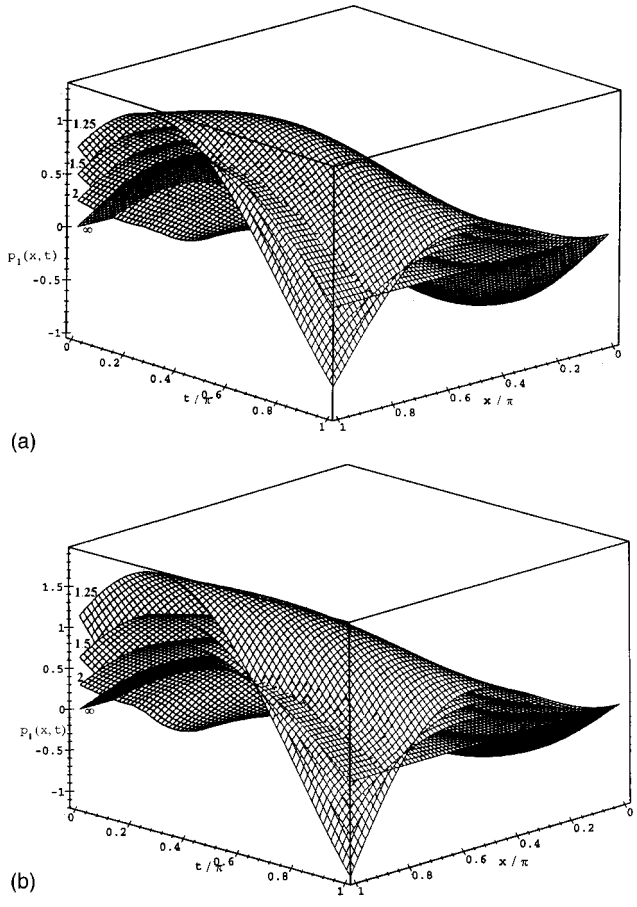

FIG. A1. Pressure distribution, $p_1(x,t)$, in the channel gap for different values of $\eta_0\sqrt{\sigma}$ shown in the figure. (a) $\sigma=0.27$ and $\gamma=5/3$, representative of a He–Xe mixture. (b) $\sigma=0.7$ and $\gamma=7/5$, representative of air.

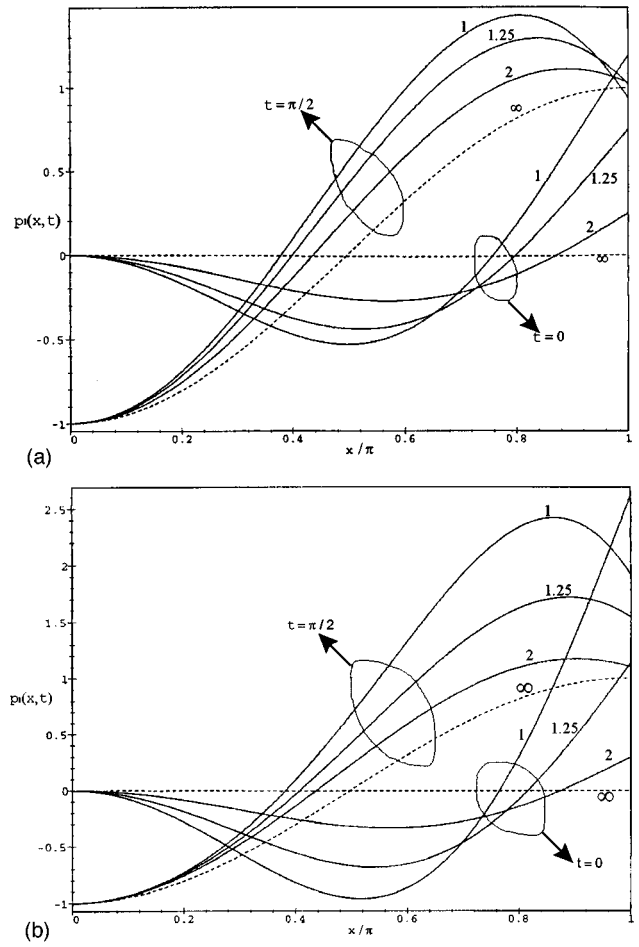

FIG. A2. Pressure traces, $p_1(x)$, for $t=0,\pi/2$, for different values of $\eta_0\sqrt{\sigma}$ shown on the figure. The dotted line represents the wide-gap limiting form. (a) $\sigma=0.27$ and $\gamma=5/3$, representative of a He–Xe mixture. (b) $\sigma=0.7$ and $\gamma=7/5$, representative of air.

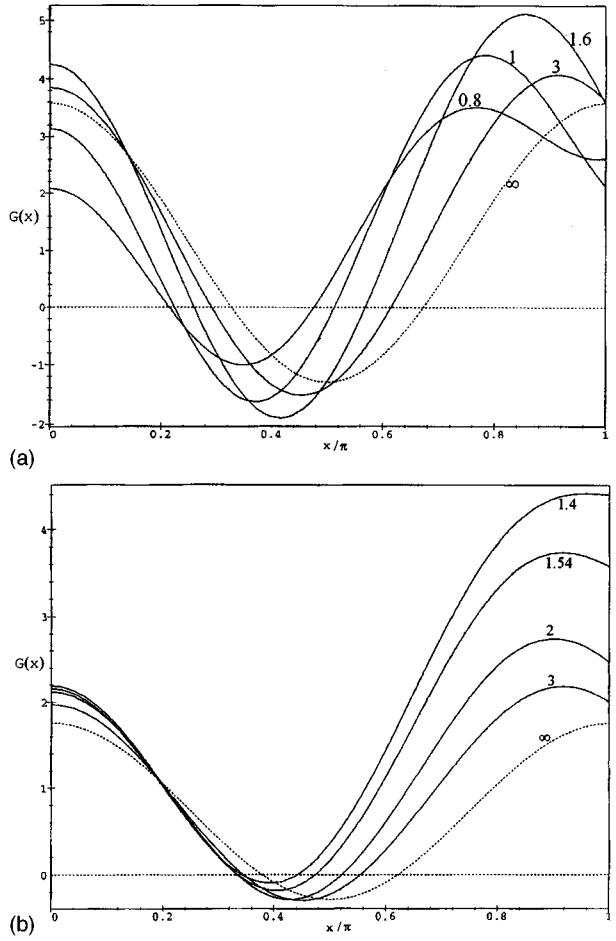

FIG. A3. Axial variation of the dimensionless wall heat flux for arbitrary gap widths as described by the function $G(x;\sigma,\gamma,\eta_0)$ from Appendix A for different values of $\eta_0\sqrt{\sigma}$ shown on the figure. The dotted line represents the wide-gap limiting form, $g(x)$, shown in Fig. 2. (a) $\sigma=0.27$ and $\gamma=5/3$, representative of a He–Xe mixture. (b) $\sigma=0.7$ and $\gamma=7/5$, representative of air.

establishing a universal baseline reference case which for convenience does not involve the blockage factor l/y_0, all channels considered are half-wavelength long with $x_1=0$ and $x_2=\pi$. No other approximations were made and the general solution of Eq. (19) (with $\epsilon_s\to 0$) was used along with the general forms of the expressions for the first harmonic quantities in Eqs. (10), (11), (16), and (18) valid for arbitrary gap widths. The resulting expression for the dimensionless heat flux [equivalent to Eq. (32)] is much too long-winded and hence prohibitively cumbersome to be reproduced here in its entirety and is available from the corresponding author (A. G.) upon request. Only the resulting behavior is discussed below.

First, it is worth pointing out that for very narrow gaps the pressure waveform, $p_1(x,t)$, in the channel is considerably distorted from its purely sinusoidal wide-gap form, as is evident from Fig. A1 which shows the pressure distribution for different gap widths for two representative cases at approximately each end of the Prandtl number spectrum for gases. Figure A2 is a plot of the pressure traces from the curves in Fig. A1 at two chosen instants of time, $t=0,\pi/2$, to further emphasize this point.

To also compare the heat flux results for the above general case of arbitrary gap widths, with that of the wide-gap limiting form $g(x)$ in Eqs. (32) and (33) or Eq. (A1), a suitable function $G(x)$ is defined as follows:

$$G(x;\sigma,\gamma,\eta_0)\equiv \frac{1}{\sigma}\left.\frac{\partial\phi_{10}}{\partial\eta}\right|_{\eta=0}$$

$$\text{such that}\quad G(x;\sigma,\gamma,\eta_0\to\infty)\equiv g(x;\sigma,\gamma), \tag{A3}$$

where the function $G(x)$ represents the arbitrary-gap analog of the wide-gap form $g(x)$.

The variation of $G(x)$ for different values of η_0 is shown in Fig. A3 for the same Prandtl numbers considered in Figs. A1 and A2. It may be deduced from Fig. A3(a) and the numerical values that, for low Prandtl number gases there clearly exists an optimum gap width of $y_0/\delta_\kappa\equiv\eta_0\sqrt{\sigma}\approx 1.5$–$1.6$ for which, the axial gradient of the thermoacoustically induced mean heat flux between the pressure node and antinode, and the lowest temperature achieved in the vicinity of the pressure node, are both maximized. For larger Prandtl numbers such as for air, Fig. A3(b) and the numerical values indicate that there is not such a clear opti-

mum and a wider range of gap widths can be used to maximize these thermoacoustic effects. However it becomes clear from a comparison of Fig. A3(a) and (b) that gases, or gas mixtures, with low Prandtl numbers (such as those studied by Hofler[22] and Giacobbe[45]) are preferred since they are capable of inducing much larger temperature gradients, and larger levels of cooling, which are the desirable features for refrigeration applications of thermoacoustic engines. The form of $G(x)$ in Fig. A3 also helps clearly establish the wide-gap criterion and confirms that for $y_0/\delta_\kappa \geqslant 4$, the more convenient results for the wide-gap approximation developed in the main body of this paper may be used with little loss in accuracy.

APPENDIX B

For the general case when Bi_1 and/or Bi_2 are nonzero, the solution of the heat conduction problem posed in Eqs. (36)–(39) may be obtained from the separation of variables method as,

$$\Phi_{10}=\sum_{n=0}^{\infty}\frac{K_{\mathrm{fs}}}{N_{\mathrm{I}}}\frac{D_n}{lk\Omega_n}\frac{\cosh\, lk\Omega_n y_s}{\sinh\, lk\Omega_n}\left[\cos\,\Omega_n(x-x_1)+\frac{\mathrm{Bi}_1}{\Omega_n}\sin\,\Omega_n(x-x_1)\right], \tag{B1}$$

where the constants, D_n, are

$$\begin{aligned}D_n=&\frac{2g_0(\sigma,\gamma)}{\Omega_n}\left[\sin\,\Omega_n\Delta x+\frac{\mathrm{Bi}_1}{\Omega_n}(1-\cos\,\Omega_n\Delta x)\right]\\&+\frac{g_2(\sigma,\gamma)}{(2+\Omega_n)}\left\{[\sin((2+\Omega_n)\Delta x+2x_1)-\sin 2x_1]\right.\\&\left.-\frac{\mathrm{Bi}_1}{\Omega_n}[\cos((2+\Omega_n)\Delta x+2x_1)-\cos 2x_1]\right\}\\&+\frac{g_2(\sigma,\gamma)}{(2-\Omega_n)}\left\{[\sin((2-\Omega_n)\Delta x+2x_1)-\sin 2x_1]\right.\\&\left.+\frac{\mathrm{Bi}_1}{\Omega_n}[\cos((2-\Omega_n)\Delta x+2x_1)-\cos 2x_1]\right\},\end{aligned} \tag{B2}$$

and the eigenvalues, Ω_n, and the normalization integral, N_{I}, are given by

$$\begin{aligned}&\cot\,\Omega_n\Delta x=\frac{\Omega_n^2-\mathrm{Bi}_1\,\mathrm{Bi}_2}{\Omega_n(\mathrm{Bi}_1+\mathrm{Bi}_2)},\\&N_{\mathrm{I}}=\Delta x\left[1+\frac{\mathrm{Bi}_1^2}{\Omega_n^2}\right]+\frac{\mathrm{Bi}_1}{\Omega_n^2}\left[1+\frac{\mathrm{Bi}_2}{\mathrm{Bi}_1}\frac{(1+\mathrm{Bi}_1^2/\Omega_n^2)}{(1+\mathrm{Bi}_2^2/\Omega_n^2)}\right].\end{aligned} \tag{B3}$$

For the special case of insulated ends, $\mathrm{Bi}_1=\mathrm{Bi}_2=0$ treated in Sec. III D, the complete unsteady form of the heat conduction equation in Eq. (6) must be considered to allow a quasi-steady analysis (for l/δ_s sufficiently large). In this case the fluid-wall interface heat flux boundary condition in Eq. (38) must be decomposed into two parts, one with a zero mean and the other with a nonzero mean, over the channel length, Δx. The part with the zero mean yields a steady-state solution with eigenvalues, $\Omega_n=n\pi/\Delta x$. The part with the nonzero mean yields the time-dependent solution (subject to the initial condition $\Phi_{10}=0$ at $t_s=0$), which may be obtained by Laplace transform methods, and consists of exponentially decaying transients along with a quasi-steady growth on the diffusive time scale. For time, t_s, large enough for which the above transients are negligible,

$$\begin{aligned}\Phi_{10}=&\sum_{n=1}^{\infty}\frac{D_n}{lk\Omega_n}\frac{\cosh\, lk\Omega_n y_s}{\sinh\, lk\Omega_n}\cos\,\Omega_n(x-x_1)\\&+K_{\mathrm{fs}}\left[g_0(\sigma,\gamma)+\frac{1}{2\Delta x}g_2(\sigma,\gamma)\right.\\&\left.\times(\sin 2x_2-\sin 2x_1)\right]\left(t_s+\frac{1}{2}y_s^2-\frac{1}{6}\right),\end{aligned} \tag{B4}$$

where the eigenvalues $\Omega_n=n\pi/\Delta x$, and the constants, D_n, are now given by

$$\begin{aligned}D_n=&K_{\mathrm{fs}}g_2(\sigma,\gamma)[(-1)^n\sin 2x_2-\sin 2x_1]\\&\times\left[\frac{1}{2\Delta x+n\pi}+\frac{1}{2\Delta x-n\pi}\right].\end{aligned} \tag{B5}$$

[1] N. Rott, ''Thermoacoustics,'' Adv. Appl. Mech. **20**, 135–175 (1980).
[2] R. L. Raun, M. W. Beckstead, J. C. Finlinson, and K. P. Brooks, ''A review of Rijke tubes, Rijke burners and related devices,'' Prog. Energy Combust. Sci. **19**, 313–364 (1993).
[3] N. Rott, ''The heating effect connected with nonlinear oscillations in a resonance tube,'' Z. Angew. Math. Phys. **25**, 619–634 (1974).
[4] P. Merkli and H. Thomann, ''Thermoacoustic effects in a resonant tube,'' J. Fluid Mech. **70**, 161–177 (1975).
[5] E. S. Jeong and J. L. Smith, Jr., ''Secondary flow in reciprocating machinery,'' *National Heat Transfer Conference, San Diego*, ASME-HTD **204**, 105–113 (1992).
[6] L. Bauwens, ''Oscillating flow of a heat-conducting fluid in a narrow tube,'' J. Fluid Mech. **324**, 135–161 (1996).
[7] J. Wheatley, T. Hofler, G. W. Swift, and A. Migliori, ''An intrinsically irreversible thermoacoustic heat engine,'' J. Acoust. Soc. Am. **74**, 153–170 (1983).
[8] J. Wheatley, T. Hofler, G. W. Swift, and A. Migliori, ''Experiments with an intrinsically irreversible thermoacoustic heat engine,'' Phys. Rev. Lett. **50**, 499 (1983).
[9] J. Wheatley, T. Hofler, G. W. Swift, and A. Migliori, ''Understanding some simple phenomena in the thermoacoustics with applications to acoustical heat engines,'' Am. J. Phys. **53**, 147–162 (1985).
[10] T. J. Hofler, ''Thermoacoustic refrigerator design and performance,'' Ph.D. Thesis, University of California at San Diego (1986).
[11] G. W. Swift, ''Thermoacoustic engines,'' J. Acoust. Soc. Am. **84**, 1145–1180 (1988).
[12] A. A. Atchley, T. J. Hofler, M. L. Muzzerall, M. D. Kite, and C. Ao, ''Acoustically generated temperature gradients in short plates,'' J. Acoust. Soc. Am. **88**, 251–263 (1990).
[13] N. Cao, J. R. Olson, G. W. Swift, and S. Chen, ''Energy flux density in a thermoacoustic couple,'' J. Acoust. Soc. Am. **99**, 3456–3464 (1996).
[14] G. W. Swift, ''Analysis and performance of a large thermoacoustic engine,'' J. Acoust. Soc. Am. **92**, 1551–1563 (1992).
[15] J. R. Olson and G. W. Swift, ''A loaded thermoacoustic engine,'' J. Acoust. Soc. Am. **98**, 2690–2693 (1995).
[16] W. P. Arnott, J. A. Lightfoot, R. Raspet, and H. Moosmüller, ''Radial wave thermoacoustic engines: Theory and examples for refrigerators and high-gain narrow-bandwidth photoacoustic spectrometers,'' J. Acoust. Soc. Am. **99**, 734–745 (1996).
[17] G. W. Swift and R. M. Keolian, ''Thermoacoustics in pin-array stacks,'' J. Acoust. Soc. Am. **94**, 941–943 (1993).
[18] W. P. Arnott, H. E. Bass, and R. Raspet, ''General formulation of ther-

moacoustics for stacks having arbitrarily shaped pore cross sections,'' J. Acoust. Soc. Am. **90**, 3228–3237 (1991).
[19] R. Raspet, H. E. Bass, and J. N. Kordomenos, ''Thermoacoustics of traveling waves: Theoretical analysis for an inviscid gas,'' J. Acoust. Soc. Am. **94**, 2232–2239 (1993).
[20] J. Kordomenos, A. A. Atchley, R. Raspet, and H. E. Bass, ''Experimental study of a thermoacoustic termination of a traveling-wave tube,'' J. Acoust. Soc. Am. **98**, 1623–1628 (1995).
[21] R. Raspet, *Erratum*, J. Acoust. Soc. Am. **100**, 673 (1996).
[22] T. J. Hofler, ''Concepts for thermoacoustic refrigeration and a practical device,'' *International Cryocooler Conference 5, Monterey*, 93–101 (1988).
[23] S. L. Garrett and T. J. Hofler, ''Thermoacoustic refrigeration,'' ASHRAE J. **34**, 28–36 (1992).
[24] S. L. Garrett, J. A. Adeff, and T. J. Hofler, ''Thermoacoustic refrigerator for space applications,'' AIAA J. Thermophys. Heat Trans. **7**, 595–599 (1993).
[25] G. W. Swift, ''Thermoacoustic engines and refrigerators,'' Phys. Today **48**, 22–28 (1995).
[26] B. L. Minner, L. Mongeau, and J. E. Braun, ''Optimization of thermoacoustic engine design variables for maximum performance,'' J. Acoust. Soc. Am. **98**, 2961 (1995); Internal Report-207, HL 96-6, Ray W. Herrick Laboratories, Purdue University (1996).
[27] M. Wetzel and C. Herman, ''Design optimization of thermoacoustic refrigerators,'' Intl. J. Refrig. **20**(1), 3–21 (1997).
[28] A. A. Atchley, H. E. Bass, T. J. Hofler, and H. T. Lin, ''Study of a thermoacoustic prime mover below onset of self-oscillation,'' J. Acoust. Soc. Am. **91**, 734–743 (1992).
[29] A. A. Atchley, ''Standing wave analysis of a thermoacoustic prime mover below onset of self-oscillation,'' J. Acoust. Soc. Am. **92**, 2907–2914 (1992).
[30] A. A. Atchley and F. M. Kuo, ''Stability curves for a thermoacoustic prime mover,'' J. Acoust. Soc. Am. **95**, 1401–1404 (1994).
[31] A. A. Atchley, ''Analysis of the initial buildup of oscillations in a thermoacoustic prime mover,'' J. Acoust. Soc. Am. **95**, 1661–1664 (1994).
[32] W. P. Arnott, J. R. Belcher, R. Raspet, and H. E. Bass, ''Stability analysis of a helium-filled thermoacoustic engine,'' J. Acoust. Soc. Am. **96**, 370–375 (1994).
[33] M. Watanabe, A. Prosperetti, and H. Yuan, ''A simplified model for linear and nonlinear processes in thermoacoustic prime-movers. Part I: Model and linear theory,'' J. Acoust. Soc. Am. **102**, 3484–3496 (1997).
[34] H. Yuan, S. Karpov, and A. Prosperetti, ''A simplified model for linear and nonlinear processes in thermoacoustic prime-movers. Part II: Nonlinear oscillations,'' J. Acoust. Soc. Am. **102**, 3497–3506 (1997).
[35] M. Wetzel and C. Herman, ''Design issues of a thermoacoustic refrigerator and its heat exchangers,'' *National Heat Transfer Conference, Houston*, ASME–HTD **331**, 137–144 (1996).
[36] A. S. Worlikar and O. M. Knio, ''Numerical simulation of a thermoacoustic refrigerator. Part I: Unsteady adiabatic flow around the stack,'' J. Comput. Phys. **127**, 424–451 (1996).
[37] J. R. Olson and G. W. Swift, ''Similitude in thermoacoustics,'' J. Acoust. Soc. Am. **95**, 1405–1412 (1994).
[38] Q. Qi, ''The effect of compressibility on acoustic streaming near a rigid boundary for a plane traveling wave,'' J. Acoust. Soc. Am. **94**, 1090–1098 (1993).
[39] D. G. Crighton,''Nonlinear Acoustics,'' in *Modern Methods in Analytical Acoustics, Lecture Notes*, by D. G. Crighton, A. P. Dowling, J. E. Ffowcs Williams, M. Heckl, and F. G. Leppington (Springer Verlag, New York, 1992), Chap. 24, pp. 648–670.
[40] P. C. Allen, W. R. Knight, D. N. Paulson, and J. C. Wheatley, ''Principles of liquids working in heat engines,'' Proc. Natl. Acad. Sci. USA **77**, 39–43 (1980).
[41] G. W. Swift, ''A Stirling engine with a liquid working substance,'' J. Appl. Phys. **65**, 4157–4172 (1989).
[42] G. W. Swift and A. M. Fusco, ''Seawater as a working fluid for thermoacoustic engines,'' J. Acoust. Soc. Am. **84**, S37 (1988).
[43] T. B. Gabrielson, ''Radiation from a submerged thermoacoustic source,'' J. Acoust. Soc. Am. **90**, 2628–2636 (1991).
[44] A. Migliori and G. W. Swift, ''Liquid-sodium thermoacoustic engine,'' Appl. Phys. Lett. **53**, 355–357 (1988), and references therein.
[45] F. W. Giacobbe, ''Estimation of Prandtl numbers in binary mixtures of helium and other noble gases,'' J. Acoust. Soc. Am. **96**, 3568–3580 (1994).

Measurements of thermoacoustic functions for single pores

L. A. Wilen
Department of Physics and Astronomy, Ohio University, Athens, Ohio 45701

(Received 25 July 1997; accepted for publication 27 October 1997)

A novel volume modulation technique is employed to measure the complex compressibility of a gas in a single pore. The complex compressibility depends on the geometry dependent thermal coupling between the gas and the pore walls, and is related to the thermoacoustic function f_κ, or equivalently, $F(\lambda)$. By measuring two different lengths of a given pore, end effects are eliminated, so that $F(\lambda)$ corresponding to a uniform, infinite length pore is determined. Pores of circular, rectangular, coaxial, and hexagonal cross sections were investigated, as well as cylinders which contained wire mesh screens. A wide range of values for the ratio of the thermal penetration depth to pore size was achieved by working down to very low frequencies. Results for circular, rectangular, and coaxial pores are in excellent agreement with theory. Hexagonal pores show behavior which is very close to similar size circular pores. Qualitative aspects of the screen results can be understood by a comparison to the theory for parallel plates. © *1998 Acoustical Society of America.* [S0001-4966(98)00503-7]

PACS numbers: 43.35.Ud, 43.20.Mv, 43.20.Ye [HEB]

INTRODUCTION

It is interesting to consider the effects of different stacks on the efficiency of thermoacoustic engines. The thermoacoustic behavior of circular and parallel plate stacks was originally calculated by Rott.[1] Arnott *et al.*[2] and also Stinson[3] extended these results to additional pore geometries. A new geometry, consisting of the channels between an array of parallel wires, was proposed by Müller.[4] Swift and Keolian[5] presented calculations which confirmed that a significant increase in efficiency for this type of geometry (termed the ''pin array'') could be obtained.

In general, the efficiency of a stack containing pores of a particular geometry is completely determined by the thermoacoustic function f_κ employed by Rott. A related function, $F(\lambda)$, was introduced by Arnott *et al.*[2] to discuss thermoacoustics for stacks having arbitrary pore geometries. The two functions are related by $F(\lambda)=1-f_\kappa^*$.

We previously described an experimental technique which allows one to measure directly the function $F(\lambda)$ for single pores.[6] Here, we present the results for a variety of pore geometries using this technique. The pores used were relatively large in diameter, but by working down to very low frequencies, a wide range of values for the ratio of the thermal penetration depth to pore size was explored. Consequently, the results are also applicable to much smaller pores at higher frequencies (as in porous materials or stacks) which have similar values for this ratio.

Measurements were performed for pores of circular, rectangular, coaxial, and hexagonal cross sections, as well as cylinders which contained wire mesh screens. For the first three types, a direct comparison with theory was possible.

I. EXPERIMENTAL TECHNIQUE

A number of improvements were made to the original apparatus described in Ref. 6. The setup is shown in Fig. 1. A 2-in. tweeter, driven by the reference output of a lock-in (buffered with a power amplifier), modulates an electroformed bellows attached to one side of a given pore. The motion of the bellows was monitored by bouncing a laser beam off a mirror on the speaker cone onto a position-sensitive detector (United Detector Technology model LSC/5D). It was important to measure only the translational part of the motion since rotation does not result in any net volume change of the cell. This was achieved by placing a lens midway between the speaker and detector which imaged the laser spot on the mirror onto the detector.[7] The amplitude of the motion varied slightly with frequency and was approximately 0.07 mm peak to peak. This corresponded to relative volume oscillations of about 0.4% for the smallest pore down to 0.04% for the largest. The resulting pressure oscillations were sensed with a silicon pressure gauge (Honeywell Microswitch model 24PCAFA1G) attached to the opposite end of the pore. The position and pressure signals were detected simultaneously with two digital vector lock-in amplifiers (Stanford Research Systems models SR850 and SR830) locked to the same reference frequency. The drive frequency was stepped from 0.5 Hz to 96 Hz in 71 equal increments of $f^{1/2}$. Both position and pressure signals were detected with a time constant of 3 s for frequencies below 3 Hz, and 1 s for the remainder. These relatively short time constants were possible because the lock-in amplifiers employ a digital filter to remove the second harmonic usually present after the phase sensitive detector. The complex pressure response was divided by the complex displacement response for all measured frequencies. This normalized pressure response will be referred to throughout the paper as $p(\omega)$.

The setup was designed so that different pore lengths and geometries could easily be inserted (and sealed) or removed. Before taking data for each pore, the cell was first flushed with dry nitrogen gas for several hours and then sealed off under approximately one atmosphere of nitrogen. The exact pressure in the cell was determined by measuring the outside pressure with a capacitance manometer (MKS

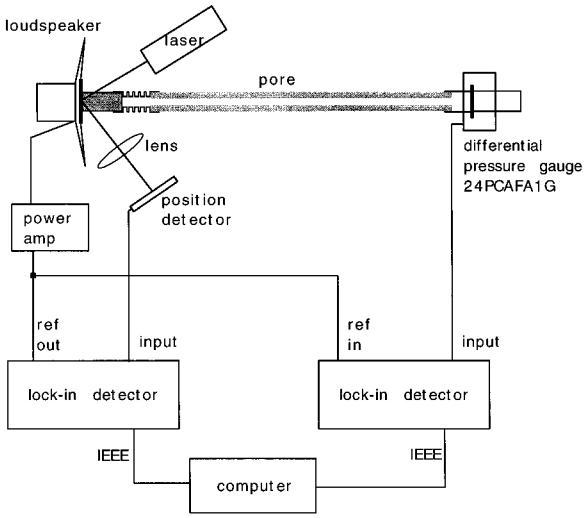

FIG. 1. Schematic diagram of the experimental setup.

Baratron model 622A 13T ED), and also the pressure difference between the inside and outside using the silicon pressure gauge, which was calibrated separately. The cell was allowed enough time to equilibrate to room temperature, which was measured with a mercury thermometer. A complete run for one pore took 35 min, during which time the drift in pressure and temperature was typically less than 1.5 Torr and 0.2 degrees Celsius, respectively. Typically, three to five runs were made with a given pore to check that the data were reproducible.

For each pore geometry, measurements were made with a longer and shorter length. From these measurements, the thermoacoustic function $F(\lambda)$ corresponding to a uniform, infinite length pore was determined as discussed below.

II. THEORY

In the low frequency limit where the acoustic wavelength in the gas is much larger than the length of the pore, the pressure response can be considered spatially uniform. To first order, the pressure and volume of the cell can be written as

$$P(t)=P_0+P_1(\omega)\exp(-i\omega t),$$
$$V(t)=V_0+V_1(\omega)\exp(-i\omega t), \tag{1}$$

where P_0 and V_0 are the equilibrium values and P_1 and V_1 are the acoustic variations. The complex compressibility is defined in terms of these quantities as:

$$C(\omega)=-\frac{1}{V_0}\frac{V_1(\omega)}{P_1(\omega)}. \tag{2}$$

The complex compressibility is also related to the experimentally measured normalized pressure response, $p(\omega)$, as follows:[6]

$$C(\omega)=\frac{p(0)}{p(\omega)}\times(P_0)^{-1}. \tag{3}$$

The thermoacoustic function $F(\lambda)$ is defined in terms of the complex compressibility $C_\infty(\omega)$ which would be measured for an infinite length pore of uniform cross section:[2,3]

$$F(\lambda)=\frac{\gamma}{\gamma-1}\,[1-P_0C_\infty(\omega)], \quad \lambda=R\sqrt{\frac{\rho_0\omega c_p}{\kappa}}. \tag{4}$$

γ is the usual ratio of specific heats, ρ_0 is the gas density, c_p is the isobaric heat capacity, κ is the thermal conductivity, and R is the characteristic pore radius defined as twice the transverse pore area divided by the pore perimeter. It is convenient to define a function $\tilde{F}(\lambda)$, which is related to the complex compressibility of arbitrary pores in the same way:

$$\tilde{F}(\lambda)=\frac{\gamma}{\gamma-1}\,[1-P_0C(\omega)]. \tag{5}$$

For a given pore inserted into the setup, $\tilde{F}(\lambda)$ [as determined from the pressure response using Eqs. (3) and (5)] represents an average of the thermoacoustic properties of the pore and the ends including the bellows and the pressure gauge. However, by measuring the pressure response for two different lengths of the desired pore, the end effects can be subtracted out to give the thermoacoustic function $F(\lambda)$.[8] Let $p_a(\omega)$ and $p_b(\omega)$ correspond to the measured pressure response functions, and V_a and V_b correspond to the volumes, with the shorter and longer pores inserted into the setup, respectively. The corresponding functions $\tilde{F}_a(\lambda)$ and $\tilde{F}_b(\lambda)$ can be calculated using Eqs. (3) and (5). The response for a uniform infinite pore is then given by[6]

$$F(\lambda)=\frac{V_a/V_b}{V_a/V_b-1}\,\tilde{F}_a(\lambda)-\frac{1}{V_a/V_b-1}\,\tilde{F}_b(\lambda). \tag{6}$$

The volume ratio in Eq. (6) is determined experimentally by

$$\frac{V_a}{V_b}=\frac{p_b(\omega=0)}{p_a(\omega=0)}\,\frac{P_a}{P_b}. \tag{7}$$

P_a and P_b are the equilibrium pressures in the cell for the runs with the short and long pores. In order to get accurate measurements for $p(\omega=0)$, the pressure response was extrapolated to zero frequency with a polynomial fit to the values of $p(\omega)$ for the ten lowest frequencies. Only the real part of the response was fit because $\mathrm{Im}[p(\omega=0)]=0$. A polynomial of the form $y=A+B\omega^2+C\omega^4$ was used because, for any geometry, the low-frequency expansion of the response function takes this form.

Values for λ were determined using $c_p=29.124$ J/mol K.[9] ρ_0 was calculated from the cell pressure and temperature assuming the ideal gas law. The thermal conductivity κ was taken to be $[25.44+0.074(T-22C)]$ mW/m K which is a simple interpolation between the literature values given for κ.[10] For γ, a value of 1.4021 was determined from the above value for c_p, and a value for c_p-c_v calculated using the second virial coefficient for nitrogen[11] and the thermodynamic relationship:

$$c_p-c_V=T\left(\frac{\partial p}{\partial T}\right)_V\left(\frac{\partial V}{\partial T}\right)_p. \tag{8}$$

Exact theoretical expressions for $F(\lambda)$ have been derived for some specific pore geometries. Cylindrical and parallel plate geometries have been worked out in the context of both thermoacoustics and porous media theory.[1,12–15] Calcu-

lations for rectangular pores are given by Stinson,[3] and also Roh *et al.*[16] Triangular pores are worked out by Stinson and Champoux.[17] A compilation of all the results can be found in Arnott *et al.*[2]

The derivation for a coaxial geometry follows a similar line to that of the pin-array model.[5] They differ only in the boundary condition at the outside radius: For the coaxial geometry, the temperature variations vanish while for the pin array the radial derivative of the same quantity vanishes. Assuming an inner radius r_i and an outer radius r_o, the result is expressed in terms of Bessel functions J and Neumann functions Y:

$$F(\lambda)=1-\frac{2}{x_2^2-x_1^2}\left\{\frac{(Y_0(x_2)-Y_0(x_1))(x_2J_1(x_2)-x_1J_1(x_1))-(J_0(x_2)-J_0(x_1))(x_2Y_1(x_2)-x_1Y_1(x_1))}{J_0(x_1)Y_0(x_2)-J_0(x_2)Y_0(x_1)}\right\},$$

$$x_1=\frac{1+i}{\sqrt{2}}\frac{r_i}{r_0-r_i}\lambda, \quad x_2=\frac{1+i}{\sqrt{2}}\frac{r_o}{r_o-r_i}\lambda. \tag{9}$$

The characteristic pore radius for this geometry is given by

$$R=\frac{2(\pi r_o^2-\pi r_i^2)}{2\pi r_o+2\pi r_i}=r_o-r_i. \tag{10}$$

III. PORE GEOMETRIES

The dimensions and shapes of the different pores used in the experiment are shown in Fig. 2. Two types of screens were measured. Both were spaced by 0.051 in. and fit into a cylinder as shown. The fine screens were brass with a wire density of 40/in. The orientation of adjacent screens was random. The coarse screens were copper, and had a wire density of 14/in. in one direction and 18/in. in the other. These were chosen so that the spacing between the screens was roughly equal to the size of the screen holes. They were oriented uniformly, but the wires on adjacent screens did not line up perfectly when viewed down the axis of the cylinder. For both types of screens, two lengths were measured to eliminate end effects but no attempt was made to eliminate edge effects at the perimeter of the cylinder.

For all of the pores, the ends were adapted to fit into a standard size hole which interfaced to the bellows on one side and a similar hole which interfaced to the pressure gauge on the opposite side. The manner in which this was done is shown at the bottom of Fig. 2 for the coaxial and screen pores.

IV. RESULTS AND DISCUSSION

The results for all of the pores are shown in Figs. 3–5. The small anomaly observed in all the experimental curves is due to pickup at 60 Hz. Except where noted, the experimental data for F are plotted versus $\lambda=(\rho_0\omega c_p/\kappa)^{1/2}R$, where R is the characteristic radius defined above. The uncertainty in the data points due to systematic effects is estimated to be about 0.002 in absolute units for the imaginary component and 0.01 for the real component. The statistical errors in most cases are smaller than this except at the very lowest frequencies where some scatter is observed. The statistical errors for the screens are somewhat larger.

For the rectangular pores, measurements were made for pores of length 1, 2, 3, and 4 in. $F(\lambda)$ was determined from the 1 in. and 3 in. pair, and also the 2-in. and 4-in. pair. This was done to check that the 1-in. pore was long enough for the thermal response in the center to be independent of the ends. For the remaining geometries, only two pore lengths were measured. Except for the screens, the nominal length of pores used were 1 in. and 3 in. For the screens, the short pore contained 1 screen and 2 spacers while the long pore contained 10 screens and 11 spacers.

The results for the circular, rectangular, and coaxial pores are plotted in Fig. 3 along with the theoretical curves. Note that these are not ''fits'' to the experimental data, i.e., there are no free parameters. The experimental measurements agree very well with theory for all three pore geometries. The disagreement at the upper end of the frequency range is due to the finite length of the cell relative to the wavelength of sound. In other words, the deviation observed is the tail of the first standing wave resonance in the tube. This effect does not severely limit the range of validity of the results; in particular, the imaginary component is practically unaffected over most of the range. The reason for this is that the effect of the resonance is most pronounced on the real part of the pressure response. At higher frequencies, the real part of the response contains the dispersive resonant line shape, while the imaginary part contains the resonant peak. Since the tail of resonant peak falls off more quickly $[(\omega-\omega_0)^{-2}]$ than the dispersive part $[(\omega-\omega_0)^{-1}]$, the imaginary part of the low-frequency behavior is less influenced by the resonance.

There is a small systematic overshoot of the dip in the imaginary part of $F(\lambda)$ by about 1.5% which is present for the circular and rectangular pore data.[18] Although this effect could be accounted for by a value of γ 0.6% larger than the one used, it seems unlikely that the literature values for the gas properties are in error by that amount. The cause for this overshoot is still open to conjecture.

The results for the circular and hexagonal pores are particularly interesting in the context of the work relating to the pin-array stack geometry. The theory employed by Swift and Keolian[5] to calculate the response for the pin-array relies on approximating a hexagonal boundary by a circular one enclosing an equal area. Recent experimental measurements by

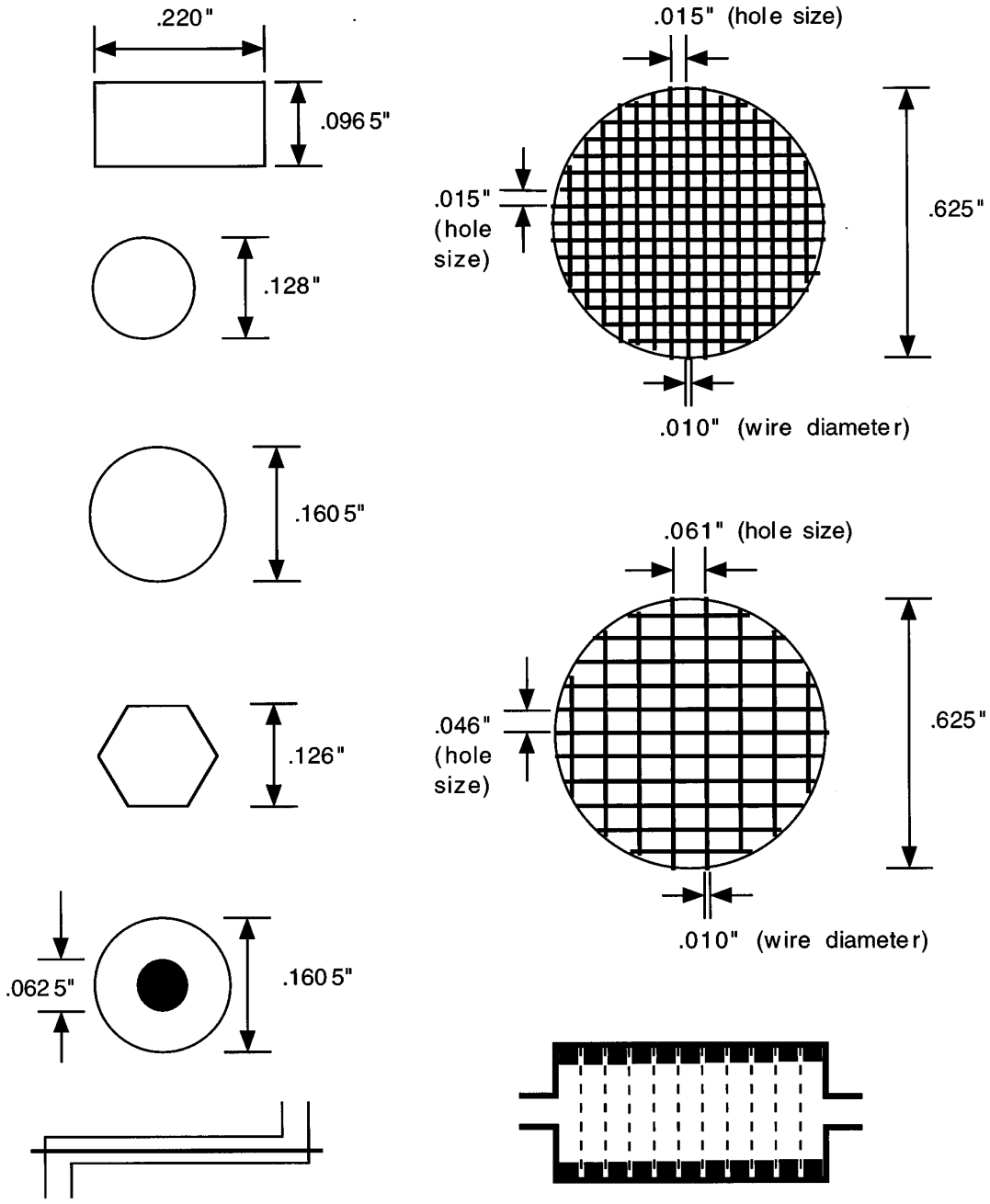

FIG. 2. Geometry and inside dimensions of the pores used in the experiment. All of the pores are made from brass, except for the coarse screens which are copper.

Hayden and Swift have shown that this approximation is well justified for the pin array.[19]

A comparison of the data for circular and hexagonal pores (Fig. 4) shows that these two geometries are almost identical if the experimental data for the hexagon are plotted as a function of $\lambda=(\rho_0\omega c_p/\kappa)^{1/2}r'$, where r' is taken to be the radius of a circle which has an equal area to that of the hexagon. At the higher frequencies, slightly better agreement (not shown) is achieved if the hexagon data are plotted as a function of $\lambda=(\rho_0\omega c_p/\kappa)^{1/2}R$, where R is the characteristic radius. This is to be expected since all geometries should agree at high frequencies (i.e., small thermal penetration depths) when plotted in this fashion.

Note that there is a subtle difference between the comparison discussed here and the pin-array calculation. For the pin array, the hexagonal geometry and the ''circle of equal area'' geometry have the same characteristic radius because the perimeter (due to the pins only) is the same for each.

Closer examination (see inset) reveals that the dip in Im $F(\lambda)$ is 1.5% smaller for the hexagonal pore compared to a circular pore. This is expected qualitatively by considering the theory for triangular, square, and circular pores. The

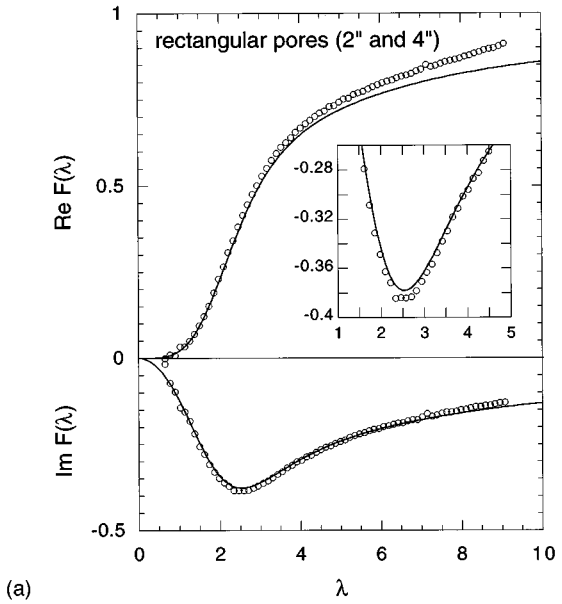

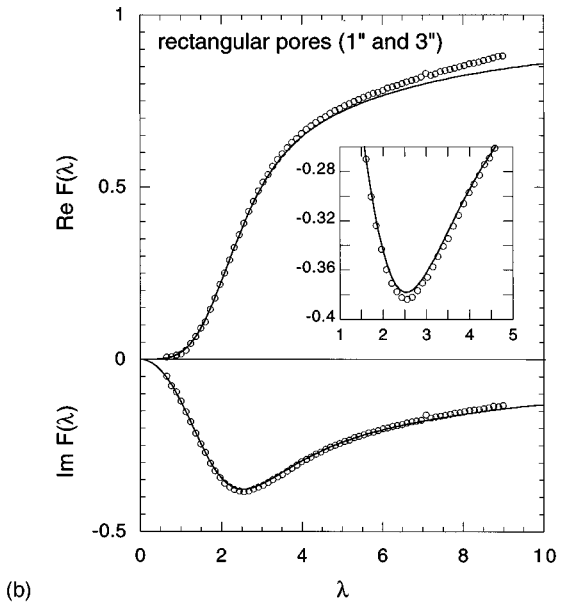

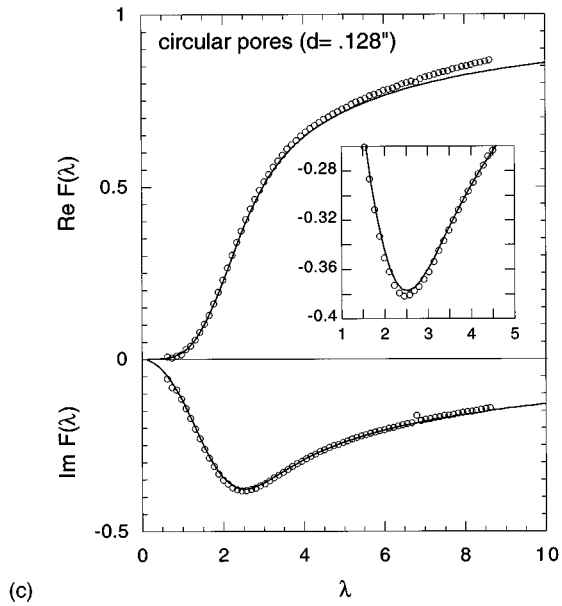

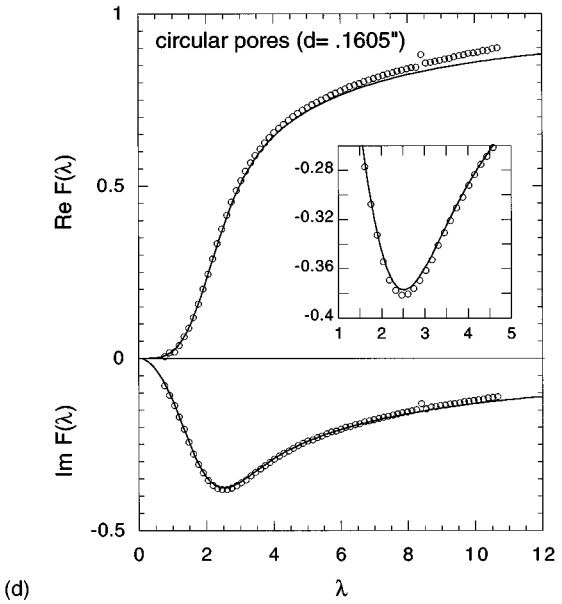

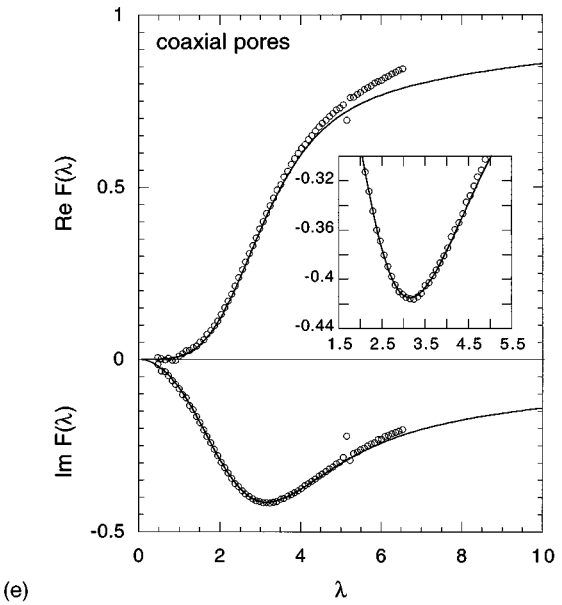

FIG. 3. $F(\lambda)$ vs λ plotted for the results from (a) the 2-in. and 4-in. rectangular pores, (b) the 1-in. and 3-in. rectangular pores, (c) the 0.128-in. diameter circular pores, (d) the 0.1605-in. diameter circular pores, and (e) the coaxial geometry pores. The solid lines are the results of the theory for the appropriate geometry. In all cases the inset shows a close-up of the minimum in Im $F(\lambda)$.

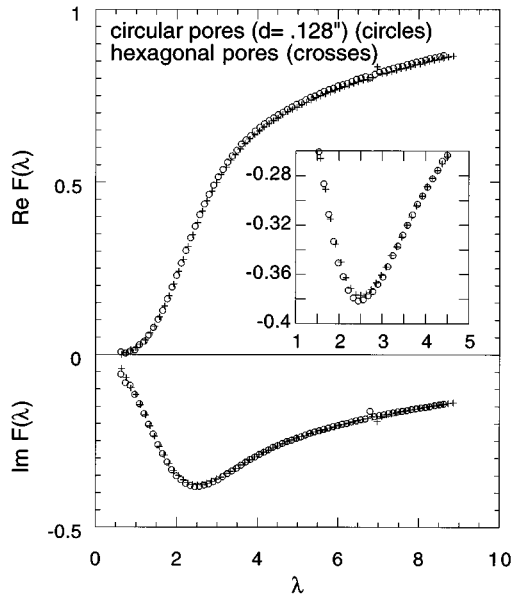

FIG. 4. $F(\lambda)$ vs λ plotted for the hexagonal pore along with the results for the 0.128-in. circular pore. For the hexagonal pore, the data is plotted as a function of $\lambda=(\rho_0\omega c_p/\kappa)^{1/2}r'$, where r' is the radius of a circle which has an area equal to that of the hexagon. The inset shows a close-up of the minimum in Im $F(\lambda)$.

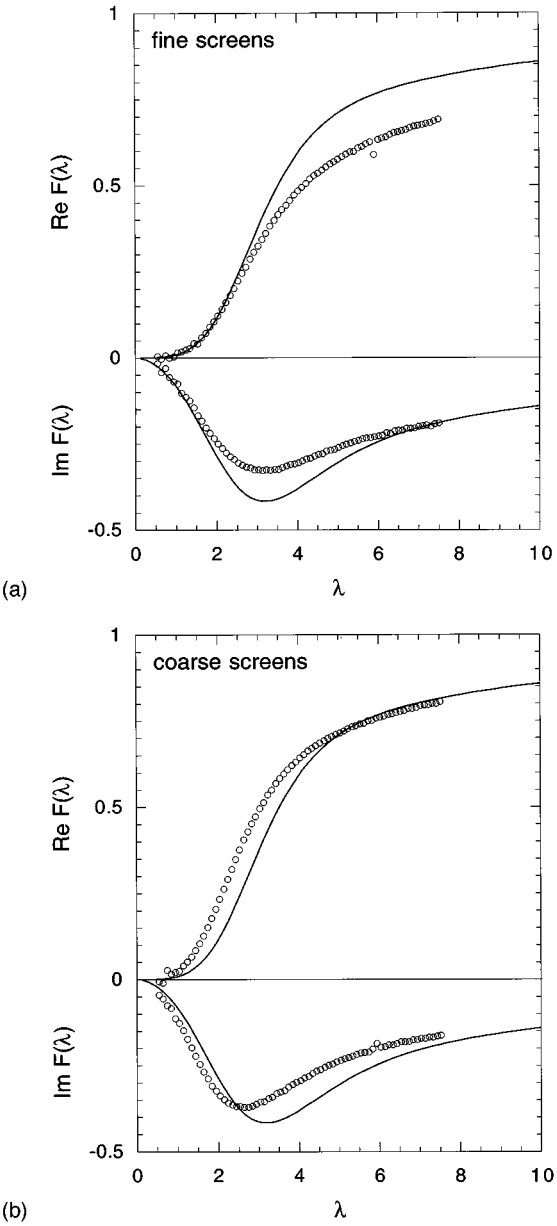

FIG. 5. $F(\lambda)$ vs λ plotted for the results of (a) the fine screens and (b) the coarse screens. In both cases, the data were plotted against $\lambda=(\rho_0\omega c_p/\kappa)^{1/2}d$, where d equals the distance between the screens. The solid curves are the theory for parallel planes.

minimum in Im $F(\lambda)$ increases (in magnitude) with the number of sides of the polygon (with a circle being thought of as having an infinite number). The minimum of Im $F(\lambda)$ for a square is 3% smaller than that of a circular pore. It is reasonable that the hexagon data fall in between the square and the circle.

Although quantitative attempts to model complex geometries similar to screens have been made in the context of porous media theory,[15] only a qualitative description will be given here. The results for the two screen geometries (Fig. 5), plotted as a function of $\lambda=(\rho_0\omega c_p/\kappa)^{1/2}d$, where d equals the distance between the screens, are compared to the theory for parallel plates. For the fine screens, the dip in Im $F(\lambda)$ occurs at a similar value of λ as the theory. Qualitatively, the picture is the following: The region between adjacent screens crosses over from isothermal to adiabatic behavior at the same frequency as that expected for parallel plates. However, the magnitude of the response is smaller because at this frequency the pressure oscillations in the volume between the small screen holes are still isothermal. Only at significantly higher frequencies do the oscillations in these regions cross over to adiabatic. It might be interesting to consider how a thermoacoustic device with a stack having this geometry would operate.

The data for the coarser screens show somewhat different behavior. A given parcel of gas between these screens is farther away from solid boundary (on the average) relative to a similar parcel between the fine screens. Therefore, the crossover from isothermal to adiabatic behavior occurs at a lower frequency. Because the holes in the screens are similar in size to the screen spacing, there is only one length scale for the transition from isothermal to adiabatic behavior. It is reasonable to conjecture that this results in the deeper minimum in Im $F(\lambda)$ seen for the coarse screens relative to the fine ones.

V. CONCLUSIONS

An experimental technique has been demonstrated which provides accurate measurements of the thermoacoustic function $F(\lambda)$ for single uniform pores and other more complicated geometries.

ACKNOWLEDGMENTS

I gratefully acknowledge Pat Arnott for the idea to investigate screens. I would also like to thank the reviewers for many helpful suggestions. This work was supported by Ohio University Research and Sponsored Programs.

[1] N. Rott, ''Damped and thermally driven acoustic oscillations in wide and narrow tubes,'' Z. Angew. Math. Phys. **20**, 230–243 (1969).
[2] W. P. Arnott, H. E. Bass, and R. Raspet, ''General formulation of thermoacoustics for stacks having arbitrarily shaped pore cross sections,'' J. Acoust. Soc. Am. **90**, 3228–3237 (1991).
[3] M. R. Stinson, ''The propagation of plane sound waves in narrow and wide circular tubes, and the generalization to uniform tubes of arbitrary cross-sectional shape,'' J. Acoust. Soc. Am. **89**, 550–558 (1991).
[4] U. A. Müller, US patent 4 625 517 (1986).
[5] G. W. Swift and R. M. Keolian, ''Thermoacoustics in pin-array stacks,'' J. Acoust. Soc. Am. **94**, 941–943 (1993).
[6] L. A. Wilen, ''Measurements of scaling properties for acoustic propagation in a single pore,'' J. Acoust. Soc. Am. **101**, 1388–1397 (1997).
[7] The distance from the cone to detector is 10.0 cm and the focal length of the lens is 2.5 cm.
[8] The result holds as long the thermoacoustic response in the center of the shorter insert is not affected by the ends. This condition is met if the pore length is at least several times the pore's characteristic radius.
[9] *CRC Handbook of Chemistry and Physics*, 75th ed., edited by D. R. Lide (CRC, Boca Raton, FL, 1994), p. 4-123.
[10] Reference 9, p. 6-20.
[11] Reference 9, p. 6-32.
[12] G. W. Swift, ''Thermoacoustic engines,'' J. Acoust. Soc. Am. **84**, 1145–1180 (1988).
[13] C. Zwikker and C. Kosten, *Sound Absorbing Materials* (Elsevier, Amsterdam, 1949).
[14] M. A. Biot, ''Theory of propagation of elastic waves in a fluid-saturated porous solid,'' J. Acoust. Soc. Am. **28**, 168–191 (1956).
[15] K. Attenborough, ''Acoustical characteristics of porous materials,'' Phys. Rep. **82**, 179–227 (1982).
[16] H. S. Roh, W. P. Arnott, J. M. Sabatier, and R. Raspet, ''Measurement and calculation of acoustic propagation constants in arrays of small air-filled rectangular tubes,'' J. Acoust. Soc. Am. **89**, 2617–2624 (1991).
[17] M. R. Stinson and Y. Champoux, ''Propagation of sound and the assignment of shape factors in model porous materials having simple pore geometries,'' J. Acoust. Soc. Am. **91**, 685–695 (1992).
[18] The overshoot is not apparent for the coaxial geometry. However, the geometry for this pore is not as precisely determined as for the other pores. For example, the centering of the inner rod is not perfect and this would cause a slightly shallower dip.
[19] M. E. Hayden and G. W. Swift, ''Thermoacoustic relaxation in a pin array stack,'' J. Acoust. Soc. Am. **102,** 2714–2722 (1997).

Scattering of ultrasonic compression waves by particulate filler in a cured epoxy continuum

Richard E. Challis, Andrew K. Holmes, John S. Tebbutt, and Richard P. Cocker
Ultrasonics and Digital Signal Processing Laboratory, Keele University, Staffs ST5 5BG, United Kingdom

(Received 5 December 1995; revised 30 September 1997; accepted 17 November 1997)

Absorption of ultrasound in adhesive materials is significant in forming ultrasonic signals obtained in nondestructive evaluation (NDE) procedures, and may also have diagnostic value in the evaluation of adhesive materials themselves. This paper investigates the effects of filler particles in adhesive polymers on ultrasonic compression wave absorption and phase velocity dispersion as functions of frequency. Wave propagation is affected by relaxations in the continuous polymer phase as well as by scattering at filler particles. The complex compression wave number for the composite material is derived on the basis of conventional theories of scattering in randomly distributed fields of particles, together with a formulation of the particle diffraction problem based on a combination of the cases for solid particles in solid continua and solid particles in liquid continua first proposed by Ying and Truell, and Allegra and Hawley, respectively. Experiments are described which demonstrate the effects of relaxations and scattering on absorption and phase velocity as functions of frequency in an epoxy material containing a mineral filler. Good agreement is obtained between theory and experiment.
[S0001-4966(98)01203-X]

PACS numbers: 43.38.Ar, 43.35.Cg [SLE]

LIST OF SYMBOLS

ω	frequency, $2\pi f$	μ	shear modulus
h_n, j_n	Heine functions	κ	thermal conductivity
a_c, a_s, a_T	radius of particle multiplied by wave number of compressional, shear, and thermal waves	η	shear viscosity
		b_c	see Eq. (7)
		b_T	see Eq. (8)

(Except in the case of j_n and h_n primes refer to physical quantities of the dispersed phase)

INTRODUCTION

The increasing use of adhesive bonding in safety critical structures brings with it an urgent need for nondestructive evaluation (NDE) of adhered structures and adhesive materials. For many reasons which are beyond the scope of this paper compression wave ultrasound provides a basis for such testing and evaluation. Absorption of ultrasound in adhesive materials is significant in forming the signals obtained in test procedures applied to thick bondlines, and could potentially provide the basis for the evaluation of cured adhesive materials if more was known about the physics of the interactions between ultrasound and the adhesive. In earlier work[1] we presented measurements of wave absorption and phase velocity as functions of frequency for a number of industrial adhesive formulations, and showed how a simple anelastic solid model could be used to approximate compression wave propagation. This model did not take into account the scattering phenomena at filler particles in the adhesives, used for bulking and modification of the engineering properties of the material. It is the purpose of this paper to consider theoretically and experimentally how scattering and other effects at filler particle boundaries in combination with loss mechanisms (relaxations) in the adhesive polymer contribute to the compression wave absorption and phase velocity as functions of frequency in the composite. There are a number of uncertainties in attempting to do this. Adhesives generally consist of a crosslinked polymer phase which may vary in structure from batch to batch of material and with variations in the temperature-time course of the cure cycle. Many different materials can be used as fillers, and filler particle dimensions may vary between 0.5 μm and 20 μm, corresponding approximately to a range of wave number particle dimension products (k_cR) of between 10^{-4} and unity. A given filler material may have a wide distribution of particle sizes within one batch, and the shapes of filler particles can take many forms, examples being; spheres, platelets, and needles, and many less well-defined geometries. In this paper we use an approximate description of filler particles as spheres whose size is identified as their Stokes radius. Due to the complex and variable molecular structure of the base polymer, its internal relaxation mechanisms can take many (unknown) forms and a detailed and generalized formulation of these processes is therefore difficult to achieve. We take a phenomenological approach to their effect on wave propagation and describe the continuous phase by means of measured compression wave absorption and phase velocity dispersion as functions of frequency.

Scattering of ultrasound in particulate mixtures can be formulated theoretically in many different ways. Anson and Chivers[2] have recently reviewed 12 models as predictors of ultrasonic phase velocity in solid-in-solid suspensions, noting that no single model could be identified as generally applicable, and that there was a need for high quality experimental data which would include measurements of absorption as well as phase velocity. Their review included mul-

tiple scattering approaches, self-consistent formulations, and incremental approaches to self-consistency.

Brill and Gaunaurd[3] and Gaunaurd and Wertman[4,5] have proposed formulations in which the scattered far field is expressed as a superposition of resonance and background contributions, taking into account shear and compression waves in the composite material. It is instructive to consider the problem of diffraction at a single particle separately from the formulation of the scattered field from an ensemble of particles randomly distributed in the composite mixture. A number of solutions to the diffraction problem are available: Ying and Truell[6] for a solid particle in a solid continuum, Epstein and Carhart[7] for a liquid particle in a liquid continuum, and Allegra and Hawley[8] for a solid particle in a liquid continuum. The first of these is appropriate for lossless solids in both phases and does not take account of thermal transport between phases. The other two[7,8] do take account of thermal transport between phases, but in their original forms they are restricted to a liquid continuous phase. The Allegra and Hawley formulation is readily adaptable to mixtures with a solid continuous phase, and we have done this in order to examine the significance of thermal transport in solid-in-solid mixtures. Given a solution to the diffraction problem at a single particle, the wave number in particulate mixtures can be obtained in the single scattering case using Foldy,[9] or in the multiple scattering case using an approximation based on concatenated slabs of composite material developed by Waterman and Truell.[10] The concatenated slab assumption is avoided in a later formulation by Lloyd and Berry.[11]

The aim of this work was to establish a computational model that would form the basis for the NDE of filled adhesives, and bonded structures that incorporated them. Of interest was the effect of the filler particle size *distribution* on the ultrasonic properties of the composite material, whether or not thermal transport between phases was significant, and which of the methods of Foldy,[9] Waterman and Truell,[10] or Lloyd and Berry[11] were appropriate to the calculation of the complex wave number in the composite which contained a distribution of particle sizes. In this paper we use a modified form of the Allegra and Hawley[8] model in order to deal with solid particles in a solid continuum, taking account of thermal transport between phases, and to provide comparison with Ying and Truell[6] who do not consider thermal effects. The three solutions for the wave number in the composite are adapted to incorporate arbitrary distributions of particle size by superposition. Experiments are then performed on cured unfilled epoxy adhesive, and then on the same material with various concentrations of a mineral filler added before cure. The complex wave number for compression waves in the unfilled adhesive is used to characterize the continuous phase in the scattering models identified above; these are then used to calculate the expected attenuation and phase velocity dispersion as functions of frequency in the filled adhesive for three filler concentrations. These simulations are then compared to experimental results for a filled adhesive, with good agreement, provided that the distribution of particle sizes is included in the calculation.

I. DIFFRACTION AT A SPHERICAL OBSTACLE

We review briefly three related theories[6–8] and the relationships between them. Allegra and Hawley[8] considered diffraction of an incident compression wave on an isotropic spherical obstacle set in a liquid continuum, and included thermal coupling between dispersed and continuous phases. The incident compression wave was assumed to cause compression, shear, and thermal waves to diffract into the particle, and compression, viscous and thermal waves to be scattered into the liquid continuum. These six wave components were described by summations of partial wave potentials (A_n', C_n', B_n', A_n, C_n, B_n, respectively) which were related to the incident compression wave and to each other through the boundary conditions at the particle boundary; these were continuity of radial stress, radial velocity, tangential stress, tangential velocity, temperature, and heat flux. The partial wave amplitudes could then be obtained from the resulting system of six equations, which can be summarized in matrix form thus:

$$[M]_{AH}\begin{bmatrix} A_n \\ C_n \\ A_n' \\ C_n' \\ B_n \\ B_n' \end{bmatrix} = \begin{bmatrix} a_c j_n'(a_c) \\ j_n(a_c) \\ \eta_s[(a_s^2-2a_c^2)j_n(a_c)-2a_c^2 j_n''(a_c)] \\ \eta_s[a_c j_n'(a_c)-j_n(a_c)] \\ b_c j_n(a_c) \\ \kappa a_c b_c j_n'(a_c) \end{bmatrix}. \tag{1}$$

The matrix $[M]_{AH}$ is given in the Appendix. $A_n B_n C_n$ are the partial amplitudes of the compression, thermal, and shear/viscous waves, respectively, and unprimed symbols apply to the continuous phase while primes refer to the dispersed phase. $j_n(x)$ is the spherical Bessel function of the first kind and $j_n'(x)=(d/dx)j_n(x)$. η_s is the shear viscosity in the continuous phase, a_c and a_s are the compression and shear wave numbers, respectively, multiplied by the particle radius, κ is the thermal conductivity of the continuous phase, and b_c is a function of the material thermal properties.[8]

If the shear modulus in the dispersed phase μ' is interpreted as a viscosity term $\eta_s=-\mu'/i\omega$, it can be shown that a system of equations results which is identical to that derived by Epstein and Carhart[7] for a liquid particle suspended in a liquid continuum. In a similar vein the Allegra and Hawley[8] model can be modified for the case of a solid particle in a solid continuum by interpreting viscosities as shear moduli, $\mu=-i\omega\eta_s$. The thermal effects implicit in the model can be removed by considering only the first four columns and the first four rows in the matrix M_{AH}. If this is done, and the differentiated Hankel and Bessel functions are substituted using the following

$$x^2 H_n''=(n(n-1)-x^2)H_n+2xH_{n+1}$$

and

$$xH_n'=nH_n-xH_{n+1}, \tag{2}$$

then, after some tedious algebra, the reduced 4×4 matrix can be shown to represent an identical system to that which results from the Ying and Truell[6] formulation for a solid sphere suspended in a solid continuum. Thus the modified

Allegra and Hawley model can be used to predict propagation in a solid-in-solid composite with thermal conduction included; with the thermal terms removed it yields results equivalent to Ying and Truell. By running the model in the two cases the significance of thermal effects can be examined with all other aspects of the computation unchanged.

For $n=0$ the second and fourth rows and the second and fourth columns in the matrix $[M]_{AH}$ are not valid; this is the monopole condition for which $[M]_{AH}$ reduces to a 4×4 matrix. For wavelengths large in relation to particle size the coefficients A_n diminish rapidly, and n can generally be restricted to $n=0,1,2$.

II. COMPRESSION WAVE NUMBER IN THE COMPOSITE

The compression wave number in a composite containing a spatially random distribution of isotropic scatterers can be calculated using the formulations cited earlier[9–11] from the following.

$$\left(\frac{\beta}{k_c}\right)^2 = 1+\frac{3\phi}{ik_c^3R^3}(A_0+3A_1+5A_2) - \frac{27\phi^2}{k_c^6R^6}(A_0A_1+5A_1A_2) - \frac{54\phi^2}{k_c^6R^6}\left(A_1^2+\frac{5}{3}A_0A_2+3A_1A_2+\frac{115}{21}A_2^2\right). \quad (3)$$

Here β is the wave number in the composite, and k_c is the wave number of the continuous phase, which is complex in the general case. On the right-hand side the first bracketed term corresponds to Foldy,[9] the first two bracketed terms correspond to Waterman and Truell,[10] while the complete expression corresponds to Lloyd and Berry.[11] For the materials in which we are interested most fillers are not of uniform particle size. We incorporate polydispersity by an approximation that incorporates volume fractions ϕ_j of particles of radius R_j and by assuming that these combine additively in the computation of wave number β. The coefficients A_n are computed for each particle radius R_j, giving A_{nj} as functions of frequency for $n=0,1,2$. With J particle sizes in the distribution Eq. (3) then becomes, for the polydisperse case,

$$\left(\frac{\beta}{k_c}\right)^2 = 1+\sum_{j=1}^{J}\left[\frac{3\phi_j}{ik_c^3R_j^3}(A_{0j}+3A_{1j}+5A_{2j}) - \frac{27\phi_j^2}{k_c^6R_j^6}(A_{0j}A_{1j}+5A_{1j}A_{2j}) - \frac{54\phi_j^2}{k_c^6R_j^6}\left(A_{1j}^2+\frac{5}{3}A_{0j}A_{2j}+3A_{1j}A_{2j}+\frac{115}{21}A_{2j}^2\right)\right]. \quad (4)$$

In practice, particle size distributions are measured and reported as histograms, and R_j is taken as the central radius of the relevant histogram bin.

III. IMPLEMENTATION OF THE ALLEGRA AND HAWLEY MODEL

The complexity of Eq. (1) and related equations has resulted in a number of analytic approximations for specific cases which can be found in the original works[6–8] and more recently in, for example, Gaunaurd and Wertman.[4,5] These are certainly instructive and lead to useful physical insight. However, to support a general interest in particulate mixtures of many different types, and with many different contrasts in physical properties, there is utility in implementing the solution of Eq. (1) in a more general way. This requires some care in dealing with Hankel and Bessel functions of small or large complex arguments, and also in dealing with situations in which the equations are otherwise poorly conditioned. We have implemented the solution of the A_n coefficients in a computer program designed for general application. The model runs with or without thermal terms and in three forms: liquid particles in liquid, solid particles in liquid, and solid particles in solid. The program has been extensively tested by comparing its outputs with analytical approximations published by many workers and by comparison with experimental data obtained by our own and other research groups. We have found generally good agreement between the predictions of our model and data from other sources.[12–14]

Our interest in adhesives implied that losses in both phases be incorporated in relevant wave numbers as frequency dependent compression and shear wave phase velocities and attenuations. For the continuous phase both of these could be measured and used to form the complex wave numbers, thus

$$k_c=\omega/c_c(\omega)+i\alpha_c(\omega) \quad (5)$$

$$k_s=\omega/c_s(\omega)+i\alpha_s(\omega). \quad (6)$$

The model provides for a similar input for the material of the dispersed phase, but in practice, for most of the materials used, only the real parts of k_c and k_s could be estimated on the basis of estimates of density and lossless elastic moduli. In a mineral filler of small k_cR the effect of absorption would be small. By similar reasoning the shear modulus μ for the two phases was either input from known physical data or was estimated from measurements of low-frequency shear wave velocity. The thermal terms b_c and b_T for both phases were estimated, following Allegra and Hawley,[8] thus

$$b_c=\frac{-\gamma}{c_1^2\beta_T}\left[\omega^2-\left(\frac{c_1^2}{\gamma}+\frac{4\mu}{3\rho}\right)k_c^2\right] \quad (7)$$

$$b_T=\frac{-\gamma}{c_1^2\beta_T}\left[\omega^2-\left(\frac{c_1^2}{\gamma}+\frac{4\mu}{3\rho}\right)k_T^2\right], \quad (8)$$

where c_1 is the speed of sound for a spherical compression wave

$$c_1^2=(\lambda+\tfrac{2}{3}\mu)/\rho. \quad (9)$$

k_T is the thermal wave number $(\omega\rho C_p/2\kappa)^{1/2}$, $\gamma=C_p/C_v$ the ratio of specific heats, β_T is the thermal dilation, ρ is density, and μ is the Lamé coefficient. Also input from tables of physical data was the thermal conductivity, κ. Since the wave number of the composite material is a squared term

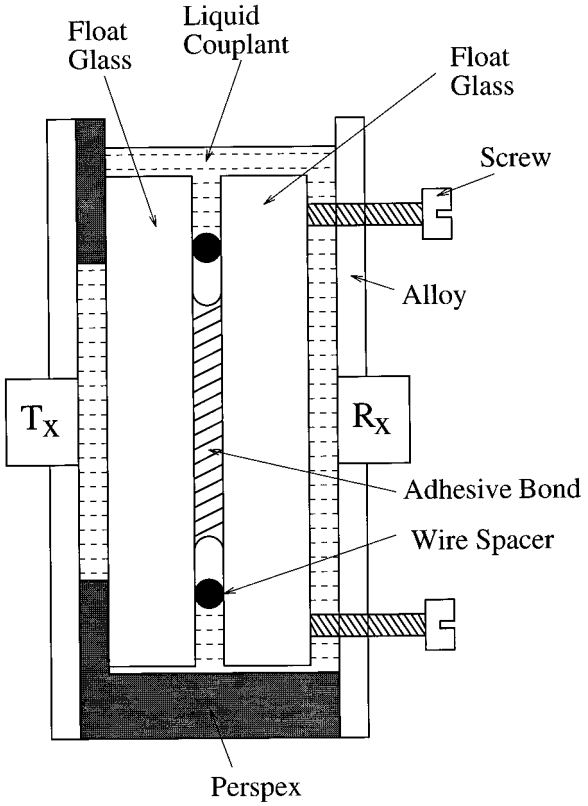

FIG. 1. Test cell with transducers and adhesive bond between float glass blocks.

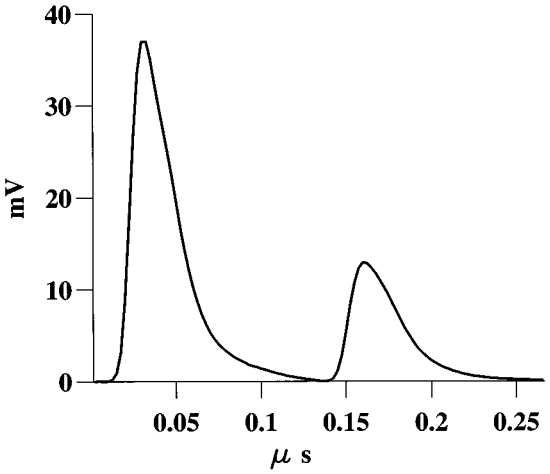

FIG. 2. Two acoustic reverberations in the signal received from the test cell.

in Eq. (3) or (4), it was evaluated from the complex number χ that resulted from the summations of Eq. (3) or (4) using de Moivre's theorem, thus

$$\beta^2 = \chi_R + i\chi_I$$

and

$$\beta = (\chi_R^2 + \chi_I^2)^{1/4} e^{i[(\arctan \chi_I/\chi_R)/2]}. \tag{10}$$

The output of the computer program was arranged to provide the absorption coefficient multiplied by wavelength $\alpha\lambda$ and phase velocity dispersion, as functions of frequency which matched our measurement range up to 70 MHz. Phase velocity dispersion was calculated as the difference between measured phase velocity at frequency f, $c(f)$, minus the phase velocity at our lower limit of measurement, which lay between 2 MHz and 15 MHz depending on experimental conditions. The nondimensional frequency scale, k_cR is also available, but only applicable to mixtures which contain particles of a single size, or which can be approximated as such.

IV. EXPERIMENTS

A. Measurement method

The basis of our technique to measure compression wave absorption and phase velocity as functions of frequency has been reported elsewhere[1] so will only be summarized briefly here. A thin adhesive layer is formed between two float glass blocks separated by cylindrical wire spacers of known diameter (Fig. 1). The external edge of the adhesive is sealed with a silicone elastomer material. This assembly is immersed in a thin water filled cell with cylinders of piezoelectric material (PZT4) fixed coaxially on its outside surface, the test bond being held perpendicular to the transducers' common axis in its two planes. The piezoelectric elements operate as thickness drive devices, one acting as transmitter and the other as receiver. The thickness of the devices (5 mm) is such that their internal acoustic reverberation time is greater than two pulse reverberation times in the adhesive layer. The transmitting device is excited by a high voltage (200 V) short pulse of duration 5 ns with rise and fall times of 2 ns. A near replica of this pulse propagates through the adhesive to the receiving transducer. The signal at the receiver is followed by later reverberations in both transducers and the glass blocks, which are all discarded in subsequent processing. The signal at the receiver terminals is amplified by a low noise linear phase amplifier with a gain of 40 dB over a 150-MHz bandwidth. Its output is digitized by a digital storage oscilloscope (LeCroy 9450) and passed to a computer network via an IEEE 488 (GPIB) interface. The part of the signal that includes reverberations within the adhesive bond is windowed out and preprocessed by digital filters to correct for baseline shift that results from piezoelectric regeneration (associated with $-C_0$ in the Mason[15] model) and radiation coupling between the transducers.[16] The resulting signal consists of two separately resolvable monopolar pulses (Fig. 2). The first of these has made a single transit across the bond while the second has made three transits, being the first reverberation component. These two pulses are windowed out and compared in the frequency domain by means of a fast Fourier transform (FFT). The ratio of the FFT moduli of the two pulses, combined with a knowledge of the adhesive thickness, yields the absorption coefficient, while comparison of the two FFT phase spectra yields phase velocity, both as functions of frequency. These two functions together give $\alpha\lambda$. Shear wave absorption and velocity is measured in thin slabs of free standing adhesive using a related technique[17] based on a goniometer stage where shear waves are generated in the adhesive by mode conversion from compression waves incident at a nonperpendicular angle on the thin slab. Details of this method will be

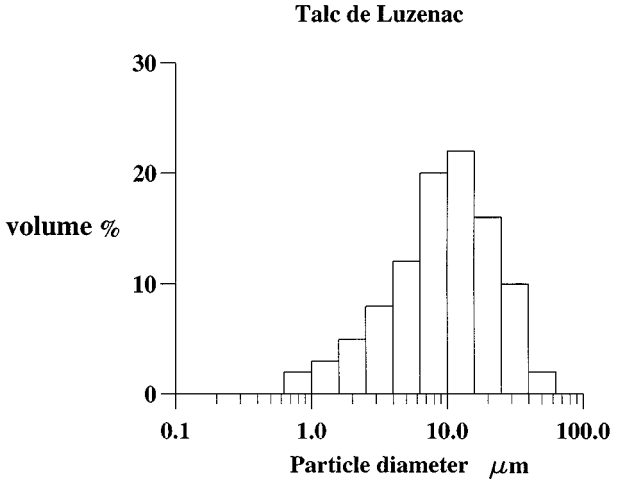

FIG. 3. Particle size distribution of the talc filler used in the experiments.

reported elsewhere. The experimental techniques, when applied to repeated measurements on the same sample, give a repeatability of better than 1% for both attenuation and propagation velocity. It is very difficult to establish their accuracy and precision in an absolute sense, although where comparison has been possible we have found agreement with other workers in the order of $\pm 2\%$ for attenuation coefficient and $\pm 1\ \mathrm{m\cdot s^{-1}}$ for *changes* in phase velocity with frequency in relation to a low frequency phase velocity value. However, due to a compromise between the need for rapid measurements on a series of samples and a requirement for precise temperature control, the values of absolute propagation velocity are likely to be in error by $\pm 5\ \mathrm{m\cdot s^{-1}}$.

B. Sample materials and preparation

The adhesive used was an epoxy resin in combination with a phenolic hardener (AY105 and HY2958, Ciba Geigy Ltd, UK). The filler used was talc (SiO_2–MgO–Al_2O_3) which had platelet shaped particles, and the particle size distribution shown on Fig. 3 which gives the Stokes diameters obtained from a sedimentation test. The physical properties of the filler particles and the continuous phase used for the theoretical computations are given in Table I. The volume

TABLE I. Physical properties of the particles and continuous phase used in the theoretical computations.

Property	Units	Epoxy	Talc de Luzenac
Velocity	$\mathrm{m\cdot s^{-1}}$	experimental[a]	5900[c]
Density	$\mathrm{kg\cdot m^{-3}}$	1190	2780
Shear rigidity	$\mathrm{kg\cdot m^{-1}\cdot s^{-2}}$	1.71×10^{9}	4.08×10^{10}[c]
Thermal conductivity	$\mathrm{W\cdot m^{-1}\cdot K^{-1}}$	2.102	10.46[c]
Volume expansion coefficient	$\mathrm{K^{-1}}$	2.03×10^{-4}	2.1×10^{-5}[c]
Specific heat	$\mathrm{J\cdot kg^{-1}\cdot K^{-1}}$	0.22	0.18[c]
$\alpha\cdot f^{-2}$	$\mathrm{Np\cdot s^{2}\cdot m^{-1}}$	experimental[b]	1.0×10^{-15}[c]

[a]Phase velocity $2640\ \mathrm{m\cdot s^{-1}}$ at 15 MHz rising to $2675\ \mathrm{m\cdot s^{-1}}$ at 65 MHz.
[b]Absorption in the continuous phase is plotted in Fig. 4 (as $\alpha\lambda$).
[c]Literature value unavailable. Value for glass substituted.

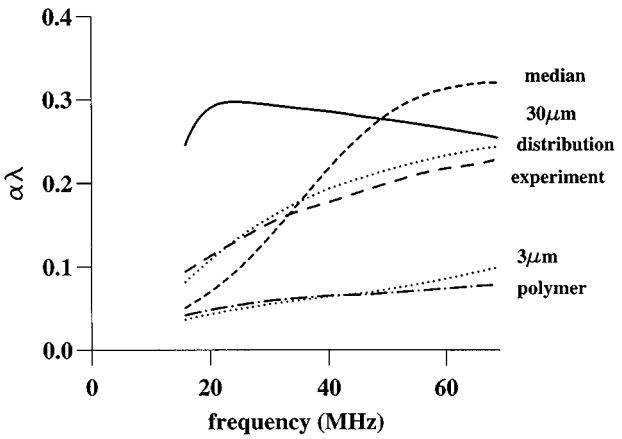

FIG. 4. Measured $\alpha\lambda$ versus frequency for the unfilled adhesive (marked polymer), and for the adhesive filled to 10% v/v with polydisperse talc particles (marked experiment). Also shown are calculations using the modified Allegra and Hawley model for the experimental distribution of particle size and for 10% volume fraction of particles of diameters 3 μm, 10 μm (distribution median), and 30 μm.

fractions of filler in the test bonds were 0%, 5%, 10%, and 15%. For the preparation of unfilled bonds the adhesive was mixed with hardener under vacuum for 10 min before forming the adhesive test layer. For the filled bonds the epoxy and filler were mixed together under vacuum for 10 min; the hardener was then added and mixing continued for a further 10 min. The bonds proper were formed between float glass blocks to a thickness of 170 μm, set with cylindrical wire spacers. They were cured for 2 h at 20 °C; during cure the bonded glass blocks were laid flat with their long dimensions horizontal and were inverted at intervals of 5 min to reduce the tendency of the fillers to sediment downward.

C. Results

Figure 4 shows compression wave absorption $\alpha\lambda$ versus frequency as measured for the unfilled cured adhesive (marked ''polymer''), and for the adhesive filled to 10% by volume with talc filler whose particle size distribution is given in Fig. 3. The Allegra and Hawley model adapted for solid particles in solid continua but including the thermal terms and with $n=0,1,2$ was used together with the first two bracketed terms in Eq. (3) or (4) (Waterman and Truell[10]) to give the predicted absorption for four cases in order to assess the effect of particle size and its distribution; these were a 10% volume fraction of particles of 3 μm diameter, a 10% volume fraction of particles of 30 μm diameter, a 10% volume fraction of particles of 10 μm diameter (the median particle size in the distribution), and finally a calculation based on Eq. (4) taking account of all size bins of Fig. 3. The necessity of including the particle size distribution in the calculation is clear.

Figure 5 shows a further comparison between the experimental data for the talc-filled adhesive with the output of the Allegra and Hawley model as run for Fig. 4 with the size distribution included, and as run with the thermal terms removed so as to correspond with the formulation of Ying and Truell,[6] also with the size distribution included. It is clear that for the higher frequencies (and higher k_cR values), the

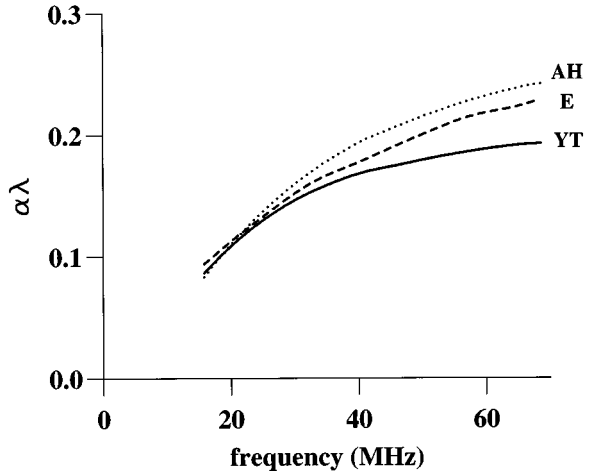

FIG. 5. The experimental result of Fig. 4 for the filled polymer (E) compared to calculations based on the modified Allegra and Hawley model with (AH) and without (YT, Ying and Truell case) thermal terms.

thermal terms implicit in the Allegra and Hawley model provide a small but significant contribution to absorption in the composite material.

In Fig. 6 the modified Allegra and Hawley model has been used to calculate absorption for a 10% volume fraction of talc at the median particle size (10 μm), using the first two bracketed terms of Eq. (3) for the wave number (Waterman and Truell case), but with the summations based on A_0 alone, A_0 and A_1, and A_0, A_1 and A_2. Also shown is the calculation for A_0 alone, with thermal terms removed (Ying and Truell case). It is clear that for the material particle sizes and frequencies in question the dominant term is A_1, but that significant contributions arise from A_0 and A_2. At frequencies above 20 MHz the thermal contribution to A_0 becomes significant.

Figure 7 compares the same experimental data as before to calculations using the Allegra and Hawley model, again applied to the whole size distribution, with the composite compression wave number calculated on the basis of A_0,

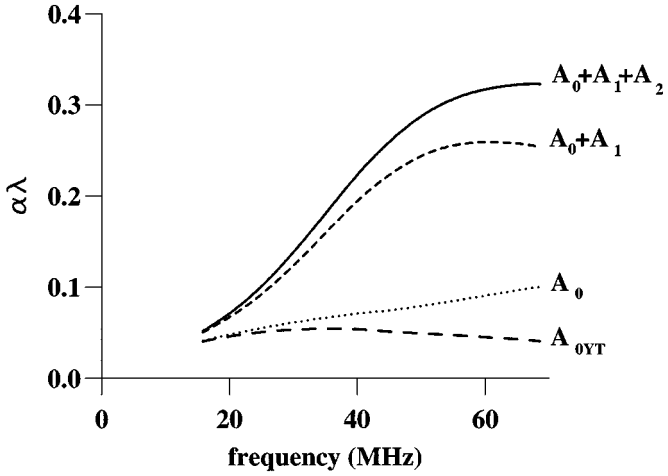

FIG. 6. Calculations of $\alpha\lambda$ for the median particle diameter (10 μm) based on the Allegra and Hawley model showing the contributions from A_0, A_0+A_1, and $A_0+A_1+A_2$. For comparison the contribution of A_0 calculated without thermal terms is included, A_{0YT}.

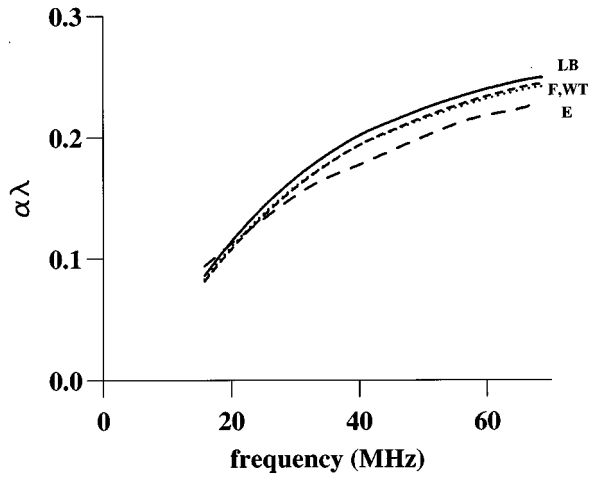

FIG. 7. Experimental data of Fig. 4 for the talc filled epoxy (E) compared to the Allegra and Hawley calculation with three calculations of the composite wave number, Eq. (4), marked F (Foldy), WT (Waterman and Truell), and LB (Lloyd and Berry).

A_1, and A_2, for the three cases in Eq. (4): the first bracketed term only (Foldy[9]), the first two bracketed terms (Waterman and Truell[10]), and the full expression (Lloyd and Berry[11]). All three calculations give closely similar results and match experimental measurements of absorption to within 8% or so at the highest frequency.

Figure 8 shows the effect of talc filler concentration at 40 MHz on absorption as measured experimentally, and as calculated from the modified Allegra and Hawley model using the Waterman and Truell case in Eq. (4). The theory predicts a near-linear increase with concentration above the value for adhesive alone, which is matched to within 10% by the experimental data.

The change in compression wave phase velocity with frequency calculated using the modified Allegra and Hawley model for the whole particle size distribution, including A_0, A_1, and A_2, but with the wave number evaluated according to the three cases in Eq. (4), is compared to experiment in Fig. 9. At low frequencies all three calculations are in close

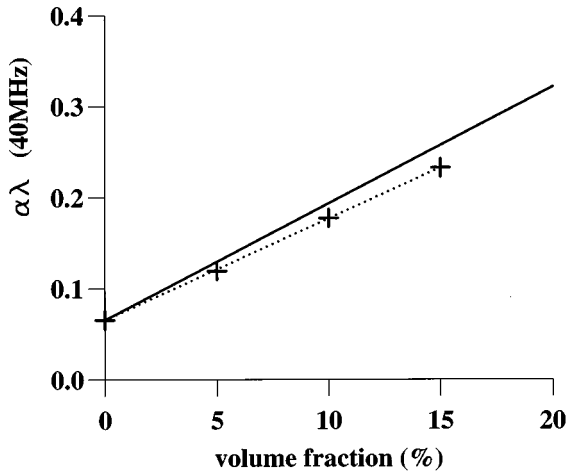

FIG. 8. $\alpha\lambda$ at 40 MHz for the talc-filled epoxy versus filler concentration (v/v): solid line, Allegra and Hawley calculation; crosses, experiment.

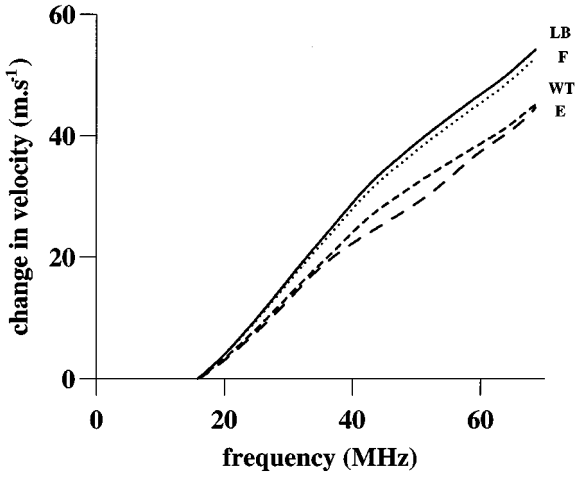

FIG. 9. Change in phase velocity for the talc filled epoxy (10% v/v): experiment compared to three calculations of wave number, Eq. (4), marked as in Fig. 7.

agreement with the experimental data, but as frequency increases agreement is most closely maintained with the Waterman and Truell simulation.

V. DISCUSSION

The range of frequencies and particle sizes in the talc-filled samples gave $0.018<k_cR<4.4$, a little over two orders of magnitude; this range of k_cR, while being relatively restricted, represents a realistic filled epoxy material and a range of frequencies appropriate to its testing. The absorption spectra in Fig. 6 include absorption in the epoxy continuous phase but show the contributions from A_0, A_1, and A_2, with the contribution of A_1 dominating, with a maximum around 60 MHz, corresponding to $k_cR=0.94$, close to unity. $\alpha\lambda$ can be approximated from the first line of Eq. (3), thus

$$\alpha\lambda=-\frac{3\pi\phi}{k_c^3R^3}\,\mathrm{Re}[A_0+3A_1+5A_2]. \tag{11}$$

The real parts of A_n corresponding to the data in Fig. 6 were $0.016(n=0)$, $0.05(n=1)$, and $0.01(n=2)$. These are close to the values calculated by Gaunaurd and Wertman[4] for glass spheres in epoxy. Their data indicated an expected large monopole $(n=0)$ resonance at around $k_cR=3$, after the first dipole resonance at around $k_cR=1$. Higher order resonances were expected at values of k_cR greater than those found for the monopole resonance. In the low k_cR range, below unity, the dipole term was expected to dominate, as we have found here. The peak at around 22 MHz for the simulation of 30-μm-diameter particles in Fig. 4 gives similar confirmation of Gaunaurd and Wertman's results.

Given our interest in NDE of cured filled adhesives and adhered structures, the most significant finding of this work is the necessity to include the distribution of particle sizes in simulations of wave propagation in filled materials, and the data in Fig. 4 show this clearly. If the median particle size is taken, then absorption is likely to be overestimated in some spectral regions and underestimated in others. The simulation, which includes the particle size distribution, matches experiment closely for these relatively low k_cR values, the divergence between theory and experiment being around 8% at 40 MHz. The single particle size data in Fig. 4 (30 μm, 3μm, and median), being significantly different from the data for the whole size distribution, indicate that simulations and measurements such as these would provide a basis for the detection of agglomeration of filler materials in adhesives.

We now consider the effect of thermal coupling between phases. The two computed curves in Fig. 5 give our modified Allegra and Hawley simulation, which includes thermal conduction between phases, and a calculation equivalent to the Ying and Truell model[6] which does not include thermal effects. Thermal wavelength is given by

$$\lambda_T=2\pi\left(\frac{2\kappa}{\omega\rho C_p}\right)^{1/2}, \tag{12}$$

which at 20 MHz gives values of 220 μm and 88 μm in epoxy and talc, respectively, both significantly greater than the Stokes particle diameters of the majority of the filler particles. We would thus expect the whole of the particle volume rather than superficial layers to contribute to this loss mechanism, and also the contribution to attenuation to be a rising function of frequency over the range of frequencies considered here.[8] This is borne out by the computations shown in Fig. 6 which show the contributions of A_0, A_1, and A_2 at the median particle size, together with a curve indicating the contribution of A_0 with the thermal terms removed (Ying and Truell case[6]). The divergence between the two computations of A_0 is clear, and in the nonthermal case the A_0 contribution falls with frequency above 30 MHz. Given that all of the computations include the absorption in the continuous phase (see Fig. 4), this is not unexpected since a significant fraction of the relatively lossy epoxy has been replaced by talc, which we have assumed to be almost lossless in the model.

Our results for change in compression wave phase velocity with frequency (Fig. 9) indicate that the Waterman and Truell approach to phase velocity calculation [first two bracketed terms of Eq. (3)] gives the best prediction of our experimental data for the distribution of particle sizes. This confirms earlier expectation and indeed observations by others workers[5] considering monodisperse systems. The other two calculations give results which are similar to each other and which are within 15% of experimental observations.

At the relatively low concentrations considered in this work the modified Allegra and Hawley model predicts a near-linear dependence of absorption with concentration of particulate material as would be expected from Eq. (3) for $\phi\ll1$, small k_cR and correspondingly small values for A_0, A_1, and A_2. The data in Fig. 8 show a similar linear dependence in the experimental results, but with a slope that differs by about 10% from theoretical expectation. While errors of 2% or so could be accounted for by experimental uncertainty, the physical basis for the remaining error is not at present understood. Strong possibilities are the nonspherical nature of the talc particles, and some agglomeration and sedimentation of filler particles during sample preparation.

VI. CONCLUSION

The motivation for this work was to establish a computational model for ultrasonic compression wave propagation in filled adhesives which could be used to support NDE of adhesive materials and adhered structures. The model was required to function in the tens of the MHz frequency range and to be applicable to polydisperse fillers with particle sizes ranging from a few μm to tens of μm. A primary consideration was whether an adequate prediction of wave absorption and/or phase velocity could be based on a single particle size, such as the median, to represent the whole distribution. It is clear that this approach does not work and that the whole size distribution must be taken into account, in which case good correlation with experimental data is possible.

The Allegra and Hawley[8] model has been adapted for solid inclusions in solid continua, and in its complete form includes the effects of thermal conduction between phases. A simplified version did not include these effects and could be shown to be exactly equivalent to the Ying and Truell[6] formulation. Thus it was possible to compare simulations which either included or did not include thermal conduction in the monopole term (A_0). It was found that the complete model, which included thermal conduction, gave a better correlation with our experimental data, although the difference between the two models was small, due to the fact that the dominant phenomena were represented by the dipole term A_1, which was identical for both models. This was expected due to the significant density contrast between phases ($\rho'/\rho = 2.44$ for talc and epoxy), although this would not be true for polymer inclusions in a polymer continuum. Three approaches of computation of the wave number have been compared; all three gave equivalent results for absorption, but the Waterman and Truell approach gave the best simulation of phase velocity.

ACKNOWLEDGMENT

We are grateful to Bill Rolfe of CIBA Polymers, Duxford, UK, for advice and assistance in sample preparation.

APPENDIX: THE MATRIX $[M]_{AH}$ FOR THE ALLEGRA AND HAWAWLEY[8] FORMULATION

$$
[M]_{AH} \equiv \begin{bmatrix}
a_c h_n'(a_c) & -n(n+1)h_n(a_s) & i\omega\alpha_c' j_n'(a_c') & -i\omega n(n+1) j_n(a_s') & a_T h_n'(a_T) & i\omega a_T' j_n'(a_T') \\
h_n(a_c) & -[h_n(a_s)+a_s h_n'(a_s)] & i\omega j_n(a_c') & -i\omega[j_n(a_s')+a_s' j_n'(a_s')] & h_n(a_T) & i\omega j_n(a_T') \\
\mu[(a_s^2-2a_c^2)h_n(a_c) & \mu 2n(n+1)[a_s h_n'(a_s) & i\omega\mu'[(a_s'^2-2a_c'^2) & i\omega 2\mu' n(n+1) & \mu[(a_s^2-2a_T^2)h_n(a_T) & i\omega\mu'[(a_s'^2-2a_T'^2) j_n(a_T') \\
-2a_c^2 h_n''(a_c)] & -h_n(a_s)] & \times j_n(a_c')-2a_c'^2 j_n''(a_c')] & \times[a_s' j_n'(a_s')-j_n(a_s')] & -2a_T^2 h_n''(a_T)] & -2a_T'^2 j_n''(a_T')] \\
\mu[a_c h_n'(a_c) & (-\mu/2)[a_s^2 h_n''(a_s) & i\omega\mu'[a_c' j_n'(a_c') & -i\omega(\mu'/2)[a_s'^2 j_n''(a_s') & \mu[a_T h_n'(a_T) & i\omega\mu'[a_T' j_n'(a_T')-j_n(a_T')] \\
-h_n(a_c)] & +(n^2+n-2)h_n(a_s)] & -j_n(a_c')] & -(n^2+n-2) j_n(a_s')] & -h_n(a_T)] & \\
b_c h_n(a_c) & 0 & i\omega b_c' j_n(a_c') & 0 & b_T h_n(a_T) & i\omega b_T' j_n(a_T') \\
\kappa a_c b_c h_n'(a_c) & 0 & i\omega\kappa' a_c' b_c' j_n'(a_c') & 0 & \kappa b_T a_T h_n'(a_T) & i\omega\kappa' b_T' a_T' j_n'(a_T')
\end{bmatrix}.
$$

[1] R. F. Challis, T. Alper, A. K. Holmes, and R. P. Cocker, ''Near-plane-wave acoustic propagation measurements in thin layers of adhesive polymer,'' Meas. Sci. Technol. **2**, 59–68 (1991).

[2] L. W. Anson and R. C. Chivers, ''Ultrasonic velocity in suspensions of solids in solids—A comparison of theory and experiment,'' J. Phys. D: Appl. Phys. **26**, 1566–1575 (1993).

[3] D. Brill and G. Gaunaurd, ''Resonance theory of elastic wave ultrasonically scattered from an elastic sphere,'' J. Acoust. Soc. Am. **81**, 1–21 (1987).

[4] G. C. Gaunaurd and W. H. Wertman, ''Resonance scattering of elastic waves by an elastic inclusion in an elastic matrix: Numerical calculations,'' IEEE Trans. Ultrason. Ferroelectr. Freq. Control **35**, 628–636 (1988).

[5] G. C. Gaunaurd and W. Wertman, ''Comparison of effective medium theories for inhomogeneous continua,'' J. Acoust. Soc. Am. **85**, 541–554 (1989).

[6] C. F. Ying and R. Truell, ''Scattering of a plane longitudinal wave by a spherical obstacle in an isotropically elastic solid,'' J. Appl. Phys. **27**, 1086–1097 (1956).

[7] P. S. Epstein and R. R. Carhart, ''The absorption of sound in suspensions and emulsions: I. Water fog in air,'' J. Acoust. Soc. Am. **25**, 553–565 (1953).

[8] J. R. Allegra and S. A. Hawley, ''Attenuation of sound in suspensions and emulsions: Theory and experiments,'' J. Acoust. Soc. Am. **51**, 1545–1564 (1972).

[9] L. L. Foldy, ''The multiple scattering of waves,'' Phys. Rev. **67**, 107–119 (1945).

[10] P. C. Waterman and R. Truell, ''Multiple scattering of waves,'' J. Math. Phys. **2**, 512–537 (1961).

[11] P. Lloyd and M. V. Berry, ''Wave propagation through an assembly of spheres. IV. Relations between different multiple scattering theories,'' Proc. Phys. Soc. London **91**, 678–688 (1967).

[12] J. S. Tebbutt, Ph.D. Thesis, Keele University, UK, 1996.

[13] A. K. Holmes, R. E. Challis, and D. J. Wedlock, ''A wide-bandwidth ultrasonic study of suspensions: the variation of velocity and attenuation with particle size,'' J. Colloid Interface Sci. **168**, 339–348 (1994).

[14] J. S. Tebbutt and R. E. Challis, ''Ultrasonic wave propagation in colloidal suspensions and emulsions: A comparison of four models,'' Ultrasonics **34**, 363–368 (1996).

[15] D. A. Berlincourt, D. R. Curran, and H. Jaffe, in *Physical Acoustics*, Vol. 1A, edited by W. P. Mason (Academic, New York, 1964).

[16] J. A. Harrison, G. N. Cook-Martin, and R. E. Challis, ''Radiation coupling between two coaxial disks of different diameter: An exact solution and detailed experimental verification,'' J. Acoust. Soc. Am. **76**, 1009–1022 (1984).

[17] R. J. Freemantle, T. Alper, and R. E. Challis, ''A model fitting approach to the broad band measurement of ultrasonic wave velocities in thin samples of engineering material,'' Meas. Sci. Technol. **4**, 1129–1137 (1993).

Electromechanical response of polymer films by laser Doppler vibrometry

François M. Guillot and Jacek Jarzynski
School of Mechanical Engineering, Georgia Institute of Technology, Atlanta, Georgia 30332-0405

Edward Balizer
Naval Surface Warfare Center, Silver Spring, Maryland 20903

(Received 3 October 1996; accepted for publication 17 November 1997)

A two-sided laser Doppler vibrometer (LDV) was designed to measure the d_{33} electromechanical coupling coefficient of piezoelectric and electrostrictive thin films. Optical fibers and optical fiber couplers were used to split the light into multiple beams and to simultaneously illuminate the same spot on both sides of the film. This probe measured the normal displacement on each side of the sample and allowed computation of the change in thickness by summing the two LDV signals. Data for PVDF films are presented to illustrate problems associated with this type of measurement. A large bending motion of the sample occurred which was responsible for a significant error in the measured thickness change. Reducing the amplitude of this motion by stacking films was an efficient way to increase the accuracy of the data. An error analysis was carried out to qualitatively explain these experimental observations. It was also discovered that the measurement accuracy improved when the ac driving voltage frequency was less than the bending resonance frequency of the sample. © *1998 Acoustical Society of America.* [S0001-4966(98)01303-4]

PACS numbers: 43.38.Ar, 43.38.Fx [SLE]

INTRODUCTION

In the past few years, the topic of electromechanical polymers has received a lot of attention because of their attractive features for transducer applications (low density, low modulus, low cost). Polyvinylidene fluoride (PVDF) is the best-known piezoelectric polymer and is widely used in the construction of acoustic devices. Its dielectric, piezoelectric, and elastic properties have been investigated for the past 20 years and their measured values are summarized by Wang.[1] Other polymers such as polyurethanes are currently being investigated, for which a very large electrostrictive response has been reported;[2,3] these materials have a high potential for use as acoustic projectors and sensors. The origins of the mechanism responsible for this large electrostriction are not yet understood. Thus, accurate measurements of the electrostrictive effect in these polyurethanes are necessary for a better understanding of its underlying mechanism. The piezoelectric or electrostrictive response of a thin film can be determined by measuring the amplitude of the thickness change when an ac voltage is applied to the film; the d_{33} piezoelectric or electrostrictive electromechanical coupling coefficient can then be computed by taking the ratio of the vibration amplitude to the voltage amplitude. Such measurements can be performed optically.

Optical techniques of measuring displacements have lead to a very flourishing research area in the past several years, and a large number of methods involving lasers as sources of coherent light have been developed. Among these methods, laser Doppler interferometry techniques[4] have been emphasized for several reasons: they are accurate for measurements of displacements associated with acoustic waves and have both a broad dynamic range (from a few tenths of a nanometer to several hundred nanometers) and frequency range (from $\sim$100 Hz to several MHz). Most importantly, they provide a noncontact method of measurement. In consequence of these facts, it appears that such a system is very suitable to study the piezoelectric and electrostrictive response of thin polymer films.

This paper presents the design of an optical probe to perform such experiments. This probe was initially tested by measuring the response of PVDF films and the feasibility of the method was established. However, some accuracy issues were encountered during these measurements, and we present and discuss here these problems which are relevant to electromechanical thin film studies. Only PVDF results are presented in this paper as a foundation for the study of the electrostrictive polyurethane materials. The system described below differs from previous optical interferometers used for measurements on polymer films.[3,5] The main difference is the dual beam design of the present system which allows independent, simultaneous measurement of surface motion on both sides of the film. Such measurements provide a complete description of the displacement of the film, since both the thickness motion and the bending motion can be determined. This paper is divided into three sections: first, the optical system is presented and compared with previous interferometers in Sec. I; Sec. II then deals with PVDF measurements and focuses on sample mounting procedures as well as experimental errors; and finally, conclusions are drawn in Sec. III.

I. DESCRIPTION OF THE OPTICAL SYSTEM

The optical system designed for the displacement measurements is a laser Doppler vibrometer (LDV) based on the theory of heterodyne interferometry, and is depicted in Fig. 1. It is a two-beam system capable of measuring normal

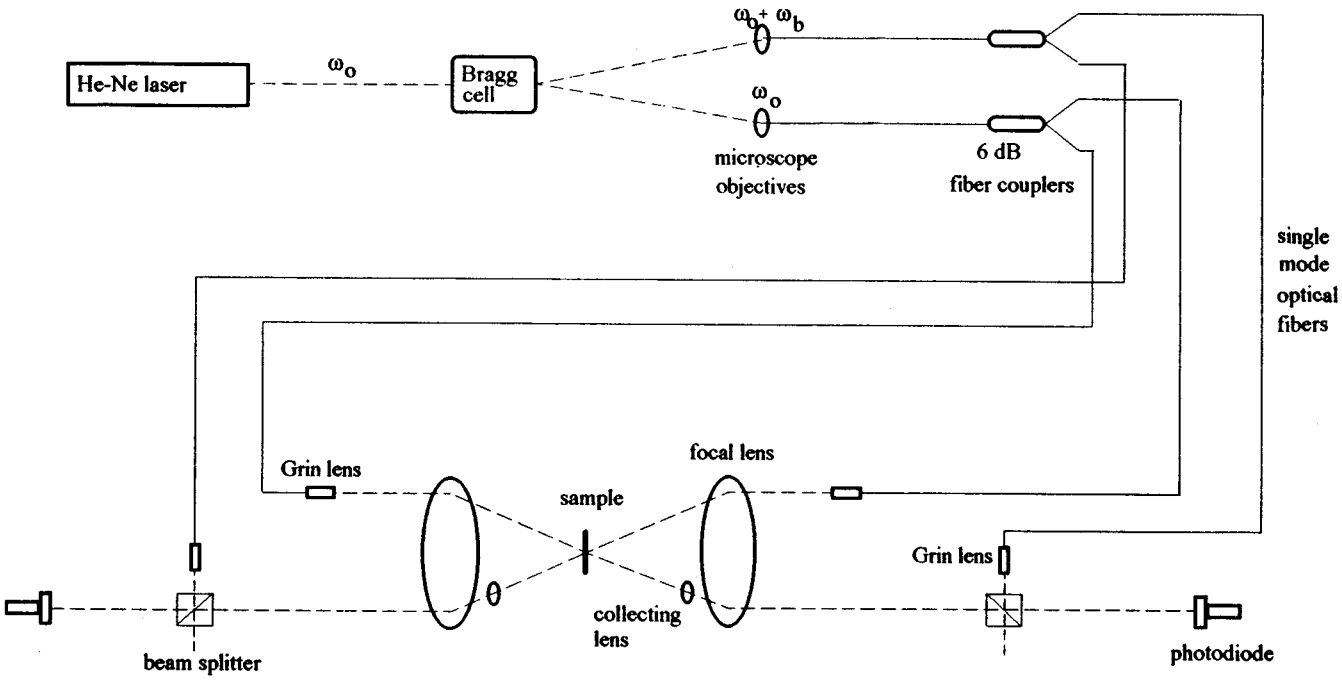

FIG. 1. Two-sided optical probe for out-of-plane displacements detection. The solid lines represent optical fibers and the dashed lines are laser beams in air.

(out-of-plane) surface displacements simultaneously on opposite sides of a thin piezoelectric film. A description of its components and working principle is given in complete detail in Ref. 6 and is outlined as follows. The source is a 10-mW helium neon laser which emits red light ($\lambda = 633$ nm) that is split into two beams (the ''reference'' and ''object'' beams) by an acousto-optic Bragg cell[7] operating at 40 MHz. Each output beam is coupled inside optical fibers using $\times 20$ microscope objectives. Single-mode optical fibers (core diameter: 4 μm) are used to facilitate the manipulation of the system. Each fiber is split into two fibers, each carrying an equal amount of light by using 6-dB fiber couplers. The system is divided into two identical sides consisting of both a reference and an object beam. The other end of the fibers is terminated by a quarter-pitch gradient index (GRIN) lens for collimating the light beam exiting the fibers. The object beam GRIN lens is positioned in front of a large aperture (127 mm diameter) converging lens (achromatic doublet) that focuses the light on the film surface from which it is reflected back through the lens. The focal distance of the lens is 30 cm and the half-angle between the incident and the reflected beam is at most 7°. A smaller lens is placed between the sample and the large aperture lens to collect the light scattered from the surface, which is sent to one side of a beamsplitter cube. The reference beam GRIN lens is positioned in front of a perpendicular side of the cube so that the two beams interfere and produce a 40-MHz optical signal (heterodyne signal). The out-of-plane motion of the film surface creates a Doppler shift (phase modulation) in the object beam; therefore, the resulting 40-MHz signal is phase modulated by a quantity proportional to the displacement of the surface. This signal is then converted into an ac voltage using a Hewlett-Packard PIN photodiode. It is then amplified and combined (via a frequency mixer) with a 40.1-MHz sine wave from a function generator, in order to get a downshifted 100-kHz heterodyne signal, which is then amplified and filtered. The FM demodulation is used to extract the displacement information contained in the phase of the heterodyne voltage. This is done using a phase-locked loop (PLL) electronic circuit, which produces an output proportional to the surface velocity.[8] After some band-pass filtering, the output of the PLL is displayed on a Tektronix digital oscilloscope (TDS 420) equipped with a GPIB board for data transfer to a microcomputer.

It is of interest to compare the laser Doppler vibrometer described in this paper with the optical interferometers previously used to study polymer films. The main difference is that the two separate interferometers that constitute the present system are designed for independent measurement of surface motion on both sides of the film while Zhenyi *et al.*[3] as well as Pan and Cross[5] configured their apparatus to measure the *difference* (by optical recombination) in displacement at opposite points on the two sides of the film which is directly related to its thickness motion. An advantage of the present system is that it determines both the thickness and the bending motion of the film, while the probes described in Refs. 3 and 5 cannot be used to assess the latter. This is important to note, because, as will be explained in the next section, the bending motion is a major source of errors in these measurements, and being able to measure it can help reduce the inaccuracies. For this procedure, the signals from each interferometer have to be digitally recombined, and it was found that 12-bit resolution in the A/D conversion was required for accurate determination of d_{33}. On the other hand, a disadvantage of the present system is that the thickness motion is determined by adding displacement signals obtained at opposite points on the two sides of the film. Therefore, any error in amplitude or phase calibration of the

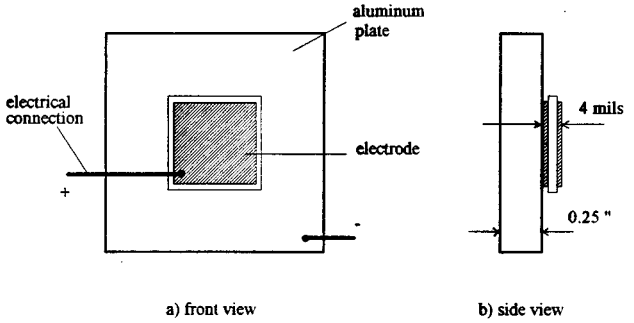

FIG. 2. The PVDF sample mounted on a $\frac{1}{4}$-in. aluminum plate.

detection electronics for either light beam will lead to an error in determination of the thickness motion. However, the data presented here show that this error can be reduced to a few percent by careful calibration of the two sets of detection electronics used in the two-beam system.

II. d_{33} PIEZOACTIVE COEFFICIENT MEASUREMENTS ON PVDF SAMPLES

A. Sample glued on a rigid backing

In order to test the accuracy and the reliability of the displacements obtained with the LDV system, a film of 4-mil (0.1 mm)-thick PVDF was glued to a 1/4 in. (6.35 mm)-thick aluminum plate using conducting epoxy, as shown in Fig. 2. This conducting epoxy was also used for all the electrical connections to the sample and to the plate. A narrow unelectroded margin around the edge of the film prevented shorting of the electrodes. This sample could expand only in the three-direction (pure thickness vibration) and had well-defined boundary conditions (in-plane motions frozen). We could then calculate the amplitude of the thickness vibrations as a function of the applied ac voltage and compare these results with the experimental data. The constitutive relations for a piezoelectric film driven by an electric field applied across the sample (in the three-direction) are given as[9]

$$\begin{aligned} S_1 &= s_{11}X_1 + s_{12}X_2 + s_{13}X_3 + d_{31}E_3, \\ S_2 &= s_{21}X_1 + s_{22}X_2 + s_{23}X_3 + d_{32}E_3, \\ S_3 &= s_{31}X_1 + s_{32}X_2 + s_{33}X_3 + d_{33}E_3, \end{aligned} \tag{1}$$

where the S_i are the strains, the X_i are the stresses, the s_{ij} are the compliance coefficients, the d_{ij} are the piezoelectric strain constants, and E_3 is the electric field. For the case depicted in Fig. 2, $S_1 = S_2 = 0$ and X_3 is due only to the acoustic radiation pressure into the fluid (air) and is negligible as the sample is much smaller than the acoustic wavelength in air. Therefore, upon substitution, Eqs. (1) become

TABLE I. The 4-mil PVDF on a rigid backing; left side measurements.

Location	1	2	3
$\Delta T(10^{-10}$ m)	4.4	4.4	4.4
$\lvert\Delta T/V\rvert(10^{-10}$ m/V)	0.11	0.11	0.11

TABLE II. The 4-mil PVDF on a rigid backing; right side measurements.

Location	1	2	3
$\Delta T(10^{-10}$ m)	3.4	3.9	3.8
$\lvert\Delta T/V\rvert(10^{-10}$ m/V)	0.9	0.10	0.10

$$\begin{aligned} 0 &= s_{11}X_1 + s_{12}X_2 + d_{31}E_3, \\ 0 &= s_{21}X_1 + s_{22}X_2 + d_{32}E_3, \\ S_3 &= s_{31}X_1 + s_{32}X_2 + d_{33}E_3. \end{aligned} \tag{2}$$

As the values of all the compliance and piezoelectric coefficients are known for PVDF,[10] the first two equations of (2) can be used to express X_1 and X_2 as a function of E_3. Substituting these expressions into the third equation, the ratio $S_3/E_3 = \Delta T/V$ is obtained, where ΔT is the amplitude of the vibrations in the three-direction when an ac voltage of amplitude V is applied to the sample. This computation gives the value of -0.11×10^{-10} m/V for $\Delta T/V$.

The measured values shown in Tables I and II were taken by separate measurements by each arm of the system. The sample was driven with a 40-V amplitude signal of 1.5 kHz, and the resulting displacements were recorded at three locations on the surface. The data was signal averaged (1024 traces) on a digital oscilloscope and then transferred to a computer for calculation of the amplitude using MATLAB®. This procedure was used for all the subsequent data presented here. Values of the ratio $\Delta T/V$ are absolute values, and one can see that they follow our theoretical predictions based upon the PVDF coefficients available in the literature. The same sample was also used to ensure that there was not any significant phase difference between the response of each arm. This is important as any phase lag can introduce errors when the displacements from each side are recombined to get the thickness motion. Finally, the reproducibility of the measurements was checked by taking data on the same sample several days apart; similar values to the ones in Tables I and II were obtained. In summary, these amplitude, phase, and reproducibility measurements established the accuracy of the LDV system.

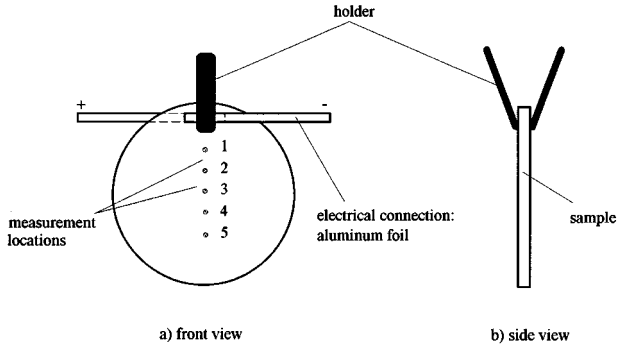

FIG. 3. Freely suspended sample mounting and electrical connections. The numbers refer to the light beam locations.

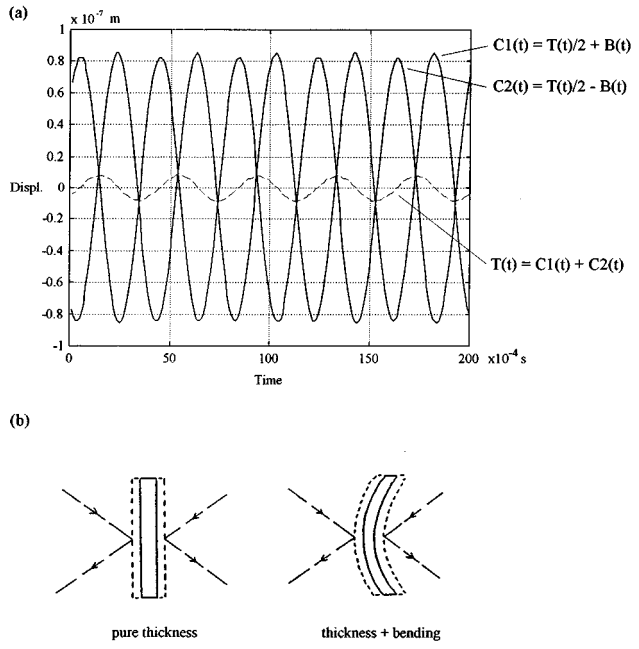

FIG. 4. Typical output of the optical probe: (a) measured displacements on each side of the film (signals C_1 and C_2) and computed thickness motion (signal T); (b) schematic representations of sample vibrations: pure thickness and thickness combined with bending; the latter case corresponds to (a) where signal B represents the bending motion.

B. Freely suspended sample

We then designed a mounting configuration with minimal constraints imposed on the film. Figure 3 illustrates this design and shows a disk-shaped, 4-mil-thick PVDF film clamped at the top, as well as electrical connections in the form of aluminum strips attached to the sample using silver paint. The disk diameter is 0.5 in. (12.7 mm) and the sample is free of mounting-induced stresses everywhere except near the clamped area. Therefore, using the third equation of (1), we find $d_{33}=S_3/E_3=\Delta T/V$, which can be directly computed from the measurements of the thickness change ΔT. The published values of this coefficient[10,11] range from -0.27×10^{-10} to -0.38×10^{-10} m/V. The motivation for measuring displacements simultaneously on both sides of the film is to eliminate the effect of any motion that would occur in addition to the thickness change. The thickness motion alone can be isolated by combining the signals corresponding to each side of the film. Figure 4(a) depicts a typical displacement output of the optical system; signals from each side are labeled $C_1(t)$ and $C_2(t)$ and one can see that they are approximately 180° out-of-phase and that their amplitudes are roughly equal. This indicates that the film undergoes a flexural motion whose amplitude is larger than that of the thickness motion. Let $B(t)$ and $T(t)$ represent the flexural and the thickness vibrations, respectively; we have then for the signal from each side:

$$C_1(t)=\frac{T(t)}{2}+B(t),$$
$$C_2(t)=\frac{T(t)}{2}-B(t). \tag{3}$$

Therefore, the thickness motion (of amplitude ΔT) can be obtained by the following straightforward combination of $C_1(t)$ and $C_2(t)$:

$$T(t)=C_1(t)+C_2(t). \tag{4}$$

1. Experimental results

The first set of data shown in Table III is for a 4-mil-thick, circular PVDF film driven with a 17-V amplitude voltage at 250 Hz. Measurements were made at five locations on the surface of the sample, 1 mm apart. This table includes the amplitudes of the measured displacements C, as well as the thickness amplitude values ΔT. The d_{33} values are much larger than the published values, and they show some scatter. It was suspected that the high level of bending (flexural) motion was responsible for this data inaccuracy. A stiffer four-layer sample (described in Fig. 5) was used next to test this hypothesis. This sample was assembled by bonding four 4-mil films together with a thin layer of shear wave couplant (viscoelastic material) whose modulus is lower than that of PVDF. The films were driven in parallel and the mounting was identical to the single layer case. This design presented several advantages as far as reducing bending: increasing the thickness of the sample increased its stiffness and also enhanced the thickness motion contribution. Finally, the parallel electrical connections created bending moments with opposite signs in each film, canceling each other. The data in

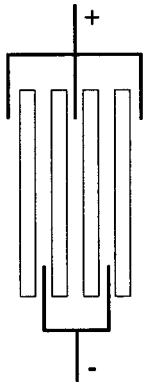

FIG. 5. Stack of four PVDF films with electrical connections.

TABLE III. Freely suspended 4-mil PVDF sample (one layer).

Location	1	2	3	4	5
$C(10^{-9}$ m)	2	31	68	110	160
$\Delta T(10^{-9}$ m)	1.7	4.8	5.4	5.3	4.2
$\lvert d_{33}\rvert(10^{-10}$ m/V)	0.95	2.75	3.12	3.03	2.40

TABLE IV. Freely suspended 4-mil PVDF sample (four layers).

Location	1	2	3	4	5
$C(10^{-9}$ m)	9	9	10	22	28
$\Delta T(10^{-9}$ m)	1.6	1.2	1.1	1.4	1.2
$\lvert d_{33}\rvert(10^{-10}$ m/V)	0.40	0.30	0.28	0.35	0.30

Table IV are from measurements performed on the four-layer sample, at five different locations, 2 mm apart (in this table, ΔT is the total thickness response of the stack divided by 4); the sample was driven with a 40-V amplitude voltage at 250 Hz. Two observations should be made: first, the bending motion amplitude is reduced by an order of magnitude, confirming that stacking films together is an efficient way to reduce bending; second, the d_{33} data are in good agreement with the published values. Therefore, it appeared that it was necessary to reduce the bending amplitude as much as possible in order to obtain more nearly accurate experimental results.

2. Error analysis

At this point, two questions remain unanswered: what are the origins of the bending motion, and why does it affect the measurement accuracy? In theory, when an electroded piezoelectric film is subjected to an electric field as in these measurements, it should only undergo a thickness deformation; this assumes that the film is perfectly symmetric. However, if any asymmetry is present in the sample, the thickness motion is likely to excite flexural waves; if an ac driving voltage is used, these waves will produce a standing wave pattern (SWP) deforming the film and giving rise to what is referred to as ''bending motion'' in this paper. Asymmetries in the sample include nonuniformity in electrode thickness, nonuniform poling across the film thickness, presence of electrical connections on both sides of the film, and mounting-induced asymmetries. In particular, if the electrodes on each side of a sample do not have the same thickness, a bending occurs due to an extensional motion by a Poisson coupling. On the thicker electrode side, this motion is more restricted (higher stiffness) than on the other side, and this situation may lead to sample bending. This bending motion has the same frequency as the driving voltage and the thickness motion, but it has been experimentally observed that it does not possess any definite phase relationship with the latter. Furthermore, its amplitude is a function of location on the sample surface. Most of the time, this amplitude is much larger (at least by a factor of 10) than the thickness amplitude, making it difficult to precisely measure the thickness effect. Typically, the bending amplitude should not exceed the thickness amplitude by more than a factor of approximately 20 in order to allow accurate computations of d_{33} values. This ratio of 20 to 1 is not to be regarded as a rigid rule, but rather provides a general guideline about the validity of the measurements; it is based on all the PVDF data that was taken during the course of this work.

In this paragraph, we take a more detailed look at the bending motion and we propose a possible cause of error related to this type of motion. First, let us recall that a bending motion is made of two components, a translation and a rotation motion, as depicted in Fig. 6. In the case of our samples, bending can be represented by a standing wave; considering only a one-dimensional model in the x direction, the bending η can be written as

$$\eta(x,t) = \eta_0 \cos(k_F x)\sin(\omega t), \tag{5}$$

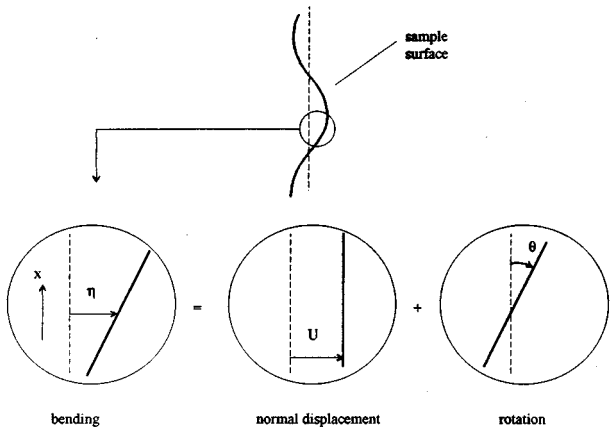

FIG. 6. Translation and rotation components of bending motion.

where η_0 is the bending amplitude, k_F is the flexural wave number, and ω is the driving angular frequency. The slope at any location is given by

$$\tan\,\theta = \frac{\partial \eta}{\partial x} = -\,\eta_0 k_F\,\sin(k_F x)\sin(\omega t), \tag{6}$$

and its amplitude is

$$|\tan\,\theta| = \eta_0 k_F\,\sin(k_F x). \tag{7}$$

What is obtained from optical measurements at any location x is the bending amplitude $[\,\eta_0 \cos(k_F x)]$. Supposing that measurements can be made at several locations on the sample surface so as to find an approximate maximum value, η_0 can be found. Thus an estimate for the *maximum* slope amplitude can be theoretically calculated according to

$$|\tan\,\theta_{\max}| = \eta_0 k_F\,. \tag{8}$$

On the other hand, it is likely that, during measurements, the light beams are not exactly positioned at the same spot on each side of the film. The procedure to align them is to stick a small piece of translucent paper on the sample (hanging over its edge), make the spots overlap on this paper, and then translate the sample so that the beams are properly located on its surface. The piece of paper is removed after the beam adjustment. Some samples also have small unelectroded areas which can be used similarly for the alignment. Since this is accomplished by eye, it is virtually impossible to avoid a small offset $(2d)$, as illustrated in Fig. 7. Let us define the different signals as follows:

$T(t)$, thickness motion (not shown in Fig. 7);

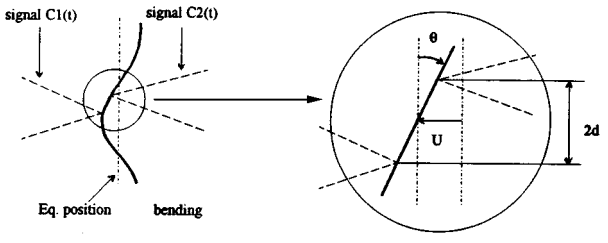

FIG. 7. Light beams misalignment.

$$\left.\begin{aligned} B_1(t) &= A_1 \sin(\omega t) \\ B_2(t) &= A_2 \sin(\omega t) \end{aligned}\right\}$$

bending motions as measured by each side of the probe;

$$\left.\begin{aligned} C_1(t) &= B_1(t) + \frac{T(t)}{2} \\ C_2(t) &= B_2(t) + \frac{T(t)}{2} \end{aligned}\right\}$$

total displacements measured by the optical probe.

In the case where the beams are slightly offset by an amount $(2d)$, the following relations hold:

$$A_1 = U + d \tan\theta, \quad A_2 = -U + d \tan\theta,$$

$$\begin{cases} C_1(t) = (U + d \tan\theta)\sin(\omega t) + \dfrac{T(t)}{2}, \\ C_2(t) = (-U + d \tan\theta)\sin(\omega t) + \dfrac{T(t)}{2}. \end{cases} \tag{9}$$

Therefore,

$$C_1(t) + C_2(t) = T(t) + (2d \tan\theta)\sin(\omega t). \tag{10}$$

One can see that, in this case, the combination of the light beams misalignment and the rotational component of bending produces an extra term $(2d \tan\theta)$ in the thickness motion computation. It is important to keep in mind that since there is no definite phase relationship between bending and thickness [in other words, in the above analysis, $T(t) = \Delta T \sin(\omega t + \varphi)$, where φ is unknown], the term $(2d \tan\theta)$ can either be added to or subtracted from the thickness amplitude, depending on the relative phase between the two signals. In fact, $(2d \tan\theta)$ is the maximum error generated by the combined effects of rotation and beam misalignment. Thus, if M is the amplitude of the measured signal $C_1(t) + C_2(t)$, one can write the following formula for the thickness change amplitude:

$$\Delta T = M \pm 2d \tan\theta. \tag{11}$$

The quantity d in the above equation is not easily determined with accuracy, because the beams are aligned by eye. For our calculations, it is assumed that $(2d)$ is on the order of 0.1 mm. On the other hand, the slope $\tan\theta$ also needs to be evaluated; Eq. (8) could only be used if the film motion were free, and one would simply need to calculate the bending wavelength of the free flexural wave. The bending motion, however, is forced, and the corresponding shape is not easily obtainable theoretically. Therefore, the slope was estimated using the experimental data obtained on the samples: for each measurement location, the amplitude of the bending motion alone was computed (thickness motion factored out) and the slope was calculated using a finite difference approximation. This approach is further justified by the simplicity of the bending shape in the case of clamped circular films: as Tables III and IV reveal, the bending amplitude increases from top to bottom, indicating a ''cantilever beam''-type motion. The average slope is approximately 4×10^{-5} for the single-layer sample and 2.8×10^{-6} for the four-layer sample. Therefore, one can compute the d_{33} errors for each sample, which are $(2d \tan\theta)/V$ and $(2d \tan\theta)/4V$, respectively. Numerically,

$$d_{33} \text{ error (1 layer)} = \pm 2.31 \times 10^{-10} \text{ m/V},$$

$$d_{33} \text{ error (4 layers)} = \pm 0.02 \times 10^{-10} \text{ m/V}.$$

These results are compatible with the data shown in Tables III and IV: one can see, for example, that the erroneously large values obtained on the single-layer sample can be explained by the above analysis. On the other hand, the d_{33} data from the stacked sample are within an acceptable range. Pan and Cross[5] also point out the need for the beams on the two sides of the sample to be collinear in order to eliminate bending effects, but do not comment further on the sensitivity of their apparatus to this adjustment.

C. Clamped sample

One of the objectives in assembling the present system was to study the polyurethane films for which a very large electrostrictive response has been reported. These measurements are now in progress. Although the results presented in the previous section suggest that reducing the bending amplitude by stacking samples is the solution to the problems encountered in this work, the mounting that was used turned out to be impractical for softer samples such as the above polyurethanes. When freely suspended, these samples exhibit a curled surface which becomes even more pronounced when a large DC bias voltage is applied to them (as is required to measure their electrostrictive response). This is a problem, because when the film surface is not flat, the laser light is not reflected in the proper direction, making the alignment of the optics difficult and time-consuming. Therefore, another holder had to be designed for their measurements according to the following requirements:

(i) minimum constraints on the films,
(ii) possibility to stack films, and
(iii) control of film flatness.

The mounting procedure that was chosen was inspired by the one used by Zhenyi *et al.*:[3] a holder clamps the film along its two vertical edges and a small tension is applied in the horizontal direction by pulling the two clamps apart, in order to get a flat surface. The whole assembly is placed on an XYZ positioner combined with a tilt platform for posi-

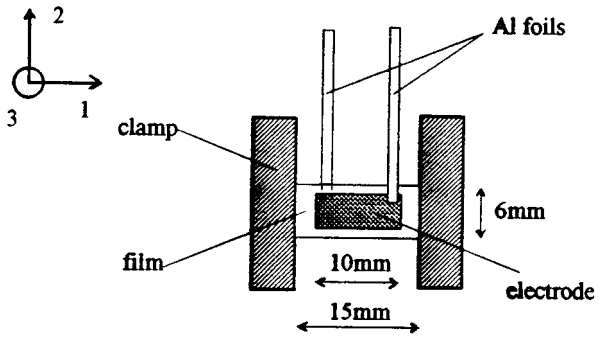

FIG. 8. Mounting configuration for clamped samples.

TABLE V. Clamped single layer PVDF sample measurements.

Frequency (Hz)	250	300	500	560
$C(10^{-9}$ m)	4	5	35	100
$\Delta T(10^{-9}$ m)	1.0	1.0	2.8	3.9
$\lvert\Delta T/V\rvert(10^{-10}$ m/V)	0.25	0.25	0.72	1.00

TABLE VI. Clamped double-layer PVDF sample measurements.

Frequency (Hz)	200	250	300	1000
$C(10^{-9}$ m)	3	9	13	3
$\Delta T(10^{-9}$ m)	3.2	1.2	3.2	1.0
$\lvert\Delta T/V\rvert(10^{-10}$ m/V)	0.22	0.18	0.20	0.16

tioning and fine tuning. Electrical connections are made with strips of aluminum foil [0.5 mil (12.7 μm) thick, 2 mm wide] attached to the electrode with a conducting paste (Eccobond 59C from Grace Polymer); this is depicted in Fig. 8. The boundary conditions are: $X_2=X_3=0$, $S_1=0$, and Eqs. (1) thus become

$$\begin{aligned} 0&=s_{11}X_1+d_{31}E_3,\\ S_2&=s_{21}X_1+d_{32}E_3,\\ S_3&=s_{31}X_1+d_{33}E_3. \end{aligned} \tag{12}$$

Combining the first and the last of the above equations gives

$$S_3=\left(-\frac{s_{31}}{s_{11}}\,d_{31}+d_{33}\right)E_3. \tag{13}$$

Therefore, what is measured by the optical probe when the sample is held this way is

$$\frac{\Delta T}{V}=\frac{S_3}{E_3}=d_{33}-\frac{s_{31}}{s_{11}}\,d_{31}. \tag{14}$$

The coefficients involved in Eq. (14) are available from Refs. 10 and 11; they respectively yield the following values for $\Delta T/V$: -0.19×10^{-10} m/V and -0.12×10^{-10} m/V. These values were confirmed by the results of a finite element simulation (using the ATILA® finite element code) modeling the sample in its holder. Tables V and VI summarize the data taken on a 4-mil single-layer and on a 2×4-mil double-layer sample, respectively (in the case of Table V, the driving voltage amplitude was 39 V, whereas it was different at each frequency for Table VI, ranging from 30 to 80 V). One can see that the double-layer results are accurate, as expected: they fall within the range of published values at all frequencies. The single-layer sample, on the other hand, did not yield bad results at 250 and 300 Hz, but did not show the expected response at higher frequencies. These two higher frequencies (500 and 560 Hz) actually correspond to the first two resonances that can be excited in the single-layer sample, and they are characterized by a relatively large bending amplitude. The double-layer sample did not exhibit any resonance over the frequency range of interest (200–1000 Hz). Calculations from experimental slope measurements on the single-layer indicate that an offset of 0.1 mm in the beams would result in a d_{33} error on the order of 0.04×10^{-10} m/V at 200 and 300 Hz, which is acceptable. At 500 and 560 Hz, however, the same offset would only result in an error on the order of 0.2×10^{-10} m/V, which cannot account for the observed discrepancies in the data at these two frequencies. The beam offset ''required'' to get the erroneous values reported in Table V would be detectable by eye, which means that the above error analysis is not sufficient to explain the large values obtained at resonance. This suggests that accuracy is not only a function of the amplitude of the bending motion at the laser beam location, but also depends on whether or not the film is excited below its fundamental resonance. When this is not the case, there seems to be a coupling effect between the resonant vibrations and the thickness change that affects the accurate detection of the latter. At this point, the mechanism responsible for this effect has not been identified; work involving numerical simulations is now ongoing to get a better understanding of it. In any case, it appears that it is preferable to measure the thickness change when the sample is driven with a frequency below its fundamental resonance frequency.

III. CONCLUSIONS

Measurements on PVDF samples proved that the optical probe was suitable for estimation of thin film thickness coefficient. This study revealed that the bending motion was a major source of error when calculating the net thickness change. The error analysis demonstrated that inaccuracies can be explained by the combined effects of the light beams' misalignment and the rotational component of the bending motion. Stacking films was proven to be an efficient way to reduce the bending amplitude and should be done in any subsequent similar work. Finally, it was observed that exciting samples below their fundamental resonance frequency was required to insure accurate measurements.

ACKNOWLEDGMENTS

This work was partially supported by the Office of Naval Research, Structural Acoustics Program, Code 332; Dr. G. L. Main, Scientific Officer. The authors wish to thank Dr. Jerry I. Scheinbeim for his helpful comments during a visit to his laboratory at Rutgers University.

[1] H. Wang, ''Electromechanical Effects in Polymeric Materials,'' Ph.D. dissertation, Pennsylvania State University, 1994, p. 25.
[2] J. E. Barger, ''Electrostrictive polyurethane projector,'' J. Acoust. Soc. Am. **95**, 2857(A) (1994).
[3] M. Zhenyi, J. I. Scheinbeim, J. W. Lee, and B. A. Newman, ''High Field Electrostrictive Response of Polymers,'' J. Polym. Sci., Part B: Polym. Phys. **32**, 2721–2731 (1994).
[4] L. E. Drain, *The Laser Doppler Technique* (Wiley, Chichester, 1980).
[5] W. Y. Pan and L. E. Cross, ''A Sensitive Double Beam Laser Interferometer for Studying High-Frequency Piezoelectric and Electrostrictive Strains,'' Rev. Sci. Instrum. **60**, 2701–2705 (1989).
[6] F. M. Guillot, ''Development of a Two-Sided Optical Probe for Displacement Detection,'' (M.S. dissertation, Georgia Institute of Technology, 1995), Chap. 4, pp. 25–36.
[7] A. Yariv, *Introduction to Optical Electronics* (Holt, Rinehart and Winston, New York, 1971), 2nd ed., Chap. 12, pp. 337–353.
[8] R. E. Best, *Phase-Locked Loops* (McGraw–Hill, New York, 1984).
[9] O. B. Wilson, *Introduction to Theory and Design of Sonar Transducers* (Peninsula, Los Altos, 1988), p. 57.
[10] H. Schewe, ''Piezoelectricity of Uniaxially Oriented Polyvinylidene Fluoride,'' IEEE Ultrason. Symp. Proc. **1**, 519–524 (1982).
[11] O. B. Wilson, *Introduction to Theory and Design of Sonar Transducers* (Peninsula, Los Altos, 1988), p. 83.

State switched transducers: A new approach to high-power, low-frequency, underwater projectors

Gregg D. Larson and Peter H. Rogers
George W. Woodruff School of Mechanical Engineering, Georgia Institute of Technology, Atlanta, Georgia 30332-0405

Walter Munk
Scripps Institution of Oceanography, University of California, San Diego, La Jolla, California 92093-0225

(Received 18 February 1997; accepted for publication 3 November 1997)

In order to produce high-amplitude, low-frequency signals, an underwater transducer must generate a relatively large volume displacement. Since water exerts a large reaction force back on the transducer, ''conventional wisdom'' dictates that such a transducer would have to be a high Q resonant device and thus not be broadband. However, a transducer does not have to be broadband in the conventional sense to meet the requirements of communication and sonar systems. A transducer that is capable of instantaneously switching between two discrete frequencies is adequate for communication and transmission of coded signals; one that is capable of switching among several frequencies could produce the chirp signals commonly used in active sonars. Ordinarily, a broadband transducer is needed to accomplish the frequency switching rapidly. A way around this difficulty is the ''state-switched'' source concept originally proposed by Walter Munk in 1980 which permits instantaneous frequency switching of a high Q resonant transducer while always maintaining the resonance state. The objective of this research has been to investigate this novel approach to the design of high-power, low-frequency, broadband transducers for use in long-range underwater communication, active sonar, and underwater research applications. This paper presents a practical realization of a ''state-switched'' source. © *1998 Acoustical Society of America.* [S0001-4966(98)03502-4]

PACS numbers: 43.38.Ar, 43.30.Yj, 43.38.Fx, 43.30.Vh [SLE]

INTRODUCTION

Communication systems, sonar systems, and underwater research such as acoustic ocean tomography require a method of generating a controllable, broadband signal with high power at low frequencies underwater. During the Heard Island Feasibility Test,[1,2] high-power, low-frequency sound was propagated over distances as great as 18 000 km. High power at low frequencies allows for greater signaling distances in communication systems and for detecting underwater objects at greater distances using active sonar. Low frequencies are desired in order to minimize the attenuation over long propagation distances as the attenuation decreases with decreasing frequency.[3] High signal level and efficiency maximize the long range performance. Additionally, higher efficiency extends the operational lifetime of unattended sources. The ability to transmit highly controllable signals such as multifrequency sweeps and pseudorandom codes is essential for successful communications and long range propagation experiments. Broad bandwidth is needed in communication systems to allow for high data rate transmission and in active sonar systems for range resolution. Accuracy of long range measurements is increased by raising the source level and increasing the bandwidth.[4]

High-power, low-frequency sound can be generated underwater by a variety of sources, namely tonpilz,[5] hydroacoustic,[6] flextensional,[7] and electrodynamic[8] transducers. Electrostatic, piezoelectric, magnetostrictive, electromagnetic, hydroacoustic, and parametric transduction mechanisms have been examined as means of producing low-frequency sound underwater.[9] Other sources such as Helmholtz resonators,[10] an air gun impulsive underwater transducer,[11] and a bubble transducer[12] have also been used. In spite of the problems associated with the design of low-frequency underwater transducers[9,13,14–16] such as transducer size, low radiation resistance, large volume velocities, and depth compensation, the difficulties of generating a high-power, low-frequency signal underwater must be overcome for applications such as communication systems, sonar systems, and underwater research.

High power, coupled with low frequencies, indicates a need for large displacements of the radiating surface. At low frequencies, the wavelength in water is typically much greater than the characteristic source dimension, resulting in a low mechanical radiation impedance, $Z_{m\mathrm{rad}}$. For example, for a baffled piston radiator, the mechanical radiation impedance[17] is given by

$$Z_{m\mathrm{rad}}=\rho c\pi a^2[R_1(2ka)-iX_1(2ka)], \tag{1a}$$

$$R_1(2ka)=1-\frac{2J_1(2ka)}{2ka}, \tag{1b}$$

$$X_1(2ka)=\frac{2H_1(2ka)}{2ka}, \tag{1c}$$

where J_1 and H_1 are the Bessel and Struve functions of the first order. At low values of $2ka$, $R_1(2ka)$ and $X_1(2ka)$ can be approximated as

 0001-4966/98/103(3)/1428/14/$10.00

$$R_1(2ka)=\frac{(2ka)^2}{4\cdot 2}-\frac{(2ka)^4}{6\cdot 4^2\cdot 2}+\frac{(2ka)^6}{8\cdot 6^2\cdot 4^2\cdot 2}-\cdots, \quad (2)$$

$$X_1(2ka)=\frac{(4/\pi)(2ka)}{3}-\frac{(4/\pi)(2ka)^3}{5\cdot 3^2}+\frac{(4/\pi)(2ka)^5}{7\cdot 5^2\cdot 3^2}+\cdots . \quad (3)$$

As the radiated acoustic power, P_a, is determined by

$$P_a=\tfrac{1}{2}|\hat{v}_n|^2\ \mathrm{Re}\{Z_{m\mathrm{rad}}\}, \quad (4)$$

where $\hat{v}_n$ is the normal surface velocity, a low mechanical radiation impedance translates into a low radiated acoustic power. To achieve high radiated acoustic power with low radiation impedance, the normal surface velocity and the radiating surface area must be large (that is, a large volume displacement is required). From Eqs. (2) and (3), it is evident that, for low ka, the radiation reactance is much larger than the radiation resistance. Hence, to maximize the surface displacement, the source must be operated near resonance as a narrow-band, or high Q, device. Thus the frequencies available for signaling and communication purposes are constrained to a relatively small band centered on the resonance frequency of the transducer.

Increasing the surface area of the radiating surface results in increased radiation damping and added mass due to the water loading.[18,19] Increased radiation damping lowers the Q and increases the bandwidth while the added mass raises the Q and lowers the operating frequencies. Direct scaling of higher frequency (tonpilz) transducers yields dimensions of 6 m in diameter and 15 m in length at 100 Hz.[16] Thus smaller dimensions are used at the expense of low radiation impedance.

Another option is to increase the internal damping of the transducer in an effort to lower the source's Q, thus increasing the bandwidth without changing the resonance frequency. The main disadvantage of lowering the Q of the transducer in this manner is that the signal level and efficiency are both reduced as the losses in the system are increased. By lowering the Q of the transducer, a greater bandwidth is realized but at the cost of decreased surface displacements, and hence reduced signal levels.

High power at low frequencies underwater requires large displacements due to the low radiation resistance and large forces due to the relatively high radiation reactance. Resonance is required to eliminate the reactance and high Q follows from the low radiation impedance. Therefore, a high Q source operated at resonance is needed. But a high Q source operated at resonance does not provide a broadband response. A low Q, or nonresonant, source is necessary for broad bandwidth but will not efficiently provide high power at low frequencies. Apparently, neither a high Q nor a low Q source, in the traditional sense, completely satisfies the requirements of a broadband, high-power, low-frequency, underwater, acoustic transducer.

This research was undertaken to determine whether or not a novel idea, state switching,[20] could be used to obtain high power at low frequencies in an underwater acoustic transducer with an ''effective bandwidth'' much larger than that of a typical high Q resonant source. Ordinarily, a broadband transducer is needed to accomplish frequency switching rapidly. However, a transducer does not have to be broadband in the conventional sense to meet the requirements of communication and sonar systems. A transducer that is capable of instantaneous switching between two discrete frequencies is adequate for communication and one that is capable of instantaneous switching among several frequencies could produce the chirp signals commonly used in active sonars. It is theoretically possible to instantaneously switch frequencies with a high Q resonant system provided that the resonance frequency of the system is altered simultaneously with the drive frequency. Moreover, it is possible to accomplish the switching without having to provide additional energy to the system. Such a ''state-switched'' transducer would retain the advantages (high power, high efficiency, and large displacements) of a high Q resonant transducer without the accompanying disadvantages (narrow bandwidth and slow response time).

I. STATE SWITCHING CONCEPT

The state switching concept was first described by Munk[20] as a ''State-Switched Acoustic Source.'' A state switched acoustic source is an acoustic source that has the ability to switch among multiple distinct resonant states, while maintaining resonance throughout the switching process. At any given time, the source has only one fundamental resonance as with any typical source. The distinction of a state switched source is that it has the ability to change its resonance by altering a property of the system. State switching is accomplished by driving the source to resonance and at a predetermined time, switching both the resonance frequency and the driving frequency of the source simultaneously.

The state switching concept is most apparent upon examination of a simple harmonic oscillator. A mass-spring system with a spring constant k_0 and mass m_0 has a resonance frequency, ω_H, given by

$$\omega_H=\sqrt{\frac{k_0}{m_0}}. \quad (5)$$

Decreasing the mass produces a new resonance frequency, ω_L, given by

$$\omega_L=\sqrt{\frac{k_0}{m_1}}, \quad (6)$$

where the new mass is represented by m_1. A second way to modify the resonance frequency of the original mass–spring system is to reduce the stiffness of the spring to k_1 such that

$$\omega_L=\sqrt{\frac{k_1}{m_0}}. \quad (7)$$

In a mass switching realization of state switching, the original mass–spring system is driven at resonance at its natural frequency, ω_H, as shown in Fig. 1. At a point of zero velocity, the mass is instantaneously replaced by the second mass, m_1, effectively changing the resonance frequency of the system to the new value, ω_L. At the same time that the mass is switched, the driving frequency is changed to corre-

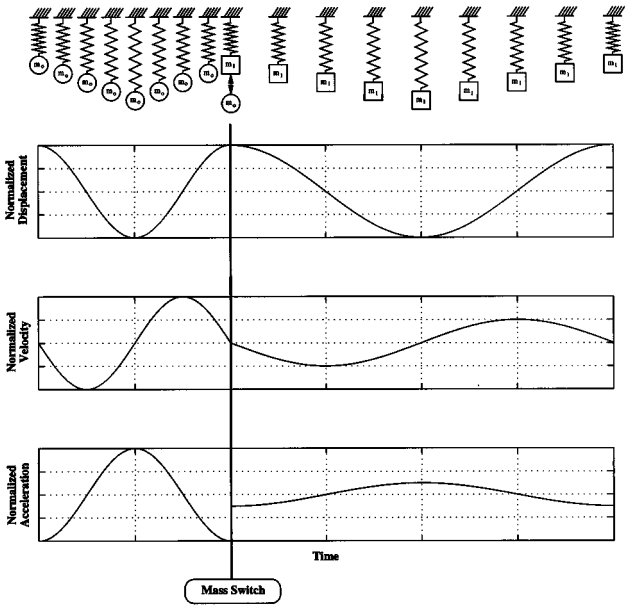

FIG. 1. Mass switching realization of state switching a simple harmonic oscillator.

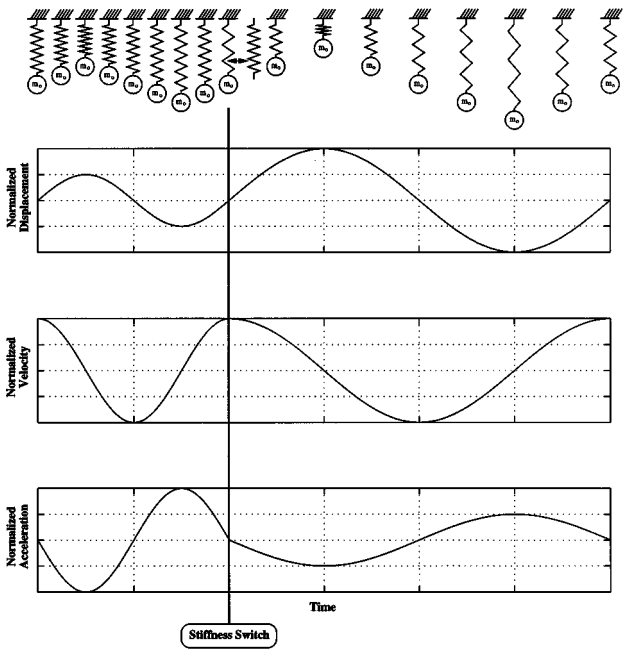

FIG. 2. Stiffness switching realization of state switching of a simple harmonic oscillator.

spond to the new resonance frequency of the system. The switch and its effect on the system are shown in Fig. 1. For the purpose of illustrating the state switching concept, the masses and stiffnesses in Fig. 1 have been chosen such that the high frequency, ω_H, is exactly twice the low frequency, ω_L (although obviously any convenient, achievable value for ω_H/ω_L could be used in an actual system). The switch takes place at a point of zero velocity where the kinetic energy of the system is zero. At this point, all of the system energy is in the spring and the potential energy of the system is a maximum. By changing the mass of the system at a point of zero kinetic energy, the total energy of the system is unchanged by the switching process. Throughout the switch, energy is conserved, hence no work is done. At any subsequent point of zero velocity, the mass may be replaced by the original mass, m_0, to return the resonance frequency to the original value of ω_H. To maintain resonance when the masses are switched, the drive frequency must always be changed to correspond to the appropriate resonance frequency.

For a mass switching realization of state switching, conservation of energy requires that the displacement amplitude remain constant through the switching process while the velocity and acceleration amplitudes change according to

$$\frac{|v_H|}{|v_L|}=\frac{\omega_H}{\omega_L}, \tag{8a}$$

$$\frac{|a_H|}{|a_L|}=\left(\frac{\omega_H}{\omega_L}\right)^2, \tag{8b}$$

where $|v_H|$ and $|a_H|$ are the amplitudes of the velocity and acceleration, respectively, at the high frequency, ω_H, and $|v_L|$ and $|a_L|$ are the amplitudes of the velocity and acceleration, respectively, at the low frequency, ω_L. The velocity amplitude is reduced by a factor of 2 and the acceleration amplitude is reduced by a factor of 4 when changing from ω_H to ω_L for the case shown in Fig. 1.

Alternatively, a state switched source can be produced by altering the stiffness of the system. Beginning again with the original mass–spring system being driven at its fundamental resonance, ω_H, the stiffness of the system is instantaneously changed (e.g., by changing springs) to a different value, k_1, at a point of zero displacement to produce a new simple harmonic oscillator. At the same time that the stiffness is changed, the drive frequency of the system is changed to correspond to the system's new resonance frequency, ω_L. The effect of the stiffness switch on the system (for $k_0=4k_1$) is shown in Fig. 2. The zero displacement point corresponds to a zero potential energy state for the system. That is, at this point all of the system energy is in the kinetic energy of the mass. By switching springs at a zero potential energy state, the total energy of the system is unaffected by the state switching and resonance is maintained. The system can be state switched back to the first resonance state at any subsequent point of zero displacement.

In the stiffness switching realization, energy conservation requires the velocity to remain constant through the switch while the displacement and acceleration amplitudes change according to

$$\frac{|x_H|}{|x_L|}=\frac{\omega_L}{\omega_H}, \tag{9a}$$

$$\frac{|a_H|}{|a_L|}=\frac{\omega_H}{\omega_L}, \tag{9b}$$

where $|x_H|$ and $|a_H|$ are the displacement and acceleration amplitudes, respectively, at the high frequency, ω_H, and $|x_L|$ and $|a_L|$ are the displacement and acceleration amplitudes, respectively, at the low frequency, ω_L. For our example, the

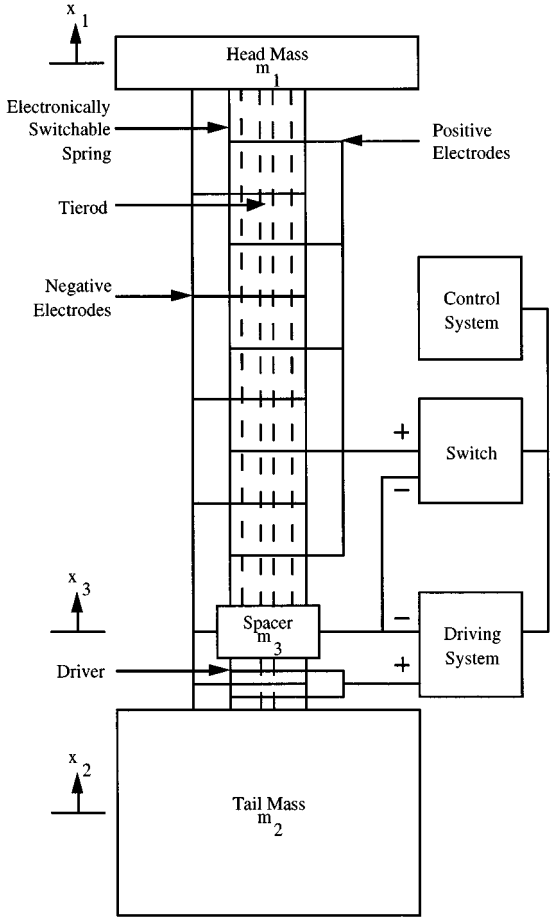

FIG. 3. Conceptual design of a state switched acoustic transducer utilizing stiffness switching.

displacement amplitude is doubled and the acceleration amplitude is halved by changing from ω_H to ω_L (see Fig. 2).

II. CONCEPTUAL DESIGN OF A STATE SWITCHED ACOUSTIC TRANSDUCER

While we have found no practical means of implementing a mass switched realization of a state switched transducer, we have found it possible to construct workable stiffness switched realizations of a state switched transducer by making use of the change in stiffness modulus which occurs due to the electromechanical coupling when electrical boundary conditions are changed in piezoelectric materials.[21,22] A conceptual design of a state switched acoustic transducer which utilizes stiffness switching is shown in Fig. 3. The transducer includes a head mass, a tail mass, a driver of piezoelectric ceramic, a switchable spring of piezoelectric ceramic, a tierod to keep the piezoelectric ceramic in compression, and a spacer as an interface between the driver and the switchable spring. All of the piezoelectric ceramic is polarized in the longitudinal direction. The transducer is driven by placing an alternating voltage across the driver at the desired frequency.

The switchable spring is made from piezoelectric ceramic which allows for modification of the spring's stiffness, and therefore, the resonance state of the transducer. The idea is to exploit the alteration in mechanical properties which occurs in a piezoelectric material when the electrical boundary condition is changed from open circuit to short circuit. Examination of the constitutive relations for a piezoelectric ceramic,[23]

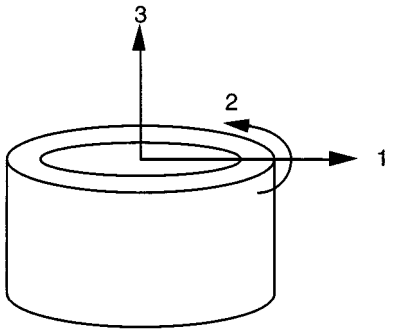

FIG. 4. Coordinate system for longitudinally polarized hollow cylinder.

$$S_1 = s_{11}^E T_1 + s_{12}^E T_2 + s_{13}^E T_3 + d_{31} E_3, \tag{10a}$$

$$S_2 = s_{12}^E T_1 + s_{11}^E T_2 + s_{13}^E T_3 + d_{31} E_3, \tag{10b}$$

$$S_3 = s_{13}^E T_1 + s_{13}^E T_2 + s_{33}^E T_3 + d_{33} E_3, \tag{10c}$$

$$S_4 = s_{44}^E T_4 + d_{15} E_2, \tag{10d}$$

$$S_5 = s_{44}^E T_5 + d_{15} E_1, \tag{10e}$$

$$S_6 = s_{66}^E T_6, \tag{10f}$$

$$D_1 = \epsilon_1^T E_1 + d_{15} T_5, \tag{10g}$$

$$D_2 = \epsilon_1^T E_2 + d_{15} T_4, \tag{10h}$$

$$D_3 = \epsilon_3^T E_3 + d_{31}(T_1 + T_2) + d_{33} T_3, \tag{10i}$$

shows that the ceramic can be stiffened both electrically and mechanically.[24,25] In Eqs. (10a) through (10i), S_i is the ith strain component, T_j is the jth stress component, E_n is the electric field in the nth direction, and D_m is the electric displacement in the mth direction. The piezoelectric material properties are given by s_{ij} (compliance), d_{ml} (piezoelectric strain coefficient), and ϵ_{mn} (dielectric permittivity). The values i of and j range from 1 to 3 for normal stress and strain and from 4 to 6 for shear stress and strain. The values of m and n range from 1 to 3 for polarization directions along the normal axes. The E superscript indicates a constant electric field while the T superscript indicates a constant stress.

The coordinate system for a longitudinally polarized hollow ceramic cylinder, the shape used in the switchable spring, is shown in Fig. 4. The polarization direction, always the ''3'' direction by convention, for the longitudinally polarized piezoelectric ceramic is in the axial direction. Assuming motion and electric field only in the longitudinal direction, application of the boundary conditions

$$E_1 = E_2 = 0, \tag{11a}$$

$$T_1 = T_2 = T_4 = T_5 = T_6 = 0, \tag{11b}$$

reduces Eqs. (10a) through (10i) to

$$S_3 = s_{33}^E T_3 + d_{33} E_3, \tag{12a}$$

$$D_3 = \epsilon_3^T E_3 + d_{33} T_3. \tag{12b}$$

For the short circuit constraint, the electric field is zero ($E_3=0$) and Eqs. (12a) and (12b) can be reduced to show that the strain and the electric displacement are proportional to the stress

$$S_3=s_{33}^E T_3, \tag{13a}$$

$$D_3=d_{33}T_3. \tag{13b}$$

The open circuit constraint requires that there be no electric displacement ($D_3=0$). Thus rearrangement of Eqs. (12a) and (12b) yields

$$S_3=s_{33}^E T_3(1-k_{33}^2), \tag{14a}$$

$$k_{33}^2=\frac{d_{33}^2}{s_{33}^E \epsilon_3^T}, \tag{14b}$$

where k_{33} is the coupling coefficient, a property of the material. Note that the proportionality constant relating stress and strain is different for the open circuit constraint [Eq. (14a)] than it is for the short circuit constraint [Eq. (13a)].

From Eq. (13a), the short circuit stiffness, k_{sc}, can be shown to be

$$k_{\mathrm{sc}}=\frac{A_c}{s_{33}^E L_c}, \tag{15}$$

where A_c and L_c are the cross-sectional area and the length of ceramic, respectively, while the open circuit stiffness, k_{oc}, can be found from Eq. (14a) to be

$$k_{\mathrm{oc}}=\frac{A_c}{s_{33}^E L_c(1-k_{33}^2)}. \tag{16}$$

The ratio of the stiffness of the piezoelectric ceramic when open circuited to the stiffness of the piezoelectric ceramic when short circuited is given by

$$\frac{k_{\mathrm{oc}}}{k_{\mathrm{sc}}}=\frac{1}{1-k_{33}^2}. \tag{17}$$

The piezoelectric coupling factor, k_{33} [defined by Eq. (14b)], determines the change in effective elastic compliance of the material. The piezoelectric coupling factor is important in determining the transduction efficiency as it is defined to be ''the ratio of the mutual elastic and dielectric energy density to the geometric mean of the elastic and dielectric self-energy densities.''[26] Thus the square of the coupling factor is the ratio of the output mechanical energy to the input electrical energy.[27,28]

We could use a thickness polarized cylindrical tube instead of the longitudinally polarized tube shown in Fig. 4. However, the change in stiffness would then be governed by k_{31} which is much smaller than k_{33} for most piezoelectric materials.

For a piezoelectric transducer, the maximum value of the transducer coupling factor is the coupling coefficient of the piezoelectric ceramic material appropriate to the ceramic polarization and the direction of motion. The actual value of the transducer coupling coefficient is reduced by the transducer structure and casing,[27–31] specifically by the compliance of the joints in the ceramic stack, the piezoelectric driver, the compression bolt, the case, and the waterproofing seals. In order to maximize the change in frequency between resonance states of the state switched transducer, the compliance of the elements in parallel with the switchable spring (i.e., the prestress tierod) should be much greater than the compliance of the switchable spring while the compliance of the elements in series with the switchable spring (i.e., the driver stack) should be much smaller than that of the switchable spring.

The joints in the stack of piezoelectric elements degrade the coupling and reduce the change in stiffness modulus. The strain in the stack of piezoelectric elements is a combination of the strain in the individual piezoelectric elements and the strain in the joints between the individual piezoelectric elements as given by

$$\frac{\delta x}{L}=\frac{\delta x_c+\delta x_j}{L}, \tag{18}$$

where δx is the total extension of the stack of total length L, δx_c is the extension of the piezoelectric elements, and δx_j is the extension of the joints. Thus, the total strain in the stack of piezoelectric elements including the effects of the joints can be written as

$$S_3=s_{33}^E T_3\left(\frac{L_c}{L}\right)\left(1+\frac{k_c}{k_j}\right)+d_{33}E_3\left(\frac{L_c}{L}\right), \tag{19a}$$

$$k_c=\frac{A_c}{s_{33}^E L_c}, \tag{19b}$$

$$k_j=\frac{A_j E_j}{L_j}, \tag{19c}$$

where k_c is the stiffness of the piezoelectric ceramic, and k_j, A_j, E_j, and L_j are the stiffness, cross-sectional area, Young's modulus, and length of the joints. The ratio of the stiffness of the piezoelectric ceramic when open circuited to the stiffness of the piezoelectric ceramic when short circuited is then

$$\frac{k_{\mathrm{oc}}}{k_{\mathrm{sc}}}=\frac{1}{1-k_{33}^2/(1+k_c/k_j)}. \tag{20}$$

Thus by making the joints as stiff as possible, the change in stiffness of the assembled stack is maximized.

The switchable spring of the conceptual design of the state switched acoustic transducer shown in Fig. 3 has an effective coupling coefficient, k_{eff}, which includes the electromechanical nature of the piezoelectric material and the effects of the joints in the stacks, the transducer case, the support structure, and the other transducer parts. The ratio of the effective stiffness modulus of the stiffness changing realization of a state switched acoustic transducer between the open and short circuit conditions for the switchable spring is given by

$$\frac{k_{\mathrm{oc}}}{k_{\mathrm{sc}}}=\frac{1}{1-k_{\mathrm{eff}}^2}. \tag{21}$$

The frequency ratio for the state switched acoustic transducer is then given by

$$\frac{f_{oc}}{f_{sc}} = \sqrt{\frac{1}{1-k_{eff}^2}}, \tag{22}$$

where f_{oc} is the open circuit resonance frequency and f_{sc} is the short circuit resonance frequency. Thus for a stiffness changing realization of a state switched acoustic transducer with an switchable spring of PZT-5H which has a piezoelectric coupling coefficient, k_{33}, of 0.75,[32] the maximum attainable increase in resonance frequency is 51%.

III. LUMPED ELEMENT STEADY STATE MODEL

To determine the frequency change between resonance states, a lumped parameter model was derived and verified experimentally.[21,22] The state switched acoustic transducer was assumed to be a monopole under free-field conditions as the characteristic dimension of the source was much less than the wavelength in both air and water for the frequency range of interest, below 1000 Hz. The magnitude of the radiated pressure, $|p|$, in the far field is related to the source dimensions and the acoustic medium by[33]

$$|p| = \frac{\rho_0}{4\pi r}|\dot{Q}|, \tag{23}$$

where ρ_0 is the density of the medium, $\dot{Q}$ is the volume acceleration of the source, and r is the distance from the source to the observation point. If the radiating surface is a piston of radius a

$$|p| = \frac{\rho_0 a^2 \omega^2 d}{4r}, \tag{24}$$

where ω is the angular frequency and d is the amplitude of the surface displacement. To increase the sound level at a prescribed distance from the source at a specific frequency, either the piston radius or the surface displacement need to be increased. Increasing the piston radius will increase the radiation damping which is proportional to the piston radius raised to the fourth power.[19] Generally, increased radiation damping will lead to higher source levels. However, the additional damping may reduce the source level when force-limited underwater. In displacement-limited transducers, the only option is to increase the surface area to raise the source level. Proper impedance matching will ensure maximum power transfer.

In the lumped parameter model, the head mass, spacer, and tail mass were treated as masses while the switchable spring, driver, and tierod were treated as stiffness elements. The effective masses of the stiffness elements of the source were included in the lumped masses of the system following the derivation of Stansfield.[34] The switchable spring and the driver stiffnesses included the piezoelectric coupling of the ceramic. Electrical, mechanical, and electromechanical losses were included for the piezoelectric ceramic.[35,36] All three losses are frequency dependent but were assumed to be constant for modeling purposes as the frequency range of interest was relatively small. The joint stiffness was included in the model for the switchable spring and the driver. The electrical resistance of the switch for the switchable spring was also included in the short circuit case as an additional loss in the system.

The effects of the surrounding medium, air or water, were modeled by lumped elements for the effective mass and damping of the surrounding medium.[19] This assumption is valid for $ka < 0.5$. Thus in water, the maximum frequency for which the added mass and damping may be modeled as lumped elements is 2350 Hz for a 2 in. radius piston. In air, the maximum frequency for using lumped elements for the added mass and damping is only 537 Hz for a 2 in. radius piston but the effect of added mass and damping in air is negligible.

The acoustic boundary condition used to calculate the radiation impedance was a piston at the end of a long rigid cylinder.[19,37] Mass loading, m_{rad}, and damping, c_{rad}, were calculated as[19]

$$m_{rad} = 1.927\rho_0 a^3, \tag{25a}$$

$$c_{rad} = \left(\frac{\pi}{4}\right)\left(\frac{\rho_0 \omega^2 a^4}{c}\right), \tag{25b}$$

where c is the speed of sound in the surrounding medium in meters per second. The surrounding medium was taken to be either air or water. A speed of sound of 343 m/s and a density of 1.21 kg/m^3 were used for air while a speed of sound of 1500 m/s and a density of 1026 kg/m^3 were used for water.[38]

Both the driver and the switchable spring were a stack of piezoelectric elements with the individual elements epoxied together. The thin-walled hollow cylinders used in the switchable spring were polarized in the direction of motion resulting in k_{33} coupling, which is only 4% lower than the optimal piezoelectric coupling factor.[39] Polarizing the cylinders radially through the thickness would have resulted in k_{31} coupling, which produces a much smaller maximum change in resonance, only 8.6%, due to a much lower coupling coefficient [$k_{31} = -0.39$ (Ref. 32)] for PZT-5H. Polarizing the cylinders through the height increased the number of joints in the stack but the advantage of the higher coupling was preferred over reducing the losses due to the stiffness of the joints.

Since motion was assumed to be only in the longitudinal direction, only one degree of freedom was required for each mass shown in Fig. 3. Model results will be shown with the experimental data in the next section.

IV. STATE SWITCHING CONCEPT DEMONSTRATION

State switching has been demonstrated with the acoustic transducer shown in Fig. 5, in air and water at frequencies between 810 and 1022 Hz.[21,22] Details of the transducer components are described in Table I. The switchable spring is a stack of 20 thin-walled hollow cylinders of piezoelectric ceramic (C-5500, Channel Industries, Inc., Santa Barbara, California) which were polarized in the longitudinal direction. The driver stack was made from four thin disks of piezoelectric ceramic (C-5400, Channel Industries, Inc., Santa

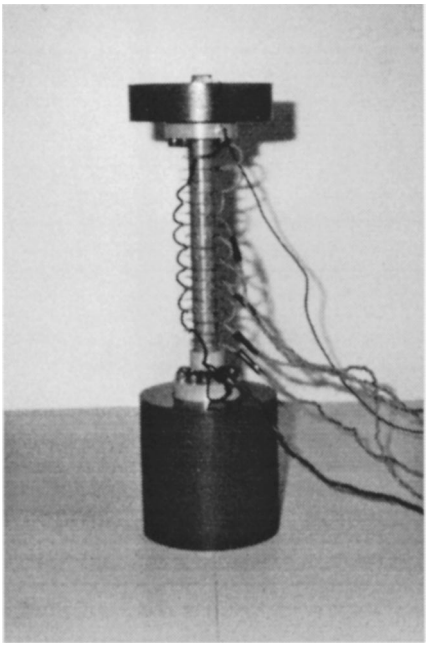

FIG. 5. State switched acoustic transducer.

Barbara, California) polarized in the longitudinal direction. The electrodes in the joints were made with flat wire mesh and conducting epoxy.

As the pressure in the far field is directly proportional to the acceleration of the head mass, an accelerometer was attached to the head mass for the in air measurements as shown in Fig. 5. Underwater measurements were made with a Brüel and Kjær 8100 Hydrophone. All data acquisition and system control operations were accomplished with a PC and a data acquisition board with appropriate amplification and filtering.

The state switched transducer resonates in air at 814 Hz when the switchable spring is completely short circuited and at 1019 Hz when the switchable spring is completely open circuited as shown in the displacement response in Fig. 6. The Q of the short circuit resonance is 56.8 and the Q of the open circuit resonance is 48.5. While both the open circuit and short circuit resonances are shown in Fig. 6, the state switched transducer does not exhibit both resonances simultaneously. At any given time, the transducer has only one resonance state. The distinction of the state switched transducer is that it can change its resonance state during operation. The frequency change between the full open circuit and full short circuit conditions is 205 Hz; the open circuit resonance is 25% larger than the short circuit resonance. Modeling results, shown in Fig. 6, closely agree with the experimental data. The difference between the experimental and modeled short circuit resonances is attributed to the variability of tabulated material properties for the piezoelectric ceramic.

Of particular importance is the high Q nature of the

TABLE I. Physical description of prototype state switched acoustic transducer.

Head mass		Electronically switchable spring	
Diameter	10.2 cm (4 in.)	Outer diameter	1.91 cm (0.75 in.)
Height (air)[a]	2.54 cm (1 in.)	Inner diameter	1.48 cm (0.584 in.)
Height (underwater)[a]	2.13 cm (0.84 in.)	Total height	15.2 cm (6 in.)
Mass (air)[a]	1.56 kg (3.44 lb)	Cylinder height	0.76 cm (0.3 in.)
Mass (underwater)[a]	1.33 kg (2.94 lb)	Number of cylinders	20
Material	Steel	Material[c]	C-5500 (PZT-5)
Tail mass		**Driver**	
Diameter	10.2 cm (4 in.)	Outer diameter	1.91 cm (0.75 in.)
Height (air)[b]	10.2 cm (4 in.)	Inner diameter	0.51 cm (0.2 in.)
Height (underwater)[b]	10.5 cm (4.125 in.)	Total height	1.02 cm (0.4 in.)
Mass (air)[b]	6.44 kg (14.2 lb)	Disk height	0.25 cm (0.1 in.)
Mass (underwater)[b]	6.04 kg (13.3 lb)	Number of disks	4
Material	Steel	Material[c]	C-5400 (PZT-4)
Spacer		**Attachment disks (head mass and tail mass)[d]**	
Outer diameter	2.54 cm (1 in.)	Outer diameter	5.08 cm (2 in.)
Inner diameter	0.676 cm (0.266 in.)	Inner diameter	0.676 cm (0.266 in.)
Height	1.27 cm (0.5 in.)	Thickness	1.27 cm (0.5 in.)
Mass	42.5 g (1.5 oz)	Mass	0.16 kg (0.36 lb)
Material	Steel	Material	Steel
Prestress rod (6-32 threaded rod)			
Outer diameter	0.351 cm (0.138 in.)		
Length	20.1 cm (7.9 in.)		
Material	Steel		

[a]Different head masses were used for the testing in air and underwater so that the transducer would resonate at approximately the same frequencies in air and underwater.
[b]The added height of the tail mass used for underwater testing compensated for the wiring access holes required to connect the piezoelectric ceramic to the electronics in the underwater case.
[c]All of the piezoelectric ceramic was manufactured by Channel Industries, Inc., Santa Barbara, California.
[d]The attachment disks were epoxied to the piezoelectric stacks and bolted to the masses.

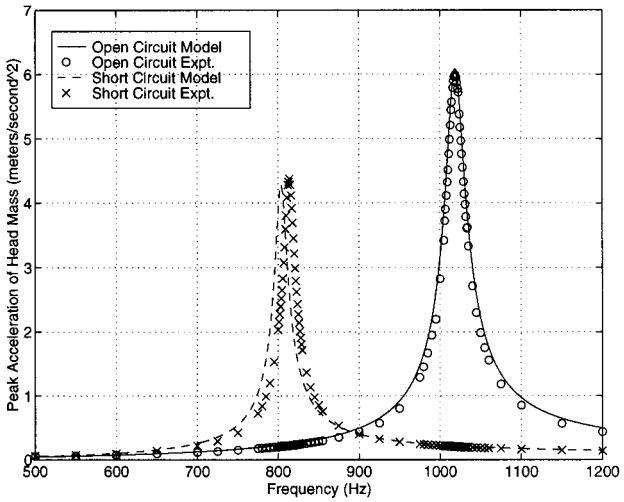

FIG. 6. Theoretical and experimental resonances of the state switched acoustic transducer in air.

response of the transducer. Specifically, the response at resonance is substantially higher than the response away from resonance. The response of the transducer when driven at the short circuit resonance frequency with the switchable spring open circuited is substantially lower than with the switchable spring short circuited. When the transducer is driven at the open circuit resonance frequency, the response is greater when the switchable spring is open circuited than when the switchable spring is short circuited.

Since the switchable spring is made from ten pairs of piezoelectric cylinders, intermediate resonances can be obtained by short circuiting only a portion of the switchable spring. In Fig. 7, nine intermediate resonances are shown between the full short circuit and full open circuit conditions. For example, short circuiting 50% of the switchable spring resulted in a resonance at 893 Hz. The segmentation of the switchable spring allows operation of the transducer at distinct resonances over a 205-Hz bandwidth. Further segmentation of the switchable spring or utilizing segments of differing lengths would increase the number of distinct resonance states over the same bandwidth.

The first step in state switching is to determine the damped natural frequency for each resonance state. The damped natural frequencies (rather than the frequencies of maximum response) are used in state switching to eliminate any transients that could be caused by interference between the drive signal and the damped natural response of the source. To state switch with a stiffness switching realization of a state switched acoustic transducer, the transducer is driven to resonance and at a zero displacement point, the resonance state of the transducer is changed and the drive frequency is simultaneously changed to the new resonance frequency. As the strain and electric field of a piezoelectric ceramic are in phase, the zero displacement point corresponds to a zero voltage point. Thus, state switching is done when the drive voltage is zero and the piezoelectric ceramic of both the driving stack and the electronically switchable spring is unstrained. The drive voltage waveform is a sinusoid whose frequency corresponds to the damped natural frequency of the transducer. Whenever the resonance state of the transducer is changed, the drive frequency is changed to the new damped natural frequency. A small change in the

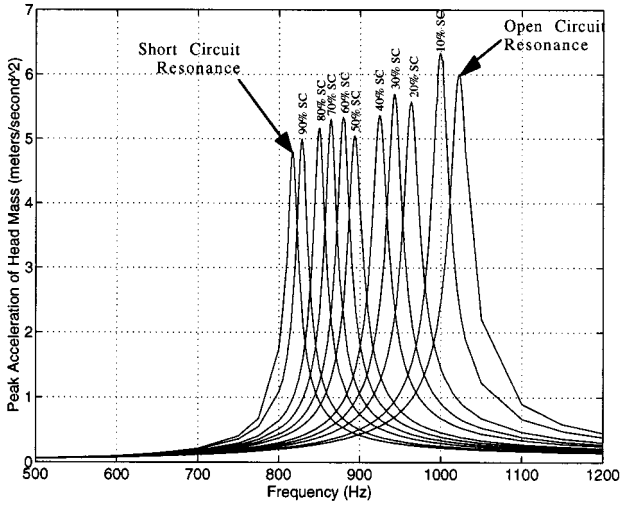

FIG. 7. Experimental intermediate resonances of state switched acoustic transducer in air.

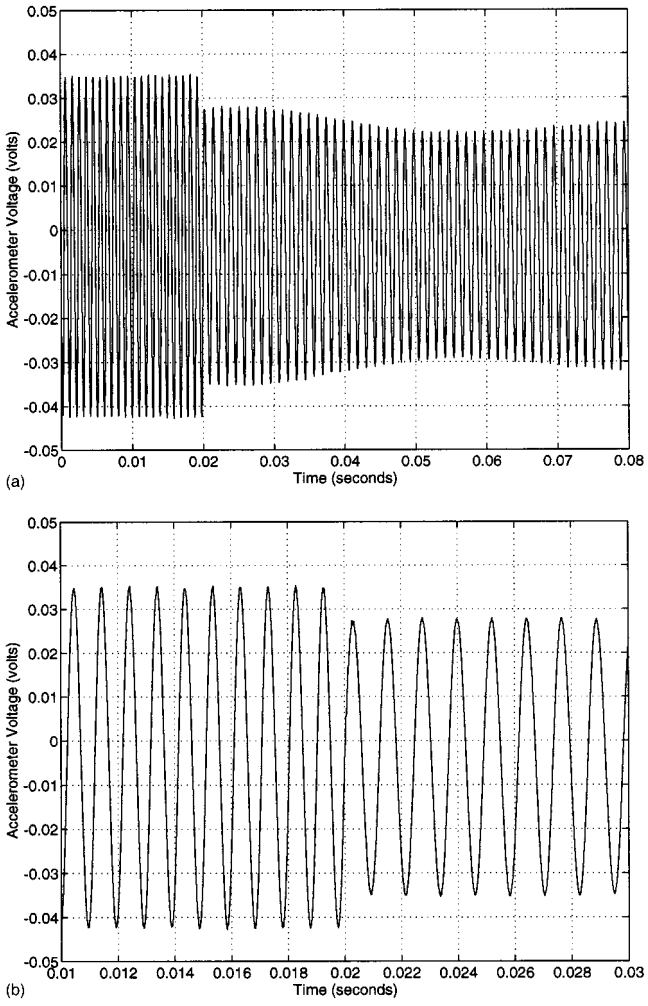

FIG. 8. State switching the state switched acoustic transducer from open to short circuit with adjusted drive voltages in air (switch at 0.02 s).

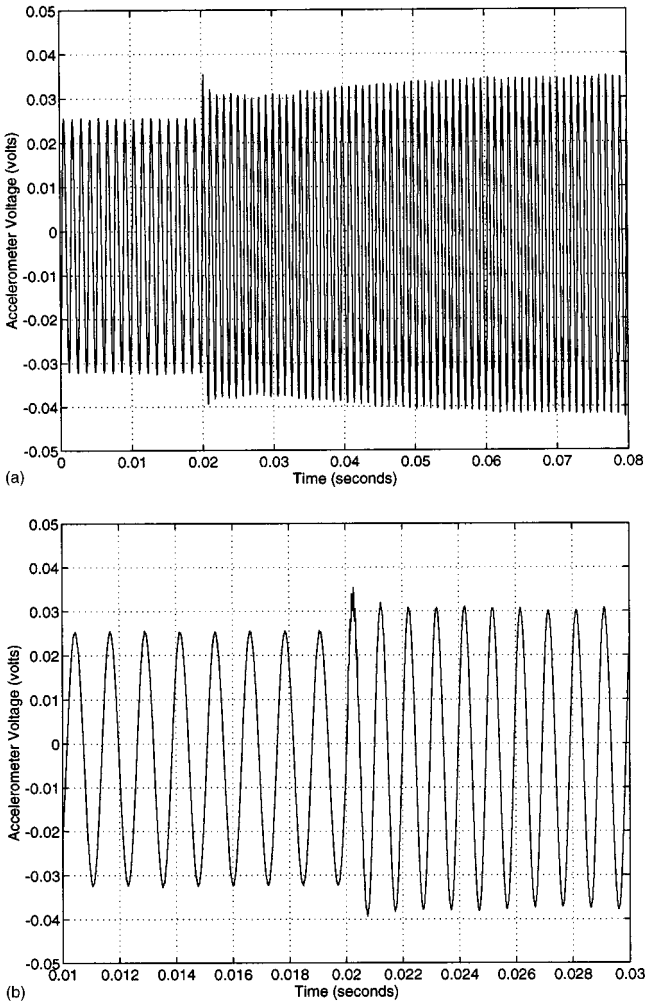

FIG. 9. State switching the state switched acoustic transducer from short to open circuit with adjusted drive voltages in air (switch at 0.02 s).

drive voltage amplitude is required to accommodate the difference between the short circuit and open circuit losses.

State switching was demonstrated with the transducer shown in Fig. 5 in air as shown in Figs. 8 and 9. The switchable spring is switched from open to short circuit in Fig. 8 while the switchable spring is switched from short to open circuit in Fig. 9. The frequency of the transmitted signal changes immediately while there is a small amplitude adjustment following the switch. Switching only the switchable spring but not the driving frequency, and vice versa, produces significant transient effects following the switch as seen in Figs. 10 and 11 (switching from open to short circuit in air). Switching the switchable spring and the driving frequency at a peak displacement (as opposed to switching at a zero displacement point for state switching) produces a high-frequency transient which decays rapidly as shown in Fig. 12. The high-frequency transient is caused by exciting the fundamental radial mode of the piezoelectric cylinders of the switchable spring by switching at the incorrect time. Similar results are seen when switching from short to open circuit.[21,22]

The transducer was mounted in a case as shown in Fig. 13 for underwater testing.[22] A membrane seal isolated the

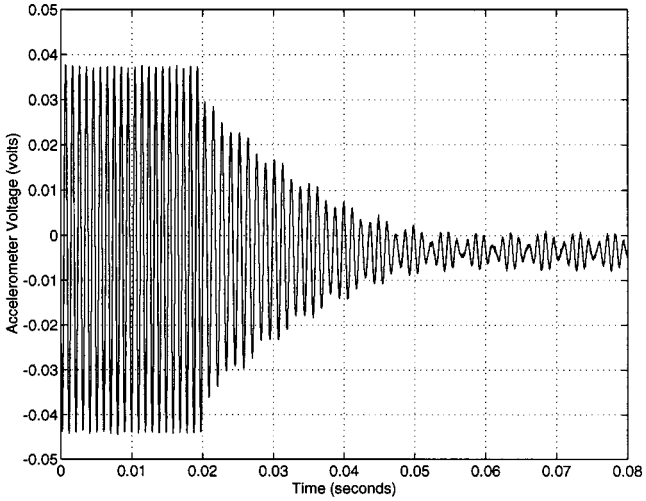

FIG. 10. Switching the switchable spring but not the driving frequency of the state switched acoustic transducer from open to short circuit in air (switch at 0.02 s).

piston from the water while O-rings sealed the interfaces between the case sections. The tail mass was suspended between two layers of corprene to vibrationally isolate the tail mass from the case so that motion of the tail mass would not radiate sound into the water. Two O-rings around the tail mass provided lateral stability for the transducer. Two wiring access holes in the tail mass allowed the electrical connections to be made at the rear of the transducer. Hence, the tail mass was lengthened to account for the mass lost to the wiring access holes in order to maintain the same resonances for the underwater testing as for the testing done in air. The electronic switch was enclosed in the case.

The water environment causes mass loading of the piston and increases the damping of the transducer, resulting in lower resonance frequencies and lower Q's underwater. For the underwater testing of the state switched acoustic transducer, the size of the head mass was reduced so that the transducer would have approximately the same resonances underwater as were observed in air in Figs. 6–12. The mod-

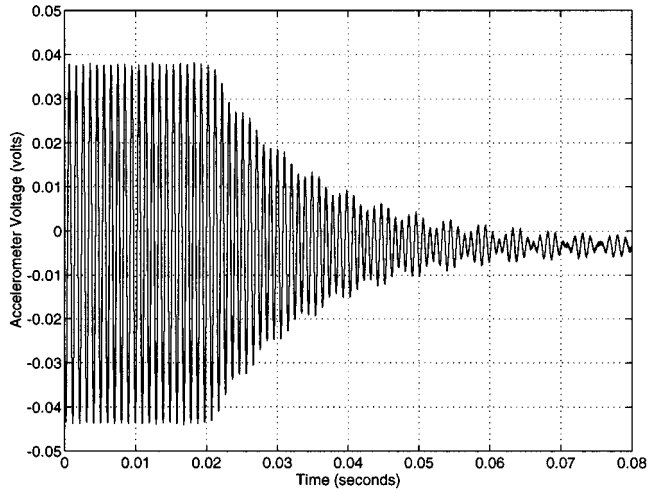

FIG. 11. Switching the driving frequency but not the switchable spring of the state switched acoustic transducer from open to short circuit in air (switch at 0.02 s).

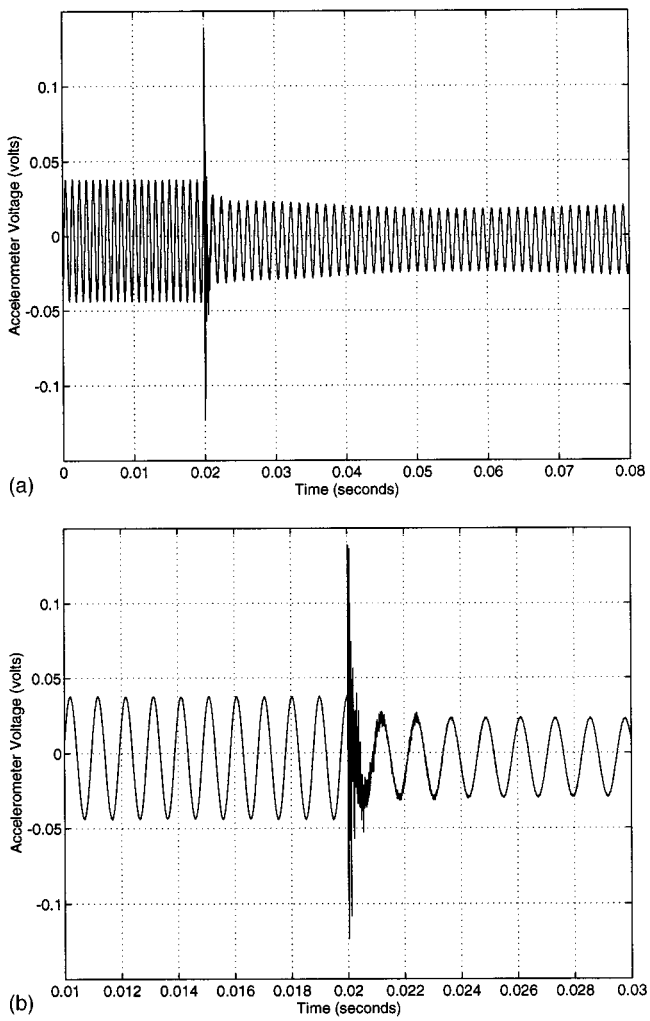

FIG. 12. Switching the switchable spring and the driving frequency of the state switched acoustic transducer from open to short circuit at a peak displacement in air (switch at 0.02 s).

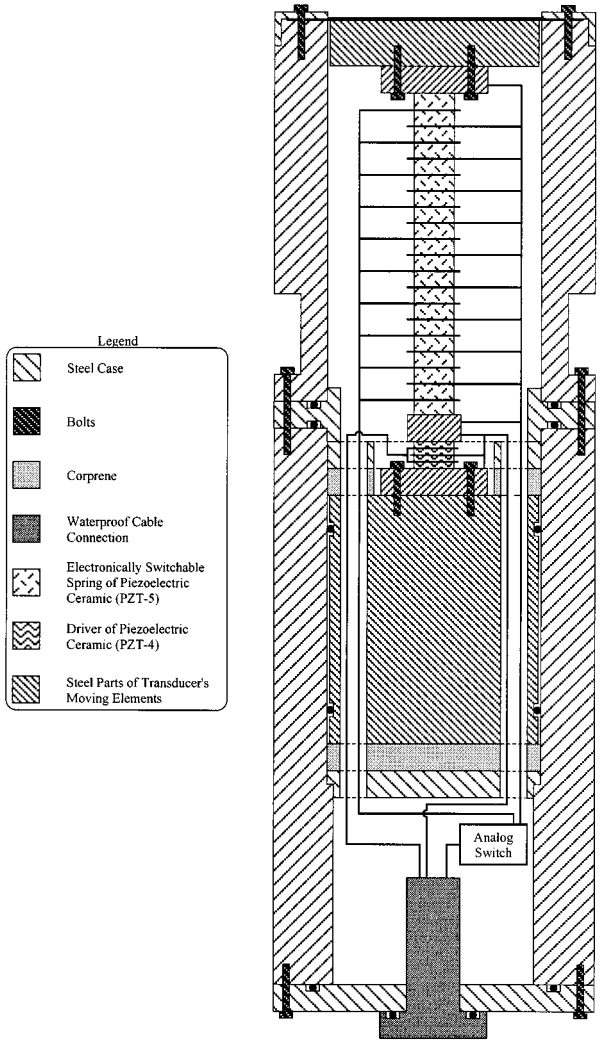

FIG. 13. Cross-sectional view of the state switched acoustic transducer in underwater case.

eled resonances of the transducer, with the thinner head mass in air and underwater, are shown in Fig. 14. The sealed transducer had a Q of 36.1 with its fundamental resonance at 1113 Hz in air with the switchable spring open circuited and a Q of 28.3 with its fundamental resonance at 892 Hz in air with the switchable spring short circuited. The damped natural frequencies were found to be 1016.2 Hz with a Q of 15.4 (open circuit switchable spring) and 817.9 Hz with a Q of 15.7 (short circuit switchable spring) underwater. State switching underwater from open to short circuit is shown in Fig. 15 and from short to open circuit in Fig. 16 (the apparent jitter in the signal is due to noise).

As shown in the experimental data, the state switched transducer can be changed between two discrete resonance states with a change of 25% in resonance frequency. With appropriate switching and control algorithms, state switching could be used to generate a wide variety of frequency modulated or frequency coded signals for data transmission, sonar, and propagation experiments. The frequency could potentially be changed as often as every half cycle since the frequency can be changed whenever the piston is at the zero displacement point.

V. ADVANTAGES OF STATE SWITCHING

Comparisons of state switched transducers with traditional tonpilz transducers indicate that their efficiencies are

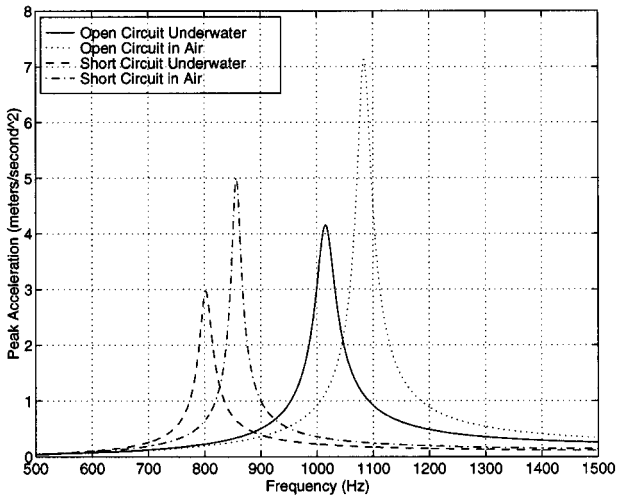

FIG. 14. Modeled response of the state switched acoustic transducer in air and underwater with thinner head mass.

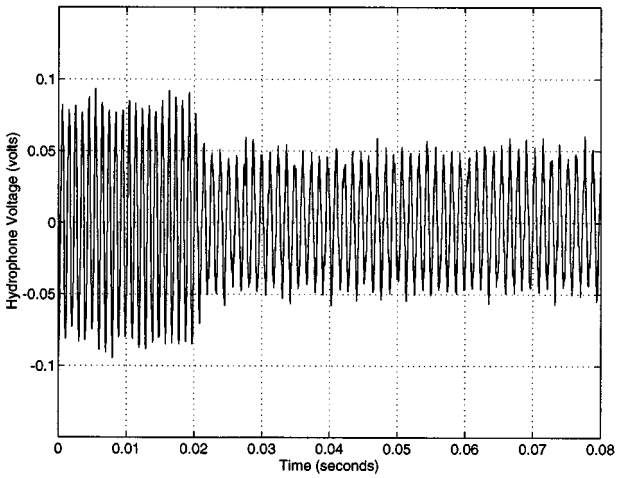

FIG. 15. State switching the state switched acoustic transducer from open to short circuit underwater (switch at 0.02 s).

comparable even though the overall coupling of the state switched transducer is decreased by the switchable spring. Woollett[27,30,31] has shown that the addition of springs to a transducer reduces the overall coupling. Moffett and Marshall[28] have shown that the overall coupling of a transducer can be reduced by a long cable, a stress rod, and glue joints. Springs in parallel with the piezoelectric ceramic[27,30,31] (i.e., seals or oil enclosed within the case for pressure compensation) reduce the overall coupling, k, according to

$$k^2=\frac{(k')^2}{1+(c_M^{I'}/c_s)}=\frac{(k')^2}{1+(1-(k')^2)(c_M^{E'}/c_s)}, \tag{26}$$

where $c_M^{I'}$ is the open circuit compliance of the piezoelectric ceramic, $c_M^{E'}$ is the short circuit compliance of the piezoelectric ceramic, c_s is the compliance of the springs in parallel, and k' is the coupling coefficient the transducer would have without the parallel springs. Thus, a parallel spring that is softer than the ceramic stack will reduce the coupling less than a spring that is stiffer than the ceramic stack would. Similarly, springs in series with the ceramic stack[27,30,31] (i.e., a passive spring used to lower the transducer's resonance frequency or the joints in the ceramic stack) reduce the coupling according to

$$k^2=\frac{(k')^2}{1+c_s/c_M^{E'}}. \tag{27}$$

In this case, springs that are stiffer than the ceramic stack will reduce the overall coupling less than springs that are much softer than the ceramic stack. In the state switched transducer, the overall coupling of the transducer is reduced from 0.71 to 0.11 due to the addition of the switchable spring (neglecting the effects of the seals, the mounting method, the joints in the stack and the prestress rod).

In spite of the low overall coupling, the electroacoustic efficiency is still high due to the high Q nature of the state switched transducer. The electroacoustic efficiency,[40] η_{ea}, of a transducer is simply the product of the electromechanical efficiency, η_{em}, and the mechanoacoustical efficiency, η_{ma}. As the state switched transducer is always operated at resonance, it is the efficiency at resonance which is of importance. The electromechanical efficiency at resonance is determined by[40]

$$\eta_{em}=\frac{1}{1+\dfrac{\tan\delta}{[k^2/(1-k^2)](Q_{MW}^E)}}, \tag{28}$$

where $\tan\delta$ is the loss tangent, k is the coupling coefficient, and Q_{MW}^E is the mechanical quality factor of the transducer when operated under constant electric field underwater. The electromechanical efficiency of the state switched transducer at resonance is then 0.9796 for $\tan\delta=0.004$, $k=0.11$, and $Q_{MW}^E=15.7$; if the coupling were 0.71, the electromechanical efficiency would be 0.9997. The obvious disadvantage is that the slightly higher electromechanical efficiency gained by not state switching is accompanied by the narrow bandwidth of the high Q resonance. As the mechanoacoustical efficiency is determined by the transducer's mechanical losses and the radiation resistance, it is not affected by the switchable spring and the reduced overall coupling.

As the state switched transducer's maximum source level is limited by the allowable strain in the switchable spring, the state switched source level is comparable to the source level attained by driving both the switchable spring and the driver stack. The transmitting voltage responses and efficiencies of the state switched acoustic transducer when used in the state switching mode at the open circuit and short circuit resonances are shown in Figs. 17 and 18 with the response when the switchable spring is driven at maximum allowable strain with the same electric field applied to the driver stack as in the state switched cases. The efficiency is defined as the ratio of the acoustic power output to the required electrical volt-amperes (both resistive and reactive) input. Low dielectric losses are included in both the driver and the switchable spring stacks in Fig. 17. In Fig. 18, higher dielectric losses are included when the piezoelectric ceramic is driven with a high electric field.

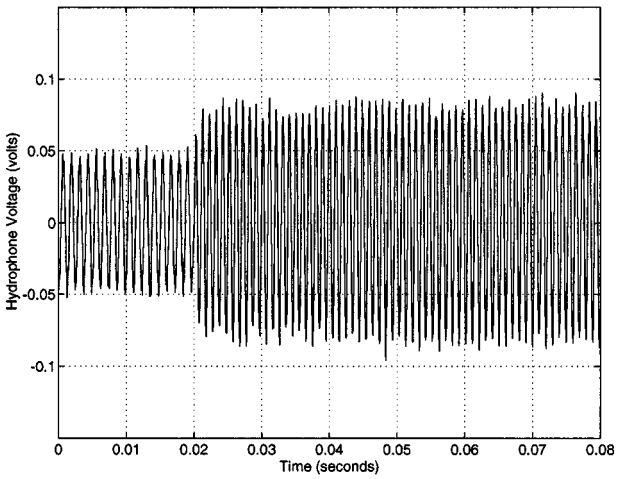

FIG. 16. State switching the state switched acoustic transducer from short to open circuit underwater (switch at 0.02 s).

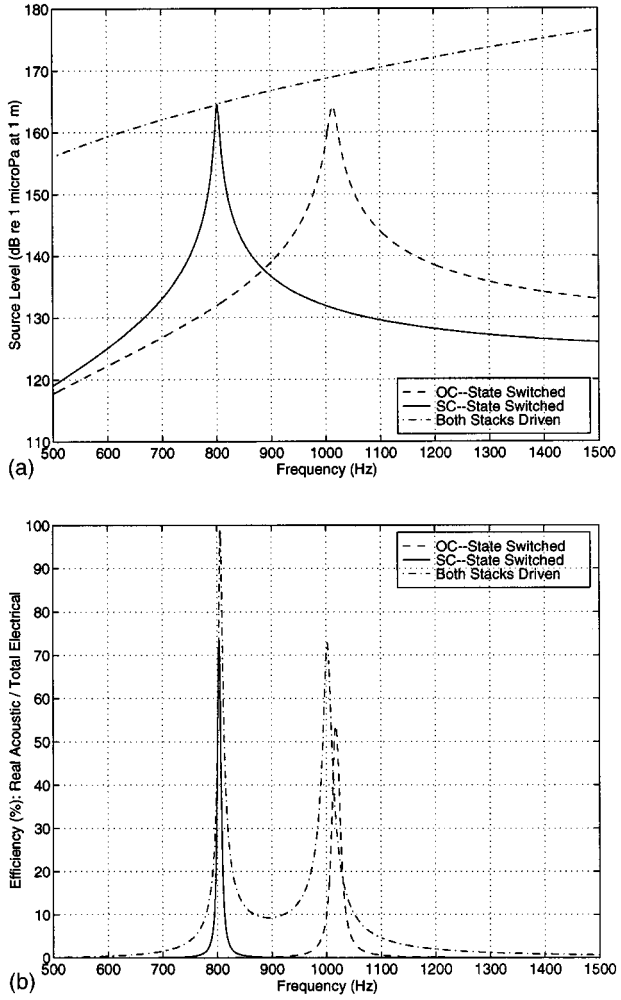

FIG. 17. Modeling of the state switched acoustic transducer in the state switching mode and with both the switchable spring and the driver stack being driven with low dielectric losses. (a) Transmitting voltage response; (b) efficiency.

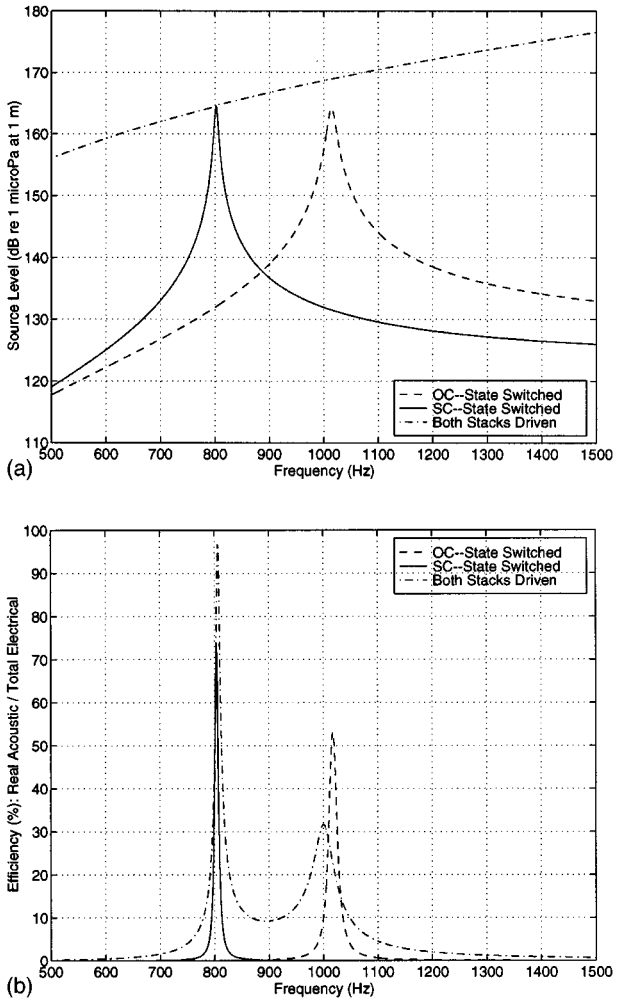

FIG. 18. Modeling of the state switched acoustic transducer in the state switching mode and with both the switchable spring and the driver stack being driven with higher dielectric losses. (a) Transmitting voltage response; (b) efficiency.

It is important to note that the maximum source level of the transducer at resonance is limited by the allowable strain in the switchable spring. Thus, driving the switchable spring will not substantially improve the source level at resonance. However, higher source levels are possible when the transducer is driven off-resonance as a tonpilz transducer (as compared to the state switched mode). The disadvantage of driving the transducer in this manner is the increased input electrical power requirement due to the low efficiencies at frequencies removed from resonance. Efficiency is not a problem if one is just going between the constant voltage and the constant current frequencies but in this case, increased effective bandwidth will not be realized since the constant voltage resonance will still have to ring up and ring down.

A tonpilz transducer has a fundamental resonance for constant driving voltage and for constant driving current as seen in Fig. 17. It may be possible to switch between these two resonances by switching the input electrical drive signal between the constant current and constant voltage conditions while simultaneously changing the driving frequency. This effectively state switches the transducer through the amplifier. However, operating the transducer in this manner limits the output signal to the constant voltage and constant current resonances; the transducer cannot be switched to intermediate resonance states. State switching by ''switching the amplifier'' would seem to produce little advantage and increase the complexity and expense of the system.

The application of state switching to a typical high Q transducer substantially increases its bandwidth for the purpose of transmitting frequency modulated or frequency coded signals. The ''effective bandwidth'' of the state switched transducer is a function of both the operational characteristics of the transducer and the transmitted signal and can be more than twice the frequency separation of the two resonances.[22] It is apparent from examination of Figs. 8, 9, 15, and 16 that the ''effective bandwidth'' is larger than the frequency separation of the two resonances.

The simulated response of a state switched acoustic transducer with a switchable spring that can be infinitely adjusted to change the resonance state between 800 and 1000 Hz is compared with simulations of two high Q ($=25$) transducers in Fig. 19. The first high Q transducer has a damped natural frequency of 800 Hz while the second high Q transducer has a damped natural frequency of 1000 Hz in Fig. 19.

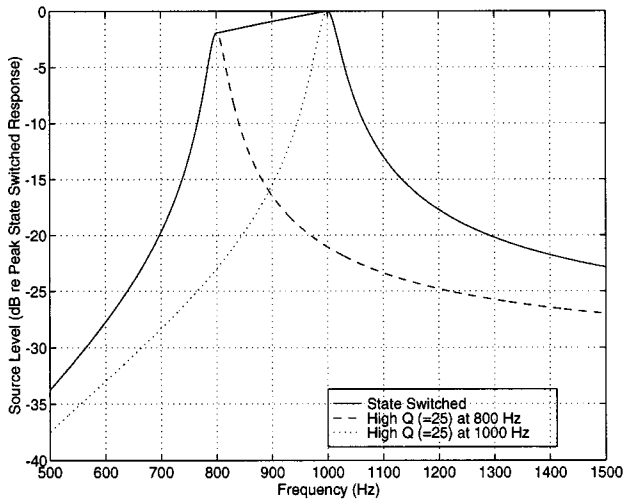

FIG. 19. Simulations of state switched transducer and typical high Q (=25) transducers (state switching between 800 and 1000 Hz with a Q of 25).

The source levels are referenced to the peak response of the state switched transducer at 1000 Hz. Below 800 Hz, the state switched transducer's response is that of a high Q (=25) transducer with a resonance at 800 Hz. Above 1000 Hz, the state switched transducer's response corresponds to a high Q (=25) transducer that is resonant at 1000 Hz. Between 800 and 1000 Hz, the state switched transducer's response is that of a transducer which is resonant at the chosen frequency since the switchable spring is assumed to be infinitely adjustable such that the transducer's resonance can be switched to any frequency between 800 and 1000 Hz. By maintaining the response at resonance between 800 and 1000 Hz, the state switched transducer's source level is maximized over that bandwidth making it particularly useful for frequency-modulated sonar. Outside the state switching region, the amplitude decreases due to the high Q of the resonance. The state switched transducer has a bandwidth of 228.4 Hz between the half-power points of the response with a peak response at 1000 Hz and an effective Q of 4.4.

The bandwidth of a typical high Q transducer without the advantage of state switching is substantially lower as seen in Fig. 19. For a transducer with a Q of 25 and a damped natural resonance at 800 Hz, the bandwidth between half-power points is 32 Hz as shown in Fig. 19. Changing the damped natural frequency to 1000 Hz produces a bandwidth of 40 Hz.

A frequency modulated signal could be transmitted with a state switched transducer utilizing the state switched bandwidth by simply changing the drive frequency and the resonance frequency of the transducer accordingly. With the infinitely adjustable switchable spring of the simulated transducer in Fig. 19, the resonance frequency and the drive frequency would always be the same. However, the state switched transducer shown in Fig. 5 did not have an infinitely adjustable switchable spring but rather had 11 distinct resonance states. By simulating the response of a state switched transducer with 11 distinct resonance states equally spaced over the frequency range from 800 to 1000 Hz at each resonance state, a maximum source level can be determined and is shown in Fig. 20. Each resonance state of the state switched transducer has a frequency range where it exhibits the maximum response. When the driving frequency of a frequency modulated signal is within a particular resonance state's frequency range, the transducer is set to that particular resonance. The source level decreases slightly when the drive frequency is different from the resonance frequency, but not substantially. A high source level is maintained throughout the state switching frequency range due to the resonance operation. Further segmentation of the switchable spring or utilizing unequal segments would increase the number of resonance states and more closely approximate an infinitely adjustable switchable spring.

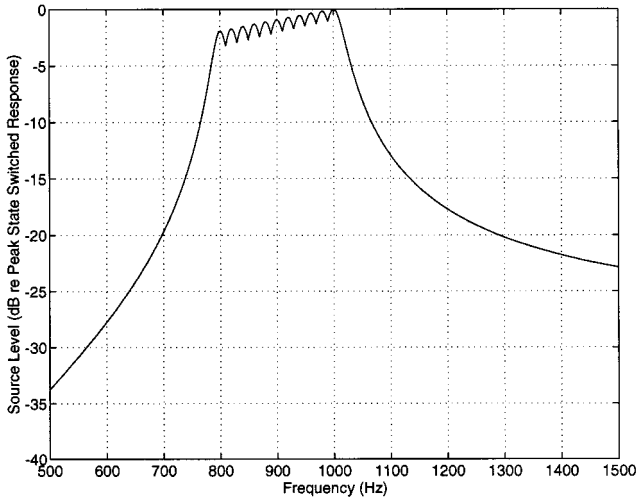

FIG. 20. Maximum source level for frequency modulated signal generation with a state switched transducer with 11 distinct resonant states.

VI. CONCLUSIONS

The ability to switch between discrete frequencies over a large bandwidth while maintaining high source levels and efficiencies makes the state switched transducer useful for active sonar systems, underwater research, and communication systems. Application of the state switching concept to an acoustic transducer makes operation possible at resonance for maximum efficiency while the operating bandwidth is determined by the magnitude of the frequency change between the distinct resonance states. A state switched transducer with two discrete resonance frequencies could transmit coded and pseudorandom signals quite easily; segmentation of the switchable spring increases the number of resonance states making it possible to produce the chirp signals commonly used in active sonar systems.

By incorporating the state switching concept into a high Q transducer, the advantages of the high Q resonance (large displacements, large forces, and high efficiency) are retained while the slow response time and narrow bandwidth of a high Q resonant source are avoided. Thus state switching provides the means of incorporating high power and broadband operation at low frequencies in an underwater transducer. Switching between signaling frequencies can be accomplished with a state switched transducer without the

transient effects observed in the response of a high Q transducer being driven by the same coded signal.[22] Further, the increased bandwidth and signal level improve the accuracy of arrival time measurements[4] for range determination.

The control of the electrical boundary condition of the piezoelectric elements of the switchable spring provides an efficient and straightforward method of changing the resonance of the state switched acoustic transducer by more than 25% (potentially up to 51% for PZT-5H). While the demonstrated state switched transducer is a tonpilz transducer which uses a stack of piezoelectric tubes as the switchable spring, other configurations are possible. Presently, designs involving displacement amplification are being considered in order to lower the resonance frequencies and increase the source level for a given size source. Other materials such as Terfenol-D®[41] or single crystal relaxors[42] may be used as the active material of the switchable spring. With coupling as high as 0.75, Terfenol-D has the potential to produce a 51% change in resonance frequency. Single crystal relaxors could increase the resonance frequency by 190% due to coupling as high as 0.938.

ACKNOWLEDGMENT

This work was supported by the Office of Naval Research.

[1] W. H. Munk, R. C. Spindel, A. Baggeroer, and T. G. Birdsall, ''The Heard Island Feasibility Test,'' J. Acoust. Soc. Am. **96**, 2330–2342 (1994).
[2] A. Baggeroer and W. Munk, ''The Heard Island Feasibility Test,'' Phys. Today **45**(9), 22–30 (1992).
[3] C. S. Clay and H. Medwin, *Acoustical Oceanography: Principles and Applications* (Wiley, New York, 1977), pp. 96–102.
[4] W. Munk and C. Wunsch, ''Observing the ocean in the 1990s,'' Philos. Trans. R. Soc. London, Ser. A **307**, 439–464 (1982).
[5] D. Stansfield, *Underwater Electroacoustic Transducers, A Handbook for Users and Designers* (Bath University, Bath, UK, and Institute of Acoustics, St. Albans, 1991).
[6] J. V. Bouyoucos, ''Hydroacoustic transduction,'' J. Acoust. Soc. Am. **57**, 1341–1351 (1975).
[7] K. D. Rolt, ''History of the flextensional electroacoustic transducer,'' J. Acoust. Soc. Am. **87**, 1340–1349 (1990).
[8] C. C. Sims, ''High-fidelity underwater sound transducers,'' Proc. IRE **47**, 866–871 (1959).
[9] W. M. Leach, Jr., T. E. Brewer, and M. R. Walls, Jr., *An Investigation of Electroacoustic Radiators for Low-Frequency Underwater Sound Generation* (Georgia Institute of Technology, School of Electrical Engineering, Atlanta, GA, 1978), pp. 25–67.
[10] T. A. Henriquez and A. M. Young, ''The Helmholtz resonator as a high-power, deep submergence source for frequencies below 500 Hz,'' J. Acoust. Soc. Am. **67**, 1555–1558 (1980).
[11] J. E. Barger and W. R. Hamblen, ''The air gun impulsive underwater transducer,'' J. Acoust. Soc. Am. **68**, 1038–1045 (1980).
[12] C. C. Sims, ''Bubble transducer for radiating high-power low-frequency sound in water,'' J. Acoust. Soc. Am. **32**, 1305–1308 (1960).
[13] D. Stansfield, *Underwater Electroacoustic Transducers, A Handbook for Users and Designers* (Bath University, Bath, UK, and Institute of Acoustics, St. Albans, 1991), pp. 345–372.
[14] J. N. Decarpigny, B. Hamonic, and O. B. Wilson, Jr., ''The design of low-frequency underwater acoustic projectors: Present status and future trends,'' IEEE J. Ocean Eng. **16**, 107–122 (1991).
[15] O. B. Wilson, *Introduction to the Theory and Design of Sonar Transducers* (Peninsula, Los Altos, CA, 1988), pp. 109–126.
[16] R. S. Woollett, ''Basic problems caused by depth and size constraints in low-frequency underwater transducers,'' J. Acoust. Soc. Am. **68**, 1031–1037 (1980).
[17] A. D. Pierce, *Acoustics, An Introduction to its Physical Principles and Applications* (Acoustical Society of America, Woodbury, NY, 1989), pp. 220–225.
[18] F. Fahy, *Sound and Structural Vibration, Radiation, Transmission, and Response* (Academic, San Diego, CA, 1985), pp. 113–125.
[19] L. L. Beranek, *Acoustics* (Acoustical Society of America, Woodbury, NY, 1993), pp. 116–128.
[20] W. Munk, D. Webb, and T. Birdsall (unpublished notes, 1980, 1981).
[21] G. D. Larson and P. H. Rogers, ''State switched acoustic source,'' J. Acoust. Soc. Am. **96**, 3317(A) (1994).
[22] G. D. Larson, ''The analysis and realization of a state switched acoustic transducer,'' Ph. D. dissertation, Georgia Institute of Technology, Atlanta, GA, May 1996.
[23] O. B. Wilson, *Introduction to the Theory and Design of Sonar Transducers* (Peninsula, Los Altos, California, 1988), pp. 69–77.
[24] W. G. Cady, *Piezoelectricity, An Introduction to the Theory and Applications of Electromechanical Phenomena in Crystals* (McGraw-Hill, New York, 1946), pp. 260–283.
[25] G. S. Kino, *Acoustic Waves: Devices, Imaging, and Analog Signal Processing* (Prentice-Hall, Englewood Cliffs, NJ, 1987), pp. 21–22.
[26] D. A. Berlincourt, D. R. Curran, and H. Jaffe, ''Piezoelectric and piezomagnetic materials and their function in transducers,'' in *Physical Acoustics, Principles and Methods*, edited by W. P. Mason (Academic, New York, 1964), Vol. I A, Chapter 3, p. 189.
[27] R. S. Woollett, ''Transducer comparison methods based on the electromechanical coupling-coefficient concept,'' IRE Convention Record, Part 9, Session 12, pp. 23–27 (1957).
[28] M. B. Moffett and W. J. Marshall, Jr., ''The importance of coupling factor for underwater acoustic projectors,'' NUWC-NPT-TD-10691, Naval Undersea Warfare Center Division, Newport, RI [Also: J. Acoust. Soc. Am. **95**, 2857(A) (1994)].
[29] D. Stansfield, *Underwater Electroacoustic Transducers, A Handbook for Users and Designers* (Bath University, Bath, UK, and Institute of Acoustics, St. Albans, 1991), pp. 179–237.
[30] R. S. Woollett, ''Effective coupling factor of single-degree-of-freedom transducers,'' J. Acoust. Soc. Am. **40**, 1112–1123 (1966).
[31] R. S. Woollett, *Sonar Transducer Fundamentals* (Naval Underwater Systems Center, Newport Laboratory, Newport, RI, New London Laboratory, New London, CT), Sec. I, pp. 156–159.
[32] Morgan Matroc, Inc., Electro Ceramics Division, *Guide to Modern Piezoelectric Ceramics* (Bedford, Ohio, 1993).
[33] A. D. Pierce, *Acoustics, An Introduction to its Physical Principles and Applications* (Acoustical Society of America, Woodbury, NY, 1989), pp. 153–155.
[34] D. Stansfield, *Underwater Electroacoustic Transducers, A Handbook for Users and Designers* (Bath University, Bath, UK, and Institute of Acoustics, St. Albans, 1991), pp. 197–198.
[35] D. Berlincourt, ''Piezoelectric crystals and ceramics,'' in *Ultrasonic Transducer Materials*, edited by O. E. Mattiat (Plenum, New York, 1971), Chap. 2, pp. 84–86.
[36] R. Holland, ''Representation of dielectric, elastic, and piezoelectric losses by complex coefficients,'' IEEE Trans. Sonics Ultrason. **SU-14**, 18–20 (1967).
[37] W. M. Leach, Jr., T. E. Brewer, and M. R. Walls, Jr., *An Investigation of Electroacoustic Radiators for Low-Frequency Underwater Sound Generation* (Georgia Institute of Technology, School of Electrical Engineering, Atlanta, GA, 1978), pp. 7–19.
[38] L. E. Kinsler, A. R. Frey, A. B. Coppens, and J. V. Sanders, *Fundamentals of Acoustics* (Wiley, New York, 1982), 3rd ed., pp. 462–463.
[39] R. S. Woollett, *Sonar Transducer Fundamentals* (Naval Underwater Systems Center, Newport Laboratory, Newport, RI, New London Laboratory, New London, CT), Section I, pp. 124–127.
[40] R. S. Woollett, *Sonar Transducer Fundamentals* (Naval Underwater Systems Center, Newport Laboratory, Newport, RI, New London Laboratory, New London, CT), Section I, pp. 73–77.
[41] J. L. Butler, *Application Manual for the Design of Etrema Terfenol-D® Magnetostrictive Transducers*, Edge Technologies, Inc., 1988.
[42] S. E. Park and T. R. Shrout, ''Characteristics of relaxor-based piezoelectric single crystals for ultrasonic transducers,'' IEEE Trans. Ultrason. Ferroelectr. Freq. Control (in press, 1997).

Theoretical and experimental study of transducers aimed at low-frequency ultrasonic atomization of liquids

Daniel Sindayihebura and Léon Bolle
Université catholique de Louvain, Department of Mechanical Engineering, Place du Levant, 2-1348 Louvain-la-neuve, Belgium

Alain Cornet and Luc Joannes
Université catholique de Louvain, Department of Physics, Chemin du Cyclotron, 2-1348 Louvain-la-neuve, Belgium

(Received 5 August 1996; accepted for publication 17 November 1997)

The fine atomization of liquids by means of low-frequency ultrasonic atomizers (about 50 kHz) results from unstable surface waves generated on the free surface of a thin liquid film. This thin liquid film develops as the liquid spreads fast over the atomizing surface of the atomizer. The displacement amplitude of the atomizing surface must be greater than 2 μm to initiate the atomization process. This may be achieved using a displacement amplitude transformer. The present study focuses on an analytical analysis of the longitudinal oscillations stimulated by the piezoelectric elements in a stepped horn which operates as an amplitude transformer. A sizing method of the stepped horn is established and experimentally tested. The influence of the materials' mechanical damping on the displacement amplitude of the atomizing surface is investigated. The comparison between theoretical and experimental results allows the determination of the internal damping coefficient. © *1998 Acoustical Society of America.* [S0001-4966(98)01103-5]

PACS numbers: 43.38.Ar, 43.35.Yb, 43.35.Zc [SLE]

LIST OF SYMBOLS

a	displacement amplitude of the atomizing surface per unit applied voltage
A_1	cross-sectional area of the backing piece
A_2	cross-sectional area of the piezoelectric element ($A_2=A_{2.1}=A_{2.2}$)
A_3	cross-sectional area of the front part of the stepped horn
A_4	cross-sectional area of the atomizing surface
b	thickness of the piezoelectric element
C_m^E	elastic stiffness under conditions of constant electric field
d_i	inside diameter of the piezoelectric element
d_0	outside diameter of the piezoelectric element
d_1	diameter of the backing piece ($d_1=d_0$)
d_2	diameter of the atomizing surface
D_m	electric displacement
e	piezoelectric coefficient
E_m	electric field
E_{ym}	Young's modulus
f	working frequency
j	complex number ($j=\sqrt{-1}$)
k_m	wave number
l_1	length of the backing piece
l_2, l_3	lengths of the parts of stepped horn
Q_m	mechanical quality factor
r_m	internal mechanical damping
S	strain ($S=\partial\xi/\partial x$)
t	time
v_m	velocity of the propagation of the acoustic waves
V_m	electric potential
V_0	amplitude of the electric potential
Z_m	acoustic impedance
μ_m	internal mechanical damping coefficient
ε^s	electric permittivity under conditions of constant strain
λ_3	wavelength in the stepped horn
ξ	displacement
ρ	density
σ, σ_m	normal stress
ω	angular frequency

Subscripts

1	pertaining to the backing piece
2.1, 2.2	pertaining to the piezoelectric elements
3, 4	pertaining to the stepped horn

Superscripts

E	related to constant electric field
S	related to constant strain
m	related to part of the transducer ($m=1$, 2.1, 2.2, 3, and 4)

INTRODUCTION

Low-frequency ultrasonic atomizers which are used most often consist of two identical piezoelectric elements sandwiched between a support and a stepped horn, the latter operating as a displacement amplitude transformer. The stepped horn is usually made of materials having a good resistance to fatigue, like magnesium, aluminum, or titanium alloys. Its free end forms the atomization surface.

Many authors have studied the vibrations of piezoelectric elements exhibiting various geometrical shapes such as rectangle, disk, and ring in order to get sufficient insight into their physical behavior.[1–3] Several versions of amplitude transformers like stepped horn, exponential horn, and conical horn also have been analyzed theoretically and experimentally.[4,5] It results that the stepped horns are suited for high displacement amplification, while piezoelectric elements which are ring shaped make easy the assembling of the transducers.

Unfortunately, very little work has been carried out on the whole system, which includes the support, the piezoelectric elements, and the amplitude transformer all together. The main reference in this respect is the theoretical study based on the electrical equivalent circuit of the transducer, which has been published by Bangviwat *et al.*[6] This study shows how to design a stepped horn aimed at maximizing the power delivery to a given load impedance. As suggested by the authors, this work could be interesting in design of ultrasonic probes like those which are used in some medical and welding applications.[5] In the field of liquid atomization, it would be helpful in determining the size of transducers appropriate for the atomization techniques based on focused acoustic beams. In this case, a high acoustic energy is applied to the liquid free surface in order to tear it. This leads to a rough liquid atomization, described as ''a volcano'' consisting of droplets of random sizes.[7] Focused acoustic energy may also be used to generate single droplets of controlled diameter and velocity.

The aim of the present work is to perform an analytical modeling of the behavior of transducers used in fine liquid atomization. Droplet formation is a consequence of the growth of surface waves generated on the free surface of a thin liquid film that develops as the liquid spreads over the atomizing surface. In other words, the droplets are produced from the peeling of the liquid/air interface. The resultant spray is characterized by a low inertia of the droplets and an uniform droplet diameter.[8] A procedure for the determination of the stepped horn dimensions leading to displacement amplitude of the atomizing surface needed to initiate such atomization process is presented. This displacement amplitude must be greater than 2 μm. The load on the atomizing surface is neglected as the liquid film, which is formed during the atomization process, remains very thin. The validity of the sizing method established is studied. Actual values of the displacement amplitude of the atomizing surface are obtained by means of an interferometric measurement technique. Finally, the influence of the internal mechanical damping on the displacement amplitude is shown.

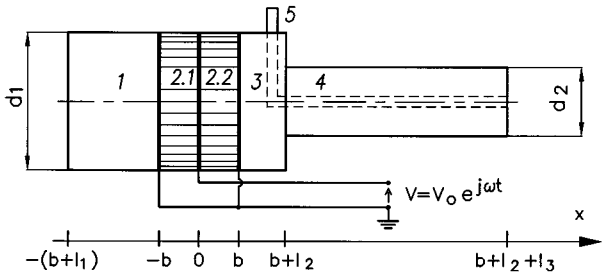

FIG. 1. Geometrical configuration of the transducer.

I. FORMULATION OF THE PROBLEM

We are interested in the propagation of longitudinal oscillations through the transducer shown in Fig. 1. l_1 represents the length of the backing piece (1), l_2 and l_3 are the lengths of the amplitude transformer parts (3 and 4), and d_2 is the outer diameter of the atomizing surface which can be varied according to the needed liquid flow rate. The liquid is supplied to the atomizing surface through hole 5. Acoustic waves are produced by two piezoelectric ceramic elements (2.1 and 2.2) whose thickness b and diameter d_1 are fixed by the manufacturer. Both the backing piece and the amplitude transformer are assumed to be made of isotropic materials and the physical properties uniformly distributed.

A. Equation of waves

The equations of plane waves in the x direction are derived from the linear momentum balance equations. Neglecting the body force, we have:

$$\frac{\partial \sigma}{\partial x} = \rho \frac{\partial^2 \xi}{\partial t^2}, \tag{1}$$

where σ denotes the normal stress, ρ the density, ξ the displacement, and t the time. The stress σ is given by the constitutive equations.

1. Constitutive equations

We distinguish the piezoelectric elements, typically anisotropic and exhibiting interactive mechanical and electrical effects, from the support and the amplitude transformer which are made of isotropic materials whose electrical effects can be neglected.

In general, the following constitutive equations characterize the piezoelectric materials.

$$\sigma_m = C_m^E \frac{\partial \xi_m}{\partial x} + r_m \frac{\partial^2 \xi_m}{\partial t \partial x} - e E_m, \tag{2}$$

$$D_m = e \frac{\partial \xi_m}{\partial x} + \epsilon^s E_m, \tag{3}$$

where $m = 1,2.1,2.2,3,4$. C_m^E represents the elastic stiffness under conditions of constant electric field (E), r_m the internal mechanical damping, e the piezoelectric coefficient, E_m the electric field, D_m the electric displacement, and ϵ^s the electric permittivity under conditions of constant strain ($S = \partial \xi / \partial x$). The subscript m refers to the transducer parts as described in Fig. 1. The electric field derives from the electric potential $V_m(x,t)$:

$$E_m = -\frac{\partial V_m}{\partial x}, \tag{4}$$

and the electric displacement satisfies the electrostatic equation for an insulator:

$$\frac{\partial D_m}{\partial x} = 0. \tag{5}$$

Equation (2) can also be used as constitutive equations for isotropic materials, if all the electric characteristics such as e, ε^S, and E_m are put equal to zero. In this case, the elastic stiffness C_m^E represents Young's modulus. In the following, it is expressed by E_{ym}.

2. Equation of longitudinal waves

Introducing Eq. (2) in Eq. (1) while taking Eq. (3) into account, we get the following equation for the propagation of longitudinal waves:

$$\rho_m \frac{\partial^2 \xi_m}{\partial t^2} = C_m^D \frac{\partial^2 \xi_m}{\partial x^2} + r_m \frac{\partial^3 \xi_m}{\partial t \partial x^2}, \tag{6}$$

where

$$C_m^D = C_m^E + \frac{e^2}{\varepsilon^S}.$$

The solution of Eq. (6) leads to the displacement $\xi_m(x,t)$ which makes it possible to calculate both the electric field $E_m(x,t)$ and the electric potential $V_m(x,t)$. This solution must satisfy the mechanical boundary conditions as well as the electric ones.

B. Boundary conditions

The piezoelectric elements are supplied with voltage at their interface ($x=0$). They are polarized in opposite directions and we assume that their interface constitutes a nodal plane.

1. Mechanical boundary conditions

We express conditions at the free ends and at the cross-sectional areas located between the different transducer parts:

$$\text{At } x=-(b+l_1): \quad \sigma_1 = 0, \tag{7}$$

$$\text{At } x=-b: \quad \xi_1 = \xi_{2.1} \text{ and } A_1\sigma_1 = A_2\sigma_{2.1}, \tag{8}$$

where A_1 and A_2 denote the cross-sectional areas of the plain backing piece and the piezoelectric elements which would be annular ($A_2 = A_{2.1} = A_{2.2}$):

$$\text{At } x=0: \quad \xi_{2.1} = 0, \tag{9}$$

$$\xi_{2.2} = 0, \tag{10}$$

$$\text{At } x=b: \quad \xi_{2.2} = \xi_3 \quad \text{and} \quad A_2\sigma_{2.2} = A_3\sigma_3. \tag{11}$$

A_3 represents the cross-sectional area of part (3):

$$\text{At } x=b+l_2: \quad \xi_3 = \xi_4 \quad \text{and} \quad A_3\sigma_3 = A_4\sigma_4. \tag{12}$$

A_4 is the cross-sectional area of the amplitude transformer free end:

$$\text{At } x=b+l_2+l_3: \quad \sigma_4 = 0. \tag{13}$$

2. Electrical boundary conditions

A voltage ($V_0 e^{j\omega t}$) is applied across the circular surfaces of the piezoelectric elements as shown in Fig. 1. Then, the boundary conditions can be written in the following way:

$$V_{2.1}(0,t) - V_{2.1}(-b,t) = V_0 e^{j\omega t}, \tag{14}$$

$$V_{2.2}(0,t) - V_{2.2}(b,t) = V_0 e^{j\omega t}. \tag{15}$$

II. DISPLACEMENT AMPLITUDE

The displacement amplitude expression is obtained from the solution of equation Eq. (6). This solution must satisfy the boundary conditions given by Eq. (7) up to Eq. (15). We use a method based on the separation of variables. It follows:

$$\xi_m(x,t) = \Xi_m(x) f_m(t). \tag{16}$$

As we are interested in the forced motion due to the voltage ($V_0 e^{j\omega t}$) applied to the piezoelectric elements, the time dependence of the motion in the whole transducer can be anticipated as:

$$f_m(t) = e^{j\omega t}. \tag{17}$$

Substituting Eq. (16) and Eq. (17) into Eq. (6) leads to

$$\frac{d^2 \Xi_m}{dx^2} + k_m^2 \Xi_m = 0, \tag{18}$$

where

$$k_m^2 = \frac{\omega^2 \rho_m}{C_m^D + j\omega r_m}.$$

The constant k_m represents a complex wave number.

The general solution of Eq. (18) can be written as follows:

$$\Xi_m(x) = B_{1m} e^{jk_m x} + B_{2m} e^{-jk_m x}. \tag{19}$$

The constants B_{1m} and B_{2m} have to be determined using the boundary conditions. This solution allows us to get explicit expressions of the electric field $E_m(x,t)$ and the electric potential $V_m(x,t)$. Assuming that

$$\begin{aligned} E_m(x,t) &= E_{1m}(x) e^{j\omega t} \\ V_m(x,t) &= V_{1m}(x) e^{j\omega t}, \end{aligned} \tag{20}$$

the following expression can be derived from Eq. (3) and Eq. (5):

$$E_{1m}(x) = jk_m \frac{e}{\varepsilon^S} (-B_{1m} e^{jk_m x} + B_{2m} e^{-jk_m x}) + B_{0m}, \tag{21}$$

where the integration constants B_{0m} still have to be determined. On the other hand, Eq. (4) and Eq. (21) lead to the expression of $V_{1m}(x)$. We get:

$$V_{1m}(x) = \frac{e}{\varepsilon^S} (B_{1m} e^{jk_m x} + B_{2m} e^{-jk_m x}) - B_{0m} x + C_{0m}. \tag{22}$$

The C_{0m} are new integration constants.

A. Explicit displacement amplitude expression

We have to calculate the constants which appear in Eq. (19) and Eq. (22) taking into account the boundary conditions expressed by Eqs. (7)–(15). As the transducer is fixed at the plane $x=0$, its left and right parts referring to this nodal plane are treated separately. For the sake of clarity, the left part will be called the first principal part and the right part the second principal part.

1. First principal part

The first principal part is composed of the support (1), where the displacement amplitude is represented by $\Xi_1(x)$, and the first piezoelectric element (2.1), where the displacement amplitude is $\Xi_{2.1}(x)$. The constants which must be calculated are: B_{11}, $B_{2.1}$, $B_{12.1}$, $B_{22.1}$, and $B_{02.1}$. This requires use of the mechanical boundary conditions given by Eqs. (7)–(9) and the electrical boundary condition described by Eq. (14). Results of the calculation are

$$\Xi_1(x)=\frac{-V_0}{\text{den } 1}\cos\, k_1(l_1^*+x) \tag{23}$$

$$\Xi_{2.1}(x)=\frac{V_0}{\text{den } 1 \sin\, k_2 b}\cos\, k_1 l_1 \sin\, k_2 x, \tag{24}$$

where

$$\text{den } 1=-\frac{\omega b Z_2 K_b}{e}\left(\frac{RZ}{K_b}\sin\, k_1 l_1+\cos\, k_1 l_1\right)$$

$$k_2=k_{2.1}=k_{2.2},\quad r_2=r_{2.1}=r_{2.2},$$

$$l_1^*=b+l_1,\quad c_1=E_{Y1}+j\omega r_1,$$

$$c_2=C_2^D+j\omega r_2,\quad RZ=\frac{Z_1A_1}{Z_2A_2},$$

$$K_b=\frac{e^2}{\omega b\varepsilon^S Z_2}-\frac{\cos\, k_2 b}{\sin\, k_2 b}.$$

Z_1 and Z_2 denote the specific acoustic impedance of the backing piece and the piezoelectric elements, respectively. The specific acoustic impedance Z_m is defined as follows:

$$Z_m=\rho_m v_m, \tag{25}$$

where v_m is the propagation velocity of the elastic wave. According to our notations, we have

$$Z_m=\rho_m v_m=\sqrt{\rho_m c_m};\quad c_m=C_m^D+j\omega r_m. \tag{26}$$

2. Second principal part

The second principal part is composed of the second piezoelectric element (2.2), where the displacement amplitude is $\Xi_{2.2}(x)$, and the two parts of the amplitude transformer (3) and (4), where the displacement amplitudes are $\Xi_3(x)$ and $\Xi_4(x)$, respectively. The constants: $B_{12.2}$, $B_{22.2}$, B_{13}, B_{23}, B_{14}, B_{24}, and $B_{02.2}$ have to be determined using the mechanical boundary conditions given by Eq. (10) up to Eq. (13) and the electrical boundary condition expressed by Eq. (15). Calculation leads to the following expressions:

$$\Xi_{2.2}(x)=\frac{-V_0}{\text{den } 2 \sin\, k_2 b}\left(\cos\, k_3 l_3 \cos\, k_3 l_2 - \frac{A_4}{A_3}\sin\, k_3 l_3 \sin\, k_3 l_2\right)\sin\, k_2 x \tag{27}$$

$$\Xi_3(x)=\frac{V_0}{\text{den } 2}\left(\frac{A_4}{A_3}\sin\, k_3 l_3 \sin\, k_3(l_2^*-x) - \cos\, k_3 l_3 \cos\, k_3(l_2^*-x)\right) \tag{28}$$

$$\Xi_4(x)=\frac{-V_0}{\text{den } 2}\cos\, k_3(l_3^*-x), \tag{29}$$

where

$$\text{den } 2=\frac{\omega b Z_2}{e}\left[(RZS\sin\, k_3 l_2+K_b\cos\, k_3 l_2)\cos\, k_3 l_3 + \frac{A_4}{A_3}(RZS\cos\, k_3 l_2-K_b\sin\, k_3 l_2)\sin\, k_3 l_3\right]$$

$$l_2^*=b+l_2,\quad l_3^*=b+l_2+l_3,$$

$$RZS=\frac{Z_3A_3}{Z_2A_2},\quad Z_3=Z_4.$$

III. TRANSDUCER DIMENSIONS

We would like to calculate the lengths l_1, l_2, and l_3 which optimize the performance of transducers, used as low-frequency ultrasonic atomizers, for any given value of (A_4/A_3) or (d_2/d_1). We first deal with the case of ideal materials $(r_m=0)$. The influence of internal mechanical damping will be analyzed later.

A. The backing piece length: l_1

The backing piece is needed to ensure good mechanical contact between the piezoelectric elements and the amplitude transformer. It must allow a sufficient torque which is about 7 Nm. For an optimized transducer, the displacement amplitude of the free end of the backing piece has to remain quite small in order to reduce vibrational energy losses.

The displacement amplitude $\Xi_1(x)$ of the backing piece free end $(x=-l_1^*)$ is deduced from Eq. (23) as follows:

$$\Xi_1(-l_1^*)=\frac{eV_0}{\omega b Z_2 K_b\left(\frac{RZ}{K_b}\sin\, k_1 l_1+\cos\, k_1 l_1\right)}. \tag{30}$$

The value of l_1 is calculated by maximizing the function:

$$\psi_1(l_1)=\frac{RZ}{K_b}\sin\, k_1 l_1+\cos\, k_1 l_1, \tag{31}$$

when the working frequency $(v=2\pi\omega)$ and the physical properties of the materials like the specific acoustic impedance and the density are known. As $\psi_1(l_1)$ represents a periodic function, we would choose the smallest favorable value of l_1 which provides good mechanical resistance.

B. Amplitude transformer length: l_2 and l_3

A well-designed amplitude transformer is required for getting optimized displacement amplitude $\Xi_4(x)$ of the atomizing surface ($x=l_3^*$), the area A_4 of this latter being large enough to atomize the desired mass flow rate. The displacement amplitude is expressed from Eq. (29) as follows:

$$\Xi_4(l_3^*)=\frac{-V_0}{\text{den } 2}. \tag{32}$$

Values of l_2 and l_3 which optimize $\Xi_4(l_3^*)$ result from the roots of den 2:

$$(RZS \sin k_3 l_2 + K_b \cos k_3 l_2)\cos k_3 l_3 + \frac{A_4}{A_3}(RZS \cos k_3 l_2 - K_b \sin k_3 l_2)\sin k_3 l_3 = 0, \tag{33}$$

where the values of the parameters RZS, K_b, k_2, and k_3, which depend on the working frequency and the physical properties of the materials, are known. In other words, the optimal dimensions of the amplitude transformer are calculated at the resonance of the transducer. Thus the fixed frequency represents the resonance frequency.

C. Application

To illustrate the theory developed above, we detail an example of determining sizes of an ultrasonic atomizer (l_1, l_2, and l_3) intended to operate at 50 kHz. The piezoelectric elements used are ring shaped and made of polycrystalline ceramic. Their thickness b, outside diameter d_0, and inside diameter d_i, as well as their mechanical and electrical properties, are

$$b=3 \text{ mm}, \quad d_0=15 \text{ mm}, \quad d_i=6 \text{ mm},$$
$$\rho_2=7700 \frac{\text{kg}}{\text{m}^3}, \quad C_2^E=65.36\cdot 10^9 \frac{\text{N}}{\text{m}^2}, \tag{34}$$
$$e=17.65 \frac{\text{C}}{\text{m}^2}, \quad \epsilon^S=61.85\cdot 10^{-10} \frac{\text{C}^2}{\text{Nm}^2}.$$

Both the backing piece and the amplitude transformer are made of aluminum alloy. Their density and Young's modulus are

$$\rho_1=\rho_3=\rho_4=2710 \frac{\text{kg}}{\text{m}^3}, \quad E_{y1}=E_{y3}=E_{y4}=69\cdot 10^9 \frac{\text{N}}{\text{m}^2}. \tag{35}$$

Different values of the area ratio A_4/A_3 can be tested, varying the atomizing surface diameter d_2.

The appropriate values of the length l_1 are those which maximize the function $\psi_1(l_1)$ [see Eq. (31), where $|RZ/K_b|=0.24$]. From a purely mathematical point of view, the smallest value of l_1 which maximizes $\psi_1(l_1)$ is zero. However, technological constraints make the backing piece essential to apply the right amount of press stress, when assembling the ultrasonic atomizer. Consequently, the value of the length l_1 should be determined in such a way that the function $\psi_1(l_1)$ deviates only slightly from its maximum value which is equal to 1. In this example, $\psi_1(l_1)>0.8$ when $l_1<0.01$ m. The length l_1 should be ranging from l_{1c} to 0.01 m, where l_{1c} represents the critical needed length.

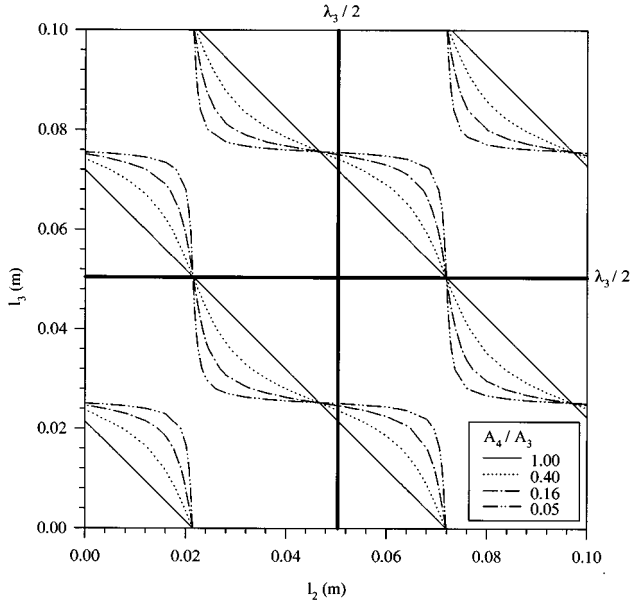

FIG. 2. Optimized values of the amplitude transformer length.

The possible values of the lengths l_2 and l_3 are determined from Eq. (33). Because periodic functions are involved, an infinite number of solutions is expected. Figure 2 shows the roots (l_2,l_3) of Eq. (33). It can be easily seen that the basic roots are located between 0 and $\lambda_3/2$ for both l_2 and l_3. For the sake of clarity, they will be written as (l_{2b},l_{3b}). Then, the infinite solutions of Eq. (33) are ($l_{2b}+\alpha\lambda_3/2$, $l_{3b}+\beta\lambda_3/2$), where α and β are any integer. λ_3 is the wavelength of acoustic waves in the stepped horn. Each couple of lengths defines a stepped horn of an ultrasonic atomizer whose resonance frequency is equal to 50 kHz without loading. Examples of calculated values are shown in Table I. They represent the lengths l_2 and l_3 of stepped horns involved in ultrasonic atomizers operating at 30, 40, 50, and 60 kHz, respectively. These atomizers have been experimentally tested as will be seen later. Periodic solutions have also been found by Bangviwat *et al.*[6] for stepped horns designed in order to get maximum power delivery to a given load. However, their solutions are different from ours. For example, they found values of l_2 and l_3 which are located on curves containing the point ($l_2=\lambda_3/4$, $l_3=\lambda_3/4$) which leads to a stepped horn, the two parts of which are one-quarter wavelength long. These values do not occur in our solutions, and experimental investigation performed using ultrasonic atomizers provided with such stepped horns did not show

TABLE I. Amplitude transformer sizes: theoretical values ($A_4/A_3=0.16$).

Amplitude transformer		Resonance frequency
l_2 (mm)	l_3 (mm)	f (kHz)
2.6	20.6	60
3.2	24.7	50
3.0	31.1	40
4.0	41.5	30

any liquid atomization, in our working conditions. We can thus conclude that the sizing method established by Bangviwat *et al.* is not appropriate for low-frequency ultrasonic atomizers.

D. Effects of the internal mechanical damping

When the internal mechanical damping is taken into account, the wavelength k_m represents complex quantities given by

$$k_m = \left(\frac{\rho_m \omega^2}{C_m^D + j\omega r_m} \right)^{1/2}. \tag{36}$$

Several authors, among whom are Bishop and Johnson,[9] introduce a nondimensional quantity μ to describe the effects of the internal damping. This coefficient is defined as

$$\mu = \frac{1}{Q}, \tag{37}$$

where Q is the mechanical quality factor. μ represents the ratio between the energy dissipated per cycle and the maximum kinetic energy. The use of μ leads to the following modifications of Eq. (36):

$$k_m = \left(\frac{\rho_m \omega^2}{C_m^D (1 + j\mu_m)} \right)^{1/2}. \tag{38}$$

Thus

$$\mu_m = \frac{\omega r_m}{C_m^D}. \tag{39}$$

We did not find anywhere in the literature experimental data over the internal mechanical damping properties μ_m or r_m of the materials in transducers operating at ultrasonic frequencies, except the piezoelectric ceramic elements ($\mu_2 = 1/Q = 1/750$). Frequencies less than 1 kHz have only been investigated. As a consequence, our approach will be limited to a sensitivity analysis.

We start from the explicit expression of the atomizing surface displacement $\xi_4(l_3^*, t)$ derived from Eqs. (16), (17), and (29). For the sake of clarity, we write this expression in the following concise form, where all the parameters are assumed to be known expected μ_3:

$$\xi_4(l_3^*, t) = \frac{V_0 e^{j\omega t}}{\eta_1 + j\eta_2}, \tag{40}$$

where $\eta_1 = \eta_1(l_2, l_3, f, \mu_3)$ and $\eta_2 = \eta_2(l_2, l_3, f, \mu_3)$. This equation can be rewritten as follows:

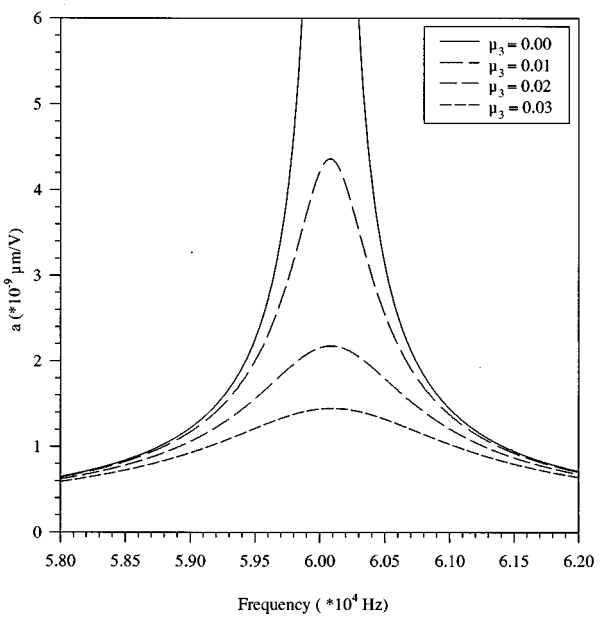

FIG. 3. Effects of the internal mechanical damping on the displacement amplitude.

$$\xi_4(l_3^*, t) = \eta_0 V_0 e^{j(\omega t - \zeta)}, \tag{41}$$

where

$$\eta_0 = (\eta_1^2 + \eta_2^2)^{1/2} \quad \text{and} \quad \zeta = \arctan\left(\frac{\eta_2}{\eta_1} \right).$$

Equation (41) leads to the following function from which the effects of the internal mechanical damping are studied:

$$\Xi_4(l_3^*) = \eta_0 V_0 e^{-j\zeta}. \tag{42}$$

Figure 3 shows the variation of the displacement amplitude $a = |\Xi_4(l_3^*)|/V_0$ when the working frequency oscillates around the transducer resonance frequency. The lengths of l_2 and l_3 have been fixed at 2.6 and 19.9 mm, respectively.

One can notice that the displacement amplitude of the atomizing surface is almost equal to zero far from the resonance frequency. A slight increase of the internal mechanical damping coefficient leads to a notable reduction of this displacement amplitude. However, its highest value remains located at the same value of the frequency (about 60 kHz) which represents the resonance frequency of the atomizer tested. Similar behaviors have been observed for various values of the lengths l_2 and l_3. Thus it can be concluded that the mechanical damping μ_3 does not change the resonance

TABLE II. Amplitude transformer: experimental data ($A_4/A_3 = 0.16$).

Amplitude transformer actual dimensions		Resonance frequency: measured	Resonance frequency: calculated	Displacement amplitude	Electric voltage
l_2 (mm)	l_3 (mm)	f (kHz)	f (kHz)	Ξ_4 (μm)	V_0 (V)
2.6	19.8	59.3	62.2	4.97	41.7
3.2	24.1	50.3	51.3	4.20	61.1
3.0	30.0	42.1	41.4	2.78	41.2
4.0	40.2	32.3	31.0	1.46	41.5

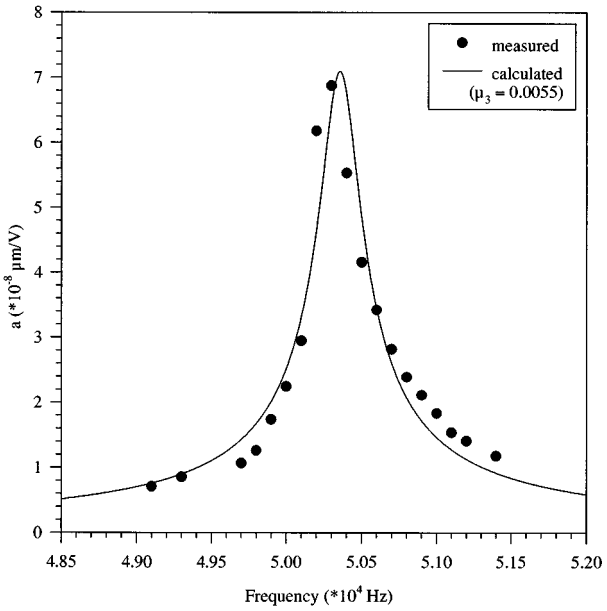

FIG. 4. Estimated value of the internal mechanical damping (the resonance frequency is equal to 50.3 kHz).

frequency of a ultrasonic transducer. It is not necessary to take into account the mechanical damping of materials in designing of ultrasonic transducers.

IV. EXPERIMENTAL RESULTS AND DISCUSSIONS

Experimental investigations have been done in order to locate and to measure the largest value of the atomizing surface displacement amplitude as well as the corresponding working frequency, called the resonance frequency. A laser interferometric technique is used to determine the amplitude displacement of the atomizing surface. The experimental setup is based on a Michelson interferometer using an He-Ne laser. The interference fringes are detected by a fast PIN photodiode (13 DSI 001 Mlles Griot) and stored by a digital oscilloscope (Lecroy 9310 A).

The design values of the resonance frequencies as well as the dimensions l_2 and l_3 are mentioned in Table II. Actual values of l_3 appear to be slightly smaller (see Table I) because of successive attempts to reach the best possible mirror quality of the atomizing surface needed for measurements. Consequently, the resonance frequency increases as shown by both the measured values and the calculated ones. The difference shown by the measured resonance frequency value of the first transducer is due to our experimental equipment, which did not allow accurate measurements of relatively high displacement amplitudes. Globally, the experimental results are in a satisfactory agreement with the theoretical ones.

Figure 4 shows the variation of the displacement amplitude $a=|\Xi_4(l_3^*)|/V_0$ as a function of the frequency when the experimental value of the resonance frequency is equal to 50.3 kHz. The theoretical curve fits reasonably well the experimental points for values of the mechanical damping around $\mu_3=0.0055$. For a resonance frequency equal to 42.1 kHz, the damping was found to be around $\mu_3=0.005$.

Experimental data found for aluminum, in the literature, correspond to internal mechanical values between 10^{-4} and 10^{-2} at 1 kHz.

V. CONCLUSIONS

A theoretical and experimental analysis of the longitudinal oscillations in ultrasonic transducers used as low-frequency ultrasonic atomizers is reported. A sizing method has been established and theoretical design has been experimentally tested. This method has been successfully applied in designing ultrasonic atomizers which are being used in our laboratory.[10] The theory developed in this work could be used in determining the sizes of transducers involved in different applications like ultrasonic piezomotors. It would also be helpful to fill the lack of experimental data on the internal mechanical damping of materials when ultrasonic frequencies are concerned, comparing theoretical values of the displacement amplitude of the stepped horn free end to the measurements.

[1] J. S. Arnold and J. G. Martner, ''Description of the resonances of short solid barium titane cylinders,'' J. Acoust. Soc. Am. **31**, 217–226 (1959).
[2] R. H. Coursaut, ''Les transducteurs ultrasonores,'' Acta Electron. **22**, 129–141 (1979).
[3] M. Brissaud, ''Characterization of piezoceramics,'' IEEE Trans. Ultrason. Ferroelectr. Freq. Control **38**, 603–617 (1991).
[4] L. G. Merkulov and A. V. Kharitonov, ''Theory and analysis of sectional concentrators,'' Sov. Phys. Acoust. **5**, 183–190 (1958).
[5] Philips, Piezoelectric ceramics: properties and applications (N. V. Philips Gloeilampenfabrieken, 1991), pp. 42–45.
[6] A. Bangviwat, H. K. Ponnekanti, and R. D. Finch, ''Optimizing the performance of piezoelectric drivers that use stepped horns,'' J. Acoust. Soc. Am. **90**, 1223–1229 (1991).
[7] S. A. Elrod, B. Hadimioglu, B. T. Khuri-Yakub, E. G. Rawson, N. N. Mansour, and T. S. Lundgren, ''Nozzleless droplet formation with focused acoustic beams,'' J. Appl. Phys. **65**, 3441–3447 (1989).
[8] D. Sindayihebura, J. Cousin, and C. Dumouchel, ''Experimental and theoretical study of sprays produced by ultrasonic atomizers,'' Part. Part. Syst. Charact. **14**, 93–101 (1997).
[9] R. E. D. Bishop and D. C. Johnson, *Mechanics of Vibration* (Cambridge University Press, Cambridge, MA, 1960), pp. 407–493.
[10] D. Sindayihebura and L. Bolle, ''Theoretical and experimental study of the behaviour of liquid film free surfaces driven by transverse ultrasonic vibrations,'' in *Computational Modelling of Free and Moving Boundary Problems III* (Bled, Slovenia, 1995), pp. 66–74.

Calculating the performance of 1–3 piezoelectric composites for hydrophone applications: An effective medium approach

Marco Avellaneda
Courant Institute of Mathematical Sciences, New York University, 251 Mercer Street, New York, New York 10012

Pieter J. Swart
Theoretical Division, MS-B284, Los Alamos National Laboratory, Los Alamos, New Mexico 87545

(Received 2 July 1994; revised 14 November 1996; accepted 29 January 1997)

A new method is presented for evaluating the performance of 1–3 polymer/piezoelectric ceramic composites for hydrophone applications. The Poisson's ratio effect, i.e., the enhancement of the hydrostatic performance which can be achieved by mixing piezoelectric ceramics with polymers, is studied in detail. Using an ''effective medium'' approach, algebraic expressions are derived for the composite hydrostatic charge coefficient d_h, the hydrostatic figure of merit $d_h g_h$, and the hydrostatic electromechanical coupling coefficient k_h in terms of the properties of the constituent materials, the ceramic volume fraction, and a microstructural parameter p. The high contrast in stiffness and dielectric constants existing between the two phases can be exploited to derive simple, geometry-independent approximations which explain quantitatively the Poisson's ratio effect. It is demonstrated that the stiffness and the Poisson's ratio of the polymer matrix play a crucial role in enhancing hydrophone performance. Using a differential scheme to model the parameter p, we evaluate d_h, $d_h g_h$, and k_h for polymer/piezoelectric ceramic systems at varying compositions. Several examples involving $Pb(Zr, Ti)O_3$ and $(Pb,Ca)TiO_3$ piezoelectric ceramics are given to illustrate the theory. [S0001-4966(97)00506-7]

PACS numbers: 43.38.Fx, 43.30.Yj, 77.84.Lf, 77.65.Bn [SLE]

LIST OF SYMBOLS

f	volume fraction of ceramic
p	microstructural parameter
q	microstructural parameter
d_h	hydrostatic charge coefficient
g_h	hydrostatic voltage coefficient
k_h	hydrostatic electromechanical coupling coefficient
κ	transverse (planar) bulk modulus
μ	transverse (planar) shear modulus
ν	Poisson's ratio
ϕ	porosity
$\mathbf{d}$	piezoelectric strain tensor
$\boldsymbol{\epsilon}^T$	free permittivity tensor
$\boldsymbol{\epsilon}^S$	clamped permittivity tensor
$\boldsymbol{\beta}^T$	free impermittivity tensor
$\mathbf{e}$	piezoelectric stress tensor
$\mathbf{g}$	piezoelectric voltage tensor
$\mathbf{u}$	displacement
$\mathbf{s}^E$	elastic compliance tensor under short-circuit boundary conditions
$\mathbf{c}^E$	elastic stiffness tensor under short-circuit boundary conditions
$\mathbf{D}$	dielectric displacement
$\mathbf{E}$	electric field
$\mathbf{S}$	strain tensor
$\mathbf{T}$	stress tensor

INTRODUCTION

Piezoelectric transducers have been used for several years as sensors and transmitters of acoustic signals. Quartz was used in the first piezoelectric transducer—in the form of a steel-quartz sandwich—invented by P. Langevin in 1917.[1] Following the discovery in the 1940s of perovskite piezoelectrics with very large electromechanical coupling ($k \cong 50\%-80\%$), poled piezoelectric ceramics such as barium titanate ($BaTiO_3$), lead zirconate-titanate [$Pb(Zr,Ti)O_3$ or PZT (Trademark of Vernitron, Inc.)], and calcium-modified lead-titanate [$(Pb,Ca)TiO_3$] have become the most commonly used transducer materials.[2] The principal applications of piezoelectric transducers are in ultrasound medical imaging, nondestructive testing and underwater acoustics, where they are used for tracking vessels, finding fish, and for deep-sea seismology (see the review in Ref. 3). Low-frequency receivers for underwater acoustics are known as hydrophones.

This paper studies an important class of composite piezoelectric materials for hydrophone applications. The composite material consists of an array of parallel piezoelectric ceramic rods embedded in a polymer matrix as shown in Fig. 1. The overall shape is that of a disk with axis aligned with the rods which are poled in the longitudinal direction. Under an incident acoustic field, the matrix transmits strain to the ceramic rods. This strain is transformed into electrical

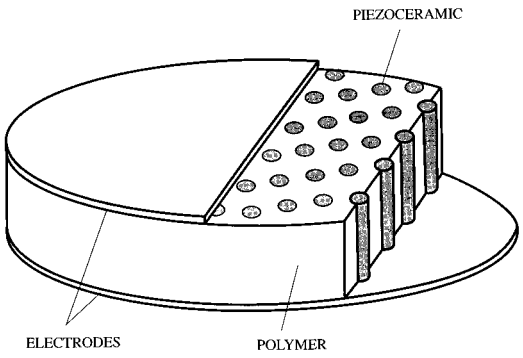

FIG. 1. Schematic representation of a 1–3 piezoelectric composite made from piezoelectric ceramic rods embedded in a polymer matrix.

polarization by the direct piezoelectric effect, producing a voltage difference between the electrodes placed at the extremities of the disk. Conversely, the application of an alternate current between the electrodes will give rise to an acoustic field, by the converse piezoelectric effect. This structure is generally referred to as a 1–3 composite, following Newnham's connectivity classification.[4]

The use of polymer/piezoelectric ceramic composites in acoustic transducers is motivated by several reasons, including design flexibility and the potential for good operating conditions in a high-pressure environment. Moreover, given the high density of piezoelectric ceramics, their impedance matching with a medium such as water is poor. Combining ceramic with a low-density material or introducing voids improves the transmission of acoustic energy. Another reason, which is the main focus of this paper, is sensitivity enhancement. It has been shown that a suitably engineered polymer/piezoelectric ceramic composite can have a much larger sensitivity in the hydrostatic mode than a conventional device in the same mode.[5–8] Several studies were successful in explaining the observed enhancement of sensitivity in polymer/piezoelectric ceramic 1–3 composites (cf. Haun and Newnham,[9] Chan and Unsworth,[10] Smith and Auld,[11] Smith[3,12,13] and Dunn and Taya[14,15]).

In this paper we take the question further. We propose an alternative method to characterize from first principles the hydrostatic response of polymer/piezoelectric ceramic composites in terms of the physical properties and the volume fractions of the constituents. (A preliminary announcement of some of these results was made in Ref. 16.) In the present approach, the composite is treated as an equivalent homogeneous continuum or effective medium and its effective properties are computed from the effective response tensor. The assumption that the material can be treated as an equivalent homogeneous continuum will not apply to all 1–3 composites: it cannot handle structures having only a few ceramic rods or large voids, which give rise to irregular field patterns. However, if the composite is made of regularly distributed, slender piezoelectric rods in a homogeneous matrix, then the effective medium treatment should provide a good approximation to the actual material response. For these ''macroscopically homogeneous'' composites, the hydrostatic charge coefficient d_h, the hydrostatic figure of merit $d_h g_h$, and the hydrostatic electromechanical coupling coefficient k_h, are studied for several material systems/compositions. We show that this treatment, which is much simpler than a full-fledged finite-element calculation, is sufficiently accurate to be used as a design tool for engineering 1–3 piezoelectric composites.

For the reader's convenience, we present a summary of the main results and applications. In Sec. I, we calculate formally the effective response tensor of a transversely isotropic piezoelectric composite. We show that the relevant constants for hydrostatic applications can be expressed algebraically in terms of the moduli of the constituents, the volume fractions, and a single ''microstructural'' parameter p. This parameter is associated with the solution of a plane elasticity problem for the transverse microgeometry. The analysis follows the works of Hill,[17] Schulgasser,[18] and Benveniste and Dvorak.[19] In Sec. II, we derive explicit formulas for the measures of hydrostatic performance d_h, g_h, $d_h g_h$, and k_h of the composite.

We analyze these measures of hydrostatic performance in Sec. III, exploiting the fact that piezoelectric ceramics are about 20–100 times stiffer and have dielectric constants 100–1000 times larger than typical polymers. This large-contrast analysis gives simple expressions for the quantities of interest. To a large extent, this analysis is independent of specific details of the microstructure (such as the shape of the cross section of the rods) and of the precise value of the unknown parameter p. The enhancement of d_h depends in a crucial way on the Poisson's ratio of the polymer matrix: The d_h coefficient for the composite will be larger than that of the piezoelectric constituent (i.e., enhancement will occur) if

$$\nu_{13}^{(m)} < -\frac{d_{13}^{(i)}}{d_{33}^{(i)}}, \tag{1}$$

where $\nu_{13}^{(m)}$ is the Poisson's ratio of the matrix and $d_{13}^{(i)}, d_{33}^{(i)}$ are the piezoelectric charge coefficients of the piezoelectric ceramic. We believe that this is an important result. It should provide a useful criterion for selecting 1–3 composite materials for hydrophone applications. We also show that, whenever this criterion is satisfied, the maximum value of d_h occurs at moderate volume fractions of piezoelectric ceramic, in the range of 5 vol % to 20 vol %. (We use vol % to indicate the volume fraction of the piezoelectric ceramic material.) The enhancement in the hydrostatic figure of merit $d_h g_h$ is mainly due to the large dielectric contrast, as pointed out earlier by Smith.[13] Finally, we also show that, if (1) holds, the effective hydrostatic electromechanical coupling coefficient k_h is of the same magnitude as the ceramic k_h in the range of compositions where d_h reaches its peak value. Therefore, composites made with a polymer matrix with low enough Poisson's ratio so that (1) holds, and with low volume fractions of ceramic, are potentially superior to homogeneous piezoelectric ceramics.

In Sec. IV we propose a method to evaluate the performance of a given polymer/piezoelectric ceramic system by modeling the parameter p. For this, we use a differential effective medium (DEM) scheme. In Sec. V we use the DEM to numerically characterize various polymer/piezoelectric ceramic systems with PZT5A and calcium-modified lead-

titanate rods. This analysis includes examples which satisfy and do not satisfy the enhancement criterion.

Finally, we use our method to investigate two interesting design issues: The use of porous polymer matrices as well as the use of materials with negative Poisson's ratio—also known as auxetic materials—to enhance the Poisson's ratio effect. The latter class of fillers was originally proposed by Smith[12] for this purpose.

Our conclusions are given in Sec. VI.

I. EFFECTIVE MEDIUM THEORY FOR 1–3 PIEZOELECTRIC COMPOSITES

We state explicitly the assumptions on the composite microstructure that are consistent with and necessary for an effective-medium treatment of material properties. We shall consider only perfectly bonded (in practice, interfaces may be imperfect and this could affect the theoretical results) composites for which the overall dimensions (thickness, transverse width) are much larger than the typical rod thickness (δ) and the typical rod separations (a). The rods are assumed to have uniform but otherwise arbitrarily shaped cross section (rectangular, square, or circular rods are allowed, but tapered rods, which break the cylindrical symmetry, are not). We assume the polymer matrix to be transversally isotropic in its material properties, with axes aligned with that of the rods. (The z or 3-coordinate is chosen to coincide with the axis of rotational symmetry.) For simplicity, we assume the array of rods to be either hexagonal or random, so as to ensure transverse isotropy. (Lower symmetry arrays, such as square arrays, can be treated in a similar fashion at the expense of slightly more complicated algebra.) The wavelengths of the incident acoustic/electric fields are also assumed to be much longer than δ and a. Under these conditions, we can regard the composite as an ''equivalent-homogeneous'' material, for which the various averaged fields are related by effective, or macroscopic physical constants. Notice that this precludes, for instance, composite structures consisting of only a few rods or extrusions of size comparable to the device itself, as well as short incident wavelengths for which strong multiple-scattering and resonances are expected. A 1–3 piezoelectric composite of dimensions 1–10 cm consisting of an epoxy matrix with PZT rodlike inclusions with $a \cong \delta$ on the order of 0.1–1 mm operating in the 1–100 kHz regime in water and the 1–10 kHz regime in air fits these assumptions well.

For low operating frequencies the acoustic and electric fields are quasistatic, so the equations of linear elasticity and Maxwell's equations reduce to[20]

$$\nabla \cdot \mathbf{T} = 0, \quad \mathbf{S} = \tfrac{1}{2}(\nabla \mathbf{u} + (\nabla \mathbf{u})^t), \tag{2}$$

and

$$\nabla \cdot \mathbf{D} = 0, \quad \nabla \times \mathbf{E} = 0, \tag{3}$$

where $\mathbf{T} = (T_{ij})$ is the stress tensor, $\mathbf{S} = (S_{ij})$ is the strain tensor, $\mathbf{u} = (u_i)$ is the displacement [$(\nabla \mathbf{u})^t$ denotes the transpose of the displacement gradient], $\mathbf{D} = (D_i)$ is the dielectric displacement and $\mathbf{E} = (E_i)$ is the electric field. We shall omit throughout the dependence of the fields on frequency. The constitutive relations satisfied by these fields in a linear piezoelectric material are

$$\begin{aligned} S_{ij} &= s^E_{ijkl} T_{kl} + d_{ijk} E_k, \\ D_i &= d_{kli} T_{kl} + \epsilon^T_{ik} E_k, \end{aligned} \tag{4}$$

where summation over repeated indices is implied. (These relations should be taken in their adiabatic form for transducer applications.) In tensor notation, we have

$$\begin{bmatrix} \mathbf{S} \\ \mathbf{D} \end{bmatrix} = \begin{bmatrix} \mathbf{s}^E & \mathbf{d} \\ \mathbf{d}^t & \boldsymbol{\epsilon}^T \end{bmatrix} \begin{bmatrix} \mathbf{T} \\ \mathbf{E} \end{bmatrix}. \tag{5}$$

Here $\mathbf{s}^E$ is the compliance tensor under short-circuit boundary conditions, $\mathbf{d}$ is the piezoelectric strain tensor and $\boldsymbol{\epsilon}^T$ is the free permittivity tensor. Other equivalent forms of the above constitutive relation that are convenient for our analysis are

$$\begin{bmatrix} \mathbf{T} \\ \mathbf{D} \end{bmatrix} = \begin{bmatrix} \mathbf{c}^E & -\mathbf{e} \\ \mathbf{e}^t & \boldsymbol{\epsilon}^S \end{bmatrix} \begin{bmatrix} \mathbf{S} \\ \mathbf{E} \end{bmatrix}, \tag{6}$$

where $\mathbf{c}^E$ is the short-circuit stiffness tensor, $\boldsymbol{\epsilon}^S$ is the clamped permittivity tensor, $\mathbf{e} = \mathbf{c}^E \mathbf{d}$ is the piezoelectric stress tensor, and

$$\begin{bmatrix} \mathbf{S} \\ \mathbf{E} \end{bmatrix} = \begin{bmatrix} \mathbf{s}^D & \mathbf{g} \\ -\mathbf{g}^t & \boldsymbol{\beta}^T \end{bmatrix} \begin{bmatrix} \mathbf{T} \\ \mathbf{D} \end{bmatrix}, \tag{7}$$

where $\mathbf{s}^D$ is the open-circuit compliance tensor, $\boldsymbol{\beta}^T$ is the free impermittivity tensor, and $\mathbf{g} = \mathbf{d}(\boldsymbol{\epsilon}^T)^{-1}$ is the piezoelectric voltage tensor. (The notation used here and throughout the paper follows the 1978 IEEE Standard.[21]) Note that (5) is a symmetric relation, whereas (6) and (7) are not.

In composite media, the tensors and fields in the constitutive relations (5), (6), and (7) are spatially varying, i.e., depend on position, reflecting the heterogeneity at the ''microscopic'' level. The effective linear response tensor, or tensor of effective properties, relates the corresponding averaged fields. Accordingly, if $\langle . \rangle$ denotes averaging over a volume large compared to the microstructure and small compared to the macrostructure, we have

$$\begin{bmatrix} \langle \mathbf{S} \rangle \\ \langle \mathbf{D} \rangle \end{bmatrix} = \begin{bmatrix} \mathbf{s}^E_{\text{eff}} & \mathbf{d}_{\text{eff}} \\ \mathbf{d}^t_{\text{eff}} & \boldsymbol{\epsilon}^T_{\text{eff}} \end{bmatrix} \begin{bmatrix} \langle \mathbf{T} \rangle \\ \langle \mathbf{E} \rangle \end{bmatrix}. \tag{8}$$

Under the above assumptions of fine-scale structure and long incident wavelengths, the effective tensor is independent of the shape of the device. Thus, relation (8) can be regarded as a constitutive relation which completely characterizes the effective electro-mechanical response of the composite. Implicit in this treatment is the assumption that contributions arising from variations of fields near the boundary of the composite are irrelevant. This implies that the effective tensors $\mathbf{s}^D_{\text{eff}}$, $\boldsymbol{\epsilon}^T_{\text{eff}}$, etc. corresponding to the alternative formulations (6), (7), can be computed self-consistently from (8) as if the material were homogeneous.

Evaluating the effective properties of composites is mathematically nontrivial. Nevertheless, in the case of 1–3 piezoelectric composites with the ceramic poled in the direction of the rods, it can be shown that the effective constants for hydrostatic applications can be expressed algebraically in

terms of the properties of the two materials and an additional microstructural parameter, p, which has a simple physical interpretation. This parameter can be computed explicitly in cases of interest and estimated in general due to the large mismatch in elastic and dielectric properties in polymer/piezoelectric ceramic composites.

Suppose that the composite material is subjected to an applied transverse strain and electric field. Let $\langle\cdot\rangle_i$ denote volume averaging over the inclusion phase (ceramic rods), and set $S_p=(S_{11}+S_{22})/\sqrt{2}$. We define two microscopic parameters p and q, respectively, by

$$p=\frac{\langle S_p\rangle_i}{\langle S_p\rangle} \tag{9}$$

for $\langle S_{33}\rangle=\langle E_3\rangle=0$, and

$$q=\frac{\langle S_{12}\rangle_i}{\langle S_{12}\rangle} \tag{10}$$

for $\langle S_p\rangle=\langle E_3\rangle=0$. Physically, p and q represent, respectively, the mean transverse hydrostatic strain and the mean transverse deviatoric strain in the inclusion phase, per unit applied transverse pressure and shear.

We are in position to state the main result of this section. For convenience, we use dyadic (Voigt) tensor notation corresponding to the relation (6), viz. (henceforth, we drop superscripts for simplicity, writing $s\equiv s^E$, $c\equiv c^E$, and $\epsilon\equiv\epsilon^S$ unless otherwise specified)

$$\begin{bmatrix} T_{11}\\ T_{22}\\ T_{33}\\ D_3\end{bmatrix}=\begin{bmatrix} c_{11} & c_{12} & c_{13} & -e_{13}\\ c_{12} & c_{11} & c_{13} & -e_{13}\\ c_{13} & c_{13} & c_{33} & -e_{33}\\ e_{13} & e_{13} & e_{33} & \epsilon_{33}\end{bmatrix}\begin{bmatrix} S_{11}\\ S_{22}\\ S_{33}\\ E_3\end{bmatrix}, \tag{11}$$

$$\begin{bmatrix} T_{i3}\\ D_i\end{bmatrix}=\begin{bmatrix} c_{15} & -e_{15}\\ e_{15} & \epsilon_{11}\end{bmatrix}\begin{bmatrix} S_{i3}\\ E_i\end{bmatrix},\quad i=1,2, \tag{12}$$

and

$$T_{12}=\tfrac{1}{2}(c_{11}-c_{12})S_{12}. \tag{13}$$

We use the superscripts m, i, and e to denote, respectively, the moduli of the matrix phase, the inclusion phase, and the effective moduli. The transverse bulk and shear moduli $\kappa=\frac{1}{2}(c_{11}+c_{12})$ and $\mu=\frac{1}{2}(c_{11}-c_{12})$ are used as well. The volume fraction of the inclusion phase is denoted by f. In this notation, the effective moduli of a 1–3 piezoelectric composite relevant for hydrostatic performance are given by:

$$\kappa^{(e)}=\kappa^{(m)}+fp(\kappa^{(i)}-\kappa^{(m)}), \tag{14a}$$

$$\mu^{(e)}=\mu^{(m)}+fq(\mu^{(i)}-\mu^{(m)}), \tag{14b}$$

$$c_{13}^{(e)}=c_{13}^{(m)}+fp(c_{13}^{(i)}-c_{13}^{(m)}), \tag{14c}$$

$$e_{13}^{(e)}=e_{13}^{(m)}+fp(e_{13}^{(i)}-e_{13}^{(m)}), \tag{14d}$$

$$c_{33}^{(e)}=c_{33}^{(m)}+f\left\{1+(p-1)\frac{(c_{13}^{(i)}-c_{13}^{(m)})^2}{(\kappa^{(i)}-\kappa^{(m)})(c_{33}^{(i)}-c_{33}^{(m)})}\right\}\times(c_{33}^{(i)}-c_{33}^{(m)}), \tag{14e}$$

$$e_{33}^{(e)}=e_{33}^{(m)}+f\left\{1+(p-1)\frac{(c_{13}^{(i)}-c_{13}^{(m)})(e_{13}^{(i)}-e_{13}^{(m)})}{(\kappa^{(i)}-\kappa^{(m)})(e_{33}^{(i)}-e_{33}^{(m)})}\right\}\times(e_{33}^{(i)}-e_{33}^{(m)}), \tag{14f}$$

$$\epsilon_{33}^{(e)}=\epsilon_{33}^{(m)}+f\left\{1-(p-1)\frac{(e_{13}^{(i)}-e_{13}^{(m)})^2}{(\kappa^{(i)}-\kappa^{(m)})(\epsilon_{33}^{(i)}-\epsilon_{33}^{(m)})}\right\}\times(\epsilon_{33}^{(i)}-\epsilon_{33}^{(m)}). \tag{14g}$$

This representation is consistent with the uniform field theory initiated by Hill[17] for the elastic case and established for general piezoelectric composites by Benveniste and Dvorak.[19] A short proof of this theorem is provided in the Appendix for the sake of completeness. Note that this result characterizes all effective moduli, except for $\epsilon_{11}^{(e)}$, $e_{15}^{(e)}$, and $c_{15}^{(e)}$. Since we are concerned only with hydrostatic applications, we will not discuss these moduli in this paper, and we refer the reader to Schulgasser[18] and Benveniste and Dvorak[19] for an analysis of these effective parameters.

II. HYDROSTATIC PERFORMANCE OF 1–3 PIEZOELECTRIC COMPOSITES

For hydrostatic applications, we are interested in the average axial dielectric displacement $\langle D_3\rangle$ arising from an applied hydrostatic compression such that $\langle T_{ij}\rangle=T\delta_{ij}$, $i,j=1,2,3$. The hydrostatic charge coefficient d_h is defined by

$$d_h=\langle D_3\rangle/T. \tag{15}$$

In the case of a homogeneous piezoelectric ceramic poled in the 3-direction, we have

$$d_h=2d_{13}+d_{33}. \tag{16}$$

For PZT, $BaTiO_3$, and other commonly used piezoelectric ceramics, the axial and transverse piezoelectric coefficients d_{13} and d_{33} have opposite signs (lateral and axial compression give rise to polarizations of opposite direction). This results in a hydrostatic coefficient d_h which is much lower than d_{33}: for instance in PZT5A, $d_{33}\cong 374$ pC/N and $d_{13}\cong -171$ pC/N, so that $d_h\cong 32$ pC/N.

The performance of the composite can be measured by its effective moduli. The two quantities most commonly used for measuring hydrostatic performance are the hydrostatic figure of merit d_hg_h, and the hydrostatic electromechanical coupling factor k_h, defined below.

According to the formulation (7), the tensor **g** measures the electric field resulting from a given applied stress. The corresponding hydrostatic voltage coefficient

$$g_h=d_h/\epsilon_{33}^T, \tag{17}$$

where ϵ_{33}^T is the free-body axial permittivity, measures the axial electric field arising from an applied hydrostatic pressure. The product

$$d_hg_h=d_h^2/\epsilon_{33}^T \tag{18}$$

is the hydrostatic figure of merit, a commonly used measure of the performance of the composite.

The hydrostatic electromechanical coupling factor, k_h, defined by

$$k_h^2=\frac{d_h^2}{\epsilon_{33}^T s_h^E}, \tag{19}$$

is a nondimensional parameter which measures the overall electromechanical power conversion. In (19) the modulus s_h^E represents the dilatational compliance

$$s_h^E=2s_{11}^E+2s_{12}^E+4s_{13}^E+s_{33}^E. \tag{20}$$

Using the representation (14) of the previous section, we can compute algebraic expressions for the effective d_h, $d_h g_h$, and k_h in terms of the material properties of each phase and the microstructural parameter p. We present these formulas hereafter.

It is convenient to introduce a reduced set of a moduli associated with the acoustic/electric couplings of primary interest. Accordingly, set

$$c_{pp}=2\kappa=c_{11}+c_{12}, \tag{21}$$

$$c_{pz}=c_{13}\sqrt{2}, \tag{22}$$

$$c_{zz}=c_{33}, \tag{23}$$

$$e_{pz}=e_{13}\sqrt{2}, \quad d_{pz}=d_{13}\sqrt{2}, \tag{24}$$

$$e_{zz}=e_{33}, \quad d_{zz}=d_{33}, \quad \epsilon_{zz}=\epsilon_{33}, \tag{25}$$

and define the field components

$$S_p=\frac{1}{\sqrt{2}}(S_{11}+S_{22}), \tag{26}$$

$$T_p=\frac{1}{\sqrt{2}}(T_{11}+T_{22}), \tag{27}$$

$$S_z=S_{33}, \tag{28}$$

$$T_z=T_{33}, \tag{29}$$

$$E_z=E_3, \tag{30}$$

$$D_z=D_3. \tag{31}$$

The constitutive relation (11) implies the reduced relation for a transversely isotropic piezoelectric material, namely

$$\begin{bmatrix} T_p \\ T_z \\ D_z \end{bmatrix}=\begin{bmatrix} c_{pp} & c_{pz} & -e_{pz} \\ c_{pz} & c_{zz} & -e_{zz} \\ e_{pz} & e_{zz} & \epsilon_{zz} \end{bmatrix}\begin{bmatrix} S_p \\ S_z \\ E_z \end{bmatrix}. \tag{32}$$

We also define, for convenience of notation,

$$\mathbf{C}=\begin{bmatrix} c_{pp} & c_{pz} \\ c_{pz} & c_{zz} \end{bmatrix}, \tag{33}$$

$$\mathbf{e}=\begin{bmatrix} e_{pz} \\ e_{zz} \end{bmatrix}, \tag{34}$$

and

$$\mathbf{d}=\begin{bmatrix} d_{pz} \\ d_{zz} \end{bmatrix}. \tag{35}$$

It can be easily shown that

$$\mathbf{d}=\mathbf{C}^{-1}\mathbf{e}, \tag{36}$$

$$d_h=[\sqrt{2},1]^t\cdot\mathbf{d}=[\sqrt{2},1]^t\cdot\mathbf{C}^{-1}\mathbf{e}, \tag{37}$$

$$\epsilon_{33}^T=\epsilon_{zz}+\mathbf{e}\cdot\mathbf{C}^{-1}\mathbf{e}, \tag{38}$$

and

$$s_h^E=\begin{bmatrix} \sqrt{2} \\ 1 \end{bmatrix}\cdot\mathbf{C}^{-1}\begin{bmatrix} \sqrt{2} \\ 1 \end{bmatrix}. \tag{39}$$

Therefore, the hydrostatic figure of merit and the coupling coefficient are given, respectively, by

$$d_h g_h=\frac{\left(\begin{bmatrix} \sqrt{2} \\ 1 \end{bmatrix}\cdot\mathbf{C}^{-1}\mathbf{e}\right)^2}{\epsilon_{zz}+\mathbf{e}\cdot\mathbf{C}^{-1}\mathbf{e}} \tag{40}$$

and

$$k_h^2=\frac{\left(\begin{bmatrix} \sqrt{2} \\ 1 \end{bmatrix}\cdot\mathbf{C}^{-1}\mathbf{e}\right)^2}{(\epsilon_{zz}+\mathbf{e}\cdot\mathbf{C}^{-1}\mathbf{e})\left(\begin{bmatrix} \sqrt{2} \\ 1 \end{bmatrix}\cdot\mathbf{C}^{-1}\begin{bmatrix} \sqrt{2} \\ 1 \end{bmatrix}\right)}. \tag{41}$$

For the calculation of the effective quantities $d_h^{(e)}$, $(d_h g_h)^{(e)}$, and $k_h^{(e)}$ for a piezoelectric composite, we must input in the above formulas the effective stiffness matrix $\mathbf{C}^{(e)}$, the effective piezoelectric stress tensor $\mathbf{e}^{(e)}$, and the effective clamped permittivity constant $\epsilon_{zz}^{(e)}=(\epsilon_{33}^S)^{(e)}$. From (14a), (14c), and (14e) it follows that

$$c_{pp}^{(e)}=c_{pp}^{(m)}+fp\Delta c_{pp}, \tag{42}$$

$$c_{pz}^{(e)}=c_{pz}^{(m)}+fp\Delta c_{pz}, \tag{43}$$

and

$$c_{zz}^{(e)}=c_{zz}^{(m)}+f\left[1+(p-1)\frac{(\Delta c_{pz})^2}{(\Delta c_{pp})(\Delta c_{zz})}\right]\Delta c_{zz}, \tag{44}$$

are the entries of $\mathbf{C}^{(e)}$, where $\Delta c_{pp}=c_{pp}^{(i)}-c_{pp}^{(m)}$, etc. The effective piezoelectric stress coefficients are, from (14d) and (14f),

$$e_{pz}^{(e)}=e_{pz}^{(m)}+fp\Delta e_{pz} \tag{45}$$

and

$$e_{zz}^{(e)}=e_{zz}^{(m)}+f\left[1+(p-1)\frac{(\Delta c_{pz})(\Delta e_{pz})}{(\Delta c_{pp})(\Delta e_{zz})}\right]\Delta e_{zz}. \tag{46}$$

Finally, the effective clamped dielectric constant is given by (14g) as

$$\epsilon_{zz}^{(e)}=\epsilon_{zz}^{(m)}+f\left[1-(p-1)\frac{(\Delta e_{pz})^2}{(\Delta c_{pp})(\Delta\epsilon_{zz})}\right]\Delta\epsilon_{zz}. \tag{47}$$

Substitution of $\mathbf{C}^{(e)}$, $\mathbf{e}^{(e)}$, and $\epsilon_{zz}^{(e)}$ into formulas (37), (40), and (41) gives the quantities measuring hydrostatic performance.

III. ANALYSIS OF THE POISSON'S RATIO EFFECT

The possibility of gaining sensitivity by ''decoupling'' the polarizations arising from transverse and longitudinal strains is a primary motivation for using 1–3 polymer/piezoelectric ceramic composites for hydrostatic applications

instead of pure piezoelectric ceramics. This decoupling is known as the Poisson's Ratio Effect (PRE). The goal of this section is to present a theoretical explanation for the PRE and the resulting nonlinear effects on $d_h g_h$ and k_h. First, we give a simple engineering argument. Then, using the prior results together with the assumption of large stiffness/dielectric mismatch, we show quantitatively how the decoupling takes place. An appealing feature of this analysis is its generality: it does not require a detailed description of the microgeometry (shape/location of the rods) or modeling of the unknown microstructural parameter p. These results capture the essential features of electro-acoustic coupling in 1–3 piezoelectric ceramic/polymer composites and are consistent with experimental results (e.g., Refs. 8–10).

This is how the PRE works: When a uniaxial piezoelectric material is subjected to a pressure field, the dielectric displacement in the axial direction (D_3) is given by

$$D_3 = d_h T, \tag{48}$$

where T is the intensity of the pressure field. For instance, PZT5H has a d_{33} and d_{13} of 593 pC/N and -274 pC/N, respectively.[22] Intuitively, the opposite signs of d_{13} and d_{33} arise because lateral compression of the ceramic implies longitudinal extension (the material has a positive Poisson's ratio). Therefore, from (16), homogeneous PZT5H has a d_h of 45 pC/N, which is quite low when compared to d_{33}. The use of a 1–3 PZT5H/polymer composite allows for the possibility of converting an applied hydrostatic field into a predominantly tensile stress on the rods.

To obtain a more nearly accurate picture one must also take into account the fact that lateral strain in the matrix will be accompanied by a vertical deformation. For matrices with positive Poisson's ratio $\nu_{13}^{(m)}$, this vertical deformation opposes the vertical deformation due to the imposed axial strain, whereas if the Poisson's ratio is either zero (as for cork) or negative (as for the cellular materials discussed in Sec. V C) it has the same sign. Thus, the basic principle is that a soft matrix with low Poisson's ratio will tend to cancel the d_{13} polarization arising from transverse strains, mostly giving rise to a d_{33} polarization in the piezoelectric ceramic rods. [We note, however, that negative values of the matrix Poisson's ratio are accompanied by a shear stiffening which will have secondary effects (cf. Sec. V).]

A. The effective hydrostatic charge coefficient d_h

Let us consider the situation in more detail. From (42), we have

$$c_{pp}^{(e)} = c_{pp}^{(m)} \hat{K}(f), \tag{49}$$

where we define

$$\hat{K}(f) \equiv 1 + fp(f) \frac{c_{pp}^{(i)} - c_{pp}^{(m)}}{c_{pp}^{(m)}} \tag{50}$$

as the nondimensional transverse rigidity of the microstructure. If we consider the asymptotic limit of large stiffness mismatch, i.e.,

$$\frac{c_{pp}^{(m)}}{c_{pp}^{(i)}} \to 0, \quad \frac{c_{pz}^{(m)}}{c_{pz}^{(i)}} \to 0, \quad \frac{c_{zz}^{(m)}}{c_{zz}^{(i)}} \to 0, \tag{51}$$

the parameter $\hat{K}(f)$ will approach a finite value $\hat{K}_\infty(f)$, corresponding to the stiffness of a material made of a matrix with moduli $\tilde{\kappa}^{(m)} = 1$, $\tilde{\mu}^{(m)} = \mu^{(m)}/\kappa^{(m)}$, containing perfectly rigid rods. Therefore,

$$fp(f) = (\hat{K}(f) - 1) \frac{c_{pp}^{(m)}}{c_{pp}^{(i)} - c_{pp}^{(m)}} \cong (\hat{K}_\infty(f) - 1) \frac{c_{pp}^{(m)}}{c_{pp}^{(i)}}, \tag{52}$$

to leading order in $c_{pp}^{(m)}/c_{pp}^{(i)}$. The nondimensional rigidity $\hat{K}_\infty$ satisfies

$$\hat{K}_\infty(f) \cong 1 + cf \quad \text{for } f \ll 1, \tag{53}$$

where c is a numerical constant depending on the shape of the rods (see Sec. IV A). This formula for a dilute dispersion of rigid cylinders is standard: For the special case of rods with ellipsoidal cross section it follows from solving the Eshelby one-inclusion problem.[23] On the other hand, if the volume fraction of rods is increased (by increasing δ/a), then $\hat{K}_\infty$ increases and $\hat{K}_\infty = \infty$ at the critical volume fraction f_c for which the rods touch each other. Note that, from (52) and (53), we obtain, to leading order,

$$p \cong c \frac{c_{pp}^{(m)}}{c_{pp}^{(i)}} \tag{54}$$

for all f sufficiently small. To evaluate the effective properties in the limit $c_{pp}^{(m)}/c_{pp}^{(i)} \to 0$, etc., we set, from (49) and (43),

$$c_{pp}^{(e)} \cong c_{pp}^{(m)} \hat{K}_\infty(f) \tag{55}$$

and

$$\begin{aligned} c_{pz}^{(e)} &\cong c_{pz}^{(m)} + fp c_{pz}^{(i)} = c_{pp}^{(m)} \left(\frac{c_{pz}^{(m)}}{c_{pp}^{(m)}} + fp \frac{c_{pp}^{(i)}}{c_{pp}^{(m)}} \cdot \frac{c_{pz}^{(i)}}{c_{pp}^{(i)}} \right) \\ &\cong c_{pp}^{(m)} (\nu^{(m)} + (\hat{K}_\infty - 1) \nu^{(i)}), \end{aligned} \tag{56}$$

where

$$\nu^{(m)} = \frac{c_{pz}^{(m)}}{c_{pp}^{(m)}} = -\frac{s_{pz}^{(m)}}{s_{zz}^{(m)}} = -\sqrt{2}\frac{s_{13}^{(m)}}{s_{33}^{(m)}} = \sqrt{2}\nu_{13}^{(m)} \text{ and } \nu^{(i)} = \frac{c_{pz}^{(i)}}{c_{pp}^{(i)}} \tag{57}$$

are, up to the factor of $\sqrt{2}$, the Poisson's ratios of the two materials. Note that

$$c_{pz}^{(e)} = \nu^{(e)} c_{pp}^{(e)} \cong \nu^{(e)} c_{pp}^{(m)} \hat{K}_\infty, \tag{58}$$

where

$$\nu^{(e)} = \frac{c_{pz}^{(e)}}{c_{pp}^{(e)}} \cong \frac{1}{\hat{K}_\infty} \nu^{(m)} + \left(1 - \frac{1}{\hat{K}_\infty} \right) \nu^{(i)} \tag{59}$$

is the effective Poisson's ratio (up to the factor of $\sqrt{2}$). Also, from (44),

$$c_{zz}^{(e)} \cong c_{zz}^{(m)} + c_{zz}^{(i)} \left[f + f(p-1) \frac{(c_{pz}^{(i)})^2}{c_{pp}^{(i)} c_{zz}^{(i)}} \right]. \tag{60}$$

Moreover, since $(c_{pz}^{(i)})^2 / c_{pp}^{(i)} c_{zz}^{(i)}$ is an $O(1)$ quantity and $p \leqslant$ const $\times (c_{pp}^{(m)}/c_{pp}^{(i)})$, we have, to leading order,

$$c_{zz}^{(e)} \cong c_{zz}^{(m)} + c_{zz}^{(i)} f\left(1 - \frac{(c_{pz}^{(i)})^2}{c_{pp}^{(i)} c_{zz}^{(i)}}\right)$$

$$= c_{zz}^{(m)} + f\left(\frac{c_{zz}^{(i)} c_{pp}^{(i)} - (c_{pz}^{(i)})^2}{c_{pp}^{(i)}}\right) = c_{zz}^{(m)} + f/s_{zz}^{(i)}, \tag{61}$$

where $s_{zz}^{(i)} = s_{33}^{(i)}$ is the axial compliance of the ceramic.

A similar asymptotic analysis can be made for the piezoelectric stress coefficients $e_{pz}^{(e)}$ and $e_{zz}^{(e)}$, using (45) and (46). This gives

$$e_{pz}^{(e)} = fpe_{pz}^{(i)} \tag{62}$$

and

$$e_{zz}^{(e)} \cong fe_{zz}^{(i)} + f(p-1)\frac{c_{pz}^{(i)}}{c_{pp}^{(i)}} e_{pz}^{(i)}. \tag{63}$$

We used here the fact that the matrix is a passive polymer. These last two relations can be summarized in matrix form:

$$\begin{bmatrix} e_{pz}^{(e)} \\ e_{zz}^{(e)} \end{bmatrix} \cong \begin{bmatrix} fp & 0 \\ f(p-1)\dfrac{c_{pz}^{(i)}}{c_{pp}^{(i)}} & f \end{bmatrix} \begin{bmatrix} e_{pz}^{(i)} \\ e_{zz}^{(i)} \end{bmatrix}. \tag{64}$$

Recalling that $\mathbf{e}^{(i)} = \mathbf{C}^{(i)}\mathbf{d}^{(i)}$, we have

$$\begin{bmatrix} e_{pz}^{(e)} \\ e_{zz}^{(e)} \end{bmatrix} \cong \begin{bmatrix} fp & 0 \\ f(p-1)\dfrac{c_{pz}^{(i)}}{c_{pp}^{(i)}} & f \end{bmatrix} \begin{bmatrix} c_{pp}^{(i)} & c_{pz}^{(i)} \\ c_{pz}^{(i)} & c_{zz}^{(i)} \end{bmatrix} \begin{bmatrix} d_{pz}^{(i)} \\ d_{zz}^{(i)} \end{bmatrix}$$

$$= \begin{bmatrix} fpc_{pp}^{(i)} & fpc_{pz}^{(i)} \\ fpc_{pz}^{(i)} & f/s_{zz}^{(i)} \end{bmatrix} \begin{bmatrix} d_{pz}^{(i)} \\ d_{zz}^{(i)} \end{bmatrix}$$

$$\cong \begin{bmatrix} c_{pp}^{(m)}(\hat{K}_\infty - 1) & c_{pp}^{(m)}(\hat{K}_\infty - 1)\nu^{(i)} \\ c_{pp}^{(m)}(\hat{K}_\infty - 1)\nu^{(i)} & f/s_{zz}^{(i)} \end{bmatrix} \begin{bmatrix} d_{pz}^{(i)} \\ d_{zz}^{(i)} \end{bmatrix}. \tag{65}$$

Using the relation $\mathbf{d}^{(e)} = (\mathbf{C}^{(e)})^{-1}\mathbf{e}^{(e)}$, we conclude that the effective charge coefficients $d_{pz}^{(e)}$ and $d_{zz}^{(e)}$ are related to the charge coefficients of the ceramic by

$$\mathbf{d}^{(e)} \cong \mathbf{M}\mathbf{d}^{(i)}, \tag{66}$$

where

$$\mathbf{M} = \mathbf{A}^{-1}\mathbf{B}, \tag{67}$$

with

$$\mathbf{A} = \begin{bmatrix} c_{pp}^{(m)}\hat{K}_\infty & c_{pp}^{(m)}\hat{K}_\infty \nu^{(e)} \\ c_{pp}^{(m)}\hat{K}_\infty \nu^{(e)} & c_{zz}^{(m)} + f/s_{zz}^{(i)} \end{bmatrix} \tag{68}$$

and

$$\mathbf{B} = \begin{bmatrix} c_{pp}^{(m)}(\hat{K}_\infty - 1) & c_{pp}^{(m)}(\hat{K}_\infty - 1)\nu^{(i)} \\ c_{pp}^{(m)}(\hat{K}_\infty - 1)\nu^{(i)} & f/s_{zz}^{(i)} \end{bmatrix}. \tag{69}$$

The effective hydrostatic charge coefficient

$$d_h = 2d_{13}^{(e)} + d_{33}^{(e)} = \sqrt{2}d_{pz}^{(e)} + d_{zz}^{(e)} \tag{70}$$

can be computed from (66). In the ''large stiffness contrast'' approximation (51), we obtain

$$d_h = 2Ad_{13}^{(i)} + Bd_{33}^{(i)}, \tag{71}$$

where

$$A = 1 - \frac{1}{\hat{K}_\infty}\left\{\frac{f + s_{zz}^{(i)}c_{zz}^{(m)} - s_{zz}^{(i)}c_{pz}^{(m)}\nu^{(e)}\hat{K}_\infty}{f + s_{zz}^{(i)}c_{zz}^{(m)} - s_{zz}^{(i)}c_{pp}^{(m)}\hat{K}_\infty\nu^{(e)^2}}\right\}$$

$$+ \frac{1}{\sqrt{2}}\left\{\frac{s_{zz}^{(i)}c_{pp}^{(m)}\nu^{(e)} - s_{zz}^{(i)}c_{pz}^{(m)}}{f + s_{zz}^{(i)}c_{zz}^{(m)} - s_{zz}^{(i)}c_{pp}^{(m)}\hat{K}_\infty\nu^{(e)^2}}\right\} \tag{72}$$

and

$$B = 1 - \frac{\sqrt{2}}{\hat{K}_\infty}\left\{\frac{f\nu^{(m)} - s_{zz}^{(i)}c_{pz}^{(m)}(\hat{K}_\infty - 1)}{f + s_{zz}^{(i)}c_{zz}^{(m)} - s_{zz}^{(i)}c_{pp}^{(m)}\hat{K}_\infty\nu^{(e)^2}}\right\}$$

$$+ \left\{\frac{s_{zz}^{(i)}c_{pz}^{(m)}\nu^{(e)} - s_{zz}^{(i)}c_{zz}^{(m)}}{f + s_{zz}^{(i)}c_{zz}^{(m)} - s_{zz}^{(i)}c_{pp}^{(m)}\hat{K}_\infty\nu^{(e)^2}}\right\}. \tag{73}$$

Notice that $s_{zz}^{(i)}c_{pp}^{(m)}$, $s_{zz}^{(i)}c_{zz}^{(m)}$, and $s_{zz}^{(i)}c_{pz}^{(m)}$ are infinitesimal quantities in the large contrast approximation (51). However, these quantities cannot be neglected without taking into account the value of f. In fact, since f appears in the denominators of (72) and (73), it is important to distinguish between the cases $f \gg c_{pp}^{(m)}/c_{pp}^{(i)}$ and $f \ll c_{pp}^{(m)}/c_{pp}^{(i)}$. In the latter case it is not difficult to show from (53), (72), and (73) that

$$\lim_{f\to 0} A = \lim_{f\to 0} B = 0, \tag{74}$$

as expected. On the other hand, if $f \gg c_{pp}^{(m)}/c_{pp}^{(i)}$, etc., we can neglect the products $s_{zz}^{(i)}c_{pp}^{(m)}$ in (72) and (73). The corresponding formulas are then very simple:

$$A = 1 - \frac{1}{\hat{K}_\infty} \tag{75}$$

and

$$B = 1 - \frac{\sqrt{2}\nu^{(m)}}{\hat{K}_\infty} = 1 - \frac{2\nu_{13}^{(m)}}{\hat{K}_\infty}. \tag{76}$$

In summary, the final formula for d_h in the large contrast limit and for intermediate volume fractions $f \gg c_{pp}^{(m)}/c_{pp}^{(i)}$ is

$$d_h \cong 2\left(1 - \frac{1}{\hat{K}_\infty}\right)d_{13}^{(i)} + \left(1 - \frac{2\nu_{13}^{(m)}}{\hat{K}_\infty}\right)d_{33}^{(i)}. \tag{77}$$

This formula should provide a good approximation for the d_h of systems such as PZT/epoxy which have stiffness contrasts of up to $c_{pp}^{(m)}/c_{pp}^{(i)} \cong 1\%$ for ''intermediate'' volume fractions in the range 0.1 or $0.2 \leqslant f \leqslant f_c$. Notice that as f becomes smaller $\hat{K}_\infty \cong 0$ and (in the aforementioned range of compositions)

$$1 - \frac{1}{\hat{K}_\infty} \cong 0, \tag{78}$$

whereas

TABLE I. Material properties used in numerical examples.

Material	(Pb,Ca)TiO_3	PZT5A	Stycast
$s_{11}^E(10^{-12}\ \mathrm{m^2/N})$	7.3	16.4	108
$s_{12}^E(10^{-12}\ \mathrm{m^2/N})$	−1.5	−5.74	−32
$s_{13}^E(10^{-12}\ \mathrm{m^2/N})$	−1.4	−7.22	−32
$s_{33}^E(10^{-12}\ \mathrm{m^2/N})$	8.5	18.8	108
$d_{13}(10^{-12}\ \mathrm{C/N})$	−2.4	−171	0
$d_{33}(10^{-12}\ \mathrm{C/N})$	70	374	0
$\epsilon_{33}^T/\epsilon_0$	207	1700	4
$\rho(\mathrm{kg/m^3})$	6940	7750	1590

$$1-\frac{2\nu_{13}^{(m)}}{\hat{K}_\infty}\cong 1-2\nu_{13}^{(m)}, \tag{79}$$

which is a positive number if the matrix is isotropic. The effect of decoupling d_{13} and d_{33} in the composite and the influence of the matrix Poisson's ratio are thus put in evidence. Of course, this formula does not hold for arbitrarily small values of f and a transition exists for $f\cong c_{pp}^{(m)}/c_{pp}^{(i)}$, with B increasing sharply from zero to its maximum value. The increase in A is much more progressive, due to (78). Notice also that for $f\cong f_c$, we have $\hat{K}_\infty \gg 1$ and we recover $d_h=2d_{13}^{(i)}+d_{33}^{(i)}$, i.e., the pure ceramic piezoelectric coefficient.

It is instructive to study the magnitude of d_h as a function of f. Can the use of a soft matrix increase the effective piezoelectric coefficient? This is made clearer by writing (77) as

$$d_h\cong d_h^{(i)}-\frac{2}{\hat{K}(f)}(d_{13}^{(i)}+\nu_{13}^{(m)}d_{33}^{(i)}),\quad f\gg\frac{c_{pp}^{(m)}}{c_{pp}^{(i)}}, \tag{80}$$

where we used $\hat{K}$ rather than the high-contrast approximation $\hat{K}_\infty$. Since $\hat{K}(f)$ increases from 1 at $f=0$ to $c_{pp}^{(i)}/c_{pp}^{(m)}$ at $f\cong 1$, it follows that the hydrostatic charge response d_h will be enhanced or weakened, depending on the sign of

$$d_{13}^{(i)}+\nu_{13}^{(m)}d_{33}^{(i)}. \tag{81}$$

(Recall that for most piezoelectric ceramics, poling along the 3-axis results in a positive $d_{33}^{(i)}$ but a negative $d_{13}^{(i)}$—otherwise decoupling would not be necessary in the first place.)

The condition on the Poisson's ratio of the matrix which guarantees enhancement of the coefficient d_h is therefore

$$\nu_{13}^{(m)}<\frac{-d_{13}^{(i)}}{d_{33}^{(i)}}. \tag{82}$$

Another consequence of (80) is that the peak value of d_h will occur at small volume fractions. As an example, we can take the PZT5A/Stycast (Trademark of Emerson and Cumings, Inc.) composite studied in Refs. 12 and 13 and Sec. V (cf. Table I), for which $-d_{13}^{(i)}/d_{33}^{(i)}=0.457$ and $\nu_{13}^{(m)}=0.3$, hence the composite should enhance d_h (the DEM calculations in Sec. V confirm this). On the other hand, the (Pb,Ca)TiO_3/Stycast composite studied in Refs. 13, 7, and 8 and Sec. V is characterized by an almost vanishing $d_{13}^{(i)}$, so that $-d_{13}^{(i)}/d_{33}^{(i)}=0.034$ compared to $\nu_{13}^{(m)}=0.3$. We therefore expect no enhancement in d_h. This is again confirmed by the DEM calculations in Sec. V.

For a given piezoelectric ceramic, (80) also shows the potential advantage in using a more compliant matrix. Choosing a more compliant matrix results in a smaller $\hat{K}(f)=c_{pp}^{(e)}/c_{pp}^{(m)}$ at each f. Therefore, if (82) holds and if the matrix is made more compliant without changing its Poisson's ratio, then d_h should increase. (This is illustrated by our DEM calculations in Sec. V B.) On the other hand, if $\nu_{13}^{(m)}>-d_{13}^{(i)}/d_{33}^{(i)}$, then employing a more compliant matrix with a similar Poisson ratio can actually weaken d_h at intermediate volume fractions of the piezoelectric ceramic inclusions (see Fig. 7 and the accompanying description in Sec. V B). This effect might explain the experimental measurements of d_h reported in Refs. 7 and 8 (Fig. 4 in Ref. 8), for calcium-modified lead-titanate/epoxy composites. (Of course, this assessment ignores experimental considerations such as interface bonding and composite preparation. It is made to illustrate the theoretical role played by the matrix stiffness and Poisson's ratio.) Replacing a Stycast matrix with a more compliant Spurr epoxy reduced d_h by approximately 40% (at 20 vol % volume fraction of the ceramic). Moreover, the increase in the Poisson's ratio of the matrix could also have further contributed to the decrease in d_h. We note that, as is shown in the calculations of Ref. 7 and the experiments of Ref. 8, the parallel-series connectivity model of Haun and Newnham[9] fails to predict this weakening in d_h.

B. Effective g_h and d_hg_h

The hydrostatic voltage coefficient $g_h=d_h/\epsilon_{33}^T$ and the hydrostatic figure of merit d_hg_h can also be analyzed in the high stiffness/dielectric contrast. The permittivity of standard piezoelectric ceramics is typically of the order of 10^{-8} F/m, while polymers have an ϵ of the order of 10^{-11} F/m (which is comparable to the permittivity of vacuum, ϵ_0). The arithmetic mean

$$\epsilon_{33}^T\cong\epsilon_{33}^{(m)}+f(\epsilon_{33}^{(i)}-\epsilon_{33}^{(m)}), \tag{83}$$

where $\epsilon_{33}^{(i)}$ is either the clamped or the free permittivity constant of the ceramic, is a good approximation to the actual value of ϵ_{33}^T. The reason for this is that corrections to (83) due to piezoelectric coupling are controlled by the ratios $(e_{13}^{(i)})^2/[(\kappa^{(i)}-\kappa^{(m)})(\epsilon_{33}^{(i)}-\epsilon_{33}^{(m)})]$ [cf. (47)] and $\mathbf{e}\cdot\mathbf{C}^{-1}\mathbf{e}$ [cf. (38)], where $\mathbf{e}$ is the vector of effective piezoelectric stress coefficients and $\mathbf{C}$ is the effective stiffness matrix. For common polymer/piezoelectric ceramic systems, these corrections are of the order of 10^{-3} to 10^{-2} in nondimensional units.

Therefore, from (17) and (18), we have

$$g_h \cong \frac{d_h}{\epsilon_{33}^{(m)} + f(\epsilon_{33}^{(i)} - \epsilon_{33}^{(m)})}$$

$$\cong \frac{1}{\left[\frac{\epsilon_{33}^{(m)}}{\epsilon_{33}^{(i)}} + f\left(1 - \frac{\epsilon_{33}^{(m)}}{\epsilon_{33}^{(i)}}\right)\right]} \cdot \left\{ \frac{d_h^{(i)}}{\epsilon_{33}^{(i)}} - \frac{1}{\hat{K}_\infty(f)} \frac{(d_{13}^{(i)} + \nu_{13}^{(m)} d_{33}^{(i)})}{\epsilon_{33}^{(i)}} \right\}. \tag{84}$$

Here we used the large-contrast approximation (80) for d_h, which is valid for ''intermediate'' volume-fractions $f \gg c_{pp}^{(m)}/c_{pp}^{(i)}$. This formula can be further simplified. For typical PZT/epoxy composites the dielectric contrast $\epsilon_{33}^{(m)}/\epsilon_{33}^{(i)}$ is of order 10^{-3} to 10^{-2}. Therefore, in the intermediate regime,

$$g_h \cong \frac{1}{f}\left(g_h^{(i)} - \frac{d_{13}^{(i)} + \nu_{13}^{(m)} d_{33}^{(i)}}{\epsilon_{33}^{(i)} \hat{K}_\infty(f)} \right). \tag{85}$$

If the composite enhances piezoelectric response, i.e., if $d_{13}^{(i)} + \nu_{13}^{(m)} d_{33}^{(i)} < 0$, then the expression in parentheses is greater than $g_h^{(i)}$. Furthermore, the prefactor of $1/f$ in this expression shows that g_h is greatly enhanced at low volume-fractions. Since the lower cutoff for f is $c_{pp}^{(m)}/c_{pp}^{(i)}$ (the stiffness contrast), we can expect enhancements in the g_h of up to 100 times with respect to pure ceramic, due to the large dielectric contrast between the two materials.

A similar analysis can be carried out for the hydrostatic figure of merit $d_h g_h$. From the above analysis, we conclude that in the intermediate regime $c_{pp}^{(m)}/c_{pp}^{(i)} \ll f < f_c$, we have

$$d_h g_h \cong \frac{1}{f}\left(g_h^{(i)} - \frac{d_{13}^{(i)} + \nu_{13}^{(m)} d_{33}^{(i)}}{\epsilon_{33}^{(i)} \hat{K}_\infty(f)} \right)\left(d_h^{(i)} - \frac{d_{13}^{(i)} + \nu_{13}^{(m)} d_{33}^{(i)}}{\hat{K}_\infty(f)} \right). \tag{86}$$

This formula shows that the hydrostatic figure of merit can be larger than $(1/f) g_h^{(i)} d_h^{(i)}$ in this range of compositions. Hence, a 100-fold enhancement in the figure of merit is feasible if a polymer/ceramic 1–3 component is used instead of pure ceramic.

Summarizing, the enhancements of g_h and $d_h g_h$ for a composite, relative to the values for pure ceramic, are largely due to the large contrast between the dielectric permittivities of the matrix and the ceramic. In general, the curves describing these parameters as a function of f have narrow, high peaks at $f \cong c_{pp}^{(m)}/c_{pp}^{(i)} = \kappa^{(m)}/\kappa^{(i)}$.

C. Effective electromechanical coupling k_h

The hydrostatic electromechanical coupling coefficient k_h characterizes the efficiency of the composite in converting acoustic power to electric power when operating in hydrostatic mode. More precisely,

$$k_h^2 = \frac{P_{\text{electric}}}{P_{\text{acoustic}}}, \tag{87}$$

where P_{acoustic} represents the power stored by subjecting the composite to a hydrostatic stress under short-circuit boundary conditions and P_{electric} is the corresponding power stored by displacement of charges. In a 1–3 composite with large stiffness contrast between the two phases, most of the strain will be concentrated outside the ceramic rods and thus the percentage of acoustic power converted to electric power is expected to be small, or at least not greater than the corresponding figure of merit for the ceramic. Thus it is important to study the dependence of k_h on the volume fraction of ceramic. In particular, we would like to see whether the figure of merit for the composite is reasonably large at the peak of d_h, i.e., whether the ''enhancement'' of d_h can offset the decrease in the figure of merit. To examine the situation in detail, we first consider the approximations valid in the intermediate regime of compositions $c_{pp}^{(m)}/c_{pp}^{(i)} \ll f < f_c$.

By definition, we have

$$k_h^2 = \frac{d_h^2}{\epsilon_{33}^T s_h^E}, \tag{88}$$

where s_h^E is the dilatational compliance defined in (20). Using similar approximations as in Sec. III A, we find that

$$s_h^E \cong \frac{1}{\hat{K}_\infty c_{pp}^{(m)}} \left\{ \frac{2(f + s_{zz}^{(i)} c_{zz}^{(m)}) + s_{zz}^{(i)} c_{pp}^{(m)} (1 - 2\sqrt{2}\nu^{(e)}) \hat{K}_\infty}{f + s_{zz}^{(i)} c_{zz}^{(m)} - s_{zz}^{(i)} c_{pp}^{(m)} \hat{K}_\infty \nu^{(e)^2}} \right\}. \tag{89}$$

In the high-contrast limit, $s_{zz}^{(i)} c_{pp}^{(m)} \cong 0$, so that to leading order

$$s_h^E \cong \frac{2}{\hat{K}_\infty c_{pp}^{(m)}}. \tag{90}$$

Hence, from (88) and (86) we obtain

$$k_h^2 \cong \frac{\hat{K}_\infty c_{pp}^{(m)}}{2f}\left(g_h^{(i)} - \frac{d_{13}^{(i)} + \nu_{13}^{(m)} d_{33}^{(i)}}{\hat{K}_\infty \epsilon_{33}^{(i)}} \right)\left(d_h^{(i)} - \frac{d_{13}^{(i)} + \nu_{13}^{(m)} d_{33}^{(i)}}{\hat{K}_\infty} \right)$$

$$= \frac{\hat{K}_\infty}{2} \cdot \frac{c_{pp}^{(m)} s_h^{(i)}}{f} \left\{ \frac{1}{s_h^{(i)}}\left(g_h^{(i)} - \frac{d_{13}^{(i)} + \nu_{13}^{(m)} d_{33}^{(i)}}{\hat{K}_\infty \epsilon_{33}^{(i)}} \right) \times \left(d_h^{(i)} - \frac{d_{13}^{(i)} + \nu_{13}^{(m)} d_{33}^{(i)}}{\hat{K}_\infty} \right) \right\}. \tag{91}$$

The term in braces is roughly comparable to $g_h^{(i)} d_h^{(i)}/s_h^{(i)} = (k_h^{(i)})^2$, the square of the piezoelectric ceramic coupling factor. Note that this number can be larger than $(k_h^{(i)})^2$ if the enhancement condition (82) is satisfied. In the intermediate regime of compositions, we have $f \gg c_{pp}^{(m)}/c_{pp}^{(i)} \cong c_{pp}^{(m)} s_h^{(i)}$. This makes the effective k_h smaller than the corresponding value for the pure ceramic. However, if the ratio

$$\frac{c_{pp}^{(m)} s_h^{(i)}}{f} \tag{92}$$

is of order unity, i.e., if we are at low compositions at the ''edge'' of the intermediate zone, the effective k_h can be comparable to that of the pure ceramic. (At these compositions, we have $\hat{K}_\infty/2 \cong \frac{1}{2}$.) Furthermore, if the enhancements of d_h and g_h due to the PRE are sufficiently large, the coupling factors can exceed that of the pure ceramic.

Summarizing, we expect a peak in the value of k_h at small volume fractions $f \cong c_{pp}^{(m)}/c_{pp}^{(i)}$, which may or may not exceed the ceramic value $k_h^{(i)}$, depending on the magnitude

of the PRE (enhancement of d_h). The examples discussed in Sec. V confirm that by carefully choosing (or manufacturing) the passive matrix material in 1–3 piezoelectric composites, one can take advantage of the PRE to compensate for the poor hydrostatic response of commercial piezoelectric ceramics.

D. Comparison with the Smith–Auld model

Smith and Auld proposed a simple physical model for the effective properties of 1–3 piezoelectric composites.[11–13] This model has been found to agree quite well with numerical and experimental observations and is currently widely used in transducer design.

It is convenient to view their model as a relation between (S_p, T_z, D_z) and (T_p, S_z, E_z). From (32) we have the equivalent form

$$\begin{bmatrix} S_p \\ T_z \\ D_z \end{bmatrix} = \begin{bmatrix} 1/c_{pp} & -\nu & e_{pz}/c_{pp} \\ \nu & 1/s_{zz} & -(e_{zz}-\nu e_{pz}) \\ e_{pz}/c_{pp} & (e_{zz}-\nu e_{pz}) & \epsilon_{zz}+e_{pz}^2/c_{pp} \end{bmatrix} \times \begin{bmatrix} T_p \\ S_z \\ E_z \end{bmatrix}. \tag{93}$$

The model equations derived by Smith and Auld[11] are mathematically equivalent to assuming that the matrix in (93) satisfy ''the rule of mixtures,'' i.e., $1/c_{pp}^{(e)} = 1/c_{pp}^{(i)} f + 1/c_{pp}^{(m)}(1-f)$, $\nu^{(e)} = \nu^{(i)} f + \nu^{(m)}(1-f)$, etc.

To derive the resulting expression for d_h, we note that (36) implies

$$d_{13} = -\nu_{13} d_{33} + e_{13}/e_{pp}, \tag{94}$$

$$d_{33} = s_{33}(e_{33} - 2\,\nu_{13} e_{13}), \tag{95}$$

and therefore

$$d_h = (1-2\,\nu_{13}) d_{33} + \frac{2e_{13}}{c_{pp}}. \tag{96}$$

The last term in (96) satisfies the rule of mixtures, and therefore, from (94) and the fact that the matrix is a passive polymer, we have

$$\frac{e_{13}^{(e)}}{c_{pp}^{(e)}} = f\frac{c_{13}^{(i)}}{c_{pp}^{(i)}} = f(d_{13}^{(i)} + \nu_{13}^{(i)} d_{33}^{(i)}). \tag{97}$$

Similarly, by applying the rule of mixtures to the quantities $(e_{zz} - \nu e_{pz})$ and $1/s_{33}$, we obtain

$$d_{33}^{(e)} = \frac{f d_{33}^{(i)}}{s_{zz}^{(i)}/s_{zz}^{(m)} + f(1 - s_{zz}^{(i)}/s_{zz}^{(m)})}. \tag{98}$$

In the limit of large stiffness contrast (51) we can neglect the $s_{zz}^{(i)}/s_{zz}^{(m)}$ terms, and thus obtain

$$d_h^{(e)} \cong 2 f d_{13}^{(i)} + (1 - 2\,\nu_{13}^{(m)}(1-f)) d_{33}^{(i)}, \tag{99}$$

for the Smith–Auld model's behavior at intermediate volume fractions.

Note that this formula is equivalent to (77), provided $\hat{K}_\infty = 1/(1-f)$. The enhancement condition (82) can therefore also be derived within the Smith–Auld model.

IV. DIFFERENTIAL EFFECTIVE MEDIUM APPROXIMATION (DEM)

To obtain more nearly precise numerical values for the effective response of a piezoelectric composite, we must evaluate the microstructural parameter p. From (14a) we have, formally,

$$p = \frac{1}{f}\left(\frac{\kappa^{(e)} - \kappa^{(m)}}{\kappa^{(i)} - \kappa^{(m)}}\right), \tag{100}$$

and hence the problem is equivalent to the calculation of the effective transverse (planar) bulk modulus $\kappa^{(e)}$ for a two-dimensional composite with transversely isotropic constituents. The value of $\kappa^{(e)}$ is determined by f, $\kappa^{(i)}$, $\mu^{(i)}$, $\kappa^{(m)}$, $\mu^{(m)}$, and also by the microstructure, i.e., the shapes of the inclusions and their spatial arrangement. Mean-field theories, bounds, and numerical calculations of various kinds have been used by many authors to solve this problem (see, for instance, the reviews of Hashin[24] and Torquato[25]). A simple mean-field theory consistent with a matrix-inclusion microstructure is the Differential Effective Medium Theory (DEM) (also known under other names) (cf. Refs. 14 and 26–28). This procedure evaluates the effective moduli and hydrostatic parameters for all volume fractions and is exact in the small volume fraction limit. It is shown below that, for polymer-ceramic systems, it provides an excellent approximation to the theoretical values essentially up to the close-packing volume fraction (see Sec. V). Since we have established that the peak values of the hydrostatic parameters occur at moderate volume fractions of ceramic, the DEM should provide a good approximation to the theoretical values in the small to intermediate vol % range. In the DEM approach, the shapes of the inclusions are given—for simplicity we shall assume that they are circular cylinders. As shown by Hill[17] and others, the result of ''inserting'' a dilute system ($f \ll 1$) of inclusions with elastic moduli $(\kappa^{(i)}, \mu^{(i)})$ in a matrix with moduli $(\kappa^{(m)}, \mu^{(m)})$ is a composite with effective moduli

$$\kappa^{(e)} = \kappa^{(m)} + f(\kappa^{(i)} - \kappa^{(m)}) \frac{\kappa^{(m)} + \mu^{(m)}}{\kappa^{(i)} + \mu^{(m)}} + O(f^2) \tag{101}$$

and

$$\mu^{(e)} = \mu^{(m)} + f(\mu^{(i)} - \mu^{(m)}) \times \frac{2\mu^{(m)}(\kappa^{(m)} + \mu^{(m)})}{(\mu^{(i)} + \mu^{(m)})\kappa^{(m)} + 2\mu^{(m)}\mu^{(i)}} + O(f^2). \tag{102}$$

If a new system of inclusions with moduli $(\kappa^{(i)}, \mu^{(i)})$ is inserted into the homogenized continuum constructed in the previous step, the increment in the effective properties can again be calculated to first-order in f. Iterating this procedure with infinitesimal increments in volume fraction at each step leads to the ordinary differential equations (ODEs)

$$\frac{d\kappa^{(e)}}{df} = \left(\frac{1}{1-f}\right)(\kappa^{(i)} - \kappa^{(e)}) \frac{\kappa^{(e)} + \mu^{(e)}}{\kappa^{(i)} + \mu^{(e)}}, \tag{103a}$$

$$\frac{d\mu^{(e)}}{df}=\left(\frac{1}{1-f}\right)(\mu^{(i)}-\mu^{(e)}) \times\frac{2\mu^{(e)}(\kappa^{(e)}+\mu^{(e)})}{(\mu^{(i)}+\mu^{(e)})\kappa^{(e)}+2\mu^{(e)}\mu^{(i)}}, \tag{103b}$$

with the ''initial'' conditions $\kappa^{(e)}=\kappa^{(m)}$ and $\mu^{(e)}=\mu^{(m)}$ at $f=0$.

Note that by first exploiting the transverse symmetry, in the form of (14), the DEM scheme reduces to solving only two ODEs. (This is much simpler than solving the full system of 81 coupled ODEs, on the basis of which the DEM has been criticized for its complexity.[14])

Milton[29] and later Avellaneda[30] showed that the DEM is a realizable effective medium scheme, in the sense that it corresponds to an actual composite of matrix-inclusion type. However, unlike the 1–3 composites with equally sized rods considered here, the microgeometry realizing the DEM exactly consists of rods with a ''hierarchy'' of different sizes, reflecting physically the separation between the successive scales implicit in this iterative approach for calculating $(\kappa^{(e)},\mu^{(e)})$. Despite this, the DEM has the major advantage of being simple to compute and of being realizable as a microstructure. For moderate values of f, this scheme reflects quite accurately the elastic and electric interactions between a single rod and the rest of the composite structure (see e.g., Ref. 31 and the numerical comparisons in Sec. V). Therefore, it should provide reliable values for $\kappa^{(e)}$ and $\mu^{(e)}$ at volume fractions such that the deviations from the mean field which arise from nearby rod interactions are weak. This means that the composition should be below the critical value f_c for which rods touch each other, but not necessarily dilute. For the analysis of polymer-ceramic piezoelectric composites, this is not a severe restriction for two reasons: (i) We have already shown that the desirable volume fractions of ceramic are in the range $\kappa^{(m)}/\kappa^{(i)}\leqslant f\leqslant 10\kappa^{(m)}/\kappa^{(i)}$ approximately. This is well below f_c for most systems of interest. (ii) In practice, one of the original reasons to introduce a polymer matrix was to match the device's impedance to that of the medium. Given the high density of typical piezoelectric ceramics this amounts to choosing f quite small.

Although exact solutions for the DEM equations (103) are not available, a high-contrast analysis can be used to estimate the parameter $\hat{K}(f)$ in (80) and thus obtain algebraic formulas for d_h, etc. From (100) and (101) we obtain a first-order approximation for $p(f)$, namely

$$p(f)=\frac{\kappa^{(m)}+\mu^{(m)}}{\kappa^{(i)}+\mu^{(m)}} +\frac{2\mu^{(m)}(\kappa^{(m)}+\mu^{(m)})\Delta\mu\Delta\kappa}{(\mu^{(i)}+\mu^{(m)})^2\{(\mu^{(i)}+\mu^{(m)})\kappa^{(m)}+2\mu^{(i)}\mu^{(m)}\}}f +O(f^2). \tag{104}$$

On the other hand, from (50), we have

$$\hat{K}(f)=1+cf+O(f^2),\quad \text{with}\ \ c=p(0)\frac{\Delta\kappa}{\kappa^{(m)}},\quad f\ll 1. \tag{105}$$

In the large contrast limit, $c_{pp}^{(m)}/c_{pp}^{(i)}\ll 1$, we obtain from (104)

$$p(0)=c=1+\frac{\mu^{(m)}}{\kappa^{(m)}}+O\left(\frac{c_{pp}^{(m)}}{c_{pp}^{(i)}}\right). \tag{106}$$

Therefore, substituting this into (105), we have

$$\hat{K}_\infty(f)\cong 1+\left(1+\frac{\mu^{(m)}}{\kappa^{(m)}}\right)f. \tag{107}$$

Note that $\mu/\kappa=1-2\nu$ if the matrix is isotropic (as for typical polymers), so

$$\hat{K}_\infty(f)\cong 1+2(1-\nu^{(m)})f+O(f^2). \tag{108}$$

A similar calculation for the model of Smith and Auld discussed in Sec. III B yields

$$\hat{K}_\infty(f)\cong 1+f+O(f^2). \tag{109}$$

In their model the reduced two-dimensional elastic problem of finding the effective κ and μ at low volume fractions therefore gives an answer consistent with $\nu^{(m)}=1/2$.

V. EXAMPLES AND APPLICATIONS

We use the DEM approximation of Sec. IV to numerically compute the effective properties of several 1–3 piezoelectric ceramic/polymer systems. These computations are used to illustrate our description of the hydrostatic response of such materials. This is done as follows. The DEM ODEs (103) in κ and μ are numerically integrated with a fourth-order Runge–Kutta scheme with variable discretization step size $df<0.0005$ (chosen small enough to resolve the sharp peaks in g_h and $d_h g_h$) and ''initial data'' $\kappa(0)=\kappa^{(m)}$ and $\mu(0)=\mu^{(m)}$. The microstructural parameter p is recovered from (100), and all the remaining effective (hydrostatic) quantities are then computed using (14). This method appears to correspond well with experimental results. For example, we obtain a good agreement with the d_{33} measurements in the PZT7A/Araldite D system studied by Chan and Unsworth.[10] Unfortunately we could find only a few such detailed experiments on carefully prepared systems at varying compositions, hence this scheme obviously requires further experimental verification. We therefore apply this approach to predict the effective response of some model systems, chosen to illustrate the analysis of Sec. III.

A. Numerical examples: Enhancement versus nonenhancement

Table I contains the values for the material parameters used in our examples, which correspond to two important and contrasting classes of piezoelectric ceramics: lead zirconate-titanates ($Pb(Zr,Ti)O_3$ or PZT) and modified lead-titanates. We use the PZT5A formulation of $Pb(Zr,Ti)O_3$ and the calcium-modified lead-titanate piezoelectric ceramic $(Pb,Ca)TiO_3$. As the matrix phase we employ Stycast, a dense and stiff epoxy. (The material parameters are identical to those used by Smith and Auld,[11] Smith,[13] and Shaulov *et al.*[7] These book values are admittedly quite dated but allow for a comparison with previous works.) Although PZT5A is one of the best commercial piezoelectric ceramic

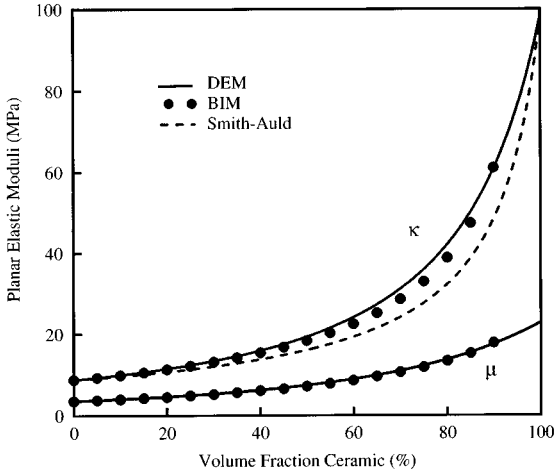

FIG. 2. Effective planar bulk and shear moduli κ and μ as a function of piezoelectric ceramic volume fraction for a composite made from PZT5A inclusions in a Stycast epoxy matrix, with material properties as in Table I. Predictions using the DEM scheme are compared with Helsing's boundary integral method (BIM)[32] and the Smith–Auld model[11] (see Sec. V A).

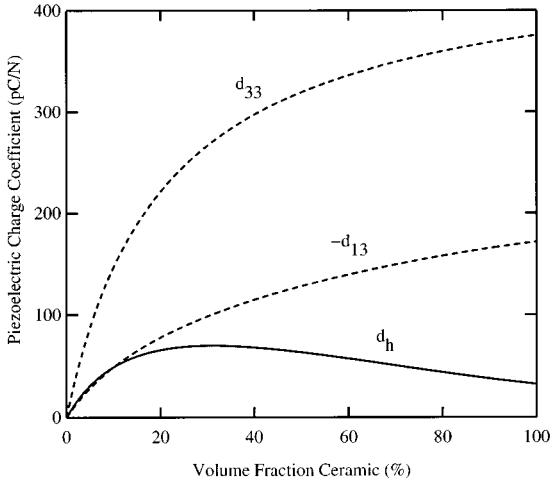

FIG. 3. Effective piezoelectric charge coefficients d_{ij} and d_h as a function of piezoelectric ceramic volume fraction for a PZT5A/Stycast composite (see Sec. V A).

materials for hydrophone applications, it has a relatively small hydrostatic d_h. The modified lead titanate piezoelectric ceramics differ from PZT in that they have an essentially vanishing transverse piezoelectric coupling, i.e., $d_{13} \cong 0$ and therefore $d_h \cong d_{33}$. For this reason, even though their d_{33} values are only about 20% of that of PZT, the modified lead titanates are often used in applications involving hydrostatic fields (e.g., underwater acoustics).

In Fig. 2 we show the values for the effective κ and μ as obtained by integrating the DEM ODEs (103) for a PZT5A/Stycast composite, with material properties as in Table I. To test the accuracy of the DEM scheme we compare our results with that of the boundary integral method (BIM) of Helsing[32] for the special case of an hexagonal array of circular disks, computed to six digit accuracy and for inclusion volume fractions up to 90%. As shown, the DEM results agree well with these predictions, and predict $\kappa^{(e)}$ and $\mu^{(e)}$ with relative error of less than 5%. This is the case for all the examples in this section. Also shown is the prediction for $\kappa^{(e)}$ as given by the Smith–Auld model (cf. III D). As discussed in IV A, since the matrix (Stycast) has a Poisson's ratio $\nu^{(m)} = 0.3$ (close to 0.5), the Smith–Auld theory gives a good approximation for $\kappa^{(e)}$.

In Fig. 3 is shown the dependence of the effective piezoelectric charge coefficients d_{13}, d_{33}, and d_h on the volume fraction ceramic for a PZT5A/Stycast composite, using DEM. As discussed in III A, in this case we have

$$\nu_{13}^{(m)} = 0.3 < -d_{13}^{(i)}/d_{33}^{(i)} = 0.457,$$

so that the condition for enhancement (82) is satisfied. The resulting decoupling of d_{13} and d_{33} prevents the cancellation typical of PZT, resulting in a significant enhancement in d_h at a low volume-fraction of ceramic.

Figure 4 shows the dependence of d_{13}, d_{33}, and d_h on the volume fraction for a composite made of modified lead-titanate and Stycast. Here $-d_{13}^{(i)}/d_{33}^{(i)} = 0.034$ compared to $\nu_{13}^{(m)} = 0.3$, and hence the condition for enhancement (82) fails. As predicted in III A, no enhancement in d_h is observed.

Figure 5 shows the sharp peaks in g_h for these two composites.

In Fig. 6 we compare the hydrostatic figure of merit $d_h g_h$ for these two composites. As predicted in III B, due to the enhancement in d_h for the PZT5A/Stycast composite, we observe a large increase in $d_h g_h$ at around 15 vol % ceramic. On the other hand, the $(Pb,Ca)TiO_3$/Stycast composite shows very little improvement in $d_h g_h$ over the pure ceramic phase.

Finally, we compare the hydrostatic coupling coefficient k_h for these two composites in Fig. 7. For the PZT5A/Stycast composite we observe a maximum k_h of 14% at about 10 vol % ceramic, which is a modest improvement over the 8% of pure PZT5A, showing that this would be the most efficient region within which to operate as a transducer. Due to the

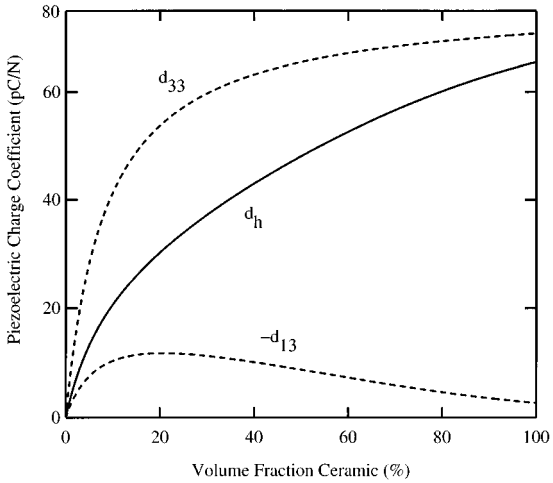

FIG. 4. Effective piezoelectric charge coefficients d_{ij} and d_h as a function of piezoelectric ceramic volume fraction for a composite made from calcium-modified lead-titanate ($(Pb,Ca)TiO_3$) piezoelectric ceramic and Stycast, with material properties as in Table I (see Sec. V A).

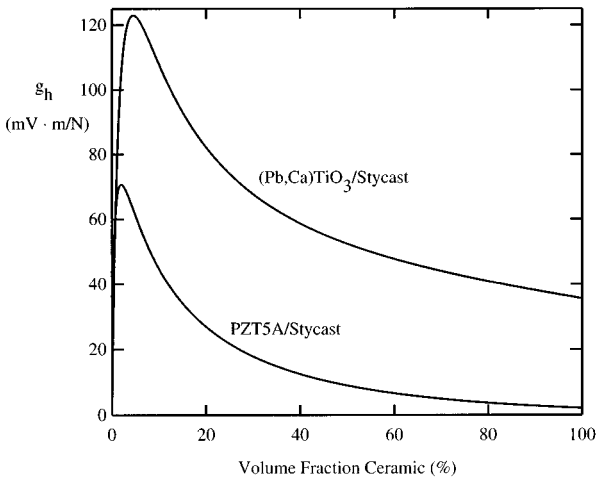

FIG. 5. Effective hydrostatic voltage coefficient g_h as a function of piezoelectric ceramic volume fraction for a PZT5A/Stycast and $(Pb,Ca)TiO_3$/Stycast composite (see Sec. V A).

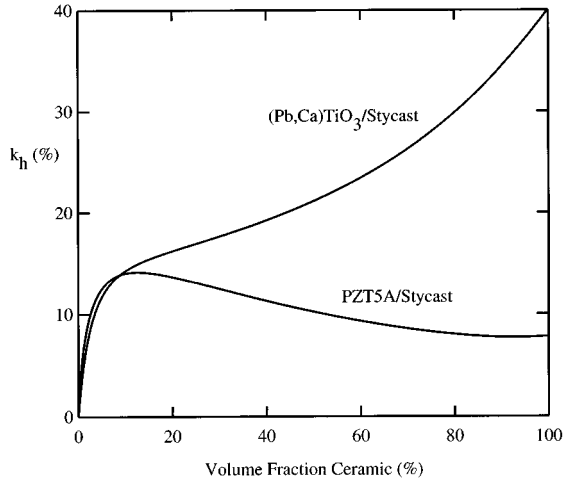

FIG. 7. Hydrostatic electromechanical coupling factor k_h as a function of piezoelectric ceramic volume fraction. The PZT5A/Stycast composite satisfies the enhancement condition (82) and its k_h exceeds that of the pure ceramic. For the modified lead-titanate composite the condition (82) fails, hence the pure ceramic phase exhibits the larger k_h.

lack of decoupling in the modified lead-titanate composite, our calculations show a near monotone growth of k_h as the volume fraction of ceramic increases, and although it compares well with the PZT5A/Stycast composite at small volume-fractions, the hydrostatic coupling coefficient of the composite remains much smaller than that of the pure ceramic.

By choosing a matrix material specifically tailored to the properties of the piezoelectric ceramic, these figures can be significantly improved. We first discuss some of the advantages of adding porosity to the matrix.

B. The effect of porosity in the matrix

A viable but poorly understood technique to further enhance the hydrostatic sensitivity of 1–3 piezoelectric ceramic-polymer composites, is to add porosity to the matrix. This can be done in many ways, for example by foaming the matrix to produce micropores (e.g., Ref. 33), or even by introducing a single large internal void (e.g., Ref. 9). Both methods have been reported to be successful in further decoupling the effective d_{33} and d_{13} coefficients and lowering the permittivity, resulting in improvements in the hydrostatic d_h and g_h coefficients.[6,9,33] (One caveat in using porous materials for deep-sea acoustic transduction is that micropores may collapse at high pressures.)

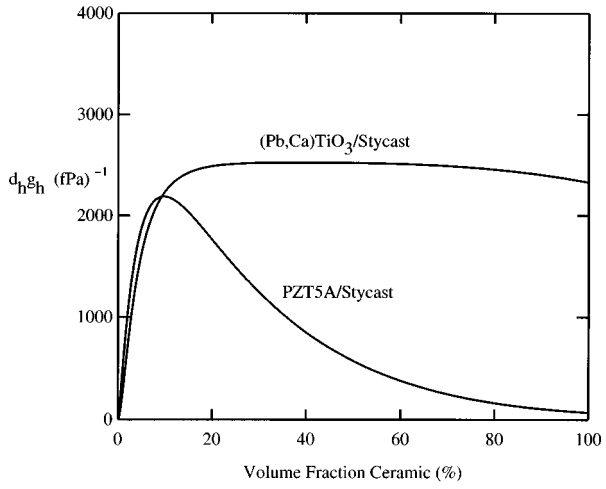

FIG. 6. Hydrostatic figure of merit $d_h g_h$ as a function of piezoelectric ceramic volume fraction. Notice the strong enhancement due to the Poisson's ratio effect in the PZT5A/Stycast composite, whereas the $(Pb,Ca)TiO_3$/Stycast composite shows very little improvement in $d_h g_h$ over the pure ceramic phase.

Here we focus on the consequences of using a cellular matrix obtained by foaming. Foaming can be applied to almost any material, and provides a well-developed technique to introduce cellular microstructure at a length-scale much smaller than that of the ceramic rod-inclusions.[34] This allows us to treat the porous matrix as a homogeneous isotropic elastic solid, for which the macroscopic elastic moduli depend only on the porosity and the cell geometry (in particular on whether the cells are open or closed), but not on the cell-size. In the case of open cells, the effective Young's modulus E and Poisson's ratio ν are well-described by

$$E^{(m)}/E^{(\text{polymer})} = (1-\phi)^2, \quad \nu^{(m)}/\nu^{(\text{polymer})} = 1, \qquad (110)$$

where $\phi = 1 - \rho^{(m)}/\rho^{(\text{polymer})}$ is the porosity expressed in terms of the relative density.[34] For such open-cell foams the Poisson's ratio is therefore unaffected by the porosity. These formulas agree well with experimental results for many polymers, elastomers, metals, and glasses, and in some cases are valid for porosities as high as 90% (see, for example, Ref. 34, Figs. 5.9–5.11). Similar expressions hold for closed-cell foams, although the expression for the effective Young's modulus is slightly more complicated (so as to account for the effects of membrane stresses and gas pressure). The Poisson's ratio is again unaffected by porosity.

Figures 8 to 13 show the hypothetical effects of using a porous foamed matrix, which we assume to satisfy (110), for the two systems above, i.e., as piezoelectric ceramic inclusions we again use PZT5A and calcium-modified lead-titanate. [Note that, by (110), increasing the porosity is

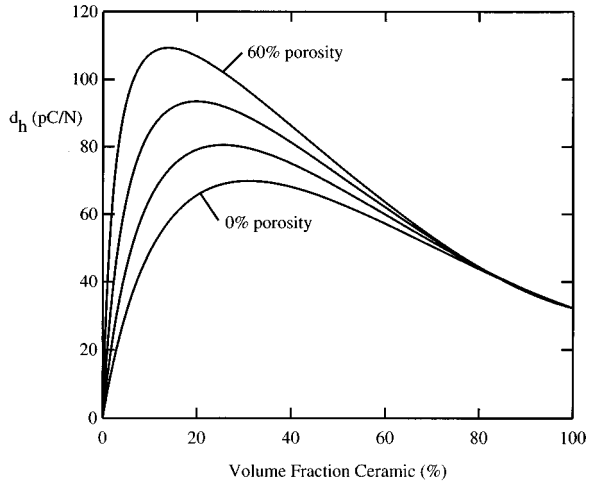

FIG. 8. Hydrostatic piezoelectric charge coefficient d_h for a composite made from PZT5A and porous Stycast, as described in Sec. V B.

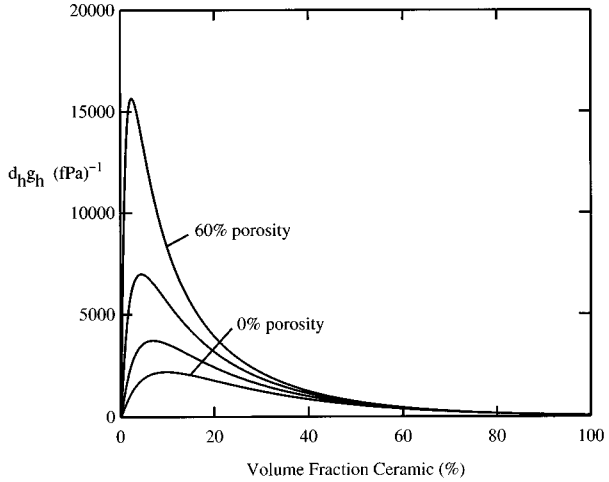

FIG. 10. Hydrostatic figure of merit $d_h g_h$ for a composite made from PZT5A and porous Stycast (see Sec. V B).

equivalent to fixing the Poisson's ratio of the matrix, and lowering its Young's modulus.] We use the elastic moduli of Stycast for the matrix backbone, and display the effective quantities at 0%, 20%, 40%, and 60% porosity. From (110), adding 60% porosity corresponds to lowering the effective Young's modulus of the matrix to 16% of its original value. We also choose $\epsilon^{(m)}$ to be equal to that of Stycast. This approximation entails small error since $\epsilon^{(m)}$ is relatively small.

Figures 8 and 9 show the effect of matrix porosity on the effective d_h for, respectively, a PZT5A and lead-titanate composite, and with porous matrix as described above. For the PZT5A composite, increasing the porosity in the matrix from 0% to 60% almost doubles the maximum d_h value (the maximum in d_h shifts from approximately 70 pC/N at 30 vol % ceramic to 110 pC/N at 15 vol % ceramic). On the other hand, for the lead-titanate composite Fig. 9 shows that although an additional enhancement is possible by increasing the matrix porosity, d_h remains rather small compared to the value for the pure ceramic.

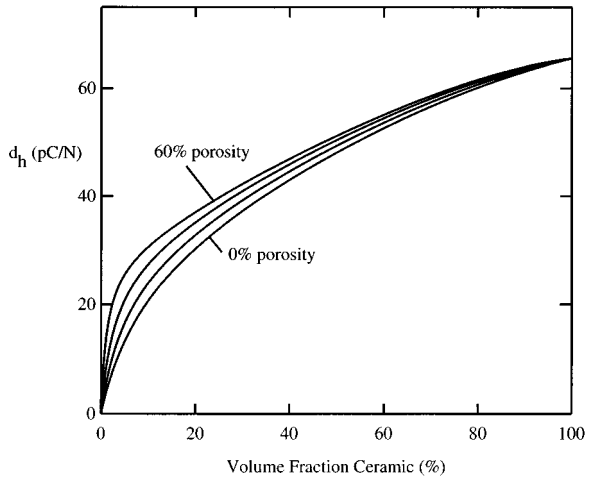

FIG. 9. Hydrostatic piezoelectric charge coefficient d_h for a composite made from calcium-modified lead-titanate and porous Stycast (see Sec. V B).

Figures 10 and 11 show the effect of matrix porosity on the hydrostatic figure of merit $d_h g_h$. For both composites we observe a substantial increase at low volume fractions. For the lead-titanate composite, the maximum value of $d_h g_h$ more than doubles when increasing porosity to 60%, while for the PZT5A composite it increases sevenfold from approximately 2000 to 15 000 fPa^{-1}. For both composites, an increase in porosity of the matrix causes $d_h g_h$ to peak more sharply and at lower volume fraction ceramic.

The effect of matrix porosity on the hydrostatic coupling coefficient k_h is shown in Figs. 12 and 13. For the PZT5A composite there is not much improvement except at very low volume fraction ceramic ($f<5$ vol %). As in the case of d_h and $d_h g_h$, the peaks in k_h sharpen and occur at increasingly lower volume fractions as the porosity is increased. At higher volume fractions the coupling can decrease substantially. Figure 13 shows that if the enhancement condition (82) fails then an increase in porosity can actually worsen the effective coupling coefficient. Due to the failure of (82), the enhancement in $d_h g_h$ is relatively small (compared to the PZT5 composite), and cannot compensate for the increase in

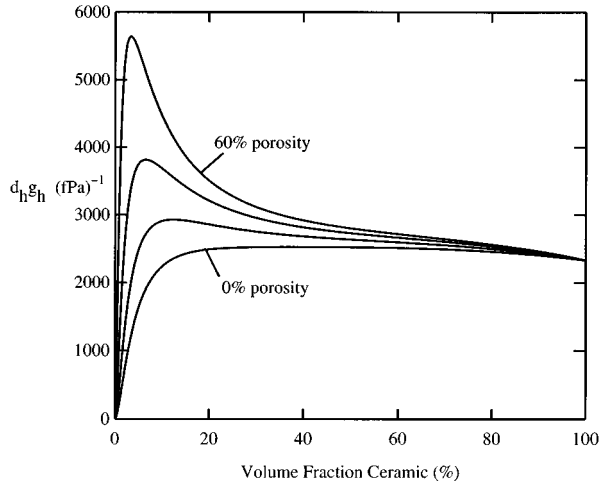

FIG. 11. Hydrostatic figure of merit $d_h g_h$ for a composite made from calcium-modified lead-titanate and porous Stycast (see Sec. V B).

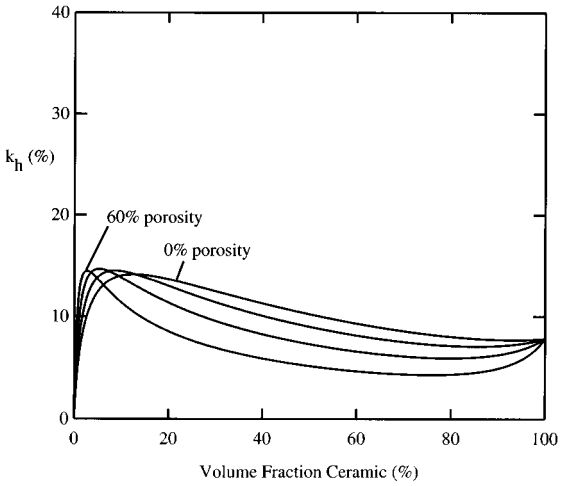

FIG. 12. Hydrostatic electromechanical coupling k_h for a composite made from PZT5A and porous Stycast. Increasing the porosity results in narrower peaks at lower volume fractions, without much change in the maximum value of k_h (see Sec. V B).

s_h. We therefore observe a systematic deterioration in the coupling as porosity is increased, with k_h decaying to almost 50% of the zero-porosity value.

C. Enhancement due to a polymer matrix with negative Poisson's ratio

The high-contrast approximation (80) suggests that a sensitivity enhancement can be achieved by using a matrix with sufficiently small Poisson's ratio. Using DEM theory, we investigate the interesting possibility, first proposed by Smith,[12] of exploiting new materials with negative Poisson's ratio to maximize the hydrostatic sensitivity and electromechanical coupling in 1–3 piezoelectric composites.

For a material described by linear isotropic elasticity, thermodynamic stability requires the stiffness matrix to be positive-definitive, thereby constraining the Poisson's ratio ν to lie between -1 and 0.5. For most materials, ν lies between 0.3 and 0.4 (e.g., $\nu=0.3$ for Stycast), approaching it's theoretical upper limit for rubbery incompressible polymers. Materials exhibiting negative Poisson's ratio do occur in nature, but are quite rare. Only recently has it become possible to tailor materials specifically for this purpose, which has led to much interest in their modeling and application.[35] The first materials specifically designed and manufactured to exploit the advantages of a negative Poisson's ratio were the reentrant open-cell polymer and metallic foams of Lakes,[36–38] with Poisson's ratio as low as -0.7. Another example is that of the microporous and highly anisotropic expanded polytetrafluoroethylene.[39–41] In the following numerical examples we restrict our attention to the isotropic case.

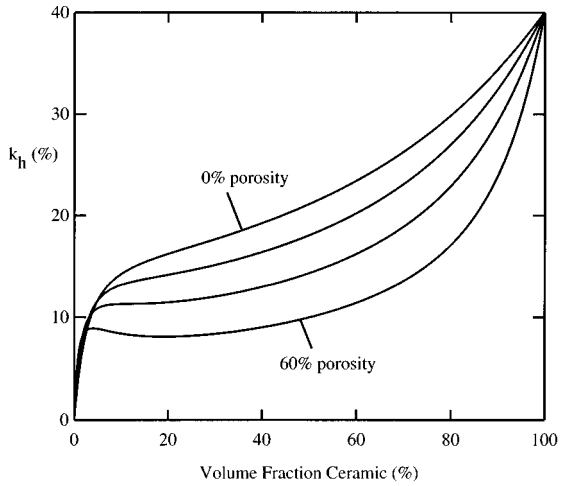

FIG. 13. Hydrostatic electromechanical coupling k_h for a composite made from calcium-modified lead-titanate ceramic and porous Stycast. Due to the failure of the enhancement condition (82), k_h decreases as matrix porosity is increased (see Sec. V B).

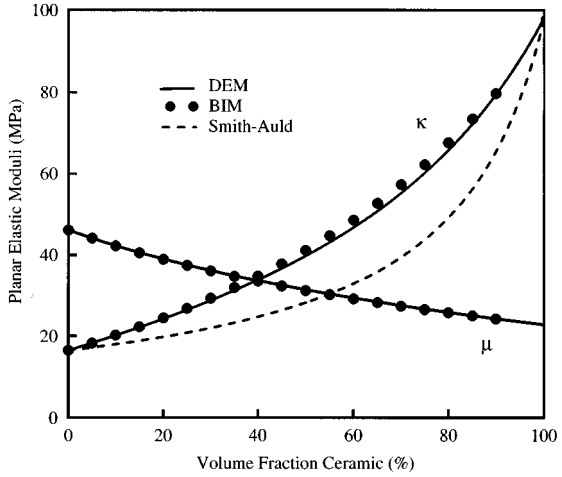

FIG. 14. Effective planar bulk and shear moduli κ and μ as a function of piezoelectric ceramic volume fraction for a composite made from PZT5A inclusions in an isotropic polymer matrix with Young's modulus equal to that of Stycast but with Poisson's ratio $\nu=-0.9$. Predictions using the DEM scheme are compared with Helsing's boundary integral method (BIM)[32] and the Smith–Auld model[11] (see Sec. V C).

As promising as these new materials are, they do introduce additional complications. In particular their highly porous nature make efficient interface bonding more difficult. Also, deep water immersion can cause aging of the microstructure and thereby affect the composite's response.

Figures 14 – 20 show the hypothetical effects of using a matrix with negative Poisson's ratio. In order to be able to compare our simulations with the previous numerical examples, we use a hypothetical isotropic matrix with Young's modulus equal to that of Stycast (i.e., $E=9.22$ GPa, which is about one-seventh that of PZT5), and Poisson's ratio $\nu^{(m)}$ chosen equal to 0.4, 0.0, -0.4, and -0.9. We also choose $\epsilon^{(m)}$ to be equal to that of Stycast.

In Fig. 14 we compare the predictions of DEM and the Smith–Auld model against the high-precision numerical results of Helsing's boundary integral method (BIM)[32] for an hexagonal array of disks. Here the Poisson's ratio is taken to be $\nu^{(m)}=-0.9$, and we display $\kappa^{(e)}$ and $\mu^{(e)}$. The DEM shows excellent accuracy, agreeing to within 5% with the BIM approximation of the theoretically exact result. The Smith–Auld model does less well since it does not take into consideration the shear stiffening which accompanies negative Poisson's ratios and which influences indirectly the value of $\kappa^{(e)}$ (cf. Sec. IV A).

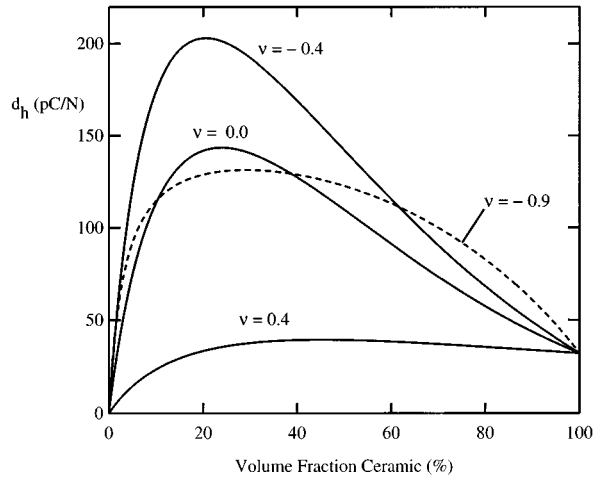

FIG. 15. Hydrostatic piezoelectric charge coefficient d_h for a composite made from PZT5A inclusions in an isotropic polymer matrix with Young's modulus equal to that of Stycast but with Poisson's ratios $\nu=0.4, 0.0, -0.4, -0.9$. For PZT5A the condition (82) is satisfied for $\nu<0.457$, and we therefore observe enhancement in all cases. At $\nu=-0.9$ the shear modulus of the matrix exceeds that of the PZT, which weakens the enhancement (see Sec. V C).

Figures 15 and 16 show the effect on d_h of lowering the Poisson's ratio from 0.4 to -0.9. For the PZT5A composite $-d_{13}^{(i)}/d_{33}^{(i)}=0.457$ and, as predicted by (80), we observe only a slight enhancement at $\nu^{(m)}=0.4$. Decreasing the Poisson's ratio to $\nu^{(m)}=-0.4$ results in a sixfold improvement in d_h, from 32 pC/N for pure PZT5A, to a maximum of 200 pC/N at 20 vol % PZT. Interestingly, when decreasing $\nu^{(m)}$ further to -0.9, the effective d_h worsens significantly at almost all volume fractions. The main reason for this lies in the assumed isotropic nature of the matrix, which forces a rapid increase in the transverse rigidity $\hat{K}_\infty(f)\cong 1+2(1-\nu^{(m)})f+O(f^2)$ [see Eq. (108)], as $\nu^{(m)}$ decreases to its allowed lower limit of -1. The result is a much smaller enhancement

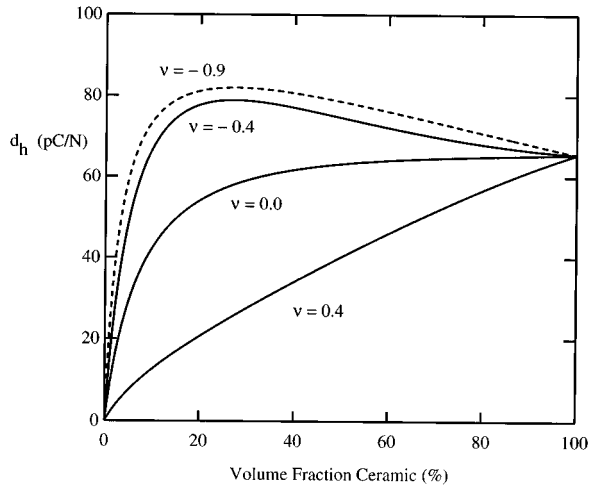

FIG. 16. Hydrostatic piezoelectric charge coefficient d_h for a composite made from calcium-modified lead-titanate inclusions and an isotropic matrix with Young's modulus equal to that of Stycast but with Poisson's ratios $\nu=0.4, 0.0, -0.4, -0.9$. In this system the condition (82) is satisfied for $\nu<0.034$, hence the enhancement in d_h for negative Poisson's ratios $\nu=-0.4$ and -0.9 (see Sec. V C).

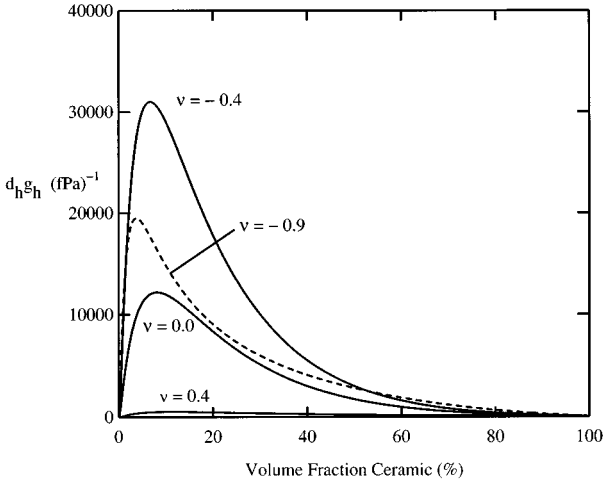

FIG. 17. Hydrostatic figure of merit $d_h g_h$ for a composite made from PZT5A inclusions and an isotropic matrix with Young's modulus equal to that of Stycast but with Poisson's ratios $\nu=0.4, 0.0, -0.4, -0.9$ (see Sec. V C).

in (80), despite the large value of the $(d_{13}^{(i)}+\nu_{13}^{(m)}d_{33}^{(i)})$ term. For the lead-titanate composite, we observe in Fig. 16 a continuing improvement in d_h as $\nu^{(m)}$ is decreased from 0.4 to -0.9. In this case $-d_{13}^{(i)}/d_{33}^{(i)}=0.034$ and, as predicted by (80), we observe enhancement once $\nu^{(m)}$ is decreased below zero. At $\nu^{(m)}=-0.4$ and -0.9, the composite's d_h actually exceeds that of the pure ceramic by as much as 30%.

Note that for an isotropic matrix the shear modulus $\mu=E/[2(1+\nu)]$ (here E is the Young's modulus) must grow to ∞ as $\nu\to-1$. In fact, choosing $\nu^{(m)}=-0.9$ gives a shear modulus of $\mu^{(m)}=46$ GPa for the PZT5A composite, which is larger than the $\mu^{(i)}=33$ GPa of the PZT5A inclusion. In this case the form of the DEM ODEs (103) implies that $\hat{K}_\infty$ increases much more rapidly with f, which offsets the benefits of a large negative $\nu^{(m)}$. Because of lead-titanate composite's high shear modulus ($\mu^{(i)}=56$ GPa), this complication is avoided for our choices of $\nu^{(m)}$. This explains the

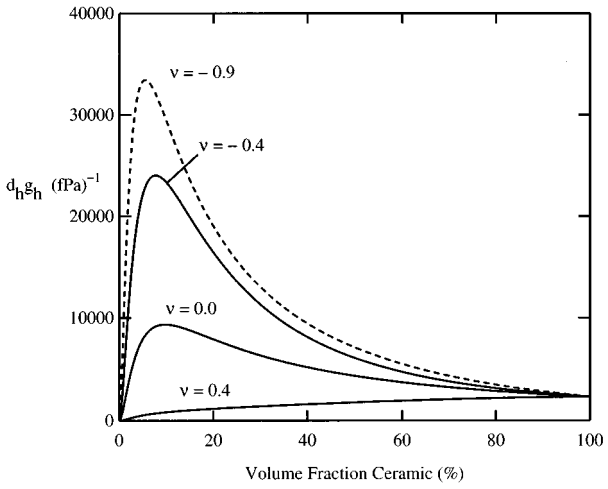

FIG. 18. Hydrostatic figure of merit $d_h g_h$ for a composite made from calcium-modified lead-titanate inclusions and an isotropic matrix with Young's modulus equal to that of Stycast but with Poisson's ratios $\nu=0.4, 0.0, -0.4, -0.9$ (see Sec. V C).

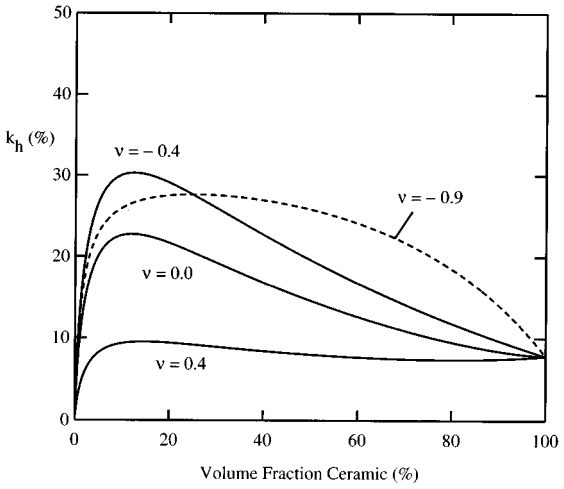

FIG. 19. Hydrostatic electromechanical coupling coefficient k_h for a composite made from PZT5A inclusions and an isotropic matrix with Young's modulus equal to that of Stycast but with Poisson's ratios $\nu = 0.4, 0.0, -0.4, -0.9$. Decreasing the Poisson's ratio of the matrix results in improved electromechanical coupling over a broader range of compositions (see Sec. V C).

different behavior at $\nu^{(m)} = -0.9$ for the two examples.

Figures 17 and 18 show the large improvement possible in $d_h g_h$ by using a matrix with negative Poisson's ratio. As in Fig. 15, the PZT5A composite shows a decrease in $d_h g_h$ when $\nu^{(m)}$ is chosen too small.

The hydrostatic coupling coefficient k_h shows substantial improvement for both composites. For the PZT5A composite with matrix having $\nu^{(m)} = -0.4$, k_h shows, in Fig. 19, a broad peak at 30% coupling coefficient, centered around 15 vol % ceramic. Further decreasing the Poisson's ratio to -0.9 lowers k_h slightly at lower volume fractions, but allows for a much broader peak. Figure 20 shows that by choosing $\nu^{(m)} = -0.9$ for the lead-titanate composite, one can more than double the k_h achievable by a Stycast matrix

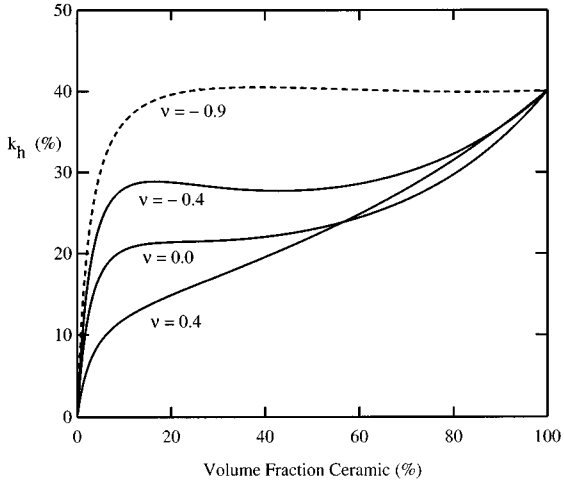

FIG. 20. Hydrostatic electromechanical coupling coefficient k_h for a composite made from calcium-modified lead-titanate inclusions and an isotropic matrix with Young's modulus equal to that of Stycast but with Poisson's ratios $\nu = 0.4, 0.0, -0.4, -0.9$. Decreasing the Poisson's ratio of the matrix phase results in large improvements in the coupling factor over a broad range of compositions (see Sec. V C).

(cf. Fig. 7). Here k_h matches the coupling coefficient of the pure ceramic at about 20 vol % and higher.

These results, obtained by using negative Poisson's ratios, can be improved even further by using anisotropic matrix materials. If one of the three independent orthotropic Poisson's ratios is negative, there is no theoretical limit on the range of possible values for the other two.[42] For example, in the highly anisotropic form of expanded polytetrafluoroethylene, Poisson's ratios as low as -12 have been measured.[39,41] Using such materials as a matrix should make additional sensitivity enhancement possible.

VI. CONCLUSIONS

We presented a first-principles description of the effective properties of 1–3 piezoelectric composites. Specifically, we showed that, for hydrostatic applications, the relevant effective properties can be expressed algebraically in terms of the volume fractions and moduli of the constituents, and a single ''microstructural'' parameter p which has a simple physical interpretation. We used this theory as well as the high contrast (soft polymer matrix, hard piezoelectric ceramic rods) typical of most applications to obtain simple expressions which describe the nonmonotone enhancement of the hydrostatic piezoelectric coefficient d_h, the hydrostatic figure of merit $d_h g_h$, and the hydrostatic electromechanical coupling coefficient k_h independently of microstructural details. In particular, we predict the size of the Poisson's ratio effect, and derived a single necessary criterion (82) for the enhancement of d_h. When using piezoelectric ceramics such as PZT, for which the piezoelectric coefficients d_{13} and d_{33} are large but cancel to give a poor hydrostatic response, it follows that by satisfying the condition (82) a significant enhancement in both the hydrostatic figure of merit $d_h g_h$ as well as the hydrostatic coupling coefficient k_h can be achieved over the pure ceramic. On the other hand, for piezoelectric ceramics with high piezoelectric anisotropy and relatively large hydrostatic response, e.g., calcium-modified lead-titanate, a matrix with Poisson's ratio much smaller than that of typical polymers is required to satisfy (82). If this constraint can be met, however, then a k_h equal to that of the pure ceramic is observed over a broad range of compositions.

We showed that the differential effective medium (DEM) approximation provides a simple, self-consistent means to numerically compute the effective properties of different piezoelectric composite systems by solving a system of two ordinary differential equations. Examples are presented which illustrate enhancement versus nonenhancement in the sensitivity parameters, in agreement with our high-contrast analysis.

Finally, this approach is used to investigate two interesting design issues: the effect of porosity in the polymer matrix, and the use of materials with negative Poisson's ratio to enhance the Poisson's ratio effect. The benefits of adding porosity (by foaming the matrix) are largely restricted to materials for which the enhancement condition (82) is valid at zero porosity. If (82) fails then this strategy can actually lower the coupling factor k_h. On the other hand, by lowering the Poisson's ratio of the matrix, one generally improves the

sensitivity and electromechanical coupling in all cases. The use of negative Poisson's ratio materials are shown to be potentially beneficial, providing optimal performance over a wide range of compositions.

ACKNOWLEDGMENTS

Marco Avellaneda is grateful to the National Science Foundation for support through Grant No. NSF/DMS-92-07085 and NSF/DMS-94-02763, and the Army Research Office for support through Grant No. ARO/DAAL-03-92-G0011. Pieter Swart thanks the Air Force Office for Scientific Research (AFOSR-90-0090) and the National Science Foundation (NSF/DMS-9112654, NSF/DMS-92-17151, and NSF/DMS-94-02763) and the Department of Energy (W-7405-ENG-36 and KC-07-01-01) for supporting this research. The authors wish to thank Dr. Yakov Benveniste for pointing out an error in an earlier draft of this work, and Dr. Johan Helsing for the use of his boundary integral code to test the numerical accuracy of the DEM scheme. Last, but not least, we are grateful to the two referees of this paper, who have helped us to substantially improve an earlier draft.

APPENDIX: DERIVATION OF FORMULAS FOR THE EFFECTIVE MODULI

We give a derivation of the fundamental relations (14) showing that the relevant effective moduli can be expressed in terms of the microstructural parameter p and the moduli of the two phases. Results in the same vein have been derived by Schulgasser[18] and Benveniste and Dvorak.[19] Our formulation emphasizes the role of the microstructural parameters p and q. These parameters are, of course, directly related to $\kappa^{(e)}$ and $\mu^{(e)}$. We give here an alternative proof based on the evaluation of the so-called Wu tensor (defined below). The basic idea, which exploits the properties of local fields for a transversely isotropic microstructure, goes back to Hill.[17]

Denote by $\mathbf{L}$, $\mathbf{L}^{(e)}$, $\mathbf{L}^{(m)}$, and $\mathbf{L}^{(i)}$, respectively, the spatially varying linear response ''tensor'' defined in (6), the effective tensor, and the tensors corresponding to the matrix and the inclusion phases. We will use the $(\mathbf{S},\mathbf{E})\leftrightarrow(\mathbf{T},\mathbf{D})$ formulation (6) for convenience. By setting

$$\mathbf{F}=\begin{bmatrix}\mathbf{S}\\ \mathbf{E}\end{bmatrix}, \tag{A1}$$

i.e., combining the stress and electric fields into a single ''field,'' we have

$$\begin{aligned}\mathbf{L}^{(e)}\langle\mathbf{F}\rangle=\langle\mathbf{L}\mathbf{F}\rangle&=\mathbf{L}^{(m)}\langle\mathbf{F}\rangle+\langle(\mathbf{L}-\mathbf{L}^{(m)})\mathbf{F}\rangle\\ &=\mathbf{L}^{(m)}\langle\mathbf{F}\rangle+\langle(\mathbf{L}^{(i)}-\mathbf{L}^{(m)})\chi^{(i)}\mathbf{F}\rangle\\ &=\mathbf{L}^{(m)}\langle\mathbf{F}\rangle+(\mathbf{L}^{(i)}-\mathbf{L}^{(m)})\langle\chi^{(i)}\mathbf{F}\rangle\\ &=\mathbf{L}^{(m)}\langle\mathbf{F}\rangle+f(\mathbf{L}^{(i)}-\mathbf{L}^{(m)})\langle\mathbf{F}\rangle_i.\end{aligned} \tag{A2}$$

Here, $\chi^{(i)}(\mathbf{r})=1$ if the position vector $\mathbf{r}$ is in the inclusion phase and $\chi^{(i)}(\mathbf{r})=0$ if $\mathbf{r}$ is in the matrix phase, i.e., $\chi^{(i)}(\mathbf{r})$ is the characteristic function of the inclusion phase. Moreover,

$$\langle\mathbf{F}\rangle_i=\frac{1}{f}\langle\chi^{(i)}\mathbf{F}\rangle \tag{A3}$$

represents the average of $\mathbf{F}$ over the inclusion phase. We introduce the Wu tensor $\mathbf{W}$ defined by

$$\langle\mathbf{F}\rangle_i=\mathbf{W}\langle\mathbf{F}\rangle. \tag{A4}$$

This tensor (which is independent of $\langle\mathbf{F}\rangle$) relates the ''applied field'' $\langle\mathbf{F}\rangle$ to the average of the local field $\mathbf{F}$ in the inclusion phase. Substituting (A4) in (A2) and eliminating $\langle\mathbf{F}\rangle$ from the equation, we obtain the general formula [cf. Dunn and Taya,[14] Eq. (19)]

$$\mathbf{L}^{(e)}=\mathbf{L}^{(m)}+f(\mathbf{L}^{(i)}-\mathbf{L}^{(m)})\mathbf{W}. \tag{A5}$$

In the case of transversely isotropic piezoelectric composites, we can write this relation in the form of two matrix relations and one scalar relation, viz.,

$$\begin{aligned}\begin{bmatrix}c_{pp}^{(e)} & c_{pz}^{(e)} & -e_{pz}^{(e)}\\ c_{pz}^{(e)} & c_{zz}^{(e)} & -e_{zz}^{(e)}\\ e_{pz}^{(e)} & e_{zz}^{(e)} & \epsilon_{zz}^{(e)}\end{bmatrix}&=\begin{bmatrix}c_{pp}^{(m)} & c_{pz}^{(m)} & -e_{pz}^{(m)}\\ c_{pz}^{(m)} & c_{zz}^{(m)} & -e_{zz}^{(m)}\\ e_{pz}^{(m)} & e_{zz}^{(m)} & \epsilon_{zz}^{(m)}\end{bmatrix}\\ &+f\begin{bmatrix}\Delta c_{pp} & \Delta c_{pz} & -\Delta e_{pz}\\ \Delta c_{pz} & \Delta c_{zz} & -\Delta e_{zz}\\ \Delta e_{pz} & \Delta e_{zz} & \Delta\epsilon_{zz}\end{bmatrix}\\ &\times\begin{bmatrix}w_{11} & w_{12} & w_{13}\\ w_{21} & w_{22} & w_{23}\\ w_{31} & w_{32} & w_{33}\end{bmatrix}\end{aligned} \tag{A6}$$

and

$$\mu^{(e)}=\mu^{(m)}+f(\mu^{(i)}-\mu^{(m)})\tilde{w}, \tag{A7}$$

where w_{ij} and $\tilde{w}$ are the components of the Wu tensor in dyadic (Voigt) tensor notation. By definition of p and q, in (9) and (10) respectively, we have

$$w_{11}=p \quad \text{and} \quad \tilde{w}=q. \tag{A8}$$

Moreover, we know that an applied axial strain such that $\langle S_p\rangle=0$ gives rise to a uniform axial strain inside the composite. Similarly, the E_3 component of the electric field is also uniform. Therefore,

$$\begin{bmatrix}w_{11} & w_{12} & w_{13}\\ w_{21} & w_{22} & w_{23}\\ w_{31} & w_{32} & w_{33}\end{bmatrix}=\begin{bmatrix}p & w_{12} & w_{13}\\ 0 & 1 & 0\\ 0 & 0 & 1\end{bmatrix}. \tag{A9}$$

The coefficients w_{12} and w_{13} can be computed using the symmetry of the effective tensor. In fact $c_{pz}^{(e)}$ can be computed from (A6) in two ways. Accordingly, multiplying the second row of $\Delta\mathbf{C}$ by the first column of $\mathbf{W}$, we obtain (14c). On the other hand, multiplying the first row of $\Delta\mathbf{C}$ by the second column of $\mathbf{W}$, we obtain

$$c_{pz}^{(e)}=c_{pz}^{(m)}+f(\Delta c_{pp}w_{12}+\Delta c_{pz}).$$

Hence,

$$\Delta c_{pp}w_{12}+\Delta c_{pz}=p\Delta c_{pz}$$

or

$$w_{12}=(p-1)\frac{\Delta c_{pz}}{\Delta c_{pp}}. \tag{A10}$$

A similar computation with $e_{pz}^{(e)}$ yields (14d) and $-e_{pz}^{(e)}=-e_{pz}^{(m)}+f(\Delta c_{pp}w_{13}-\Delta e_{pz})$, which gives

$$w_{13}=-(p-1)\frac{\Delta e_{pz}}{\Delta c_{pz}}. \tag{A11}$$

Substituting these values in (A9), we obtain equations (14e), (14f), and (14g). The proof of the representation formulas (14) is complete.

[1] E. Klein, ''Underwater sound and naval acoustical research and applications before 1939,'' J. Acoust. Soc. Am. **43**, 931–947 (1968).

[2] O. B. Wilson, *An Introduction to the Theory and Design of Sonar Transducers* (Peninsula, Los Altos, CA, 1988).

[3] W. A. Smith, ''The application of 1–3 piezocomposites in acoustic transducers,'' *Proceedings of the 1990 IEEE 7th International Symposium on Ferroelectrics* (IEEE, New York, 1991), pp. 145–152.

[4] R. E. Newnham, ''Composite electroceramics,'' Ferroelectrics **68**, 1–32 (1986).

[5] W. D. Wilder, ''Electroacoustic sensitivity of ceramic cylinders,'' J. Acoust. Soc. Am. **62**, 769–771 (1977).

[6] A. Safari, G. Sa-gong, J. Giniewicz, and R. E. Newnham, ''Composite piezoelectric sensors,'' in *Proceedings of the 21st University Conference on Ceramic Science* (Plenum, New York, 1985), Vol. 20, pp. 445–454.

[7] A. A. Shaulov, W. A. Smith, and R. Y. Ting, ''Modified-lead-titanate/polymer composites for hydrophone applications,'' Ferroelectrics **93**, 177–182 (1989).

[8] R. Y. Ting, A. A. Shaulov, and W. A. Smith, ''Evaluation of the properties of 1–3 piezocomposites of a new lead titanate in epoxy resins,'' Ferroelectrics **132**, 69–77 (1992).

[9] M. J. Haun and R. E. Newnham, ''An experimental and theoretical study of 1–3 and 1–3–0 piezoelectric PZT-polymer composites for hydrophone applications,'' Ferroelectrics **68**, 123–139 (1986).

[10] H. L. W. Chan and J. Unsworth, ''Simple model for piezoelectric ceramic/polymer 1–3 composites used in ultrasonic transducer applications,'' IEEE Trans. Ultrason. Ferroelectr. Freq. Control **36**, 434–441 (1989).

[11] W. A. Smith and B. A. Auld, ''Modeling 1–3 composite piezoelectrics: thickness-mode oscillations,'' IEEE Trans. Ultrason. Ferroelectr. Freq. Control **38**, 40–47 (1991).

[12] W. A. Smith, ''Optimizing electromechanical coupling in piezocomposites using polymers with negative Poisson's ratio,'' *Proceedings of the IEEE 1991 Ultrasonics Symposium* (IEEE, New York, 1991), pp. 661–666.

[13] W. A. Smith, ''Modeling 1–3 composite piezoelectrics: hydrostatic response,'' IEEE Trans. Ultrason. Ferroelectr. Freq. Control **40**, 41–49 (1993).

[14] M. L. Dunn and M. Taya, ''Micromechanics predictions of the effective electroelastic moduli of piezoelectric composites,'' Int. J. Solids Struct. **30**, 161–175 (1993).

[15] M. L. Dunn and M. Taya, ''An analysis of piezoelectric composite materials containing ellipsoidal inhomogeneities,'' Proc. R. Soc. London, Ser. A **443**, 265–287 (1993).

[16] M. Avellaneda and P. J. Swart, ''Effective moduli and electro-acoustic performance of epoxy-ceramic 1–3 piezocomposites,'' in *Smart Structures and Materials 1994: Mathematics and Control in Smart Structures*, edited by H. T. Banks (SPIE 1994), Proc. SPIE 2192, 394–402.

[17] R. Hill, ''A self-consistent mechanics of composite materials,'' J. Mech. Phys. Solids **13**, 213–222 (1965).

[18] K. Schulgasser, ''Relationships between the effective properties of transversely isotropic piezoelectric composites,'' J. Mech. Phys. Solids **40**, 473–479 (1992).

[19] Y. Benveniste and G. J. Dvorak, ''Uniform fields and universal relations in piezoelectric composites,'' J. Mech. Phys. Solids **40**, 1295–1312 (1992).

[20] H. F. Tiersten, *Linear Piezoelectric Plate Vibrations* (Plenum, New York, 1969), pp. 30–32.

[21] ''IEEE Standard on Piezoelectricity,'' ANSI/IEEE Std. 176–1978.

[22] Landolt–Börnstein, *Elastic, Piezoelectric, Pyroelectric, Piezooptic, Electrooptic Constants, and Nonlinear Dielectric Susceptibility of Crystals* (Springer-Verlag, Berlin, 1984), Vol. III, Table 16.

[23] J. G. Berryman, ''Long-wavelength propagation in composite elastic media. II. Ellipsoidal inclusions,'' J. Acoust. Soc. Am. **68**, 1820–1831 (1980).

[24] Z. Hashin, ''Analysis of composite materials—a survey,'' Trans. ASME, J. Appl. Mech. **50**, 481–505 (1983).

[25] S. Torquato, ''Random heterogeneous media: Microstructure and improved bounds on effective properties,'' Appl. Mech. Rev. **44**, 37–76 (1991).

[26] R. McLaughlin, ''A study of the differential scheme for composite materials,'' Int. J. Eng. Sci. **15**, 237–244 (1977).

[27] A. N. Norris, ''A differential scheme for the effective moduli of composites,'' Mech. Mater. **4**, 1–16 (1985).

[28] A. N. Norris, A. J. Callegari, and P. Sheng, ''A generalized differential effective medium theory,'' J. Mech. Phys. Solids **33**, 525–543 (1985).

[29] G. W. Milton, ''Microgeometries corresponding exactly with effective medium theories,'' in *Physics and Chemistry of Porous Media*, edited by D. L. Johnson and P. N. Sen, AIP Conf. Proc. No. **107** (AIP, New York, 1983).

[30] M. Avellaneda, ''Iterated homogenization, differential effective medium theory and applications,'' Commun. Pure Appl. Math. **40**, 527–554 (1987).

[31] R. Landauer, ''Electrical conductivity in inhomogeneous media,'' in *Electrical Transport and Optical Properties of Inhomogeneous Media*, edited by J. C. Garland and D. B. Tanner (AIP, New York, 1978), pp. 1–45.

[32] J. Helsing, ''An integral equation method for elastostatics of periodic composites,'' J. Mech. Phys. Solids **43**, 815–828 (1995).

[33] K. A. Klicker, J. V. Biggers, and R. E. Newnham, ''Composites of PZT and Epoxy for hydrostatic transducer applications,'' J. Am. Ceram. Soc. **64**, 5 (1981).

[34] L. J. Gibson and M. F. Ashby, *Cellular Solids: Structures & Properties* (Pergamon, New York, 1988).

[35] G. W. Milton, ''Composite materials with Poisson's ratios close to -1,'' J. Mech. Phys. Solids **40**, 1105–1137 (1992).

[36] R. Lakes, ''Foam structures with a negative Poisson's ratio,'' Science **235**, 1038–1040 (1987).

[37] E. A. Friis, R. S. Lakes, and J. B. Park, ''Negative Poisson's ratio polymeric and metallic foams,'' J. Mater. Sci. **23**, 4406–4414 (1988).

[38] R. Lakes, ''Deformation mechanisms in negative Poisson's ratio materials: structural aspects,'' J. Mater. Sci. **26**, 2287–2292 (1991).

[39] B. D. Caddock and K. E. Evans, ''Microporous materials with negative Poisson's ratios: I. Microstructure and mechanical properties,'' J. Phys. D **22**, 1877–1882 (1989).

[40] K. E. Evans, ''Tensile network microstructures exhibiting negative Poisson's ratios,'' J. Phys. D **22**, 1870–1876 (1989).

[41] K. E. Evans and B. D. Caddock, ''Microporous materials with negative Poisson's ratios: II. Mechanisms and interpretation,'' J. Phys. D **89**, 1883–1887 (1989).

[42] B. M. Lempriere, ''Poisson's Ratio in Orthotropic Materials,'' AIAA J. **6**, 2226–2227 (1968).

A numerical approach to determining the transient response of nonrectangular bars subjected to transverse elastic impact

Yiching Lin, Wei-Kuang Lai, and Kuo-Lung Lin
Department of Civil Engineering, National Chung-Hsing University, Taichung 40227, Taiwan, Republic of China

(Received 8 April 1997; revised 25 September 1997; accepted 19 November 1997)

The objectives of the studies presented in this paper are to propose an efficient numerical approach to determining the transient response of nonrectangular bars subjected to transverse elastic impact. It is shown that the response of nonrectangular bars, such as T- and I-beams, subjected to transverse impact is composed of frequencies corresponding to the cross-sectional modes of vibration of the nonrectangular bar. In this study, eigenvalue analyses of plane-strain finite-element models of T- and I-sections were performed first to solve for the cross-sectional mode shapes and the corresponding natural frequencies. Three-dimensional resonant analyses were used to verify the existence of the cross-sectional modes obtained from the eigenvalue analyses. Three-dimensional finite-element models were also used to determine the transient response of T- and I-beams subjected to transverse elastic point impact. Numerical results were verified by experimental studies on a 0.5-m-deep concrete T-beam and a 0.72-m-deep concrete I-beam. Good agreement was obtained between the numerical and experimental results. It is concluded that the proposed numerical models are valid and efficient for determining the transient response of nonrectangular bars subjected to transverse impact.
[S0001-4966(98)01503-3]

PACS numbers: 43.40.Cw, 43.40.Kd [CBB]

INTRODUCTION

This paper presents an efficient numerical approach to determining the transient response of non-rectangular bars subjected to transverse elastic point impact. The exact elasticity solution has been found for the vibrational modes produced in isotropic bars of infinite length by waves traveling along the length of the bars. Pochammer and Chree[1,2] solved the problem for circular bars and Mindlin and Fox[3] found the solution for rectangular bars. In addition, several researchers used the Rayleigh–Ritz method to find approximate solutions for vibration of noncircular cross sections.[4–7] However, these existing solutions cannot be used to determine the three-dimensional transient response of a bar subjected to transverse impact.

Gazis[8] and Bird[9] proposed approximate analyses of vibrations of thick-walled cylinders. Armenakas *et al.*[10] obtained the exact solutions for free vibrations of circular cylindrical shells because of their simple geometric shapes. Lin and Sansalone[11] showed that these exact solutions can be used to solve for frequencies corresponding to the cross-sectional modes of vibration of a thick hollow cylinder which are present in the response of the cylinder subjected to transverse point impact. In practice, elements used in civil engineering structures are often designed to have special shapes, such as T- and I-shaped beams. It is very difficult to obtain the exact solutions for problems involving transient stress wave propagation in such bounded solids. For the case of square and rectangular bars, Lin and Sansalone[12,13] determined the transverse impact response numerically and experimentally.

The purposes of the studies presented in this paper are to propose an efficient numerical approach for determining the transient response of nonrectangular bars subjected to transverse elastic impact. These studies were designed to establish the basis for using the impact-echo technique for nondestructive evaluation of nonrectangular concrete elements, such as T- and I-beams which are commonly used in civil engineering structures.[14] In the impact-echo technique, a transient stress pulse is introduced into a test object by mechanical impact. A displacement transducer (receiver) located close to the impact point is used to monitor surface displacements caused by the arrival of waves reflected by internal defects and external boundaries of the test object.[15,16] Time domain waveforms are transformed into the frequency domain using the fast Fourier transform technique. The resulting spectra are used to determine the integrity of the test object.[17] The success of the technique relies on identifying changes in the frequencies in the spectra between the solid element and the element containing defects.

In this paper, numerical studies include eigenvalue analyses of plane-strain models of T- and I-sections, resonant analyses and transient impact analyses of three-dimensional finite element models. Eigenvalue analyses of plane-strain finite element models of T- and I-sections were performed first to solve for the cross-sectional mode shapes and the corresponding natural frequencies. Second, three-dimensional finite-element models subjected to transverse, sinusoidal, point loads with specified frequencies (resonant analyses) were used to verify the existence of the cross-sectional modes obtained from the eigenvalue analyses of plane-strain finite-element models. Finally, three-dimensional finite-element models were also used to deter-

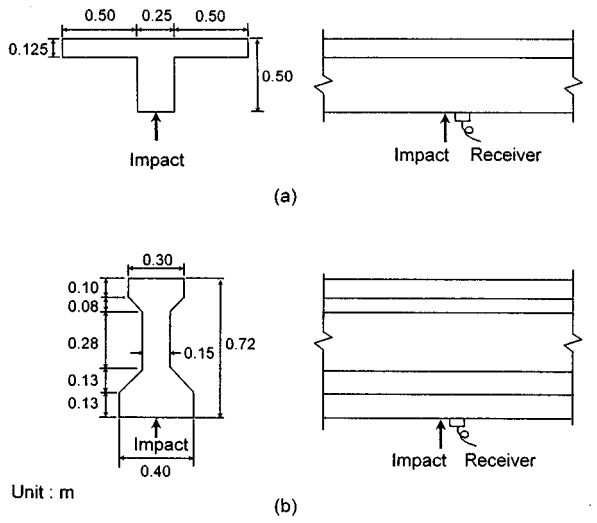

FIG. 1. Schematic illustration of impact-echo tests on (a) T-beam and (b) I-beam.

mine the transient response of T- and I-beams subjected to transverse elastic point impact. To verify the results obtained from the numerical analyses, experimental studies were performed on a 0.5-m-deep T-beam and a 0.72-m-deep I-beam. These specimens were representative of full-size concrete elements.

I. BACKGROUND

Prior to discussing the results of numerical and experimental studies, background information is provided on the impact-echo technique, on the numerical method for obtaining approximate solutions to problems involving wave propagation in bounded solids, and on the experimental specimens.

A. Impact-echo method

Figure 1(a) and (b) are schematic representations of impact-echo tests on a T-beam and an I-beam, respectively. The figures show the cross-sectional dimensions for the T- and I-beams. The impact-echo test configuration shows the locations of the impact and the receiving transducer. The impact is applied at the center of the bottom surface of the cross sections. The stress pulse generated by the point impact propagates into the solid as spherical dilatational (P) and distortional (S) waves. In addition, a Rayleigh (R) wave is produced which propagates along a circular wavefront across the impact surface. These waves are reflected by traction-free boundaries. The receiving transducer located adjacent to the impact point monitors normal surface displacement caused by the arrival of each wave reflection from the free boundaries.

In our studies, small hardened steel spheres on spring steel rods are used to produce elastic impact. The force-time history of the elastic impact of a sphere can be approximated as a half-cycle sine curve[17] defined by the impact duration t_c and the maximum force $F_{\max}$. The impact duration determines the frequency content of the stress pulse that is generated. Most of the energy in the pulse can be considered to be contained in frequencies less than $1.5/t_c$. A shorter duration impact produces a broader range of frequencies in the waves, however, the amplitude of each component frequency is lower.

The receiver is a broadband displacement transducer consisting of a small, conically-shaped, piezoelectric element cemented to a brass cylinder.[18] The output signal of this transducer is proportional to normal surface displacement. A thin sheet of lead is used between the conical piezoelectric element and the concrete surface to complete the transducer circuit and to couple the element to the rough concrete surface.

In the impact-echo method, the recorded time-domain waveforms are transformed into the frequency domain using the fast Fourier transform technique. The resulting spectra are used to determine whether the test object is solid or not. When testing platelike elements, wave reflections from the side boundaries do not have a significant effect on the impact response. The resulting amplitude spectrum contains a single large-amplitude peak at a frequency associated with multiple wave reflections between the top and bottom surfaces of the plate. The presence of a flaw in the plate disrupts the spectral pattern, and thus make it easy to identify the presence of the flaw. In contrast, the problems of wave propagation in bar-like elements, such as T- and I-beams, subjected to transverse impact are complex due to the significant effects caused by the close proximity of the side boundaries.

B. Numerical models

It is extremely difficult to solve problems involving wave propagation in bounded solids. Exact solutions have been obtained for only the most fundamental types of wave motion. However, the finite-element method provides a powerful tool for finding numerical solutions for wave propagation in bounded solids.

It was shown that the response of a rectangular bar subjected to transverse impact is composed of frequencies corresponding to the cross-sectional modes of vibration of the rectangular bar.[13] For the case of nonrectangular bars, it will be shown that the response is also composed of a number of natural frequencies associated with the cross-sectional modes of vibration. Eigenvalue analyses of plane-strain finite-element models of T- and I-sections were used to solve for the cross-sectional mode shapes and the corresponding natural frequencies. Such plane-strain models can be used to accurately predict the cross-sectional modes for the case when the bar is long relative to the cross-sectional dimensions. In addition, three-dimensional finite-element models subjected to transverse, sinusoidal, point loads with specified frequencies were used to verify the eigensolutions obtained from plane-strain model. When the specified frequency is one of the natural frequencies of the structure, the corresponding mode of vibration is excited. Subsequently, three-dimensional finite-element models were also used to determine the transient response of T- and I-beams subjected to transverse elastic point impact.

In impact-echo testing, impact is generated by dropping a small steel sphere (typically 4–12 mm in diameter) on the surface of a concrete specimen. The strain response in con-

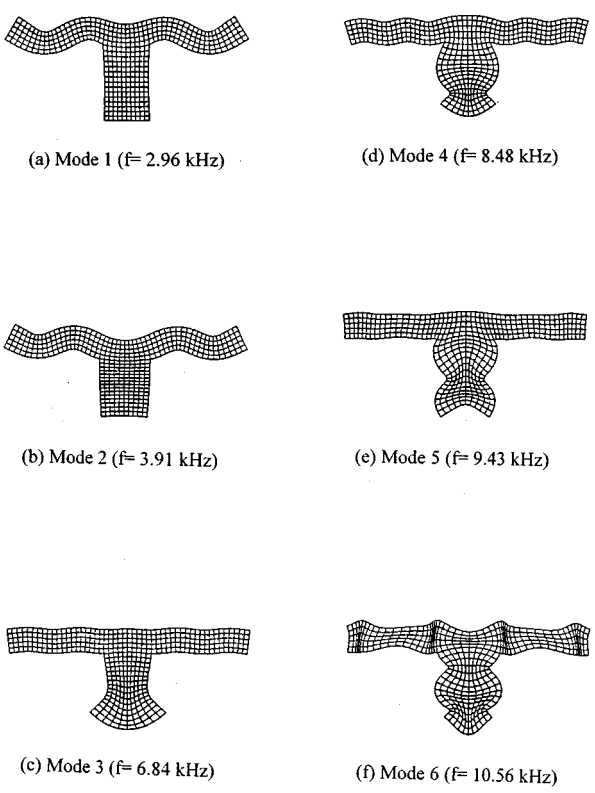

FIG. 2. Plane-strain cross-sectional modes of a T-beam and their corresponding frequencies.

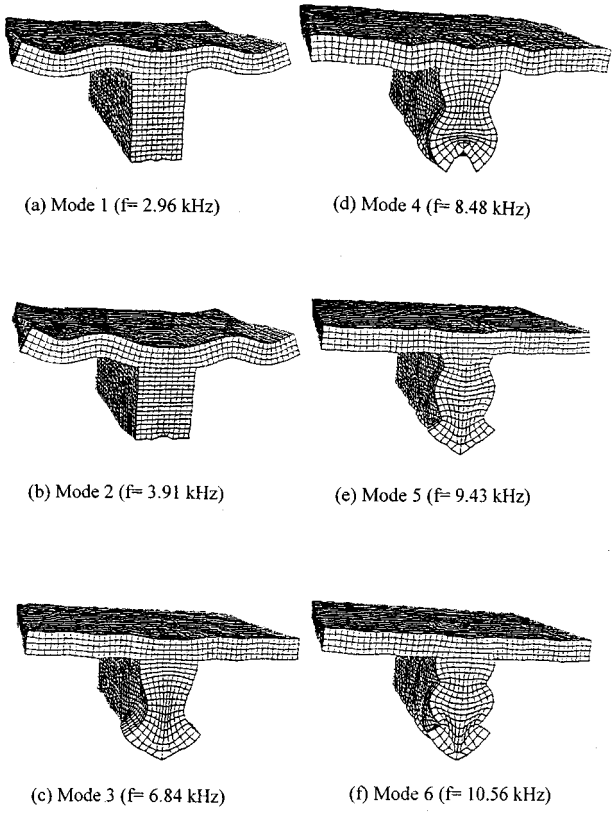

FIG. 3. Three-dimensional mode shapes for a T-beam and their corresponding frequencies.

crete produced by the waves generated by impact is low. Thus, a linear, elastic material model is valid for concrete at low strain levels. For the range of impact durations used in impact-echo testing (20–80 μs), the frequencies in the stress pulse generated by impact are sufficiently low so that scattering at the many interfaces between the aggregate particles and cement binder in concrete is not significant. Concrete appears homogeneous to the propagating waves. Therefore, numerical models can make use of linear, elastic, isotropic material models. The values of density, Young's modulus of elasticity, and Poisson's ratio used to define the material model for concrete were 2300 kg/m^3, 33100 Mpa, and 0.2, respectively. These values resulted in dilatational, distortional, and Rayleigh wave velocities in infinite media of 4000, 2440, and 2240 m/s, respectively.

An explicit, finite-element code, DYNA3D,[18] was used to perform the three-dimensional finite-element analyses of nonrectangular bars subjected to transverse elastic impact. An input generator, INGRID,[19] was used to create the finite-element models. An interactive, graphic postprocessor, TAURUS,[20] was used to obtained deformed shapes, contour plot of stress at selected times, and time-history responses of displacements at specific nodes. The impact of a sphere on a bar was simulated by applying a pressure loading with a force-time history of a half-cycle sine curve over a small number of elements. In the analyses, the concrete T- and I-beams were unsupported. To reduce the number of elements used in the analyses, nonreflecting boundaries were used at the ends of the bars to simulate the response of an infinitely long bar.

In each of the analyses, eight-noded solid elements were used to represent the continuum, and numerical integration of the equations of motion was accomplished using the central difference method. The wavelengths of the propagating waves are important factors in determining the size of elements in the finite element models. Typically, when linear elements are used, as in the models presented in this paper, the elements should have dimensions less than approxi-

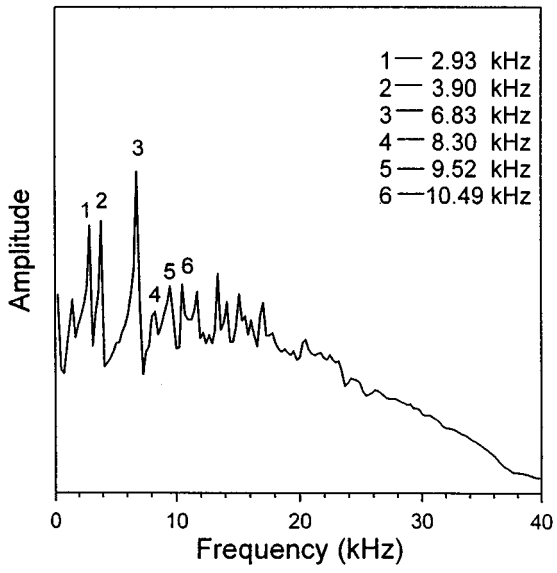

FIG. 4. Amplitude spectrum obtained from numerical analysis of a T-beam subjected to transverse impact.

TABLE I. Frequency values (kHz) of the first six cross-sectional modes of a T-beam.

Mode	Eigensolution (Cp=4000 m/s)	Finite element[a] (Cp=4000 m/s)	Experiment[a] (Cp=3800 m/s)	Experiment[a] (Cp=4000 m/s)
1	2.96	2.93	2.93	3.08
2	3.91	3.90	3.66	3.85
3	6.84	6.83	6.34	6.67
4	8.48	8.30	8.05	8.47
5	9.43	9.52	9.27	9.76
6	10.56	10.49	10.00	10.52

[a]Resolution in spectra is 0.244 kHz.

mately one-tenth the wavelength of the highest frequency of interest. The dimensions of elements used in the finite-element models discussed in this paper was 0.01 m. Thus, frequencies up to about 40 kHz could be accurately captured in the response.

C. Experimental specimens

To verify the results obtained from the numerical analyses, laboratory studies on nonrectangular bars were carried out. Two specimens used in the studies were constructed of concrete. One was a 3-m-long T-beam having a depth of 0.5 m, a flange width of 1.25 m, and the relevant dimensions as illustrated in Fig. 1(a). The other was a 3-m-long I-beam having a depth of 0.72 m and the relevant dimensions as shown in Fig. 1(b). The concrete mixture ingredients (proportion of cement, aggregate, and water) were chosen to result in hardened concrete with a strength of about 28 MPa. The P-wave speed in the specimens was measured to be about 3800 m/s. This value is 95% of the 4000-m/s P-wave speed which was used in the numerical analyses.

II. IMPACT RESPONSE OF A T-BEAM

Figure 1(a) is a schematic illustration of a T-beam subjected to transverse point impact. The configuration shows the locations of the impact and the receiving transducer.

A. Cross-sectional modes of vibration

It was shown that the response of a rectangular bar subjected to transverse impact is composed of frequencies corresponding to the cross-sectional modes of vibration of the rectangular bar.[13] For the case of a T-beam, it will be shown that the response is also composed of a number of natural frequencies associated with the cross-sectional modes of vibration. In this section, results obtained from eigenvalue analyses of a T-section having dimensions as illustrated in Fig. 1(a) are presented. A global stiffness matrix for the plane-strain, finite-element meshed T-section was assembled, and a consistent mass matrix was also formed. Subsequently, a computer code for eigenvalue problems was used to solve for the cross-sectional mode shapes (eigenvectors) and their corresponding natural frequencies (eigenvalues). Figure 2(a)–(f) shows the shapes of the first six cross-sectional modes of the T-beam. The frequency corresponding to each of these mode shapes is also shown in the figure.

B. Resonant analysis

To verify the existence of the cross-sectional modes as obtained from the plane-strain analyses, resonant analyses of three-dimensional finite-element models were performed. In resonant analysis, a point load with a time history defined by a continuous sine curve having a specific frequency is applied to a structure. When the frequency of the applied force-time function matches one of the natural frequencies of the structure, a resonant condition is set up and the corresponding mode of vibration is generated. The first six mode frequencies of 2.96, 3.91, 6.84, 8.48, 9.43, and 10.56 kHz obtained previously from plane-strain eigenvalue analyses for a T-section as shown in Fig. 2(a)–(f) were used to perform the resonant analyses one at a time. Figure 3(a)–(f) shows the first six resonant mode shapes, respectively. These cross-sectional shapes are identical to the mode shapes obtained from the eigenvalue analyses which were presented in Fig. 2(a)–(f). Thus as shown in the studies of square and rectangular bars by Lin and Sansalone,[12,13] plane-strain finite-element models can be used to obtain the cross-sectional modes and natural frequencies of a T-beam subjected to transverse impact when the length of the beam is large relative to the cross-sectional dimensions.

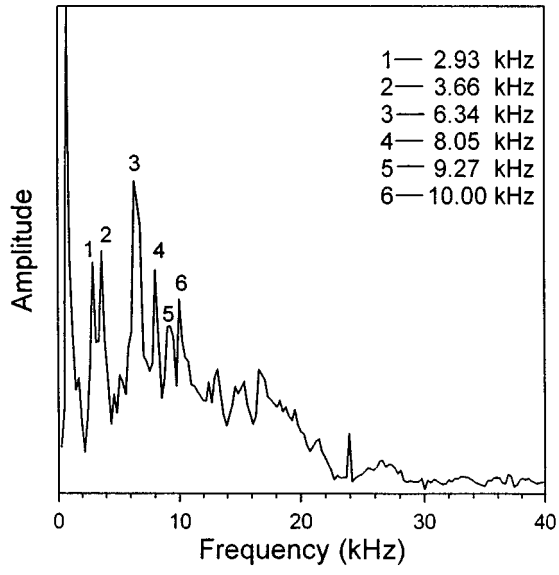

FIG. 5. Amplitude spectrum obtained from laboratory test on a T-beam.

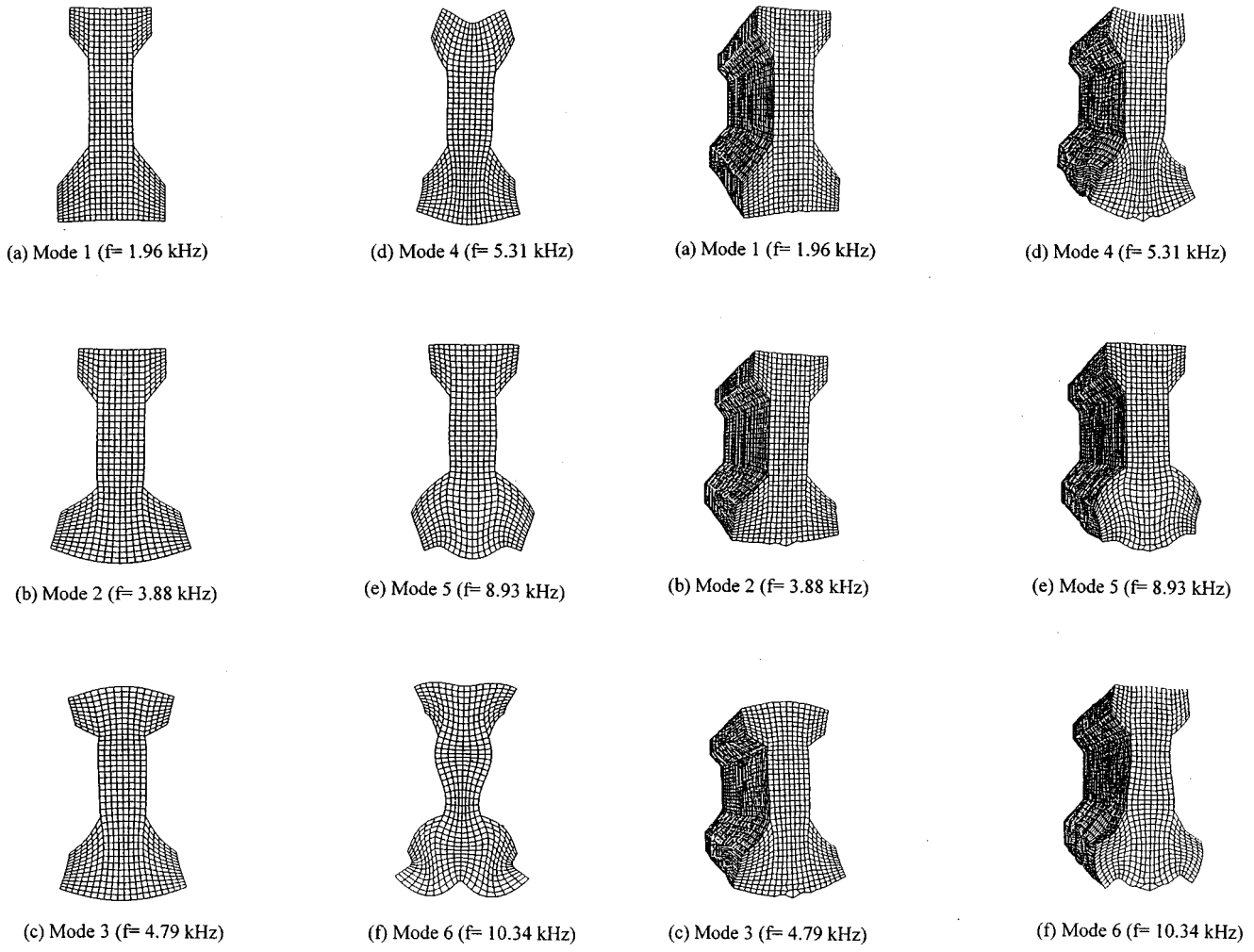

FIG. 6. Plane-strain cross-sectional modes of an I-beam and their corresponding frequencies.

FIG. 7. Three-dimensional mode shapes for an I-beam and their corresponding frequencies.

C. Impact response

Three-dimensional finite-element analyses were performed to study the transient response of T-beams subjected to transverse point impact. In the analyses, the impact of a spherical mass on a large bar was simulated as a uniform pressure load over 20 mm (two elements) at the center of the T-beam bottom as well as the longitudinal dimension [see Fig. 1(a)]. Because of biaxial symmetry, only one-quarter of the problem was analyzed to reduce the computational time.

The stress waves generated by point impact propagate into the T-beam. Wave reflections occur at the cross-sectional boundaries. Because of the close proximity of these cross-sectional boundaries, waves propagate back and forth across the cross section of the T-beam. These multiple wave reflections give rise to cross-sectional modes of vibration. Figure 4 shows an amplitude spectrum obtained from the FFT of a displacement-time history calculated at a node point at a distance of 0.03 m to the impact location. The spectral response exhibits a number of peaks at frequencies which correspond to the cross-sectional modes of vibration of the T-beam. The resolution in the spectrum is 0.244 kHz. The frequencies of the first six cross-sectional modes are 2.93, 3.90, 6.83, 8.30, 9.52, and 10.49 kHz; these values are close to the natural frequencies of 2.96, 3.91, 6.84, 8.48, 9.43, and 10.56 kHz obtained from the eigenvalue analysis (see Fig. 2). For comparison, these frequencies are tabulated in Table I. The table also shows experimental results which will be discussed in the following section.

D. Experimental verification

To verify the results obtained from the numerical analyses, experimental studies on a concrete T-beam having the same dimensions as in the numerical models were carried out. The P-wave speed in the concrete specimen was measured to be about 3800 m/s. This value is 95% of the 4000-m/s P-wave speed which was used in the numerical analyses. In the test, the impactor was applied at the center of the longitudinal as well as lateral dimensions of the T-beam. The spacing between the impactor and receiving transducer was 0.03 m, as in the finite element analyses. Surface displacement waveforms consisted of 1024 points recorded at a sampling rate of 250 kHz (4 μs) for a record length of 4096 μs and a resolution in the amplitude spectrum of 0.244 kHz (the same as in the numerical analyses).

Figure 5 shows the amplitude spectrum obtained from a test carried out at the bottom center of the 0.5-m-deep con-

crete T-beam. In the spectrum, the largest amplitude peak is caused by the transducer resonance. There are six other large amplitude peaks as indicated in the spectrum. Because the P-wave speed in the concrete specimen is 95% of that used in the numerical models, the frequency values associated with the six large amplitude peaks in the experimental spectrum must be divided by 0.95 for comparison purpose. The last column of Table I shows the converted frequency values. The experimental spectrum shown in Fig. 5 can be compared with the numerical spectrum shown in Fig. 4. A comparison of frequency peaks produced by the cross-sectional modes shows that there is good agreement between numerical and experimental results with regard to both the frequency values associated with each large amplitude peak (see Table I) and the relative amplitude of the peaks produced by the cross-sectional modes.

The results of the experiments clearly show the validity of using the proposed numerical models for studying transient stress wave propagation in nonrectangular bars.

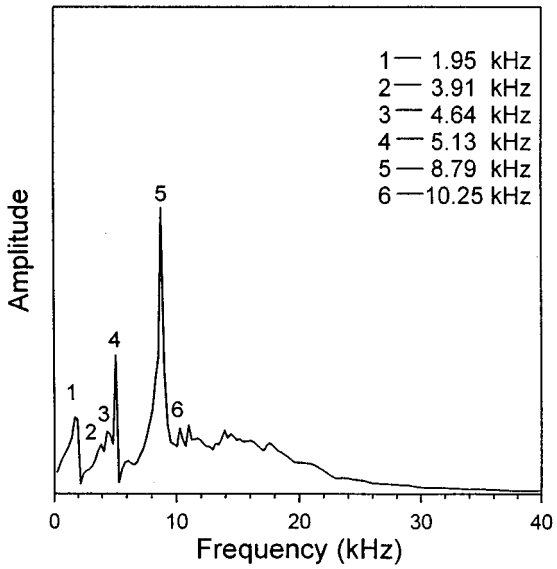

FIG. 8. Amplitude spectrum obtained from numerical analysis of an I-beam subjected to transverse impact.

III. IMPACT RESPONSE OF AN I-BEAM

The same analytical procedures as described in the previous section were also employed to determine the impact response of an I-beam. The objective of this study was to ascertain whether the proposed numerical models are suitable for determining approximately the transient response of a bar with complicated cross-sectional boundaries subjected to elastic transverse impact.

In this section, results obtained from both numerical and experimental studies on an I-beam having dimensions as illustrated in Fig. 1(b) are presented. Numerical studies also include eigenvalue analyses of plane-strain models, resonant analyses, and transient impact analyses of three-dimensional finite-element models. Experimental studies were performed to verify the results obtained from the numerical analyses.

Figure 6(a)–(f) shows the shapes of the first six cross-sectional modes obtained from eigenvalue analyses of plane-strain finite-element models of the I-section. The frequency corresponding to each of these mode shapes is also shown on the figure. Accordingly, Fig. 7(a)–(f) shows the first six resonant three-dimensional finite-element mode shapes, respectively. These cross-sectional shapes are identical to the mode shapes which were presented in Fig. 6(a)–(f). Thus, it is concluded again that, as shown in the previous studies of T-beams, plane-strain finite element models can be used to obtain the cross-sectional modes and natural frequencies of an I-beam subjected to transverse impact when the length of the beam is large relative to the cross-sectional dimensions.

Figure 8 shows an amplitude spectrum obtained from the transient impact analyses of the three-dimensional I-beam finite element models. The spectral response exhibits a number of peaks at frequencies which correspond to the cross-sectional modes of vibration of the I-beam. The resolution in the spectrum is 0.244 kHz. The frequencies of the first six cross-sectional modes are 1.95, 3.91, 4.64, 5.13, 8.79, and 10.25 kHz; these values are close to the natural frequencies of 1.96, 3.88, 4.79, 5.31, 8.93, and 10.34 kHz obtained from the eigenvalue analysis (see Fig. 6). For comparison, these frequencies are tabulated in Table II. The table also shows experimental results which will be discussed subsequently.

Figure 9 shows the amplitude spectrum obtained from a test carried out at the bottom center of the 0.72-m-deep concrete I-beam. For comparison purposes, the frequency values associated with the first six large amplitude peaks in the experimental spectrum must be divided by 0.95 to account for the lower P-wave speed in the concrete specimen. The converted frequency values are listed in the last column of Table II. A comparison of frequency peaks in the spectra (Figs. 8 and 9) obtained from numerical and experimental studies shows good agreement with regard to both the frequency

TABLE II. Frequency values (kHz) of the first six cross-sectional modes of an I-beam.

Mode	Eigensolution (Cp=4000 m/s)	Finite element[a] (Cp=4000 m/s)	Experiment[a] (Cp=3800 m/s)	Experiment[a] (Cp=4000 m/s)
1	1.96	1.95	1.71	1.80
2	3.88	3.91	3.66	3.85
3	4.79	4.64	4.39	4.62
4	5.31	5.13	4.88	5.14
5	8.93	8.79	8.30	8.74
6	10.34	10.25	9.52	10.02

[a]Resolution in spectra is 0.244 kHz.

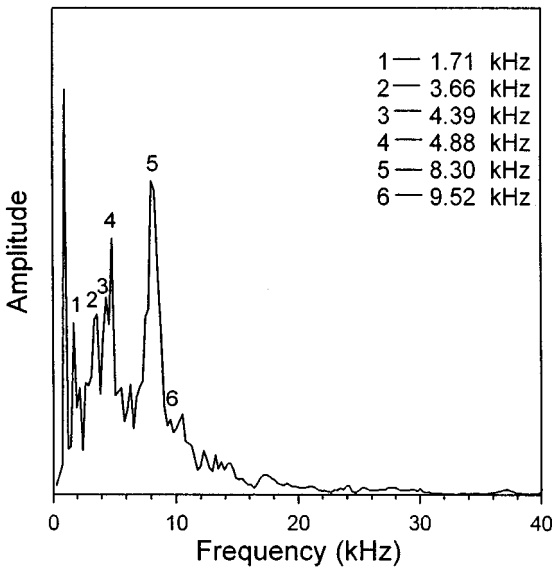

FIG. 9. Amplitude spectrum obtained from laboratory test on an I-beam.

values associated with each large amplitude peak (see Table II) and the relative amplitude of the peaks produced by the cross-sectional modes. Again, the experimental results clearly show the validity of the proposed numerical models for determining the transient response of a bar with complicated cross-section boundaries subjected to transverse impact.

IV. CONCLUSIONS

The objective of the studies presented in this paper is to propose an efficient numerical approach to determining the transient response of non-rectangular bars subjected to transverse elastic impact. Numerical studies include eigenvalue analyses of plane-strain models of T- and I-sections, resonant analyses, and transient impact analyses of three-dimensional finite-element models. Experimental studies were performed to verify the results obtained from the numerical analyses. Good agreement was obtained between the numerical and experimental results. It is shown that the response of non-rectangular bars, such as T- and I-beams, subjected to transverse impact is composed of frequencies corresponding to the cross-sectional modes of vibration of the nonrectangular bar. Eigenvalue analyses of plane-strain finite element models can be used efficiently to obtain the cross-sectional modes and natural frequencies of a nonrectangular bar subjected to transverse impact when the length of the bar is large relative to the cross-sectional dimensions. Three-dimensional resonant analyses can be used to verify the existence of the cross-sectional modes obtained from the eigenvalue analyses.

ACKNOWLEDGMENTS

Numerical studies presented in this paper were performed by using DYNA3D provided by the National Center for High-Performance Computing, Taiwan, ROC. The research summarized in this paper was funded through grants from the Sinotech Foundation for Research & Development of Engineering Science and Technologies, Taiwan.

[1] L. Pochammer, ''Uber die Fortpflanzungsgeschwindigkeiten kleiner Schwingungen in einem unbergrenzten isotropen Kreizylinder,'' Z. Reine Angew. Math. (Crelle) **81**, 324–336 (1876).
[2] D. Chree, ''The equations of an isotropic elastic cylinder in polar and cylindrical coordinates, their solutions and applications,'' Trans. Cambridge Philos. Soc. **14**, 250–369 (1889).
[3] R. D. Mindlin and E. A. Fox, ''Vibrations and waves in elastic bars of rectangular cross section,'' J. Appl. Mech. **27**, 152–158 (1960).
[4] N. J. Nigro, ''Steady-state wave propagation in infinite bars of noncircular cross section,'' J. Acoust. Soc. Am. **40**, 1501–1508 (1966).
[5] W. B. Fraser, ''Stress wave propagation in rectangular bars,'' Int. J. Solids Struct. **5**, 379–397 (1969).
[6] B. Aalami, ''Waves in prismatic guides of arbitrary cross section,'' J. Appl. Mech. **40**, 1067–1072 (1973).
[7] G. R. Liu, J. Tani, K. Watanabe, and T. Ohyoshi, ''A semi-exact method for the propagagtion of harmonic waves in anisotropic laminated bars of rectangular cross section,'' Wave Motion **12**, 361–371 (1990).
[8] D. C. Gazis, ''Exact analysis of the plane-strain vibrations of thick-walled hollow cylinders,'' J. Acoust. Soc. Am. **30**, 786–794 (1958).
[9] J. F. Bird, ''Vibration of thick-walled hollow cylinders: Approximate theory,'' J. Acoust. Soc. Am. **32**, 1413–1419 (1960).
[10] A. E. Armenakas, D. C. Gazis, and G. Herrmann, *Free vibrations of circular cylindrical shells* (Pergamon, New York, 1969), 1st ed.
[11] J. M. Lin and M. Sansalone, ''The transverse elastic impact response of thick hollow cylinders,'' J. Nondestruct. Eval. **12**, 139–149 (1993).
[12] Y. Lin and M. Sansalone, ''Transient response of thick circular and square bars subjected to transverse elastic impact,'' J. Acoust. Soc. Am. **91**, 885–893 (1992).
[13] Y. Lin and M. Sansalone, ''Transient response of thick rectangular bars subjected to transverse elastic impact,'' J. Acoust. Soc. Am. **91**, 2674–2685 (1992).
[14] Y. Lin and K. L. Lin, ''The Transient Impact Response of Bridge I-Girders with and without Flaws,'' J. Bridge Eng. ASCE **2**(4), 131–138 (November 1997).
[15] M. Sansalone and N. J. Carino, ''Impact-echo: a method for flaw detection in concrete using transient stress waves,'' NBSIR 86-3452, NTIS PB No. 87-104444/AS, Springfield, VA (September 1986).
[16] N. J. Carino and M. Sansalone, ''Impact-echo: a new method for inspecting construction materials,'' in *Proceedings of the Conference on NDTE for Manufacturing and Construction*, University of Illinois at Urbana-Champaign, August 1988.
[17] N. J. Carino, M. Sansalone, and N. N. Hsu, ''Flaw detection in concrete by frequency spectrum analysis of impact-echo waveform,'' Int. Adv. Nondestruct. Test **12**, 117–146 (1986).
[18] J. O. Hallquist, ''DYNA3D user's manual (nonlinear dynamic analysis of structures in three dimensions),'' Lawrence Livemore National Laboratory, Report No. UCID-19592, Rev. 5 (May 1989).
[19] D. W. Stillman and J. O. Hallquist, ''User's manual for INGRID: a three-dimensional mesh generator for modeling nonlinear system,'' Lawrence Livermore National Laboratory, Report No. UCID-20506 (revised July 1985).
[20] B. E. Brown and J. O. Hallquist, ''User's manual for TAURUS: an interactive post-processor for the analysis code NIKE3D, DYNA3d, TACO3D, and GEM-INI,'' Lawrence Livermore National Laboratory, Report No. UCID-19392 (revised May 1984).

Structural intensity of torsional vibration in solid and hollow cylindrical bars

Jiaqiang Pan[a] and Jie Pan
Department of Mechanical and Materials Engineering, University of Western Australia, WA 6907, Australia

(Received 3 October 1996; revised 11 August 1997; accepted 28 October 1997)

This paper presents an exact analytical solution to the vibrational intensity of torsional waves in three-dimensional solid and hollow cylindrical bars of finite length. As the torsional response in circular cylindrical bars to the excitation of pure torsional moments is uncoupled with the motion of other degrees of freedom, its characteristics can be investigated independently. After verifying the orthogonal properties of the eigenfunctions of the torsional waves in a bar with fixed-free ends, the steady state response of the bar to a torsional moment was obtained analytically. The solution of the response was then utilized to calculate the vibrational intensity. Examples are used to illustrate the features of the torsional intensity in a hollow cylindrical bar. © *1998 Acoustical Society of America.* [S0001-4966(98)02902-6]

PACS numbers: 43.40.Cw [CBB]

INTRODUCTION

n the past decades, techniques have been developed to use vibrational power flow and structural intensity in the identification of intensity paths, positions of sources, and sinks of mechanical energy. Previous calculations and measurements of structural intensity were largely limited to simple structures such as thin beams, plates, and shells. However, when the technique is applied to more complicated structures and broader frequency ranges, the validity of engineering models for simple structures has not been established. For example, the existing bending wave intensity expression was developed on the basis of classical bending wave theory and is only valid for homogeneous thin beams of low frequencies. The description of high-frequency structural waves in large practical structures often requires the inclusion of the shear deformation and rotatory inertia in the structural intensity formulation. The objective of this paper is to calculate vibrational intensity using the solution of three-dimensional elastic equations for solid and hollow cylindrical rods. Traditionally, even the solution of the free vibration of a three-dimensional circular cylindrical rod requires significant numerical calculation.[1] However, examination of the boundary value problems of the three-dimensional elastic equations showed that the torsional response in circular bars to the excitation of pure torsional moments is uncoupled from the motion of other degrees of freedom, and the dynamic equation of the torsional waves is separable from the full elastic equations. Consequently, analytical solution of torsional response becomes possible, and the response obtained can be used to investigate the properties of the vibrational power flow and structural intensity in solid and hollow cylindrical bars.

Study of the vibrational intensity of torsional waves in solid and hollow cylindrical bars may provide understanding of vibrational and absorption characteristics of various machine components such as turbine rotors and heavily loaded gears. Clark[2] has studied the free-torsional wave propagation in hollow cylindrical bars of infinite length using the three-dimensional analytical approach. His work provided the solution of propagating modes in the bars and demonstrated the characteristics of torsional wave velocity in hollow bars. Recently Leissa and So[3,4] used the three-dimensional Ritz analysis for the resonance frequencies of a solid cylindrical rod of finite length. Their study has shown a significant effect of Poisson's ratio on the resonance frequencies.

To obtain the steady state response for the computation of power flow and structural intensity,[5] the eigensolutions obtained by Clark[2] and Leissa[3,4] are utilized for a modal expansion of the response and excitation moment. Using the orthogonal properties of the eigenfunctions and solution of the modal normalization factors, this paper presents an analytical solution to the forced torsional response of solid and hollow bars to excitation of a pure torsional moment due to axial symmetrical body forces. The solution is used for the computation of structural intensity in the bars. Two examples are used to illustrate the power flow properties in a hollow cylindrical bar. The results show the potential of using three-dimensional solutions for calculation of structural intensity for the conditions where the engineering models of structures may not be valid, and for the precise determination of the error which the conventional method may bear for the measurement of the power flow in one-dimensional beam structures.

I. TORSIONAL VIBRATION IN THE SOLID CYLINDRICAL BAR

Figure 1 shows a circular cylindrical bar with fixed-free ends in a cylindrical coordinates (r,θ,z), where $u(r,\theta,z;t)$, $v(r,\theta,z;t)$, and $w(r,\theta,z;t)$ represent the displacements at location (r,θ,z) and in the r, θ, and z directions, respectively. The bar is assumed to be excited by an torsional moment M_z about the z axis due to axially symmetric body forces:

$$M_z = m_z e^{j\omega t}, \tag{1}$$

where ω is the radian frequency of excitation. For this excitation, only forced torsional vibration is generated in the

[a]Present address: Department of Mechanical Engineering, Zhejiang University, Hongzhou, 310027, People's Republic of China.

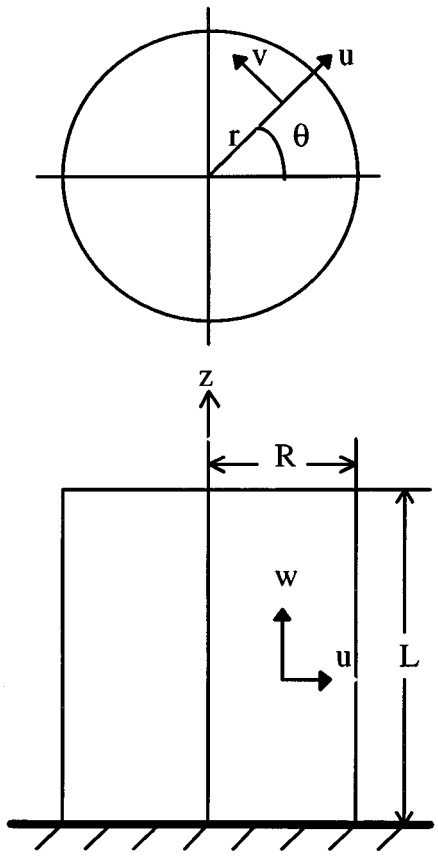

FIG. 1. A fixed-free circular cylindrical bar and corresponding coordinates.

bar.[3,4] With $u=w=0$ and ν independent of θ, the dynamic equation is

$$\frac{\partial^2\nu}{\partial r^2}+\frac{1}{r}\frac{\partial\nu}{\partial r}-\frac{\nu}{r^2}+\frac{\partial^2\nu}{\partial z^2}+\frac{\tilde{\Theta}e^{j\omega t}}{G}=\frac{\rho}{G}\frac{\partial^2\nu}{\partial t^2}, \tag{2}$$

where G is the shear modulus and ρ is the volume density. Here, $\tilde{\Theta}=\tilde{\Theta}(r,z)$ is the axial symmetric body force in the θ direction. It produces a torsional moment m_z:

$$\int_0^{2\pi}\int_0^R\int_0^L r\tilde{\Theta}(r,z)dV=m_z, \tag{3}$$

where $dV=r\,dr\,dz\,d\theta$. Using the eigenfunctions for the torsional displacement in a solid cylindrical bar with fixed-free ends,[3] $\nu(r,\theta,z;t)$ can be expressed by the following expansion:

$$\nu(r,\theta,z;t)=\left\{\sum_m^\infty\left[A_{0m}r+\sum_i^\infty A_{im}J_1(\beta_i r)\right]\sin\alpha_m z\right\}e^{j\omega t}, \tag{4}$$

where J_1 is the first-order Bessel function of the first kind. The boundary conditions at two ends ($u=\nu=w=0$ at $z=0$; $\sigma_z=\tau_{z\theta}=\tau_{zr}=0$ at $z=L$) give rise to

$$\alpha_m=(m-\tfrac{1}{2})\pi/L \quad (m=1,2,3,...) \tag{5}$$

and the boundary conditions on the cylinder surface ($r=R$, $\sigma_r=\tau_{r\theta}=\tau_{rz}=0$) induce an eigenvalue equation for determining β_i:

$$J_2(\beta_i R)=0, \tag{6}$$

where J_2 is the second-order Bessel function of the first kind.

Substituting Eq. (4) into Eq. (2), multiplying both sides of the resultant equation with the eigenfunctions of the circular bar, integrating over the whole volume of the bar, and using the orthogonal properties of the eigenfunctions, the coefficients in the displacement response $\nu(r,\theta;z,t)$ can be obtained:

$$A_{0m}=\frac{16\pi}{R^4L\rho(\omega_{0m}^2-\omega^2)}\int_0^L\int_0^R\tilde{\Theta}(r,z)r^2\sin\alpha_m z\,dr\,dz, \tag{7a}$$

$$A_{im}=\frac{4\pi}{N_iL\rho(\omega_{im}^2-\omega^2)}\int_0^L\int_0^R\tilde{\Theta}(r,z)rJ_1(\beta_i r)\times\sin\alpha_m z\,dr\,dz, \tag{7b}$$

where

$$\omega_{0m}^2=\alpha_m^2\frac{G}{\rho},\quad \omega_{im}^2=(\alpha_m^2+\beta_i^2)\frac{G}{\rho} \tag{8}$$

and the normalization factors are

$$N_i=\int_0^R J_1^2(\beta_i r)r\,dr=\frac{1}{2}R^2J_1^2(\beta_i R). \tag{9}$$

To highlight the application of the analytic method in calculating the vibration intensity, two special cases of body force $\tilde{\Theta}(r,z)$ were selected. They correspond to a linearly distributed force in the cross section $z=z_0$ (case A):

$$\tilde{\Theta}=\frac{2m_z}{\pi R^4}r\delta(z-z_0), \tag{10}$$

and a cubically distributed body force in the cross section $z=z_0$ (case B):

$$\tilde{\Theta}=\frac{3m_z}{\pi R^6}r^3\delta(z-z_0). \tag{11}$$

Both of the distributed force will only produce axial symmetrical moments.

Using Eqs. (7a) and (7b), the coefficients for case A are

$$A_{0m}=\frac{8m_z\sin\alpha_m z_0}{R^4L\rho(\omega_{0m}^2-\omega^2)}, \tag{12a}$$

$$A_{im}=0, \tag{12b}$$

and those for case B are

$$A_{0m}=\frac{8m_z\sin\alpha_m z_0}{R^4L\rho(\omega_{0m}^2-\omega^2)}, \tag{13a}$$

$$A_{im}=\frac{48m_zJ_1(\beta_i r_0)\sin\alpha_m z_0}{\beta_i^2R^5L\rho(\omega_{im}^2-\omega^2)J_1^2(\beta_i R)}. \tag{13b}$$

Therefore, the torsional displacement response for case A is expressed as

$$\nu=\frac{8m_z r}{R^4 L\rho}\left\{\sum_m \frac{\sin\alpha_m z_0 \sin\alpha_m z}{\omega_{0m}^2-\omega^2}\right\}e^{j\omega t}, \tag{14}$$

and for case B:

$$\nu=\frac{8m_z}{R^4 L\rho}\left\{\sum_m\left[\frac{r}{\omega_{0m}^2-\omega^2}+\sum_i \frac{6J_1(\beta_i r)}{\beta_i^2 R(\omega_{im}^2-\omega^2)J_1(\beta_i R)}\right]\sin\alpha_m z_0 \sin\alpha_m z\right\}e^{j\omega t}. \tag{15}$$

II. TORSIONAL VIBRATION IN HOLLOW CYLINDRICAL BARS

In this section the forced torsional vibration in a hollow cylindrical bar, with R_1 and R_2 as its inner and outer radius, is investigated. Similar to the excitation of the solid bars, two kinds of axial symmetrical body forces $\tilde{\Theta}(r,z)$, which produce torsional moment m_z acting in the section $z=z_0$ ($L\geqslant z_0>0$), are considered. One is linearly distributed along the r direction and in the cross section $z=z_0$ (case C):

$$\tilde{\Theta}=\frac{2m_z}{\pi(R_2^4-R_1^4)}\, r\,\delta(z-z_0), \tag{16}$$

and the other has a cubic distribution in the cross section $z=z_0$ (case D):

$$\tilde{\Theta}=\frac{3m_z}{\pi(R_2^6-R_1^6)}\, r^3(z-z_0). \tag{17}$$

Using the eigenfunctions for the torsional displacement in a hollow cylindrical bar with fixed-free ends, $\nu(r,z;t)$ can be expressed as

$$\nu(r,z;t)=\left\{\sum_{m=0}^{\infty}\left\{A_{0m}r+\sum_{i=1}^{\infty}A_{im}[J_2(\beta_i R_2)Y_1(\beta_i r)-Y_2(\beta_i R_2)J_1(\beta_i r)]\right\}\sin\alpha_m z\right\}e^{j\omega t}. \tag{18}$$

There the eigenvalue equation for β_i is

$$J_2(\beta_i R_1)Y_2(\beta_i R_2)=J_2(\beta_i R_2)Y_2(\beta_i R_1), \tag{19}$$

where Y_1 and Y_2 are, respectively, the first- and second-order Bessel functions of the second kinds. Although $1/r$ is also one of the general solutions of Eq. (2) for hollow cylindrical bars, its coefficient has to be equal to zero because of the requirement of boundary condition $\tau_{r\theta}=\partial\nu/\partial r-\nu/r=0$ at $r=R_1$ and $r=R_2$.

Substituting Eq. (18) into Eq. (2) and using the orthogonal properties of the eigenfunctions the coefficients in the displacement response [Eq. (18)] $\nu(r,z;t)$ are obtained as

$$A_{0m}=\frac{16\pi}{(R_2^4-R_1^4)L\rho(\omega_{0m}^2-\omega^2)}\int_0^L\int_{R_1}^{R_2}\tilde{\Theta}(r,z)r^2\times\sin\alpha_m z\, dr\, dz, \tag{20a}$$

$$A_{im}=\frac{4\pi}{\tilde{N}_i L\rho(\omega_{im}^2-\omega^2)}\int_0^L\int_{R_1}^{R_2}\tilde{\Theta}(r,z)r\tilde{V}_i(r)\sin\alpha_m z\, dr\, dz, \tag{20b}$$

where

$$\tilde{N}_i=\int_{R_1}^{R_2}[\tilde{V}_i(r)]^2 r\, dr=\tfrac{1}{2}\{R_2^2[\tilde{V}_i(R_2)]^2-R_1^2[\tilde{V}_i(R_1)]^2\} \tag{21a}$$

and

$$\tilde{V}_i(r)=J_2(\beta_i R_2)Y_1(\beta_i r)-Y_2(\beta_i R_2)J_1(\beta_i r). \tag{21b}$$

Thus for case C:

$$A_{0m}=\frac{8m_z}{(R_2^4-R_1^4)L\rho}\,\frac{\sin\alpha_m z_0}{\omega_{0m}^2-\omega^2}, \tag{22a}$$

$$A_{im}=0 \tag{22b}$$

and for case D,

$$A_{0m}=\frac{8m_z}{(R_2^4-R_1^4)L\rho}\,\frac{\sin\alpha_m z_0}{\omega_{0m}^2-\omega^2}, \tag{23a}$$

$$A_{im}=\frac{24m_z}{\tilde{N}_i\beta_i^2(R_2^6-R_1^6)L\rho}\,\frac{[R_2^3\tilde{V}_i(R_2)-R_1^3\tilde{V}_i(R_1)]\sin\alpha_m z_0}{\omega_{im}^2-\omega^2}. \tag{23b}$$

Therefore, the displacement response for case C is expressed as

$$\nu=\frac{8m_z r}{(R_2^4-R_1^4)L\rho}\left\{\sum_m\frac{\sin\alpha_m z_0\sin\alpha_m z}{\omega_{0m}^2-\omega^2}\right\}e^{j\omega t} \tag{24}$$

and for case D,

$$\nu=\frac{8m_z}{L\rho}\left\{\sum_m\left\{\frac{1}{R_2^4-R_1^4}\,\frac{r}{\omega_{0m}^2-\omega^2}+\sum_i\frac{3[R_2^3\tilde{V}_i(R_2)-R_1^3\tilde{V}_i(R_1)]}{\tilde{N}_i\beta_i^2(R_2^6-R_1^6)}\,\frac{\tilde{V}_i(r)}{\omega_{im}^2-\omega^2}\right\}\times\sin\alpha_m z_0\sin\alpha_m z\right\}e^{j\omega t}. \tag{25}$$

III. THE POWER FLOW OF TORSIONAL VIBRATION IN SOLID AND HOLLOW CYLINDRICAL BARS

The structural intensity (time averaged) vector $I=(I_r I_\theta I_z)^T$ in elastic structures is defined as follows:[5]

$$I=\begin{pmatrix}I_r\\ I_\theta\\ I_z\end{pmatrix}=-\frac{1}{2}\,\mathrm{Re}\left\{\begin{pmatrix}\sigma_r & \tau_{r\theta} & \tau_{rz}\\ \tau_{\theta r} & \sigma_\theta & \tau_{\theta z}\\ \tau_{zr} & \tau_{z\theta} & \sigma_z\end{pmatrix}\begin{pmatrix}\dot{u}^*\\ \dot{v}^*\\ \dot{w}^*\end{pmatrix}\right\}, \tag{26}$$

where the dot over u, v, and w represents their derivatives with respect to time. Because $u=w=0$ and $v=v(r,z;t)\neq 0$, the relevant stress components are

$$\tau_{r\theta}=G\left(\frac{\partial v}{\partial r}-\frac{v}{r}\right),\quad \sigma_\theta=0,\quad \tau_{z\theta}=G\,\frac{\partial v}{\partial z}. \tag{27}$$

Therefore, the components of the intensity are:

$$I_r=-\tfrac{1}{2}\,\mathrm{Re}\{\tau_{r\theta}\dot{v}^*\},\quad I_\theta=0,\quad I_z=-\tfrac{1}{2}\,\mathrm{Re}\{\tau_{z\theta}\dot{v}^*\}, \tag{28}$$

where symbol * and Re{ } represent the conjugation and the real part of a complex value, respectively.

To obtain a nonzero average power flow I, the shear modulus, G, is assumed to be complex to take the internal losses of structures into account, that is,

$$G=G_0(1+j\,\eta), \tag{29}$$

where η is the structural loss factor and G_0 is the real shear modulus. Note that according to Eq. (8), the natural frequencies, ω_{im}, are now complex.

For solid bars, $\tau_{r\theta}$, $\tau_{z\theta}$, and $\dot{v}^*$ in Eq. (28) can be expressed, respectively, as

1. Case A:

$$\tau_{r\theta}=0, \tag{30}$$

$$\tau_{z\theta}=\frac{8m_zGr}{R^4L\rho}\left\{\sum_m\ \alpha_m\,\frac{\sin\,\alpha_mz_0\,\cos\,\alpha_mz}{\omega_{0m}^2-\omega^2}\right\}e^{j\omega t}, \tag{31}$$

$$\dot{v}^*=\frac{8m_z\omega r}{R^4L\rho}\left\{\sum_m\ \frac{\sin\,\alpha_mz_0\,\sin\,\alpha_mz}{\omega_{0m}^{*2}-\omega^2}\right\}e^{-j(\omega t+\pi/2)}. \tag{32}$$

2. Case B:

$$\tau_{r\theta}=-\frac{48m_zG}{R^5L\rho}\left\{\sum_m\sum_i\ \frac{J_2(\beta_ir)}{\beta_i^2J_1(\beta_iR)(\omega_{im}^2-\omega^2)}\times\sin\,\alpha_mz_0\,\sin\,\alpha_mz\right\}e^{j\omega t}, \tag{33}$$

$$\tau_{z\theta}=\frac{24m_zG}{R^4L\rho}\left\{\sum_m\ \alpha_m\left[\frac{r}{3(\omega_{0m}^2-\omega^2)}+\sum_i\ \frac{2J_1(\beta_ir)}{\beta_i^2R(\omega_{im}^2-\omega^2)J_1(\beta_iR)}\right]\times\sin\,\alpha_mz_0\,\cos\,\alpha_mz\right\}e^{j\omega t}, \tag{34}$$

$$\dot{v}^*=\frac{8m_z\omega}{R^4L\rho}\left\{\sum_m\left[\frac{r}{\omega_{0m}^{*2}-\omega^2}+\sum_i\ \frac{6J_1(\beta_ir)}{\beta_i^2R(\omega_{im}^{*2}-\omega^2)J_1(\beta_iR)}\right]\times\sin\,\alpha_mz_0\,\sin\,\alpha_mz\right\}e^{-j(\omega t+\pi/2)}. \tag{35}$$

For hollow bars, $\tau_{r\theta}$, $\tau_{z\theta}$, and $\dot{v}^*$ in Eq. (28) can be expressed, respectively, as

1. Case C:

$$\tau_{r\theta}=0, \tag{36}$$

$$\tau_{z\theta}=\frac{8m_zGr}{(R_2^4-R_1^4)L\rho}\left\{\sum_m\ \alpha_m\,\frac{\sin\,\alpha_mz_0\,\cos\,\alpha_mz}{\omega_{0m}^2-\omega^2}\right\}e^{j\omega t}, \tag{37}$$

$$\dot{v}^*=\frac{8m_z\omega r}{(R_2^4-R_1^4)L\rho}\times\left\{\sum_m\ \frac{\sin\,\alpha_mz_0\,\sin\,\alpha_mz}{\omega_{0m}^{*2}-\omega^2}\right\}e^{-j(\omega t+\pi/2)}. \tag{38}$$

It can be seen from Eqs. (30)–(32) and (36)–(38) that for the excitation of torsional moment due to linearly distributed body force (cases A and C), the vibrational intensity will be characterized by a distribution function $Z(z)$ as follows:

$$I_z=m_z^2Z(z)r^2. \tag{39}$$

For example, the distribution function of the hollow cylindrical bars is

$$Z(z)=\frac{32G_0\omega}{(R_2^4-R_1^4)^2L^2\rho^2}\,\mathrm{Re}\left\{(\eta-j)\sum_m\ \alpha_m\times\frac{\sin\,\alpha_mz_0\,\sin\,\alpha_mz}{\omega_{0m}^2-\omega^2}\sum_n\ \frac{\sin\,\alpha_nz_0\,\sin\,\alpha_nz}{\omega_{0n}^{*2}-\omega^2}\right\}. \tag{40}$$

2. Case D:

$$\tau_{r\theta}=-\frac{24m_zG}{(R_2^6-R_1^6)L\rho}\left\{\sum_m\sum_i\ \frac{[R_2^3\tilde{V}_i(R_2)-R_1^3\tilde{V}_i(R_1)]}{\tilde{N}_i\beta_i}\cdot\frac{[J_2(\beta_iR_2)Y_2(\beta_ir)-Y_2(\beta_iR_2)J_2(\beta_ir)]}{\omega_{im}^2-\omega^2}\times\sin\,\alpha_mz_0\,\sin\,\alpha_mz\right\}e^{j\omega t}, \tag{41}$$

$$\tau_{z\theta}=\frac{8m_zG}{L\rho}\left\{\sum_m\ \alpha_m\left\{\frac{r}{(R_2^4-R_1^4)(\omega_{0m}^2-\omega^2)}+\sum_i\ \frac{3[R_2^3\tilde{V}_i(R_2)-R_1^3\tilde{V}_i(R_1)]\tilde{V}_i(r)}{\tilde{N}_i\beta_i^2(R_2^6-R_1^6)(\omega_{im}^2-\omega^2)}\right\}\times\sin\,\alpha_mz_0\,\cos\,\alpha_mz\right\}e^{j\omega t}, \tag{42}$$

TABLE I. Parameters of hollow aluminum bar used in example 1.

E	2.7346×10^{10}	Nm^{-2}	R_2	0.1	m
ν	0.3		R_1	0.05	m
G_0	1.0518×10^{10}	Nm^{-2}	L	5.0	m
ρ	2740	kgm^{-3}	η	0.1	

TABLE II. Parameters of hollow aluminum bar used in example 2.

E	2.7346×10^{10}	Nm^{-2}	R_2	2.5	m
ν	0.3		R_1	1.25	m
G_0	1.0518×10^{10}	Nm^{-2}	L	2.0	m
ρ	2740	kgm^{-3}	η	0.1	

$$\cdot\dot{\nu}^{*}=\frac{8m_z}{L\rho}\left\{\sum_m\left\{\frac{r}{(R_2^4-R_1^4)(\omega_{0m}^{*2}-\omega^2)}+\sum_i\frac{3[R_2^3\tilde{V}_i(R_2)-R_1^3\tilde{V}_i(R_1)]\tilde{V}_i(r)}{\tilde{N}_i\beta_i^2(R_2^6-R_1^6)(\omega_{im}^{*2}-\omega^2)}\right\}\times\sin\ \alpha_m z_0\ \sin\ \alpha_m z\right\}e^{-j(\omega t+\pi/2)}. \tag{43}$$

IV. EXAMPLES

The torsional power flow in two hollow aluminium bars corresponding to cases C (as example 1) and D (as example 2) are calculated and used to explain the analytical results obtained. The parameters used for the two structures are listed in Tables I and II, respectively. Dimensionless parameters are used in both examples. The eigenvalues $x_i=\beta_i R_2$ are listed in Table III for $R_2/R_1=2$. The first five resonance frequencies of the bars used in the examples are listed in Table IV.

For the excitation of a torsional moment due to linearly distributed body force, the vibrational intensity in the hollow cylinder of the first example has only one component I_z. This component can be represented by $Z(z)$ as shown in Eq. (41) as its quadratic dependence of the intensity on r is obvious. Figure 2 shows the negative value of $Z(z)$ in bar used in the first example with excitation moment at $z_0=L$ ($f=200$ Hz and $\eta=0.1$). For this case, the positive values of $-Z(z)$ correspond to the vibrational intensity in the negative z direction. The effect of modal truncation on the intensity is shown in Fig. 2 when two different numbers of modes ($M=50$ and 800) were used in the calculation. It can be seen that the modal truncation error has more significant effect on the intensity at the cross sections near the source. For effective computation of the results shown in Figs. 3–6, 800 modes were used in calculating the near field intensity, while only 50 modes for the far field intensity.

TABLE III. The first 15, $\beta_i R_2$ for a hollow bar with $R_2:R_1=2$.

i	$\beta_i R_2$
1	6.8138
2	12.8553
3	19.0457
4	25.2808
5	31.5347
6	37.7982
7	44.0673
8	50.3399
9	56.6149
10	62.8915
11	69.1692
12	75.4479
13	81.7273
14	88.0072
15	94.290

TABLE IV. The first five modal frequencies in the examples.

Example 1	f_{im}, (Hz)	98.0	293.9	489.8	685.7	881.7
	(i, m)	(1,0)	(2,0)	(3,0)	(4,0)	(5,0)
Example 2	f_{im}, (Hz)	244.9	734.7	884.5	1123.4	1224.5
	(i, m)	(1,0)	(2,0)	(1,1)	(2,1)	(3,0)

Figure 3 shows $-Z(z)$ as a function of excitation frequencies $\omega/2\pi$ at the section $z=0.3L$. It can be seen that the vibrational intensity in elastic structures could vary in a large range at any cross section, depending on whether the excitation frequency is close to the resonance frequencies, particularly of the lower order modes.

Figure 4 shows the $-Z(z)$ curves at first four resonance frequencies: $f_{1-4}=98.0$, 239.9, 489.8, and 685.7 Hz of the first example. The shapes of the curves are dominated by the modal vibration of the bar at the resonances. In those regions where torsional vibration has large amplitude, the power flow curves have large slope, as the large amplitude vibration corresponds to a large dissipation of the energy. Figure 5 shows $-Z(z)$ for the location of driving moment at $z_0=0.4L$. For this case the intensity flows away from the external driving moment. A large amount of the energy is dissipated between the driving moment and the free end where the torsional displacement is large.

The three-dimensional analysis of the torsional wave in the hollow cylindrical bars also suggested that the distributed intensity vector field is contributing to the power flowing in bars. The complexity of the intensity field may be observed when the driving frequency is high and the diameter of the structure is large. Figure 6 shows a typical example of the intensity vector field in a hollow cylindrical aluminium bar with parameters listed in Table II. The aluminum bar is driven by a torque ($m_z=1$ Nm) due to cubically distributed body force concentrated on the free end ($z_0=L$) of the bar and the excitation frequency is at 900 Hz. Because the axially symmetric excitation of the moment, the intensity field is also axially symmetric. For this case, Fig. 6 represents the

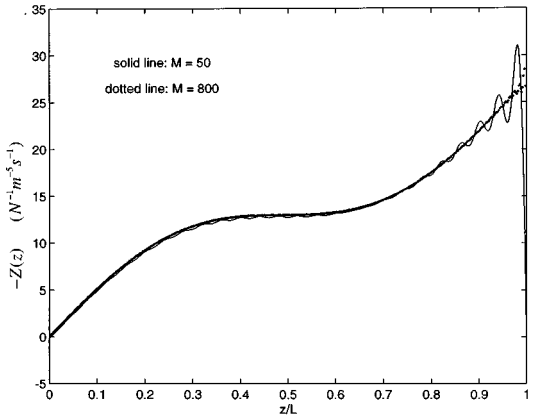

FIG. 2. Effect of the number of modes on the calculations of vibrational intensity (solid curve: $M=50$; dotted curve: $M=800$).

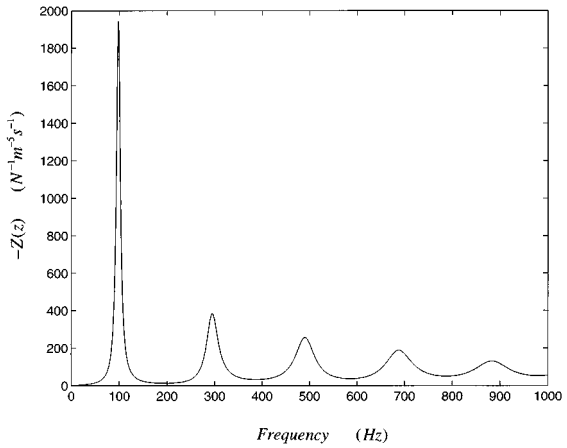

FIG. 3. $-Z(z)$ as a function of frequency at $z=0.3L$ (case C, $z_0=L$, $\eta=0.1$).

intensity vector field in any lateral cross section of the bar.

Because of the large moment input near the outer surface of the hollow bar, a large intensity vector flowing towards the negative z direction can be observed. This part of the intensity field carries the major part of the input power. While attenuated along their flow path in the region of $1.5\ \text{m}<z<2.0\ \text{m}$, the intensity vectors flow towards the inner surface. Between $z=0.9$ m and $z=1.5$ m, the major part of the power flow is carried out by the intensity field close to the inner surface. Around $z=0.9$ m, the intensity vectors start to flow towards the outer surface and in the positive z direction. As a result, a vortex of structural intensity field can be identified in Fig. 6.

V. COMPARISON WITH THE ONE-DIMENSIONAL THEORY

The structural intensity obtained from the three-dimensional modeling is compared with that from the one-dimensional torsional wave theory. The results are summarized as follows:

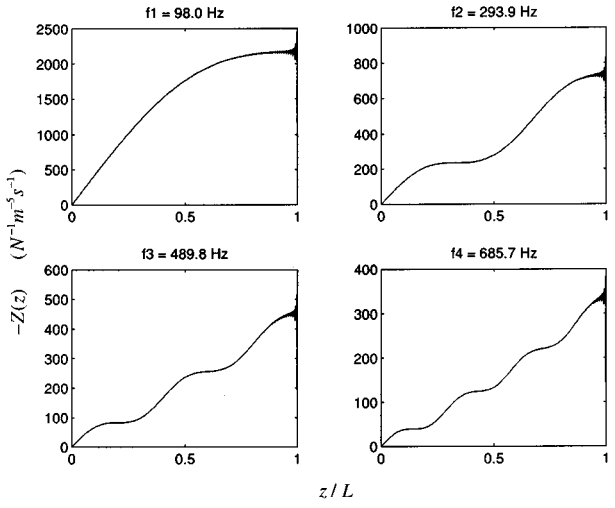

FIG. 4. $-Z(z)$ curves at first four resonance frequencies: $f_1=98.0$ Hz, $f_2=293.9$ Hz, $f_3=489.8$ Hz, $f_4=685.7$ Hz (case C, $z_0=L$, $\eta=0.1$).

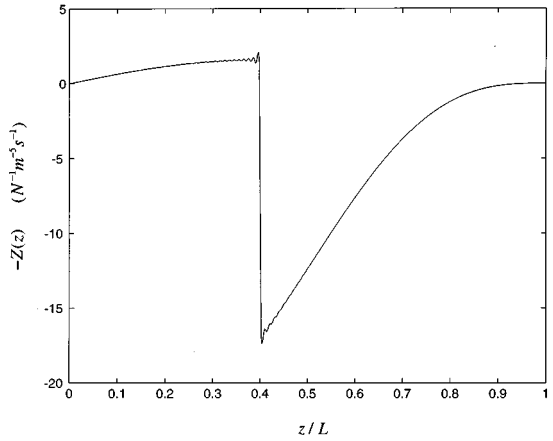

FIG. 5. $-Z(z)$ curve for case C ($z_0=0.4L$, $\eta=0.1$, $f=200$ Hz).

(1) Under the excitation of a moment due to symmetric and linearly distributed forces [Eqs. (10) and (16)], the torsional displacement can be written as $\nu=r\hat{\theta}(z,t)$ as shown in Eqs. (14) and (24). $\hat{\theta}$ represents the angular displacement of the bar's cross section and is independent of r (corresponding to the rigid cross-section model). Therefore, for this type of moment excitation, Eq. (2) is equivalent to the equation of torsion in the one-dimensional theory:

$$\frac{\partial^2\hat{\theta}}{\partial z^2}-\frac{\rho}{G}\frac{\partial^2\hat{\theta}}{\partial t^2}=-\frac{1}{GI_0}m_z\delta(z-z_0)e^{j\omega t},$$

where GI_0 is the torsional rigidity of the bar. The corresponding vibrational intensity is a quadratic function of r.

(2) If the external moment is not due to linearly distributed forces [e.g., Eqs. (11) and (17)], the structural intensity predicted by the three-dimensional model will be different from that by the one-dimensional torsional wave equation. As shown in this analysis, the distribution of structural intensity component I_z in the z direction will not be dependent on r quadratically. In addition, the component I_r will not be zero for this case.

Figure 7(a) and (b) shows the vibrational intensity components I_z and I_r at four cross sections ($z=0.3$, 1.0, 1.75, and 1.95 m) of the hollow bar described in Table II under the excitation of a unit moment due to cubically distributed body

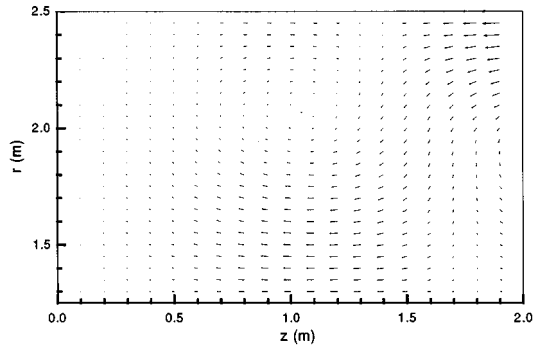

FIG. 6. Structural intensity vector field (case D, $\eta=0.1$, $f=900$ Hz, $m_z=1$ Nm).

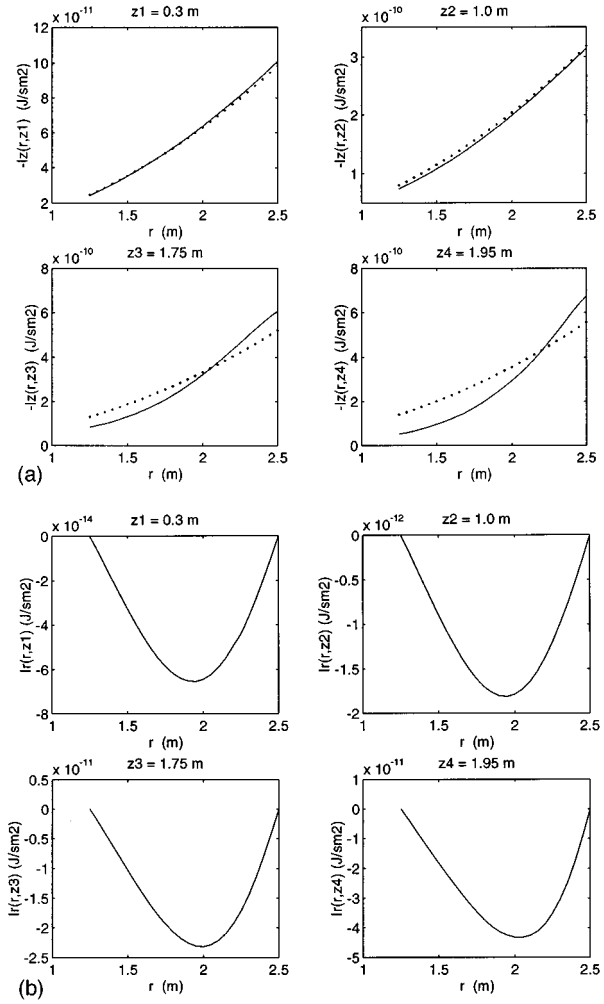

FIG. 7. Comparison with one-dimensional model at the lower frequency ($f=100$ Hz, $\eta=0.1$ $m_z=1$ Nm). (a) I_z; (b) I_r (solid curve: exact solution; dotted curve: 1-D model).

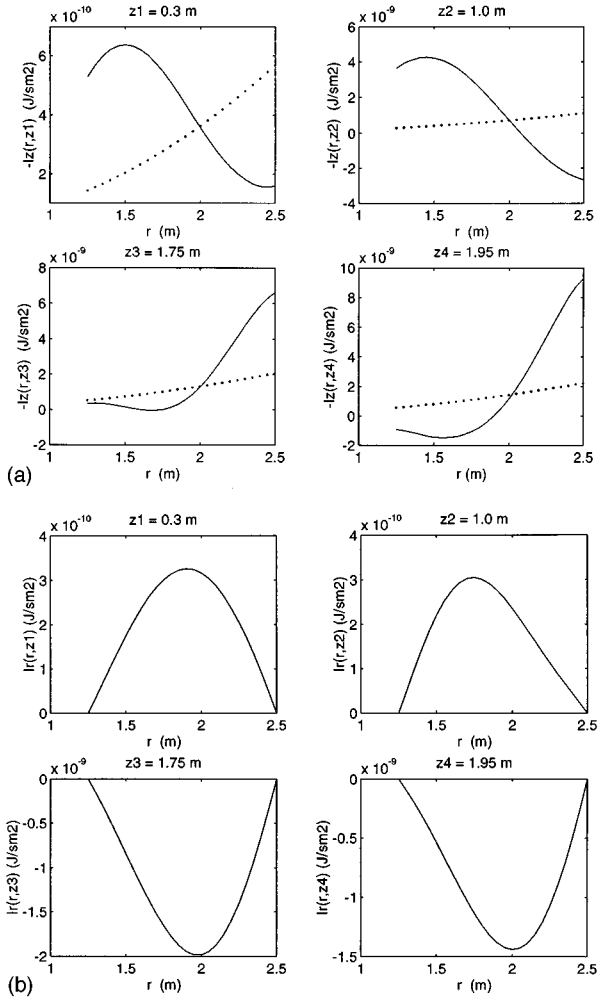

FIG. 8. Comparison with one-dimensional model at the higher frequency ($f=900$ Hz, $\eta=0.1$ $m_z=1$ Nm). (a) I_z; (b) I_r (solid curve: exact solution; dotted curve: 1-D model).

force applied at $z_0=L$. The driving frequency is at 100 Hz which is lower than the first resonance frequency (244.9 Hz). The intensity components are calculated respectively using the three dimensional model and the one dimensional torsional theory. For such a low-frequency excitation, the two models give similar intensity distribution along the r direction at those cross sections away from the driving moment. Near the driving moment, a difference occurs. The 3-D solution tends to show the dependence of the intensity on r in a nonquadratic relationship, while the result from the classical torsional theory shows the quadratic dependence on r. However, the total power flow in the z direction calculated from these two models are still very close. The calculated results of the power flow components $p_z=\int_S I_z\, dS$ at the four cross sections obtained from the two models show the deviation between the two predictions is less than 3% away from the driving location. Very close to the driving location the deviation is about 13%. This large derivation comes from the fact that near the driving location a significant portion of the structural intensity is in the negative r direction, while the one-dimensional theory fails to predict that. In Fig. 7(b), it is clearly shown that the intensity flow in the r direction does exist, while the one-dimensional torsional theory can only give zero intensity component in this direction. Near the driving location at $z=1.95$ m, large intensity component in the r direction can be identified. This explains why the 3-D solution gives smaller power flow in the z direction at the cross section near the driving moment.

The second example shows the characteristics of the torsional intensity field due to a high-frequency excitation. The driving frequency is at 900 Hz, which is above the third resonance frequency of the bar (884.5 Hz). The vibrational intensity components I_z are presented in Fig. 8(a), where the 3-D intensity differs markedly from that predicted by the 1-D theory. For this case, the one-dimensional theory simply cannot provide any relevant information. The components I_r are presented in Fig. 8(b). They show that the intensity flows along the r axis are not all in the same direction, which indicates a possible vortex pattern, as shown in Fig. 6.

VI. CONCLUSIONS

The vibrational intensity of torsional waves in solid and hollow cylindrical bars is analytically investigated in this paper. The expressions of the three-dimensional torsional re-

sponse in the bars are obtained and they satisfy exactly the governing elastic equations and prescribed boundary conditions. The significance of the analytical results is illustrated using two examples (pipelike and turbinelike hollow bars). Useful observations are summarized as follows:

(1) Except for the moment excitation due to body forces linearly distributed in the r direction, the axial symmetrically excited torsional intensity usually have two nonzero components in both the z direction and r directions of cylindrical bars. Complex intensity vector field patterns may be observed for the excitation at higher frequencies. For this case, the largest intensity values may not necessarily occur near the outer surface of the bar, and vortex patterns may be observed in the intensity vector field.
(2) When the bars are excited by a moment excitation due to linearly distributed body forces (axially symmetric), the predicted torsional response and intensity using the three-dimensional results are identical to that obtained from the one-dimensional torsional wave theory. If the moment excitations are due to axial symmetrical body forces other than the linearly distributed one, the one-dimensional theory can only give useful results in predicting low frequency power flows. For the intensity distribution at the high frequencies, the 3-D solution has to be employed to obtain the intensity component in the radial direction and the intensity vector near the source of the excitation. For this type of moment excitation at high frequencies, the three-dimensional solution has to be used in the prediction of the structural intensity field, because the one-dimensional torsional theory fails to provide any useful information.

ACKNOWLEDGMENT

Financial support for this work from Australia Research Council is gratefully acknowledged.

[1] A. W. Leissa, *Vibration of Shells* (Acoustical Society of America, Woodbury, NY, 1993).
[2] S. K. Clark, ''Torsional wave propagation in hollow cylindrical bars,'' J. Acoust. Soc. Am. **28**, 1163–1165 (1956).
[3] A. W. Leissa and J. So, ''Comparisons of vibration frequencies for rods and beams from one-dimensional and three-dimensional analyses,'' J. Acoust. Soc. Am. **98**, 2122–2135 (1995).
[4] A. W. Leissa and J. So, ''Accurate vibration frequencies of circular cylinders from three-dimensional analyses,'' J. Acoust. Soc. Am. **98**, 2136–2141 (1995).
[5] G. Pavic, Intensity induced by structural vibrations of elastic bodies, Proceedings of the 3rd International Congress on Intensity Techniques, Senlis, France, 21–28 August 1990.

Vibroacoustic analysis of an unbaffled rotating disk

André F. Côté and Noureddine Atalla
Groupe d'Acoustique de l'Université de Sherbrooke, Département de Génie Mécanique, Université de Sherbrooke, 2500 boul. Université, Sherbrooke, Quebec J1K 2R1, Canada

Jean-Louis Guyader
Laboratoire Vibrations-Acoustique, Institut National de Sciences Appliquées, Lyon, France

(Received 10 January 1997; revised 19 August 1997; accepted 24 November 1997)

The dynamic and acoustic response of an unbaffled rotating disk, subjected to a space-fixed harmonic lateral force, is investigated. The plate is supposed to be clamped at the inside and free at the outer boundary. The exciting force being space-fixed, the mass and stiffness matrices, obtained from the variational method combined with the Rayleigh–Ritz approach in the rotating frame, are converted back to the nonrotating frame, where the generalized force and the displacements of the plate are evaluated. The related acoustic pressure, neglecting fluid loading, is determined using a boundary element formulation. Special attention has been given to ensure correct modeling of the unbaffled condition on the radiation of the plate. Results are presented to show the effect of rotation for both dynamic response and acoustic radiation. A practical case is also investigated: the circular saw. To simulate the exciting force of the saw, a measurement of the force induced by one tooth has been done. Then, a retarded-time sum has been performed to account for the exact number of teeth.
 [S0001-4966(98)02903-8]

PACS numbers: 43.40.Dx, 43.40.Rj [CBB]

INTRODUCTION

The vibration analysis of a circular or annular plate has generated a lot of interest. This interest naturally comes from the similarity with industrial application such as compact and computer disks, train wheels, circular saws, etc. Most of this interest, however, has been concentrated on the free vibration. Weisensel (1989) has reported 19 papers on the annular plate (rotating or not) and even more than that for the circular plate. The subject is well covered.

Possibly due to the fact that all the main vibration phenomena have been studied with free vibration analyses, the forced response has received less attention. Honda *et al.* (1985) have studied the modal response of an annular plate to a rotating force. Although in their analysis it was the force instead of the plate that was rotating, it is still a similar problem. Their results were consistent with the results on the free vibration. This subject is also well mastered.

On the acoustic radiation, three papers (Lee and Singh, 1992, 1994; Beslin and Nicolas, 1996) have been found. Those studies were focused mainly on the modal radiation efficiency. Lee and Singh (1992, 1994) determined analytically the modal radiation efficiency and modal radiation power of a rotating baffled plate, in a rotating frame of reference. The effect of rotation was considered through centrifugal stresses (Sinha, 1987) and the retarded source Green's function, but the doubling of modes due to a nonrotating frame of reference was not considered (Tobias and Arnold, 1957). Since most applications involve nonbaffled plates, the Lee and Singh methods and calculations do not apply directly. Furthermore, the calculations were performed in the rotating frame of reference, which is restrictive since the human observer is obviously not in that frame for most applications (circular saws, compact and computer disks, etc.).

Recently, Beslin and Nicolas (1996) considered the modal radiation efficiency of an unbaffled rotating annular disk, in both frames of reference (rotating and nonrotating). Hence the doubling of modes due to rotation is considered, however, the centrifugal stresses are not. For most applications (circular saws, compact and computer disks, train wheels) this is a good approximation. Indeed, studies (Côté, 1994) have shown that the effect of centrifugal stresses is not very important when the rotation speed is low. Beslin and Nicolas (1996) have developed a criterion to classify the modes as radiating or nonradiating modes, based on the radiation efficiency at the natural frequencies of the plate, considering that all modes have the same imposed velocity (amplitude). Using this criterion Beslin and Nicolas have concluded that only the modes with a high number of nodal circles can radiate. In the case of a mode with a low number of nodal circles, it can radiate but only if its number of nodal diameters is very high. They have also concluded that the effect of rotation, namely the doubling of modes, has negligible effects on the radiation. Beslin and Nicolas's work gives good insight into the radiation mechanism of an unbaffled rotating plate. However, it is the belief of the authors that most applications violate their main assumption (equally excited modes using an imposed velocity).

To summarize the literature review, the free and forced vibration analysis of an annular plate has been well covered. However, for the acoustic radiation, only the radiation efficiencies have been studied and the assumptions made are somewhat limiting. Indeed, Lee and Singh (1992, 1994) used a baffled plate, and neglected the doubling of modes due to the nonrotating frame of reference. Beslin and Nicolas (1996) did include those characteristics in their model but they considered an *equally imposed velocity (amplitude)* on each mode. The present analysis eliminates these limitations.

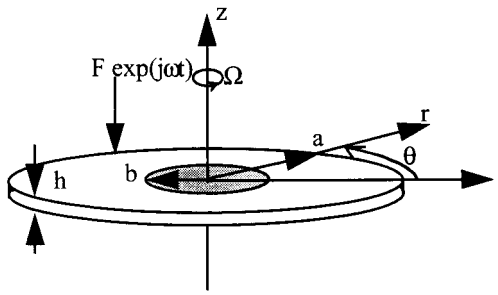

FIG. 1. Harmonic force acting on a rotating clamped-free annular plate.

It investigates the specific response of an unbaffled annular plate due to an exciting force. Using this approach, this paper studies the vibroacoustic behavior of an unbaffled rotating plate. The presented analysis especially shows the influence of the rotation and the excitation on the vibroacoustic response of the plate. Due to the more general assumptions of the presented analysis, in certain situations, conclusions different from those of Beslin and Nicolas (1996) are obtained.

The paper is organized as follows. After a brief description of the model and assumptions in Sec. I, the analysis continues by presenting the vibration response of the disk to an exciting force (Sec. II). This section does not show any new phenomena but helps in understanding the acoustic radiation phenomena presented in Secs. III and IV. In Sec. III, the vibroacoustic frequency response of the plate is analyzed. This section presents the particularities of the acoustic response. And, in Sec. IV, an excellent first approximation of a circular saw's response is presented, simply by considering an estimation of the nonconstant exciting force. Using this numerical model, conclusions of the effect of rotation on the acoustic response of a circular saw are drawn.

I. MODEL AND ASSUMPTIONS

The geometry of the model is given in Fig. 1. A rotating annular plate clamped on the inside and free at the outer boundary is excited by a harmonic force. The force is oscillating at frequency ω and is acting normal to the plate. Note that an in-plane force could also be modeled but since only the transverse displacement is important to the acoustic radiation, the in-plane force is ignored. The acoustic medium is air with no boundary (infinite space) and the plate is unbaffled except at the center (gray area in Fig. 1). A cylindrical set of coordinates, rotating with the plate, is used. In addition, the following assumptions are made:

The material is isotropic and homogeneous.
The thickness is constant.
The displacements are small (within linear theory).
The torsion is neglected.
The fluid loading on the plate is neglected.
The in-plane displacements are neglected.

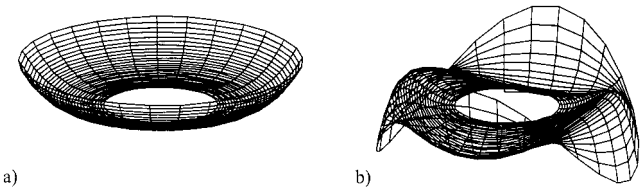

FIG. 2. (a) mode shape (0,0) and (b) mode shape (1,2).

II. VIBRATION

A. Equation of motion in the rotating frame of reference

Côté (1994) has investigated the free vibration of a thick rotating annular plate in the rotating frame of reference, for calculation convenience. The free motion of the disk is described using the variational principle. To solve for the plate motion, the method of assumed modes is used where the displacement field variables are expanded over an admissible polynomial set of trial functions with unknown amplitudes. One should note here that, due to the circular geometry of the plate, the chosen set of trial functions separates into two types of orthogonal waves: the symmetric and antisymmetric waves.

$$w=\sum_{p,n} r^p(r-\xi)^2[\underbrace{C^s_{pn}\cos(n\theta)}_{\text{symmetric waves}} + \underbrace{C^a_{pn}\sin(n\theta)}_{\text{antisymmetric waves}}]e^{j\omega t}, \tag{1}$$

where C^s_{pn} and C^a_{pn} are unknown constants (amplitudes). Superscripts s and a refer to symmetric and antisymmetric waves, respectively.

Using Hamilton's principle, Côté (1994) obtained the generalized equation of motion expressed in the rotating frame of reference

$$[M_R]\{\ddot{X}\}_{\text{Rot}}+[K_R]\{X\}_{\text{Rot}}=\{0\}, \tag{2}$$

where $[M_R]$ and $[K_R]$ are the mass and stiffness matrices, and $\{X\}_{\text{Rot}}$ contains the unknown amplitudes in the Rayleigh–Ritz expansion (terms C^s_{pn} and $C^{a\ 1}_{pn}$). Explicit expressions for $[M_R]$ and $[K_R]$ can be found in Côté (1994). It must be emphasized that those matrices account for the effect of shear deformation, rotatory inertia, Coriolis acceleration, variation of inertia due to plate vibration, and the centrifugal stresses. Therefore the model is very general.

Resolution of Eq. (2) yields the natural frequencies and the mode shapes of the system in the rotating frame of reference. Mode shapes are defined with two indices (m,n), where m defines the number of modal circles and n defines the number of nodal diameter. Figure 2 shows a sketch of mode shapes (0,0) and (1,2).

B. Equation of motion in the fixed frame of reference

It is preferable to have the response of the plate in the observer's reference frame. For several applications (circular saw, train wheels, computer disk, etc.), the observer's refer-

ence frame is the space-fixed frame of reference. Therefore the equations of motion are transformed into the fixed reference frame.

For a given circumferential order n [see Eq. (1)], the symmetric and antisymmetric waves, rotating with the plate, are related to the corresponding space-fixed symmetric and antisymmetric waves by the following equation,

$$\begin{Bmatrix} \text{sym. wave} \\ \text{antisym. wave} \end{Bmatrix}_{\text{Rot}} = \begin{bmatrix} \cos(n\Omega t) & -\sin(n\Omega t) \\ \sin(n\Omega t) & \cos(n\Omega t) \end{bmatrix} \times \begin{Bmatrix} \text{sym. wave} \\ \text{antisym. wave} \end{Bmatrix}_{\text{Fix}}, \tag{3}$$

where Ω is the angular speed of rotation. The theoretical development to obtain this equation is formulated in the Appendix. Thus the global vector $\{X\}_{\text{Rot}}$ given in Eq. (2) may be related to the corresponding vector in the space-fixed frame of reference $\{X\}_{\text{Fix}}$. Using this transformation matrix [Eq. (3)], Eq. (2) becomes,

$$[M_R]\{\ddot{X}\}_{\text{Fix}} + (2n\Omega[M_R][R])\{\dot{X}\}_{\text{Fix}} + ([K_R] - n^2\Omega^2[M_R])\{X\}_{\text{Fix}} = \{0\}, \tag{4}$$

where $[R]$ is a block diagonal matrix with each block defined as

$$[R_b] = \begin{bmatrix} 0 & -1 & 0 & 0 & 0 & 0 \\ 1 & 0 & -1 & 0 & 0 & 0 \\ 0 & 1 & 0 & -1 & 0 & 0 \\ 0 & 0 & 1 & 0 & -1 & 0 \\ 0 & 0 & 0 & 1 & 0 & -1 \\ 0 & 0 & 0 & 0 & 1 & 0 \end{bmatrix}.$$

Equation (4) is the generalized equation of motion expressed in the space-fixed frame of reference. Two points should be noted here. First, one must not be mistaken by Eq. (4), rotation does not have the effect of adding damping. Indeed, this equation may be separated into two equations: one for symmetric waves and the other for nonsymmetric waves (Côté, 1994) with classic eigenvalue form. Second, resolution of those equations yields the natural frequencies and the mode shapes defined in the nonrotating frame of references. The mode shapes are the same in both references (rotating or not) but the natural frequencies follow the relationship (Tobias and Arnold, 1957; Côté, 1994)

$$\omega_{mn} = \omega_{mn}^R \pm n\Omega, \tag{5}$$

where ω_{mn} and ω_{mn}^R are the circular frequencies of the fixed and rotating frame, respectively, and where Ω is the angular speed of rotation.

To calculate the forced response of the rotating disk, the work done by the harmonic point force is added to the Lagrangian of the system. Expanding the transverse displacement of the disk over the polynomial set of trial functions, with the constants expressed in the nonrotating frame of reference, one obtains,

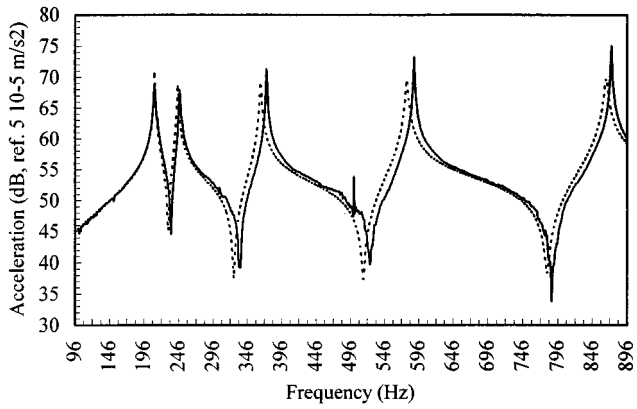

FIG. 3. Forced vibration of a disk: theory versus experiment [$a=173$ mm, $b=63.5$ mm, $h=3.048$ mm, $\rho=7800$ kg/m^3, $E=215$ Gpa, $\nu=0.32$, $F=1$ N, $\eta=0.009$], ———: experiment. – – –: theory.

$$\{F_g\} = \int_S \left(F(r,\theta,t) \sum_{p,n} r^p (r-\xi)^2 [\bar{C}_{pn}^s \cos(n\theta) + \bar{C}_{pn}^a \sin(n\theta)] e^{i\omega t} \right) dS, \tag{6}$$

where $F(r,\theta,t)$ is a force acting normal to the plate and S is the surface of the plate.

With the addition of Eq. (6) into Eq. (4), the following linear system is obtained for the forced response,

$$[M_R]\{\ddot{X}\}_{\text{Fix}} + (2n\Omega[M_R][R])\{\dot{X}\}_{\text{Fix}} + ([K_R]f - n^2\Omega^2[M_R])\{X\}_{\text{Fix}} = \{F_g\}. \tag{7}$$

It is important to note that, even though the plate is rotating, the system is still linear: A force acting at a certain frequency will generate a displacement at this same frequency. For the rest of this paper, all the calculations and results are done in the fixed reference frame.

C. Validation of the vibration calculation

The proposed approach has been validated for a nonrotating disk by comparing it with experimental data. The disk used for the purpose of the experiment was a circular saw made of steel without the teeth. The excitation was produced at a radius of 16 cm with a Brüel & Kjaer type 8292 impact hammer equipped with a type 8200 force transducer. The response was taken at the same point by a laser vibrometer (Polytec OFV302 head and OFV2600 controller) and analyzed with the Brüel & Kjaer dual channel type 2032 analyzer. The measurement setup and technique are described by Couture and Champoux (1994).

The outer diameter of the saw is not constant to allow evacuation of cut wood. The analytical formulation is not adapted to model such variation in the outer diameter, the average outer diameter was used instead (17.3 cm). The exact thickness ($h=3.048$ mm) and the inner diameter (6.35 cm) of the saw were used in the model. The typical density ($\rho=7800$ kg/m^3), structural damping coefficient[2] ($\eta=0.009$), and Young's modulus ($E=215$ GPa) of steel were used. The results are given in Fig. 3. The agreement between

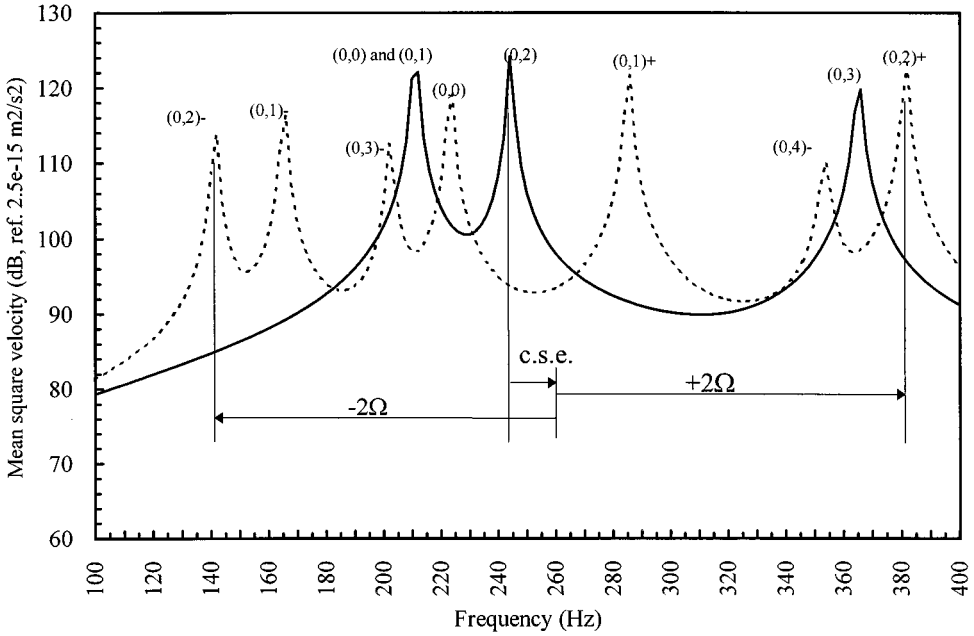

FIG. 4. Effect of rotation [$a=173$ mm, $b=63.5$ mm, $h=3.048$ mm, $\rho=7800$ kg/m^3, $E=215$ Gpa, $v=0.32$, $F=1$ N], ———: 0 rpm, – – –: 3600 rpm; $(m,n)^+$: mode with an increased natural frequency; $(m,n)^-$: mode with a decreased natural frequency.

the model and experiment is excellent. The only exception is the experimental peak at 496 Hz which is due to a problem with the analyzer used. The analyzer creates a lot of noise at the medium frequency when performing a zoom. Concerning the validation of the forced vibration of a *rotating* disk, the authors are not aware of any published experimental or analytical results. However, the validation of the proposed approach may be assumed from the correctness of the free vibration analysis of a rotating plate (Côté *et al.*, 1997), and the forced response of the stationary disk.

D. Review of the main phenomena for the vibration response

In this section, a number of conclusions drawn from the proposed approach will be discussed. It must be noted that these phenomena are well known. The idea is to recall these phenomena as they will serve in the acoustic radiation analysis. In Fig. 4, the effect of rotation on the mean-square velocity of a steel disk is presented. The same disk used in the validation section is considered. The mean-square velocity of the disk due to a point force excitation at a radius of 16 cm, where the disk is stationary, is compared to the case where the disk is rotating ($\Omega=3600$ rpm).

It may be observed that apart from the (0,0) mode, rotation doubles the number of natural frequencies for each mode. This is a consequence of the fact that the solution is expressed in a space-fixed frame of reference. In this frame, a mode is the superposition of a forward and a backward traveling wave (Tobias and Arnold, 1957). This effect is illustrated for mode (0,2) in Fig. 4. One may see that the (0,2) resonant frequency initially at 242 Hz is now ''doubled,'' appearing at 142 Hz for $(0,2)^-$ and 382 Hz for $(0,2)^+$. This effect may be very important from a practical viewpoint, since the vibration behavior of the disk will be conditioned by the spectra of the excitation force. As a consequence, by doubling the number of natural frequencies, the chances of a coincidence between the vibration of the disk and the exciting spectrum are substantially increased (Honda *et al.*, 1985). For a narrow-band excitation, this can lead to a significant change in the vibration output of the plate. This is crucial from a design viewpoint. However, this is not the same for a broadband excitation case. Indeed, the overall mean-square velocity level over the frequency range presented in Fig. 4 (100–400 Hz) does not change noticeably (127.3 dB with rotation and 127.7 dB without rotation).

Another classical effect of rotation (Sinha, 1987), apparent in Fig. 4, is the increase of the natural frequencies due to the centrifugal stresses (CSE). This effect is more apparent for mode (0,0) since the frame of reference has no doubling effect on this mode. Its frequency has been increased by 13 Hz (7%). Also, it must be noted that the phenomena of mode separation and frequency shift are the main rotation influence on the forced response. The Coriolis acceleration and variation of inertia have been included but were found to be negligible (Côté, 1994).

III. ACOUSTIC RADIATION

A. Theory

The vibration response calculated in the last section will now be used as an input to obtain sound radiation. Note that the acoustic radiation calculations can all be performed in the fixed reference frame, since the velocity distribution is given in that frame.

The acoustic pressure radiated by the disk is given by the Helmholtz integral equation (Pierce, 1980),

$$p(\mathbf{x}) = \int_{S_r} \left[p(\mathbf{y}) \frac{\partial G(\mathbf{x},\mathbf{y})}{\partial n_y} - G(\mathbf{x},\mathbf{y}) \frac{\partial p}{\partial n_y} \right] dS_y, \tag{8}$$

where $\mathbf{x}$ denotes a point in the fluid, $\mathbf{y}$ a point on the plate, n_y is the outward normal to the plate surface at point $\mathbf{y}$, $G(\mathbf{x},\mathbf{y}) = e^{-jkr}/4\pi r$ is the free-field Green's function with r the Euclidean distance between points $\mathbf{x}$ and $\mathbf{y}$, k is the acoustic wave number, and S_T the total surface of the disk (including the two faces).

Since the disk is assumed to be thin, there is a continuity of the normal velocity through the disk plane and a discontinuity of the acoustic pressure. Denoting $\mu = p^+ - p^-$, the pressure jump through the disk, and defining the normal to be in the direction from p^- to p^+, Eq. (8) reduces to

$$p(\mathbf{x}) = \int_S \mu(\mathbf{y}) \frac{\partial G(\mathbf{x},\mathbf{y})}{\partial n_y} dS_y, \tag{9}$$

where S denotes the upper surface of the disk.

Using the continuity condition between the annular plate and the fluid displacement at the surface of the plate, Eq. (9) becomes

$$\rho_0 \omega^2 (\mathbf{u}\cdot\mathbf{n}_x) = \frac{\partial}{\partial n_x} \int_S \mu(\mathbf{y}) \frac{\partial G(\mathbf{x},\mathbf{y})}{\partial n_y} dS_y, \tag{10}$$

where $(\mathbf{u}\cdot\mathbf{n}_x)$ denotes the normal displacement at point $\mathbf{x}$ of the disk. Note that the surface integral is to be taken in the sense of Hadamard's finite part. To evaluate Eq. (10) and alleviate the hypersingularity, a variational approach is used (Hamdi, 1981). First, Eq. (10) is multiplied by an arbitrary regular function $\delta\mu$ and the result is then integrated over the plate surface. Since we have no pressure jump along the edges of a thin plate, the following relation is found:

$$\rho_0 \omega^2 \int_S \delta\mu(\mathbf{x})(\mathbf{u}\cdot\mathbf{n}_x) dS_x = \int \int_S \frac{\partial^2 G(\mathbf{x},\mathbf{y})}{\partial \mathbf{n}_x \, \partial \mathbf{n}_y} \delta\mu(\mathbf{x})\mu(\mathbf{y}) dS_y \, dS_x. \tag{11}$$

In the case of a thin structure, the singular integral in Eq. (11) may be regularized using the procedure described in Hamdi (1981) which leads to

$$\begin{aligned} \rho_0 \omega^2 \int_\Sigma \delta\mu(\mathbf{x})(\mathbf{u}\cdot\mathbf{n}_x) dS_x &= \int \int_\Sigma k^2 (\mathbf{n}_x\cdot\mathbf{n}_y) G(\mathbf{x},\mathbf{y}) \delta\mu(\mathbf{x})\mu(\mathbf{y}) dS_y \, dS_x \\ &\quad - \int \int_\Sigma [\mathbf{n}_x \wedge \nabla_x \delta\mu(\mathbf{x})]\cdot[\mathbf{n}_y \wedge \nabla_x \mu(\mathbf{y})] G(\mathbf{x},\mathbf{y}) dS_y \, dS_x. \end{aligned} \tag{12}$$

To solve Eq. (12) a boundary element method is used. In this paper Eq. (12) is first discritized using linear triangular elements. Since the pressure jump decreases rapidly at the disk's outer boundary, a finer mesh should be used near the boundary. The numerical evaluation of the singular integrals (=cross influence terms) is made through a Radau-hammer integration scheme while the integration of the singular term (=self-influence terms) is made using a semianalytical approach. Next, using the variational principle, the solution of Eq. (12) is found.

Once the acoustic pressure jump is determined, the acoustic indicators can be calculated (e.g., acoustic power and radiation efficiency) using a simple numerical integration technique (Gauss quadrature).

B. Validation of the acoustic radiation

The results of the acoustic radiation method have also been validated. The comparison is made with results obtained by Williams (1983) on an unbaffled piston. Figure 5 shows the mesh used. This mesh has been checked to ensure that convergence is reached. Figure 6 presents the comparison of the pressure on the surface of the disk calculated using the methods presented in this paper and the data from Williams (1983). The piston characteristics are given in the caption of this figure. The agreement is excellent.

C. Results and discussion on the acoustic radiation

The same disk, as in the forced vibration section, is used. The acoustic power and the mean-square velocity of this plate is presented in Figs. 7 and 8. For the nonrotating case, it can be seen in Fig. 7 that only a few modes are radiating. Indeed, the contributions of mode (0,0) and mode (0,1) are so strong that it masks all the other modes in this frequency range. It is difficult to know the real contribution of mode (0,1) since it has almost the same natural frequency as mode (0,0). But, we can expect it to be between those of mode (0,0) and mode (0,2). This is especially apparent when mode (0,2) is resonant where only a tiny peak was able to emerge. It is no surprise that modes (0,2), (0,3), and (0,4) are radiating much less since they have 2, 3, and 4 nodal diameters respectively, creating a recirculation process of the energy at the surface of the plate that allows less energy to escape to the far field (Krishnappa and McDougall, 1989). The radiation efficiency of mode (0,0), (0,1), and (0,2) presented in Fig. 9 confirms this fact. It is quite clear that over

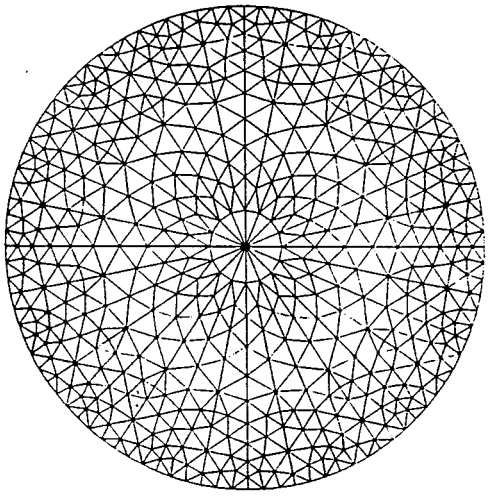

FIG. 5. Mesh of the plate.

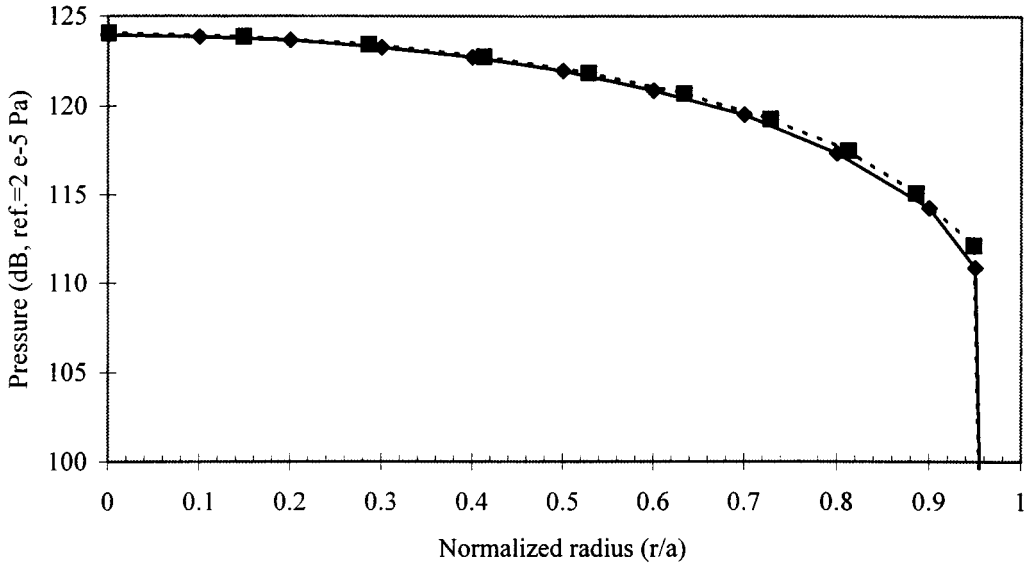

FIG. 6. Comparison of pressure on the surface of an unbaffled piston [$a=0.2$ m, $W=1\times10^{-5}$ m/s, $ka=2$, $c=340$ m/s, $\rho_0=1.2$ kg/m^3] —◇—: Williams (1983), ---■---: present study.

the 0–700-Hz frequency range, mode (0,0) has the highest radiation efficiency, then (0,1) and finally (0,2).

In Fig. 8, the acoustic response of the rotating plate is shown. A first look at the figure tells that rotation has the effect of increasing the number of radiating modes. Five peaks are clearly visible in the figure. All these peaks come from modes with high-shifted natural frequencies except for mode (0,1), where the natural frequency has been decreased. The explanation for this is in the modal radiation efficiency which increases with frequency [for frequencies under the critical frequency of radiation (Junger and Feit, 1993)]. The modes whose natural frequency have been reduced radiate less and the modes whose natural frequency have been increased radiate more. The contribution of mode (0,1) is now visible since its natural frequency has been shifted. Its contribution is between those of mode (0,0) and mode (0,2) as expected. Since it has only one nodal line (one nodal diameter), it has been able to emerge from the contribution of mode (0,0).

In summary, rotation increases the number of radiating modes due to both the doubling of modes and the fact that radiation efficiency increases with the frequency. The practical importance of this result depends on the excitation, as for the forced vibration. When the plate is excited by a narrow-band excitation, the effect of rotation might be very important since the number of radiating modes has increased.

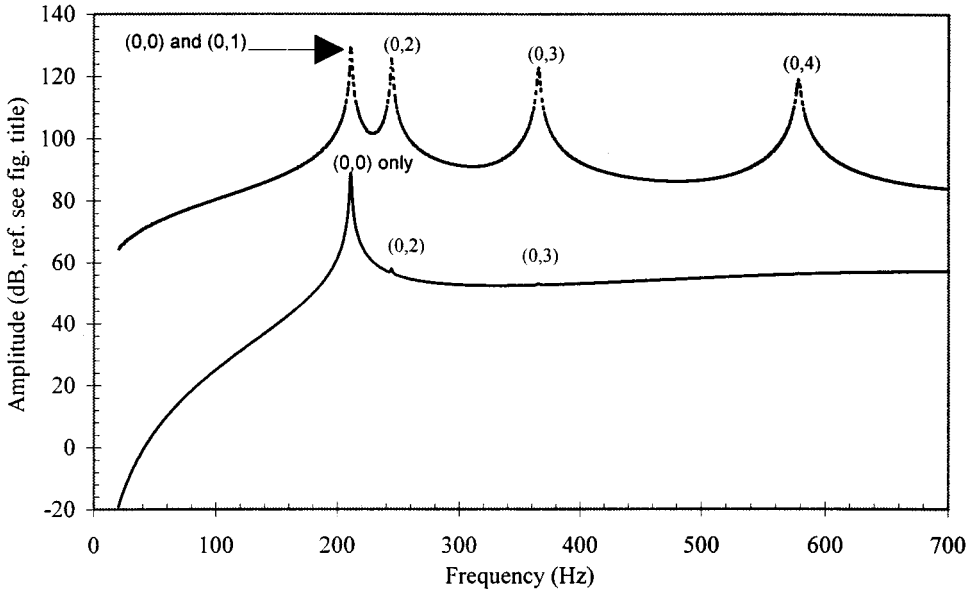

FIG. 7. Acoustic power and mean-square velocity of a disk excited by a harmonic point force [$a=173$ mm, $b=63.5$ mm, $h=3.048$ mm, $\rho=7800$ kg/m^3, $E=215$ GPa, $\upsilon=0.32$, $F=1$ N] ———: acoustical power, ref. 1×10^{-12} W, ----------: mean-square velocity, ref. 2×10^{-15} m^2/s^2.

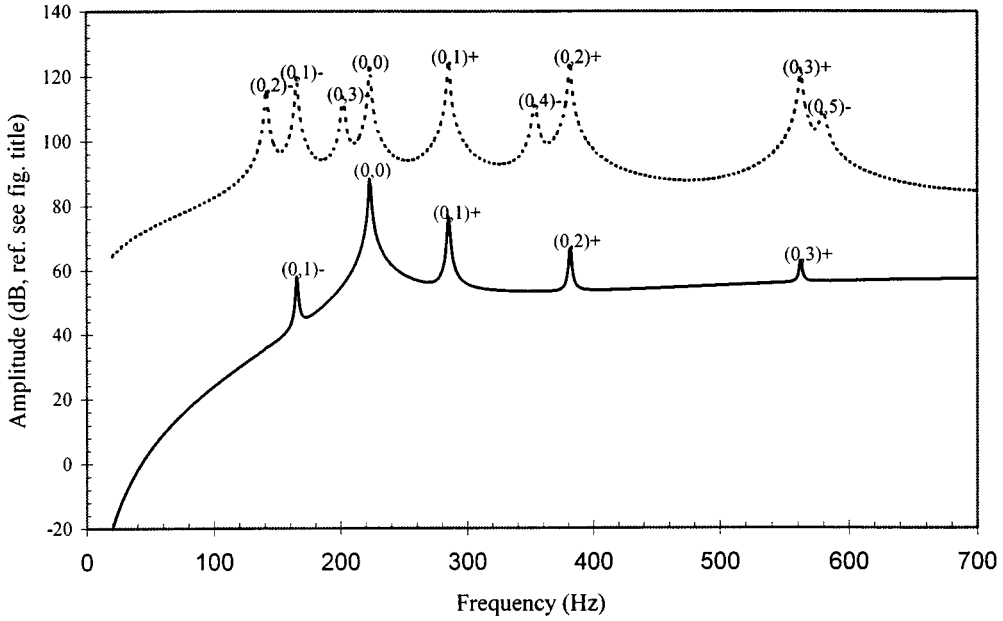

FIG. 8. Acoustic power and mean-square velocity of a rotating disk excited by a harmonic point force [$a=173$ mm, $b=63.5$ mm, $h=3.048$ mm, $\rho=7800$ kg/m^3, $E=215$ GPa, $\upsilon=0.32$, $\Omega=3600$ rpm, $F=1$ N] ———: Acoustical power, ref. 1×10^{-12} W, ----------: mean-square velocity, ref. 2×10^{-15} m^2/s^2; $(m,n)^+$: mode with an increased natural frequency; $(m,n)^-$: mode with a decreased natural frequency.

The chances of hitting a natural frequency are therefore increased. In contrast, for a wide spectral excitation several modes are excited anyway and the total radiated sound power is the same with or without rotation (93 dB when rotating, 94 dB with no rotation).

IV. PRACTICAL CASE: A CIRCULAR SAW

Using the general method developed, a simple yet quite real numerical model of a practical application can be obtained by using an estimation of the input force. This section will study the case of a circular saw.

A. Determination of the input force

First, the input force must be estimated. The transverse input force of a single saw tooth has been measured (Wojtowicki, 1993). Figure 10 presents the results of the measurement.

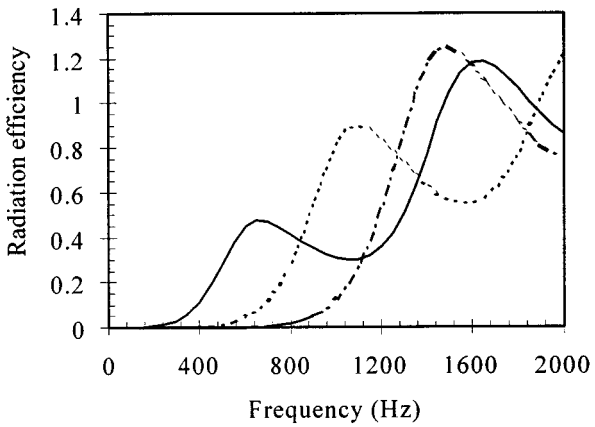

FIG. 9. Radiation efficiency of mode (0,0), (0,1), and (0,2). ———; (0,0); --------; (0,1); and –·–·–·–·; (0,2).

To account for the exact number of saw teeth, the total input force equals the retarded-time sum of all the teeth. Considering that $s_0(t)$ is the input force of one tooth, one finds that the total input force is

$$s(t)=s_0(t)+s_0\left(t-\frac{2\pi}{\Omega N_d}\right)+s_0\left(t-\frac{2\pi*2}{\Omega N_d}\right)+\cdots+s_0\left(t-\frac{2\pi*(N_d-1)}{\Omega N_d}\right),$$

where N_d is the number of teeth and Ω is the speed of rotation as usual.

This equation can be rewritten in a more compact form,

$$s(t)=s_0(t)*\sum_{i=0}^{N_d-1}\delta\left(t-\frac{2\pi i}{\Omega N_d}\right),$$

where the asterisk represents a convolution product.

Performing a Fourier transform, one obtains,

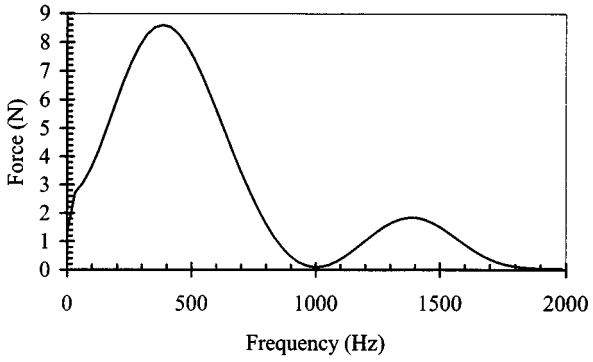

FIG. 10. Transversal input force spectrum of a saw tooth.

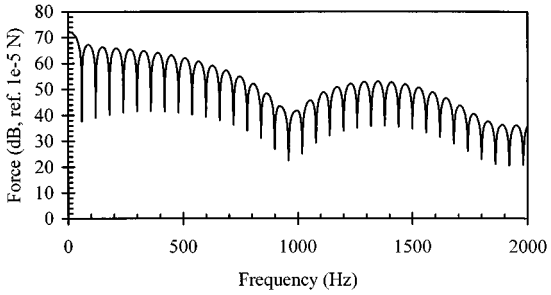

FIG. 11. Estimation of the input force spectrum of a circular saw.

$$s(\omega)=s_0(\omega)\sum_{i=0}^{N_d-1} e^{-j(2\pi i/\Omega N_d)\omega}. \tag{13}$$

This last equation is the equation used as the input force of the circular saw. Figure 11 presents this force over the frequency range 0–2000 Hz.

B. Vibroacoustic analysis of a circular saw

The next two figures (Figs. 12 and 13) present the response of an annular plate (the same as the forced vibration and acoustic radiation sections) subjected to the input force of Fig. 11. Each figure has two curves: one for a rotating plate and one for a nonrotating plate. It must be noted that it is a theoretical case: The force of Fig. 11 cannot exist if the circular saw is not rotating. Still, this force can be theoretically injected into the model of a nonrotating and a rotating plate. Hence the effect of rotation can be evaluated.

Figure 12 presents the mean-square velocity of the plate while Fig. 13 presents the sound power. The two main influences on the response of the plate are visible in those figures: the excitation and the modal responses. Indeed, the pattern of the input force (Fig. 11) is clearly apparent in Figs. 12 and 13. The main difference is the peaks that Figs. 12 and 13 have. Those peaks are due to the modal response of the plate: each peak is a mode. Although the number of modes and their natural frequency are quite different for the nonrotating and the rotating plate, the global response does not change very much. That confirms what we expected from the analysis of the annular plate with a constant force over frequency.

Over the frequency range shown, the amplitude of vibration and sound radiation is governed by the first modes, meaning modes (0,0), (0,1), and (0,2). Therefore to reduce the vibration and acoustic output of the circular saw, work must be done on those modes first, whether or not rotation is considered. In that sense, rotation is negligible.

This result is in contradiction with Beslin and Nicolas' (1996) conclusions that modes $(1,x)$ and $(2,x)$ should radiate more than mode $(0,x)$, especially for a low number of nodal diameters. As stated in the Introduction, Beslin and Nicolas' (1996) conclusions were reached by considering the same amplitude for each mode. This is certainly not the case here (see Fig. 12 for mean-square velocity). Therefore Beslin and Nicolas' (1996) conclusions do not apply in this case.

In summary, the effect of rotation on a circular saw is negligible, in terms of vibration and acoustic radiation. This is due to the fact that the excitation of a circular saw is a wideband excitation, thus every mode is excited to a certain degree. The fact that rotation shifts and increases that number of modes does not have an important effect on the global response since it is already very rich. In passing, one must note that rotation is important from the instability viewpoint. Indeed, at certain speeds the plate becomes unstable. Those

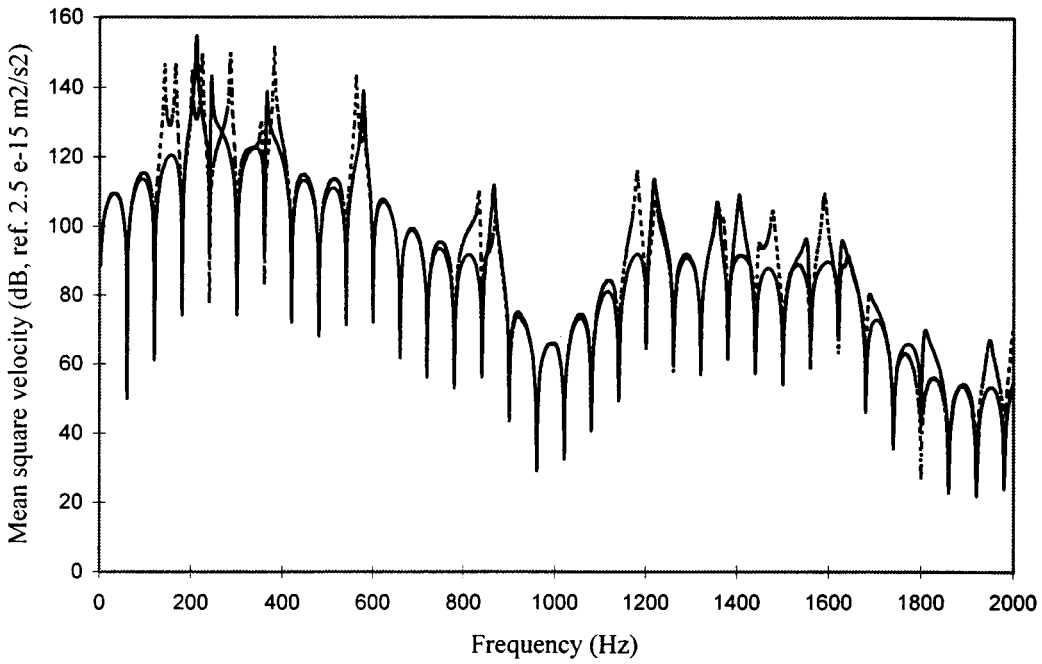

FIG. 12. Mean-square velocity of a circular saw [$a=173$ mm, $b=63.5$ mm, $h=3.048$ mm, $\rho=7800$ kg/m^3, $E=215$ GPa, $\nu=0.32$]. ———: stationary plate, ----------: rotating plate.

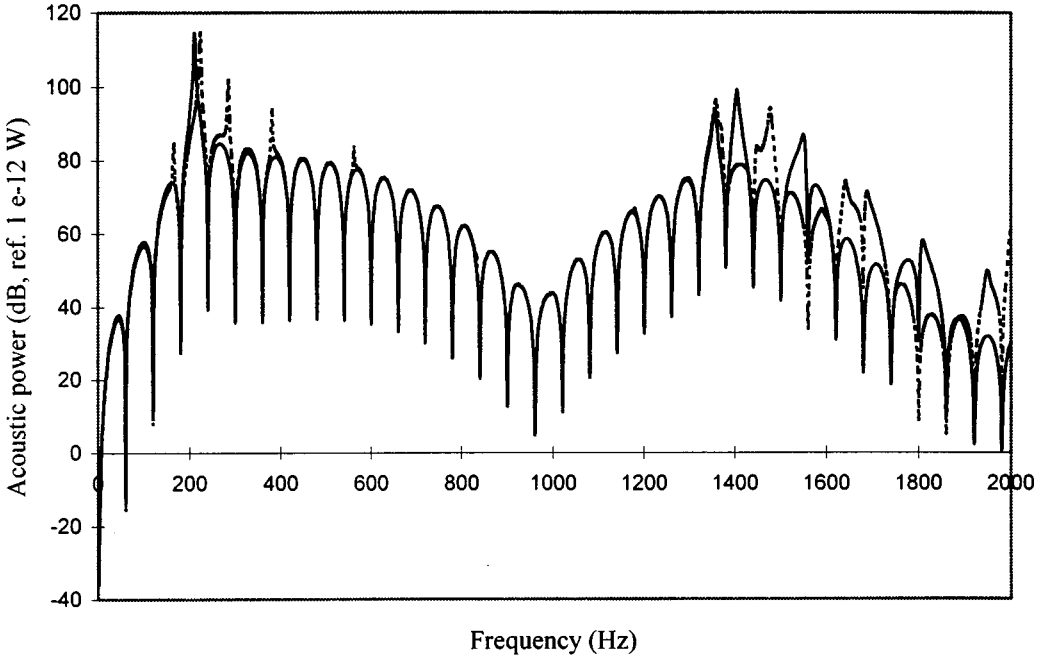

FIG. 13. Acoustic power of an annular plate subjected to a circular saw's input force [$a=173$ mm, $b=63.5$ mm, $h=3.048$ mm, $\rho=7800$ kg/m^3, $E=215$ GPa, $\upsilon=0.32$]. ———: Stationary plate, ----------: Rotating plate.

speeds are called critical speeds of rotation (Mote and Szymani, 1978).

V. CONCLUSION

The effect of rotation on the forced response and acoustic output of an unbaffled disk excited by a fixed harmonic force has been investigated. The generalized equation of motion expressed in a rotating plate obtained by Côté (1994) has been transformed in the space-fixed frame of reference where they have been solved for the transverse displacements. The related pressure on the surface of the plate has been obtained by a boundary element method.

The effect of rotation on the forced response, which is to double the number of natural frequencies, has been discussed. For a narrow-band excitation, this might have a very important effect since the probability of hitting a natural frequency has doubled. But, for a wide spectral excitation, the total mean-square velocity has not been found to change significantly between disks that rotate and those that do not rotate.

The acoustical response of the plate was first investigated for a nonrotating plate. It has been found that a mode with one (or more) nodal diameters radiates less than a mode with no nodal diameter. The rotation changes that. Indeed, for the cases studied more modes were found to radiate. The new radiating modes where the ones with an increased natural frequency. Finally, from a practical viewpoint, rotation has a similar effect on the acoustic response and the forced response. That is, a narrow-band excitation might give very different results with or without the rotation while for a wide spectral excitation there is no significant change. This has been confirmed with a practical case: the circular saw.

APPENDIX: CONVERSION OF REFERENCE SYSTEM

The objective is to obtain a relation between the vector of symmetric and antisymmetric waves expressed in the rotating frame of reference and the vector of symmetric and antisymmetric waves expressed in the nonrotating frame of reference. Starting with Eq. (1) which has been reproduced here,

$$w(r,\theta,t)=\sum_{p,n} r^p(r-\xi)^2[C^s_{pn}\cos(n\theta) + C^a_{pn}\sin(n\theta)]e^{jwt}, \tag{A1}$$

one uses the relation between a rotating and a nonrotating frame,

$$r\Rightarrow r, \quad \theta\Rightarrow\theta+\Omega t, \tag{A2}$$

to obtain

$$w(r,\theta,t)=\sum_{p,n} r^p(r-\xi)^2[C^s_{pn}\cos(n\theta+n\Omega t) + C^a_{pn}\sin(n\theta+n\Omega t)]e^{jwt}. \tag{A3}$$

With the development of the trigonometric functions

$$w(r,\theta,t)=\sum_{p,n} r^p(r-\xi)^2[\cos(n\theta)(C^s_{pn}\cos(n\Omega t) + C^a_{pn}\sin(n\Omega t))+\sin(n\theta)(-C^s_{pn}\sin(n\Omega t) + C^a_{pn}\cos(n\Omega t))]e^{jwt}. \tag{A4}$$

This equation expressed this way,

$$w(r,\theta,t)=\sum_{p,n} r^p(r-\xi)^2[\overline{C}^s_{pn}\cos(n\theta) + \overline{C}^a_{pn}\sin(n\theta)e^{jwt} \tag{A5}$$

where

$$\begin{Bmatrix}\overline{C}^s_{pn}\\ \overline{C}^a_{pn}\end{Bmatrix}=\begin{bmatrix}\cos(n\Omega t) & \sin(n\Omega t)\\ -\sin(n\Omega t) & \cos(n\Omega t)\end{bmatrix}\begin{Bmatrix}C^s_{pn}\\ C^a_{pn}\end{Bmatrix} \tag{A6}$$

relates the amplitude of the assumed modes from the rotating frame to the nonrotating frame of reference, which is exactly the inverse of what Eq. (3) presents.

[1]To alleviate the presentation only the transverse displacement has been shown, but rotations and in-plane displacements have also been discretized in the model.

[2]Damping has been included in the model by the use of a complex Young's modulus: $E=E(1+\eta)$.

Beslin, O. B., and Nicolas, J. R. (**1996**). ''Modal radiation from an unbaffled rotating disk,'' J. Acoust. Soc. Am. **100**, 3192–3202.

Côté, A. F. (**1994**). ''Réponse Vibratoire et Acoustique d'un Disque Annulaire Non-Baffle en Rotation,'' Master's Thesis, Sherbrooke University, Sherbrooke, Québec, Canada.

Côté, A. F., Atalla, N., and Nicolas, J. (**1997**). ''Effects of shear deformation and rotary inertia on the free vibration of a rotating annular plate,'' J. Vib. Acoust. **119**, 641–643.

Couture, D., and Champoux, Y. (**1994**). ''Quadratic surface velocity measurement of a light structure using accurate modal analysis data'' *Proceedings of the 12th International Modal Analysis Conference*, Honolulu, Hawaii (Union College, Schenectady, NY), Vol. 2, pp. 1048–1053.

Hamdi, M. A. (**1981**). ''Une formulation variationelle par équations intégrales pour la résolution de l'équation de Helmoltz avec des conditions aux limites mixtes,'' C. R. Acad. Sci. Paris, Ser. II **292**, 17–20.

Honda, Y., Matsuhisa, H., and Sato, S. (**1985**). ''Modal response of a disk to a moving concentrated harmonic force,'' J. Sound Vib. **102**(4), 457–472.

Junger, M. C., and Feit, D. (**1993**). *Sound, Structures, and Their Interaction* (Acoustical Society of America, Woodbury, NY, 1993).

Krishnappa, G., and McDougall, J. M. (**1989**). ''Sound intensity distribution and energy flow in the nearfield of a clamped circular plate,'' J. Vib., Acoust., Stress Reliability Des. **111**, 465–471.

Lee, M., and Singh, R. (**1992**). ''Sound radiation characteristics of a computer disk,'' Inter-noise, 601–606.

Lee, M., and Singh, R. (**1994**). ''Analytical formulations for annular disk sound radiation using structural modes,'' J. Acoust. Soc. Am. **95**, 3311–3323.

Mote, Jr., C. D., and Szymani, R. (**1978**). ''Circular saw vibration research,'' Shock Vib. Digest **10**, 15–30.

Pierce, A. D. (**1991**). *Acoustics: An Introduction to its Physical Principles and Applications* (Acoustical Society of America, Woodbury, NY).

Sinha, S. K. (**1987**). ''Determination of natural frequencies of a thick spinning annular disk using a numerical Rayleigh–Ritz's trial functions,'' J. Acoust. Soc. Am. **81**, 357–369.

Tobias, S. A., and Arnold, R. N. (**1957**). ''The Influence of dynamical imperfection on the vibration of rotating disks,'' *The Institution of Mechanical Engineers—Proceedings*, Vol. 171, pp. 669–690.

Weisensel, G. N. (**1989**). ''Natural frequency information for circular and annular plates,'' J. Sound Vib. **133**, 129–134.

Williams, E. G. (**1983**). ''Numerical evaluation of the radiation from unbaffled, finte plates using the FFT,'' J. Acoust. Soc. Am. **74**, 343–347.

Wojtowicki, J. L. (**1993**). ''Forces dynamiques entrant dans le procédé de coupe par les scies ciruclaires,'' GAUS, Université de Sherbrooke.

Active control of sound radiation from a plate using a polyvinylidene fluoride volume displacement sensor

F. Charette[a] and A. Berry
G.A.U.S., Mechanical Engineering Department, Université de Sherbrooke, Sherbrooke, Québec J1K 2R1, Canada

C. Guigou
V.A.L., Mechanical Engineering Department, Virginia Polytechnic Institute and State University, Blacksburg, Virginia 24061-0238

(Received 18 April 1997; accepted for publication 19 November 1997)

This paper presents a new volume displacement sensor (made of shaped strips of PVDF film) and the experimental implementation of this sensor in an active control system. A design strategy for a PVDF sensor detecting the volume displacement induced by a vibrating 2D structure is presented. It is based on the modal representation of the plate response. It actually consists in designing a PVDF sensor, composed of several shaped PVDF strips bonded to the surface of the structure, in such a way that the output signal of the sensor is directly proportional to the volume displacement. The design methodology is based on the experimental measurements of the plate mode shapes (eigenfunctions) and is valid for any type of boundary conditions. The experimental implementation of such a volumetric sensor in an active control system is then presented. The experimental results obtained validates this new type of volume displacement sensor. © *1998 Acoustical Society of America.* [S0001-4966(98)00703-6]

PACS numbers: 43.40.Vn, 43.38.Fx [PJR]

INTRODUCTION

The two main strategies for actively controlling sound fields are active noise control (ANC) and active structural acoustic control (ASAC), first proposed by Fuller.[1,2] The ANC approach is based on controlling the acoustic field by using loudspeakers as acoustic secondary sources, while the ASAC approach directly modifies the response of the radiating structure by applying structural inputs as secondary sources, i.e., modal restructuring.[2] In general, the ASAC approach has been proved to require a smaller number of secondary sources for a global control of the acoustic field. Recently, piezoceramic actuators embedded in or bonded to the structure have been successfully used as structural secondary sources for ASAC applications.[3,4] These integrated-distributed actuators overcome many of the disadvantages of shakers.

In ASAC, the other component of prime importance is the error sensor, which defines the type of information to be minimized by the controller. Polyvinylidene fluoride (PVDF) materials have been suggested as error sensors in the active control of structural vibration,[5,6] and more recently in the active control of sound radiation.[7–10] In the latter case, the type of information measured on the structure by such sensors has to be carefully defined so that the minimization of this information effectively leads to a global attenuation of the sound field. In this instance, PVDF materials provide distributed sensors for which spatial filtering techniques can be applied by tailoring the sensor shape, in order to select, for example, the most efficient radiating modes in the structural response.

Since active control is most efficient at low frequencies, the development of appropriate sensors to be used in ASAC should be based on the low-frequency mechanisms of the sound radiation from vibrating structures. For planar radiators, it is well known that the sound radiation is directly related to the velocity distribution over the surface of that structure, for frequencies lower than the critical frequency. It was shown[11,12] that velocity distributions corresponding to certain modes, i.e., odd–odd or symmetric modes for simply supported and clamped boundary conditions, are the most efficient radiators. Therefore, the sensor to be designed should be able to mainly detect these well-radiating velocity distributions. A strategy originally investigated by Fuller *et al.*[13] is to detect only the supersonic (radiating) components of the structural wave number spectrum. Another approach is based on the ''radiation modes'' concept; it was shown[14,15] that the sound power can be written in terms of radiation modes, which correspond to the eigenvectors of the radiation impedance operator of the structure and radiate sound independently. Recently, Snyder *et al.*[10] have implemented the active control of sound radiation from a simply supported panel using PVDF film shaped in order to observe the radiation modes of the panel. The first and most radiating of these radiation modes was found to be the piston-type mode. Such a mode actually represents the monopole behavior of the structure and can be detected by measuring the net volume displacement over the surface of the structure. Based on this assumption, Rex and Elliott[16] developed a ''quadratically weighted strain integrating sensor,'' i.e., a quadratically

[a]F. Charette is currently working at the Vibration and Acoustics Laboratories (VAL) of Virginia Polytechnic Institute & State University.

weighted sensor measuring the volume velocity of the structure. This sensor can be implemented in practice in the form of a piezoelectric cable or an optical fiber bonded on or embedded in the structure. Using the same approach, Johnson and Elliott[17] showed that the volume velocity of a two-dimensional structure can be measured by quadratically weighting the sensitivity or the thickness of an extended PVDF sensor covering the whole surface of the structure. This solution being unrealistic in practice, it was approximated by shaping the sensor into quadratic or rectangular strips.[18] They successfully implemented active control of volume displacement using such sensor on a plate and observed significant reductions in the sound radiations. However, the disadvantage of their sensor design is that it has to cover the whole plate surface, which may not be available in many applications. Recently, Guigou *et al.*[8] have successfully implemented active control of volume displacement in the case of flexural beams, by using a single shaped PVDF strip, and they observed significant attenuation of the radiated sound field. The shape of the PVDF strip was based on the mode shapes (eigenfunctions) of the beam. This last work provides the basis of the present investigation.

The objective of this paper is to extend the concepts of the abovementioned paper in the case of 2D structures. The implementation of an extended, shaped PVDF sensor as a volume displacement sensor is discussed in the case of a rectangular panel with arbitrary boundary conditions; the sensor shape is shown to be independent of the frequency and type of excitation. Moreover, the strategy of minimizing the volume velocity keeps the control architecture very simple (single input control system). Experimental results of the volume displacement sensor and its use in an active control system are presented and discussed.

I. VOLUME DISPLACEMENT PVDF SENSOR

A. Description of the system considered

The mechanical system studied in this paper consists of a rectangular clamped plate on which two piezoelectric actuators are bonded; see Fig. 1. A piezoelectric actuator is composed of two identical colocated piezoceramic patches on each side of the plate. The piezoceramic patches are assumed to be perfectly bonded to the plate surface. A symmetric actuation (pure flexion) is induced in the plate when the two piezoceramic patches are driven 180° out of phase.[2] Here, one of the piezoelectric actuators is used to induce the unwanted vibration (i.e., primary actuator) while the second actuator is the control (i.e., secondary) actuator. The plate dimensions and material properties are described in Table I. The piezoceramic actuators characteristics and locations are given in Table II.

TABLE I. Properties of the clamped plate.

L_x^{pl}	50.0 cm
L_y^{pl}	39.8 cm
L_z^{pl}	3.15 mm
Young's modulus (E)	6.5×10^{10} Pa
Density (ρ)	2800 kg/m^3

The total transverse displacement of the plate under the action of the primary and secondary actuators can be written as a linear combination of modes,

$$w(x,y)=\sum_{i=1}^{I}\hat{W}_i\Psi_i(x,y), \tag{1}$$

where $\hat{W}_i$ is the modal amplitude and $\Psi_i(x,y)$ is the ith eigenfunction. The modal sum in Eq. (1) is truncated to ''I'' modes.

B. Experimentally determined eigenfunctions

The design of the volume displacement sensor starts with the determination of the plate eigenfunctions. In this work, these eigenfunctions are determined experimentally, even though theoretical approximations are available in the case of clamped plate. The experimental determination of the eigenfunctions can lead to a better representation of a particular ''real'' (i.e., experimental) plate displacement, since it takes into account the imperfections in the boundary conditions, plate material, external loading, etc. Furthermore, using experimentally measured eigenfunctions would be natural for more complex plates for which no theoretical approximations are easily available.

The plate was excited between 100 and 500 Hz, using the primary PZT actuator, in order to obtain its modal characteristics. A Bruel & Kjaer analyser was used to measure the transfer function between the velocity signal from a laser vibrometer [at a total of 144 (12×12) regularly spaced measurement points] and the excitation signal. The modal analysis STAR SYSTEMS V5.0 package was then used to process the data. This software uses a frequency domain curve-fitting analysis to determine the modal characteristics. The experimental mode shapes $\Psi_i(x,y)$ are then represented as a combination of polynomial trial functions,

$$\Psi_i(x,y)=\sum_{p=0}^{P-1}\sum_{q=0}^{Q-1}A_{i,pq}\left(\frac{x}{L_x^{pl}}\right)^p\left(\frac{y}{L_y^{pl}}\right)^q. \tag{2}$$

Such trial functions are very general and may be used for plates with arbitrary boundary conditions. In order to determine the unknown coefficients $A_{i,pq}$ of a mode shape, the following system of equations has to be solved for each mode ''i,''

$$[\varphi_{mnpq}]\{A_{i,pq}\}=\{w_{i,mn}\}. \tag{3}$$

The vector $\{w_{i,mn}\}$ contains the ith modal displacement of the mnth measurement point as provided by the STAR SYSTEMS package. The vector $\{w_{i,mn}\}$ thus contains 144 elements. The coefficients of the matrix $[\varphi_{mnpq}]$ are given by

$$\varphi_{mnpq}=\left(\frac{x_m}{L_x^{pl}}\right)^p\left(\frac{y_n}{L_y^{pl}}\right)^q, \tag{4}$$

where x_m and y_n are the positions of the mnth measurement point.

Reasonably small values of P and Q in Eq. (2) are sufficient to reconstruct the first few modes of the plate. Consequently, the values of P and Q are usually smaller than the

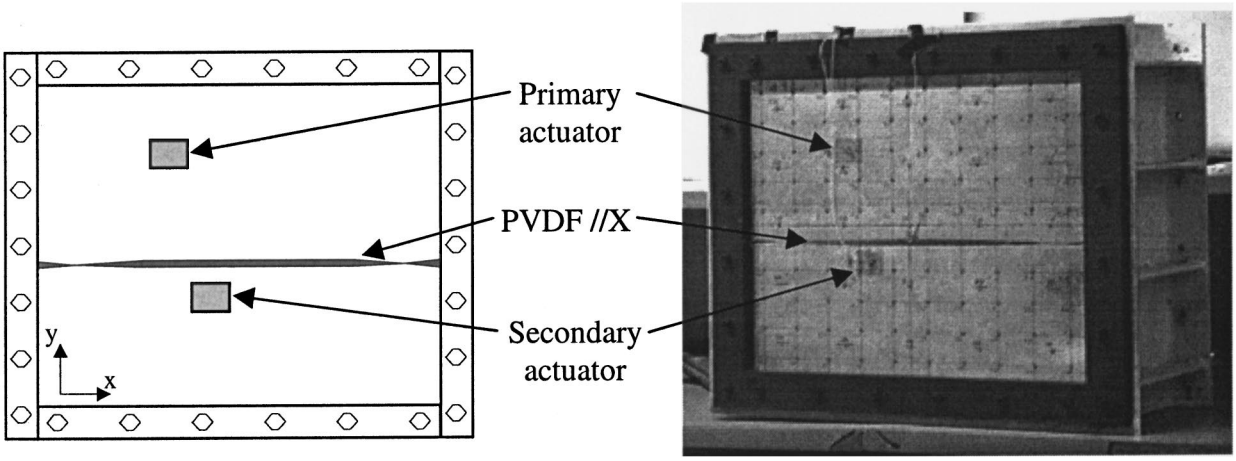

(a) Front of the plate

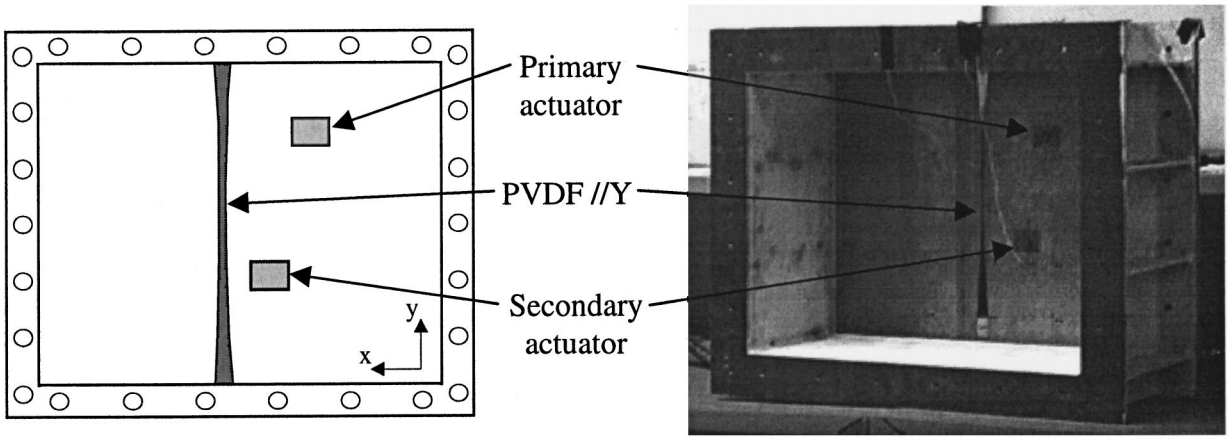

(b) Back of the plate

FIG. 1. Clamped plate studied.

number of measurement points in each direction of the plate and the linear system represented by Eq. (3) is overdetermined. Therefore, a least mean square technique is used and the following system has to be solved,

$$[\varphi_{mnpq}]^T[\varphi_{mnpq}]\{A_{i,pq}\}=[\varphi_{mnpq}]^T\{w_{i,mn}\}. \tag{5}$$

The superscript T indicates the transpose operator. A criterion must be used to evaluate the accuracy of the polynomial approximation obtained. The criterion suggested by Gerald and Wheatley[19] is to increase the degree of the approximation polynomials until a statistically significant decrease in the variance of the approximation error is obtained. The variance of the error is defined as

$$\chi_i^2=\frac{\Sigma_{m=1}^{M}\Sigma_{n=1}^{N}(\Psi_i(x_m,y_n)-w_{i,mn})^2}{M\cdot N-P\cdot Q-1}, \tag{6}$$

where ''M'' and ''N'' are the total number of measuring points in the x and y directions, respectively. Thus the orders ''P'' and ''Q'' of the approximation polynomials are selected independently for each mode ''i'' using Eq. (6) as criterion.

C. Structural volume displacement of a plate

In the present work, the cost function considered for the active control system is the structural volume displacement

TABLE II. Ceramic piezo-characteristics.

	Primary	Secondary
L_x^{pz}	3.81 cm	3.81 cm
L_y^{pz}	3.18 cm	3.18 cm
L_z^{pz}	0.19 mm	0.19 mm
Pos. of the center along the x axis	16.0 cm	19.0 cm
Pos. of the center along the y axis	30.0 cm	15.0 cm
Young's modulus (E_{11})	6.3×10^{10} Pa	6.3×10^{10} Pa
Density (ρ)	7750 kg/m^3	7750 kg/m^3

of the plate. The structural volume displacement is defined as the integral of the transverse displacement over the surface of the plate,

$$D=\int_0^{L_y^{pl}}\int_0^{L_x^{pl}} w(x,y)dx\ dy. \tag{7}$$

Introducing Eqs. (1) and (2) into Eq. (7) and performing the double integration yields the volume displacement of the plate, which can be written in matrix form as

$$D=L_x^{pl}L_y^{pl}\langle\hat{W}_i\rangle[A_{i,pq}]\{D_{pq}\}. \tag{8}$$

The dimensions of the matrix $[A_{i,pq}]$ are ''I'' rows by ''$P\times Q$'' columns. Each row of the matrix $[A_{i,pq}]$ contains the coefficients of a given eigenfunctions $\Psi_i(x,y)$ over the polynomial trial functions. The line vector $\langle\hat{W}_i\rangle$ contains the modal amplitudes. The components of the column vector $\{D_{pq}\}$ are simply given by $1/[(p+1)(q+1)]$.

The volume velocity of the plate is simply Eq. (8) multiplied by $j\omega$ as harmonic excitation is assumed. Thus for pure tone excitation, it is equivalent to minimize the volume velocity or the net volume displacement. The strategy of using the volume displacement as a cost function for an active control system have been shown previously[8,15,18] to be very efficient to reduce sound radiation in the low-frequency range (i.e., $k_0L\ll1$, k_0 is the wave number in air, and L is the characteristic dimension of the structure).

D. Design of a volume displacement sensor using shaped PVDF film

The charge response of an arbitrarily shaped strip of PVDF sensor applied to a two-dimensional structure has been derived by Lee *et al.*[5] It was shown that the charge response of the sensor is a function of the integral of the strain over the surface of application and is expressed as

$$q=-\frac{L_z^{pl}+L_z^s}{2}\int_0^{L_y^{pl}}\int_0^{L_x^{pl}}\left[e_{31}\frac{\partial^2w(x,y)}{\partial x^2}+e_{32}\frac{\partial^2w(x,y)}{\partial y^2}+2e_{36}\frac{\partial^2w(x,y)}{\partial x\partial y}\right]\cdot F(x,y)\cdot dx\ dy, \tag{9}$$

where L_z^{pl} and L_z^s are, respectively, the plate thickness and PVDF sensor thickness. The e_{ij} are the PVDF sensor stress/charge coefficients. It is assumed that no skew angle is associated with the polarization of the PVDF film used in this study, $e_{36}=0$. The function $F(x,y)$ represents the variation of the film sensitivity with the position on the surface of application. In practice, this variation of sensitivity is more easily achieved by shaping the PVDF film as described in the following.

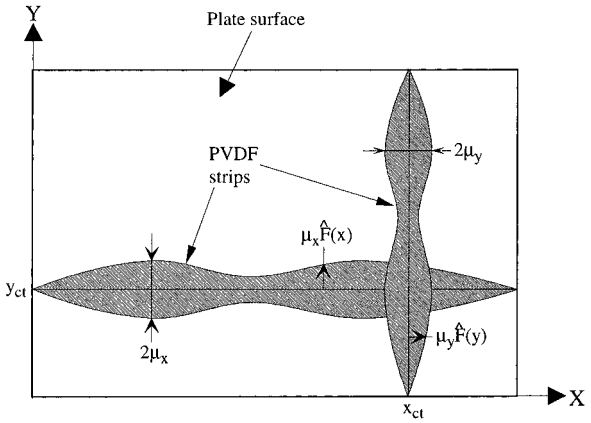

FIG. 2. Top view of the finite plate with a typical shaped PVDF strips configuration.

First, consider a single PVDF strip parallel to the x direction of the plate, whose center line is located at $y=y_{ct}$, as shown in Fig. 2. The maximum width of the strip is noted $2\mu_x$, and the width at the position x is $2\mu_x\hat{F}(x)$, where $\hat{F}(x)$ is a function varying between -1 and $+1$. Negative values of $\hat{F}(x)$ correspond to an inversion of the PVDF film polarity. It is assumed that the strip axis coincides with the direction of maximum stress/charge coefficient e_{31}. It is desired to find the output response of this strip when the function $\hat{F}(x)$ is given by

$$\hat{F}(x)=\sum_{r=0}^{R-1}\hat{\alpha}_r\left(\frac{x}{L_x^{pl}}\right)^r. \tag{10}$$

In this case, the charge response of the PVDF strip can be written as

$$q_x=-\frac{L_z^{pl}+L_z^s}{2}\int_0^{L_x^{pl}}\int_{y_{ct}-\mu_x\hat{F}(x)}^{y_{ct}+\mu_x\hat{F}(x)}\left[e_{31}\frac{\partial^2w(x,y)}{\partial x^2}+e_{32}\frac{\partial^2w(x,y)}{\partial y^2}\right]dy\,dx. \tag{11}$$

Introducing Eqs. (1) and (2) into Eq. (11) and integrating with respect to the variable y leads to

$$q_x=-\frac{L_z^{pl}+L_z^s}{2}\sum_{i=1}^{l}\hat{W}_i\sum_{p=0}^{P-1}\sum_{q=0}^{Q-1}A_{i,pq}\int_0^{L_x^{pl}}\left\{\frac{e_{31}p(p-1)L_y^{pl}}{(q+1)(L_x^{pl})^2}\times\left(\frac{x}{L_x^{pl}}\right)^{p-2}\cdot\left(\frac{y_{ct}}{L_y^{pl}}\right)^{q+1}\cdot\left[\left(1+\frac{\mu_x\hat{F}(x)}{y_{ct}}\right)^{q+1}-\left(1-\frac{\mu_x\hat{F}(x)}{y_{ct}}\right)^{q+1}\right]+\frac{e_{32}qL_y^{pl}}{(L_y^{pl})^2}\left(\frac{x}{L_x^{pl}}\right)^{p}\cdot\left(\frac{y_{ct}}{L_y^{pl}}\right)^{q-1}\cdot\left[\left(1+\frac{\mu_x\hat{F}(x)}{y_{ct}}\right)^{q-1}-\left(1-\frac{\mu_x\hat{F}(x)}{y_{ct}}\right)^{q-1}\right]\right\}dx. \tag{12}$$

At this point, it is necessary to introduce a simplifying assumption before integrating along the strip axis: If the width μ_x of the strip is small enough such that $|\mu_x \hat{F}(x)/y_{ct}| \ll 1$ then

$$\left(1+\frac{\mu_x \hat{F}(x)}{y_{ct}}\right)^{q+1} \approx 1+\frac{(q+1)\mu_x \hat{F}(x)}{y_{ct}} + \frac{q(q+1)}{2}\left(\frac{\mu_x \hat{F}(x)}{y_{ct}}\right)^2. \tag{13}$$

Similar assumptions are made for

$$\left(1-\frac{\mu_x \hat{F}(x)}{y_{ct}}\right)^{q+1}, \quad \left(1+\frac{\mu_x \hat{F}(x)}{y_{ct}}\right)^{q-1},$$

and

$$\left(1-\frac{\mu_x \hat{F}(x)}{y_{ct}}\right)^{q-1}.$$

Inserting these approximations into Eq. (12) and performing the integration along the x axis, the charge of the PVDF strip parallel to the x axis can be written in matrix form as

$$q_x = -\frac{L_z^{pl}+L_z^s}{2}\langle \hat{W}_i \rangle [A_{i,pq}][T1_{pq,r}]\{\hat{\alpha}_r\}, \tag{14}$$

where $\{\hat{\alpha}_r\}$ is the vector of the shape coefficients of the PVDF strip. The coefficients of the matrix $[T1_{pq,r}]$ are given by

$$T1_{pq,r} = \frac{2\mu_x e_{31} p(p-1)}{L_x^{pl}(p+r-1)}\left(\frac{y_{ct}}{L_y^{pl}}\right)^q + \frac{2\mu_x L_x^{pl} e_{32} q(q-1)}{(L_y^{pl})^2(p+r+1)}\left(\frac{y_{ct}}{L_y^{pl}}\right)^{q-2}. \tag{15}$$

Similarly, for a PVDF strip parallel to the y direction at $x = x_{ct}$, with a maximum width $2\mu_y$ (see Fig. 2) and a shape described by

$$\hat{F}(y) = \sum_{s=0}^{S-1} \hat{\beta}_s \left(\frac{y}{L_y^{pl}}\right)^s, \tag{16}$$

the charge response is given by

$$q_y = -\frac{L_z^{pl}+L_z^s}{2}\sum_{i=1}^{l}\hat{W}_i \sum_{p=0}^{P-1}\sum_{q=0}^{Q-1} A_{i,pq}\int_0^{L_y^{pl}} \left\{ \frac{e_{31} q(q-1) L_x^{pl}}{(p+1)(L_y^{pl})^2} \times \left(\frac{y}{L_y^{pl}}\right)^{q-2} \cdot \left(\frac{x_{ct}}{L_x^{pl}}\right)^{p+1} \cdot \left[\left(1+\frac{\mu_y \hat{F}(y)}{x_{ct}}\right)^{p+1} - \left(1-\frac{\mu_y \hat{F}(y)}{x_{ct}}\right)^{p+1} \right] + \frac{e_{32} p}{L_x^{pl}} \left(\frac{y}{L_y^{pl}}\right)^q \cdot \left(\frac{x_{ct}}{L_x^{pl}}\right)^{p-1} \cdot \left[\left(1+\frac{\mu_y \hat{F}(y)}{x_{ct}}\right)^{p-1} - \left(1-\frac{\mu_y \hat{F}(y)}{x_{ct}}\right)^{p-1} \right] \right\} dy. \tag{17}$$

Using approximations similar to Eq. (13) for the terms $(1+[\mu_y \hat{F}(y)/x_{ct}])^{p+1}$, etc., and performing the integration along the y axis, the charge of the PVDF strip parallel to the y axis can be written in matrix form as

$$q_y = -\frac{L_z^{pl}+L_z^s}{2}\langle \hat{W}_i \rangle [A_{i,pq}][T2_{pq,s}]\{\hat{\beta}_s\}, \tag{18}$$

where

$$T2_{pq,s} = \frac{2\mu_y e_{31} q(q-1)}{L_y^{pl}(q+s-1)}\left(\frac{x_{ct}}{L_x^{pl}}\right)^p + \frac{2\mu_y L_y^{pl} e_{32} p(p-1)}{(L_x^{pl})^2(q+s+1)}\left(\frac{x_{ct}}{L_x^{pl}}\right)^{p-2}. \tag{19}$$

The total output charge $q = q_x + q_y$ written in matrix form is

$$q = -\frac{L_z^{pl}+L_z^s}{2}\langle \hat{W}_i \rangle \{[A_{i,pq}][T1_{pq,r}]\{\hat{\alpha}_r\} + [A_{i,pq}][T2_{pq,s}]\{\hat{\beta}_s\}\}. \tag{20}$$

It is required that the sum of the output charges be proportional to the net volume displacement of the plate. In this case, the sensor formed by the 2 PVDF strips is a volume displacement sensor. This requirement allows the unknown coefficients $\hat{\alpha}_r$ and $\hat{\beta}_s$ of the strip shapes to be determined. Equating Eqs. (8) and (20) row by row implies that the modal volume displacements of the plate are equal to the modal charge response of the sensor, which ensures that the sensor is independent of the frequency; this yields

$$-\frac{L_z^{pl}+L_z^s}{2}\{[A_{i,pq}][T1_{pq,r}]\{\hat{\alpha}_r\} + [A_{i,pq}][T2_{pq,s}]\{\hat{\beta}_s\}\} = L_x^{pl} L_y^{pl} [A_{i,pq}]\{D_{pq}\}. \tag{21}$$

Equation (21) forms a system of I linear equations to be solved for the $R+S$ unknown coefficients $\hat{\alpha}_r$ and $\hat{\beta}_s$. A unique solution is obtained if $R+S=I$, I being the total number of modes considered in the plate response. So, this uniqueness condition relates the total number of modes to the order of the polynomials used to shape the strips of PVDF. Note that high order polynomials yield complicated shapes of PVDF strips (with possibly many zeros, thus many polarity changes) implying difficulties in experimental implementation. Therefore, when the number of modes I considered is large, it is worthwhile to consider more than one strip in the x and/or y directions. Adding strips on the plate allows the order of the shape polynomials to be kept small for each strip. Equation (21) can easily be extended to consider more than one strip in the x or y direction. It is also interesting to note that since matrix $[A_{i,pq}]$ is rectangular, it cannot be easily dropped from Eq. (21). Furthermore, the goal is to obtain a linear equation for each mode considered in the frequency range of interest [eliminating matrix $[A_{i,pq}]$ would remove the modal representation in Eq. (21)].

It is important to note that the volume displacement sensor given by Eq. (21) is independent of the excitation frequency and of the type, magnitude, and location of the excitation. Also, the use of polynomial functions to reconstruct the plate response and to design the sensor shape, makes the methodology valid for arbitrary boundary conditions that do not allow rigid modes. It should be noted that since the PVDF film is a strain sensor, it is not sensitive to rigid (whole body) modes.

TABLE III. PVDF film characteristics.

e_{31}	0.046 N/(V m)
e_{32}	0.006 N/(V m)
L_z^s	0.028 mm
μ_x	1.0 cm
μ_y	1.0 cm
Young's modulus (E_{11})	2.0×10^9 Pa
Density (ρ)	1780 kg/m^3

II. EXPERIMENTAL RESULTS

A. Experimental implementation of the volume displacement sensor

The procedure described in Sec. D of Part I was implemented experimentally on the clamped plate described in Table I. Two piezoceramic actuators (a primary ''disturbance'' actuator and a secondary ''control'' actuator) were bonded to the plate. The characteristics and locations of the piezoceramic actuators are described in Table II. The properties of the PVDF film used in the experiments are listed in Table III.

The shapes of the strips were determined using $I=7$ modes for the plate response and polynomial functions of order $R=4$, $S=3$ for the shape functions of the strips in the x and y directions. Once the positions x_{ct} and y_{ct} of the strips have been chosen, the solution of Eq. (21) yields the coefficients of the two PVDF strip shapes which form the volume displacement sensor. The accuracy of the PVDF volume displacement sensor turns out to be quite sensitive to the positions x_{ct} and y_{ct}. This is partly due to the approximation introduced in Eq. (13) to design the shapes of the PVDF strips. Therefore, after fixing the positions of the PVDF strips and solving Eq. (21) for the shape function [$\hat{F}(x)$ and $\hat{F}(y)$] coefficients, Eqs. (12) and (17) are numerically integrated and their sum is compared to the volume displacement measured directly. If the comparison shows that the two curves corresponds well, then the chosen positions x_{ct} and y_{ct} are valid ones. If not, other positions for x_{ct} and y_{ct} have to be tested.

The velocity at a total of 144 (12×12) regularly spaced points on the plate [i.e., $j\omega w(x_{ix},y_{iy})$ for ix and $iy=1$ to 12] was measured using a laser vibrometer. A Bruel & Kjaer analyzer was used to acquire the transfer functions between the excitation signal (to the PZT actuator) and the laser signal. The measured volume displacement can then be evaluated as

$$D_{\text{measured}}=\frac{L_x^{pl}L_y^{pl}}{144}\sum_{ix=1}^{12}\sum_{iy=1}^{12}w(x_{ix},y_{iy}), \tag{22}$$

which is a discrete version of Eq. (7). Figure 3 presents the results for $x_{ct}=0.259$ m and $y_{ct}=0.176$ cm. Figure 3(a) and (b) shows the shapes of the PVDF strips in the x and y direction, respectively. Figure 3(c) presents the comparison of the measured volume displacement (with a laser vibrometer) and the numerically calculated charge response [Eqs. (12) and (17)] of the PVDF sensor when the excitation is induced by the primary actuator. Note, there is no ordinate scale in Fig. 3(b) because the two curves were superposed to facilitate comparison (i.e., the charge response of the PVDF does not have the same unit/scale as the volume displacement response). Figure 3(c) shows an excellent agreement between the numerically calculated signal and the measured volume displacement, which confirms that the chosen positions x_{ct} and y_{ct} are valid. Note that the shapes of the strips [Fig. 3(a), (b)] are almost symmetric. This is intuitively understandable since the experimental mode shapes of the plate to be observed by the PVDF strips are also symmetric (monopole modes).

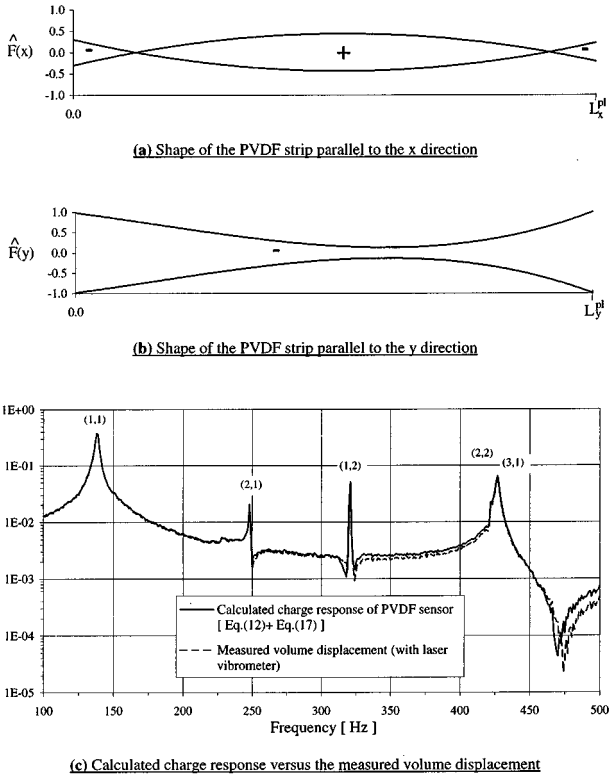

(a) Shape of the PVDF strip parallel to the x direction

(b) Shape of the PVDF strip parallel to the y direction

(c) Calculated charge response versus the measured volume displacement

FIG. 3. Results obtained for the positions $x_{ct}=0.259$ and $y_{ct}=0.176$ m.

The sensor strips shown in Fig. 3(a) and (b) were implemented experimentally and taped to the clamped plate. The total electrical signal from the PVDF sensor (the added signal of the two PVDF strips) was first passed through a preamplifier (with high input impedance and variable gain) and then measured with a Bruel & Kjaer analyzer. Figure 4 and

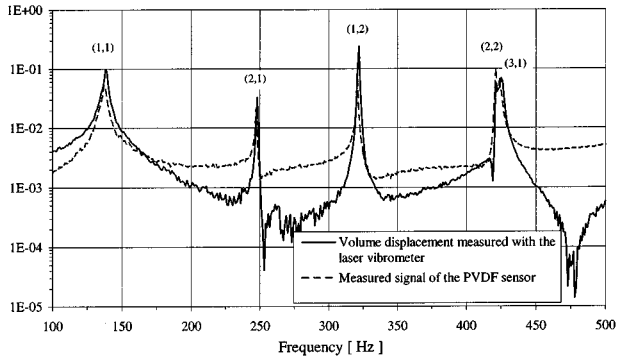

FIG. 4. Performance of sensor when the primary actuator induces the vibrations.

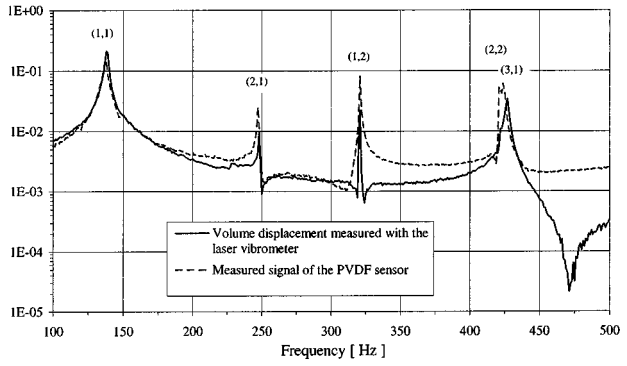

FIG. 5. Performance of sensor when the secondary actuator induces the vibrations.

Fig. 5 present the PVDF sensor signal compared to the direct measurement of the volume displacement when the vibration of the plate is induced by the primary PZT actuator and the secondary PZT actuator respectively. Note that the signal from the PVDF sensor was scaled to be equivalent to the measured volume displacement at 170 Hz. It must be recalled that the sensor is designed using the first seven experimental modes of the plates, so that the contribution of higher order modes is not considered in the shape of the sensor. Thus it is expected that the sensor signal deviates from the volume displacement in higher frequencies. Also, the off-resonance differences between the sensor signal and the measured volume displacement are presumably due to the higher order modes contributions in the flexural strain of the plate. PVDF materials measure strain and are thus more sensitive to higher order modes. In effect, this is more apparent in the case of the primary actuator excitation, which is significantly off-center and thus excites more efficiently the higher order modes of the plate. Note that in both cases the response of the (2,1) and (1,2) modes is large, indicating that these modes have a nonzero volume displacement and are thus not perfectly antisymmetric (this is mainly due to the presence of the PZT on the plate and the imperfections in the experimental boundary conditions). The fact that modes (2,1) and (1,2) have a volume displacement, shows that it is worthwhile to base the design of the sensor from experimentally measured mode shapes (i.e., eigenfunctions). It allows to take into account all the experimental imperfections (i.e., boundary conditions, added mass, added stiffness, plate imperfections, etc.) of the actual experimental setup. The sensor is designed from the measured modal characteristics. Therefore, any modifications of the structure mechanical properties (added mass, stiffness, boundary conditions, etc.) after the design stage will affect the response of the sensor.

B. Active control of volume displacement

This section describes the active control experiment using the volume displacement sensor developed previously. The plate was located in a semi-anechoic chamber for the experiments. Sound pressure levels were measured at nine discrete points equally distributed over a 1.2 m radius from the center of the plate in the plane $x = L_x^{pl}/2$. Note, the main purpose of these sound pressure measurements was to get a good indication of the reduction that could be expected in a realistic application. Therefore, no baffle was installed around the plate. Furthermore, in order to have a single sound pressure value to quantify the reduction obtained by the control, an average sound pressure level in the plane $x = L_x^{pl}/2$ is defined as

$$\langle \tilde{p} \rangle = \frac{R^2}{\rho_0 c_0} \int_{-\pi/2}^{\pi/2} |p(R,\theta)|^2 |\sin(\theta)| d\theta, \tag{23}$$

where R is the radius between the center of the plate and the positions of the measurements point, ρ_0 is the density of air, and c_0 is the speed of sound in air. θ is the angle between the line perpendicular to the plate surface and the line that joins the considered point on the radius R to the center of the plate. Since the sound pressure measurements were done at nine angles θ_i, the discrete version of the last equation is

$$\langle \tilde{p} \rangle = \frac{\pi R^2}{9 \rho_0 c_0} \sum_{i=1}^{9} |p(R,\theta_i)|^2 |\sin(\theta_i)|. \tag{24}$$

The displacement of the plate before and after control was measured using a laser vibrometer at 144 regularly spaced points on the plate surface. The primary actuator was used to induce the unwanted vibration while the secondary actuator was used as the control actuator. The voltage applied on these actuators was typically between 80 and 120 V peak to peak. A feedforward filtered X-LMS controller was used. A number of single frequency was tested (i.e., harmonic control was performed here). The control results are presented for three typical frequencies, two on-resonance and one off-resonance frequency. For each of these frequencies, the measured displacement field as well as the sound pressure levels in the plane $x = L_x^{pl}/2$ are displayed before and after control is applied.

Figure 6 presents the results obtained at 125 Hz, corresponding to an off-resonance frequency of the clamped plate (below the first mode). The structural displacement field before control clearly shows that the plate acts like a monopole type radiator with a maximum displacement close to the primary (i.e., disturbance) actuator location. After control, the plate is forced to act as a dipole type radiator by the secondary (i.e., control) actuator. One can note that the vibration level before and after control are globally the same in this case (the absolute maximum displacement value is approximately 0.08 μm before control, 0.06 μm after control). The experimental sound pressure levels in the plane $x = L_x^{pl}/2$ are shown in Fig. 6(b). The reduction of the average sound pressure level is around 16 dB. This reduction can be attributed solely to the fact that the plate deformation is changed from a monopole type radiator to a dipole type radiator (i.e., modal restructuring[2]). The control of the volume displacement has no appreciable effect on the vibration level at this frequency and only the radiation efficiency, which represents the capacity of the plate the generate sound, is decreased.

Figure 7 presents the results obtained at 140 Hz, which corresponds to the resonance frequency of the first mode, i.e., mode (1,1). As seen in Fig. 7(a), the plate displacement before control corresponds to the (1,1) mode shape, with maximum displacement at the center of the plate. This mode

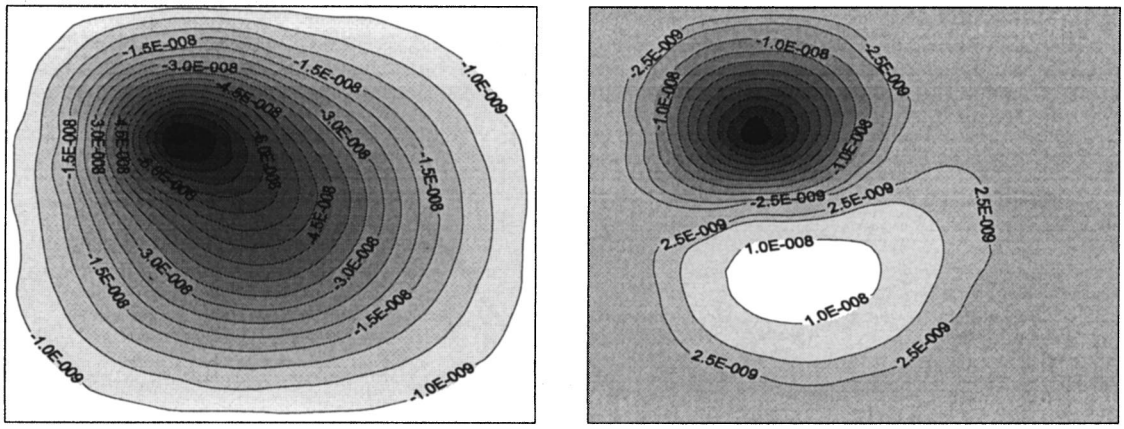

Before control After control

(a) Measured transversal displacements

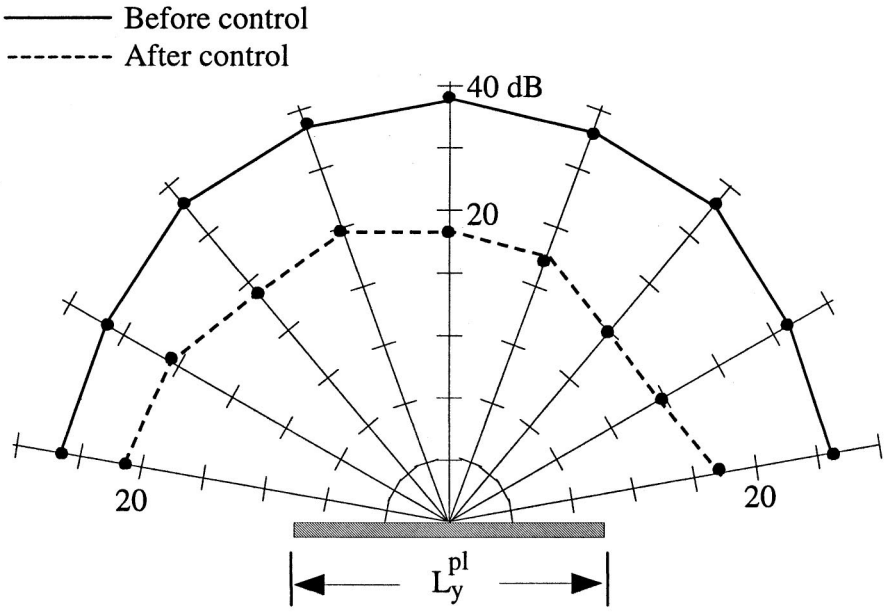

(b) Measured sound pressure levels (plane $x=L_x^{pl}/2$).

FIG. 6. Experimental results at 125 Hz (off-resonance).

is a monopole-type radiator.[2,11] Once again, after control the secondary actuator forces the plate to act as a dipole-type radiator. Note here the vibration levels after control are much lower than before control which indicates that in this case the control combines both vibration restructuring and vibration reduction. Figure 7(b) presents the measured sound pressure levels. The reduction of the average sound pressure level is around 40 dB. The results of the volume displacement control at 140 Hz (Fig. 7) shows that the sound attenuation on resonance of a symmetric mode is associated with a decrease of the radiation efficiency (passage from a monopole type radiator to a dipole-type radiator), combined with a decrease of the vibration amplitudes.

Finally, Fig. 8 presents the results for 320-Hz resonance of mode (1,2). Note that the shape of the displacement after control is globally the same as the one before control. On the other hand, the maximum displacement has been reduced significantly. Therefore, the 14-dB reduction of the average sound pressure level is associated with the reduction of the vibration levels. In this case, the sensor acts as a vibration

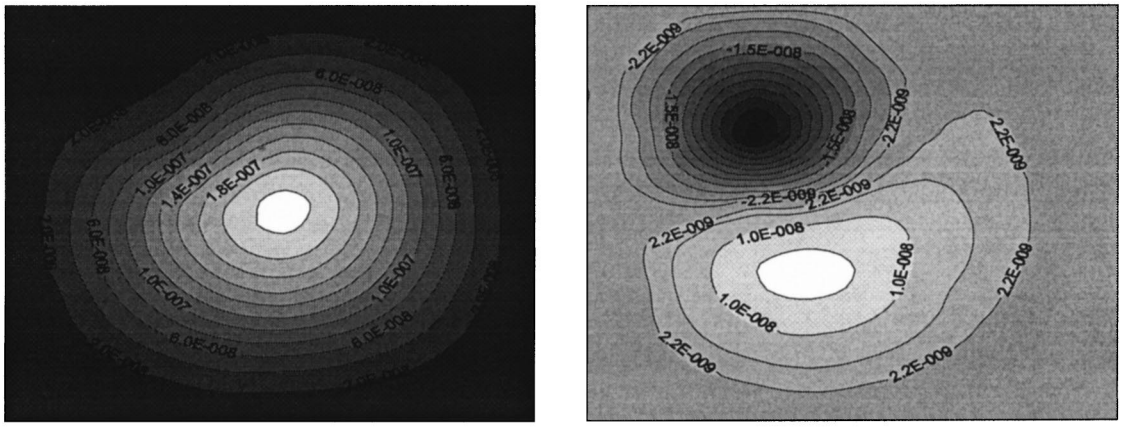

(a) Measured transversal displacements

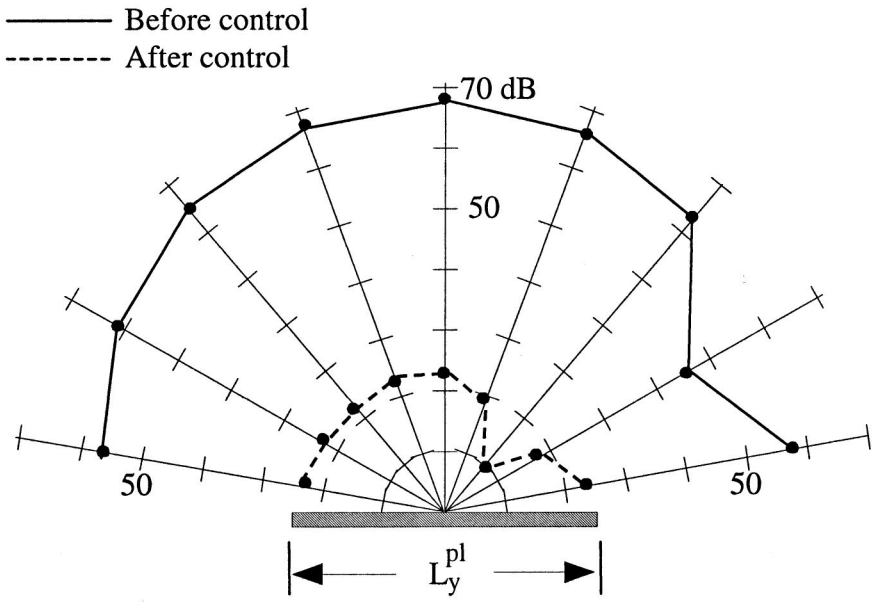

(b) Measured sound pressure levels (plane $x=L_x^{pl}/2$).

FIG. 7. Experimental results at 140 Hz [resonance of mode (1,1)].

sensor, since the plate displacement before control was already a dipole-type radiator. It is interesting to note that the measured pressure directivity in the $x=L_x^{pl}/2$ plane correspond to that of a monopole-type radiator (as expected). At this frequency, it can be deduced from Fig. 8(a) that the pressure directivity in the $y=L_y^{pl}/2$ plane would be that of a dipole-type radiator before and after control. Since the control only reduces the vibrational levels, pressure reductions in the $y=L_y^{pl}/2$ plane are expected to be similar to that measured in the $x=L_x^{pl}/2$ plane.

III. CONCLUSIONS

This paper presents the development of a novel volume displacement sensor for plates and its use in an active control system. The sensor is made of shaped strips of PVDF film in the x and y directions and is independent of the type and frequency of excitation. The approach is very general, since it is based on experimentally determined mode shapes. This allows consideration of any boundary conditions (that do not allow rigid modes), and plates with added punctual mass/

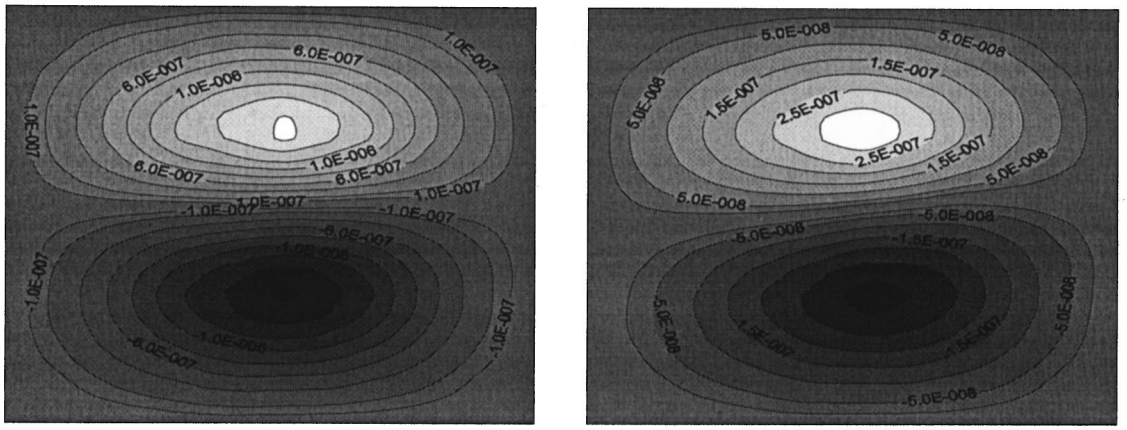

(a) Measured transversal displacements

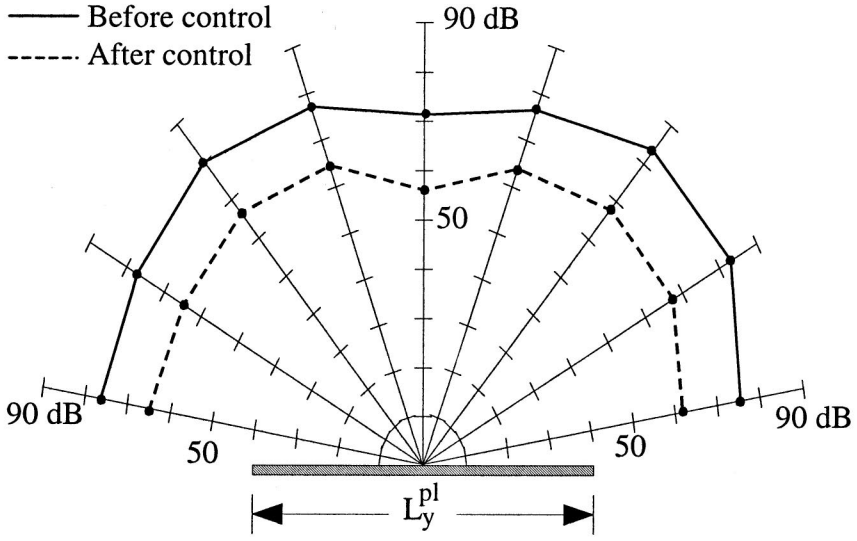

(b) Measured sound pressure levels (plane $x=L_x^{pl}/2$).

FIG. 8. Experimental results at 320 Hz [resonance of mode (1,2)].

stiffness and/or with internal defects. Results were presented for a clamped plate. The sensor was validated by comparing the volume displacement measured with a laser vibrometer to the measured signal from the PVDF sensor. The contribution of high order modes of the plate in the sensor response, as well as the location of the PVDF strips, is sensitive parameters in the sensor design.

A global reduction in the plane $x=L_x^{pl}/2$ of about 16 dB was obtained in the average sound pressure level for the off-resonance frequency case (125 Hz). This reduction is principally associated with a decrease in the radiation efficiency (the plate goes from a monopole-type radiator to a dipole one). For the on resonance case of mode (1,1), at 140 Hz, the obtained reduction in the average sound pressure level is 40 dB. This large reduction for this resonance case is attributed to the fact that the control of volume displacement decreases simultaneously the radiation efficiency and the vibration levels. Finally, for the results at 320 Hz, which correspond to the resonance of mode (1,2), the reduction of 14 dB of the average sound pressure level is associated with the reduction of the vibration levels. In this case, the plate was already acting like a dipole-type radiator before control. Therefore, the controller mainly reduced the vibration levels at this frequency.

The transversal displacement fields and the sound pressure levels obtained experimentally before and after control clearly validates the use of PVDF film directly bonded to a plate as a volume displacement sensors in an active structural

acoustic control (ASAC) system for harmonic excitation. This sensor could be used for ASAC under wide-band excitation if an appropriate digital controller is implemented.

ACKNOWLEDGMENTS

The authors wish to thank Professor Bruno Paillard and his student Martin Bouchard for the development and implementation of the control code on the DSP card. This work was funded in part by the F.C.A.R. (Formation de Chercheurs et l'Aide à la Recherche).

[1] C. R. Fuller, ''Active control of sound transmission/radiation from elastic plates by vibrational inputs: I. Analysis,'' J. Sound Vib. **136**, 1–15 (1990).
[2] C. R. Fuller, S. J. Elliott, and P. A. Nelson, *Active Control of Vibration* (Academic, London, 1996).
[3] C. R. Fuller, C. H. Hansen, and S. D. Snyder, ''Active control of structurally radiated noise using piezoceramic actuator,'' Proceedings of Inter-Noise **89**, 509–511 (1989).
[4] R. L. Clark and C. R. Fuller, ''Experiments on active control of structurally radiated sound using multiple piezoelectric actuators,'' J. Acoust. Soc. Am. **91**, 3313–3320 (1992).
[5] C. K. Lee and F. C. Moon, ''Modal sensors/actuators,'' J. Appl. Mech. **57**, 434–441 (1990).
[6] Y. Gu, R. L. Clark, C. R. Fuller, and A. C. Zander, ''Experiments on active control of plate vibration using piezoelectric actuators and polyvinylidene fluoride (PVDF) modal sensors,'' J. Vib. Acoust. **116**, 303–308 (1994).
[7] R. L. Clark and C. R. Fuller, ''Modal sensing of efficient acoustic radiators with PVDF distributed sensors in active structural acoustic approaches,'' J. Acoust. Soc. Am. **91**, 3321–3329 (1992).
[8] C. Guigou, F. Charette, and A. Berry, ''Active control of finite beam volume velocity using shape PVDF sensor,'' Acta Acust. (China) **82**, 772–783 (1996).
[9] R. L. Clark, R. A. Burdisso, and C. R. Fuller, ''Design approaches for shaping polyvinylidene fluoride sensors in active structural acoustic control (ASAC),'' J. Intell. Mater. Syst. Struct. **4**, 354–365 (1993).
[10] S. D. Snyder, C. H. Hansen, and N. Tanaka, ''Shaped vibration sensors for feedforward control of structural radiation,'' Proceedings of the Second Conference on Recent Advances in Active Control of Sound and Vibration, April 28–30, 1993, Blacksburg, Virginia, pp. 177–188 (1993).
[11] C. E. Wallace, ''Radiation resistance of a rectangular panel,'' J. Acoust. Soc. Am. **51**, 946–952 (1972).
[12] A. Berry, J. L. Guyader, and J. Nicolas, ''A general formulation for the sound radiation from rectangular, baffled plates with arbitrary boundary conditions,'' J. Acoust. Soc. Am. **88**, 2792–2802 (1990).
[13] C. R. Fuller and R. A. Burdisso, ''A wave number domain approach to active control of structure-borne sound,'' J. Sound Vib. **148**, 355–360 (1991).
[14] S. J. Elliott and M. E. Johnson, ''A note on the minimization of the radiated sound power,'' ISVR Technical Memorandum (1992).
[15] M. E. Johnson and S. J. Elliot, ''Active control of sound radiation using volume velocity cancellation,'' J. Acoust. Soc. Am. **98**, 2174–2186 (1995).
[16] J. Rex and S. J. Elliott, ''The QWSIS—A new sensor for structural radiation control,'' 1st International Conference on Motion and Vibration Control Yokohama, pp. 339–343 (1992).
[17] M. E. Johnson and S. J. Elliott, ''Volume velocity sensors for active control,'' Proc. Inst. Acoust. **15**, Part 3, 411–420 (1993).
[18] M. E. Johnson and S. J. Elliott, ''Experiments on the active control of sound radiation using a volume velocity sensor,'' Proceedings of SPIE 1995 conference on Smart Structures and Integrated Systems, Vol. 2443, 658–669 (1995).
[19] C. F. Gerald and P. O. Wheatley, *Applied Numerical Analysis* (Addison-Wesley, New York, 1989).

Sensor systems for global vibration and noise control

J. Q. Sun,[a] S. M. Hirsch,[b] and V. Jayachandran[b]
Department of Mechanical Engineering, University of Delaware, Newark, Delaware 19716

(Received 21 May 1997; accepted for publication 10 December 1997)

An important issue in sensor studies is to define sensor configurations such that the reduction of a performance measure based on the sensor measurements will guarantee a decrease in a global response measure of the system. This paper presents a study of sensors along this line. In the paper, the concept of global sensor systems is introduced. The condition for such a sensor system is derived. This concept is then applied to structural and acoustic control problems. It is shown in the paper that the nodal placement of sensors always leads to a global sensor system, and allows a single sensor gain to scale the sensor based performance measure in such a way that it is identical to the true global performance measure of the system response. Tonal and narrow-band problems are also considered where a global sensor system may be redundant. The rank of a reduced performance matrix is used to determine the number of sensors needed in these applications. The theory of the paper is demonstrated by using simple examples. Further work needs to be done to extend the present study to more complex systems. Nevertheless, the study presented in this paper may have significant implications in designing practical sensor systems for both structural and acoustic control problems. © *1998 Acoustical Society of America.* [S0001-4966(98)05003-6]

PACS numbers: 43.40.Vn [PJR]

INTRODUCTION

Sensors and actuators are two key elements in active vibration and noise control systems. An important issue in sensor studies is to define sensor configurations such that the reduction of a performance measure based on the sensor measurements by the controller will guarantee a decrease in a global response measure of the system. Such a sensor configuration is referred to as a global sensor system. This paper presents a study of global sensor configurations for both structural and acoustic control systems.

There have been many sensor studies in the literature. Sensor placement is often optimized for best modal extraction and identification[1–6] as well as for damage detection.[7,8] In conjunction with the controller design, sensor placement can be optimized to obtain an optimal feedback gain,[9,10] to minimize spillover,[5,11] and to guarantee the stability of the control system.[12] In Refs. 3 and 13 the optimal sensor and actuator locations for controlling flexible structures are obtained based on a consideration of the controllability and observability grammians. In Ref. 14, on the other hand, the locations of sensors and actuators are optimized together to move the transmission zeros of the system farther to the left of the imaginary axis in the complex s plane. Reference 15 presents some practical microphone configurations for global interior sound control in a cylindrical shell. In the present paper, we focus on the sensor configurations that can lead to a global reduction of the system response.

The remainder of the paper is organized as follows. In Sec. I, we present the concept of global sensor systems. In Sec. II, we study sensor systems for structural control problems. In particular, we consider the nodal placement of structural sensors, and show that it always leads to a global sensor system. In Sec. III, we consider acoustic control problems. We present a study of nodal placement of microphones for the acoustic enclosure. We also consider other practical configurations of acoustic sensors that are placed on the boundary of the enclosure. In Sec. IV, we turn our attention to tonal and narrow-band structural and acoustic control problems where far fewer sensors may be needed for a global reduction of the system response.

I. GLOBAL SENSOR SYSTEMS

Consider a field variable $p(\mathbf{r},t)$ defined on a domain $\mathbf{r} \in \mathbf{D} \subset \mathbf{R}^3$. The field variable can be approximated in the following finite series form:

$$p(\mathbf{r},t) = \sum_{i=1}^{N} p_i(t)\,\phi_i(\mathbf{r}) \equiv \mathbf{p}^T \boldsymbol{\phi}, \tag{1}$$

where $p_i(t) \in C^1$, $\phi_i \in R^1$, $\mathbf{p} = \{p_1, p_2, \ldots p_N\}^T$, and $\boldsymbol{\phi} = \{\phi_1, \phi_2, \ldots, \phi_N\}^T$. C^1 represents the complex space. $\boldsymbol{\phi}$ is a set of real-valued base functions for the series solution. We define a global measure of the field variable as

$$J_g = \int_{\mathbf{D}} |p(\mathbf{r},t)|^2 \, d\mathbf{r} = \sum_{i=1}^{N} \sum_{j=1}^{N} p_i^*(t) p_j(t) \int_{\mathbf{D}} \phi_i(\mathbf{r})\,\phi_j(\mathbf{r})\, d\mathbf{r} \equiv \mathbf{p}^H \mathbf{A} \mathbf{p}, \tag{2}$$

where $\mathbf{A}$ is an $N \times N$ positive definite real-valued symmetric matrix and the superscript ''H'' denotes the Hermitian transpose. Very often, the control objective of an active system is to reduce this global measure. Hence, J_g is also referred to as the performance measure. However, J_g is not readily measurable by using a finite number of sensors. Consider N_s sensors which read the field variable $p(\mathbf{r},t)$ at $\mathbf{r}_i$ $(i = 1,2,\ldots N_s)$. In practice, we often define a quadratic perfor-

[a] Assistant Professor. To whom correspondence should be addressed.
[b] Graduate student.

mance measure based on the sensor signals as follows

$$J_s=\sum_{i=1}^{N_s}|p(\mathbf{r}_i,t)|^2$$
$$=\sum_{i=1}^{N}\sum_{j=1}^{N}p_i^*(t)p_j(t)\sum_{k=1}^{N_s}\phi_i(\mathbf{r}_k)\phi_j(\mathbf{r}_k)\equiv\mathbf{p}^H\mathbf{B}\mathbf{p}, \quad (3)$$

where $\mathbf{B}$ is an $N\times N$ real-valued symmetric matrix. By reducing J_s, we are hoping to ultimately reduce J_g. When does this happen? To address this question, we introduce a definition of global sensor systems by making use of the above two performance measures J_g and J_s.

A. Definition of global sensor systems

Let ∇J_g be the gradient of J_g at any $\mathbf{p}\in\mathbf{C}^N$, and ∇J_s be the gradient of J_s at the same point in $\mathbf{C}^N$. If $\nabla J_g\cdot\nabla J_s>0$ for all $\mathbf{p}\in\mathbf{C}^N$, then, the sensor system is said to be global.

The condition $\nabla J_g\cdot\nabla J_s>0$ implies that as $\mathbf{p}$ ranges through $\mathbf{C}^N$, these two performance measures will increase and decrease together. Hence, when a sensor system is global, reduction of the performance measure J_s guarantees a global reduction of the field variable $p(\mathbf{r},t)$. By using the quadratic forms in the above equations, we can derive the following condition for global sensor systems:

$$\mathbf{p}^H\mathbf{B}^T\mathbf{A}\mathbf{p}=\mathbf{p}^H\mathbf{B}\mathbf{A}\mathbf{p}>0, \quad \text{for all } \mathbf{p}\in\mathbf{C}^N. \quad (4)$$

In other words, the matrix $\mathbf{BA}$ has to be positive definite. In the special case when $\boldsymbol{\phi}$ is chosen to be a set of orthonormal eigenfunctions of the physical system, $\mathbf{A}=\mathbf{I}$ (the identity matrix). Hence, the condition for global sensor systems becomes that $\mathbf{B}$ is positive definite.

II. STRUCTURAL PROBLEMS

A. One-dimensional structures

We first consider a one-dimensional simply supported beam. The orthonormal eigenfunctions of the beam can be obtained as

$$\phi_n(x)=\sqrt{2}\,\sin(n\pi x), \quad 0\leqslant x\leqslant 1, \quad n=1,2,...,N. \quad (5)$$

It can be readily shown that $\mathbf{A}=\mathbf{I}$ for the beam. In this case, $p(x,t)$ represents the deflection of the beam.

1. Nodal placement

Let x_i $(i=1,2,...,N)$ be the nodes of the $(N+1)$st mode of the beam, excluding the support locations. Then, it can be shown[16,17] that

$$\mathbf{B}=\mathbf{X}\mathbf{X}^T=(N+1)\mathbf{I}, \quad \mathbf{X}=[X_{ni}]=[\phi_n(x_i)], \quad 1\leqslant n,i\leqslant N. \quad (6)$$

Hence, $J_s=(N+1)J_g$. This result implies that with the nodal placement and a proper gain for all the sensors, the performance measure J_s can be made identical to the true global measure J_g. Note that this sensor gain is simply the square root of $1/(N+1)$ which is independent of the response of the structure. With a similar mathematical analysis to the nodal control studies in Refs. 16 and 17, we can show that the nodal placement of sensors on one-dimensional structures with other boundary conditions leads to a performance measure $J_s=\alpha_N J_g$, where α_N is a constant depending on the number of terms N.

As an extension to the Nodal Control Theorem in Refs. 16 and 17, we state a Global Nodal Sensor Theorem as follows:

2. Global nodal sensor theorem

For one-dimensional structures with the boundary conditions considered in the Nodal Control Theorem, N sensors located at the nodes of the $(N+1)$st mode of the structure will always lead to a global sensor system for the structure represented by the first N modes.

B. Two-dimensional structures

Consider a two-dimensional simply supported rectangular plate. The orthonormal eigenfunctions of the plate are given by

$$\phi_{nm}(x,y)=\phi_n(x)\psi_m(y), \quad 0\leqslant x\leqslant a, \quad 0\leqslant y\leqslant b,$$
$$\phi_n(x)=\sqrt{\frac{2}{a}}\sin\left(\frac{n\pi x}{a}\right), \quad n=1,2,...,N, \quad (7)$$
$$\psi_m(y)=\sqrt{\frac{2}{b}}\sin\left(\frac{m\pi y}{b}\right), \quad m=1,2,...,M.$$

It can be shown that $\mathbf{A}=\mathbf{I}$ for the simply supported plate. Here, $p(x,y,t)$ represents the deflection of the plate. Let x_i $(i=1,2,...,N)$ be the nodes of the function $\phi_{N+1}(x)$, and y_j $(j=1,2,...,M)$ be the nodes of the function $\psi_{M+1}(y)$. Consider now the system of $N\times M$ sensors located at (x_i,y_j). Then, it can be shown that

$$\mathbf{B}=\mathbf{Z}\mathbf{Z}^T=(N+1)(M+1)\mathbf{I}, \quad (8)$$

where

$$\mathbf{Z}=\mathbf{X}\otimes\mathbf{Y}, \quad \mathbf{X}=[X_{ni}]=[\phi_n(x_i)],$$
$$\mathbf{Y}=[Y_{mj}]=[\psi_m(y_j)]. \quad (9)$$

The symbol $\otimes$ denotes the Kronecker matrix product. Equation (8) indicates that $J_s=(N+1)(M+1)J_g$. As in the case of one-dimensional structures, with the nodal placement and a proper gain for all the sensors, the performance measure J_s for the plate can be made identical to the true global measure J_g. The sensor gain is the square root of $1/(N+1)(M+1)$ which is independent of the response of the structure.

For rectangular plates with different boundary conditions such that the eigenfunction of the plate deflection can be expressed as a product of two one-dimensional orthonormal beam mode functions satisfying the boundary conditions in the x and y directions that are covered in the nodal control studies,[16,17] it can be shown that the global nodal sensor theorem still holds. That is to say, both matrices $\mathbf{A}$ and $\mathbf{B}$ are diagonal, and $J_s=\alpha_N\alpha_M J_g$, where α_N and α_M are constants depending on the number of terms N and M.

Extension of the nodal control studies and the global nodal sensors to two-dimensional structures with a different geometry such as circular plates has yet to be made because of the complication of eigenfunctions for such structures. A global nodal sensor theorem for such structures is hence not available at the present time.

It should be noted that the mathematical representation of the matrix **B** involving the Kronecker matrix product renders the programming for computing this matrix extremely compact and efficient. This representation can be easily extended to three dimensional structures whose eigenfunctions consist of a product of three functions of the spatial variables, or whose series solutions are expressed in terms of expansion functions which are comprised of a product of three beam mode functions.

1. Another condition for global sensor systems

By way of construction, the matrix **B** is always nonnegative because the performance measure J_s is a sum of squared terms. In order for **B** to be positive definite, it must necessarily have a full rank. Using the above matrix representations of **B**, we can show that the condition for a global sensor system is that the matrix **X** has a full rank for one-dimensional structures, and that the matrix **Z** has a full rank for two-dimensional structures. It should also be pointed out these conditions can be readily shown to be true for the acoustic problems considered in Sec. III.

2. Some remarks

Nodal placement considered above requires that the number of sensors be the same as the number of modes participating in the response. This agrees with the conventional one-mode–one-sensor theory. As a matter of fact, other placement strategies such as uniform placement can lead to a global sensor system when the number of sensors is the same as the number of modes. The placement should be such that the matrices **X** in Eq. (6) and **Z** in Eq. (8) are nonsingular. Besides the guaranteed full rank of **X** and **Z**, the advantages of nodal placement are: (1) it allows a single sensor gain to scale the sensor based performance measure so that it is identical to the true global performance measure; (2) it produces the least observer spillover, and can work together with the nodally placed actuators to provide a decentralized control system with uniform damping to all the controlled modes.[16–18] It can also be shown that nodal sensors will lead to an observable control system.

III. ACOUSTIC PROBLEMS

A. One-dimensional wave solutions

Consider the one-dimensional enclosed sound field in a finite duct. The acoustic pressure distribution is given by

$$p(x,t)=\sum_{n=0}^{N} p_n(t)\,\phi_n(x), \tag{10}$$

where

$$\phi_n(x)=\epsilon_n \cos(n\pi x),\quad 0\leqslant x\leqslant 1,\quad n=0,1,2,...,N,$$
$$\epsilon_0=1,\quad \epsilon_n=\sqrt{2},\quad n>0. \tag{11}$$

The matrix **A** of J_g is again the identity matrix. Let x_i ($i=1,2,...,N+1$) be the nodes of the mode function $\phi_{N+1}(x)$. Consider a set of microphones located at these nodes. We can show that the matrix **B** for the performance index based on the microphones is given by $\mathbf{B}=(N+1)\mathbf{I}$. Hence, the global nodal sensor theorem also holds for the one-dimensional enclosed sound field. It is not hard to show that the theorem also holds for the one-dimensional sound fields in a finite duct with open ends.

B. Two-dimensional wave solutions

Let us consider a simple geometry: a rectangular enclosure. The acoustic pressure can be obtained as

$$p(x,y,t)=\sum_{n=0}^{N}\sum_{m=0}^{M} p_{nm}(t)\,\phi_n(x)\,\psi_m(y),$$
$$0\leqslant x\leqslant a,\quad 0\leqslant y\leqslant b, \tag{12}$$

where

$$\phi_n(x)=\epsilon_n \cos\left(\frac{n\pi x}{a}\right),\quad n=0,1,2,...,N,$$
$$\epsilon_0=\frac{1}{\sqrt{a}},\quad \epsilon_n=\sqrt{\frac{2}{a}},\quad n>0,$$
$$\psi_m(y)=\gamma_m \cos\left(\frac{m\pi y}{b}\right),\quad m=0,1,2,...,M, \tag{13}$$
$$\gamma_0=\frac{1}{\sqrt{b}},\quad \gamma_m=\sqrt{\frac{2}{b}},\quad m>0.$$

We define column vectors $\boldsymbol{\phi}^N(x)=\{\phi_1(x),\phi_2(x),...,\phi_N(x)\}^T$ and $\boldsymbol{\psi}^M(y)=\{\psi_1(y),\psi_2(y),\ldots,\psi_M(y)\}^T$. Let x_i ($i=1,2,...,N+1$) be the nodes of the function $\phi_{N+1}(x)$, and y_j ($j=1,2,...,M+1$) be the nodes of the function $\psi_{M+1}(y)$. If we are allowed to place sensors in the acoustic interior, we would have a system of $(N+1)\times(M+1)$ microphones located at (x_i,y_j). In this case, we can show that this sensor system is global and that the matrix **B** of the sensor based performance measure is given by $\mathbf{B}=(N+1)(M+1)\mathbf{I}$. This conclusion can be extended to the three-dimensional rectangular enclosure.

However, unlike one-dimensional acoustic problems or structural problems where the sensors are allowed inside the domain **D**, for higher dimensional acoustic problems, we have to assume that the acoustic interior is a valuable space for occupancy. The acoustic sensors should be placed on the boundary of the enclosure. In Ref. 15, several configurations of microphones placed at the structural–acoustic interface have been studied for reducing the interior noise of a cylindrical shell. In the active sound control studies reported in Ref. 19, microphones are routinely placed at the corners of the rectangular enclosure. Here, we shall examine the properties of these practical configurations for active sound control.

Consider a set of microphones placed along the x and y directions on the edge as well as at the four corners of the two-dimensional enclosure. The placement along the edges in each direction is nodal as defined earlier. In the following, we present as an example, the formulas of the performance measure from the sensors along one side of the enclosure and from a sensor located at a corner.

$$J_s=\sum_{i=1}^{N+1}|p(x_i,0,t)|^2+|p(a,b,t)|^2\equiv\mathbf{p}^H\mathbf{B}\mathbf{p}, \tag{14}$$

where the summation represents the contribution from the sensors along the edge $y=0$ and the other term comes from a microphone located at the corner $(x,y)=(a,b)$. By making use of the vector notation introduced earlier, the matrix $\mathbf{B}$ is given below:

$$\begin{aligned}
&\mathbf{z}_{x_i}=\mathbf{x}_i^1\otimes\mathbf{y}^0, \quad \mathbf{x}_i^1=\boldsymbol{\phi}^N(x_i), \ \ \mathbf{y}^0=\boldsymbol{\psi}^M(0),\\
&\mathbf{z}_c=\mathbf{x}^c\otimes\mathbf{y}^c, \quad \mathbf{x}^c=\boldsymbol{\phi}^N(a), \ \ \mathbf{y}^c=\boldsymbol{\psi}^M(b),\\
&\mathbf{Z}_x=[\mathbf{z}_{x_1},\mathbf{z}_{x_2},\ldots,\mathbf{z}_{x_{N+1}}],\\
&\mathbf{B}=\mathbf{Z}_x\mathbf{Z}_x^T+\mathbf{z}_c\mathbf{z}_c^T.
\end{aligned} \tag{15}$$

The performance measure including other sensors can be easily constructed by adding appropriate terms of the form $\mathbf{Z}\mathbf{Z}^T$ or $\mathbf{z}\mathbf{z}^T$ to the matrix $\mathbf{B}$. To study these sensor placements, we simply consider the rank of $\mathbf{B}$ as a function of the number of sensors.

We have found from numerical simulations that for a set of $N+M+2$ microphones placed along the x and y directions on the edge at the nodal coordinates defined earlier, the rank of $\mathbf{B}$ is always $N+M+1$, while the number of acoustic modes is equal to $(N+1)(M+1)$. Adding four microphones located at the corners makes the number of sensors $N+M+6$, while the rank of $\mathbf{B}$ is improved only by one, to $N+M+2$. It is evident that this configuration with fewer sensors than the acoustic modes will not lead to a global sensor system as defined in this paper. However, we have seen in many applications that the sensors placed in this way do lead to a global sound reduction in the enclosure in tonal and narrow-band applications. This is the issue we shall look into next.

IV. TONAL OR NARROW-BAND APPLICATIONS

It should be noted that the global sensor system is defined for all possible response modal vectors $\mathbf{p}\in\mathbf{C}^N$. Hence, this definition is particularly suitable for broadband applications where $\mathbf{p}$ can be arbitrary. For tonal or narrow-band applications, however, there may be only a few dominant modes in the system response, indicating that there are only a few dominant elements of $\mathbf{p}$ that determine the global measure of the field variable. In this case, a global sensor system may be redundant. A much smaller set of sensors may be needed to provide a performance measure that leads to a global reduction of the field variable for a wide range of frequencies. In this section, we consider the rank of the submatrix of $\mathbf{B}$ which multiplies the dominant modes of the system response. We select the dominant modes as those with amplitude greater than a certain cutoff percentage of the largest modal amplitude at a given frequency.[20] The remaining modes can be neglected, allowing us to extract a subvector of dominant modes, $\mathbf{p}_d$, and a corresponding submatrix, $\mathbf{B}_d$, so that the cost function is now approximated by

$$J_s\approx J_d=\mathbf{p}_d^H\mathbf{B}_d\mathbf{p}_d. \tag{16}$$

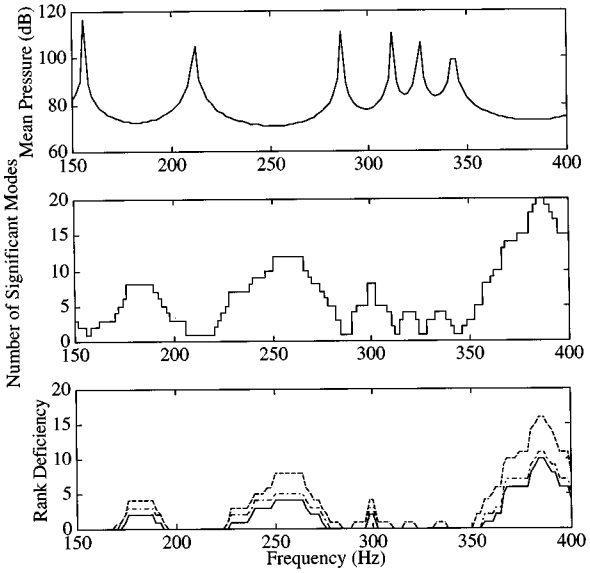

FIG. 1. Top: Mean pressure in the 2-D enclosure. Middle: Number of modes contributing significantly at each frequency. Bottom: Rank deficiency of $\mathbf{B}_d$. Dashed line: Error sensors at the corners only. Dashed-dot line: Error sensors placed nodally along the edges in the x- and y-directions. Solid line: All the sensors.

It is evident that if $\mathbf{B}_d$ is full rank, the control performance will be comparable to that of a global sensor system (to the extent to which J_d accurately approximates J_g). Studies reported in Refs. 15, 20, and 21 are such examples where the finite sensor systems have been shown to lead to a global interior sound reduction over a broad range of frequencies when the problem is tonal. The example considered in the previous section with microphones placed along the edge of the enclosure as well as at the corners may lead to a global noise reduction for tonal applications. In the following, we present a numerical study of this sensor configuration for tonal applications.

We consider a two-dimensional rectangular acoustic enclosure of size 1.1 m by 1.2 m with an acoustic source placed at one corner. Six microphone sensors are placed along each of the two edges adjacent to this corner, at the nodes of the sixth mode. Additionally, one sensor is placed at each corner. Thirty-six modes are included in the model ($N=M=5$). We consider the performance of three sensor configurations: (1) the corner sensors; (2) the nodally positioned sensors along the edges; and (3) all of these sensors together. The top frame of Fig. 1 presents the mean pressure ($\sqrt{J_g}$) in the enclosure as a function of frequency. The sharp peaks are at resonance frequencies of the enclosure where the sound field is dominated by only a few modes. Away from resonance frequencies, the modal amplitudes will be much lower, but more uniformly distributed. The middle frame of Fig. 1 shows the number of dominant modes at each frequency where the cutoff for dominant modes is 10%. The lower frame of Fig. 1 shows the rank deficiency of $\mathbf{B}_d$, i.e., the difference between the number of dominant modes and the rank of $\mathbf{B}_d$, for the three sensor configurations. Zero values indicate that the sensor configuration is sufficient for global control of the dominant modes. As expected, the rank defi-

ciency is smallest near resonance frequencies, because the sensors need to detect only a few modes. Rank deficiency is worst between resonance frequencies, as the sound field is a diffuse combination of a large number of modes. Note that the difference between the total number of modes in the model and the number of sensors for these three cases are 32, 24, and 20, respectively. In general, rank deficiencies can be attributed to two factors: (1) fewer number of sensors than significant modes; and (2) the redundancy of the sensors due to poor displacement.

It should be noted that the rank deficiency of the matrix $\mathbf{B}_d$ simply suggests that for some special combinations of modal amplitudes in $\mathbf{p}_d$, a reduction of J_s may not lead to a decrease of J_g, but it will never increase J_g. It has been observed in many experiments that interior active noise control systems reduce the sound level at sensor locations, and increase the noise elsewhere. From the sensor point of view, this may be due to the fact that the control system moves the acoustic energy from the sensor locations to other places resulting in a zero net change of the total energy. Of course, the control spillover in those systems may contribute to an increase in the overall sound pressure level. However, this is not an issue we are concerned with in this paper.

The performance loss off-resonance is typical in active noise control systems, but often acceptable because sound pressure levels are already much lower at these frequencies. This becomes a problem only in the presence of prominent noise sources which excite the enclosure off-resonance. We have found in our studies that the control performance is best with all the sensors considered here, and worst with the corner sensors only. It should be noted that the addition of the corner sensors to the two linear sensor arrays again decreases the rank deficiency by one at best.

The above results suggest that a few strategically placed sensors in an acoustic enclosure can provide sensing performance comparable to that from a true global control system for tonal or narrow band applications. The exception, which could require many more sensors, is when the enclosure is excited off acoustic resonance, for example, by the sound radiation from a structural source vibrating at its own resonance frequency.

V. CONCLUDING REMARKS

We have presented the concept of global sensor systems and derived conditions for such a system. We have found that the nodal placement of sensors always leads to a global sensor configuration for structural and acoustic systems represented by the same number of modes as the number of sensors. In particular, the nodal placement allows the use of a single gain for all sensors such that the sensor-based performance measure can be made identical to the real global measure of the system response. Furthermore, this sensor gain is independent of the system response. We have studied the tonal and narrow-band problems where there may be only a few dominant modes determining the global measure of the system response. In this case, the global sensor system can be redundant. A much smaller number of sensors may be needed for effective global control. Here, we have proposed using the rank of a reduced performance measure matrix to determine whether a sensor system is global. We have demonstrated our discussion by using a two-dimensional interior noise control problem. We have found that, indeed, at the acoustic resonance frequencies, only a few sensors are needed, and between the acoustic resonance frequencies, more sensors will be needed to better sense the sound field because there are many contributing modes. This conclusion can be readily extended to structural systems as well. Finally, this paper has demonstrated the procedure for designing global sensor systems by using simple examples. The extension of this research to more complex systems depends on the availability of the modal information. In designing active control systems, however, a modal survey of the system is often needed.[22,23]

ACKNOWLEDGMENTS

This work is supported in part by a grant (CMS-9634672) from the National Science Foundation, and a grant from the State of Delaware Research Partnership program and Lord Corporation. We would also like to acknowledge the support for S. M. Hirsch by the Delaware Space Grant College Fellowship Program, and the support for Vijay Jayachandran by the University of Delaware Competitive Fellowship.

[1] H. Baruh and K. Choe, ''Sensor placement in structural control,'' J. Guid. Control. Dyn. **13**, 524–533 (1990).
[2] D. C. Kammer and L. Yao, ''Enhancement of on-orbit modal identification of large space structures through sensor placement,'' J. Sound Vib. **171**, 119–139 (1994).
[3] T. W. Lim, ''Actuator/sensor placement for modal parameter identification of flexible structures,'' Modal Analysis: The International Journal of Analytical and Experimental Modal Analysis **8**, 1–13 (1993).
[4] C. Liu and F. A. Tasker, ''Sensor placement for multi-input multi-output dynamic identification,'' Proceedings of AIAA/ASME/ASCE/AHS Structures, Structural Dynamics & Materials Conference, 3327–3337 (1995).
[5] G. Obinata, S. Kizawa, and H. Doki, ''Sensor placement and model reduction in stabilization of flexible beams,'' Trans. Jpn. Soc. Mech. Eng., Ser. C **59**, 75–80 (1993).
[6] L. Yao, A. Sethares-William, and C. Kammer-Daniel, ''Sensor placement for on-orbit modal identification via a genetic algorithm,'' AIAA J. **31**, 1922–1928 (1993).
[7] T. A. L. Kashangaki, ''Mode selection for damage detection using the modal sensitivity parameter,'' Proceedings of AIAA/ASME/ASCE/AHS Structures, Structural Dynamics & Materials Conference, 1535–1542 (1995).
[8] F. A. Tasker and C. Liu, ''Variance-based sensor placement for modal identification of structures,'' J. Guid. Control. Dyn. **18**, 627–630 (1995).
[9] S. Kondoh, C. Yatomi, and K. Inoue, ''The positioning of sensors and actuators in the vibration control of flexible systems,'' JSME Intl. J. Ser. III **33**, 145–152 (1990).
[10] K. K. Krishna, R. Swaminathan, and L. Montgomery, ''Multiple optimal solutions for structural control using genetic algorithms with niching,'' J. Guid. Control. Dyn. **17**, 1374–1377 (1994).
[11] T. Meressi and B. Paden, ''Buckling control of a flexible beam using piezoelectric actuators,'' J. Guid. Control. Dyn. **16**, 977–980 (1993).
[12] J. N. Juang and M. Phan, ''Robust controller designs for second-order dynamic systems: A virtual passive approach,'' J. Guid. Control. Dyn. **15**, 1192–1198 (1992).
[13] K. B. Lim, ''Method for optimal actuator and sensor placement for large flexible structures,'' J. Guid. Control. Dyn. **15**, 49–57 (1992).
[14] P. G. Maghami and S. M. Joshi, ''Sensor/actuator placement for flexible space structures,'' IEEE Trans. Aerosp. Electron. Syst. **29**, 345–351 (1993).
[15] W. Shen and J. Q. Sun, ''A study of shell interior noise control,'' Proceedings of the SPIE Smart Structures and Materials '97 (1997).

[16] L. Silverberg, ''Conjecture about orthogonal function,'' AIAA J. Guid. Control Dyn. **20**, 198–202 (1996).
[17] L. Weaver, Jr. and L. Silverberg, ''Node control of uniform beams subject to various boundary conditions,'' J. Appl. Mech. **59**, 983–990 (1992).
[18] D. J. Rossetti and J. Q. Sun, ''Uniform modal damping of rings by an extended node control theorem,'' AIAA J. Guid. Control Dyn. **18**, 373–374 (1995).
[19] A. J. Bullmore, ''The active minimization of harmonic enclosed sound fields with particular application to propeller induced cabin noise,'' Ph.D. thesis, University of Southampton (1987).
[20] S. M. Hirsch and J. Q. Sun, ''Numerical studies of acoustic boundary controls for interior sound suppression,'' J. Acoust. Soc. Am. (in review).
[21] J. Q. Sun and S. M. Hirsch, ''An acoustic boundary control method for interior noise suppression,'' Proceedings of the SPIE Smart Structures and Materials '97 (1997).
[22] *Advances in Acoustics Technology*, edited by J. M. M. Hernandez (Wiley, New York, 1995).
[23] E. Benzaria and V. Martin, ''Secondary source locations in active control: Selection or optimization?,'' J. Sound Vib. **173**, 137–144 (1994).

A study of the medium frequency response of sound field in a panel–cavity system

K. S. Sum and J. Pan
Department of Mechanical and Materials Engineering, The University of Western Australia, Nedlands, Western Australia 6907, Australia

(Received 19 June 1997; revised 12 November 1997; accepted 17 November 1997)

Vibration and absorption properties of structures which are used to form an enclosure have significant effects on the acoustical response of the enclosed sound field. Boundary structures such as panels and partitions found in real enclosures like buildings and vehicles are often elastic, thus their perturbational/coupling effect cannot be isolated from the vibrational motion of boundary-induced acoustic modes in the enclosed sound field. The effect of acoustic-structural coupling on the transient and steady-state responses of the sound field has been investigated in both low- and high-frequency ranges. In the medium-frequency range, acoustic–structural coupling problems are not well understood. In this paper, acoustic–structural interactions at medium frequencies are investigated using the modal coupling method and the effect of the coupling on the medium frequency response of the sound field in a panel–cavity system is studied. Features associated with the sound field response are then obtained when modal properties of the boundary structures are varied. © *1998 Acoustical Society of America.* [S0001-4966(98)02303-0]

PACS numbers: 43.55.Br, 43.55.Dt, 43.20.Ks [JDQ]

INTRODUCTION

The interaction between a boundary structure and a sound field in an enclosure is a complicated process. The presence of a flexible structure such as a panel as one of the boundaries of the enclosure has a substantial effect on the acoustic response inside the enclosure. The acoustic–structural interaction controls the energy exchange between the boundary and the sound field. It also controls the sound absorption at the boundary which the resultant transient and steady-state behaviors of the sound field are dependent on. Traditionally, the effect of acoustic–structural interactions on the sound field behavior is described by the concept of the sound absorption coefficient which physically represents the characteristics of sound energy exchange over the boundary. The sound absorption coefficient of the boundary is related to the reverberation time of the enclosure in the well-known Sabine's reverberation formula. The introduction of the concept of acoustic impedance allows this absorption coefficient to be related to the physical properties of the boundary structure.[1] To reduce mathematical complexity in solving the wave equation for the enclosed sound field, the structural boundary is assumed to be locally reactive.[2] This means that the response on each portion of the boundary is dependent only on the incident sound pressure in front of it and independent of the response on other portions of the boundary.

Pan and Bies[3–5] have shown both theoretically and experimentally that the locally reactive modeling for the boundary conditions of an enclosure has limited application and most practical structures are modally (extensively) reactive. In this case, the motion at each point on a boundary surface is not only dependent on the local sound pressure but also on the motion at other parts of the surface. When the parts of the surface are correlated, a modal description is applicable and the response of the boundary is different for different incident sound waves. The behavior of the enclosed sound field is then controlled by the coupling between its acoustic modes and the boundary structural modes. It has been shown that for acoustic–structural coupled systems such as a panel–cavity system, both the resonance frequency and decay time of each acoustic mode can be adjusted by varying the amount of coupling between structural modes and the acoustic mode.[4,5] However, there are three regions where the sound field in such a coupled system may exhibit different response behavior, namely the low-, medium-, and high-frequency regions.

The comparatively large wavelengths of the sound field, relative to the dimensions of the system in the low-frequency range suggested that the sound field response can be described in terms of the response of lumped-parameter systems such as mass–spring–damper oscillators. The frequency response of the amplitude of an uncoupled sound field is then characterized by distinguishable and well-separated resonance peaks, and corresponding phase drops are observed in its phase response because of the sparse modal distribution. Each peak and phase drop is dominated by, and associated with, a single acoustic mode of the sound field. If the sound field is now coupled to a boundary structure near resonance, then the dominant acoustic mode is responsible for a large portion of the total power flow between the sound field and the structure. The sound field response at or close to resonance can then be characterized in terms of modal resonance frequency, modal decay time, and mode shape of the dominant mode. The relevant works in the low-frequency range have been presented by Pan *et al.*[4–6]

In the high-frequency range, there is difficulty and uncertainty in the determination of modal information of each dominant mode due to the high modal density of the sound field. Wavelengths of the sound field are also comparably smaller than the system dimensions. Many acoustic modes will be simultaneously excited although the driving fre-

quency is a very narrow band or even discrete. Therefore the modes will overlap and resonance peaks in the sound field amplitude response which correspond to each mode will tend to superimpose, thus it is difficult to distinguish one mode from another. Statistical Energy analysis (SEA) has been used for such cases. It suggests that modal information for individual modes is not required, but rather the effect of acoustic–structural coupling on the sound field response is related to the averaged behavior of all dominant acoustic and structural modes.[7]

In the medium-frequency range, the distribution of acoustic modes is not as dense as in the high-frequency range, but the modes still overlap and are difficult to distinguish from one another. There might be several modes within the averaged bandwidth of one mode (assumed as 2–5 modes). Thus the sound field behavior cannot be fully described by the modal properties of individual modes even though the excitation frequency is at or very close to the natural frequencies of the modes. In addition, the use of statistical techniques is unreliable because the sound field is not diffuse and the modal density of the sound field is not sufficiently high. Because of these limitations, the effect of acoustic–structural coupling on the medium-frequency response of the sound field is not well understood. In this paper, the well-established modal coupling theory is used to analytically study acoustic–structural interactions and to investigate the effect of coupling on the sound field response in the medium-frequency range. The objective is to obtain new understanding into the physical mechanisms involved in acoustic–structural coupling at medium frequencies. Significant features associated with coupling and the effect of coupling on the sound field response will be explained using numerical examples. The modal coupling theory used here has been experimentally and numerically validated by many authors (see the bibliography of Ref. 4). This paper briefly reviews the theory for the case of a forced excitation of the sound field.

I. DESCRIPTION OF THE PHYSICAL MODEL

To study the problem of acoustic–structural interaction in the medium-frequency range, the panel–cavity system used by Pan[6] is used here. This system consists of a rectangular box of dimensions (0.868, 1.150, 1.000) m with five slightly absorptive walls and a simply supported flexible aluminium panel on top (i.e., $z=1.000$ m) to form the sixth wall. The five walls are modeled as locally reactive boundaries and the panel is modeled as a modally reactive boundary. In this case, the effect of the panel perturbations on the sound field response in the cavity can be clearly observed when the panel modal properties are varied. The sound field inside the cavity is directly excited by using a loudspeaker which is placed at the origin of the coordinate system, $(x,y,z)=(0,0,0)$ m.

II. THEORY OF SOUND FIELD RESPONSE

A. Review of the modal coupling theory

The sound pressure in the cavity, p, is described by the three-dimensional inhomogeneous wave equation,

$$\nabla^2 p + k^2 p = -j\rho_0 \omega q, \tag{1}$$

where k is the wave number, q is the volume velocity of the sound source per unit volume of the cavity, ρ_0 is air density, and ω is the angular excitation frequency. This equation is subject to two boundary conditions for the continuity of normal air particle velocity and normal surface velocity at the cavity boundaries. At any of the five locally reactive walls, the incident sound pressure in front of it is described by the specific acoustical impedance of the boundary surface, Z_{AC}, and the boundary condition is

$$\frac{\partial p}{\partial n} = \frac{-j\rho_0 \omega p}{Z_{\mathrm{AC}}}, \tag{2}$$

where n indicates the direction normal to the boundary surface (positive outwards). At the flexible panel, the boundary condition is

$$\frac{\partial p}{\partial n} = -j\rho_0 \omega v, \tag{3}$$

where the panel surface velocity, v, satisfies the following plate equation for flexural vibration:

$$j\omega\rho_p h v - jD_p \nabla^4 v/\omega = p - p_{\mathrm{ext}}. \tag{4}$$

Here, D_p is the panel bending stiffness, h is the panel thickness, p_{ext} is the total sound pressure on the panel external surface, and ρ_p is the panel density. Within the accuracy of the present analysis, the effect of external pressure on panel vibration is neglected when compared to the sound pressure inside the cavity. Pan and Bies[4] discuss the significance of sound radiation from the panel to the external space and it is only important when the panel is thin and its damping is low, otherwise the panel response behavior is controlled by the internal sound pressure of the cavity.

To use the modal coupling method, the fluctuating quantities p and v are expressed in terms of the eigenfunction of the cavity, $\Phi_i(\mathbf{r})$, and the eigenfunction of the panel, $S_j(\boldsymbol{\sigma})$, using the method of orthogonal expansion:

$$p(\mathbf{r},\omega) = \sum_{i=1}^{N} P_i(\omega)\Phi_i(\mathbf{r}), \tag{5}$$

$$v(\boldsymbol{\sigma},\omega) = \sum_{j=1}^{M} V_j(\omega) S_j(\boldsymbol{\sigma}). \tag{6}$$

In the above, P_i and V_j are, respectively, the complex pressure and velocity amplitudes of the ith cavity mode and jth panel mode and $\mathbf{r}$ and $\boldsymbol{\sigma}$ are, respectively, the location vectors in the cavity sound field and on the panel surface. By substituting Eqs. (5) and (6), respectively, into Eqs. (1) and (4) and using the Green's function method,[8] one can obtain the modal-interaction equations which are expressed in matrix form as follows:

$$[P_N] = [Z_A][V_M] + [Q_N] \tag{7}$$

for the cavity and

$$-[Z_{PP}][V_M] = [B_{PA}][P_N] \tag{8}$$

for the panel. Physical meanings of the above matrices have been provided in Ref. 9. The matrices are written as follows:

$$[P_N]=[P_1,P_2,\ldots,P_N]^T, \tag{9}$$

$$[V_M]=[V_1,V_2,\ldots,V_M]^T, \tag{10}$$

$$[Q_N]=[Q_1,Q_2,\ldots,Q_N]^T, \tag{11}$$

$$[Z_A]=\rho_0 c_0 \begin{pmatrix} B_{1,1}/\chi_{a1} & \cdots & B_{1,M}/\chi_{a1} \\ \vdots & \ddots & \\ B_{N,1}/\chi_{aN} & & B_{N,M}/\chi_{aN} \end{pmatrix}, \tag{12}$$

$$[Z_{PP}]=\rho_0 c_0 \begin{pmatrix} \chi_{p1} & & 0 \\ & \ddots & \\ 0 & & \chi_{pM} \end{pmatrix}, \tag{13}$$

$$[B_{PA}]=\begin{pmatrix} B_{1,1} & \cdots & B_{1,N} \\ \vdots & \ddots & \\ B_{M,1} & & B_{M,N} \end{pmatrix}, \tag{14}$$

where

$$Q_i=\frac{-\rho_0 c_0}{A_p \chi_{ai}} \int_{V_0} q\Phi_i \, dV, \tag{15}$$

$$\chi_{ai}=\frac{jV_0\Lambda_{ai}}{\omega c_0 A_p}(\omega_{ai}^2-\omega^2+j\eta_{ai}\omega_{ai}^2), \tag{16}$$

$$\chi_{pj}=\frac{j\rho_p h\Lambda_{pj}}{\omega\rho_0 c_0}(\omega_{pj}^2-\omega^2+j\eta_{pj}\omega_{pj}^2), \tag{17}$$

$$\Lambda_{ai}=\frac{1}{V_0}\int_{V_0}\Phi_i^2(\mathbf{r})dV, \tag{18}$$

$$\Lambda_{pj}=\frac{1}{A_p}\int_{A_p}S_j^2(\boldsymbol{\sigma})dA, \tag{19}$$

$$\eta_{ai}=4.4\pi/T_{ai}\omega_{ai}, \tag{20}$$

$$\eta_{pj}=4.4\pi/T_{pj}\omega_{pj}, \tag{21}$$

$$B_{j,i}=\frac{1}{A_p}\int_{A_p}S_j(\boldsymbol{\sigma})\Phi_i(\mathbf{r})dA. \tag{22}$$

In the above, T_{ai}, T_{pj}, η_{ai}, η_{pj}, ω_{ai}, and ω_{pj} are respectively the cavity and panel modal decay times, modal loss factors, and angular resonance frequencies; A_p is the panel surface area, $B_{j,i}$ is the modal coupling coefficient between the ith cavity mode and jth panel mode, c_0 is the speed of sound in air, and V_0 is the volume of the cavity. Expression for $B_{j,i}$ for the panel–cavity system used here is provided in Ref. 4. Rigid-walled cavity eigenfunctions and simply supported panel eigenfunctions are used. Expressions for the eigenfunctions and corresponding resonance frequencies are also provided. By substituting Eq. (8) into (7) and eliminating $[V_M]$, it can be shown that

$$[P_N]=\begin{bmatrix} 1+\sum_{j=1}^{M}\frac{B_{1,j}B_{j,1}}{\chi_{a1}\chi_{pj}} & \cdots & \sum_{j=1}^{M}\frac{B_{1,j}B_{j,N}}{\chi_{a1}\chi_{pj}} \\ \vdots & \ddots & \\ \sum_{j=1}^{M}\frac{B_{N,j}B_{j,1}}{\chi_{aN}\chi_{pj}} & & 1+\sum_{j=1}^{M}\frac{B_{N,j}B_{j,N}}{\chi_{aN}\chi_{pj}} \end{bmatrix}^{-1}[Q_N]. \tag{23}$$

The acoustic amplitude and phase responses at any desired position in the cavity can then be evaluated from Eq. (5) since $[P_N]$ is a complex matrix.

B. Definition of medium-frequency range

The modal overlap index, M_a, rather than the modal density, n_a, of the sound field is used to define the medium-frequency range. It combines both the damping in the sound field and the modal density and is defined as[10]

$$M_a=\Delta f_{3\mathrm{dB}} n_a(f), \tag{24}$$

where

$$\Delta f_{3\mathrm{dB}}=2.2/T_{60}, \tag{25}$$

$$n_a(f)=\frac{4\pi V_0 f^2}{c_0^3}+\frac{\pi S f}{2c_0^2}+\frac{L}{8c_0}. \tag{26}$$

Here f is the excitation frequency, $\Delta f_{3\,\mathrm{dB}}$ is the half-power bandwidth of a cavity mode, L is the total edge lengths of the cavity, S is the total surface area inside the cavity, and T_{60} is the cavity reverberation time.

Modal overlap index is often used as a factor to identify the bound between two frequency ranges at which certain parameters of coupled systems (e.g., acoustic–structural, structural–structural coupled systems, etc.) follow a particular statistical distribution.[11,12] However there are no definitions for the medium-frequency range of an enclosed sound field in terms of this index because both the lower and upper frequency bounds of the frequency range are required. It is generally difficult to establish the corresponding values of the modal overlap index at the bounds for given reverberation time and dimensions of the cavity which are consistent with the change of characteristics in the sound field response. In this paper, the definition of the medium-frequency range is related to physical mechanisms which are unique to the response in this frequency range. These mechanisms are described in the next section. The medium-frequency range is defined to contain at least two overlapping cavity modes either in the space domain of an uncoupled sound field or in both the space and frequency domains. Statistical treatment to the sound field response is also not permissible. Modal overlapping in the frequency domain will occur if the average frequency spacing between adjacent modes of an uncoupled sound field [i.e., reciprocal of Eq. (26)] is less than the half amplitude bandwidth of a mode. The half-amplitude bandwidth of a mode is defined as the bandwidth where the linear amplitude response of the mode is equal to or greater than half of its linear maximum response. By using the expression for the ratio of modal response to maximum re-

sponse of a cavity mode in Ref. 13 and with some algebraic manipulation, it can be shown that the half-amplitude bandwidth is approximately $\sqrt{3}\Delta f_{3\,\mathrm{dB}}$. Modal overlapping in the space domain can occur even though cavity modes are well separated in frequency as long as the excitation frequency bandwidth, Δf, contains at least two resonance modes. By considering only the first term on the right-hand side of Eq. (26), the half-amplitude bandwidth, and a given excitation bandwidth, Morse[14] obtains a lower limiting frequency where the sound field response is fairly uniform in frequency and space. However, the medium-frequency range is not defined. By considering a minimum of two overlapping modes, using Eq. (26) with the second term included, and using a similar approach as Morse, it can be shown that the lower frequency bound for the medium-frequency range is given by

$$f_{\mathrm{LM}}=\frac{c_0 S}{16V_0}\left(\sqrt{1+\frac{64c_0T_{60}V_0}{\pi S^2(T_{60}\Delta f+4)}}-1\right). \tag{27}$$

By substituting Eq. (27) into (24), the corresponding sound field modal overlap index is

$$M_a=2.2/(T_{60}\Delta f+4). \tag{28}$$

Above this value, one generally observes, with the exception of degenerated modes, that each group of clustered modes will have an average of two or more overlapping modes either in the space domain or in both the space and frequency domains. For pure tone excitation, $\Delta f=0$ Hz and thus $M_a=0.55$. For band excitation, M_a is below 0.55 and the modes overlap only in the space domain and are well separated in the frequency domain.

The Schroeder cutoff frequency, which is given by[15]

$$f_{\mathrm{MH}}=2000\sqrt{T_{60}/V_0}\ \ \mathrm{Hz}, \tag{29}$$

provides a rough estimate of the lowest frequency where statistical treatment to the sound field is permissible when noise excitation is a pure tone. It can be shown that $M_a=3$ at the Schroeder frequency. By substituting Eq. (29) into (26) and considering the half amplitude bandwidth of a mode, it can be shown that there are at least five to six overlapping modes in both the space and frequency domains for excitation above the Schroeder frequency. This is also consistent with the criterion for broadband excitation that there be at least five resonance modes for reliable use of statistical techniques.[12,16] By considering a minimum of five to six overlapping modes, the upper frequency bound for the medium-frequency range for the case of band excitation can be derived in a similar way to the lower frequency bound and is obtained as

$$f_{\mathrm{MH}}=4000\sqrt{T_{60}/V_0(T_{60}\Delta f+4)}. \tag{30}$$

For pure tone excitation, $\Delta f=0$ Hz and Eq. (30) is equal to the Schroeder frequency. The bandwidth of the medium-frequency range, Δf_{MF}, can be obtained by subtracting Eq. (27) from (30). For pure tone excitation, it is given by

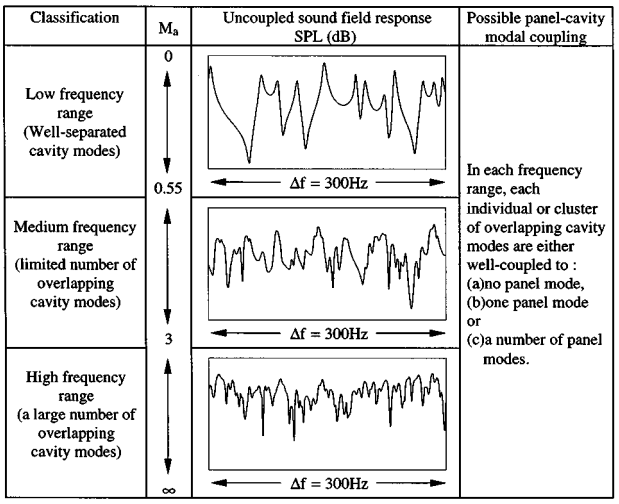

FIG. 1. Definition of medium-frequency range of a sound field and possible panel–cavity modal coupling for each frequency range.

$$\Delta f_{\mathrm{MF}}=\left\{2000-\frac{c_0 S}{16\sqrt{T_{60}V_0}}\left(\sqrt{1+\frac{16c_0T_{60}V_0}{\pi S^2}}-1\right)\right\}\sqrt{\frac{T_{60}}{V_0}}. \tag{31}$$

Equation (31) shows the dependency of the medium-frequency bandwidth on the reverberation time and physical dimensions of the cavity. For a cavity reverberation time of 1.0 s and dimensions used in this analysis, $f_{\mathrm{LM}}=780$ Hz, $f_{\mathrm{MH}}=2000$ Hz, and thus $\Delta f_{\mathrm{MF}}=1220$ Hz.

Defining the medium-frequency range for the uncoupled sound field corresponds only to one part of the panel–cavity system. Consideration must also be given to the panel part of the system as far as panel–cavity modal coupling is concerned. By modeling the panel as a modally reactive boundary, its uncoupled vibration response associated with the medium frequency range can also be defined in a similar way to the uncoupled sound field response but in terms of the panel modal overlap index, M_p. For pure tone excitation, the panel response is in the medium frequency range when $0.55<M_p<3$.

There exist three possibilities of panel–cavity modal coupling as far as the medium-frequency sound field response is concerned. Each cluster of a limited number of overlapping cavity modes can either well couple with none, one panel mode, or a number of panel modes in terms of proximity of natural frequencies[17] and/or mode shape matching. In the low-frequency range, panel–cavity modal coupling at or close to a cavity resonance involves only an individual cavity mode. In the high-frequency range, the coupling at a given frequency involves a cluster of a large number of overlapping cavity modes. Classification of frequency ranges, the corresponding characteristics in the frequency response of an uncoupled sound field, the definition of medium-frequency range for the sound field, and the possible panel–cavity modal coupling are summarized in Fig. 1.

III. RESULTS AND DISCUSSION

It is known that energy transfer between the sound field and panel is dependent on both spatial and frequency matchings between their uncoupled modes. The panel modal density controls the distribution of panel modes that will significantly couple with dominant cavity modes in terms of natural frequencies' proximity. This is because the frequency spacing between coupled modes of the panel–cavity system will be adjusted once the panel modal density is varied and the energy transfer will be affected. It is also known that the amount of coupling between those cavity and panel modes can be adjusted by varying their damping. This is because damping is not only a measure of the ability to dissipate energy but is also a measure of the tendency of both subsystems to resist acquiring energy. In this section, numerical examples for a number of panel modal overlaps (i.e., modal density and internal damping) are presented to illustrate that physical mechanisms are involved in panel–cavity modal coupling at medium frequencies. The mechanisms are used to describe how the coupling controls the occurrence of maxima and minima in the medium-frequency response of the sound field. Results for the case where cavity modes are not coupled to the panel modes (i.e., all the cavity walls are modeled as locally reactive boundaries) are also included for comparison. For each example, a sufficient number of uncoupled panel and cavity modes have been used to avoid modal truncation errors.

In the sound field low-frequency range, panel–cavity modal coupling splits any single resonance peak in the amplitude response which is dominated by an individual cavity mode into two peaks, namely the cavity-controlled peak and the panel-controlled peak.[4–6] The phase response is also split into two phase drops corresponding to the peaks. It has been shown that properties of the coupled sound field response at or close to the peaks such as resonance frequency, amplitude and phase responses, mode shape, and decay time can be described using the corresponding modal details of the dominant and coupled cavity mode. Therefore the effect of coupling on the low-frequency sound field response at any peak can be realized from details of individually dominant cavity modes.

In the high-frequency range, panel–cavity modal coupling at a given frequency involves a large number of overlapping cavity modes. Thus the effect of the coupling on the sound field response cannot be realized in terms of individual modal properties because there are no single dominant modes. Detailed investigation of each individual mode is also impractical and therefore description in terms of averaged modal properties is applicable. When the amplitude and phase of the overlapping cavity modes is adjusted by the coupling such that out-of-phase destructive superposition dominates, the sound field response is a minimum. However, when in-phase constructive superposition dominates, the response becomes a maximum.

The sound field response in the medium-frequency range is somewhat different to the low- and high-frequency ranges because of the presence of a limited number of overlapping cavity modes. The width of maxima in the medium-frequency response is often broader than the bandwidth of the modes because of the modal overlapping. Thus the presence of cavity-controlled peaks associated with each cavity mode and panel-controlled peaks due to coupling with panel modes becomes difficult to identify. Panel-controlled peaks are often submerged in the cavity-controlled peaks. There are three types of panel–cavity modal interaction which are often observable in the medium-frequency range as far as clusters of overlapping cavity modes are concerned. The first type involves one panel mode which is well coupled in terms of resonance frequency proximity (proximate modal coupling[17]) to only one of the overlapping cavity modes. Figure 2 shows an example of a sound field medium-frequency response at a corner $[(x,y,z)=(0.868, 1.150, 0)\ \mathrm{m}]$ for such a case. The frequency range chosen here is consistent with the definition of medium-frequency range in the previous section. Modal indices and uncoupled natural frequencies of all dominant modes [(3,2,8,), (6,6,2) and (5,7,3) cavity modes and (8,6) panel mode] are tabulated in Table I. The sound field is modally decomposed at two driving frequencies (1529 and 1531 Hz, which correspond to maxima in the uncoupled response) and modal amplitude and phase of the overlapping cavity modes as a function of panel thickness are shown in Fig. 3. At 1529 Hz and $h=5.79$ mm, energy transfer from the (5,7,3) mode to the

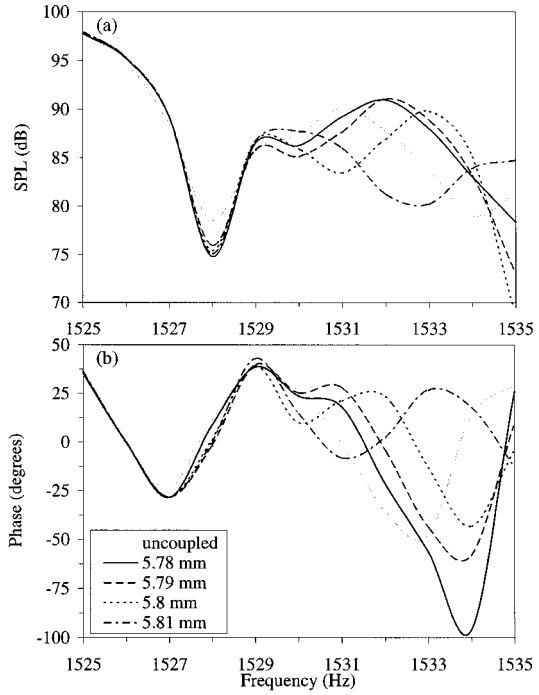

FIG. 2. The (a) SPL and (b) phase response of the sound field at (0.868, 1.150, 0) m in a medium-frequency range for several different panel thickness (type 1).

TABLE I. Dominant cavity and panel modes between 1528 and 1535 Hz.

l	m	f_a (Hz)	u	v	5.78 mm f_p (Hz)	5.79 mm f_p (Hz)	5.80 mm f_p (Hz)	5.81 mm f_p (Hz)
3	2	1528.5	8	6	1529.2	1531.8	1534.5	1537.1
6	6	1528.8						
5	7	1531.0						

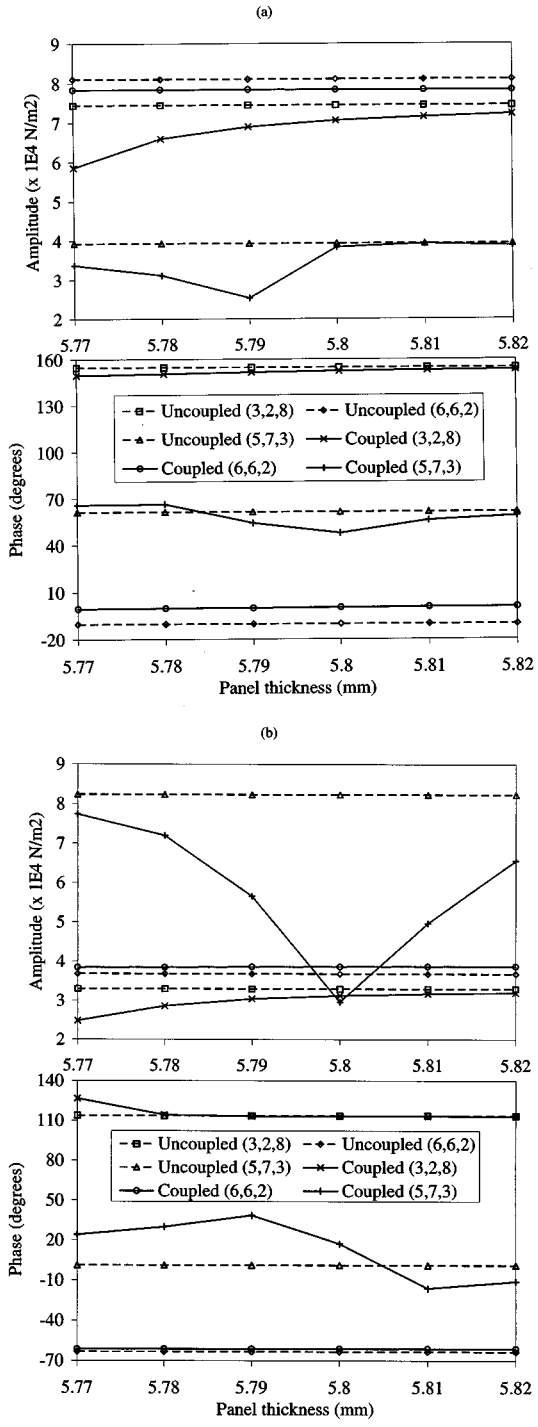

FIG. 3. Complex sound pressure modal amplitude and phase of three overlapping cavity modes as a function of panel thickness at (a) 1529 Hz and (b) 1531 Hz.

(8,6) mode is maximum when the modes are proximately coupled. Thus the (5,7,3) mode undergoes a minimum amplitude and a phase jump [Fig. 3(a)]. The coupling from all other panel modes not in the vicinity of natural frequency to the (3,2,8) and (6,6,2) modes only causes slight offsets in the amplitude and phase responses of these two modes. However, since these modes are dominant over the (5,7,3) mode which is in contrast to the case at 1531 Hz [Fig. 3(b)], effect of the (8,6) panel modal coupling through the (5,7,3) mode is insignificant on the sound field response. Thus there is only a small difference in SPL and phase between the uncoupled and coupled cases at 1529 Hz in Fig. 2 while the difference is significant at 1531 Hz.

The effect of panel–cavity modal coupling on the medium-frequency sound field response cannot be directly realized from details of individual cavity modes. Examination of Figs. 2 and 3 reveals no common features between the sound field response and the response of each mode. Thus the use of modal details such as modal resonance frequency as one of the descriptors for the sound field response becomes inappropriate. This is because there is no assurance that there is a maximum in the amplitude response (and a corresponding phase drop in the phase response) of the sound field at a modal resonance. It is the overall interaction between the overlapping coupled cavity modes that determines the occurrence of maxima and minima. The effect of panel–cavity coupling on the medium-frequency sound field response can then be realized by two mechanisms, namely the modal domination mechanism and the modal superposition mechanism. These mechanisms are dependent on the modal distribution of the panel. The first mechanism is defined as the case where there is only one dominant cavity mode to the sound field response with significant contribution from other overlapping modes. The second mechanism is the case where the amplitude response of overlapping cavity modes is comparable and none of them can be regarded as the dominant mode. The sound field response is then related to the averaged superposition of the modes. For example, the amplitude of the (5,7,3) mode at 1531 Hz and $h = 5.77$ mm is greater than the others [see Fig. 3(b)]. Thus the sound field response is a maximum although this mode is out-of-phase with the other overlapping modes (modal domination mechanism). When the panel modal density is adjusted (e.g., 5.8 mm) such that the amplitude of other overlapping cavity modes is comparable to the (5,7,3) mode, out-of-phase superposition now yields a minimum in the sound field response (modal superposition mechanism) [see Fig. 2(a)].

The SPL distribution of the sound field is also affected by the change in panel modal density. Mode shape of the dominant mode can be observed in the SPL response when the sound field is controlled by the modal domination mechanism. This indicates that the sound field still responds modally but disturbance from modal superposition with other overlapping modes causes the mode shape to distort. Thus the modal response is termed as weak. When the modal superposition mechanism is dominant, the response becomes more uniform.

The second type of medium-frequency panel–cavity modal interaction involves one panel mode which is proximately coupled to more than one overlapping cavity modes. Figure 4 shows an example of the sound field frequency response for this case for several panel thicknesses. Natural frequencies of the dominant panel and cavity modes are tabulated in Table II. At 1016 Hz, for example, cavity modes (3,3,4), (3,5,2), and (5,1,1) undergo a minimum amplitude and a phase jump when proximately coupled to the (6,6) panel mode (see Fig. 5). The modal domination mechanism

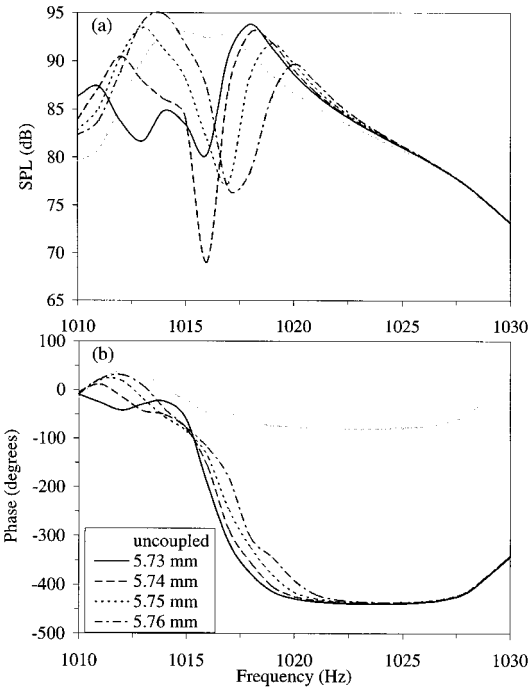

FIG. 4. The (a) SPL and (b) phase response of the sound field at (0.868, 1.150, 0) m in a medium-frequency range for several different panel thickness (type 2).

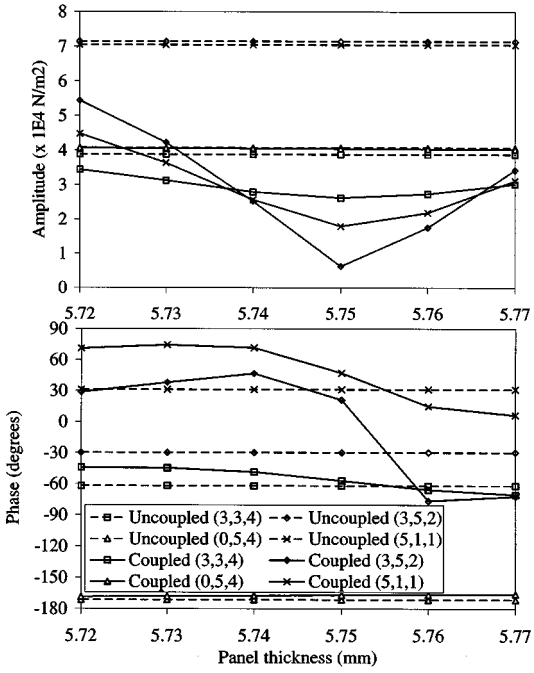

FIG. 5. Complex sound pressure modal amplitude and phase of four overlapping cavity modes as a function of panel thickness at 1016 Hz.

by mode (0,5,4) is at work when $h=5.75$ mm. For $h=5.73$ mm, the sound field response is no longer dominated by this mode and is controlled by the modal superposition mechanism. Out-of-phase destructive superposition of the overlapping modes then yields a minimum in the sound field response [Fig. 4(a)].

The third type of medium-frequency panel-cavity modal interaction is a multiple panel-cavity modal coupling in which there is more than one overlapping cavity mode proximately coupled to more than one panel mode. An example of the sound field frequency response for this case is shown in Fig. 6. It can be seen that the response is extremely sensitive to the panel modal density. Even a change of 2×10^{-4} Hz^{-1} in modal density or 2×10^{-5} m in panel thickness can cause significant changes in the sound field response. Sound field modal decomposition results for the overlapping (3,3,2), (0,3,4), (0,5,2), and (4,1,1) cavity modes at two driving frequencies (821 and 825 Hz) are shown in Fig. 7 for different panel thickness. The results clearly exhibit minimum amplitude and phase jump when the cavity modes proximately couple with the (6,4), (3,8), and (5,6) panel modes. Information of all the modes is tabulated in Table III. The sound field response is not describable by response characteristics of any individual cavity mode because it is determined by the superposition of the modes. For a certain panel thickness and driving frequency, the amplitude of one mode is greater than the others and the resulting response is a maximum although the modes superimpose out-of-phase (e.g., $h=5.76$ mm at 821 and 825 Hz) (modal domination mechanism). For other panel thicknesses, ampli-

TABLE II. Dominant cavity and panel modes between 1013 and 1020 Hz.

l	m	f_a (Hz)	u	v	5.73 mm f_p (Hz)	5.74 mm f_p (Hz)	5.75 mm f_p (Hz)	5.76 mm f_p (Hz)
3	3	1013.94	6	6	1013.69	1015.46	1017.23	1019.00
3	5	1015.37						
0	5	1016.16						
5	1	1016.66						

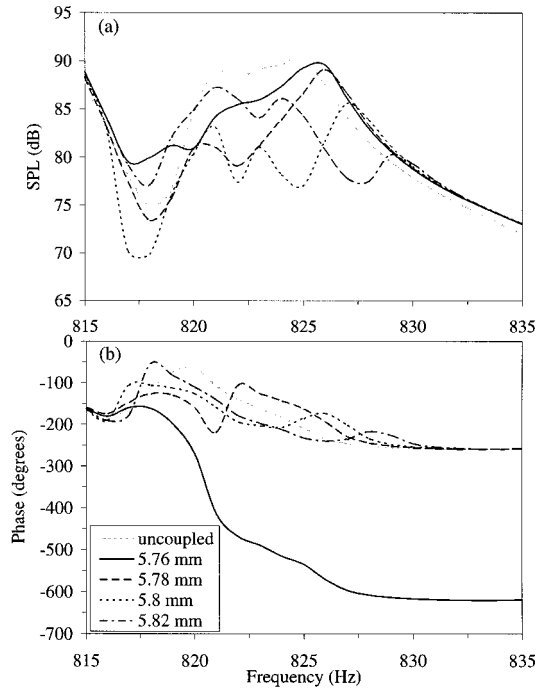

FIG. 6. The (a) SPL and (b) phase response of the sound field at (0.868, 1.150, 0) m in a medium-frequency range for several different panel thickness (type 3).

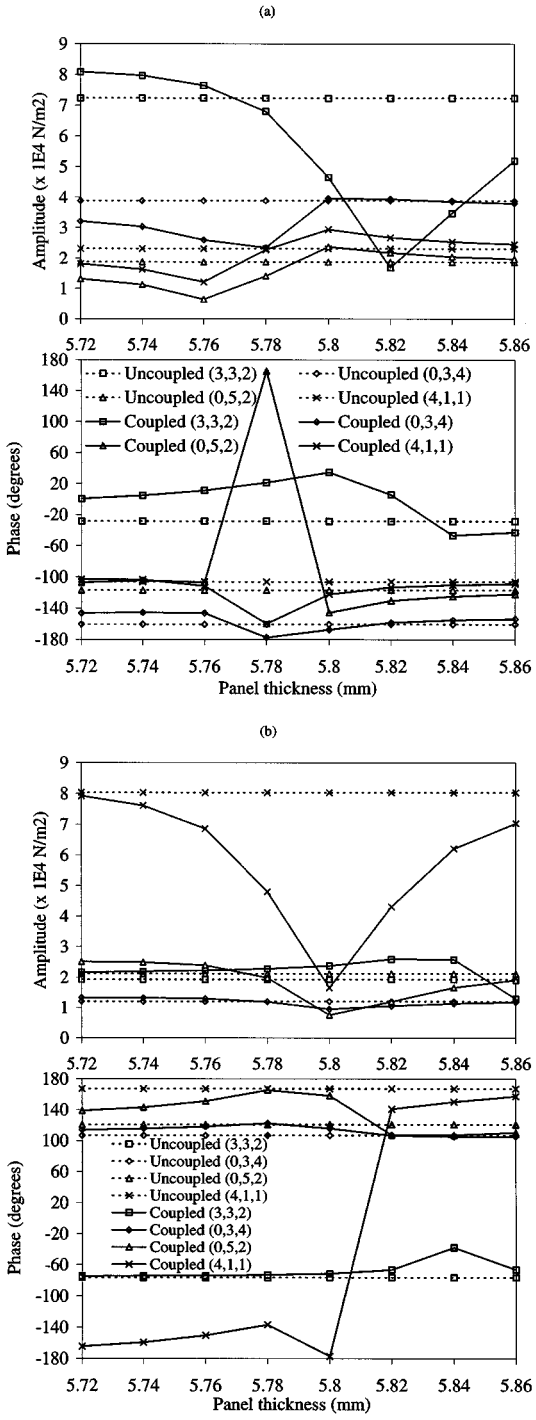

FIG. 7. Complex sound pressure modal amplitude and phase of four overlapping cavity modes as a function of panel thickness at (a) 821 Hz and (b) 825 Hz.

TABLE III. Dominant cavity and panel modes between 820 and 830 Hz.

l	m	f_a (Hz)	u	v	5.76 mm f_p (Hz)	5.78 mm f_p (Hz)	5.80 mm f_p (Hz)	5.82 mm f_p (Hz)
3	3	820.40	6	4	813.54	816.36	819.19	822.01
0	3	821.38	3	8	819.77	822.61	825.46	828.31
0	5	823.15	5	6	820.64	823.49	826.34	829.19
4	1	824.75						

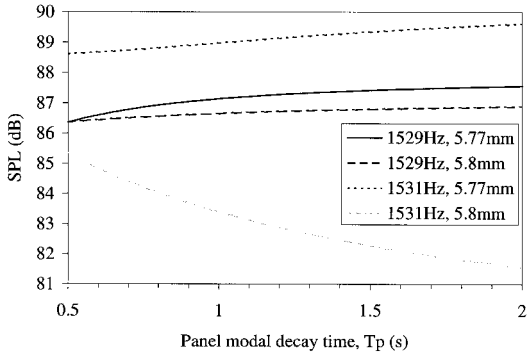

FIG. 8. The SPL at (0.868, 1.150, 0) m as a function of panel modal decay time.

tudes of the modes are comparable. Out-of-phase superposition then yields a minimum (e.g., $h=5.8$ mm at 825 Hz) and in-phase superposition yields a maximum in the sound field response (e.g., $h=5.82$ mm at 821 Hz) (modal superposition mechanism) (see Figs. 6 and 7). The phenomena show that there are two physical mechanisms involved in panel–cavity modal interaction at medium frequencies, namely, the modal domination and modal superposition mechanisms. These mechanisms control the occurrence of maxima and minima in the sound field response.

The effect of panel modal decay time on the medium-frequency sound field response is also significant when panel and cavity modes are proximately coupled. An example is shown in Fig. 8 [$h=5.8$ mm at 1531 Hz where mode (5,7,3) proximately couples with mode (8,6)]. However, effect of the decay time will not be reflected much in the SPL when modal amplitude of the (5,7,3) mode is not dominant compared to other overlapping cavity modes [see Fig. 3(a)] regardless of whether this cavity mode is proximately coupled to any panel modes or not (e.g., at 1529 Hz and $h=5.77$ mm or 5.8 mm in Fig. 8).

When the sound field response is controlled by the modal superposition mechanism, variation in decay time of each of the overlapping cavity modes has a comparable significance to the SPL [see Fig. 9(a) and (b) for $h=5.8$ mm and $Tp=0.5$ s]. When the sound field response is controlled by the modal domination mechanism, variation in modal decay time of the dominant cavity mode has more pronounced effect on the SPL than other overlapping modes [e.g., $h=5.77$ mm at 1531 Hz in Fig. 9(a) where variation in Ta of mode (6,6,2) or (3,2,8) is insignificant to the SPL compared to mode (5,7,3) and $h=5.76$ mm at 825 Hz in Fig. 9(b) where variation in Ta of mode (0,5,2), (0,3,4) or (3,3,2) is insignificant to the SPL compared to mode (4,1,1)]. The panel modal decay time has an insignificant effect on the SPL when the sound field response is controlled by the modal domination mechanism and the dominant mode is not proximately coupled to any panel modes, i.e., this mode remains dominant [e.g., mode (5,7,3) for $h=5.77$ mm at 1531 Hz in Fig. 9(a) and mode (4,1,1) for $h=5.76$ mm at 825 Hz in Fig. 9(b)] even though the panel modal decay time is increased fourfold (e.g., from $Tp=0.5$ s to $Tp=2.0$ s). This is explained by the fact that modal amplitude of the dominant mode is not attenuated much as panel modal decay time

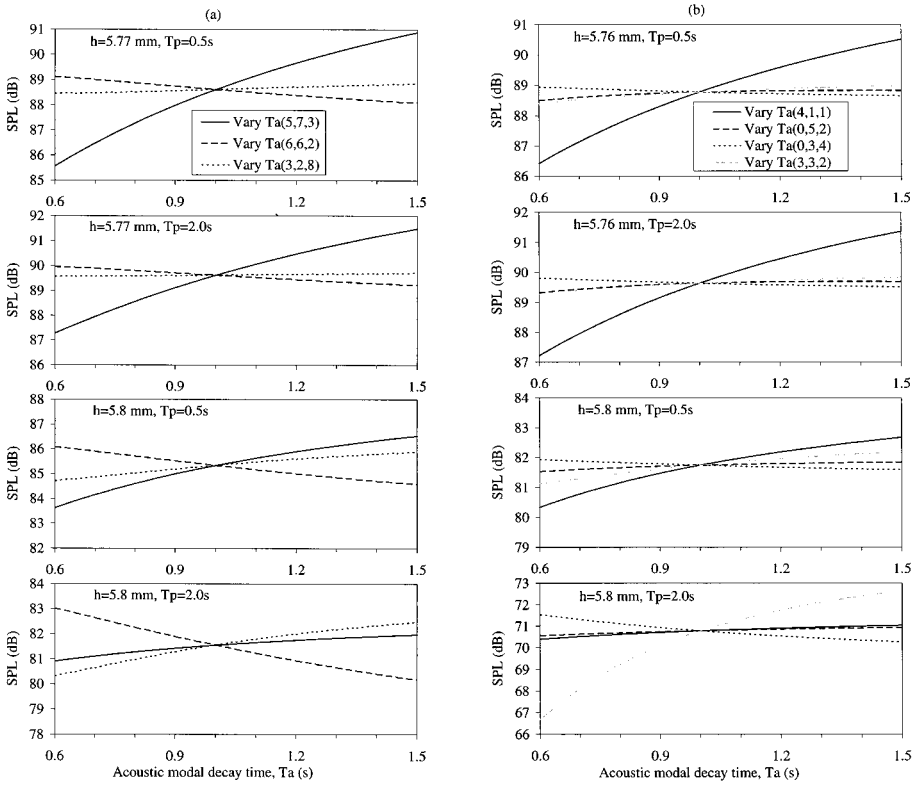

FIG. 9. The SPL at (0.868, 1.150, 0) m as a function of modal decay times of dominant cavity modes for different panel thicknesses and different panel modal decay times, at (a) 1531 Hz and (b) 825 Hz.

is varied [e.g., see Fig. 10(a) for $h=5.76$ mm at 825 Hz]. If the dominant mode is proximately coupled to the panel modes, then the panel modal decay time has a significant effect on the SPL because the contribution of the dominant mode is significantly affected. For example, the contribution of the dominant mode to the SPL is reduced [e.g., mode (5,7,3) in Fig. 9(a) and mode (4,1,1) in Fig. 9(b) for $h=5.8$ mm] as the panel modal decay time is increased from 0.5 to 2.0 s, which indicates that the panel resistance to acquiring vibrational energy has decreased. Thus more energy is flowing from the dominant cavity mode to the proximately coupled panel modes and its energy content is reduced. On the other hand, it is also possible to change the sound field control mechanism by adjusting the panel modal decay time if panel and cavity modes are proximately coupled. For example, the sound field response which is modal superposition controlled [$h=5.8$ mm and $Tp=0.5$ s in Fig. 9(b)] becomes modal domination controlled [$h=5.8$ mm and $Tp=2.0$ s in Fig. 9(b)] when amplitudes of proximately coupled cavity modes are all attenuated [see Fig. 10(b)] as the panel modal decay time is increased. [For $Tp=0.5$ s, variation in Ta of each of the overlapping cavity modes has comparable significance to the SPL. For $Tp=2.0$ s, variation in Ta of mode (4,1,1), (0,5,2), or (0,3,4) is insignificant to the SPL compared to mode (3,3,2) although natural frequencies of these modes are closer to the excitation frequency of 825 Hz than mode (3,3,2). Thus mode (3,3,2) becomes dominant at this driving frequency.]

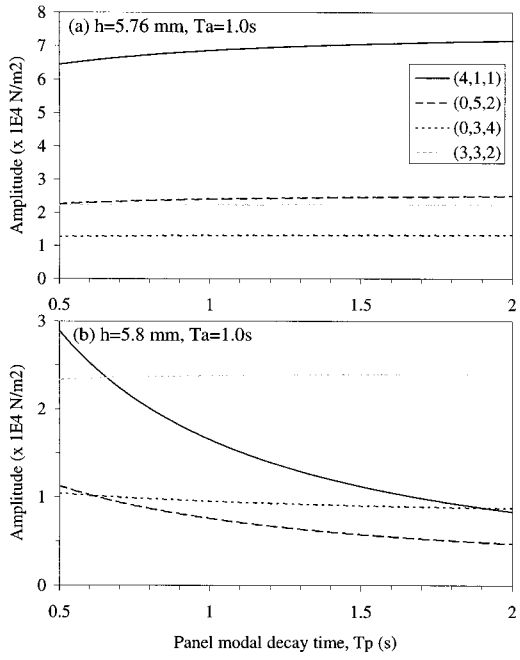

FIG. 10. Modal amplitude of four overlapping cavity modes as a function of panel modal decay time at 825 Hz for panel thicknesses of (a) 5.76 mm and (b) 5.8 mm.

IV. CONCLUSIONS

The medium-frequency range of an enclosed sound field for a given reverberation time and physical dimensions of cavity has been defined in this paper. Panel–cavity modal coupling and the effect of the coupling on the medium-frequency sound field response have also been studied.

Physical mechanisms associated with the coupling and the corresponding features have been obtained. These mechanisms control the occurrence of maxima and minima in the sound field frequency response. Results have shown great dependency of the sound field response on modal properties (e.g., modal density or modal decay time) of boundary structures. These properties determine if the sound field is controlled by modal domination mechanism or by modal superposition mechanism. When the modal properties are adjusted such that there is only one dominant cavity mode with significant contribution from other overlapping modes, the mode shape of the dominant mode observed in the sound field response is distorted and the modal response of the sound field is then weak (modal domination mechanism). This shows that the dominant mode is not unique and the presence of averaged contribution from other proximate modes is also equally important. When the modal properties are adjusted such that amplitudes of the overlapping cavity modes are comparable, the average superposition of the modes now controls the sound field response (modal superposition mechanism). Thus in contrast to the low-frequency range where modal domination mechanism dominates and the high-frequency range where modal superposition mechanism dominates, both mechanisms are at work in the medium-frequency range. This study has also shown that sound field response at medium frequencies can neither be described by the current understanding in acoustic–structural interaction at low frequencies nor by the understanding in acoustic–structural interaction at high frequencies.

ACKNOWLEDGMENTS

Financial support from Australia Research Council for this research is gratefully acknowledged.

[1] P. M. Morse and K. U. Ingard, ''Sound waves in ducts and rooms,'' Chap. 9 in *Theoretical Acoustics* (McGraw–Hill, New York, 1968).
[2] P. M. Morse and R. H. Bolt, ''Sound waves in rooms,'' Rev. Mod. Phys. **16**, 69–150 (1944).
[3] J. Pan and D. A. Bies, ''An experimental investigation into the interaction between a sound field and its boundaries,'' J. Acoust. Soc. Am. **83**, 1436–1444 (1988).
[4] J. Pan and D. A. Bies, ''The effect of fluid-structural coupling on sound waves in an enclosure—Theoretical part,'' J. Acoust. Soc. Am. **87**, 691–707 (1990).
[5] J. Pan and D. A. Bies, ''The effect of fluid-structural coupling on sound waves in an enclosure—Experimental part,'' J. Acoust. Soc. Am. **87**, 708–717 (1990).
[6] J. Pan, ''The forced response of an acoustic-structural coupled system,'' J. Acoust. Soc. Am. **91**, 949–956 (1992).
[7] J. Pan and D. A. Bies, ''The effect of fluid-structural coupling on acoustical decays in a reverberation room in the high frequency range,'' J. Acoust. Soc. Am. **87**, 718–727 (1990).
[8] E. H. Dowell, G. F. Gorman, and D. A. Smith, ''Acoustoelasticity: general theory, acoustic natural modes and forced response to sinusoidal excitation, including comparisons with experiment,'' J. Sound Vib. **52**, 519–542 (1977).
[9] J. Pan, C. H. Hansen, and D. A. Bies, ''Active control of noise transmission through a panel into a cavity: I. Analytical study,'' J. Acoust. Soc. Am. **87**, 2098–2108 (1990).
[10] M. J. Crocker and A. J. Price, ''Acoustics of enclosures,'' Chap. 4 in *Noise and Noise Control* (CRC, Boca Raton, FL, 1975), Vol. 1.
[11] R. H. Lyon, ''Statistical analysis of power injection and response in structures and rooms,'' J. Acoust. Soc. Am. **45**, 545–565 (1969).
[12] F. J. Fahy and A. D. Mohammed, ''A study of uncertainty in applications of SEA to coupled beam and plate systems, Part 1: computational experiments,'' J. Sound Vib. **158**, 45–67 (1992).
[13] F. V. Hunt, ''Investigation of room acoustics by steady-state transmission measurements I.,'' J. Acoust. Soc. Am. **10**, 216–227 (1939).
[14] P. M. Morse, ''Standing waves of sound,'' Chap. 8 in *Vibration and Sound* (American Institute of Physics, New York, 1976).
[15] M. R. Schroeder and K. H. Kuttruff, ''On frequency response curves in rooms. Comparison of experimental, theoretical, and Monte Carlo results for the average frequency spacing between maxima,'' J. Acoust. Soc. Am. **34**, 76–80 (1962).
[16] D. A. Bies and C. H. Hansen, ''Sound in enclosed areas,'' Chap. 7 in *Engineering Noise Control* (Unwin Hyman, London, 1988).
[17] F. J. Fahy, ''Vibration of containing structures by sound in the contained fluid,'' J. Sound Vib. **10**, 490–512 (1969).

On the multiple microphone method for measuring in-duct acoustic properties in the presence of mean flow

Seung-Ho Jang and Jeong-Guon Ih[a)]
Center for Noise and Vibration Control, Department of Mechanical Engineering, Korea Advanced Institute of Science and Technology, Science Town, Taejon 305-701, Korea

(Received 19 February 1997; accepted for publication 21 November 1997)

Nowadays, the two-microphone method is accepted as the standard as specified in ASTM E1050-90 for measuring in-duct acoustic properties. However, research results on using the least square method with multiple measurement points and broadband excitation have been reported for enhancing the frequency response of the two-microphone method. In this paper, the effects of varying the relative measurement positions on errors in the estimation of the acoustic quantities is studied for the multiple microphone method. Both the theoretical and experimental results show that, among possible sensor positioning configurations, the equidistant positioning of sensors yields the smallest error within the effective measurement frequency range. In addition, it is noted that the measurement accuracy can be increased and the effective frequency range can be widened by increasing the number of equidistant sensors. Measurement examples are shown and the results support the findings. © *1998 Acoustical Society of America.* [S0001-4966(98)01703-2]

PACS numbers: 43.58.Bh, 43.55.Rg, 43.55.Ev, 43.60.Qv [SLE]

INTRODUCTION

The standing wave ratio (SWR) method and the two-microphone method (TMM) are practiced very well nowadays for measuring in-duct acoustic properties and the two techniques have been standardized by ASTM C384-90a[1] and E1050-90,[2] respectively. Although the SWR method can yield very accurate results, it is very time consuming, especially in measuring the acoustic properties for a wide frequency range with a linear frequency step. By using the TMM with broadband excitation, acoustic properties can be determined over a very wide frequency range and the measurement can be much faster than with the SWR method. However, it is not possible to find the microphone spacing which can cover the whole frequency range of interest satisfying the desired accuracy bound.[3] In this regard, many works have been devoted to the analysis of the accuracy.[4–9]

Fujimori *et al.*[10] introduced the least square method based on the data sampled at multiple measurement points, and Pope[11] showed that the least square method using the broadband excitation and the transfer function between two measuring points is actually equivalent to the TMM. Chu[3] reported that the least square method gives more accurate results than the TMM if the measurement is performed at multiple points. However, the measuring sensor positions were chosen arbitrarily in the previous works and no guideline based on the analytical investigation has been given on this matter. Jones and Parrott[12] suggested the multi-point method using the least square estimation with pure tone excitation. They showed that only two properly positioned sensors are required for repeatable measurements, but the more consistent results can be obtained by adopting the additional measurement points that are evenly spaced within a half-wavelength.

In this paper, the effects of varying the relative measurement positions on errors of the estimated acoustic quantities are investigated by using the least square method with broadband excitations, and the guideline for selecting the proper sensor positions is suggested.

I. THEORY

A. Least squares method

The sound field in a duct in the presence of mean flow is considered as depicted in Fig. 1. At one end of the duct exists an acoustic source and a linear passive termination at the opposite end. The sound field for a plane wave propagating in the duct can be expressed as

$$P(x,f)=P_+(f)\exp(i\Gamma_+x)+P_-(f)\exp(i\Gamma_-x), \quad (1)$$

where $P(x,f)$ is the frequency spectrum of the measured acoustic pressure at a position x, and P_+ and P_- are the spectra of incident and reflected pressures, respectively. Here Γ_+ and Γ_- denote the incident and reflected plane wave propagation constants, respectively, defined as

$$\Gamma_+=-(k-i\delta)/(1+M), \quad (2a)$$

$$\Gamma_-=(k-i\delta)/(1-M), \quad (2b)$$

where k is the wave number, M is the mean flow Mach number, and δ is the attenuation constant. The attenuation constant originates from the viscothermal and turbulent effects as[9,13]

$$\delta=\delta_\nu+\delta_t, \quad (3)$$

where

$$\delta_\nu=\frac{\omega}{2\sqrt{2}a_0c_0}\left[\sqrt{\frac{\mu}{\rho_0\omega}}+(\gamma-1)\sqrt{\frac{\kappa}{\rho_0\omega c_p}}\right], \quad (4a)$$

a)Electronic mail: ihih@sorak.kaist.ac.kr

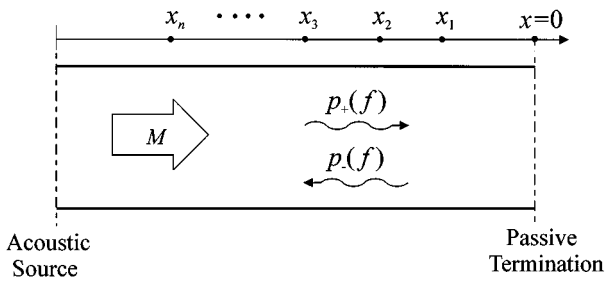

FIG. 1. Sound field in the acoustic duct with mean flow.

$$\delta_t = \frac{\Psi M}{2a_0}\left(1+\frac{\Psi' \mathrm{Re}}{2\Psi}\right). \tag{4b}$$

Here, ω denotes the angular frequency, a_0 is the ratio of duct area to perimeter (if a circular duct of diameter D is used, $a_0 = D/4$), c_0 is the speed of sound, ρ_0 is the density of the fluid medium, μ is the shear viscosity coefficient, γ is the specific heat ratio, κ is the heat conduction coefficient, c_p is the specific heat at constant pressure, Re is the Reynolds number of the flow, Ψ is the coefficient of friction for turbulent flow, and Ψ' denotes $\partial\Psi/\partial\mathrm{Re}$. If a smooth duct is involved, Ψ can be calculated from the Prandtl universal resistance law as given by[14]

$$\frac{1}{\sqrt{\Psi}} = 2\log_{10}(\mathrm{Re}\ \sqrt{\Psi}) - 0.8. \tag{5}$$

Based on Eq. (1) and by assembling all $P_j(f)$ measured at x_j as can be seen in Fig. 1, the overdetermined linear matrix equation can be obtained as

$$\mathbf{Ax} = \mathbf{b}, \tag{6}$$

where

$$\mathbf{A} = \begin{bmatrix} \exp(i\Gamma_+ x_1) & \exp(i\Gamma_- x_1) \\ \exp(i\Gamma_+ x_2) & \exp(i\Gamma_- x_2) \\ \vdots & \vdots \\ \exp(i\Gamma_+ x_n) & \exp(i\Gamma_- x_n) \end{bmatrix},$$
$$\mathbf{x} = \begin{Bmatrix} P_+(f) \\ P_-(f) \end{Bmatrix}, \quad \mathbf{b} = \begin{Bmatrix} P_1(f) \\ P_2(f) \\ \vdots \\ P_n(f) \end{Bmatrix}. \tag{7}$$

Then, the following least-squares solution of Eq. (6) can be obtained by using the Moor–Penrose generalized inverse $\mathbf{A}^+$:

$$\mathbf{x} = \mathbf{A}^+\mathbf{b} = (\mathbf{A}^{\mathrm{H}}\mathbf{A})^{-1}\mathbf{A}^{\mathrm{H}}\mathbf{b}. \tag{8}$$

Here, $\mathbf{A}^{\mathrm{H}}$ denotes the Hermitian matrix of $\mathbf{A}$. It is well known that Eq. (8) yields ''the best approximate solution'' of Eq. (6).[15] By applying Cramer's rule to Eq. (8), the complex pressure reflection coefficient $R(f)$ for the cross section at $x=0$ can be derived as

$$R(f) = \frac{P_-(f)}{P_+(f)} = \frac{\det\begin{bmatrix} \sum_j \exp[i(\Gamma_+ - \Gamma_+^*)x_j] & \sum_j P_j \exp(-i\Gamma_+^* x_j) \\ \sum_j \exp[i(\Gamma_+ - \Gamma_-^*)x_j] & \sum_j P_j \exp(-i\Gamma_-^* x_j) \end{bmatrix}}{\det\begin{bmatrix} \sum_j P_j \exp(-i\Gamma_+^* x_j) & \sum_j \exp[i(\Gamma_- - \Gamma_+^*)x_j] \\ \sum_j P_j \exp(-i\Gamma_-^* x_j) & \sum_j \exp[i(\Gamma_- - \Gamma_-^*)x_j] \end{bmatrix}}, \tag{9}$$

where $\det[\cdots]$ means the determinant of the matrix and (*) denotes the complex conjugate. The acoustic impedance at the cross section at $x=0$ can be obtained as

$$\frac{Z(f)}{\rho_0 c_0} = \frac{1+R(f)}{1-R(f)}. \tag{10}$$

Without mean flow, Eq. (8) reduces to the reflection coefficient derived in the previous works.[10,11]

From the fact that Eq. (1) never changes by multiplying any complex constant to the reflection coefficient R,[11] the transfer function $H_j(f)$, i.e., $P_j(f)/P_{\mathrm{ref}}(f)$, can be used instead of $P_j(f)$ in Eq. (9). In this regard, the reference signal $P_{\mathrm{ref}}(f)$ can be the signal driving the source or the sound pressure at a microphone at a fixed position, whichever is common to all measurements. When the transfer function between two measurement positions, $H_{12}(f)$ $[=P_2(f)/P_1(f)]$, is used ignoring the attenuation, Eq. (8) coincides with the expression for the pressure reflection coefficient stated in ASTM E1050-90.[2]

B. Sensitivity of the method to measurement errors

The input $\mathbf{b}$ in Eq. (6) is always contaminated by the measurement errors, and the solution $\mathbf{x}$ will have large errors if $\mathbf{A}$ becomes singular. The singular value decompositions of $\mathbf{A}$ and the Moor–Penrose generalized inverse matrix $\mathbf{A}^+$ can be given by[15]

$$\mathbf{A} = \mathbf{U}\Lambda\mathbf{V}^{\mathrm{H}}, \tag{11a}$$

$$\mathbf{A}^+ = \mathbf{V}\Lambda^{-1}\mathbf{U}^{\mathrm{H}}, \tag{11b}$$

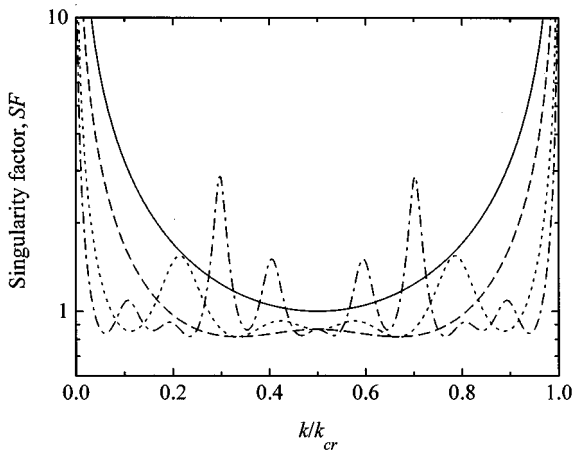

FIG. 2. Singularity factors for various measurement setups using two or three microphones. ———, $n=2$; – – –, $n=3$, $r=1$, $q=1$; ----, $n=3$, $r=4$, $q=1$; – – –, $n=3$, $r=3$, $q=7$.

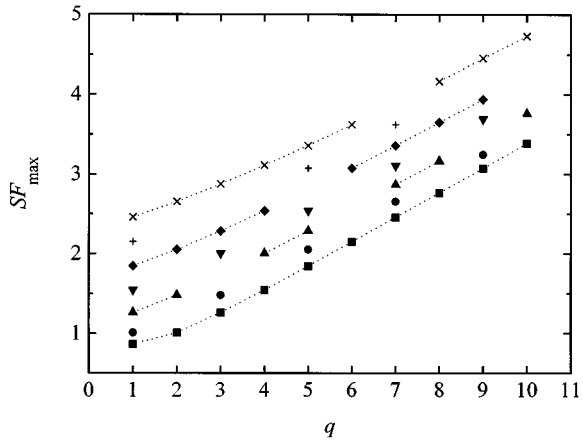

FIG. 3. Comparison of maximum singularity factors varying the sensor spacing in $n=3$ case. ■, $r=1$; ●, $r=2$; ▲, $r=3$; ▼, $r=4$; ◆, $r=5$; +, $r=6$; ×, $r=7$.

where Λ and Λ^{-1} are $n\times 2$ and $2\times n$ real diagonal matrices containing the singular values and its inverse values as diagonal elements, respectively, and **U** and **V** are $n\times n$ and 2×2 unitary matrices, respectively. From Eq. (6), the following relation can be written:

$$\tilde{\mathbf{b}}=\mathbf{b}+\mathbf{m}=\mathbf{A}\mathbf{x}+\mathbf{m}=\mathbf{A}\tilde{\mathbf{x}}. \tag{12}$$

Here, **m** denotes the measurement error in **b** and ($\tilde{}$) represents the estimated value. Then, one can express the estimation error as

$$\tilde{\mathbf{x}}-\mathbf{x}=\mathbf{A}^{+}\mathbf{m}. \tag{13}$$

The expected value of the squared norm of the estimation error can be obtained as

$$\begin{aligned} E[\|\tilde{\mathbf{x}}-\mathbf{x}\|^2] &= E[(\mathbf{A}^{+}\mathbf{m})^{\mathrm{H}}(\mathbf{A}^{+}\mathbf{m})] \\ &= E[\mathbf{m}^{\mathrm{H}}\mathbf{U}(\Lambda^{-1})^{\mathrm{T}}\Lambda^{-1}\mathbf{U}^{\mathrm{H}}\mathbf{m}] \\ &= E[\mathrm{Tr}((\Lambda^{-1})^{\mathrm{T}}\Lambda^{-1}\mathbf{U}^{\mathrm{H}}\mathbf{m}\mathbf{m}^{\mathrm{H}}\mathbf{U})], \end{aligned} \tag{14}$$

where $E[\ ]$ and Tr( ) mean the expected and the trace values, respectively. If the elements of the measurement noise **m** are assumed to be the uncorrelated white noises having the same variance of σ^2, then one can put $E[\mathbf{m}\mathbf{m}^{\mathrm{H}}]=\sigma^2\mathbf{I}$, where **I** denotes the identity matrix. Equation (14) can be rewritten as

$$\begin{aligned} E[\|\tilde{\mathbf{x}}-\mathbf{x}\|^2] &= \mathrm{Tr}(\sigma^2(\Lambda^{-1})^{\mathrm{T}}\Lambda^{-1}\mathbf{U}^{\mathrm{H}}\mathbf{U}) \\ &= \sigma^2\ \mathrm{Tr}((\Lambda^{-1})^{\mathrm{T}}\Lambda^{-1})=\sigma^2\ \mathrm{SF}^2, \end{aligned} \tag{15}$$

where the SF denotes the *singularity factor* defined as[16,17]

$$\mathrm{SF}=\sqrt{\sum_j\ \Lambda_j^{-2}}. \tag{16}$$

In order to get a small estimation error, SF should be held to the minimum possible. The sensitivity of the method to the measurement input errors can be obtained by using the SF.

Considering Eq. (16), it follows that the smallest singular value is 0 and **A** is singular if $\det(\mathbf{A}^{\mathrm{H}}\mathbf{A})=0$. If the attenuation effects are neglected, the following singular condition can be derived:

$$\left(\sum_j\ \exp\left[i\left(\frac{2k}{1-M^2}\right)x_j\right]\right)\left(\sum_j\ \exp\left[-i\left(\frac{2k}{1-M^2}\right)x_j\right]\right) - n^2=0. \tag{17}$$

If this condition is met, a large error can occur in the solution **x** and the smallest and nonzero wave number satisfying Eq. (17) is called as the *critical wave number*, k_{cr}. It is noted that Eq. (17) reduces to the well-known half-wavelength restriction of the TMM[3–9] when $n=2$.

C. Selection of the best sensor positions of sensors

In order to estimate the in-duct acoustic properties over a wide frequency range of interest, the broadband noise is used for the source signal and the transfer functions $[H_j(f)=P_j(f)/P_{\mathrm{ref}}(f)]$ between measuring points are taken as the elements of the input **b** in Eq. (6). Chu[3] analyzed a similar measurement condition experimentally and the results were compared with those by the SWR technique without mean flow. The least square method was employed by using the multiple sensor positions and the broadband excitation. It was found that the least square method is quicker but slightly less accurate than the pure tone excitation method. In his study, the measuring positions were determined empirically. It is thought that the proper choice of the measuring positions is necessary for obtaining the acoustic properties with precision. In this regard, the error sensitivity related to the relative positions of the measurement sensors should be investigated and the following discussion will be devoted on this matter. However, the attenuation effects will be neglected because the presence of attenuation has little effect on the singular values.

When $n=2$, the measurement situation is equivalent to the TMM and the corresponding singular condition can be easily derivable from Eq. (17) as

$$\cos\left(\frac{2kx_{21}}{1-M^2}\right)=1, \tag{18}$$

where x_{21} denotes the distance between the two measuring positions 1 and 2. In order to avoid the sensor placement at

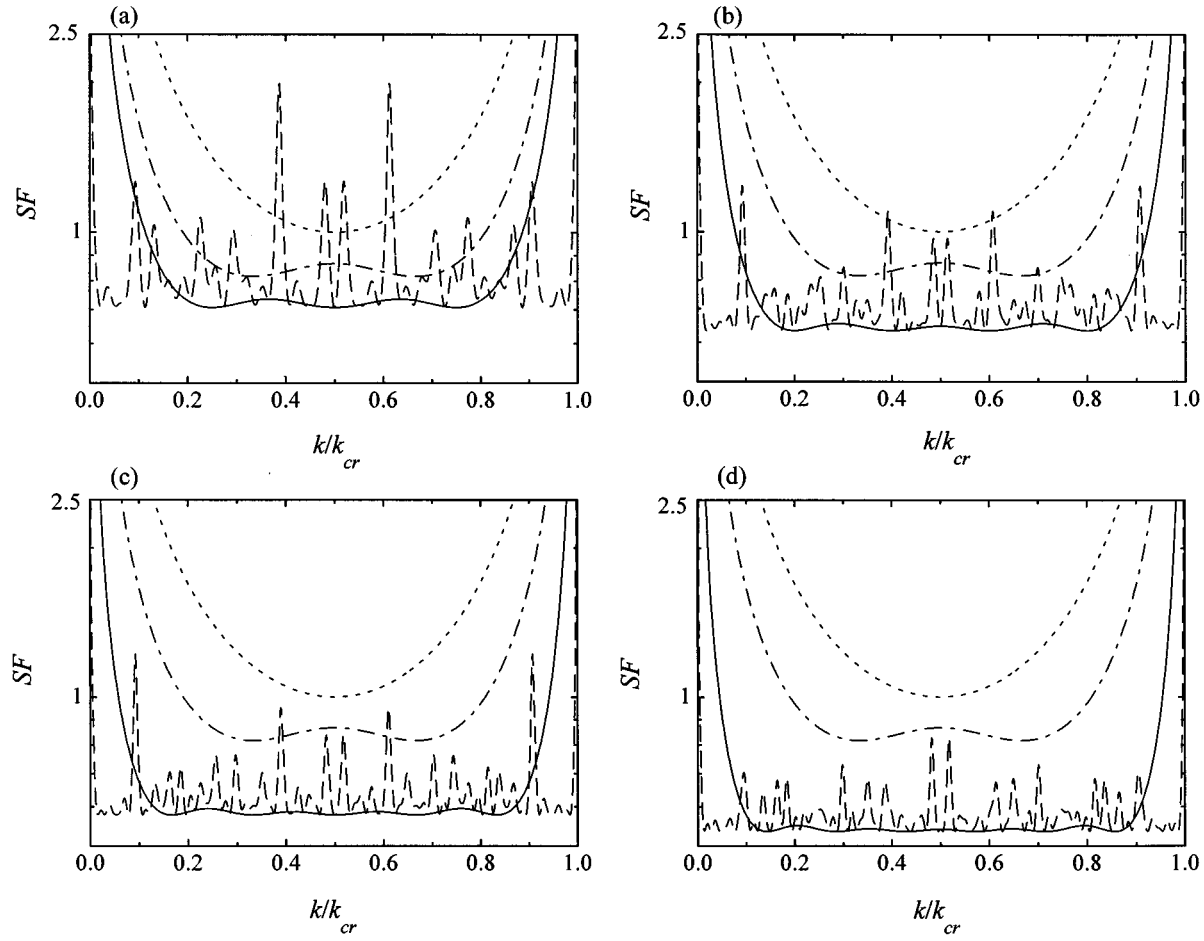

FIG. 4. Comparison of singular factors by increasing the number of measuring points. ———, uniform spacing; – – –, arbitrary spacing ($x_{21}=1.0$, $x_{32}=1.3$, $x_{43}=0.8$, $x_{54}=1.2$, $x_{65}=1.1$, $x_{76}=0.6$); ---, two microphones; –·–, three microphones ($r=1$, $q=1$). (a) $n=4$, (b) $n=5$, (c) $n=6$, and (d) $n=7$.

singular points, one should choose x_{21} satisfying the criterion given by

$$kx_{21}<\pi(1-M^2) \tag{19}$$

within the desired frequency range of interest. In Fig. 2, the degree of measurement accuracy is expressed by using the SF, where the wave number is normalized by the *critical wave number*, k_{cr}, i.e., $\pi(1-M^2)/x_{21}$. One can observe that the SF for $n=2$ case is smallest when $k/k_{\mathrm{cr}}=0.5$ and goes to infinity for $k/k_{\mathrm{cr}}=0$ and 1. This means that the effective range of the wave number for the accurate measurement is confined within a narrow range centered at $k/k_{\mathrm{cr}}=0.5$. It is noted that the same degree of accuracy for all frequencies of interest is not attainable with only a single pair of measurement sensors and this agrees with the results of the previous works.[3–9]

When three sensors are used simultaneously ($n=3$), the corresponding singular condition can be derived from Eq. (17) as

$$\cos\left[\frac{2kx_{21}}{(1-M^2)}\right]+\cos\left[\frac{2kx_{31}}{(1-M^2)}\right]+\cos\left[\frac{2kx_{32}}{(1-M^2)}\right]=3, \tag{20}$$

where $x_{31}=x_1-x_3$ and $x_{32}=x_2-x_3$. Both $kx_{21}/(1-M^2)$ and $kx_{32}/(1-M^2)$ must be integer multiples of π to satisfy Eq. (20). When $x_{32}/x_{21}=q/r$ (r and q are integers) and q/r is an irreducible fraction, the critical wave number k_{cr} can be obtained as

$$k_{\mathrm{cr}}x_{21}=r\pi(1-M^2). \tag{21}$$

The singularity factors of several sets of the three-sensor arrangement are shown in Fig. 2, where the wave number is normalized by k_{cr} as specified in Eq. (21). Local maxima of

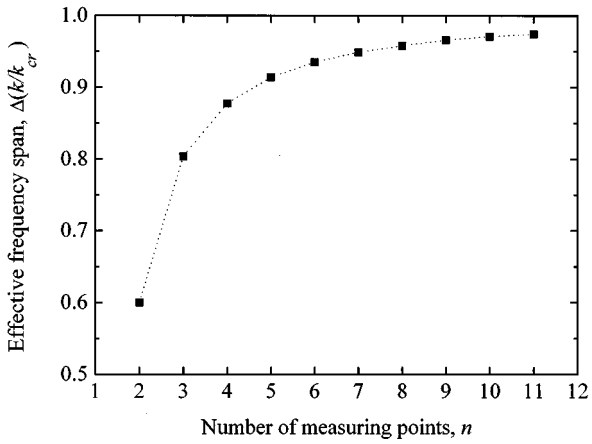

FIG. 5. Effective frequency spans varying the number of measuring points having the uniform spacing.

TABLE I. Frequency range where the SF is approximately the same with that at $k/k_{cr}=0.5$.

n	3	4	5	6	7
$\Delta\varphi$	0.23	0.19	0.16	0.14	0.12

the SF can be observed and the smallest local maximum near $k/k_{cr}=0.5$ can be found when $r=1$ and $q=1$, i.e., the equidistant positioning of sensors. It is noted that the SF for $n=3$ is smaller than that for $n=2$ case for the entire effective frequency range of interest and, furthermore, the effective frequency range is widened when $r=1$, $q=1$ or $r=4$, $q=1$ conditions are met. The largest local maximum of the SF, viz., SF_{max}, within the effective frequency range is plotted in Fig. 3 by varying r and q for several possible sensor arrangements of $n=3$ case. One can find that the SF_{max} increases as r and q increases and SF_{max} is smallest when $r=1$, $q=1$.

For sensor arrangements with more than three measurement points, similar procedures as above can be followed in choosing the proper sensor positions that minimize the measurement errors. Figure 4 shows the example calculations of the singularity factors for various layouts of multiple measurement points. Especially, the comparison is made between

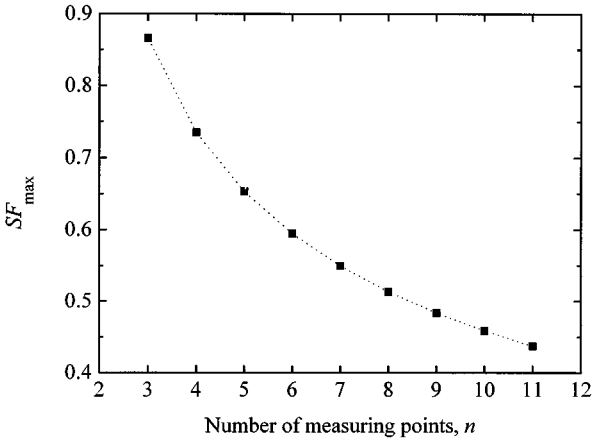

FIG. 6. Maximum singularity factors varying the number of measuring points having the uniform spacing.

the uniform and the random spacings of measuring positions for each sensor set. It is noted that every set of measurement points having uniform spacings provides smaller singularity factors than those having nonuniform spacings at all frequencies except the ranges near to $k/k_{cr}=0$ and $k/k_{cr}=1$. As the number of measuring points increases, the SF within effec-

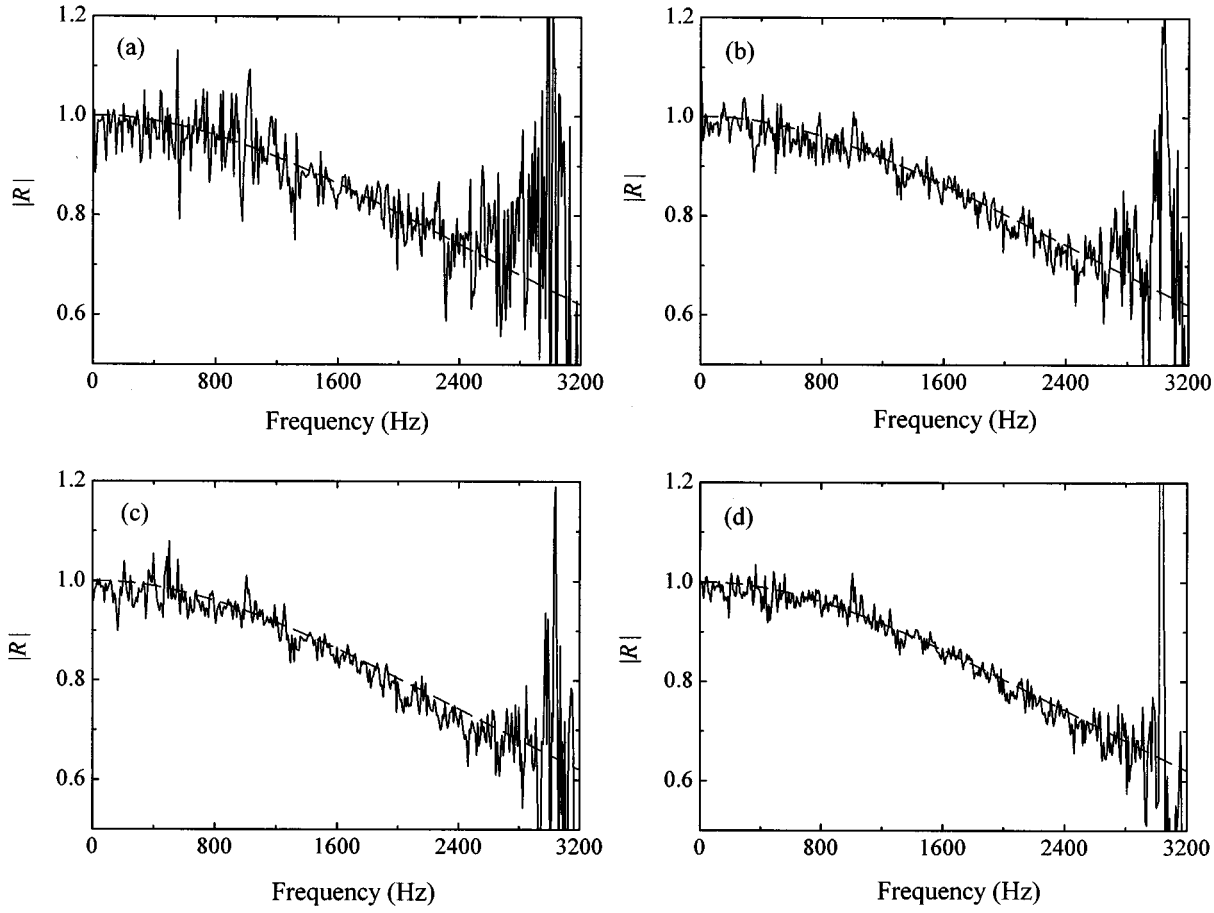

FIG. 7. Comparison of the magnitudes of the pressure reflection coefficient of an unflanged open pipe without mean flow. ———, measured by using the equidistant measuring points; – – –, theory (Ref. 18). (a) $n=2$, (b) $n=3$, (c) $n=4$, and (d) $n=5$.

tive frequency span becomes small, especially for $k/k_{cr}=0.5$. Consequently, by recalling that the SF within the effective frequency range is usually set as less than 1.7 for the TMM, it is thought that the effective frequency range widens more and more as the number of measuring points increases. The effective frequency spans satisfying $SF \leqslant 1.7$ are shown in Fig. 5 for various number of uniformly spaced measuring points. When multiple measurement points greater than 2 are used, the frequency range where the SF is approximately the same with that at $k/k_{cr}=0.5$ can be determined from Figs. 2 and 4 as $\Delta\varphi < k/k_{cr} < 1-\Delta\varphi$.

Table I lists the values of $\Delta\varphi$ for each multiple-sensor set. Figure 6 shows the decreasing trend of the SF_{max} as the number of measuring points increases. Although the frequency range can be widened and the singularity can be reduced by increasing the number of measuring points, the efficiency of these favorable effects becomes marginal when n is greater than about 7, as can be seen in Figs. 5 and 6.

II. EXPERIMENTS

A. Experimental setup

In order to confirm the analytical findings in the foregoing section, measurements were performed for the reflection coefficient of the unflanged open end of which the theoretical value is available.[18,19] An acrylic circular tube 0.53 m long and 0.04 m in diameter was used, where the cutoff frequency of the first higher-order mode is approximately 5 kHz. A signal analyzer (HP 35670A) was used to feed the stationary random signal for the acoustic driver mounted at one end of the tube and to calculate the spectra from measured signals. The frequency range of the acoustic driver was from 0.3–3.2 kHz. The acoustic transfer functions were measured with flush mounted $\frac{1}{4}''$ microphones (B&K 4135) and the source signal of the acoustic driver was used as the reference signal. The correlation technique was adopted to suppress the flow-generated noise from the turbulent flow.[7] For all measurements, the first measurement position x_1 was fixed at 30.0 mm from the open end.

B. Results and discussions

In Fig. 7, a comparison is made between the measured and the analytical pressure reflection coefficients of the unflanged open pipe without mean flow. The spacing between the adjacent measurement positions was uniformly set as 57.1 mm, giving the critical frequency of 3034 Hz for $c_0=346.5$ m/s, and the number of averaging was 80 for all measurements. It is noted that large errors occur for frequencies higher than about 3 kHz. For $n=2$, errors are relatively large except at frequencies between 1.5 and 1.8 kHz and this

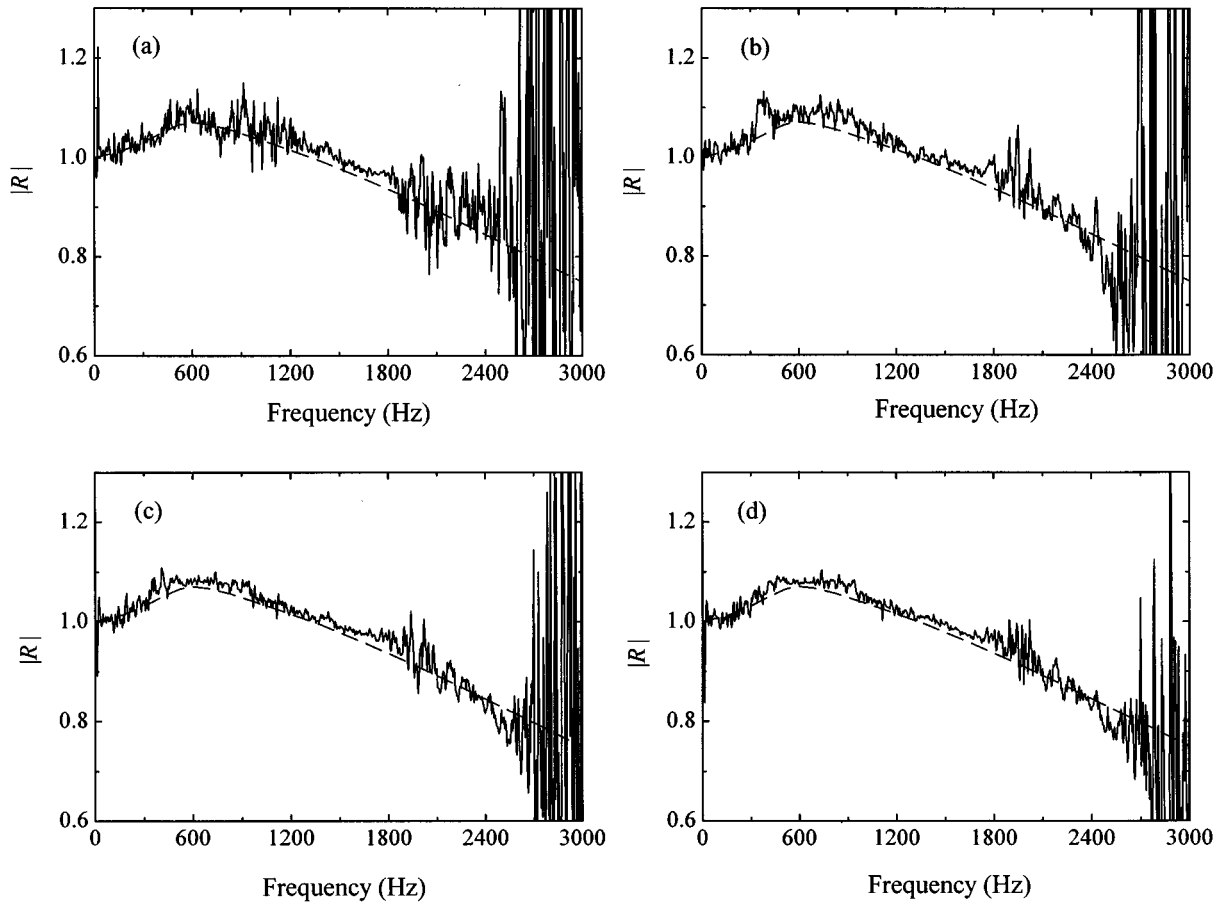

FIG. 8. Comparison of the magnitudes of the pressure reflection coefficient of an unflanged open pipe with mean flow ($M=0.1$). ———, measured by using the equidistant measuring points; – – –, theory (Ref. 19). (a) $n=2$, (b) $n=3$, (c) $n=5$, and (d) $n=6$.

range corresponds to $k/k_{cr}=0.45-0.55$. For $n=3$, errors are smaller than the $n=2$ case for most of the frequency range of interest, but are still relatively large at low frequencies and near the critical frequency. One can observe that the measured result becomes more nearly accurate with the increase of the number of measuring points, except at near 3 kHz. Although one can find the widening of the effective measurement range at high frequencies as expected in Fig. 4, the errors are not symmetrically decreasing about $k/k_{cr}=0.5$. This is due to the fact that the source signal was cut off below about 300 Hz and the transfer functions become incoherent.

In the presence of mean flow for $M=0.1$, the measured results are compared with the theoretical values[19] in Fig. 8. The sensor spacing was given by 57.1 mm in a uniform manner. The critical frequency was 3005 Hz and the number of averaging was 300. Large errors can be observed at around 3 kHz for all measurements, although the error becomes small as the number of measuring points increases.

III. CONCLUSION

The errors associated with the relative positioning of sensors have been investigated for the measurement of in-duct acoustic quantities by using the least square method with multiple measurement points and broadband excitation. The sensitivity of the method to measured input errors was expressed by using the singular factors and it is found that the equidistant positioning of sensors yields the smallest SF_{max} within the effective frequency range of the measurement. It is noted that this effective frequency range can be widened and the singularity factor at every frequency within the interested range can be reduced by increasing the number of measurement points. Therefore, the measurement method by using the multiple, uniformly spaced sensors can be a good candidate for overcoming the shortcomings of the well-known two-microphone method.

[1] (ASTM) C384-90a, ''Standard method for impedance and absorption of acoustical materials by the impedance tube method'' (American Society for Testing and Materials, Philadelphia, 1990).

[2] (ASTM) E1050-90, ''Standard test method for impedance and absorption of acoustical materials using a tube, two microphones, and a digital frequency analysis method'' (American Society for Testing and Materials, Philadelphia, 1990).

[3] W. T. Chu, ''Impedance tube measurements—a comparative study of current practices,'' Noise Control Eng. J. **37**, 37–44 (1991).

[4] A. F. Seybert and B. Soenarko, ''Error analysis of spectral estimates with application to the measurement of acoustic parameters using random sound fields in ducts,'' J. Acoust. Soc. Am. **69**, 1190–1199 (1981).

[5] J. Y. Chung and D. A. Blaser, ''Transfer function method of measuring in-duct acoustic properties. I. Theory,'' J. Acoust. Soc. Am. **68**, 907–913 (1980); ''Transfer function method of measuring in-duct acoustic properties. II. Experiment,'' J. Acoust. Soc. Am. **68**, 914–921 (1980).

[6] H. Bodén and M. Åbom, ''Influence of errors on the two-microphone method for measuring acoustic properties in ducts,'' J. Acoust. Soc. Am. **79**, 541–549 (1986).

[7] M. Åbom and H. Bodén, ''Error analysis of two-microphone measurements in ducts with flow,'' J. Acoust. Soc. Am. **83**, 2429–2438 (1988).

[8] H. Hudde and U. Letens, ''Untersuchungen zum Akustischen Messleitungsverfahren mit festen Messorten,'' Acustica **56**, 258–269 (1984).

[9] M. L. Munjal and A. G. Doige, ''The two-microphone method incorporating the effects of mean flow and acoustic damping,'' J. Sound Vib. **137**, 135–138 (1990).

[10] T. Fujimori, S. Sato, and H. Miura, ''An automated measurement system of complex sound pressure reflection coefficients,'' Proc. Inter Noise **84**, 1009–1014 (1984).

[11] J. Pope, ''Rapid measurement of acoustic impedance using a single microphone in a standing wave tube,'' Proc. ICA **12**, Paper M3-3 (1986).

[12] M. G. Jones and T. L. Parrott, ''Evaluation of a multi-point method for determining acoustic impedance,'' Mech. Syst. Signal Proc. **3**, 15–35 (1989).

[13] U. Ingard and V. K. Singhal, ''Sound attenuation in turbulent pipe flow,'' J. Acoust. Soc. Am. **55**, 535–538 (1974).

[14] S. W. Yuan, *Foundation of Fluid Mechanics* (Prentice–Hall, Englewood Cliffs, NJ, 1967), Chap. 10, pp. 383–384.

[15] G. Golub and C. Van Loan, *Matrix Computations* (Johns Hopkins U.P., Baltimore, 1985), Chap. 6, pp. 136–140.

[16] D. Oh and Y. Park, ''Order reduction based on singular values of modal matrix,'' Mech. Syst. Signal Proc. **8**, 63–79 (1994).

[17] B.-K. Kim and J.-G. Ih, ''On the reconstruction of vibro-acoustic field over the surface enclosing an interior space using the boundary element method,'' J. Acoust. Soc. Am. **100**, 3003–3016 (1996).

[18] H. Levine and J. Schwinger, ''On the radiation of sound from an unflanged circular pipe,'' Phys. Rev. **73**, 383–406 (1948).

[19] R. M. Munt, ''Acoustic transmission properties of a jet pipe with subsonic jet flow: I. The cold jet reflection coefficient,'' J. Sound Vib. **142**, 413–436 (1990).

Suppression of distortion product otoacoustic emissions (DPOAE) near $2f_1-f_2$ removes DP-gram fine structure—Evidence for a secondary generator

Jürgen Heitmann, Bernd Waldmann, and Hans-Ulrich Schnitzler
Department of Animal Physiology, University of Tuebingen, Auf der Morgenstelle 28, D-72076 Tübingen, Germany

Peter K. Plinkert[a] and Hans-Peter Zenner
Department of Otolaryngology, University of Tuebingen, Silcherstrasse 5, D-72076 Tübingen, Germany

(Received 22 January 1997; accepted for publication 21 November 1997)

Since the discovery of distortion product otoacoustic emissions (DPOAE) there has been a controversial discussion about their cochlear generation sites. Suppression experiments suggest that the place near f_2 is the main generation site. On the other hand, the fact that DPOAE can be perceived subjectively indicates that there is also a cochlear excitation at the place of $2f_1-f_2$ resulting in a stimulus frequency otoacoustic emission (SFOAE). The contribution of this SFOAE to the overall emission is still unknown. Different studies showed contradictory results. We demonstrate a secondary generator by successive suppression of the SFOAE with a sine wave close to the frequency $2f_1-f_2$. Suppression growth functions (SGF) showed a three-step behavior. For low suppressor levels, the emission either decreased or increased when increasing the suppressor. For intermediate suppressor levels, DP amplitude was constant and independant of suppressor level. For high suppressor levels, the emission always decreased with further increase of the suppressor. The behavior of the SGF in the first section depends on the fine structure of the DP-gram, which shows minima and maxima. Emissions at a maximum decreased while emissions at a minimum increased in the first section of the SGF. We conclude that the fine structure of the DP-gram is produced by alternate constructive and destructive interference of the two generators. By adding a third tone near $2f_1-f_2$ the SFOAE and thus the interference are suppressed. The fine structure of the DP-gram vanishes and the resulting DP-gram should be more closely related to the cochlear status near f_2. © *1998 Acoustical Society of America.* [S0001-4966(98)01803-7]

PACS numbers: 43.58.Ry, 43.64.Jb, 43.64.Yp [SLE]

INTRODUCTION

Stimulating the ear with two tones at frequencies f_1 and f_2 leads to a cochlear response at $2f_1-f_2$ distortion product otoacoustic emissions (DPOAE), which is regarded as an epiphenomenon of cochlear amplification (Kemp, 1979). Usually, emission amplitude is recorded at multiple stimulus frequencies with constant levels and frequency ratio. Emission amplitude plotted versus frequency is called a DP-gram, in analogy to the audiogram. The region of overlap of the two traveling waves evoked by the two primaries is undoubtedly the main generation site of the emissions (Harris *et al.*, 1993). This can be demonstrated by adding a suppressor tone between f_1 and f_2 which effectively diminishes the emission amplitude (Brown and Kemp, 1983).

DPOAE can be perceived subjectively, which indicates that there is also a cochlear excitation at the place of $2f_1-f_2$ (Jones, 1935). This excitation will result in a stimulus frequency otoacoustic emission (SFOAE) which might contribute to the DPOAE signal measured in the external ear canal (Kemp and Chum, 1980). The contribution of this secondary generator has been the subject of controversial discussion, evidence both in favor of (Stover *et al.*, 1996) and against a secondary generator (He and Schmiedt, 1996) has recently been put forward.

The attempt to investigate the contribution of a secondary generator with suppression experiments leads to ambiguous results (Kummer *et al.*, 1995). These studies did not take into account the fine structure of the DP-gram. Small variations of the frequencies of the primaries can result in large changes in DP amplitude (up to 20 dB for a 50-Hz step) (He and Schmiedt, 1993; Heitmann *et al.*, 1996). Interference of the two generators has been proposed as an explanation of this fine structure (Shera and Zweig, 1991; Zweig and Shera, 1995).

The working hypothesis in the present study is that fine structure of the DP-gram is responsible for the variability of the effect of a suppressor that other authors have reported, and that this fine structure is caused by interference of two emission sources. To investigate this, we tested the effect of a third tone of various intensities near the frequency of the suspected second emission source. For these experiments, a range of the DP-gram was selected that showed pronounced rippling.

I. MATERIAL AND METHODS

DPOAE were evoked with constant primary levels of $L_1=65$ dB SPL and $L_2=55$ dB SPL. Primary frequency ratio $f2/f1$ was constant at 1.22 (Harris *et al.*, 1989). A third

[a]Corresponding author: Electronic mail: peter.plinkert@uni-tuebingen.de

tone was added 25 Hz above the emission frequency $2f1-f2$ at a level varying from −20 to +80 dB SPL. The effect of this third tone is shown in suppression growth functions (SGF), where the DP level is plotted versus the level of the third tone, with all frequencies and primary levels constant.

First, DP-grams were measured at the conventional 12 audiogram frequencies in each ear (0.5, 0.75, 1, 1.5, 2, 2.5, 3, 3.5, 4, 5, 6, and 8 kHz). Then, fine structure was measured in 12.5-Hz steps between 1.7 kHz and 2.2 kHz. In all subjects, otoscopy was inconspicuous and pure-tone audiometry (500 Hz–6 kHz) was within the normal range.

Measurements were performed with a custom-made setup consisting of an IBM compatible personal computer and two digital signal processor (DSP) boards (ASPI, Elf-31) with 16 bit A/D and D/A converters at a common 25.6-kHz sampling rate. The stimuli were presented using Etymotic ER-2 transducers connected to a custom-made probe via Teflon tubes. The probe contained a Knowles 1843 low noise miniature microphone. The microphone signal was amplified 200-fold and band limited from 500 Hz to 10 kHz using a custom-made amplifier and filter. The amplified signal was fed back to the DSP board and was analyzed with a 2048 points fast Fourier transform, resulting in 12.5-Hz frequency resolution. Stimulus generation and frequency analysis were performed concurrently using custom-made software for the TMS320C31 processor.

Since signal input and output were phase locked, the input signal could be averaged in the time domain. The number of averages was 100, resulting in a noise floor of −15 to −20 dB SPL in the frequency range of interest.

System generated distortions were at least 80 dB below the level of the primaries. Cross talk between sound delivery tube and the microphone was measured by sealing the tip of the microphone tube with a drop of glue. Attenuation was 50–80 dB over the entire frequency range.

For calibration, the microphone tube was inserted in a 1-ccm calibration coupler (B&K UA 0922) together with a 1/4′-in. microphone (B&K 4135) and a transducer taken from a miniature headphone. The transducer was stimulated with white noise and the comparison of the two microphone signals gave the frequency response of the probe microphone. Transducers were calibrated in the ear canal at the beginning of each measurement.

II. RESULTS

For stimulus conditions that produce a maximum in the fine structure (trace a in Fig. 1), suppression occurs in three steps. Low suppressor levels from 30 to 50 dB (region 1) reduced DP amplitude. Intermediate levels from 50 to 60 dB (region 2) have no further effect. High suppressor levels above 60 dB (region 3) diminish DP amplitude until it disappears in the noise floor.

For stimulus conditions that produce a minimum in the fine structure (trace i in Fig. 1), low suppressor levels surprisingly result in an increase of DP amplitude. Intermediate suppressor levels have no effect and high levels diminish DP amplitude similarly to trace a.

SGF measured between minima and maxima of the fine

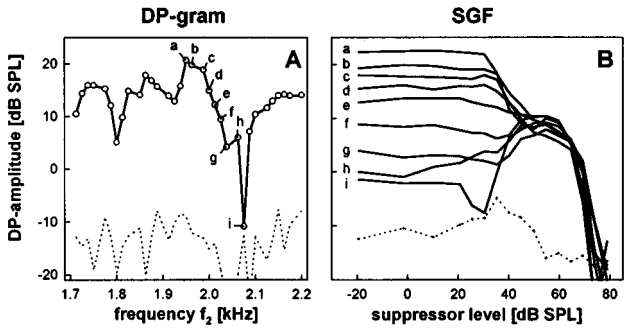

FIG. 1. DP-gram fine structure (A) and suppression growth function (B) in a single ear. Traces a–i in graph B were recorded with f_2 at the frequency marked with corresponding labels in graph A and a suppressor tone 25 Hz above $2f_1-f_2$. Frequency ratio $f_2:f_1$ was fixed at 1.22 and levels L_1, L_2 were 65 and 55 dB SPL, respectively. Dotted lines show noise floor. Depending on the location of f_2 within the fine structure (minimum or maximum), suppression near $2f_1-f_2$ can either increase or decrease the emission amplitude; for suppressor levels around 55 dB SPL, all DP amplitudes converge to a common value.

structures have shapes that gradually change between the two extremes described above (Fig. 1 b–h).

Summarizing, the effect of a low level suppressor (region 1) depends on the position within the DP fine structure. Intermediate suppressor levels (region 2) always clamp DP amplitude to a value independent of fine structure. High suppressor levels (region 3) always produce a large decrease of DP amplitude.

Recording DP-gram fine structure while presenting an intermediate level suppressor (55 dB SPL) results in a flat DP-gram (Fig. 2). The mean amplitude of this DP-gram lies between the minimum and maximum of the original rippling pattern.

Fine structures with less pronounced or less regular rippling patterns will also be flattened in the presence of an intermediate suppressor level (Fig. 3, rows 4 and 5). All the corresponding sets of SGF traces converge at the level of the ''true'' DP amplitude for a suppressor level of 50–60 dB.

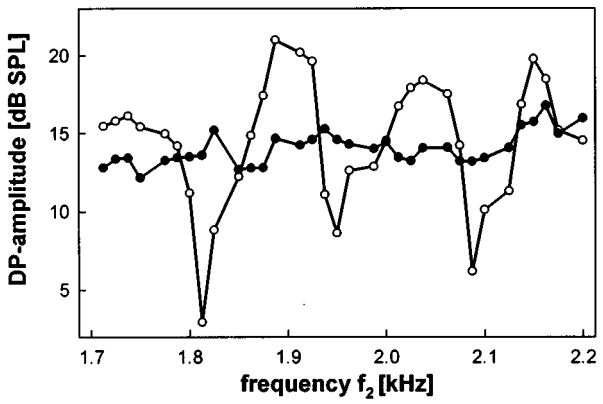

FIG. 2. DP-gram fine structure with conventional DPOAE measurement (open circles) and with a 55 dB SPL suppressor 25 Hz above $2f_1-f_2$ (filled circles). The new measurement paradigm greatly reduces the prominent rippling of the DP-gram fine structure, presumably by suppressing the interfering second generator at $2f_1-f_2$.

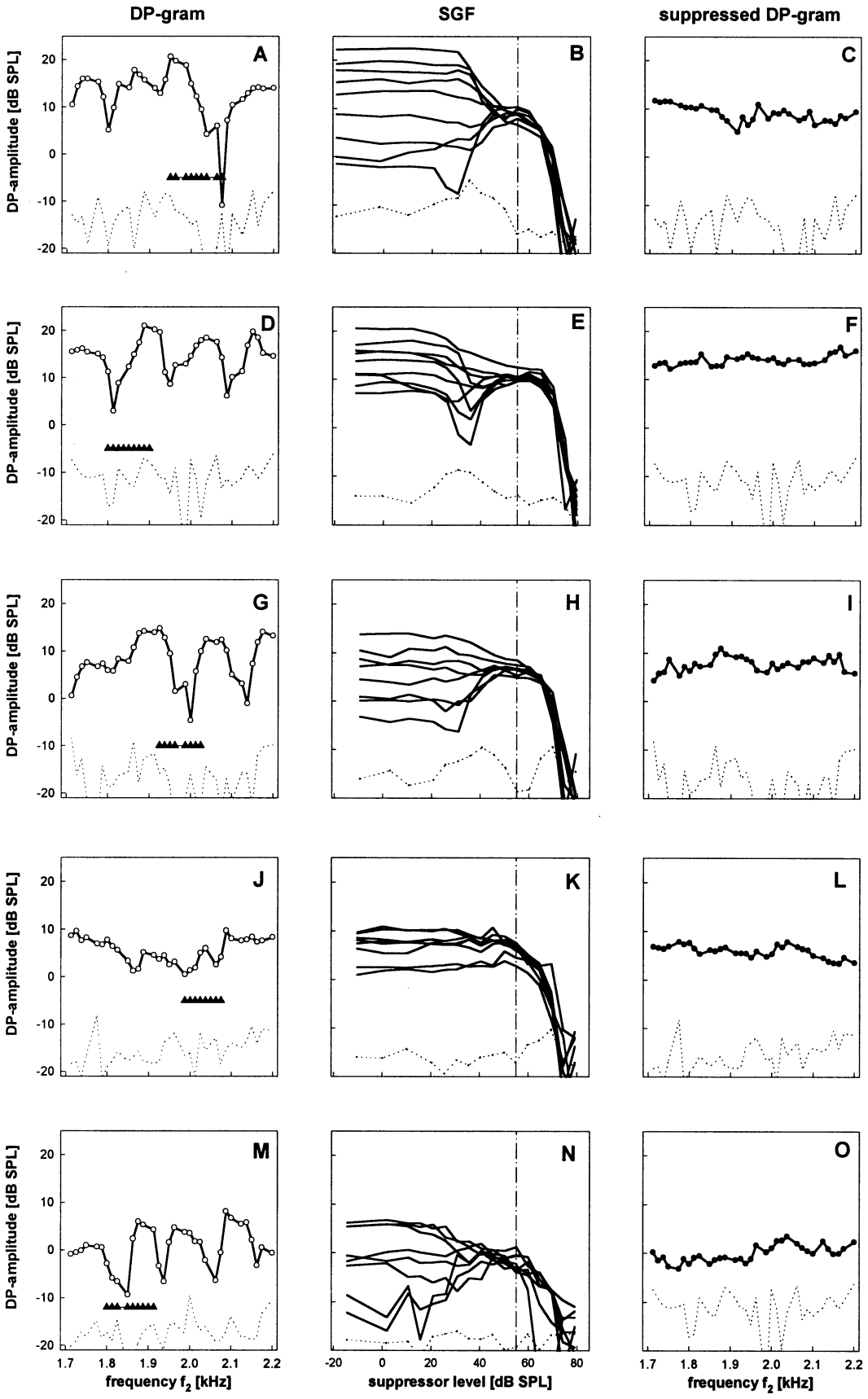

FIG. 3. Conventional DP-gram fine structure (left column), suppression growth functions (SGF, middle column) and sgDPOAE DP-gram fine structure (right column) in five ears (rows 1–5). Triangles in left graphs mark f_2 primary frequencies used in the SGF graphs. Dotted lines show noise floor. In all cases, a 55 dB SPL (vertical line in SGF graphs) suppressor near $2f_1-f_2$ removes the rippling pattern of the DF-gram fine structure.

III. DISCUSSION

Stimulation of the cochlea with two tones f_1 and f_2 leads to a distortion product (DPOAE) with the frequency of $2f_1-f_2$. Adding a third tone close to $2f_1-f_2$ can influence the amplitude of DPOAE, even for low tone levels. The third tone can either increase or decrease the emission amplitude depending on the tone level and on the position in the DP-gram fine structure. High DP amplitudes (fine structure peaks) are decreased by low or intermediate level third tones, whereas low DP amplitudes (fine structure dips) are increased in response to the same stimulus. High level stimuli will always suppress the emission irrespective of the position in the fine structure.

This suppression behavior can be explained by assuming the existence of two separate generators for the $2f_1-f_2$ emission. The first generator resides in the region of overlap of f_1 and f_2. The DP generated here propagates throughout the cochlea and excites the place with the characteristic frequency $2f_1-f_2$, leading to a psychoacoustic perception. Presumably, this tonal excitation at $2f_1-f_2$ will evoke an active cochlear response (stimulus frequency otoacoustic emission, SFOAE). Both the DPOAE generated between f_1 and f_2 and the SFOAE generated at $2f_1-f_2$ propagate toward the oval window.

The result of the interference of these two sine wave oscillations of equal frequency can be recorded in the external ear canal. Depending on the relative phase between the two signals, the result can be either larger (constructive interference) or smaller (destructive interference) than the individual signals (Kemp and Chum, 1980; Shera and Zweig, 1991; Zweig and Shera, 1995). If the phase between the two generators gradually varies along the cochlea, this results in the interference pattern of Fig. 4A, which closely resembles the actual fine structure measured in many ears (Fig. 4B; from Heitmann *et al.*, 1996). According to this theory, peaks in the fine structure are caused by constructive interference of the two generators, and dips are due to destructive interference. Suppressing the secondary generator will therefore decrease the overall amplitude at a maximum and vice versa.

Low level tones (up to 50 dB SPL) near $2f_1-f_2$ will lead to a locally restricted excitation pattern on the basilar membrane; this will suppress the secondary generator, leaving only the response from the primary generator to be recorded in the external ear canal. Further increase of the suppressor level up to 65 dB SPL can have no further effect at $2f_1-f_2$ and will be too weak to influence the distant primary generator. High suppressor levels above 65 dB SPL start to suppress the primary generator, perhaps due to their wide traveling wave envelope which extends to the f_2 site.

A range of intermediate suppressor levels can be specified which completely suppress the secondary generator without influencing the primary generator. DPOAE recorded with these intermediate suppressor levels result in a smoothed DP-gram without any rippling (Fig. 2). Emissions recorded while presenting such an intermediate suppressor tone depend only on cochlear status near f_2 and not at $2f_1-f_2$. We propose to call the new stimulus regime ''single generator'' distortion product otoacoustic emissions (sgDPAOE).

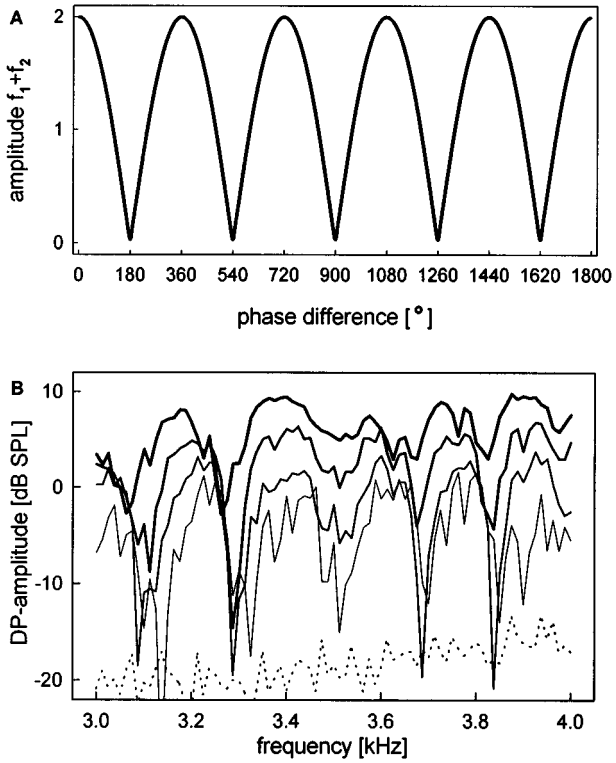

FIG. 4. Interference between two sine waves produces sharp minima and shallow peaks (A, simulation) depending on relative phase (overall amplitude proportional to $|\cos \varphi/2|$). This pattern closely resembles the actual DP-gram fine structure (B, data from a single ear, from Heitmann *et al.*, 1996).

IV. CONCLUSION

In contrast to conventional DP measurements, single generator DPOAE make a frequency specific statement about a single region in the cochlea, the site of the primary generator. The ''single generator DP-gram'' may even show a closer correlation to auditory threshold and thus improve objective audiometry.

ACKNOWLEDGMENTS

Kerstin Just helped with the experiments. The project was supported by BMBF 01VJ93127.

Brown, A. M., and Kemp, D. T. (**1983**). ''Otoacoustic emissions: the iso-suppression tuning properties of the distortion product $2f1-f_2$ in gerbil and man,'' Br. J. Audiol. **17**, 123–124.

Harris, F. P., Lonsbury-Martin, B. L., Stagner, B. B., Coats, A. C., and Martin, G. K. (**1989**). ''Acoustic distortion products in humans: systematic changes in amplitudes as a function of $f2/f1$ ratio,'' J. Acoust. Soc. Am. **85**, 220–229.

Harris, F. P., Probst, P., Plinkert, P. K., and Xu, L. (**1993**). ''Influence of interference tones on $2f_1-f_2$ acoustic distortion products,'' in *Biophysics of Hair Cell Sensory Systems*, edited by H. Duifhuis, J. W. Horst, P. van Dijk, and S. M. van Netten (World Scientific, Singapore), pp. 87–93.

He, N.-J., and Schmiedt, R. A. (**1993**). ''Fine structure of the $2f1-f2$ acoustic distortion product: changes with primary level,'' J. Acoust. Soc. Am. **94**, 2659–2669.

He, N.-J., and Schmiedt, R. A. (**1996**). ''On the generation site of the fine structure of $2f1-f2$ acoustic distortion product,'' Association for Research in Otolaryngology **179** (Abstract).

Heitmann, J., Waldmann, B., and Plinkert, P. K. (**1996**). ''Limitations in the use of distortion product otoacoustic emissions in objective audiometry as the result of fine structure,'' Eur. Arch. Otorhinolaryngol. **253**, 167–171.
Jones, A. T. (**1935**). ''The discovery of difference tones,'' Am. Phys. Teacher **3**, 49–51.
Kemp, D. T. (**1979**). ''Evidence of mechanical nonlinearity and frequency selective wave amplification in the cochlea,'' Arch. Otorhinolaryngol. **224**, 37–45.
Kemp, D. T., and Chum, R. A. (**1980**). ''Properties of the generator of stimulated acoustic emissions,'' Hearing Res. **2**, 213–232.
Kummer, P., Janssen, T., and Arnold, W. (**1995**). ''Suppression tuning characteristics of the $2f_1-f_2$ distortionproduct otoacoustic emission in humans,'' J. Acoust. Soc. Am. **98**, 197–210.
Shera, C. A., and Zweig, G. (**1991**). ''Reflection and retrograde waves within the cochlea and at the stapes,'' J. Acoust. Soc. Am. **89**, 1290–1305.
Stover, L. J., Neely, S. T., and Gorga, M. P. (**1996**). ''DPOAE ''filter'' responses from hearing impaired subjects,'' Association for Research in Otolaryngology **178** (Abstract).
Zweig, G., and Shera, C. A. (**1995**). ''The origin of periodicity in the spectrum of evoked otoacoustic emissions,'' J. Acoust. Soc. Am. **98**, 2018–2047.

Temperature measurements inside the oscillatory boundary layer produced by acoustic waves

Guadalupe Huelsz and Eduardo Ramos
Centro de Investigación en Energía, UNAM, A.P. 34, 62580, Temixco, Morelos, Mexico

(Received 13 January 1997; accepted for publication 3 November 1997)

In this work experimental techniques developed for acoustic temperature oscillation measurements in gases using a cold wire anemometer are reported. The techniques also proved accurate for measuring of the relative phase between temperature and pressure oscillations. Specifically, the structure of the oscillatory thermal boundary layer with isothermal conditions in the solid boundary of an acoustic standing wave in air with 130-Hz frequency and pressure oscillation amplitude up to 200 Pa is determined. Experimental results are satisfactorily compared to theoretical results of a linear theory. © *1998 Acoustical Society of America.* [S0001-4966(98)03402-X]

PACS numbers: 43.58.Vb [SLE]

INTRODUCTION

The interaction of a sound wave in a compressible fluid in contact with solid boundaries produces thermoacoustic effects: acoustic power production and heat flux. These effects have practical importance due to their applications in thermoacoustic engines and refrigerators, respectively.[1] Measurements inside the oscillatory thermal boundary layer are of interest because the acoustic power production and the hydrodynamic heat flux takes place inside it.[2] Moreover, the relative phase between temperature and pressure oscillations in standing waves are related to the interpretation of the acoustic power production given by Rayleigh.[3–5]

A sound wave in a compressible fluid consists of coupled displacement, density, pressure, and temperature oscillations. The frequency of these oscillations, in the audible range, runs from 20 to 20 000 Hz. The amplitude of the temperature oscillation is proportional to the amplitude of the pressure oscillation and for air at room conditions, the temperature oscillation amplitude is very small. For example, for pressure oscillation with amplitude of 200 Pa, the temperature oscillation amplitude is about 0.05 °C. Near the solid boundary, the temperature oscillation amplitude reduces due to the solid thermal inertia, producing the thermal boundary layer. Therefore, in order to measure temperature oscillations due to acoustic waves, especially in the thermal boundary layer, a sensitive instrument with extremely low thermal inertia has to be used. Besides, this boundary layer depth is very small ($\sim 10^{-4}$ m), and in order to have good spatial resolution, the sensor has to be at least two orders of magnitude smaller than the boundary layer depth.

Taking into account these conditions, the ''cold wire anemometer'' (or ''constant current anemometer'') has been suggested as a convenient instrument that complies with the requirements of small thermal inertia, sensitivity, and size. The ''cold wire anemometer'' is not really an anemometer, but takes its name from a very similar instrument, the ''hot wire anemometer'' used to measure flow velocities in gases.[6] In order to measure temperature fluctuations, the wire overheat is much smaller than that used for velocity measurement and thus the name ''cold wire anemometer.'' Currently, to measure velocities, a constant temperature in the wire is maintained using an electronic circuit. In contrast, if the temperature is to be measured, it is more convenient to maintain constant the electric current through the wire, thus the alternative name of ''constant current anemometer.'' The ''cold wire anemometer'' is extensively used in turbulent flow measurements; also, it has been used to measure temperature fluctuations in nonisothermal gases with zero time-average velocity.[7] Højstrup *et al.*[8] used acoustic waves for the dynamic calibration of cold wire anemometers in still air. They made measurements of the magnitude of the transfer function[9] for frequencies up to 10 kHz. They also reported the magnitude of the temperature oscillation near a wall, but they did not report any phase measurements.

In this work experimental techniques for acoustic temperature oscillation measurements using a cold wire anemometer and for the measurement of the relative phase between temperature and pressure oscillations are developed. Measurements inside the oscillatory thermal boundary layer produced by a standing acoustic wave, with isothermal conditions in the solid boundary, are presented and satisfactorily compared to theoretical results[4] based on a linear theory developed by Rott[10] and Swift.[2] The main assumptions made in the theoretical model are the existence of a one-dimensional acoustic standing wave of angular frequency ω propagating parallel to the wall, the two-dimensional boundary layer approximation, and the neglect of body forces.

I. EXPERIMENTAL SETUP

The experimental facility used to perform the measurements is shown schematically in Fig. 1. It consists of the following main components: waveguide, instrumentation, data acquisition and analysis system, and auxiliary equipment.

A. Waveguide

The waveguide used is a duct with a rectangular internal cross section of $0.098\,\text{m}\times 0.054\,\text{m}$ and 0.60 m internal length. These dimensions satisfy the requirements for the establishment of a one-dimensional wave inside a waveguide.[11] One end ($x^*=0$) is closed with a massive coldroll cap, while a loudspeaker is placed at the other end

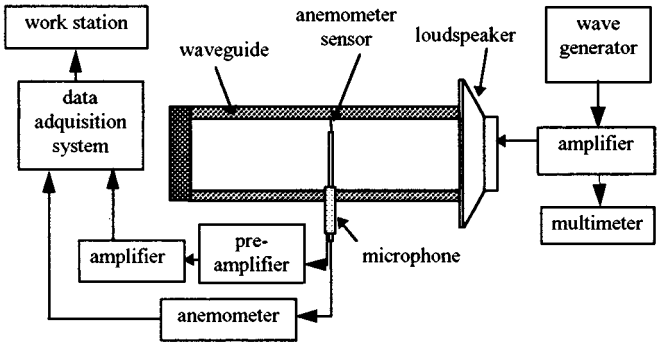

FIG. 1. Experimental setup.

($x^* = 0.60$ m). The loudspeaker input signal is provided by a Wavetek model 29 function generator and amplified by a Onkyo model PI amplifier. There is a flexible foam junction between the loudspeaker and the waveguide and they are mounted on two separate tables in order to reduce unwanted vibrations from the loudspeaker to the waveguide. The waveguide vertical faces are made of transparent plexiglas in order to permit visualization inside the duct; the top and bottom walls are made of Naylamid. Due to future uses of this system, a patch of ceramic material was imbedded in the wall at the location at which boundary layer measurements were made. The waveguide is filled with air at atmospheric pressure. Eight ports are located along the waveguide bottom wall to flush mount the microphone. Whenever a port is not in use, it is closed with a rubber plug. Also, the anemometer probe support is introduced at the central part of the waveguide bottom wall. With this arrangement, all ports are properly sealed and they do not modify the acoustic properties of the wave.

B. Instrumentation

The pressure oscillations are measured with a $\frac{1}{2}''$-diam, Brüel & Kjaer 4165 model condenser microphone, connected to a B&K 2619 model preamplifier and a B&K 2610 model measuring amplifier. The microphone with the preamplifier is conventionally calibrated using a B&K 4230 model calibrator system, obtaining a sensitivity of 43.5 ± 0.2 mV/Pa. The temperature oscillations are measured with a DISA M55 cold wire anemometer, using Dantec 55P11 probes with 1-μm diam Wollaston wire. In all experiments, the cold wire anemometer is operated with a constant current of 0.200 ± 0.005 mA. For these conditions, the wire overheat[12] is very small (2.4×10^{-4}), thus the sensitivity of the wire to velocity fluctuations was expected to be negligible.[13] This was experimentally confirmed by setting the probe at a different axial position along the standing acoustic wave, where the ratio between the amplitude of temperature oscillation and the amplitude of velocity oscillation goes from zero to infinity.

C. Data acquisition and analysis system

A Hewlett–Packard 3852A data acquisition system (10^5 samples/second) and a HP 9000-386 work station with the HP-Veetest code are used to register microphone and cold wire anemometer output signals. The data analysis is made with the same work station and code.

D. Auxiliary equipment

The cold wire anemometer sensor is placed in a desired position with an XYZ Melles–Griot micrometric positioning device. This device has a 0.01 mm precision in all directions.

II. DEVELOPMENT OF THE MEASURING TECHNIQUES

The experimental techniques for temperature oscillations measurements and for measuring the relative phase between temperature and pressure oscillations in acoustic waves were developed according to the following steps.

A. Acoustic standing wave

The natural frequency of the waveguide is found according to the following procedure. Setting a constant amplitude harmonic wave in the wave generator, the frequency is varied to find the resonance frequency (f^*) of the waveguide–loudspeaker system, the maximum amplitude registered by the microphone determines a resonance frequency value of $f^* = 130 \pm 1$ Hz. All the tests are performed at this frequency. The existence and properties of a quarter-wavelength acoustic standing wave inside the waveguide are verified by measuring the amplitude of the pressure oscillations as a function of the axial position for different amplitudes of the loudspeaker input signal. The wavelength (λ^*) is determined making a fitting to the experimental data, resulting in $\lambda^* = 2.65 \pm 0.01$ m. The pressure amplitude at the antinode (p_A^*) can vary up to 200 Pa (140 dB). Besides, the Fourier analysis of the microphone output signal shows that, in this range, the wave is basically monochromatic, the second harmonic contribution being less than 2% and the high-frequency noise less than 0.1%.

B. Cold wire anemometer calibration

First, a narrow-band pass filter (127.5 to 132.5 Hz) is used to select the desired 130-Hz frequency of the cold wire anemometer output signal. This process eliminates all unwanted noise contamination, mostly due to electric and electronic noise. The calibration of the cold wire anemometer response to the acoustic temperature oscillations is made using, as the reference, the temperature oscillation amplitude calculated ($T^*_{a\,\mathrm{calc}}$) through the measurement of the local pressure oscillation amplitude (p_a^*) and their relation in adiabatic conditions[14]

$$T^*_{a\,\mathrm{calc}} = \frac{\beta_m T_m^*}{\rho_m^* C_p}\, p_a^*, \tag{1}$$

where T_m^* is the time-average temperature, and β_m, ρ_m^*, and C_p are, respectively, the thermal expansion coefficient, the density, and the isobaric specific heat of air at T_m^*.

The cold wire anemometer probe is put at the center of the waveguide cross section, where adiabatic conditions can be confidently assumed. Making use of the fact that in a

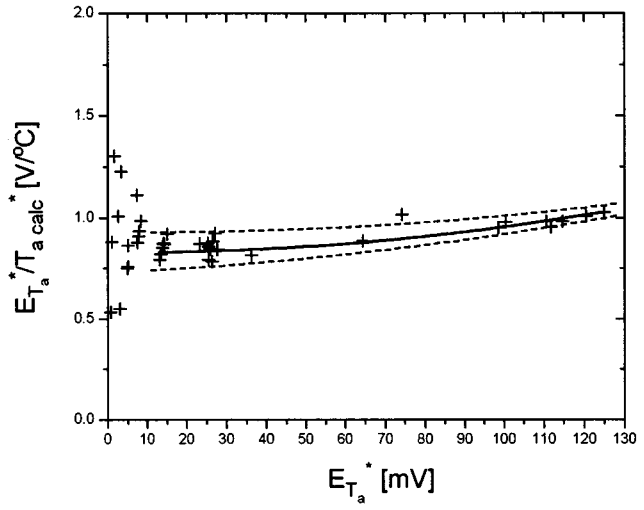

FIG. 2. Response of the cold wire anemometer using a sensor with $R_{T_{\text{amb}}} = 56\,\Omega$) as the ratio of the output voltage amplitude over the calculated temperature oscillation amplitude ($E^*_{T_a}/T^*_{a\text{calc}}$) plotted as a function of the anemometer output voltage amplitude ($E^*_{T_a}$). The magnitude of the associated uncertainty to each individual experimental point is not significant. Data fitting determines the calibration curve $E^*_{T_a}/T^*_{a\text{calc}} = 0.83 + 0.000E^*_{T_a} + 0.00001E^{*2}_{T_a} \pm (0.1 - 0.0005E^*_{T_a})$

one-dimensional wave the pressure oscillation only depends on the axial coordinate and does not depend on transversal coordinates, the microphone is sealed flush mounted in the bottom waveguide wall at the same axial position of the anemometer ($x = 2\pi x^*/\lambda^* = 0.24\pi$).

Figure 2 shows the response of the cold wire anemometer using a sensor with ambient temperature resistance of $R_{T_{\text{amb}}} = 56\,\Omega$ as the ratio of the output voltage amplitude over the calculated temperature oscillation amplitude ($E^*_{T_a}/T^*_{a\text{ calc}}$) plotted as a function of the anemometer output voltage amplitude obtained by varying the amplitude of the acoustic wave of 130 Hz frequency. Scatter of less than $\pm 17\%$ is observed for $E^*_{T_a} > 10$ mV ($T^*_{a\text{ calc}} > 0.012\,^\circ$C), while for $E^*_{T_a} < 10$ mV the scatter presents a considerable increase (up to 100%), therefore, only measurements in the range $E^*_{T_a} > 10$ mV are considered. A minimum squares fitting to data over this range determines the calibration equation. It must be stressed that the calibration equation depends on both the specific cold wire sensor and the acoustic wave frequency. The dependence of $E^*_{T_a}/T^*_{a\text{ calc}}$ on output voltage $E^*_{T_a}$ is due to the nonlinearity response of the amplifier of DISA55M system.[15]

C. Phase difference measurements

The phase difference between the microphone and anemometer output signals (α_{exp}) is measured in two ways, both of which use the filtered signals. In the first method, use is made of the following equation:

$$|\alpha_{\text{exp}}| = \arccos\left(\frac{2}{E^*_{p_a}E^*_{T_a}\Delta t^*}\int_0^{\Delta t^*} E^*_p(t)E^*_T(t)\,dt^*\right), \tag{2}$$

where $E^*_p(t)$ is the voltage output filtered signal from microphone and $E^*_{p_a}$ is its amplitude. Here, $E^*_T(t)$ is the voltage output filtered signal from anemometer and $E^*_{T_a}$ is its respective amplitude. Δt^* is the sampling period. The sign of α_{exp} is determined by visually observing the output filtered signals. By definition, a positive α_{exp} means an anemometer signal lag with respect to the microphone signal.

The second way of obtaining α_{exp} is using a fast Fourier transform that gives information about the phase of Fourier components of the signal. The phase difference is just the subtraction between the anemometer 130 Hz component phase (α_T) and the microphone 130-Hz component phase (α_p): $\alpha_{\text{exp}} = \alpha_T - \alpha_p$.

Results obtained by both methods coincide in all cases with a maximum error of $\pm 5.5 \times 10^{-4}\pi$, which is typically less than 0.03% of the whole range.

D. Temperature and pressure oscillations phase difference calibration

In adiabatic conditions, the temperature and pressure oscillations of an acoustic wave have zero phase difference. Nevertheless, setting the cold wire anemometer probe in the center of the waveguide cross section and the microphone in the bottom waveguide wall at the same axial position, as discussed in Sec. II, the phase difference between the microphone and anemometer output signals is not zero. This phase difference will be denominated base phase difference (α_b). There is a clearly identifiable source of dephasing and consists of the lag in the acquisition of each temperature value with respect to the pressure. This delay is 10^{-5} s, equivalent to a phase difference of 0.003π. α_b was measured for different amplitudes of the loudspeaker input signal finding that it depends on the amplitude of the acoustic wave and is of order 0.125π. In all measurements realized in adiabatic conditions, pressure and temperature amplitudes change proportionally [see Eq. (1)], but this is not the case in boundary layer measurements. According to B&K microphone[16] and amplifier[17] specifications, there is no phase difference between pressure oscillation and voltage output signal for frequencies smaller than 1 kHz. Thus the value of $\alpha^*_b = \alpha_b - 0.003\pi$ is only due to the cold wire anemometer. In order to investigate whether this phase difference is due to the heat transfer to the wire or is due to the system electronics, a two-dimensional heat transfer analysis for the wire, neglecting the convective heat transfer (justified by the small overheat value) but considering the effect of the stubs and prongs,[18–20] was carried on. The phase difference between the temperature oscillation of air and the temperature in the platinum wire obtained by this analysis is -0.009π, which is much smaller than α^*_b. The analysis of the available circuits diagrams allows the acceptance of a possible phase shift due to electronics up to $\pi/4$, but no definitive conclusion can be reached. According to these results, the value of α^*_b is assumed to be due to the system electronics and that it is only a function of the voltage output signal amplitude of the cold wire anemometer. Figure 3 shows typical results for $\alpha_b(E^*_{T_a})$. As before, only measurements with $E^*_{T_a} > 10$ mV are considered where maximum error is less than $\pm 0.05\pi$.

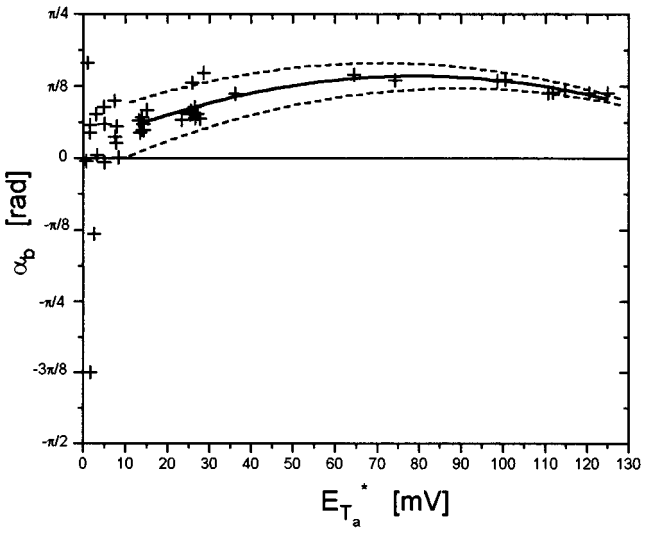

FIG. 3. Base phase difference (α_b) as a function of the anemometer output voltage amplitude ($E_{T_a}^*$). The magnitude of the associated uncertainty to each individual experimental point is not significant. Data fitting determines the calibration curve: $\alpha_b = 0.02\pi + 0.003\pi E_{T_a}^* - 0.000019\pi E_{T_a}^{*2} \pm (0.05\pi - 0.0004\pi E_{T_a}^*)$

To obtain the relative phase between temperature and pressure oscillations (α) the base phase is subtracted from the phase difference between the microphone and anemometer output signals: $\alpha = \alpha_{\text{exp}} - \alpha_b$.

It must be pointed out that increasing the ambient temperature resistance of the sensor ($R_{T_{\text{amb}}}$), the sensitivity of the probe is increased, and, therefore, the scatter in the plot of α_b as a function of $E_{T_a}^*$ (Fig. 3) is reduced. But at the same time, the scatter in the $E_{T_a}^*/T_{a\,\text{calc}}^*$ plot as a function of $E_{T_a}^*$ (Fig. 2) increases for high values of $R_{T_{\text{amb}}}$. This behavior is due to the fact that a sensor having a higher $R_{T_{\text{amb}}}$ has a longer section of the Wollaston wire that has been etched to remove the silver cover and that it has a 1-μm diameter. Therefore, the sensor has a longer sensitive zone, but also is more fragile and susceptible to vibrations. Best results in amplitude and phase calibrations are obtained for $R_{T_{\text{amb}}} \sim 60\ \Omega$.

III. MEASUREMENTS IN THE OSCILLATORY THERMAL BOUNDARY LAYER

The experimental techniques described in the previous sections were used to determine the structure of the thermal boundary layer generated by the interaction of a standing acoustic wave with a rigid, isothermal boundary. Also, the relative phase between temperature and pressure oscillations inside the oscillatory thermal boundary was obtained as a function of the distance to the wall. As it was mentioned in the Introduction, this last quantity is of relevance in the study of the thermoacoustic effect.

The standing wave was generated inside the waveguide described in Sec. I A. Data were obtained in four different experiments, using two local pressure oscillation amplitudes ($p_a^* = 20$ and 123 Pa). In all of them the time-averaged temperature of the air was $T_m^* = 23\ ^\circ\text{C} \pm 1\ ^\circ\text{C}$ and the frequency of oscillation was 130 ± 1 Hz as dictated by the length of the waveguide. The microphone is flush mounted at the bottom waveguide wall and the cold wire anemometer sensor is at the same axial position, 0.314 m from the rigid end ($x = 0.24\pi$). Before each experiment was realized, a previous calibration of the cold wire anemometer sensor used was made. In all of the experiments, the cold wire anemometer sensor distance to the plate (y^*) is varied and it is reported in a nondimensional form $y = y^*/\delta_k$, where δ_k is the thermal boundary layer depth defined by $\delta_k \equiv \sqrt{2k/\rho_m^* C_p \omega^*}$, k being the thermal conductivity of air and ω^* the angular frequency $\omega^* = 2\pi f^*$. Also, temperature oscillation amplitude results are reported in a nondimensional form $T_a = T_a^*/T_{a\text{calc}}^*$.

The structure of the thermal boundary layer was found by recording the amplitude of the temperature oscillation as a function of the distance to the wall. The results are shown in Fig. 4. The maximum error bar is calculated from the uncertainties due to the cold wire anemometer calibration (see Fig. 2). The value of T_a^* attained at $y \gg 1$ coincides with $T_{a\text{calc}}^*$ ($T_a \to 1$) within the experimental bar in all cases, as it must for a standing wave far away from rigid boundaries. The boundary layer extends to approximately $3\delta_k$ and data could be obtained as close as $0.8\delta_k$ in the 20-Pa case and up to $0.06\delta_k$ in the 123-Pa case. No further approach was possible in the 20-Pa measurements because the anemometer output signal amplitude was less than 10 mV, and data were not considered reliable as discussed in Sec. II 2. The largest scatter of data was found near the edge of the boundary layer. The structure of the thermal boundary layer is neatly defined as a region starting with a temperature with $T_a \sim 0.1$ at $y \sim 0$ and then displaying a large temperature gradient that levels off at $y \sim 3\delta_k$.

Experimental data are compared with theoretical results obtained with a simplified theory and reported in a previous paper.[4] The theory indicates that the expression for the temperature amplitude in the boundary layer next to a constant temperature wall is $T_a(y) = 1 - (e^{-y}\ \cos y)/(1+\epsilon)$ where ϵ is a parameter that relates fluid and solid properties and is defined by $\epsilon = \sqrt{k\rho_m^* C_p / k_s \rho_s^* C_s}$. Air properties are substituted by their corresponding value at time-average temperature. Properties of the wall material are not known with accuracy, but ceramics in air are estimated to have $\epsilon \sim 0.01$.[20] In Fig. 4, the theoretical curve using this value is given. The coincidence of theoretical result with the experimental observations is excellent. The experimental error prevents us from discerning which value of ϵ is the best fit. For the same reason, the shallow local maximum predicted by the theory could not be confirmed by the experimental observations. Included in this figure are experimental points obtained by Højstrup *et al.*[8] for $1 < y < 6$. Their results are in coincidence with those obtained in the present study.

Figure 5 shows the relative phase between temperature and pressure oscillations (α) as a function of the distance to the wall, for the same experiments presented in the previous paragraphs. At $y > 4$, the relative phase is zero, evidencing the presence of a standing, adiabatic wave. In the region $1 < y < 4$, $\alpha(y)$, diminishes monotonically and at $y \sim 0.5$, the data display a minimum with an approximate value of

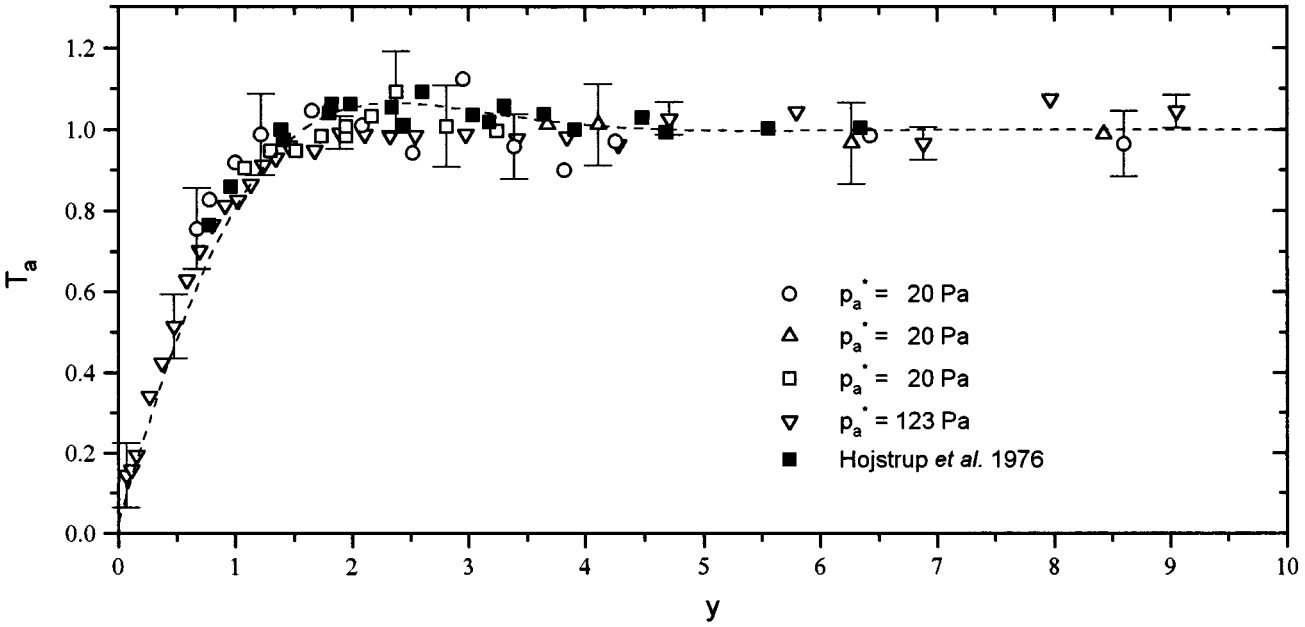

FIG. 4. Nondimensional temperature oscillation amplitude (T_a^*) as a function of the nondimensional distance to the plate (y). Line corresponds to theoretical prediction, using $\epsilon = 0.01$. Maximum estimated experimental uncertainty is indicated for representative points.

$-3\pi/16$. The relative phase approaches zero with a steep gradient as $y \to 0$. A maximum error bar is also reported in the figure, and it has been found that the main source of error is associated to the uncertainty estimated for the base phase difference (see Fig. 3). Due to the regularity of the data points, it is believed that the actual error involved is much smaller than the error reported formally. Also shown in Fig. 5 is the theoretical curve for $\alpha(y)$ calculated using the expression in Huelsz and Ramos[4] with $\epsilon = 0.01$. As can be appreciated, the qualitative agreement is very good, confirming the validity of the approximations made in the theory. Experimental errors prevent us from discerning the precise value of ϵ that best fits the experimental observations; $\epsilon = 0.01$ gives a maximum difference between theoretical and experimental values of 0.06π.

IV. CONCLUSIONS

Experimental techniques were developed for measuring temperature oscillation using a cold wire anemometer. The same techniques could also be used to determine the relative phase between temperature and pressure oscillations in

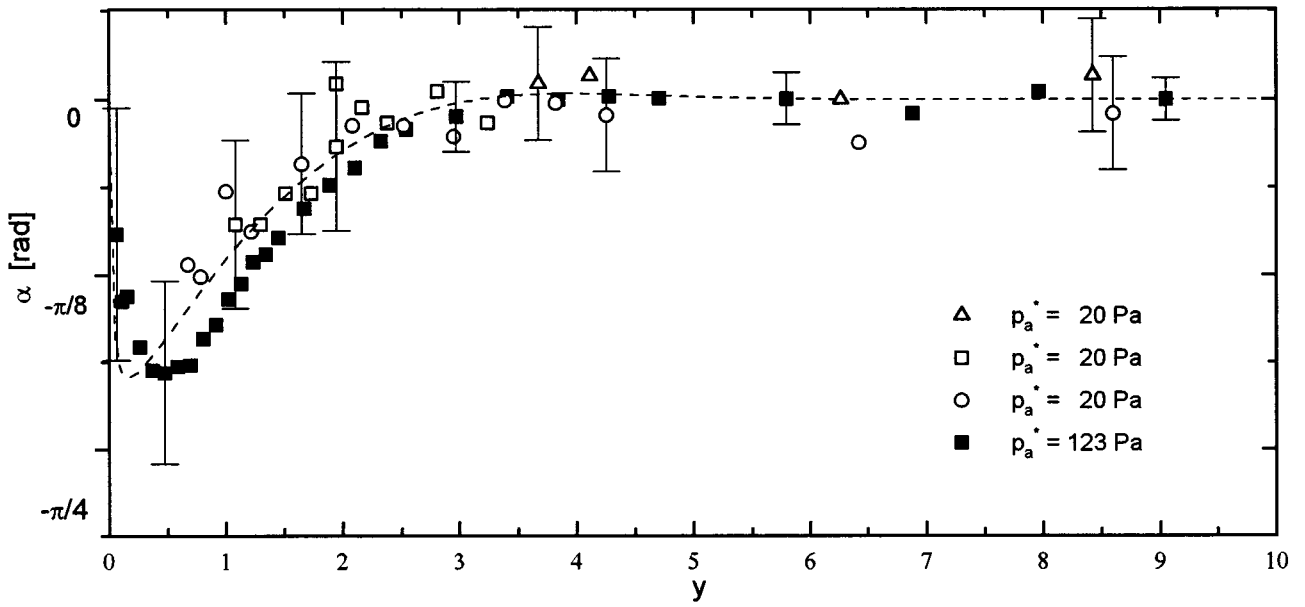

FIG. 5. Phase difference between temperature and pressure oscillations as a function of the nondimensional distance to the plate (y). Line corresponds to theoretical prediction using $\epsilon = 0.01$. Maximum estimated experimental uncertainty is indicated for some representative points.

acoustic waves. The amplitude of the temperature oscillation in the thermal boundary layer produced by a standing acoustic wave in air with isothermal conditions in the solid boundary was precisely mapped and the structure of the boundary layer determined to have a thickness of approximately $3\delta_k$. Also, the relative phase of the temperature and pressure oscillations could be recorded as a function of the distance to the plate. The profile is nonmonotonic with a minimum at a distance of approximately $0.5\delta_k$ from the wall. Qualitative agreement with the simplified theory[4] based on Rott[10] and Swift[2] works is very good.

ACKNOWLEDGMENTS

Useful discussions with Professor Mihir Sen from Notre Dame University, Professor Zellman Warhaft and Mr. Edward Jordan of Cornell University, Professor Ricardo Ruiz Bullosa from CI-UNAM, and Professor Raúl Espejel from IF-UNAM are gratefully acknowledged. This work has been partially supported by CONACYT under project G0044E.

[1] G. W. Swift, ''Thermoacoustic engines and refrigerators,'' Phys. Today **48**(7), 22–28 (1995).
[2] G. W. Swift, ''Thermoacoustic engines,'' J. Acoust. Soc. Am. **84**, 1145–1180 (1988).
[3] Lord Rayleigh (J. W. Strutt) *The Theory of Sound* (Dover, New York, 1945), 2nd ed., Vol. 2, Sec. 322.
[4] G. Huelsz and E. Ramos, ''On the phase difference of the temperature and pressure waves in the thermoacoustic effect,'' Int. Commun. Heat Mass Transf. **22**(1), 71–80 (1995).
[5] G. Huelsz and E. Ramos, ''A physical interpretation of the thermoacoustic effect,'' J. Non Equilibrium Thermodyn. **21**(3), 278–284 (1996).
[6] H. H. Bruun, *Hot Wire Anemometry. Principles and Signal Analysis* (Oxford Science, Oxford, UK, 1995).
[7] J. C. LaRue, T. Deaton, and C. H. Gibson, ''Measurement of high-frequency turbulent temperature,'' Rev. Sci. Instrum. **46**, 757–764 (1975).
[8] J. Højstrup, K. Rasmussen, and S. E. Larsen, ''Dynamic calibration of temperature wires in still air,'' DISA Inf. **20**, 22–30 (1976).
[9] The transfer function is defined as the ratio between the wire temperature oscillation and the air temperature oscillation.
[10] N. Rott, ''Damped and thermally driven acoustic oscillations in wide and narrow tubes,'' Z. Angew. Math. Mech. **20**, 230–243 (1969).
[11] L. E. Kinsler, A. R. Frey, A. B. Coppens, and J. V. Sanders, *Fundamentals of Acoustics* (Wiley, New York, 1982), pp. 200.
[12] The wire overheat is defined as $a_m(T_w^*-T_m^*)$, where T_w^* is the time-average temperature of the wire, T_m^* is the time-average temperature of the gas, and a_m is the thermal coefficient of resistance of the wire at T_m^*.
[13] A. J. Smits, A. E. Perry, and P. H. Hoffmann, ''The response to temperature fluctuations of a constant-current hot-wire anemometer,'' J. Phys. E **11**, 909–914 (1978).
[14] H. B. Callen, *Thermodynamics* (Wiley, New York, 1960), pp. 54–56.
[15] DISA, *DISA55M system with 55M20 temperature bridge manual* (DISA, Denmark, 1973).
[16] Brüel & Kjær, *Calibration chart for condenser microphone cartridge type 4165* (Brüel & Kjær, Denmark, 1979).
[17] Brüel & Kjær, *Measuring Amplifier Type 2610, Instruction Manual* (Brüel & Kjær, Denmark, 1979).
[18] C. Petit, P. Paranthoen, and J. C. Lecordier, ''Influence of Wollaston wire and prongs on the response of cold wires at low frequencies,'' Lett. Heat Mass Transf. **8**, 281–291 (1981).
[19] H. E. Boyer and T. L. Gall, *Metals Handbook, Desk Edition* (American Society for Metals, Metals Park, OH, 1985), pp. 13-1 and 1-66.
[20] J. R. Welty, R. E. Wilson, and C. E. Wicks, *Fundamentals of Momentum Heat and Mass Transfer* (Wiley, New York, 1976), pp. 731 and 734.

Inverse imaging of the breast with a material classification technique

Charles W. Manry, Jr.[a)]
Department of the Navy, SPAWARSYSCEN D851 (PL-MR), 53560 Hull Street, San Diego, California 92152-5001

Shira L. Broschat[b)]
School of Electrical Engineering and Computer Science, Washington State University, Pullman, Washington 99164-2752

(Received 18 March 1996; accepted for publication 18 November 1997)

In recent publications [Chew *et al.*, IEEE Trans. Blomed. Eng. **BME-9**, 218–225 (1990); Borup *et al.*, Ultrason. Imaging **14**, 69–85 (1992)] the inverse imaging problem has been solved by means of a two-step iterative method. In this paper, a third step is introduced for ultrasound imaging of the breast. In this step, which is based on statistical pattern recognition, classification of tissue types and *a priori* knowledge of the anatomy of the breast are integrated into the iterative method. Use of this material classification technique results in more rapid convergence to the inverse solution—approximately 40% fewer iterations are required—as well as greater accuracy. In addition, tumors are detected early in the reconstruction process. Results for reconstructions of a simple two-dimensional model of the human breast are presented. These reconstructions are extremely accurate when system noise and variations in tissue parameters are not too great. However, for the algorithm used, degradation of the reconstructions and divergence from the correct solution occur when system noise and variations in parameters exceed threshold values. Even in this case, however, tumors are still identified within a few iterations. © *1998 Acoustical Society of America.* [S0001-4966(98)03803-X]

PACS numbers: 43.60.Pt, 43.60.Lq, 43.58.Bh [JLK]

INTRODUCTION

Breast cancer is a major health issue for women today. In the United States, cancer is the leading cause of death in women ages 35–50 with breast cancer responsible for the majority of cancer-related deaths. In 1995, approximately 182 000 new cases of breast cancer were diagnosed and 46 000 women died from this disease.[1] The earlier a breast tumor is detected, the greater the chance of survival of the victim.[2] If a tumor is detected when it is small (with a diameter of 5 mm or less, a so-called *minimal tumor*), the patient's post-treatment life span is on the order of 20 years, the normal life expectancy of a middle-aged woman.[2] Thus it is critical to develop breast imaging techniques with sufficient resolution to detect small tumors.

In current ultrasound mammography techniques it is assumed that scattering of energy in the breast is weak. This assumption has allowed the development of simple and efficient imaging algorithms. However, recent research has shown that fat lobes near the surface of the breast significantly refract, or bend, the ultrasound energy as it passes through the breast.[3–5] This strong refraction violates the weak scattering assumption. Consequently, to increase the likelihood of detecting minimal tumors, imaging algorithms must account for strong scattering. This requires the use of full-wave inversion techniques.

In recent publications, the full-wave inverse imaging problem has been solved using an iterative approach based on moment methods and the Gauss–Newton (GN) method.[6] This iterative technique (and similar methods[7–12]) assumes that the scattering object is bounded within a region of space but that no additional information is known. It consists of two steps which are repeated in sequence until a termination criterion is satisfied. In the first step, the total field is computed for the scattering object; in the second, the scattering object is updated using the measured scattered fields and the calculated total field. The iterative technique can be computationally expensive since a large number of iterations is typically required to adequately reconstruct the scattering object.

A third step has been developed by the authors to reduce the computational expense. When the scattering object is composed of a known set of materials, but with an unknown configuration, the convergence rate and accuracy of the inverse solution can be increased using *a priori* knowledge of the material characteristics. This is the basis of the third step, material classification. In the classification procedure a histogram is constructed for the tissue loss in the image of the scattering object. Gaussian distributions are fitted to the histogram, and classification decisions are based on the location and spread of the Gaussian modes. The decision process is a Bayes, or maximum likelihood, classifier with an option to reject a classification.[13,14] When the decision is made to accept a classification, a region of the image (pixel sized) is set equal to the appropriate material. When the decision is made to reject a classification, the region is left unmodified.

In this paper, inverse imaging with material classifica-

[a)]Electronic mail: cmanry@spawar.navy.mil
[b)]Electronic mail: shira@eecs.wsu.edu

tion is studied. Simulations are performed using a simple two-dimensional model of the human breast. The model contains both minimal tumors (less than 1 mm in size) and small cysts as well as larger tumors and cysts. It also includes a fat layer. The results show that when the signal-to-noise ratio (SNR) is large and tissue parameter values have little variation, addition of the third step reduces the number of iterations by 40%, reduces the CPU time required by 48%, and increases the accuracy of the reconstructions. However, when the SNR is not large or the spread of the sound velocity in the tissue is appreciable, location of minimal tumors still occurs early in the iterative process but reconstructions are poor. The poor performance is attributed mainly to the use of an approximation in the GN method. This approximation greatly reduces the computational cost of the GN algorithm but at the price of reconstruction accuracy.

In the next section a brief review of the GN inverse imaging technique is presented. In Sec. II, breast tissue parameters are given and discussed. The method for obtaining the initial value for the iterative method is explained in Sec. III, and in Sec. IV the material classification technique is presented. The two-dimensional breast model used in the simulations is described in Sec. V, and the simulation results are presented in Sec. VI. Finally, in Sec. VII, concluding remarks are given and future work is discussed.

I. THE GAUSS–NEWTON ITERATIVE METHOD

In the Gauss–Newton iterative method, we start with the Fredholm integral equations

$$f^{\text{inc}}_{\omega\phi}(\mathbf{x}) = f_{\omega\phi}(\mathbf{x}) - \int_{\infty}^{\infty} f_{\omega\phi}(\mathbf{x}')\,\gamma(\mathbf{x}') \times G(|\mathbf{x}-\mathbf{x}'|)\,d\mathbf{x}', \tag{1}$$

$$f^{s}_{\omega\phi}(\mathbf{x}) = \int_{\infty}^{\infty} f_{\omega\phi}(\mathbf{x}')\,\gamma(\mathbf{x}')\,G(|\mathbf{x}-\mathbf{x}'|)\,d\mathbf{x}', \tag{2}$$

where $\mathbf{x}$ is the two-dimensional position vector, $f^{\text{inc}}_{\omega\phi}(\mathbf{x})$is the scalar incident field, $f_{\omega\phi}(\mathbf{x})$ is the total field, $f^{s}_{\omega\phi}(\mathbf{x}) = f(\mathbf{x}) - f^{\text{inc}}(\mathbf{x})$ is the scattered field, and the subscript $\omega\phi$ indicates that the equations are applied for all source frequencies and positions. The scattering object is given by $\gamma(\mathbf{x}) = k_0^2(k^2(\mathbf{x})/k_0^2 - 1)$, k_0 is the incident wave number, and $k(\mathbf{x}) = \omega/c(\mathbf{x}) + i\alpha(\mathbf{x})$where $c(\mathbf{x})$ is the speed of sound and $\alpha(\mathbf{x})$ is the loss. Finally, $G(|\mathbf{x}-\mathbf{x}'|) = (-i/4)H_0^{(2)}(k_0|\mathbf{x}-\mathbf{x}'|)$ is the two-dimensional Green's function where $H_0^{(2)}$ is the Hankel function of the second kind.[17]

Equations (1) and (2) can be recast in the operator notation of Borup *et al.*:[6]

$$\mathbf{f}^{\text{inc}}_{\omega\phi} = (I - C_{\omega}[/\boldsymbol{\gamma}/])\mathbf{f}_{\omega\phi}, \tag{3}$$

$$\mathbf{f}^{s}_{\omega\phi} = D_{\omega}[/\mathbf{f}_{\omega\phi}/]\boldsymbol{\gamma}, \tag{4}$$

where C_{ω} and D_{ω} are $N\times N$ and $N\times N_d$ matrix operators, respectively, N_d is the number of detectors, and I is the $N\times N$ identity operator. $\boldsymbol{\gamma}$, $\mathbf{f}^{\text{inc}}_{\omega\phi}$, and $\mathbf{f}_{\omega\phi}$ are N-length vectors representing the unknown scattering object, incident field, and total field, respectively, and $\mathbf{f}^{s}_{\omega\phi}$ is of length N_d. The notation $[/\boldsymbol{\gamma}/]$ indicates a diagonal operator that multiplies $\boldsymbol{\gamma}$ with the vector to its right. Field quantity vectors include information for all frequencies and source positions. The total number of measurements in $\mathbf{f}^{s}_{\omega\phi}$ is $M = N_d\times\Omega\times\Phi$ where Ω is the number of frequencies and Φ is the number of source positions.

In a clinical situation, measurements of the scattered field would be obtained in the following manner. A patient would lie face down on a platform. Underneath this platform would be a water tank containing an annular array of equally spaced transducers. The patient's breast would be suspended through a hole in the platform into the water tank and centered in the array. Each transducer would, in turn, transmit a pulse through the breast and the fields would be measured at all transducers, allowing data collection for multiple views of the breast. This setup is similar to the one used in a study at the University of Pennsylvania where linear arrays rather than an annular array were used.[3,4]

Given a scattering object vector $\boldsymbol{\gamma}$ and the incident field vector $\mathbf{f}^{\text{inc}}_{\omega\phi}$, the total field vector $\mathbf{f}_{\omega\phi}$ can be uniquely determined from Eq. (3). This is accomplished using the bi-stabilized fast Fourier transform conjugate gradient method (BI-STAB FFT-CG).[18,19] However, Eq. (4) is ill-posed when both the scattered field vector $\mathbf{f}^{s}_{\omega\phi}$ and the total field vector $\mathbf{f}_{\omega\phi}$ are given,[20] and direct solution for $\boldsymbol{\gamma}$ is not possible. Thus an iterative method is employed to obtain estimates for the object. Here the unknown scattering object $\boldsymbol{\gamma}$ is estimated using the Gauss–Newton method. A Frechet variation (Jacobian) of the difference between the measured scattered field and the estimated scattered field is found with respect to the object. The Jacobian is given by (see Ref. 6 for details)

$$J_{\omega\phi} = \frac{\partial r_{\omega\phi}}{\partial \boldsymbol{\gamma}} = -D_{\omega}(I - [/\boldsymbol{\gamma}/]C_{\omega})^{-1}[/\mathbf{f}_{\omega\phi}/]. \tag{5}$$

Where the residual error is given by $\mathbf{r}^{(i)}_{\omega\phi} = \mathbf{f}^{s(m)}_{\omega\phi} - \mathbf{f}^{s(i)}_{\omega\phi}$, $\mathbf{f}^{s(m)}_{\omega\phi}$ is the measured scattered field, and $\mathbf{f}^{s(i)}_{\omega\phi}$ is the current estimate for the scattered field at the measurement locations. The term $(I - [/\boldsymbol{\gamma}/]C_{\omega})^{-1}$ cannot be found explicitly. It can be calculated using the BI-STAB FFT-CG method, but this requires a large number of additional computations. To reduce the cost, the Jacobian is approximated using a binomial expansion. The final form for this approximation is given by

$$J_{\omega\phi} = \frac{\partial r_{\omega\phi}}{\partial \boldsymbol{\gamma}} = -D_{\omega}(I + [/\boldsymbol{\gamma}/]C_{\omega})[/\mathbf{f}_{\omega\phi}/]. \tag{6}$$

Borup *et al.* have found this approximation to be adequate since it accommodates phase changes for low contrast objects where the magnitude of the object, $|\boldsymbol{\gamma}|$, ranged from 0.0 to 0.1; for these values, refraction is minimal.[6] The breast model used for this work has a similar range of approximately $0.07 \leqslant |\boldsymbol{\gamma}| \leqslant 0.11$. Phase change alone is not enough in this case since it does not account for refraction at the fat–glandular interface.[6] However, for this work it is assumed that a combination of the material classification scheme (see Sec. V) and the binomial approximation for the Jacobian is adequate for imaging complex-valued breast tissues.

A summary of the steps of the Gauss–Newton algorithm follows (see Ref. 6 for details):

TABLE I. Material parameters for tissue types used in the human breast model and the mean value of the imaginary part of the object profile γ.

Tissue	Sound speed [m/s]	Loss [m^{-1}]	Mean
Water	1490.0	0.0	0.0
Cysts	1584.0	0.46	22.55
Fat	1439.0	1.66	82.55
Glandular	1581.0	2.90	128.77
Skin	1586.0	3.36	149.79
Tumors	1573.0	6.58	295.85

(1) For $\boldsymbol{\gamma}^{(i)}$, where the superscript (i) represents the ith iteration, choose an initial value, $\boldsymbol{\gamma}^{(0)}$ and set $i=0$.
(2) Solve the forward operator equation for the current estimate of the total field $\mathbf{f}_{\omega\phi}^{(i)}$ using the estimate for the object $\boldsymbol{\gamma}^{(i)}$:

$$\mathbf{f}_{\omega\phi}^{\text{inc}}=(I+C_{\omega}[/\boldsymbol{\gamma}^{(i)}/])\mathbf{f}_{\omega\phi}^{(i)} \quad \forall\omega,\phi.$$

(3) Compute the residual error:

$$\mathbf{r}_{\omega\phi}^{(i)}=\mathbf{f}_{\omega\phi}^{s(m)}-\mathbf{f}_{\omega\phi}^{s(i)}.$$

(4) If $\Sigma_{\omega,\phi}\|\mathbf{r}_{\omega\phi}^{(i)}\|/\Sigma_{\omega,\phi}\|\mathbf{f}_{\omega\phi}^{s(m)}\|<\epsilon$, the desired convergence limit, then stop.
(5) Solve the following minimization equation for $\partial\boldsymbol{\gamma}^{(i)}$ using the FFT-CG[21] method for N_{inv} iterations using the approximate Jacobian:

$$\min\partial\boldsymbol{\gamma}^{(i)}\sum_{\omega,\phi}\|J_{\omega\phi}^{(i)}\cdot\partial\boldsymbol{\gamma}^{(i)}+\mathbf{r}_{\omega\phi}^{(i)}\|^2.$$

(6) Update $\boldsymbol{\gamma}^{(i)}$: $\boldsymbol{\gamma}^{(i+1)}=\boldsymbol{\gamma}^{(i)}+\partial\boldsymbol{\gamma}^{(i)}$.
(7) Set $i=i+1$. Go to step 2 to start the next iteration.

In step 5 the minimization is performed for a set number of iterations. Normally (as in step 2 for the forward solution) enough iterations are performed to solve the equations to within a chosen error bound. For the inverse minimization (step 5) $\partial\boldsymbol{\gamma}^{(i)}$ conforms to the current estimates of the total field and object if the solution for $\partial\boldsymbol{\gamma}^{(i)}$ is carried out to a small error (large N_{inv}). This makes the iterative GN solution converge to an incorrect answer after only a few iterations. If N_{inv} is too small, the image solution converges very slowly. Thus N_{inv} must be found by trail and error for a given class of objects or images to be reconstructed. The exact requirements for successful reconstruction depend on the number of source frequencies, detectors N_d, and source positions Φ, and vary for each type of problem considered. The computational cost, dominated by FFTs, is on the order of $(4N_{\text{fwd}}+4N_{\text{GN}}N_{\text{inv}})\Phi N\log_2 N$ where N_{GN} is the number of GN steps and N_{fwd} is the total number of iterations in the BI-STAB FFT-CG for all N_{GN} iterations.

II. BREAST MODEL TISSUE PARAMETERS

For imaging of the breast, the material classification technique requires *a priori* knowledge of the mean values of both the loss and speed of sound for each tissue type of interest. The values used in this study are given in Table I. Note that the speeds of sound are similar, approximately 1570 m/s, for all tissue types except fat and water. The sound speed information is used in the imaging procedure, but it is the loss that provides significant distinction between tissue types. In Table I loss is given for a frequency of 400 kHz at body temperatures.[15,16] Tumors have a loss of 6.58 m^{-1} while skin has a loss of 3.19 m^{-1}. Thus tumors can be identified from their high loss relative to the surrounding tissue values. Similarly, cysts have low loss and can be identified relative to the surrounding tissue values.

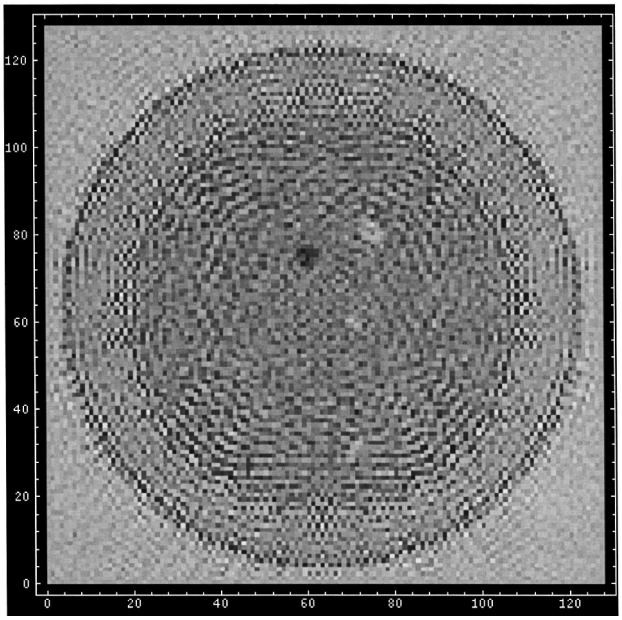

FIG. 1. Loss reconstruction of the 2-D breast model using the approximate GN method and the Born approximation for the initial value. White represents the highest loss (15.42 m^{-1}) and black the lowest loss (-9.13 m^{-1}).

III. CHOICE OF THE INITIAL VALUE

An initial value for the scattering object $\boldsymbol{\gamma}^{(0)}$ is needed for the GN algorithm. Several standard approaches were considered, including use of the Born approximation. In general, these approaches work well for reconstruction of the sound speed, but they do not work well for reconstruction of loss (see Fig. 1). Since reconstruction of loss is required to distinguish tumors, a new approach for obtaining a suitable initial value is needed. The method developed here is based on the difference in sound speeds of tissues together with knowledge of the anatomy of the breast. The human breast can be partitioned roughly into an external skin layer, then a fat layer, and finally a glandular interior. Water and fat have sound speeds that are less than 1500 m/s while skin and glandular tissue have speeds that are over 1500 m/s. This information is used to obtain the initial value for a breast suspended in water and comprised only of skin, fat, and glandular regions.

To obtain the initial value a good estimate of the sound speed profile is needed. This is acquired using the Born approximation or the GN method constrained to real-valued objects only—that is, with the loss set to zero. Once the speed profile is calculated, the water, skin, fat, and glandular regions are located in the following manner: Starting in the center of the image (in the glandular region) march outward at a given angle looking for a change in speed from greater

than 1500 m/s to less that 1500 m/s and record the distance from the center. This corresponds to the fat-glandular boundary. Then continue out toward the skin layer looking for a speed change from less than 1500 m/s to a greater than 1500 m/s and record this distance from the center. Repeat the process for other angles. A decision boundary is then formed using the average value between the inner and outer points at each angle. Once this decision boundary is determined, the water, skin, fat, and glandular regions are easily located. For example, if an image pixel is on or inside the decision boundary for the fat-glandular interface and the speed is greater than 1500 m/s, it is glandular tissue; otherwise, it is fat. Similar rules are used to distinguish the fat and skin layers and the skin from the surrounding water. Once identified, the material in each region is set to the mean loss value listed in Table I, and the initial value is obtained. This method is referred to as the initial classification (IC) method. The results for reconstruction using the IC method are discussed in Sec. VII.

IV. THE MATERIAL CLASSIFICATION TECHNIQUE

The motivation for adding the material classification step, which is used after the update of the image between steps 6 and 7, is to obtain faster convergence. The *a priori* information used to make this step possible includes knowledge of the material parameters and information about the structure of the breast. For example, it is known that skin tissue does not exist in the interior of the breast. When a pixel can be classified as a particular tissue type, it is set to the mean values of the speed and loss for that tissue.

The algorithm used to make the classification decision is the Bayes, or maximum-likelihood, classifier:[13]

$$\mathscr{P}=\mathrm{Max}_C\frac{\rho(C)P(x|C)}{p(x)}, \tag{7}$$

where C is the tissue type or class (e.g., fat, cyst, skin, tumor), $\rho(C)$ is the prior probability of class C, $P(x|C)$ is the conditional probability density function given a class C for observation x, and $p(x)=\Sigma_C\rho(C)P(x|C)$ is the total probability density of x. $\mathscr{P}$ is a number from zero to one that represents the probability of the most likely class. For example, for a given observation point, if the most likely tissue is fat, then $C=$fat, and $\mathscr{P}$ is the largest value for all classes considered.

A method is needed to estimate the conditional probability density function, $P(x|C)$, and prior probability, $\rho(C)$, for each tissue type. Since loss is the key distinction between tissue types, the classification is based on tissue loss. This is analogous to classifying the imaginary part of the image. The tissue parameters are assumed to be Gaussian random variables with the mean values given in Table I. $P(x|C)$ is assumed to have the same Gaussian form. An estimate is then needed for the height of the individual Gaussian—that is, $\rho(C)$—and its variance for each tissue type.

Estimates of the height and variance are made using a histogram of the imaginary part of the image. For a more convenient scale, values are weighted by a factor of 4×10^4. Mean values for the Gaussians used in the histogram are listed in Table I. A window is centered at each mean value and the height estimate is obtained by finding the area of the histogram under each window. The variance estimate is found in a similar manner. The sum of the heights is normalized to one—that is, $\Sigma_C\rho(C)=1$. Also thresholds are chosen for the variances to ensure they are in a proper range for each of the tissue types. Estimates that are too large or too small cause poor classification choices. The Bayes classifier is tuned using knowledge of where tissue losses should appear in the histogram. An example of a histogram is given in Fig. 2. Once the estimates for $\rho(C)$ and $P(x|C)$ are obtained the object can be classified by examining each image pixel and calculating which tissue type it most likely is. However, there are situations when no decision should be made—for example, when it is equally likely that a pixel is two different tissue types. Another class is introduced to handle such situations, the ''rejection'' class, for which a pixel is left unmodified until the next GN iteration where an attempt is made to classify it again. The rule for determining a rejection is

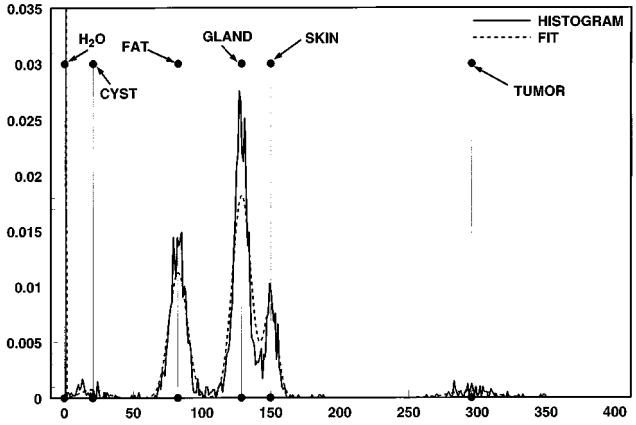

FIG. 2. Example of a histogram of the image loss and its Gaussian fit from the 2-D breast model under reconstruction. Also shown are the mean values for the loss of the various tissues.

$$\begin{aligned}&\text{If } \mathscr{P}\geqslant 1-\mathscr{R}, \text{ set tissue to } C,\\ &\text{Else, reject,}\end{aligned} \tag{8}$$

where $0\leqslant\mathscr{R}\leqslant1$ is the rejection rate and a controlling parameter for each GN iteration. If $\mathscr{R}=0$, then all decisions from the Bayes classifier are rejected; if $\mathscr{R}=1$, then all decisions are accepted. Thus $\mathscr{R}$ is used as a measure of confidence in the ability to classify. Initially, $\mathscr{R}$ is kept small to allow separation of tissue types. As the tissues in the image become distinct, $\mathscr{R}$ is increased, allowing classification of tissue types. There is a trade-off in the choice of $\mathscr{R}$. The more slowly it is increased, the more slowly convergence is obtained. However, if it is increased too rapidly, degradation in the reconstruction occurs because of incorrect classifications. A linear ramp from $\mathscr{R}=0$ to $\mathscr{R}=1$ was chosen for the rejection rate because of its simplicity, and rejection was initiated at the fourth GN iteration. This was found to give reasonable results. However, further research is needed to determine an optimal method for choosing $\mathscr{R}$ at each GN iteration.

The technique described above selects the tissue type using the imaginary part of the image, an estimate of the Gaussian curves, and the rejection rate $\mathscr{R}$. However, the decisions made by the Bayes classifier can be incorrect. For example, cysts (low loss) and tumors (high loss) are initially set to glandular tissue (medium loss). During early iterations, cyst locations are identified as fat because of the low-loss classification. Similarly, tumors are classified as skin. This incorrect identification can cause the image to diverge from the desired result. To prevent this from occurring, a ''clean-up'' step is inserted after the Bayes classification step. The speed and loss of recognizable, nonrejected pixels are checked to ensure that they fall within acceptable bounds. If they do not, the pixel identification is rejected. The location of the tissue type is also checked. For example, if a pixel is identified as skin tissue in the breast interior, it is rejected. The ''clean-up'' procedure insures selection of tissue types that will most likely lead to a convergent solution in the iterative process.

V. THE TWO-DIMENSIONAL BREAST MODEL AND SCATTERING GEOMETRY

The two-dimensional breast model used in the numerical simulations is presented in this paper is shown in Fig. 4(b). The model is discretized into 128 by 128 pixels ($N=128\times128$). The simulations are performed at a frequency of 400 kHz with the pixel set to 0.93 mm ($\lambda/4$ in water). The model is comprised of a skin layer 2 pixels (1.86 mm) wide with an outer radius of 60 pixels (5.59 cm). Next a fat layer is constructed with an annular layer 5 mm wide and 1-cm fat lobes placed along its inner radius. As shown in an earlier paper,[5] this creates a highly refractive fat–glandular interface which provides a rigorous test of our imaging method. The breast interior is composed of glandular tissue and tumors and cysts of various sizes and shapes. Minimal tumors and a cyst the size of one pixel (0.93 mm) are used to test the capability of imaging small objects. The model is illuminated by $\Phi=128$ plane waves equally spaced around the breast. The scattered field is measured along the four edges of the images for each source rotation; thus $N_d=4\times\Phi\times128$. Finally $N_{\text{inv}}=22$. The scattered field measurements for the true image are calculated using the BI-STAB CG-FFT method to a residual error of 1.0×10^{-9}. Similarly the forward field (step 2) for each GN iteration is solved to a residual error of 1.0×10^{-5}. The GN iterations terminate when (1) the condition in step 4 is met with the convergence limit $\epsilon=1.0\times10^{-5}$, (2) the image has no rejected classifications, (3) 20 GN iterations are reached, or (4) no change occurs in the total field.

VI. SIMULATION RESULTS

Before presenting the results of our simulations, terminology and error measures are introduced. Initial classification (IC) refers to use of the initial value described in Sec. IV with no addition to the GN iterative method. Full classification (FC) refers to use of the initial value with addition of the material classification step to the GN iterative method. When the mean values of the tissue parameters (see Table I) are used with no variation, and no signal noise is added to the scattered field measurements, the simulation is noiseless. When tissue losses are allowed to vary by 10% around the mean values, tissue sound speeds are allowed to vary by 2%, and the signal-to-noise ratio (SNR) of the scattered field measurements is set to 70 dB, the simulation is termed noisy. The noise added to the scattered field measurements represents system, detector, or external noise sources. The 10% spread in tissue loss has been chosen because fat and glandular tissue values start to overlap beyond this; it has been assumed that there is no significant overlap in tissue loss values.

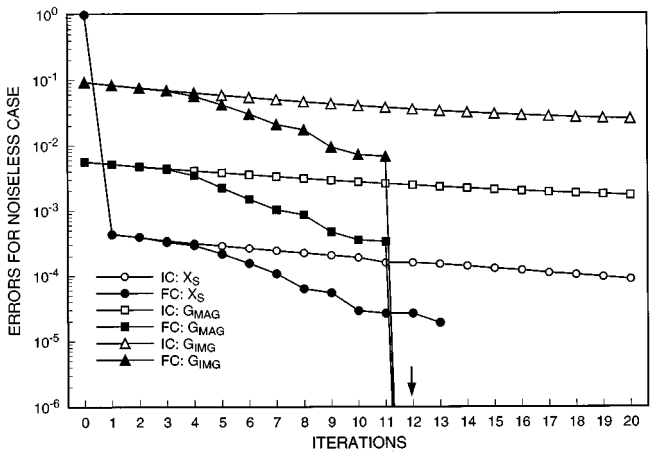

FIG. 3. Error curves for the noiseless case using the initial classification (IC) and full classification (FC) simulations. The arrow indicates that the error is zero at the 12th iteration.

Error is tracked via (1) the mean-square error between the measured and computed scattered fields, (2) the mean-square error between the true and reconstructed image, and (3) the mean-square error between the imaginary part of the true and reconstructed images. The first two are standard error measures; the third is added to evaluate reconstruction of the loss. Recall that loss provides the best means of distinguishing tissue types. The error measures are given by

$$X_s=\text{SQRT}\left(\sum_{\omega,\phi}\|\mathbf{r}_{\omega\phi}^{(i)}\|^2\Big/\sum_{\omega,\phi}\|\mathbf{f}_{\omega\phi}^{s(m)}\|^2\right), \tag{9}$$

$$G_{\text{mag}}=\text{SQRT}\left(\sum_{j}\|\gamma^{(T)}-\gamma^{(i)}\|^2\Big/\sum_{j}\|\gamma^{(T)}\|^2\right), \tag{10}$$

$$G_{\text{img}}=\sum_{j}|\text{IMAG}(\gamma^{(T)}-\gamma^{(i)})|/|\text{IMAG}(\gamma^{(T)})|, \tag{11}$$

where $\gamma^{(T)}$ is the true object and Σ_j is over all image positions.

Simulation results for the noiseless IC and FC cases are shown in Figs. 3–5. In Fig. 3 and in Table II the different error rates are shown. For the IC simulation the error curves demonstrate that the GN method converges from the initial value to the true image. However, convergence is slow. After 20 iterations, the final IC image is shown in Fig. 4(a). The tumors and cysts are clearly reconstructed, but some ripple occurs around them as well as in the water region.

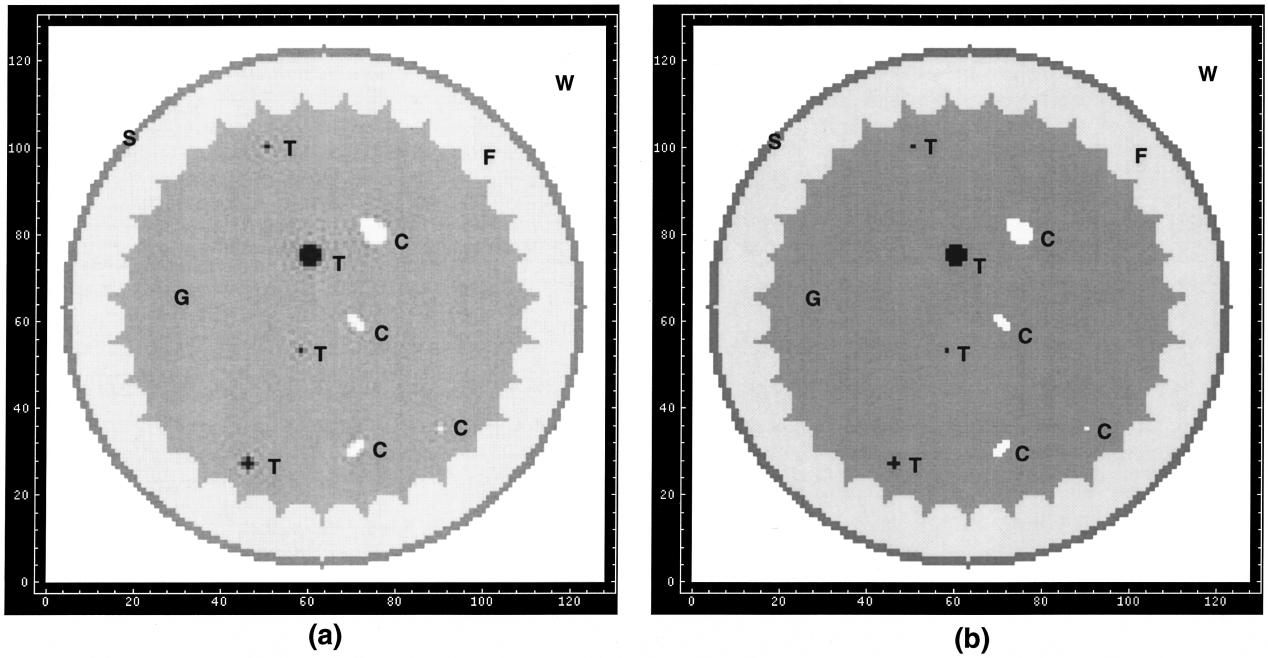

FIG. 4. Loss reconstructions for the noiseless case using (a) the IC simulation at the 20th iteration and (b) the FC simulation at the 12th iteration. White represents the lowest loss and black the highest loss. For the IC simulation the range is -0.0526 m^{-1} to 7.619 m^{-1} and for the FC simulation the range is 0.0 m^{-1} to 6.585 m^{-1}. The symbols represent water (W), skin (S), fat (F), glandular (G), cyst (C), and tumor (T).

This simulation and all other simulations were performed on a Paragon supercomputer using 128 parallel nodes. Calculations for all simulations took approximately 30–60 wall-clock minutes.

For the noiseless FC simulation, reconstruction of the image is complete by the twelfth iteration, and the algorithm terminates at the thirteenth iteration. The error for the scattered field is $X_s = 1.914 \times 10^{-5}$, an improvement over the IC result of nearly an order of magnitude. The final image is shown in Fig. 4(b). There is no ripple in the water region and the tumors and cysts are reconstructed perfectly. The rejection rate $\mathscr{R}$ for all FC simulations is set to zero for the first five ($i = 5$) iterations. From the sixth through eleventh iterations ($i = 6-11$) it is increased linearly to 0.75. From the twelfth iteration ($i \geqslant 12$) it is held constant at 1.0. The FC simulation requires 40% fewer iterations and 48% less CPU time than the IC simulation for the noiseless case.

In Fig. 5 classification decision plots for both the sixth and last iterations are shown. Tissue types have been assigned a gray value according to the decisions made during the classification step. In the case of a rejection the pixel is assigned a white value. Note that for the sixth iteration, when the rejection rate is nonzero for the first time, all tumors are located and correctly classified. The material classification technique locates and identifies tumors, including minimal tumors, quickly. However, the cysts, particularly larger ones, take longer for full reconstruction.

Simulation results for the noisy IC and FC cases are

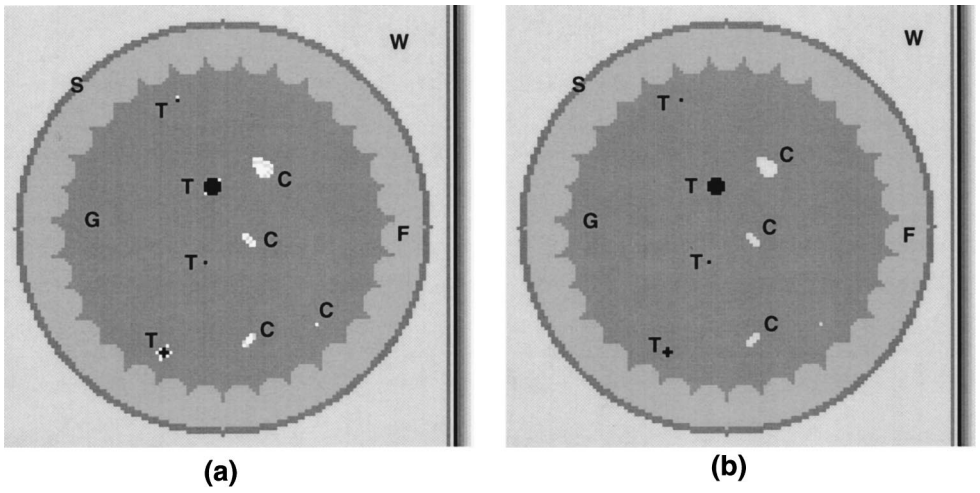

FIG. 5. Decision plots using the FC simulation for the noiseless case at (a) the 6th iteration and (b) the 12th iteration. White pixels show locations of rejections. Symbols are the same as in Fig. 4.

TABLE II. Error rates for the IC and FC simulations for both noiseless and noisy cases.

Error	Noiseless	With noise	
		9th Iter.	20th Iter.
IC X_s	8.897×10^{-4}	4.077×10^{-4}	3.593×10^{-4}
IC G_{mag}	1.726×10^{-3}	1.945×10^{-2}	1.938×10^{-2}
IC G_{img}	1.726×10^{-2}	0.1170	0.1222
FC X_s	1.914×10^{-5}	4.161×10^{-4}	4.207×10^{-4}
FC G_{mag}	0.0	1.9201×10^{-2}	1.923×10^{-2}
FC G_{img}	0.0	0.1008	0.1024

shown in Figs. 6–10. The results are not as good as for the noiseless case. As shown in Fig. 6 and listed in Table II, there is very little improvement in the error value with increasing iterations. In fact the image error curves for both the IC and FC simulations start diverging after the ninth iteration. If the SNR is decreased or the spread in the speed is increased, the results get worse. Both the IC and FC images after the ninth iteration are shown in Fig. 7; the contrast is better in the FC image, but tumors and cysts are visible in both. The final results after 20 iterations (Fig. 8) are similar. Note that there is more speckle in the IC image after the twentieth iteration, which is the cause of the divergence. For the FC results, the divergence is caused by errors that occur during the material classification step. Pixels near the cross-shaped tumor are incorrectly identified as tumor (marked ''E'' in the figure). Also, as image locations are identified during the classification step, more pixels are set to the mean values of the tissues, increasing the error.

In Fig. 9 classification decision plots for both the ninth and last iterations are shown. An incorrect identification is labeled ''E;'' the number of mis-identifications increases by one, while the number of rejections in the skin layer decreases. Note that at the sixth iteration (Fig. 10) the classification scheme has detected all but one of the minimal tumors, and the remaining tumor is located in the following iteration. Even when the reconstruction results are poor, the imaging method identifies tumors quickly.

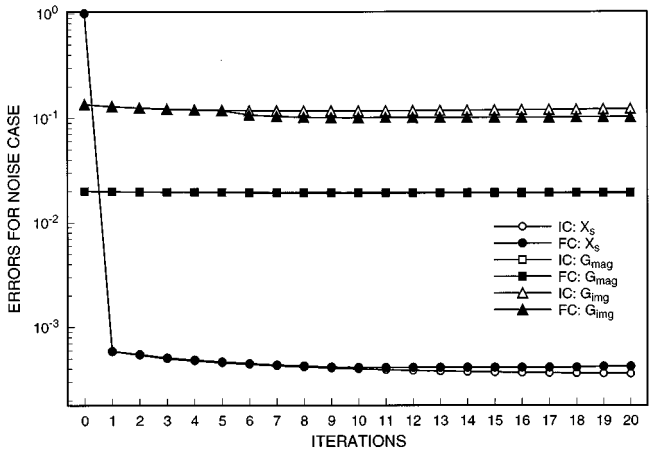

FIG. 6. Error curves for the noisy case using the IC and FC simulations.

The main cause of the divergence discussed above is the use of the approximate Jacobian in the GN method. This approximation works well for low contrast materials and has the advantage of considerably decreasing the computational cost. Initially, it was hoped that addition of the classification step would allow good reconstruction even for high contrast materials. Apparently the approximate Jacobian is not accurate enough for perfect reconstruction of the breast in the presence of strong refraction, but it is accurate enough to allow identification of even minimal tumors.

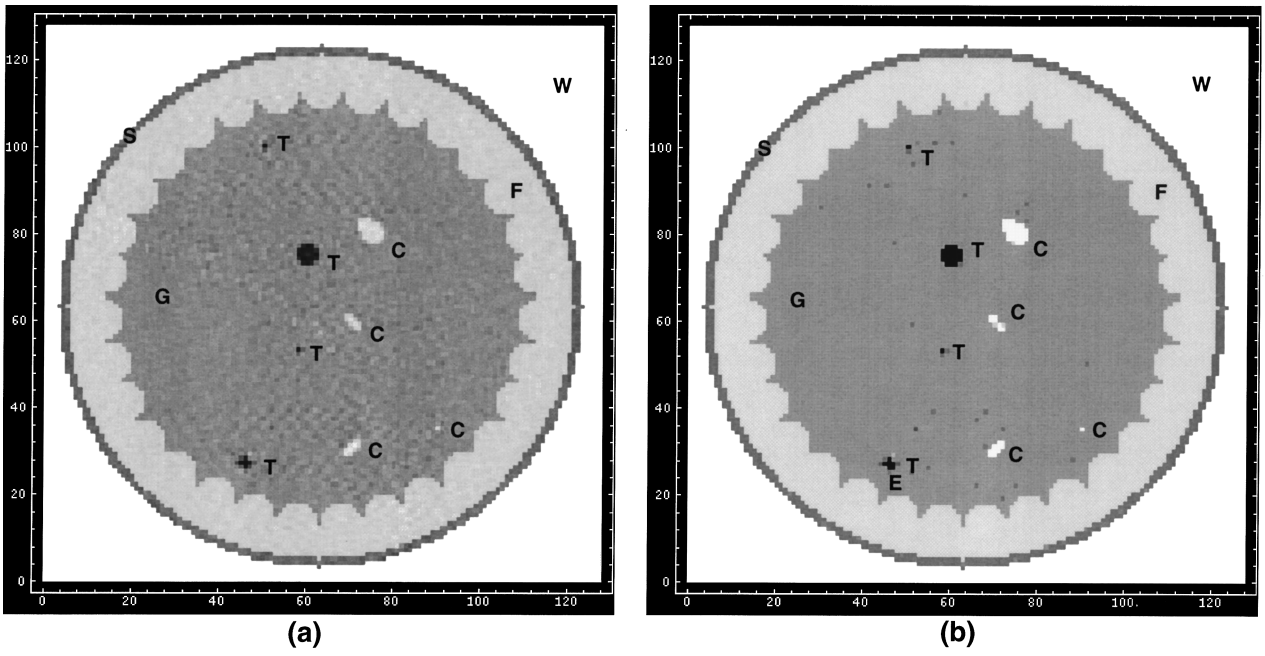

FIG. 7. Loss reconstructions for the noisy case using (a) the IC simulation and (b) the FC simulation at the 9th iteration. For the IC simulation the range is -0.5241 m^{-1} to 6.909 m^{-1} and for the FC simulation the range is 0.0 m^{-1} to 6.585 m^{-1}.

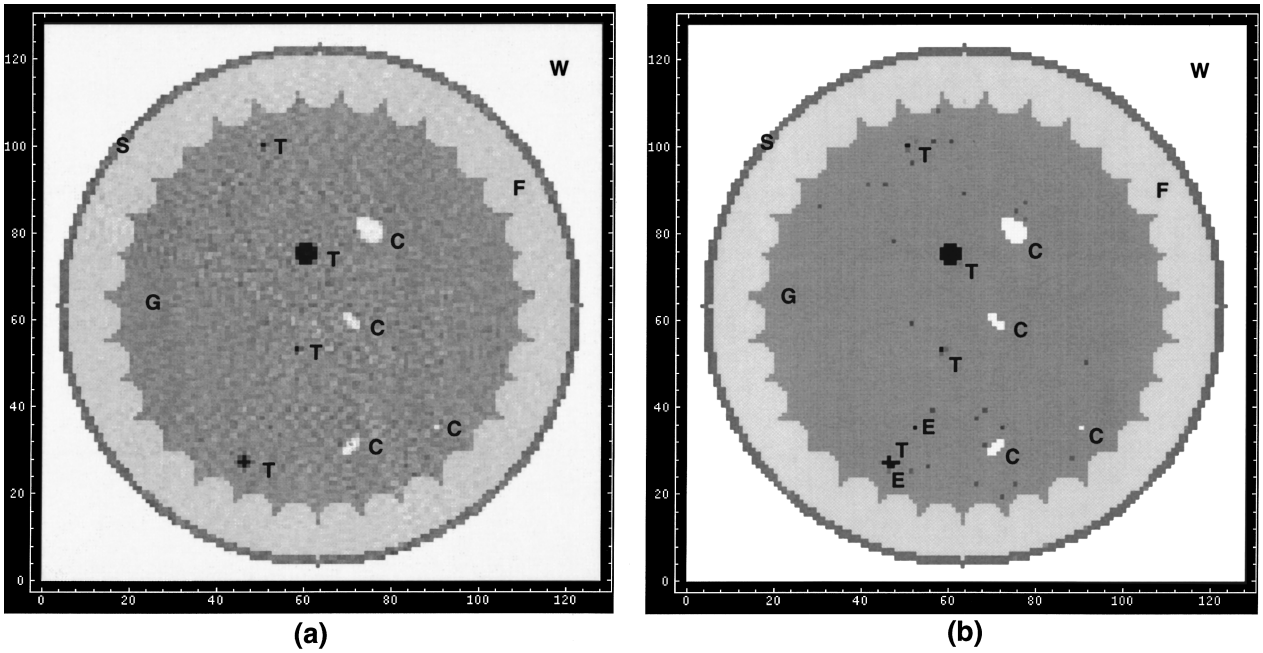

FIG. 8. Same as Fig. 7 but at the 20th iteration. (a) For the IC simulation the range is -0.7467 m^{-1} to 7.5454 m^{-1} and (b) for the FC simulation the range is 0.0 m^{-1} to 6.585 m^{-1}.

VII. SUMMARY

In this paper a new step for use in the Gauss–Newton iterative inverse imaging algorithm has been presented. This step, known as material classification, is added to increase the rate of convergence; it uses a Bayes classifier that identifies and sets image points to the known mean values of the tissue sound speed and loss. Classification decisions are based on Gaussian curves fitted to a histogram of image loss. Image loss allows a clear distinction between tissue types. After initial values have been chosen, a ''clean-up'' phase is used to insure that material classification leads to a convergent and correct solution. To save significant computation time, the Jacobian appearing in the Gauss–Newton method is approximated. Because of this approximation, choice of a proper initial value is critical for obtaining convergence to the correct solution. The initial value is found using tissue parameters and *a priori* knowledge of the breast structure.

Simulations using only the initial value, referred to as initial classification (IC), are performed for a simple two-dimensional model of the human breast. The results for the noiseless case are quite good, but convergence is slow. When the material classification step is used in addition to the initial value, referred to as full classification (FC), better results are obtained at approximately 60% of the cost. However, when system noise and variations in tissue parameter values are added, both classification methods give divergent results. For the FC simulations, the divergence is attributed primarily to use of the approximate Jacobian. If the signal-to-noise ratio is decreased or the sound speed variation is increased, the results are more divergent. Nonetheless, minimal tumors

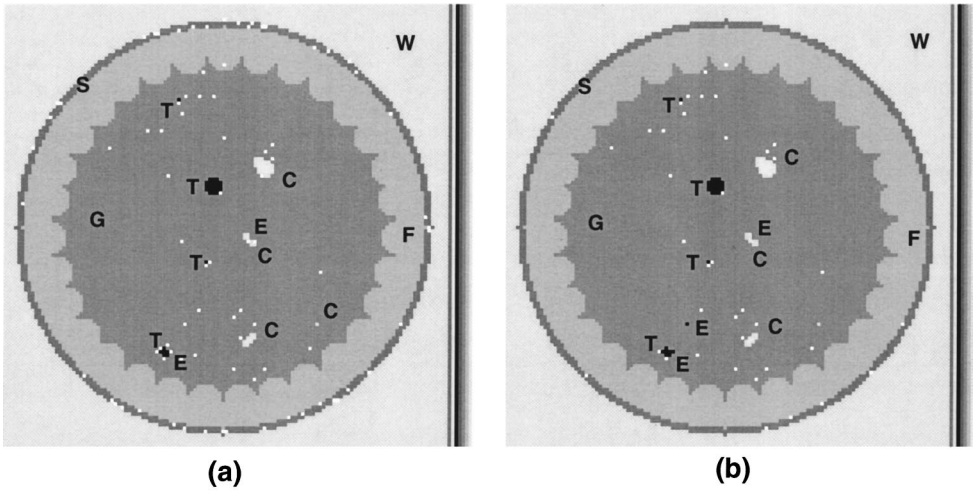

FIG. 9. Same as Fig. 5 but for the noisy case and at (a) the 9th iteration and (b) the 20th iteration. The symbol ''E'' denotes classification errors made during the material classification step.

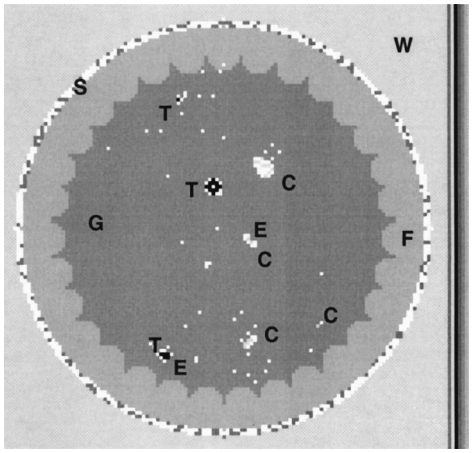

FIG. 10. Same as Fig. 9, but at the 6th iteration.

(less than 1 mm) are reconstructed for both types of simulations, and the material classification technique still identifies and locates tumors early in the iterative process.

Another possible factor in the divergence of the results is the rigidity of the classification method. Pixels are forced to a single value after each iteration, causing incorrect convergence with variation in the sound speed. In future work modification of this method will be examined. Further research is also needed to find a technique for selecting an optimal rejection rate ($\mathscr{R}$) at each GN iteration. Finally, use of alternate approximations to the Jacobian and use of the full Jacobian will be considered.

ACKNOWLEDGMENTS

The authors would like to thank Dr. Roberto Bamberger for use of the NeXT computer laboratory. The authors would also like to thank Dr. Patrick J. Flynn for helpful discussions on the use of the Bayes classifier and for his assistance in the early stages of developing the material classification step. This work was supported by the San Diego Supercomputer Center where all simulations were performed, by the National Science Foundation under Grant No. ECS-9253547, and by the Carl M. Hansen Foundation.

[1] American Cancer Society, *Cancer Facts and Figures 1995*, Atlanta, 1-800-ACS-2345 (1995).

[2] E. Kelly-Fry, ''Breast cancer screening for younger United States women,'' *Proc. Third International Congress on Ultrasound Examination of the Breast*, Tokyo, edited by J. Jellins and T. Kobayashi (Wiley, New York, 1984).

[3] Q. Zhu and B. D. Steinberg, ''Wavefront amplitude distribution in the female breast,'' J. Acoust. Soc. Am. **96**, 1–9 (1994).

[4] R. J. Pauls and B. D. Steinberg, ''A refraction-based simulation to explore wavefront distortion in ultrasound mammography: refraction-induced amplitude effects,'' Internal Report UP-14-92, Valley Forge Research Center, University of Pennsylvania, March 1992.

[5] C. W. Manry, Jr. and S. L. Broschat, ''The FDTD method for ultrasound propagation through a two-dimensional model of the human breast,'' J. Acoust. Soc. Am. **94**, 1774–1775 (1993). (Also submitted to Ultrason. Imaging.)

[6] D. T. Borup, S. A. Johnson, W. W. Kim, and M. J. Berggren, ''Nonperturbative diffraction tomography via Gauss-Newton iteration applied to the scattering integral equation,'' Ultrason. Imaging **14**, 69–85 (1992).

[7] S. A. Johnson and M. L. Tracy, ''Inverse scattering solutions by a sinc basis, multiple source, moment method—Part I: Theory,'' Ultrason. Imaging **5**, 361–375 (1983).

[8] Y. M. Wang and W. C. Chew, ''An iterative solution of two-dimensional inverse scattering problem,'' Int. J. Imaging Syst. Technol. **1**, 100–108 (1989).

[9] T. J. Cavicchi and W. D. O'Brien, ''Numerical study of higher-order diffraction tomography via the sinc basis moment method,'' Ultrason. Imaging **11**, 42–74 (1989).

[10] W. C. Chew and Y. M. Wang, ''Reconstruction of two-dimensional permittivity distribution using the Distorted Born Iterative method,'' IEEE Trans. Biomed. Eng. **BME-9**, 218–225 (1990).

[11] Y. M. Wang and W. C. Chew, ''Reconstruction of two-dimensional refractive index distribution using the Born Iterative and Distorted Born iterative method,'' Acoust. Imaging **18**, 105–114 (1991).

[12] M. Moghaddam and W. C. Chew, ''Nonlinear two-dimensional velocity profile inversion using time domain data,'' IEEE Trans. Geosci. Remote Sens. **30**, 147–156 (1992).

[13] A. K. Jain and R. C. Dubes, *Algorithms for Clustering Data* (Prentice-Hall, Englewood Cliffs, 1988), Chaps. 2 and 3.

[14] P. A. Devijver and J. Kittler, *Pattern Recognition: A Statistical Approach* (Prentice-Hall, Englewood Cliffs, 1992), Chap. 2.

[15] E. L. Madsen, J. A. Zagzebski, G. R. Frank, J. F. Greenleaf, and P. L. Carson, ''Anthropomorphic breast phantoms for assessing ultrasonic imaging system performance and for training ultrasonographers: Part 1,'' J. Clin. Ultrasound **10**, 10–75 (1982).

[16] E. L. Madsen, J. A. Zagzebski, G. R. Frank, J. F. Greenleaf, and P. L. Carson, ''Anthropomorphic breast phantoms for assessing ultrasonic imaging system performance and for training ultrasonographers: Part 2,'' J. Clin. Ultrasound **10**, 91–100 (1982).

[17] M. Abramowitz and I. A. Stegun, Eds., *Handbook of Mathematical Function with Formulas, Graphs, and Mathematical Tables* (Dover, New York, 1972).

[18] D. T. Borup and O. P. Gandhi, ''Calculation of high-resolution SAR distributions in biological bodies using the FFT algorithm and conjugate gradient method,'' IEEE Trans. Microwave Theory Tech. **MTT-33**, 417–419 (1985).

[19] H. A. Van Der Vorst, ''BI-CGSTAB: A fast and smoothly converging variant of BI-CG for the solution of nonsymmetric linear systems,'' SIAM (Soc. Ind. Appl. Math.) J. Sci. Stat. Comput. **13**, 631–644 (1992).

[20] A. J. Devaney, ''Nonuniqueness in the inverse scattering problem,'' J. Math. Phys. **19** (1978).

[21] T. K. Sarkar and E. Arvas, ''On a class of finite step iterative method (conjugate directions) for the solution of an operator equation arising in electromagnetics,'' IEEE Trans. Antennas Propagat. **AP-33**, 1058–1066 (1985).

Signal processing of the echo signatures returned by submerged shells insonified by dolphin "clicks:" Active classification

Guillermo C. Gaunaurd,[a] Donald Brill,[a] and Hanson Huang[b]
Naval Surface Warfare Center, White Oak, Silver Spring, Maryland 20903-5640

Patrick W. B. Moore
Naval Command, Control & Oceans Systems Center, NRaD, San Diego, California 92152-6267

Hans C. Strifors
National Defense Research Establishment, S-17290, Stockholm, Sweden

(Received 19 July 1996; accepted for publication 25 November 1997)

A large set of dolphin-emitted acoustic pulses (''echolocation clicks'') have been examined, which were reflected from various elastic shells that were suspended, underwater, 4.5 m in front of the animal in a large test site in Kaneohe Bay, Hawaii. A carefully instrumented analog-to-digital system continuously captured the emitted clicks and also the returned, backscattered echoes (A/D conversion at 500 kHz). Using standard conditioning techniques and food reinforces, the dolphin is taught to push an underwater paddle when the ''correct'' target—the one he has been trained to identify—is presented to him. He communicates his consistently correct identifying choices in this manner. Many echoes returned by three types of cylindrical shells in both the time and frequency domains as well as in the *joint* time-frequency (t-f) domain, by means of Wigner-type distributions have been examined. It will be shown exactly how specific features observable in these displays are directly related to the physical characteristics of the shells. This processing takes advantage of certain fundamental resonance principles to show which echo features contain information about the size, shape, wall thickness, and material composition of both the shell and its filler substance. In the same fashion that these resonance features give the identifying characteristics of each shell, it is believed they may also give them to the dolphin. These echo features may allow him to extract the target properties by inspection without any need for computations. It is claimed that this may be the fundamental physical explanation of the dolphin's amazing target ID feats, upon which they base their recognition choices. This claim may be substantiated by the detailed analysis of many typical echoes returned by various shells, when they are interrogated by several dolphins. Thus far, this analysis of many echoes from many shells has only been carried out for a single dolphin. [S0001-4966(98)03603-0]

PACS numbers: 43.60.Ft, 43.40.Ey, 43.20.Gp, 43.80.Ka [JLK]

INTRODUCTION

Dolphins have an unsurpassed ability to identify underwater objects using their biological sonar. Extensive prior efforts have been devoted to train and test these animals, and to gather data in order to try to understand: (i) how they generate their echolocating clicks; (ii) what is the limit of their auditory ability; (iii) how they perceive or analyze the echoes returned from targets. Much of this earlier echo-analysis work has simply described the performance of selected animals (i.e., successes versus failures) in carrying out certain feats, such as distinguishing between various simple shapes or materials. Some of the existing literature on this general topic has been summarized in recent books.[1,2] The present paper makes use of a database gathered during a matching-to-sample experiment conducted at the NRaD, Hawaii, Laboratory. It contains a large collection of clicks emitted by trained dolphins when they are insonifying or echolocating cylindrical metal shells that contain various fillers. The database also contains the backscattered echoes returned to the animal. These data together with theoretical predictions of ours for the same conditions are compared and analyzed here. We also use an inverse scattering technique we have developed that permits the total identification of the target characteristics from certain features in the echoes. These features are present in both the measured *and* in the predicted responses, even though these two are not always identical replicas of each other. The three basic spectral features are: Δx, $\Delta x'$, and x^*. These quantities and their time-counterparts (Δt, $\Delta t'$, and $t_1 - t^*$) are explained in detail in later sections. Here we define Δx (and $\Delta x'$) as certain longer (or shorter) *spacings* between the resonance peaks that are observable in the spectrum of the echoes. The quantity x^* is the (nondimensional) frequency location of the first spectral peak. We will show below that *we* can extract all the characteristics of the targets (i.e., shape, size, shell composition, shell thickness and filler composition) from these features in a simple fashion that hardly requires any calculation. In view of this, and since these clues are also available to the dolphin, we claim, and would like to believe, that this is the simple procedure also used by the dolphins to carry out their

[a]Current address: Naval Surface Warfare Center, Carderock Division—Code 684, 9500 MacArthur Boulevard, W. Bethesda, MD 20817-5700.
[b]Retired consultant.

amazing identification feats. The automation of this procedure seems to be straightforward. The important properties of the incident clicks which best bring out the abovementioned identifying features in the echo are that the pulses are short (i.e., broadband) and energetic enough (i.e., of high S/N) to overcome the ambient noise levels that might be present. Both these conditions are met in the experiment described here.

I. BACKGROUND ON SOUND SCATTERING BY SUBMERGED SHELLS

The echo returned by a submerged, elastic, shell of, say, cylindrical shape contains features due to various effects.[3] These are: (a) the specular reflection from the outer (i.e., $r=a$) shell surface; (b) the diffracted circumferential waves which revolve around the shell, starting somewhere near the edge of the shadow boundary; (c) the elastic waves transmitted into the shell that are scattered from the inner (i.e., $r=b$) shell surface and bounce repeatedly within the shell thickness (i.e., the region: $b \leqslant r \leqslant a$); and (d) the symmetric and anti-symmetric circumferential Lamb waves of zero order. In general, these Lamb waves are of the flexural type, a_n, and of the longitudinal or extentional type, s_n. These also revolve around the shell, within its thickness, and $n=0,1,2,\ldots$. At low frequencies, the $n=0$ type seems to be dominant.

The contribution of type (a) causes no peaks or dips in the graph of the form function, $|f_\infty|$. The contribution of type (b) is close to that of a rigid object, and it generates very weak peaks or dips in $|f_\infty|$. Extrema in the graph of $|f_\infty|$ caused by type (c) contributions can only occur at very high frequencies. Therefore, for a relatively thin shell [i.e., $h/a=(a-b)/a \leqslant 5\%$], only contributions of type (d) can cause the extrema that may be present in a plot of $|f_\infty|$ versus frequency. In fact, only those due to s_0 and a_0 are important. The effect of s_0 appears at much lower frequencies than that of a_0 for a thin shell. Hence, for the present purposes, only s_0 has to be considered.

II. THEORETICAL PREDICTION OF BACKSCATTERED PULSES

Given any pulse $g(t)$, of spectrum $G(f)$, incident on a submerged shell, the ''echo,'' or backscattered pressure pulse returned by the shell is given by[4]

$$p_{sc}(\tau)\,\frac{2r}{a}=\frac{1}{2\pi}\int_{-\infty}^{\infty}[f_\infty(ka)G(ka)]\times\exp\left[-ika\left(\tau-\frac{r}{a}\right)\right]d(ka), \tag{1}$$

where τ is a nondimensional time: $\tau=ct/a$; ka is a nondimensional frequency: $ka=x=2\pi(a/c)f$; $G(ka)$ is the spectrum of whatever incident pulse one has in terms of the nondimensional variable $x\equiv ka$; and $f_\infty(ka)$ is the form function of the target in the steady-state case. The above integral is usually evaluated numerically since $f_\infty(ka)$ is generally a complicated function, even for the simplest of targets. For a cylindrical metal shell of inner/outer radii, b/a, containing an internal filler substance, which is insonified normally to its axis by an infinite plane wave, the form function is given by the series:

$$|f_\infty(ka)|=\left|\frac{2}{\sqrt{i\pi ka}}\sum_{n=0}^{\infty}(-1)^n(2-\delta_{n0})b_n\right|, \tag{2}$$

where the coefficients b_n are obtained from the boundary conditions of the problem. They turn out to be the ratios of two 6×6 determinants, as follows:

$$b_n=\frac{\begin{vmatrix} A_1 & d_{12} & d_{13} & d_{14} & d_{15} & 0 \\ A_2 & d_{22} & d_{23} & d_{24} & d_{25} & 0 \\ 0 & d_{32} & d_{33} & d_{34} & d_{35} & 0 \\ 0 & d_{42} & d_{43} & d_{44} & d_{45} & d_{46} \\ 0 & d_{52} & d_{53} & d_{54} & d_{55} & d_{56} \\ 0 & d_{62} & d_{63} & d_{64} & d_{65} & 0 \end{vmatrix}}{\begin{vmatrix} d_{11} & d_{12} & d_{13} & d_{14} & d_{15} & 0 \\ d_{21} & d_{22} & d_{23} & d_{24} & d_{25} & 0 \\ 0 & d_{32} & d_{33} & d_{34} & d_{35} & 0 \\ 0 & d_{42} & d_{43} & d_{44} & d_{45} & d_{46} \\ 0 & d_{52} & d_{53} & d_{54} & d_{55} & d_{56} \\ 0 & d_{62} & d_{63} & d_{64} & d_{65} & 0 \end{vmatrix}}. \tag{3}$$

The 30 nonzero elements of these determinants are functions depending on Bessel and Hankel functions and their derivatives, all of arguments depending on ka. One of these elements, for example, is

$$d_{21}=-kaH_n^{(1)\prime}(ka). \tag{4}$$

The entire list was obtained earlier.[5] Also, δ_{mn} is the Kronecker delta. The above elasticity-based formulation is computerized and can be used to predict the scattered pressure pulse for any incident pulse (i.e., ''click'') when the shell's dimensions and material are known.

We remark that our prediction is approximate. We are using an exact but two-dimensional model for the shell motions—the only one possible in closed form—in the three-dimensional formulation for the echo. The three-dimensional Green's function for the Helmholtz equation is used in Eq. (1) since the echoes *must be* three dimensional. Since the incidences are normal to the cylindrical axis and the end effects are small, the resulting echo predictions are adequate. The identifying features (i.e., $\Delta x, \Delta x', x^*, \ldots$) in the predicted curves match those in the measured responses even though the complete curves are not their identical replicas. The spectrum of the target response is obtained from the relation:

$$\left|P_{sc}(ka)\,\frac{2r}{a}\right|=|G(ka)f_\infty(ka)|. \tag{5}$$

Equation (1) gives the target response in the nondimensional time-domain τ, and Eq. (5) in the nondimensionalized frequency domain, $ka=x$. The conversion to real time and frequency follows immediately from the definitions of τ and x. It can be shown that Eq. (1) is equivalent to a convolution and can also be interpreted as the inverse Fourier transform

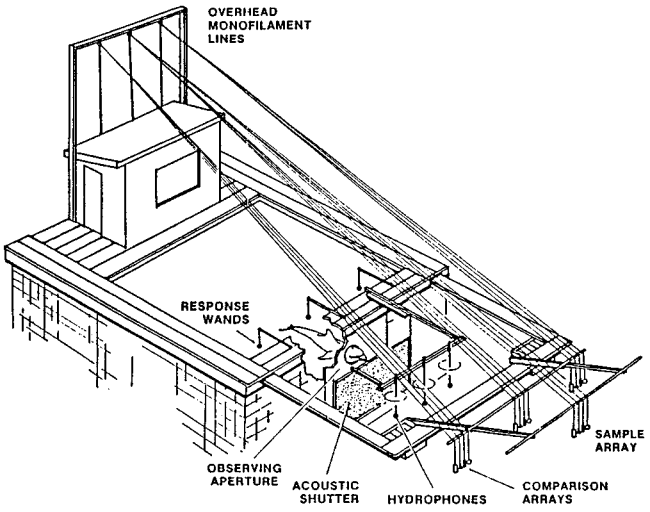

FIG. 1. Experimental setup for dolphin training, testing, and monitoring.

of the form function (in retarded time) as viewed through a ''spectral window,'' which is the spectrum of whatever incident pulse is used. The dolphin ''click'' is the pulse in this case. Equation (1) holds for any target. The quantity varying with different targets is $f_\infty(x)$. Most of the theoretical predictions shown here use this formulation to produce the plots.

We remark that from Eq. (5), the form function, $f_\infty(x)$, can be obtained as the ratio of the F.T. of the backscattered pulse, divided by the F.T. of the incident click. This would also follow from basic considerations of F.T.'s. This would only be valid within the (broad) band of the incident pulse (i.e., 30–130 kHz, as shown later in Figs. 6 and 10). An analogous relation also exists in the time domain. The features $\Delta x, \Delta t, \ldots$ obtained in this fashion coincide with the ones we have shown in our figures.

III. EXPERIMENTAL MEASUREMENT OF BACKSCATTERED PULSES

In a test site in Kaneohe Bay, Hawaii, a dolphin was trained to introduce his head in a hoop and echo locate a target placed in the water in front of him; see Fig. 1. For the purpose of the present experiment, the targets were elastic cylindrical shells that were suspended vertically at a distance of 4.5 m. The shells here filled with different substances. A carefully instrumented analog-to-digital system was used to capture the emitted echo-location clicks and returned backscattered echoes. The A/D conversion was at 500 kHz. By means of standard conditioning techniques and food reinforces, the dolphin is taught to push an underwater paddle whenever the ''correct'' target—the one he has been trained to identify—is presented to him. This is the way in which the animal communicates to us his consistently correct choices. The animal correctly identifies the shell every time. (Further details are given in Ref. 6.) We have collected and examined a large set of these emitted pulses (''clicks'') and the corresponding backscattered echoes from the shells. We have found exactly how certain specific features observable in the echoes (measured and predicted) are related to the physical characteristics of the pertinent shells.[7] Our procedure to examine the echoes makes use of certain basic resonance principles to show which echo features contain information about the size, shape, wall thickness, and material composition of both the shell and its filler substance. It then extracts the information from the features.

TABLE I. The properties of the fillers.

	c (cm/s)	ρ (g/cm^3)
Glycerol ($C_3H_8O_3$)	1.906×10^5	1.26
Beeswax[a]	1.3×10^5	0.96
Salt water (@25 °C & 35 ppt)	1.53×10^5	1.0241
Pure water (25 °C)	1.48×10^5	1.000
Air	0.33×10^5	0.0012

[a]Beeswax has properties close to paraffin.

Our procedure, to be illustrated and explained below (see Secs. V and VI), tells us how to extract the details of the target that has backscattered the dolphin's insonifying signal, thus identifying it completely. We believe that the animal instantaneously processes the echoes and looks for the same features which immediately tell him the target properties, without any need for calculations, and prompts him to push (or not) the rewarding paddle when the ''right'' (or ''wrong'') target is presented. We point out that we have computed here predicted responses only to compare them to the measured data, which is always a reassuring confirmation that ''things are right.'' We remark that any retentive subject, after a learning period, can also extract the target characteristics in a simple fashion from the measured *data*, with hardly any calculation, by just noticing the pertinent features. We believe that this procedure is the fundamental physical explanation of the dolphin's extraordinary target ID feats. This procedure seems to be sufficiently simple to be quickly automated.

IV. PARAMETERS REQUIRED TO GENERATE THEORETICAL PREDICTIONS

In order to make echo predictions, the target properties must be known *a priori*. As stated above, the targets can be totally identified from the measured data, with hardly any need for calculations. If we can do that, we believe the dolphin can also. Theoretical predictions are merely obtained here as a reassuring confirmation that the echoes observed and those calculated by our elasticity-based formulation contain very similar ''features.'' The theoretical predictions for $|p_{sc}(\tau)|$ and $|P_{sc}(ka)|$ [and also for $f_\infty(ka)$] are obtained from Eqs. (1) to (5), using the material parameters given below.

The shell dimensions are: $a=3.25$ cm, $b=3.19$ cm, and length $L=8.5$ cm. Clearly the shell's thickness is: $h=a-b=0.6$ mm. The shell material is aluminum, of density: $\rho=2.79$ g/cm^3, and dilatational and shear speeds, $c_d=6.38\times10^5$ cm/s and $c_s=3.10\times10^5$ cm/s, respectively. The fillers are substances such as glycerol, beeswax, and salt water. Their properties, plus those of air and pure water, are summarized in Table I.

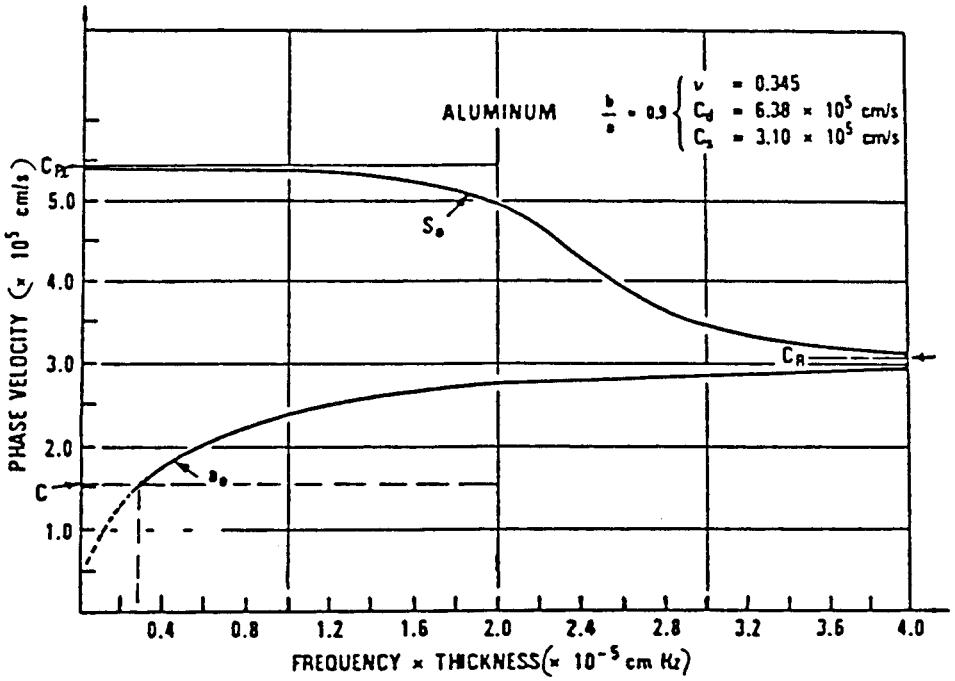

FIG. 2. Dispersion plot of the phase velocity of the first two (i.e., a_0 and s_0) Lamb waves in an aluminum plate.

These are all the parameters required to generate theoretical predictions with the formulation in Sec. I. There are some additional relations that can be used to obtain other properties that we will have occasion to use. Some of these are given below. Young's modulus E and Poisson's ratio ν in terms of the dilatational and shear speeds are

$$E=\rho c_s^2\left[\frac{3c_d^2-4c_s^2}{c_d^2-c_s^2}\right], \quad \nu=\frac{c_d^2-2c_s^2}{2(c_d^2-c_s^2)}. \tag{6}$$

Using the above values for aluminum, we find

$$E=7.21\times 10^{11}\ \text{dyn/cm}^2, \quad \nu=0.345. \tag{7}$$

The ''plate speed,'' $c_{\rm pl}$, of an aluminum shell is

$$c_{\rm pl}=\sqrt{\frac{E}{\rho(1-\nu^2)}}=5.42\times 10^5\ \text{cm/s}. \tag{8}$$

The ratio: $c_{\rm pl}/c$, where c is the sound speed in salt water, will be later denoted as Δx where

$$\Delta x\cong\frac{c_{\rm pl}}{c}=\frac{5.42\times 10^5}{1.53\times 10^5}=3.54. \tag{9}$$

The ka scale is related to the frequency scale (in kHz) for a shell of radius 3.25 cm in salt water by

$$ka=\left(\frac{2\pi a}{c}\right)f=0.13f. \tag{10}$$

The relative shell thickness is

$$\frac{h}{a}=\frac{0.6\ \text{mm}}{32.5\ \text{mm}}=1.85\% \quad \text{(thin shell case)}. \tag{11}$$

The ''coincidence (normalized) frequency'' of this aluminum shell[8] can be estimated from the relation: $(ka)_c(h/a)\sim 1$. Thus $(ka)_c\approx 54.1$. The corresponding ''coincidence frequency,'' f_c is $f_c\approx 405.5$ kHz. This value is way above the threshold of hearing for dolphins, which is at about 150 kHz, and thus it is of no use in the present analysis. For this thin shell, in the present low-frequency band (i.e., $ka\leqslant 20$), only the s_0 Lamb wave is present, and it accounts for all the observable features. This wave propagates almost without dispersion and thus,

$$c_0^{\rm group}=c_0^{\rm phase}=c_{\rm pl}=\frac{\sqrt{1-2\nu}}{1-\nu}\,c_d. \tag{12}$$

All the above quantities equal 5.42×10^5 cm/s, which is the value already found for $c_{\rm pl}$. The Rayleigh wave speed, c_R, for this aluminum shell is: $c_R\cong 0.98\ c_s\cong 3.0\times 10^5$ cm/s. The dispersion plots for the phase speeds versus fh' in the plate for the s_0 and a_0 Lamb waves in an aluminum plate are shown[3] in Fig. 2. The plate thickness is $h'=a-b$. To use this figure, which is valid for a plate, in the present case of a cylindrical shell, one must relate fh' in the plate to ka in the shell by $fh'=(c/2\pi)(h'/a)ka$. In our case: $ka=222(fh')\times 10^{-5}$. Since each ''tick'' in Fig. 2 corresponds to a value of $fh'\times 10^{-5}\approx 0.2$, then it will also correspond to a ka value of 44.5. For the present situation ($ka\leqslant 20$), we are within half of the initial ''tick'' for the s_0 curve. The a_0 curve is shown dotted before it crosses the horizontal line for the sound speed, c, in the water, because the a_0 wave is not activated until $c^{\rm phase}\geqslant c$. This occurs at ''coincidence,'' which here occurs at $ka\approx 54$. So, in the region of interest, there is only s_0, which propagates with a nearly constant phase speed, equal to $c_{\rm pl}$.

An approximate way to estimate the ratio c_d/c, which provides an alternative way to identify the shell material, is from the empirical relation:

$$\frac{c_d}{c}\cong\left[\frac{10a}{c(t_1-t^*)}\right]^2. \tag{13}$$

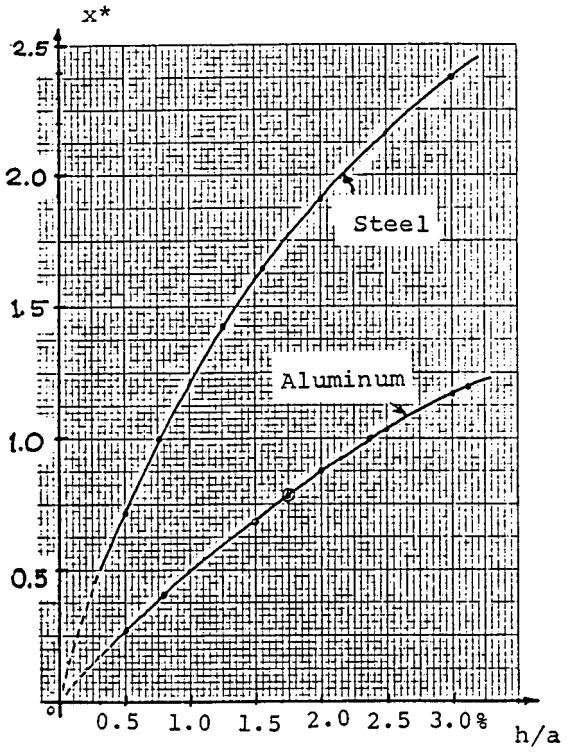

FIG. 3. Location of the first resonance peak, x^*, in the form function of a cylindrical shell of various materials, versus the relative shell thickness, h/a.

Here t_1 is the arrival time of the first wave packet or peak due to the s_0 Lamb wave, and t^* is the arrival time of the spectral pulse. The time interval $t_1 - t^*$ is usually very brief, and the formula is obtained from numerical experimentation. Previous numerical experimentation has also shown that the frequency, x^*, for the first maximum in the spectrum of the target response varies with relative shell thickness, h/a, as shown in Fig. 3. We note that h/a can also be found from the coincidence frequency using $h/a \sim 1/(ka)_c$. However, in the present case, the coincidence frequency is too high for this relation to be applicable. Figure 3 shows results for aluminum and steel shells. Analogous curves for shells of other materials can also be obtained. The so called ''quasi-thickness resonance'' [8] can be used, in some instances, to determine the composition of the internal filler. However, in the present case it occurs at such high frequencies (viz., for $ka \approx 707$, or $f \cong 5.3$ Mhz) that it is of no practical use.

To identify the sound speed in the filler it is useful to consider the time interval, $\Delta t'$, for a ''ray'' incident on one side of the shell to travel back-and-forth through the shell and the internal filler. If c_3 is the sound speed in the filler, then, obviously,

$$\Delta t' = 2\left[\frac{2h}{c_d} + \frac{2b}{c_3}\right]. \tag{14}$$

If $\Delta t'$ is measured, then c_3 is

$$c_3 = \frac{4bc_d}{c_d \Delta t' - 4h} = \frac{4bc_d \Delta f'}{c_d - 4h\Delta f'}, \tag{15}$$

where we have used the time-frequency relation: $\Delta t' \Delta f' \sim 1$. One final, auxiliary relation gives directly the value of

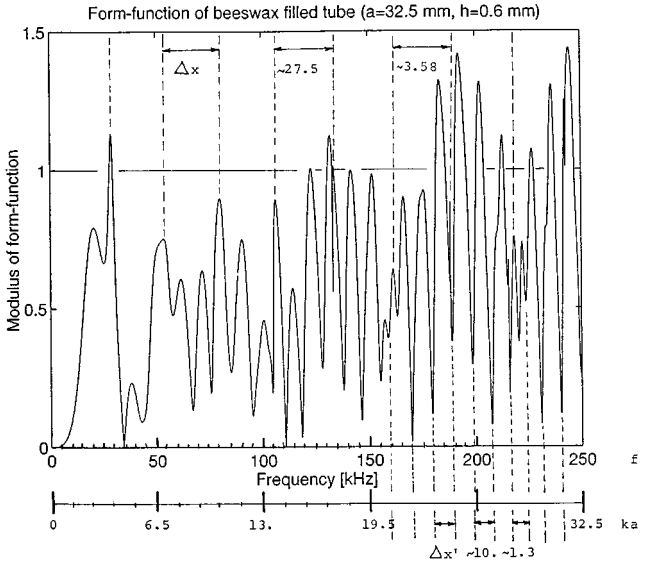

FIG. 4. Form function of an elastic tube filled with beeswax. The abcissas are frequency f (in kHz) and nondimensional frequency ka, both in parallel scales.

Poisson's ratio ν in terms of the ratio: $c_{\rm pl}^2/c_d^2 \equiv A$. It is

$$\nu = \frac{1}{A}\,[A - 1 + \sqrt{1 - A}]. \tag{16}$$

This relation is obtained from the known expression:[3]

$$\frac{c_{\rm pl}}{c_d} = \frac{\sqrt{1-2\nu}}{1-\nu}, \tag{17}$$

by solving it for ν. The above approach becomes more accurate after the (low-frequency) diffraction effects have diminished and ray theory begins to dominate. This concludes the list of auxiliary relations between the various problem parameters that are useful in the present situation.

As an example of a theoretical prediction, we evaluate and plot the form function $|f_\infty(ka)|$ of a cylindrical aluminum shell of dimensions: $a = 32.5$ mm, $h = a - b = 0.6$ mm, in the frequency range: $0 \leqslant ka \leqslant 32.5$. For the given value of ''a,'' this corresponds to a band of: $0 \leqslant f \leqslant 250$ kHz. The shell is filled with beeswax, and is submerged in salt water. All the material properties are given in Table I. The result, obtained from Eqs. (2) and (3), with the elements d_{ij} given in Ref. 5, is shown in Fig. 4. The features in it, will be discussed and used below.

V. EXTRACTION OF TARGET INFORMATION FROM THE ECHOES

We have examined a large number of dolphin emitted echolocation ''clicks'' in the database. A typical one (i.e., #31 in the series R0521S02) is shown in Fig. 5. This short pulse has a broad spectrum as seen in Fig. 6, which is the modulus of the Fourier transform of the pulse in Fig. 5. The spectrum amplitude is very low above $f \cong 150$ kHz, which is about the threshold of hearing for a dolphin. Since these spectra are within the animal's auditory range, they are not wasting any energy when they generate their emitted clicks. The corresponding ka scale is also shown in Fig. 6, as ob-

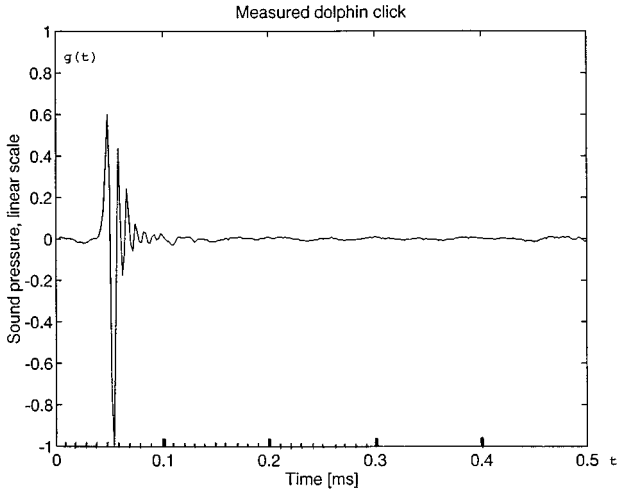

FIG. 5. One of the measured dolphin ''clicks'' in the database versus time.

tained from Eq. (10). This actual dolphin ''click'' is now made to hit the cylindrical shell filled with bee's wax described before, which has the form function shown in Fig. 4. The backscattered pressure waveform is calculated from Eq. (1), using the $|f_\infty(ka)|$ in Fig. 4, and the $G(f)$ [or $G(ka)$] in Fig. 6. The result is given in Fig. 7 in the (real) time domain. The nondimensional variable τ is transformed to t by: $t = a\tau/c$. The spectrum of this backscattered echo is displayed in Fig. 8 as obtained from Eq. (5). Both f and ka scales are shown in Fig. 8. Superimposed—in dotted line—in Fig. 8 is the spectrum, $G(f)$, of the incident click, which acts as a low-pass filter function and suppresses most of the spectrum above $f \cong 150$ kHz. The predicted target response in Fig. 8 is the portion of the form function in Fig. 4 that ''fits'' under the spectrum $G(f)$ shown in Fig. 6, which acts as a modulating envelope for the spectral response. We note that the ''features'' in the $|f_\infty(ka)|$ (cf. Fig. 4) are also present in $|P_{sc}(ka)|$ (cf. Fig. 8), but only within the band bounded by $G(f)$ (i.e., up to $f \cong 150$ kHz). We also note that although the incident click $g(t)$ in Fig. 5 is very short (i.e., under 0.1 ms), the target response in Fig. 7 lasts ten or more times that

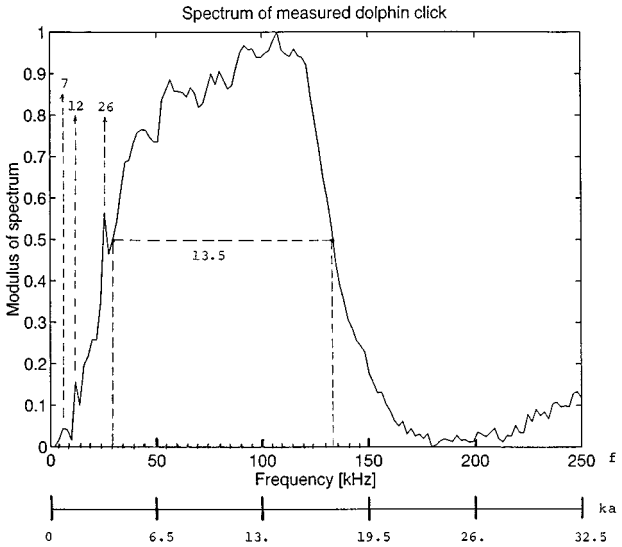

FIG. 6. Spectrum of the measured dolphin ''click'' in Fig. 5.

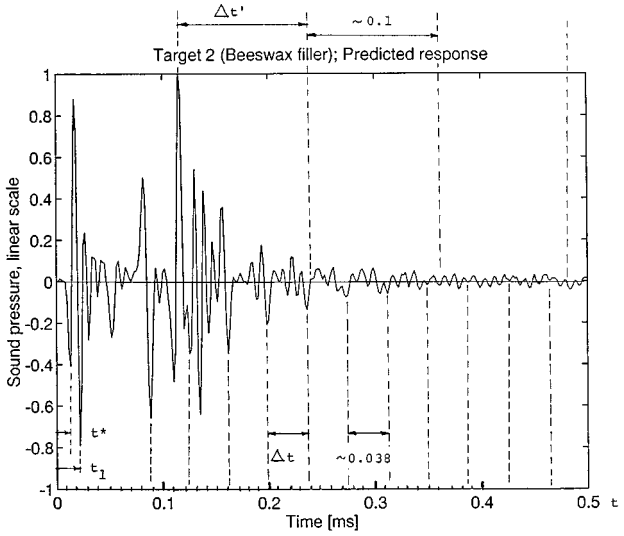

FIG. 7. Predicted time signature of the echo from the aluminum cylindrical shell filled with beeswax. Features spaced Δt and $\Delta t'$ are observed.

amount. Figures 7 and 8 are predicted calculations. Figures 9 and 10 display the same information as measured at the experimental site and as recorded in the database. We will first examine the predicted responses.

Figure 8 shows a series of successive (resonance) peaks caused by the circumnavigating s_0 Lamb wave in the shell, that are spaced a uniform distance: $\Delta x \cong 27.5$ kHz. In the ka scale, this separation is $\Delta x \cong 3.58$. The ka scale is the same as in Fig. 6. In the time-domain response of Fig. 7, after the initial spike due to the specular return, there follows a ''tail'' of resonance peaks, also due to the revolving s_0 wave. The spacing or time interval between successive dips is also uniform, and it has the value: $\Delta t \cong 0.038$ ms. In agreement with

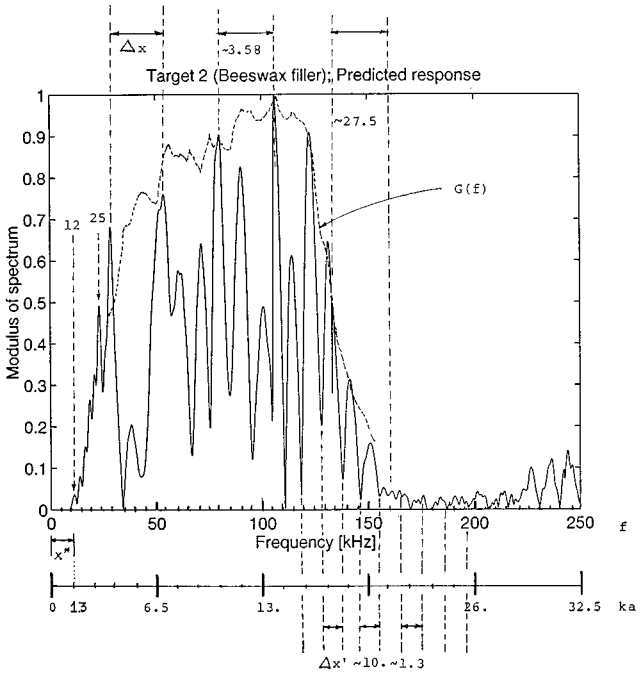

FIG. 8. Predicted spectrum of the echo returned by the beeswax-filled shell. Features spaced Δx and $\Delta x'$ are observed.

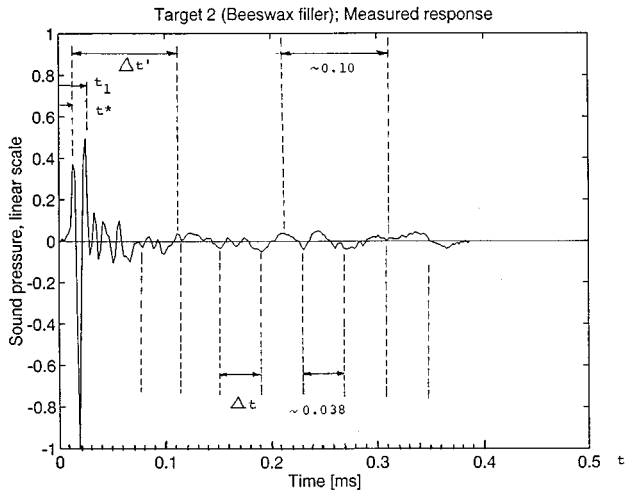

FIG. 9. Measured time signature of the beeswax-filled shell. Features spaced Δt and $\Delta t'$, similar to those in Fig. 7, are observed.

the ''uncertainty principle,'' it can be verified that

$$\Delta x \Delta t = (27\,500)(0.038\times 10^{-3}) \approx 1. \tag{18}$$

Closely spaced features in Fig. 7 correspond to widely spaced features in Fig. 8. There is also another set of features in Fig. 8 that appears at higher frequencies, that are spaced an amount: $\Delta x' \cong 10.0$ kHz. In the ka scale, this separation is: $\Delta x' \cong 1.30$. In the time domain (cf. Fig. 7) we also see repeated features separated a larger amount: $\Delta t' \cong 0.10$ ms. These two sets of features also obey a relation similar to Eq. (18), viz.,

$$\Delta x' \Delta t' = (10.0\times 10^{3})(0.10\times 10^{-3}) \cong 1. \tag{19}$$

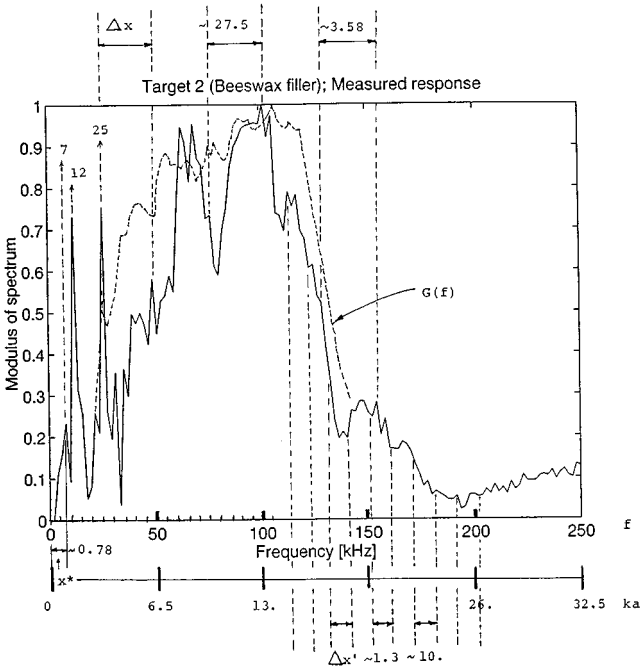

FIG. 10. Measured spectral response of the beeswax-filled aluminum shell insonified by the ''click'' in Fig. 5. Features spaced Δx and $\Delta x'$ are observed. These are similar to those in Fig. 8.

These features are due to ''rays'' incident on the shell, that travel back-and-forth through the shell and its filler, in the time interval given by Eq. (14).

The spacing Δx in the ka scale of Fig. 8 was: $\Delta x \cong 3.58$. This is essentially the ratio: $c_{\rm pl}/c$ [see Eq. (9)]. Since c in salt water is known, this relation determines the $c_{\rm pl} = c\Delta x \cong 5.47\times 10^{5}$ cm/s, which comes out very close to the value in aluminum [cf. Eq. (8)], and identifies it. The spacing $\Delta t \cong 0.038$ ms in Fig. 7 corresponds to the time it takes the s_0 Lamb wave to travel once around the shell (i.e., $2\pi a$) at the speed of the s_0 wave, which is the plate speed, $c_{\rm pl}$, just determined above. We can use the relation $\Delta t = 2\pi a/c_{\rm pl}$, to determine the shell radius ''a,'' viz.,

$$a = \frac{c_{\rm pl}\Delta t}{2\pi} \cong 3.3 \ \text{cm}, \tag{20}$$

which is a close estimate of the true value (3.25 cm). Since there is no observable ''giant resonance'' feature at low frequencies, typical of bodies with two curvatures (i.e., spheroids, ellipsoids, etc.) it can be concluded that this is a single-curvature object, like a cylinder. The location of the first maximum in Fig. 8 is about $x^* \cong 1$. Using the curve for aluminum (already identified) in Fig. 3 we find: $h/a \cong 2.3\%$, a slightly higher value than the true shell thickness of: $h/a = 1.85\%$ [cf. Eq. (11)]. We will see below that the measured response in Fig. 10 gives an even closer estimate. Since the radius ''a'' was determined above, the shell thickness comes out to be: $h = 0.023\times 3.3$ cm $= 0.76$ mm, which is the estimate obtained for the true value of 0.6 mm. Figure 7 shows the time interval $(t_1 - t^*)$ to be ~ 0.01 ms. This can be used in Eq. (13) to determine c_d, which comes out to be: 6.38×10^{5} cm/s, as assumed from the start for aluminum. Figure 8 shows features spaced an amount: $\Delta x' \cong 10.0$ kHz at the high-frequency end of the spectrum. Figure 7 shows repeated time features spaced an amount: $\Delta t' \cong 0.10$ ms. Here, $\Delta x'$ and $\Delta t'$ obey Eq. (19). We can verify that $\Delta t'$ is precisely the time required for the back-and-forth travel of a ray through the shell and the filler, as predicted by Eq. (14), viz.,

$$\Delta t' = 4\left(\frac{0.06}{6.38\times 10^{5}} + \frac{3.19}{1.3\times 10^{5}}\right) \cong 0.1 \ \text{ms},$$

$$\Delta x' = \frac{1}{\Delta t'} = 10.0 \ \text{kHz} \quad (\text{or } 1.30 \text{ on the } ka \text{ scale}).$$

It is then clear that Eq. (15) can be used to determine the sound speed in the filler. It is,

$$c_3 \cong \frac{4b}{\Delta t'} = \frac{4(3.19)}{10^{-4}} \cong 1.28\times 10^{5} \ \text{cm/s},$$

which is close to the value in Table I. (We have used here the fact that: $c_d \Delta t' \gg 4h$.) The value of Poisson's ratio in the shell can also be extracted. Since $c_{\rm pl}$ and c are already known, then $A = (c_{\rm pl}/c)^2 \cong 0.722$, and using this value in Eq. (16) yields $\nu \cong 0.345$, the value we started with. Hence, the predicted plots in Figs. 7 and 8 determine all the characteristics of the shell and its filler. They do not give the length (L) of the shell because the model is two dimensional, but that could be determined experimentally, by other means.

We now examine the measured responses in Figs. 9 and 10. The measured signatures in Fig. 9 (and 10) do not exactly coincide with the predicted ones in Fig. 7 (and 8). However, the features [i.e., the various spacings Δx, Δt, $\Delta x'$, $\Delta t'$, and the frequency or time parameters, x^* and $(t_1 - t^*)$] are nearly the same as those in Figs. 7 and 8. Hence, the identification procedure follows the same steps. The value $\Delta x \cong 3.58$ yields the same $c_{\rm pl}$ value found before, which identifies the shell material as aluminum. Also, $\Delta t = 0.038$ ms yields the same shell radius ''a'' (3.3 cm), and fixes the ka scale, as before. The first maximum of Fig. 10 now occurs at $x^* \cong 0.78$, which corresponds to a relative shell thickness (cf. Fig. 3) of $h/a = 1.75\%$, which is a closer estimate to the true thickness (of 1.85%) than that found from the theoretically predicted plot (i.e., Fig. 8). This yields a thickness: $h = (0.0175) \times (3.3\ \text{cm}) \cong 0.58$ mm. Figure 9 shows that $t_1 - t^* = 0.01$ ms which, again, yields the true value: $c_d \cong 6.38 \times 10^5$ cm/s. From $\Delta t' \cong 0.10$ (cf. Fig. 9) we find the sound speed in the filler as before, viz., $c_3 = 4b/\Delta t' \cong 1.28 \times 10^5$ cm/s, which is essentially the true sound speed in beeswax, and serves to identify it as such. We could have also used: $c_3 \cong 4b\Delta x'$, with $\Delta x' = 10.0$ kHz as seen in Fig. 10, and found the same value for c_3. Since $c_{\rm pl}$ is the same as before, then $A = c_{\rm pl}^2/c^2$ still has the same value 0.722, which yields the same value found earlier for the Poisson's ratio of the shell (i.e., $\nu = 0.345$), when substituted into Eq. (16). Hence, both the predicted *and* the measured responses, in the time *and* frequency domains totally characterize *all* the details of the targets, even when predicted and measured responses are not exact replicas of each other. This procedure has been repeated in various cases with several different fillers and a large number of dolphin clicks. The results are found to be essentially the same in all these cases.

VI. ANALYSIS OF THE ECHOES IN THE JOINT TIME-FREQUENCY DOMAIN

Thus far, our analysis was independently carried out in the frequency and in the time domains, separately. We now analyze the returned echoes in the combined time-frequency (t-f) domain using more advanced signal processing techniques. These techniques are based on the use of Wigner-type distributions. The basic properties of these distributions have been extensively discussed elsewhere[9] and need not be repeated. Our own earlier work[10] has already indicated how these distributions are used to analyze acoustic echoes from submerged structures.[11,12] A mini-summary of the key results to be used here, follows.

The pseudo-Wigner distribution (PWD) associated with a signal $f(t)$ is defined by

$$\overline{W}_f(t,\omega) = \int_{-\infty}^{+\infty} f\left(t + \frac{\tau}{2}\right) f^*\left(t - \frac{\tau}{2}\right) w_f\left(\frac{\tau}{2}\right) \times w_f^*\left(-\frac{\tau}{2}\right) e^{-i\omega\tau}\, d\tau, \tag{21}$$

where the asterisk (*) denotes complex conjugation and $w_f(t)$ is a window function, which here will be chosen to be a Gaussian of the form:

$$w_f(t) = \exp(-\alpha t^2). \tag{22}$$

The positive number α controls the width of the time window and emphasizes or de-emphasizes some selected features that may be present in the signal, $f(t)$. The PWD differs from the standard Wigner distribution (WD) by the presence of the window function, which is absent in the WD. The window function can be made to slide along the time axis with the instant t at which the WD is being evaluated. Different windows place different weights on the time segments of the time-varying function, $f(t)$.

The WD belongs to a more general class of bilinear distributions of the form:

$$C_f(t,\omega;\Phi) = \frac{1}{2\pi} \int_{-\infty}^{+\infty} du \int_{-\infty}^{+\infty} d\tau \int_{-\infty}^{+\infty} \Phi(\tau,\xi) \times \exp[i(\xi t - \omega\tau - \xi u)] f\left(u + \frac{\tau}{2}\right) f^*\left(u - \frac{\tau}{2}\right) d\xi. \tag{23}$$

Different choices of the kernel function $\Phi(\tau,\xi)$ yield the numerous time-frequency distributions used in current work. For example, if $\Phi(\tau,\xi) \equiv 1$, then, the WD is obtained, viz.,

$$W_f(t,\omega) = \int_{-\infty}^{+\infty} f\left(t + \frac{\tau}{2}\right) f^*\left(t - \frac{\tau}{2}\right) e^{-i\omega\tau}\, d\tau, \tag{24}$$

which, as mentioned above, is similar to Eq. (21) with the window function absent. For a kernel of the important form:

$$\Phi_s(\tau,\xi) = \int_{-\infty}^{+\infty} w\left(u + \frac{\tau}{2}\right) w\left(u - \frac{\tau}{2}\right) e^{-i\xi u}\, du, \tag{25}$$

the so-called spectrogram results, viz.,

$$\text{SPEC}_f(\omega,t) = \left| \int_{-\infty}^{+\infty} f(\tau) w(\tau - t) e^{-i\omega\tau}\, d\tau \right|^2 = |\text{STFT}_f(t,\omega)|^2. \tag{26}$$

This is the modulus squared of a standard Fourier transform viewed through a window $w(\cdot)$. The quantity within the absolute value signs is often called the short-time Fourier transform (STFT). The STFT provides good time resolution but does not provide good enough combined time *and* frequency resolution, simultaneously. More general approaches than that provided by the STFT were conceived from a hope to obtain a joint time *and* frequency distribution of the energy in a signal. All bilinear distributions can be interpreted[9] as smoothed or transformed versions of the WD with their particular type of smoothing—determined by the window function—which controls the amount of attenuation of the (unavoidable) interference terms, and the loss of time-frequency concentration of features. All continuous t-f distributions admit discrete representations in the usual way.[12,9] The Gabor spectrogram (GS^D) of order D is:[13,14]

$$\text{GS}_f^D(k,l) = \sum_{d=0}^{D} \sum_{\lambda(d)} a(t_\mu, f_\mu) H(k - t_\mu, l - f_\mu), \tag{27}$$

where $\lambda(d) = \{(m,n),(m',n') \,|\, |m-m'| + |n-n'| = d\}$ for each d is a set of pairs of coordinates separated by d, and

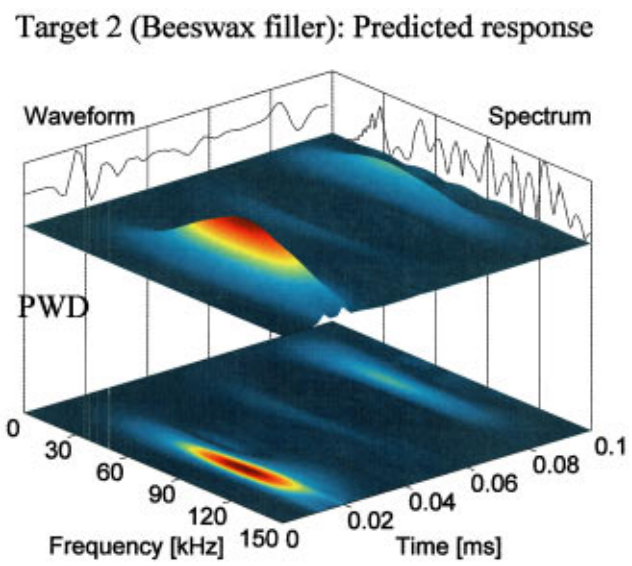

FIG. 11. Pseudo-Wigner distribution (PWD) of the echo-signature returned by the beeswax-filled tube. This is the prediction of the analytic model presented here [Eq. (21)].

$$a(t_\mu, f_\mu) = C_{m,n} C^*_{m',n'} \exp\left(i \frac{2\pi}{N} f_d t_\mu \right), \tag{28}$$

$$H(k,l) = 2 \exp\left\{ -\left[\frac{k^2}{\sigma^2} + \left(\frac{2\pi}{N} \sigma l \right)^2 \right] \right\} \times \exp\left\{ -i \left[\frac{2\pi}{N} (t_d l - f_d k) \right] \right\}, \tag{29}$$

and where the $C_{m,n}$ are the orthogonal-like Gabor coefficients,[13] $t_\mu = (m+m')\Delta M/2$, $f_\mu = (n+n')\Delta N/2$ the time and frequency centers, $t_d = (m-m')\Delta M$, $f_d = (n-n')\Delta N$ the time and frequency difference between two individual Gabor basis functions, and σ the variance.

For larger D, the Gabor spectrogram converges to the WD. The higher the value of D the higher the amount of

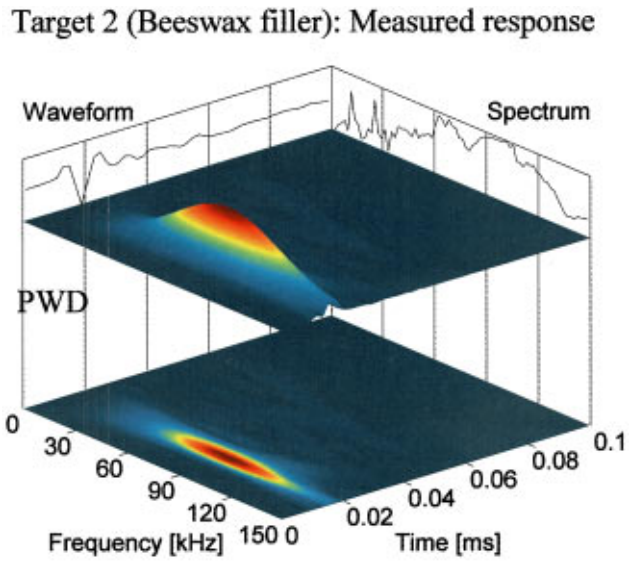

FIG. 12. PWD of the echo from the beeswax-filled shell insonified by the ''click'' in Fig. 5. This response is obtained from measured data in the database.

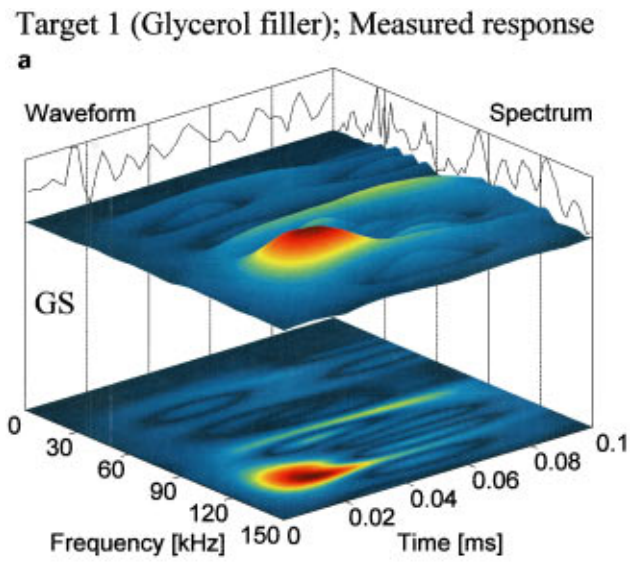

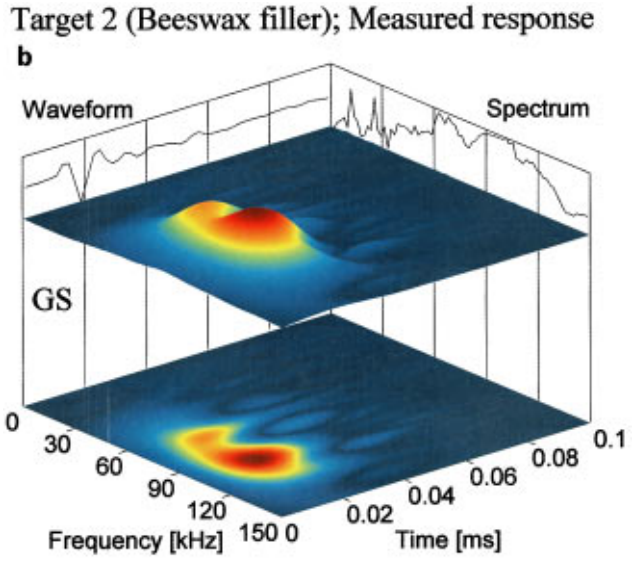

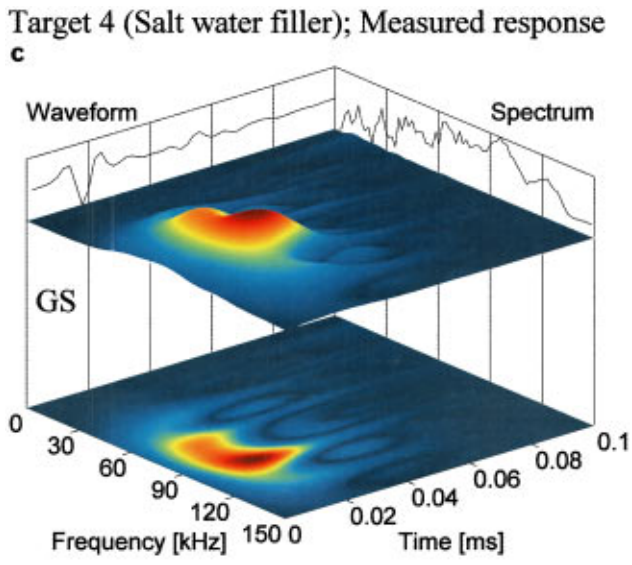

FIG. 13. Gabor spectrogram of order $D=4$ (GS) of the echoes from the shell filled with: (a) glycerol; (b) beeswax; (c) salt water [from Eq. (27)]. These plots are generated from measured data in the database.

computations that are required. An optimum value of D seems to be about three or four, for which the resolution is high and the cross-term interference becomes minimal. Among other distributions that reduce this unavoidable interference is the appropriately called, the ''reduced interference distribution.'' [15] For the present work we will only be concerned with the Gabor spectrogram of order D (GS), and with the PWD, as given above.

Figures 11 and 12 display the three-dimensional plots of the PWD obtained from Eq. (21) with a narrow window, for the predicted and measured shell responses, respectively, when the aluminum shell is filled with beeswax. The figures also show the usual[12] colorized projection in 2D in the bottom, time-frequency plane, as well as the waveform and spectrum on the lateral planes. Comparing Figs. 11 and 12 shows that the initial prominent feature of the response plots (up to 0.02 ms) exhibit great resemblances. The second strong feature in the predicted response (Fig. 11, 0.08–0.10 ms) is not observable in the measured response, because it appears later (for $t>0.1$ ms), outside the range of the plot. Analogous figures (not shown) for the case when the shell filler is glycerol, shows both of these features within the plot range and agreeing quite well with each other. The results in Figs. 11 and 12—in the ranges shown—are in general good agreement with those in Figs. 7, 8, 9, and 10; the smoothed-out differences being caused by the window effect in the PWD plots.

Finally, Fig. 13(a), (b), (c) displays analogous plots for shells with three different fillers (i.e., glycerol, beeswax, and salt water, respectively), but now generated using the GS [Eq. (27)]. The lateral planes show the waveform and spectrum. These types of t-f plots can also be generated using many other distributions as we have illustrated earlier in other publications.[12,16] Even with the naked eye a minimaly trained observer can easily distinguish the differences caused by the three fillers. Although Fig. 13(a), (b), (c) contains the information required for a detailed quantitative analysis[12] relating ''features'' to actual target characteristics as in the previous Section, if the classification task were just to distinguish among these three cases, such differentiation could be easily accomplished without calculations. It would only be required to simply inspect these patterns visually or auditorily, since they contain the same data, but in a more easily recognizable form. If there were more targets to choose from, the patterns could be fed to an automatic comparator to speed up the process. We also note that Fig. 13(b) is not very similar to Fig. 12 even though it pertains to the same target, because it was generated using a different distribution. This is not always the case. In some instances different distributions extract similar features and generate nearly the same plots. We remark in closing that the measured target responses analyzed here were preprocessed by deleting small initial portions (i.e., the first 0.15 ms in the time record; see Figs. 9 and 12). This was done because in many cases the *emitted* dolphin clicks had some frequency components of, as yet, unexplained origins at about 7, 12, and 25 kHz. These are noticeable in Fig. 6 and consequently, in Fig. 10. We used the click *tail* rather than the entire click to retain those (7, 12, and 25 kHz) features which otherwise would not be discernible, until their origin is better understood.

VII. CONCLUSIONS

We have presented a simple and systematic technique to extract all the physical characteristics of selected submerged targets containing different fillers, from the echoes they return when insonified by actual dolphin clicks. Theoretical predictions partially based on an earlier elasticity model[5] for an insonified shell were also generated, mainly to reassure us that the signatures we were analyzing were close to what they were ''expected'' to be. The time or frequency clues or features (i.e., Δx, $\Delta x'$, x^*, Δt, and $\Delta t'$) that we ended up using for the complete identification of *all* the physical characteristics of these targets (i.e., shape, size, shell material, shell thickness, and filler composition) appeared both in the predicted responses *and* also in the measured waveforms from the database. Interestingly, this happens even though the measured echoes were not exact replicas of the predicted ones. This simple method is amenable to quick automation. It gives *us* the necessary clues for identification. We believe that these same clues can be used by the dolphin. We also analyzed the echo signatures in the joint time-frequency domain using modern signal processing techniques relying on pseudo-Wigner distributions (PWD) and generalized (Gabor) spectrograms (GS). These useful color plots basically contain the same ''data'' as the separate frequency and/or time displays mentioned above, but the *joint* time-frequency plots (in either 3D or 2D) provide an easier and faster way to distinguish one target from another[16] by simple inspection. That is the basic advantage of an advanced signal processing technique: it gets more and cheaper mileage out of the same data. The present approach seems to scientifically explain the secret of the dolphin's consistent successes. However, the exact physiological or neuronal mechanisms the animal may use to extract these features and identify the target are still not understood, and have not been addressed here. We remark that had the *features* in the received echoes been blurred due to poor S/N, or had they been simply missing for whatever reason, this would have led to wrong choices or ''confusion'' in the selection of the resulting outcomes.

ACKNOWLEDGMENTS

The authors wish to acknowledge support from the Office of Naval Research (Code 321) and also from the Independent Research Boards of their own Institutions.

[1] P. E. Nachtigall and P. W. B. Moore, Editors, *Animal Sonar: Processes and Performance* (Plenum, New York, 1988).
[2] W. W. Au, *The Sonar of Dolphins* (Springer-Verlag, New York, 1993).
[3] G. C. Gaunaurd and M. Werby, ''Resonance response of submerged, acoustically excited thick and thin shells,'' J. Acoust. Soc. Am. **77**, 2081–2093 (1985) (see Fig. 14).
[4] G. C. Gaunaurd and W. Wertman, ''Transient acoustic scattering by fluid-loaded elastic shells,'' Int. J. Solids Struct. **27**, 699–711 (1991).
[5] G. C. Gaunaurd and D. Brill, ''Acoustic spectrogram and complex-frequency poles of a resonantly excited elastic tube,'' J. Acoust. Soc. Am. **75**, 1680–1693 (1984).
[6] H. L. Roitblat, P. W. B. Moore, D. A. Helweg, and P. E. Nachtigall, ''Representation and processing of acoustic information in a biomimetic neural network,'' in *Animals to Animals 2: Simulation of Adaptive Behav-*

ior, edited by J. A. Myer, H. A. Roitblat, and S. W. Wilson (MIT, Cambridge, MA, 1993), pp. 1–10.
[7] Some examples for other target shapes and frequency ranges have appeared in G. C. Gaunaurd, ''Active classification via transient resonant scattering,'' J. Opt. Eng. **31**, 2553–2561 (1992).
[8] G. C. Gaunaurd and M. Werby, ''Lamb and creeping waves around submerged spherical shells resonantly excited by sound scattering II,'' J. Acoust. Soc. Am. **89**, 1656–1667 (1991).
[9] L. Cohen, *Time-Frequency Analysis* (Prentice-Hall, Englewood Cliffs, NJ, 1995).
[10] G. C. Gaunaurd and H. C. Strifors, ''Time-frequency processing of underwater echoes generated by explosive sources,'' Ultrasonics **33**, 147–153 (1995).
[11] G. C. Gaunaurd, H. C. Strifors, and W. H. Wertman, ''Transient effects in the scattering of arbitrary electromagnetic pulses by dielectric spherical targets,'' J. Electromagn. Waves Appl. **5**, 75–92 (1991).
[12] G. C. Gaunaurd and H. C. Strifors, ''Signal analysis by means of time-frequency (Wigner-type) distributions: Applications to Sonar and Radar Echoes,'' Proc. IEEE, Special issue on ''Time-Frequency Analysis of Signals'' (invited) **84**, 1231–1248 (1996).
[13] S. Qian and D. Chen, ''Discrete Gabor transform,'' IEEE Trans. Signal Process. **41**, 2429–2438 (1993).
[14] S. Qian and D. Chen, ''Signal representation using adaptive normalized Gaussian functions,'' Signal Process. **36**, 1–11 (1994).
[15] J. Jeong and W. J. Williams, ''Kernel design for reduced interference distributions (RID),'' IEEE Trans. Signal Process. **40**, 402–412 (1992).
[16] G. C. Gaunaurd and H. C. Strifors, ''Transient resonance scattering and target identification,'' Appl. Mech. Rev. **50**(3), 131–149 (1997).

The mammalian auditory hair cell: A simple electric circuit model

F. Rattay and I. C. Gebeshuber
University of Technology, Vienna, Austria

A. H. Gitter
Institut für klinische Physiologie, Freie Universität, Berlin, Germany

(Received 5 February 1997; revised 1 November 1997; accepted 2 November 1997)

A model based on the potassium current pathway through the hair cell is used to analyze the electrical behavior of mammalian inner and outer hair cells. Without taking into account the effects of calcium it is possible to simulate experimental results concerning the shape and strength of the receptor potential and the frequency dependent ac (alternating current) and dc (direct current) components of the receptor current. This model and a simplified form of it are utilized to explain: (1) Transduction latencies: that the receptor potential follows a stimulating signal with a very short delay, under the assumption of a constant number of open K^+ channels in the lateral part of the cell membrane. (2) Transduction gains: why higher potential changes are measured in inner hair cells than in outer hair cells, although the outer hair cells are expected to be exposed to higher stereociliary motions: in inner hair cells a decrease in the conductance of the basolateral membrane causes higher gain (receptor potential increases) and together with an increase of membrane capacitance slower reaction (a larger time constant). (3) Transduction channel kinetics: that the shortest (0.1 ms) as well as the longest (20 ms) possible open times of the transduction channels in the stereocilia have different frequency related effects on the shape of the receptor potentials.
 [S0001-4966(98)03503-6]

PACS numbers: 43.64.Ld, 43.64.Bt, 43.64.Nf [RDF]

INTRODUCTION

In vertebrates, hair cells are found in all peripheral structures used in hearing and balance. They play the key role in the mechano-electrical transduction mechanism. Inner hair cells (IHC) and outer hair cells (OHC) are found in the mammalian cochlea. Figure 1 schematically illustrates a typical inner hair cell. The apical part of the cell including the hairs (stereocilia) enters the endolymphatic fluid, which is characterized by its high electrical potential and its high K^+ concentration. The stereocilia of one hair cell are connected through tip links and lateral links. The transmembrane voltage of -70 mV for OHC and -40 mV for IHC is mainly caused by the K^+ concentration gradient between cell body and cortilymph. Current influx that changes the receptor potential occurs mainly through the transduction channels of the stereocilia: stereociliary displacement to the lateral side of the cochlea causes an increase of transduction channel open probability and hence depolarization of the receptor potential, whereas stereociliary displacement to the medial side results in a decrease of the transduction channel open probability and hence hyperpolarization. The transduction channel is cation selective and although Ca^{++} ions are important in regulating the opening mechanism of the transduction channels our electric model considers the main current component, carried by K^+ ions entering the cell.

The relation between hair deflection and receptor potential change is asymmetric and saturates (Hudspeth and Corey, 1977; Markin *et al.*, 1993). Small variations of the receptor potential (about 0.1 mV) cause a release of at least one quantum of neurotransmitter which may cause spiking in the most sensitive fibers of the auditory nerve (Hudspeth, 1989). In this respect the effectiveness of synaptic transmission from the hair cell to the auditory nerve fiber is extraordinary compared to common synaptic transmission, e.g., Katz and Miledi (1967) report that there is a threshold for neurotransmitter release at about 45 mV depolarization in the presynaptic terminal of the squid stellate ganglion.

Several hypotheses are concerned with the opening mechanism of the transduction channels in the stereocilia. The most prominent is the gating-spring theory from Hudspeth which proposes that the tip links which connect neighboring stereocilia are elastic elements, called gating springs, that directly open the transduction channels (Pickles *et al.*, 1984). Even the assumption that the gating springs are localized in the horizontal links would not influence the functionality of the transduction mechanism (Gitter, 1994, 1996). Because of the lack of experimental data, our model does not suggest a detailed transduction mechanism process.

Mammalian hair cells are very sensitive and because of their short latency in generating the receptor potential a second messenger system is highly unlikely to be involved. In the present paper we show that a model of the hair cell that just takes into account its electrical properties yields results comparable to those from experiments.

I. ELECTRICAL MODEL OF A HAIR CELL

The main task of hair cells in sensory systems is to detect forces which deflect their stereocilia. Differences in the hair cells of the cochlea and of the vestibular organ appear in ion concentrations, in geometries and membrane

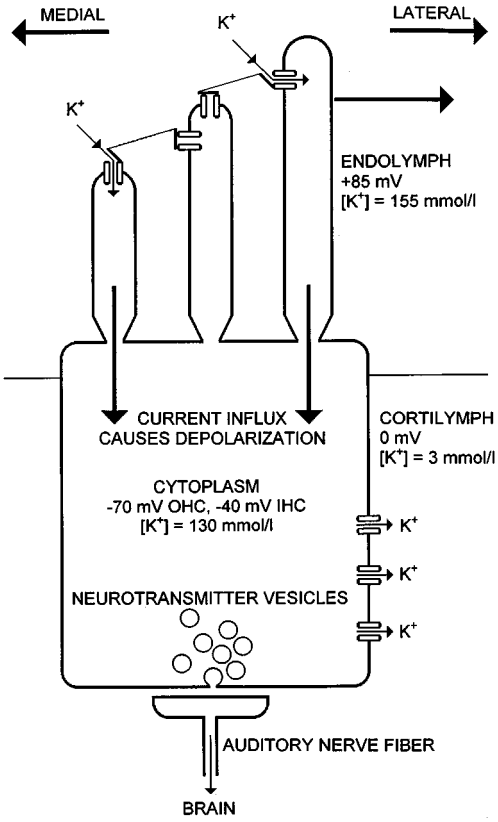

FIG. 1. Scheme of a mammalian cochlear inner hair cell. Experimental results indicate that there are only one or two transduction channels close to the tip of each stereocilium. K^+ influx through open transduction channels causes depolarization inside the hair cell, repolarization occurs then because of K^+ outflux through the lateral cell body membrane.

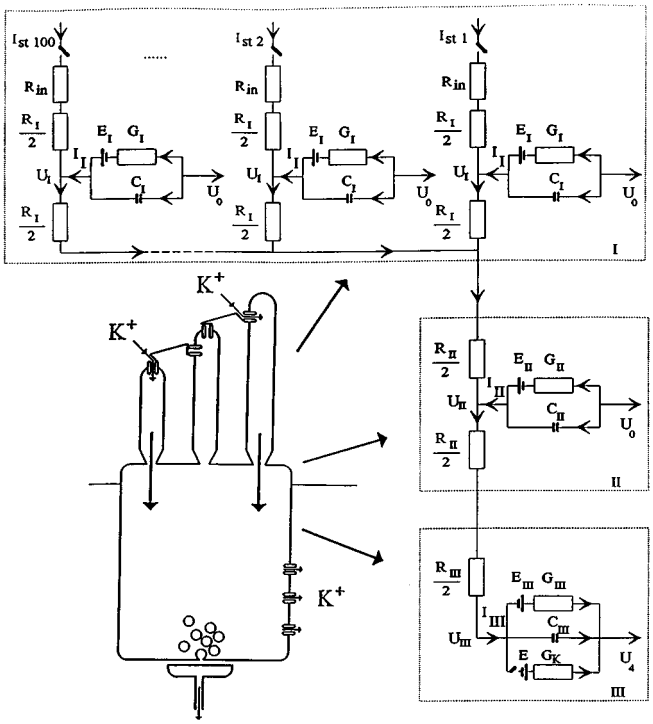

FIG. 2. Equivalent electric circuit diagram of the hair cell's three main regions in our model. Each of the compartments is represented by its mean inside potential U, membrane conductance G, membrane capacitance C, Nernst potential E and cytoplasm resistance R. The K^+ influx through the jth stereociliary transduction channel is represented by the stimulating current I_{stj}. G_K represents the conductance of a K^+ channel in the basolateral cell membrane. U_0 and U_4, the potentials in the endolymph and cortilymph are constant, whereas the potentials in the different hair cell regions, U_I, U_{II} and the receptor potential U_{III}, depend upon stereociliary movement. Note that the values of G_I and C_I depend on the individual stereocilia lengths.

properties. Even in the same cochlea there are remarkable differences between receptor potentials from inner hair cells and outer hair cells (comp. inset of Fig. 3). Konishi and Salt (1983) measured the K^+ activities in the mammalian cochlea at $[K^+]_{\text{endolymph}} = 113.8$ mM, $[K^+]_{\text{cortilymph}} = 1.98$ mM and $[K^+]_{\text{hair cell}} = 64.8$ mM. In our model we used data from Zenner (1994) as shown in Fig. 1 (see also Ma *et al.*, 1996). In the cochlea, the electrical potential of endolymph and cortilymph are 84.7 mV (Konishi and Salt, 1983) and 0 mV (Dallos *et al.*, 1982), respectively. According to Russell and Sellick (1978) and Cody and Russell (1987), the resting potential of cochlear IHC is about -40 mV. The resting potential of OHC is about -70 mV (Dallos *et al.*, 1982).

Our equivalent electric circuit model of a hair cell consists of three different compartments (Fig. 2). The part of the cell body which is surrounded by cortilymph forms compartment III. U_{III} represents the voltage in the center of this compartment, i.e., U_{III} equals the receptor potential. So, when no stimulus is applied U_{III} equals the resting potential. The transition between the cell body and the stereocilia is modeled by compartment II, a spherical part with center voltage U_{II}, whose membrane is surrounded by endolymph-like compartment I, the stereocilia. The current flux through the transduction channels into the stereocilia is modeled individually by subcompartments containing switches, which simulate the opening/closing kinetics of the transduction channels. The single channel transduction current is calculated using the cortilymph-cytoplasm potential difference with constant single channel conductance resulting in 10 and 12 pA for IHC and OHC, respectively. However, our model does not suggest a detailed mechanism for the transduction process since further experimental evidence on the molecular movement associated with transduction is necessary, and the single channel transduction current in our model was assumed to be constant (according to Crawford *et al.*, 1991, the fluctuations in receptor potential do not significantly influence the total charge movement while the transduction channels are open). The open probability of transduction channels depends in a non-linear way on the deflection of the stereocilia; we used the data from Markin *et al.* (1993) for modeling. U_I represents the voltage in the center of each of the stereocilia. On IHC the stereocilia are arranged in three parallel rows, on OHC the three rows of stereocilia are parallel and additionally arranged in W shape. Zetes (1995) reports in IHC stereocilia lengths of 2.024 ± 1.411 μm, and in OHC of 2.070 ± 1.184 μm. In our model we have investigated the influence of stereocilia lengths on the receptor potential changes. We have averaged the stereocilia lengths reported in Zetes (1995), such that the stereocilia bundle is composed of three rows of stereocilia of increasing heights, with equal heights in each row and we have also calculated the influence of uniform stereocilia lengths across the hair bundle.

Each compartment consists of capacity, resistance and

TABLE I. Parameters used for modeling cochlear hair cells.

Parameter	IHC	OHC
number of stereocilia (human, Zenner, 1994)	$n=60$	$n=100$
average length of stereocilia (guinea pig, Zetes, 1995; humans: Zenner, 1994)	$l_I=2$ μm	$l_I=2$ μm
average diameter of stereocilia (guinea pig, Zetes, 1995; Zenner, 1994)	$d_I=0.2$ μm	$d_I=0.2$ μm
length of cell body (Zenner, 1994)	$l_{III}=20$ μm	$l_{III}=50$ μm
diameter of cell body (guinea pig, Preyer *et al.*, 1994)	$d_{III}=8$ μm	$d_{III}=10$ μm
cell body area involved (calculated)	$a_{III}=552$ μm^2	$a_{III}=1649$ μm^2
open probability of transduction channels at rest (bullfrog, Hudspeth, 1989)	0.15	0.15
single transduction channel current (guinea pig, lateral OHC K^+ channel, Gitter *et al.*, 1992)	$I_{tc}=10$ pA	$I_{tc}=12$ pA
input resistance of transduction channel	$R_{in}=0$ Ω	$R_{in}=0$ Ω
cytoplasm resistance (Rattay, 1990)	$\rho_i=100$ Ω cm	$\rho_i=100$ Ω cm
membrane resistance (Rattay, 1990)	$\rho_m=5$ kΩ cm^2	$\rho_m=5$ kΩ cm^2
membrane capacitance (Rattay, 1990; see text)	$c=2$ μF/cm^2	$c=1$ μF/cm^2
cortilymph potential (Zenner, 1994)	$U_4=0$ V	$U_4=0$ V
endolymph potential (Zenner, 1994)	$U_0=85$ mV	$U_0=85$ mV
Nernst potential endolymph-cytoplasm (calculated)	$E_I=E_{II}=4$ mV	$E_I=E_{II}=4$ mV
Nernst potential cytoplasm-cortilymph (calculated)	$E_{III}=43$ mV	$E_{III}=71$ mV
number of K^+ channels in the lateral cell membrane (always open; fitted)	$Kch=260$	$Kch=900$
conductance of a lateral K^+ channel (guinea pig, Gitter *et al.*, 1992)	$G_K=200$ pS	$G_K=200$ pS
cytoplasm resting potential (Russell and Sellick, 1978 and Cody and Russell, 1987; Dallos *et al.*, 1982)	-39.7 mV	-69.9 mV

battery to model the various currents through the membrane. Battery potentials were calculated using data of Zenner (1994). The compartments are connected by resistances, which represent the electrical properties of the cytoplasm. The currents from the open transduction channels combine to a current which flows through compartment II. This current then leads to a receptor potential change in compartment III and leaves the receptor cell through K^+ channels in the basolateral membrane. In the resting state, e.g. when the stereocilia are not deflected, about 15% of the transduction channels are open (Hudspeth, 1989).

There are few data available on the kinetics of transduction channels. Crawford *et al.* (1991) report for a 150-nm displacement of the stereocilia a mean open time of 1.1 ms and a distribution that could be well fitted by a single exponential. Because of this we modeled the open/close kinetics by a Markovian process without memory. The shortest possible transduction channel open time was assumed to be 0.1 ms, the longest 20 ms, as reported for K^+ channels in the lateral cell body membrane of guinea pig outer hair cells (Zenner, 1994).

This model can be used for all kinds of hair cells. Parameters for typical mammalian IHC and OHC which we have used for our calculations are given in Table I. We used an average number of 60 stereocilia for IHC and 100 for OHC, respectively. Note that this does not generally hold in mammalian cochleas, e.g., in the apex of the guinea pig cochlea OHC in the second and third rows frequently have less than three rows of stereocilia. IHC cell body lengths show small variations within a single cochlea, OHC cell body lengths, however, vary, at the apex of the cochlea they can be three times as long as they are at the base (Spoendlin, 1970). We modeled IHC with a length of 20 μm and OHC with an average length of 50 μm, according to Zenner (1994).

Our results show that for the prediction of the receptor potential in compartment III, the compartments I and II can be omitted because the leakage through the membranes of these two compartments is very small.

II. RESULTS

There are differences in the time constants and amplitudes of receptor potential reactions of inner and outer hair cells to a stimulus of 1 ms duration, which is strong enough to open all of the transduction channels (Fig. 3). Here we assume that 15% of the transduction channels are always open, and the rest switches from closed to open state while the stimulus pulse is applied. The main differences between IHC and OHC in physiological parameters are (see also Table I): Compared to an OHC an IHC has fewer stereocilia with a larger variance in lengths, a smaller cell body, a higher membrane capacitancy, and fewer K^+ channels because of the smaller basolateral membrane area involved (leading to a smaller resting potential). In our view OHC are also expected to be exposed to higher stereociliary motions because of their localization close to the mainly moving parts of the basilar membrane. The inset of Fig. 3 shows the relating experimental data from Dallos (1983).

A. Transduction latencies

Modeling an OHC without any open lateral K^+ channels results in a time constant of the receptor potential change of 5 ms, because only current outflux via the membrane is possible in this situation. The IHC capacitance is modeled

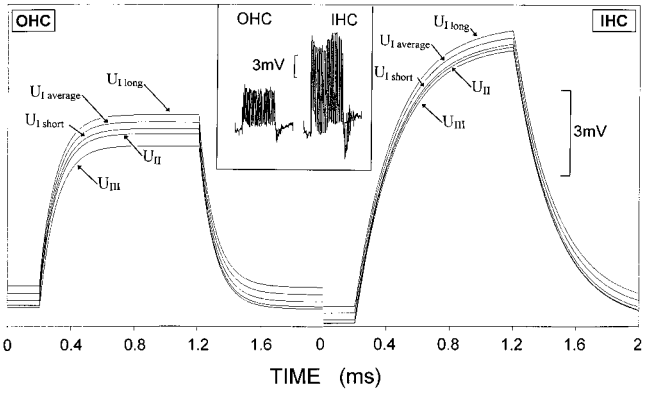

FIG. 3. Simulated receptor potentials of an inner and an outer hair cell. The voltages in the stereocilia, $U_{I\,short}$, $U_{I\,average}$ and $U_{I\,long}$, increase with lengths (OHC stereocilia lengths: 2.070 ± 1.184 μm, IHC stereocilia lengths: 2.024 ± 1.411 μm). These voltages are slightly higher than U_{II} because of the leakage through the stereocilia and compartment II. The receptor potential U_{III} is the smallest because of additional leakage through the cell body membrane. In the resting state 15% of the transduction channels are open, after 0.2 ms all transduction channels open for 1 ms. Note the following basic differences between IHC and OHC: (1) the higher gain of the IHC transduction mechanism; (2) the larger time constant of an IHC does not allow for saturation of the receptor potential within 1 ms; (3) different resting potentials, IHC: -40.9 mV and OHC: -70.4 mV. Inset (from Dallos, 1983): Receptor potentials from one inner hair cell and one outer hair cell measured in the same cochlea at a stimulation frequency of 1 kHz, 80 dB SPL. Both cells follow the stimulus simultaneously.

with the OHC value doubled. This has several reasons: Capacitance decreases when the distance between the charged particles increases, and as 70% of the OHC surface are covered with large particles of putative motor proteins (Forge, 1991) a smaller capacitance for OHC is justified. Gitter and Zenner (1990) report that IHC membrane of guinea pigs appear to be softer and less rigid than those of OHC. This makes a higher capacitance for IHC reasonable. Furthermore, a variation in membrane capacitance also occurs in generally accepted models for the membranes of the nodes of myelinated nerve fibers: Sweeney *et al.* (1987) takes for the rabbit 2.5 μF cm^{-2} as membrane capacitance and Frankenhaeuser and Huxley (1964) assume for the frog 1 μF cm^{-2}. These values are necessary for the proper shape of the action potentials.

The OHC is modeled with 900 open K^+ channels with a single channel conductance of 200 pS leading to a time constant $R_{m\,III} \cdot C_{III} = 0.1$ ms [Dallos (1984) reports a time constant of 0.127 ms]. For the IHC just 260 of those K^+ channels were assumed because of the smaller cell body area involved, this gives a time constant of 0.255 ms. Russell and Sellick (1983) report IHC time constants from 0.19 to 0.89 ms with a mean of 0.387 ms.

B. Transduction gains

The OHC is of remarkable sensitivity: In our model, a 1 ms stimulus of 12 pA (one additional open transduction channel during this time) leads to a change in receptor potential of 0.065 mV. The maximum possible range of receptor potential change is 6.6 mV. Preyer *et al.* (1994) report 5 mV.

The simulation demonstrates the higher gain to equivalent stimuli of an IHC compared to an OHC: A 1 ms stimulus of 10 pA (one additional open transduction channel during this time) leads to a receptor potential change of 0.19 mV. A receptor potential change of 0.1 mV is assumed to lead to neurotransmitter release and thereby to an action potential in the auditory nerve fiber (Hudspeth, 1989). In the case of IHC the maximum possible range of receptor potential change is 11.1 mV. This is also in accordance with experimental results (compare the inset of Fig. 3).

We have investigated the electrical influence of different stereociliary lengths on the receptor potential in order to justify a possible simplification of the model. Decreasing amplitudes of the voltages occur in the three rows of the stereocilia (U_{Ii}) in the small transition compartment (U_{II}), and in the cell body (U_{III}) (Fig. 3). Since only U_{III}, the voltage changes at the bottom of the cell, triggers neurotransmitter release, we propose the following reduction: The calculations of U_I and U_{II} can be omitted, the transduction current and some additional current, that always flows into the hair cell because of membrane leakage in the apical part (about 50 pA) are assumed to flow directly into compartment III (reduced model).

C. Transduction channel kinetics

The computer simulation allows the investigation of the influence of constant open times for all transduction channels. According to experimental results, the open times are assumed to range between 0.1 and 20 ms. Various open times at different stimulation frequencies lead to quite different results (Fig. 4). In all examples the sinusoidal stimulus is equivalent to a 20 nm amplitude, this means a 20 nm deflection of the stereocilia. For such small amplitudes the open probability of the transduction channels is a linear function of stereociliary deflection (Markin *et al.*, 1993). As we will see below, for larger displacement this function becomes asymmetric and saturating.

For this simulation each sinusoidal stimulus period is segmented in its four quadrants. The transduction channels are assumed to be stretch sensitive and therefore their opening depends not only on the deflection but also on the direction of the movement of the stereocilia: Only in the first quadrant of the stimulating signal (stereociliary motion to the lateral side) transduction channels open—and one additional channel opens for every signal step of 1 nm. The transduction channels hold their open status for a given time [0.1 ms in Fig. 4(a), 1 ms in (b) and 18 ms in (c)]. During the second quadrant of the stimulating signal, when the stereocilia move back to the initial position, the stretch on the channels is reduced again and therefore no additional channels open. In the third quadrant the stereocilia are deflected from the initial position to the medial side, some of the transduction channels that were open in the initial resting state are forced to close, for every signal step of -1 nm one channel closes. Note that in this modeling situation 20 channels are open in the initial resting state. We investigated the receptor potential reaction to a 100 Hz signal for three different transduction channel open times: 0.1, 1, and 18 ms (Fig. 4). Special effects occur when the open time of the transduction channels

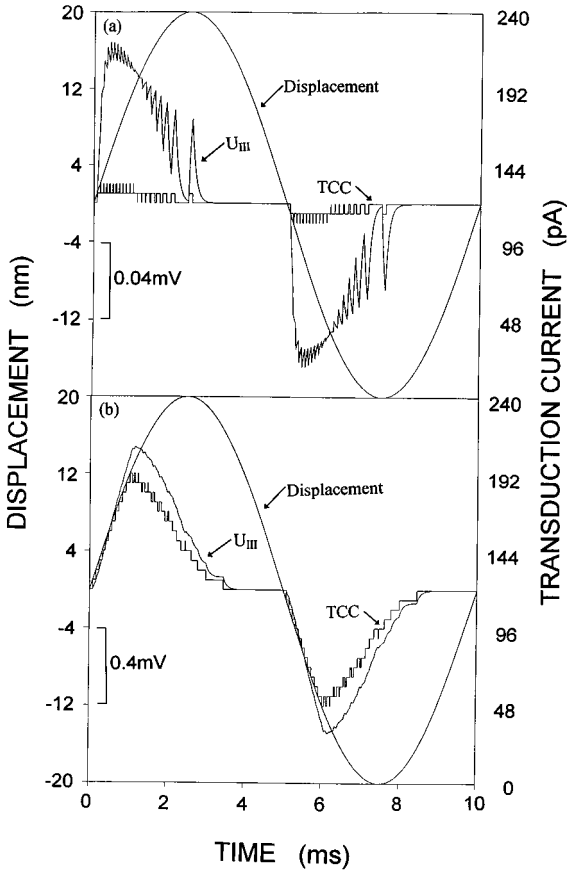

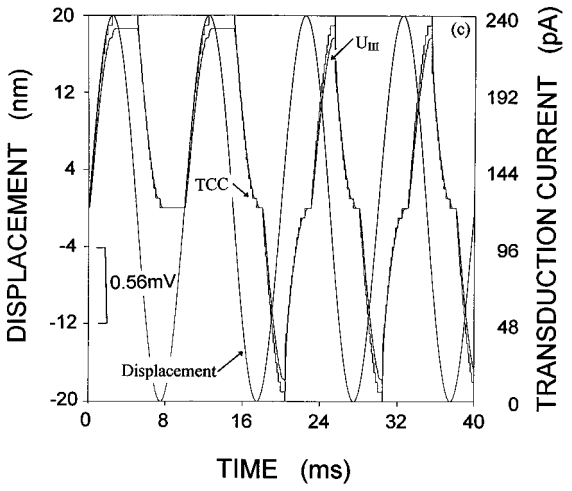

FIG. 4. Transduction channel current (TCC) and receptor potential as a function of transduction channel open time. (a) and (b) show one period, (c) shows four periods of the stimulating sinusoidal 100 Hz signal (displacement of the stereocilia) and the transduction channel current influx which rises and falls in steps of 12 pA corresponding to the single channel current. In (a) the channel open time is 0.1 ms, this is in the range of the OHC time constant $R_{m\,III} \cdot C_{III}$. Note that U_{III} accumulates more than the transduction channel current influx, but it does not reach a 0.1 mV change when two channels are open. In (b) the channel open time is 1 ms. Because of the membrane capacitance the curve for U_{III} is smoother than the steplike transduction channel current curve. Note the different voltage scale compared to (a) and that U_{III} exceeds a change of 0.1 mV. In (c) the channel open time is 18 ms and as a consequence U_{III} becomes periodical not before 18 ms. The steplike curve is the transduction channel current, because of the OHC time constant of 0.1 ms the receptor potential is nearly in phase with TCC, but smoother. Calculations with OHC parameters of Table I, reduced model.

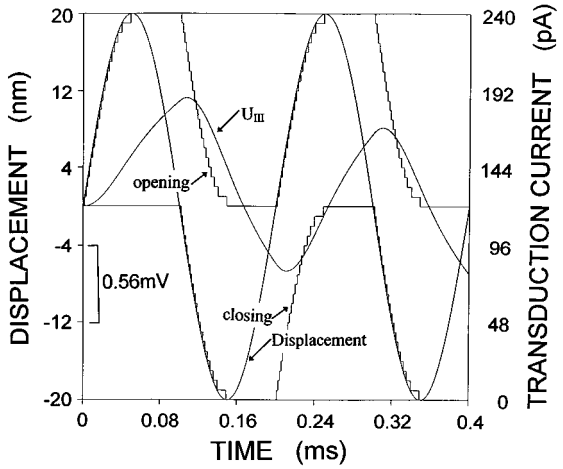

FIG. 5. Receptor potential for a 5000-Hz stimulus and a channel open time of 0.1 ms. For clarity in the TCC curve is divided into two parts: the contribution from the number of transduction channels that are open additionally to the 20 channels open at the resting state (upper step-like curve), and the contribution from the number of channels that are open at rest but closed because of stereociliary movement to the hyperpolarizing side (lower step-like curve). The sum of these two curves gives the TCC. Compared to Fig. 4(c) the phase shift of U_{III} is larger relative to the stimulating signal (OHC time constant 0.1 ms), because of its higher frequency. Calculations with OHC parameters of Table I, reduced model.

is long compared to stimulus period. Figure 4(c) demonstrates this effect for a transduction channel open time of 18 ms and stimulus period of 10 ms. During the first cycle of the stimulus, rectification of TCC and the receptor potential U_{III} occur: The transduction channel open time is 18 ms. However, during the third quadrant of the stimulating signal, other channels are forced to close. Note that compared to (a) and (b) no hyperpolarization of U_{III} occurs during the first period of the stimulus. In the second period of the stimulating signal hyperpolarization takes place, because the channels that opened during the starting phase of the stimulus close again.

For higher frequencies the transduction channel currents accumulate even for shortest open times (Fig. 5). Our results show that in the region where low frequencies are detected, longer transduction channel open times increase the amplitude of the receptor potential, whereas in high-frequency regions short transduction channel open times are of advantage because they enable hyperpolarization within a few periods of the stimulating signal.

It is known from experiments that receptor potentials in auditory hair cells are asymmetric. Markin *et al.* (1993) published an asymmetric sigmoidal relation between stereociliary displacement and the open probability of the transduction channels. This relation contributed to the results of Fig. 6 and is shown as the inset of Fig. 6(a). In (a) and (c) stimuli with an amplitude of 100 nm are used, in Fig. 6(b) the stimulus amplitude is 20 nm. Stereociliary displacements with an amplitude less than 20 nm are in a region of a linear relation to the open probability, and therefore U_{III} in Fig. 6(b) is symmetrical. Stronger stimuli lead to asymmetry in the receptor potential [Fig. 6(a) and (c)]. Stimuli in the kHz range lead because of the time constant to a steady component in U_{III} (caused by the dc component of the receptor current)

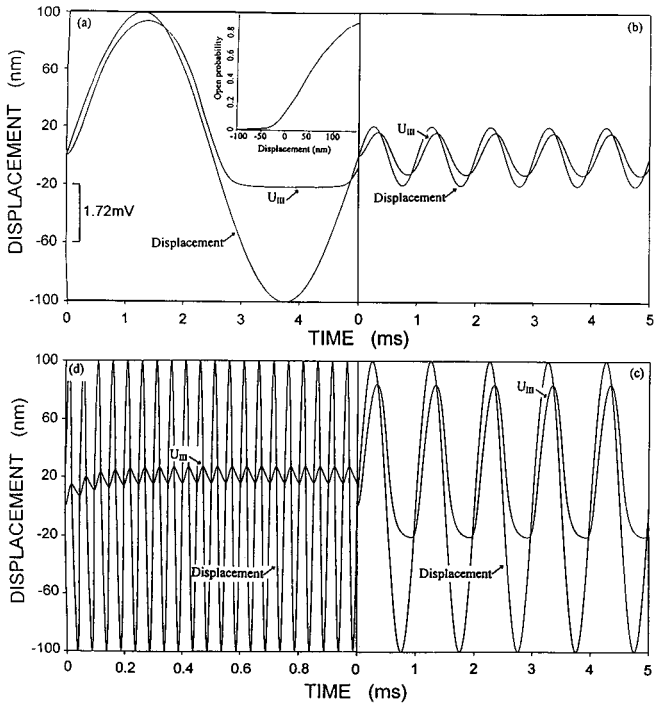

FIG. 6. Receptor potential reactions to different stimulating frequencies. Figure 6(a) shows the asymmetric receptor potential following a 200-Hz stimulus with 100-nm amplitude. The inset shows the relation between stereociliary displacement and open probability of a transduction channel according to Markin *et al.* (1993). Figure 6(b) and (c) shows the changes in U_{III} caused by 1000-Hz stimuli with amplitudes of 20 and 100 nm, respectively. In (b) U_{III} is symmetric as a consequence of the low amplitude stimulus (amplitude $<$ 20 nm), but when in (c) the high amplitude stimulus is applied, the displacement-open probability relation is not linear any more for the sinusoidal stimulus and therefore the depolarization is stronger than the hyperpolarization. In Fig. 6(d) U_{III} consists of alternating and steady components because of the high frequency stimulation: 20 kHz with 100-nm amplitude. Calculations with OHC parameters of Table I, reduced model. (a)–(d) are in the same scale regarding displacement and voltage.

which increases with frequency. The steady component in Fig. 6(d) is in the range of 1 mV, which is in accordance with experimental results from Dallos (1983) (comp. inset of Fig. 3). However, in auditory hair cells a high variance is found regarding the sensitivity and the strengths of the alternating and steady components (Mountain, 1989; Russell and Sellick, 1983; Palmer and Russell, 1986; Preyer *et al.*, 1994).

III. DISCUSSION

Taking only into account the pathway of K^+ ions through the cell and the capacitative currents results in a model that is able to represent basic properties of receptor potential changes in mammalian inner and outer hair cells. The results of our simulations are in accordance with measured receptor potentials and membrane currents, comp. the inset of Fig. 3 (from Dallos, 1983) that shows one of the rare measurements of receptor potentials for IHC and OHC from the same organ of Corti and demonstrates the higher gain of IHC. Furthermore, the asymmetric shape of the receptor potential caused by a sinusoidal stimulus [depolarizing portion is essentially larger than the hyperpolarizing one in Fig. 6(a) and (c)] was reported among others by Kros *et al.* (1993). The steady components in the receptor potential which appear at higher frequency stimulation, e.g. in Fig. 6(d), are also well known from experiments (Palmer and Russell, 1986).

Because we do not model adaptation our results reflect the behavior of hair cells with the highest sensitivity. The large dynamic range of the auditory system of $1{:}10^6$ can be explained by at least three facts: (1) for strong stimuli adaptation takes place in the hair cell; (2) the synapses of the auditory nerve fibers connecting to a single hair cell have different sensitivity; and (3) different sensitivity between neighboring hair cells.

A comparison of our results with former models shows that:

(1) Some of the former investigations did not account for the capacitance of the cell membrane because the analysis was limited to low frequencies (e.g., Mountain, 1989). Our model holds for all frequencies, calculates appropriate time constants for IHC and OHC and enables investigation of their influence on the receptor potential changes regarding different transduction channel open times and stereocilia lengths (Figs. 3, 4 and 5).
(2) Some authors use RC networks for analyzing parts of the cortical organ, but they mainly concentrate on other features than potential changes within the hair cell (e.g., Mountain and Hubbard, 1994; Dallos and Evans, 1995).
(3) A model of the receptor potential of hair cells utilizing a simple model circuit and ideas of stretch activated channels shows interesting results yet it is focused on hair cells of the lateral line organ of mudpuppy (Bell and Holmes, 1986).

Our simple electric circuit model of the mammalian auditory hair cell can be utilized to explain the following important basic features:

(1) Transduction latencies: The receptor potential follows a stimulating signal with a very short delay, i.e., with time constants of 0.1 and 0.255 ms for OHC and IHC, respectively (see Figs. 3, 5, and 6). Thus, OHC react faster. The larger IHC time constant results from an IHC membrane capacitance which is the OHC value doubled; reasons for this assumptions have been given in Sec. II. Note that these time constants (τ=RC) do not depend on the surface area since C is proportional and R is inverse proportional to the basolateral membrane area involved. The difference between IHC and OHC is, therefore, not affected by the variation in length of the OHC.
(2) Transduction gains: IHC show higher receptor potential changes to the same stimulus than OHC. This is caused by different electrical properties of both kinds of hair cells: In IHC, which are generally smaller compared to OHC of the same region, the decrease in conductance of the basolateral membrane causes higher gain.
(3) Transduction channel kinetics: In a single living hair cell the transduction channels in the stereocilia show a mixture of open times ranging from 0.1 to 20 ms. The computer simulation allows exploration of the influence of

possible channel open time distributions on the receptor potential changes. Furthermore, constant channel open times are used in order to analyze the significance of the wide range of channel open times. We have demonstrated that longer transduction channel open times cause higher gain whereas the shorter open times are of advantage for the encoding of high frequency stimuli.

In Sec. II C we used the displacement dependent open probability of the transduction channels to show the effects of different but constant open times on the receptor potential at various frequencies. A refinement of our model should investigate stochastic distributions in the transduction channel open times for the different stereocilia within one hair cell and show their effects on the receptor potential and the ability of the brain to detect the auditory signal. In that model it will be of importance to consider the fact that OHC length changes are associated with a charge movement within the cell membrane, as this charge movement manifests itself as a nonlinear membrane capacitance that contributes up to 40% of the cell's total capacitance (Santos-Sacchi, 1991).

A refinement of the model should also include the voltage dependence of the potassium channels in the basolateral cell body membrane (Gitter *et al.*, 1986; Gitter *et al.*, 1992) and the role of calcium which performs various local tasks (Jaramillo, 1995). For example, at the basal end of the hair cell depolarization-induced locally increased Ca^{++} triggers neurotransmitter release from microdomains, called active zones or ''hot spots'' (Tucker and Fettiplace, 1995).

Some interesting models deal with the macro- and micromechanical behavior of the cochlea and reproduce experimental phenomena (e.g., Furness *et al.*, 1997). Our model, which is concentrated on the electrical properties of hair cells, adequately reproduces the receptor potential changes and so is a suitable component in a multicellular model for peripheral auditory coding (Gebeshuber *et al.*, 1998).

APPENDIX: MATHEMATICAL FORMULATION OF THE MODEL

The set of equations for the voltages in the hair cell (potential earth: cortilymph potential) is the following:

$$U_{o\mathrm{I}i}=\int \frac{I_{tc}-I_{oi}-(U_{o\mathrm{I}i}+E_1-U_0)\cdot G_{\mathrm{I}i}}{C_{\mathrm{I}i}}dt, \tag{A1}$$

$$U_{v\mathrm{I}i}=\int \frac{I_{st}-I_{vi}-(U_{v\mathrm{I}i}+E_1-U_0)\cdot G_{\mathrm{I}i}}{C_{\mathrm{I}i}}dt, \tag{A2}$$

$$U_{c\mathrm{I}i}=\int \frac{-I_{ci}-(U_{c\mathrm{I}i}+E_1-U_0)\cdot G_{\mathrm{I}i}}{C_{\mathrm{I}i}}dt, \tag{A3}$$

$$U_{\mathrm{II}}=\int \frac{I_{12}-I_{23}-(U_{\mathrm{II}}+E_{\mathrm{II}})\cdot G_{\mathrm{II}}}{C_{\mathrm{II}}}dt, \tag{A4}$$

$$U_{\mathrm{III}}=\int \frac{I_{23}-(U_{\mathrm{III}}+E_{\mathrm{III}})\cdot (G_{\mathrm{III}}+Kch\cdot G_K)}{C_{\mathrm{III}}}dt, \tag{A5}$$

where $U_{o\mathrm{I}i}$, $U_{v\mathrm{I}i}$ and $U_{c\mathrm{I}i}$ are the voltages in the middle of stereocilia with open transduction channels, with transduction channels changing their state from open to closed (or vice versa) and with transduction channels that are closed all the time, respectively; the index i ($i=1,2,3$) represents short, average and long stereocilia. U_{II} and U_{III} are the voltages in the middle of compartment II and the cell body, respectively. The value of the single channel current I_{tc} and other parameters taken from the literature and used for modeling are listed in Table I. I_{oi}, I_{vi} and I_{ci} represent the currents in the stereocilia, definition of the indices same as above, I_{12} is the current from the stereocilia into compartment II and I_{23} is the current from compartment II into the cell body. I_{st} denotes the stimulating transduction current in a single stereocilium, i.e. when the transduction channel is open, I_{st} equals I_{tc}, otherwise 0 pA. For the calculation of the maximum receptor potential changes, I_{st} is modeled as a current pulse with strength I_{tc} and all transduction channels are open (Fig. 3) or closed. The transduction channel open probabilities are a nonlinear and saturating function of the deflection of the stereocilia [inset Fig. 6(a)] and determine the time course of I_{st} for each stereocilium (Figs. 4, 5, and 6; the sum of the currents I_{st} through all stereocilia gives the whole cell transduction channel current TCC).

The membrane conductivities and capacities in Eqs. (A1)–(A5) are

$$C_{\mathrm{I}i}=a_{\mathrm{I}i}\cdot c, \quad G_{\mathrm{I}i}=a_{\mathrm{I}i}\cdot gm, \quad \text{with } a_{\mathrm{I}i}=d_1\cdot\pi\cdot l_{\mathrm{I}i}+d_{\mathrm{I}}^2\cdot\frac{\pi}{4}, \tag{A6}$$

$$C_{\mathrm{II}}=a_{\mathrm{II}}\cdot c, \quad G_{\mathrm{II}}=a_{\mathrm{II}}\cdot gm, \quad \text{with } a_{\mathrm{II}}=d_{\mathrm{II}}^2\cdot\frac{\pi}{4}-n\cdot d_{\mathrm{I}}^2\frac{\pi}{4}, \tag{A7}$$

$$C_{\mathrm{III}}=a_{\mathrm{III}}\cdot c, \quad G_{\mathrm{III}}=a_{\mathrm{III}}\cdot gm,$$
$$\text{with } a_{\mathrm{III}}=d_{\mathrm{III}}\cdot\pi\cdot l_{\mathrm{III}}+d_{\mathrm{III}}^2\cdot\frac{\pi}{4}, \tag{A8}$$

where a denotes area, d diameter and l length: $d_{\mathrm{I}}=0.2$ μm, $d_{\mathrm{II}}=d_{\mathrm{III}}=10$ μm, $l_{\mathrm{I}1}=0.886$ μm (short), $l_{\mathrm{I}2}=2.07$ μm (average), $l_{\mathrm{I}3}=3.254$ μm (long), $l_{\mathrm{II}}=1$ μm, $l_{\mathrm{III}}=50$ μm.

The currents in the hair cell are calculated as follows:

$$I_{oi}=\frac{U_{o\mathrm{I}i}-U_{\mathrm{II}}}{\frac{R_{\mathrm{I}i}}{2}+\frac{R_{\mathrm{II}}}{2}}, \quad I_{vi}=\frac{U_{v\mathrm{I}i}-U_{\mathrm{II}}}{\frac{R_{\mathrm{I}i}}{2}+\frac{R_{\mathrm{II}}}{2}}, \quad I_{ci}=\frac{U_{c\mathrm{I}i}-U_{\mathrm{II}}}{\frac{R_{\mathrm{I}i}}{2}+\frac{R_{\mathrm{II}}}{2}}, \tag{A9}$$

$$I_{\mathrm{I}2i}=I_{oi}\cdot m_{oi}+I_{vi}\cdot m_{aoi}+I_{ci}\cdot(n_i-m_{oi}-m_{aoi}), \tag{A10}$$

$$I_{\mathrm{I}2}=I_{\mathrm{I}21}+I_{\mathrm{I}22}+I_{\mathrm{I}23}, \quad I_{23}=\frac{U_2-U_3}{R_2/2+R_3/2}. \tag{A11}$$

The cytoplasm resistances in Eq. (A9) are

$$R_{\mathrm{I}i}=\frac{\rho_i\cdot l_{\mathrm{I}i}}{0.25\pi\cdot d_1^2}, \quad R_{\mathrm{II}}=\frac{\rho_i\cdot l_{\mathrm{II}}}{0.25\pi\cdot d_{\mathrm{II}}^2}, \quad R_{\mathrm{III}}=\frac{\rho_i\cdot l_{\mathrm{III}}}{0.25\pi\cdot d_{\mathrm{III}}^2},$$

m_o is the number of open transduction channels, m_{ao} is the number of transduction channels additionally open to the 15% open at rest [m_{ao} ranges from -15 (i.e., all TC closed) to $+85$ (i.e., all TC open) for OHC, and from -9 to $+51$ for IHC] and n_i denotes the number of stereocilia in each row.

Bell, J., and Holmes, M. H. (**1986**). ''A nonlinear model for transduction in hair cells,'' Hearing Res. **21**, 97–108.

Cody, A. R., and Russell, I. J. (**1987**). ''The responses of hair cells in the basal turn of the guinea-pig cochlea to tones,'' J. Physiol. (London) **383**, 551–569.

Crawford, A. C., Evans, M. G., and Fettiplace, R. (**1991**). ''The actions of calcium on the mechanoelectrical transducer current of turtle hair cells,'' J. Physiol. (London) **434**, 369–398.

Dallos, P. (**1983**). ''Cochlear electroanatomy: influence on information processing,'' in: *Hearing—Physiological Bases and Psychophysics*, edited by R. Klinke and R. Hartmann, Proc. 6th Int. Symp. on Hearing (Springer, Berlin), pp. 32–38.

Dallos, P. (**1984**). ''Some electrical circuit properties of the organ of Corti. II. Analysis including reactive elements,'' Hearing Res. **14**, 281–291.

Dallos, P., and Evans, B. N. (**1995**). ''High-frequency motility of outer hair cells and the cochlear amplifier,'' Science **267**, 2006–2009.

Dallos, P., and Santos-Sacchi, J. (**1982**). ''Intracellular recordings from cochlear outer hair cells,'' Science **218**, 582–584.

Forge, A. (**1991**). ''Structural features of the lateral walls in mammalian cochlear outer hair-cells,'' Cell Tissue Res. **265**, 473–483.

Frankenhaeuser, B., and Huxley, A. L. (**1964**). ''The action potential in the myelinated nerve fibre of Xenopus Laevis as computed on the basis of voltage clamp data,'' J. Physiol. (London) **171**, 302–315.

Furness, D. N., Zetes, D. N., Hackney, C. M., and Steele, C. R. (**1997**). ''Kinematic analysis of shear displacement as a means for operating mechanotransduction channels in the contact region between adjacent stereocilia of mammalian cochlear hair cells,'' Proc. R. Soc. London, Ser. B **264**, 45–51.

Gebeshuber, I. C., Mladenka, A., Rattay, F., and Svrcek-Seiler, W. A. (**1998**). ''Brownian motion and the ability to detect weak auditory signals,'' in *Chaos and Noise in Biology and Medicine* edited by C. Taddei-Ferretti (World Scientific, Singapore, in press).

Gitter, A. H. (**1994**). ''Sind 'tip links' Grundlage der Mechanosensitivität von Haarzellen?'' HNO **42**, 327–333.

Gitter, A. H. (**1996**). ''Row-to-row horizontal links may be associated with the transduction channels of hair cells,'' ORL **58**, 1–3.

Gitter, A. H., Frömter, E., and Zenner, H. P. (**1992**). ''C-type potassium channels in the lateral cell membrane of guinea-pig outer hair cells,'' Hearing Res. **60**, 13–19.

Gitter, A. H., Zenner, H. P., and Frömter, E. (**1986**). ''Membrane potential and ion channels in isolated outer hair cells of guinea pig cochlea,'' ORL J. Otorhinolaryngol. Relat. Spec. **48**, 68–75.

Gitter, A. H., and Zenner, H. P. (**1990**). ''The cell potentials of isolated inner hair cells *in vitro*,'' Hearing Res. **45**, 87–94.

Hudspeth, A. J. (**1989**). ''How the ear's works work,'' Nature (London) **341**, 397–404.

Hudspeth, A. J., and Corey, D. P. (**1977**). ''Sensitivity, polarity, and conductance change in the response of vertebrate hair cells to controlled mechanical stimuli,'' Proc. Natl. Acad. Sci. USA **74**, 2407–2411.

Jaramillo, F. (**1995**). ''Signal transduction in hair cells and its regulation by calcium,'' Neuron **15**, 1227–1230.

Katz, B., and Miledi, R. (**1967**). ''A study of synaptic transmission in the absence of nerve impulses,'' J. Physiol. (London) **192**, 407–436.

Konishi, T., and Salt, A. N. (**1983**). ''Electrochemical profile for potassium ions across the cochlear hair cell membranes of normal and noise-exposed guinea pigs,'' Hearing Res. **11**, 219–233.

Kros, C. J., Rüsch, A., Lennan, G. W. T., and Richardson, G. P. (**1993**). ''Voltage dependence of transducer currents in outer hair cells of neonatal mice,'' in *Biophysics of Hair Cell Sensory Sytems* edited by H. Duifhuis, J. W. Horst, P. van Dijk, and S. M. van Netten (World Scientific, Singapore), pp. 141–150.

Ma, Y. L., Rarey, K. E., Gerhardt, K. J., Curtis, L. M., and Rybak, L. P. (**1996**). ''Electrochemical potentials and potassium concentration profiles recorded from perilymph, endolymph and associated inner ear tissues in adrenalectomized rats,'' Hearing Res. **96**, 151–156.

Markin, V. S., Jaramillo, F., and Hudspeth, A. J. (**1993**). ''The three-state model for transduction-channel gating in hair cells,'' Biophys. J. **64**, A93.

Mountain, D. C. (**1989**). ''Measurement of low-frequency receptor potentials in inner hair cells: a theoretical analysis,'' Hearing Res. **41**, 101–106.

Mountain, D. C., and Hubbard, A. E. (**1994**). ''A piezoelectric model of outer hair cell-function,'' J. Acoust. Soc. Am. **95**, 350–354.

Palmer, A. R., and Russell, I. J. (**1986**). ''Phase-locking in the cochlea nerve of the guinea-pig and its relation to the receptor potential of inner hair cells,'' Hearing Res. **24**, 1–15.

Pickles, J. O., Comis, S. D., and Osborne, M. P. (**1984**). ''Cross-links between the stereocilia in the guinea pig organ of Corti, and their possible relation to sensory transduction,'' Hearing Res. **15**, 103–112.

Preyer, S., Hemmert, W., Pfister, M., Zenner, H. P., and Gummer, A. W. (**1994**). ''Frequency response of mature guinea-pig outer hair cells to stereociliary displacement,'' Hearing Res. **77**, 116–124.

Rattay, F. (**1990**). *Electrical Nerve Stimulation: Theory, Experiments and Applications* (Springer Wien/New York).

Russell, I. J., and Sellick, P. M. (**1978**). ''Intracellular studies of hair cells in the mammalian cochlea,'' J. Physiol. (London) **284**, 261–290.

Russell, I. J., and Sellick, P. M. (**1983**). ''Low-frequency characteristics of intracellularly recorded receptor potentials in guinea-pig cochlear hair cells,'' J. Physiol. (London) **338**, 179–206.

Santos-Sacchi, J. (**1991**). ''Reversible inhibition of voltage-dependent outer hair-cell motility and capacitance,'' J. Neurosci. **11**, 3096–3110.

Spoendlin, H. (**1970**). ''Vestibular labyrinth,'' in *Ultrastructure of the Peripheral Nervous System and Sense Organs*, edited by A. Bischoff (Georg Thieme Verlag, Stuttgart), p. 264.

Sweeney, J. D., Mortimer, J. T., and Durand, D. (**1987**). ''Modeling of mammalian myelinated nerve for functional neuromuscular electrostimulation,'' IEEE 9th Annual Conference Eng. Med. Biol. Soc. Boston, 1577–1578.

Tucker, T., and Fettiplace, R. (**1995**). ''Confocal imaging of calcium microdomains and calcium extrusion in turtle hair cells,'' Neuron **15**, 1323–1335.

Zenner, H. P. (**1994**). ''Physiologische und biochemische Grundlagen des normalen und gestörten Gehörs,'' in *Oto-Rhino-Laryngologie in Klinik und Praxis*, edited by J. Helms (Georg Thieme Verlag, Stuttgart), Vol. 1: Ohr, pp. 81–230.

Zetes, D. E. (**1995**). ''Mechanical and morphological study of the stereocilia bundle in the mammalian auditory system.'' Ph.D. Thesis, Stanford University.

Effectiveness of intermittent and continuous acoustic stimulation in preventing noise-induced hearing and hair cell loss

David R. White, Flint A. Boettcher, Lesa R. Miles, and Michael Anne Gratton
Department of Otolaryngology and Communicative Sciences, Medical University of South Carolina, Charleston, South Carolina 29425-2242

(Received 3 April 1997; revised 2 November 1997; accepted 3 November 1997)

Resistance to noise-induced hearing loss (NIHL) was studied in gerbils exposed either to intermittent or continuous low-level noise prior to an intense noise. Auditory-evoked brainstem response (ABR) thresholds, distortion product otoacoustic emissions (DPOAEs), $Q_{10\ dB}$ values from compound action potential (CAP) tuning curves, and outer hair cell (OHC) loss were measured for each group. Subjects were exposed to A-weighted noise (octave band noise centered at 2 kHz) on an intermittent (80 dB, 6 h/day) or continuous schedule (74 dB, 24 h/day) for 10 days, allowed to rest in quiet for 2 days, then exposed to intense A-weighted noise (107 dB, 24 h/day) for 2 days. A ''noise-only'' group was exposed only to the intense noise. Gerbils exposed in both the ''intermittent'' and ''continuous'' groups had less (15–30 dB) temporary threshold shift (TTS) than those in the noise-only group. In addition, the continuous group had less (10–15 dB) permanent threshold shift (PTS) than the other groups. These data suggest that resistance to NIHL is evident in both the intermittent and continuous groups when TTS is measured, but resistance to PTS is afforded only by the continuous paradigm. Both paradigms decreased OHC loss as compared to the noise-only group, with the continuous paradigm being most effective. However, neither paradigm conserved DPOAE amplitudes or tuning curve $Q_{10\ dB}$ values relative to the noise-only group. © *1998 Acoustical Society of America.* [S0001-4966(98)03303-7]

PACS numbers: 43.64.Wn, 43.64.Pg, 43.64.Jb, 43.64.Ri [RDF]

INTRODUCTION

Recent data suggest that noise-induced hearing loss (NIHL) is reduced by prior acoustic stimulation. When a subject is exposed to intermittent low-level noise, the temporary threshold shift (TTS) measured after each exposure becomes progressively smaller until no TTS is observed. This phenomenon of ''resistance to NIHL'' was first noted by Miller *et al.* (1963), in the cat, but it was not studied again until Clark *et al.* (1987) reported the same phenomenon in chinchillas. Resistance to NIHL has been demonstrated with behavioral techniques (Miller *et al.*, 1963; Clark *et al.*, 1987), evoked potentials from the brainstem (Subramaniam *et al.*, 1991; Boettcher, 1993) and cochlea (Boettcher *et al.*, 1992), single unit recordings in the auditory nerve (Sinex *et al.*, 1987), and in distortion-product otoacoustic emissions (Franklin *et al.*, 1991; Subramaniam *et al.*, 1994; Boettcher and Schmiedt, 1995).

A second series of experiments has demonstrated that permanent threshold shift (PTS) due to an intense noise can be reduced if the subject is first exposed to a lower-level sound. This was first demonstrated by Canlon *et al.* (1988) who exposed guinea pigs to a 1-kHz, 81-dB SPL pure tone continuously for 24 days, after which no TTS was noted. Three hours after completing the preliminary exposure, the subjects were exposed to the same tone for three days at an intensity (105 dB SPL) known to cause PTS in control groups. The pre-exposed subjects experienced significantly less TTS and PTS after the intense tone than control subjects exposed to the intense tone only. Protection from PTS can be afforded likewise by first exposing the subject to intermittent low-level noise (Campo *et al.*, 1991; Subramaniam *et al.*, 1992; Henselman *et al.*, 1994). For example, Campo *et al.* (1991) exposed chinchillas to a 6-hour intense noise 5 days after completing a 10-day, low-level intermittent exposure. In this case, the subjects were found to have less TTS and PTS after the intense noise than similar subjects exposed to an intense noise only. More recent work by McFadden *et al.* (1997) showed that the protection from NIHL is long-lasting; chinchillas exposed to intense noise 60 days after a preliminary low-level intermittent exposure demonstrated resistance to TTS and PTS.

Noise-induced cochlear damage may also be reduced by prior exposure to a low-level noise. Subramaniam *et al.* (1994, 1995) exposed monaural chinchillas to an intermittent noise before an intense noise that resulted in a reduction of hair cell loss compared to intense noise alone. Canlon (1996) reported that guinea pigs exposed to a low-level, continuous pure tone before exposure to an intense tone showed less hair cell loss than those exposed to the intense stimulus alone. Bohne and colleagues have also demonstrated that an interrupted low- or high-frequency noise exposure causes less hair cell loss than an equal-energy, continuous noise (Bohne *et al.*, 1985, 1987).

Thus, two experimental paradigms have been used to exemplify the protective effect of prior acoustic stimulation. In the first model, the ear becomes resistant to TTS (Clark *et al.*, 1987) or PTS (Campo *et al.*, 1991) after intermittent exposure to noise. In the second model, the ear becomes resistant to TTS and PTS after exposure to a continuous,

low-level tone (Canlon *et al.*, 1988). While variations of each of these paradigms have been studied extensively, a direct comparison of the two paradigms (intermittent versus continuous preliminary exposures) has not been performed. The purpose of this experiment was to compare the effectiveness of intermittent and continuous preliminary exposures in protecting the ear from PTS and cochlear hair cell loss. Here, preliminary exposures which caused no TTS were followed by an intense exposure which, in itself, caused significant TTS, PTS, and OHC loss. Thresholds were estimated from auditory brainstem responses (ABRs) to tone pips. The condition of the cochlea was also monitored with DPOAEs and tuning curves derived from forward masking of the CAP response. Outer hair cell counts were performed with standard surface preparation techniques.

I. METHODS

A. Subjects

Thirty one young (6–14 months) Mongolian gerbils (*Meriones unguiculatus*) were used as subjects. The gerbils were raised in a sound-treated vivarium with a median A-weighted sound level of 35–40 dB. Each gerbil was checked for otologic obstruction and infection. All subjects had clear, healthy ears, and no otologic abnormalities were found. Each subject received a preliminary ABR; thresholds of all subjects were 25 dB SPL or less at 1, 2, 4, 8, and 16 kHz. Subjects were assigned randomly to one of three groups: (1) an ***intermittent group*** ($n=12$), exposed to intermittent (6 hours on, 18 hours off) noise for 10 days followed by 2 days of quiet and 2 days of intense noise, (2) a ***continuous group*** ($n=12$), exposed to low-level, continuous noise for 10 days followed by 2 days of quiet and 2 days of exposure to an intense noise; and (3) a ***noise-only group*** ($n=7$), exposed only to intense noise for 2 days. Typical data for an unexposed ***control*** group was used for comparison of DPOAE and tuning curve data (data from Boettcher, 1996).

B. Noise exposures

Noise exposures were performed in a reverberant chamber. Subjects remained in home cages with *ad lib* food and water throughout the exposures. Each noise exposure was an octave band noise centered at 2 kHz (see Fig. 1). The 80-dB intermittent A-weighted noise was presented for 6 h per day over a 10-day period. The continuous noise was presented for 10 days at 74 dB. These exposures were not intended to be energy equivalents. Rather, they were chosen to provide maximum resistance to NIHL without independently causing TTS. The levels were chosen based on unpublished preliminary data from our lab. Thresholds measured by ABR showed less than 2 dB of TTS at 1, 2, 4, 8, and 16 kHz for each of the exposure paradigms after a 10-day exposure. Following the preliminary period of intermittent or continuous noise, the subjects rested in a quiet vivarium for 48 h before being exposed to a 107 dB noise for 48 h. Resistance to noise has been observed with rest periods of 3 h to 60 days between a protective and an intense exposure (Canlon *et al.*, 1988; McFadden *et al.*, 1997). The goal of this study was to compare the intermittent and continuous paradigms and thus

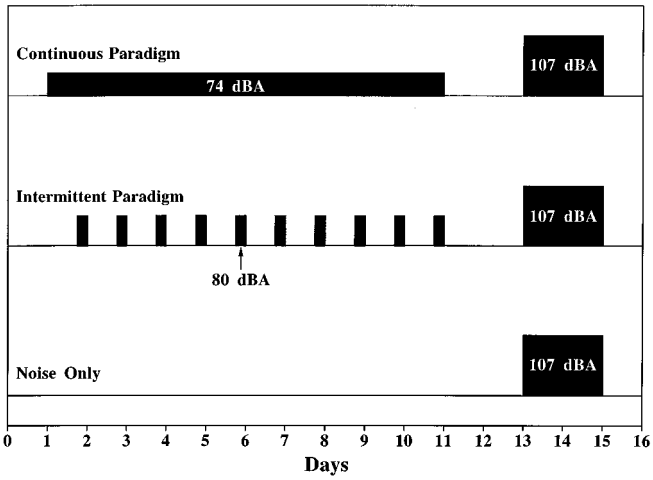

FIG. 1. Noise exposure schedules are shown for the three groups of animals. An octave band noise centered at 2 kHz was presented to each group. The ''continuous paradigm'' consisted of continuous A-weighted 74-dB noise (24 hrs/day, 10 days) which ended 48 hours prior to the intense noise exposure (107 dB, 48 h). The ''intermittent paradigm'' consisted of an 80 dB noise presented intermittently (6 h/day, 10 days) and ending 48 h prior to the intense noise. The ''noise-only'' group was exposed only to the intense noise.

the rest period was chosen to maximize the possible protective effects of the exposures while allowing for recovery from anesthesia following testing at the end of the protective exposure. Subjects in the ''Noise-only'' group were exposed only to the final, intense noise. Animals in the (unexposed) control group received no noise exposures.

C. ABR collection

For each ABR procedure, subjects were anesthetized with a mixture of ketamine (35 mg/kg) and xylazine (8 mg/kg) injected intramuscularly. Smith and Mills (1989) have shown that this combination of drugs does not affect ABRs measured in the gerbil. Each subject was placed inside of a double-walled, sound-treated booth (I.A.C. 402A) and body temperature (37 °C) was maintained using a closed loop heating pad system.

ABR stimulus generation and presentation as well as data collection and analysis were controlled using a Tucker-Davis Technology (TDT) system including a personal computer, 16-bit A/D's and D/A's, programmable attenuators, mixers, and a headphone buffer. Stimuli were digitally synthesized using SigGen© software. Tone pips (1.8-ms duration; 0.75-ms rise–fall times) were presented at octave intervals from 1 to 16 kHz. Stimuli were presented through a Beyer DT-48 earphone calibrated at the ear canal entrance with a Knowles microphone. Neurological activity was recorded with subcutaneous needle electrodes placed at vertex and in the mastoid regions behind each pinna. A bite bar served as the ground electrode. Activity was routed from the electrodes to a Grass model 12 biological amplifier, where it was filtered (300 to 3000 Hz) and amplified (100 000×) and then routed to the 16-bit A/D convertor. Data were collected and analyzed using AeP© software from TDT. Thresholds were determined off-line visually with a criterion amplitude of 0.25 μV.

ABR waveforms were collected before the low-level (continuous or intermittent) noise exposure to establish a baseline. Subjects in the intermittent and continuous groups were tested immediately following the tenth day of preliminary exposure; immediately after the intense exposure (to determine TTS from the intense exposure); and 30 days after ending the intense exposure (to determine PTS from the intense exposure). Noise-only animals were tested before the exposure to the intense noise, immediately following the intense noise (TTS), and 30 days after the intense noise (PTS).

D. Compound action potential and DPOAE testing

Two to seven days after the final ABR had been collected, the subject was weighed and deeply anesthetized with Nembutal (50 mg/kg, i.p.). Depth of anesthesia was tested by the withdrawal reflex, and supplemental doses of Nembutal (20 mg/kg) were given as needed. The gerbil was then placed in a head holder in a double-walled, sound-treated booth. A closed-loop heating pad system maintained body temperature at 37 °C. A tracheotomy was performed in order to maintain a clear airway for the subject. The pinna was removed, the bulla was exposed and moistened, then the bulla was opened with a slowly revolving drill bit to minimize surgical noise trauma. A silver-wire electrode was inserted through the bulla to rest on the bone above the round window, and a ground electrode was placed at vertex. The compound action potential (CAP) from the auditory nerve was recorded from the round window electrode and monitored via an online oscilloscope. Stimuli were presented through a Beyer DT-48 headphone. The headphone was located in a customized sound source incorporating a B&K 4134 microphone for calibration. The sound source was placed in the external auditory meatus, 1–2 mm above the tympanic membrane, creating a sealed acoustic system.

DPOAEs were collected using Ariel signal processing boards and CUB^{e}DIS system (Mimosa Acoustics). This system was described in Boettcher and Schmiedt (1995). Primary levels were calibrated with a ''chirp'' signal and adjusted prior to collection of each data set. DPOAEs were recorded in 4-s intervals using the probe microphone equalized to a flat response, then stored on disk. DPOAEs were collected at 8 points per octave over the range of 0.5–20 kHz, using signal levels of 40, 50, and 60 dB SPL (Schmiedt, 1984, 1986; Boettcher and Schmiedt, 1995).

CAP tuning curves were recorded at 1, 2, 4, 8, and 16 kHz using a forward masking procedure described by Dallos and Cheatham (1976) and modified by Schmiedt (1984). Briefly, the probe tone was 1.8 ms in duration (0.75-ms rise–fall times), presented at a level 10–15 dB above threshold. The probe was preceded by a 70-ms masker (5 ms duration from masker offset to probe onset). The masker level was varied in 10-dB steps; at each level, the frequency was controlled manually to determine the frequency at which masking occurred. The masked threshold was determined visually on-line from the oscilloscope.

E. Cochlear histology

The cochleae of five animals from each group were analyzed for hair cell damage using the soft surface preparation technique (Axelsson *et al.*, 1974). Immediately following acquisition of the DPOAE measures, the deeply anesthetized animal was sacrificed by decapitation. The temporal bones were quickly excised, the cochlea exposed and the stapes removed. The cochlea was perfused via a slit made in the round window membrane with 1.0 ml of 4% paraformaldehyde in a 0.1 M phosphate buffer (PB) (1 ml, *p*H 7.4, RT). The cochlea was then immersed in the fixative solution and stored (4 °C) prior to post-fixation and staining via perfusion of cold 1% OsO4 in 0.1 M PB for 20–30 min. The cochlea was then drilled to thin the otic capsule and decalcified (50 ml, 0.35M 4SS [sodium salt] EDTA, *p*H 8.0, RT, 2h). The decalcified cochlea was microdissected and the organ of Corti mounted in glycerin for microscopic study.

Using differential interference contrast (DIC) microscopy at 400×, the number of missing inner and outer hair cells was quantified by row from cochlear apex to base. The cells were considered present if the cell body, cuticular plate and stereocilia were intact. Missing cells were identified by the presence of a phalangeal scar. Counts of the cells by type and condition were normalized and plotted in 2% intervals as a function of percent distance from the apex (i.e., frequency location in the cochlea; based on Tarnowski *et al.*, 1991) to obtain a cochleogram. Cell data for all animals in a group were averaged to obtain a group mean cochleogram (Gratton *et al.*, 1990).

II. RESULTS

A. Threshold shifts

The mean ABR temporary threshold shifts (TTS) with standard errors of the mean for the noise-only, intermittent, and continuous groups are shown in Fig. 2 (upper panel). The intermittent and continuous noise exposure groups incurred less TTS than the noise-only group at most frequencies. The intermittent group had significantly less TTS at 1–8 kHz (10–20 dB) than the noise-only group (unpaired *t*-test, $p<0.05$), but not at 16 kHz. The continuous noise group had significantly less TTS (25–30 dB difference, unpaired *t*-test, $p<0.05$) than the noise-only group at each frequency tested. The continuous paradigm provided significantly more protection (unpaired *t*-test, $p<0.05$) from TTS than the intermittent paradigm at 4 and 16 kHz.

The mean permanent threshold shifts (PTS) for the three subject groups are shown in Fig. 2 (lower panel). The intermittent and noise-only groups had similar amounts of PTS (10–25 dB) at each frequency. However, the subjects preexposed to continuous noise had significantly less PTS than the noise-only group at 4, 8, and 16 kHz (unpaired *t*-test, $p<0.05$). The differences between the noise-only and continuous-paradigm groups were 11 to 14 dB at 4 through 16 kHz. Furthermore, the continuous exposure paradigm proved to be significantly (unpaired *t*-test, $p<0.05$) better at protecting the ear from PTS than the intermittent paradigm at 4, 8, and 16 kHz, respectively, with 12, 9, and 9 dB less PTS in the continuous group.

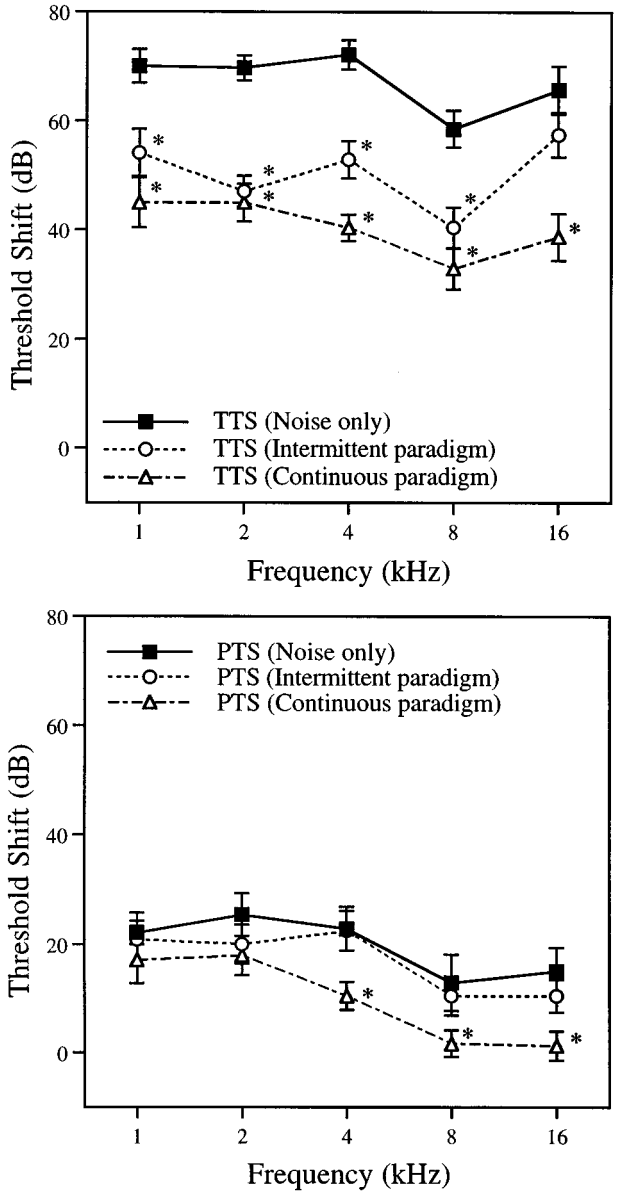

FIG. 2. Mean ABR threshold shifts for each group plotted against frequency. Threshold shift was determined by pre- and post-exposure ABR thresholds for each animal. The upper panel shows TTS for the noise-only, intermittent, and continuous groups. The lower panel shows PTS for the same groups. Error bars represent the standard error of the mean. Asterisks denote significant difference from the noise-only group ($p<0.05$).

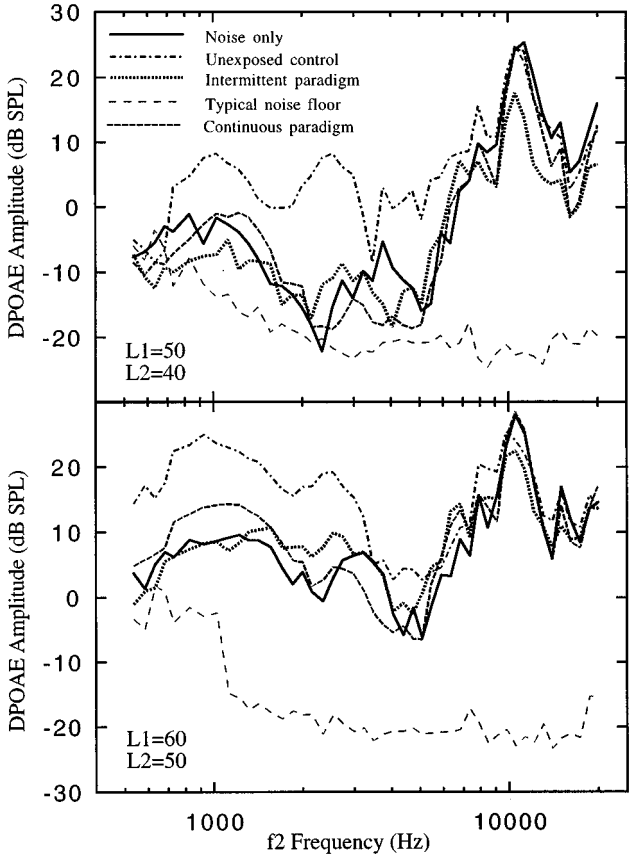

FIG. 3. Mean DPOAE amplitude ($2f_1-f_2$) is plotted as a function of f_2 frequency (0.54–20.1 kHz, eight points per octave) for the groups shown. A typical noise floor is shown in each panel; $L1$ and $L2$ values are indicated in the lower left corner of each panel. The intermittent group is compared to noise-only and unexposed controls in the panels on the left; the continuous group is compared to noise-only and unexposed controls in the panels on the right. Standard errors for the noise-only group range from 0.57 to 7.64 dB SPL; standard errors for the intermittent group range from 1.16 to 5.98 dB SPL; and standard errors for the continuous group ranged from 0.95 to 3.97 dB SPL.

B. DPOAEs

The average DPOAE's from the intermittent and continuous paradigms were plotted with the noise-only group and unexposed controls. The upper panel of Fig. 3 shows data collected with primary levels of 40 and 50 dB SPL (L_2 and L_1, respectively) and the lower panel shows data collected with levels of 50 and 60 dB SPL. The lowest dotted line in each panel represents a typical noise floor for the recording environment. At lower primary levels (upper panel), animals exposed to intense noise, whether intense noise alone or those with continuous or intermittent preexposure, have lower DPOAE amplitudes than control (unexposed) subjects, at f_2 frequencies below approximately 10 kHz. The three exposed groups have similar, although reduced, amplitudes from approximately 5 through 10 kHz. Below 4 kHz, the relative amplitudes vary; for example, the noise-only group has the highest amplitude of the exposed groups at approximately 4 kHz whereas the intermittent group has the highest amplitude at 2–3 kHz and the continuous group had the highest amplitude at 1–2 kHz. Thus, whereas each exposed group had reduced DPOAE amplitudes below 10 kHz for the lower-level primaries, there was no consistent pattern as to which group had the lowest emission amplitudes.

Results for the higher-level primaries (L_1 of 60 dB SPL, L_2 of 50 dB SPL) were qualitatively similar to the results for the lower-level primaries. Each of the three exposed groups had similar DPOAE amplitudes as the unexposed subjects at f_2 frequencies of approximately 5.5 kHz and higher. The amplitudes from the exposed groups were reduced relative to controls at lower frequencies, but there was no consistent pattern as to which group had the greatest deficit in emission amplitudes. For example, the continuous group had the largest amplitudes of the exposed groups at frequencies below

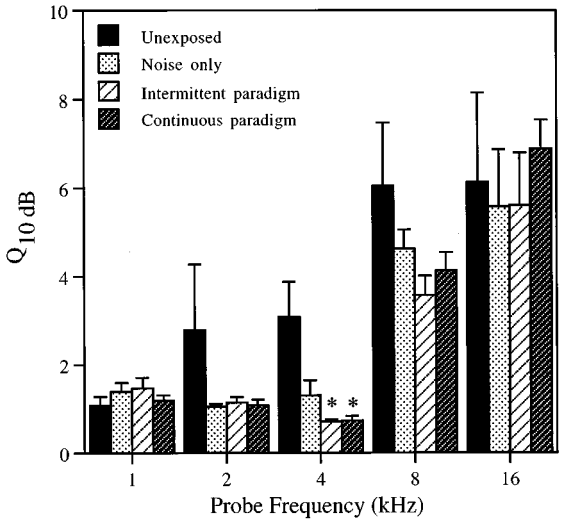

FIG. 4. $Q_{10\ dB}$ values (width of the tuning curve 10 dB above the tip divided by probe frequency) are plotted against probe frequency. Error bars represent the standard error of the mean. The intermittent group, continuous group, and noise-only group are shown along with the unexposed controls. Asterisks denote significant differences of the preexposed groups from the noise-only group.

approximately 1.8 kHz, with the intermittent and noise-only groups having higher amplitudes than the continuous group at 2–5 kHz.

C. Tuning of the CAP

Because DPOAE amplitude decreases into the noise floor as noise-induced hearing loss increases, tuning curves were examined. Tuning curves from the CAP are measurable except in cases of severe hearing loss and thus were included as a secondary measure of cochlear nonlinearities. Tuning curves were measured in terms of $Q_{10\ dB}$ values (width of the tuning curve 10 dB above the tip divided by the probe frequency). Figure 4 shows mean $Q_{10\ dB}$ values at 1, 2, 4, 8, and 16 kHz for unexposed control, noise-only, intermittent, and continuous groups with error bars representing the standard error of the mean. Each noise-exposed group had decreased $Q_{10\ dB}$ values at 2, 4, and 8 kHz when compared to unexposed animals; all groups had normal values at 16 kHz. Both the intermittent and continuous groups had significant reductions (unpaired t-test, $p<0.05$) in $Q_{10\ dB}$ at 4 kHz when compared to the noise-only group. No significant difference was noted between the $Q_{10\ dB}$ values when the intermittent and continuous were compared.

D. Hair cell loss

No loss of inner hair cells occurred in the intermittent, continuous, or noise-only groups. Approximately 20% of the OHCs in the region corresponding to 12–16 kHz were found to be missing in the group exposed only to the intense noise (Fig. 5, top panel). This loss was evident in all three rows of OHCs and was accompanied by another focal region of OHC loss at 18 kHz in which 10%–12% of second and third row OHCs were missing. In contrast to the loss of OHCs in all three rows in the noise-only group, losses in the intermittent

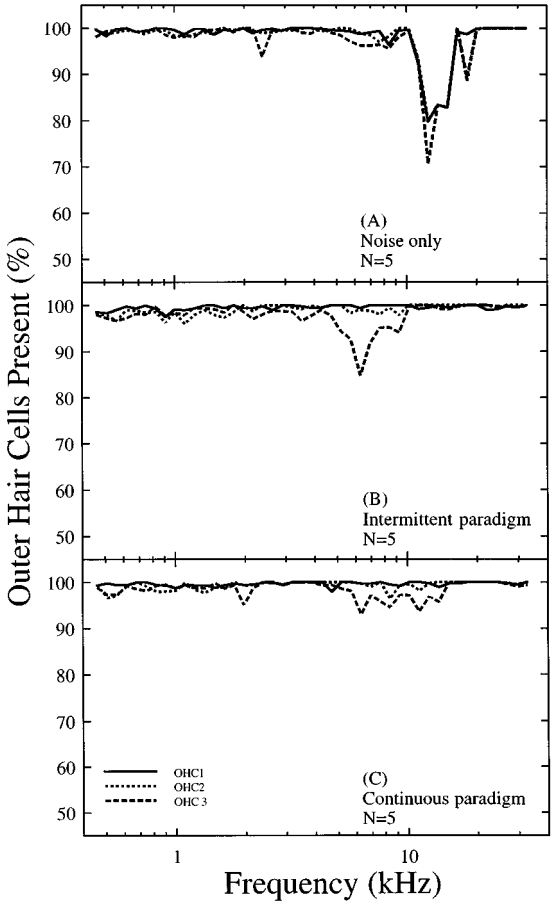

FIG. 5. Percent of outer hair cells (OHCs) present is plotted against frequency for each group. Data for each row of OHCs are shown separately as indicated in the legend.

group (Fig. 5, middle panel) were limited to the third row of OHCs. The damage (with a peak of 15% OHC loss at 6.3 kHz) was found in the region corresponding to 4–11 kHz. The maximal losses for the noise-only and the intermittent groups occur at different frequencies, but the lesions occur in adjoining areas of the cochlea and differ anatomically by only a few millimeters. Figure 5 (bottom panel) shows that the continuous group had virtually no OHC loss. The sporadic and minimal OHC loss observed ($<7\%$) was confined to the third OHC row and was found in the regions corresponding to 4–15 kHz.

III. DISCUSSION

A. Comparison of intermittent and continuous paradigms

The continuous preexposure provided more protection against TTS, PTS, and hair cell loss, than the intermittent paradigm. The data are consistent with the observation of Canlon *et al.* (1988) that a low-level preexposure may reduce both TTS and PTS caused by a subsequent intense exposure. Our work, using continuous noise preexposures, extends Canlon's observations on continuous pure tone preexposures. Furthermore, the results are consistent with observations of Campo *et al.* (1991) or Subramaniam (1992) that an inter-

mittent preexposure may reduce TTS from a subsequent exposure. However, in contrast with Campo or Subramaniam, there is little or no evidence of reduced PTS from the intense noise in the intermittent group.

The discrepancy between the current results and those of Campo, Subramaniam, and colleagues may be due to differences in the noise levels of the preliminary exposures or species differences. For example, the protective exposure used in the present study (80 dB) caused no TTS by itself, whereas the exposures used by Campo *et al.* (95 dB SPL) resulted in significant TTS on the first few days of exposure. It is thus possible that some degree of TTS is needed in the intermittent paradigm to observe resistance. However, a TTS-inducing intermittent exposure such as that used by Campo *et al.* has been shown to cause some degree of damage to the cochlea by itself, in terms of displacement of OHC stereocilia and loss of OHCs (Boettcher *et al.*, 1992). Such damage could in theory ultimately make the cochlea *more* susceptible to PTS and hair cell damage by subsequent noise exposures. Indeed, Subramaniam and colleagues (1992) have shown that in some cases (such as when the spectra of the preexposure and the intense exposure do not match), the hearing loss from the intense noise is greater when preceded by the lower-level exposure. Furthermore, the chinchilla is typically more susceptible to noise exposure than the gerbil, which may account for some differences between studies. However, it is difficult to resolve why a TTS-producing intermittent exposure should reduce PTS when the spectra of the exposures match (Campo *et al.*, 1991), but a nontraumatic exposure such as used in the present experiment does not provide protection from PTS.

It is also difficult to understand why, in the present study, the protection differed between the intermittent and continuous paradigms. Neither paradigm in itself caused TTS at any time during the exposure, thus it is unlikely that either paradigm caused any degree of cochlear damage. For example, OHC changes are apparently not seen after a protective exposure with continuous tone which causes no TTS in itself (Canlon, 1996). Our data showed greater loss of OHCs in those animals exposed to the intermittent paradigm when compared to the minimal OHC loss of animals in the continuous group. Of course, this is difficult to resolve when the data are compared to Campo and colleagues, as they most likely induced significant cochlear damage with their intermittent exposure, yet observed protection from PTS caused by a subsequent intense noise.

A second factor which could potentially contribute to differences between the intermittent and continuous exposures is the levels of the exposures. For example, the noise level of the intermittent exposure may have been insufficient to induce resistance to NIHL in these animals. This, however, seems improbable since the many paradigms studied have shown resistance at several different noise levels; thus resistance is unlikely to be related to the precise level of the intermittent exposure. The levels were not matched to provide equal energy, but instead were designed, based on preliminary data, to be the upper bounds of the exposures which caused no TTS by themselves.

B. Mechanism of resistance

The mechanisms involved in the development of resistance to NIHL are not understood. Because resistance to NIHL occurs in the absence of middle ear muscles (Ryan *et al.*, 1994; Henderson *et al.*, 1994), it is unlikely to occur due to hypertrophy of middle ear muscles. Resistance has been observed in compound action potential (CAP) recordings from the auditory nerve as well as single nerve fibers (Sinex *et al.*, 1987), thus the mechanism of resistance must be a cochlear phenomenon. The OHC is the most likely site for development of resistance to NIHL since it seems to be responsible for most of the cochlear amplification present in the inner ear. Canlon *et al.* (1992, 1993) reported increased vesicle content in the presynaptic region of the OHC and decreases in cytoplasmic calcium buffer levels after a conditioning stimulus. Increases in the amount of smooth endoplasmic reticulum at the apical surface of the OHC were reported by Boettcher and Gratton (1993) following intermittent noise exposures. However, Boettcher *et al.* (1992) reported increased OHC death and stereocilia damage over the course of a 15-day intermittent noise exposure.

More recently, several groups have examined the role of the efferent auditory system in resistance to NIHL. Zheng *et al.* (1997) exposed chinchillas to an intermittent noise (OBN centered at 4 kHz, 85 dB SPL) for ten days followed by exposure to a similar 95-dB noise. One ear of each animal was surgically de-efferented. Those ears with complete deefferentation (only two subjects) had more reduction in DPOAE amplitudes from the intense noise than did the control ears. Preliminary work by Kujawa *et al.* (1996) also suggests that the medial efferent system may play a part in resistance to NIHL. Although the mechanism(s) of resistance to NIHL remain unknown, the OHC is implicated by physiological, histological and biochemical evidence and the efferent system is implicated in preliminary physiological data.

C. Consistency across measures of NIHL

There was little consistency across PTS, OHC loss, and measures of cochlear nonlinearity (DPOAE amplitudes and Q_{10dB} values of CAP tuning curves) in this study. These results are consistent with recent work of several groups (Schmiedt, 1986; Davis *et al.*, 1989; Subramaniam *et al.*, 1994, 1995; Hamernik *et al.*, 1996) and others which have shown a lack of correlation across such measures. For example, whereas Davis *et al.* (1989) observed a high correlation coefficient between PTS and OHC loss in chinchillas exposed to noise, for a given PTS, a wide range of OHC loss (from near zero to nearly complete loss) might occur. Similarly, DPOAE changes are often not correlated with PTS or OHC loss. Hamernik *et al.* (1996) illustrated a 10–30 dB SPL loss of DPOAE amplitude in chinchillas with less than 20 dB PTS (see Hamernik *et al.*, 1996, Figs. 12–15). Furthermore, some of these animals' DPOAE amplitudes were comparable to the noise floor at frequencies where no PTS and minimal OHC loss occurred (Hamernik *et al.*, 1996, Figs. 12 and 14). Thus, reductions in DPOAE amplitudes and tuning of the CAP may occur despite minimal OHC loss or loss of sensitivity.

IV. SUMMARY AND CONCLUSIONS

Gerbils were exposed to a low-level intermittent or continuous octave band of noise for ten days, then 2 days later were exposed to an intense noise for 2 days. A third group was exposed only to the 2-day intense noise. Both groups with preliminary exposures had less temporary threshold shift from the intense noise. However, only the animals receiving the continuous preexposure had reduced permanent threshold shift from the intense exposure. All exposed subjects had similar reductions in distortion-product otoacoustic emission amplitudes and reductions in $Q_{10\ \mathrm{dB}}$ values of CAP tuning curves. The pre-exposed groups had reductions in OHC loss compared to the noise-only group, with the least hair cell loss in the continuous group. The data suggest that a low-level, continuous noise exposure (which in itself causes no TTS) protects the ear from PTS and OHC loss caused by subsequent intense noise exposure.

ACKNOWLEDGMENTS

The authors would like to thank Dr. Richard A. Schmiedt for advice on the tuning and suppression procedures and Dr. Schmiedt, Dr. Judy R. Dubno, and Dr. John H. Mills for comments on an earlier version of the manuscript. Work supported by a grant from the Deafness Research Foundation to FAB and NIH-NIDCD Grant No. P01-DC-00422.

Axelsson, A., Miller, J., and Holmquist, J. (**1974**). ''Studies of cochlear vasculature and sensory structures: A modified method,'' Ann. Otol. Rhinol. Laryngol. **83**, 537–549.

Boettcher, F. A. (**1993**). ''Auditory brain-stem response correlates of resistance to noise-induced hearing loss in the Mongolian gerbil,'' J. Acoust. Soc. Am. **94**, 3207–3214.

Boettcher, F. A. (**1996**). ''Diltiazem does not protect the ear from noise-induced hearing loss in mongolian gerbils,'' Laryngoscope **106**, 772–776.

Boettcher, F. A., and Gratton, M. A. (**1993**). ''Resistance to noise-induced hearing loss in the mongolian gerbil,'' Abstr. Soc. Neurosci. **19**, 1421.

Boettcher, F. A., and Schmiedt, R. A. (**1995**). ''Distortion-product otoacoustic emissions in Mongolian gerbils with resistance to noise-induced hearing loss,'' J. Acoust. Soc. Am. **98**, 3215–3222.

Boettcher, F. A., Spongr, V. P., and Salvi, R. J. (**1992**). ''Physiological and histological changes associated with the reduction in threshold shift during interrupted noise exposure,'' Hearing Res. **62**, 217–236.

Bohne, B. A., Zahn, S., and Bozzay, D. (**1985**). ''Damage to the cochlea following interrupted exposure to low frequency noise,'' Ann. Otol. Rhinol. Laryngol. **94**, 122–130.

Bohne, B. A., Yohman, I., and Grunner, M. M. (**1987**). ''Cochlear damage following interrupted exposure to high-frequency noise,'' Hearing Res. **29**, 251–264.

Campo, P., Subramaniam, M., and Henderson, D. (**1991**). ''The effect of 'conditioning' exposures on hearing loss from traumatic exposure,'' Hearing Res. **55**, 195–200.

Canlon, B. (**1996**). ''The effects of sound conditioning on the cochlea,'' in *Auditory System Plasticity and Regeneration*, edited by R. J. Salvi, D. Henderson, F. Fiorino, and V. Colletti (Thieme Medical Publishers, New York), pp. 128–142.

Canlon, B., Borg, E., and Flock, A. (**1988**). ''Protection against noise trauma by preexposure to a low level acoustic stimulus,'' Hearing Res. **34**, 197–200.

Canlon, B., Borg, E., and Lofstrand, P. (**1992**). ''Physiological and morphological aspects to low-level acoustic stimulation,'' in *Noise-Induced Hearing Loss*, edited by A. Dancer, D. Henderson, R. Salvi, and R. Hamernik (Mosby Yearbook, St. Louis), pp. 489–499.

Canlon, B., Lofstrand, P., and Borg, E. (**1993**). ''Ultrastructural changes in the presynaptic region of outer hair cells after acoustic stimulation,'' Neurosci. Lett. **150**, 103–106.

Clark, W. W., Bohne, B. A., and Boettcher, F. A. (**1987**). ''Effect of periodic rest on hearing loss and cochlear damage following exposure to noise,'' J. Acoust. Soc. Am. **82**, 1253–1264.

Dallos, P., and Cheatham, M. A. (**1976**). ''Compound action potential (AP) tuning curves,'' J. Acoust. Soc. Am. **59**, 591–597.

Davis, R. I., Ahroon, W. A., and Hamernik, R. P. (**1989**). ''The relation among hearing loss, sensory cell loss, and tuning characteristics in the chinchilla,'' Hearing Res. **41**, 1–14.

Franklin, D. J., Lonsbury-Martin, B. L., Stagner, B. B., and Martin, G. K. (**1991**). ''Altered susceptibility of 2 $f1$-$f2$ acoustic-distortion products to the effects of repeated noise exposure in rabbits,'' Hearing Res. **53**, 185–208.

Gratton, M. A., Salvi, R. J., Kamen, B. A., and Saunders, S. S. (**1990**). ''Interaction of cisplatin and noise on the peripheral auditory system,'' Hearing Res. **50**, 211–224.

Hamernik, R. P., Ahroon, W. A., and Lei, S.-F. (**1996**). ''The cubic distortion product otoacoustic emissions from the normal and noise-damaged chinchilla cochlea,'' J. Acoust. Soc. Am. **100**, 1003–1012.

Henderson, D., Subramaniam, M., Papazian, M., and Spongr, V. P. (**1994**). ''The role of middle ear muscles in the development of resistance to noise induced hearing loss,'' Hearing Res. **74**, 22–28.

Henselman, L. W., Henderson, D., Subramaniam, M., and Sallustio, V. (**1994**). ''The effect of 'conditioning' exposures on hearing loss from impulse noise,'' Hearing Res. **78**, 1–10.

Kujawa, S. G., Brown, M. C., and Liberman, M. C. (**1996**). ''Sound conditioning enhances responses and peripheral effects of olivocochlear neurons,'' Abstr. Soc. Neurosci. **22**, 256.

McFadden, S. L., Henderson, D., and Shen, Y.-H. (**1997**). ''Low-frequency 'conditioning' provides long-term protection from noise-induced threshold shifts in chinchillas,'' Hearing Res. **103**, 142–150.

Miller, J. D., Watson, C. S., and Covell, W. P. (**1963**). ''Deafening effects of noise on the cat,'' Acta Oto-Laryngol. Suppl. **176**, 1–91.

Ryan, A. F., Bennett, T. M., Woolf, N. K., and Axelsson, A. (**1994**). ''Protection from noise-induced hearing loss by prior exposure to a nontraumatic stimulus: Role of the middle ear muscles,'' Hearing Res. **72**, 23–28.

Schmiedt, R. A. (**1984**). ''Acoustic injury and the physiology of hearing,'' J. Acoust. Soc. Am. **76**, 1293–1317.

Schmiedt, R. A. (**1986**). ''Acoustic distortion in the ear canal. I. Cubic difference tones: Effects on acute noise injury,'' J. Acoust. Soc. Am. **79**, 1481–1490.

Sinex, D. G., Clark, W. W., and Bohne, B. A. (**1987**). ''Effect of periodic rest on physiological measures of auditory sensitivity following exposure to noise,'' J. Acoust. Soc. Am. **82**, 1265–1273.

Smith, D. I., and Mills, J. H. (**1989**). ''Anesthesia effects: Auditory brainstem response,'' EEG Clin. Neurophysiol. **72**, 422–428.

Subramaniam, M., Campo, P., and Henderson, D. (**1991**). ''The effect of exposure level on the development of progressive resistance to noise,'' Hearing Res. **52**, 181–188.

Subramaniam, M., Henderson, D., Campo, P., and Spongr, V. (**1992**). ''The effect of 'conditioning' on hearing loss from a high frequency traumatic exposure,'' Hearing Res. **58**, 57–62.

Subramaniam, M., Henselman, L. W., Spongr, V., Henderson, D., and Powers, N. L. (**1995**). ''Effect of high-frequency interrupted noise exposures on evoked-potential thresholds, distortion-product otoacoustic emissions, and outer hair cell loss,'' Ear Hear. **16**, 372–381.

Subramaniam, M., Salvi, R. J., Spongr, V. P., Henderson, D., and Powers, N. L. (**1994**). ''Changes in distortion product otoacoustic emissions and outer hair cells following interrupted noise exposures,'' Hearing Res. **74**, 204–216.

Tarnowski, B. I., Schmiedt, R. A., Hellstrom, L. I., Lee, F. S., and Adams, J. C. (**1991**). ''Age-related changes in cochleas of mongolian gerbils,'' Hearing Res. **54**, 123–134.

Zheng, X.-Y., Henderson, D., McFadden, S. L., and Hu, B.-H. (**1997**). ''The role of the cochlear efferent system in acquired resistance to noise-induced hearing loss,'' Hearing Res. **104**, 191–203.

Comparison of monaural (CMR) and binaural (BMLD) masking release

Steven van de Par and Armin Kohlrausch
IPO Center for Research on User-System Interaction, P.O. Box 513, NL-5600 MB Eindhoven, The Netherlands

(Received 6 May 1997; accepted for publication 2 December 1997)

Release of masking for a sinusoidal signal of 5 kHz masked by a 25-Hz-wide noise band centered around 5 kHz was measured. The masking release was provided by a second noise band that was comodulated with the on-frequency masker band. For CMR configurations the second noise band was centered at 3 kHz and presented to the ipsi-lateral or to the contra-lateral ear. For BMLD configurations the second band was centered at 5 kHz and presented to the contra-lateral ear. In another condition the second noise band also contained the signal presented with such a phase that maximal differences in the envelope resulted. For both the CMR and the BMLD paradigm, the masking release for the latter condition was larger than for the former condition. To assess further the similarity between monaural and binaural masking release, a sinusoidal masker and either a noise or a sinusoidal signal were used. The data indicate that, at high frequencies, envelope correlation may be a valuable cue for CMR as well as for the BMLD. © *1998 Acoustical Society of America.* [S0001-4966(98)03703-5]

PACS numbers: 43.66.Ba, 43.66.Dc, 43.66.Pn [JWH]

INTRODUCTION

When a tone is masked by a narrow band of noise, the amount of masking can be decreased by simultaneously presenting a flanking band which has a different center frequency than the masker and signal. Such a release from masking can be observed provided that the flanking band is comodulated with the masker band (Hall *et al.*, 1984a). The release from masking has been termed comodulation masking release (CMR). Since the first reports about CMR (Hall and Haggard, 1983; Hall *et al.*, 1984a), several mechanisms have been proposed to account for the observations. Some of these mechanisms are based on information within only one auditory channel (Schooneveldt and Moore, 1987; Verhey and Dau, 1996, 1997), others are based on the assumption that information across two or more auditory channels is compared (Buus, 1985; Hall, 1986; Richards, 1987).

In order to exclude within-channel processing, several experiments have been conducted where the spectral components responsible for the masking release are presented in the ear opposite to the masker and signal ear (Hall *et al.*, 1984b; Cohen and Schubert, 1987; Schooneveldt and Moore, 1987). Also, for these conditions some release from masking is observed, indicating that across-channel mechanisms are involved.

Several hypotheses have been made about the nature of these across-channel mechanisms. Hall *et al.* (1984a) suggested that a dynamic profile analysis mechanism compares the temporal envelope patterns of the various frequency components and makes inferences from these comparisons.

Another mechanism, initially proposed to account for the CMR obtained by modulating a noise masker with a low-pass noise, is based on the assumption that the addition of the signal to the masker band leads to a change in the modulation depth in the auditory filter centered around the signal. By comparing this modulation depth to that of other auditory filters, for which the modulation depth is unaltered, subjects would increase their sensitivity to the presence of the signal (Hall, 1986). Such a mechanism could also be effective in various other experiments that revealed CMR where stimuli consist of a narrow-band masker with one or more flanking bands which are comodulated with the masker (e.g., Hall *et al.*, 1984a; McFadden, 1986; Cohen and Schubert, 1987).

A different explanation for CMR was proposed by Buus (1985), who suggested that the comodulated flanking bands give valuable information about the moments at which the masker band has a relatively low energy. By attributing more weight to these valleys in the masker, the effective signal-to-noise ratio increases and detection improves. This mechanism was termed ''listening in the valleys.''

Also proposed by Buus (1985) is an equalization and cancellation (EC) mechanism which was originally introduced by Durlach (1963) to account for various binaural masking release data. According to this mechanism, the envelopes of masker and flanking band are first equalized and are then subtracted. The output of such a mechanism will have a considerable increase in signal-to-noise ratio provided that the masker and the flanking bands are comodulated.

These last two mechanisms have been compared in a recent study by Buus *et al.* (1996), which revealed that for their CMR-type of experiment, detection is dominantly based on the valleys present within the masker and flanking bands, supporting the listening-in-the-valleys hypothesis. However, it is also noted by Buus *et al.* that a combination of peripheral compression (Yates, 1990; Oxenham and Plack, 1997) followed by an EC mechanism may also account for the data.

A fourth mechanism has been proposed by Richards (1987). In this view it is assumed that the cross covariance between the envelopes of the masker and the flanking band is

used for signal detection. Due to the addition of the signal to the masker band, the envelope cross covariance decreases, a cue to which subjects are assumed to be sensitive. Such a mechanism is, however, difficult to reconcile with data by Eddins and Wright (1994). They used two 100% sinusoidally amplitude modulated (SAM) sinusoids of different center frequencies. Subjects had to detect the in-phase addition of a sinuoid to one of the SAM sinusoids. Although the envelope pattern is altered by the addition of the in-phase sinusoid, the envelope cross covariance does not change. Therefore, if envelope cross covariance is essential for obtaining a CMR, this type of stimulus should not lead to a CMR. However, a CMR was observed, and the authors rejected the envelope cross-covariance hypothesis.

Green (1992) showed the equivalence of an EC mechanism to an envelope correlation mechanism. However, Green's derivation may be interpreted to apply either to the envelope cross correlation or to the envelope cross covariance (cf. Bernstein and Trahiotis, 1996). One cannot regard such a different interpretation as a trivial issue since these two measures of envelope coherence have been shown to give very different relations between the change in coherence (correlation or covariance) and the signal-to-masker ratio (van de Par and Kohlrausch, 1995, 1998). With this in mind it is interesting to note that a CMR would have been predicted for the stimuli which Eddins and Wright (1994) used on the basis of the presumed sensitivity of subjects to a change in envelope cross *correlation*. In connection to these different measures of coherence it has been found that binaural detection at high frequencies is better described in terms of an envelope cross correlation mechanism than in terms of an envelope cross covariance mechanism (Bernstein and Trahiotis, 1996).

In this paper we investigate various mechanisms which might account for CMR by measurements with a set of stimuli which predict different results depending on the mechanism that is assumed. The mechanisms which we consider in this paper are: (1) the comparison of modulation depth across several components of the stimulus; (2) the listening-in-the-valleys hypothesis; and (3) the subject's sensitivity to a change in envelope cross correlation (which in terms of the resulting decision process is equivalent to an EC mechanism).

Furthermore, a comparison is made between CMR and high-frequency binaural detection since for both it has been suggested that envelope disparities play an important role in the detection process. For this purpose, the constituent noise-bands of each stimulus were presented in three different configurations: (1) both components were presented to the same ear and the two components had center frequencies of 3 and 5 kHz (ipsi-lateral CMR); (2) both components were presented to opposite ears and had center frequencies of 3 and 5 kHz (contra-lateral CMR); and (3) both components were presented to opposite ears and had equal center frequencies of 5 kHz (binaural). The stimulus generation was such that, independent of the configuration for which they were generated, the properties of the envelopes of each pair of noise bands were identical.

I. EXPERIMENTS

A. Procedure

A 3-interval forced-choice procedure with adaptive signal-level adjustment was used to determine the lowest signal level for which the test interval could be distinguished from the reference intervals. The three masker intervals of 400-ms duration were separated by gaps of 200 ms. A signal of 300-ms duration was added in the temporal center to one of these intervals. The subject's task was to indicate which of the three intervals contained the signal. For some conditions, the signal was added to the test interval as well as to the reference intervals, but with different phase relations. In this case, the subjects could only select the test interval by listening to disparities in the envelopes of the stimulus constituents.

The signal level was adjusted according to a two-down one-up rule (Levitt, 1971). The initial step size for adjusting the level was 8 dB. After every second reversal of the level track, the step size was halved until a step size of 1 dB was reached. The run was then continued for another 8 reversals. From the level of these last eight reversals the median was calculated and used as a threshold value. At least four threshold values were obtained for each parameter value and subject from which the median value was selected.

B. Stimuli

The stimuli were presented in three configurations; the binaural, the CMR ipsi-lateral, and the CMR contra-lateral configuration.

For the binaural configuration, thresholds were measured under five conditions:

1. A condition for which the masker was a 25-Hz-wide noise and the signal a sinusoid. Masker and signal were interaurally in phase, resulting in identical envelopes in both ears (BNoSo).
2. Similar to condition 1, but the signal was added only to the left ear (BNoSm). Thus envelopes are different in both ears.
3. Similar to condition 1, but the signal was interaurally out-of-phase (BNoSπ).
4. The masker was an interaurally in-phase sinusoid while the signal was a 25-Hz-wide noise in antiphase (BSoNπ). An in-phase noise at the same level as the signal was added to the reference intervals to avoid within-channel detection due to the high sensitivity of subjects to changes in a flat envelope (Kohlrausch *et al.*, 1997).
5. Similar to condition 4, but instead of noise as a signal, sinusoids were used with a 12.5-Hz higher frequency than the masker (BSoSπ). Here the reference intervals contained the in-phase sinusoidal signal for similar purposes as in condition 4.

Although it is not the actual way in which stimuli were generated, the CMR ipsi-lateral and the CMR contra-lateral stimuli are in principle derived from the binaural stimuli. To obtain a CMR contra-lateral stimulus the spectral components of the right channel of the binaural stimulus are shifted downwards in frequency to 3 kHz, preserving the amplitudes

and phases of all the spectral components. In this way, the envelopes of the original waveform, at 5 kHz, and the down-shifted waveform, at 3 kHz, are identical.

To obtain a CMR ipsi-lateral stimulus, the 3-kHz waveform that is presented to the right ear for the CMR contra-lateral configuration is now presented to the left ear in addition to the 5-kHz waveform that is already present in the left ear. The same five conditions that were measured for the binaural configuration, were also measured for the two CMR configurations.

In order to emphasize the equivalence between the binaural and the CMR ipsi- and contra-lateral stimuli, a similar notational convention which is normally only used for binaural stimuli will be used for all stimuli throughout the rest of this paper. Thus for the CMR ipsi-lateral configuration, CiNoSm denotes a conventional CMR stimulus which is presented monaurally (to the left ear) with a 5-kHz signal, a masker band at 5 kHz and a comodulated flanking band at 3 kHz, while for CcNoSm, the flanking band is presented contralaterally. When discussing three conditions together, the prefix is omitted.

All stimuli were generated digitally and converted to analog signals with a two-channel (left and right), 16-bit D/A converter at a sampling rate of 32 kHz. For subject JB, the stimuli were presented over Beyerdynamic DT 990 headphones; subject HB used both Beyerdynamic and TDH-49P headphones; and subject SP listened only through TDH-49P headphones. Each masking band was presented at an overall sound pressure level of 70 dB.

The actual generation of the stimuli in the experiments was done by selecting samples from a set of pregenerated buffers. Before each threshold measurement, a two-channel 2000-ms cyclic masker buffer was generated containing FFT-filtered noises or sinusoids depending on the measurement condition. For the binaural configuration, both channels contained the same signals at 5 kHz. For the CMR contra-lateral configuration, the 5-kHz signal in the left channel was shifted down to 3 kHz and presented in the right channel. This was done by taking the FFT of the 5-kHz signal and translating all Fourier components down by 2 kHz. For the CMR ipsi-lateral configuration the same procedure was followed but now both the 5-kHz and the 3-kHz signals were presented to the left ear, while the right ear contained no signal. During the measurement, 400-ms two-channel intervals were selected at random from this buffer to serve as a masker and were presented to both ears. A new random entry was selected for each interval. Similarly, a two-channel signal buffer was generated, again, either containing FFT-filtered noises or sinusoids. The same temporal interval which was selected from the masker buffer was also selected from the signal buffer to serve as a signal. Since the signal duration was 300 ms, only the central 300 ms of the 400-ms interval was added to the masker. Since the phases of the two buffers were set in an appropriate way in advance, selecting the same temporal interval from the masker and signal buffers enabled us to create stimuli with the properties described above.

C. Subjects

Three normal-hearing subjects participated in the experiments varying in age from 27 to 34 years. Subjects were trained for at least 1 h before data collection started. As a criterion for selecting a subject for the listening tests the subject had to be able to distinguish the test and the reference intervals for the CiSoNπ condition. We found that more than 50% were not able to do this at any signal-to-masker ratio.

D. Results

The results for the five conditions described above are shown in Fig. 1 for the three subjects in the upper 2 and the lower left panel. In addition mean thresholds across subjects are shown in the lower right panel. Thresholds are specified as the power of one signal component relative to the power of one masker band. The dark gray bars show results for the binaural configuration, the light gray and white bars show results for the CMR ipsi-lateral and contra-lateral configurations, respectively.

A first inspection of the results shows that the pattern of results for the three configurations is rather similar for each of the three subjects. Thresholds are lowest for conditions 3, 4, and 5 (NoSπ) where a signal is added to both masker bands. Thresholds for condition 2 (NoSm) are on average 6.2 dB higher than for condition 3. Thresholds for the reference condition 1 (NoSo) are higher than thresholds for conditions 2 and 3, which implies that release of masking was found in the latter conditions.

Both ipsi- and contra-lateral CMR configurations give fairly similar thresholds for two of the three subjects. This suggests, that since for the contra-lateral configuration only across-channel cues can be used, across-channel cues were also dominant in the ipsi-lateral configuration and that therefore, within-channel cues did not significantly contribute to detection.

II. DISCUSSION

For condition 1 there are no across-channel disparities and thus detection is likely based on an energy detection process. Therefore this condition can serve as a reference condition. A comparison of thresholds for this reference with thresholds for condition 2 in Fig. 1 indicates that there is a release from masking for the NoSm condition.

For condition 2, the introduction of the signal to one of the masker bands leads to a difference in modulation depth between the two bands, and thus this may also be a detection cue. In addition, listening in the valleys can provide a benefit for signal detection. In this condition the masker component without signal can provide useful information as to when the masker component to which the signal is added has a high signal-to-masker ratio. Furthermore, the disparities in envelope that are introduced by the addition of the signal to one of the masker bands leads to a decrease in the envelope correlation. Thus on the basis of all three cues, both for the binaural configuration and for the two CMR configurations, a release from masking could in principle be expected.

In condition 3, the sinusoidal signal was added to both noise masker components with a phase such that NoSπ

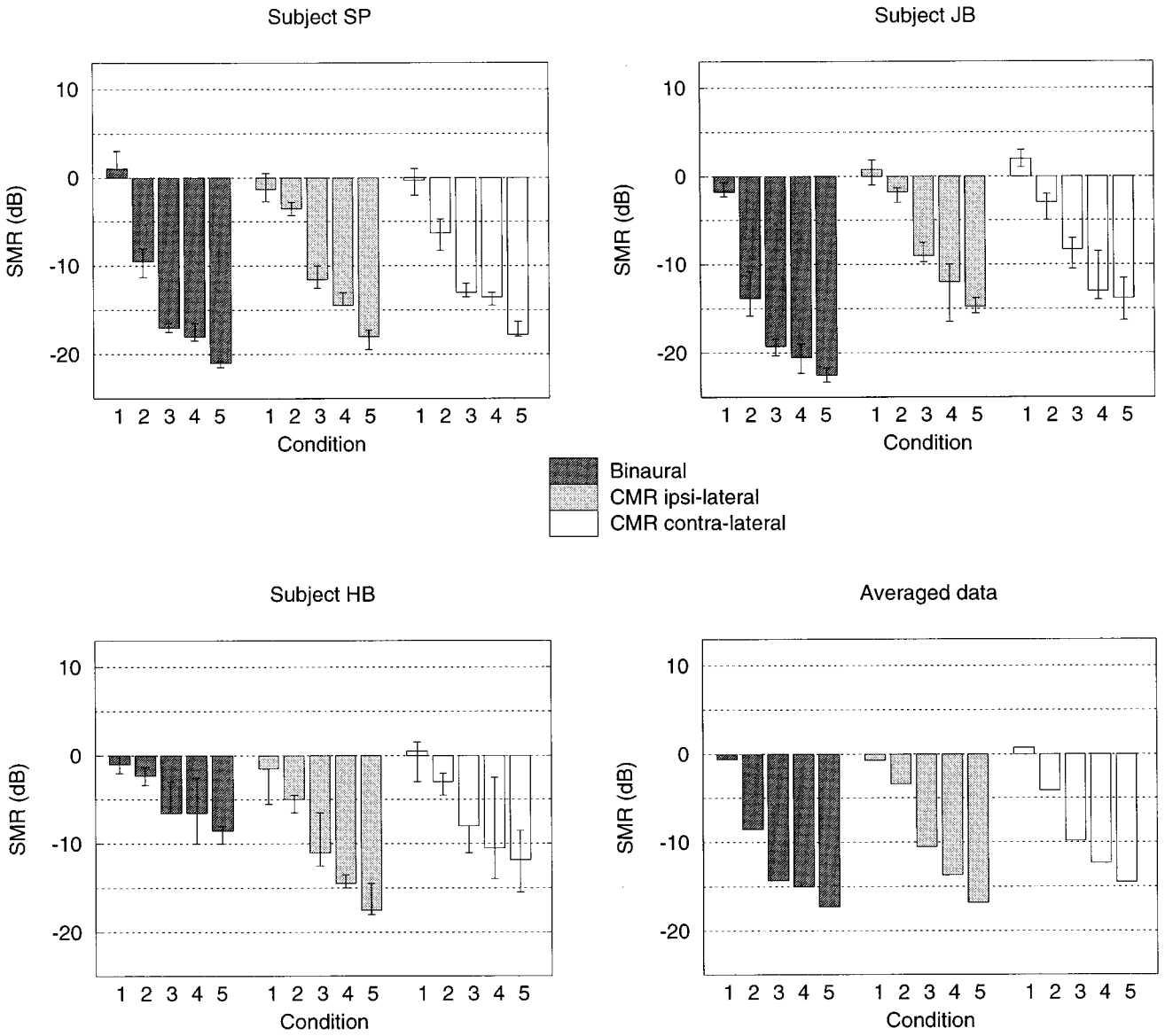

FIG. 1. The median thresholds, expressed as signal to maskerband ratio (SMR), for three subjects. In addition mean thresholds across subjects are plotted in the lower right panel. The binaural, the CMR ipsi-lateral, and the CMR contra-lateral configurations are shown by the dark gray, light gray, and white bars, respectively. In conditions 1–3, the two masker components are noise bands with identical envelopes. In condition 1, the signal is added in-phase to both masker components. In condition 2, the signal is added to only one masker component. In condition 3, the signal is added out-of-phase to both masker components. In conditions 4 and 5 the masker is an in-phase sinusoid and the signal is a pair of noise bands or a pair of sinusoids presented out-of-phase, respectively. In conditions 5, the signal sinusoids are 12.5 Hz higher in frequency than the masker sinusoids. The errorbars show lower and upper quartiles.

stimuli were obtained. In this case the difference in the envelopes of the two stimulus components is larger than for the NoSm stimuli (condition 2). Averaged across the three configurations, this results in thresholds which are 6.2 dB lower than for condition 2. When it is assumed that the envelope correlation is the cue used by subjects a decrease of 6 dB in thresholds is expected (van de Par and Kohlrausch, 1998). A mean difference of 5.7 dB was observed between the BNoSm and BNoSπ conditions, in line with the theoretically expected value. For the CMR ipsi-lateral and the CMR contra-lateral configurations, mean differences of 7.1 dB and 5.7 dB were found, respectively, also in good agreement with the assumption that subjects are sensitive to envelope correlation.

Because in condition 3 the signal is added in anti-phase to the masker bands, both masker bands will contain a signal and thus the modulation depth averaged across many samples will not be different in the two bands. However, the modulation depth across bands can still be very different for each specific stimulus. In order to show this, the difference in modulation depth can be expressed as the difference in the normalized fourth moment (cf. Hartmann and Pumplin, 1988) of both masker components. At threshold, average absolute differences in the normalized fourth moment were found to be 0.49 and 0.45 for conditions 2 and 3, respectively.

The absolute difference across bands in the normalized fourth moment was used as a decision variable in a simulated adaptive procedure with the same stimuli that were used in the experiment. A Gaussian stochastic variable with an rms

TABLE I. The median SMRs of the three subjects are shown for all five conditions of the CMR ipsi-lateral configuration. In addition, predictions by a simple model based on listening in the valleys are presented for the same five conditions. For the model, 24 thresholds were simulated for each condition.

	CiNoSo	CiNoSm	CiNoSπ	CiSoNπ	CiSoSπ
Subjects	−1.3 dB	−3.5 dB	−11 dB	−14.5 dB	−17.5 dB
Model	0 dB	−4 dB	−13 dB	−6 dB	−8.5 dB

of 0.4 was added to the decision variable to limit performance such that the median of the simulated thresholds for condition 3 was near to experimentally measured thresholds. In order to include the use of purely monaural (within channel) cues in this procedure it was simply assumed that performance was perfect for signal-to-masker ratios above 0 dB. For conditions 2 and 3, median thresholds of −5.5 and −10.5 dB were found based on 24 threshold simulations per condition. This result comes close to the experimental results.

Although, it is less straightforward to see than for an NoSm condition, the listening-in-the-valleys mechanism may also provide a benefit for condition 3 (NoSπ condition). For these stimuli there is no component band without signal. However, one of the component bands can still be used to determine the times corresponding to low-energy portions of the masker. Thus, a listening-in-the-valleys strategy may provide a sufficient cue for detection, as shown in the model predictions described below and in Table I.

Thus it seems that listening in the valleys, detection of differences in modulation depth and the envelope cross correlation provide good mechanisms for describing the experimentally observed thresholds of conditions 2 and 3.

For condition 4, a sinusoidal masker and a Gaussian-noise signal were used. The sinusoidal masker which has a flat envelope interacts in an interesting way with the noise signal. The fluctuations that are created in the envelopes of the two masker bands by adding the signal are nearly opposite in sign. Therefore it is expected that the difference in modulation depth across bands is rather small. Indeed for stimuli at threshold, average absolute differences in the normalized fourth moment were found to be only 0.02, a factor 20 smaller than values found for conditions 2 and 3. Furthermore, simulating a decision process based on the absolute differences across bands in the normalized fourth moment such as described above resulted in a median threshold of −3 dB, much too high in comparison to the experimental results.

Another aspect of the stimuli used in condition 4 as well as in condition 5 using a sinusoidal signal is that at small signal-to-masker ratios, the signal will only introduce small fluctuations in the otherwise flat envelope. Therefore, the momentary signal-to-noise ratio will fluctuate only marginally and there will not be much benefit in listening in the valleys. This implies that if subjects have to rely on this cue, a considerably higher threshold can be expected for conditions 4 and 5 as compared to condition 3.

In order to investigate this expectation quantitatively, some simulations were done with a simple model based on a single-channel energy detector which can just discriminate 1-dB level differences. In order to incorporate the listening-in-the-valleys mechanism, the stimulus that is present within the detection channel was weighted with the reciprocal value of the envelope of the other, nondetection channel. For the CiNoSm condition the weighting function was derived from the band not containing the signal. For the CiNoSπ, CiSoSπ, and CiSoSπ conditions there is no band without a signal, therefore one band was used to derive a weighting function for the other band. The weighting function was made level independent by normalizing the envelope of the nondetection channel to a constant rms of 1. Simulation results using the same CMR stimuli that were used in the experiments and using the same adaptive procedure as in the experiments, are shown in Table I together with the median subject results for the CMR ipsilateral configuration. It appears that this simple model can account reasonably well for conditions 2 and 3 with the fluctuating masker, but not for conditions 4 and 5 with a flat envelope masker. The fact that the predicted thresholds are rather high for conditions 4 and 5 indicates that some cue other than listening in the valleys is used by the subjects.

Since for conditions 4 and 5, the signal is added in antiphase to the two masker components there will be no consistent differences in modulation depth for these conditions. Similarly to condition 3, the results of condition 4 and 5 lead us to conclude that listening for modulation depth disparities is not necessary for discriminating between stimuli with identical and slightly different envelopes.

If we now consider that in conditions 4 and 5 the listener's strategy is not listening in the valleys nor detecting differences in the modulation depth of the two stimulus components, it appears that some measure of envelope disparity is responsible for the rather low detection thresholds for conditions as used in this study. Such a measure of disparity could be the envelope cross correlation. Let us assume for a moment that this is indeed the cue used by subjects.

According to the analysis of the envelope correlation by van de Par and Kohlrausch (1995, 1998) it is expected that all thresholds should be identical for the NoSπ, SoNπ, and SoSπ conditions (conditions 3, 4, and 5) while thresholds should be 6 dB higher for the condition where the signal is added to only one of the masker components (condition 2). For condition 1, there are no envelope differences between both masker components and therefore the envelope correlation will not provide a useful cue for this condition. Thus the difference in threshold for condition 1 on the one hand and conditions 2–5 on the other hand is consistent with the subject's sensitivity to changes in envelope correlation.

In most cases, there is a trend for thresholds in conditions 4 and 5 to be lower than in condition 3 while they were expected to be equal on theoretical grounds. Although we have no good understanding of this, possibly this may be an indication that the envelopes are not represented in an exact linear way internally. A speculation is that the dc components may be partially removed as was considered by Bernstein and Trahiotis (1996) in the context of high-frequency binaural stimuli. Removing part of the dc component for a stimulus with a sinusoidal masker (like condition 4) can be

shown to lead to a decrease in correlation value, improving thresholds. This decrease can be shown to be larger than for a stimulus with a noise masker (like condition 3) with the same signal-to-masker ratio (cf. Bernstein and Trahiotis, 1996). This would explain the decrease in thresholds for conditions 4 and 5. The difference of 6 dB between conditions 2 and 3 is not expected to be changed since the 6-dB difference has been shown to hold with or without the preservation of the dc component (cf. van de Par and Kohlrausch, 1995, 1998).

Since there seems to be a mechanism that in essence is fairly similar to an envelope correlation mechanism which can account for the performance of subjects in conditions 4 and 5 and since this mechanism by itself would be sufficient to account for the detection in conditions 2 and 3, it seems unnecessary to assume additional cues in these conditions, such as listening in the valleys and detection of differences in modulation depth.

At first sight, this may seem to contradict the finding of Buus *et al.* (1996) that detection in CMR ipsi-lateral CiNoSm conditions is predominantly based on the information that is present within the minima of the masker. However, Buus *et al.* also noted that the results which lead them to this finding may also be explained if one assumes a compressive nonlinearity followed by an EC mechanism. As already mentioned, an EC mechanism can be shown to be equivalent, in terms of the resulting detection process, to a decision device based on the normalized cross correlation. Thus a combination of peripheral compression and a normalized cross correlation mechanism should equally well explain their data.

When the results for the binaural and the two CMR configurations are compared we find that, on average, the binaural conditions give the lowest thresholds. However, this is not generally the case for each subject. For subject HB, monaural masking release is larger than the binaural masking release. The two CMR conditions give almost the same results for subjects JB and SP, while for subject HB, who was less sensitive in the binaural configuration, the contra-lateral CMR configuration gives higher thresholds. In fact, for this subject the binaural and the CMR contra-lateral configuration are fairly similar. Thus for each subject, the performance in the CMR contra-lateral configuration seems to be determined by the processing mode with the highest average thresholds (either binaural or CMR ipsi-lateral). It is interesting that averaged across the three listeners, the performance in the CMR and binaural tasks is not too different. Furthermore, the pattern of results is fairly similar for all three configurations suggesting a strong similarity in at least the effective processing involved.

Summarizing, the pattern of results suggests that a detection cue related to the disparity between the envelopes of the masker components, such as the envelope cross correlation, is used by subjects in the binaural and the CMR configurations. Although, such a hypothesis for CMR has been rejected on the basis of several experiments (e.g., Hall *et al.*, 1988; Moore and Emmerich, 1990; Eddins and Wright, 1994) we have shown that in at least some studies this rejection is due to the specific choice of the authors for the envelope cross covariance as a measure of envelope coherence (van de Par and Kohlrausch, 1998). Had the authors used the normalized envelope cross correlation instead, they would have had a measure of envelope disparity that is in line with their results.

ACKNOWLEDGMENTS

The authors thank Andrew Oxenham and both reviewers for their comments on an earlier version of this manuscript. We are especially grateful to reviewer A for suggesting the normalized fourth moment as a means to compare modulation depth and for stimulating us to look in more quantitative detail at the listening-in-the-valleys hypothesis.

Bernstein, L. R., and Trahiotis, C. (**1996**). ''On the use of the normalized correlation as an index of interaural envelope correlation,'' J. Acoust. Soc. Am. **100**, 1754–1763.

Buus, S. (**1985**). ''Release from masking caused by envelope fluctuations,'' J. Acoust. Soc. Am. **78**, 1958–1965.

Buus, S., Zhang, L., and Florentine, M. (**1996**). ''Stimulus-driven, time-varying weights for comodulation masking release,'' J. Acoust. Soc. Am. **99**, 2288–2297.

Cohen, M. F., and Schubert, E. D. (**1987**). ''Influence of place synchrony on detection of a sinusoid,'' J. Acoust. Soc. Am. **81**, 452–458.

Durlach, N. I. (**1963**). ''Equalization and cancellation theory of binaural masking-level differences,'' J. Acoust. Soc. Am. **35**, 1206–1218.

Eddins, D. A., and Wright, B. A. (**1994**). ''Comodulation masking release for single and multiple rates of envelope correlation,'' J. Acoust. Soc. Am. **96**, 3432–3442.

Green, D. M. (**1992**). ''On the similarity of two theories of comodulation masking release,'' J. Acoust. Soc. Am. **91**, 1769.

Hall, J. W. (**1986**). ''The effect of across-frequency differences in masking level on spectro-temporal patteren analysis,'' J. Acoust. Soc. Am. **79**, 781–787.

Hall, J. W., and Haggard, M. P. (**1983**). ''Co-modulation—A principle for auditory pattern analysis in speech,'' Proc. 11th ICA **4**, 69–71.

Hall, J. W., Haggard, M. P., and Fernandes, M. A. (**1984a**). ''Detection in noise by spectro-temporal pattern analysis,'' J. Acoust. Soc. Am. **76**, 50–56.

Hall, J. W., Haggard, M. P., and Harvey, A. D. G. (**1984b**). ''Release from masking through ipsilateral and contralateral comodulation of a flanking band,'' J. Acoust. Soc. Am. **76**, S76.

Hall, J. W., Grose, J. H., and Haggard, M. P. (**1988**). ''Comodulation masking release for multicomponent signals,'' J. Acoust. Soc. Am. **83**, 677–686.

Hartmann, W. M., and Pumplin, J. (**1988**). ''Noise power fluctuation and the masking of sine signals,'' J. Acoust. Soc. Am. **83**, 2277–2289.

Kohlrausch, A., Fassel, R., van der Heijden, M., Kortekaas, R., van de Par, S., Oxenham, A. J., and Püschel, D. (**1997**). ''Detection of tones in low-noise noise: Further evidence for the role of envelope fluctuations,'' Acust. Acta Acust. **83**, 659–669.

Levitt, H. (**1971**). ''Transformed up–down methods in psychoacoustics,'' J. Acoust. Soc. Am. **49**, 467–477.

McFadden, D. (**1986**). ''Comodulation masking release: Effects of varying the level, duration, and time delay of the cue band,'' J. Acoust. Soc. Am. **80**, 1658–1667.

Moore, B. C. J., and Emmerich, D. S. (**1990**). ''Monaural envelope correlation perception, revisited: Effects of bandwidth, frequency separation, duration, and relative level of the noise bands,'' J. Acoust. Soc. Am. **87**, 2628–2633.

Oxenham, A. J., and Plack, C. J. (**1997**). ''A behavioral measure of basilar-membrane nonlinearity in listeners with normal and impaired hearing,'' J. Acoust. Soc. Am. **101**, 3666–3675.

Richards, V. M. (**1987**). ''Monoaural envelope correlation perception,'' J. Acoust. Soc. Am. **82**, 1621–1630.

Schooneveldt, G. P., and Moore, B. C. J. (**1987**). ''Comodulation masking release (CMR): Effects of signal frequency, flanking-band frequency,

masker bandwidth, flanking-band level, and monotic versus dichotic presentation of the flanking band,'' J. Acoust. Soc. Am. **82**, 1944–1956.

van de Par, S., and Kohlrausch, A. (**1995**). ''Analytical expressions for the envelope correlation of certain narrow-band stimuli,'' J. Acoust. Soc. Am. **98**, 3157–3169.

van de Par, S., and Kohlrausch, A. (**1998**). ''Analytical expressions for the envelope correlation of narrow-band stimuli used in CMR and BMLD research,'' J. Acoust. Soc. Am. (submitted).

Verhey, J., and Dau, T. (**1996**). ''Simulationen zu comodulation masking release (CMR),'' DAGA'96, Deutsche Gesellschaft für Akustik e.V., Oldenburg, 330–331.

Verhey, J., and Dau, T. (**1997**). ''Modeling comodulation masking release,'' in *Contributions to Psychological Acoustics*, edited by A. Schick and M. Klatte (Bibliotheks- und Informationssystem der Universität Oldenburg), pp. 389–396.

Yates, G. K. (**1990**). ''Basilar-membrane nonlinearity and its influence on auditory-nerve rate-intensity functions,'' Hearing Res. **50**, 145–162.

Auditory continuity and loudness computation[a)]

Stephen McAdams[b)]
Laboratoire de Psychologie Expérimentale (CNRS), Université René Descartes, EPHE, 28 rue Serpente, F-75006 Paris, France and Institut de Recherche et de Coordination Acoustique/Musique (IRCAM), 1 place Igor-Stravinsky, F-75004 Paris, France

Marie-Claire Botte and Carolyn Drake
Laboratoire de Psychologie Expérimentale (CNRS), Université René Descartes, EPHE, 28 rue Serpente, F-75006 Paris, France

(Received 21 August 1996; revised 6 October 1997; accepted 4 November 1997)

Sequences composed of alternating bursts of different levels with no silences separating them can give rise to a perception of a continuous sound upon which is superimposed an intermittent stream. These experiments sought to determine how the perceived loudness of the intermittent stream depends on the level difference between higher-level and lower-level bursts in the sequence in cases in which continuity is either heard or not heard. In the main experiment, listeners were asked to adjust the level of continuous or intermittent comparison sequences to match the loudness of components that appeared to be either continuous or intermittent in an alternating-level reference sequence, thus urging them to focus on the two-stream percept. Loudness matches of the continuous comparison stimulus were close to physical levels of the lower-level bursts, whereas matches of the intermittent comparison stimulus were well below the physical levels of higher-level bursts. These results are discussed in terms of Bregman's [*Auditory Scene Analysis* (MIT, Cambridge, MA, 1990)] ''old-plus-new'' hypothesis: The loudness of the intermittent stream should result from the subtraction of the lower level from the higher level under the assumption that the higher-level burst represents a simultaneous mixture of sounds including the continuation of the lower-level burst. Additional experiments verified that, in the absence of the continuity phenomenon, matched levels were very close to the physical levels and that matches to fixed-level continuous and intermittent sequences were precise. The matching results from the main experiment support predictions of neither classical loudness models that do not take auditory organization processes into account nor schema-based models that presume a selection of information from the higher-level burst that does not affect the perceptual content of this burst. The matched levels fell between predictions of models based on subtraction of acoustic pressure and acoustic power, but were very different from subtraction of loudness measured in sones, suggesting that loudness is computed subsequent to auditory organization processes.
[S0001-4966(98)04602-5]

PACS numbers: 43.66.Cb, 43.66.Mk, 43.66.Lj [WJ]

INTRODUCTION

To recover a veridical representation of the acoustic environment, it would be useful for the auditory system to be able to group together acoustic components that originate from the same source into coherent mental descriptions (variously referred to as auditory ''streams,'' ''objects,'' ''images,'' or ''entities''). Once the streams are organized, the auditory system can compute the perceptual attributes (loudness, pitch, timbre, etc.) of the events belonging to each stream. Our experiments aimed to measure the effect of auditory organization on the computation of loudness.

Consider the stimulus sequence in Fig. 1(a) in which a pure tone or a noise signal alternates between a higher level (L_H) and a lower one (L_L). There are several ways that such a signal might be generated, three of which are shown in Fig. 2. Given that the signal might result from several acoustic configurations, it is interesting to understand how the auditory system analyses the situation. One might imagine that a listener would hear an alternating sequence of loud and soft tones or noise bursts (hypothesis 1). If this were the case, one would expect that when listeners are asked to adjust the level of a comparison stimulus to match the loud or soft parts of the reference stimulus, we should obtain matches in the vicinity of L_H and L_L, respectively, with perhaps some deviations due to temporal masking effects and temporal integration of energy within each burst. Such a prediction would be made by classical time-varying loudness models (Zwicker, 1977). This class of model, as currently implemented in several so-called psychoacoustic measurement devices available on the market, does not consider the incident waveform to be

[a)]Preliminary work leading to this study was reported at the Troisième Congrès Français d'Acoustique, Toulouse (McAdams *et al.*, 1994a). Portions of the present data were first presented at the ATR Workshop on ''A Biological Framework for Speech Perception and Production,'' Kyoto (McAdams *et al.*, 1994b).

[b)]Address correspondence to S. McAdams, Laboratoire de Psychologie Expérimentale, 28 rue Serpente, F-75006 Paris, France, Electronic mail: smc@ircam.fr

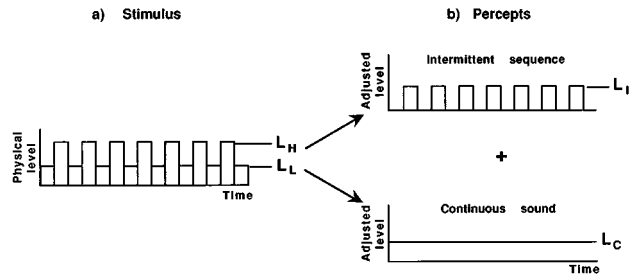

FIG. 1. (a) Stimulus sequence alternating between levels L_L and L_H. (b) Percepts resulting from the alternating sequence: a continuous sound with perceived level L_C and a sequence of intermittent bursts with perceived level L_I.

composed of temporally overlapping sound signals originating from separate sources of overlapping or even identical frequency content.[1]

However, Warren *et al.* (1972) have demonstrated that such a stimulus can be heard in a different way. A level difference between L_H and L_L of about 3–10 dB generally gives rise to a perception not of alternation but of an intermittent sequence superimposed on a continuous sound [Fig. 1(b)]. This perception of continuity is heard under certain conditions that depend on the difference between levels L_L and L_H (Houtgast, 1972; Thurlow, 1957; van Noorden, 1977), on the abruptness of the transition (Bregman and Rousseau, 1991), on the presence or absence of silences between bursts (van Noorden, 1977), as well as on other secondary factors (Houtgast, 1972; Thurlow, 1957; van Noorden, 1975; Verschuure *et al.*, 1976). This phenomenon has been called ''auditory continuity'' (Thurlow and Elfner, 1959) since the low-level signal is heard to continue through the intermittent signal, or ''auditory induction'' (Warren *et al.*, 1972) since the high-level part induces a perception of continuity in the low-level part. Similar types of phenomena have been demonstrated for speech interrupted by noise, in which a continuous speech signal appears to be perceptually

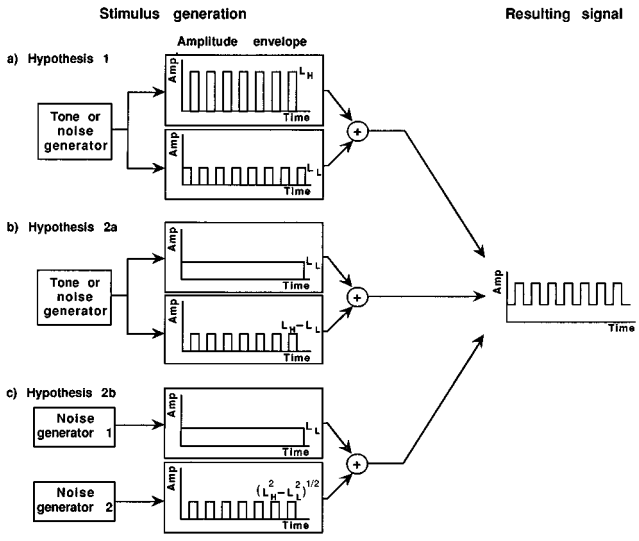

FIG. 2. Three different stimulus generation methods that would give similar resulting signals. Methods a, b, and c correspond to hypotheses 1, 2a, and 2b, respectively (see text).

restored during the noise burst (see Warren, 1984, for a review). In these cases, the auditory system would appear to have interpreted the signal as being composed of a continuous sound upon which another signal is superimposed. This interpretation depends on the presence of contextual evidence that the restored sound may be present, i.e., there must be no evidence that the low-level sound stopped and, in addition, the peripheral units stimulated by the interrupting sound must include those that would be stimulated by the anticipated fainter sound (Bregman, 1990; Warren *et al.*, 1972). Of particular interest to our present concerns is what this phenomenon might tell us about how the auditory system disentangles the respective perceptual attributes of superimposed signals.

Bregman (1990) proposes the existence of a general-purpose, bottom-up perceptual heuristic, called the ''old-plus-new'' strategy, which makes some qualitative predictions about this phenomenon: an interpolation is performed between the properties of the lower-level sounds occurring before and after the higher-level interrupting sound (Ciocca and Bregman, 1987). However, this computation is performed only if the auditory information indicates that the low-level sound could have been present during the occurrence of the high-level sound and that the transition between the high-level and low-level sounds is not a continuous one. Subsequently, the signal in the time interval occupied by the high-level sound is interpreted as resulting from a mixture of the low-level (old) sound and an additional (new) sound. The computation of the loudness of the intermittent stream would thus be based on a *subtraction* of the level of the restored part of the continuous sound from the global level of the intense part of the sequence. This kind of subtractive mechanism was first proposed by Warren (1982).[2]

According to this strategy, if we ask listeners to adjust the level of a comparison stimulus to match the loudness of either the continuous or the intermittent parts of this reference stimulus (see Fig. 1), we should obtain an adjusted level in the vicinity of L_L for the continuous part (L_C) and an adjusted level for the intermittent part (L_I) that would depend on the underlying psychological scale used by the subtraction mechanism to derive the loudness of this latter part. If a continuous sound and an intermittent sequence of identical frequency content are added in phase and presented to one or both ears [Fig. 2(b)], one might expect a law computed on acoustic pressure ($L_I = L_H - L_L$, where L is in units of pressure) (hypothesis 2a), whereas for similar, independent stimuli with incoherent phase relations [Fig. 2(c)] (e.g., signals of unknown properties, or even known signals presented in a reverberant environment), one might expect a law computed on acoustic power ($L_I^2 = L_H^2 - L_L^2$, where L is in units of pressure since power is proportional to the square of pressure) (hypothesis 2b). In both cases, and in contradistinction to the predictions from classical loudness models that do not include an organizational stage in their computations, adjusted level L_I would be *less* than the physical level L_H and the more so as $L_H - L_L$ becomes smaller. Since the periodicity of the waveform may affect the operation of these latter two hypothetical mechanisms, we decided to use both pure-tone and narrow-band noise bursts in our experiments.

Note that these models both presume that the signal is organized into continuous and intermittent parts *prior* to loudness computation. Another approach would presume that the loudness is computed on the raw signal levels, and that auditory organization would occur *subsequent* to this computation, in which case some additional loudness computation process would perform the subtractions in sone units (Stevens, 1957) (hypothesis 2c). For pure tones and narrow-band noise, identical results would be obtained from Zwicker's loudness model by subtracting specific loudness patterns and summing the specific loudnesses over critical bands in the residual pattern (Zwicker, 1960; Zwicker and Feldtkeller, 1967; Zwicker and Scharf, 1965). Pressure, power, and loudness calculations give different results for a given $L_H - L_L$ level difference.

All three of the aforementioned models that embody hypotheses 2a, 2b, and 2c presume that some kind of subtractive segregation process is employed, the operation of which is based on the available sensory data. Another possibility has been suggested by Repp (1992). He proposed that when an obliterated phoneme is replaced by a noise burst, its perceptual restoration is illusory since some higher-level, schema-driven, phonological completion is performed in a top-down fashion: the necessary information is selected from the noise burst (the top-down process is thus constrained by the sensory information), but this information is not *subtracted* per se from the noise burst, leaving the perceptual properties of the burst unaffected (hypothesis 3).

To summarize, the competing hypotheses to be tested are the following:

H1) classical loudness model without subtraction;
H2) old-plus-new type subtraction models, the computations of which are based on:
  a) acoustic pressure,
  b) acoustic power,
  c) loudness (in sones);
H3) top-down information-selection model.

Note that H1 and H3 make identical predictions for alternating-level sequences.

To test these various hypotheses, we presented listeners with sequences of events that alternated between a high level (L_H) and a low level (L_L), as in Fig. 1(a). The events were identical in spectral content. Listeners were asked to adjust the level of a comparison stimulus so that its loudness matched that of a specific part of the reference stimulus that varied with the experiment or within a block of trials. Stimulus parameters were varied to test the dependence of adjusted levels L_C and L_I on physical levels L_L and L_H under conditions in which listeners either clearly experienced auditory continuity or could not hear it. In the main experiment (experiment 1), conditions were presented in which continuity was heard. The adjusted levels were compared to those predicted by hypotheses H1, H2a–c, and H3. According to the old-plus-new heuristic, when continuity is not perceived, the classical model should be satisfactory and no subtraction of levels should be evident. Experiments 2 and 3 studied loudness matching to H and L bursts in alternating-level sequences in which continuity was impaired either by sending H and L bursts to separate ears or by introducing silences between them, respectively. Finally, a control experiment (experiment 4) was performed to verify listeners' loudness matching precision with fixed-level intermittent and continuous sequences.

To test for the possibility that temporal integration and/or loudness enhancement affect loudness computation in the continuity phenomenon, various duty cycles between H and L bursts were also employed in experiments 1 and 2. If temporal integration plays a role, one would expect differences in loudness matches between H bursts with durations of 200 ms and 100 ms, as well as between 100-ms L bursts and longer duration L bursts (Zwislocki, 1960). If loudness enhancement effects, originally investigated in two-burst stimuli, can be generalized to alternating sequences, one would expect greater loudness enhancement of L bursts (and thus less loudness difference between L and H bursts) in stimuli with shorter L-burst durations (100 and 200 ms; Zwislocki and Sokolich, 1974).

I. GENERAL METHOD

A. Stimuli

Sequences were composed of one of two types of stimulus bursts: a 1-kHz pure tone or a subcritical band, 140-Hz noise band centered on 1 kHz. Individual bursts had 5-ms linear onset and offset ramps. Sequences with alternating levels were composed of eight low-level (L) bursts interleaved with seven higher-level (H) bursts (Fig. 1). In experiments 1, 2, and 4, the sequences were presented with four different duty cycles to study effects of the time course of loudness growth and decay (D_H/D_L in ms: 200/200, 100/100, 100/300, 100/700). The total duration of the reference stimulus varied with duty cycle, being 3.0, 1.5, 3.1, and 6.3 s, respectively. In experiment 3, only the 100/300 duty cycle was used.

The H and L burst onsets and offsets either overlapped by 2.5 ms (no silence, experiments 1 and 2) or were separated by 30- or 100-ms silent intervals (experiment 3). With overlapping bursts, both pure-tone and noise-band signals were added in phase, i.e., they were derived from the same sound generator as in Fig. 2(b). In this latter condition, the continuity percept is quite strong if the sequence is presented diotically (experiment 1), but it is absent if H and L bursts are presented to separate ears (experiment 2). With silent intervals, continuity is generally absent or quite weak with 30-ms silences at the levels we used and is almost never perceived with 100-ms silences (experiment 3).

L_L in the reference stimulus was varied randomly within the A-weighted set $60 \pm \{1,3,5\}$ dB. In all analyses and plots, levels are presented relative to the mean of the roving range (60 dB). L_H was either 2, 6, or 10 dB greater than L_L. The prediction was that when auditory continuity was perceived, the loudness of the intermittent stream would vary systematically with this level difference, always being adjusted to a level below L_H (see Table I). For a mechanism operating on acoustic pressure, ideal listeners perceiving continuity should adjust an intermittent comparison stimulus to levels that are below L_H by 13.7, 6.0, and 3.3 dB, for L_H/L_L level differ-

TABLE I. Subtraction of low level from high level in units of pressure, power, and sones for a difference between H and L bursts of 6 dB (L_L=60 dB SPL, L_H=66 dB SPL, Pr_{ref}=20 μPa, Po_{ref}=1 pW).

	Pressure (μPa) ($Pr=10\ \text{dB}/20\cdot Pr_{\text{ref}}$)	Power (pW) ($Po=10\ \text{dB}/10\cdot Po_{\text{ref}}$)	Loudness (sones) ($S=0.01\cdot Pr^{0.6}$)
L_L	20 000	1 000 000	3.8073
L_H	40 000	3 981 072	5.7626
L_H-L_L	20 000	2 981 072	1.9553
L_I (dB)	60.0	64.7	50.4
L_I-L_H (dB)	−6.0	−1.3	−15.6

ences of 2, 6, and 10 dB, respectively. For a mechanism operating on acoustic power, the adjusted levels should be below L_H by 4.3, 1.3, and 0.5 dB, respectively. And for a mechanism operating on sone units, the adjusted levels should be below L_H by 29.7, 15.6, and 10.1 dB, respectively. These latter values are obtained by converting L_H and L_L from dB to sones (S_H and S_L) by Stevens' law: $S=kp^{0.6}$, where S is the loudness in sones, $k\approx 0.01$, and p is the pressure in μPa (cf. Botte, 1989). Then $S_I=S_H-S_L$, and S_I is reconverted to L_I in dB by the same law in reverse. This relation is only valid for levels above 30 phones (30 dB for pure tones and narrow noise bands in the vicinity of 1 kHz) (cf. Scharf, 1978).

To the contrary, if the classical loudness model or the schema-driven model is appropriate, the level adjusted to match the intermittent part of the sequence should be close to L_H. The same result should obtain when continuity is not perceived (experiments 2 and 3). All models predict that the level adjusted to match the continuous stream when continuity is heard or to the lower-level part of the sequence when continuity is not heard should be near L_L. Departures from the physical levels in reference stimuli not producing auditory continuity may indicate biases induced by the stimulus context and/or by the matching strategy. Such biases would need to be taken into account when interpreting the results for stimuli producing continuity.

B. Procedure

Each experiment was preceded by a familiarization phase in which the stimuli were presented to the subjects who were questioned as to what they heard in order to verify whether or not auditory continuity was perceived for all stimulus conditions. They were also allowed to practice the adjustment procedure. One or two blocks containing all the stimuli for a given condition presented in random order were usually sufficient.

Each trial consisted of the repeated alternation between the reference stimulus and a comparison stimulus. During this alternation, the level of the comparison stimulus could be adjusted with a single-turn potentiometer. Subjects could listen to the alternation as many times as necessary to make a satisfactory loudness match, at which point they signaled the computer to record the level of the comparison stimulus by pressing a button. The listener aligned the turn-pot to a fixed reference point at the beginning of each trial. The starting levels of the reference stimulus were chosen at random from $L_L\pm\{7,8,9,10\}$ dB for that trial. The duration of the silent intervals separating the two stimuli varied with the experiment and will be specified for each one below. For reference stimuli producing continuity, subjects were asked on a given trial either to adjust the level of a continuous comparison stimulus to match the level of what appeared to be continuous in the reference, or to adjust the level of an intermittent sequence to match the level of what appeared to be intermittent in the reference. For sequences not producing continuity, intermittent reference stimuli of similar temporal structure were presented and the subjects were asked to match either the higher or the lower level in the reference stimulus using ear of presentation or duration cues to focus on the target stream (experiments 2 and 3, respectively).

Stimuli were presented in blocks comprising a given burst type (pure-tone or noise-band) and duty cycle. All combinations of burst type and duty cycle tested in a given experiment were completed before any one was repeated. They were block randomized for each subject and five blocks of each type were completed by each subject in each experiment. Different subjects were recruited for each experiment and for the different silent-duration and burst-type conditions in experiment 3. Each experiment was conducted in a series of sessions varying from 60 to 90 min. Subjects were allowed to take breaks between blocks as desired. In all experiments, the dependent variable was the matching ''error'' (in dB) between the adjusted level of the comparison stimulus and the level of the targeted part of the reference stimulus (H or L bursts).

C. Apparatus

Sinusoidal and white noise signals were synthesized at a sampling rate of 20 kHz with 16-bit resolution on an Oros DSP card controlled by a Compaq 386 computer. In the case of alternating-level signals, H and L bursts were processed in different channels. The signals were then filtered with a Kemo VBF/24 bandpass filter with cutoff frequencies of 930 and 1070 Hz and −48 dB/oct slopes. The filtering served both for anti-aliasing and for obtaining the narrow-band noise. The filtered signals were then routed through Charybdis D programmable attenuators with 0.25-dB resolution that were controlled by the computer. The final signals were either sent separately to the two earpieces of a TDH-49 headset for the dichotic conditions or were mixed and sent to both earpieces for the diotic conditions. Experimental sessions took place in an IAC single-walled sound isolation chamber. Subjects adjusted levels for comparison stimuli with a single-turn potentiometer and signaled their satisfaction with

the match by pressing a button on the response box. At this point, the computer presented the next trial. Levels at each earpiece were verified using a Bruel & Kjaer 4153 artificial ear and a 2230 sound-pressure meter.

II. EXPERIMENT 1: DIOTIC ALTERNATING-LEVEL SEQUENCES PRODUCING CONTINUITY

The goal of this experiment was to test the main competing hypotheses that the loudness of an alternating sequence organized into continuous and intermittent streams is, on the one hand, partitioned into two quantities that may be computed either on the basis of pressure (H2a), power (H2b), or specific loudness (H2c) subtraction, or, on the other hand, is perceived as corresponding to the physical values presented (H1 and H3).

A. Method

On each trial the reference stimulus (sequence of overlapping H and L bursts) was alternated with an adjustable comparison stimulus that was either continuous or intermittent. The silence separating the end of the reference stimulus and the beginning of the comparison stimulus was 800 ms. A 1500-ms silence separated the end of the comparison stimulus and the next presentation of the reference stimulus. The four duty cycles were presented (200/200, 100/100, 100/300, 100/700). The continuous adjustable comparison stimulus had the same total duration as the reference stimulus and the intermittent adjustable comparison stimulus had the same temporal structure as the H bursts in the reference stimulus. Eight subjects that reported having normal hearing participated in the experiment and were paid for their services. Each subject completed five repetitions of the 48 conditions: 2 burst types $\times 4$ duty cycles $\times 3$ H/L level differences $\times 2$ comparison stimulus types.

B. Results

In the familiarization phase, all subjects reported the continuity percept for each condition, although the effect was weaker for the 2-dB difference in level between L_L and L_H, sometimes heard more as a fluctuating level. Subjects also reported that the bursts composing the intermittent stream in the alternating sequence were degraded in terms of the attack quality and tone color compared with the isolated intermittent sequence (similarly to results reported by Warren *et al.*, 1994).

From the adjusted level of the continuous comparison stimulus (L_C) and that of the intermittent comparison (L_I), the dependent variable (matching ''error'') was computed for each ($L_C - L_L$ and $L_I - L_H$, respectively). These values are plotted as a function of the H/L level difference in Fig. 3. For continuous stimuli, plotted data are averaged over burst type, duty cycle, subjects, and repetitions. For intermittent stimuli, data are averaged over subjects, repetitions, and duty cycle, with the exception of noise stimuli for which the stimuli with 200-ms H bursts are plotted separately from those with 100-ms H bursts (mean over 100/100, 100/300, and 100/700 duty cycles). Separate repeated-measures

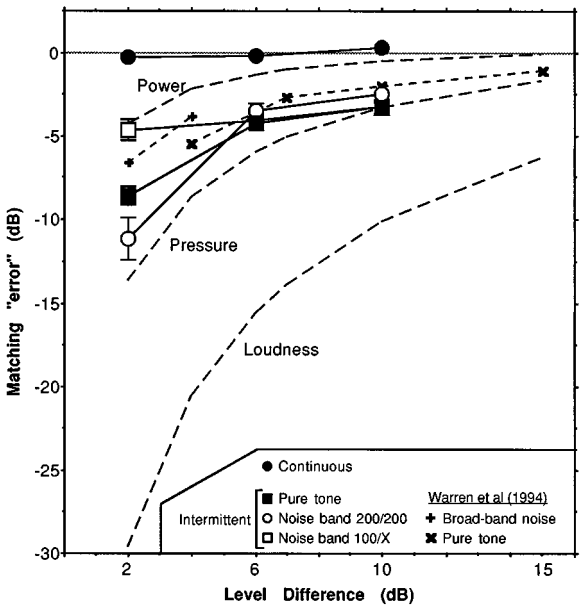

FIG. 3. Summary data for experiment 1. Mean loudness matching ''error'' (see text) as a function of H/L level difference. ''Errors'' for matches to the intermittent stream that are predicted by power, pressure, and loudness subtraction models are shown by dashed lines. All points would lie on the line at zero for models predicting matches to the physical values. All models predict zero error for matches to the continuous stream. For comparison, the data for similar (homophonic) conditions in Warren *et al.* (1994) are shown. (Pure-tone data were derived from Figs. 2 and 3 and broadband noise data from Fig. 7 in that study.) Vertical bars (where visible) show ± 1 standard error.

ANOVAs were performed for continuous and intermittent comparison stimuli with repeated factors burst type (2), H/L duty cycle (4), and H/L level difference (3).

1. Continuous comparison stimuli

There was a nearly perfect match of the comparison stimulus to the level of the continuous stream, matching error being within 1 dB of L_L. There was a significant difference of 0.6 dB between adjusted levels for pure-tone and noise-band stimuli [$F(1,7)=10.67$, $p<0.05$],[3] the stimuli being adjusted 0.3 dB below L_L for pure tones and 0.3 dB above L_L for noise bands. The two means are also both reliably different from the hypothesized value of 0 dB [single sample $t(479)=-2.92$, $p<0.005$; $t(479)=2.98$, $p<0.005$, respectively]. This difference, while significant, is quite small (less than the differential threshold for intensity discrimination, e.g., Luce and Green, 1974). There were no effects of duty cycle or of H/L level difference.

2. Intermittent comparison stimuli

The intermittent stream was adjusted on average to a level less than L_H. The range of the mean matching errors across subjects and repetitions was from -2.4 to -11.2 dB. Classical loudness models would predict mean adjusted intermittent levels near L_H, but these were very rare across subjects (17 out of 192 matching errors averaged across repetitions were above -1.0 dB). The effect of H/L level difference depended on both burst type and duty cycle, as witnessed by the significant triple interaction [$F(6,42)=5.42$,

$p<0.05$]. For pure-tone stimuli, a separate repeated-measures ANOVA on factors duty cycle and H/L level difference revealed that there was no effect of duty cycle [$F(3,21)=1.09$, n.s.], while a significant main effect of H/L level difference [$F(2,14)=6.16$, $p<0.05$] was found: matching ''errors'' decreased with increasing level difference. A similar analysis for noise-band stimuli showed that the duty cycle by H/L level difference interaction was significant [$F(6,42)=5.14$, $p<0.05$]. This interaction results from the fact that for the 200/200 duty cycle and a 2-dB H/L difference, the comparison stimulus was adjusted to much lower values compared both to those at larger H/L differences for the same duty cycle, as well as to the other duty cycles at the 2-dB difference (all of the cited differences between means were greater than the critical Tukey–Kramer difference of 3.4 dB). There was no effect of H/L level difference for the three duty cycles with 100-ms H bursts [$F(1,42)=0.65$, n.s., for 2 dB versus 6 dB; $F(1,42)=1.05$, n.s., for 6 dB versus 10 dB; $F(1,42)=3.35$, $p<0.10$, for 2 dB versus 10 dB]. There was no difference between pure-tone and noise-band stimuli at the 6-dB and 10-dB H/L level differences. The source of this triple interaction thus seems to be related to matches for noise-band stimuli at the 2-dB H/L level difference: the adjusted level of the 200/200 duty cycle was low (a value commensurate with those obtained for pure-tone stimuli at all duty cycles) and the adjusted levels of the duty cycles with 100-ms H bursts were high.

C. Discussion

This pattern of data corresponds to predictions of neither the classical loudness models (H1) nor the schema-driven models (H3), i.e., listeners do not systematically adjust levels of the intermittent sequence close to the physically presented levels. We can thus reject both of these classes of models. The data are, however, in qualitative agreement with the prediction of the ''old-plus-new'' subtraction strategy: the smaller the H/L level difference, the greater the matching error. In fact, L_I was, on average, adjusted even lower than L_I for a difference of 2 dB. This effect is broadly consistent with results obtained by Darwin (1995) for synthetic vowel stimuli and by Warren *et al.* (1994) for pure tones and broadband noise. The matching errors are much smaller in magnitude than those predicted by the loudness subtraction model (see Fig. 3). So whatever the auditory representation of level used for subtracting the continuous portion from the high-level burst, it is clearly not related to loudness as defined in Stevens' power law, suggesting that the signal is organized into streams before loudness is computed rather than afterward. For these homophonic stimuli, the auditory representation of level at the stage of stream organization appears to be closer to physical units like pressure or power. Our data fall between the predictions based on pressure and power subtraction, as do those of Warren *et al.* (1994). Single-sample t-tests, adjusted for multiple tests, were performed on mean matching errors against values predicted by power and pressure subtraction. They revealed that neither subtraction method predicts all of the experimental data. At the 2-dB level difference, matches for noise-band stimuli with the 200/200 duty cycle are not different from the pressure calculation, while those with 100-ms H bursts are not different from the power calculation. At the 10-dB difference, none of the matches is different from the pressure calculation. In all other cases, the mean matching errors are significantly different from both pressure and power calculations. Clearly, neither of these units explains the data and there are some troubling differences due to duty cycle and burst type, particularly at the smallest H/L level difference.

There may be a number of reasons for these discrepancies. Subjects noted that with the 2-dB level difference, the task was more difficult and they were more uncertain in their matches. They also felt the difficulty and uncertainty were increased with the noise stimuli compared to the pure tone stimuli. The former impression is borne out for 2-dB conditions, which have much higher standard deviations (7–8 dB) than do conditions with a larger level difference (2.5–3.0 dB). However, this pattern is very similar for both pure-tone and noise-band stimuli, and indeed for noise stimuli the 200/200 duty cycle has a larger standard deviation than that for the other three duty cycles taken together. This result belies the latter impression and argues against listeners' having difficulty estimating the level in these stimuli due to short-term level fluctuations in narrow-band noise signals. Although our results globally support a subtractive segregation mechanism, they may also suggest that subjects had difficulty in segregating the intermittent stream composed of 100-ms bursts for the 2-dB difference for noise-band stimuli: the stochastic nature of the signal may have hindered the segregation process to some extent making the percept itself somewhat fuzzy. While this interpretation is coherent with the introspective reports of subjects during the familiarization phase described above, seven of the eight subjects adjusted comparison levels *below* the physical level in conformity with predictions of a subtraction model which presumes a segregation of the sequence into two streams.

Another potential problem is that the alternating-level stimulus context may have induced biases in the level matches. It was therefore necessary to verify that listeners adjust comparison stimuli to levels that are close to the physically presented levels in alternating-level stimuli that do not produce continuity. Further, it was also necessary to estimate the precision with which listeners adjust continuous and intermittent sequences to such alternating sequences and to rule out the possibility that alternating-level sequences affect the matching of loudness more generally.

III. EXPERIMENT 2: DICHOTIC ALTERNATING-LEVEL SEQUENCES

This experiment had two goals: verify the prediction that adjusted levels of comparison sequences are close to physically presented levels when continuity is not heard and test the precision of such matches. A reference stimulus was used that had the same temporal configuration as that of the reference stimulus producing continuity in experiment 1, but which did not itself produce the continuity percept. The breakdown of continuity is obtained by sending the H and L bursts to separate ears.

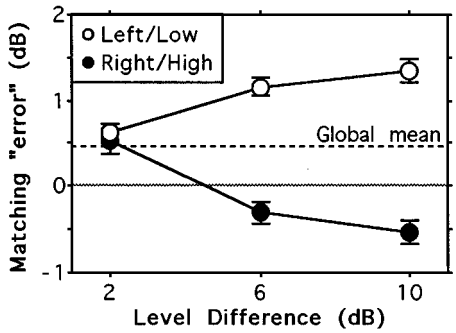

FIG. 4. Summary data for experiment 2. Mean loudness matching ''error'' as a function of H/L level difference for matches to higher-level intermittent sequences in the right ear (Right/High) and lower-level intermittent sequences in the left ear (Left/Low). Vertical bars show ± 1 standard error.

A. Method

H and L bursts were routed to the right and left earphones, respectively. These ear-specific target sequences will be denoted R/H (Right/High) and Le/L (Left/Low). The adjustable comparison stimulus was presented to the target ear and consisted of a series of bursts identical in duration to those of the sequence presented to the same ear in the reference stimulus. At the beginning of the experiment all three level differences were presented to subjects who were asked what they heard. No subject reported a sensation of continuity. Eight subjects reporting no hearing problems were recruited and paid for their participation. Each subject completed five repetitions of the 48 conditions: 2 burst types $\times 4$ duty cycles $\times 3$ H/L level differences $\times 2$ comparison stimulus types (R/H) vs (Le/L).

B. Results

The dependent variable was the ''error'' in adjusted level of the comparison stimulus relative to the physical level presented in the reference stimulus. Mean matching errors are presented in Fig. 4 for each ear as a function of H/L level difference and in Fig. 5 for each ear as a function of duty cycle. The mean errors across burst types, subjects, and repetitions varied from -1.3 to $+2.6$ dB. A repeated-measures ANOVA was performed on factors comparison stimulus type (2), burst type (2), duty cycle (4), level difference (3), and repetitions (5). No difference was found between noise and tone stimuli $[F(1,7)<1]$. The effect of comparison stimulus type was significant $[F(1,7)=14.4,\ p<0.005]$, the global error being -0.1 dB for the R/H sequences and 1 dB for the Le/L sequences. There is a global overestimation of 0.5 dB that was not present in the first experiment for the continuous stream. It may therefore be related to adjusting a simple intermittent sequence to part of an alternating sequence, although Marks (1978) noted a greater sensitivity of the right ear on the order of 1 dB in subjects performing loudness magnitude estimations on binaural stimuli.

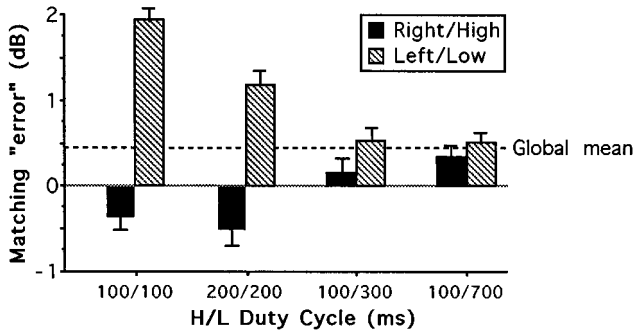

FIG. 5. Summary data for experiment 2. Mean loudness matching ''error'' as a function of duty cycle for matches of Right/High and Left/Low sequences. Vertical bars show $+1$ standard error.

A significant interaction between comparison stimulus type and level difference results from a divergence between matching errors for R/H and Le/L conditions $[F(2,14)=31.8,\ p<0.0001]$ (see Fig. 4): listeners increasingly overestimated the level of the Le/L sequence as the level difference increased and they moved from a slight overestimation of R/H sequences at a 2-dB difference to an equivalent underestimation at a 10-dB difference. This divergence is nearly symmetrical about the global average matching error and suggests a bias in matches to the target sequence in the direction of the level of the nontarget sequence.

A significant interaction was also found between comparison stimulus type and duty cycle $[F(3,21)=23.2,\ p<0.0001]$ (see Fig. 5): matching errors were significantly different from the global average in a positive direction for Le/L conditions and in a negative direction for R/H conditions, but only for the 100/100 and 200/200 duty cycles. So the matching bias in the direction of the nontarget sequence appears to disappear when the duration of the L bursts is at least 300 ms. It seems unlikely that this effect is due to temporal integration of loudness over the first 200 ms of the tone (Zwicker and Fastl, 1990), since the effect is symmetric for duty cycles of similar duration in the two ears.

C. Discussion

The first thing to note about these results is that they are strikingly different from those of experiment 1. On average, matching errors are within 2 dB of the physically presented values at all duty cycles for all level differences. Indeed in this experiment departures from perfect matches are greater for greater H/L level difference, whereas in experiment 1 errors were greater for smaller H/L level difference. It would appear that these results, obtained with stimuli not producing the continuity phenomenon, can be roughly predicted by the classical loudness models.

These results may also reflect biases in matches to intermittent sequences embedded in alternating-level sequences. They suggest that an isolated intermittent sequence is heard globally with a level of about 0.5 dB less than the same sequence embedded in an alternating context. They also suggest that increasing the level difference between the embedded target sequence and the nontarget sequence results in an increasing bias in the direction of the nontarget sequence, amounting to about 1 dB for a 10-dB H/L difference. This effect is more pronounced for stimuli with shorter-duration L bursts. The values found in this experiment, however, are neither big enough nor consistently in a given direction to explain the departure of data for matches to intermittent tar-

gets in experiment 1 from either pressure or power subtraction predictions. Further, the large difference between noise-band stimuli with 100-ms H bursts and those with 200-ms H bursts that was found in experiment 1 is not found in this experiment. It may be that the dichotic presentation made this set of stimuli too different from those in experiment 1 for the biases revealed to be directly comparable to the former conditions.

IV. EXPERIMENT 3: DIOTIC ALTERNATING-LEVEL SEQUENCES WITH INTER-BURST SILENCES

The aims of this experiment were identical to those of experiment 2. However, in this experiment we used diotically presented stimuli similar in structure to those of the main experiment but in which continuity was not heard. Continuity was broken by introducing brief silences between H and L bursts. The prediction was that matches would be close to physically presented levels.

A. Method

Only the 100/300 duty cycle was used. Silences of 30 or 100 ms were introduced to separate the low- and high-level tone bursts. The 30-ms silences were used only with pure-tone stimuli, whereas both pure-tone and noise-band stimuli were tested with 100-ms silences. To focus subjects' attention on the perception of intermittent streams in the reference stimulus, the adjustable comparison stimuli were always intermittent and corresponded identically in temporal structure (300-ms bursts for lower-level and 100-ms bursts for higher-level streams) to the targeted high- or low-level part of the reference stimulus. These comparison stimuli will be denoted Lo/L (long/low) and S/H (short/high). Subjects' verbal reports indicated that 30-ms silences could at times give a weak impression of continuity, but they could also learn not to hear the percept. Van Noorden (1975) had found that with 40-ms pure-tone bursts and silences of 22 ms, the H/L level difference necessary to obtain the continuity effect was over 20 dB, which is well above the maximum level difference employed in this study. For the stimuli with 30-ms silences, some subjects found it difficult to focus on one level at the beginning. To the contrary, the 100-ms silences never gave the continuity percept and presented fewer problems of attentional focus. Three independent groups of subjects were paid for their participation in the experiment. Seven heard pure-tone stimuli with 30-ms silences, eight heard pure-tone stimuli with 100-ms silences, and eight heard noise-band stimuli with 100-ms silences. All reported having normal hearing. Each subject completed five repetitions of the six conditions: 3 H/L level differences $\times 2$ comparison stimulus types (S/H vs Lo/L).

B. Results

The dependent variable was the ''error'' in final adjusted level of the comparison stimulus relative to the physical level presented. Mean matching errors are presented in Fig. 6 for each comparison stimulus type as a function of H/L level difference. The mean matching errors across subjects and repetitions varied from -1.9 to $+1.6$ dB. A mixed ANOVA was performed with independent groups on the combinations of silent-duration and burst-type factors and with repeated measures on factors comparison stimulus type (2), level difference (3), and repetitions (5). There was no difference between the two durations of silence separating H and L bursts [$F(1,20)<1$]. The variability in matches was slightly lower for the 100-ms silences, perhaps due to the better impairment of continuity than was obtained with 30-ms silences. There was a significant interaction of comparison stimulus type, level difference, and burst type [$F(2,40)=16.2$, $p<0.0001$]. For S/H sequences, matching errors were increasingly negative with increased H/L level difference, while the reverse was the case for matches to the Lo/L sequences, mirroring the results from experiment 2. The triple interaction results from the fact that this effect is slightly less marked for pure-tone than for noise-band stimuli (see Fig. 6).

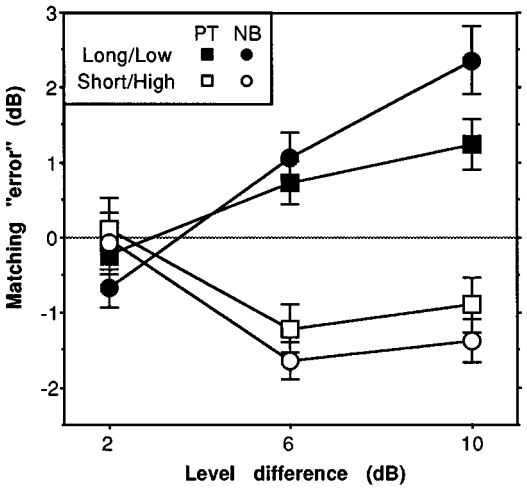

FIG. 6. Summary data for experiment 3. Mean loudness matching ''error'' as a function of H/L level difference for matches to intermittent sequences of higher-level, short-duration bursts (Short/High) or lower-level, long-duration bursts (Long/Low) for both pure-tone (PT: $N=75$) and narrow-band noise stimuli (NB: $N=40$). Vertical bars show ± 1 standard error.

C. Discussion

As for the results of experiment 2, these results are globally consistent with the predictions of classical loudness models. Further, these results also reveal a dependence of adjusted levels on level difference in the alternating sequence. It would seem, therefore, that the context effect of a sequence with alternating levels induces overestimation of lower-level sounds and underestimation of higher-level sounds. This effect is much larger than the small bias found in nonalternating sequences (see experiment 4 below). It is roughly equivalent to that found for dichotic alternating sequences (experiment 2), although the global positive bias in matches present in the latter experiment was not present in the current one, suggesting the previous result may have its origins in the dichotic presentation. Similarly to experiment 2, the matching biases found here are insufficient to explain the departures from pressure or power predictions for inter-

mittent streams in experiment 1, particularly concerning the large difference between pure-tone and noise-band stimuli found in the latter experiment.

V. EXPERIMENT 4: DIOTIC FIXED-LEVEL STIMULI

The goal of this control experiment was to verify whether the intermittence of the reference or comparison stimuli systematically influenced matching errors for either continuous or intermittent sequences.

A. Method

Two types of diotically presented stimuli were used that resemble those in Fig. 1(b): a continuous (CONT) sound and an intermittent (INT) sequence composed of seven sounds having the duration of *H* bursts separated by silences having the duration of *L* bursts. Comparison stimuli were adjusted to match the level of reference stimuli of the same type (INT or CONT).[4] For INT conditions, both pure-tone and noise-band stimuli with four duty cycles were employed. For CONT conditions, four sequence durations were used that corresponded to the total sequence duration for each duty cycle. Eight subjects, all of whom reported having normal hearing, were paid to participate in the study. Each subject completed five repetitions of the 16 conditions: 2 burst types $\times 4$ duty cycles $\times 2$ stimulus types.

B. Results and discussion

The matching precision was good with mean matching errors across burst types, subjects, and repetitions varying from -0.4 to 0.5 dB for INT conditions and from 0.0 to 0.3 dB for CONT conditions. Separate repeated-measures ANOVAs were performed for INT and CONT stimuli on factors burst type (2), duty cycle (4), and repetitions (5). Note that duty cycle corresponds simply to a difference in stimulus duration for CONT stimuli. The only significant effect in both analyses was for the duty cycle factor in INT stimuli [$F(3,21)=4.1$, $p<0.05$]. Matching errors for all duty cycles were positive except for 100/700. However, only one of these mean matching errors was significantly different from zero by single-sample *t*-tests adjusted for multiple tests. This condition was INT 100/100 for which subjects overestimated the level by about 0.5 dB [$t(79)=3.61$, corrected $p<0.005$]. In general therefore, listeners are quite precise at adjusting both continuous and intermittent sequences, mean matching errors being well within the differential threshold for intensity (Luce and Green, 1974). The differences between adjusted levels and power and pressure predictions in experiment 1 would not appear to be attributable to imprecise level matching between intermittent sequences.

VI. GENERAL DISCUSSION

The data presented above demonstrate that the perceived loudness of an auditory event depends on the way the event sequence is organized perceptually. In the case of an alternating-level sequence perceived as a sequence of intermittent events imposed on a continuous sound, the level of the continuous sound is heard as being equal to the physical level of the lower-level bursts. Level matches of a continuous comparison sound to the continuous stream of the reference stimulus are within 0.4 dB of the physical level and are unaffected by the level difference in the alternating-level context (experiment 1). Indeed, a comparable degree of precision is found for matches to a fixed-level continuous sound (experiment 4). However, matches to the intermittent part of the percept are far below the physical levels presented and are clearly consistent with some kind of subtractive process. The pattern of the data in the present study confirms and extends that of Warren *et al.* (1994) and suggests that the higher-level part of the signal is processed by the auditory system as if it were composed of two parts, each with its own share of the neural input corresponding to the incident energy of the stimulus sequence.[5] Loudness matches fall between values predicted by subtraction based on acoustic pressure and acoustic power. They are very different from computations based on loudness as represented in sone units. The results are thus consistent with the hypothesis that auditory organization takes place prior to loudness computation and that the auditory sensory representation of level at this stage of processing is close to the physical stimulus. For small differences between higher and lower levels, loudness matches also depend both on the relative durations of the *H* and *L* bursts and on the spectral content of the signal. The means for most conditions are nearer the predictions based on pressure with the exception of small *H*/*L* level differences for noise-band stimuli with short-duration *H* bursts.

When the continuity of such an alternating-level sequence is broken by routing alternate events to separate ears (experiment 2) or by introducing a silence between successive events (experiment 3), mean matches are much closer to the physically presented values and are even at times greater than these values, a situation *never* found when continuity was heard. With the stimuli of experiments 2 and 3, a dependence of the matches to the lower-level bursts on the level difference is found: as the level difference increases, the level of these bursts is progressively overestimated, i.e., in the direction of the higher-level bursts. This overestimation attains about 1–2 dB on average for a level difference of 10 dB. Clearly the matching of loudness in the two cases is influenced by the perceptual context, and these kinds of matching biases are similar to what Poulton (1989) has characterized as ''centering tendencies'' in psychophysical judgment strategies. However, the pattern of results is completely different from that found when the sequence is organized into two streams. In the former case, matches are consistent with classical loudness models (plus judgment biases) whereas in the latter case they are consistent with a subtraction model.

These results are not consistent with effects related to temporal integration, loudness enhancement, loudness adaptation or the ''recalibration'' of sensory input. We can rule out loudness summation as the origin of these effects (Zwicker *et al.*, 1957) since stimuli were confined to a single critical band. We can also rule out loudness adaptation (Botte *et al.*, 1982) as the stimulus sequences were not long enough in duration. Further, it is hard to imagine how loudness enhancement (Zwislocki and Sokolich, 1974) might be playing a role in these stimuli even it if can be considered to

generalize to alternating levels: there is clearly no enhancement of the lower-level bursts, the level of the continuous stream being adjusted very near the physical level. However, one might imagine that the loudness of the low-level intermittent stream could be enhanced by a louder continuous stream. This relation is predicted by pressure and power subtraction for the 2-dB H/L level difference, but adjusted levels appear to be very sensitive to both the waveform and the duration of intermittent bursts. It is unclear how loudness enhancement could account for these latter results. Finally, the ''slippery context effect'' or ''recalibration'' of loudness described by Marks and Warner (1991) and Marks (1994), respectively, do not explain these data either. In those studies, the loudness of a soft pure tone could be increased when presented within the context of trials containing relatively higher-level tones at another frequency. First, this effect completely disappears when the tones are of the same frequency (Marks, 1994), and second, the loudness of the higher-level tone is unaffected by the context, while that of the lower-level tone is increased. Their results are thus quite the opposite of ours and most likely reflect a completely different level of the loudness computation mechanism.

A comparison of these data with those obtained in similar sequences that do not produce auditory continuity (experiments 2 and 3) demonstrates that while the alternating context induces matching biases (the bigger the level difference, the greater the compensation of the match in the direction of the nontargeted part of the sequence), this kind of compensation is not at all found for the lower-level continuous stimuli in experiment 1 and the matching ''errors'' for intermittent stimuli are much larger. Further, the pattern of bias is very different in experiments 2 and 3 compared with the deviations from the physical levels in experiment 1. The largest deviations are found for small alternating level differences in experiment 1 and for large differences in experiments 2 and 3. Also, the biases exist for both L and H bursts (in opposite directions) in experiments 2 and 3, while no appreciable deviation is found for the lower-level continuous stimuli in experiment 1. Therefore, we may conclude that the divergence from physical levels in experiment 1 cannot be explained simply by biases induced by the alternating-level context. The results are consistent with a subtractive process based on the perceptual interpretation that H bursts are composed of the continuation of L bursts and an additional superimposed burst.

There remains the problem of determining the nature of the subtraction process which seems to correspond to neither pressure nor power computations. It is possible that the nature of the task may be responsible for these deviations in experiment 1. On a given trial, the listener is asked to focus either on the continuous sound or on the intermittent sequence and to estimate the loudness in order to match it with a comparison stimulus. This focusing may create an imprecise partitioning of the stimulus energy which is mixed together in the same auditory channels since the two streams are spectrally identical. If a pressure subtraction law is used, one could imagine that the focusing process results in too much energy being assigned to the attended stream, which would lead to an overestimation of the levels. The data suggest that if this is the case, a greater difference between the alternating levels results in smaller errors in estimation. They further suggest that for short-duration stimuli with uncertain levels (as is the case with the 100-ms H bursts of narrowband noise), the overestimation is exaggerated for very small level differences. The question of a possible influence of temporal structure (as well as of experimental instructions) on perceived continuity will be addressed in a subsequent paper (Drake and McAdams, submitted).

If, on the other hand, the auditory system uses power computation, the focusing process would have to result in too little energy being assigned to the target stream. This error would be greatest at small level differences for pure tones and noise bands with longer-duration H bursts, but would be smallest at the same level difference for short-duration H bursts. For larger level differences, the error would be constant for all stimuli tested.

It is important to recall that in the everyday world, pressure calculations would only be appropriate for signals added in coherent phase (an unlikely occurrence) while power calculations would be appropriate for independent signals, the phases of which are unknown. While the stimuli in our experiments were added in coherent phase, Warren *et al.* (1994) demonstrated that randomizing the phase relations between successive bursts had no appreciable effect on the data.

Another possibility is that the auditory system is no more precise than it has to be to get the job done correctly.[6] There may be an inherent ambiguity in the partitioning process, since it is rarely possible on the basis of locally available sensory information to determine the exact properties of the signals that compose a mixture. In more realistic situations than the repetitive alternation between two levels used here, there would normally be separate instants where the ''old'' signal is present alone, the ''new'' signal is present alone, and both signals are mixed. If a significant proportion of the ''old'' signal can be removed at an instant of mixture, the resulting rough estimate of the intensity of the ''new'' one could be corrected by estimates obtained either at earlier or at later instants when it was present by itself. The conjunction of a number of estimates at different instants could lead to a reasonably, although not perfectly, accurate conclusion concerning this property of the target source. This was clearly the case in our study as evidenced by the precise matches to the continuous stream in experiment 1.

VII. CONCLUSIONS

(1) A process akin to the ''old-plus-new'' strategy (Bregman, 1990) seems to operate on alternating-level homophonic sequences. This process subtracts from an interrupting high-level sound the part that is perceptually assigned to another sound perceived to continue through it. The level of the residue thus depends on the level difference between the higher-level sound and the lower-level sound. This result is in contradistinction to predictions by classical loudness models (e.g., Zwicker, 1977) that do not take auditory organization processes into account, or by models that postulate a selection of information on the basis of some kind of mental schema (Repp, 1992) in which the restored

part of the continuous sound is not subtracted from the mixture. However, the law by which the loudness *is* partitioned does not correspond across all conditions to either pressure or power subtraction and is very different from predictions based on loudness subtraction in sone units. The same law would appear to operate on pure tone and narrow-band noise stimuli for larger differences between lower- and higher-level bursts. Observed effects due to the duty cycle of the alternation for noise-band stimuli do not seem to be attributable to the uncertainty in estimation of loudness of short-duration narrow-band noise bursts nor to effects of loudness enhancement.

(2) Loudness matches to fixed-level continuous and intermittent stimuli are very accurate when reference and comparison stimuli have the same temporal structure.

(3) For alternating sequences in which continuity is not heard (dichotically presented sequences or sequences with intervening silences), the level of the softer, intermittent stream is overestimated by an amount that increases with the level difference between higher and lower levels. The reverse was true of the louder stream, suggesting that matching biases are made in the direction of the level of the nontarget stream. Aside from these small matching biases, matches are consistent with predictions of classical loudness models, suggesting that such models are most appropriate for situations in which sound sequences are perceptually organized into a single stream.

(4) The loudness matching biases found in conditions where continuity was not perceived do not explain the deviations measured in the continuity conditions. It is likely that a process akin to the old-plus-new subtraction strategy is employed, though the task used, which requires the listener to focus on a targeted part of the stimulus sequence, may affect the perceived loudness. On the other hand, the auditory system may not need to be more precise in its loudness computations to deal appropriately with real-world situations.

ACKNOWLEDGMENTS

This research was funded in part by a grant from the French Ministry of the Environment to Marie-Claire Botte shortly before her untimely death. François Banide, Xavier Durot, and Sophie Savel helped run subjects and Anne-Marie Argenti helped with DSP programming. Neil Todd suggested the duty cycle conditions. Albert Bregman, Bertram Scharf, Richard Warren, and one anonymous reviewer made thought provoking comments on an earlier version of the manuscript.

[1]The classical approach to loudness has of course investigated the perception of loudness of individual components of complex signals, such as pure tones in noise (Zwicker and Fastl, 1990), but the models currently published in the literature do not segregate the signal into pure-tone and noise components and then perform the loudness calculation on the separate components. The experimenter has to know where to focus on the model output to perform the appropriate calculations. Further, these results do not generalize to temporally varying signals of constant spectral content, which is the case being considered here.

[2]Other linear effects in loudness have also been investigated. Most notably, the difference in loudness between monaural and binaural presentation can for the most part be explained by a linear summation of the individual loudnesses in sone units of the signals at the two ears (Marks, 1979; Scharf, 1969; Scharf and Fishken, 1970).

[3]Degrees of freedom for the F-statistic are adjusted where necessary with the Geisser–Greenhouse epsilon to compensate for inherent correlation among repeated factors.

[4]All four combinations of intermittent and continuous reference and comparison stimuli were presented to subjects. Only the same-type pairs are reported here as they are the only ones cogent to this study.

[5]It should be noted that subjects' reports of qualitative differences between the intermittent comparison stimulus and the intermittent stream in the reference sequence, in both the present study and in Warren *et al.*'s study, cannot be accounted for by a simple subtraction of stimulus level and may reflect a more complex partitioning of the neural response as suggested by Warren *et al.* (1994).

[6]We are grateful to Albert Bregman for pointing out this ecologically pragmatic possibility to us.

Botte, M.-C., Canévet, G., and Scharf, B. (**1982**). ''Loudness adaptation induced by an intermittent tone,'' J. Acoust. Soc. Am. **72**, 727–739.

Bregman, A. S. (**1990**). *Auditory Scene Analysis: The Perceptual Organization of Sound* (MIT, Cambridge, MA).

Bregman, A. S., and Rousseau, L. (**1991**). ''Auditory intensity changes can cue perception of transformation, accompaniment or replacement.,'' Bull. Psychonom. Soc. **29**, 476 (A).

Ciocca, V., and Bregman, A. S. (**1987**). ''Perceived continuity of gliding and steady-state tones through interrupting noise,'' Percept. Psychophys. **42**, 476–484.

Darwin, C. J. (**1995**). ''Perceiving vowels in the presence of another sound: a quantitative test of the ''old-plus-new'' heuristic,'' in *Levels in Speech Communication: Relations and Interactions*, edited by C. Sorin, J. Mariani, H. Meloni, and J. Schoentgen (Elsevier, Amsterdam), pp. 1–12.

Drake, C., and McAdams, S. (**submitted**). ''The continuity illusion: Role of temporal sequence structure.''

Houtgast, T. (**1972**). ''Psychophysical evidence of lateral inhibition in hearing,'' J. Acoust. Soc. Am. **51**, 1885–1894.

Luce, R. D., and Green, D. M. (**1974**). ''Neural coding and psychophysical discrimination data,'' J. Acoust. Soc. Am. **56**, 1554–1564.

Marks, L. E. (**1978**). ''Binaural summation of the loudness of pure tones,'' J. Acoust. Soc. Am. **64**, 107–113.

Marks, L. E. (**1979**). ''A theory of loudness and loudness judgments,'' Psychol. Rev. **86**, 256–285.

Marks, L. E. (**1994**). ''''Recalibrating'' the auditory system: The perception of loudness,'' J. Exp. Psychol. **20**, 382–396.

Marks, L. E., and Warner, E. (**1991**). ''Slippery context effect and critical bands,'' J. Exp. Psychol. **17**, 986–996.

McAdams, S., Botte, M.-C., and Drake, C. (**1994a**), ''Le phénomène de la continuité auditive et la répartition de la sonie entre flux auditifs,'' J. Physique **4**(C5), 383–386.

McAdams, S., Botte, M.-C., Banide, F., Durot, X., and Drake, C. (**1994b**). ''The computation of loudness in the auditory continuity phenomenon,'' ATR Workshop on ''A Biological Framework for Speech Perception and Production,'' Kyoto, ATR Technical Report TR-H-121, pp. 81–86.

Poulton, E. C. (**1989**). *Bias in Quantifying Judgments* (Erlbaum, Hillsdale, NJ).

Repp, B. H. (**1992**). ''Perceptual restoration of a missing speech sound: Auditory induction or illusion?,'' Percept. Psychophys. **51**, 14–32.

Scharf, B. (**1969**). ''Dichotic summation of loudness,'' J. Acoust. Soc. Am. **45**, 1193–1205.

Scharf, B., and Fishken, D. (**1970**). ''Binaural summation of loudness reconsidered,'' J. Exp. Psychol. **86**, 374–379.

Scharf, B. (**1978**). ''Loudness,'' in *Handbook of Perception*, Vol. 4: Hearing, edited by E. C. Carterette and M. P. Friedman (Academic, New York), pp. 187–242.

Stevens, S. S. (**1957**). ''Concerning the form of the loudness function,'' J. Acoust. Soc. Am. **29**, 603–606.

Thurlow, W. R. (**1957**). ''An auditory figure-ground effect,'' Am. J. Psychol. **70**, 653–654.

Thurlow, W. R., and Elfner, L. F. (**1959**). ''Continuity effects with alternately sounding tones,'' J. Acoust. Soc. Am. **31**, 1337–1339.

van Noorden, L. P. A. S. (**1975**). ''Temporal coherence in the perception of tone sequences,'' unpublished doctoral thesis, Eindhoven University of Technology.

van Noorden, L. P. A. S. (**1977**). ''Minimum differences of level and frequency for perceptual fission of tone sequences ABAB,'' J. Acoust. Soc. Am. **61**, 1041–1045.

Verschuure, J., Rodenburg, M., and Maas, A. J. J. (**1976**). ''Presentation conditions of the pulsation threshold method,'' Acustica **35**, 47–54.
Warren, R. M. (**1982**). *Auditory Perception: A New Synthesis* (Pergamon, New York).
Warren, R. M. (**1984**). ''Perceptual restoration of obliterated sounds,'' Psychol. Bull. **96**, 371–383.
Warren, R. M., Bashford, J. A., Healy, E. W., and Brubaker, B. S. (**1994**). ''Auditory induction: Reciprocal changes in alternating sounds,'' Percept. Psychophys. **55**, 313–322.
Warren, R. M., Obusek, C. J., and Ackroff, J. M. (**1972**). ''Auditory induction: Perceptual synthesis of absent sounds,'' Science **176**, 1149–1151.
Zwicker, E. (**1960**). ''Ein Verfahren zu Berechnung der Lautstärke,'' Acustica **10**, 304–308.
Zwicker, E. (**1977**). ''Procedure for calculating loudness of temporally variable sounds,'' J. Acoust. Soc. Am. **62**, 675–682.
Zwicker, E., and Fastl, H. (**1990**). *Psychoacoustics: Facts and Models* (Springer-Verlag, Berlin).
Zwicker, E., and Feldtkeller, R. (**1967**). *Das Ohr als Nachrichtenempfänger* (S. Hirzel Verlag, Stuttgart).
Zwicker, E., Flottorp, G., and Stevens, S. S. (**1957**). ''Critical band width in loudness summation,'' J. Acoust. Soc. Am. **29**, 548–557.
Zwicker, E., and Scharf, B. (**1965**). ''A theory of loudness summation,'' Psychol. Rev. **72**, 3–26.
Zwislocki, J. (**1960**). ''Theory of temporal auditory summation,'' J. Acoust. Soc. Am. **32**, 1046–1060.
Zwislocki, J., and Sokolich, W. G. (**1974**). ''On loudness enhancement of a tone burst by a preceding tone burst,'' Percept. Psychophys. **16**, 87–90.

Change in envelope beats as a possible cue in comodulation masking release (CMR)

Emily Buss, Joseph W. Hall III, and John H. Grose
Department of Surgery, Division of Otolaryngology, University of North Carolina, Chapel Hill, North Carolina 27599-7070

(Received 3 February 1997; accepted for publication 25 September 1997)

The detection advantage associated with masker envelope coherence across frequency has typically been described in terms of comparisons of information across auditory channels. More recently it has been suggested that analysis of the output of a wider initial filter, similar to that suggested for the TMTF, can account for the data [B. G. Berg, J. Acoust. Soc. Am. **100**, 1013–1023 (1996)]. This approach suggests that a change in envelope beats could serve as the cue to the addition of a pure-tone signal. Data are presented here for the detection of a tone added to multiple maskers with coherent envelopes. In one condition a change in envelope beats was an accurate potential cue, whereas in others the change was too unreliable to serve as an indicator of the presence of the signal. All conditions employing maskers with coherent envelopes produced very similar thresholds, and all showed improved sensitivity over the case of detecting a signal added to a single masker centered on the signal frequency. Results are interpreted as evidence that a change in envelope beats does not form the basis of detection in CMR.
[S0001-4966(98)01903-1]

PACS numbers: 43.66.Dc [WJ]

INTRODUCTION

Comodulation masking release (CMR) is the detection advantage associated with maskers that have a coherent pattern of amplitude modulation across frequency. This coherence of amplitude modulation, or comodulation, of maskers at the signal frequency and at frequencies distant from the signal tends to improve sensitivity for detection of an added pure tone. The typical finding is that thresholds in the case of a single narrow-band masker centered on the signal decrease with the addition of comodulated maskers up to an octave away from the signal frequency, while addition of noncomodulated maskers increases thresholds slightly (e.g., Moore *et al.*, 1990).

The basis of CMR is typically described as an across-channel, envelope-based process. In fact, some care is usually taken to prevent within-channel cues from contributing to detection so that ''true CMR'' (Schooneveldt and Moore, 1987), an across-channel phenomenon, can be more directly examined. The types of models that have been proposed to account for CMR can be broadly characterized as falling into two categories: envelope comparisons across frequency and cued listening. Envelope comparison models are based on the observation that the addition of a signal to one of several comodulated masker bands decreases the coherence of amplitude modulation (AM) for those bands. Specific detection cues of this type that have been proposed include envelope correlation (Richards, 1987) and differencing of normalized envelopes (Buus, 1985; Hall, 1986). Cued listening models (Buus, 1985), on the other hand, are based on the observation that the signal-to-noise ratio at the signal frequency is best during the masker modulation minima. If maskers are comodulated across frequency, the auditory system could potentially use modulation minima of the maskers distant from the signal to cue listening at the signal frequency. This cueing would lead to an improved signal-to-noise ratio in the ''samples'' for stimuli with coherent AM.

Both the envelope comparison and the cued listening models take as a starting point the idea that the envelopes of the central and flanking maskers (i.e., the masker centered on the signal and those at flanking frequencies) are represented separately in the auditory system, as in different frequency channels. The study of CMR has often been motivated by the desire to characterize the (assumed) across-channel process occurring after auditory filtering. More recently, Berg (1996) has challenged this assumption by proposing a model that accounts for the basic phenomenon of CMR by dispensing with the initial stage of auditory filtering and the subsequent across-channel comparisons. According to this model, described in terms of the output of a leaky integrator, the characteristics of the amplitude spectrum of the envelope of the summed waveform falling within a relatively wide predetection band (e.g., as proposed to account for modulation detection threshold data; Viemeister, 1979) serve as the basis for detection. In order to arrive at these characteristics, multiple samples of the stimulus are amassed and their envelopes extracted via half-wave rectification and low-pass filtering. These envelopes are then subjected to a Fourier analysis, the results of which are assessed for correlates with the presence of a signal. Those characteristics of the envelope amplitude spectrum which are predictive then form the cue for detection. In simulations of the leaky integrator output, Berg (1996) pointed out that one particular aspect of the envelope amplitude spectrum that could cue the presence of a signal was related to the frequency separation between masker bands: The signal-absent case is characterized by a more pronounced peak in envelope energy at the beat frequency.

The example given in Berg's paper consists of two masker bands separated in frequency by 100 Hz. These

maskers are comprised of two sets of tones, either with the same starting phases for analogous tones in the two bands (producing coherent AM), or with different randomly selected starting phases for analogous tones in the two bands (producing incoherent AM). In the case of coherent AM, the average envelope amplitude spectrum is dominated by beats at the frequency of masker separation (in this example 100 Hz, the separation of the pairs of tones with a shared starting phase). The addition of a signal reduces the prominence of this beating, and this relative reduction in energy at the beat frequency is proposed as a possible cue to detection. In the case of incoherent AM, no such stable peak at the frequency of masker separation is present even in the absence of the signal, so change in the relative amount of envelope energy at the beat frequency does not form such a reliable cue for the signal.

The top two panels of Fig. 1 illustrate those aspects of the envelope amplitude spectrum which differ reliably between signal-present and signal-absent cases.[1] The maskers used to produce these plots were 40 Hz wide, computed as the sum of seven equal amplitude tones, and the envelope of each masker was controlled via the starting phase of each component tone. One masker was centered at 900 and the other at 1000 Hz, and the signal-present case included a 10-dB increment in level of the masker component at 1000 Hz. Each panel shows the mean-to-sigma ratio ($n=2000$) of the first 200 Hz of the envelope amplitude spectrum for the signal-present (dotted line) and the signal-absent (solid line) cases. A large value reflects consistency in the amplitudes obtained for that point, indicating a frequency that could potentially be used as a reliable cue to the identity of the stimulus (provided it differentiates the signal-present from the signal-absent cases). The first panel shows the results for the case of two maskers with perfectly coherent AM, with the starting phases for the component tones in the two maskers chosen anew on each ''trial.'' The salient peak at 100 Hz in the signal-absent case represents the envelope beats at the frequency of masker separation. These beats arise because components 1–7 of the two maskers share a common starting phase and are all separated by 100 Hz, so the seven sets of tones all beat in phase and at the same frequency, resulting in the beat pattern in the summed waveform. The second panel shows the results for maskers with incoherent AM, but that are otherwise identical to the previous case. (Notice the reduced range of ordinate values.) There is no peak at 100 Hz in this case. This is because starting phase of the component tones of the two bands are randomly assigned so that the pairs of tones separated by any given interval do not necessarily beat in phase. Despite the lack of a peak, the functions are not identical in the signal-present and signal-absent cases, and these (less distinctive) differences could be hypothesized to support detection, although with lower sensitivity.[2]

The reduction of envelope beats as a detection cue in CMR successfully addresses some aspects of monaural CMR: the basis for improved sensitivity in the presence of maskers with coherent AM, the deleterious effect of increased frequency separation between maskers eliciting CMR (e.g., Cohen and Schubert, 1987), and the disruptive

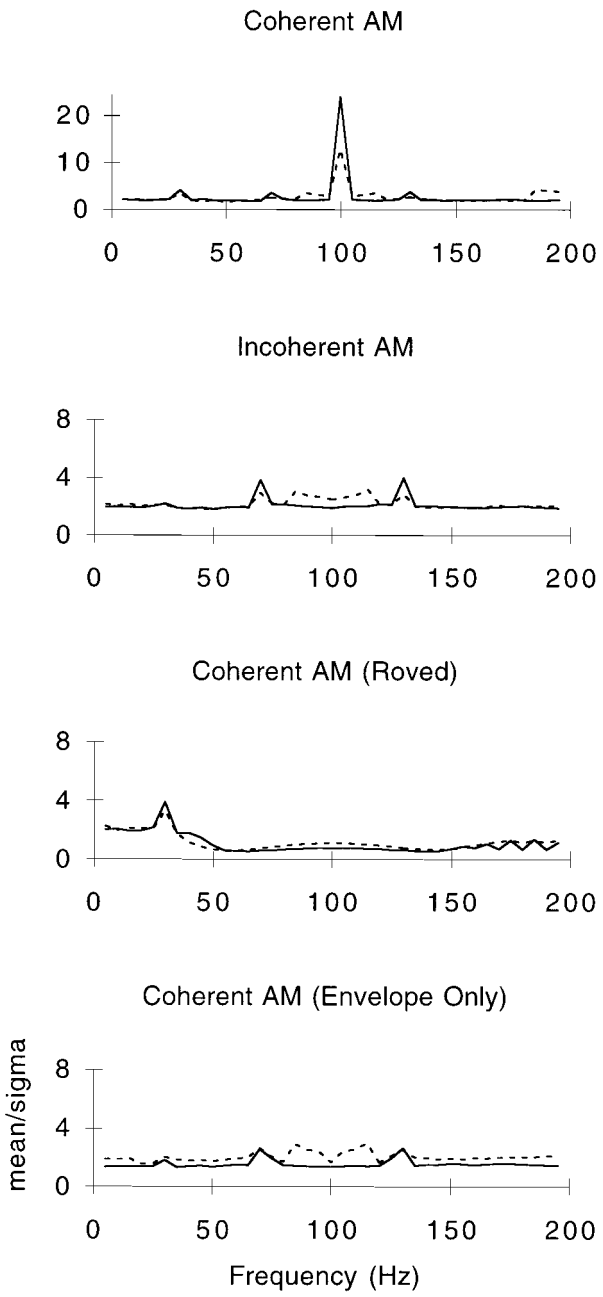

FIG. 1. Characteristics of the amplitude spectrum of the envelope for four conditions: The envelopes for 2000 maskers were generated separately for the signal-absent and signal-present stimuli. The mean-to-sigma ratio for the first 200 points of the amplitude spectrum of the envelope is plotted as a function of frequency (in Hz). The solid lines show results for the signal-absent cases, dotted lines for the signal-present cases. Stimuli used to generate panel 1 consist of two maskers (40 Hz wide, centered at 900 and 1000 Hz) with coherent AM and a signal consisting of a 10-dB increment in the masker component at 1000 Hz. Stimuli used to generate panel 2 consist of two maskers which lack coherent AM, but are otherwise identical to those from panel 1. Panel 3 shows results for two maskers with coherent AM, the one centered on the signal frequency (1000 Hz) and the other roved in frequency over a range of 50 Hz (875–925 Hz). Panel 4 was generated using stimuli identical to those from panel 1 except that the phases of the masker components were assigned so as to reduce envelope beat regularity (while maintaining coherence of AM).

effects of the addition of a pure tone distant in frequency from the signal (Berg, 1996). There are several issues that are not as clearly addressed, however. For example, as pointed out by Berg (1996), envelope beats are not present as

a reliable cue for wide-band AM noise maskers, a stimulus configuration for which robust CMRs can be obtained (e.g., Hall *et al.*, 1984). It is also not obvious how this cue would predict improved performance with increasing numbers of perfectly comodulated masker bands separated in frequency, more maskers leading to a peak at the beat frequency that is more consistent and less susceptible to disruption by the addition of the signal. These examples suggest that the reduction of envelope beats might be an insufficient cue for modeling observer performance across the range of stimuli for which CMR is observed. That is not to say that Berg's leaky integrator model would not exploit some other predictive correlate of the presence of the signal based on the amplitude spectrum of the envelope for those stimuli.

The question of interest is whether the auditory system can make use of a reduction in envelope beats in cases where this change could reliably cue the presence of the signal. The data discussed below are based on stimuli for which envelope beats either do or do not serve as a reliable cue to the presence of a signal, but which are otherwise as similar as possible (e.g., narrow-band maskers separated in frequency). By comparing results of conditions with and without the potential cue of change in envelope beats, we attempted to test whether this cue is employed when it is present.

If CMR is based on reduction of energy at the beat frequency of the masker envelopes, identified via examination of many samples of the stimulus, then a rove of the flanking masker frequency should interfere dramatically with detection as compared to the more commonly used condition of fixed flanking masker frequency. Masker frequency rove would introduce substantial variability in the average amplitude spectrum of the stimulus envelope across trials, resulting in a greatly reduced (or absent) peak at the (average) frequency of masker separation. Panel 3 of Fig. 1 illustrates this effect. This panel shows the mean-to-sigma ratios for the amplitude spectra of envelopes of signal-absent (solid line) and signal-present (dotted line) stimuli. The stimuli were similar to those used in creating panel 1 except that the low frequency masker took on a new center frequency for each ''trial,'' chosen from a uniform distribution 50 Hz wide and centered on 900 Hz (center frequencies ranging from 875 to 925 Hz). As in the case of incoherent AM (Fig. 1, panel 2), there is no peak at the frequency of the (average) masker separation in the signal-absent case. The amplitude spectra of the envelopes in the case of roving flanking masker frequency do appear to differ reliably, providing a potential cue for Berg's leaky integrator model, but the nature of that difference is quite dissimilar from the case of coherent AM with fixed flanking masker frequency (Fig. 1, panel 1).

While the detection strategy of Berg's leaky integrator model (and the plots in Fig. 1) are based on the reliable properties of a particular component in the long-term envelope amplitude spectrum across many samples of the stimulus, it is also possible that a change in envelope beats could be used in signal detection on an interval-by-interval basis. For example, the amplitude spectrum of the envelope in a single sample of a signal-absent stimulus tends to have a peak at the beat frequency, whereas the amplitude spectrum of the envelope for the signal-present case tends to be less elevated at the beat frequency. If the beat frequency is identified on an interval-by-interval basis, then roving flanking masker frequency would not necessarily be expected to interfere substantially with detection. The amplitude spectrum of the envelope of the signal-absent stimulus would tend to contain a pronounced peak at the frequency of separation chosen for that particular interval. The amplitude spectrum of the envelope of the signal-present stimulus would tend to contain a smaller peak at the frequency separation chosen for that interval. The detection decision, then, could be based on the size of the largest peak across a range of possible beat frequencies, a large peak reflecting a regular beat pattern in the signal-absent case.

It is possible to generate masker bands with identical envelopes that do not exhibit a regular beat pattern when summed via assignment of magnitude and phase to the component tones (e.g., Richards, 1988). For this illustration, component tones 1–7 were equal amplitude and with starting phases in band 2 assigned as negative one times the starting phase of the mirror image component in band 1. In this way pairs of tones separated by a constant interval in frequency did not beat in phase, a fact reflected in the relative lack of beats in the summed waveform. If the regularity of envelope beats within a signal-absent interval forms the detection cue, then this type of coherently modulated masker lacking a regular beat pattern should not produce a CMR. The bottom panel of Fig. 1 shows the mean-to-sigma ratio for this type of stimulus. The plot of mean-to-sigma ratio for this type of stimulus resembles the graph based on stimuli with incoherent AM (panel 2). While this plot is based on many samples of the stimulus, it should be noted that the cue being examined is the relative reduction in energy at the beat frequency associated with a particular sample of the stimulus, not the average beat frequency across samples. One way to quantify the regularity of envelope beats is to ask how much energy is present in the most prominent peak of the envelope amplitude spectrum in the frequency region where envelope beats might occur. Based on the signal-absent stimuli used to produce Fig. 1, the largest peak between 50 and 150 Hz for any single sample of the stimuli with irregular beats is on average approximately 55% of that for the fixed-frequency, coherent AM condition. If beat regularity within interval is the basis for detection, then the stimulus with coherent AM and irregular beats should be associated with a greatly reduced CMR.

The data presented below suggest that envelope beats do not underlie detection of a tone added to maskers with coherent AM. Roving flanking masker frequency failed to increase thresholds either with sinusoidally amplitude modulated (SAM) maskers or with narrow-band noise maskers. The coherently modulated maskers with irregular beats, a manipulation employing narrow-band noise maskers, also failed to disrupt CMR. Poor performance in a condition employing pure-tone flanking maskers and a SAM central masker confirmed that the detection advantage observed for the inclusion of flanking maskers with coherent AM can be attributed to the coherence of envelopes rather than a profile-type cue based on long-term amplitude spectra (Fantini and Moore, 1994; Green, 1988).

I. STIMULI

The signal was a 100-ms tone burst at 1 kHz and temporally centered in a 600-ms masker (onset occurring 250 ms after masker onset and offset occurring 250 ms before masker offset). For SAM maskers, this positioning centered the signal in a masker modulation minimum. The signal was gated with a 50-ms $\cos^2$ rise-fall time and was added in phase to the masker component at 1 kHz.

There were three basic masker conditions for both the SAM and the narrow-band noise masker stimuli. All of the SAM masker conditions included a SAM tone centered on the signal frequency (1 kHz) with a modulation rate of 10 Hz and a $-\cos$ starting phase. The condition employing just this masker will be referred to as the narrow-band (NB) condition. In a second condition the SAM tone at 1 kHz was accompanied by SAM tones at 500, 700, 1300, and 1500 Hz that were also SAM at 10 Hz, with a $-\cos$ starting phase. This condition will be referred to as the fixed-comodulation (f−CO) condition, as all maskers were comodulated and had fixed flanking masker center frequencies. A third condition consisted of the SAM tone at 1 kHz and four additional comodulated SAM maskers, each with a center frequency chosen randomly from a uniform distribution for each presentation of the stimulus. In order to reduce the possibility of within-channel effects, the range of frequencies that a flanking masker could take on was restricted to ± 25 Hz from the frequency of the analogous masker in the f-CO condition (e.g., 500 ± 25 Hz for the lowest frequency masker).[3] This condition will be referred to as the roved-comodulation (r-CO) condition, reflecting the fact that the center frequencies for the four comodulated SAM flanking maskers were roved. Limited data were also collected in a fourth condition, which included a SAM tone masker at 1 kHz and four unmodulated pure tones at 500, 700, 1300, and 1500 Hz, gated on and off with 50-ms $\cos^2$ ramps and scaled to have power equal to the SAM tones present in the other conditions. This condition will be referred to as the pure-tone (TONE) condition.

Conditions analogous to the three basic SAM conditions were also completed with 12-Hz-wide narrow-band maskers, which had an approximate equivalent average rate of modulation of 8 Hz (Rice, 1953). A band consisted of a set of five pure tones all with equal amplitude, spaced at intervals of 2.44 Hz (as dictated by the sampling rate and FFT buffer size), and each tone had a randomly chosen starting phase. A new set of starting phases was chosen at the beginning of each stimulus presentation, and coherence of AM across frequency was achieved by assigning the same set of starting phases for the tones comprising each band. As with the SAM maskers, all narrow-band noise masker conditions included one masker centered on the signal frequency (1 kHz). The NB condition consisted of just this masker. The f-CO condition included comodulated maskers centered at 500, 700, 1300, and 1500 Hz, with the starting phases of the analogous component tones in each band being identical for all maskers. The r-CO condition consisted of the narrow-band masker centered on 1 kHz and four additional maskers with roved center frequency, chosen from a uniform distribution ± 25 Hz the frequency of the analogous masker in the f-CO condition. As in the f-CO condition, the starting phases of the component tones 1–5 were identical for all maskers. Finally, the envelope-only (ENV-ONLY) condition was identical to the f-CO condition in all respects except in the manner that the starting phases of the component tones of the central masker were assigned. Starting phases for each tone of this masker were negative one times the phase of the analogous mirror image component of a flanking masker (cf., Richards, 1988). This produces bands with coherent AM but reduced beat regularity in the summed waveform (Richards, 1990). All maskers were gated on and off with 50-ms $\cos^2$ rise-fall times.

All stimuli were digitally computed (AP2, TDT), presented at 10 kHz via a DAC (DD1, TDT), low-pass filtered at 3 kHz (Kemo, 85 dB/oct), attenuated (PA4, TDT) and presented diotically over headphones (Sony, MDR-V6). Maskers in the SAM condition were presented at 60 dB SPL per SAM tone (i.e., carrier and two sidebands), and each masker band in the narrow-band noise condition was presented at 65 dB SPL.

II. PROCEDURES

Four observers participated in the experiment. All had pure-tone thresholds better than 20 dB HL for frequencies between 250 and 8000 Hz. Observers 1–3 were all very experienced in psychophysical procedures, having participated in CMR and other previous experiments. Observer 4 had some previous exposure to psychophysical procedures, although none with CMR stimuli. Both observers 1 and 4 had one or more hours of additional practice on earlier versions of this experiment.

Observers were tested in a double-walled sound-proof booth. Stimuli were presented in a 2AFC paradigm with an interstimulus interval of approximately 400 ms. The signal was equally likely to appear in the first as the second interval, and feedback was provided visually after each trial. A 3-down 1-up tracking procedure estimated 79% correct (Levitt, 1971). The initial step size of 8 dB was reduced to 4 dB after the second track reversal, and reduced again to 2 dB after the fourth reversal. Trials continued until a total of ten reversals were obtained. Threshold estimates were computed as the average of the levels at the last six track reversals. Practice trials were available at the beginning of each track.

All observers began with the SAM masker conditions. Because of time constraints, only observers 1–3 completed the TONE condition. The order of SAM masker conditions was quasi-random across observers, with thresholds taken in blocks by condition. A total of five threshold estimates were taken for each condition, with the first discarded as practice. After completing the SAM masker conditions, observers began the narrow-band noise masker conditions. Only observers 1–3 completed the ENV-ONLY condition, and the order of the narrow-band noise conditions was completed in quasi-random order. Visual inspection of the data revealed no effect of practice across the four threshold estimates taken as data. This would be surprising were it not for the fact that all but one of the observers was highly practiced in CMR tasks.

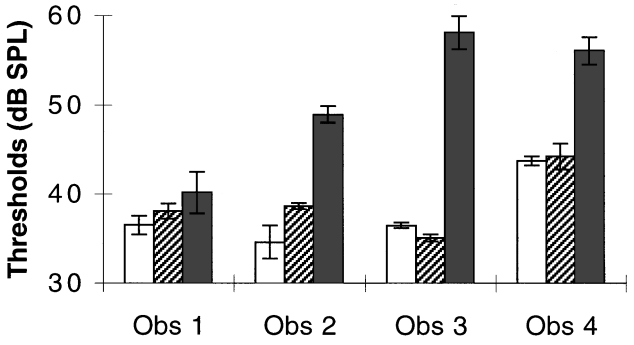

FIG. 2. Results for the SAM masker conditions: Thresholds (in dB SPL) are plotted separately for each condition and each observer. Left to right, bars represent results for the f-CO, r-CO, and NB conditions.

III. RESULTS

Results for the SAM masker conditions appear in Fig. 2. Average thresholds for the four observers, indicated on the abscissa, are plotted separately. Left to right the bars in each cluster show thresholds in the f-CO, r-CO, and NB conditions. Error bars show the standard error of the mean (sem) across the four threshold estimates. Average thresholds from the TONE condition, not shown on this graph, were well above those in the other conditions for all three of the observers who completed this condition; the average threshold across observers in the TONE condition was 60.0 dB (sem $=0.5$ dB), significantly higher than thresholds in the f-CO condition (1-tailed, paired t-test: $t_2=9.72$, $p<0.01$). Results for the narrow-band noise maskers appear in Fig. 3. As in Fig. 2, data for the four observers, indicated on the abscissa, are plotted separately. Left to right the bars in each cluster show thresholds in the f-CO, r-CO, and NB conditions. Thresholds in the ENV-ONLY condition, not shown on this graph, averaged 62.8 dB (sem$=2.6$ dB). These thresholds were not significantly higher than those in the f-CO condition (1-tailed, paired t-test: $t_2=0.52$, $p=0.33$). Data for both the SAM and narrow-band noise masker conditions indicate a reliable CMR; results from 1-tailed, paired t-tests show thresholds in the f-CO condition to be lower than those in the NB condition in both cases ($t_3=3.52$, $p<0.05$ and $t_3=2.72$, $p<0.05$ for the SAM and narrow-band noise conditions, respectively), though this trend was not evident in the data of all observers (e.g., observer 4's data with narrow-band noise maskers). Masker frequency rove did not significantly raise thresholds as compared to the fixed-frequency case (f-CO versus r-CO conditions) for either the SAM or narrow-band noise masker conditions ($t_2=1.04$, $p=0.19$; $t_2=0.28$, $p=0.40$).

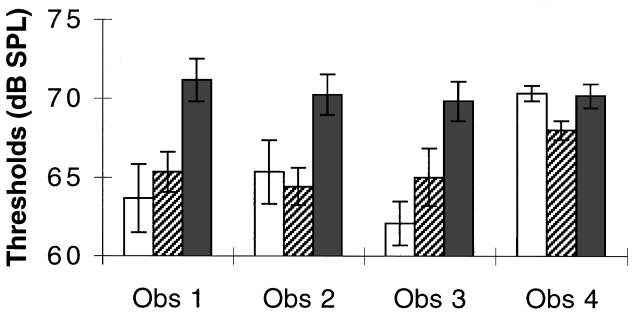

FIG. 3. Results for the narrow-band noise masker conditions: As in Fig. 2, thresholds (in dB SPL) are plotted separately for each condition and each observer. Left to right, bars represent results for the f-CO, r-CO, and NB conditions.

IV. DISCUSSION

The results presented here do not support the hypothesis that a change in envelope beats serves as a cue for detecting a signal added to maskers with coherent AM. The data fail to show an adverse effect of roving flanking masker center frequency, as would be predicted if the reduction of envelope energy at the beat frequency (identified by comparing envelope amplitude spectra across samples) were the cue to the addition of the signal in the case of comodulated maskers. Instead, CMRs in the roved frequency condition appear to be uncompromised relative to those obtained with maskers fixed in frequency. The lack of an effect of reduced beat regularity (in the ENV-ONLY condition) is inconsistent with the possibility that envelope beats, as identified on an interval-by-interval basis, form the cue for detection. The elevation of thresholds in the presence of pure-tone maskers in the TONE condition suggests that the long-term amplitude spectrum (e.g., profile analysis; Green, 1988) was not responsible for improved sensitivity associated with the inclusion of comodulated flanking maskers. While it is quite plausible that Berg's leaky integrator model could be fitted to these data, detection would be based on very different aspects of the amplitude spectra of the envelope in each case—the decrease of energy at the beat frequency in the case of fixed-frequency flanking masker, and much subtler changes in energy across a broader range of frequencies in the case of roved flanking masker frequency or reduced beat regularity (detection perhaps also relying heavily on covariance across points in the envelope amplitude spectrum). It is also possible that detection could be based on cues other than those derived from the envelope amplitude spectrum, particularly in the r-CO and ENV-ONLY conditions. Given the similarities in the patterns of results obtained for these three conditions, however, it seems somewhat unlikely that such different cues would be utilized equally efficiently, particularly given the limited exposure these observers had to stimuli with roved flanking masker frequency and reduced envelope beat regularity.[4]

ACKNOWLEDGMENTS

This work was supported by Grant No. RO1 DC00418 from NIH-NIDCD. We would like to thank Bruce Berg for his input in the development of these ideas and for making his software available to us. Two anonymous reviewers provided helpful comments on earlier versions of this paper.

[1]This figure resembles Fig. 1 in Berg (1996).

[2]Introduction of channel and central noise to this basic model, necessary to fit observers' data, complicates this picture somewhat. The inclusion of additive noise has a large affect on the mean-to-sigma ratio of envelope energy at the beat frequency (this energy being relatively low, particularly after the lowpass filter). As a result, envelope cues at frequencies other than the beat frequency [somewhat similar to those discussed in Green *et al.* (1992) although that study used very different stimuli and different methods] increase in relative reliability. This issue will not be pursued, however, because the hypothesis under consideration in this study is whether the

decision statistic underlying CMR is based on a change in envelope beats.

[3]Based on Schooneveldt and Moore's (1987) data in the region of 1000 Hz, all of the masker frequencies tested here fall outside the range thought to produce within-channel effects.

[4]Observers 1–2 have had over 100 h of previous exposure to stimuli similar to those in the f-CO condition, as compared to less than 1-h exposure to stimuli in the r-CO and ENV-ONLY conditions in the course of the present experiment.

Berg, B. G. (**1996**). ''On the relation between comodulation masking release and temporal modulation transfer functions,'' J. Acoust. Soc. Am. **100**, 1013–1023.

Buus, S. (**1985**). ''Release from masking caused by envelope fluctuations,'' J. Acoust. Soc. Am. **78**, 1958–1965.

Cohen, M. F., and Schubert, E. D. (**1987**). ''Influence of place synchrony on detection of a sinusoid,'' J. Acoust. Soc. Am. **81**, 452–458.

Fantini, D. A., and Moore, B. C. J. (**1994**). ''Profile analysis and comodulation detection differences using narrow bands of noise and their relation to comodulation masking release,'' J. Acoust. Soc. Am. **95**, 2180–2191.

Green, D. (**1988**). *Profile Analysis: Auditory Intensity Discrimination* (Oxford University Press, Oxford).

Green, D. M., Berg, B. G., Dai, H., Eddins, D. A., Onsan, Z., and Nguyen, Q. (**1992**). ''Spectral shape discrimination of narrow-band sounds,'' J. Acoust. Soc. Am. **92**, 2586–2597.

Hall, III, J. W. (**1986**). ''The effect of across-frequency differences in masking level on spectro-temporal pattern analysis,'' J. Acoust. Soc. Am. **79**, 781–787.

Hall, J. W., Haggard, M. P., and Fernandez, M. A. (**1984**). ''Detection in noise by spectro-temporal pattern analysis,'' J. Acoust. Soc. Am. **76**, 50–56.

Levitt, H. (**1971**). ''Transformed up-down methods in psychoacoustics,'' J. Acoust. Soc. Am. **49**, 467–477.

Moore, B. C. J., Glasberg, B. R., and Schooneveldt, G. P. (**1990**). ''Across-channel masking and comodulation masking release,'' J. Acoust. Soc. Am. **87**, 1683–1694.

Rice, S. O. (**1953**). ''Mathematical analysis of random noise,'' in *Selected Papers on Noise and Stochastic Processes*, edited by N. Wax (Dover, New York), pp. 133–294.

Richards, V. M. (**1987**). ''Monaural envelope correlation perception,'' J. Acoust. Soc. Am. **82**, 1621–1630.

Richards, V. M. (**1988**). ''Components of monaural envelope correlation perception,'' Hearing Res. **35**, 47–58.

Richards, V. M. (**1990**). ''The role of single-channel cues in synchrony perception: The summed waveform,'' J. Acoust. Soc. Am. **88**, 786–795.

Schooneveldt, G. P., and Moore, B. C. J. (**1987**). ''Comodulation masking release (CMR): Effects of signal frequency, flanking-band frequency, masker bandwidth, flanking-band level, and monotic versus dichotic presentation of the flanking band,'' J. Acoust. Soc. Am. **82**, 1944–1956.

Viemeister, N. F. (**1979**). ''Temporal modulation transfer functions based upon modulation thresholds,'' J. Acoust. Soc. Am. **66**, 1364–1380.

Basilar-membrane nonlinearity and the growth of forward masking

Christopher J. Plack
Laboratory of Experimental Psychology, University of Sussex, Brighton BN1 9QG, England

Andrew J. Oxenham[a)]
Institute for Perception Research (IPO), P.O. Box 513, 5600 MB Eindhoven, The Netherlands

(Received 10 June 1997; accepted for publication 19 November 1997)

Forward masking growth functions were measured for pure-tone maskers and signals at 2 and 6 kHz as a function of the silent interval between the masker and signal. The inclusion of conditions involving short signals and short masker-signal intervals ensured that a wide range of signal thresholds were recorded. A consistent pattern was seen across all the results. When the signal level was below about 35 dB SPL the growth of masking was shallow, so that signal threshold increased at a much slower rate than masker level. When the signal level exceeded this value, the masking function steepened, approaching unity (linear growth) at the highest masker and signal levels. The results are inconsistent with an explanation for forward-masking growth in terms of saturating neural adaptation. Instead the data are well described by a model incorporating a simulation of the basilar-membrane response at characteristic frequency (which is almost linear at low levels and compressive at higher levels) followed by a sliding intensity integrator or temporal window. Taken together with previous results, the findings suggest that the principle nonlinearity in temporal masking may be the basilar membrane response function, and that subsequent to this the auditory system behaves as if it were linear in the intensity domain. © *1998 Acoustical Society of America.* [S0001-4966(98)02003-7]

PACS numbers: 43.66.Dc, 43.66.Ba, 43.66.Mk [WJ]

INTRODUCTION

One of the main goals of psychoacoustic research is to provide an account of auditory perception that is physiologically realistic, computationally tractable, and parsimonious. These efforts are complicated by the considerable nonlinearities that are observed in certain aspects of auditory processing. A dramatic example of this nonlinear behavior is forward masking, in which the detectability of a signal is reduced by a masker terminated before the onset of the signal. It is a well-established fact that on-frequency forward masking grows nonlinearly: A given increase in masker level requires a smaller increase in signal level in order for the signal to remain at detection threshold (Jesteadt *et al.*, 1982; Moore and Glasberg, 1983). In other words, the masker becomes relatively less effective as its level is increased. The result is in contrast to that for on-frequency simultaneous masking, in which the signal-to-masker ratio at threshold is almost independent of masker level (Hawkins and Stevens, 1950; Viemeister, 1972).

These findings have been taken as evidence that forward masking is, at least in part, a consequence of nonlinear processes in the auditory nerve; specifically, neural adaptation (Bacon, 1996; Duifhuis, 1973; Jesteadt *et al.*, 1982; Kidd and Feth, 1982). According to this account, the sensitivity of a neuron is reduced after stimulation, leading to a decrease in the detectability of a subsequent signal. Neural adaptation is compressive and saturating (Smith, 1977, 1979), so that the relative effectiveness of the adaptor decreases with level. These characteristics are consistent, *qualitatively*, with the nonlinearity observed behaviorally in the majority of forward-masking experiments, although more recent physiological studies suggest that the *amount* of forward masking observed in single auditory nerve fibers is not sufficient to account for the *amount* of psychophysical forward masking (e.g., Relkin and Turner, 1988). Even though the adaptation account as described here is based on the response of single neurons measured in isolation, for the present purposes this should be a sufficient analysis. The characteristics of adaptation that are important here (saturation with increasing level, and dependence of adaptation on masker level, not signal level) will apply even if a larger number of neurons are employed in a given forward-masking situation.

An alternative explanation for forward masking is that it is a consequence of more ''central'' processes relating to the limited temporal resolution of the auditory system: The neural representation of the masker is smoothed over time by an integration device, or temporal window (Festen *et al.*, 1977; Moore *et al.*, 1988; Penner *et al.*, 1972), so that the representation of the masker overlaps with the representation of the signal at some stage in the auditory system. In this account it is the ''persistence'' of masker excitation that produces the masking (Plomp, 1964; Zwislocki *et al.*, 1959). Classically, however, the temporal window has been taken to be linear, so that the model is unable to account for the nonlinearities observed in forward masking without assuming that the duration of the temporal window is reduced as stimulus level is increased (Plack and Moore, 1990). Not only does this considerably complicate the temporal window model, but it is also inconsistent with other data that suggest that temporal

[a)]Present address: Communication Research Laboratory, Department of Speech–Language Pathology and Audiology, Northeastern University, Boston, MA 02115.

resolution is almost independent of level (Buus and Florentine, 1985; Moore and Glasberg, 1988; Peters *et al.*, 1995; Plomp, 1964; Viemeister, 1979). In addition, a temporal-window model operating on stimulus intensity cannot account for the nonlinear additivity of forward and backward maskers (Penner, 1980).

Despite these failings, the temporal-window model has considerable appeal, mainly perhaps because of its simplicity. It has been suggested that the model can be rescued by assuming that there is a compressive nonlinearity prior to the temporal window (Oxenham and Moore, 1994; Penner, 1980). Furthermore, it has been suggested that the compressive nonlinearity may be related to the nonlinear response of the basilar membrane (Oxenham and Moore, 1994, 1995). In these studies, however, basilar-membrane compression was modeled using a simple (level-invariant) power law. Thus while the additivity of forward and backward masking could be well accounted for, the nonlinear growth of forward masking could not.

Physiological measurements of basilar-membrane vibration have shown that the response to a pure tone at its ''nominal'' characteristic frequency (CF; defined as the pure-tone frequency that produces the maximum excitation at *low* levels) is approximately linear for tone levels below about 40 dB SPL (Murugasu and Russell, 1995; Ruggero *et al.*, 1997; Russell and Nilsen, 1997). Above these levels, the response is highly compressive, with a compression ratio of roughly 5:1 (in dB units). It is possible to distinguish two characteristics of basilar-membrane nonlinearity that may determine the compressive behavior at CF. One is the compressive response of the basilar membrane *per se*, which has been linked to an active physiological mechanism. The other is the reduction in the best frequency (BF, the frequency that produces the maximum response) of each place on the basilar membrane as level is increased (McFadden and Yama, 1983; Ruggero *et al.*, 1997; Russell and Nilsen, 1997). As BF shifts downward, the tone fixed at CF (which is no longer the optimum frequency) produces *relatively* less excitation, leading to a compressive response function. The account implies that the response at BF should be less compressive than at CF, and indeed this is observed in some of the basilar membrane measurements (see for example, Ruggero *et al.*, 1997, Fig. 8; Russell and Nilsen, 1997, Fig. 4). Both the compression at BF and the shift in BF may contribute to the measured compression at CF, although it should be emphasized that these characteristics are probably the consequence of a single underlying mechanism.

The nonlinear growth of forward masking can be explained in terms of basilar-membrane nonlinearity as follows (Oxenham and Moore, 1995). Because the amount of masking produced by a forward masker is usually quite small, at least in comparison to simultaneous masking, the threshold signal levels in forward-masking experiments have generally been low. If the masker level is high enough to be in the compressive region of the basilar membrane function, a 10-dB increase in masker level may produce only a 2-dB increase in masker excitation (5:1 compression). If the signal level is always in the low-level, more linear, portion of the basilar-membrane function, then the signal excitation will increase in proportion to the physical signal level. Assuming that threshold corresponds to a constant internal signal-to-masker ratio, the signal *level* only has to increase by the same amount as the masker *excitation* (i.e., about 2 dB) in order for the signal to remain at threshold (see also Moore, 1996). The hypothesis can account, in principle, for the shallow growth of forward masking. Furthermore, since cochlear damage leads to a loss of basilar-membrane compression, the hypothesis also predicts more linear growth of forward masking in listeners with cochlear hearing impairment. This prediction is consistent with the available data (Oxenham and Moore, 1995, 1997). In further support of the hypothesis, Oxenham and Moore (1997) showed that their modification of the temporal window model, including a simulation of the basilar-membrane response function, provided a good account of the growth of forward masking for both normal and impaired listeners.

The aim of the present experiments was to distinguish between the neural and mechanical explanations for the nonlinear behavior of forward masking. As will be explained, the predictions of the two hypotheses, while similar when signal threshold is low, differ when signal threshold is high. The experiments were designed to exploit this distinction.

I. GENERAL METHOD

A. Stimuli

The sinusoidal stimuli were generated digitally on a Silicon Graphics workstation at a sampling rate of 32 kHz, with 16-bit resolution. Anti-aliasing was provided by built-in filters. Analog waveforms were delivered directly via the headphone output on the computer. Level changes were implemented in the digital domain, although for conditions requiring low signal thresholds the built-in analog attenuators were used to decrease the overall output level by up to 18 dB.

B. Procedure

A 2I, 2AFC paradigm was adopted throughout. In one interval the masker and the signal were presented; in the other interval the masker alone was presented. The interstimulus interval was 500 ms. A two-down, one-up adaptive tracking rule was used to estimate the 71% correct point on the psychometric function (Levitt, 1971). The level of the signal was increased and decreased by 4 dB for the first four turnpoints, and by 2 dB thereafter. Sixteen turnpoints were recorded in each experimental block and the threshold estimate was taken as the mean of the values at the last 12 turnpoints. At least four such estimates were made for each listener and the results were averaged.

Listeners were tested individually in an IAC single-walled sound-attenuating booth. Stimuli were presented over one earphone of a Sony MDRV6 headset. Listeners made their responses using the numeric keypad on the computer keyboard. ''Lights'' were presented in a graphical display on the computer monitor to delineate the observation intervals, and to provide feedback after each trial.

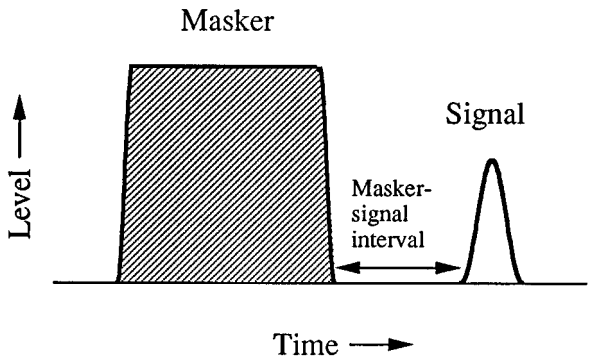

FIG. 1. A schematic illustration of the temporal characteristics of the stimuli.

II. EXPERIMENT 1: FORWARD MASKING OF 10-MS TONE BURSTS AS A FUNCTION OF LEVEL

A. Rationale

While the two explanations (neural and mechanical) for the nonlinearity in forward masking produce similar predictions when the signal level is low, the predictions of the hypotheses diverge when the signal level enters the compressive region of the basilar-membrane response function. In terms of the neural adaptation account, the amount of adaptation is dependent only on masker level. This means that the growth of masking should still be shallow at high signal levels, since the adaptation produced by the masker will still be saturated. However, in terms of the basilar-membrane nonlinearity account, if the masker and the signal are *both* being compressed then the effects should cancel out to some degree, so that the masking function should be steeper, i.e., more linear, at high signal levels than at low.

The experiment was designed to test these predictions using a brief signal presented shortly after the masker. The stimulus parameters were chosen to ensure a large amount of masking so that signal threshold at high masker levels would be within the compressive region of the basilar membrane. High signal frequencies were tested, so that the masker and signal would not overlap on the basilar membrane due to ''ringing'' in the auditory filters (Duifhuis, 1973; Oxenham and Plack, 1997), and so that the spectral spread of the short signal would be small compared to the auditory filter bandwidth.

B. Conditions

The sinusoidal stimuli are illustrated schematically in Fig. 1. The masker had a steady-state duration of 20 ms with 2-ms raised-cosine onset and offset ramps. The signal had no steady-state portion and 5-ms onset and offset ramps. The masker had the same frequency as the signal and frequencies of 2 and 6 kHz were tested. At each frequency, masker-signal intervals (specified from zero-voltage points) of 2, 20, and 40 ms were tested. At each masker-signal interval, thresholds were measured for masker levels of 30–100 dB SPL in 10-dB steps. In addition, absolute threshold measurements were made in the absence of the masker.

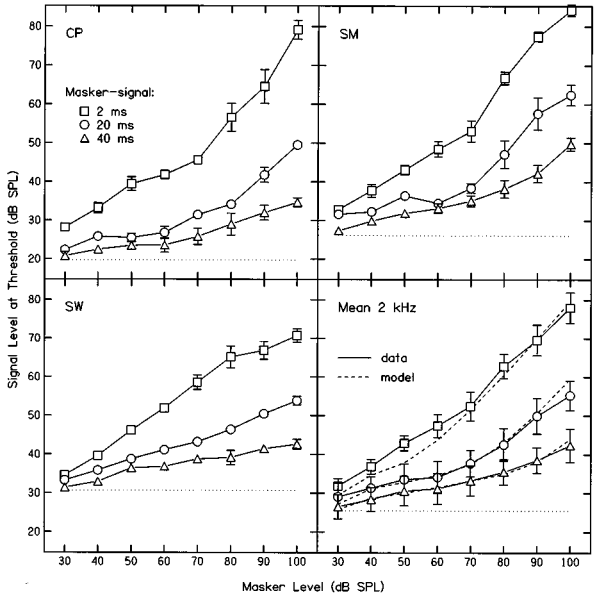

FIG. 2. The individual and mean results from experiment 1 for the 2-kHz signal showing signal threshold as a function of masker level with masker-signal interval as the parameter. The dotted lines show the absolute thresholds for the signal in the absence of the masker. The dashed lines show the predictions of the model described in the text. Error bars show standard errors between replications for the individual data and between listeners for the mean data.

C. Listeners

Three normally hearing listeners took part. Absolute thresholds for the signal (for CP, SM, and SW, respectively) were 19.7, 26.1, and 30.6 dB SPL at 2 kHz, and 22.3, 29.1, and 17.3 dB SPL at 6 kHz. Listeners were given at least 4 h practice on the task before data collection began.

D. Results and discussion

The individual and mean data at 2 and 6 kHz are shown in Figs. 2 and 3, respectively. The horizontal dotted lines show the absolute thresholds in the absence of the masker. The dashed lines show the threshold values estimated by a model that will be described later.

The data for the two signal frequencies are broadly similar. For the 2-ms masker-signal interval the masking function is relatively steep (compared to the 20- and 40-ms intervals) over the entire level range, although there is a slight tendency for the function to steepen with increasing masker level, approaching a value of unity at the highest levels. The 20-ms data show an initial very shallow growth of masking, consistent with previous measures of forward masking, followed by an increase in slope. The same pattern is seen for the 40-ms data, although the function first begins to steepen at a higher masker level. The only deviation from this general pattern is for listener SW at 2 kHz, where the 2-ms data appear to flatten off slighty at high masker levels, although this is also where the variability is highest.

Figure 4 shows a scatter plot of the slope of the masking function against signal level at threshold. Each point was obtained by plotting the mean of each two consecutive signal thresholds from the mean data in Figs. 2 and 3 against the

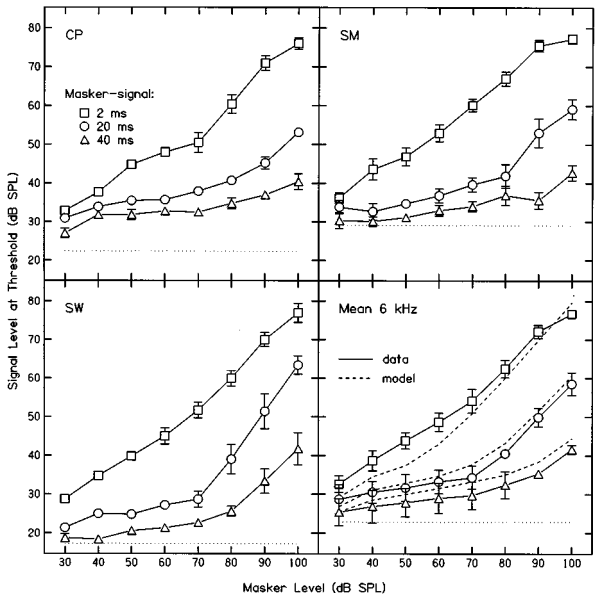

FIG. 3. As Fig. 2 except showing the results from experiment 1 for the 6-kHz signal.

slope of the straight line connecting them. There is a very clear tendency for the slopes to increase with increasing signal level. For signal levels below about 35 dB SPL the slope of the masking function is low, with the values clustered around 0.2 dB/dB. Above this cutoff value the slopes are much greater. The correlation between signal level and slope was measured separately for the 2- and 6-kHz data. In both cases the correlation was positive, strong, and highly significant (respectively: $r=0.826$, $p<0.001$; $r=0.722$, $p<0.001$). Also pertinent is the finding that the correlation between *masker* level and slope was much weaker ($r=0.480$, $p<0.02$, at 2 kHz; and $r=0.560$, $p<0.01$, at 6 kHz). It is possible that the correlation with masker level may be largely a result of the correlation between signal level and masker level. A test devised by Williams (1959) was used to determine the significance of the difference in correlations. Grouping the data from 2 and 6 kHz together, it was found that the masking function slope was significantly more highly correlated with signal level than with masker level ($t=2.691$, $p<0.01$). It can be concluded that it is predominantly signal level that determines the shape of the masking function. The analysis supports the view that the masking function steepens because of changes in the compression applied to the signal as threshold level increases.

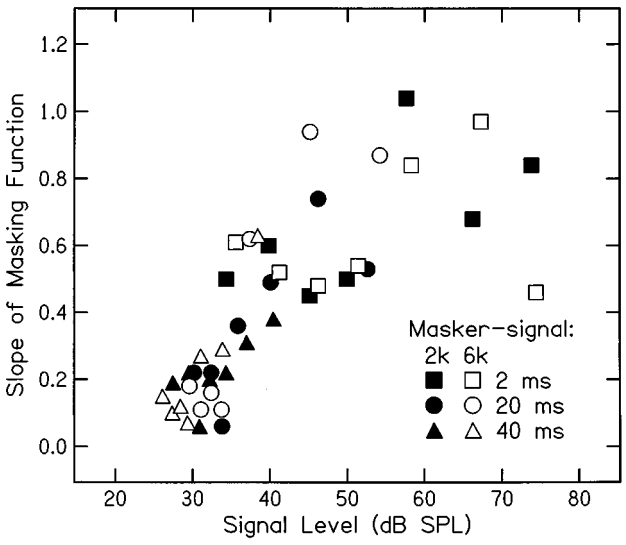

FIG. 4. A scatter plot of signal level at threshold against the slope of the masking function. The data were derived from the mean results of experiment 1 (see text for details).

The shape of the masking function is inconsistent with the hypothesis that the nonlinearities in forward masking are the result of saturating neural adaptation produced by the masker. If the hypothesis were correct then the masking function should be dependent only on masker level, and should be shallow at high masker levels where adaptation is most saturated. Neither of these characteristics are evident in the results. The shape of the masking function is consistent, however, with a basilar membrane input–output function that is steep below 35 dB SPL and shallow (i.e., highly compressive) for levels above this. When the signal is in the linear region and the masker is compressed the masking function is shallow, and when both masker and signal are in the compressive region the masking function is more linear.

III. EXPERIMENT 2: FORWARD MASKING OF 50-MS TONE BURSTS AS A FUNCTION OF LEVEL

A. Rationale

The aim of experiment 2 was to confirm the generality of the results from experiment 1 using longer maskers and signals. The masked threshold for a long signal is lower than that for a short signal, so that the upper, linear, portion of the growth of masking function is less prominent. However, the long signal also has a lower absolute threshold, allowing the masking function to be measured at lower masker levels. This is of interest since, according to the basilar-membrane hypothesis, when both the signal and the masker are at low levels (i.e., within the linear region) the growth of masking should again be linear. Such a pattern is seen in the classic results of Munson and Gardner (1950).

B. Conditions

The masker had a steady-state duration of 100 ms with 2-ms raised-cosine onset and offset ramps. The signal had a steady-state duration of 30 ms with 10-ms onset and offset ramps. Signal frequencies of 2 and 6 kHz were tested. At each frequency, masker-signal intervals (specified from zero-voltage points) of 2 and 20 ms were tested. At each masker-signal interval, thresholds were measured for masker levels of 20–100 dB SPL in 10-dB steps. Absolute threshold measurements were made in the absence of the masker.

C. Listeners

Three normally hearing listeners took part, only one of whom had taken part in experiment 1. Absolute thresholds for the signal (for DP, SM, and PB, respectively) were 12.9,

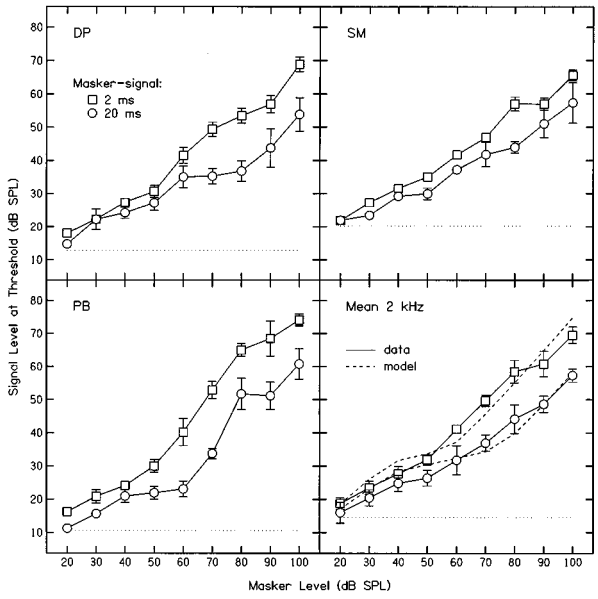

FIG. 5. As Fig. 2 except showing the results from experiment 2 for the 2-kHz signal.

20.2, and 10.6 dB SPL at 2 kHz, and 17.5, 20.7, and 24.2 dB SPL at 6 kHz. Listeners were given at least four hours practice on the task before data collection began.

D. Results and discussion

The individual and mean data at 2 and 6 kHz are shown in Figs. 5 and 6, respectively. The mean results at 6 kHz are similar to the on-frequency results of Munson and Gardner (1950) at 1 kHz. There is an initial, relatively steep, increase in signal threshold over the lowest three masker levels; a broad, shallow mid-level region; and a dramatic steepening in the masking function at high masker levels. The steepening begins at a lower masker level for the 2-ms data. The

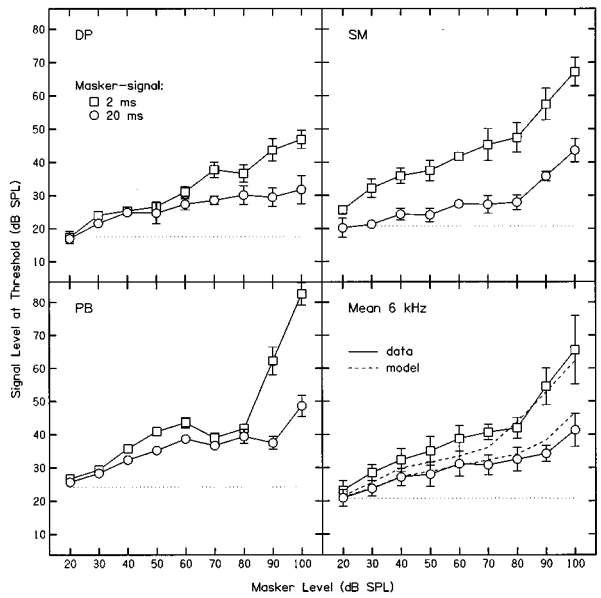

FIG. 6. As Fig. 2 except showing the results from experiment 2 for the 6-kHz signal.

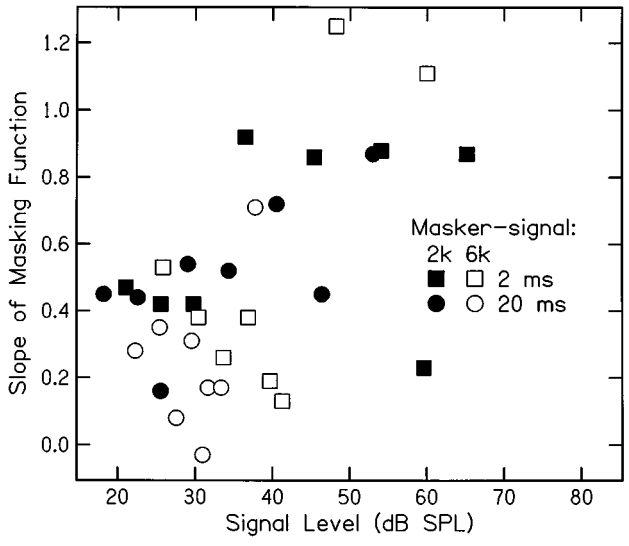

FIG. 7. As Fig. 4 except showing a scatter plot derived from the mean results of experiment 2.

masking functions at 2 kHz are relatively steep throughout the level range, although there is also a tendency for the functions to steepen with increasing masker level.

Figure 7 shows a scatter plot of the slope of the mean masking function against signal level. Once again, there is a clear tendency for the slopes to increase with increasing signal level, although the effect is more variable than it was in experiment 1. Part of this variability is possibly a result of the increase in slope for low *masker* levels. The correlation between signal level and slope was measured separately for the 2- and 6-kHz data. At both frequencies the correlation was positive and significant (respectively: $r=0.486$, $p<0.05$; $r=0.628$, $p<0.005$). Again, the overall correlation with masker level was weaker, although only marginally so at 2 kHz ($r=0.452$, $p<0.1$, at 2 kHz; and $r=0.391$, $p>0.1$, at 6 kHz). Grouping the data from 2 and 6 kHz together, it was found that masking function slope was significantly more highly correlated with signal level than with masker level ($t=1.768$, $p<0.05$).

Considering only masker levels up to 70 dB, at 6 kHz there was a significant *negative* correlation between masker level and slope ($r=-0.622$; $p<0.05$). This confirms that the lower part of the masking function, where both masker and signal levels are within the linear region, has a more linear slope than the masking function at medium masker levels. Because of the earlier steepening in the growth of masking function at 2 kHz, the negative correlation was not seen over the same range of masker levels for this data set. Overall, however, the results are consistent with the basilar-membrane hypothesis and confirm that the nonlinear growth of forward masking is not explicable in terms of saturating neural adaptation.

As can be seen in Fig. 6, the results for the highest masker levels at 6 kHz were highly variable between listeners. Widin and Viemeister (1979) also comment on the large variation in thresholds between their listeners. In some respects this is to be expected. First, a slight between-listener variation in the shape of the basilar-membrane function, for

instance, the level at which the basilar membrane changes from being linear to compressive, can have a dramatic effect on signal thresholds. For example, if the transition from the linear to the compressive region is at 35 dB, then the masking function would become almost linear for signal levels above this, perhaps resulting in an increase in signal threshold from 35 to 55 dB for a 20-dB increase in masker level. If the transition level is 40 dB, however, the masking function should be shallow up to this value, so the signal threshold may only increase from 35 to 39 dB for the same 20-dB increase in masker level (given 5:1 compression). In other words, a 5-dB between-listener variation in the transition level (well within the range of values observed physiologically) can produce a 16-dB between-listener variation in signal threshold that was not evident for a masker level 20 dB lower. Similarly, any variation in the efficiency of the detection mechanism between listeners has a much larger effect at high levels, because of the compression. If the internal signal-to-masker ratio at threshold is increased by 2 dB, the physical signal level has to be increased by 10 dB under 5:1 compression.

While all the individual results in Fig. 6 vary at high levels, the largest discrepancy is seen in the results for listener PB, where there is a dramatic steepening in the growth function for the 2-ms masker-signal interval at high levels. The slope here is greater than unity and is not compatible with a basilar membrane function that is equally compressive above a low-level cutoff point. While the results for this listener may be attributable to random variation, there is an alternative explanation. Until recently, physiological measurements of the basilar membrane response at CF often showed a three stage function, with a linear low-level region, a compressive mid-level region, and a linear high-level region (Ruggero, 1992; Ruggero and Rich, 1991; Ruggero *et al.*, 1993). The absence of compression at very high levels has been linked to a reduction in sensitivity caused by a deterioration in the physiological condition of the animal (Ruggero *et al.*, 1997). If PB's hearing is very slightly impaired at 6 kHz (indeed, his absolute threshold was the highest of the three listeners), then it is conceivable that his basilar-membrane function followed the steep–shallow–steep pattern. This being the case, when the masker enters the high-level linear region and the signal is in the compressive region then the masking function should become very steep (greater than linear) since now the signal threshold needs to increase at a much higher rate than masker level to overcome the compression (the reverse of the situation for low signal levels and medium masker levels). It is possible that PB's results may be explained in this way, although this does not appear to be a general rule. For the 2-kHz data in experiment 1, for example, SW has the highest absolute threshold of the three listeners, but a shallower slope at high levels (see Fig. 2). In any case, PB's data are clearly not consistent with the adaptation account.

Although there were clear individual differences in the 6-kHz condition in experiment 2, the remaining results were reasonably consistent between listeners, at least in terms of the overall form of the data, and the subsequent analysis will focus on the mean data. If the mechanical hypothesis is accepted, it is reasonable to regard the mean data as providing a first approximation to the ''average'' basilar-membrane response, while acknowledging that the shape of the function may differ between individuals.

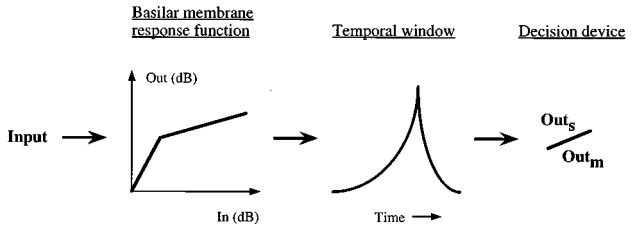

FIG. 8. An illustration of the processing stages of the model described in the text.

IV. THE REVISED TEMPORAL-WINDOW MODEL

In order to provide a quantitative test of the basilar-membrane hypothesis, a version of the temporal-window model was implemented that could estimate signal thresholds in forward-masking paradigms. In its present form the model consists of three stages: a level-dependent compressor, a sliding temporal integrator, and a decision device (see Fig. 8). As the masker and the signal were pure tones with the same frequency, and since the temporal smearing due to ringing was considered to be negligible at the CFs tested, the effects of the auditory filter were ignored for the present purposes.

The model assumes that the detectability of the signal is determined by the response at the place on the basilar membrane with CF equal to the signal frequency. Since the early years of research on frequency selectivity, models of masking have often made this assumption (Fletcher, 1940; Moore, 1995), and it would seem to be a reasonable one to make in the present case, where the spectrum of the signal is small compared to the critical band and hence the utility of ''off-frequency listening'' (Johnson-Davies and Patterson, 1979) is minimized. The model also assumes that threshold is determined by the ratio of signal intensity to masker intensity at some central stage in the auditory system. Again, this is an assumption commonly used in models of masking, and is consistent with the finding that the Weber fraction for intensity discrimination is approximately constant over a wide range of levels (Viemeister, 1988). In terms of traditional signal detection theory (Green and Swets, 1966), the approach assumes that the standard deviation of the internal representation is proportional to its mean.

A. Stage 1: The compressor

This stage simulates the nonlinear input-output function of the basilar membrane. The most recent direct measurements of basilar-membrane vibration have shown that the response at CF can be divided into two level regions: A roughly linear region for input levels below about 40 dB SPL, and a compressive region for higher levels (Murugasu and Russell, 1995; Ruggero *et al.*, 1997; Russell and Nilsen, 1997). It was decided to produce a rough approximation to the overall response function using two straight lines on dB/dB coordinates.

In an earlier article (Oxenham and Plack, 1997) the response of the basilar membrane was measured behaviorally using a forward masker an octave below the signal frequency. The experiment was a modification of an earlier procedure that used the growth of simultaneous masking to estimate basilar-membrane response functions (Nelson and Schroder, 1997; Stelmachowicz *et al.*, 1987; Yates *et al.*, 1990). The reasoning is that the excitation produced by the low-frequency masker should grow linearly at the CF corresponding to signal frequency (Murugasu and Russell, 1995; Yates *et al.*, 1990), so that the change in masker level with signal level provides an estimate of the amount of signal compression at CF. In other words, the plot of masker level at threshold as a function of signal level is an estimate of the basilar-membrane input–output function. The results obtained were consistent with physiological measurements.

The mean masker levels obtained by Oxenham and Plack at 6 kHz, for signal levels of 30–80 dB SPL, were used to estimate the nonlinear function in the first stage of the model. Because the 4-ms signal used in the main experiment of Oxenham and Plack had a high absolute threshold, meaningful masker thresholds could only be measured for signals levels of 40 dB SPL and greater. Therefore, for the purposes of the present analysis, for signal levels above 35 dB SPL the results for the 4-ms signal were used, but for the lower signal levels of 30 and 35 dB SPL the results for a 14-ms signal were used, with the masker levels at threshold decreased by a constant 6.56 dB. This was the mean difference between the masker levels needed to mask the 4-ms and 14-ms signals at signal levels of 40, 45, 50, 55, and 60 dB SPL. The manipulation corrects for the greater detectability of the longer signal.

The data were fitted with two straight lines, with the slope of the lines and the position of the ''knee'' in the function where the two lines meet as free parameters. The value of these free parameters was found that minimized the squared deviations of the experimental results from the fitted function. It was found that the Oxenham and Plack data were well fit by two straight lines with slopes of 0.78 and 0.16 on dB/dB coordinates. The lines meet at a signal level of 45 dB SPL. This value is 10 dB above the cutoff value of 35 dB suggested by the present data from experiment 1; it was decided to use the latter value here. Both values are within the range observed physiologically.

Following this somewhat crude analysis, the compressive function in the first stage of the temporal window model is given by:

$$L_{\text{out}} = 0.78\, L_{\text{in}} \quad (L_{\text{in}} <= 35 \text{ dB SPL}) \tag{1}$$

$$L_{\text{out}} = 0.16\, L_{\text{in}} + 21.7 \quad (L_{\text{in}} > 35 \text{ dB SPL}), \tag{2}$$

where L_{in} is input level expressed in dB SPL, and L_{out} is the output of the compressive function expressed in dB. The constant of 21.7 is added to Eq. (2) so that L_{out} is the same for Eqs. (1) and (2) when $L_{\text{in}} = 35$. The output of this stage is expressed in units of intensity. This is consistent with the transfer function of auditory nerve fibers, for which firing rate has been found to be linearly related to stimulus intensity (Yates *et al.*, 1990).

B. Stage 2: The temporal window

In the second stage the waveform is smoothed by a sliding temporal integrator, or temporal window. The output of this stage is the integrated product of the input waveform (in units of intensity) with the temporal window, as a function of the center time of the window. (This is equivalent to a convolution of the input waveform with the time-reversed temporal window.) The shape of the temporal window is described by a combination of exponential functions:

$$W(t) = 0.975 \exp(t/4) + 0.025 \exp(t/29) \tag{3}$$

for times before the center of the window $(t = 0)$ and

$$W(t) = \exp(-t/3.5) \tag{4}$$

for times after the center of the window, where $W(t)$ is an intensity-weighting function and t is time measured relative to the center (or maximum) of the weighting function (in ms). These equations are taken from Oxenham and Moore (1994) with the parameters derived for listener AO.

The temporal window simulates masking by causing the masker and the signal to effectively overlap in time. The shape of the temporal window determines the relative threshold values for different masker-signal intervals in forward masking, and also determines the effect of increases in masker duration.

C. Stage 3: The decision device

The decision device is particular to the task being simulated. In the present case, the statistic used is simply the ratio of the output of the window in response to the signal to the output in response to the masker (the signal-to-masker ratio), referred to subsequently, in dB units, as the parameter k. The fitting procedure described below uses an adaptive algorithm to find the optimum value of k as a function of the center time of the window. k_{thr} is the optimum value of k at signal threshold, and is a measure of the efficiency of the decision mechanism.

Although it has taken a few lines to describe, the temporal-window model is in essence an extremely simple description of auditory processing, which ignores all the complications and nonlinearities of neural physiology in favor of a scheme based around a simple intensity integrator. It should be emphasized that the primary purpose of the model described here is to provide a quantitative evaluation of the mechanical hypothesis, and not to provide an all-encompassing description of temporal masking. Other factors, including the temporal effects of auditory filtering and possible ''cognitive'' influences, would have to be taken into consideration to account for thresholds in all possible conditions.

D. Implementing the model

The model was fitted to the present results in the following way. For each condition, digital representations of the intensity envelope of the masker and of the signal were generated. The masker level was set at the value for the particular condition but the signal level was varied by the fitting procedure. A continuous intensity envelope was added to the

masker to act as a ''noise floor.'' This simulates the influence of absolute threshold for the lowest masker levels. The effect of the noise floor is relatively insignificant except for the lowest signal levels. The level of the noise floor was chosen so that, in the absence of the masker, the thresholds predicted by the model were similar to the mean absolute thresholds for the signal in quiet. The levels used for simulating the results of experiment 1 were 19 dB at 2 kHz and 17 dB at 6 kHz. The levels used for simulating the results of experiment 2 were 6 dB at 2 kHz and 15 dB at 6 kHz. The predicted absolute thresholds at 2 and 6 kHz, respectively, were 25.2 and 23.3 dB for the experiment 1 simulations, and 14.4 and 20.7 dB for the experiment 2 simulations.

The model was fitted to the mean data independently for each signal frequency from each experiment. The fitting procedure predicted data values based on a given value of k_{thr}. It was assumed that the temporal window was centered on the time that produced the highest value of k, i.e., the maximum detectability. The center time was usually on the offset ramp of the signal. The parameter k_{thr} was varied adaptively to find the value (to the nearest 0.05 dB) that minimized the sum of the squared deviations of the predicted data values from the measured values. The signal thresholds derived with this optimum value of k_{thr} were taken as the predictions of the model.

The only free parameter in the fitting procedure itself was the parameter k_{thr} although clearly the knee in the compressive function was also constrained by the data (to a limited extent) and the level of the noise floor was constrained by the absolute threshold measurements. Aside from these three, all the other parameters in the fit were taken from independent measures of basilar-membrane nonlinearity and of temporal resolution, selected before data collection began.

E. Evaluating the model

The thresholds predicted by the model are shown by the dashed lines in Figs. 2, 3, 5, and 6. Consider first the fits to the data from experiment 1 (Figs. 2 and 3). The model accounts very well for the overall shape of the data at both frequencies, although it is slightly more accurate at 2 kHz than at 6 kHz. The only consistent deviation of the predictions from the data is for the 50- and 60-dB masker levels for a 2-ms masker-signal interval. The optimum values of k_{thr} at 2 and 6 kHz were -0.15 and -0.05 dB, respectively.

The results of experiment 2 are also reasonably well described by the model (Figs. 5 and 6). The model captures the initial steep growth from absolute threshold in the 6-kHz data, although it underestimates somewhat the signal thresholds in the mid-level region for the 2-ms masker-signal interval. The model also captures the steeper, more linear function at 2 kHz. This is achieved by simply using a high value of k_{thr}: 5.75 dB compared to 3.65 dB at 6 kHz. When k_{thr} is high, the signal threshold is increased so that the signal level enters the compressive region at a lower masker level, leading to a more linear function overall.

When both the signal and the masker are in the linear portion of the basilar-membrane function (levels below about 35 dB) then it might be expected that the slope of the masking function would be unity. However, both the data and the simulations show a slope shallower then unity, albeit steeper than at medium masker levels. The results can be explained in terms of the proximity of absolute threshold, represented by the noise floor in the simulation. When the signal level is close to absolute threshold, a substantial part of the masking is attributable to the fixed-level noise floor, so that changes in masker level have a smaller effect on signal threshold than would be the case if the noise floor were absent. The result is a masking slope shallower than unity even when both masker and signal are in the linear region of the response function.

Both the values of k_{thr} derived from the experiment 2 data are higher than those derived from the experiment 1 data. While it is not unreasonable to attribute this variation solely to the different listeners used in the two experiments, fits to the individual data of the listener (SM) who was common to both experiments revealed that this was not the case. For these fits the noise floor was adjusted to match the listener's absolute thresholds (see above), but otherwise the model was the same as that fitted to the mean data. The resulting values of k_{thr} at 2 and 6 kHz were 0.05 and 0.25 dB for experiment 1, and 5.55 and 4.20 dB for experiment 2. In other words, the results of the fitting procedure suggest that there was some additional performance deficit associated with the stimulus configuration used in experiment 2. The deficit is not simply a consequence of the longer masker having more energy, since this should be taken into account by the integration of the temporal window (Oxenham and Moore, 1994). One possibility is that the long masker used in experiment 2 made it hard to focus attention on the subsequent signal. Moore and Glasberg (1982) provided evidence that temporal uncertainty may affect thresholds in forward masking by demonstrating that performance can be improved by gating a ''cue'' stimulus with the masker or the signal. Another possibility, however, is that the parameters of the temporal window used in the model were inaccurate. To illustrate this idea, the mean 2-kHz data from experiments 1 and 2 were fitted with the time constant for the skirt of the window [the number 29 in Eq. (3)] increased by a factor of 3. The manipulation increases the amount of energy that is integrated from the long forward masker in experiment 2. The optimum values of k_{thr} in the new fits were much more similar between the two experiments (-3.4 and -2.1 dB, respectively), although the overall goodness of fit was worse. It is possible that a temporal-window shape could be found that would enable all the data to be fit reasonably well with a single value of k_{thr}. The window shape used here was derived using a different initial compression and this factor can have a large effect on the estimated shape of the window.

Overall, the results appear to be broadly consistent with the temporal-window model: The mean data can be described using a very small number of free parameters. In all the simulations, the same basilar-membrane function and the same temporal-window function were used. The level of the noise floor was determined by the absolute threshold measurements. The only parameter allowed to vary between the different frequencies and experiments was the efficiency of the detector mechanism, k_{thr}.

The sum-of-squared deviations of the predicted values from the measured values was 79 dB^2 for the 2-kHz data

from experiment 1. When the slope of the compressive part of the basilar membrane function in the model was increased by 50% from 0.16 to 0.24 the best sum-of-squared deviations that could be obtained for this data set increased to 390 dB^2. In other words, the predictions are highly sensitive to the overall form of the basilar membrane function. Since the function used in the simulations was derived from an independent measure of basilar membrane nonlinearity (Oxenham and Plack, 1997), the analysis adds further support to the hypothesis that the nonlinearities in forward masking are the result of basilar-membrane nonlinearities, as opposed to other nonlinearities in the auditory pathway.

F. Modeling results from other studies

As a final test of the general applicability of the model, the data from three other studies of forward masking growth using sinusoidal maskers and signals (Jesteadt *et al.*, 1982, Fig. 1; Kidd and Feth, 1981, Fig. 3; Moore and Glasberg, 1983, Table A1) were fit with the temporal-window model. It was decided to only use data for signal frequencies of 2 kHz and above, since the form of the basilar-membrane function, which is crucial for the success of the model, is not known for lower frequencies. In these three papers the results are quoted in units of dB SL, i.e., level above absolute threshold. For the present purposes the values were converted into dB SPL by adding 15 dB, which was the mean absolute threshold from experiment 2 at 2 kHz. Although the mean absolute thresholds from the individual papers differed slightly from this value, it was hoped that using the same mean threshold might correct for any calibration differences between the studies. For example, if the responses of the headphones at high frequencies varied substantially between the different studies then this may be reflected by differences in the absolute thresholds, and hence differences in the masked thresholds when expressed in dB SPL. The current approach assumes that the ''true'' mean absolute threshold in each case was the same as that measured in experiment 2 at 2 kHz. In effect, the mean absolute thresholds are being used to calibrate the individual experiments.

The stimulus parameters in the three studies were fairly similar. The signal duration was 20 ms in each case. Kidd and Feth used a 300-ms masker and a masker-signal interval of 10 ms. Jesteadt *et al.* also used a 300-ms masker and Moore and Glasberg used a 210-ms masker. The latter two studies used a range of masker-signal intervals.

The data were fitted using the procedure described earlier, with the noise floor fixed at 6 dB (as for the 2-kHz results from experiment 2). A different value of k_{thr} was derived for each set of data. The transformed data and the predictions of the model are illustrated in Fig. 9. It can be seen that the model fits the data fairly well. The biggest discrepancy is for the data of Jesteadt *et al.* where the model underestimates the threshold for the 60-dB masker with a delay of 5 ms. It will be remembered that a similar discrepancy was seen in the predictions of the results from experiment 1. The model also underestimates the thresholds for the 20-dB masker for the 4-kHz data of Moore and Glasberg. It would appear that the noise floor used by the model is too low in this case.

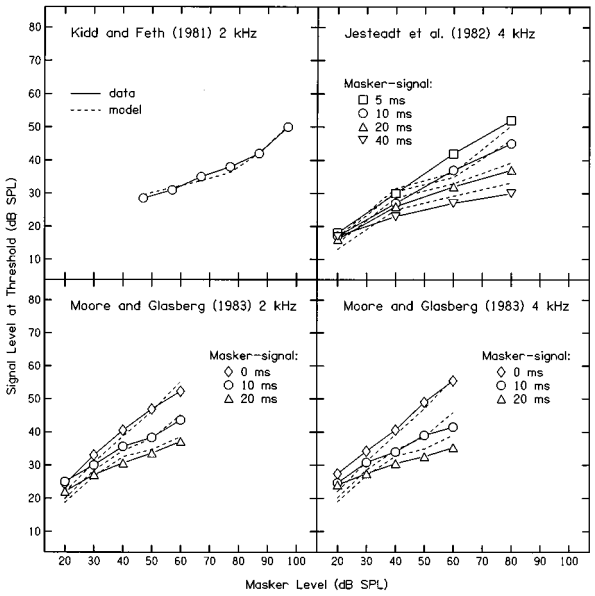

FIG. 9. Mean results from three previous forward-masking studies together with the predictions of the model described in the text.

The values of k_{thr} were -2.25 dB for the data of Kidd and Feth, -0.30 dB for the data of Jesteadt *et al.*, and 2.70 and 2.85 dB for the 2- and 4-kHz data of Moore and Glasberg, respectively. Although k_{thr} does vary between studies, the variability is not great, and the values are broadly consistent with those derived from the present study. There was little variation in k_{thr} with frequency for the data of Moore and Glasberg.

V. GENERAL DISCUSSION

A. Previous forward-masking studies

While (to the authors' knowledge) the present experiments are unique in terms of the stimulus configurations employed (to ensure high signal thresholds while avoiding temporal overlap on the basilar membrane), there are other forward-masking studies that also provide support for the hypothesis presented here. Oxenham and Plack (1997) measured forward-masking functions with a 6-kHz masker and a very brief 6-kHz signal. Because of the large amount of masking produced by the design, the signal level at threshold was roughly equal to masker level. They found a nearly linear masking function at all levels, which is entirely consistent with the model: When the signal and masker are at similar levels they are both compressed (or not compressed) equally, and the masking function is linear, just as in simultaneous masking.

Other studies have generally measured low signal thresholds which are not expected to lead to a dramatic steepening in the growth function. Some of these were examined in Sec. IV F. Using noise maskers, Moore and Glasberg (1983) found a slight steepening in the growth function at high masker levels. Across the different masker-signal intervals they used, the steepening appears to be related to signal level, consistent with the basilar-membrane hypothesis. Similarly, the data of Jesteadt *et al.* (1982), Kidd and

Feth (1981), and Widin and Viemeister (1979) show a steepening in the masking function as masker-signal delay is decreased and signal threshold is increased, although the shortest masker-signal intervals used by these authors may have resulted in a temporal overlap of the masker and signal on the basilar membrane, particularly at low frequencies where the temporal response of the auditory filter is longer (Kiang *et al.*, 1965). Some of the results of Kidd and Feth in particular (see Fig. 5 in their article) are similar in form to those reported here. Other studies (Bacon and Jesteadt, 1987; Kidd and Feth, 1982) have shown a steepening in the growth function as signal threshold is increased due to an increase in masker duration. As described earlier, the classic data of Munson and Gardner (1950), with the more linear low-level region, also offer support for the basilar-membrane account.

Finally, the fact that sensorineural hearing-impaired listeners show more linear forward-masking functions (Oxenham and Moore, 1995, 1997) provides quite strong evidence that the nonlinearities in forward masking are a consequence of healthy, nonlinear, cochlear function.

B. Is the central auditory system intensity linear?

In the present experiments and subsequent analysis it has been shown that a simple model incorporating a compressive function and an intensity integrator can account, quantitatively, for the nonlinear growth of forward masking. Oxenham and Moore (1994) have demonstrated that a very similar approach can account for both the increase in signal threshold with increasing forward-masker duration (Kidd and Feth, 1982) and for the nonlinear additivity of forward and backward masking (Penner, 1980). Both of these phenomena are examples of the nonlinear summation of masker intensity over time. In contrast, hearing-impaired listeners, who are assumed to have more linear basilar-membrane functions, show a *linear* additivity of intensity in these situations (Oxenham and Moore, 1995). Taken together, the results suggest that the principle nonlinearity in temporal masking (at least for the range of masker-signal intervals studied here) is the basilar-membrane response function. While a saturating neural nonlinearity cannot account for the present results, it is conceivable that forward masking is due in part to some form of linear adaptation rather than to a persistence of activity. Unlike the temporal-window model, however, an explanation based on adaptation cannot account for backward masking, or for the additivity of forward and backward masking.

The simple hypothesis described here has important consequences since it implies that, after the compressive basilar membrane, the auditory system may behave *as if* it were intensity linear with respect to temporal masking. Despite the severe nonlinearities involved in neural transduction, synaptic transmission, and neural spike generation, when the auditory system integrates activity over time it seems to use a transform that is equivalent to integrating intensity. This may prove to be a very useful property with regard to modeling normal and impaired hearing. Furthermore, it has been shown that auditory-nerve firing rate is proportional to stimulus intensity after the effects of the basilar membrane have been factored out (Yates *et al.*, 1990). The implication may be that the auditory system integrates by effectively counting neural spikes.

C. Applications of the approach

Oxenham and Plack (1997) measured the masker level needed to forward mask a signal an octave above as a function of signal level. They argued that the function provides a direct estimate of the CF basilar-membrane response to the signal. In a similar way, the present experiments suggest that the growth of on-frequency forward masking provides an estimate of the basilar-membrane response to the masker. The approach assumes that the basilar-membrane response function is approximately linear at low levels, and that threshold corresponds to a constant ''internal'' signal-to-masker ratio. As long as the signal level is within the linear region, then the growth of signal threshold with masker level should be equivalent to the basilar membrane input–output function in response to the masker. The particular stimuli chosen by Munson and Gardner (1950) may be ideal for these type of measurements. They used a 400-ms masker and an 80-ms signal separated by a 20-ms silent interval. The long masker ensured a reasonable amount of masking and the long signal ensured a low absolute threshold and hence a reasonable dynamic range within the low-level region. The 20-ms masker-signal interval was sufficient to avoid an overlap of responses on the basilar membrane. The growth of masking they observed for a 1-kHz masker and signal for masker levels up to about 80 dB SPL is similar to recent physiological measurements of the basilar membrane response at CF.

Unfortunately, the technique of using an on-frequency forward masker requires a large dynamic range so that the masker and the signal can be in clearly distinct regions of the basilar-membrane function. While it may prove to be a useful tool for measuring peripheral nonlinearity in normal listeners, it has little application to the study of impaired hearing.

VI. CONCLUSIONS

The main findings presented in this article can be summarized as follows:

(1) The function relating signal threshold to forward-masker level is shallow for signal levels below about 35 dB SPL, but becomes steeper at higher levels. There is a highly significant positive correlation between signal threshold level and masking function slope, but the correlation between masker level and masking function slope is weaker: Signal level seems to be the principle determinant of masking function slope.
(2) The steepening with level and dependence of slope on signal level are inconsistent with an explanation for the growth of forward masking in terms of saturating neural adaptation.
(3) The data can be described by a simple model involving a nonlinear transfer function (representing the response function of the basilar membrane) and a sliding intensity integrator, or temporal window. The success of the ap-

proach here and elsewhere suggests that the principle nonlinearity in temporal masking may be the basilar-membrane response function, and that subsequent to this the auditory system behaves as if it were linear in the intensity domain.

ACKNOWLEDGMENTS

We are most grateful to Armin Kohlrausch for helpful comments on an earlier version of this manuscript, and to three anonymous reviewers whose careful criticism improved the clarity and content of the article. The first author was supported by a Royal Society University Research Fellowship and the second author by a Wellcome Trust Research Fellowship (0044215/Z/95/Z).

Bacon, S. P. (**1996**). ''Comments on 'Manipulations of the duration and relative onsets of two-tone forward maskers' [J. Acoust. Soc. Am. **94**, 1269–1274 (1993)],'' J. Acoust. Soc. Am. **99**, 3246–3248.

Bacon, S. P., and Jesteadt, W. (**1987**). ''Effects of pure-tone forward masker duration on psychophysical measures of frequency selectivity,'' J. Acoust. Soc. Am. **82**, 1925–1932.

Buus, S., and Florentine, M. (**1985**). ''Gap detection in normal and impaired listeners: The effect of level and frequency,'' in *Time Resolution in Auditory Systems*, edited by A. Michelsen (Springer-Verlag, New York), pp. 159–179.

Duifhuis, H. (**1973**). ''Consequences of peripheral frequency selectivity for nonsimultaneous masking,'' J. Acoust. Soc. Am. **49**, 1155–1162.

Festen, J. M., Houtgast, T., Plomp, R., and Smoorenburg, G. F. (**1977**). ''Relations between interindividual differences of auditory functions,'' in *Psychophysics and Physiology of Hearing*, edited by E. F. Evans and J. P. Wilson (Academic, London).

Fletcher, H. (**1940**). ''Auditory patterns,'' Rev. Mod. Phys. **12**, 47–65.

Green, D. M., and Swets, J. A. (**1966**). *Signal Detection Theory and Psychophysics* (Wiley, New York).

Hawkins, J. E., and Stevens, S. S. (**1950**). ''The masking of pure tones and of speech by white noise,'' J. Acoust. Soc. Am. **22**, 6–13.

Jesteadt, W., Bacon, S. P., and Lehman, J. R. (**1982**). ''Forward masking as a function of frequency, masker level, and signal delay,'' J. Acoust. Soc. Am. **71**, 950–962.

Johnson-Davies, D. B., and Patterson, R. D. (**1979**). ''Psychophysical tuning curves: Restricting the listening band to the signal region,'' J. Acoust. Soc. Am. **65**, 765–770.

Kiang, N. Y.-S., Wantanabe, T., Thomas, E. C., and Clark, L. F. (**1965**). ''Discharge patterns of single fibers in the cat's auditory nerve,'' Res. Monogr. No. 35 (MIT, Cambridge, MA).

Kidd, G., and Feth, L. L. (**1981**). ''Patterns of residual masking,'' Hearing Res. **5**, 49–67.

Kidd, G., and Feth, L. L. (**1982**). ''Effects of masker duration in pure-tone forward masking,'' J. Acoust. Soc. Am. **72**, 1384–1386.

Levitt, H. (**1971**). ''Transformed up-down methods in psychoacoustics,'' J. Acoust. Soc. Am. **49**, 467–477.

McFadden, D., and Yama, M. F. (**1983**). ''Upward shifts in the masking pattern with increasing masker intensity,'' J. Acoust. Soc. Am. **74**, 1185–1189.

Moore, B. C. J. (**1995**). ''Frequency analysis and masking,'' in *Hearing*, edited by B. C. J. Moore (Academic, New York), pp. 161–205.

Moore, B. C. J. (**1996**). *An Introduction to the Psychology of Hearing* (Academic, New York).

Moore, B. C. J., and Glasberg, B. R. (**1982**). ''Contralateral and ipsilateral cueing in forward masking,'' J. Acoust. Soc. Am. **71**, 942–945.

Moore, B. C. J., and Glasberg, B. R. (**1983**). ''Growth of forward masking for sinusoidal and noise maskers as a function of signal delay: Implications for suppression in noise,'' J. Acoust. Soc. Am. **73**, 1249–1259.

Moore, B. C. J., and Glasberg, B. R. (**1988**). ''Gap detection with sinusoids and noise in normal, impaired, and electrically stimulated ears,'' J. Acoust. Soc. Am. **83**, 1093–1101.

Moore, B. C. J., Glasberg, B. R., Plack, C. J., and Biswas, A. K. (**1988**). ''The shape of the ear's temporal window,'' J. Acoust. Soc. Am. **83**, 1102–1116.

Munson, W. A., and Gardner, M. B. (**1950**). ''Loudness patterns—a new approach,'' J. Acoust. Soc. Am. **22**, 177–190.

Murugasu, E., and Russell, I. J. (**1995**). ''Salicylate ototoxicity: The effects on basilar membrane displacement, cochlear microphonics, and neural responses in the basal turn of the guinea pig cochlea,'' Aud. Neurosci. **1**, 139–150.

Nelson, D. A., and Schroder, A. C. (**1997**). ''Linearized response growth inferred from growth-of-masking slopes in ears with cochlear hearing loss,'' J. Acoust. Soc. Am. **101**, 2186–2201.

Oxenham, A. J., and Moore, B. C. J. (**1994**). ''Modeling the additivity of nonsimultaneous masking,'' Hearing Res. **80**, 105–118.

Oxenham, A. J., and Moore, B. C. J. (**1995**). ''Additivity of masking in normally hearing and hearing-impaired subjects,'' J. Acoust. Soc. Am. **98**, 1921–1934.

Oxenham, A. J., and Moore, B. C. J. (**1997**). ''Modeling the effects of peripheral nonlinearity in listeners with normal and impaired hearing,'' in *Modeling Sensorineural Hearing Loss*, edited by W. Jesteadt (Erlbaum, Hillsdale, NJ).

Oxenham, A. J., and Plack, C. J. (**1997**). ''A behavioral measure of basilar-membrane nonlinearity in listeners with normal and impaired hearing,'' J. Acoust. Soc. Am. **101**, 3666–3675.

Penner, M. J. (**1980**). ''The coding of intensity and the interaction of forward and backward masking,'' J. Acoust. Soc. Am. **67**, 608–616.

Penner, M. J., Robinson, C. E., and Green, D. M. (**1972**). ''The critical masking interval,'' J. Acoust. Soc. Am. **52**, 1661–1668.

Peters, R. W., Moore, B. C. J., and Glasberg, B. R. (**1995**). ''Effects of level and frequency on the detection of decrements and increments in sinusoids,'' J. Acoust. Soc. Am. **97**, 3791–3799.

Plack, C. J., and Moore, B. C. J. (**1990**). ''Temporal window shape as a function of frequency and level,'' J. Acoust. Soc. Am. **87**, 2178–2187.

Plomp, R. (**1964**). ''The rate of decay of auditory sensation,'' J. Acoust. Soc. Am. **36**, 277–282.

Relkin, E. M., and Turner, C. W. (**1988**). ''A reexamination of forward masking in the auditory nerve,'' J. Acoust. Soc. Am. **84**, 584–591.

Ruggero, M. A. (**1992**). ''Responses to sound of the basilar membrane of the mammalian cochlea,'' Curr. Op. Neurobiol. **2**, 449–456.

Ruggero, M. A., and Rich, N. C. (**1991**). ''Furosemide alters organ of Corti mechanics: Evidence for feedback of outer hair cells upon the basilar membrane,'' J. Neurosci. **11**, 1057–1067.

Ruggero, M. A., Rich, N. C., and Recio, A. (**1993**). ''Alteration of basilar membrane responses to sound by acoustic overstimulation,'' in *Biophysics of Hair Cell Sensory Systems*, edited by H. Duifhuis, J. W. Horst, P. v. Dijk, and S. M. v. Netten (World Scientific, Singapore), pp. 258–264.

Ruggero, M. A., Rich, N. C., Recio, A., Narayan, S. S., and Robles, L. (**1997**). ''Basilar-membrane responses to tones at the base of the chinchilla cochlea,'' J. Acoust. Soc. Am. **101**, 2151–2163.

Russell, I. J., and Nilsen, K. E. (**1997**). ''The location of the cochlear amplifier: Spatial representation of a single tone on the guinea pig basilar membrane,'' Proc. Natl. Acad. Sci. USA **94**, 2660–2664.

Smith, R. L. (**1977**). ''Short-term adaptation in auditory nerve fibers: Some poststimulatory effects,'' J. Neurophysiol. **40**, 1098–1112.

Smith, R. L. (**1979**). ''Adaptation, saturation, and physiological masking in single auditory-nerve fibers,'' J. Acoust. Soc. Am. **65**, 166–178.

Stelmachowicz, P. G., Lewis, D. E., Larson, L. L., and Jesteadt, W. (**1987**). ''Growth of masking as a measure of response growth in hearing-impaired listeners,'' J. Acoust. Soc. Am. **81**, 1881–1887.

Viemeister, N. F. (**1972**). ''Intensity discrimination of pulsed sinusoids: The effects of filtered noise,'' J. Acoust. Soc. Am. **51**, 1256–1269.

Viemeister, N. F. (**1988**). ''Intensity coding and the dynamic range problem,'' Hearing Res. **34**, 267–274.

Viemeister, N. F. (**1979**). ''Temporal modulation transfer functions based upon modulation thresholds,'' J. Acoust. Soc. Am. **66**, 1364–1380.

Widin, G. P., and Viemeister, N. F. (**1979**). ''Pure-tone forward masking,'' J. Acoust. Soc. Am. **66**, 388–395.

Williams, E. J. (**1959**). ''The comparison of regression variables,'' J. Royal Stat. Soc. (B) **21**, 396–399.

Yates, G. K., Winter, I. M., and Robertson, D. (**1990**). ''Basilar membrane nonlinearity determines auditory nerve rate-intensity functions and cochlear dynamic range,'' Hearing Res. **45**, 203–220.

Zwislocki, J., Pirodda, E., and Rubin, H. (**1959**). ''On some poststimulatory effects at the threshold of audibility,'' J. Acoust. Soc. Am. **31**, 9–14.

Binaural detection as a function of interaural correlation and bandwidth of masking noise: Implications for estimates of spectral resolution

Marcel van der Heijden and Constantine Trahiotis
Surgical Research Center, Department of Surgery (Otolaryngology) and Center for Neurological Sciences, University of Connecticut Health Center, Farmington, Connecticut 06030

(Received 4 August 1997; revised 20 October 1997; accepted 8 November 1997)

Detection thresholds were measured for an antiphasic ($S\pi$) 500-Hz tone masked by a binaural noise, as a function of the bandwidth of the noise. Several values of interaural correlation of the masking noise were used, ranging from -1 to $+1$. The bandwidth dependence of the thresholds showed a pattern consistent with a 100-Hz-wide critical band for most values of interaural correlation, even for those values which resulted in a considerable binaural release of masking. Only when the interaural correlation of the masking noise was very close to, or equal to, unity was the bandwidth dependence of the thresholds in accord with an approximately 300-Hz-wide ''binaural'' critical band measured in previous studies. Our analysis of the data calls into question the commonly stated notion that binaural processing is characterized by a wider critical band than is monaural processing.
 [S0001-4966(98)00303-8]

PACS numbers: 43.66.Pn, 43.66.Dc, 43.66.Ba [DWG]

INTRODUCTION

This investigation concerns estimates of spectral resolution, or critical bandwidths, obtained in binaural psychoacoustical experiments. By binaural, we refer to experiments in which interaural differences of stimuli serve as cues. Such experiments are to be differentiated from ''monaural'' experiments in which interaural differences are either absent or uneffective. It is the case that some estimates of binaural critical bandwidth are essentially equal to their monaural counterparts (e.g., Hall *et al.*, 1983; Kohlrausch, 1988; Kollmeier and Holube, 1992), while other estimates seem to be distinctly larger, sometimes by a factor of 4 or so (Bourbon and Jeffress, 1965; Bourbon, 1966; Cokely and Hall, 1991). In addition, estimates of binaural critical bandwidth are extremely variable and appear to depend on the particular task or paradigm employed (e.g., Hall *et al.*, 1983).

An important difference between monaural and binaural detection thresholds is how they vary as a function of bandwidth of the masker. We will discuss this in terms of the findings of Bourbon (1966), who appears to have conducted the first band-widening experiment utilizing monaural and binaural processing conditions. Bourbon held the spectrum level of the noise constant and employed 500-Hz tones as signals. He found that the detection thresholds in the $NoS\pi$ condition increased 3 dB per doubling of bandwidth of the diotic masker until the masker was about 400 Hz wide. For wider bandwidths of the masker, thresholds remained essentially constant as bandwidth was increased further. In contrast, Bourbon found that thresholds obtained in diotic (NoSo) conditions increased at a rate of about 1.5 dB per doubling of bandwidth and reached asymptote at a bandwidth of approximately 100 Hz. The differences between the two sets of data have led many to assume that the auditory system has two underlying processing mechanisms, one monaural and one binaural, each having its own spectral resolving power.

The purpose of this study was to examine the assumption that monaural and binaural processing are mediated by different degrees of frequency resolution. Our approach was to obtain binaural detection data under a continuum of conditions wherein, at one extreme, only binaural cues could mediate performance while, at the other extreme, only monaural cues could mediate performance. Of particular interest was whether one critical bandwidth would be indicated from data collected in conditions in which both types of processing might be involved.

It will be seen that binaural detection data obtained while varying the interaural correlation and the bandwidth of masking noise do not support the assumption that there are two independent critical bands, one underlying monaural processing and one underlying binaural processing.

I. EXPERIMENT

A. Procedure

Detection of 500-Hz tones presented in the $S\pi$ configuration was measured in the presence of Gaussian noise. The bandwidth of the masking noise, which was centered at 500 Hz, was either 30, 100, 300, or 900 Hz. The overall level of the noise was held constant at 75 dB SPL, independent of bandwidth. Several interaural correlations of the masking noise were employed for each bandwidth.[1] They were 1.000, 0.998, 0.992, 0.968, 0.874, 0.498, and -1.000. Values of interaural correlations that were equally spaced on a linear scale were avoided because such a spacing generally results in highly nonuniform effects on detection thresholds (Robinson and Jeffress, 1963; Grantham and Wightman, 1979). The desired values of interaural correlation were realized by appropriately mixing two independent binaural Gaussian noise

stimuli, one interaurally in phase, the other interaurally out of phase (van der Heijden and Trahiotis, 1997).

The total duration of the signals was 280 ms (including 10-ms, cosine-squared, rise/decay times). The signals were temporally centered within the maskers, which had a total duration of 300 ms, also including 10-ms, cosine-squared, rise/decay times. All stimuli were generated digitally with a sampling rate of 20 kHz via an array processor (Tucker-Davis Technologies AP2). The noises were constructed using inverse FFTs that yielded 32 768 points in the time domain. This yielded a 1.64-s long buffer of noise from which samples were randomly chosen in a manner that provided independent waveforms in each interval of the psychophysical task. A new, independent, buffer was generated for each adaptive run. Tonal signals were generated in the time domain and added to noise waveforms prior to D/A conversion. All stimuli were low-pass filtered at 8.5 kHz (TDT FLT2) and presented via TDH-39 earphones (mounted in MX/41-AR cushions) to listeners seated in single-walled, IAC booths. Four young adults, three male (one being the first author) and one female, with no evidence or history of hearing loss served as listeners. All listeners received extensive practice before the collection of data began.

The stimuli were presented in a 2-cue, 2-alternative, forced-choice task. Each trial consisted of a warning interval (300 ms) and four 300-ms observation intervals separated by 400 ms. Intervals were marked by a visual display on a computer monitor. The first and fourth intervals contained only the masker. The Sπ signal was presented with equal *a priori* probability in either the second or the third interval. The remaining interval, like the first and fourth intervals, contained only the masker. Masker waveforms were randomly chosen both within and across trials. Correct-answer feedback was provided after each response.

The level of the signal was adaptively varied in order to estimate 70.7% correct (Levitt, 1971). The initial step size of the adaptive track was 4 dB and was reduced to 2 dB and to 1 dB after two reversals occurred at each of the former step sizes. A run was terminated after 12 reversals using the 1-dB step size and estimates of threshold were calculated using the average level of the signal across the last 10 reversals. Final thresholds were calculated by averaging four estimates of threshold for each listener and for each stimulus condition.

The ordering of the stimulus conditions was determined by first selecting at random one of the values for the bandwidth of the masking noise. Then an estimate of threshold was obtained after choosing randomly, without replacement, each of the values for the interaural correlation of the masking noise. This procedure was repeated using newly obtained random orders of presentation in order to provide the second estimate of threshold. The final two estimates of thresholds were obtained by visiting the original conditions in reverse (i.e., counterbalanced) order.

B. Results and discussion

Figure 1 contains the thresholds of detection obtained as a function of the bandwidth of the masking noise. The symbols represent thresholds obtained with particular values of interaural correlation, ρ, as indicated by the legend. The data

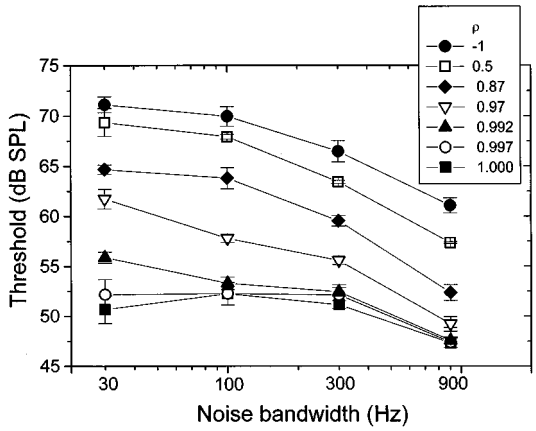

FIG. 1. Detection thresholds of an antiphasic 500-Hz tone as a function of the bandwidth of the masking noise. Different curves correspond to different values of interaural correlation of the masker as indicated in the legend. The data points indicate mean thresholds calculated across four listeners. Error bars indicate ± one standard error of the mean.

points represent means computed across the four listeners' thresholds. The error bars indicate ± one standard error of the mean. Note that the standard errors, and therefore differences across individuals, are very small. Therefore, only the mean values of the thresholds will be presented and discussed.

The reader is reminded that the overall level of the masking noise was held constant as bandwidth was increased from 30 Hz to 900 Hz. Following Fletcher (1940), thresholds obtained with subcritical or critical bandwidths of the masker are expected to be constant (independent of bandwidth), whereas thresholds obtained with supracritical bandwidths of the masker are expected to fall at a rate of 3 dB/oct.

Our description of the data begins with thresholds obtained when $\rho=1$ (solid squares). These are commonly termed No Sπ thresholds. No Sπ thresholds are approximately constant for bandwidths of noise of 30, 100, and 300 Hz. The threshold obtained when the bandwidth of the noise was 900 Hz is about 4 dB lower than the threshold obtained when the bandwidth was 300 Hz. Taken at face value, this decrease in thresholds indicates a binaural critical bandwidth slightly larger than 300 Hz. This agrees with the findings of Bourbon (1966).

Let us now turn to the thresholds obtained when $\rho=-1$ (solid circles). These are commonly termed NπSπ thresholds and reflect the processing of ''monaural'' cues because this stimulus configuration does not provide binaural information useful for detection of the signal. Note that thresholds are 15–20 dB higher than their No Sπ counterparts, indicating masking level differences consistent with those obtained in several other studies using similar stimuli (e.g., Bourbon, 1966; Zurek and Durlach, 1987).

Note that thresholds obtained in this NπSπ condition decreased monotonically with bandwidth and, more importantly, decreased about 9 dB as bandwidth was increased from 100 to 900 Hz. This is what would be expected were the size of the monaural critical bandwidth about 90–100 Hz, a value quite close to that obtained by several other investigators (e.g., Scharf, 1970, Table I page 162).

The patterning of data obtained in these $N\pi S\pi$ and $NoS\pi$ conditions is very much like the patterning of data obtained in previous binaural detection experiments used to infer that different critical bands mediate performance in monaural and binaural processing modes, respectively (e.g., Bourbon, 1966). It should be noted that Bourbon varied bandwidth while maintaining a constant spectrum level of the noise. We varied bandwidth while maintaining a constant overall level. Consequently, the appearances of the plots in the two studies are different even though both sets of data support the same inferences *vis a vis* the relative sizes of putative monaural and binaural critical bands.

We now consider the data obtained with intermediate values of interaural correlation. The reader is reminded that the major purpose of this investigation was to determine if the patterning of thresholds in these conditions is compatible with the assumption that two different critical bandwidths are involved in the detection of the $S\pi$ signals, one monaural and one binaural.

The data displayed in Fig. 1 that were obtained with intermediate values of correlation clearly indicate that thresholds generally increased (i.e., MLDs decreased) as the value of ρ was decreased. We begin with thresholds obtained when ρ was either 0.97 (open inverted triangles), 0.87 (solid diamonds), or 0.5 (open squares). Note that these conditions all resulted in thresholds clearly and substantially *below* those obtained when ρ equaled -1, a condition devoid of binaural cues. This means that detection for those three values of ρ had to be mediated primarily, if not exclusively, by binaural information. The patterning of the data obtained with these three values of ρ is surprising, however, because, like the data obtained in the $N\pi S\pi$ condition, they reflect a *small* ''*monaural-like*,'' critical bandwidth rather than a *large* ''*binaural-like*'' critical bandwidth. Thus a partitioning of the data on the basis of whether the listeners used monaural or binaural cues is not consistent with a partitioning of the data based on whether monaural or binaural critical bands mediate performance. In that sense, to derive monaural and critical bands from the curves relating detection threshold and bandwidth, if not entirely without merit, is highly suspect because of inconsistencies between theoretical expectations and trends in the data.

One could argue, however, that what we have considered to be thresholds mediated by the binaural processor could have been mediated by a *combination* of monaural and binaural processors. It was not intuitively apparent what the patterning of the data would be if detection thresholds depended on a combination of information of monaural and binaural processors. It is possible that,under those conditions, the patterning of the data, as a function of bandwidth, could reflect an appropriate ''mix'' of monaural and binaural critical bands that matched the data.

We felt that this possibility deserved attention and, therefore, went through a laborious exercise to derive, mathematically, estimates of thresholds from that point of view. First, we postulated that there really are separate critical bandwidths characterizing monaural and binaural processing. Next, from this viewpoint, we derived predictions of detection thresholds for the conditions used in our experiment. Finally, we compared these predictions with the data.

Specifically, we assumed: (1) a ''monaural'' processor whose outputs are not affected by binaural information present in the stimulus and (2) a binaural processor whose outputs are solely affected by binaural information present in the stimulus. The only assumptions made regarding the spectral resolution of the two processors are the important assumption that the spectral resolution of the two processors is independent and the trivial assumption that the input of each processor is subject to some stage of filtering. The bandwidth dependence of the two processors was derived from the behavioral data. Within our schema, the relative contribution of the two processors to detectability will depend on the relative impact of spectral filtering in a given task, as compared to the impact of binaural processing in that same task.

The import of spectral resolution depends on the *bandwidth* of the masking noise and the import of binaural information depends on the *interaural correlation* of the masking noise. Detectability using the *monaural* processor is affected by bandwidth and, of course, is unaffected by interaural correlation of the masking noise. Detectability using the *binaural* processor is affected by *both* bandwidth and interaural correlation of the noise and these two factors are assumed to produce essentially independent effects. The assumption of independence is necessarily tied to the straightforward interpretation of curves relating masker bandwidth and detection threshold in terms of critical bands. Any interaction between the effects of bandwidth and correlation would make such an interpretation invalid.

Subsets of the data in Fig. 1 were used to derive how the performances of the supposed monaural and binaural processors depend on bandwidth and interaural correlation of the masking noise. These dependencies were then used to predict performance for the complete set of conditions used in the experiment. We only outline the basic ideas concerning the derivation of the predictions here. Derivations and computational details are presented in the Appendix.

The subset of thresholds obtained when $\rho=-1$ (i.e., the $N\pi S\pi$ thresholds) corresponds to monaural processing only; there is no binaural information in the stimuli. For that reason, the manner in which the $N\pi S\pi$ thresholds depend on noise bandwidth is taken to reflect the spectral resolution of the monaural processor. That is, the spectral resolution of the binaural processor plays no role.

The subset of thresholds obtained when $\rho=+1$ (i.e., the $NoS\pi$ thresholds) represents the ''most binaural'' of the conditions used in our experiment. The MLDs of 15–25 dB obtained with this stimulus assure that the monaural system played very little, or no, role in detection in these conditions. It is therefore reasonable to interpret the bandwidth dependence of the $NoS\pi$ thresholds as essentially reflecting the spectral resolution of the binaural processor. This is precisely how similar data have traditionally been interpreted (e.g., Bourbon, 1966) and such an interpretation is at the heart of this investigation.

The subset of thresholds obtained when the bandwidth of the noise was 30 Hz was used to derive how the performance of the binaural processor depends on the interaural correlation of the noise. A bandwidth of 30 Hz is well below

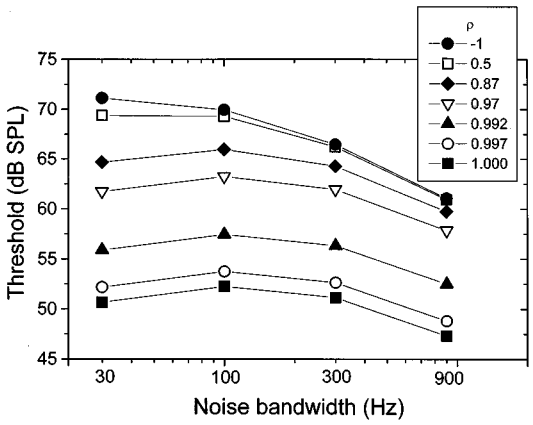

FIG. 2. Predicted thresholds of an antiphasic 500-Hz tone as a function of the bandwidth of the masking noise. The predictions are plotted in the same way as the data of Fig. 1.

both monaural and binaural critical bandwidths. Consequently, the spectral resolution of the two processors plays no role in their respective performances and the spacing of thresholds obtained with this bandwidth isolates effects of interaural correlation on performance. Because the obtained thresholds, by assumption, always reflect the *combined* operation of the monaural and binaural processors, the exclusive effects of interaural correlation on the performance of the binaural processor were derived by eliminating the contribution of the monaural processor from the data.

At this point, the individual performances of the monaural and binaural processor were known as a function of the bandwidth and the interaural correlation of the masker. This permitted us to generate predictions of thresholds based on the combination of information that is available from the two processors. We assumed that information from the (independent) monaural and binaural processors is combined optimally using sums of squares of *d*-primes, as explained in detail in the Appendix.

Figure 2 shows the predictions for all the conditions employed in our experiment. They are plotted in the same way as the data in Fig. 1. The most striking feature in the predictions is that the curves are parallel for values of ρ ranging from $+1.00$ down to 0.87. Further, these predictions all show the same dependence on bandwidth expected from processing via a ''binaural'' critical band. The relatively uniform increases in predicted thresholds with decreasing ρ correspond to losses of binaural information that occur with decorrelation of the noise. This outcome is in accord with the assumption that, for the binaural processor, effects due to interaural decorrelation and bandwidth are independent. A very different pattern of predictions was obtained when $\rho = 0.5$. Those predictions parallel the ones obtained in the $N\pi S\pi$ condition and, therefore, their dependence on bandwidth is ''monaural-like.'' For that stimulus condition, it is evident that the loss of binaural information was so large that contribution from the monaural processor became significant.

The predictions can be generally summarized as follows: with decreasing ρ, thresholds are uniformly elevated with the ''monaural'' thresholds obtained in the $N\pi S\pi$ condition acting as a ''ceiling.'' In addition, as expected, those predicted thresholds that reflect a significant contribution of *binaural* processing (as indicated by sizeable MLDs) show a ''binaural'' (rather than a ''monaural'') bandwidth dependence.

These trends in the predictions differ greatly from the data plotted in Fig. 1 both qualitatively and quantitatively. For example, the predicted curves for $\rho = 0.992$ and $\rho = 0.97$ are parallel to the curve corresponding to the $NoS\pi$ condition ($\rho = +1$). For the data, the curves obtained for $\rho = 0.992$ and $\rho = 0.97$ are not at all parallel to the curves obtained with the $NoS\pi$ stimulus. That is, the data show a clear bandwidth effect for bandwidth *smaller* than the binaural critical band.

In addition, it is generally true that predicted thresholds are *higher* than observed thresholds. The mismatches range from 0.5 to 8.5 dB. Thus the overall patterning and accuracy of the predictions *do not* support the hypothesis that the patterning of binaural detection thresholds, as a function of interaural correlation and bandwidth, stems from a combination of information from independent monaural and binaural processors.

C. Potential explanations and thoughts concerning the bandwidth dependence of binaural detection thresholds

The data in Fig. 1 indicate that the bandwidth dependence of the $NoS\pi$ threshold differs from the bandwidth dependence of thresholds obtained with the other values of interaural correlation of the masker. It appears that, as the interaural correlation of the masker approaches $+1$, thresholds decrease unless and until a certain ''noise floor'' of binaural processing is reached. Such a ''noise floor'' is consistent with ''internal'' or processing noise, a construct often employed in quantitative models of binaural hearing (e.g., Durlach, 1963; Durlach, 1972).

In order to account for the $NoS\pi$ detection data, one can postulate that the limiting internal or processing noise is *bandwidth dependent* in such a way that broadband stimuli are processed less accurately than narrow-band stimuli. This effect would tend to elevate $NoS\pi$ thresholds as the bandwidth of the noise is increased. This elevation would be superimposed on the nominal effects of increasing the bandwidth of the masker leading to an overestimation of the width of the noise that contributes to the masking of the signal (the critical bandwidth).

It should also be mentioned that a bandwidth-dependent accuracy of processing is in line with, and may help account for, data presented by Gabriel and Colburn (1981). Their correlation-discrimination data indicate that sensitivity to changes of interaural correlation, from a value of $+1$, is degraded for bandwidths of noise more than 100 Hz wide. This finding has been especially puzzling because it is the opposite of what would be expected from statistical arguments concerning the effects of sample size on detectability.

We now present some speculations concerning how increasing the bandwidth of our maskers, and binaural stimuli, in general, could, effectively, reduce the accuracy of binaural processing.

Increasing the bandwidth of the masker results in increasing rates of change of interaural differences. To the degree that additional spectral components are ''passed'' by the monaural critical band, performance could be degraded by limitations in the temporal resolution of the binaural processor (i.e., binaural sluggishness, Grantham and Wightman, 1978).

It is also the case that if there were any differences between the ''auditory filters'' of the left and right ears, then the effective interaural correlation of the inputs would be reduced. Even small reductions of interaural correlation result in appreciable degradation of binaural detection (Fig. 1). Left/right differences of auditory filters will primarily act to degrade interaural correlation for the *broader* bands of noise because they are more affected by auditory filtering than are narrower bands of noise.

A third possibility is that increasing masker bandwidth degrades performance because it leads to a reduction of the effective level of the *whole* stimulus (signal plus noise) through the operation of a type of gain control. It is known that efficiency of binaural detection is poorer with relatively low stimulus levels (e.g., McFadden, 1966; Yost, 1988). Consequently, a gain-control mechanism could result in thresholds that are increasingly elevated as bandwidth of the masker is increased. Such elevated thresholds could be mistaken for effects due to a broader underlying critical bandwidth. A gain control that ''kicks in'' at relatively high stimulus levels also could help explain why wider critical bands are more often reported with higher masker levels than with lower masker levels (Bourbon, 1966; Hall *et al.*, 1983).

One other factor that came to mind is ''off-frequency listening.'' With a narrow-band noise stimulus, the information available in neighboring channels not centered on the signal frequency could contribute to the detection of the signal. However, broadening the noise will render this strategy of ''off-frequency listening'' ineffective. This will happen because the signal will be attenuated in the off-frequency channels. Such an attenuation of the signal will result in off-frequency channels having a decreased signal-to-noise ratio, as compared to the signal-to-noise ratio in on-frequency channels. This kind of application of off-frequency listening in binaural detection is mentioned in Hall *et al.* (1983) and is the focus of ongoing investigations conducted by van de Par and his colleagues (1997).

Although off-frequency listening cannot be ruled out, we believe that it cannot provide a satisfactory interpretation of the trends found within our data. We cannot understand why off-frequency listening should not play similar roles in *all* of the stimulus conditions that we tested. Consequently, off-frequency listening, in and of itself, is not able to explain why the bandwidth dependence of $\mathrm{NoS}\pi$ thresholds differs from the bandwidth dependence of all the other thresholds.

II. GENERAL CONCLUSION

We believe that the patterning of binaural detection data obtained while varying both interaural correlation and bandwidth of masking noise is *inconsistent* with the interpretation that separate monaural and binaural critical bands of differing size mediated performance. That belief is based on the qualitative and quantitative arguments presented above. In addition, our results strongly suggest that derivations of *binaural* critical bandwidths from traditional ''band-widening'' experiments using an $\mathrm{NoS}\pi$ stimulus configuration may be invalid. The patterning of detection thresholds versus bandwidth in the $\mathrm{NoS}\pi$ condition is distinctly different from the patterning of detection thresholds versus bandwidth in other conditions that produce large masking differences. In closing, we believe that this investigation has revealed inconsistencies that vitiate common interpretations of binaural detection data *vis a vis* critical bandwidths.

ACKNOWLEDGMENTS

This research was supported by research Grant No. NIH DC-00234. We thank Dr. Les Bernstein for his extensive contributions. We also thank Dr. Armin Kohlrausch and an unidentified reviewer and Dr. Wes Grantham, the responsible Associate Editor, for their helpful comments.

APPENDIX

In this Appendix we present the derivations of the predicted thresholds shown in Fig. 2. It is assumed that detection is accomplished by an optimal combination of information stemming from two independent processors, one monaural and one binaural. This implies that the squared d-prime of the combined system, d'_C equals the sum of the squared d-primes of the individual (monaural and binaural) processors, d'_M and d'_B, respectively:

$$d'^2_C = d'^2_M + d'^2_B. \tag{A1}$$

Our task is to cast this ''combination rule'' in terms of detection thresholds. In order to do that, we assume that, for both processors, d' is related to signal-to-noise ratio (S/N) by a simple exponential rule (Egan *et al.*, 1969):

$$d' = m(\mathrm{S/N})^k, \tag{A2}$$

where m is an efficiency factor. The exponent, k, describes the rate at which d-prime increases with signal-to-noise ratio (for our purposes, the exponent, k, was taken to be unity because that value well-characterized the set of psychometric functions generated from our empirical data, across all stimulus conditions). Given Eq. (A2), we define the signal power at detection threshold, T, as that value of signal power that corresponds to the ''threshold'' value of d-prime. That quantity is indicated by d'_0. Using these terms, the relation between the physical signal power S and d' becomes:

$$d' = d'_0(S/T)^k. \tag{A3}$$

Appropriate substitution of this equation into the ''combination rule'' (A1) yields a relation between the ''combined'' detection threshold, T_C, and the ''individual'' detection thresholds T_M and T_B, which represent the detection thresholds that would result if only the monaural or the binaural processor were available, respectively. After rearrangement and simplification this relation reduces to:

$$(1/T_C)^{2k} = (1/T_M)^{2k} + (1/T_B)^{2k}. \tag{A4}$$

In the following, this equation is used in two ways. First it is used to separate the individual contributions of the monaural and binaural processors. For example, the data indicate that, when ρ was 0.5 and bandwidth was 30 Hz, the threshold was 69.4 dB. The corresponding *monaural* threshold (i.e., the NπSπ threshold obtained with the same bandwidth) was 71.2 dB. These two thresholds, respectively, correspond to the T_C term (the combined threshold) and the T_M (the monaural threshold) in Eq. (A4). Substitution of these thresholds (after conversion to arbitrary power units) into Eq. (A4) leads to the ''unknown,'' T_B. T_B is the threshold that would result if only the binaural processor were present. In our example, with a ρ of 0.5 and bandwidth of 30 Hz, this ''purely binaural'' threshold (after conversion from power units) turns out to be 70.6 dB. As described at the end of this Appendix, the second way in which Eq. (A4) is used is to obtain the combined threshold, T_C, once predictions for T_M and T_B have been derived.

The monaural thresholds, T_M, depend only on bandwidth. Their value is obtained from the ''monaural'' data (thresholds obtained when $\rho=-1$). The binaural thresholds, T_B, as explained in the body of the paper, depend on two parameters: bandwidth (W) and interaural correlation (ρ). Effects of these parameters are assumed to be independent:

$$T_B(W,\rho)=T_B(W,1)\cdot E(\rho), \tag{A5}$$

where $E(\rho)$ expresses the effect of interaural correlation. $E(\rho)$ is derived from the thresholds obtained with a noise bandwidth of 30 Hz. In order to do that, we first extracted the exclusive contribution of the binaural processor from those thresholds by eliminating the contribution of the monaural processor using Eq. (A4). Next, we substituted these ''purely binaural'' thresholds into Eq. (A5) so as to determine $E(\rho)$. Then, having $E(\rho)$, the predictions of ''purely binaural thresholds'' were derived for each of the other bandwidths by substituting $E(\rho)$ and the NoSπ thresholds [again ''corrected'' for monaural processing by means of Eq. (A4)] into Eq. (A5). The final predictions were obtained by combining the purely binaural thresholds, T_B, with the purely monaural thresholds, T_M, with the help of Eq. (A4).

[1]We used values of interaural correlation, which, when transformed to the quantity $10\log\frac{1}{2}(1-\rho)$, yield the numbers $-\infty$, -30, -24, -18, -12, -6, and 0, respectively. The quantity $10\log\frac{1}{2}(1-\rho)$ is what van der Heijden and Trahiotis (1997) term the ''power of the Nπ component'' of a masking noise of arbitrary interaural correlation. As shown in their paper, the power of the Nπ component is the portion of the external noise that, in the contex of optimal binaural processing, is internally effective in masking an Sπ signal. Note that the transformed values of interaural correlation utilized are equally spaced and 6 log units apart (save for the interaural correlation of $+1$ for the NoSπ stimulus that is transformed to a value of $-\infty$).

Bourbon, W. T. (**1966**). ''Effects of bandwidth and level of masking noise on detection of homophasic and antiphasic tonal signals,'' unpublished dissertation, University of Texas, Austin, Texas.

Bourbon, W. T., and Jeffress, L. A. (**1965**). ''Effect of bandwidth of masking noise on detection of homophasic and antiphasic tonal signals,'' J. Acoust. Soc. Am. **37**, 1180(A).

Cokely, J. A., and Hall, J. W. (**1991**). ''Frequency resolution for diotic and dichotic listening conditions compared using the bandlimiting measure and a modified bandlimiting measure,'' J. Acoust. Soc. Am. **89**, 1331–1339.

Durlach, N. I. (**1963**). ''Equalization and cancellation theory of binaural masking-level differences,'' J. Acoust. Soc. Am. **35**, 1206–1218.

Durlach, N. I. (**1972**). ''Binaural signal detection: Equalization and cancellation theory,'' in *Foundations of Modern Auditory Theory*, edited by J. V. Tobias (Academic, New York), Vol. II.

Egan, J. P., Lindner, W. A., and McFadden, D. (**1969**). ''Masking-level differences and the form of the psychometric function,'' Percept. Psychophys. **6**, 209–215.

Fletcher, H. (**1940**). ''Auditory patterns,'' Rev. Mod. Phys. **12**, 47–65.

Gabriel, K. G., and Colburn, H. S. (**1981**). ''Interaural correlation discrimination: I. Bandwidth and level dependence,'' J. Acoust. Soc. Am. **69**, 1394–1401.

Grantham, D. W., and Wightman, F. L. (**1978**). ''Detectability of varying interaural temporal differences,'' J. Acoust. Soc. Am. **63**, 511–523.

Grantham, D. W., and Wightman, F. L. (**1979**). ''Detectability of a pulsed tone in the presence of a masker with time-varying interaural correlation,'' J. Acoust. Soc. Am. **65**, 1509–1517.

Hall, J. W., Tyler, R. S., and Fernandez, M. A. (**1983**). ''Monaural and binaural auditory frequency selectivity resolution measured using band-limited noise and notched-noise masking,'' J. Acoust. Soc. Am. **73**, 894–898.

van der Heijden, M. L., and Trahiotis, C. A. (**1997**). ''A new way to account for binaural detection as a function of interaural noise correlation,'' J. Acoust. Soc. Am. **101**, 1019–1022.

Kohlrausch, A. (**1988**). ''Auditory filter shape derived from binaural masking experiments,'' J. Acoust. Soc. Am. **84**, 573–583.

Kollmeier, B., and Holube, I. (**1992**). ''Auditory filter bandwidths in binaural and monaural listening conditions,'' J. Acoust. Soc. Am. **92**, 1889–1901.

Levitt, H. (**1971**). ''Transformed up–down methods in psychacoustics,'' J. Acoust. Soc. Am. **49**, 467–477.

McFadden, D. (**1968**). ''Masking-level differences determined with and without interaural disparities in masker intensity,'' J. Acoust. Soc. Am. **44**, 212–223.

Par, S. van de (**1997**). Personal communication.

Robinson, D. E., and Jeffress, L. A. (**1963**). ''Effect of varying the interaural noise correlation on the detectability of tone signals,'' J. Acoust. Soc. Am. **35**, 1947–1952.

Scharf, B. (**1970**). ''Critical bands,'' in *Foundations of Modern Auditory Theory*, edited by J. V. Tobias (Academic, New York), Vol. I, pp. 159–202.

Yost, W. A. (**1988**). ''The masking level difference and overall masker level: Restating the internal noise hypothesis,'' J. Acoust. Soc. Am. **83**, 1517–1521.

Zurek, P. M., and Durlach, N. I. (**1987**). ''Masker-bandwidth dependence in homophasic and antiphasic tone detection,'' J. Acoust. Soc. Am. **81**, 459–464.

A dynamic biomechanical model for neural control of speech production

Vittorio Sanguineti[a)]
Dipartimento di Informatica, Sistemistica e Telematica, Università di Genova, Via Opera Pia 13, 16145 Genova, Italy

Rafael Laboissière
Institut de la Communication Parlée, 46, av. Felix Viallet, F-38031 Grenoble, France

David J. Ostry
McGill University, 1205, Dr. Penfield Avenue, Montréal, Quebec H3A 1B1, Canada

(Received 23 April 1997; accepted for publication 2 October 1997)

A model of the midsagittal plane motion of the tongue, jaw, hyoid bone, and larynx is presented, based on the λ version of equilibrium point hypothesis. The model includes muscle properties and realistic geometrical arrangement of muscles, modeled neural inputs and reflexes, and dynamics of soft tissue and bony structures. The focus is on the organization of control signals underlying vocal tract motions and on the dynamic behavior of articulators. A number of muscle synergies or ''basic motions'' of the system are identified. In particular, it is shown that systematic sources of variation in an x-ray data base of midsagittal vocal tract motions can be accounted for, at the muscle level, with six independent commands, each corresponding to a direction of articulator motion. There are two commands for the jaw (corresponding to sagittal plane jaw rotation and jaw protrusion), one command controlling larynx height, and three commands for the tongue (corresponding to forward and backward motion of the tongue body, arching and flattening of the tongue dorsum, and motion of the tongue tip). It is suggested that all movements of the system can be approximated as linear combinations of such basic motions. In other words, individual movements and sequences of movements can be accounted for by a simple additive control model. The dynamics of individual commands are also assessed. It is shown that the dynamic effects are not neglectable in speechlike movements because of the different dynamic behaviors of soft and bony structures. © *1998 Acoustical Society of America.* [S0001-4966(98)04801-2]

PACS numbers: 43.70.Aj, 43.70.Bk [AL]

INTRODUCTION

In this paper, we report on a midsagittal plane model of the motion of the tongue, jaw, hyoid bone, and larynx. We describe both the development of the biomechanical model and, in the context of the model, we consider the way control signals to muscles are organized to produce multi-articulator motion. We consider in addition the effects of articulator dynamics on the motions of the tongue and jaw. We will report analyses which suggest that the control of speech movements can be accounted for by a small set of independent commands. We will also suggest that to understand the control of orofacial motions, realistic physical and biomechanical models as well as modeled control signals are needed. Initial versions of the jaw and hyoid model (Laboissière *et al.*, 1996) and the tongue model have been reported previously (Sanguineti *et al.*, 1997).

Most modeling work to date has focused on individual orofacial structures, and models of the face and lips (Müller *et al.*, 1984; Terzopoulos and Waters, 1990; Lee *et al.*, 1995), tongue (Perkell, 1974; Kiritani *et al.*, 1976; Hashimoto and Suga, 1986; Wilhelms-Tricarico, 1995; Sanguineti *et al.*, 1997; Payan and Perrier, 1997), jaw (Baragar and Osborn, 1984; Throckmorton and Throckmorton, 1985a, 1985b; Otten, 1987; van Eijden *et al.*, 1988; Laboissière *et al.*, 1996), hyoid bone, and larynx have been proposed. The models include graphical animations, models of muscle mechanical properties, and static force estimation. More complete models, which include muscle properties, dynamics, and simulated neural mechanisms have been reported (Otten, 1987; Laboissière *et al.*, 1996; Sanguineti *et al.*, 1997; Payan and Perrier, 1997).

Although the majority of modeling studies deal with individual articulators, many problems in orofacial research can only be addressed in terms of the combined action of multiple articulators. These problems include the basis of coordination in speech and mastication, the complexity of interarticulator coupling at the level of the control signals, and the determinants of interarticulator coarticulation (Ostry *et al.*, 1996). The presence of vocal tract mechanical interactions underscores the need for multi-articulator models. It is essential to account for the interactions between soft tissue and bony structures in order to have accurate prediction of vocal tract motion (Honda *et al.*, 1994; Sanguineti *et al.*, 1997).

The model presented here is based on the λ version of the equilibrium point hypothesis of motor control. The model

[a)]Mailing address: Department of Physiology, Northwestern University Medical School, 303 East Chicago Ave., Chicago, IL 60611. Electronic mail: sangui@parker.physio.nwu.edu

includes muscle properties and realistic muscle geometry, modeled neural inputs and reflexes, and articulator dynamics. As in our jaw and hyoid simulations (Laboissière *et al.*, 1996) and our recent model of the tongue (Sanguineti *et al.*, 1997), we have assumed that control signals to individual muscles are coordinated to enable the nervous system to produce a number of independent motions.

In the present paper, we consider a number of problems relating to the identification of the control signals underlying orofacial movements and how they are coordinated to produce multi-articulator motion. We first perform a model-based factor analysis of the Strasbourg x-ray data base (Bothorel *et al.*, 1986) in order to identify the basic motions of the system and to infer their associated commands. This relates control in the model to empirical data, addresses the extent to which control signals are organized in a low-dimensional control space, and provides a basis for comparison with purely geometric articulatory models.

We examine the extent to which the effects of commands which we derive are additive. Additivity removes the need for context specificity in central commands. Purely geometric articulatory models such as that proposed by Maeda (1990) assume that the effect of the individual articulators on vocal tract shape is additive. However, this may not necessarily be the case given the complex mechanics of the orofacial system. To the extent that additivity in control signals can be demonstrated in the present model, it suggests that the predictions related to additivity in geometric models may still hold.

We focus as well on the predicted dynamics of motions associated with the individual commands. This is motivated by the observation that speech involves relatively synchronous articulator motions and therefore complex command patterns may be necessary if the dynamics of individual articulators differ.

I. THE MODEL

Jaw motions in the model have two degrees of freedom—orientation in the sagittal plane and translation along the articular surface of the temporal bone; also see Laboissière *et al.* (1996); the hyoid has three degrees of freedom, horizontal and vertical position and sagittal plane orientation. The larynx is modeled as a point mass with a single degree of freedom—vertical position, which has the largest kinematic effect. Midsagittal plane tongue movements are modeled, as described below, using finite element techniques (Schwarz, 1984).

Previous studies have suggested that interactions between the individual vocal tract structures—between hard and soft tissues (Sanguineti *et al.*, 1997) and between the larynx and the tongue or the hyoid bone (Honda *et al.*, 1994)—are significant in determining the global mechanical behavior of the system. For these reasons, care has been taken in modeling the interaction between individual structures, by deriving the global equations of motion for this system (see the Appendix). This ensures that mechanical interactions including reaction forces and velocity-dependent forces are accounted for.

The model geometry (see Fig. 1) is that of a young female speaker, for whom an x-ray data set of midsagittal plane vocal tract images is available (Bothorel *et al.*, 1986). The modeled jaw position and orientation at occlusion were estimated by superimposing a normative model of the jaw (Scheideman *et al.*, 1980) on the x-ray data. The tongue surface contour, the hyoid position and orientation, and the larynx height were likewise obtained from the x-ray data set.

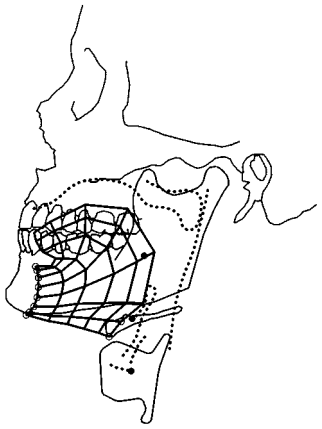

FIG. 1. Biomechanical model of the mid-sagittal section of the oral cavity. Circles indicate the nodes of the tongue mesh which are fixed with respect to either the jaw or the hyoid bone. Dots indicate the centers of mass of the jaw, the hyoid bone, and the larynx. Dotted lines indicate the approximate boundaries of the oral cavity. Thick lines correspond to the tongue mesh.

A. The tongue

The tongue is the main determinant of vocal tract shape. It has been modeled as a viscoelastic continuum whose behavior has been assumed, as a first approximation, to be linear and isotropic. The coefficient of elasticity, or Young's Modulus, E, is that of passive muscle tissue (Duck, 1990)—$E=6.2$ kPa. A Poisson's ratio of $\nu=0.49$ is used (Hashimoto and Suga, 1986). This approximates conservation of volume at a microscopic level. (By microscopic level, we mean here the limit behavior for an infinitely small discretization of the continuous tongue tissue. As our FE (finite element) discretization is quite coarse, volume conservation is not completely guaranteed in our model.) We assumed that there is no deformation in the transverse direction, and that the X and Y components of deformation only depend on position on the XY plane (this corresponds to the hypothesis of plane strain).

Tongue mass has been assumed to be $m_t=0.1$ kg. Its density has been taken to be that of muscle tissue, which is $d_t=1040$ kg/m^3 (Duck, 1990). This is slightly greater than the density of water.

The interaction of the tongue and the palate has also been accounted for. Contact forces are assumed to be elastic (depending of the level of ''penetration'' of each node into the palate), and directed normally. It is thus assumed that there is zero friction.

By applying standard finite element (FE) techniques (Schwarz, 1984), the tongue configuration has been approximated by a discrete mesh (Fig. 1), whose configuration is completely specified by the vector $\mathbf{x}$ that includes the X and Y coordinates of each of the nodes in the mesh. We used a

6×8 mesh to describe the tongue, thus yielding a 96-dimensional configuration vector **x**. However, some of the nodes are fixed with respect to either the jaw or the hyoid bone (see the Appendix and Fig. 1 for details).

B. Jaw, hyoid bone, and larynx

The geometrical arrangement of jaw and hyoid bone is based on Laboissière *et al.* (1996). The jaw is represented as a rigid body that can rotate about the temporomandibular joint and translate along the articular surface of the temporal bone. The shape of this surface has been described by a third-order polynomial, $y=a_1x^3+a_2x^2$ (see Laboissière *et al.*, 1996). Thus, if x_0 is the X coordinate of the center of rotation of the jaw, the corresponding Y coordinate is $y_0=y(x_0)$. Accordingly, jaw configuration $\mathbf{q}_j$ is a vector with two components: x_0, and the orientation angle α_j, relative to the occlusal plane. As in Laboissière *et al.* (1996), jaw mass and inertia have been estimated to be $m_j=1$ kg and $I_j=0.0042$ kg m^2.

The hyoid bone has been modeled as a free rigid body, characterized by its position and orientation. In particular, hyoid configuration is described by the vector $\mathbf{q}_h=[\mathbf{x}_{Gh}^T\alpha_h]^T$, where $\mathbf{x}_{Gh}$ represents the X and Y coordinates of the center of mass, and α_h is the orientation. Hyoid mass has been assumed to be $m_h=0.1$ kg; its corresponding moment of inertia (relative to the center of mass) has been calculated to be $I_h=2.8\times10^{-5}$ kg m^2. This value has been estimated by approximating the hyoid bone as a U-shaped object of midsagittal length of 3 cm and radius 1.5 cm, with uniformly distributed mass.

The larynx is a complex musculo-cartilagenous structure whose main function is to control vocal fold configuration. Only the thyroid cartilage is attached to the bony structures of our model, namely the hyoid bone and the sternum. As we assume that the muscles originating on these bony structures insert on the thyroid at a single point, the larynx is modeled as a point mass with $m_l=0.1$ kg. We assume also that it can only translate vertically, which is a good approximation for our x-ray data. In summary, the height of the larynx is assumed to correspond to the observed height of the vocal folds as determined from the x-ray tracings (see Sec. II).

Other degrees of freedom of the laryngeal system, related to the motion of the vocal folds and to the relative motions of the cricoid and the thyroid cartilage, have not been modelled. Although horizontal thyroid motion is important acoustically (Honda *et al.*, 1994), its amplitude is small. It has been omitted since the primary focus here is on biomechanics rather than acoustics.

C. Muscle properties and neural control

The λ model assumes that neural control signals produce voluntary movement by acting on motoneurone (MN) membrane potentials. The effect at the level of the muscle is to change the threshold muscle length (λ) at which α MN recruitment begins (Feldman *et al.*, 1990). By changing the values of λ's over time, the musculoskeletal system may be caused to move to a new equilibrium position.

This mechanism is modeled by assuming that muscle activation (A) develops in proportion to the difference between λ and a reflex component, depending on actual muscle length (l) and its rate of change:

$$A(t)=[l(t-d)-\lambda(t)+\mu\dot{l}(t-d)]^+, \tag{1}$$

where $[x]^+=\max[x,0]$ and d is reflex delay. The parameter μ characterizes the dependence of the muscle's threshold length on velocity and provides damping due to proprioceptive feedback. Damping due to muscle intrinsic properties is also included (see below). For simplicity, we have assumed that μ is the same for all muscles and constant (0.07 s). The value for μ was set on the basis of simulation studies carried out with a multi-joint arm model (Gribble *et al.*, 1998)—the value of μ was adjusted so that simulated joint viscosity in statics matched empirically obtained estimates for this variable (Tsuji *et al.*, 1995, see Gribble *et al.*, 1998 for details). We have used a reflex delay, d, of 15 ms for all muscles. The value was based on observed delays in human jaw openers and closer muscles (Lamarre and Lund, 1975; Ostry *et al.*, 1997b).

It should be noted that the model assumes that afferent input associated with muscle length and velocity is combined with descending input to α MNs to yield muscle activation. Position- and velocity-dependent afferent input in limb muscles arises from muscle spindle receptors. However, several orofacial muscles including the jaw opener, anterior digastric, and the jaw protruder, lateral pterygoid, have few if any muscle spindles. We have nevertheless recently demonstrated both phasic and tonic stretch reflexes in human jaw opener muscles (Ostry *et al.*, 1997). This suggests that these reflexes are not necessarily mediated exclusively by muscle spindle afferents. In tongue muscles, stretch responses have also been reported (see Sanguineti *et al.*, 1997 for review).

Increases in muscle activation due to changes in λ are associated with MN recruitment and increases in firing rate and muscle force. Active force, M, has been modeled as an exponential function of the form

$$M=\rho[\exp(cA)-1], \tag{2}$$

which has been suggested by the experimental studies of Feldman and Orlovsky (1972) and accounts for both the intrinsic and reflex components of active force. The parameter ρ is assumed to vary with muscle force generating ability, and may be estimated from each muscle's maximum force capability. In particular, a value of ρ equal to 25% of maximum muscle force has been found (see Gribble *et al.*, 1997 for details) to be consistent with the static stiffness observed in the human arm. Here c is a form parameter, related to the MN recruitment gradient, and is assumed to be equal for all muscles (see Laboissière *et al.*, 1996). The exponential relationship between force and muscle length is consistent with the size principle (Henneman *et al.*, 1965), that is, as the difference between the actual and threshold muscle length increases, progressively larger motor units are recruited and larger increments in force are obtained.

We also included in the model (see Fig. 2 for a schematic diagram) the dependence of muscle force on muscle lengthening or shortening velocity (Joyce and Rack, 1969),

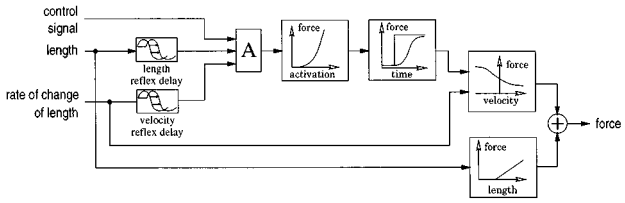

FIG. 2. Block diagram of the muscle model (see text for details).

the graded development of force over time (Huxley, 1957), and the passive elastic stiffness of muscle (Feldman and Orlovsky, 1972); see Laboissière *et al.* (1996) for details. The force–velocity relation was modeled with a sigmoidal function (Laboissière *et al.*, 1996) which was obtained by fitting data for cat soleus muscle. Separate parameter estimates were obtained for tongue muscles and for other orofacial muscles. The parameters were selected to match empirically reported force-velocity functions for fast (tibialis) and slow (soleus) muscle, respectively (Wells, 1965). The gradual development of muscle force was modeled using a second-order low pass filtering of active muscle force, M. The filter was critically damped and had a time constant of 15 ms which led to an asymptotic response to a step input in about 90 ms (Miller, 1991). Passive muscle stiffness was assumed to vary with physiological cross-section area.

D. The muscle system

The muscles of the oral cavity have a complex geometrical arrangement. The individual fibers within a muscle may have very different lines of action and their paths may be curved. Thus, the directions of muscle action may not be simply approximated as a straight line.

In the present model, we have assumed that some muscles are made of a discrete number of ''macro-fibers'' that are formed by division of a distributed muscle into a number of spatially segregated compartments. The number of compartments used for each muscle depends upon the shape of the muscle and in particular upon its directions of action. The geometric arrangement of each macro-fiber is approximated by a series of line segments that connect the nodes of the tongue mesh or connect the tongue mesh to specific points on the bony structures. Each macro-fiber is treated as a single entity. Its length and velocity are defined as the sum of the lengths and velocities of the individual segments.

The geometrical arrangement of modeled muscles is based on anatomical descriptions (Miyawaki, 1974; Dickson and Maue-Dickson, 1982; McDevitt, 1989) and on previous modeling work (Laboissère *et al.*, 1996; Sanguineti *et al.*, 1997). In the tongue model, we have included three extrinsic muscles, genioglossus (GG), hyoglossus (HG), and styloglossus (SG), and three intrinsic muscles, superior longitudinalis (SL), inferior longitudinalis (IL), and verticalis (VE). Muscles acting on the jaw include a jaw opener (OP), which models the effects of geniohyoid and the anterior belly of digastric, a jaw closer (CL), which represents the effects of the masseter and medial pterygoid, anterior and posterior temporalis (AT and PT), and superior and inferior lateral

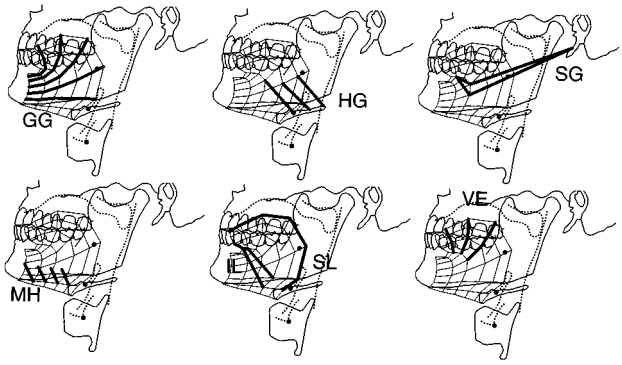

FIG. 3. The geometric arrangement of tongue muscles. Top, from left to right: genioglossus (GG, 5 macro-fibers); hyoglossus (HG, 3 macro-fibers); styloglossus (SG, 2 macro-fibers). Bottom: mylohyoid (MH, 4 macro-fibers), superior (SL, 6 macro-fibers) and inferior (IL, 2 macro-fibers) longitudinalis, verticalis (VE, 3 macro-fibers). Thick lines represent the macro-fibers that were used to model each muscle.

pterygoid (SP and IP). The mylohyoid (MH) originates on the jaw and inserts onto the tendinous median raphé and on the hyoid bone. In the present model, we focused on its role in forming the tongue floor, and accordingly its attachments to the hyoid bone are not included. However, its effect on the hyoid bone is taken into account by the finite element modeling of the tongue floor. In other words, despite the fact that no connection is explicitly modeled between MH and the hyoid, the model accounts correctly for the effect of MH contraction, i.e., raising and protrusion of the hyoid bone.

Additional muscles that act on the hyoid bone and larynx include a hyoid retractor (RE), which models the effects of the posterior belly of digastric and the stylohyoid, the thyrohyoid (TH), the sternohyoid (SH), and the sternothyroid (ST). It should be noted that by modeling the larynx as a point mass, the attachments of muscles to the larynx had to be restricted to this point. This results in some inaccuracy in the lines of action of TH and ST. The musculo-skeletal geometry of the model is depicted in Figs. 3 and 4.

Individual λ's are associated with each muscle and each macro-fiber in the model. The latter point requires comment. Relatively little is known about the neural organization of

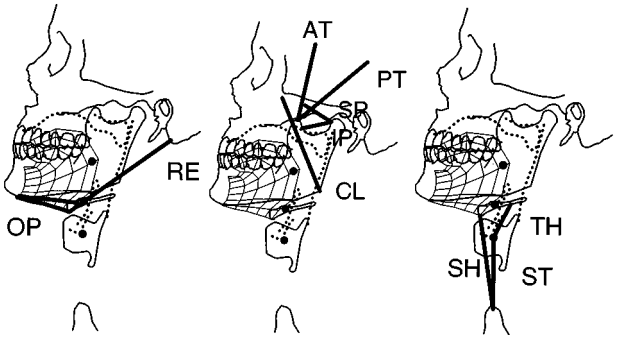

FIG. 4. The geometric arrangement of jaw, hyoid, and laryngeal muscles. Left: opener (OP, 2 macro-fibers) and retractor (RE). Middle: closer (CL), anterior (AT), and posterior (PT) temporalis, superior (SP) and inferior (IP) pterygoid. Right: thyrohyoid (TH), sternohyoid (SH), and sternothyroid (ST). Thick lines represent the macro-fibers that were used to model each muscle.

TABLE I. The estimated muscle parameters.

Muscle	CSA (mm^2)	f_m^{max} (N)	ρ (N)	K_p (N/m)
Genioglossus (GG)	309	67.8	13.6	0
Hyoglossus (HG)	296	65.1	13.0	0
Styloglossus (SG)	110	24.2	4.84	0
Mylohyoid (MH)	186	40.9	8.18	32.2
Superior longitudinalis (SL)	65	14.3	2.86	0
Inferior longitudinalis (IL)	88	19.4	3.88	0
Verticalis (VE)	66	14.5	2.90	0
Jaw opener (OP)		115	23.0	34.7
Jaw closer (CL)		639	128	192
Retractor (RE)		86.3	17.6	23.1
Superior pterygoid (SP)		126	25.2	38.0
Inferior pterygoid (IP)		252	50.4	76.0
Anterior temporalis (AT)		362	72.6	109
Posterior temporalis (PT)		197	39.4	59.4
Thyrohyoid (TH)		28.7	5.74	8.65
Sternohyoid (SH)		28.7	5.74	8.65
Sternothyroid (ST)		28.7	5.74	8.65

control signals in distributed muscle structures such as the tongue. There is some evidence in the context of empirical electromyographic data of functional partitioning of the genioglossus muscle (Baer *et al.*, 1988) and some suggestion that the superior longitudinalis may not behave as a single muscle (Dickson and Maue-Dickson, 1982). However, our decision, in the present context to associate a separate λ with each macro-fiber, arises as a compromise. Since the dimensionality of control to individual muscles is essentially unknown, by providing individual λ's to each macro-fiber we are able to analyze the dimensionality of control on the basis of the patterns of covariation of λ's which arise in fitting the tongue model to the x-ray data base (see Sec. II for details).

The maximum forces for tongue muscles, f_m^{max}, have been determined from estimates of their cross-sectional areas on the basis of anatomic atlases (see Sanguineti *et al.*, 1997 for details), and by assuming a maximum specific tension of 22 N/mm^2, reported in Wilhelms-Tricarico (1995) for the geniohyoid muscle. In the case of jaw and hyoid muscles, the values of maximum force and passive stiffness, K_p, reported by Laboissière *et al.* (1996) were used (see Table I).

E. Organization of control signals

A number of additional assumptions may be made concerning the organization of control signals to individual muscles. The λ model proposes that central control variables can be interpreted as geometric quantities, namely, threshold muscle lengths. In the case of multiple muscle systems, because of their springlike behavior, the set of λ's associated with individual muscles (or muscle compartments) specify an equilibrium configuration for the system. This does not mean that the individual λ's are independently controlled. Indeed, control is presumably organized into a relatively small number of different combinations of λ changes, which we will refer to as ''commands.'' Commands in effect define muscle synergies that correspond to elementary or primitive motor behaviors. All possible movements may result from the combination of these basic motions.

How can such muscle synergies or basic motions be identified for the jaw–hyoid–tongue–larynx system? A first possible criterion is that of independent motions. In the case of jaw motion, the observation of a variety of different patterns of coordination between jaw protrusion and rotation has suggested (Ostry and Munhall, 1994) that in speech its mechanical degrees of freedom can be controlled independently. Moreover, the data of Westbury (1988) suggest that the observed patterns of motion of the hyoid bone are largely uncorrelated with jaw movements. On the other hand, simulation studies (Honda *et al.*, 1994) have demonstrated a close mechanical coupling between the hyoid bone, the larynx and the tongue. These findings suggest that, although the hyoid–larynx system and the jaw are not mechanically independent, these structures are controlled by different muscle synergies.

A second criterion is that of independent muscle groups. Öhman (1967) and Perkell (1969) have suggested that the tongue system consists of a number of separately controlled muscle groups. In particular, it appears that the tongue tip can move independently of the tongue body. However, unlike jaw movements, there is no *a priori* basis for the identification of functional degrees of freedom of tongue motions (Maeda, 1990; Sanguineti *et al.*, 1997).

Our approach to this identification problem is essentially data driven, as will be described in Sec. II. Central commands (i.e., synergies of muscle λ's) are inferred from an empirical data set using a numerical optimization technique and a factor analysis. The obtained results reflect the variability of vocal tract configurations present in the corpus.

II. RESULTS

In this section, we focus on the organization of control and its relation to the mechanical properties of the system and the anatomical arrangement of muscles. In Sec. II A, we identify the basic motions of the system and their associated commands. In Sec. II B, we examine the related issue of whether the individual compartments of the spatially distributed muscles of the tongue are independently controlled. In

Sec. II C, we explore the extent to which summation applies to the system's basic motions. Finally, in Sec. II D we present simulations of the dynamic behavior of the system in response to simple rhythmic commands that act on individual articulators. These results provide initial predictions concerning the dynamic behavior of the tongue/jaw system.

A. Determination of independent commands

Based on empirical evidence which shows that the behavior of orofacial structures may each be characterized by a small number of independent motions (see Sec. II E), we have used the Strasbourg x-ray data set (Bothorel *et al.*, 1986) in conjunction with our model to identify these basic motions, and to infer the mapping between their associated commands and the control signals to individual muscles.

Consistent with experimental evidence and with related simulation studies (Laboissière *et al.*, 1996; Sanguineti *et al.*, 1997), each of these motions can be represented as a different combination of changes to muscle λ's. One combination of λ's results in an increase of the global stiffness of the system, without accompanying motion.

We will show that systematic sources of variation in the x-ray data can be accounted for with six independent commands, each corresponding to a direction of articulator motion, or more specifically, to a linear combination of control signals to individual muscles (λ's). There are two commands for the jaw corresponding to sagittal plane jaw rotation and jaw protrusion, one command controlling larynx height, and three commands for the tongue corresponding to forward and backward motion of the tongue body, arching and flattening of the tongue dorsum, and motion of the tongue tip.

The Strasbourg data base consists of 519 frames of midsagittal plane x-ray images of a single female speaker (subject number 3, PB) during the continuous production of ten short sentences, pronounced in a normal-to-fast rate. The sentences were chosen to be representative of the phonetic variation of French. The sampling frequency for x-ray images is 50 Hz. The midsagittal tongue contours and those of the bony structures were estimated by hand tracing from the x-ray lateral views.

For each x-ray image, we ran a constrained optimization procedure, in order to determine the set of individual muscle λ's and the corresponding model configuration. The constraints were the requirements that the system be in mechanical equilibrium, and that the nodes on the upper side of the tongue mesh lay on the empirically observed tongue contour. The observed positions and orientations of jaw, hyoid, and larynx were also extracted from the x-ray image, thus determining the positions of the associated model articulators. The criterion to be minimized was the level of cocontraction, which was defined as the squared distance between actual muscle lengths and λ's:

$$C(\mathbf{Q},\boldsymbol{\lambda}) = [\mathbf{l}(\mathbf{Q}) - \boldsymbol{\lambda}]^T \cdot [\mathbf{l}(\mathbf{Q}) - \boldsymbol{\lambda}], \tag{3}$$

where $\mathbf{Q}$ is the system configuration (see the Appendix). The quantities $\mathbf{l}(\mathbf{Q})$ and $\boldsymbol{\lambda}$ are, respectively, the vectors of lengths and λ's for each of the muscles and macro-fibers in the model.

The procedure resulted in a set of λ's that can be interpreted as the representation, in the space of muscle control signals, of the variety of configurations that the system can assume during speech movements.

Commands associated with the motion of individual articulators were derived from the above set of muscle λ's by means of a two-step factor analysis [see Maeda (1990) for a similar approach]. First, the contributions of jaw rotation, jaw protrusion, and larynx elevation to muscle λ's were derived by linear regression. This step was motivated by empirical observations which suggest that the nervous system controls jaw and larynx motion in terms of their mechanical degrees of freedom (Ostry and Munhall, 1994; Laboissière *et al.*, 1996). In total, 15.8% of variance in the set of muscle λ's (derived from the x-ray data base) was attributable to the motion of the jaw and larynx.

The contributions of tongue motion to muscle λ's were derived by carrying out a principal components analysis in the subspace of muscle λ's that were not correlated with jaw and larynx motions. In fact, principal components in λ space define a number of muscle groups that act independently and have orthogonal directions of action (Sanguineti *et al.*, 1997). This is a property of the geometric arrangement of tongue muscles that is implied in the conjecture (Öhman, 1967; Perkell, 1969) that tongue motions are determined by a small number of independently controlled components, or articulators.

Each of the factors or regression coefficients described above is a vector specifying a direction of change in λ space. The application of the vector corresponds to a shift of the equilibrium configuration of the system. Movements of different amplitude can be obtained by varying the magnitude of the vector. This vector thus defines a ''command'' for the system.

The factor analysis led to the identification of three commands for tongue motion: tongue dorsum arching/flattening, tongue tip raising/lowering, and tongue body front/back. The tongue movement commands accounted for 40.5% of the total variance in the set of muscle λ's derived from the x-ray data. Note that while the tongue, jaw, and laryngeal commands taken together account for only 57% of the total variance in λ space, the residual factors have almost no observable effects on the posture or configuration of the system.

In addition to the commands which result in tongue, jaw, and larynx motion, a command controlling the global level of muscle cocontraction could be defined. The cocontraction command was determined by finding, in the space of the residual factors (the factors not already included in the set of jaw, tongue, and larynx commands), a direction of λ change which resulted in an increase in force in each of the modeled muscles. By changing the magnitude of the cocontraction command, global stiffness may be increased without movement.

Figure 5 shows the effects of the above commands. Each panel shows three tracings corresponding to the effects of a single command on the configuration of the system. All panels show a neutral configuration (corresponding to the statistical mean of all λ's) plus two additional tracings representing ± 4 times the standard deviation of the factor associated

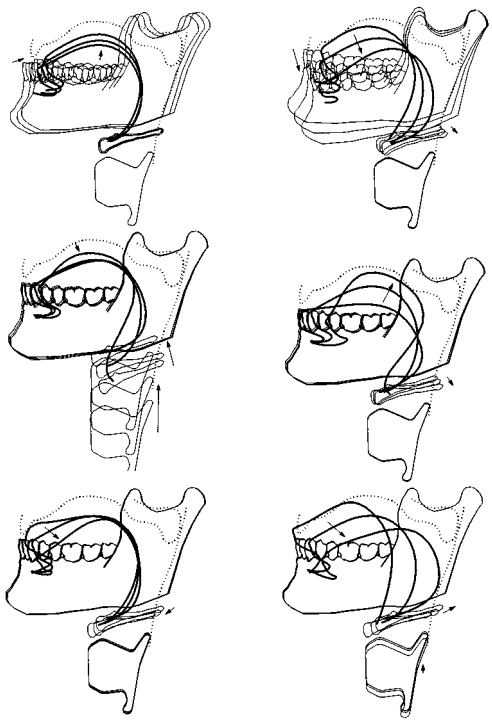

FIG. 5. Effect of individual commands on vocal tract configuration. Top, from left to right: jaw protrusion, jaw rotation. Middle: larynx height, tongue dorsum. Bottom: tongue tip, tongue body. Arrows indicate the motion of each structure; arrow lengths reflect actual movement magnitude. The penetration of the palate in the lower right-hand panel is a consequence of modeling contacts with elastic forces.

with that command. These outer tracings are the extreme positions for each command.

The top two panels of Fig. 5 show the results of the jaw commands. The protrusion command produces, in addition to jaw protrusion and retraction, small but noticeable changes in tongue elevation (in particular during retraction) but little movement of the hyoid bone. The command for jaw rotation affects both jaw orientation and tongue position. Both lowering and raising appear to have an active effect on tongue postures. In both cases greater movements of the tongue blade are observed than would be expected if the tongue simply moved passively with the jaw. Such a synergistic action of jaw and tongue—when the jaw opens, the tongue is actively lowered—can be observed in this particular x-ray data set, and is therefore reflected in our factor analysis.

The middle panel of Fig. 5 (left-hand side) shows the effect of the larynx height command. Changes in larynx height are observed to affect hyoid vertical position but have little effect on hyoid orientation or upon the positions of the jaw and tongue.

The three tongue commands affect the tongue and hyoid, and, in one case, the elevation of the larynx. The tongue dorsum command produces arching and flattening of the tongue, the tongue tip commands produce raising and lowering of the tip with almost no effect on the posterior profile of the tongue, and the tongue body command advances and retracts the tongue.

It should be noted that the set of the commands derived in this fashion are primarily dependent upon the geometrical arrangement of muscles and not upon the cost function used to do the optimization. This was shown by repeating the procedure using a different cost function. One cost function, shown in Eq. (3), determines the set of λ's which minimize the average squared distances between actual muscle lengths and λ's. A second cost function determines λ's which minimize the average squared muscle force (normalized for muscle cross-sectional area). While both cost functions can be interpreted as measures of cocontraction, they are not linearly related and therefore they should yield different values of the optimal λ's.

Differences between the resulting commands and their effects were assessed quantitatively by computing the angles between each of the six tongue, jaw, and larynx commands, obtained by using the two different cost functions. The angles ranged from 14 to 42 deg, with an average 29.5 deg (in the space of λ changes). Moreover, the commands derived with the second cost function resulted in vocal tract configurations that were comparable to those shown in Fig. 5. This was assessed quantitatively in terms of the positions of three selected nodes on the tongue surface, namely (from anterior to posterior) tongue tip (TT), tongue blade (TB), and tongue dorsum (TD) (see also Sec. II C). The directions of motion of these points as a result of the application of each of the commands (ranging from -4 to 4 as in Fig. 5) were compared for the two different cost functions. The average angle between the directions of motion was found to be 18 deg.

In summary, the muscle λ's for tongue, jaw, hyoid, and larynx muscles were derived by fitting the model to the Strasbourg x-ray data base. Commands corresponding to basic motions of the tongue, jaw, and larynx were obtained using factor analysis. The commands are associated with maximally independent sources of λ variation and may be interpreted as corresponding to the muscle synergies which underlie motions of this system.

B. Functional independence of muscle compartments

No direct empirical evidence exists on which to identify the organization of control signals to spatially distributed muscles. In the present section, we attempt to infer this organization in the context of the tongue on the basis of pattern of variation of tongue muscle λ's.

The spatially distributed nature of tongue muscles was represented by a number of macro-fibers which were treated as if they were independently controlled. This leads to an increase in the number of degrees of freedom of the tongue. However, systematic patterns of correlation were found among the set of λ's for the macro-fibers associated with individual muscles. To assess the dependence among the λ's of the macro-fibers of each muscle, we carried out, for each muscle separately, a principal components analysis on the set of λ's associated with all macro-fibers for that muscle (for the entire data set). Figure 6 gives the cumulated proportion of variance accounted for by the principal components of each muscle. The figure shows that 75% or more of the variance in λ's in extrinsic tongue muscles can be accounted for by two factors for genioglossus, one each for styloglossus

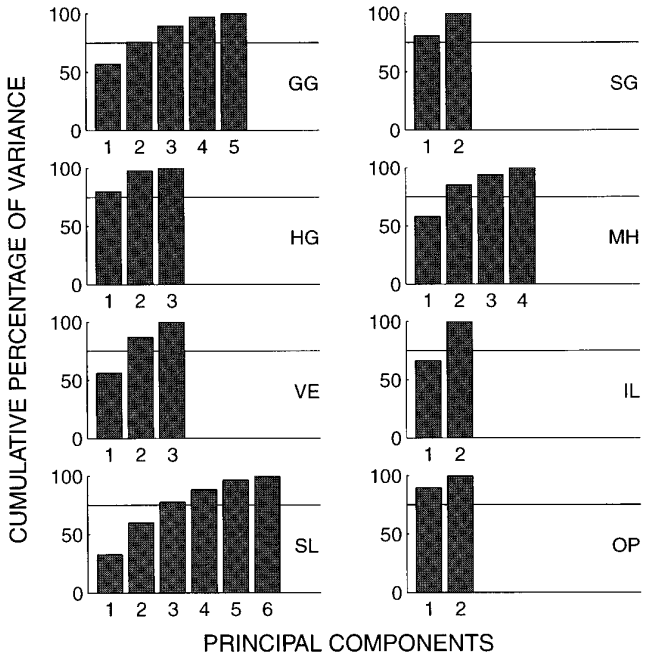

FIG. 6. Cumulative percentage of variance accounted for by the principal components associated with the macro-fibers of each tongue muscle (75% of total variance is shown with solid lines). See text for muscle labels.

and hyoglossus and two for mylohyoid. For the intrinsic tongue muscles, two factors are required for verticalis and inferior longitudinalis and three for superior longitudinalis. One factor is sufficient to account for control signals to the jaw opener muscles (anterior digastric and geniohyoid). Thus, the analysis suggests that control signals to the spatially distributed fibers which comprise each of the muscles of the tongue may themselves be grouped into a small number of independent commands.

C. Additivity of commands

Articulatory models sometimes assume that the effects of commands are additive (for example, Maeda, 1990). However, it is unclear whether this assumption holds in systems that have complex geometry and mechanics.

In the case of the present model, predicted changes to articulator positions resulting from the commands derived above were found to be largely independent of the initial vocal tract configuration. That is, when a given command was applied at different initial vocal tract configurations, similar changes in configuration were produced.

System behavior was characterized in terms of the positions of three selected nodes on the tongue surface, namely tongue tip (TT), tongue blade (TB), and tongue dorsum (TD), and of the tip of the mandibular incisor (MN). Changes of their positions were assessed as a result of the application of each of the commands. The procedure was repeated for a wide range of initial vocal tract configurations.

Figure 7 shows, for each command, the displacement of nodes as arrows connecting the initial to final positions. In some cases, the arrows overlap and thus the number of lines may appear to differ.

The top two panels show the jaw protrusion and jaw rotation commands, the middle panels are for larynx height and for the tongue dorsum command, and the bottom panels give the tongue tip and tongue body commands. The critical aspect of each figure is the behavior of the node most closely associated with a particular command. Hence, with the exception of the larynx command which results in little movement of the tongue and jaw, each of the other commands produces movements of its associated node that change little in direction as a result of changes in the configuration of the tongue and jaw.

We have assessed the extent to which the individual commands (except for the larynx command) produce movements of comparable direction in their associated nodes (MN for jaw commands, TD for tongue dorsum, TT for tongue tip, TB for tongue body) when initiated from different vocal tract configurations. For each of the tongue and jaw commands, the standard deviation of the direction of node movements, shown in Fig. 7, was computed about their respective population means. The resulting standard deviations of command directions with changes in vocal tract configuration were protrusion command, 3 deg, jaw rotation command 0.8 deg, tongue dorsum command, 6.5 deg, tongue tip command, 1.9 deg, and tongue body command 3.8 deg.

These findings are consistent with the idea that the effects of different commands are additive, in terms of positioning of points on the tongue surface inside the oral cavity. Since a given command has essentially the same effect in terms of postural change for any workspace configuration, this means that a postural change which results from a combination of the above commands can be interpreted as the combination of the changes elicited by the individual commands.

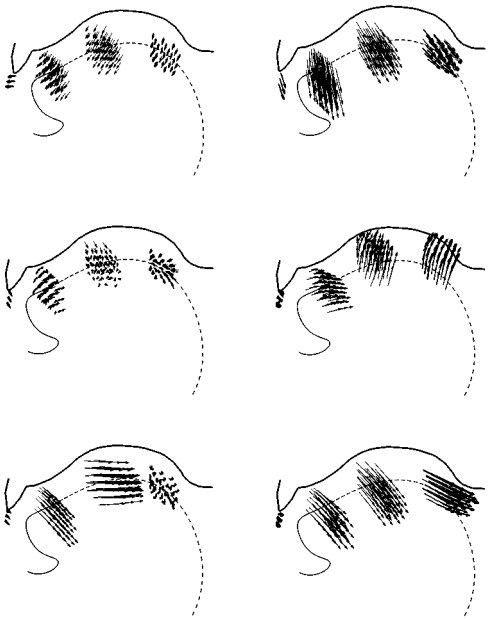

FIG. 7. Effect of each individual command in different initial configurations. Top, from left to right: jaw protrusion, jaw rotation. Middle: larynx height, tongue dorsum. Bottom: tongue tip, tongue body. In each panel, the displacement of selected nodes (from left to right, MN, TT, TB, and TD) is represented by arrows connecting their initial and final positions.

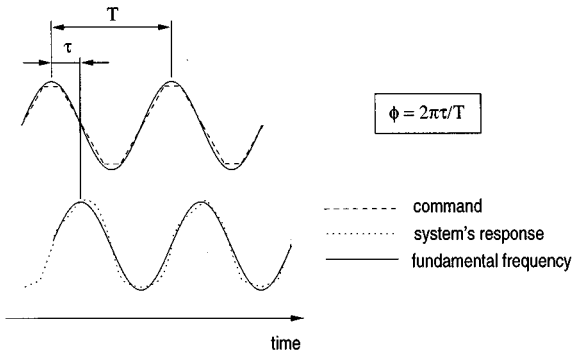

FIG. 8. The phase lag of the fundamental Fourier component of the response with respect to the control signal.

D. Dynamics of articulators

Aspects of the dynamic behavior of the system have been assessed by examining simulated movements which result from simple periodic commands. Simulations were carried out for each of the jaw, larynx, and tongue commands individually. The tests used cyclic (stepwise linear) control signals at different frequencies (namely, 1, 3, and 5 Hz) and, to test system nonlinearity, at different amplitudes (two and three times the standard deviation; see Fig. 5). The simulations were repeated at different levels of cocontraction: 0%, i.e., no cocontraction, and 25% (a level of 100% corresponding to the situation in which at least one of the muscles has reached its maximum force capability). The above commands and levels of cocontraction are assumed to be representative of the working conditions of the system during speech.

System behavior was characterized in terms of the time-varying trajectories of MN, TT, TB, and TD. For both the *X* and *Y* coordinates of these nodes, we estimated amplitude and phase lag of the fundamental Fourier component (corresponding to the frequency of the command); see Fig. 8. In the case of jaw rotation and protrusion, tongue motion can be decomposed into a ''passive'' component due to jaw movement, and an ''active'' tongue deformation. In this situation, the estimation procedure was carried out for tongue movements relative to the jaw.

This procedure allows us not only to assess the general dynamic behavior of the system, but also to identify differences in the dynamics of individual structures (e.g., jaw and tongue, i.e., bony and soft structures), and also of different portions of the tongue. It may be predicted, for instance, that the tongue can move faster than the jaw due to its smaller mass, and also to the larger proportions of ''fast'' fiber types that are found in tongue muscles. Figure 9 summarizes the phenomena observed in the simulations, averaged across command amplitudes and levels of cocontraction. As expected, in jaw rotation movements the vertical motion of MN displays a phase lag that is much larger than that observed in tongue nodes; see Fig. 9 (top).

The vertical motion of tongue nodes results from the combined effect of a ''slow'' component, due to jaw rotation, and a ''fast'' component, due to active tongue lowering. The relative contributions of these ''slow'' and ''fast'' components to the overall tongue motion can be assessed by estimating the motion of each tongue node with respect to the jaw, and its corresponding phase lag. The phase lag of this ''fast'' component of tongue motion is comparable to those observed in pure tongue movements.

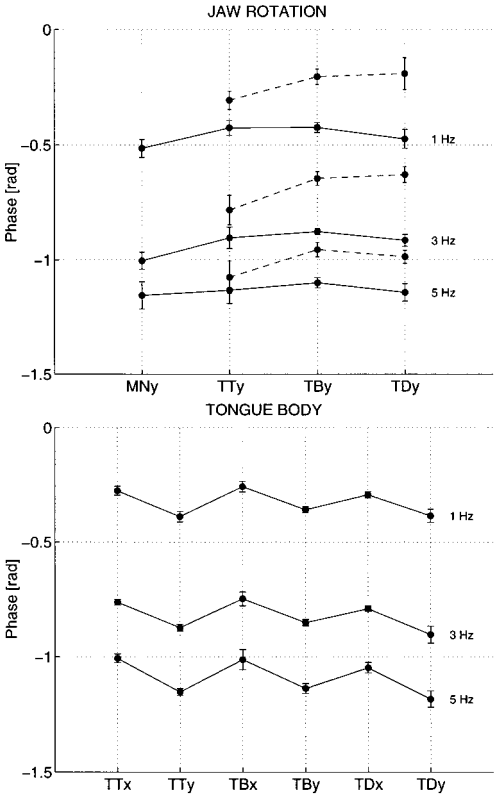

FIG. 9. Averaged phase lags observed in motions of jaw and tongue nodes, during jaw rotation (top) and tongue body (bottom) movements. Continuous lines represent absolute motions, dashed lines (top panel) indicate motion of tongue nodes relative to the jaw. Error bars reflect variability across command amplitudes and levels of cocontraction. The three families of lines correspond to the three different command frequencies; from top to bottom, 1, 3, and 5 Hz.

The simulations also show that, regardless of the particular command, horizontal tongue movements tend to be faster than the vertical ones. This effect can be observed in Fig. 9 (bottom), which shows movements resulting from the tongue body command. The pattern observed here may be due to mechanics of muscular hydrostats, for which movements along the main dimension (the long axis) are larger and faster than the transverse ones (Chiel *et al.*, 1992). Changes in the level of cocontraction result in small but observable modifications of the phase lags of the observed movements. Figure 10 shows this effect in the typical case of jaw rotation. In particular, it can be observed that increases in the level of cocontraction result in a smaller phase lag, thus suggesting a decrease in the apparent ''damping'' of the system. This is consistent with the notion that cocontraction controls the stiffness of the entire system.

III. DISCUSSION

We have presented a physiological model of the motions of the tongue, jaw, larynx, and hyoid bone, based on the λ version of the equilibrium point hypothesis.

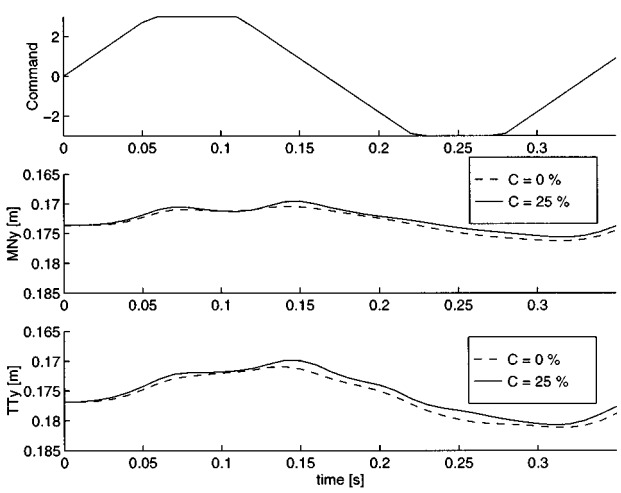

FIG. 10. Effect of cocontraction on vertical motion of mandibular incisor and tongue tip, in the case of jaw rotation commands of amplitude 3 S.D. and frequency of 3 Hz.

Using empirical x-ray data in conjunction with the model, we have shown that the motions of these articulators can be accounted for by a small number of independent commands in λ space. For the jaw and larynx, we identified commands that are related to the mechanical degrees of freedom of these articulators. For the tongue, the commands correspond to different combinations of control signals to individual muscles which produce maximally independent motions. We have shown that these commands have essentially similar effects regardless of the vocal tract configuration and therefore any movement can be expressed as the composition of such independent commands or basic motions.

The idea that control is organized in terms of coordinated commands or muscle synergies derives in part from observations that, in the jaw, independent motions may be produced in the jaw's mechanical degrees of freedom (Ostry and Munhall, 1994; Ostry *et al.*, 1997a). Data on tongue motions are also consistent with the idea that muscles act synergistically to produce the basic or elementary vocal tract motions. Öhman (1967), for example, suggested that there was independent motion of different parts of the tongue depending on phonetic context. Harshman *et al.* (1977) and Maeda (1990) have shown that tongue shapes and tongue motions can be partitioned into statistically independent components.

Accordingly, in the context of the model, we explored a hypothesis of organization of control signals that is based on the following assumptions: (i) for the jaw, rotation and protrusion/retraction movements are separately controlled; (ii) vertical motions of the larynx–hyoid complex can be carried out independently of jaw movements; (iii) the tongue can move independently of the bony parts; and (iv) the basic motions of the tongue reflect the geometric arrangement of tongue muscles.

In particular, consistent with related approaches (Maeda, 1990), we have found that tongue movements can be accounted for by three independent commands. While the effects of the commands are similar to those reported by Maeda and Honda (1994), the effects arise in different ways. Whereas in previous work functional subdivisions in tongue motion have been associated with disjoint subsets of tongue muscles (Maeda and Honda, 1994; Perkell, 1969), in the present model, the control signals to all tongue muscles contribute to the production of each of the basic motions (also see Smith, 1992).

Moreover, consistent with previous findings, our correlation analyses suggest that the tongue muscles which contribute to these synergies may not act as unitary structures. Thus, we have been able to observe a functional subdivision, based on groupings of λ change, of genioglossus and mylohoid, each of which contributes to tongue movements in two different ways. It should be noted, however, that the subdivisions observed in the pattern of control signals to tongue muscles does not appear to have direct parallels to anatomical subdivisions (see, for example, Baer *et al.*, 1988).

A particularly interesting and indeed somewhat surprising finding was that individual tongue and jaw command changes result in similar changes in tongue and jaw position regardless of the initial configuration of the system. The result is surprising since with changes to vocal tract configurations, the distribution of forces associated with commands defined in terms of λ shifts might have varied considerably and led to significant variation in the resulting movements. The observed invariance in the effects of these commands presumably occurs as a result of compensations which arise at the geometrical level. A consequence of invariance is that it permits an exceedingly simple organization of commands (namely, an additive model) in which computations are unneeded to account for changes in workspace geometry (Laboissière *et al.*, 1996; Ostry *et al.*, 1996).

Few models of orofacial motion have explicitly included dynamics—see Laboissière *et al.* (1996) for the jaw–hyoid system, and Wilhelms-Tricarico (1995) and Payan and Perrier (1997) for the tongue. Those which have assume that the individual structures are mechanically independent. In the present paper, we show that consideration of the dynamic interaction of vocal tract bony and soft structures is needed to correctly account for orofacial dynamics. Failure to account for these structures results in a model which does not account for forces acting on the tongue and as a result leads to incorrect predictions of tongue movements and achieved tongue positions in behaviors such as speech. Thus, the jaw is not simply a moving frame of reference for the tongue but jaw motion imparts force to the tongue which changes its shape. In the case of the larynx, changes in tongue shape have been shown to be capable of producing changes in pitch due to the mechanical coupling of the tongue and the larynx (Honda *et al.*, 1994).

The ''simplicity'' of the central commands that the nervous system must provide is a major problem in understanding how speech production is planned. In the case of human arm movements, it has been suggested (Gribble *et al.*, 1997) that muscle viscoelastic properties and the peripheral neural circuitry have a built-in capability to ''compensate'' for dynamic effects such as inertia and Coriolis/centrifugal forces, a feature that is captured by the λ model. Such a compensatory ability of muscles and reflexes suggests that the nervous

system may not need precise information about the dynamics of the body and of the external world in order to plan movements. Hence, ''central'' control commands may be ''simple'' in the sense that they only need to account for the kinematic aspects of the desired movement.

In the neural control of speech production, this feature would be particularly desirable because of the mechanical complexity of the system and of the performance requirements of speech movements (speed, precision, need for an accurate synchronization of motions of different articulators). However, the differences in jaw and tongue dynamics, which emerge from our simulations, appear to challenge the hypothesis of command ''simplicity,'' in particular with regards to their coordination.

In fact, orofacial movements in speech must satisfy precise timing constraints. For instance, what makes voiced and voiceless stops perceptually distinguishable is the difference in the timing between glottal opening and release of occlusion. If the individual structures differ in their dynamic behavior, such a synchronization can only be achieved at the planning level, by means of some form of prediction of system dynamics. For instance, it has been suggested (Perrier *et al.*, 1996) that the amplitude of equilibrium shifts for the different commands may be varied to maintain the basic temporal synchrony of movement. More specifically, the commands related with slower structures may overshoot the spatial endpoint of the movement. Or, the different structures could well be controlled by commands that have a completely different temporal structure, and synchrony of movements could emerge as the result of mechanical interactions. It must be noted, however, that these and other hypotheses can only be addressed by interpreting empirical observations by means of a realistic physiological model that accounts for the mechanical interaction among the different structures.

ACKNOWLEDGMENTS

This research was supported by National Institutes of Health Grant No. DC-00594 from the National Institute on Deafness and Other Communication Disorders—USA, NSERC—Canada, FCAR—Québec, and by a postdoctoral fellowship to VS from the University of Genova (Italy). The authors thank the Institut de Phonetique de Strasbourg (IPS) for providing the data set, and Arturo Galvan for the port of the data to MATLAB. We are also indebted to the reviewers (K. Honda, E. Saltzman, and an anonymous reviewer) for their detailed comments and suggestions.

APPENDIX: DERIVATION OF THE EQUATIONS OF MOTION

The dynamic behavior of the whole system is completely specified by its global kinetic and potential energy function.

In the case of the jaw, kinetic energy is given by $T_j = \frac{1}{2}\dot{\mathbf{q}}_j^T \cdot M_j(\mathbf{q}_j) \cdot \dot{\mathbf{q}}_j$, where

$$M_j(\mathbf{q}_j) = \begin{bmatrix} m_j[1 + y'(x_0)^2] & m_j[1 y'(x_0) \cdot R(\alpha_j - \theta + \pi/2) \cdot \hat{\mathbf{x}}_{Gj}] \\ m_j[1 y'(x_0)] \cdot R(\alpha_j - \theta + \pi/2) \cdot \hat{\mathbf{x}}_{Gj} & I_j \end{bmatrix} \tag{A1}$$

is the matrix of inertia of the jaw; m_j and I_j are, respectively, jaw mass and its moment of inertial with respect to the center of the condyle, whereas $\hat{\mathbf{x}}_{Gj}$ is the position of the center of mass relative to the center of the condyle, θ is jaw orientation at occlusion (constant, estimated from the x-ray data), and $y'(x_0) = dy(x)/dx|_{x_0}$.

The matrix $R(\alpha)$ represents a rotation of an angle α. The only contribution to potential energy is that of gravity and, therefore, supposing that gravity is directed vertically:

$$V_j = m_j g[x_0 \cos \theta + y(x_0) \sin \theta + \hat{x}_{Gj} \cos \alpha_j + \hat{y}_{Gj} \sin \alpha_j],$$

where $\hat{x}_{Gj}$ and $\hat{y}_{Gj}$ are the components of $\hat{\mathbf{x}}_{Gj}$.

In the case of the hyoid bone, kinetic energy is defined as $T_h = \frac{1}{2}\dot{\mathbf{q}}_h^T \cdot M_h \cdot \dot{\mathbf{q}}_h$, where the matrix of inertia, diagonal, is

$$M_h = \begin{bmatrix} m_h & 0 & 0 \\ 0 & m_h & 0 \\ 0 & 0 & I_h \end{bmatrix}, \tag{A2}$$

whereas the potential energy is given by $V_h = m_h g y_{Gh}$.

Finally, the kinetic and potential energy functions for the larynx are simply expressed, respectively, by $T_t = 1/2 m_l \dot{y}_l^2$ and $V_l = m_l g y_l$.

As regards the tongue, kinetic energy is $T_t = 1/2 d_t \int \dot{\mathbf{u}}^T \cdot \dot{\mathbf{u}}\, dV$, where $\mathbf{u}$ is the deformation field and d_t is tongue density, assumed uniform; potential energy is $V_t = 1/2 \int \boldsymbol{\sigma}^T \cdot \boldsymbol{\varepsilon}\, dV - d_t \mathbf{g}^T \cdot \int \mathbf{u}\, dV$, where $\boldsymbol{\sigma}$ and $\boldsymbol{\varepsilon}$ are, respectively, the stress and the strain fields; $\mathbf{g}$ is the constant gravity acceleration.

Strain is the gradient of the deformation field, i.e.,

$$\boldsymbol{\varepsilon} = \begin{bmatrix} \frac{\partial}{\partial x} & 0 \\ 0 & \frac{\partial}{\partial y} \\ \frac{\partial}{\partial x} & \frac{\partial}{\partial y} \end{bmatrix} \mathbf{u}. \tag{A3}$$

Stress is related to strain through the Hooke's law that, in the case of the plane strain hypothesis, is defined as

$$\boldsymbol{\sigma} = \frac{E}{(1+\nu)(1-2\nu)} \begin{bmatrix} 1-\nu & \nu & 0 \\ \nu & 1-\nu & 0 \\ 0 & 0 & (1-2\nu)/2 \end{bmatrix} \boldsymbol{\varepsilon}. \tag{A4}$$

After application of FE techniques, the above expressions for T_t and V_t can be rewritten as $T_t = 1/2\dot{\mathbf{x}}^T \cdot M_t \cdot \dot{\mathbf{x}}$ and $V_t = 1/2(\mathbf{x}-\mathbf{x}_0)^T \cdot K_t \cdot (\mathbf{x}-\mathbf{x}_0) + \mathbf{f}_g^T \cdot \mathbf{x}$, where $\mathbf{x}_0$ is the rest, undeformed configuration and the constant matrices M_t and K_t are, respectively, tongue inertia and stiffness. The constant vector $\mathbf{f}_g$ represents the distribution of tongue weight on the nodes of the mesh.

Some of the nodes of the tongue mesh are fixed with respect to the jaw or the hyoid bone; we will suppose that nodes are ordered so that we can write: $\mathbf{x} = [\mathbf{x}_t^T \mathbf{x}_j(\mathbf{q}_j)^T \mathbf{x}_h(\mathbf{q}_h)^T]^T$.

The equations of motion that describe the dynamics of the jaw-hyoid-tongue-larynx system can be obtained from the global Lagrangian function, $L = T - V$, where $T = T_t + T_j + T_h + T_l$ and $V = V_t + V_j + V_h + V_l$ are, respectively, the total kinetic and potential energy. We can define a global configuration vector for the jaw–hyoid–tongue–larynx system: $\mathbf{Q} = [\mathbf{x}_t^T \mathbf{q}_j^T \mathbf{q}_h^T y_l]^T$.

The global kinetic energy can be rewritten as $T = 1/2\dot{\mathbf{Q}}^T \cdot M(\mathbf{Q}) \cdot \dot{\mathbf{Q}}$, where the ''global'' matrix of inertia, $M(\mathbf{Q})$, is now defined as

$$M(\mathbf{Q}) = \begin{bmatrix} 0 & 0 & 0 & 0 \\ 0 & M_j(\mathbf{q}_j) & 0 & 0 \\ 0 & 0 & M_h & 0 \\ 0 & 0 & 0 & m_l \end{bmatrix} + J^T(\mathbf{Q}) M_t J(\mathbf{Q}) \tag{A5}$$

and the ''global'' jacobian matrix, $J(\mathbf{Q})$, is given by

$$J(\mathbf{Q}) = \begin{bmatrix} I_t & 0 & 0 & 0 \\ 0 & J_j(\mathbf{q}_j) & 0 & 0 \\ 0 & 0 & J_h(\mathbf{q}_h) & 0 \end{bmatrix}, \tag{A6}$$

where I_t is an unit matrix, $J_j(\mathbf{q}_j) = \partial \mathbf{x}_j / \partial \mathbf{q}_j$, and $J_h(\mathbf{q}_h) = \partial \mathbf{x}_h / \partial \mathbf{q}_h$. Similarly, the ''global'' potential energy can be rewritten as $V = V(\mathbf{Q})$.

It is now possible to derive the global equation of motion for the jaw–hyoid–tongue–larynx system, which has the form

$$M(\mathbf{Q}) \cdot \ddot{\mathbf{Q}} + C(\mathbf{Q}, \dot{\mathbf{Q}}) \cdot \dot{\mathbf{Q}} = \mathbf{G}(\mathbf{Q}) + J_l(\mathbf{Q})^T \cdot \mathbf{f}_m(\mathbf{l}, \boldsymbol{\lambda}), \tag{A7}$$

where

$$C_{ij}(\mathbf{Q}, \dot{\mathbf{Q}}) = \Sigma_k \partial M_{ij} / \partial Q_k \cdot \dot{Q}_k - 1/2 \Sigma_k \partial M_{kj} / \partial Q_i \cdot \dot{Q}_k$$

defines a velocity-dependent interaction term, and $J_L(\mathbf{Q}) = \partial \mathbf{l} / \partial \mathbf{Q}$ is the Jacobian of the transformation between the configuration $\mathbf{Q}$ and the vector $\mathbf{l} = \mathbf{l}(\mathbf{Q})$ of muscle lengths. The term $\mathbf{G}(\mathbf{Q}) = -\partial V / \partial \mathbf{Q}$ accounts for gravity and for the passive elastic properties of the tongue, whereas $\mathbf{f}_m(\mathbf{l}, \dot{\mathbf{l}}, \boldsymbol{\lambda})$ is the vector of muscle forces.

The above equation completely describes the forward dynamics of the whole system, relating the forces generated by muscles to motion generated in the mechanical degrees of freedom of the system. The equation was numerically integrated by using Gear's algorithm for stiff systems. Jaw, hyoid, larynx, and tongue motions were therefore obtained simultaneously.

Baer, T., Alfonso, P. J., and Honda, K. (**1988**). ''Electromyography of the tongue muscles during vowels in /pVp/ environment,'' Annu. Bull., Res. Inst. Logoped. Phoniatr. Univ. Tokyo **22**, 7–19.

Baragar, F. A., and Osborn, J. W. (**1984**). ''A model relating patterns of human jaw movement to biomechanical constraints,'' J. Biomech. **17**, 757–767.

Bothorel, A., Simon, P., Wioland, F., and Zerling, J. P. (**1986**). ''Cinéradiographie des voyelles et consonnes du français,'' Technical report, Travaux de l'Institut de Phonétique de Strasbourg, France.

Chiel, H. L., Crago, P., Mansour, J. M., and Hathi, K. (**1992**). ''Biomechanics of a muscular hydrostat: a model of lapping by a reptilian tongue,'' Biol. Cybern. **67**, 403–415.

Dickson, D. R., and Maue-Dickson, W. (**1982**). *Anatomical and Physiological Bases of Speech* (Little, Brown and Co., Boston).

Duck, F. A. (**1990**). *Physical properties of tissue: A comprehensive reference book* (Academic, London).

Feldman, A. G., and Orlovsky, G. N. (**1972**). ''The influence of different descending systems on the tonic reflex in the cat,'' Exp. Neurol. **37**, 481–494.

Feldman, A. G., Adamovich, S. V., Ostry, D. J., and Flanagan, J. R. (**1990**). ''The origins of electromyograms—Explanations based on the equilibrium point hypothesis,'' in *Multiple Muscle Systems—Biomechanics and Movement Organization*, edited by J. M. Winters and S. L.-Y. Woo (Springer-Verlag, New York).

Gribble, P. L., Ostry, D. J., Sanguineti, V., and Laboissière, R. (**1998**). ''Are complex computations required for the control of arm movement?,'' J. Neurophysiol. (in press).

Harshman, R., Ladefoged, P., and Goldstein, L. (**1977**). ''Factor analysis of tongue shapes,'' J. Acoust. Soc. Am. **62**, 693–707.

Hashimoto, K., and Suga, S. (**1986**). ''Estimation of the muscular tensions of the human tongue by using a three-dimensional model of the tongue,'' J. Acoust. Soc. Jpn. (E) **7(1)**, 39–46.

Henneman, E., Somjen, G., and Carpenter, D. O. (**1965**). ''Functional significance of cell size in spinal motoneurons,'' J. Neurophysiol. **28**, 560–580.

Honda, K., Hirai, H., and Dang, J. (**1994**). ''A physiological model of speech production and the implication of tongue-larynx interaction, in *International Congress on Spoken Language Processing*, Yokohama, pp. 175–178.

Huxley, A. F. (**1957**). ''Muscle structure and theories of contraction,'' Prog. Biophys. Chem. **7**, 255–318.

Joyce, G. C., and Rack, P. M. H. (**1969**). ''Isotonic lengthening and shortening movements of cat soleus muscle,'' J. Physiol. (London) **204**, 475–491.

Kiritani, S., Miyawaki, K., and Fujimura, O. (**1976**). ''A computational model of the tongue,'' Res. Instit. Logoped. Phoniatr. Annu. Bull. **10**, 243–252.

Laboissière, R., Ostry, D. J., and Feldman, A. G. (**1996**). ''Control of multimuscle systems: Human jaw and hyoid movements,'' Biol. Cybern. **74(3)**, 373–384.

Lamarre, Y., and Lund, J. P. (**1975**). ''Load compensation in human masseter muscles,'' J. Physiol. (London) **253**, 31–35.

Lee, Y., Terzopoulos, D., and Waters, K. (**1995**). ''Realistic modeling for facial animation,'' in *Computer Graphics Proceedings, Annual Conference Series*, pp. 55–62.

Maeda, S. (**1990**). ''Compensatory articulation during speech: evidence from the analysis and synthesis of vocal-tract shapes using an articulatory model,'' in *Speech Production and Speech Modelling*, edited by W. J. Hardcastle and A. Marchal (Kluwer Academic, Dordrecht), pp. 131–149.

Maeda, S., and Honda, K. (**1994**). ''From EMG to formant patterns of vowels: The implication of vowel spaces,'' Phonetica **51**(1–3), 17–29.

McDevitt, W. E. (**1989**). *Functional Anatomy of the Masticatory System* (Wright, London, UK).

Miller, A. (**1991**). *Craniomandibular Muscles: Their Role in Function and Form* (CRC, Boca Raton, FL).

Miyawaki, K. (**1974**). ''A study on the musculature of the human tongue.'' Annu. Bull. Res. Instit. Logoped. Phoniatr., Univ. Tokyo **8**, 23–50.

Müller, E. M., Milenkovic, P. H., and MacLeod, G. E. (**1984**). ''Perioral tissue mechanics during speech production,'' In *Proceedings of the Second IMAC International Symposium on Biomedical Systems Modeling*, edited by C. DeLisi and J. Eisenfeld (North-Holland, Amsterdam).

Öhman, S. E. G. (**1967**). ''Numerical model of coarticulation,'' J. Acoust. Soc. Am. **41**, 310–320.

Ostry, D. J., and Munhall, K. G. (**1994**). ''Control of jaw orientation and position in mastication and speech,'' J. Neurophysiol. **71**, 1515–1532.
Ostry, D., Gribble, P., and Gracco, V. (**1996**). ''Coarticulation of jaw movements in speech production: Is context sensitivity in speech kinematics centrally planned?,'' J. Neurosci. **16**(4), 1570–1579.
Ostry, D. J., Vatikiotis-Bateson, E., and Gribble, P. L. (**1997a**). An examination of the degrees of freedom of human jaw motion in speech and mastication, J. Speech Lang. Hear. Res. **40**(6), 1341–1352.
Ostry, D. J., Gribble, P. L., Levin, M. F., and Feldman, A. G. (**1997b**). ''Phasic and tonic stretch reflexes in muscles with few muscle spindles: Human jaw opener muscles,'' Exp. Brain Res. **116**(2), 299–308.
Otten, E. (**1987**). ''A myocybernetic model of the jaw system of the rat,'' J. Neurosci. Meth. **21**, 287–302.
Payan, Y., and Perrier, P. (**1997**). ''Synthesis of V–V Sequences with a 2D Biomechanical Tongue Model Controlled by the Equilibrium Point Hypothesis,'' Speech Commun. (in press).
Perkell, J. (**1969**). *Physiology of Speech Production* (MIT, Cambridge, MA).
Perkell, J. (**1974**). ''A Physiologically-Oriented Model of Tongue Activity in Speech Production,'' unpublished doctoral dissertation, Departement of Electrical Engineering, MIT.
Perrier, P., Ostry, D. J., and Laboissière, R. (**1996**). ''The Equilibrium Point Hypothesis and Its Application to Speech Motor Control,'' J. Speech Hear. Res. **39**, 365–378.
Sanguineti, V., Laboissière, R., and Payan, Y. (**1997**). ''A control model of human tongue movements in speech,'' Biol. Cybern. **77(1)**, 11–22.
Scheideman, G. B., Bell, W. H., Legan, H. L., Finn, R. A., and Reisch, J. S. (**1980**). ''Cephalometric analysis of dentofacial normals,'' Am. J. Orthod. **78**(4), 404–420.
Schwarz, H. R. (**1984**). *Finite Element Methods* (Academic, London).
Smith, A. (**1992**). ''The Control of Orofacial Movements in Speech,'' Crit. Rev. Oral Biol. Med. **3**(3), 233–267.
Terzopoulos, D., and Waters, K. (**1990**). ''Physically-based facial modeling, analysis and animation,'' J. Visual Comput. Animat. **1**, 73–80.
Throckmorton, G. S., and Throckmorton, L. S. (**1985a**). ''Quantitative calculations of temporomandibular joint reaction forces—I. The importance of the magnitude of the jaw muscle forces,'' J. Biomech. **18**, 445–451.
Throckmorton, G. S., and Throckmorton, L. S. (**1985b**). ''Quantitative calculations of temporomandibular joint reaction forces—II. The importance of the direction of the jaw muscle forces,'' J. Biomech. **18**, 453–461.
Tsuji, T., Morasso, P. G., Goto, K., and Ito, K. (**1995**). ''Human hand impedance characteristics during arm posture,'' Biol. Cybern. **72**, 475–485.
van Eijden, T. M. G., Klok, E. M., Weijs, W. A., and Koolstra, J. H. (**1988**). ''Mechanical capabilities of the human jaw muscles studied with a mathematical model,'' Arch. Oral Biol. **33**, 819–826.
Wells, J. B. (**1965**). ''Comparison of mechanical properties between slow and fast mammalian muscles,'' J. Physiol. (London) **178**, 252–269.
Westbury, J. R. (**1988**). ''Mandible and hyoid bone movements during speech,'' J. Speech Hear. Res. **31**, 405–416.
Wilhelms-Tricarico, R. (**1995**). ''Physiological modeling of speech production: Methods for modelling of soft-tissue articulators,'' J. Acoust. Soc. Am. **97**, 3085–3098.

Selection and combination of acoustic features for the description of pathologic voices

Dirk Michaelis, Matthias Fröhlich, and Hans Werner Strube
Drittes Physikalisches Institut, Universität Göttingen, Bürgerstr. 42-44, D-37073 Göttingen, Germany

(Received 12 December 1996; accepted for publication 10 November 1997)

The glottal to noise excitation ratio (GNE) is an acoustic measure designed to assess the amount of noise in a pulse train generated by the oscillation of the vocal folds. So far its properties have only been studied for synthesized signals, where it was found to be independent of variations of fundamental frequency (jitter) and amplitude (shimmer). On the other hand, other features designed for the same purpose like NNE (normalized noise energy) or CHNR (cepstrum based harmonics-to-noise ratio) did not show this independence. This advantage of the GNE over NNE and CHNR, as well as its general applicability in voice quality assessment, is now tested for real speech using a large group of pathologic voices ($n=447$). A set of four acoustic features is extracted from a total of 22 mostly well-known acoustic voice quality measures by correlation analysis, mutual information analysis, and principal components analysis. Three of these measures are chosen to assess primarily different aspects of signal aperiodicity, while the fourth one indicates the noise content of the signal. All analysis methods lead to the same feature set that consists of a measure of period correlation, jitter, shimmer, and GNE. The two-dimensional projection of this set named ''hoarseness diagram'' allows a graphical illustration of voice quality that can be easily interpreted. [S0001-4966(98)00603-1]

PACS numbers: 43.70.Dn, 43.70.Gr, 43.72.Ar [AL]

INTRODUCTION

The use of acoustic features in the description of pathological voice quality has been tested in various contexts and with a variety of goals. Some of its attractiveness stems from the idea that they might supply a way to quantitatively assess voice characteristics that are otherwise difficult to measure (e.g., Kreiman and Gerratt, 1996). Studies on pathological voices have correlated acoustic features with perceptual qualities (Murry *et al.*, 1977; Hammarberg *et al.*, 1980, 1981; Fritzell *et al.*, 1983a; Askenfelt and Hammarberg, 1986; Hirano *et al.*, 1986, 1988; Eskenazi *et al.*, 1990; Rammage *et al.*, 1992; Kreiman *et al.*, 1992; Kreiman and Gerratt, 1994; Dejonckere, 1995; de Krom, 1995; Bielamowicz *et al.*, 1996; Hillenbrand and Houde, 1996) or, to a lesser extent, with physiologic conditions at the glottis (Hirano *et al.*, 1986; Rammage *et al.*, 1992). However, the results are often ambiguous, and sometimes even contradictory, so the choice of the appropriate acoustic measures as well as their interpretation are still unsolved problems.

Acoustic features may be grouped according to the signal characteristics they are supposed to measure. Although there are many different possible categories, the terms ''aperiodicity features'' and ''noise features'' can be considered as two important labels. ''Aperiodicity features'' have been used to describe perceptual roughness (Hirano *et al.*, 1988; Hillenbrand, 1988; Arends *et al.*, 1990; Dejonckere, 1995) or the periodicity of glottal vibration (Dejonckere, 1995). ''Noise features'' have been found by some researchers to be indicators of breathiness (Hammarberg *et al.*, 1981; Klatt and Klatt, 1990; Hillenbrand *et al.*, 1994; Dejonckere, 1995; Hillenbrand and Houde, 1996), although these findings are controversial. Also, ''noise features'' have been related to certain physiological conditions during the phonatory cycle such as a glottal gap (Södersten and Lindestad, 1990) or softer closure (Hillenbrand *et al.*, 1994).

''Aperiodicity features'' are designed to capture the various forms of periodicity disturbances in the acoustic signal (Klingholz, 1987). One special kind of aperiodicity is related to changes in the waveform shape between glottal cycles. This effect can be measured by the mean correlation coefficient calculated for all pairs of successive cycles. Two other kinds result from variations of the fundamental frequency (F_0) and of the cycle-to-cycle peak amplitude or energy. These aperiodicities are described by the ''classical'' features jitter and shimmer, respectively. In the long history of the description of signal aperiodicity many different definitions of jitter and shimmer measures have evolved (for overviews see, e.g., Kasuya *et al.*, 1986a; Pinto and Titze, 1990; Bielamowicz *et al.*, 1996). In spite of their widespread application in voice quality assessment, recent findings of Schoentgen and de Guchteneere (1997) may lead to the necessity to rethink the general concept underlying these two acoustic features.

To the ''noise feature'' group belong the features designed to measure the relative noise component in a speech signal. Prominent members of this group are the harmonics-to-noise ratio (HNR; Yumoto *et al.*, 1982) and the normalized noise energy (NNE; Kasuya *et al.*, 1986a) that have been studied in various contexts (Hirano *et al.*, 1988; Eskenazi *et al.*, 1990; Childers and Lee, 1991; Kreiman *et al.*, 1993; Dejonckere, 1995; Bielamowicz *et al.*, 1996; Qi and Hillman, 1997). A recently developed feature belonging to this group is the glottal-to-noise excitation ratio (GNE; Michaelis and Strube, 1995).

One of the main problems with grouping acoustic features according to their principal use is that most of them are

 0001-4966/98/103(3)/1628/12/$10.00

sensitive to several acoustic properties. This mutual dependence may be one of the reasons for the difficulty in interpreting seemingly contradictory results found in the literature. With regard to the two groups mentioned above, it is obvious that waveform correlation, jitter, and shimmer (especially amplitude shimmer) will be noise sensitive to some extent depending on the particular algorithm. On the other hand, NNE and HNR were found to be sensitive to jitter and shimmer for synthetic signals (Michaelis *et al.*, 1997a).

The question now arises, which are the features to supply the *best independent assessment* of irregularity and additive noise in pathologic voices. Only if these two voice properties can be measured independently should conclusions be drawn about their relevance with regard to different perceptual qualities, like roughness or breathiness, or to the underlying physiologic conditions at the glottis.

In this paper we address this issue, with particular emphasis on whether GNE is the ''noise feature'' supplying more additional information about a pathological voice than NNE and HNR. We will proceed as follows: first, correlations are calculated for a total of 22 voice quality measures (13 of aperiodicity, 9 of noise). Second, using a technique from information theory, a mutual information analysis is performed to find the best jitter and shimmer measures of our list. Once these features have been determined, mutual information analysis is used again to find the best additional ''noise measure.'' Third, the underlying dimensionality of the thus obtained four-feature sub-space is determined by principal components analysis (PCA). After it is found to be two dimensional, PCA of the complete 22-dimensional feature space is used to confirm the former results. Finally, a two-dimensional graphical representation named ''hoarseness diagram'' is derived that allows an easy interpretation of the acoustic features.

I. METHODS

A. Speech material

The German vowel [ɛ:] was recorded for 447 different speakers (male and female) between the ages of 10 and 80 (mean: 48). They showed a variety of organic and functional voice disorders (see Table I). Eighty-eight normal voices (persons with no history of voice problems) aged 18 to 90 (mean: 47) were recorded as the reference group. The vowel was sustained by the subject at comfortable pitch and loudness for several seconds. It was digitally recorded in a soundproof room using the Kay Computer Speech Lab (CSL 4300) at a sampling frequency of 50 kHz. One second of the middle part of the signal was used for acoustic analysis, which was performed in a completely automated and unsupervised way. No segments were rejected since perturbation measures were extrapolated to highly disturbed voices as will be described in the following section. This data set is the one used in the experiments unless stated otherwise.

In order to increase the significance of the mutual information analyses, a second data set was generated. Here the same 447 recordings of the first set were used, plus additional recordings of the same patients taken at other times. For the resulting 1099 recordings, the acoustic features described in the following were calculated on 500-ms frames with a shift of 250 ms. In this way a total of $n=13\,414$ analyzed segments (i.e., data points) were obtained. The Wilcoxon test showed no significant differences in the feature distributions between the regular pathological group ($n=447$) and the large pathological group ($n=13414$).

TABLE I. List of functional and physiological disorders.

Number of occurrences	Diagnosis/description
56	vocal fold paresis
22	vocal fold fixation
34	post-operative status after partial laryngectomy
21	pre-operative status before micro surgery (glottal carcinoma)
39	polyps
16	nodules
19	laryngeal granuloma
28	cysts
12	mutational dysphonias
11	papillomas
24	Reinke's Oedema
47	hypo functional dysphonia
45	status/dysphonia after micro surgery (benign tumors)
11	laryngitis
62	others (less than 5 patients per diagnose)

B. Acoustic features

1. Jitter, shimmer, and period correlation

The energy sequence $E(\nu)$ for a periodic signal is given by the sum of the squared sample values of the νth glottal cycle [$\nu=0,..,N-1$ (last complete cycle)]. For the present study the glottal cycle length $P(\nu)$ of the νth period is determined by the waveform matching algorithm (Milenkovic, 1987; Titze and Liang, 1992). The time range to be tested by this algorithm is set to 0.5 and 1.5 times the time lag (restricted to 2.5 ms$\leqslant\delta_t\leqslant$15 ms) of the maximum of the autocorrelation function calculated for the current frame.

As jitter and shimmer measures the perturbation factor (PF; Hollien *et al.*, 1975) and the perturbation quotient (PQ; Koike, 1971) were chosen. They come as part of commercial analysis systems such as the CSL system of Kay Elemetrics and allow a good comparability of the results to other studies because of their widespread application. For a sequence $u(\nu)$ the following definitions were used according to Kasuya *et al.* (1993):

$$\mathrm{PF}=\frac{100\%}{N-1}\sum_{\nu=1}^{N-1}\left|\frac{u(\nu)-u(\nu-1)}{u(\nu)}\right|, \tag{1}$$

$$\mathrm{PQ}=\frac{100\%}{N-K}\times\sum_{\nu=(K-1)/2}^{N-[(K-1)/2]-1}\left|\frac{u(\nu)-\frac{1}{K}\sum_{k=-(K-1)/2}^{(K-1)/2}u(\nu+k)}{\frac{1}{K}\sum_{k=-(K-1)/2}^{(K-1)/2}u(\nu+k)}\right|. \tag{2}$$

TABLE II. List of the acoustic features. For each feature the monotonic transformation used to obtain an approximately normal distribution is stated. Mean and standard deviation (s.d.) are calculated separately for the normal and the pathological group. Symbols and abbreviations (see also text): MWC—mean waveform matching coefficient; PPF (EPF)—period (energy) perturbation factor; PPQ (EPQ)—period (energy) perturbation quotient; GNE—glottal-to-noise excitation ratio; NNE—normalized noise energy; CHNR—cepstrum based harmonics to noise ratio; n—number of recordings; log—base 10 logarithm.

					Mean (y)	s.d. (y)	Mean (y)	s.d. (y)
Feature	Symbol	Description	Unit	Transformation $y=f(x)$	normal ($n=88$)		pathologic ($n=447$)	
MWC	MWC			$\log(1-x)$	−2.021	0.335	−1.614	0.574
jitter	$j2$	PPF	%	$\log x$	−0.492	0.234	−0.089	0.611
	$j3$	PPQ $K=3$	%	$\log x$	−0.792	0.246	−0.374	0.645
	$j5$	PPQ $K=5$	%	$\log x$	−0.734	0.203	−0.323	0.626
	$j7$	PPQ $K=7$	%	$\log x$	−0.673	0.211	−0.276	0.610
	j^{11}	PPQ $K=11$	%	$\log x$	−0.588	0.206	−0.210	0.584
	$j15$	PPQ $K=15$	%	$\log x$	−0.522	0.199	−0.161	0.563
shimmer	$s2$	EPF	%	$\log x$	0.572	0.212	0.848	0.421
	$s3$	EPQ $K=3$	%	$\log x$	0.268	0.224	0.550	0.424
	$s5$	EPQ $K=5$	%	$\log x$	0.347	0.199	0.617	0.407
	$s7$	EPQ $K=7$	%	$\log x$	0.403	0.204	0.662	0.398
	$s11$	EPQ $K=11$	%	$\log x$	0.476	0.203	0.717	0.384
	$s15$	EPQ $K=15$	%	$\log x$	0.531	0.204	0.757	0.368
GNE	gne1	1000-Hz bandwidth		$\log(1-x)$	−1.612	0.291	−1.062	0.515
				x	0.969	0.022	0.834	0.189
	gne2	2000-Hz bandwidth		$\log(1-x)$	−1.360	0.331	−0.870	0.485
				x	0.940	0.056	0.768	0.222
	gne3	3000-Hz bandwidth		$\log(1-x)$	−1.120	0.345	−0.690	0.428
				x	0.892	0.106	0.695	0.242
NNE	nne1	60–5000 Hz	dB	x	−19.425	3.634	−16.025	5.853
	nne2	60–2000 Hz	dB	x	−22.831	3.606	−19.492	6.830
	nne3	1000–5000 Hz	dB	x	−11.715	3.734	−7.441	4.448
CHNR	chnr1	60–5000 Hz	dB	x	25.169	3.649	20.088	7.001
	chnr2	60–2000 Hz	dB	x	29.157	3.833	23.877	8.261
	chnr3	1000–5000 Hz	dB	x	17.345	4.123	11.609	5.397

If $u(\nu)$ is chosen as the period length sequence $P(\nu)$, the *period perturbation factor* (PPF) and the *period perturbation quotient* (PPQ) define different jitter measures. In the following, PPF will be abbreviated as $j2$. For PPQ, different choices of K (3, 5, 7, 11, 15) lead to the jitter measures abbreviated as $j3, j5, j7, j11, j15$ (see Table II). Analogously, shimmer is measured by the *energy perturbation factor* (EPF) (abbreviated as $s2$) or the *energy perturbation quotient* (EPQ) if $u(\nu)$ is chosen as $E(\nu)$. Again, different values for K result in the measures $s3, s5, s7, s11, s15$ (see Table II). Since the shimmer measures are based on the energy sequence, they are expected to be considerably less susceptible to noise than the amplitude shimmer often used in acoustic voice analyses.

Titze and Liang (1992) came to the conclusion that jitter and shimmer cannot be determined accurately for highly disturbed voices. Indeed, for increasingly aperiodic signals those features more and more loose their meaning as indicators of deviations from *periodicity*. However, the waveform matching algorithm does not depend *a priori* on the degree of signal periodicity and therefore can be applied to any kind of voice signal. For whispered voices (i.e., totally aperiodic signals) the algorithm is found to position the period markers in a seemingly random manner (Fröhlich *et al.*, 1997). Therefore PF and PQ show high values for these voices. This behavior is found to be consistent for any intermediate deviations from periodicity and therefore allows an interpretable quantitative classification of any voice (Michaelis *et al.*, 1997b; Fröhlich *et al.*, 1997, 1998a,b).

The mean of all correlation coefficients evaluated for every pair of consecutive periods is used as the acoustic measure termed *mean waveform matching coefficient* (MWC). It indicates the overall similarity between the cycles of the time signal. The algorithmic evaluation of the MWC is relatively robust compared to the jitter and shimmer calculation. Its upper limit of 1 is reached for signals with identical period shapes (i.e., strictly periodic signals). MWC decreases with increasing differences in length or shape between consecutive periods, i.e., with short-term variations of the time signal.

2. NNE, CHNR, and GNE

Normalized noise energy (NNE) (Kasuya *et al.*, 1986b) and *cepstrum based harmonics-to-noise ratio* (CHNR) (de Krom, 1993) are designed to measure the relative noise content of a signal. Both NNE and CHNR were found to be sensitive to jitter and shimmer for synthetic signals (Michaelis *et al.*, 1997a). A recently developed feature designed to measure the additive noise in a speech signal is the *glottal-to-noise excitation ratio* (GNE) (see the Appendix).

The use of three different bandwidths leads to different GNE measures (see Table II): gne1 is calculated using a bandwidth of 1 kHz, gne2 using 2 kHz, and gne3 using 3 kHz. Similarly, several different realizations of NNE and

CHNR were tested: nne1 and chnr1 are calculated for the frequency range 60–5000 Hz, nne2 and chnr2 for 60–2000 Hz, and nne3 and chnr3 for 1000–5000 Hz.

C. Rank correlation analysis

Correlation analysis was applied to the set of 22 acoustic measures stated in Table II in order to determine interdependencies between different features. The statistic applied was the Spearman rank-order correlation coefficient (Press *et al.*, 1989) which is independent of the shape of the underlying data distribution. Pairwise correlations were calculated for all combinations of the acoustic measures ($n=0.5\cdot 22\cdot 21=231$). For further interpretations the significance of the difference between correlation coefficients was calculated by Fisher z-transformation of the correlation coefficients and testing the difference for being normal distributed (van den Brink and Koele, 1987).

The significance levels for all correlations and differences of correlations were calculated applying the Bonferroni–Holm correction (Holm, 1979), which was performed separately for the normal and pathological voice group. The number of tests used for the correction was 369 for the pathological and 261 for the normal group. These totals result from the 231 correlations for each group, 30 ($=2\cdot 0.5\cdot 6\cdot 5$) differences of all intra-jitter/intra-shimmer correlations (i.e., correlations of all combinations of the 6 jitter (shimmer) measures) and the $\{j3,s15\}$ correlation for each group, and—for the pathological group only—108 ($=3\cdot 0.5\cdot 9\cdot 8$) differences between all the correlations of the ''noise measures'' with $j3$, $s15$, and MWC (the specific choice of the measures for these tests will become apparent in the specific sections). Throughout this paper results will be interpreted at a significance level of $p\leqslant 0.05$.

D. Mutual information analysis

1. Generalization of the mutual information

The calculation of the mutual information (Fraser and Swinney, 1986) between different acoustic features is based on their probability distributions. Its derivation will be explained in detail for the simple case of a two-dimensional data distribution. Throughout this section, for a given measure the frequency of occurrence within a certain value range will be interpreted as the probability of the measure to be found in this interval.

For the two acoustic features x_1 and x_2 the data are binned to M intervals. These intervals are uniformly distributed along each feature axis and cover the whole corresponding value ranges. Let $n_i(x_1)$ be the number of x_1-values to be found in bin i [analogously $n_i(x_2)$ for feature x_2] while $n_{ij}(x_1,x_2)$ is the number of x_1-values found in bin i and x_2-values found in bin j simultaneously. Using this binned description of the data distribution for x_1 and x_2, the estimated probability to find feature x_1 or x_2 in bin i is given by $p_i(x_\eta)=n_i(x_\eta)/M;\ i=1,...,M;\ \eta=1,2$. The estimated joint probability that x_1 will be found in bin i and x_2 in bin j is given by $p_{ij}(x_1,x_2)=n_{ij}(x_1,x_2)/M^2;\ i,j=1,...,M$. Using these expressions the one-dimensional and the two-dimensional entropy are given by

$$H(x_1)=-\sum_{i=1}^{M} p_i(x_1)\,\mathrm{ld}(p_i(x_1)), \tag{3}$$

$$H(x_1,x_2)=-\sum_{i,j=1}^{M} p_{ij}(x_1,x_2)\,\mathrm{ld}(p_{ij}(x_1,x_2)), \tag{4}$$

with ld denoting the base 2 logarithm.

With definitions (3) and (4) the mutual information between two features is expressed by $I_2=I(x_1,x_2)=H(x_1)+H(x_2)-H(x_1,x_2)$. I_2 can be interpreted as the average number of bits that are predictable of x_2 if x_1 is known, and vice versa. It can be generalized easily to μ dimensions:

$$I_\mu=I(x_1,\ldots,x_\mu)=\sum_{i=1}^{\mu} H(x_i)-H(x_1,\ldots,x_\mu). \tag{5}$$

The number of bins M should be as high as possible in order to yield a good approximation of the μ-dimensional probability distribution. However, it is limited by the data available since the number of μ-dimensional hyper-bins necessary to cover the whole μ-dimensional feature space is M^μ. This means that for, e.g., $\mu=4$ and $M=8$ (which represent values actually used in the analysis) at least 4096 data points are necessary to guarantee statistically the occurrence of at least one point per hyper-bin.

2. Normalized increase of information

If a measure is added to a given set of measures, generally not all bits of the new measure can be predicted by the old ones. The remaining, unpredictable part can be regarded as additional information about the data that is described exclusively by the added measure. However, the interpretation of this informational gain is up to the experimenter as the resulting numerical value does not tell whether the gain is due to random (and therefore unpredictable) noise or whether it indeed indicates new, meaningful properties of the data. In the present study, all acoustic features are known to describe different aspects of voice quality in a meaningful way. Therefore the quantitative value of the informational gain can be used to determine the (in this sense) optimal four-feature set starting from a three-feature set.

The maximum information B (in units ''bit'') for one feature is $B=\mathrm{ld}(M)$. Using Eqs. (3) and (5) ($\mu=3,4$), we define the *normalized additional information* that results from adding x_4 to the set $\{x_1,x_2,x_3\}$ similar to the *marginal redundancy* of Kumar and Mullik (1996) as

$$\Delta I_R=\frac{B-(I_4-I_3)}{B}. \tag{6}$$

The mutual information has been shown to be independent of monotonic coordinate transformation (Fraser and Swinney, 1986). Therefore replacing the data values by their ranks as performed in this study is permissible. If the feature values are in this way uniformly distributed, the one-dimensional entropy is maximum: $H(x_i)=B;\ i=1,...,\mu$. Now a value of $\Delta I_R=0$ indicates that the fourth feature does

not add new information (e.g., if it is chosen as one of the features x_1, x_2, or x_3 already present). On the other hand, $\Delta I_R = 1$ indicates the maximum increase of information possible.[1]

E. Principal components analysis

The underlying dimensionality of a data distribution, as well as its most significant components, can be determined by principal components analysis (PCA). The technique applied in this study is the singular value decomposition (SVD; Press *et al.*, 1989). SVD projects correlated measures onto the same principal axis of the data distribution. If the variances in some principal directions are negligible, the data space can be described in the new, lower-dimensional coordinate system defined by the principal vectors.

One advantage of this linear method is that the dimensionality of the data distribution can be estimated simply by counting the number of principal components that account for most of the data variance. The description in a low-dimensional coordinate system often facilitates the interpretation of the data.

All 13 ''aperiodicity measures'' show asymmetric distributions. Jitter and shimmer are found with a much higher probability at small values, while for MWC most values are close to 1. However, Gaussian data distributions are preferable for principal components analysis. On the other hand, monotonic transformations do not influence the other two analysis techniques (rank correlation analysis and mutual information analysis). Therefore the transformed measures using the different monotonic functions stated in Table II were used for all the analyses.

In order to apply the SVD the data have to be normalized. This is done by first subtracting the mean of the group (pathological/normal as stated in Table II), then dividing the result by the corresponding standard deviation.

II. RESULTS AND DISCUSSION

A. Acoustic analysis of normal and pathologic voices

Table II states means and standard deviations (s.d.) for each measure for the normal and the pathological group. The means of the jitter measures are of similar magnitude. The same is found for the shimmer measures. Compared to jitter, shimmer means are about ten times higher, which shows in differences of approximately one for the logarithmic values stated in the table.

The mean GNE increases with decreasing bandwidth, which is in accordance with results on synthesized signals (Michaelis *et al.*, 1997a). NNE and CHNR show an estimated noise energy that is about 8 dB higher for the frequency range 1–5 kHz than for 60–5000 Hz due to the relative attenuation of the harmonics at higher frequencies with regard to the noise level.

The differences between the means of the pathological and the normal group are significant for all measures according to the Wilcoxon two-sample test. Nevertheless, the s.d.'s for all measures are higher in the pathological group than in the normal group. At the same time the means are less than one s.d. of the pathological group apart for any given measure. This overlap signifies that a discrimination of voice quality based on just one measure cannot be considered complete or unique.

B. Rank correlation analysis

1. Correlations between jitter and shimmer

Rank correlations for all combinations of jitter and shimmer measures are significant. For the pathological voice group the correlation between the different jitter features is very high (0.84–0.99). For the different shimmer features these correlations are even exceeded (0.90–0.99). The correlation between jitter and shimmer measures is still relatively high, but clearly lower (0.74–0.87). The lowest correlation (0.74) is found between $j3$ and $s15$.

For the normal voices the correlations are generally lower than for the pathologic group but still significant. They range from 0.66 to 0.98 for jitter, 0.73 to 0.98 for shimmer, and 0.46 to 0.76 for the correlation between jitter and shimmer measures. The lowest correlation (0.46) is found again for $\{j3,s15\}$.

Since for both groups $j3$ and $s15$ are correlated the least, this measure combination supplies the most information on the signal (given this particular set of measures). Therefore, the differences of all intra-jitter correlations (i.e., all combinations of jitter measures) and intra-shimmer correlations were tested against the correlation of this set.[2] For the pathological group, all intra-jitter/intra-shimmer correlations are found to be significantly higher than the $\{j3,s15\}$ correlation (0.74). For the normal group, the correlations are significantly higher than the $\{j3,s15\}$ correlation (0.46) with the exception of $\{j3,j11\}$, $\{j3,j15\}$, and $\{s3,s15\}$ (correlations 0.75, 0.66, 0.73, respectively).

These findings suggest that for pathological voices the ''locality'' of the jitter or shimmer measure (i.e., the number of averaged cycles) is of secondary importance. The significant correlations between jitter and shimmer indicate that both measures assess similar voice characteristics. This was to be expected on theoretical grounds since they represent different aspects of signal aperiodicity (Klingholz, 1987) that may be caused by the same phenomenon (e.g., an asymmetry of the vocal folds due to pathological tissue changes) and since jitter automatically introduces shimmer to a signal (Hillenbrand, 1987).

On the other hand, the minimum correlations of 0.74 and 0.46 for the pathological and normal group, respectively, reflect that jitter and shimmer are not assessing identical aspects of signal irregularity. While variations of correlation coefficients may in principle be—to some extent—due to chance if a great number of correlations is calculated, the significant difference between intra-jitter/intra-shimmer correlations and the $\{j3,s15\}$ correlation can also be interpreted in that this particular combination of jitter and shimmer measures gives a significant advantage over the use of just one jitter or shimmer measure or a combination of two jitter or two shimmer measures. This interpretation is in accordance with the variety of findings described in the literature on which grounds no preference can be given to either jitter or shimmer over the other.

TABLE III. Rank correlation coefficients of different GNE(log), NNE, and CHNR features for the pathological group and the normal group (for the abbreviations of the features see Table II). Insignificant correlations are marked by an asterisk (*).

	Pathological group								Normal group							
	gne2	gne3	nne1	nne2	nne3	chnr1	chnr2	chnr3	gne2	gne3	nne1	nne2	nne3	chnr1	chnr2	chnr3
gne1	0.95	0.89	0.53	0.53	0.79	−0.68	−0.71	−0.86	0.81	0.67	−0.09*	−0.12*	0.33*	−0.09*	−0.08*	−0.48
gne2		0.96	0.49	0.50	0.78	−0.64	−0.67	−0.85		−0.89	−0.24*	−0.21*	0.27*	0.06*	0.02*	−0.44
gne3			0.45	0.45	0.75	−0.60	−0.62	−0.82			−0.27*	−0.22*	0.14*	0.14*	0.10*	−0.31*
nne1				0.93	0.76	−0.91	−0.86	−0.69				0.86	0.60	−0.91	−0.79	−0.44
nne2					0.72	−0.83	−0.88	−0.64					0.46	−0.73	−0.86	−0.28*
nne3						−0.83	−0.83	−0.96						−0.71	−0.65	−0.94
chnr1							0.94	0.83							0.85	0.66
chnr2								0.83								0.58

2. Correlations between NNE, CHNR, and GNE

The correlation coefficients among GNE, NNE, and CHNR features are given in Table III. For the pathological voices the correlation between the different GNE measures is very high (0.89–0.96). The smallest value is found for the combination {gne1,gne3} which represents the largest difference in bandwidth.

Of the NNE and CHNR measures, the ones defined for the high-frequency region (nne3 and chnr3) are found to be the ones most similar to GNE (correlation 0.75–0.79 for nne3, 0.82–0.86 for chnr3). Correlations of the other NNE and CHNR measures with GNE are considerably lower (0.45–0.53 for nne1/nne2, 0.60–0.71 for chnr1/chnr2). The importance of the higher-frequency region in the description of pathological voices has already been pointed out by researchers using the NNE (Kasuya *et al.*, 1986b).

If the same frequency ranges are compared, the correlations between CHNR and NNE measures are very high (0.88–0.96). Taking into account the design of the two features that both relate the harmonic energy to the nonharmonic energy, it seems plausible to interpret this covariance as an indication that CHNR and NNE measure similar voice properties. The correlations also indicate that the choice of the frequency range has a greater effect than the specific method used (i.e., NNE or CHNR).

For the normal voices all NNE and CHNR measures are significantly correlated with the one exception of {chnr3,nne2}. However, no significant correlations are found between GNE measures and NNE/CHNR (with the exceptions of {chnr3/gne1} and {chnr3/gne2}). While one possible explanation may be the limited value range for the normal voices, these findings can also be interpreted as indication that for normal voices GNE is sensitive to other voice characteristics than NNE and CHNR.

3. Correlations of jitter and shimmer with NNE, CHNR, and GNE

Table IV shows the correlations of GNE, NNE, and CHNR with jitter and shimmer. For the pathological group all values are significant. The correlations between jitter/shimmer and GNE are smaller than between jitter/shimmer and NNE/CHNR. The minimum correlation of any ''noise measure'' with jitter or shimmer measures is found for gne3. All pairwise differences between the correlation coefficients of any of the nine ''noise measures'' with both $j3$ or $s15$ were tested for their significance (i.e., all combinations of values in the $j3$ column and in the $s15$ column for the pathological voice group in Table IV). It was found that correlations of gne2 or gne3 were significantly smaller than correlations of CHNR or NNE measures.

For the normal group no significant correlation between any GNE measure and any jitter or shimmer measure is found. On the other hand, all CHNR and NNE measures are correlated significantly with jitter and shimmer. The insignificant correlations between GNE and the aperiodicity measures for the normal group and the significantly lower correlation for the pathologic group, together with the significant correlations of NNE/CHNR measures with jitter or shimmer, can be interpreted that GNE measures additive noise independently of jitter and shimmer. This is in accordance with results on synthetic signals where gne3 was found to be independent of jitter and shimmer (Michaelis *et al.*, 1997a).

The observation that the correlation of GNE with jitter and shimmer only occurs for pathologic voices can be interpreted as follows: GNE on the one hand and jitter and shimmer on the other hand measure two different voice qualities that often appear together in pathological voices [as has been argued by, e.g., Eskenazi *et al.* (1990); Dejonckere (1995)]. Jitter and shimmer have been associated with irregularities of oscillation that may be due to morphological changes of tissue properties (e.g., changes of the oscillating masses for tumors or cysts, changes of the elastic properties for vocal fold paralysis) (Lieberman, 1963; Dejonckere, 1995). Additive noise may be attributed to air passing through a glottal leak (e.g., for tumors, vocal fold paralyses, post-operative conditions for tumor patients) (Kasuya *et al.*, 1986a; Dejonckere, 1995). Under these assumptions it is reasonable to expect measures of aperiodicity and noise content to covary for pathological voices (Lieberman, 1963; Dejonckere, 1995). Since voice quality of normal voices is generally regarded to possess many independent degrees of freedom, this covariance is not to be expected for the normal group.

4. Correlations of MWC

The correlations of MWC with the other acoustic measures are stated in Table V. The left two columns show the correlation coefficients with jitter and shimmer. The high values for the pathological group (0.78–0.89) can be inter-

TABLE IV. Rank correlation coefficients of different GNE(log), NNE, and CHNR features with jitter and shimmer for the pathological and the normal group (for the abbreviations of the features see Table II). Insignificant correlations are marked by an asterisk (*).

	*j*2	*j*3	*j*5	*j*7	*j*11	*j*15	*s*2	*s*3	*s*5	*s*7	*s*11	*s*15
pathological group												
gne1	0.66	0.65	0.66	0.66	0.65	0.64	0.60	0.60	0.60	0.60	0.58	0.57
gne2	0.62	0.62	0.63	0.63	0.61	0.59	0.55	0.56	0.56	0.56	0.54	0.53
gne3	0.58	0.58	0.59	0.59	0.57	0.55	0.52	0.53	0.53	0.52	0.50	0.49
nne1	0.82	0.77	0.81	0.83	0.83	0.82	0.85	0.84	0.85	0.86	0.85	0.83
nne2	0.79	0.74	0.78	0.81	0.83	0.83	0.84	0.81	0.83	0.84	0.85	0.84
nne3	0.81	0.78	0.81	0.82	0.80	0.77	0.72	0.71	0.72	0.72	0.71	0.70
chnr1	−0.84	−0.80	−0.84	−0.84	−0.84	−0.82	−0.87	−0.86	−0.88	0.87	−0.85	−0.83
chnr2	−0.81	−0.78	−0.82	−0.83	−0.84	−0.83	−0.86	−0.85	−0.86	−0.86	−0.85	−0.83
chnr3	−0.79	−0.77	−0.79	−0.79	−0.77	−0.75	−0.70	−0.70	−0.71	−0.70	−0.69	−0.67
normal group												
gne1	0.11*	0.14*	0.10*	0.07*	0.00*	−0.02*	0.15*	0.21*	0.17*	0.11*	0.05*	0.03*
gne2	0.00*	0.05*	0.02*	−0.03*	−0.11*	−0.14*	0.00*	0.07*	0.02*	−0.03*	−0.09*	−0.12*
gne3	−0.09*	−0.05*	−0.08*	−0.13*	−0.20*	−0.22*	−0.05*	−0.00*	−0.04*	−0.08*	−0.13*	−0.17*
nne1	0.59	0.48	0.60	0.66	0.68	0.64	0.71	0.63	0.69	0.73	0.73	0.71
nne2	0.57	0.44	0.58	0.64	0.68	0.66	0.72	0.62	0.70	0.74	0.76	0.74
nne3	0.70	0.65	0.72	0.72	0.67	0.61	0.45	0.43	0.43	0.44	0.45	0.46
chnr1	−0.62	−0.56	−0.64	−0.68	−0.67	−0.62	−0.73	−0.70	−0.73	−0.74	−0.71	−0.69
chnr2	−0.62	−0.53	−0.66	−0.70	−0.69	−0.65	−0.74	−0.70	−0.74	−0.76	−0.74	−0.72
chnr3	−0.60	−0.58	−0.62	−0.61	−0.53	−0.47	−0.39	−0.41	−0.39	−0.38	−0.35	−0.36

preted as indication that MWC measures indeed one aspect of aperiodicity. For the normal group the only insignificant correlation is with *j*3, which again suggests to use both MWC and this specific jitter measure.

The correlations of MWC with GNE, NNE, and CHNR are stated in the right column. For the pathological group differences between correlations of MWC and the nine ''noise measures'' were also tested for their significance. It was found that MWC correlates significantly less with GNE (0.58–0.65) than with NNE/CHNR (0.77–0.95), while for normal voices there is no significant correlation for MWC with GNE measures. In contrast, MWC is significantly correlated with NNE/CHNR (0.43–0.80) for normal voices. This can be interpreted that for normal voices deviations from the periodic structure that are measured by MWC are mainly due to variations in shape and period length. If they resulted primarily from additive noise, correlations should be found between MWC and the noise-sensitive GNE measures.

In summary, the correlations of jitter, shimmer, or MWC with GNE, are generally either insignificant or significantly smaller than the ones with NNE or CHNR measures. Comparing the different GNE measures, the lowest correlation with different ''aperiodicity measures'' is found for gne3. We conclude that rank-order correlation points to gne3 as the best supplement to the three features jitter, shimmer, and MWC and, more specifically, to the combination {*j*3,*s*15,MWC,gne3}.

C. Mutual information

A nonlinear approach to find the best feature combination in the description of pathological voices is taken from information theory. According to this approach, the one feature that adds the least mutual information to a given set is regarded as the optimal supplement. For the analyses in this section the data values were replaced by their ranks.

TABLE V. Rank correlation coefficients of MWC with the other acoustic features for the pathological and the normal group (for the abbreviations see Table II). Insignificant correlations are marked by an asterisk (*).

	MWC			MWC			MWC	
	pathol.	normal		pathol.	normal		pathol.	normal
*j*2	0.81	0.41	*s*2	0.88	0.65	gne1	0.65	0.06*
*j*3	0.78	0.34*	*s*3	0.87	0.59	gne2	0.61	−0.07*
*j*5	0.81	0.42	*s*5	0.89	0.65	gne3	0.58	−0.12*
*j*7	0.82	0.46	*s*7	0.88	0.67	nne1	0.91	0.78
*j*11	0.82	0.46	*s*11	0.86	0.63	nne2	0.82	0.61
*j*15	0.81	0.43	*s*15	0.84	0.59	nne3	0.77	0.48
						chnr1	−0.95	−0.80
						chnr2	−0.87	−0.66
						chnr3	−0.77	−0.43

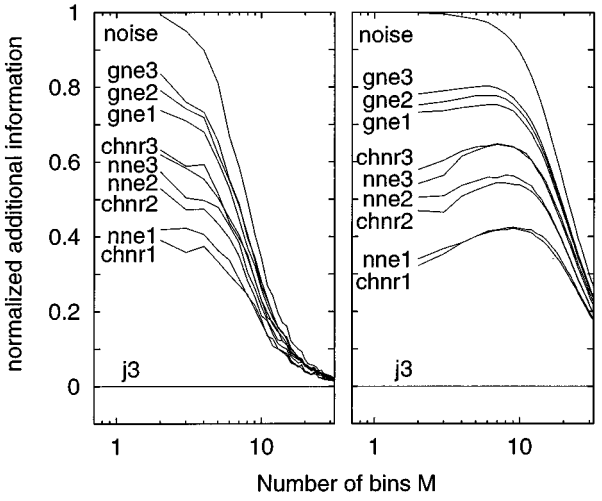

FIG. 1. The normalized additional information ΔI_R for different acoustic features as function of the number of bins M per axis (left: pathological group, $n=447$; right: large pathological group, $n=13\,414$).

Under the assumption that any irregularity in pathological voices may be found in the F_0 sequence, the energy sequence, or the waveform shape of the glottal cycles (Klingholz, 1987), the best choice of jitter and shimmer measures from our list was determined. This was achieved by calculating the three-dimensional mutual information for all combinations of one jitter measure ($j2$, $j3$, $j5$, $j7$, $j11$, $j15$), one shimmer measure ($s2$, $s3$, $s5$, $s7$, $s11$, $s15$), and MWC. The lowest mutual information was found for the combination $\{\text{MWC},j3,s15\}$.

Next, the ''noise measure'' of our list best supplementing this three-feature set was to be determined. Therefore in this second step the four dimensional normalized additional information (ΔI_R) was calculated for all combinations of the set $\{\text{MWC},j3,s15\}$ plus one of the GNE, NNE, or CHNR measures. Also, a sequence of random numbers (referred to simply as ''noise'' in the following) was used as fourth ''feature'' to supply a reference.[3] Theoretically, the predictability of such a ''feature'' should be zero (corresponding to the highest normalized additional information possible, i.e., $\Delta I_R=1$).[4] Theory predicts that the addition of one of the measures already present should amount to a zero increase of information. Therefore $j3$ was used as yet another fourth feature to test the performance of the algorithm.

The results for the pathological group are displayed in Fig. 1 (left). The general drop of the curves reflects the rapid decrease of the average number of data points per hyper-bin when the number of bins per feature axis is increased. For this reason the upper limit of ΔI_R (realized by using noise as fourth feature) has already dropped to approximately 0.95 for $M=4$. This indicates that in this case ΔI_R can be stated only with a 5% accuracy while four bins per axis still give a relatively crude approximation of the probability density of the corresponding measure.

For this reason the same analysis was performed again using the large pathological group ($n=13414$). Now the drop of the curves starts at higher values of M (Fig. 1, right). In this case the curves reach maximum values for $M=8$. At this point the value for noise is still greater than 0.95. This signifies that the number of data points per hyper-bin is still sufficiently large to yield dependable results while eight bins per axis give a much better approximation of the probability distribution than the previous four bins. In any case, the ranking of the features with respect to the normalized additional information is not affected by the choice of M and is the same for either data group. As conclusion, the best additional measure indicated by the curves in Fig. 1 is gne3.

Summarizing the results of this section: generally, the ranking of the ''noise features'' corresponds to the results of the correlation analysis of the previous section—the lower the correlation with the ''aperiodicity measures,'' the higher the normalized additional information. Analysis of the normalized additional information consistently shows for both data sets of pathological voices that about 80% of the possible increase of information can be obtained by gne3 supplementing the set $\{\text{MWC},j3,s15\}$. This is about 20% more than the informational gain realized by adding any NNE or CHNR measure. Since GNE gives interpretable information about a voice (in contrast to random noise), the results of this section point to $\{\text{MWC},j3,s15,\text{gne3}\}$ as the optimal four-item set out of the given 22 acoustic measures.

D. Principal components analysis using singular value decomposition (SVD)

1. Analysis of four-dimensional feature spaces

In the previous section the combination of $\{\text{MWC},j3,s15\}$ was determined as the best choice of the list of ''aperiodicity features'' from an information theory perspective. Now principal components analysis is applied to the four-dimensional data space defined by this three-feature set and one additional ''noise measure'' to determine the underlying dimensionality of the data space.

The results for the three data groups (normal, small, and large pathological) are listed in Table VI. The values for the pathological groups show that gne3 consistently maximizes the variance of the second principal axis compared to the NNE and CHNR measures. In particular, the variance of the second principal axis is higher for gne3 (16%) than for chnr3 (9%) and nne3 (10%).

Generally, for the pathological groups only 5%–8% of the variance are located outside the plane defined by the first two axes. Therefore the informational loss by projecting the four-dimensional space onto a two-dimensional subspace is relatively small. The statistical congruence of the small and large pathological group is again confirmed by the observation that the differences in the results for both groups never exceed 1%.

For the normal group the four-feature space cannot be projected onto a two-dimensional subspace without considerable loss of information. A possible interpretation is that for normal voices the four measures vary independently and that a higher-dimensional description is needed for an adequate classification of voice quality.

TABLE VI. Variance accounted for by the first four principal axes for the combination of {*j*3,*s*15,MWC} with one of the GNE(log), NNE, and CHNR measures for the pathological group ($n=447$), the extended pathological group ($n=13414$), and the normal group ($n=88$).

	Pathological group ($n=447$)				Pathological group ($n=13414$)				Normal group ($n=88$)			
Par	1	2	3	4	1	2	3	4	1	2	3	4
gne1	0.80	0.12	0.05	0.03	0.79	0.12	0.05	0.03	0.51	0.25	0.16	0.09
gne2	0.78	0.14	0.05	0.03	0.77	0.15	0.05	0.03	0.50	0.26	0.15	0.08
gne3	0.76	0.16	0.05	0.03	0.76	0.16	0.05	0.03	0.51	0.25	0.16	0.08
nne1	0.88	0.06	0.03	0.02	0.89	0.06	0.04	0.01	0.68	0.18	0.09	0.05
nne2	0.87	0.06	0.04	0.03	0.88	0.05	0.04	0.03	0.67	0.18	0.10	0.06
nne3	0.82	0.10	0.05	0.03	0.82	0.10	0.05	0.03	0.63	0.18	0.12	0.08
chnr1	0.89	0.06	0.04	0.01	0.89	0.06	0.04	0.01	0.69	0.17	0.09	0.04
chnr2	0.88	0.06	0.04	0.03	0.88	0.06	0.04	0.02	0.68	0.17	0.09	0.06
chnr3	0.83	0.09	0.05	0.03	0.83	0.09	0.05	0.03	0.60	0.19	0.13	0.07

2. Analysis of the complete feature space

PCA supplies a means to analyze the complete 22-dimensional feature space simultaneously and was therefore used to test whether GNE is indeed the main contributor to the second principal axis. With this motivation SVD was performed for the complete set of the 22 acoustic measures stated in Table II. The variance accounted for by the different principal axes is shown in Fig. 2. A two-dimensional space results for the pathological group and a four-dimensional space for the normal group if principal components accounting for less than 5% of the variance are considered negligible. For both groups the first axis is the predominant one, accounting for 80% of the variance for the pathological group and 59% for the normal group.

A deeper insight into the structure of the principal directions is gained by a closer look at the components of the first two principal vectors (Fig. 3). For the pathological group the absolute values of the contribution to the first principal axis are approximately constant (0.2) with the exception of the GNE measures at clearly lower values (Fig. 3, top). For the normal group, where GNE hardly contributes to the first principal axis at all, this difference between GNE and the

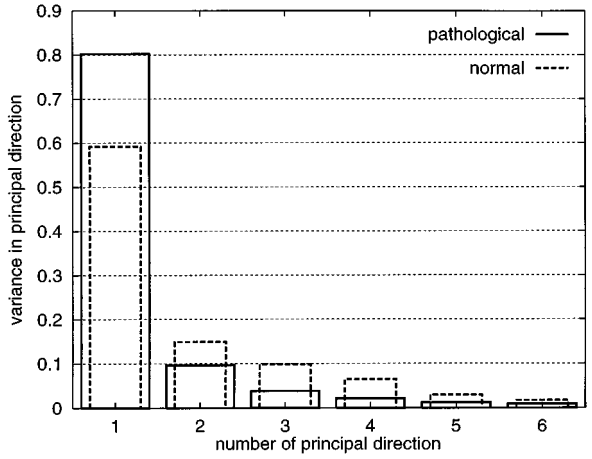

FIG. 2. Variance accounted for by the first six principal components extracted from a 22-dimensional data space for the normal and pathological group (sorted in descending order).

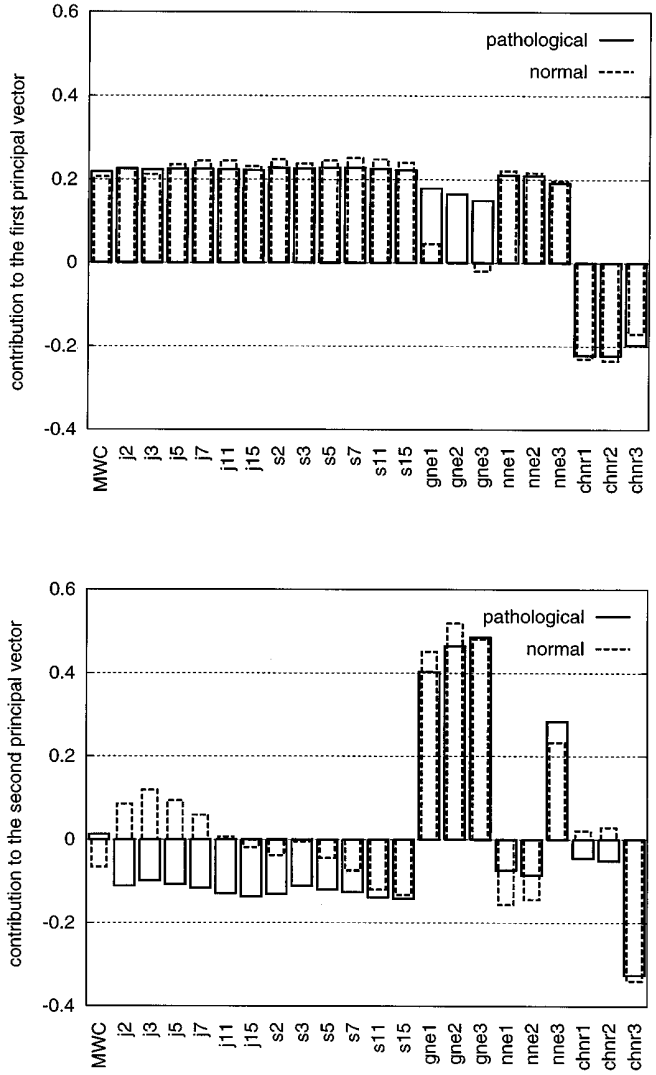

FIG. 3. Contribution of the acoustic features to the first and second principal axis obtained by SVD of the 22-dimensional feature space. The variance in the first principal direction (top) is 80% for the pathological group and 59% for the normal group, in the second principal direction (bottom) 9.7% for the pathological group and 15% for the normal group.

TABLE VII. Relative contribution of the four features MWC, $j3$, $s15$, and gne3 to the two principal axes rotated by 63.9 degrees. The rotation to a minimization of the fourth feature (gne3) in the first principal direction (top: exact values, bottom: balanced idealization used for the ''hoarseness diagram'').

Principal direction	MWC	$j3$	$s15$	gne3
1	0.499	0.606	0.619	0.000
2	−0.172	0.078	0.063	0.980
factors used in the ''hoarseness diagram'':				
1	0.577	0.577	0.577	0.000
2	0	0	0	1

other measures is even more pronounced. However, the three GNE measures are found to be the main contributors to the second principal axis (Fig. 3, bottom). This indicates GNE as the dominant feature for the data distribution to be two-dimensional instead of just one-dimensional. These findings support the previous results of the SVD on four-feature subsets.

E. The ''hoarseness diagram''

The results of the last section cannot be interpreted easily without a deeper understanding of the analysis methods applied. However, for a clinical application a concise (yet suggestive) way to present the results is desirable. Since the data space of the pathological voices was found to be two dimensional, a two-dimensional graphical representation seems to be the most obvious way to present the acoustic analysis.

In order to obtain a suitable graph, the coordinate system defined by the first two principal components of the {MWC,$j3$,$s15$,gne3} system is rotated by 63.9 degrees. This leads to a minimization of the gne3 component in the first principal direction (see Table VII, top). Simplifying further, not these exact factors are used but a balanced idealization (Table VII, bottom). An offset of 5 and 1.5 is chosen for the x-axis and the y-axis, respectively, in order to obtain positive values for all data. The GNE enters the y-coordinate linearly (instead of the logarithmic feature gne3) to supply a better possibility to distinguish between normal and pathologic voices.

The coordinates in this plot of the normalized data are thus given by the equations:

$$x\text{-coordinate} = 5 + \frac{1}{\sqrt{3}}\left(\frac{\text{MWC}+1.614}{0.574} + \frac{j3+0.374}{0.645} + \frac{s15-0.757}{0.368}\right), \tag{7}$$

$$y\text{-coordinate} = 1.5 + \frac{0.695-(1-10^{\text{gne3}})}{0.242}. \tag{8}$$

From Eq. (7) it can be seen that only ''aperiodicity measures'' enter the x-coordinate so that this axis is named *irregularity component*. Equation (8) shows that the y-axis is based entirely on the ''noise feature'' GNE. Therefore the ordinate is labeled *noise component*. These two coordinates

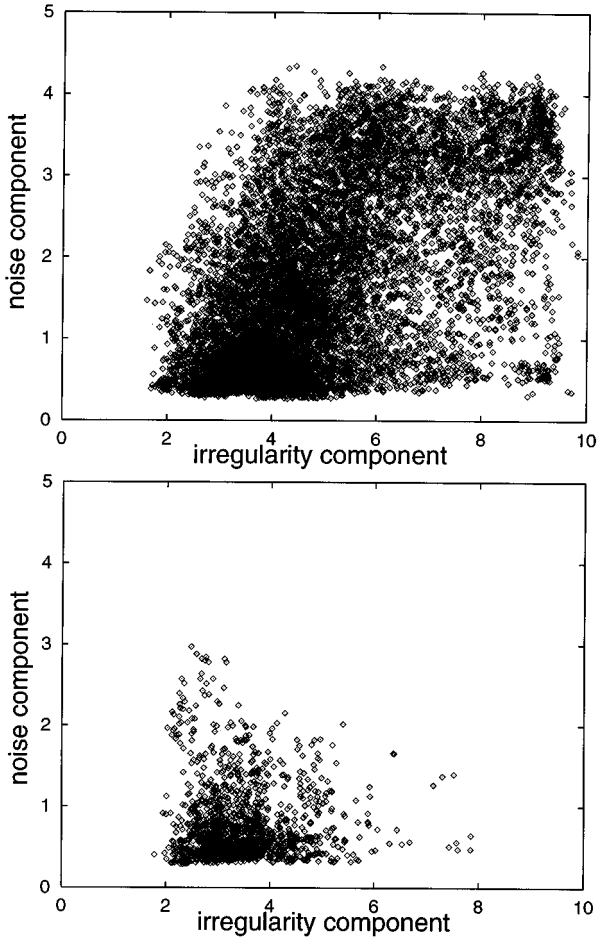

FIG. 4. ''Hoarseness diagram'' for the large pathological group (top) and the normal group (bottom). Each analysis frame is represented by one point with the coordinates given by Eqs. (7) and (8).

define the ''hoarseness diagram'' that allows a quantitative description and graphical interpretation of pathological voice quality (Michaelis *et al.*, 1997b; Fröhlich *et al.*, 1997, 1998a, b).

The ''hoarseness diagrams'' of the large pathological group and the normal group in Fig. 4 reveal that a large area is covered by the pathologic voices. The normal voices are clustered in the lower left region and supply a reference when looking at the undifferentiated pathological group.

III. CONCLUSION

A two-dimensional description of voice quality was derived from four acoustic voice quality measures. Three features (jitter, shimmer, mean period correlation MWC) describe different aspects of the signal irregularity. Mutual information analysis revealed that the best jitter and shimmer measures chosen from a list of 12 possible ones were the PPQ averaging 3 periods ($j3$) and the EPQ averaging 15 periods ($s15$). Results of the PCA suggest that these three measures contribute in roughly equal parts to a common dimension.

An additional feature supplying new information about a pathological voice was determined from a list of measures capable to describe the noise content of a speech signal. Cor-

relation analysis, mutual information analysis, and principal components analysis consistently showed GNE with a 3-kHz bandwidth of the Hilbert envelopes as the best additional measure. Compared to CHNR and NNE, GNE correlated less with jitter and shimmer for pathologic voices and not significantly for normal voices. Therefore GNE should be given preference for the independent measurement of additive noise.

The four features found to give the best description of a pathological voice were used to define the ''hoarseness diagram.'' In this diagram jitter, shimmer, and period correlation contribute in equal parts to the x-coordinate while a linear function of the GNE defines the y-coordinate. The ''hoarseness diagram'' has already proven to be valuable in differentiating between various phonation mechanisms and specific vocal pathologies (Michaelis *et al.*, 1997b; Fröhlich *et al.*, 1998a,b), as well as in monitoring the progress of voices during voice rehabilitation (Fröhlich *et al.*, 1998a, b). Its correlation to perceptual voice qualities has been shown (Zwirner *et al.*, 1998).

ACKNOWLEDGMENTS

We wish to express our gratitude to Professor E. Kruse for his encouragement and cooperation. We thank the anonymous reviewers for the many helpful suggestions and comments. Also, we want to thank I. Titze, R. Baken, R. Orlikoff, and J. Sundberg for the discussions of our results. This work is part of a project funded by the Deutsche Forschungsgemeinschaft under Kr 1469/2-1.

APPENDIX

The glottal-to-noise excitation ratio (GNE) is designed as an acoustic measure to assess noise in a pulse train that is typically generated by the oscillation of the vocal folds (Michaelis and Strube, 1995; Michaelis *et al.*, 1997a). It is based on the assumption that glottal pulses resulting from the collision of the vocal folds lead to a synchronous excitation of different frequency bands. Turbulent noise generated at a constriction, on the other hand, leads to an uncorrelated excitation. The synchronism is expressed by the correlations between envelopes calculated for the different frequency bands.

The algorithm to calculate the GNE (more precisely to calculate gne3 according to Table II) looks as follows (for a more detailed description see Michaelis *et al.*, 1997a): (1) linear-predictive inverse filtering of the speech signal to obtain glottal pulses (if present); (2) bandpass filtering of the residual signal in the frequency domain by applying Hanning windows (3000 Hz width) at different center frequencies; (3) calculation of the Hilbert envelopes for each frequency band in the frequency domain and back-transformation to the time domain; (4) calculation of correlation coefficients between the different Hilbert envelopes for lags in the range $-0.3\ \text{ms} \leqslant t \leqslant 0.3\ \text{ms}$ (difference of center frequencies has to be at least 1500 Hz); (5) maximum correlation coefficient defines the GNE.

GNE is sensitive to broadband noise, which was tested in a study using synthetic signals (Michaelis *et al.*, 1997a). It reaches its maximum value of 1.0 if the envelopes in two different frequency bands are exactly the same.

However, a general restriction for the generalization of results on synthetic signals lies in the appropriateness of the model used to generate the data. Therefore tests on real speech are equally important. The performance of the GNE has already been discussed for several case studies of various voice conditions (Fröhlich *et al.*, 1997). Generally, for real voices, white or high-frequent noise might be present in the speech signal at a level at which it already affects the higher harmonics (due to the spectral tilt) while the lower harmonics still remain relatively unchanged. Since voice signals contain most energy at the low frequencies, in this case the signal periodicity—insofar as it existed—would be hardly affected. However, the correlation between the envelopes in the different bands would be diminished considerably. Therefore, a lower GNE would result.

In such a situation, both an increase of the noise level and a stronger spectral tilt would show up as a further decrease in the GNE. Both aspects have been correlated with breathy voice quality (Hammarberg *et al.*, 1981; Klatt and Klatt, 1990; Hillenbrand *et al.*, 1994; Dejonckere, 1995) which in turn indicates the glottal phonation conditions according to some studies (Fritzell *et al.*, 1983b; Södersten and Lindestad, 1990). Therefore GNE is a promising acoustic feature in the assessment of voice quality with regard to perceptual qualities (Zwirner *et al.*, 1998) or to physiological conditions (Fröhlich *et al.*, 1998a, b).

[1]Since B is a function of M, the definition of ΔI_R in a strict sense is given by $\Delta I_R = \lim_{M\to\infty}(B-(I_4-I_3))/\mathrm{ld}(M)$. Due to the finite amount of data this equation cannot be applied, but care has to be taken to use enough data points for Eq. (6).

[2]$\{j3,s15\}$ will also be determined as the best combination of jitter and shimmer measures by mutual information analysis in Sec. II C. Therefore only differences between correlation coefficients with regard to this specific pair of measures were tested for their significance in order to keep the number of tests down to a manageable size.

[3]Two-dimensional plots for different sets of random numbers generated by the internal random number algorithm of the computer exhibited clustered structures. These structures indicated that a uniform distribution using this random number generator was not realized. A much better way of obtaining uniformly distributed values was by taking the sample values of a recording of a whispered voice.

[4]This illustrates again the restrictions that apply to results of the mutual information analysis. The numerical value of ΔI_R does not allow to draw conclusions as to the ''knowledge'' gained by the addition of the new ''feature.'' However, once the usefulness of a feature is established by other methods or by theory, ΔI_R represents a ''gain of information'' in the conventional meaning.

Arends, N., Povel, D.-J., van Os, E., and Speth, L. (**1990**). ''Predicting voice quality of deaf speakers on the basis of glottal characteristics,'' J. Speech Hear. Res. **33**, 116–122.

Askenfelt, A. G., and Hammarberg, B. (**1986**). ''Speech waveform perturbation analysis: A perceptual-acoustical comparison of seven measures,'' J. Speech Hear. Res. **29**, 50–64.

Bielamowicz, S., Kreiman, J., Gerratt, B. R., Dauer, M. S., and Berke, G. S. (**1996**). ''Comparison of voice analysis systems for perturbation measurement,'' J. Speech Hear. Res. **39**, 126–134.

Childers, D., and Lee, C. (**1991**). ''Vocal quality factors: Analysis, synthesis, and perception,'' J. Acoust. Soc. Am. **90**, 2394–2410.

de Krom, G. (**1993**). ''A cepstrum-based technique for determining a harmonics-to-noise ratio in speech signals,'' J. Speech Hear. Res. **36**, 224–266.

de Krom, G. (**1995**). ''Some spectral correlates of pathological breathy and rough voice quality for different types of vowel fragments,'' J. Speech Hear. Res. **38**, 794–811.
Dejonckere, P. (**1995**). ''Principal components in voice pathology,'' Voice **4**, 96–105.
Eskenazi, L., Childers, D., and Hicks, D. (**1990**). ''Acoustic correlates of vocal quality,'' J. Speech Hear. Res. **33**, 298–306.
Fraser, A. M., and Swinney, H. L. (**1986**). ''Independent coordinates for strange attractors from mutual information,'' Phys. Rev. A **33**, 1134–1140.
Fritzell, B., Gauffin, J., Hammarberg, B., Karlsson, I., and Sundberg, J. (**1983a**). ''Measuring insufficient vocal fold closure during phonation,'' Speech Transmission Lab.—Quarterly Progress and Status Report (KTH Stockholm) 4/1983, 50–59.
Fritzell, B., Hammarberg, B., Gauffin, J., and Sundberg, J. (**1983b**). ''Acoustic inverse filtering of breathy phonation,'' XIX Congress of the International Association of Logopaedics and Phoniatrics.
Fröhlich, M., Michaelis, D., Strube, H. W., and Kruse, E. (**1997**). ''Acoustic voice quality description: Case studies for different regions of the hoarseness diagram,'' in *Advances in Quantitative Laryngoscopy, 2nd 'Round Table,' Erlangen 1997*, edited by T. Wittenberg, P. Mergell, M. Tigges, and U. Eysholdt (Abt. Phoniatrie Univ. Göttingen, Göttingen, 1997), pp. 143–150.
Fröhlich, M., Michaelis, D., Strube, H. W., and Kruse, E. (**1998a**). ''Stimmgütebeschreibung mit Hilfe des Heiserkeits-Diagramms: Untersuchung verschiedener pathologischer Gruppen,'' in *Aktuelle phoniatrisch-pädaudiologische Aspekte 1997*, edited by M. Gross (Renate Gross Verlag, Berlin, 1998), Vol. 5 (in press).
Fröhlich, M., Michaelis, D., Strube, H. W., and Kruse, E. (**1998b**). ''Voice quality assessment using the hoarseness diagram,'' submitted.
Hammarberg, B., Fritzell, B., Gauffin, J., Sundberg, J., and Wedin, L. (**1980**). ''Perceptual and acoustic correlates of abnormal voice qualities,'' Acta Oto-Laryngol. **90**, 441–451.
Hammarberg, B., Fritzell, B., and Schiratzki, H. (**1981**). ''Teflon injection in 16 patients with paralytic dysphonia—Perceptual and acoustic evaluations,'' Speech Transmission Lab.—Quarterly Progress and Status Report (KTH Stockholm) 1/1981, 38–57.
Hillenbrand, J. (**1987**). ''A methodological study of perturbation and additive noise in synthetically generated voice signals,'' J. Speech Hear. Res. **30**, 448–461.
Hillenbrand, J. (**1988**). ''Perception of aperiodicities in synthetically generated voices,'' J. Acoust. Soc. Am. **83**, 2361–2371.
Hillenbrand, J., and Houde, R. A. (**1996**). ''Acoustic correlates of breathy vocal quality: Dysphonic voices and continuous speech,'' J. Speech Hear. Res. **39**, 311–321.
Hillenbrand, J., Cleveland, R. A., and Erickson, R. L. (**1994**). ''Acoustic correlates of breathy vocal quality,'' J. Speech Hear. Res. **37**, 769–778.
Hirano, M., Hibi, S., Terasawa, R., and Fujiu, M. (**1986**). ''Relationship between aerodynamic, vibratory, acoustic and psychoacoustic correlates in dysphonia,'' J. Phonetics **14**, 445–456.
Hirano, M., Hibi, S., Yoshida, T., Hirade, Y., Kasuya, H., and Kikuchi, Y. (**1988**). ''Acoustic analysis of pathological voice,'' Acta Oto-Laryngol. **105**, 432–438.
Hollien, H., Michel, J., and Doherty, E. (**1975**). ''A method for analyzing vocal jitter in sustained phonation,'' J. Phonetics **1**, 85–91.
Holm, S. (**1979**). ''A simple sequentially rejective multiple test procedure,'' Scand. J. Statist. **6**, 65–70.
Kasuya, H., Endo, Y., and Saliu, S. (**1993**). ''Novel acoustic measurements of jitter and shimmer characteristics from pathological voice,'' in *Eurospeech '93 Proceedings*, edited by K. Fellbaum (Berlin, 1993), Vol. 3, pp. 1973–1976.
Kasuya, H., Ogawa, S., Kikuchi, Y., and Ebihara, S. (**1986a**). ''An acoustic analysis of pathological voice and its application to the evaluation of laryngeal pathology,'' Speech Commun. **5**, 171–181.
Kasuya, H., Ogawa, S., Mashima, K., and Ebihara, S. (**1986b**). ''Normalized noise energy as an acoustic measure to evaluate pathologic voice,'' J. Acoust. Soc. Am. **80**, 1329–1334.
Klatt, D. H., and Klatt, L. C. (**1990**). ''Analysis, synthesis, and perception of voice quality variations among female and male talkers,'' J. Acoust. Soc. Am. **87**, 820–857.
Klingholz, F. (**1987**). ''The measurement of the signal-to-noise ratio (SNR) in continuous speech,'' Speech Commun. **6**, 15–26.
Koike, Y. (**1971**). ''Application of some acoustic measures for the evaluation of laryngeal dysfunction,'' Stud. Phonol. (Kyoto University) **7**, 45–50.
Kreiman, J., and Gerratt, B. R. (**1994**). ''The multidimensional nature of pathologic vocal quality,'' J. Acoust. Soc. Am. **96**, 1291–1302.
Kreiman, J., and Gerratt, B. R. (**1996**). ''The perceptual structure of pathologic voice quality,'' J. Acoust. Soc. Am. **100**, 1787–1795.
Kreiman, J., Gerratt, B. R., Precoda, K., and Berke, G. S. (**1992**). ''Individual differences in voice quality perception,'' J. Speech Hear. Res. **35**, 512–520.
Kreiman, J., Gerratt, B. R., Kempster, G. B., Erman, A., and Berke, G. S. (**1993**). ''Perceptual evaluation of voice quality: Review, tutorial, and a framework for future research,'' J. Speech Hear. Res. **36**, 21–40.
Kumar, A., and Mullik, S. (**1996**). ''Nonlinear dynamical analysis of speech,'' J. Acoust. Soc. Am. **100**, 615–629.
Lieberman, P. (**1963**). ''Some acoustic measures of the fundamental periodicity of normal and pathologic larynges,'' J. Acoust. Soc. Am. **35**, 344–353.
Michaelis, D., and Strube, H. W. (**1995**). ''Empirical study to test the independence of different acoustic voice parameters on a large voice database,'' in *Eurospeech '95 Proceedings*, edited by J. M. Pardo, E. Enriquez, J. Ortega, J. Ferreiros, J. Macias, and F. J. Valverde (Madrid, 1995), Vol. 3, pp. 1891–1894.
Michaelis, D., Gramss, T., and Strube, H. W. (**1997a**). ''Glottal to noise excitation ratio—A new measure for describing pathological voices,'' Acust. Acta Acust. **83**, 700–706.
Michaelis, D., Strube, H. W., and Kruse, E. (**1997b**). ''Reliabilität und Validität des Heiserkeits-Diagramms,'' in *Aktuelle phoniatrisch-pädaudiologische Aspekte 1996*, edited by M. Gross (Renate Gross Verlag, Berlin, 1997), Vol. 4, pp. 25–26.
Milenkovic, P. (**1987**). ''Least mean square measures of voice perturbation,'' J. Speech Hear. Res. **30**, 529–538.
Murry, T., Singh, S., and Sargent, M. (**1977**). ''Multidimensional classification of abnormal voice qualities,'' J. Acoust. Soc. Am. **61**, 1630–1635.
Pinto, N. B., and Titze, I. R. (**1990**). ''Unification of perturbation measures in speech signals,'' J. Acoust. Soc. Am. **87**, 1278–1289.
Press, W. H., Flannery, B. P. Teukolsky, S. A., and Vetterling, W. T. (**1989**). *Numerical Recipes in C* (Cambridge U.P., Cambridge, MA, 1989).
Qi, Y., and Hillman, R. E. (**1997**). ''Temporal and spectral estimations of harmonics-to-noise ratio in human voice signals,'' J. Acoust. Soc. Am. **102**, 537–543.
Rammage, L. A., Peppard, R. C., and Bless, D. M. (**1992**). ''Aerodynamic, laryngoscopic, and perceptual-acoustic characteristics in dysphonic females with posterior glottal chinks: A retrospective study,'' J. Voice **6**, 64–78.
Schoentgen, J., and de Guchteneere, R. (**1997**). ''Predictable and random components of jitter,'' Speech Commun. **21**, 255–272.
Södersten, M., and Lindestad, P.-Å. (**1990**). ''Glottal closure and perceived breathiness during phonation in normally speaking subjects,'' J. Speech Hear. Res. **33**, 601–611.
Titze, I. R., and Liang, H. (**1992**). ''Comparison of $f0$ extraction methods for high precision voice perturbation measurement,'' NCVS Status and Progress Report **3**, 97–115.
van den Brink, W., and Koele, P. (**1987**). *Statistiek, deel 3, Toepassingen* (Boom Meppel, Amsterdam, 1987).
Yumoto, E., Gould, W. J., and Baer, T. (**1982**). ''Harmonic-to-noise ratio as an index of the degree of hoarseness,'' J. Acoust. Soc. Am. **71**, 1544–1550.
Zwirner, P., Michaelis, D., Fröhlich, M., Strube, H. W., and Kruse, E. (**1998**). ''Korrelationen zwischen perzeptueller Beurteilung von Stimmen nach dem RBH-System und akustischen Parametern,'' in *Aktuelle phoniatrisch-pädaudiologische Aspekte 1997*, edited by M. Gross (Renate Gross Verlag, Berlin, 1998), Vol. 5 (in press).

Effects of local speaking rate context on the perception of voice-onset time in initial stop consonants

Jennifer Aydelott Utman[a)]
Brown University, Department of Cognitive and Linguistic Sciences, Box 1978, Providence, Rhode Island 02912

(Received 12 December 1996; revised 12 September 1997; accepted 6 October 1997)

This study explored the prediction that local speaking rate context affects the perception of voice-onset time (VOT) in initial stop consonants not only for ambiguous stimuli at the category boundary, but also for good exemplars from the category center [Volaitis and Miller, J. Acoust. Soc. Am. **92**, 723–735 (1992)]. Naturally produced exemplars of the voiceless phonetic category were presented in the context of syllables produced at fast or slow speaking rates in a series of perceptual tasks, including phonetic discrimination, identification, and goodness rating. The results from all three tasks revealed no effects of speaking rate context on the perception of VOT in initial stop consonants. Rather, it appears that listeners perceive longer VOTs as better exemplars of the voiceless phonetic category, irrespective of the rate context. Further, an additional condition, in which the instructions and familiarization tasks presented prior to the administration of the perceptual tests were similar to those used by Volaitis and Miller [J. Acoust. Soc. Am. **92**, 723–735 (1992)], revealed that the previous results may have been influenced by the experimental design. [S0001-4966(98)05201-1]

PACS numbers: 43.71.−k, 43.71.An, 43.71.Es [WS]

INTRODUCTION

Voice-onset time, i.e., the amount of time between the release of a consonant and the onset of glottal phonation, is a well-established acoustic cue to the perception of the voicing contrast in initial stop consonants. Voiceless stops in English are associated with long voice-onset times (VOTs) relative to voiced stops, and listeners demonstrate a clear perceptual boundary between voiced and voiceless phonetic categories that corresponds to differences in VOT. Nonetheless, the production of VOT is influenced by speaking rate. At slower speaking rates, overall syllable duration increases, and VOT values for voiceless and (to a lesser extent) voiced stop consonants are longer than at faster rates (Diehl *et al.*, 1980; Summerfield, 1975). In addition, the frequency distribution of VOT values for voiceless consonants is wider at slow rates than at fast rates, and the VOT value that optimally distinguishes between the voiced and voiceless categories shifts toward longer values at slower rates (Miller *et al.*, 1986).

Some evidence suggests that the perception of VOT is also affected by speaking rate. The influence of the duration of the target syllable on phonetic identification has been investigated in a number of studies. In particular, Summerfield (1981) examined the effect of rate on the perception of the voicing contrast in initial stops using synthetic VOT continua from /biz/ to /piz/ that differed in overall syllable duration. An identification task revealed that, as syllables became longer, the perceptual boundary between voiced and voiceless stops and the distribution of identification responses for both categories shifted toward longer VOT values, although this shift was smaller in magnitude than that observed in VOT analyses of speech production across speaking rates (cf. Pind, 1995).

Some researchers have suggested that, like other perceptual categories (e.g., Rosch, 1975), phonetic categories are arranged in terms of a best exemplar or prototype, and that acoustic tokens are judged in terms of their distance from this prototype. Samuel (1982) investigated this possibility in voiced and voiceless stop consonants using a selective adaptation paradigm. Goodness judgments of the syllable /ga/ along a VOT continuum from /ga/ to /ka/ were obtained, and syllables from the extreme end of the category, the category center, and closest to the category boundary were used as adapters in a phonetic identification task. Significantly greater adaptation was found for the central stimuli than for either of the lower-rated stimuli. These findings indicate that the best-rated central stimulus acted as a category prototype, and was more likely to influence phonetic categorization than surrounding stimuli on the continuum. Thus phonetic categories appear to possess an internal structure consisting of a central prototype and a surrounding distribution of less typical exemplars, which may be closer to or further from the category boundary (cf. Kuhl, 1991).

The effect of speaking rate on phonetic prototypes was explored by Miller and Volaitis (1989), who synthesized VOT continua from /bi/ to /pi/ to /*pi/ (an ''exaggerated, breathy version'' of the syllable /pi/), keeping syllable duration constant at either 125 or 325 ms. The two syllable durations were representative of a fast and a slow speaking rate, respectively. Subjects were asked to identify stimuli from the two continua as B, P, or *P, and to rate the goodness of each stimulus as a member of the phonetic category /p/ on a scale of 1–10. Results of the identification task revealed significant effects of syllable duration on both boundary location

[a)]Now at the Center for Research in Language, University of California, San Diego, CA.

and category distribution, such that at the longer syllable duration, the B-P and P-*P boundaries shifted toward longer VOT values, and the overall distribution of the B, P, and *P categories broadened to include a wider range of values than at the shorter syllable duration. Mean goodness judgments of the same stimuli showed that the range of values defining a good exemplar of the /p/ category broadened at the longer syllable duration, and that this range moved toward longer VOT values. In a similar study examining velar as well as labial stop consonants, Volaitis and Miller (1992) demonstrated that both the peak of the category distribution for voiceless stops and the best-exemplar range shift significantly toward longer VOT values at longer syllable durations. In addition, shifts in the phonetic boundary and category distributions for voiced and voiceless stops have also been obtained when the rate of a context sentence, rather than overall syllable duration, serves as a cue to speaking rate (Wayland *et al.*, 1992).

Taken together, the above findings indicate that speaking rate context affects the perception of voicing in initial stop consonants. Of particular importance is the claim made by Volaitis and Miller (1992) that rate context cued by syllable duration affects not only ambiguous stimuli at the category boundary, but good exemplars from the category center. Volaitis and Miller (1992) observe that ''as syllable duration increased [for their stimuli], so too did the VOT values of stimuli considered to be the best exemplars—the prototypic members—of the voiceless category'' (p. 731). They go on to suggest that ''context-dependent processing ...might, in general, operate beyond the boundaries between phonetic categories, well within the categories themselves'' (p. 732). This claim marks a departure from the conclusions made in previous studies of speaking rate, which have typically only shown shifts in the perception of boundary stimuli in VOT continua. This view predicts that the perception of stimuli that are good exemplars of the voiceless phonetic category should also be influenced by the speaking rate context in which they are perceived. Specifically, a VOT value that is perceived as a good exemplar of a phonetic category in one speaking rate context may be perceived as a poorer exemplar in a different speaking rate context.

The present study tested this prediction by examining the effects of speaking rate context on the perception of naturally produced VOTs that represent good exemplars of the voiceless phonetic category. The stimuli consisted of a set of CVC words with initial voiceless stops. These stimuli were produced at two different speaking rates, a fast rate and a slow rate. Thus rather than representing a continuum of VOT values from voiced to voiceless with an ambiguous boundary region, the initial consonant of each stimulus was an unambiguous exemplar of a voiceless consonant spoken at a fast or a slow speaking rate. These consonants were presented in the context of syllables spoken at fast and slow rates. That is, each VOT was presented with a fast rate syllable context, and a slow rate syllable context. Thus each VOT was either compatible or incompatible with the speaking rate of the remainder of the syllable.

It is important to note that studies using syllable duration as a rate cue have for the most part based their perceptual findings on synthetic continua in which syllable duration is held constant and VOT is varied across a considerable range. For example, Miller and Volaitis (1989) maintained the duration of CV syllables at 125 and 325 ms, while varying VOT in 10-ms steps from 10 to 120 ms and 10 to 320 ms, respectively. However, one effect of this manipulation is that vowel duration varies concomitantly with VOT, such that at longer VOTs the vowel can be as brief as 5 ms (approximately the length of a single pitch period). Data from studies of rate effects on speech production indicate that as VOT increases at slower speaking rates, vowel duration also increases, contributing to the overall increase in syllable duration at slower rates (Miller *et al.*, 1986; cf. Kessinger and Blumstein, 1996). Thus increasing VOT while decreasing vowel duration may exaggerate the magnitude of the effects of overall syllable duration on phonetic perception in natural speech, by producing a trading relation between VOT and vowel duration. However, such a trading relation does not naturally occur as a result of a change in speaking rate. The present research avoids this potential difficulty by using natural speech syllables spoken at different rates, holding the duration of the following vowel (rather than the overall syllable duration) constant at a particular rate as VOT varies (cf. Summerfield, 1981).

Tests of accuracy and reaction time in phoneme discrimination and identification were administered to determine whether compatibility with the speaking rate context influences the way in which VOT is perceived. These tasks have been used in previous studies of phonetic perception as measures of acoustic sensitivity, and as a means of comparing the relative goodness of a set of phonetic exemplars. Specifically, listeners have shown increased reaction times in phonetic discrimination tasks for ''same'' responses to stimulus pairs that are acoustically different, suggesting that they are perceptually sensitive to the acoustic difference (Pisoni and Tash, 1974; Utman *et al.*, 1996; Utman, 1997). Further, increased response times and reduced accuracy to acoustically manipulated stimuli in phonetic identification tasks have been interpreted as an indication that these stimuli are perceived as poorer exemplars of the intended phonetic category (Andruski *et al.*, 1994). In the phoneme discrimination task in the present experiment, listeners were asked to judge as ''same'' or ''different'' pairs of words that contain VOTs for voiceless stops produced at the same rate (e.g., p_{fast}eace-p_{fast}eace) and VOTs for voiceless stops produced at different rates (e.g., p_{slow}eace-p_{fast}eace). In the identification task, VOTs from fast and slow speaking rates were presented in a compatible rate context (e.g., $p_{fast}eace_{fast}$; $p_{slow}eace_{slow}$) and an incompatible rate context (e.g., $p_{fast}eace_{slow}$; $p_{slow}eace_{fast}$). Listeners were asked to identify these VOTs as belonging to the voiced or voiceless category. Response times and accuracy were measured for both tasks.

Based on the previous findings of Volaitis and Miller (1992), it was predicted that listeners would be perceptually sensitive to the acoustic difference between VOTs produced at fast and slow speaking rates. Thus whereas listeners were expected to judge VOTs from fast and slow speaking rates as belonging to the same phonetic category in the discrimination task, they were expected to show longer reaction times

to VOTs from different speaking rates than to VOTs from the same speaking rate. Further, VOTs that were compatible with the rate context were expected to be perceived as better exemplars of their phonetic category. Therefore these VOTs were expected to be identified faster and more accurately than VOTs that were incompatible with the rate context in the phonetic identification task.

I. EXPERIMENT 1: PHONEME DISCRIMINATION AND IDENTIFICATION

A. Method

1. Stimuli

The stimulus list consisted of 26 CVC(C) words that began with the phonemes /p/, /t/, or /k/. The stimuli were recorded by a 37-year-old phonetically trained male speaker of English who had lived in the Providence, RI area for approximately six years. The stimuli were presented to him for recording in orthographic form, and the speaker was asked to read through the stimulus list silently before taping began. All stimuli were read at two rates: 40 words per minute (wpm) and 120 wpm. A metronome was used to time the utterances produced by the speaker, who was asked to articulate each item between the clicks of the metronome. The clicks, which were presented over a single earphone, were audible only to the speaker and were not detected by the recording equipment. At each rate, the speaker produced eight repetitions of each stimulus item. The utterances were recorded in a sound-treated room using a Nagra 4.5 reel-to-reel tape recorder with a Sony electret condenser microphone.

Items were digitized onto a MicroVAX computer at a 20-kHz sampling rate with a 9.0-kHz low-pass filter and a 12-bit quantization. The eight repetitions of each /p,t,k/ word were analyzed using the Bliss waveform editor. Voice onset times (VOTs) were measured by placing cursors at zero-crossings demarcating the burst onset and the onset of phonation (i.e., the onset of the first glottal pulse). Vowel durations were measured from the onset of phonation to the end of the vowel, which was defined as follows: for stimuli ending in a stop or affricate, the offset of phonation or the onset of the closure interval; for stimuli ending in a fricative, the onset of the fricative noise; and for stimuli ending in a nasal consonant or a liquid, the offset of the vowel as determined visually by a change in the overall shape of the waveform, as well as auditorily. Vowel and VOT durations were evaluated separately for each token. At the fast rate (120 wpm), the shortest durations obtained for both VOTs and vowels were selected for splicing; at the slow rate (40 wpm), the longest durations were selected. These extreme values were chosen in order to maximize the duration difference between stimuli produced at different speaking rates; however, tokens were rejected if they were deemed by the experimenter to be poor or ambiguous exemplars of the intended phonetic category. If the most extreme VOT and vowel duration for a particular test item were obtained for the same token of that test item, a similar VOT or vowel duration from another token of that utterance was used in splicing. This was done so that no stimulus item would contain a VOT and a syllabic offset from the same token. At the fast rate, the mean VOT of selected items was 48 ms, and the mean vowel duration was 140 ms; at the slow rate, the mean VOT was 148 ms, and the mean vowel duration was 444 ms. Thus the temporal relationship between segments spoken at a slow rate and segments spoken at a fast rate (both VOTs and vowels) was about 3:1. The stimuli were then cross-spliced as follows (see Table I): VOTs from both the fast and slow rates were spliced onto the final portions of the test syllables (onset of phonation to termination of the final consonant) from both the fast and slow rates, so that, at each rate, test items consisted of a syllable offset with a fast VOT, and a syllable offset with a slow VOT. Syllable offset therefore served as the local speaking rate context, and VOTs were either compatible or incompatible with this context. In other words, while all test items were cross-spliced in the same manner, in some cases the VOT was compatible with the speaking rate of the following vowel and final consonant, and in some cases the VOT was incompatible with this rate. All test stimuli (compatible and incompatible) were edited in this way to eliminate a possible artifact of acoustic manipulation: if items in the incompatible condition were edited and items in the incompatible condition were not, it would not be possible to separate the effects of rate compatibility from possible effects of stimulus editing (e.g., potential discontinuities in formant trajectories). Cross-splicing resulted in four types of test items (a total of 104 stimuli), illustrated in Table I: fast VOT-fast rate (compatible, 26 items); fast VOT-slow rate (incompatible, 26 items); slow VOT-fast rate (incompatible, 26 items); and slow VOT-slow rate (compatible, 26 items). Spectrograms of a representative series of test items are shown in Figs. 1 and 2.

TABLE I. Examples of cross-spliced stimuli for the target word ''peace.'' Stimuli for which the VOT and syllable speaking rates are compatible are shown in shaded cells.

		VOT	
		Fast rate	Slow rate
Rate (syllable) context	Fast rate	$p_{fast}eace_{fast}$	$p_{slow}eace_{fast}$
	Slow rate	$p_{fast}eace_{slow}$	$p_{slow}eace_{slow}$

2. Subjects

Forty students at Brown University, all monolingual native speakers of English between the ages of 18 and 35, were paid for their participation. None of the subjects reported any hearing impairment, and all were naive to the purpose of the experiment.

3. Procedure

Subjects were seated in a sound-treated booth in front of a response box. Prior to each testing session, subjects were instructed to respond to the stimuli as quickly and as accurately as possible, to use only their dominant hand, and to respond even if they were unsure of their answer. Subjects were tested in groups of 1 to 3 in a single testing session. All stimuli were presented via Sony MDR-V2 headphones at a comfortable listening level.

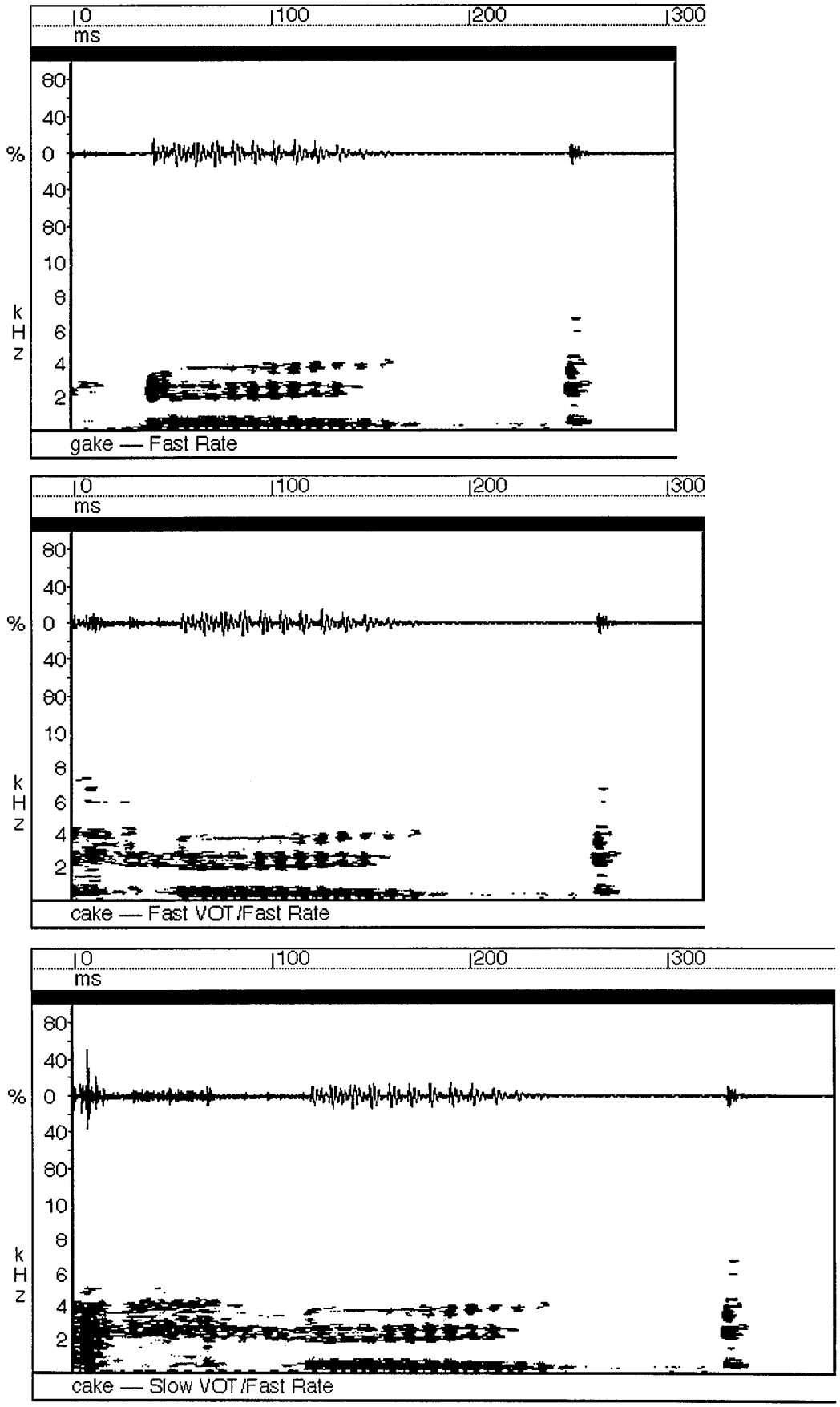

FIG. 1. Spectrograms of a series of cross-spliced stimuli in the fast rate condition (i.e., syllabic offsets produced at a fast speaking rate), with VOTs ranging from voiced to fast (voiceless) to slow (voiceless). In the center panel, the VOT is compatible with the rate context (fast VOT-fast rate), and in the bottom panel, the VOT is incompatible with the rate context (slow VOT-fast rate). In the top panel, the voiced counterpart of the initial voiceless stop (spoken at a fast rate) has been spliced on to the same syllabic offset.

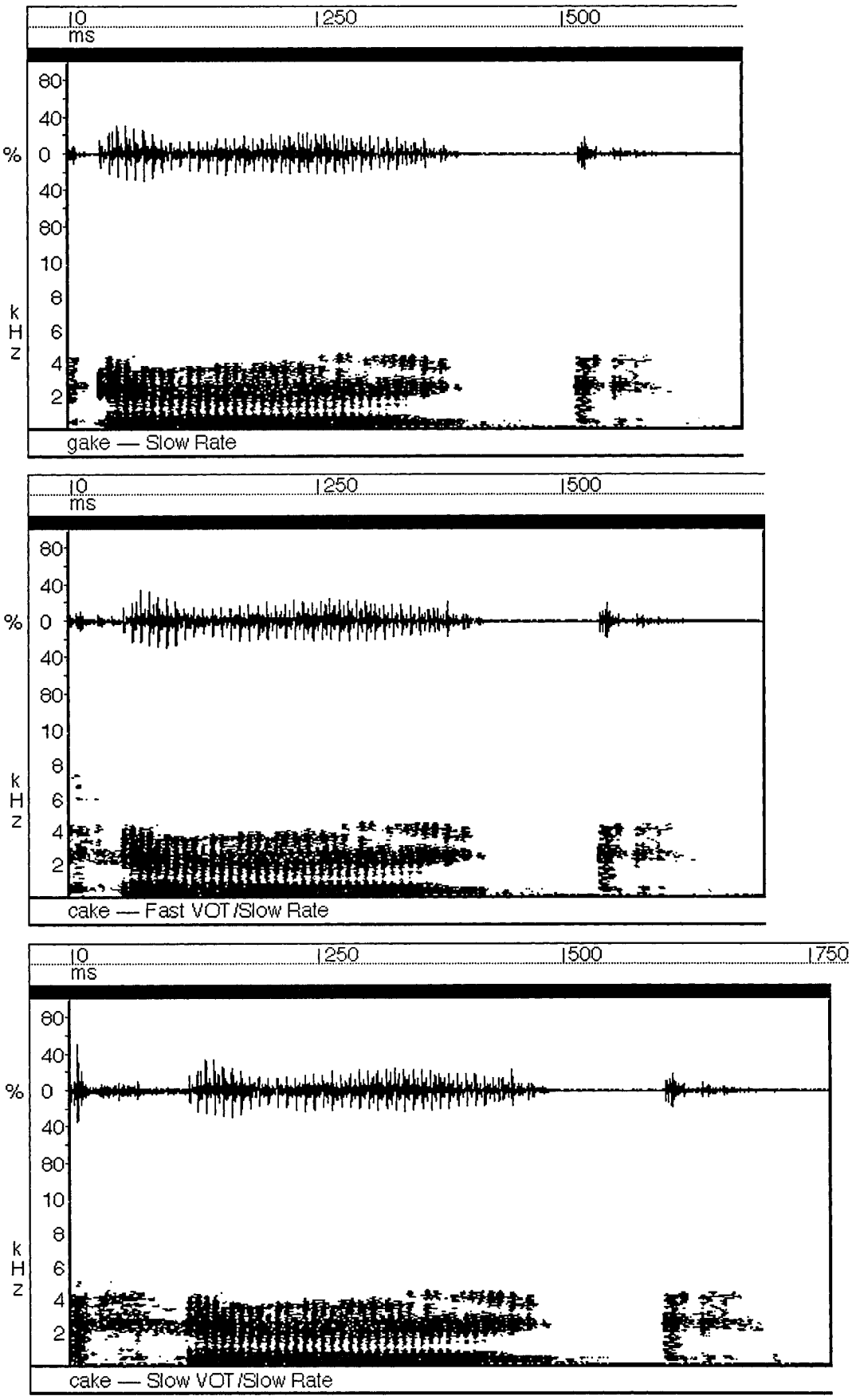

FIG. 2. Spectrograms of a series of cross-spliced stimuli in the slow rate condition, with VOTs ranging from voiced to fast (voiceless) to slow (voiceless). In the center panel, the VOT is incompatible with the rate context (fast VOT-slow rate), and in the bottom panel, the VOT is compatible with the rate context (slow VOT-slow rate). In the top panel, the voiced counterpart of the initial voiceless stop (spoken at a slow rate) has been spliced on to the same syllabic offset.

As discussed above, local speaking rate context was defined as the rate at which the syllabic offset was produced. To preserve the overall naturalness of the stimulus list, stimuli were blocked by rate context for presentation to subjects. Thus 20 of the 40 subjects were presented with syllabic contexts recorded at a fast rate, and the remaining 20 subjects received the slow rate condition. Stimuli were blocked by rate between subjects in this manner for both the discrimination and identification tasks.

The discrimination task was designed to ensure that listeners were perceptually sensitive to the acoustic difference between fast VOTs and slow VOTs within a single speaking rate context. The stimuli for this task consisted of the spliced test items, with items from compatible VOT conditions preceded either by the same compatible VOT word, e.g., $p_{fast}eace_{fast}$-$p_{fast}eace_{fast}$ (fast rate condition); $p_{slow}eace_{slow}$-$p_{slow}eace_{slow}$ (slow rate condition), or by the incompatible VOT word, e.g., $p_{slow}eace_{fast}$-$p_{fast}eace_{fast}$ (fast rate condition); $p_{fast}eace_{slow}$-$p_{slow}eace_{slow}$ (slow rate condition), for a total of 52 test pairs. Thus the VOTs for the voiceless stop consonants in each test pair were either acoustically identical (i.e., from the same speaking rate) or acoustically different (i.e., from two different speaking rates). Distractors (i.e., different trials) were created by splicing voiced onsets from compatible rates onto the VC offsets of the test stimuli and pairing these with compatible VOT words in the same manner described above for the test stimuli, e.g., $b_{fast}eace_{fast}$-$p_{fast}eace_{fast}$ (fast rate condition); $b_{slow}eace_{slow}$-$p_{slow}eace_{slow}$ (slow rate condition), for a total of 52 distractor pairs. The syllabic offsets in each pair (both test pairs and distractor pairs) were always acoustically identical. Spectrograms of representative voiced distractor stimuli at both speaking rates are shown in Figs. 1 and 2. The 104 stimulus pairs (52 test pairs and 52 distractors) were presented to subjects in random order with a 50-ms interstimulus interval (ISI) and a 3000-ms inter-trial interval (ITI). A practice test consisting of 16 pairs (eight test pairs and eight distractors) was presented prior to the beginning of the test series. Subjects were asked to indicate whether each pair sounded the same or different using their own criterion by pressing one of two buttons marked ''same'' and ''different.'' Listeners were not given an explicit criterion on which to base their judgments, in order to avoid influencing their perception of the acoustic characteristics of the stimuli. It was expected on the basis of previous results (Pisoni and Tash, 1974; Utman *et al.*, 1996; Utman, 1997) that listeners would use a phonetic criterion. That is, listeners were expected to respond ''same'' to stimuli from the same phonetic category even for pairs that were not acoustically identical, and to respond ''different'' to stimuli belonging to different phonetic categories. Further, if listeners were perceptually sensitive to the acoustic difference between fast VOTs and slow VOTs, response times were expected to be slower for ''same'' responses to pairs containing acoustically different VOTs than to pairs containing acoustically identical VOTs. Listeners were expected to demonstrate sensitivity to this acoustic difference in both rate contexts.

The identification task was designed to determine whether the perception of VOTs as exemplars of the voiceless phonetic category is influenced by local speaking rate context. The stimuli consisted of test items with compatible and incompatible VOTs, presented in isolation. The initial voiced tokens from the discrimination task served as distractors, and were presented twice so that there were an equal number of voiceless test items and voiced distractors. The 52 test items and 52 distractors were presented in random order, with an ITI of 3000 ms. A practice test consisting of 16 items (eight test words and eight distractors) was presented prior to the beginning of the test series. Subjects were asked to indicate whether each item began with the sound /p/, /t/, /k/, /b/, /d/, or /g/ by pressing one of two response buttons, one marked with the letters ''p t k'' and the other marked ''b d g.'' Based on the findings of Volaitis and Miller (1992), it was predicted that listeners would be faster and more accurate in identifying VOTs that were compatible with the speaking rate context than VOTs that were incompatible with the speaking rate context.

Responses and reaction times for both tasks were recorded by the Gateway 486 that controlled the experiment. Reaction times were measured from the offset of the second stimulus in the test pair for the discrimination task, and from the offset of the isolated word in the identification task.

B. Results

1. Discrimination task

The results of the discrimination task were scored for responses (''same'' or ''different'') and reaction time. Reaction times that were more than two standard deviations from the mean for each subject in each condition were eliminated from the analysis. As predicted, subjects responded ''same'' to both identical and acoustically different pairs: in the fast rate condition, on average subjects responded ''same'' to 91.9% of identical (fast VOT-fast VOT pairs) and to 86.0% of acoustically different (slow VOT-fast VOT pairs), and in the slow rate condition, on average subjects responded ''same'' to 93.5% of identical (slow VOT-slow VOT) pairs and to 91.2% of acoustically different (fast VOT-slow VOT) pairs. A two-way analysis of variance (ANOVA) was performed across subjects with rate context (fast versus slow syllabic offset) as a between-subjects factor and VOT (identical versus different) as a within-subjects factor. In addition, to determine whether the pattern of results generalized across stimulus items and thus avoid the fixed-effect fallacy (Church, 1973), an additional ANOVA was performed with items as the sampling variable. Rate and VOT were treated as within-subjects factors in the item analysis. Both the subject and item analyses revealed a significant main effect of VOT [subject $F(1,38)=25.184$; $p<0.0001$, item $F(1,25)=10.108$; $p<0.01$], reflecting a greater number of ''same'' responses when the VOTs within a stimulus pair were identical than when they were acoustically different. Thus listeners were perceptually sensitive to the acoustic difference between fast VOTs and slow VOTs in both rate contexts. A significant main effect of rate was obtained in the subject analysis [$F(1,38)=8.573$; $p<0.01$], due to a greater number of ''same'' responses in the slow rate context than in the fast rate context. Thus listeners may have been more sensitive to

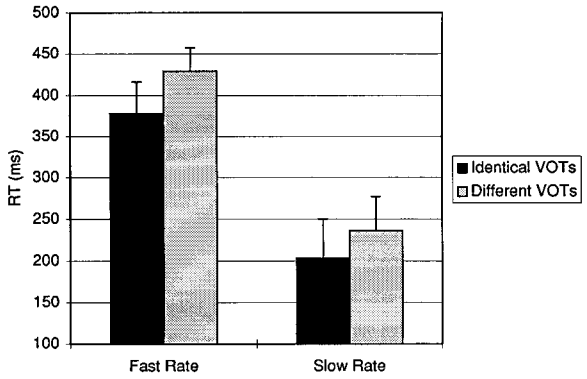

FIG. 3. Mean response times in milliseconds for ''same'' responses to test pairs containing acoustically identical and acoustically different VOTs across speaking rate contexts in the discrimination task (experiment 1).

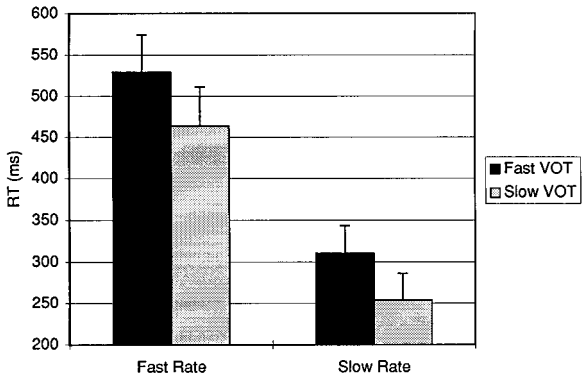

FIG. 4. Mean response times in milliseconds for correct (voiceless) responses to fast VOTs and slow VOTs across speaking rate contexts in the identification task (experiment 1).

the acoustic difference between fast VOTs and slow VOTs at the fast rate than at the slow rate, which suggests that rate context may have influenced perceptual sensitivity to the VOT difference. This possibility was supported by the significant rate×VOT interaction in the subject analysis [$F(1,38)=4.917$; $p<0.05$], which was attributable to the smaller number of ''same'' judgments to acoustically different VOTs at the fast rate than at the slow rate. However, neither the main effect of rate nor the rate×VOT interaction were significant in the item analysis, suggesting that any influence of rate context on perceptual sensitivity was weak and did not generalize across items.

A bar plot of the reaction time data for ''same'' responses is shown in Fig. 3. Two-way subject and item ANOVAs were performed on the response times to ''same'' responses with rate (fast versus slow) as a between-subjects factor and VOT (identical versus different) as a within-subjects factor in the subject analysis and rate and VOT as within-subjects factors in the item analysis. These revealed a significant main effect of rate [subject $F(1,38)=12.106$; $p<0.01$, item $F(1,25)=38.488$; $p<0.0001$] such that subjects' response times were shorter in the slow rate condition than in the fast rate condition. This effect is not surprising, given that stimuli were longer in duration in the slow rate condition, and reaction times were measured from stimulus offset. A significant main effect of VOT [subject $F(1,38)=7.283$; $p<0.05$, item $F(1,25)=11.936$; $p<0.01$] was also obtained, such that response times for ''same'' judgments to acoustically different pairs were significantly longer than response times to identical pairs. As in the analysis of ''same'' responses, this effect indicates that listeners were sensitive to the acoustic difference between fast VOTs and slow VOTs in both rate contexts. However, unlike the analysis of ''same'' responses, the rate×VOT interaction was not significant in the subject analysis or in the item analysis for the reaction time data. Thus there was no significant effect of rate context on reaction times in the discrimination task. Taken together, the results of the ''same'' response and reaction time analyses demonstrate that listeners were able to detect the acoustic difference between fast VOTs and slow VOTs. Further, any effect of rate context on perceptual sensitivity to this difference was weak, emerging only in the subject analysis of responses and failing to emerge in the reaction time data.

2. Identification task

The results of the identification task were scored for errors and reaction time. Response times that were more than two standard deviations from the mean for each subject in each condition were eliminated from the analysis. In the fast rate condition, on average subjects correctly identified 92.9% of initial segments in the fast VOT condition and 94.0% in the slow VOT condition as voiceless. In the slow rate condition, results were similar; on average subjects identified 92.9% of initial segments in the fast VOT condition and 93.8% in the slow VOT condition as voiceless. These results indicate that subjects did in fact consistently identify the initial segments as belonging to the voiceless category. Two-way subject and item ANOVAs were performed on the incorrect responses in the identification task with rate (fast versus slow) as a between-subjects factor and VOT (fast versus slow) as a within-subjects factor in the subject analysis and rate and VOT as within-subjects factors in the item analysis. A significant main effect of VOT emerged [subject $F(1,38)=7.158$; $p<0.05$, item $F(1,25)=4.355$; $p<0.05$] such that across speaking rates, subjects made more errors in the fast VOT condition than in the slow VOT condition. Thus on average more fast VOTs were misidentified as voiced consonants than slow VOTs, irrespective of rate context. Further, there was no significant main effect of rate and no rate×VOT interaction, suggesting that the effect of VOT on phoneme identification was independent of rate context. However, the fact that listeners were highly accurate in identifying the test stimuli as voiceless in all conditions raises the possibility that the lack of an interaction represents a ceiling effect. Thus it was necessary to examine the pattern of response times before concluding that rate context failed to influence phonetic identification.

Analyses of subjects' response times for correct responses in the identification task supported the findings of the accuracy analysis. Mean response times are plotted in Fig. 4. Two-way subject and item ANOVAs, with rate (fast versus slow) as a between-subjects factor and VOT (fast versus slow) as a within-subjects factor in the subject analysis and rate and VOT as within-subjects factors in the item analysis, were performed on the reaction time data. These analyses revealed a significant main effect of rate [subject

$F(1,38)=14.705$; $p<0.001$, item $F(1,25)=209.387$; $p<0.0001$], such that response times were significantly shorter in the slow rate condition than in the fast rate condition. As in the discrimination analysis, this effect is attributable to the measurement of reaction time from stimulus offset: in the slow rate condition, target stimuli are longer, giving listeners more time to identify the initial segment before the offset of the stimulus. A significant main effect of VOT was also obtained [subject $F(1,38)=70.190$; $p<0.0001$, item $F(1,25)=12.111$; $p<0.01$], such that response times to fast VOTs were significantly longer than to slow VOTs. Thus listeners were faster to identify slow VOTs as voiceless than fast VOTs, suggesting that slow VOTs represent better exemplars of the voiceless category. As in the accuracy analysis, no significant rate×VOT interaction emerged, indicating that the effect of VOT on reaction times in the identification task was independent of rate context. Taken together, the results of the accuracy and reaction time analyses indicate that speaking rate context did not influence VOT identification. That is, subjects identified targets in the slow VOT condition more accurately and more rapidly than targets in the fast VOT condition, irrespective of rate.

C. Discussion

The results of the discrimination task indicate that, as predicted, listeners were perceptually sensitive to the acoustic difference between fast VOTs and slow VOTs presented in both rate contexts. That is, listeners demonstrated longer reaction times and decreased ''same'' responses when a stimulus pair contained VOTs from two different speaking rates. Listeners in the fast rate condition were slightly more sensitive to this difference than listeners in the slow rate condition. One possible explanation for this finding is the duration of the stimuli in each rate condition. At the slow rate, stimuli were longer overall than at the fast rate. Thus there was more acoustic information intervening between the presentation of the first stimulus and the presentation of the second stimulus in the slow rate condition. Listeners may therefore have had more difficulty in detecting the acoustic difference between the two stimuli. Nevertheless, the effect of rate context on perceptual sensitivity was weak, and failed to emerge in the reaction time analysis or to generalize across items in the analysis of ''same'' responses.

The pattern of performance obtained in the identification task does not support the previous findings of Volaitis and Miller (1992) that speaking rate affects VOT perception even for good exemplars of the voiceless phonetic category. Listeners were faster and more accurate at identifying slow VOTs than fast VOTs, irrespective of rate context. That is, the compatibility of a VOT with the rate context did not influence its identification as a member of the voiceless category. That listeners showed better performance for slow VOTs may reflect the fact that slow VOTs were further from the phonetic category boundary than fast VOTs, and hence less potentially confusable with a voiced stimulus.

It is important to note that the methodology of the current study differs substantially from that used in previous investigations of speaking rate and phonetic category structure. Specifically, Miller and Volaitis (1989) and Volaitis and Miller (1992) used a phonetic identification task consisting of three choices, e.g., B, P, and *P, and a rating task in which listeners judged the goodness of each stimulus relative to the others in the set. In their investigations, the change in rate primarily affected the P-*P boundary and the upper bound of good exemplars for the voiceless category. As *P is not a true phonetic category, it is difficult to interpret changes in its distribution or perceptual boundaries relative to actual phonetic categories. Further, it is not possible to determine the extent to which this additional category influenced the number of values identified as /p/ at the short syllable duration. The use of a third category in the identification task may have artificially narrowed the best-exemplar range for voiceless consonants by causing subjects to interpret these stimuli as falling into one of two categories.

Nevertheless, significant shifts in the peak of the distribution for /p/ as well as the /b/-/p/ boundary were also obtained as a function of rate context in these studies. Thus the failure of the present experiment to demonstrate significant effects of rate context on phonetic identification for good exemplar stimuli requires further examination.

II. EXPERIMENT 2: GOODNESS RATINGS

In experiment 2, the stimuli in experiment 1 were presented in both a three-choice phonetic identification paradigm and a goodness rating paradigm, modeled after those used in Miller and Volaitis (1989) and Volaitis and Miller (1992). In these investigations, listeners were presented with a familiarization series consisting of the test stimuli presented in order from shortest to longest VOT, and were informed that the series represented a continuum from /b/ to /p/ to /*p/. Listeners were then given the three-choice identification task, or the rating task. It was predicted that listeners in the present experiment would show similar performance on this task to that obtained in Miller and Volaitis (1989) and Volaitis and Miller (1992). Specifically, listeners were expected to give higher goodness ratings to VOTs that were compatible with the rate context than to VOTs that were incompatible with the rate context. Moreover, identification responses were expected to vary systematically as a function of speaking rate. At the fast rate, listeners were expected to identify a greater number of fast VOTs as /p/ and a greater number of slow VOTs as /*p/ than at the slow rate when the category choices included B, P, and *P.

In addition, a goodness rating task was administered to a separate group of participants without a preceding familiarization or identification series. The purpose of this additional condition was to establish whether listeners without prior specific information about the test series would rate the stimuli in the same manner as listeners who had been instructed as to the nature of the stimuli before being asked to rate them. The rationale for this condition was as follows: because listeners in the Miller and Volaitis (1989) and Volaitis and Miller (1992) studies were informed that the test stimuli represented a continuum from voiced to voiceless to ''breathy'' and were presented with an example of this continuum, they were in essence given an external model on which to base their goodness judgments. This external model may have differed from the listeners' internal representation

of the voiceless phonetic category (cf. Kuhl, 1991; Kuhl *et al.*, 1991), and may therefore have produced a set of goodness ratings that failed to accurately reflect this internal representation. The behavioral data in experiment 1 suggest that listeners perceive slow VOTs as better exemplars of the voiceless phonetic category than fast VOTs at both speaking rates. Thus it is possible that in the absence of a familiarization or identification series, listeners would give higher goodness ratings to slow VOTs than to fast VOTs irrespective of rate context.

A. Method

1. Stimuli

The same cross-spliced /p,t,k,/-initial word stimuli and voiced distractors as in experiment 1 were used for both rating tasks.

2. Subjects

Forty-eight students at Brown University, all monolingual native speakers of English between the ages of 18 and 35, were paid for their participation. None of the subjects reported any hearing impairment, and all were naive to the purpose of the experiment. None of the subjects had participated in experiment 1.

3. Procedure

Subjects were seated in a sound-treated booth in front of response boxes. Prior to each testing session, subjects were instructed to respond to the stimuli as quickly and as accurately as possible, to use only their dominant hand, and to respond even if they were unsure of their answer. Subjects were tested individually in a single testing session. All stimuli were presented via Sony MDR-V2 headphones at a comfortable listening level.

As in experiment 1, half of the subjects were presented with stimuli from the fast rate condition (i.e., stimuli with syllabic offsets produced at a fast speaking rate), and the remaining subjects received the slow rate condition. Stimuli were blocked by rate between subjects in this manner for both of the instruction conditions described below. In addition, the stimuli were blocked by place of articulation as in Volaitis and Miller (1992). All subjects received all places of articulation, and the order of presentation of these blocks was counterbalanced across subjects.

Twenty-four of the 48 subjects were assigned at random to the explicit instruction condition. Subjects in this condition were given specific instructions regarding the nature of the stimuli as well as familiarization tasks prior to receiving the rating task, similar to the methodologies described in Miller and Volaitis (1989) and Volaitis and Miller (1992). For each place of articulation, a familiarization series and an identification task were administered before the rating task. The familiarization series consisted of a voiced counterpart, followed by a short (fast) VOT and then a long (slow) VOT (e.g., beace-p_{fast}eace-p_{slow}eace). The series was presented in this order at both speaking rates. Subjects were told that the first word in the series began with the voiced stop (e.g., ''B''), the second word with the voiceless stop (e.g., ''P''), and the third word with an ''exaggerated, breathy version'' of the voiceless stop, which was labeled with an asterisk (e.g., ''*P''). Subjects were instructed to listen carefully to each word in the series, and were then presented with the three-way forced-choice identification task. The identification task consisted of the test items and voiced counterparts presented in random order with an ITI of 2000 ms. Subjects were instructed to identify the first sound of each word as voiced, voiceless, or breathy by pressing one of three buttons marked with phonetic category labels (e.g., ''B,'', ''P,'' or ''*P''). Following the familiarization and identification series, subjects in the explicit instruction condition received a goodness rating task. The test stimuli and their voiced counterparts for each place of articulation were presented in random order with an ITI of 2000 ms. Subjects were told that the first sound in each word was an example of either /p/, /t/, or /k/ (depending upon the place of articulation for that block), and that for some words this sound would be a good example of the phoneme and for others this sound would be a poorer example of the phoneme. Subjects were then instructed to listen to each word and rate the first sound on a scale of 1 (very poor) to 7 (very good). Subjects responded by pressing one of seven numbered buttons on a response box, and were told to use all of the numbers in the scale and to rate each word in relation to the other words in the list. A practice test consisting of eight items (two test items with VOTs compatible with the rate context, two with incompatible VOTs, and four voiced distractors) was presented prior to the beginning of the test series for each place of articulation.

The remaining 24 subjects were assigned to the implicit instruction condition. Subjects in this condition were expected to rate the stimuli based on their own internal criteria, and were given minimal instruction regarding the nature of the stimuli prior to the rating task. These subjects received the same goodness rating task administered to subjects in the explicit instruction condition, *identical in every respect* including the instructions, the practice test, and the stimulus items. However, in order that they not be given any external model of the stimulus set that might influence their responses, these subjects did not receive the familiarization or forced-choice identification series prior to receiving the goodness rating task.

B. Results

1. Explicit instructions

The identification pretest was scored according to the mean percentage of voiced (e.g., B), voiceless (e.g., P), and breathy (e.g., *P) responses to fast VOTs and slow VOTs across rate conditions. These data are shown in Table II.

To determine whether speaking rate context influenced the identification of the test stimuli as members of the voiceless phonetic category in the present experiment, two-way subject and item ANOVAs were performed on the number of voiceless responses across conditions, with rate (fast versus slow) as a between-subjects factor in the subject analysis and a within-subjects factor in the item analysis, and VOT (fast VOT versus slow VOT) as a within-subjects factor in both

TABLE II. Percentage of voiced, voiceless, and ''breathy'' responses to fast VOTs and slow VOTs (voiceless stop consonants) as a function of speaking rate context. Due to rounding, percentages within a condition may not sum to 100.

		Fast VOT	Slow VOT
Fast rate context	Voiced	0	0
	Voiceless	89	40
	''Breathy''	8	59
Slow rate context	Voiced	1	0
	Voiceless	73	41
	''Breathy''	24	56

analyses. Results revealed a significant main effect of VOT [subject $F(1,24)=75.83$, $p<0.0001$; item $F(1,25)=271.24$, $p<0.0001$], such that there were significantly more voiceless responses to fast VOTs than to slow VOTs at both speaking rates. This effect may be due to a large number of slow VOTs being categorized as breathy (see Table II). The main effect of rate was marginally significant in the subject analysis [$F(1,24)=3.911$, $p=0.05$] and highly significant in the item analysis [$F(1,25)=11.751$, $p<0.01$], such that there were significantly more voiceless responses in the fast rate context than in the slow rate context. Thus listeners were more likely to categorize both fast and slow VOTs as voiceless in the fast rate context than in the slow rate context. In addition, the rate×VOT interaction was marginally significant in the subject analysis [$F(1,24)=3.123$, $p=0.09$] and highly significant in the item analysis [$F(1,25)=21.285$, $p<0.0001$]. *Post-hoc* Neuman–Keuls means comparisons revealed significantly more voiceless responses to fast VOTs in the fast rate context than in the slow rate context. Thus rate context influenced the identification of fast VOTs as members of the voiceless phonetic category. However, there was no significant difference in the number of voiceless responses to slow VOTs across rate contexts.

The increase in voiceless responses for fast VOTs at the fast rate supports the findings of Miller and Volaitis (1989) and Volaitis and Miller (1992). However, it should be noted that this increase in voiceless responses reflects a concomitant decrease in breathy responses for fast VOTs at the fast rate (see Table II). Based on the previous findings, it was predicted that breathy responses would *increase* in a fast rate context as a result of the shorter overall syllable duration. That is, it was expected that VOTs presented in a shorter syllable context would be perceived as more breathy and exaggerated than VOTs presented in a longer syllable context. The present results indicate that, rather than perceiving these VOTs as more breathy and exaggerated in a shorter (fast) syllable context, listeners labeled the VOTs as closer to the phonetic category center, i.e., as *less* breathy and exaggerated.

Mean goodness ratings were calculated for each subject in each condition. A bar plot of these data is shown in Fig. 5. Three-way subject and item ANOVAs with VOT (fast versus slow) as a within subjects factor in both analyses, rate as a between-subjects factor in the subject analysis and as a within-subjects factor in the item analysis, and place of articulation (/p/ vs /t/ vs /k/) as a within-subjects factor in the

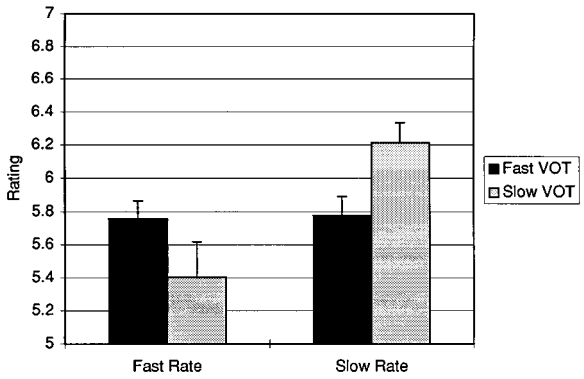

FIG. 5. Mean goodness ratings for fast VOTs and slow VOTs across speaking rate contexts in the explicit instruction condition (experiment 2).

subject analysis and as a between-subjects factor in the item analysis, were performed on the goodness rating data. A significant rate×VOT [subject $F(1,22)=4.225$, $p<0.05$; item $F(2,23)=110.488$, $p<0.0001$] interaction emerged. *Post-hoc* Newman–Keuls means comparisons revealed that subjects rated fast VOTs higher (i.e., better exemplars) than slow VOTs in the fast rate condition, and rated slow VOTs higher than fast VOTs in the slow rate condition. Thus subjects gave higher goodness ratings to VOTs that were compatible with the rate context. This finding is compatible with previous results obtained by Miller and Volaitis (1989) and Volaitis and Miller (1992). No significant main effects of rate, VOT, or place were obtained, and there were no other significant interactions.

2. Implicit instructions

Mean goodness ratings were calculated for each subject in each condition. A bar plot of these data is shown in Fig. 6. The pattern of goodness ratings in the implicit instruction condition differs substantially from that obtained in the explicit instruction condition. In fact, the results of the implicit instruction condition are more compatible with the reaction time and accuracy data obtained for the identification task (experiment 1). Three-way subject and item ANOVAs with VOT (fast versus slow) as a within-subjects factor in both analyses, rate (fast versus slow) as a between-subjects factor in the subject analysis and as a within-subjects factor in the item analysis, and place of articulation (/p/ vs /t/ vs /k/)

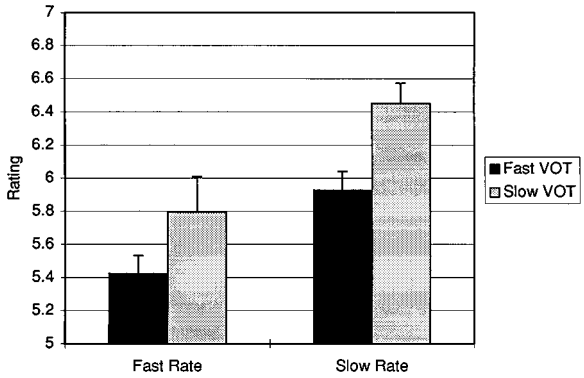

FIG. 6. Mean goodness ratings for fast VOTs and slow VOTs across speaking rate contexts in the implicit instruction condition (experiment 2).

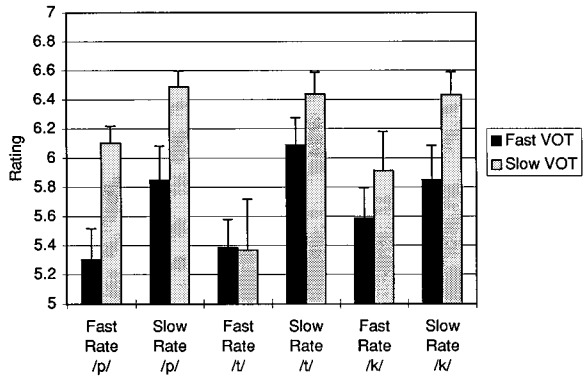

FIG. 7. Mean goodness ratings as a function of place of articulation for fast VOTs and slow VOTs across speaking rate contexts in the implicit instruction condition (experiment 2).

as a within-subjects factor in the subject analysis and as a between-subjects factor in the item analysis, were performed on the rating data. Significant main effects of rate [subject $F(1,22)=5.907$, $p<0.05$; item $F(1,23)=51.057$, $p<0.0001$] and VOT [subject $F(1,22)=15.95$, $p<0.001$; item $F(1,23)=29.638$, $p<0.0001$] emerged. Subjects rated slow VOTs significantly higher (i.e., as better exemplars) than fast VOTs across rates, and rated VOTs higher overall in the slow rate condition than in the fast rate condition. As in the identification task (experiment 1), no significant rate×VOT interaction emerged. Thus in the absence of explicit instructions and familiarization tasks, rate context did not affect the pattern of goodness ratings for fast VOTs and slow VOTs. While there was no significant main effect of place, a significant place×VOT [subject $F(2,44)=10.758$, $p<0.001$; item $F(2,23)=4.323$, $p<0.05$] interaction emerged, owing to the fact that listeners rated fast VOTs and slow VOTs for /t/ equally, while slow VOTs were rated higher than fast VOTs for both /p/ and /k/. The place×rate×VOT interaction was significant in the item analysis [item $F(2,23)=6.084$, $p<0.01$] and marginally significant in the subject analysis [subject $F(2,44)=2.769$, $p=0.07$]. Thus it appears that the /t/ place of articulation showed a different pattern of goodness ratings from /p/ and /k/. The data are plotted as a function of place of articulation in Fig. 7. *Post-hoc* Newman–Keuls means comparisons revealed that listeners rated fast VOTs and slow VOTs for /t/ equally at the fast rate, but gave higher goodness ratings to slow VOTs for /t/ at the slow rate.

C. Discussion

The results of the explicit instruction condition show clear effects of speaking rate on goodness ratings and, to a lesser extent, phonetic identification. When listeners were instructed that the test stimuli represented a series from voiced to voiceless to ''breathy'' and were given a three-choice identification task prior to the goodness rating task, their goodness ratings were consistent with the findings of Miller and Volaitis (1989) and Volaitis and Miller (1992). That is, listeners gave higher goodness ratings to VOTs that were compatible with the rate context than to incompatible VOTs. This finding demonstrates that listeners are sensitive to both within-category differences in VOT resulting from a change in speaking rate and to the rate context in which a VOT occurs.

Effects of speaking rate context were also apparent in the three-choice identification task in the explicit instruction condition. Listeners' responses to fast VOTs differed significantly according to the rate context. At the fast rate, listeners labeled a larger percentage of fast VOTs as voiceless than at the slow rate. However, the increase in voiceless responses at the fast rate does not reflect a concomitant decrease in voiced responses as a result of the shorter syllable context, as would be predicted based on the results of Miller and Volaitis (1989). Rather, the increase in voiceless responses reflected a decrease in ''breathy'' responses for fast VOTs at the fast rate. That is, at the fast rate, listeners labeled fewer of these VOTs as ''breathy'' than at the slow rate. This effect is in the opposite direction from the results obtained by Miller and Volaitis (1989) and Volaitis and Miller (1992), who found increased ''breathy'' responses in a fast rate/short syllable context. Further, no significant effects of rate context emerged for slow VOTs. Thus although the findings of the three-choice identification task show effects of speaking rate on phonetic identification, these effects are not consistent with previous findings. It is possible that the use of a test series containing only three VOTs (voiced, fast, and slow), rather than a full continuum, produced differing results. Specifically, listeners may have been reluctant to label the naturally produced voiceless stop consonants as voiced, and thus may have used the ''breathy''/starred category to indicate poorer exemplars of the voiceless category closer to the phonetic category boundary, i.e., exemplars that were perceived as closer to the voiced category. This would account for the greater number of ''breathy'' responses in the fast rate condition, and thus the apparent decrease in ''breathy'' responses in the slow rate condition.

In contrast to the results obtained in the explicit instruction condition, the findings of the goodness rating task with implicit instructions are compatible with the results of experiment 1. When listeners were given minimal specific information about the nature of the speech stimuli, they rated slow VOTs higher than fast VOTs, irrespective of rate context. The results of experiment 1 demonstrate that listeners are also faster and more accurate at identifying slow VOTs than fast VOTs across rate contexts. Thus it appears that listeners regard slow VOTs as better exemplars of the voiceless phonetic category than fast VOTs, regardless of the rate context. Slow VOTs are longer in duration than fast VOTs and are therefore further from the phonetic category boundary, which may serve as a possible explanation for this pattern of results.

The only effect of rate that was apparent in the implicit instruction condition emerged for the alveolar place of articulation. Specifically, listeners rated slow VOTs for /t/ as better exemplars than fast VOTs in the slow rate condition, whereas there was no difference in goodness ratings for /t/ in the fast rate condition. While this finding is somewhat suggestive of a speaking rate context effect, it should be noted that earlier studies of speaking rate and phonetic category

structure investigated the labial and velar places of articulation (Miller and Volaitis, 1989; Volaitis and Miller, 1992). The implicit instruction condition in experiment 2 revealed no context effects for either labial or velar consonants. Further, the goodness ratings for alveolar stops in the implicit instruction condition did not reflect the predicted interaction of VOT with rate. Listeners did not rate VOTs that were compatible with the rate context higher than incompatible VOTs across rates.

In interpreting the results obtained in the implicit instruction condition, it is important to take into account other methodological differences between Volaitis and Miller (1992) and the present study. Specifically, because the purpose of the present study was to examine the effects of rate context exclusively on stimuli from the category center, the stimulus set included only three phonetic exemplars. In contrast, Volaitis and Miller (1992) used a full continuum which included ambiguous stimuli from the phonetic category boundary. Thus, as discussed above, the restricted set of stimuli in the present experiment may have contributed to the differing results. However, the fact that the predicted effect of local rate context on phonetic identification did emerge for these stimuli in the explicit instruction condition suggests that it was the instruction condition, and not the stimulus set, that influenced the results.

Another potential concern with regard to the present set of results is the fact that all of the test tokens were produced by a single talker. Thus generalizations based upon these findings should be made with caution. Nevertheless, if VOT is perceived in a context-dependent manner, the predicted effects should have emerged in the implicit instruction condition for this talker. The findings for the implicit instruction condition in experiment 2 therefore do not support the claim that phonetic category structure for voiced and voiceless stop consonants is necessarily influenced by speaking rate context.

III. CONCLUSIONS

The purpose of this study was to investigate the effects of speaking rate on the perception of voice-onset time as a cue to voicing in naturally produced initial stop consonants. To this end, VOTs for voiceless stop consonants spoken at fast and slow rates were placed in the context of syllables spoken at fast and slow rates. Based on previous findings, it was predicted that VOTs that were compatible with the speaking rate context would be perceived as better exemplars of the voiceless phonetic category than incompatible VOTs.

To the extent that the methodology used to explore this question reproduced the methods of the previous experiments (Miller and Volaitis, 1989; Volaitis and Miller, 1992), this prediction was confirmed. When listeners were given specific instructions that the stimuli reflected a series from voiced to voiceless to ''exaggerated, breathy'' versions of stop consonants, and were given a familiarization series prior to performing the goodness rating task, their rating responses reflected the compatibility of VOT with speaking rate context. Specifically, listeners rated VOTs that were compatible with the rate context as better exemplars of the voiceless phonetic category than incompatible VOTs.

However, the presentation of familiarization tasks prior to the rating task may have influenced the results of the present experiment, as well as the findings of the previous studies. For example, the description of longer VOTs as ''exaggerated'' and ''breathy'' may have produced an expectation that these stimuli should be rated more poorly, and this expectation would have been reinforced by the three-choice identification task in which consonants were to be classified as either voiced (short), voiceless (longer), or breathy (longest). The presence of such an expectation may have resulted in listeners rating slow (longer) VOTs as poorer exemplars than fast (shorter) VOTs in the fast rate condition. Nevertheless, in the slow rate condition, slow VOTs were rated as better exemplars than fast VOTs. This interaction may have been due to the perceptual effects of the syllabic context in the fast and slow rate conditions. The discrimination task in experiment 1 demonstrated that listeners were more perceptually sensitive to the difference between fast and slow VOTs in the fast rate condition than in the slow rate condition. Thus listeners may have been better able to judge the relative ''breathiness'' of slow VOTs in the fast rate condition.

The results of the discrimination task arguably reflect an effect of speaking rate: listeners showed slightly more sensitivity to the acoustic difference in one rate context than in another. However, an alternative explanation is that the amount of acoustic information intervening between the presentation of the first VOT and the second VOT influenced perceptual sensitivity. At the slow rate, the intervening acoustic information was longer in duration than at the fast rate, and may have interfered with listeners' ability to compare the difference between fast VOTs and slow VOTs. Thus, rather than reflecting a contextual effect specific to speaking rate, the pattern of results may be due to a more general perceptual effect, which in turn may have influenced the results of the rating task.

In any case, the pattern of results that emerged in the rating task in the presence of explicit instructions and familiarization tasks differed substantially from the findings obtained when listeners made independent judgments of the stimuli, presumably based on a comparison with an internal phonetic representation. In the absence of explicit instructions, listeners rated slow VOTs as better exemplars than fast VOTs irrespective of the rate context. Interestingly, these findings are supported by the behavioral data obtained in experiment 1: at both speaking rates, listeners were faster and more accurate at identifying slow VOTs than fast VOTs. Taken together, the data suggest that listeners judge slow VOTs, which are longer in duration and therefore further from the voiced-voiceless category boundary, as better exemplars of the voiceless phonetic category than fast VOTs, and that this effect is not influenced by the speaking rate context.

This result does not support the predictions of intrinsic timing models of speech perception, in which the relative timing of acoustic events within a syllable determines phonetic perception (Fowler, 1977, 1980, 1984). Under this view, the differences in consonant/vowel ratio across rate contexts would be expected to strongly affect identification

performance. In fact, the pattern of results obtained was consistent across rates, indicating that listeners' categorization of the segments under investigation was unaffected by the duration of the following vowel. Similar results were obtained by Pind (1995), who investigated the relationship between the ''optimal boundary shift'' observed in the production of VOT at different speaking rates (Miller *et al.*, 1986) to the boundary shifts obtained in VOT perception. Pind (1995) observed that, if a phonetic contrast is processed in a truly rate-dependent manner, the perceptual boundary for the contrast should shift in accord with the variable optimal boundary that correctly categorizes the largest number of segments produced at a given speaking rate. Pind (1995) found that there was a close relationship between changes in the optimal boundary and shifts in the perceptual boundary for a phonetic contrast that involved a trading relation between consonant and vowel duration in Icelandic. Thus consonant/vowel ratio provided a consistent relational cue to this phonetic contrast across speaking rates in both perception and production, providing evidence of rate-dependent processing for this contrast. However, in the case of VOT, there was no consistent relationship between the boundary shifts obtained in perception and the variation in the optimal boundary location observed in production. In fact, rate-dependent effects on the perception of VOT were quite small, and were restricted to the ambiguous stimuli separating the voiced and voiceless categories. Taken with the results of the present study, these findings indicate that VOT is not perceived in a rate-dependent manner, and that consonant/vowel ratio does not provide a consistent acoustic cue to voicing in initial stops. Nevertheless, the Pind (1995) data suggest that rate-dependent processing of this sort may occur for other phonetic contrasts, specifically those involving a durational trading relation between two phonetic segments. Thus consonant/vowel ratio may provide a relational cue across speaking rates for contrasts such as voicing in medial stops in English (cf. Hodgson and Miller, 1991) and gemination in Italian (cf. Pickett *et al.*, 1998).

Whereas the present results indicate that VOTs can be perceived independently of speaking rate context, it is not clear whether contextual effects might emerge if the acoustic signal were degraded. Natural speech is typically perceived under noisy conditions, such as the presence of background noise or multiple talkers, and therefore may be characterized as a degraded signal. A number of studies have demonstrated that stimuli that do not show contextual effects under quiet conditions begin to show these effects when presented in noise. For instance, Shinn *et al.* (1985) demonstrated that shifts of the phonetic boundary between /ba/ and /wa/ as a function of vowel duration disappear when test stimuli mirror the acoustic parameters of natural speech. However, Miller and Wayland (1993) found that small boundary shifts could be induced for more natural speech stimuli when the stimuli were presented in a multitalker babble noise. Further, speaking rate has been found to affect word identification for natural speech targets when the targets are presented at signal-to-noise ratios of $+5$ to -10 (Sommers *et al.*, 1992). Thus listeners may not need to attend to rate context when all acoustic information relevant to a phonetic contrast is available and perceptible, whereas listeners may begin to rely on contextual information when the signal is degraded and the acoustic information is incomplete.

The results of the present study do not address the question of whether extrinsic rate information affects phonetic identification. Numerous studies have indicated that the rate of articulation of a precursor phrase can produce a shift in the boundary between two phonetic categories (Summerfield, 1981; Miller *et al.*, 1984; Wayland *et al.*, 1992; Kidd, 1989). The effects of extrinsic rate information tend to differ somewhat from syllable-internal rate effects, either in terms of the shape of the goodness function for a phonetic category at different rates (Wayland *et al.*, 1992) or the size of the boundary shift (Kidd, 1989; Summerfield, 1981). Extrinsic rate information has been shown to have an influence on the perception of natural speech continua in which VOT was varied independently of vowel duration (Kidd, 1989), similar to the acoustic manipulations used here. Thus the predicted effects of rate on phonetic identification that failed to emerge as a result of intrinsic cues might occur in the presence of extrinsic rate information, such as a precursor syllable or phrase.

In conclusion, the results of the present experiments demonstrate that the identification of naturally produced exemplars of the voiceless phonetic category is not affected by the duration of the remainder of the syllable. Further, the data suggest that the findings of previous studies showing effects of rate context on the perception of stimuli from the center of the voiceless category may have been influenced by the use of explicit instructions and familiarization tasks presented prior to the administration of the behavioral measures. When listeners in the present study were given similar instructions and pretests, the results replicated these earlier findings. However, when listeners' judgments were based on their own internal representation, their performance on phonetic identification and goodness rating tasks did not show an influence of speaking rate context. Whether contextual effects might emerge if the stimuli were presented in noise, or if speaking rate were cued by extrinsic information, remain topics for future research. Nevertheless, the present findings do not support the claim that syllable-internal acoustic cues to speaking rate are crucial for the perception of voicing in initial stop consonants.

ACKNOWLEDGMENTS

I would like to thank Sheila Blumstein, who advised me on all aspects of this research and provided many helpful comments on an earlier draft of this paper. I would also like to thank Winifred Strange and two anonymous reviewers for their comments on this manuscript, as well as Rachel Kessinger for many useful discussions of this project. This research was supported by NIMH Individual National Research Service Award 1 F31 MH11030-01A1 to Jennifer Aydelott Utman, and by NIH Grant No. NIDCD000142 to Brown University. Address reprint requests to Jennifer Aydelott Utman, Center for Research in Language, University

of California, San Diego, Dept. 0526, 9500 Gilman Drive, La Jolla, CA 92093. Electronic mail:Jennifer_Utman@crl.ucsd.edu.

Andruski, J. E., Blumstein, S. E., and Burton, M. W. (**1994**). ''The effect of subphonetic differences on lexical access,'' Cognition **52**, 163–187.

Church, H. H. (**1973**). ''The language-as-fixed-effect fallacy: a critique of language statistics in psychological research,'' J. Verb. Learn. Verb. Beh. **12**, 335–359.

Diehl, R. L., Souther, A. F., and Convis, C. L. (**1980**). ''Conditions on rate normalization in speech perception,'' Percept. Psychophys. **27**, 435–443.

Fowler, C. A. (**1977**). *Timing Control in Speech Production* (Indiana University Linguistics Club, Bloomington).

Fowler, C. A. (**1980**). ''Coarticulation and theories of extrinsic timing,'' J. Phon. **8**, 113–133.

Fowler, C. A. (**1984**). ''Segmentation of coarticulated speech in perception,'' Percept. Psychophys. **36**, 359–368.

Hodgson, P., and Miller, J. L. (**1991**). ''The role of multiple acoustic properties in specifying the internal structure of phonetic categories,'' J. Acoust. Soc. Am. **89**, 1997(A).

Kessinger, R. H., and Blumstein, S. E. (**1996**). ''Effects of speaking rate on voice-onset time and vowel length as a function of syllable duration'' (unpublished).

Kidd, G. R. (**1989**). ''Articulatory-rate context effects in phoneme identification,'' J. Exp. Psychol.: Human Percept. Perform. **15**, 736–748.

Kuhl, P. K. (**1991**). ''Human adults and human infants show a 'perceptual magnet effect' for the prototypes of speech categories, monkeys do not,'' Percept. Psychophys. **32**, 542–550.

Kuhl, P. K., Williams, K. A., and Meltzoff, A. N. (**1991**). ''Cross-modal speech perception in adults and infants using nonspeech auditory stimuli,'' J. Exp. Psychol.: Human Percept. Perform. **17**, 829–840.

Miller, J. L., Green, K., and Reeves, A. (**1986**). ''Speaking rate and segments: A look at the relation between speech production and speech perception for the voicing contrast,'' Phonetica **43**, 106–115.

Miller, J. L., Grosjean, F., and Lomanto, C. (**1984**). ''Articulation rate and its variability in spontaneous speech: A reanalysis and some implications,'' Phonetica **41**, 215–225.

Miller, J. L., and Volaitis, L. E. (**1989**). ''Effect of speaking rate on the perceptual structure of a phonetic category,'' Percept. Psychophys. **46**, 505–512.

Miller, J. L., and Wayland, S. C. (**1993**). ''Limits on the limitations of context-conditioned effects in the perception of [b] and [w],'' Percept. Psychophys. **54**, 205–210.

Pickett, E. R., Burton, M. W., and Blumstein, S. E. (**1998**). ''Acoustic characteristics of gemination in Italian,'' under review, Phonetica.

Pind, J. (**1995**). ''Speaking rate, voice-onset time, and quantity: The search for higher-order invariants for two Icelandic speech cues,'' Percept. Psychophys. **57**, 291–304.

Pisoni, D. B., and Tash, J. (**1974**). ''Reaction times to comparisons within and across phonetic categories,'' Percept. Psychophys. **15**, 285–290.

Rosch, E. (**1975**). ''The nature of mental color codes for color categories,'' J. Exp. Psychol.: Human Percept. Perform. **1**, 303–322.

Samuel, A. G. (**1982**). ''Phonetic prototypes,'' Percept. Psychophys. **31**, 307–314.

Shinn, P. C., Blumstein, S. E., and Jongman, A. (**1985**). ''Limitations of context-conditioned effects in the perception of [b] and [w],'' Percept. Psychophys. **38**, 397–407.

Sommers, M. S., Nygaard, L. C., and Pisoni, D. B. (**1992**). ''Stimulus variability and spoken word recognition. I. Effects of variability in speaking rate and overall amplitude,'' J. Acoust. Soc. Am. **96**, 1314–1324.

Summerfield, A. Q. (**1975**). ''Aerodynamics versus mechanics in the control of voicing onset in consonant-vowel syllables,'' Speech Perception **4**, 61–72.

Summerfield, Q. (**1981**). ''Articulatory rate and perceptual constancy in phonetic perception,'' J. Exp. Psychol.: Human Percept. Perform. **7**, 1074–1095.

Utman, J. A. (**1997**). ''Effects of subphonetic acoustic variability on lexical access in neurologically intact adults and patients with Broca's aphasia,'' doctoral dissertation, Brown University (unpublished).

Utman, J. A., Blumstein, S. E., and Burton, M. W. (**1996**). ''Effects of unsystematic and rule-governed variation on word recognition'' (unpublished).

Volaitis, L. E., and Miller, J. L. (**1992**). ''Phonetic prototypes: Influence of place of articulation and speaking rate on the internal structure of phonetic categories,'' J. Acoust. Soc. Am. **92**, 723–735.

Wayland, S. C., Miller, J. L., and Volaitis, L. E. (**1992**). ''The influence of sentence articulation rate on the internal structure of phonetic categories,'' J. Acoust. Soc. Am. **92**, 2495(A).

Auditory models of formant frequency discrimination for isolated vowels[a)]

Diane Kewley-Port[b)] and Yijian Zheng[c)]
Department of Speech and Hearing Sciences, Indiana University, Bloomington, Indiana 47405

(Received 26 February 1997; revised 20 November 1997; accepted 24 November 1997)

Thresholds for formant discrimination of female and male vowels are significantly elevated by two stimulus factors, increases in formant frequency and fundamental frequency [Kewley-Port *et al.*, J. Acoust. Soc. Am. **100**, 2462–2470 (1996)]. The present analysis systematically examined whether auditory models of vowel sounds, including excitation patterns, specific loudness, and a Gammatone filterbank, could explain the effects of stimulus parameters on formant thresholds. The goal was to determine if an auditory metric could be specified that reduced variability observed in the thresholds to a single-valued function across four sets of female and male vowels. Based on Sommers and Kewley-Port [J. Acoust. Soc. Am. **99**, 3770–3781 (1996)], four critical bands around the test formant were selected to calculate a metric derived from excitation patterns. A metric derived from specific loudness difference (ΔSone) was calculated across the entire frequency region. Since analyses of spectra from Gammatone filters gave similar results to those derived from excitation patterns, only the 4-ERB (equivalent rectangular bandwidth) and ΔSone metrics were analyzed in detail. Three criteria were applied to the two auditory metrics to determine if they were single-valued functions relative to formant thresholds for female and male vowels. Both the 4-ERB and ΔSone metrics met the criteria of reduced slope, reduced effect of fundamental frequency, although ΔSone was superior to 4-ERB in reducing overall variability. Results suggest that the auditory system has an inherent nonlinear transformation in which differences in vowel discrimination thresholds are almost constant in the internal representation. © *1998 Acoustical Society of America.* [S0001-4966(98)03403-1]

PACS numbers: 43.71.An, 43.66.Fe, 43.71.Es [WJ]

INTRODUCTION

Formant frequency discrimination measures the resolving power of the human auditory system for spectral peaks or resonances of vowel sounds. Results have shown that when optimal listening conditions are applied, including minimal stimulus uncertainty and the use of well-trained subjects, the estimated thresholds are reliable measures of the basic capabilities of the human auditory system (Sinnott and Krieter, 1991; Kewley-Port and Watson, 1994; Hawks, 1994). However, thresholds for the discrimination of formant frequencies of vowels are significantly affected by some stimulus factors, such as the center formant frequencies, fundamental frequency (Kewley-Port *et al.*, 1996), and consonantal contexts (Kewley-Port, 1995). In the case of steady-state vowel sounds, stimuli can be described as a harmonic series with an intensity envelope of peaks and troughs that reflects the formant resonances. Although vowels are complex stimuli, work by Green and his colleagues on profile analysis (Green, 1988), Moore and his colleagues on excitation patterns (Moore and Glasberg, 1987) and Sachs, Le Prell, and their colleagues on the neural representation of vowel spectra (Sachs *et al.*, 1988; Le Prell *et al.*, 1996) suggests that auditory models might be capable of explaining the variations in formant discrimination thresholds observed for various stimulus factors. The purpose of this investigation was to quantify the success of several metrics based on auditory models to explain the variation in formant discrimination thresholds observed for female and male vowels.

Although the studies of discrimination abilities for changes in frequency of a formant began in the 1950s (Flanagan, 1955), only recently have investigations systematically varied factors under minimal stimulus uncertainty conditions (Sinnott and Krieter, 1991; Hawks, 1994). In our first study (Kewley-Port and Watson, 1994), reliable thresholds for ten synthetic female vowels were best described by a piecewise-linear function of frequency, such that the thresholds were flat in the $F1$ region with constant values of ΔF about 14 Hz and linearly increased in the $F2$ region with a slope of about 10 Hz in ΔF for 1000 Hz in formant frequency (Fig. 1). A subsequent study of the discrimination of formant frequency for six male vowels produced with two fundamental frequencies has shown that those thresholds were also well fit by a piecewise-linear function of frequency (Kewley-Port *et al.*, 1996). The piecewise-linear functions shown in Fig. 1 indicate that thresholds are systematically elevated as fundamental frequency ($F0$) increases. The analysis of variance for the thresholds for the female and male vowels indicated that formant thresholds were significantly elevated by increases in either $F0$ or formant frequency, and that these two sources of variability act independently of one another. Based on knowledge of the processing of harmonics in the auditory periphery, a successful model for formant thresholds should reduce the effects of these

[a)]Some material in this manuscript was presented at the 128th Meeting of the Acoustical Society of America [J. Acoust. Soc. Am. **96**, 3284 (A) (1994)].
[b)]Electronic mail: kewley@indiana.edu
[c)]Electronic mail: yizheng@indiana.edu

 0001-4966/98/103(3)/1654/13/$10.00

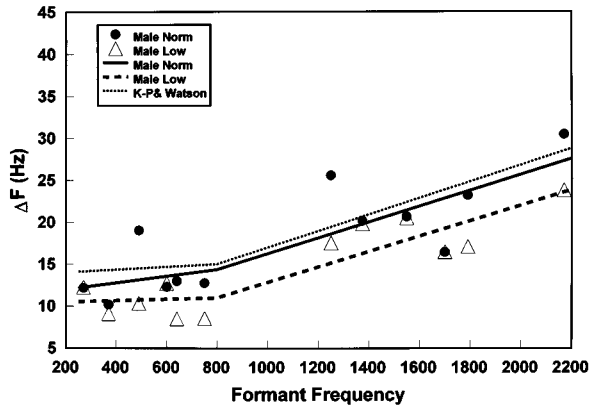

FIG. 1. The piecewise linear functions fit to three different sets of data are shown for male vowels with a normal $F0$ (solid line), male vowels with a low $F0$ (dashed line), and female vowels in Kewley-Port and Watson (1994) (dotted line). The thresholds as ΔF for the male vowels are shown, solid circles for the normal $F0$ and solid triangles for the low $F0$.

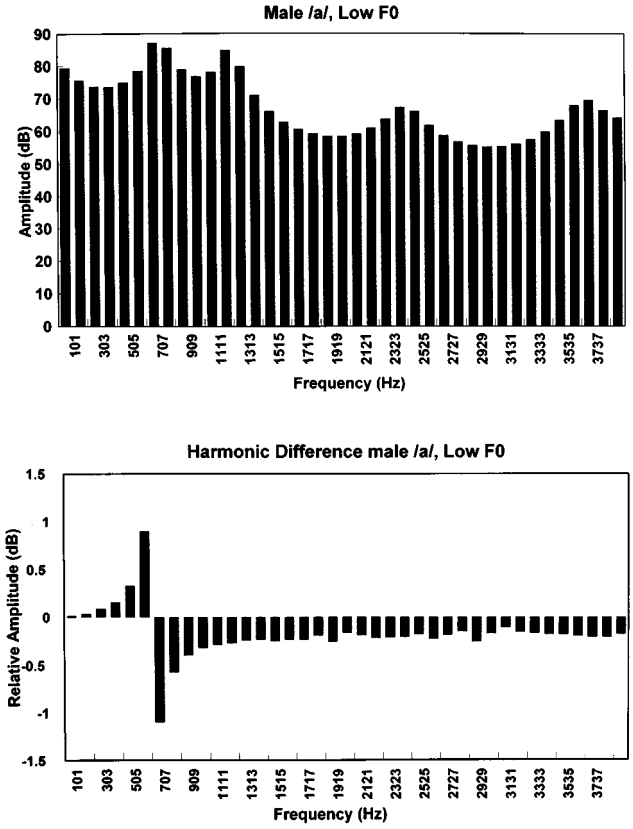

FIG. 2. The spectrum from DFT of the digital waveform for the standard /a/ vowel with the low $F0$ (101 Hz) is shown in the upper panel. Difference in the intensities of the harmonics between spectra for the standard and the just discriminable /a/ vowel with the low $F0$ (101 Hz) is shown in the lower panel.

sources of variability. That is, at threshold the listener's percept of a just-noticeable change in formant frequency is presumably based on a constant increment in sensation regardless of changes in stimulus parameters. To model this constant percept, our approach is to discover an auditory metric that is an inverse transform, such that when applied to vowel stimulus differences observed at threshold, this metric converges on the same small value. Visually, graphs of a successful metric would transform the thresholds for the three piecewise-linear functions in Fig. 1 to approximately three overlapping straight lines or single-valued functions of formant frequency. This observation suggested two criteria that could be used to evaluate the auditory metric. The first is that the slope of a metric as a function of formant frequency should approach zero (i.e., become flat) in relation to the positive slope observed for ΔF thresholds. Second, the significant effect of $F0$ should be reduced such that the average values of the thresholds for each $F0$ are almost identical.

This goal of obtaining single-valued functions for an auditory metric is quite ambitious when other, less well-understood sources of variability are also considered. In the experiment that estimated the female vowel thresholds it was discovered that when a harmonic aligned exactly with the center frequency of a formant, unusually high elevations or jumps in thresholds were obtained (Kewley-Port and Watson, 1994). It appears that this is the outcome of interactions between the harmonics and formant shape (Lyzenga and Horst, 1995), although a detailed explanation is not known. In the female vowel study, there were five harmonically aligned formants and four of them had threshold jumps in ΔF [in Table II and seen as outliers in Fig. 6 from Kewley-Port and Watson (1994)]. Therefore an attempt was made in the next study using male vowels (Kewley-Port *et al.*, 1996) to select parameters that avoided harmonic alignment. However, there appear to be three jumps in discrimination thresholds for the male vowels with normal $F0$ (Fig. 1). Although these thresholds are apparent outliers as measured in Hz, the percept of these just-noticeable differences should still be associated with a constant sensation for the listener. Thus a third criterion for a successful inverse transform is to test whether the substantial variability observed for the ΔF thresholds is significantly reduced.

In the sections that follow, the overall approach to modeling the behavioral measures of formant discrimination by transformations of sound in the auditory system is presented. Then several auditory models are described in terms of their spectral representation of vowel waveforms. Auditory metrics derived from these auditory models are defined to capture the differences in the vowel spectra discriminated at threshold. This is followed by the statistical analyses of the metrics and results.

I. MODELING FORMANT FREQUENCY DISCRIMINATION

A. Comparison of vowel spectra

For both female and male formant discrimination studies, steady-state vowels were carefully synthesized after real speakers with the KLTSYN synthesizer (Klatt, 1980). Formant frequencies of the resonators are seen as formant peaks in the resulting harmonic series (upper panel of Fig. 2), although measurements of the spectra using spectrograms or LPC analysis result in formant values that deviate by 1%–2% from the Klatt parameters (Hillenbrand *et al.*, 1995). In the discrimination task, the human listener hears, in a random order, the standard vowel and a test vowel with a small change in one formant frequency. The assumption is

that a comparison of the two acoustic signals is made by the listener, and at the threshold this is a constant auditory perceptual difference for all the vowel formants.

In terms of the physical signal, the spectral shape is shown by means of a DFT (discrete Fourier transform) that yields a harmonic series as shown in the top panel of Fig. 2. Differences between two vowel spectra are measured as changes in the intensities of the harmonics. For the standard vowel and the just-discriminable vowel at threshold, harmonics from the two harmonic series are subtracted and the intensity difference profile is shown in the bottom panel of Fig. 2. As discussed in Kewley-Port and Watson (1994), a change in formant frequency can cause changes in the intensity distribution of the vowel harmonics far from the altered formant peak. Kewley-Port and Watson (1994) examined several metrics to measure the stimulus difference between two vowel spectra at the threshold including the Euclidean distances or absolute distances in dB between the harmonic components. Analyses of these metrics did not explain the variability shown in the discrimination performance of human subjects (Kewley-Port and Watson, 1994). Of course, it was expected that physical spectral differences would not successfully describe human subjects' abilities of discrimination in terms of internal auditory perceptual thresholds. However, a clear outcome of those analyses was the need for additional data on whether or not humans attend primarily to harmonic differences near the test formant in the discrimination task.

Sommers and Kewley-Port (1996) reported on a set of experiments designed specifically to determine whether harmonics spectrally remote from the test formant affect formant discrimination performance. Thresholds were obtained for $F1$ and $F2$ in two female vowels, /e/ and /ʊ/, when: (1) all 24 harmonics were allowed to vary as in the previous female and male vowel experiments; (2) harmonic level variations were restricted to a subset of components spectrally close to the test formants; and (3) harmonics remote from the shifted formant were excluded from the stimuli. The results indicated that the thresholds for conditions (1) and (2) did not differ until level variations were restricted to between two and three components. Thresholds for condition (3) were not significantly different than those obtained for vowels with a full complement of harmonics. Sommers and Kewley-Port (1996) concluded that formant frequency discrimination is mediated by the selective attention to harmonic level variations in the components immediately adjacent to the frequency region of the shifted formant. Preliminary analyses of an excitation pattern model in Sommers and Kewley-Port (1996) were consistent with the hypothesis that listeners require a fixed perceptual difference in the excitation level to discriminate changes in $F1$ or $F2$ frequencies. These conclusions are critical to the selection of parameters for one of the auditory metrics (the 4-ERB metric) evaluated in the present study. We note, however, that the conclusion that selective attention is employed in the auditory processing of vowel spectra is compatible with the recent neurophysiological experiments reported by May and his colleagues (May *et al.*, 1996). Specifically, May *et al.* (1996) noted that discrimination performance was predicted from the best neural representation across fiber unit types. Discrimination models that represented profiles of neural discharge across the entire vowel spectrum demonstrated maximum change near the shifted formant. May *et al.* also noted that optimal neural models predicted performance that exceeded that observed in the behavioral data.

B. Approach to auditory metrics to model formant discrimination

In order to explain the human subjects' performance for formant discrimination tasks and to explore the internal mechanism of the auditory system, auditory metrics were developed and applied to the female and male vowel stimuli. The traditional model of the cochlea as a bank of overlapping bandpass filters has been commonly used to represent spectral analysis and frequency selectivity in the auditory periphery. Based on that power-spectrum model, Zwicker (1975) conceived excitation patterns to explain a variety of behavioral data in human auditory perception (Zwicker and Fastl, 1990). Excitation patterns have been successful in accounting for the experimental results of intensity discrimination (Florentine and Buus, 1981). Two versions of excitation pattern models, single-band and multiband, were evaluated in the study of Florentine and Buus. Their calculations indicated that the multiband version of the excitation pattern model predicted experimental data well.

The multiband model suggested that information across all bands was used for listeners in an intensity discrimination task. Profile analysis and comodulation masking release have provided additional evidence that listeners sometimes make simultaneous comparisons across auditory filters (Green, 1988; Hall and Grose, 1988). Kewley-Port (1991) applied the excitation pattern models from Moore and Glasberg (1987) to the results of a detection task for isolated female vowels. She found that one of the auditory metrics calculated from a multiband analysis successfully accounted for the variance in detection thresholds.

As an extension of previous studies with simpler acoustic stimuli, we applied both excitation pattern models and loudness models of Moore and Glasberg (1986, 1987) to vowels. Another model of current interest, Gammatone filter bank models described by Patterson *et al.* (1992) and Slaney (1993), was also evaluated.

Several metrics were proposed to compare auditory spectra of the standard vowel and the just-discriminable vowel at threshold. Algorithms calculated one value from the distributed difference functions between the two auditory spectra. Metrics included Euclidian distance, sums of the absolute values of spectral differences, maximum peak-to-trough difference (Lyzenga and Horst, 1995), and integration of the difference functions. In addition, for some auditory metrics, the frequency range was restricted to a region adjacent to the test formant based on results from Sommers and Kewley-Port (1996). The auditory metrics were calculated separately for the female and male vowels. Metrics for each data set were evaluated using the three criteria of reduced slope, reduced effect of $F0$, and reduced overall variability. These criteria determine the extent to which an auditory metric is a successful inverse auditory transform of

TABLE I. Formant frequencies for male and female vowels. Frequencies in Hz for formants $F1$ and $F2$ used in synthesizing the vowels.

	Female		Male	
Vowel	$F1$	$F2$	$F1$	$F2$
/i/	325	2900	270	2170
/I/	450	2300	370	1790
/e/	550	2500		
/ɛ/	600	2200	490	1700
/æ/	1000	1950	640	1550
/a/	875	1175	750	1250
/ʌ/	700	1400	600	1375
/o/	500	800		
/ʊ/	500	1350		
/u/	250	850		

threshold variability, thereby modeling the constant percept with approximately a single-valued function. Below we report on only the more successful auditory metrics.

II. METHODS

A. Stimuli

Vowel stimuli were investigated previously in two separate studies of the formant frequency discrimination for female vowels (Kewley-Port and Watson, 1994) and male vowels (Kewley-Port *et al.*, 1996). These studies estimated the thresholds for formant frequencies of $F1$ or $F2$ from isolated, steady-state vowels as shown in Table I. The vowels were synthesized using the cascade branch of the KLTSYN synthesizer (Klatt, 1980). Female vowels consisted of the ten vowels, /i, ɪ, e, ɛ, æ, ʌ, a, o, ʊ, u/, synthesized after a female speaker (the first author) with an $F0 = 200$ Hz. Male vowels consisted of the six vowels /i, ɪ, ɛ, æ, ʌ, a/, synthesized after spectral measurements of a male phonetician with two fundamental frequencies, $F0 = 101$ Hz (low $F0$) and $F0 = 126$ Hz (normal $F0$). The vowel durations were always set to 160 ms. The standard vowels in these data sets are the vowels synthesized with these parameters and are more fully described in Kewley-Port and Watson (1994) and Kewley-Port *et al.* (1996). The test sets with shifts in formant frequency for a specific vowel contained 14 modified vowels. The step size for a shift in formant frequency was calculated using a log ratio such that steps 10–15 would be easily discriminable from the standard. For the male vowels, only increments in formant frequency were tested, while for female vowels both increments and decrements were tested.

Since these vowels were steady-state stimuli, it is appropriate to consider them as a harmonic series of the fundamental frequency in which the envelope of spectral peaks reflects the formants specified in the vocal tract transfer function. Thus a discrete Fourier transform (DFT) of the vowel waveform calculates the intensities of each of the harmonics and is the spectrum of a vowel prior to any filtering introduced by the earphones or auditory system. The DFT spectrum of the digital waveform of the male /a/ vowel for the low $F0$ is shown in the top panel of Fig. 2.

B. Threshold data sets

Thresholds of formant frequency discrimination estimated from the female and male formants were previously reported in Kewley-Port and Watson (1994) and Kewley-Port *et al.* (1996). Vowels were calibrated to the highest harmonic in a vowel and varied over a 7-dB range (similarly to naturally produced vowels) near the 77-dB SPL presentation level of a calibration vowel. Thresholds were measured based on the average of the mean reversals from the last four blocks by using Levitt's (1971) adaptive-tracking method. Thresholds of ΔF were calculated in Hz based on the formant frequency parameters used in synthesizing the vowels. The *just discriminable vowels* refer to the vowels with formant frequencies shifted from standard vowels either for $F1$ or $F2$, for which listeners could just discriminate the difference from the standard vowels. To represent the difference between the standard vowel and the just discriminable vowel at threshold, a difference profile between the spectra of DFT from each vowel is calculated. The resulting difference in harmonics for the male /a/ low $F0$ vowel is shown in the bottom panel of Fig. 2. As previously described in Kewley-Port and Watson (1994), although the largest differences in harmonics are on either side of the test formant, measurable differences of 0.1 dB or more are located at frequencies substantially higher than the test formant. This is the normal function of the Klatt (1980) cascade synthesizer that emulates interactions of the resonances associated with actual vocal tract shapes.

In the analyses, thresholds from the female and male formants will be grouped into four separate data sets. The female thresholds are separated into two sets of 20 depending on whether the thresholds were estimated from an *increment* or *decrement* in frequency from the test formant. The rationale for this division is related to the threshold jumps observed for the five harmonically aligned formants. Because the variability of these threshold jumps was somewhat higher for formant increments than decrements (Figs. 6 and 7), the data sets were kept separate. The 24 thresholds for male vowels are divided into two sets, one for the low (101 Hz) and one for the normal (126 Hz) $F0$. The vowels, formant frequencies, and ΔF thresholds for the female data sets are found in Table II and for the male sets in Table III.

C. Spectral models

The rate/place theory of auditory processing states that an acoustic stimulus evokes internal neural activity distributed along the basilar membrane that maps frequency to place. Corresponding to that neural excitation, there has been a psychophysical counterpart defined as a psychophysical excitation from the masked audiogram or masking patterns (Zwicker, 1975). One model employed here is based on a more recent formulation proposed by Moore and Glasberg (1987)[1] of psychophysical excitation patterns calculated from the output of a bank of overlapping auditory filters. This output is excitation level in dB per ERB. ERB is the equivalent rectangular bandwidth of an auditory filter shape that is obtained from masking experiments using notched-noise (Patterson, 1976). The Moore and Glasberg (1987)

TABLE II. Comparison of 4-ERB and ΔSone metrics with ΔF thresholds for female vowels with formant increments and decrements (total 40 formants). Values of the formant frequencies in Hz and ERB shown on the left. ΔF thresholds in Hz and values of the two auditory metrics are shown for each of the formant increments and decrements.

Vowel-formant	Formant frequencies		Formant increments		Formant decrements			
	Hz	ERB	ΔF	4-ERB	ΔSone	ΔF	4-ERB	ΔSone
u-$F1$	250	6.4	14.6	6.52	0.78	13.9	7.49	0.90
i-$F1$	325	7.7	13.1	9.43	1.32	14.1	9.99	1.43
ɪ-$F1$	450	9.6	12.6	7.09	0.86	12.9	5.49	0.64
o-$F1$	500	10.3	16.6	7.67	1.13	14.2	7.34	1.05
ʊ-$F1$	500	10.3	13.9	7.67	0.74	22.3	9.77	0.93
e-$F1$	550	10.9	14	11.45	1.49	12.9	7.14	0.90
ɛ-$F1$	600	11.5	14.6	2.49	0.76	17.5	6.6	1.27
ʌ-$F1$	700	12.6	12.4	4.76	0.56	12.2	4.62	0.54
o-$F2$	800	13.6	21.9	3.59	0.42	16.6	5.46	0.67
u-$F2$	850	14	20.7	8.38	0.38	19.4	7.94	0.35
a-$F1$	875	14.3	12.9	6.32	1.12	15.7	6.68	1.10
æ-$F1$	1000	15.3	36	14.11	1.51	22	10.73	1.19
a-$F2$	1175	16.6	18.4	5.69	0.92	16.3	7.24	1.04
ʊ-$F2$	1350	17.7	27.2	14.74	0.71	16.9	7.22	0.32
ʌ-$F2$	1400	18	54.8	17.38	1.29	27.3	16.37	1.26
æ-$F2$	1950	20.7	23.4	8.92	0.57	25.7	11.32	0.71
ɛ-$F2$	2200	21.7	56.4	15.45	1.28	36.7	13.11	1.11
ɪ-$F2$	2300	22.1	28.5	7.68	0.44	19.3	4.84	0.27
e-$F2$	2500	22.8	33.9	7.14	0.64	36.8	7.17	0.61
i-$F2$	2900	24	36.9	9.85	0.90	38.4	6.36	0.53

model uses an auditory filter shape simplified to a roex function. ERB was calculated using the following formula derived from experimental data:

$$\text{ERB} = 6.23F^2 + 93.4F + 28.5, \quad (1)$$

where F is center frequency in kHz. The variation of the auditory filter shape with intensity levels was implemented by fitting data from asymmetric notched-noise masking experiments to produce formulas for an asymmetric roex function (Moore and Glasberg, 1987). An example excitation pattern for the standard male vowel /a/ with $F0 = 101$ Hz is plotted with the abscissa in ERB (see the upper panel of Fig. 3). This is the same vowel stimulus used to illustrate the use of amplitude spectra in Fig. 2. The DFT of all vowel spectra are input to the ERB model after adjusting the level of the harmonics to dB SPL based on the calibration procedures.

The audiogram incorporating the transmission effects of the outer and middle ear was estimated by the ISO-1961 MAF in Moore and Glasberg (1986, 1987). However, this was replaced with MAP ANSI-1969 in the present model because our subjects used TDH-39 earphones (Kewley-Port, 1991). Overall, the excitation pattern was calculated as the total output of each auditory filter in units of dB as a function of its center frequency in 0.1-ERB steps.

In order to model the discrimination performance of lis-

TABLE III. Comparison of four auditory metrics with ΔF thresholds for male vowels with normal $F0$ (126 Hz) and low $F0$ (101 Hz). Values of the formant frequencies in Hz and ERB are shown on the left. ΔF thresholds in Hz and values of the four auditory metrics are shown for each of normal and low $F0$'s as described in the text.

Vowel-formant	Formant frequencies		$F0 = 126$ Hz					$F0 = 101$ Hz				
	Hz	ERB	ΔF	4-ERB	ΔSone	Gamma tone	Total loudness	ΔF	4-ERB	ΔSone	Gamma tone	Total loudness
i-$F1$	270	6.7	12.17	6.32	0.71	5.3	0.48	12.24	10.78	1.67	6.5	1.55
ɪ-$F1$	370	8.4	10.17	4.79	0.61	4.4	−0.84	9.1	7.63	0.83	3.8	0.69
ɛ-$F1$	490	10.2	19.01	9.58	1.25	11.1	−1.25	10.34	6.59	0.97	3.9	0.84
ʌ-$F1$	600	11.5	12.29	12.63	1.50	5.77	1.35	12.7	3.33	0.56	3.4	0.41
æ-$F1$	640	12	13.0	4.79	0.65	3	0.02	8.49	4.05	0.74	2.6	0.20
a-$F1$	750	13.1	12.74	3.71	0.52	2.5	0.43	8.55	4.15	0.76	2.5	0.35
a-$F2$	1250	17.1	25.6	5.3	0.56	4.1	0.26	17.53	6.05	0.72	4.3	−0.16
ʌ-$F2$	1375	17.8	20.17	7.05	0.82	3.7	0.63	19.79	10.56	0.73	5	0.51
æ-$F2$	1550	18.8	20.66	7.52	0.54	3.9	−0.39	20.52	5.65	0.61	3.6	−0.21
ɛ-$F2$	1700	19.6	16.44	6.31	0.44	3.4	0.12	16.46	6.05	0.63	3	0.50
ɪ-$F2$	1790	20	23.2	12.4	0.54	6	−0.40	17.1	9.37	0.83	3.8	0.72
i-$F2$	2170	21.6	30.47	11.49	0.51	6	−0.37	23.81	5.35	0.75	2.9	0.62

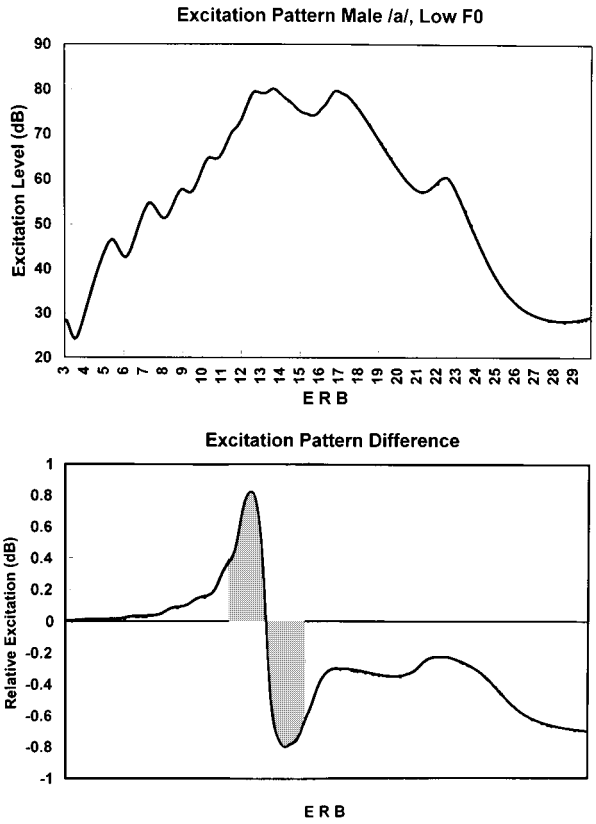

FIG. 3. The excitation pattern level in dB for the standard /a/ vowel with the low $F0$ (101 Hz) is shown in the upper panel. Excitation level distance between excitation patterns for the standard and the just discriminable /a/ vowel with the low $F0$ (101 Hz) is shown in the lower panel. The shaded area represents a 4-ERB excitation distance with a frequency region 4-ERB wide.

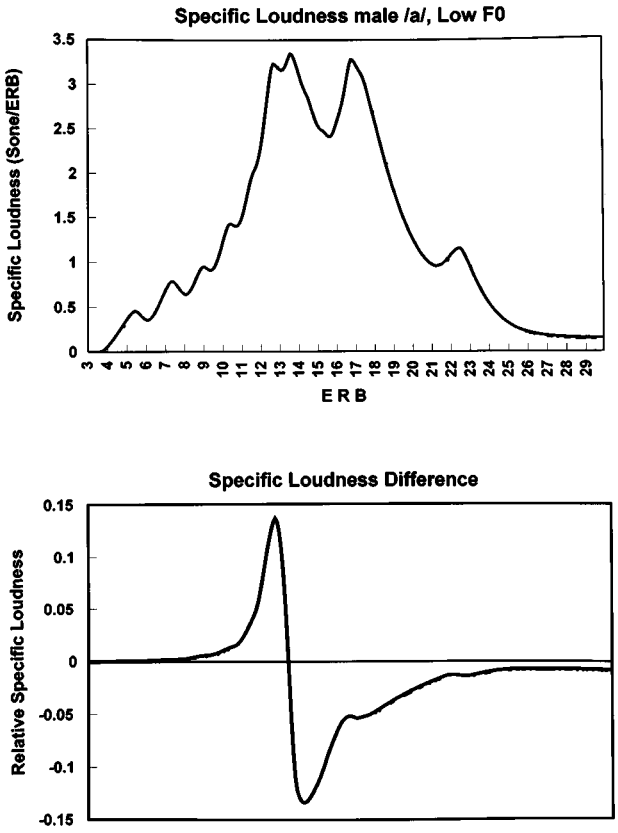

FIG. 4. The specific loudness in sones/ERB for the standard /a/ vowel with the low $F0$ (101 Hz) is shown in the upper panel. The specific loudness difference, ΔSones, for the standard and the just discriminable /a/ vowel with the low $F0$ (101 Hz) is shown in the lower panel.

teners in formant frequency discrimination tasks, a difference profile was calculated by subtracting the just discriminable excitation pattern from the pattern for the standard vowel (the lower panel of Fig. 3) and these will be called excitation profiles. The excitation difference profile is very similar to the rate difference profiles derived from single neuron recordings in cats used as a basis for describing vowel formant discrimination by Conley and Keilson (1995) and May *et al.* (1996). We note that the high-frequency tail observed in the harmonic differences in Fig. 2 is also prominent in the excitation difference profile. Preliminary analyses of auditory metrics including this tail had little apparent success in reducing threshold variation across stimulus conditions. Therefore we implemented a model of neural excitation in terms of loudness as another auditory transform of vowel spectra.

Consider the excitation profile model associated with a pattern of differences in the distribution of neural excitation along the basilar membrane. This pattern reflects intensity changes in the harmonics of the stimulus and will also be associated with listeners' judgements of loudness at more central levels of processing. Traditionally the definition of loudness uses a 1-kHz tone at a level of 40 dB SPL as the reference sound, and loudness judged relative to this standard has units of the sone (Moore, 1989; Zwicker and Fastl, 1990). Based on the rate/place theory, the specific loudness (N') is defined as the loudness or sones per unit ERB. Zwicker and Fastl (1990) have suggested that specific loudness versus critical-band (ERB-rate scale) functions are the most appropriate for representing human auditory processing. Zwicker (1975) suggested that specific loudness can be calculated from the excitation level. Moore and Glasberg (1986) modified Zwicker's original formulation as shown below:

$$N' = A\left(\frac{E_{\mathrm{TH}}}{E_0}\right)^{0.23}\left[\left(0.5\,\frac{E}{E_{\mathrm{TH}}}+0.5\right)^{0.23}-1\right], \tag{2}$$

where N' is the specific loudness, E is the excitation, E_{TH} is the excitation at absolute threshold, and E_0 is the reference excitation corresponding to the intensity $I_0 = 10^{-12}$ W/m^2. A, a constant, was chosen experimentally so that the total loudness integrated over the specific loudness function of a 40-dB, 1-kHz tone is one sone. Figure 4 shows the specific loudness pattern calculated at 0.1-ERB intervals using Eq. (2) for the same /a/ vowel shown in Figs. 2 and 3. A difference profile for specific loudness was calculated similarly to the excitation difference profile and is shown in the lower panel of Fig. 4. Specific loudness appears to be a more appropriate model than excitation level because the compressive nature of loudness enhances the high-intensity, formant peaks of the spectrum relative to the lower intensity regions remote from the peaks.

Another auditory model that has received broad attention is the Gammatone filter bank model of Patterson *et al.*

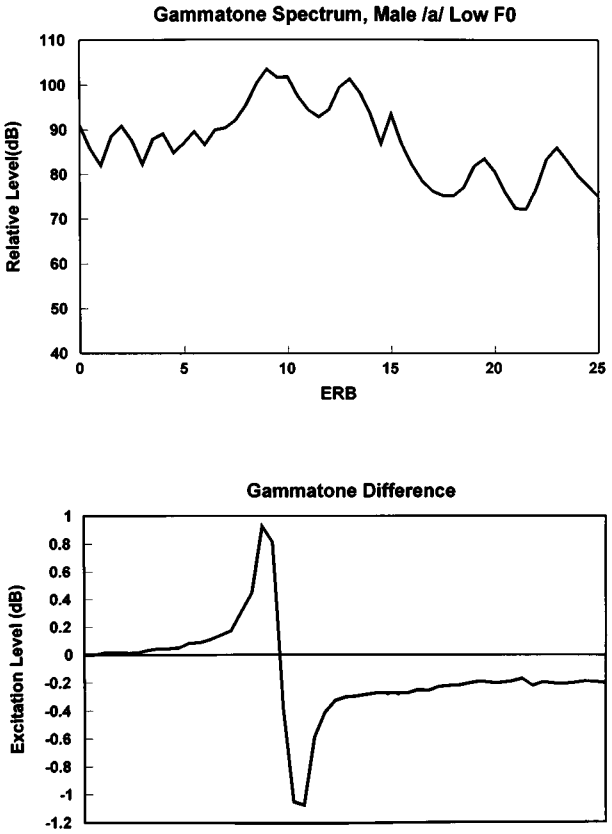

FIG. 5. The Gammatone spectrum in dB for the standard /a/ vowel with the low $F0$ (101 Hz) is shown in the upper panel. The Gammatone distance for the standard and the just discriminable /a/ vowel with the low $F0$ (101 Hz) is shown in the lower panel.

(1992). This model is also based on ERB spaced filters, but they are calculated in a time-domain implementation of the difference equations for Gammatone filters defined by their individual impulse response,

$$gt(t) = at^{(n-1)}\exp(-2\pi bt)\cos(2\pi f_c t + \Phi) \quad (t>0), \tag{3}$$

where n is the order of the filter, f_c is a center frequency of the filter, and b is a parameter that determines the bandwidth of the filter. Our implementation was taken from Slaney's *Auditory Toolbox* (1993). This is a Matlab implementation of the Patterson–Holdworth filter bank using 50 overlapping Gammatone filters to span 25 ERB, each filter implemented as a cascade of four second-order filters. In our model, a vowel was filtered by the difference equation for the full Gammatone filter bank. Subsequently, a single 20-ms FFT spectral slice was calculated near the peak amplitude of the vowel. Figure 5 shows the Gammatone spectrum calculated at 0.5-ERB intervals for the same /a/ vowel as shown in Figs. 2–4. Comparing the Moore and Glasberg excitation pattern (Fig. 3) and the Gammatone spectrum suggests that the primary difference between the spectra at low frequencies is the lack of filtering to represent the MAF audiogram in the Gammatone analyses. At high frequencies, the spectral roll off in the excitation pattern is due to the lack of higher harmonics in the auditory filters, a flaw not observed in the time-domain analyses of the Gammatone filters. A difference profile for the Gammatone spectra was calculated similarly to the excitation profiles (the lower panel of Fig. 5).

D. Auditory metrics

Several auditory metrics were examined to capture the distributed differences across the profiles into a single value. A general distance metric D as the L_p norm is defined as

$$D = \left(\sum_{i=1}^{N} \Delta x_i^p \right)^{1/p} \tag{4}$$

for Δx_i, each profile difference value in 0.1-ERB steps for total N steps. The Euclidian distance with $p=2$ was the obvious choice. Detailed examination of this distance metric for an exponent different from 2, or the absolute sum of Δx_i, were not systematically explored, but did not appear to effectively reduce threshold variability. Thus Euclidian distance was the basic auditory metric for the excitation, loudness, and Gammatone profiles.

For the excitation profile, it was obvious that the calculation of D over the entire ERB range was highly variable due to the high-frequency tail. Sommers and Kewley-Port (1996) showed that although changes caused by a shift of a formant frequency are distributed across the whole frequency region, listeners only attended to a restricted region around an altered formant frequency, encompassing two or three harmonics. These results suggest that to model the performance of listeners, a metric for the excitation profile can be restricted to a small number of auditory filters around the shifted formant frequency. Therefore a frequency region 4-ERB wide, centered on the formant frequency of the standard vowel, was selected to calculate the Euclidian distance for the excitation profiles, called the 4-ERB metric. In Fig. 3, the 4-ERB metric, with the units of dB, is calculated only within the shaded area. Clearly the effects of the ''tail'' in the high-frequency region of the excitation difference are omitted in the 4-ERB metric. We note that this restriction, while somewhat arbitrary in its implementation, is well grounded on the experimental results from Sommers and Kewley-Port (1996). Informal analyses showed that other possible metrics for excitation patterns were more variable than the 4-ERB metric, including a 2-ERB and 3-ERB metric, and a maximum peak-to-trough difference (Lyzenza and Horst, 1995). Moreover, the 4-ERB metric is compatible with the analyses of vowel discrimination based on single-unit recording described by both Conley and Keilson (1995) and May *et al.* (1996).

Auditory metrics for the loudness difference between the standard vowel and the just discriminable vowel were modeled from two different points of view. First, the total loudness is the area integrated under the specific loudness curve and measures the overall loudness of a sound in sones. The total loudness difference is the difference between the total loudness of the standard vowel and the just discriminable vowel. Second, based on the rate/place theory of distributed neural excitation, we defined another loudness difference measure, ΔSone, as the difference between the specific loudness of the standard vowel and the just discriminable vowel. ΔSone is calculated as the Euclidian distance of the specific

loudness profile in the bottom panel of Fig. 4. Thus the ΔSone metric captures the differences in the distribution of specific loudness that are greatest near the test formant in contrast to the total loudness difference which focuses on aggregate, integrated loudness shown in the top panel of Fig. 4. Note that since there was only a small ''tail'' in the high-frequency region of the specific loudness difference, the 4-ERB restriction was not imposed for the ΔSone metric.

Overall, four auditory metrics were evaluated. The metrics were the Gammatone distance in dB, the 4-ERB excitation level difference in dB, total loudness difference in sones, and ΔSones in sones/ERB. To measure how well variability was accounted for by each metric, several analyses were calculated including comparisons of the slopes and variances of metrics as a function of frequency. Because each metric had a different unit, additional justification of the slope and variance comparisons is presented. Kewey-Port and Watson (1994) and Kewley-Port *et al.* (1996) have previously discussed that from the perspective of speech processing the most appropriate unit for formant thresholds is ΔF in Hz rather than $\Delta F/F$. The rationale, based on the four different sets of thresholds, is that ΔF functions in Hz, displaying formant resolution in the $F1$ region, are constant and very good, in contrast to $\Delta F/F$ functions that display resolution as becoming increasingly poor as $F1$ decreases. For the baseline behavioral thresholds, ΔF in units of Hz as shown in Fig. 1 is about ten times greater than thresholds for pure tones (for brief stimuli, at 1000 Hz, ΔF is about 1.5 Hz for tones versus 15 Hz for formants) similar to ΔF thresholds for other complex stimuli (Kewley-Port and Watson, 1994; Watson *et al.*, 1976; Moore, 1973). For excitation patterns, Moore and Glasberg's model (1987) was designed to match behavioral data such that there is a 1-dB increment in excitation level for a 1-dB increase in intensity of a 1000-Hz tone at presentation levels from 20 to 90 dB SPL. Since Zwicker (1970) and others have argued that changes in frequency are discriminable when a difference of about 1 dB is observed in the excitation pattern, the units of dB are appropriate for behavioral thresholds. Similarly, guided by behavioral data, models that define sones increase sones roughly 1:1 for presentation levels greater than 40 dB SPL for a 1000-Hz tone (Moore and Glasberg, 1986). The goal of the present analysis was to model psychoacoustic thresholds for complex formant stimuli based on models developed to explain human perception of simpler acoustic stimuli. Thus if the magnitude of the units observed across the models for the formant stimuli correspond reasonably well with expectations for thresholds for simpler stimuli, then a comparison across the output of the models seems adequately justified.

To support this claim, consider the output of the models for a typical psychophysical task, namely the discrimination of an increment in intensity of a 1000-Hz tone at our calibration level of 77 dB SPL. The ΔI threshold is estimated to be less than 0.5 dB (Zwicker and Fastl, 1990, Fig. 7.5). Our excitation pattern and specific loudness algorithms were applied to a 1000-Hz tone at 77 dB SPL and 77.5 dB SPL to simulate this just noticeable increment in intensity. The resulting excitation profiles had a large high-frequency tail (>1 dB), similar to the vowel profiles. The value for the 4-ERB metric was 3.34 dB. The total loudness for the 77 dB SPL tone was 15.74 sones, with a 0.60 sone increment for the 77.5 dB SPL tone. The ΔSone metric was 0.574 sones/ERB, or as expected very close to the difference in total loudness for a pure tone. Thus a magnitude of ΔSone of around 0.6 sones/ERB is representative of the intensity threshold for midfrequency, high-level tones, similar in value to the ΔI increment (0.5 dB) and the total loudness (0.6 sones). These values for a 1000-Hz tone serve as referents in the comparisons across units for the analyses of the slopes and variances presented below.

Three criteria were used to evaluate the success of various metrics to reduce threshold variability, flatness, reduced effect of $F0$, and reduced overall variability. The baseline of comparison for all three criteria is the ΔF discrimination thresholds as a function of frequency. The model proposed by Kewley-Port *et al.* (1996) that best fit ΔF as a function of formant frequency was a piecewise-linear function, although each of the four data sets had strong linear components with correlation coefficients exceeding 0.80. Therefore for the purposes of this analysis, simple linear regression was selected to represent the slopes for all metrics. If a metric is not increasing or decreasing as a function of formant frequency, the slope should approach zero. To determine if the significant effect of $F0$ was removed, analysis of variance was applied to three different $F0$'s (101, 126, 200 Hz) separately for each metric. Finally, to test for the overall reduced variability of the metrics, the F-ratio test was calculated for pairs of metrics. The purpose of these analyses was to use the three criteria to select the best auditory metric for discrimination thresholds that represents the hypothesized constancy of the internal mechanism of the auditory system.

III. RESULTS

A. Gammatone distance

From the beginning of the analyses, two of the models examined had unacceptable problems, the Gammatone distance and the total loudness difference. The Gammatone profiles were calculated for the two male data sets first (Table III). One of these profiles (/ɛ/$F1$, normal $F0$) had substantial differences between the Gammatone spectra at frequency regions remote from the test formant for no explicable reason. In the Gammatone model (Slaney, 1993), the lack of a filter to model the audiogram resulted in an emphasis of harmonics in the low frequencies that is not acceptable as a complete model of spectral processing in the periphery. In addition, for time-domain filtering, it is not clear how to adjust for actual calibration of sound pressure. The Gammatone analysis is intended to model the auditory filtering of the cochlea in the time domain. Thus for our vowels, the associated spectra calculated from the Gammatone model should be similar to the Moore and Glasberg (1987) excitation patterns. For formant peaks in the midfrequency range, this appeared to be the case. Correlation between the auditory metrics for the Gammatone and excitation profiles (4-ERB) for all 23 male formants was $r=0.84$ (excluding the /ɛ/ outlier) and demonstrated that the two analyses were very similar. Since it was not obvious how to incorporate the required audiogram fil-

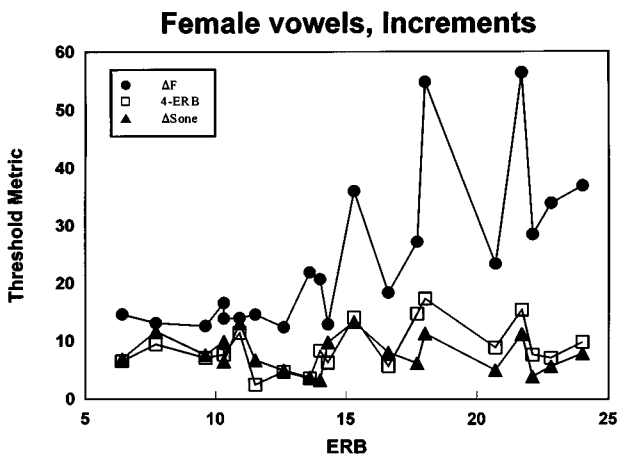

FIG. 6. Comparison of the experimental ΔF thresholds with 4-ERB distance and ΔSone metrics for female vowels with formant increments. The thresholds as ΔF in Hz are shown with solid circles, 4-ERB in dB with open squares, and ΔSone (normalized sones) with solid triangles.

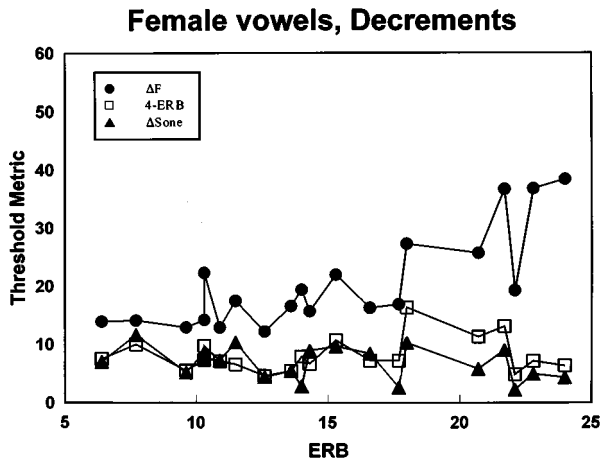

FIG. 7. Comparison of the experimental ΔF thresholds with 4-ERB distance and ΔSone metrics for female vowels with formant decrements. The thresholds as ΔF in Hz are shown with solid circles, 4-ERB in dB with open squares, and ΔSone (normalized sones) with solid triangles.

ters in the time domain and the Gammatone and excitation models were otherwise quite similar, additional analyses were not pursued with the Gammatone model.

B. Total loudness difference

The total loudness difference in sones, calculated by subtracting total loudness of the standard vowel form that of the just discriminable vowel, was evaluated with the male data sets (Table III). Since the calculation of total loudness integrates loudness across a whole frequency region, the contrast between loud and soft areas near the altered formant peak as shown in Fig. 3 was not accounted for, i.e., the loud and soft areas generally canceled in the total loudness metric. Thus an increment in formant frequency resulted in a wide range of positive and negative values of total loudness, from -1.25 to $+1.55$ sones. This included about half of the values less that the 0.6 sone threshold obtained for the 1000-Hz tone. Thus the total loudness difference metric had many subthreshold values in sones, as well as high variability, indicating that it is inappropriate as a measure of a constant internal sensation.

C. 4-ERB and ΔSone metrics

The metrics for the excitation and loudness profiles were evaluated for all four data sets. The results are presented in Figs. 6–9 and in Tables II and III. Each figure displays the value of the 4-ERB and ΔSone metrics in comparison to the thresholds of ΔF for one data set. The abscissa represents the formant frequencies in units of ERB (called ERB-rate scale or E scale, Moore and Glasberg, 1987). The ordinate labeled ''threshold metric'' represents the behavioral thresholds of ΔF in Hz and the excitation levels for the 4-ERB metrics in dB. The ordinate for the ΔSone metric is in sones/ERB normalized to match the range of 4-ERB metric for display purposes only in order to compare visually the variability in the two auditory metrics. Tables II and III list the actual values for ΔF (Hz), and the 4-ERB (dB) and ΔSone sones/ERB metrics. The average values across all four data sets of the 4-ERB metric is 8 dB and the ΔSone metric is 0.8 sones/ERB. The magnitude of these values appear reasonable as expected values for the thresholds of complex vowel stimuli based on the analysis of the 1000-Hz tone which yielded 3.3 dB (4-ERB) and 0.6 sones/ERB (ΔSone) modeled at threshold.

1. Slope analysis

The slopes calculated from the linear regression analysis are shown in Table IV for each data set. Since all functions in Figs. 6–9 are not U shaped, the linear regression slopes reflect linear trends with probabilities of significance of the fit related to the slopes of the regressions. Slopes for both the 4-ERB metric and the ΔSone metric are closer to zero and therefore much flatter across changes in formant frequency than the experimental thresholds of ΔF (see Figs. 6–9). The average slope of the ΔF thresholds is 1.23 Hz/ERB, each with a significant regression of $p<0.003$. The averages for the 4-ERB metric and ΔSone metric are 0.14 dB/ERB and -0.09 sones/ERB/ERB, respectively, each with a nonsignificant regression fit because slopes approach zero. In order to visualize how the slopes of the regression lines compare, there needs to be a referent for the maximum value of the y axis for each metric. A referent can be established from the average values of the metrics for formants less than 800 Hz (13.6 ERB) which our previous analyses of the piecewise-linear functions demonstrated to be flat (constant valued). The averages across the ΔF, 4-ERB, and ΔSone metrics are 14.6 Hz, 7.4 dB, and 0.9 sones/ERB. Thus a ratio of these

TABLE IV. Slopes of the regression lines for ΔF thresholds and the two metrics, 4-ERB and ΔSone. The last column shows the average slope of the regression line across four data sets for ΔF and the metrics.

Metric	Female, increment	Female, decrement	126 Hz	101 Hz	Average
ΔF	1.81	1.25	0.99	0.86	1.23
4-ERB	0.26	0.10	0.20	0.001	0.14
ΔSone	-0.10	-0.19	-0.029	-0.03	-0.09

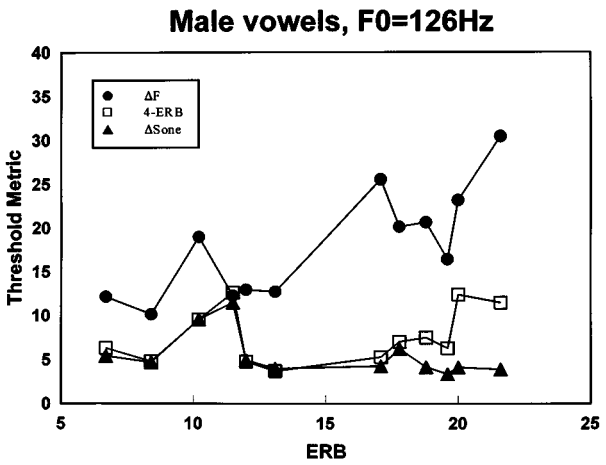

FIG. 8. Comparison of the experimental ΔF thresholds with 4-ERB distance and ΔSone metrics for male vowels with the normal $F0$ (126 Hz). The thresholds as ΔF in Hz are shown with solid circles, 4-ERB in dB with open squares, and ΔSone (normalized sones) with solid triangles.

that can be used to select the maxima of the y axis across metrics is approximately 14 to 7 to 1 (e.g., the maxima of 45 to 25 to 32 is 15 to 8 to 1). The regression lines for the three metrics for each of the four data sets are displayed in Fig. 10 using these ratios as scale factors for the ordinate.

Slopes for the regression lines displayed in Fig. 10 show that the slopes approach zero for both the 4-ERB metric and the ΔSone metric, but that there is not much difference between the two auditory metrics. The slopes for the ΔSone metric are negative for the four vowel sets apparently reflecting some differences between processing high frequencies versus low frequencies. Slopes for the 4-ERB metric are slightly larger in absolute values (0.14 to 0.09) compared to the ΔSone metric, but the direction of this difference is not consistent in pairwise comparisons. Overall, it is clear that these two auditory metrics are both successful in removing the effect that increased formant frequency elevates thresholds, with the ΔSone metric being slightly more flat than the 4-ERB metric.

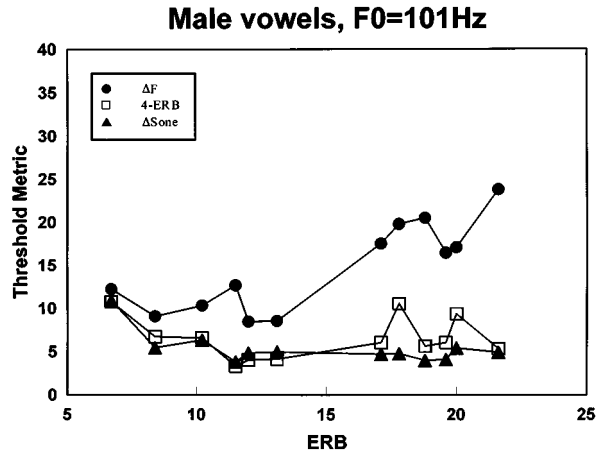

FIG. 9. Comparison of the experimental ΔF thresholds with 4-ERB distance and ΔSone metrics for male vowels with the low $F0$ (101 Hz). The thresholds as ΔF in Hz are shown with solid circles, 4-ERB in dB with open squares, and ΔSone (normalized sones) with solid triangles.

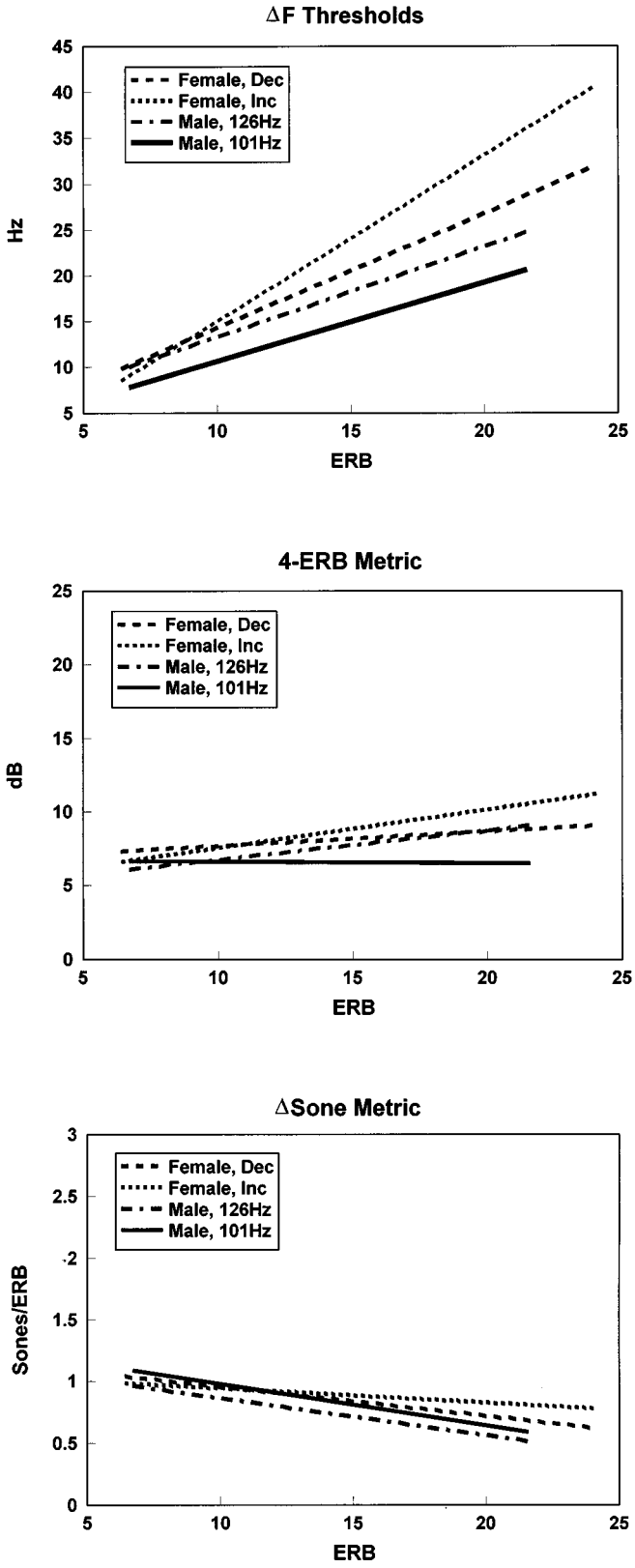

FIG. 10. The upper, middle, and lower panels show the regression lines for ΔF thresholds, 4-ERB metric, and ΔSone metric, respectively, for each of the four data sets for male vowels with a normal $F0$ (dashed-dotted line), male vowels with a low $F0$ (solid line), female vowels with formant increments (dotted line), and female vowels with formant decrements (dashed line). The slopes of both 4-ERB and ΔSone metrics are close to zero without much difference between them.

2. F0 effects

Fundamental frequency ($F0$) was shown to be an independent factor from formant frequency, a factor that also elevates thresholds. This is shown in Fig. 1 as separation between the piecewise-linear functions fit to a subset of the male and female data sets from Kewley-Port *et al.* (1996). This subset included only 12 of the 20 female formants from the formant decrement set as a match to the 12 male formants in each of the normal and low $F0$ sets. The two-way ANOVA for that subset of ΔF thresholds demonstrated that both factors were significant. For the 4-ERB metric, however, a two-way ANOVA demonstrated that the $F0$ effect on thresholds was not significantly different [$F(2,22) = 1.26$, $p > 0.30$]. An analogous two-way ANOVA for the ΔSone metric also showed that $F0$ was no longer a significant factor [$F(2,22) = 3.3$, $p < 0.055$]. Thus for this subset of data, the effect of $F0$ on thresholds was removed by both metrics, but somewhat more effectively by the 4-ERB metric.

Another analysis was undertaken to examine whether the $F0$ effect was reduced for all vowel formants in the data sets based on observation of the regression lines in Fig. 10. Here it can be seen that there is a spacing between the regression lines at high frequencies as a function of $F0$ for the ΔF thresholds that is reduced for both the 4-ERB and ΔSone metrics. The difference between the regression lines for the female increment and decrement sets is due to unusually high thresholds for the harmonically aligned formants for the increment set. Therefore in this analysis, the female decrement set was selected for the comparison of $F0$ effects as it was in Kewley-Port *et al.* (1996).

To determine whether there was a significant elevation in threshold as a function of $F0$, the effect of formant frequency can be ignored by examining the residual of the regression of a data set when the mean value is added back. A one-way analysis of variance for these adjusted residuals across the $F0$ values of 200, 126, and 101 Hz with 20, 12, and 12 formants, respectively, was calculated for ΔF thresholds and each of the auditory metrics. ΔF thresholds were significantly different as a function of $F0$ as expected [$F(2,41) = 7.04$, $p < 0.005$]. For the 4-ERB metric the effect of $F0$ was no longer significant [$F(2,41) = 1.21$, $p > 0.3$]. For the ΔSone metric, the effect of $F0$ was also not significant, but just barely [$F(2,41) = 3.14$, $p = 0.054$]. Thus two analyses of the effect of $F0$ on formant frequency show that the auditory metrics of 4-ERB and ΔSone remove the effect of $F0$ across three $F0$ variations, and therefore are representative of a more constant internal threshold. In this analysis of $F0$ effects, the 4-ERB metric may be slightly better than the ΔSone metric in producing a constant valued function.

3. Overall variability

Variability in the ΔF thresholds is quite high, especially since the threshold jumps due to harmonic alignment were included in the full data sets (Figs. 6–9). However, the auditory percept for all the formant shifts at threshold should be about constant. Therefore an F ratio for variance was calculated to see if the variability for either auditory metric is significantly reduced compared to that for ΔF. To eliminate the factors of $F0$ and formant frequency from an analysis of variability, the residual values of the linear regressions for each data set were compared. The F-ratio test selected was that for independent samples. Since the thresholds ΔF are from behavioral data and the modeled 4-ERB and ΔSone metrics are based on analyses of vowel stimuli, their independence is justified. However, the argument for independence of the 4-ERB and ΔSone metrics is less clear because it is based on the fact that specific loudness is a nonlinear transform of excitation level. An additional caution is noted for this analysis since comparison of the variances across different units may be more sensitive to magnitude differences than was the slope analysis. The F ratios for the 4-ERB and ΔSone variance of the residuals compared to that for ΔF are shown in Table V.

TABLE V. Comparison between pairs of ΔF thresholds, 4-ERB, and ΔSone, of the variance of the residuals of the regressions. The variance of each metric is measured using the F ratio. [$F(10,10)$ and $F(18,18)$ for male and female vowels, respectively].

Pairs of metrics	Female, increment	Female, decrement	126 Hz	101 Hz
ΔF/4-ERB	6.33[a]	3.07[a]	1.72	1.35
ΔF/ΔSone	731.67[b]	255.42[b]	177.30[b]	151.10[b]
4-ERB/ΔSone	115.60[b]	83.20[b]	103.32[b]	115.56[b]

[a]($p < 0.05$).
[b]($p < 0.00001$).

For the female data sets with high variability in ΔF, the 4-ERB metric significantly reduced variability. However, for the male data sets, variability was not significantly reduced. The ΔF versus ΔSone comparison showed that variability was greatly reduced for all data sets ($p < 0.00001$). Thus it appears that the 4-ERB metric reduces variability somewhat since there was a significant reduction for the data sets (female) with the large number of threshold jumps. However, the compressive ΔSone metric was clearly more successful in reducing variability.

D. Comparisons of 4-ERB and ΔSone metrics

In the analyses thus far, the criteria for demonstrating that an auditory metric is nearly constant valued showed that the ΔSone metric was more successful in reducing the variability observed in the ΔF thresholds. The slopes for the ΔSone (Table IV), although negative, were somewhat flatter in absolute values than the 4-ERB metric across all four data sets. The analysis of $F0$ effects suggested that the 4-ERB metric was slightly better than the ΔSone metric in producing a constant valued function. The variability of 4-ERB and ΔSone metrics was directly compared to see if they differed from one another using the F-ratio test of the residuals from the regressions. As shown in Table V, the F ratio between 4-ERB and ΔSone variances showed that these metrics were very different. For all data sets, the F values were highly significant at a criteria of $p < 0.00001$. Thus the overall variability is significantly different between the 4-ERB and ΔSone metrics.

Given the particularly large differences in the variances for the ΔSone comparisons, the issue of justifying the analy-

ses across metrics was reconsidered. The overriding justification is that models of behavioral thresholds with long traditions of appropriate units for simple stimuli have been applied here to thresholds for more complex (vowel) stimuli. The magnitude of metrics for vowels were indeed in the expected range. If the residuals of the regressions were to be normalized externally on principled grounds, many possibilities can be proposed. As one of several examples attempted, the values for the metrics for the 1000-Hz tone were selected (the 4-ERB metric of 3.35 dB and ΔSone of 0.6 sones/ERB) as ''equivalent'' at threshold. The residuals for the 4-ERB and ΔSone data sets were normalized with these values and the F-ratio test of variances computed (analogous to the normalization used in Figs. 6–9). The 4-ERB variance was significantly higher than the ΔSone for the female-increment ($p<0.007$), female-decrement ($p<0.04$) and male-101 Hz ($p<0.05$), while the male-126 Hz just missed significance ($p=0.059$). Thus it appears that the result that the ΔSone metric reduces variability significantly compared to the 4-ERB metric is robust. Moreover, the 4-ERB metric was calculated over a restricted and somewhat arbitrary spectral range in order to reduce variability introduced from the high-frequency tail. The ΔSone metric is calculated across the full ERB range and is thus an inherently more appealing metric.

IV. DISCUSSION AND CONCLUSIONS

Four auditory metrics for comparing vowel sounds were systematically evaluated based on the hypothesis that there exists a constant percept in the auditory system for formant frequency at threshold. A metric for total loudness difference could not explain the variability in discrimination tasks because the loudness contrast around the test formant was canceled out. The Gammatone auditory filterbank simulates cochlear processing of complex sounds and performs a spectral analysis by converting a complex time-domain signal into a multichannel representation of the pattern of neural activity. This representation of neural activity should closely resemble excitation pattern models. In fact, the high correlation between Gammatone and excitation pattern metrics for male vowels was obtained. Given that the current implementation of the Gammatone filters do not include the transfer functions of the outer and middle ear or the earphones (as represented in the audiogram), further analyses of Gammatone spectra were not pursued.

When metrics for excitation patterns based on Moore and Glasberg (1987) formulations were examined, level differences remote from the test formant were observed. To reduce the detrimental effect of these remote differences, a 4-ERB metric was calculated from excitation patterns based on the findings that listeners only attended to the spectrum in a salient region near the altered formant (Sommers and Kewley-Port, 1996). Since the specific loudness calculated from the excitation pattern showed the enhancement of peaks and the suppression of energy in the low- and high-frequency regions, the proposed ΔSone distance metric was able to include differences across the whole frequency region without any exclusion. While restricting the ΔSone metric to a 4-ERB region might make an even better approximation to a single-valued function, in fact benefits of this restriction appeared minimal.

The studies on the neural rate representation of changes in $F2$ frequency of vowels (Conley and Keilson, 1995; May *et al.*, 1996; LePrell *et al.*, 1996) strongly support our hypothesis of a single-valued function as an auditory percept in formant discrimination tasks. The neural rate difference profile and its d' for $F2$ changes has almost the same pattern as those shown in 4-ERB, ΔSone, and Gammatone difference profiles in our analyses. The combination of response patterns of auditory-nerve fibers with high, medium, and low spontaneous rates (SRs) provides an adequate representation of the difference between two steady-state vowels. May *et al.* (1996) suggested that the d' statistic can describe the neural representation of a change in $F2$ based on the magnitude of rate difference and the variability of responses. When the d' value exceeds 1, the change of neural rate, either decreased or increased, is detectable or discriminable in terms of auditory-nerve fiber responses. Therefore d' can be considered as a common criterion for discrimination of formant frequency changes on the basis of auditory-nerve representation. The 4-ERB and ΔSone metrics are derived from vowel thresholds for a $d'=1$ in our experiments. Thus our approach to discover a single-valued auditory metric corresponds to the argument presented for the physiological data that discrimination is constant for a d' criterion.

4-ERB excitation pattern metric and specific loudness difference metric (ΔSone) calculated for each data set both satisfy the criteria of reduced slope and reduced effects of $F0$. Compared to the behavioral thresholds in ΔF for formant discrimination for female and male vowels described by a piecewise-linear function of formant frequency, the measures of 4-ERB metric and ΔSone metric shown in Fig. 10 do approximate single-valued functions of frequency. This single-valued function can be considered as an internal representation of auditory perceptual thresholds for formant discrimination thresholds.

The final criteria for selecting a metric was that of reduced variability. F-ratio tests across the metrics were calculated from the residuals of the regression analyses after the effects of slope and $F0$ were removed. Thus the primary remaining known source of variability is that of harmonic alignment which appears to cause abnormally high thresholds. This high degree of variability (accidentally introduced into the stimulus generation) is a particularly challenging test for the models. The F-ratio tests (Table V) were relatively clear; the ΔSone metric was far better at reducing variability than the 4-ERB metric. This result may be viewed with some caution because of the comparison across metrics and some concern about justifying the assumptions of independence. However, as a first effort to model thresholds for vowel formants, the ΔSone metric is the metric which accounts best for variability observed in these data sets. This conclusion supports the claim of Zwicker and Fastl (1990, p. 208) that specific loudness versus critical-band rate ''best illustrate'' information processing abilities in the human hearing system.

In conclusion, the evaluation of these metrics suggest that models based on excitation patterns and distributed spe-

cific loudness can be successfully applied to explain the variability observed in psychophysical tasks with complex stimuli such as vowel formant discrimination. The present analyses imply that there are some inherent nonlinear transformations that can successfully model thresholds of formant discrimination of vowels as a constant auditory percept.

ACKNOWLEDGMENTS

This research was supported by the National Institutes of Health Grant Nos. NIHDCD-02229 and NIHDCD-00250 to Indiana University. We are especially grateful to our colleague, Larry Humes, for commenting on an earlier draft of the manuscript and for consulting with us on many aspects of the auditory models.

[1]The revised formula for ERB presented in Glasberg and Moore (1990) is a somewhat simpler expression. The resultant values deviate very slightly from their original expression [shown in Eq. (1)] over the range of frequencies (100–3000 Hz) of interest in this study.

Conley, R. A., and Keilson, S. E. (**1995**). ''Rate representation and discriminability of second formant frequencies for /ε/-like steady-state vowels in cat auditory nerve,'' J. Acoust. Soc. Am. **98**, 3223–3234.

Flanagan, J. (**1955**). ''A difference limen for vowel formant frequency,'' J. Acoust. Soc. Am. **27**, 288–291.

Florentine, M., and Buus, S. (**1981**). ''An excitation pattern model for intensity discrimination,'' J. Acoust. Soc. Am. **70**, 1646–1654.

Glasberg, B., and Moore, B. C. J. (**1990**). ''Derivation of auditory filter shapes from notched-noise data,'' Hearing Res. **47**, 103–138.

Green, D. M. (**1988**). *Profile Analysis: Auditory Intensity Analysis* (Oxford U.P., New York).

Hall, J. W., and Grose, J. H. (**1988**). ''Comodulation masking release: Evidence for multiple cues,'' J. Acoust. Soc. Am. **84**, 1669–1675.

Hawks, J. W. (**1994**). ''Difference limens for formant patterns of vowel sounds,'' J. Acoust. Soc. Am. **95**, 1074–1084.

Hillenbrand, J., Getty, L. A., Clark, M. J., and Wheeler, K. (**1995**). ''Acoustic characteristics of American English vowels,'' J. Acoust. Soc. Am. **97**, 3099–3111.

Kewley-Port, D. (**1991**). ''Detection thresholds for isolated vowels,'' J. Acoust. Soc. Am. **89**, 820–829.

Kewley-Port, D. (**1995**). ''Thresholds for formant-frequency discrimination of vowels in consonantal context,'' J. Acoust. Soc. Am. **97**, 3139–3146.

Kewley-Port, D., Li, X., Zheng, Y., and Beardsley, A. (**1996**). ''Fundamental frequency effects on thresholds for vowel formant discrimination,'' J. Acoust. Soc. Am. **100**, 2462–2470.

Kewley-Port, D., and Watson, C. S. (**1994**). ''Formant-frequency discrimination for isolated English vowels,'' J. Acoust. Soc. Am. **95**, 485–496.

Klatt, D. H. (**1980**). ''Software for cascade/parallel formant synthesizer,'' J. Acoust. Soc. Am. **67**, 971–995.

Le Prell, G. S., Sachs, M. B., and May, B. J. (**1996**). ''Representation of vowel-like spectra by discharge rate responses of individual auditory-nerve fibers,'' Aud. Neurosci. **2**, 275–288.

Levitt, H. (**1971**). ''Transformed up-down methods in psychoacoustics,'' J. Acoust. Soc. Am. **49**, 971–995.

Lyzenga, J., and Horst, J. W. (**1995**). ''Frequency discrimination of band-limited harmonic complexes related to vowel formants,'' J. Acoust. Soc. Am. **98**, 1943–1955.

May, B. J., Huang, A., Le Prell, G., and Hienz, R. D. (**1996**). ''Vowel formant discrimination in cats: Comparison of auditory nerve representations and psychophysical thresholds,'' Aud. Neurosci. **3**, 135–162.

Moore, B. C. J. (**1973**). ''Frequency difference limens for short-duration tones,'' J. Acoust. Soc. Am. **54**, 610–619.

Moore, B. C. J. (**1989**). *An Introduction to the Psychology of Hearing* (Academic, London), 3rd ed.

Moore, B. C. J., and Glasberg, B. (**1986**). ''The role of frequency selectivity in the perception of loudness, pitch and time,'' in *Frequency Selectivity in Hearing*, edited by B. Moore (Academic, London).

Moore, B. C. J., and Glasberg, B. (**1987**). ''Formulae describing frequency selectivity as a function of frequency and level, and their use in calculating excitation patterns,'' Hearing Res. **28**, 209–225.

Patterson, R. D. (**1976**). ''Auditory filter shapes derived with noise stimuli,'' J. Acoust. Soc. Am. **68**, 640–654.

Patterson, R. D. Robinson, K. Holdsworth, J. W., McKeown, D. Zhang, C., and Allerhand, M. (**1992**). ''Complex sounds and auditory images,'' in *Auditory Physiology and Perception*, edited by Y. Cazals, L. Demany, and K. Horner (Pergamon, Oxford), pp. 429–446.

Sachs, M. B., Blackburn, C. C., and Young, E. D. (**1988**). ''Rate-place and temporal-place representations of vowels in the auditory-nerve and anteroventral cochlear nucleus,'' J. Phon. **16**, 37–53.

Sinnott, J. H., and Kreiter, N. A. (**1991**). ''Differential sensitivity to vowel continua in Old World monkeys (Macaca) and humans,'' J. Acoust. Soc. Am. **89**, 2421–2429.

Slaney, M. (**1993**). ''An efficient implementation of the Patterson-Holdsworth filter bank,'' Apple Technical Report #35.

Sommers, M., and Kewley-Port, D. (**1996**). ''Modeling formant frequency discrimination of female vowels,'' J. Acoust. Soc. Am. **99**, 3770–3781.

Watson, C. S., Kelly, W. J., and Wroton, H. W. (**1976**). ''Factors in the discrimination of tonal patterns. II. Selective attention and learning under various levels of stimulus uncertainty,'' J. Acoust. Soc. Am. **60**, 1176–1186.

Zwicker, E. (**1970**). ''Masking and psychological excitation as consequences of the ear's frequency analysis,'' in *Frequency Analysis and Periodicity Detection in Hearing*, edited by R. Plomp and G. F. Smoorenburg (Sijthoff, Leiden).

Zwicker, E. (**1975**). ''Scaling,'' in the *Handbook of Sensory Physiology*, edited by W. D. Keidel and W. D. Neff (Springer-Verlag, Berlin), Vol. 5(3), pp. 401–448.

Zwicker, E., and Fastl, J. (**1990**). *Psychoacoustics* (Springer-Verlag, Berlin).

LETTERS TO THE EDITOR

This Letters section is for publishing (a) brief acoustical research or applied acoustical reports, (b) comments on articles or letters previously published in this Journal, and (c) a reply by the article author to criticism by the Letter author in (b). Extensive reports should be submitted as articles, not in a letter series. Letters are peer-reviewed on the same basis as articles, but usually require less review time before acceptance. Letters cannot exceed four printed pages (approximately 3000–4000 words) including figures, tables, references, and a required abstract of about 100 words.

On inferring speed of sound in aquatic organisms

Zhen Ye[a)]
Ocean Acoustics, Institute of Ocean Sciences, Sidney, British Columbia, Canada and Department of Physics, National Central University, Chungli, Taiwan, Republic of China

Sam McClatchie
National Institute of Water and Atmospheric Research, Wellington, New Zealand

(Received 3 February 1997; revised 20 September 1997; accepted 5 November 1997)

A previous formula used for inferring speed of sound in marine organisms is considered and compared with the result from a wave scattering theory. Comparison indicates that there exists a difference between the two results, and the difference increases with the relative sound-speed contrast, and with the ratio between the dimension of animals and the acoustic wavelength. However, it is shown analytically that in the Rayleigh scattering regime and when the mass density difference between the target organisms and the medium is negligible that the earlier formula can be recovered by the result from the wave scattering theory, thereby providing a further physical and mathematical basis to the previous formula.
[S0001-4966(98)04702-X]

PACS numbers: 43.20.Gp, 43.20.Hq, 43.80.Cs [JEG]

INTRODUCTION

An important physical parameter required for theoretical modeling of acoustic scattering by marine organisms is the speed of sound through their tissues. Several attempts have been made to measure sound speed in zooplankton (e.g., Greenlaw, 1977; Greenlaw and Johnson, 1982; Foote, 1990). The underlying principle is based on measurement of the time-of-flight of acoustic pulses through a uniform mixture of water and marine organisms, where the volume of water and animals is estimated.

To infer the sound speed in marine organisms, a time average approach was used previously. In this method, an empirical equation is used to relate the measured sound speed (c_f) in the mixture to the fraction of the volume filled by animals (β) and the speed of sound in these animals as (Foote, 1990)

$$\frac{1}{c_f}=\frac{1-\beta}{c}+\frac{\beta}{c_a}, \tag{1}$$

where c and c_a are the speed of sound in the pure medium and the animals, respectively. Since c is assumed to be known, c_a can be deduced once c_f and β are measured. Equation (1) can be rearranged into

$$\frac{c}{c_f}=1-\beta+\frac{\beta}{h}, \tag{2}$$

where $h=c_a/c$ denotes the sound speed ratio between the animal and the medium.

In using Eq. (1), it has been believed that the formula, in which no scattering features appear, is usable for inferring the speed of sound of marine organisms when: (1) multiple scattering is negligible (Greenlaw, 1997); (2) the acoustic wavelength is small compared to the projected dimension of the scatterer along the sound path; and (3) the scatterers are uniformly and randomly distributed along the acoustic path (Foote, 1990). However, no mention has been made of the precise physical mechanism for Eq. (1). The rigorous mathematical derivation of this equation is also lacking.

The purpose of this paper is two-fold. It is to inspect Eq. (1) in the context of wave scattering theory, on the one hand, and to provide a further physical and mathematical foundation for this equation on the other hand. We will show that, in contrast to the previous presumptions, Eq. (1), or equivalently, Eq. (2), may be accurate in the Rayleigh scattering regime, i.e., where the acoustic wavelength is much larger than the size of scatterers, and when the mass density ratio between the scatterer and the medium can be approximated by 1. Although it is focused on the marine animals, the discussion in this paper equally applies to other systems, such as marine porous sediments. An important implication of the

[a)]Now at Department of Physics and Center for Complex Systems, National Central University, Chung-li, Taiwan, ROC.

work is that more accurate measurement of sound speed in marine animals is needed for modeling sound scattering, so as to improve stock estimate.

I. WAVE SCATTERING THEORY

When acoustic waves propagate through a medium containing many randomly distributed scatterers, multiple scattering of acoustic waves will occur, resulting in a change in wave speed. This problem can be studied by wave scattering theories (Foldy, 1945; Lax, 1951; Waterman and Truell, 1961). In the presence of many scatterers, the wave equation for the pressure field p can be generically written as

$$(\nabla^2+k^2)p=J[p,n,f_s], \tag{3}$$

where ∇^2 is the usual Laplacian operator, k is the wave number without scattering, $J[p,n,f_s]$ denotes the interaction term resulting from scattering, and n and f_s refer to the numerical density and scattering function of the scatterers, respectively. The numerical density relates to the volume fraction filled by animals as $\beta=nv$, with v being the volume of an individual scatterer. For simplicity, in this paper we approximate the scatterers as spheres of the same size. Upon an appropriate ensemble average the effective equation for the averaged field can be written as

$$(\nabla^2+\kappa^2)p=0, \tag{4}$$

where the effective wave number, ignoring high order multiple scattering, is related to the bare wave number k as (Lax, 1951)

$$\kappa^2=k^2+4\pi n f_s(\mathbf{k},\mathbf{k}), \tag{5}$$

with $f_s(\mathbf{k},\mathbf{k})$ being the forward scattering function in the direction of wave propagation, abbreviated as $f_s(0)$ in the following.

For weak scattering, i.e., $|4\pi n f_s|/k^2 \ll 1$, Eq. (5) can be further approximated as

$$\kappa \approx k+\frac{2\pi n f_s(0)}{k}. \tag{6}$$

Writing κ as $(\omega/c_f)+i\alpha$ with α being the acoustic attenuation coefficient, the effective sound speed c_f in the mixture can be determined from

$$\frac{c}{c_f}=1+\frac{2\pi n\ \mathrm{Re}[f_s(0)]}{k^2}, \tag{7}$$

where $\mathrm{Re}[\cdot]$ means taking the real part of a complex number. Equation (7) represents an alternative formula for sound speed in the presence of scatterers in the weak scattering regime, not to be confused with the Rayleigh scattering discussed later. Apparently Eq. (7) has a more rigorous physical and mathematical interpretation. A detailed discussion of this equation can be found in Waterman and Truell (1961). Equation (7) has been widely used in the bubble population estimate. It is based on the assumption that the scattering by targets is a perturbative correction to the wave propagation through the pure medium. Generally speaking, such a perturbation theory is valid when the numerical density and scattering strength are not too large. It is thus conceivable that this assumption is valid for relatively low volume fractions (β). When the volume fraction approaches 1, the scattering by targets can no longer be regarded as a perturbative correction, and the result in Eq. (7) may not be accurate in general. We will come back to this later. Next we compare the results in Eqs. (1) and (7).

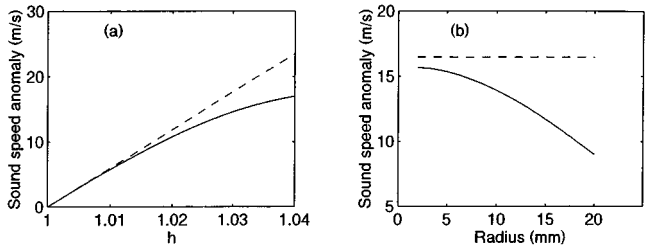

FIG. 1. The sound-speed anomaly as (a) a function of sound-speed contrast h for $a=5$ mm, and as (b) a function of radii. In these plots, the solid and dashed lines refer to the results from Eqs. (7) and (1), respectively. The frequency is 500 kHz.

Equations (7) and (1) differ in two important ways. First, according to a Kramers–Kronig relation (Temkin, 1990), $c/c_f \to 1$ as k goes to infinity in Eq. (7), whereas in Eq. (1) the sound speed ratio is independent of frequency. Second, Eq. (7) depends on scattering properties of the scatterers, while Eq. (1) does not. Differences between the two approaches are illustrated by the following numerical examples.

II. NUMERICAL COMPARISON

For the sake of convenience and illustration, yet without losing generality, we approximate marine animals as fluid spheres which have the same physical and acoustic properties as the marine organisms. The further reasons why we do not consider the actual shape of marine animals in the present calculation are as follows. First, we recognize that models for actual targets are not conclusive. Using a simpler model will not only make the problem manageable but facilitate our discussion, so that the essential points can be conveyed more clearly. Second, considering actual targets would involve many complicated and uncertain issues, such as animal orientation distribution and the ensemble average over this distribution. This would make it unfocused when the main purpose of this paper is to show the difference between Eqs. (1) and (7). Third, as Eq. (7) indicates, it is the forward scattering function that enters into the formula. And, recent studies have shown that unlike backscatter the forward scattering function for a marine animal, not necessarily modeled as a spherical object, varies rather smoothly with regards to frequencies and incident angles (Ding, 1997).

Consider the measurement of speed of sound in *Euphausia superba* as an example (Foote, 1990). The radius is assumed to vary within the range 2–20 mm to cover the actual size variability. The acoustic frequency is 500 kHz. The volume fraction filled by krill, β, varies from 0.29 to 0.4. We take $\beta=0.4$ as the extreme case. The density ratio is about 1.049–1.068 (Greenlaw and Johnson, 1982; Foote, 1990), we take $g=1.049$, and we consider h varying from 1 to 1.04. At 500 kHz used in the sound-speed measurement, we cal-

culate $|4\pi n f_s|/k^2 < 0.0208 \ll 1$ for all values of radius and h. Therefore the above theory for weak multiple scattering is applicable.

For convenience, we consider the forward problem; namely, given the targets, what will be the sound speed anomaly in the presence of the targets predicted from Eqs. (1) and (7)? Figure 1(a) presents the sound-speed anomaly, defined as $\Delta c \equiv c_f - c$, as a function of the sound speed contrast h for the radius 10 mm. The dashed line is from Eq. (1) and the solid line is from Eq. (7). Here we see that the two approaches converge as h decreases, i.e., weak scatter scenario. At $h=1.0279$, the discrepancy in the sound-speed anomaly between the two approaches amounts to about 20%. Conversely, if there is a 20% difference in estimating the sound speed anomaly, it would imply about 1.2% discrepancy in the h estimation according to Fig. 1(a). This may in turn result in large variations of the target strength of the scatterer, depending on the scattering models. For example, one model (Johnson, 1977) predicts 40% change in scattered energy for even 1% change in h (with $h \sim 1.034$). Such a large variability would make the stock estimate of marine animals very inaccurate. Note that it is shown clearly in Fig. 1(a) that the time average approach always underestimates h, consistent with what will be discussed later.

The measurement based on Eq. (1) indicates that speed of sound in *Euphausia superba* relative to seawater is about 1.0279 times that in seawater. For this value of h, we plot the sound speed anomaly as a function of the radius of scatterers in Fig. 1(b) from Eqs. (1) and (7), respectively. We note that varying the radius at a fixed frequency is equivalent to varying the frequency at a fixed radius. It shows that the results from the two approaches seem to approach each other as the size of scatterers decreases, falling into the Rayleigh scattering region. The discrepancy between the two theories increases as the size increases, and goes up from 5% to 80% as the radius increases from 2 mm to 20 mm. As will be demonstrated later, the disagreement would become more severe as the density difference increases.

III. LOW-FREQUENCY LIMIT

We consider the low-frequency limit of the result from wave scattering theory. As $ka \to 0$, i.e., in the Rayleigh scattering region, the scattering function can be derived as (Anderson, 1950)

$$f_s(\theta) = \frac{(ka)^3}{k}\left[\frac{1-gh^2}{3gh^2} - \frac{1-g}{1+2g}\cos\theta\right], \tag{8}$$

where θ is the angle between the scattering and incident directions. For forward scattering, we have

$$f_s(0) = \frac{(ka)^3}{k}\left[\frac{1-gh^2}{3gh^2} - \frac{1-g}{1+2g}\right]. \tag{9}$$

Substituting this equation into Eq. (7) and using $\beta = (4\pi/3)a^3 n$, we obtain

$$\begin{aligned}\frac{c}{c_f} &= 1-\beta+\beta\left[\frac{1+gh^2}{2gh^2}+\frac{3(g-1)}{2(1+2g)}\right] \\ &= 1-\beta+\frac{\beta(1+h^2)}{2h^2}-\frac{\beta(g-1)}{2gh^2}+\frac{3\beta(g-1)}{2(1+2g)} \\ &= 1-\beta+\frac{\beta(1+h^2)}{2h^2}+\frac{\beta(g-1)}{2}\left[\frac{3}{1+2g}-\frac{1}{gh^2}\right]. \end{aligned} \tag{10}$$

When h is close to 1, as usually true for marine animals, we write $h \equiv 1+\Delta h$ with Δh being a small positive value and referring to the relative sound speed increase in the animals. Ignoring higher orders in Δh, Eq. (10) becomes

$$\begin{aligned}\frac{c}{c_f} &= 1-\beta+\beta(1-\Delta h+O(\Delta h^2)) \\ &\quad +\frac{\beta(g-1)}{2}\left[\frac{3}{1+2g}-\frac{1}{gh^2}\right] \\ &\approx 1-\beta+\frac{\beta}{1+\Delta h}+\frac{\beta(g-1)}{2}\left[\frac{3}{1+2g}-\frac{1}{gh^2}\right] \\ &= 1-\beta+\frac{\beta}{h}+\frac{\beta(g-1)}{2}\left[\frac{3}{1+2g}-\frac{1}{gh^2}\right]. \end{aligned} \tag{11}$$

Clearly Eq. (11) will be essentially identical to Eq. (2) in the time average approach when the last term on the right-hand side is negligible. This can be satisfied if either g is close to 1, or the last term in the bracket is close to zero, i.e., when $g \sim 1-6\Delta h$, which is smaller than 1. The later case is not true for zooplankton because they are negatively buoyant. Therefore, rigorously speaking the time average approach may be applicable only for low frequencies, i.e., Rayleigh scattering, and when the mass density ratio is close to 1. This seems to contradict some of the previous assumptions, e.g., the aforementioned presumptions (1) and (2). As mentioned earlier, as β approaches 1, Eq. (10) may not be accurate because it is based on the assumption that the scattering by targets is a perturbative correction to the wave propagation through the pure medium. When β approaches 1, the scattering by the fraction of volume filled by water should rather be regarded as a correction to the wave propagation through the pure target medium. In this case, Eq. (10) is replaced by

$$\frac{c_a}{c_f} = \beta' + (1-\beta')\left\{\frac{1+gh^2}{2}+\frac{3(1-g)}{2(2+g)}\right\}, \tag{12}$$

where β' is the fraction of volume filled by the water and equals $1-\beta$. Under the condition that $g \sim 1$, $h \sim 1$, however, both Eq. (10) and Eq. (12) are equivalent. Theoretical description of the transition from Eq. (10) to Eq. (12) for arbitrary g and h is an unsolved problem, and is beyond the scope of this paper. We also note that Eq. (11) can also be derived for nonspherical fluid scatterers by the Börn approximation in the Rayleigh scattering limit. It can be further shown that when g is nearly one, Eq. (10) becomes also equivalent to the classical result of Wood (1930).

Consider the effect of the density contrast g on the estimate of h in the Rayleigh scattering limit. From Eq. (10), we can derive to the first order in Δh (see the Appendix)

TABLE I. Comparison of the time average approach and wave scattering theory.

	β	g	h	Frequency
TAA[a] in Eq. (1)	arbitrary	~ 1	~ 1	low
WST[b] in Eq. (10)	low	arbitrary	arbitrary	arbitrary

[a]TAA=time average approach.
[b]WST=wave scattering theory.

$$\Delta h = \frac{g}{\beta}\left(1 - \frac{c}{c_f} + \frac{\beta(g-1)^2}{2g(1+2g)}\right). \tag{13}$$

When $g=1$, this equation reduces to the formula derived from Eq. (2):

$$\Delta h_0 = \frac{1}{\beta}\left(1 - \frac{c}{c_f}\right). \tag{14}$$

The discrepancy between the two estimates of the sound speed increase is

$$\begin{aligned} D &\equiv \frac{\Delta h - \Delta h_0}{\Delta h_0} \\ &= g - 1 + \frac{(g-1)^2}{2(1+2g)\Delta h_0} \\ &= (g-1)\left(1 + \frac{1}{2(1+2g)}\frac{(g-1)}{\Delta h_0}\right). \end{aligned} \tag{15}$$

This equation shows that Eq. (1) always underestimate the value of h as $g>1$, and that in the low-frequency limit the discrepancy between the relative sound speed increases from the two approaches is on the order of $g-1$, if $g-1$ and Δh_0 are of the same order of magnitude. Again, when g is close to one, the discrepancy will be small. Consider *Euphausia superba* as an example. If we take Δh_0 as 0.0279, and g as 1.049, D is calculated as 6.3%, which results in less than 0.1% change in h, and less than 4% change in the scattered energy. Since in most marine animals the density increase $g-1$ and the sound speed increase are only a few percent, from Eq. (15) we conclude that the estimate of h from Eq. (1) or (2) is accurate for the low frequencies.

IV. SUMMARY

In summary, in this paper we compared a previous formula from the time average approach for inferring sound speed in marine organisms with that from a wave scattering theory. The comparison shows that while there exist general differences, the two formulas are in good agreement in the low frequency limit and when the mass density difference between the animals and the medium is negligible, thereby providing a further basis to the previous formula. The general comparison of the two approaches is summarized in Table I.

ACKNOWLEDGMENTS

The work was completed when one of us (Z.Y.) visited the National Institute of Water and Atmospheric Research (NIWA), New Zealand. Comments from Roger Coombs at NIWA are greatly appreciate. Two referees are thanked for constructive suggestions and comments. Z. Ye sincerely thanks the financial support from the NIWA visiting scientist program, and the hospitality from the staff in the acoustics group. The work also received support from Department of Fisheries an Oceans, Canada, and the National Science Council of the Republic of China under Grant No. NSC 87-2112-M-008-008.

APPENDIX

In this Appendix, we derive Eq. (13). Equation (10) can be rearranged into

$$\frac{1}{h^2} = \frac{2g}{\beta}\left(\frac{c}{c_f} - 1 + \frac{\beta(4-g)}{2(1+2g)}\right). \tag{A1}$$

Writing $h=1+\Delta h$, to the first order in Δh the above equation gives

$$1 - 2\Delta h = \frac{2g}{\beta}\left(\frac{c}{c_f} - 1 + \frac{\beta(4-g)}{2(1+2g)}\right). \tag{A2}$$

From this, Δh can be solved as

$$\Delta h = \frac{1}{2}\left\{1 - \frac{2g}{\beta}\left(\frac{c}{c_f} - 1 + \frac{\beta(4-g)}{2(1+2g)}\right)\right\}, \tag{A3}$$

which can be rearranged into Eq. (13).

Anderson, V. C. (**1950**). ''Sound scattering from a fluid sphere,'' J. Acoust. Soc. Am. **22**, 426–431.

Ding, L. (**1997**). ''Direct laboratory measurement of forward scattering by individual fish,'' J. Acoust. Soc. Am. **101**, 3398–3404, and references therein.

Foldy, L. L. (**1945**). ''The multiple scattering of waves,'' Phys. Rev. **67**, 107–119.

Foote, K. (**1990**). ''Speed of sound in *Euphausia superba*,'' J. Acoust. Soc. Am. **87**, 1405–1408.

Greenlaw, C. F. (**1977**). ''Backscattering spectra of preserved zooplankton,'' J. Acoust. Soc. Am. **62**, 44–52.

Greenlaw, C. F., and Johnson, R. K. (**1982**). ''Physical and acoustic properties of zooplankton,'' J. Acoust. Soc. Am. **72**, 1706–1710.

Johnson, R. K. (**1977**). ''Sound scattering from a fluid sphere revisited,'' J. Acoust. Soc. Am. **61**, 375–377.

Lax, M. (**1951**). ''Multiple scattering of waves,'' Rev. Mod. Phys. **23**, 287–310.

Temkin, S. (**1990**). ''Attenuation and dispersion of sound in bubbly fluids via the Kramers–Kronig relations,'' J. Fluid Mech. **211**, 61–72.

Waterman, P. C., and Truell, R. (**1961**). ''Multiple scattering of waves,'' J. Math. Phys. **2**, 512–537.

Wood A. B. (**1930**). *A Textbook of Sound* (Bell, London), pp. 326–329.

A simplified formula for viscous and chemical absorption in sea water

Michael A. Ainslie and James G. McColm
BAeSEMA Ltd., Apex Tower, 7 High Street, New Malden, Surrey KT3 4LH, England

(Received 6 June 1997; accepted for publication 16 December 1997)

A simplified expression is presented for predicting the absorption of sound in sea water, retaining the essential dependence on temperature, pressure, salinity, and acidity of the more complicated formula on which it is based [R. E. Francois and G. R. Garrison, ''Sound absorption based on ocean measurements. Part II: Boric acid contribution and equation for total absorption,'' J. Acoust. Soc. Am. **72**, 1879–1890 (1982)]. The accuracy of the simplified formula is demonstrated by comparison with the original one for a range of oceanographic conditions and frequencies between 100 Hz and 1 MHz. © *1998 Acoustical Society of America.* [S0001-4966(98)05203-5]

PACS numbers: 43.30.Es [SAC-B]

INTRODUCTION

Ocean sound is attenuated by two main mechanisms: viscous absorption, which is significant at high frequency (above 100 kHz); and chemical relaxation effects, primarily due to boric acid at low frequency (up to a few kHz), and magnesium sulphate at intermediate frequencies (up to a few 100 kHz). The magnitude of these effects varies in a complicated way with frequency, pressure, temperature, salinity, and acidity.[1,2] Here we present a simplified version of the Francois–Garrison equation which makes the dependence on these variables more transparent, while retaining similar accuracy.

A third chemical relaxation due to magnesium carbonate is sometimes included in absorption equations.[3] The Francois–Garrison equation does not incorporate an explicit $MgCO_3$ relaxation, but because it is based on ocean measurements, any effect is included implicitly in the other terms.

For notation and units we use α for attenuation in dB/km, f for frequency in kHz, z for depth in km, T for temperature in °C, and S for salinity in ppt. This notation is identical to that of Francois and Garrison.[2]

I. SIMPLIFIED FORMULA

To simplify the full Francois–Garrison formula (referred to hereafter as FG) we first expand temperature, salinity and acidity about reference values of $T=0\,^{\circ}\mathrm{C}$, $S=35$ ppt, and $p\mathrm{H}=8$, respectively. Retaining only highest order terms, this immediately simplifies the boric acid and magnesium sulphate relaxation frequencies (in kHz)

$$f_1 = 0.78(S/35)^{1/2} e^{T/26} \quad \text{(for boron)}, \tag{1}$$

$$f_2 = 42 e^{T/17} \quad \text{(for magnesium)}. \tag{2}$$

Applying a similar analysis to the coefficient terms, and in particular fitting a simple exponential to the bicubic expression for the temperature dependence of the pure water contribution (A_3 in FG), we obtain our end result (in dB/km)

$$\alpha = 0.106 \frac{f_1 f^2}{f^2+f_1^2} e^{(p\mathrm{H}-8)/0.56} + 0.52\left(1+\frac{T}{43}\right)\left(\frac{S}{35}\right)\frac{f_2 f^2}{f^2+f_2^2} e^{-z/6} + 0.00049 f^2 e^{-(T/27+z/17)}. \tag{3}$$

We have found that this simplified formula retains reasonable accuracy (to within 10% of FG between 100 Hz and 1 MHz) for the following oceanographic conditions:

$$-6<T<35\,^{\circ}\mathrm{C} \quad (S=35 \text{ ppt}, \ p\mathrm{H}=8, \ z=0)$$

$$7.7<p\mathrm{H}<8.3 \quad (T=10\,^{\circ}\mathrm{C}, \ S=35 \text{ ppt}, \ z=0)$$

$$5<S<50 \text{ ppt} \quad (T=10\,^{\circ}\mathrm{C}, \ p\mathrm{H}=8, \ z=0)$$

$$0<z<7 \text{ km} \quad (T=10\,^{\circ}\mathrm{C}, \ S=35 \text{ ppt}, \ p\mathrm{H}=8).$$

II. RESULTS

Figure 1 shows predicted volume attenuation plotted versus frequency using FG and Eqs. (1)–(3) above for four oceans of differing characteristics (Table I), based on Fig. 3 of Ref. 3 and Table VII of Ref. 4. On a logarithmic scale the differences between the two equations are almost imperceptible so we have also plotted the percentage difference for the same four oceans (Fig. 2). Departures from FG are mostly less than 5% and always less than 10% for these cases. These differences are comparable with the stated accuracy (±5%–10%) of FG itself.[2]

III. CONCLUSIONS

We apply Occam's razor to the absorption equation of Francois and Garrison.[2] The resulting equations [see Eqs. (1)–(3) above] are much simpler than the original, but retain similar accuracy. This simplicity makes it possible to reach some simple conclusions by inspection. For example we observe that:

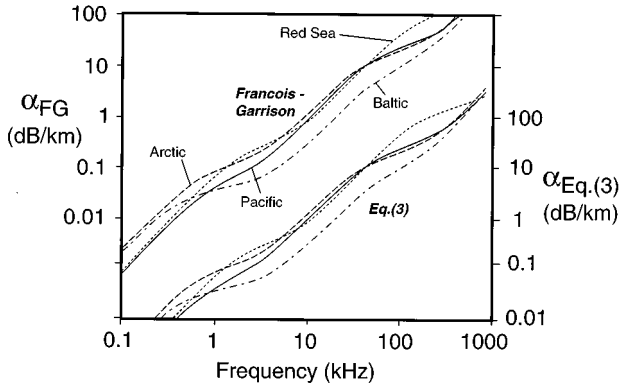

FIG. 1. Volume absorption coefficients for the four oceans from Table I, calculated using FG (upper curves) and Eq. (3) (lower curves).

- increasing acidity (decreasing pH) decreases low frequency absorption (up to the boron relaxation at f_1), with no effect at higher frequencies (hence the low absorption below 1 kHz in the Pacific Ocean);
- increasing salinity decreases absorption at low frequency ($\ll f_1$) and increases absorption at high frequency ($\gtrsim f_1$), hence the low absorption above 1 kHz in the Baltic Sea;
- increasing temperature decreases absorption at all frequencies except in the immediate vicinity of the relaxation frequencies f_1 and f_2, where absorption is *increased* (hence the high absorption at the relaxation frequencies in the Red Sea and the high absorption at all other frequencies in the Arctic Ocean);

TABLE I. Oceanographic parameters used for Figs. 1 and 2.

	pH	S(ppt)	T(°C)	z(km)
Pacific Ocean	7.7	34	4.0	1.0
Red Sea	8.2	40	22.0	0.2
Arctic Ocean	8.2	30	−1.5	0.0
Baltic Sea	7.9	8	4.0	0.0

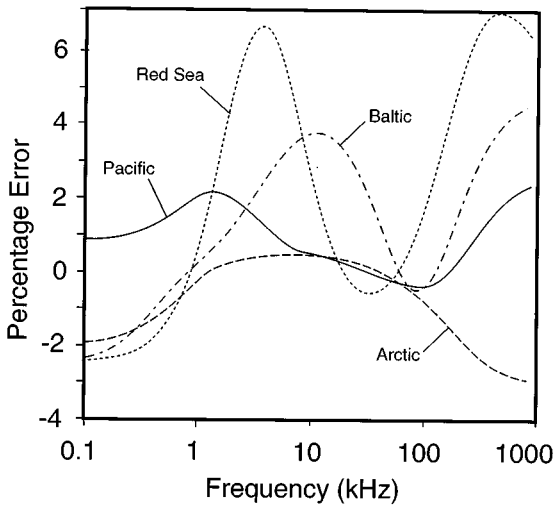

FIG. 2. Percentage difference between Eq. (3) and FG for the four oceans of Table I, calculated as $100\,[\alpha_{\text{Eq. (3)}}-\alpha_{\text{FG}}]/\alpha_{\text{FG}}$.

- increasing depth (or pressure) decreases absorption at high frequency ($\gtrsim f_1$), with no effect at lower frequencies.

Of course, all of these conclusions follow also from the original FG equation, but they are not obvious by straightforward inspection.

ACKNOWLEDGMENT

This work has been carried out with the support of the U.K. Ministry of Defence.

[1] R. E. Francois and G. R. Garrison, ''Sound absorption based on ocean measurements. Part I: Pure water and magnesium sulfate contributions,'' J. Acoust. Soc. Am. **72**, 896–907 (1982).
[2] R. E. Francois and G. R. Garrison, ''Sound absorption based on ocean measurements. Part II: Boric acid contribution and equation for total absorption,'' J. Acoust. Soc. Am. **72**, 1879–1890 (1982).
[3] D. G. Browning and R. H. Mellen, ''Attenuation of low-frequency sound in the sea: Recent results,'' in *Progress in Underwater Acoustics*, edited by H. M. Merklinger (Plenum, New York, 1987), pp. 403–410.
[4] F. H. Fisher and V. P. Simmons, ''Sound absorption in sea water,'' J. Acoust. Soc. Am. **62**, 558–564 (1977).

Active vibration control of waves in simple structures with multiple error sensors

X. Pan and Colin H. Hansen
Department of Mechanical Engineering, University of Adelaide, Adelaide, South Australia 5005

(Received 3 April 1997; accepted for publication 10 December 1997)

A numerical study is carried out to determine the improvement in vibration control of simple structures gained by using two sets rather than one set of error sensors. The structures considered are a beam, a plate, and a cylindrical shell. The control sources are driven to minimize the sum of the mean squared flexural displacement signal from all sensors with the view to reducing downstream vibration transmission. Results show that over a large frequency range there is an overall improvement in downstream attenuation resulting from the introduction of the second set of error sensors for each simple structure. © *1998 Acoustical Society of America.*
[S0001-4966(98)04903-0]

PACS numbers: 43.40.Vn [PJR]

INTRODUCTION

In the feed-forward active control of structural vibration, the design of the physical system including the error sensor and control source configuration has attracted considerable attention in recent years.[1–6] In general, the optimal error sensor configuration is relatively simpler and cheaper to achieve than the control source configuration. In previous papers,[1,2] the authors indicated that a lower reduction of power transmission occurs using active control in a beam when an error sensor is located at a standing wave node,[1] and in a plate when a line of error sensors are located at a standing wave nodal line.[2] To the authors' knowledge, there has been limited work[3] involving the use of two error sensors on a beam, and the earlier work was not extended to the use of a second set of error sensors in a plate or a cylindrical shell.

It is important to study the possibility of improving attenuation of vibratory power transmission in simple structures (beams, plates, and cylindrical shells) in the situation where the first set of error sensors is located at a nodal line. Here, the effect of a second set of error sensors is investigated and the cost function used is the sum of the mean square signal from all error sensors.

I. THEORY

A. Minimizing displacement at two error sensors in a beam

The coordinate system for a beam with a primary point force, a control point force and an error sensor is shown in Fig. 1(a).

The total flexural displacement (in the time domain) due to a harmonic primary force F_p and control force F_c acting together is[4]

$$w = F_p w_{p-f} + F_c w_{c-f}, \tag{1}$$

where w_{p-f} is the displacement normal to the beam axis due to a unit primary force and w_{c-f} is the displacement due to a unit control force. If one error sensor is located at x_e, the optimal control force for minimizing flexural displacement can be written as[4]

$$F_c = -\frac{\mathbf{PE}}{\mathbf{CE}} F_p, \tag{2}$$

where **P** and **C** are row vectors (of length 4) of primary and control forces, respectively, and

$$\mathbf{E} = \begin{bmatrix} e^{k_f x_e} \\ e^{-k_f x_e} \\ e^{jk_f x_e} \\ e^{-jk_f x_e} \end{bmatrix}. \tag{3}$$

If a second error sensor is introduced at some location x_e' downstream from the first error sensor x_e and a single control force driven in a way so as to optimally reduce vibration at both locations, the optimal control force can be obtained by minimizing the sum of the mean squares of displacement at the two locations. This is achieved by setting the partial derivatives of the sum with respect to each of the real and imaginary components of the control force equal to zero. The optimal control force can be shown to be given by

$$F_c = -\frac{1}{2}\left(\frac{\mathbf{PE}}{\mathbf{CE}} + \frac{\mathbf{PE}'}{\mathbf{CE}'}\right) F_p, \tag{4}$$

where $\mathbf{E}'$ is obtained by replacing x_e with x_e' on the right-hand side of Eq. (3).

B. Minimizing displacement at two lines of error sensors on a plate

If a plate [Fig. 1(b)] is driven by a line of in-phase radial primary point forces and a line of three independent control point forces directed normal to the plate surface, the total plate response is[2]

$$w = F_p w_{p-f} + F_{c1} w_{c-f1} + F_{c2} w_{c-f2} + F_{c3} w_{c-f3}. \tag{5}$$

The optimal control forces for minimizing the displacement at a line of error sensors $x = x_e$ may be found by integrating (across the plate) the mean square of the displacement defined in Eq. (5) and setting the partial derivatives of the integration with respect to each of the real and imaginary components of the control forces equal to zero. The result is an optimal set of control forces[2]

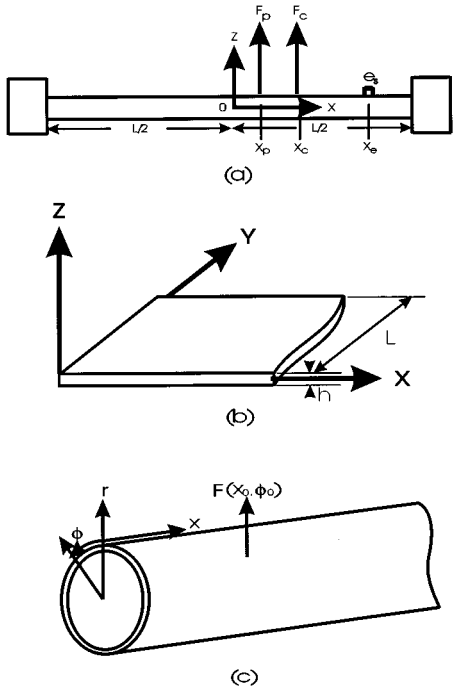

FIG. 1. (a) Beam model with a point force excitation, an applied point controlled force and an error sensor; (b) semi-infinite plate model; (c) semi-infinite cylindrical shell model with excitation F at location (x,ϕ).

$$\mathbf{F}_c = -\mathbf{D}^{-1}\mathbf{B}F_p, \tag{6}$$

where each element in **D** and **B** are matrixes, in which each element is a function of displacement at x_e. If a second line of error sensors $x=x_e'$ is introduced downstream from the first line of error sensors $x=x_e$, the optimal set of control forces can be obtained by repeating the process described in Sec. I A but for the two lines of error sensors. The result is

$$\mathbf{F}_c = -[\mathbf{D}^{-1}+(\mathbf{D}')^{-1}](\mathbf{B}+\mathbf{B}')F_p, \tag{7}$$

where $\mathbf{D}'$ and $\mathbf{B}'$ are obtained by replacing x_e with x_e' in each element of **D** and **B**, respectively.

The total power transmitted past a line across the plate at an axial location x, can be written in matrix form as[2]

$$P_{xa} = \frac{1}{2}\int_0^{L_y} \mathrm{Re}[\mathbf{F}^H\mathbf{A}\mathbf{F}]dy, \tag{8}$$

where **F** is a 1×4 matrix in which the elements are the primary force and the three control forces obtained from Eq. (6), and **A** is a 4×4 matrix in which each element is a function of the displacement due to unit force excitation, the first derivative, the second derivative, and the third derivative of the displacement, respectively.

C. Minimizing displacement at two rings of error sensors in a cylindrical shell

If the cylindrical shell [Fig. 1(c)] is driven by a ring of in-phase radial primary forces and a ring of three independent radial control point forces, the flexural displacement has the same form as shown in Eq. (5). The optimal set of control forces for the use of one ring/two rings of error sensors has the same form as shown in Eq. (6)/Eq. (7), but with the integral from 0 to L_y with respect to y replaced by an integral from 0 to 2π with respect to angular location ϕ in each integral term.

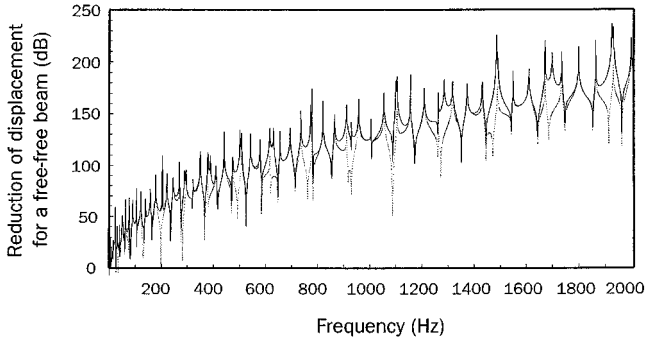

FIG. 2. Mean reduction of displacement as a function of excitation frequency in a free–free beam. ····· one error sensor; ——— two error sensors.

The total power transmitted past a ring at an axial location x is[5]

$$P_{xa} = \frac{r}{2}\int_0^{2\pi} \mathrm{Re}[\mathbf{F}^H\mathbf{A}\mathbf{F}]d\phi. \tag{9}$$

II. NUMERICAL RESULTS

A. Effect of two error sensors in a beam

A free–free aluminum beam with a cross section of 50 $\times$25 mm and extending from $x=-5$ m to $x=5$ m was used. The primary force was at $x=0$ m, the control force was at $x=1.08$ m, the first error sensor was at $x=2.16$ m, and the second error sensor was at $x=2.26$ m.

Figure 2 shows the calculated mean attenuation of displacement downstream of the second error sensor in the free–free beam as a function of the excitation frequency for one and two error sensors. It can be seen that there is an overall improvement in attenuation resulting from the introduction of the second error sensor. In particular, the original minima in attenuation using one error sensor are generally made higher or even eliminated by the introduction of the second error sensor.

The peaks and troughs in the curves in Fig. 2 are presented correctly, and finer frequency resolution would not cause them to be significantly higher or lower. The peaks are achieved at frequencies corresponding to a half flexural wavelength separation between the primary and control forces. Most of the troughs in the curve represented by the dotted line (one error sensor only) occur when the first error sensor is at a standing wave node where it cannot work effectively. The remaining troughs occur as the control force locates at a node of the standing wave due to reflection from the downstream end of the beam. It is expected that these latter troughs could be significantly reduced by using more than one control force.

B. Effect of two lines of error sensors in a plate

Numerical results are calculated for vibration transmission along a semi-infinite plate, free at one end, anechoically

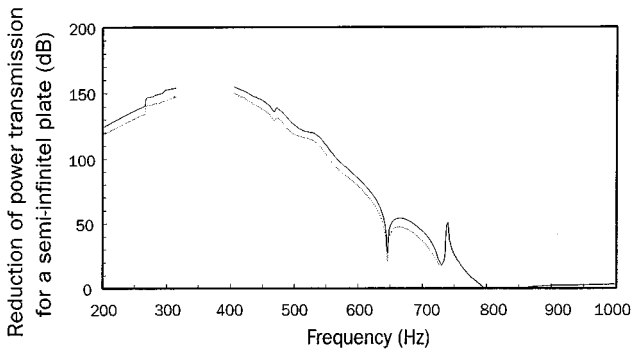

FIG. 3. Reduction of power transmission as a function of excitation frequency in a semi-infinite plate. ····· one line of error sensors; ——— two lines of error sensors.

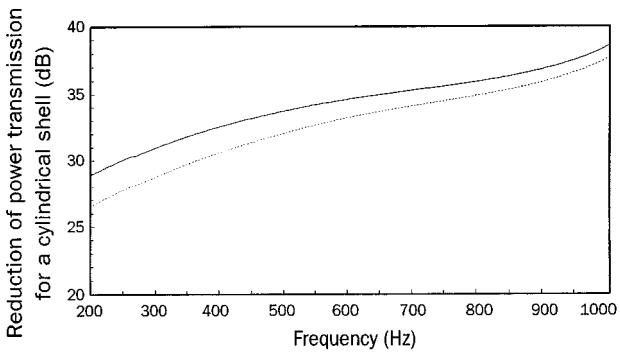

FIG. 4. Reduction of power transmission as a function of excitation frequency in a semi-infinite cylindrical shell. ····· one ring of error sensors; ——— two rings of error sensors.

terminated at the other end and simply supported along the other two sides. The plate is with thickness $h=0.003$ m and width $L_y=0.5$ m. The primary forces are located at $x=0.025$ m, the control forces are located at $x=0.138$ m, the first line of error sensors is located at $x=0.8884$ m, and the second line of error sensors is located at $x=0.9884$ m.

Figure 3 shows the power transmission reduction as a function of the excitation frequency for both one line and two lines of error sensors. The results for frequencies between 320 and 400 Hz are omitted because of numerical difficulties; that is, the matrix **D** in Eq. (6) is too ill-conditioned to be inverted to obtain a valid solution. Similar to the results shown in Fig. 2, there is an overall improvement in attenuation resulting from the introduction of the second line of error sensors. In particular, the original minima in attenuation achieved using one line of error sensors are made higher by the introduction of the second line of error sensors. The trough at 646 Hz where the control force amplitude is very large, as a result of the control force being located at a node in the standing wave generated by waves reflected from the free end of the plate. The trough at 739 Hz corresponds to the cut-on frequency of the fifth mode. In Fig. 3, it can be seen that the achievable power transmission reduction obtained by driving the control forces independently is more than 10 dB for all frequencies lower than the cut-on frequency of the fifth mode. Thus for the plate, excitation, and control force configuration considered here, good control can be achieved over the frequency range for which only the first five modes are propagating. The reduction in achievable control at higher frequencies is because the complexity of the vibration response increases as the mode order increases, so that the three control forces at particular locations are not enough to control high order modes.

C. Effect of two rings of error sensors in a cylindrical shell

Numerical results are calculated for the active control of vibration transmission along a semi-infinite shell, simply supported at one end and anechoically terminated at the other end. The shell has a radius of 0.25 m and a thickness of 0.003 m. The primary forces are at an axial location of 0.025 m, the control forces are at an axial location of 0.075 m, the first ring of error sensors is at an axial location of 0.565 m, and the second ring of error sensors is at an axial location of 0.965 m.

Figure 4 shows the reduction of power transmission as a function of the excitation frequency for both one and two rings of error sensors. Similar to the results shown in Figs. 2 and 3, there is an overall improvement in attenuation resulting from the introduction of the second ring of error sensors. Over a wide frequency range the reduction of power transmission obtained by using two rings of error sensors is about 1–2.5 dB more than that obtained by using only one ring of error sensors. The peaks and troughs have disappeared in Fig. 4 because there is no axial resonance frequency in the semi-infinite cylindrical shell.[5] The reduction of power transmission increases as the excitation frequency increases for both one ring of error sensors and two rings of error sensors because in a shell the flexural wavelength decreases as the excitation frequency increases.[5] Therefore, in terms of the flexural wavelength, the distance between the control forces and error sensors increases as the excitation frequency increases, so that the reduction of power transmission increases[5] due to a reduction in the near-field effect.

III. CONCLUSIONS

The additional benefit derived from using two sets of error sensors in actively controlled simple structures has been investigated analytically. The investigation of three examples was carried out by minimizing the sum of the mean squared flexural displacement at each error sensor. Over a large frequency range, it was found that there is an overall improvement in attenuation resulting from the introduction of a second set of error sensors. In particular, in a beam, the original minima in attenuation using one error sensor was generally made higher or even eliminated by the introduction of the second error sensor, thus indicating good potential improvement for feedforward control of broad band vibration provided a suitable reference signal can be obtained. However, for the semi-infinite plate and semi-infinite cylindrical shell, the improvement in attenuation due to the second line or second ring of error sensors was relatively small.

ACKNOWLEDGMENTS

Support for this work from the Sir Ross and Sir Keith Smith Fund and the University of Adelaide is gratefully acknowledged.

[1] X. Pan and C. H. Hansen, ''Effect of error sensor location and type on the active control of beam vibration,'' J. Sound Vib. **165**, 497–510 (1993).
[2] X. Pan and C. H. Hansen, ''Active control of vibratory power transmission along a semi-infinite plate,'' J. Sound Vib. **184**, 585–610 (1995).
[3] A. J. Young, ''Active control of vibration in stiffened structures,'' Ph.D. thesis, University of Adelaide (1995).
[4] X. Pan and C. H. Hansen, ''Effect of end conditions on the active control of beam vibration,'' J. Sound Vib. **168**, 429–448 (1993).
[5] X. Pan and C. H. Hansen, ''Active control of vibration transmission in a cylindrical shell,'' J. Sound Vib. **203**, 409–434 (1997).
[6] C. R. Fuller and L. O. Gonidou, ''Active vibration control of flexural power flow in beams,'' J. Acoust. Soc. Am. Suppl. 1 **84**, S47 (1988).

A predictive model of noise for Delhi

Krishan Kumar[a] and Vinod K. Jain
School of Environmental Sciences, Jawaharlal Nehru University, New Delhi 110067, India

Dwivedula N. Rao
Centre for Economic Studies and Planning, Jawaharlal Nehru University, New Delhi 110067, India

(Received 7 February 1994; revised 10 June 1997; accepted 29 October 1997)

Noise levels have been measured at several sites spread throughout Delhi. Based on these observations and taking into account the specific site characteristics, a linear regression model has been fitted to predict the noise levels for Delhi. It is found that noise levels are primarily determined by vehicular traffic. The residential areas have considerably lower noise levels than commercial areas. The results indicate that the vegetation has a role in attenuation of noise levels. © *1998 Acoustical Society of America.* [S0001-4966(98)04002-8]

PACS numbers: 43.50.Lj [GAD]

INTRODUCTION

Vehicular traffic is a major source of noise in urban areas. Most of the predictive models developed to date pertain to traffic noise. As traffic noise is stochastic in nature its prediction becomes a difficult problem. The early models (Johnson and Saunders, 1968; Mulholland, 1979; Delany *et al.*, 1976; Burgess, 1977) developed for the prediction of traffic noise were empirical in nature. A few attempts have also been made to develop multiple linear regression models of noise (Attenborough *et al.*, 1976; Prabhu and Chakraborty, 1978; Ohta *et al.*, 1995). In the United Kingdom, area-based prediction models based on considerations of land use and road traffic have been validated and found to be robust and reliable (Baverstock *et al.*, 1991).

In the context of Indian metropolitan cities, with the exception of a predictive regression model for the city of Calcutta (Prabhu and Chakraborty, 1978), no model has been developed to date. However, empirical models for prediction of road traffic noise have been developed for the cities of Visakhapatnam (Rao *et al.*, 1989) and Calcutta (Chakrabarty *et al.*, 1997). In the present study an attempt has been made to develop a predictive model of noise for Delhi, the capital city of India.

I. METHOD

Sampling was done at a number of sites situated in residential, commercial, and industrial zones and in areas with high traffic density for a period of 8 h. The instrument used for sampling was RION NL 10 precision integrated sound level meter, having the facility for both analog and digital displays. The measurements were made at a height of 1.2 m above the ground level and at a distance of 5 m from the outer edge of the roads. In all of the 34 areas selected for the present study, 5 apparently noisy sites were selected and numbered after preliminary survey of each area. One of these sites was then selected at random using a random number table. Eight-hour L_{eq} values were obtained for all the sites. The observed L_{eq} values at various sites are given in Table I. Based on these observations, a multiple linear regression model has been developed. The model equation is

$$Y=\alpha+\sum_{i=1}^{5}\beta_i X_i, \tag{1}$$

where Y is the dependent variable representing noise levels, α is a constant, and the β_i's are regression coefficients. The X_i's are explanatory variables characterizing each site. The criterion for selecting these variables was based on all those factors which directly or indirectly affect noise levels.

First the sites were classified into four categories, namely traffic intersections, residential, commercial, and industrial. For this purpose, three dummy variables X_1, X_2, and X_3, which take either the value zero or one, were used as shown in Table II. Further, two more binary variables, X_4 and X_5, were created to represent respectively the presence of vegetation and traffic. The vegetation in our study implies the existence of grass cover, dense interlocking hedges, and trees between noise sources and the observation point. These independent variables X_i take a value of 1 and 0 depending on the presence or absence of a particular characteristic at the site of observation.

For traffic density, the variable X_5 was assigned value ''1'' if there was a continuous stream of vehicles for a large part ($\geqslant 50\%$) of the measurement duration. In all such cases the number of vehicles passing the observation point was $\geqslant 1500$ per hour.

II. RESULTS AND DISCUSSION

The data on noise levels (L_{eq} values) and the site-specific variables shown in Table I are used for estimating the regression coefficients in Eq. (1). The regression analysis has been done using the statistical software package Statgraphics (version 3.0). Model results are shown in Table III. An examination of t values obtained for various regression coefficients in Table III suggests that significance level of all the coefficients is reasonably good. Whereas t test is used for testing the null hypothesis of an individual slope coefficient (i.e., β_i) is zero, the analysis of variance is used to test the

[a]Present address: Department of Environmental Sciences, Guru Jumbeshwar University, Hissar, Haryana, India.

TABLE I. The L_{eq} levels and site characteristics for different sampling locations in Delhi.

Sites	Traffic intersection X_1	Residential X_2	Industrial X_3	Vegetation X_4	Traffic density X_5	L_{eq} (dB)
1. PUN. BAGH	1	0	0	0	1	79.1
2. AZADPUR	1	0	0	0	1	79.3
3. ISBT	1	0	0	0	1	79.9
4. REDFORT	1	0	0	0	1	80.3
5. ITO	1	0	0	0	1	78.9
6. ASHARAM	1	0	0	0	1	79.9
7. AIIMS	1	0	0	0	1	78.3
8. MOTIBAGH	1	0	0	1	1	76.7
9. JANPATH	1	0	0	0	1	78.4
10. MINTO ROAD	1	0	0	0	1	81.6
11. R. K. PURAM	0	1	0	0	0	52.9
12. SAKET	0	1	0	1	0	52.6
13. UTTAM NAGAR	0	1	0	1	0	56.6
14. JANAK PURI	0	1	0	1	0	50.9
15. PITAMPURA	0	1	0	1	0	55.7
16. MINTO ROAD	0	1	0	0	0	53.8
17. NARAYANA IND. AREA	0	0	1	0	0	62.0
18. MAYAPURI IND. AREA	0	0	1	1	0	59.4
19. WAZIRPUT IND. AREA	0	0	1	1	0	63.1
20. OKHALA IND. AREA	0	0	1	0	0	65.6
21. BHIKAHI CAMA PLACE	0	0	0	0	0	65.3
22. SOUTH EX	0	0	0	0	1	69.6
23. NEHRU PLACE	0	0	0	0	1	69.4
24. YASHWANT PLACE	0	0	0	0	0	59.2
25. CANNAUGHT PLACE	0	0	0	1	1	66.3
26. CHANDNI CHOWK	0	1	0	0	1	64.1
27. SADAR BAZAR	0	1	0	0	1	66.4
28. KAROL BACH	0	1	0	0	1	68.5
29. RAJENDRA PLACE	0	0	0	0	0	58.6
30. NAUROJI NAGAR	0	0	0	1	1	71.9
31. DEFENCE COLONY	0	1	0	0	1	63.8
32. NEHRU NAGAR	0	1	0	0	1	76.2
33. SEVA NAGAR	0	1	0	0	1	77.7
34. MAHARANI BAGH	0	0	0	0	1	71.2

overall significance of the multiple regression by testing the hypothesis that all slope coefficients are simultaneously zero. This is done by computing the F ratio and comparing it with the critical F value associated with the degrees of freedom in the model at a given level of significance. The results of analysis of variance are shown in Table IV. The computed F value is the ratio of the mean sum of squares due to model and error. The mean sum of squares is calculated by dividing the explained sum of squares (ESS) and residual sum of squares (RSS) by associated degrees of freedom, respectively. The computed F ratio $=49.5523$ is very large compared with critical value of $F=2.56$ for degrees of freedom (5,28) at 5% level of significance. This indicates that the null hypothesis is rejected. The values of coefficients of determination (R^2) and R^2 (adj.), adjusted for degrees of freedom, and standard error of estimate which is the square root of mean sum of squares due to error (residuals), are 0.898463, 0.880331, and 3.33235 respectively.

Although the value of R^2 and the F ratio are fairly high, the coefficients of as many as three variables X_2, X_3, and X_4 (in Table III) have high standard errors. This could be on account of multicolinearity in the data since it is possible that the explanatory variables X_1 to X_5 may be intercorrelated. In order to eliminate the possibility of multicoliniarity, a correlation analysis of the explanatory variables was carried out. As all these variables are ordinal in nature, polychoric correlations were computed using LISREL software package

TABLE II. Values of variables for various area types.

Variable name	Area type			
	Traffic intersections	Residential	Industrial	Commercial
X_1	1	0	0	0
X_2	0	1	0	0
X_3	0	0	1	0

TABLE III. Model fitting results [R sq. (Adj.) $=0.880331$; SE $=3.332353$].

Independent variables	Coefficient	Standard error	t value	Significance level
Constant	59.329421	1.613421	36.7724	0.0000
X_1	7.799888	1.680612	4.6411	0.0001
X_2	−3.087989	1.534317	−2.0126	0.0539
X_3	4.425186	2.251571	1.9654	0.0594
X_4	−2.459215	1.390152	−1.7690	0.0878
X_5	12.356612	1.55078	7.9680	0.0000

TABLE IV. Analysis of variance for the full regression [R sq. $=0.898463$; standard error of est.$=3.33235$; R sq. (Adj.)$=0.880331$].

Source	Sum of squares	DF	Mean sum of squares	F ratio	P value
Model (ESS)	2751.29	5	550.258	49.5523	0.0000
Error (RSS)	310.928	28	11.1046		
Total	3062.22	33			

(Jöreskog and Sörbom, 1989). The results presented in Table V reveal significant intercorrelations between some of the variables. After careful examination of these correlations, variables X_2, X_4, and X_5 were selected as regressors.

The model results are shown in Table VI. The value of the constant ($=62.648130$) in Table VI represents the noise levels for those commercial sites where traffic density and vegetation cover are negligible ($X_4=X_5=0$). It is also seen that the coefficient of variable X_5 is rather high, which indicates that noise levels at various places in Delhi are mainly determined by the traffic density. The dominance of traffic in contributing towards environmental noise in Indian cities is also borne out from the studies of Rao *et al.* (1989) and Chakrabarty *et al.* (1997). The coefficient of variable X_2 suggests that the noise levels in residential areas are expected to be significantly lower than those in commercial areas.

The negative value of the coefficient of X_4 is in the anticipated direction and confirms the fact that existence of vegetation plays a role in attenuating noise, but the t value of the coefficient is significant at $\sim$15% only. The maxima in attenuation of noise by vegetation is known to occur at both low (200–500 Hz) and high frequencies (>2 kHz) with an acoustic window having low or zero attenuation in the mid-frequencies (1–2 kHz) (Huddard, 1990). The low-frequency attenuation can be attributed to ground effect with soft, porous ground being more absorbent than hard ground, whereas the high-frequency attenuation is associated with absorption and scattering by vegetation. The literature review presented in Huddart's report mentions several studies on the attenuation of noise by vegetation. These studies give widely varying values for attenuation of noise with respect to the thickness of the vegetation belt. For example, Whitcombe and Stowers (1973) show a reduction of up to 6 dB by a hedge 0.9–2.4 m thick. In a separate study, Yamada *et al.* (1977) mention attenuation up to 4 dB by a hedge 0.7 to 1.6 m thick. In the light of these studies it seems reasonable to accept the coefficient (-2.65) for vegetation variable X_4 obtained in our model. The authors, however, would like to point out that the depth of dense hedges in the present study was never more than 1–1.5 m and the belt of grass cover was not more than 5–6 meters.

TABLE V. Polychoric correlations matrix.

	X_1	X_2	X_3	X_4	X_5
X_1	1.000				
X_2	-0.981	1.000			
X_3	-0.928	-0.941	1.000		
X_4	-0.464	0.194	0.376	1.000	
X_5	0.984	-0.285	-0.981	-0.551	1.000

TABLE VI. Model fitting results with X_2, X_4, and X_5 as explanatory variables [R sq. (Adj.)$=0.798764$; SE$=4.321298$].

Independent variables	Coefficient	Standard error	t-value	Significance level
Constant	62.648130	1.6083344	38.952179	0.0000
X_2	-7.1298798	1.5787125	-4.5162624	0.0001
X_4	-2.6577350	1.7968595	-1.4791001	0.1495
X_5	13.935322	1.6470018	8.461.240	0.0000

It is possible that if the vegetation cover had been graded in several categories depending on its type and its extent, the results would have been sharper and a more definite conclusion could have been drawn about planting vegetation along roads and growing hedges on the central dividers as possible measures for noise abatement. It is suggested that better results could be obtained if actual traffic composition and density are incorporated in the model.

ACKNOWLEDGMENTS

K. Kumar would like to thank the University Grants Commission, Government of India, for providing a Junior Research Fellowship during this study. We would also like to thank Mr. B. B. Singh and Mr. B. K. Singh for help in obtaining the required data. We are grateful to reviewers for their valuable comments.

Attenborough, K., Clark, S., and Utley, W. A. (**1976**). ''Background noise levels in United Kingdom,'' J. Sound Vib. **48**, 359–375.

Baverstock, S. J., Pocock, R. L., and Attenborough, K. (**1991**). ''Development of Area-based methods for predicting ambient noise,'' Appl. Acoust. (U.K.) **33**, 303–312.

Burgess, M. A. (**1977**). ''Noise prediction for urban traffic conditions—Related to measurements in Sydney Metropolitan Area,'' Appl. Acoust. (U.K.) **10**, 1–7.

Chakrabarty, D., Santra, S. C., Mukherjee, A., Roy, B., and Das, P. (**1997**). ''Status of road traffic noise in Calcutta metropolis, India,'' J. Acoust. Soc. Am. **101**, 943–949.

Delany, M. E., Harland, D. G., Hood, R. A., and Scholes, W. E. (**1976**). ''The prediction of noise levels L_{10} due to road traffic,'' J. Sound Vib. **48(3)**, 305–325.

Huddart, L. (**1990**). ''The use of vegetation for traffic noise screening,'' Transport and Road Research Laboratory, Research Report 238, Crowthorne, Berkshire, U.K.

Johnson, D. R., and Saunders, E. G. (**1968**). ''The evaluation of noise from freely flowing road traffic,'' J. Sound Vib. **7**, 287–309.

Jöreskog, K. G., and Sörbom, Y. D. (**1989**). ''LISREL 7: User's Reference Guide,'' Scientific Software, Inc., Chicago.

Mulholland, K. A. (**1979**). ''The prediction of traffic noise using a scale model,'' Appl. Acoust. (U.K.) **12**, 459–478.

Ohta, M., Ikuta, A., and Mitani, Y. (**1995**). ''An improved method for road traffic noise prediction of L_{eq} based on the extended regression model (Theory and Experiment),'' J. Acoust. Soc. Jpn. **51**(9), 672–678.

Prabhu, B. T. S., and Chakraborty, R. L. M. (**1978**). ''An urban noise model for planners,'' J. Sound Vib. **58**(4), 595–596.

Rao, M. G. S., Rao, P. R., Dev. K. S., and Rao, K. V. (**1989**). ''A model for computing environmental noise level due to motor vehicle traffic in Visakhapatnam city,'' Appl. Acoust. (U.K.) **27**, 129–136.

Whitecombe, C. E., and Stowers, J. F. (**1973**). ''Sound abatement with hedges,'' Hortscience **8**(2), 128–129.

Yamada, S., Watnabe, T., Nakamura, S., Yokoyama, H., and Takeoka, S. (**1977**). ''Noise reduction by vegetation,'' Internoise 77. International Conference on noise control engineering, 1–3 March 1997, Zurich, Switzerland, pp. B599–B606.

Comments on "A consonance-based approach to the harpsichord tuning of Domenico Scarlatti" [J. Acoust. Soc. Am. 101, 2332–2337 (1997)]

Carl Sloane
43 Holwood Avenue, Toronto, Ontario M6M 1P4, Canada

(Received 25 August 1997; accepted for publication 8 October 1997)

Issue is taken with the finding that Domenico Scarlatti probably used a harpsichord tuning with no wolf fifth. Arguments indicating that he used a tuning with a substantial wolf are presented.
 [S0001-4966(98)00803-0]

PACS numbers: 43.75.Bc [WJS]

In their paper, Sankey and Sethares[1] find a strong likelihood that Domenico Scarlatti used a temperament similar to d'Alembert's ''temperament ordinaire,'' a tuning with no wolf fifth. My own findings[2] strongly suggest the use of regular meantone (RMT), and thus the presence of a wolf of some magnitude between G♯ and E♭. The evidence includes the following:

- Contemporary use of RMT in Italy and Spain, especially as attested to by Antonio Soler, once a student of Scarlatti. A later Portuguese tuning[3] unknown to me in 1992 also seems to represent an attenuated RMT if it is reconstructed using only the tuning instructions, and the error-ridden numerical description is ignored.
- The large drop in incidence between the tonic keys B♭ major and E♭ major on the one hand and between A major and E major on the other. E♭ and E majors are the simplest (least inflected) keys containing false notes in RMT.
- The rough grouping of A♭ major with B♭ minor and of B major with C♯ minor in the two most important sources (both contemporary with Scarlatti), suggesting that retuning of an enharmonic note was necessary before these keys could be used as tonics. None of these keys were allowed as tonics by Gasparini,[4] who almost certainly had RMT in mind. Although retuning for A♭ or even B might be justifiable in temperament ordinaire, the need is less apparent for two minor keys. The absence of other similar pairings in the sources, and Gasparini's somewhat rigid position, indicate that retuning was *not* a common practice.

I also have one or two quibbles with the fundamental methodology. Although it is doubtless that a composer would, in general, avoid dissonant intervals, it is almost equally certain that poor intervals in the music do not rule out a temperament, and it does not seem that Sankey and Sethares, in their attempt to ''minimize the dissonance over all intervals actually used by Scarlatti'' (p. 2332) make sufficient allowance for the apparent unconcern with which poor intervals were used, or for the practice in some quarters of softening their effect by the quick release of one of the dissonant notes.[5] They also fail to state whether the auditor is used to hearing music played in RMT.

In addition, Sankey and Sethares deal almost exclusively with intervals, the only concrete reference to chords (p. 2337) involving particular examples in the (organ!) sonata K 328, none of which are minor chords. The behavior of the minor chord,[6] however, is probably a critical factor in explaining both Gasparini's allowing F minor as a tonic (Ref. 3), and Scarlatti's fondness for it in this capacity: in RMT, F minor has poorly tuned thirds. Thus the failure of Sankey and Sethares to consider chords has probably biased their results somewhat.

[1] J. Sankey and W. A. Sethares, ''A consonance-based approach to the harpsichord tuning of Domenico Scarlatti,'' J. Acoust. Soc. Am. **101**, 2332–2337 (1997).
[2] C. Sloane, Continuo **16**, 15–16 (1992).
[3] F. I. Solano, *Novo Tratado de Música métrica, e rythmica* (Lisbon, 1779), pp. 4–8. Reproduced in G. Doderer, Actas—Encontro Nacional de Musicologia, Boletim da Associação Portuguesa de Educação Musical, fasc. **48**, 40–43 (1986).
[4] F. Gasparini, *L'Armonico Pratico al Cimbalo* (Bortoli, Venice, 1708, facs. ed. Broude Bros., New York, 1967), pp. 83–86.
[5] P. Barbieri, *Acustica, Accordatura e Temperamento nell'Illuminismo Veneto* (Torre d'Orfeo, Rome, 1987), pp. 152–158.
[6] C. Sloane, J. Sound Vib. **170**, 261–262 (1994).

Response to "Comments on 'A consonance-based approach to the harpsichord tuning of Domenico Scarlatti'" [J. Acoust. Soc. Am. 103, 1680 (1998)]

John Sankey
1369 Matheson Road, Gloucester, Ontario K1J 8B5, Canada

William A. Sethares
Department of Electrical and Computer Engineering, University of Wisconsin, Madison, Wisconsin 53706-1691

(Received 29 September 1997; accepted for publication 12 November 1997)

This Letter briefly responds to Carl Sloane's arguments regarding Scarlatti's use of wolf fifths. It is believed that the historical record is sufficiently unclear that firm conclusions are not possible.
 [S0001-4966(98)00903-5]

PACS numbers: 43.75.Bc [WJS]

We would like to thank Carl Sloane for his comments, which stem from a detailed analysis of the scant historical literature. We believe that it is important to consider all possible avenues of investigation when trying to uncover information about an insufficiently documented past, and we hope that someday it may be possible to integrate historical, theoretical, and psychoacoustic approaches.

Our paper applied a culture-independent psychoacoustic measure of consonance and dissonance to a body of Scarlatti's work in the hopes of determining the kinds of tunings most likely to have been used. As we noted, there exists no direct evidence for the tuning practices of Domenico Scarlatti, and we consider the relevance of second hand (and often self-contradictory) sources such as the Spanish musicians mentioned by Sloane to be suspect. Since Scarlatti was an Italian, living in Spain only after the age of 43, who left no writings regarding his tuning preferences, the historical record is unclear.

Regular mean tone (RMT) tunings were extensively analyzed in our paper (cf. Fig. 2). The consonance method does not support Sloane's conclusion that an RMT best matches the tonal character of the sonatas of Domenico Scarlatti. Most tunings of the period, d'Alembert included, have their largest fifth between G♯ and E♭, so it is to be expected that Sloane would find that to be consistent with these sonatas. We agree with Sloane, however, that Scarlatti's sonatas are compatible with a stronger tuning than most published in Italy at the time.

The consonance method deals solely with chords (simultaneously sounding notes), as did our discussion. It is sequential nonoverlapping notes (melodic intervals) which are ignored by the method. Although the omission of such intervals might introduce a bias in a study of vocal music, we see no reason why it should affect an analysis of keyboard works.

Generation and growth of bilayer defects induced by ultrasound

M. S. Malghani, Jie Yang, and Junru Wu
Department of Physics, University of Vermont, Burlington, Vermont 05405

(Received 2 October 1997; revised 29 November 1997; accepted 11 December 1997)

Transdermal drug delivery is handicapped by the low skin permeability caused by highly ordered structure of lipid bilayers in the outer human skin layer. It has been reported that ultrasound can increase the permeability of human skin. The enhancement was attributed to acoustic cavitation but the underlying physical mechanism is not fully understood. As a model, dipalmitoylphosphatidylcholine (DPPC) lipid bilayers are insonicated by ultrasound of two submegahertz frequencies (168 kHz and 707 kHz). The free-field spatial peak pressure amplitudes of both are measured to be 6×10^5 Pa. Bilayer defects, which have average diameters of tens to hundreds of nanometers and can be detected by an atomic force microscope, are generated within less than 0.5 min. The number of the defects grows with time. The defect growth rate at the 168-kHz frequency is about 3.5 times that at the 707-kHz frequency. © *1998 Acoustical Society of America.* [S0001-4966(98)04503-2]

PACS numbers: 43.80.Sh, 43.80.Gx, 43.35.Wa [FD]

INTRODUCTION

Development of technologies for enhancing the transport of small as well as large molecules across the skin (transdermal drug delivery) is an important avenue of drug delivery research. The low skin permeability is mainly caused by the stratum corneum (SC), the outermost skin layer. The SC is usually about 15 μm thick. It consists of keratinocytes which are dead cells and filled with keratin fibers surrounded by lipid bilayers.[1] The bilayers have highly ordered structure that makes the SC impermeable.

Over the last two decades, ultrasound has been applied to enhance transdermal drug delivery. This method is called sonophoresis. Experimental work was reported in 1986 by Kost *et al.*[2] They used 1.5-MHz ultrasound of pressure amplitude 1×10^5 Pa and increased transdermal permeation of mannitol and physostigmine across rat skin *in vivo* by up to 15-fold. The enhancement of systemic drug delivery by sonophoresis was also reported by several other investigators.[3,4] The work reported before 1995 used primarily frequencies in the megahertz range and were limited to small molecules.

Recently, it has been shown that low-frequency (20-kHz) ultrasonic tonebursts (duty cycle$=10\%$ and pressure amplitude$=2.6\times10^5$ Pa) can increase the permeability of human skin to drugs, including high molecular weight proteins such as insulin, γ-interferon (given to enhance the immune response of patients suffering from AIDS, cancer, or any viral infection), and erythropoietin (given to patients suffering from severe anemia to enhance the process by which the red blood cells are formed) by several orders of magnitude.[5,6] Acoustic cavitation was proposed as the possible cause of the enhancement.

Acoustic cavitation is commonly defined as acoustically induced bubble activity;[7] it may involve complex phenomena. At a moderate ultrasonic intensity, small gaseous bodies that play the role of nuclei of cavitation in a liquid may experience volume oscillations and the gas bodies may grow larger through a process of rectified diffusion[8] and bubble coalescence.[9] The oscillations of the gas bodies (or bubbles) excited by ultrasound of moderate acoustic intensity usually are nonlinear. The bubbles become the secondary ultrasound source; the spectrum of ultrasound radiated from them contains harmonics, subharmonics and other frequencies. Transverse waves (ripples) may be set up at the gas–liquid interfaces and bubbles may be trapped at liquid–solid interfaces. Near the bubbles and the interfaces, a dc flow which is called acoustic streaming may be generated. The shear stress associated with a high streaming velocity gradient within boundary layers of the bubbles and the interfaces may be destructive. At a high-pressure amplitude, implosions (jets) may occur and bubbles may collapse. These events may be violent and can generate localized high temperature (thousands of degrees Kelvin) and pressure elevation (hundreds to thousands of atmospheres) within the bubbles with accompanying production of shock waves;[8–13] these phenomena are associated with the so-called inertial cavitation.

One possible scenario of the enhancement is that ultrasound introduces defects that are devoid (holes) of lipid molecules in bilayer. When the number of defects grows and their sizes become large enough to allow the passage of some drug molecules through bilayers, the permeability of the skin to the drug is significantly increased. However, to our knowledge there has been no direct microscopic experimental evidence that ultrasound of moderate pressure amplitude in the order of submega Pascal can disorganize bilayers. Using supported dipalmitoylphosphatidylcholine (DPPC) lipid bilayers and an atomic force microscope (AFM), we were able to show that defects of average sizes between tens to hundreds of nanometers were created and grew with time when the bilayers were insonified by 168-kHz ultrasound, the spatial peak pressure amplitude of which was measured to be 6×10^5 Pa in a free-field condition.

I. EXPERIMENTAL METHOD

An atomic force microscope (A NanoScope E AFM, Digital Instruments, Santa Barbara, CA), equipped with

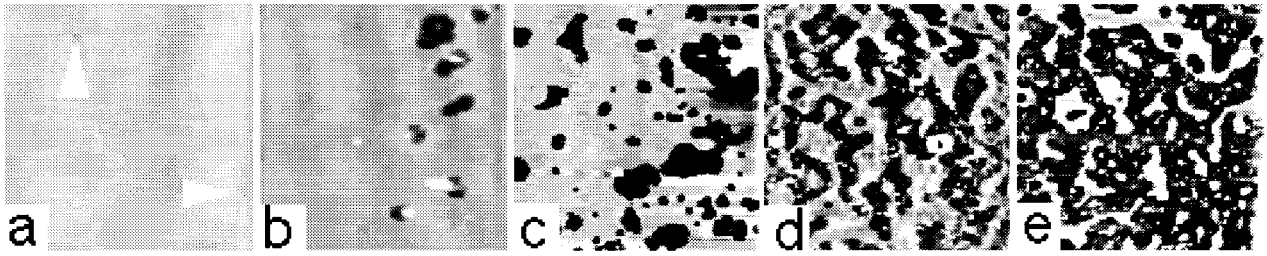

FIG. 1. Here we show five typical DPPC bilayers imaged by AFM in water, with (a) the original bilayer (the two arrow points to two very small bilayer defects, about 40 nm in diameter); and (b)–(e) under different insonification (168 kHz, SPPA=6×10^5 Pa) time periods—(b) 0.5 min; (c) 1 min; (d) 1.5 min; and (e) 2 min. Image size for each is 2 μm$\times$2 μm. Dark regions in these images are bilayer defects (holes), noting that in (e) defects are large.

oxide-sharpened Si_3N_4 tips with a nominal spring constant of 0.06 N/m was used in this work. All images were obtained under a probe force of about 0.5 nN in the contact mode, at a pixel number of 512×512, and with a scanning line speed of about 5 Hz. The piezo scanner used had a scanning range of 10 μm.

Each prepared bilayer was first examined by AFM and then irradiated with ultrasound and examined by AFM again to detect the creation of bilayer defects after insonification. The total period of the above series was less than 2 days for each bilayer used. It had been shown previously that during a 2 day period natural occurrence of bilayer defects due to the lipid loss is negligible.[14] In other words, the bilayers are quite stable in a period longer than two days. Thus the creation of bilayer defects in our experiments should be the result of insonification.

The lipids were obtained from Avanti Polar Lipids (Albaster, AL) and used without further purification. The bilayer was prepared as described elsewhere.[14] Briefly, a droplet of lipids dissolved in chloroform was placed in a glass culture tube and dried under nitrogen for about 2 h. The bottom of the tube was then coated by a film of dried lipids. About 1-ml 20-mM NaCl was placed in the culture tube and the tube was sealed after flushing the air with nitrogen gas. The concentration of lipids in the lipid suspension was about 0.5 mg/ml. The sealed tube was sonicated in an ultrasonic cleaning bath until the lipid suspension became clear. The above procedure broke large vesicles into smaller ones with the radius of curvature below the wavelength of visible light. A droplet (0.05–0.2 ml) of the sonicated lipid suspension was applied to freshly cleaved thin mica and the sample was incubated at 4 °C overnight. Afterwards, the sample was heated to 55 °C for 30 min. A supported bilayer on mica was formed and residual vesicles were removed by solution exchange. During the above operation, the piece of mica was always immersed in solution without being directly exposed to air. The dimension of the bilayer samples is about 3 mm$\times$5 mm. The sizes of mica are slightly larger than those of the bilayer sample. The thickness of the mica is less than 0.2 mm. The prepared specimen then was mounted facing vertically upward in a glass container filled with distilled water. Absorbers were present to minimize the standing-wave formation. Temperature of the water in the container was 25 °C. A 55-mm-diameter unfocused PZT ultrasonic transducer whose fundamental resonance frequency is 168 kHz was placed facing downward above the specimen. The distance between the specimen and the front face of the transducer was about 1 cm. The thickness of the bilayer prepared was about 6 nm measured by AFM. The specimen was insonified continuously for the desired time. The spatial peak pressure amplitudes (SPPA) of the sound field *in situ* was determined using a calibrated pvdf needle hydrophone, which has a 0.6-mm-diam sensing element (NTR Systems, Inc., Seattle, WA).

II. EXPERIMENTAL RESULTS

Figure 1 contains five typical AFM images; one is for an original bilayer before insonification [Fig. 1(a)] and the rest are bilayers after insonification [Fig. 1(b)–(e)] by 168-kHz ultrasound for different time periods. The creation and the growth of bilayer defects of tens to hundreds of nanometers can be observed from these images. In short time scales ($<$2 min), the decrease in bilayer coverage is accompanied with relatively uniform increase of the number of defects.

The spatial uniformity of defects is further demonstrated by our optical studies of DPPC bilayers containing 10-mol % fluorescence tag: 1-Palmitoyl-2--[6-[(7-nitro-2-1,3-benzoxadiazol-4-yl)aminol]caproyl]-sn-Glycero-3-phosphocholine (PC-NBD). After insonification at 168 kHz for 8 min, only a uniform gray background was observed using the fluorescence microscopy. This fact indicates that most defects in bilayers are smaller than that can be resolved with optical microscopy; it is consistent with the isotropic distribution of the defects detected by AFM after the short time ultrasound exposure described earlier. However, longer insonification resulted in anisotropic growth of bilayer defects. Figure 2 shows an optical microscopic image of a bilayer of DPPC with 10-mol % PC-NBD after the same ultrasonic exposure for 13 min, in which the black regions are bilayer defects and the gray areas are bilayers containing small defects. The insert in the figure shows an AFM image of a bilayer of DPPC with 10-mol % PC-NBD after 1-min insonification at 168 kHz.

A similar experiment was repeated using 707-kHz ultrasound of the same spatial peak pressure amplitude. Some typical results are shown in Fig. 3. Figure 3(a) is an original bilayer and 3(b)–(d) are for bilayers after insonifying for 2,

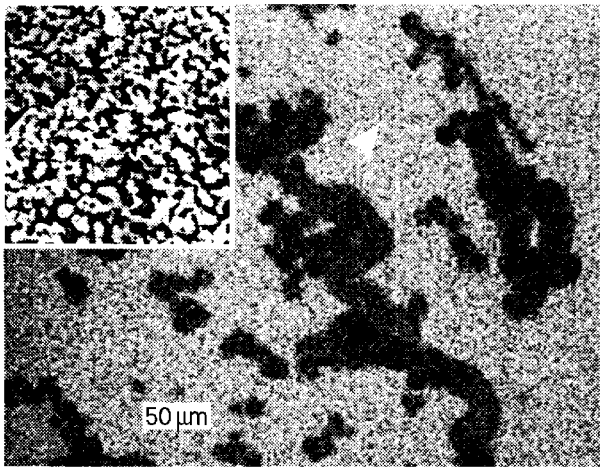

FIG. 2. A video image of a supported DPPC bilayer that contained 10 mol % of the fluorescence tag PC-NBD. The supported bilayer gave a uniform background as seen with a CCD camera (CCD-500E from CCTV Corp, South Hakensack, NJ) upon excitation with blue light. After exposure to 168-kHz insonification for 13 min, large black areas appeared, indicating regions devoid of any bilayers. The insert shows an AFM image ($3\ \mu m \times 3\ \mu m$) of a bilayer of DPPC containing 10-mol % PC-NBD after 1-min insonification, in which many bilayer defects are seen. Note that the sizes of these defects are beyond the resolution with the optical microscopy. Thus the region within bilayers, as indicated by the arrow, must contain small bilayer defects.

4, and 8 mins. The decrease of bilayer coverage is similar to the case with 168-kHz insonification, but the time required is much longer.

Figure 4 summarizes the two cases corresponding to the two different frequencies. The results are obtained with several specimens at each frequency. The large standard deviations in both cases may have resulted from the intrinsic random nature of the creation of bilayer defects. Despite this randomness, it clearly shows that the defect growth rate is much slower for 707 kHz than for the 168-kHz case.

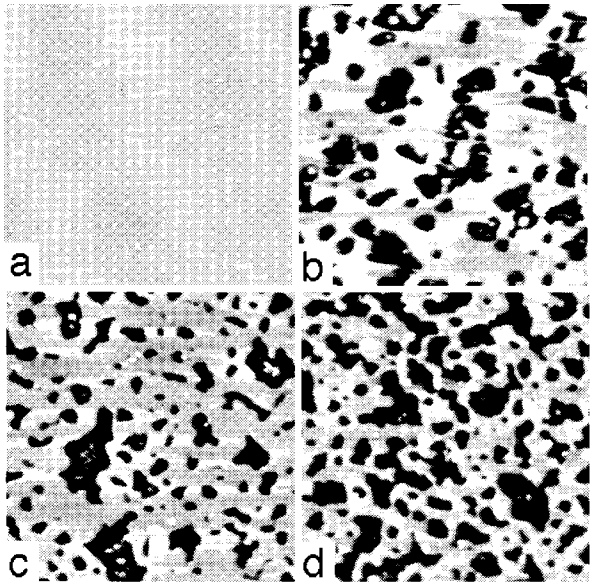

FIG. 3. Four typical images of DPPC bilayers in water, with (a) the original bilayer and (b)–(d) under different insonification (707 kHz, SPPA=6×10^5 Pa) time periods of 2, 4, and 8 min, respectively. Similarly, dark regions are bilayer defects. Image size for each: $2\ \mu m \times 2\ \mu m$.

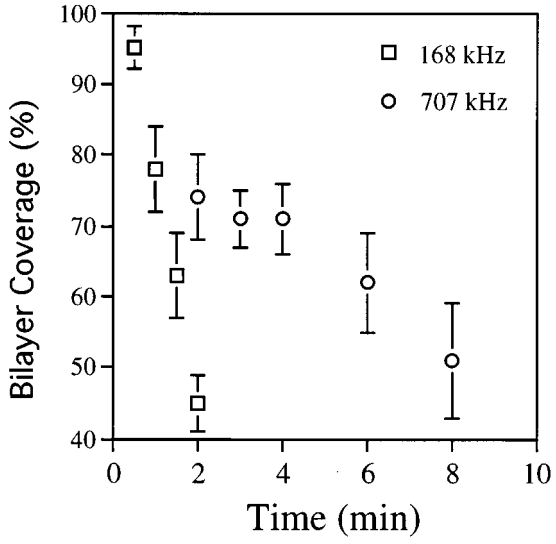

FIG. 4. A summary plot of bilayer coverage after different exposures to insonification at two frequencies of the same spatial peak pressure amplitude. Each datum point was averaged over several specimens with 5–6 AFM images taken for each specimen after exposure to ultrasound for a selected time. Error bars correspond to the standard deviation.

III. DISCUSSION

According to the numerical calculation made by Flynn and Church,[15] we note that for the frequencies and pressure amplitude used by us, initial bubbles which may grow and generate inertial cavitation have sizes in the range between submicron to tens of microns. They are much larger than typical dimensions of bilayer defects. This result suggests that the bubbles which would cause the most damage should exist in the water and near the bilayer. These bubbles may pulsate violently and generate acoustic streaming, shock waves, and jets. The stress associated with them may be great enough to break the hydrophobic binding among lipid molecules in the bilayers and drive lipid molecules out of the bilayer plane and leave defects.[16,17] The short time scale defects shown in Figs. 1 and 3 may result from this mechanism. Since the wave length corresponding to 168 kHz is about 9 mm, which is much larger than the dimension of the sample, it is reasonable that the overall induced bilayer defects were uniformly distributed.

It usually takes time for small bubbles to develop to larger bubbles either through rectified diffusion or bubble coalescence. It is quite likely that these larger bubbles once formed may be driven by the ultrasound and move to very close to the surface of the bilayer. If the air bubbles are in direct contact with the bilayer, the hydrophobic binding of lipid molecules is disrupted and large defects are generated.[18] The force causing bubble coalescence is short-range force. Therefore, the bubble-fusion process occurs only when two bubbles get very close to each other. The anisotropy of large defects shown in Fig. 3 may reflect the undeterministic-nature of the bubble motion. The large bi-

layer defects after the long time ultrasound exposure shown in Fig. 2 which have dimensions of the order of micrometer to tens of micrometer may be caused by this process.

It is known[19] that the probability to generate acoustic cavitation in a fluid by low frequency is greater than by high frequency if the acoustic pressure amplitude used is the same. If acoustic cavitation is the main cause of the generation and growth of the bilayer defects, the effects should be less dramatic at a higher frequency. Our results seems to support this hypothesis. It should be noted that the term of the cavitation used here is in a broad sense; i.e., the abovementioned acoustic streaming, jet formation, and shock wave effects related to bubbles' activity may all have contributions.

In summary, our experimental results have provided the microscopic evidence that ultrasound of submegahertz frequency and moderate pressure amplitude can generate defects in a lipid bilayer. They also suggest that the damages for a unilamellar bilayer which have pore sizes of hundreds of nanometers uniformly distributed in the bilayer plane after a short period of insonification, is likely caused by the stress generated by shock waves and jets associated with vibrating bubbles. It is clear our experimental situation is quite different from that used in an application of ultrasound enhanced drug delivery. Nevertheless, it is likely that the similar physical mechanism also play an important role in transdermal ultrasonic drug delivery applications. In real *in vivo* applications, the bioeffects related to the structure change in bilayers induced by moderate ultrasound may be reversible. Furthermore, submegahertz frequency ultrasound has its advantage compared to 20-kHz ultrasound used in the previous publications[5,6] as small piezoelectric ceramic transducers can be used as effective ultrasound sources. A portable ultrasound delivery device may make transdermal ultrasound drug delivery quite promising.

ACKNOWLEDGMENTS

The authors wish to thank useful discussions with Dr. W. L. Nyborg. The work was partially supported by the US Army Research Office (JY) and by NIH-AR42231 and NSF VT-EPSCoR (JW).

[1] W. Montagna and W. C. Lobitz, Jr., *The Epidermis* (Academic, New York, 1964).
[2] J. Kost, D. Levy, and R. Langer, Proc. Int. Control. Rel. Bioact. Mater. Control. Rev. Soc. **13**, 177 (1986).
[3] S. Miyzaki, O. Mizuoka, and M. Takada, J. Pharm. Pharmacol. **43**, 115 (1990).
[4] D. Bommannan, H. Okuyama, P. Stauffer, and R. H. Guy, Pharm. Res. **9**, 559 (1992).
[5] S. Mitragotri, D. Blankschtein, and R. Langer, Science **269**, 850 (1995).
[6] S. Mitragotri, D. A. Edwards, D. Blankschtein, and R. Langer, J. Pharm. Sci. **84**, 697 (1995).
[7] R. E. Apfel, J. Acoust. Soc. Am. **101**, 1227 (1997).
[8] A. I. Eller, J. Acoust. Soc. Am. **52**, 1447 (1972).
[9] W. L. Nyborg, ''Basic physics of low frequency therapeutic ultrasound,'' in *Ultrasound Angioplasty*, edited by R. J. Siegel (Kluwer Academic, Boston, 1996).
[10] D. L. Miller, Ultrasound Med. Biol. **13**, 443 (1987).
[11] J. A. Rooney, ''Hemolysis near an ultrasonically pulsating gas bubble'' Science **169**, 869 (1970).
[12] A. R. Williams, D. E. Hughes, and W. L. Nyborg, Science **169**, 871 (1970).
[13] J. Wu and G. Du, J. Acoust. Soc. Am. **101**, 1899 (1997).
[14] Y. Fang and J. Yang, Biochim. Biophys. Acta **1324**, 309 (1997).
[15] H. G. Flynn and C. C. Church, J. Acoust. Soc. Am. **84**, 985 (1988).
[16] M. Fechheimer, J. F. Boylan, and S. Parker, Proc. Natl. Acad. Sci. USA **84**, 8463 (1987).
[17] R. P. Holmes, L. D. Yeaman, R. G. Taylor, and D. L. McCullough, J. Urol. (Baltimore) **147**, 267 (1992).
[18] J. N. Israelachvili, S. Marcelja, and R. G. Horn, Q. Rev. Biophys. **13**, 121 (1980).
[19] AIUM, American Institute of Ultrasound in Medicine, Standard of real-time display of thermal and mechanical acoustic indices on diagnostic ultrasound equipment, Laurel, MD (1992).